

055.612:977/v.2



# Collected Reprints

1977

Atlantic Oceanographic and Meteorological Laboratories

## Volume II



June 1978

**U.S. DEPARTMENT OF COMMERCE**  
National Oceanic and Atmospheric Administration







# Collected Reprints

# 1977

Atlantic Oceanographic and Meteorological Laboratories  
Miami, Florida 33149

Volume II

June 1978

Boulder, Colorado

## **U.S. DEPARTMENT OF COMMERCE**

Juanita M. Kreps, Secretary

National Oceanic and Atmospheric Administration

Richard A. Frank, Administrator

Environmental Research Laboratories

Wilmot Hess, Director



## FORWARD

This is the eleventh consecutive year in which the Collected Reprints of NOAA's Atlantic Oceanographic and Meteorological Laboratories have been published for distribution to the libraries of scientific institutions here and abroad. The series provides a single reference source for articles by AOML personnel that have appeared in a broad spectrum of scientific and technical publications.

The Atlantic Oceanographic and Meteorological Laboratories conduct research programs in the areas of physical, chemical, and geological oceanography, sea-air interaction, and marine acoustics. The 1977 edition presents the papers published in that year plus a few that were published in 1976 but were not available for inclusion in that year's volume. The papers are arranged in alphabetical order by first author within each of five groups:

Office of the Director  
Physical Oceanography Laboratory  
Marine Geology and Geophysics Laboratory  
Sea-Air Interaction Laboratory  
Ocean Chemistry Laboratory

It is hoped that those recipients with whom we do not already have an exchange arrangement would add the AOML Library to the distribution list for any relevant publications from their institution.

Harris B. Stewart, Jr.  
Director  
Atlantic Oceanographic  
and Meteorological  
Laboratories  
15 Rickenbacker Causeway  
Virginia Key, Florida 33149





# CONTENTS

## VOLUME I

### OFFICE OF THE DIRECTOR

	Page
1. Stewart, H. B.	
And Now, IOCARIBE: Carribbean Cooperation: It Works. NOAA Magazine <u>7</u> , No. 1, 36-38.	1

### PHYSICAL OCEANOGRAPHY LABORATORY

2. Beardsley, R.C., H. Mofjeld, M. Wimbush, C.N. Flagg, and J.A. Vermersch, Jr.	
Ocean Tides and Weather-Induced Bottom Pressure Fluctuations in the Middle-Atlantic Bight. Journal of Geophysical Research <u>82</u> , No. 21, 3175-3182.	4
3. Behringer, D.W., R.L. Molinari, and J.F. Festa.	
The Variability of Anticyclonic Current Patterns in the Gulf of Mexico. Journal of Geophysical Research <u>82</u> , No. 34, 5469-5476.	12
4. Bush, P.A.	
Bathymetry of the MODE-I Region. Deep Sea Research <u>23</u> , 1105-1113. (Charts omitted.)	20
5. Chew, F.	
The Advection Effect of Planetary Vorticity on Sea Level Slope in a Western Boundary Current. Marine Geodesy <u>1</u> , No. 1, 103-116.	35
6. Culverhouse, B.	
Self-Contained Digital Tide Measurement System. NOAA Technical Memorandum ERL AOML-24, 47 pages.	49
7. Festa, J.F.	
Book Review: Physical Oceanography of Estuaries (and Associated Coastal Waters). Bulletin of the American Meteorological Society <u>58</u> , No. 2, 179-180.	96

	Page
8. Hansen, D.V.	
A Lagrangian Buoy Experiment in the Sargasso Sea. American Institute of Aeronautics and Astronautics, Technical Committee on Marine Systems and Technologies, Drift Buoy Symposium, Hampton, Virginia, May 22-23, 1976. NASA CP-2003, Session C, Simulation, Sensors, and Data (Dr. Donald Hansen, Chairman) 173-192.	97
9. Hazelworth, J.B.	
Oceanographic Variations Across the Gulf Stream Off Charleston, South Carolina, During 1965 and 1966. NOAA Technical Report ERL 383-AOML 25, 73 pages.	116
10. Hazelworth, J.B., S.R. Cummings, S.M. Minton, and G.A. Berberian.	
MESA New York Bight Project, Expanded Water Column Characterization Cruise (XWCC 11) NOAA Ship RESEARCHER, September 1976. NOAA Data Report ERL MESA-29, 192 pages.*	192
11. Hazelworth, J.B., S.R. Cummings, R.B. Starr, and G.A. Berberian.	
MESA New York Bight Project, Expanded Water Column Characterization Cruise (XWCC 8) NOAA Ship GEORGE B. KELEZ, April 1976. NOAA Data Report ERL MESA-27, 111 pages.*	211
12. Herman, A., and C. Cardwell.	
Computer Programs for Simple Lagrangian Processing (SLAP), Users' Guide. NOAA Technical Memorandum ERL AOML-28, 110 pages.	225
13. Herman, A. and D.V. Hansen.	
Objective Analysis of Lagrangian Trajectory Data. Proceedings of the American Congress on Surveying and Mapping, 37th Annual Meeting. Washington, D.C., February 27-March 5, 1977, 177-185.	335

\* Text only; complete data available from the authors or National  
Technical Information Service (NTIS).



	Page
14. Lee, T.N. and D.A. Mayer. Low-Frequency Current Variability and Spin-Off Eddies Along the Shelf Off Southeast Florida. Journal of Marine Research <u>35</u> , No. 1, 193-220.	344
15. Leetmaa, A. Book Review: Physical Oceanography of Estuaries (and Associated Waters). Limnology and Oceanography <u>22</u> , No. 5, 975.	372
16. Leetmaa, A. Effects of the Winter of 1976-1977 on the Northwestern Sargasso Sea. Science <u>198</u> , No. 4313, 188-189.	373
17. Leetmaa, A. Observations of Large-Scale Depth Perturbations of the Main Thermocline. Journal of Physical Oceanography <u>7</u> , No. 5, 746-748.	375
18. Leetmaa, A. A Study of MODE Dynamics. Deep-Sea Research <u>24</u> , 733-742.	378
19. Leetmaa, A., P. Niiler, and H. Stommel. Does the Sverdrup Relation Account for the Mid-Atlantic Circulation? Journal of Marine Research <u>35</u> , No. 1, 1-10.	388
20. Maul, G.A. The Annual Cycle of the Gulf Loop Current-Part I: Observations During a One-Year Time Series. Journal of Marine Research <u>35</u> , No. 1, 29-47.	398
21. Maul, G.A. Recent Progress in the Remote Sensing of Ocean Surface Currents. Marine Technology Society Journal <u>11</u> , No. 1, 5-13.	417
22. Maul, G.A. Variability in the Gulf Stream System. Gulfstream <u>11</u> , No. 10, 2-7.	426

	Page
23. Maul, G.A. and M. McCaslin.	
An Assessment of the Potential Contributions to Oceanography From Skylab Visual Observations and Handheld-Camera Photographs. SKYLAB Explores the Earth, NASA SP 380, 339-352.	432
24. Mofjeld, H.O. and M. Wimbush.	
Bottom Pressure Observations in the Gulf of Mexico and Caribbean Sea. Deep-Sea Research <u>24</u> , 987-1004.	446
25. Molinari, R.L.	
Synoptic and Mean Monthly 20°C Topographies in the Eastern Gulf of Mexico. NOAA Technical Memorandum ERL AOML-27, 33 pages.	464
26. Molinari, R.L. and A.D. Kirwan, Jr.	
Calculations of Differential Kinematic Properties From Lagrangian Observations. American Institute of Aeronautics and Astronautics, Technical Committee on Marine Systems and Technologies, Drift Buoy Symposium, Hampton, Virginia, May 22-23, 1976. NASA CO-2003, 193-209.	499
27. Molinari, R.L. and R.E. Yager.	
Upper Layer Hydrographic Conditions at the Yucatan Strait During May, 1972. Journal of Marine Research <u>35</u> , No. 1, 11-20.	516
28. Molinari, R.L., S. Baig, D.W. Behringer, G.A. Maul, and R. Legeckis.	
Winter Intrusions of the Loop Current. Science <u>198</u> , 505-507.	526
29. Starr, R.B., J.B. Hazelworth, S.R. Cummings, G.A. Berberian.	
MESA New York Bight Project Expanded Water Column Characterization Cruise (XWCC 10) NOAA Ship GEORGE B. KELEZ, 28 June-1 July 1976. NOAA Data Report ERL MESA-28, 93 pages.*	529

\* Text only; complete data available from the authors or National Technical Information Service (NTIS).

## OCEAN CHEMISTRY LABORATORY

30. Atwood, D.K.  
Regional Oceanography as it Relates to Present and Future Pollution Problems and Living Resources - Caribbean. Proceedings of IOC/FAO/UNEP International Workshop on Marine Pollution in the Caribbean and Adjacent Regions, Port-of-Spain, Trinidad, 13-18 December 1976. Workshop Report No. 11, 47-79. 539
31. Cantillo, A.Y. and D.A. Segar.  
Metal Species Identification in the Environment a Major Challenge for The Analyst. Symposium Volume of the International Conference on Heavy Metals in the Environment, Toronto, Canada, 1977, 183-204. 572
32. Hatcher, P.G. and L.E. Keister.  
Carbohydrates and Organic Carbon in New York Bight Sediments as Possible Indicators of Sewage Contamination. Middle Atlantic Continental Shelf and the New York Bight, Special Symposia 2, 1976, M.G. Gross, ed. (the American Society of Limnology and Oceanography, Inc.) 240-248. 594
33. Hatcher, P.G. and D.A. Segar.  
Chemistry and Continental Margin Sedimentation. Marine Sediment Transport and Environmental Management, D.J. Stanley and D.J.P. Swift, eds. (John Wiley & Son, Inc.). Chapter 19, 461-477. 603
34. Hatcher, P.G., L.E. Keister, and P.A. McGillivray.  
Steroids as Sewage Specific Indicators in New York Bight Sediments. Bulletin of Environmental Contamination and Toxicology 17, No. 4, 491-498. 620
35. Segar, D.A. and G.A. Berberian.  
Oxygen Depletion in the New York Bight Apex: Causes and Consequences. Middle Atlantic Continental Shelf and the New York Bight, Special Symposia 2, 1976, M.G. Gross, ed. (the American Society of Limnology and Oceanography, Inc.) 220-239. 628



	Page
36. Segar, D.A. and A.Y. Cantillo.	
Trace Metals in the New York Bight. Middle Atlantic Continental Shelf and the New York Bight, Special Symposia <u>2</u> , 1976, M.G. Gross, ed. (the American Society of Limnology and Oceanography, Inc.) 171-198.	648

## VOLUME II

### MARINE GEOLOGY AND GEOPHYSICS LABORATORY

37. Bennett, R.H.	
Pore-Water Pressure Measurements: Mississippi Delta Submarine Sediments. Marine Geotechnology <u>2</u> , 177-189.	677
38. Bennett, R.H. and J.R. Faris.	
AOML Pore Pressure Measurements. Ocean Engineering Technical Bulletin (NDBO) <u>3</u> , No. 4, p. 3.	690
39. Bennett, R.H., W.R. Bryant, and G.H. Keller.	
Clay Fabric and Geotechnical Properties of Selected Submarine Sediment Cores From the Mississippi Delta. NOAA Professional Paper 9, 94 pages. (Pocket insert omitted.)	691
40. Bennett, R.H., D.N. Lambert, and M.H. Hulbert.	
Geotechnical Properties of a Submarine Slide Area on the U.S. Continental Slope Northeast of Wilmington Canyon. Marine Geotechnology <u>2</u> , 245-261.	785
41. Clark, T.L.	
FET Pair and Op Amp Linearize Voltage-Controlled Resistor. Electronics <u>50</u> , No. 9, 111-112.	803
42. Dietz, R.S.	
Plate Tectonics: A Revolution in Geology and Geophysics. Tectonophysics 38, 1-6.	805

43. Freeland, G.L. and G.F. Merrill.  

The 1973 Bathymetric Survey in the New York Bight Apex: Maps and Geological Implications. NOAA Technical Memorandum ERL MESA-19, 22 pages.

811
44. Freeland, G.L., D.J.P. Swift, W.L. Stubblefield, and A.E. Cok.  

Surficial Sediments of the NOAA-MESA Study Areas in the New York Bight. Middle Atlantic Continental Shelf and the New York Bight, Special Symposia 2, 1976, M.G. Gross, ed. (the American Society of Limnology and Oceanography, Inc.) 90-101.

833
45. Goldsmith, V., G.L. Shideler, J.F. McHone, and D.J.P. Swift.  

Beach Response in the Vicinity of a Shoreface Ridge System: False Cape, Virginia. Virginia Institute of Marine Science, SRAMSOE, No. 143, June 10-11, 1977, 23-1 - 23-17.

845
46. Hunt, R.E., D.J.P. Swift, and H. Palmer.  

Constructional Shelf Topography, Diamond Shoals, North Carolina. Geological Society of American Bulletin 88, 299-311.

862
47. McGregor, B.A.  

Geophysical Assessment of Submarine Slide Northeast of Wilmington Canyon. Marine Geotechnology 2, 229-244.

875
48. McGregor, B.A. and R.H. Bennett.  

Continental Slope Sediment Instability Northeast of Wilmington Canyon. American Association of Petroleum Geologists Bulletin 61, No. 6, 918-928.

891
49. McGregor, B.A., C.G.A. Harrison, J.W. Lavelle, and P.A. Rona.  

Magnetic Anomaly Patterns on Mid-Atlantic Ridge Crest at 26°N. Journal of Geophysical Research 82, No. 2, 231-238.

902
50. Nelsen, T.A., D.A. Mayer, P.G. Hatcher, and W.N. Hess.  

New England Offshore Mining Environmental Study: The Character of Particle Dispersion and Water Movement in Massachusetts Bay and Adjacent Waters. Estuarine and Coastal Marine Science 5, 455-465.

910

	Page
51. Neumann, A.C., J.W. Kofoed, and G.H. Keller.  Lithoherms in the Straits of Florida, <i>Geology</i> <u>5</u> , No. 1, 4-10.	921
52. Rona, P.A.  Paleobathymetry of the Crest of Spreading Ridges Related to the Age of Ocean Basins - Comment. <i>Earth and Planetary Science Letters</i> , <u>35</u> , No. 3, 454-456.	928
53. Rona, P.A.  Plate Tectonics, Energy and Mineral Resources: Basic Research Leading to Payoff. <i>EOS</i> <u>58</u> , No. 8, 629-639.	931
54. Rona, P.A.  Reply to A.A. Archer's "Comments on 'Plate Tectonics and Mineral Exploration' by P.A. Rona." <i>Natural Resources Forum</i> <u>1</u> , 196-197.	942
55. Stubblefield, W.L., R.W. Permenter, and D.J.P. Swift.  Time and Space Variation in the Surficial Sediments of the New York Bight Apex. <i>Estuarine and Coastal Marine Science</i> <u>5</u> , 597-607.	944
56. Swift, D.J.P.  Shelf-Sediment Dynamics. <i>Geotimes</i> <u>2</u> , No. 6, 19-20.	963
57. Swift, D.J.P., G.L. Freeland, P.E. Gadd, G. Han, J.W. Lavelle, and W.L. Stubblefield.  Morphologic Evolution and Coastal Sand Transport, New York - New Jersey Shelf. Middle Atlantic Continental Shelf and the New York Bight, Special Symposia <u>2</u> , 1976, M.G. Gross, ed. (the American Society of Limnology and Oceanography, Inc.) 69-89.	965
58. Swift, D.J.P., T. Nelsen, J. McHone, B. Holliday, H. Palmer, and G. Shideler.  Holocene Evolution of the Inner Shelf of Southern Virginia. <i>Journal of Sedimentary Petrology</i> <u>47</u> , No. 4, 1454-1474.	986



59. Turekian, K.K. and P.A. Rona.

Eastern Atlantic Fracture Zones as Potential Disposal Sites for Radioactive Waste. *Environmental Geology* 2, 59-62.

1007

60. Young, R.A.

Seaflume: A Device for In-Situ Studies of Threshold Erosion Velocity and Erosional Behavior of Undisturbed Marine Muds. *Marine Geology* 23, M-11 - M-18.

1011

#### SEA-AIR INTERACTION LABORATORY

61. Cardone, V.J., D.B. Ross, and M.R. Ahrens.

An Experiment in Forecasting Hurricane Generated Sea States. Proceedings 11th Technical Conference on Hurricanes and Tropical Meteorology of the American Meteorological Society, Miami Beach, Florida, December 13-16, 1977, 688-695.

1019

62. Cardone, V.J., D. Ross, M. Ahrens, J.A. Greenwood, C. Greenwood, and R. Salfi.

Forecasting Hurricane Winds and Waves: A Pilot Study. Final Report to: NOAA Sea-Air Interaction Laboratory and Shell Development Company, December 1976, 45 pages (Abstract only).

1027

63. Hasselmann, K., D.B. Ross, P. Muller, and W. Sell.

Reply to "Comments on 'A Parametric Wave Prediction Model'", by Willard J. Pierson. *Journal of Physical Oceanography* 7, No. 1, 134-137.

1028

64. Johnson, R.W., I.W. Duedall, R.M. Glasgow, J.R. Proni, and T.A. Nelson.

Quantitative Mapping of Suspended Solids in Wastewater Sludge Plumes in the New York Bight Apex. *Journal Water Pollution Control Federation*, 2063-2073.

1032

	Page
65. Newman, F.C., J.R. Proni, and D.J. Walter.	
Acoustic Imaging of the New England Shelf-Slope Water Mass Interfaces. <i>Nature</i> <u>269</u> , No. 5631, 790-791.	1043
66. Ostapoff, F., S. Worthem, W. Everard.	
Surface Meteorological Observations on R/V COLUMBUS ISELIN During Phase III of GATE. NOAA Technical Memorandum ERL AOML-25, 129 pages.	1045
67. Thacker, W.C.	
A Spliced Numerical Grid Having Applications to Storm Surge. NOAA Technical Memorandum ERL AOML-26, 22 pages.	1174
68. Thacker, W.C.	
A Transformation Relating Temporal and Spatial Spectra of Turbulent Kinetic Energy. NOAA Technical Report ERL 385-AOML 26, 10 pages.	1196
69. Thacker, W.C.	
Irregular Grid Finite-Difference Techniques: Simulations of Oscillations in Shallow Circular Basins. <i>Journal of     Physical Oceanography</i> <u>7</u> , No. 2, 284-292.	1206
70. Thacker, W.C.	
Reply to "Comments on 'Irregular Grid Finite-Difference Techniques: Simulations of Oscillations in Shallow Circular Basins'" by J.D. Wang. <i>Journal of Physical     Oceanography</i> <u>7</u> , No. 6, 933-934.	1216
71. Thacker, W.C.	
"Shear Dispersion" in Time-Varying Flows. NOAA Technical Report ERL 386-AOML 27, 9 pages.	1218
72. Thacker, W.C. and J.W. Lavelle.	
Two-Phase Flow Analysis of Hindered Settling. <i>The Physics     of Fluids</i> <u>20</u> , No. 9, 1577-1579.	1227

## Pore-Water Pressure Measurements: Mississippi Delta Submarine Sediments

RICHARD H. BENNETT\*

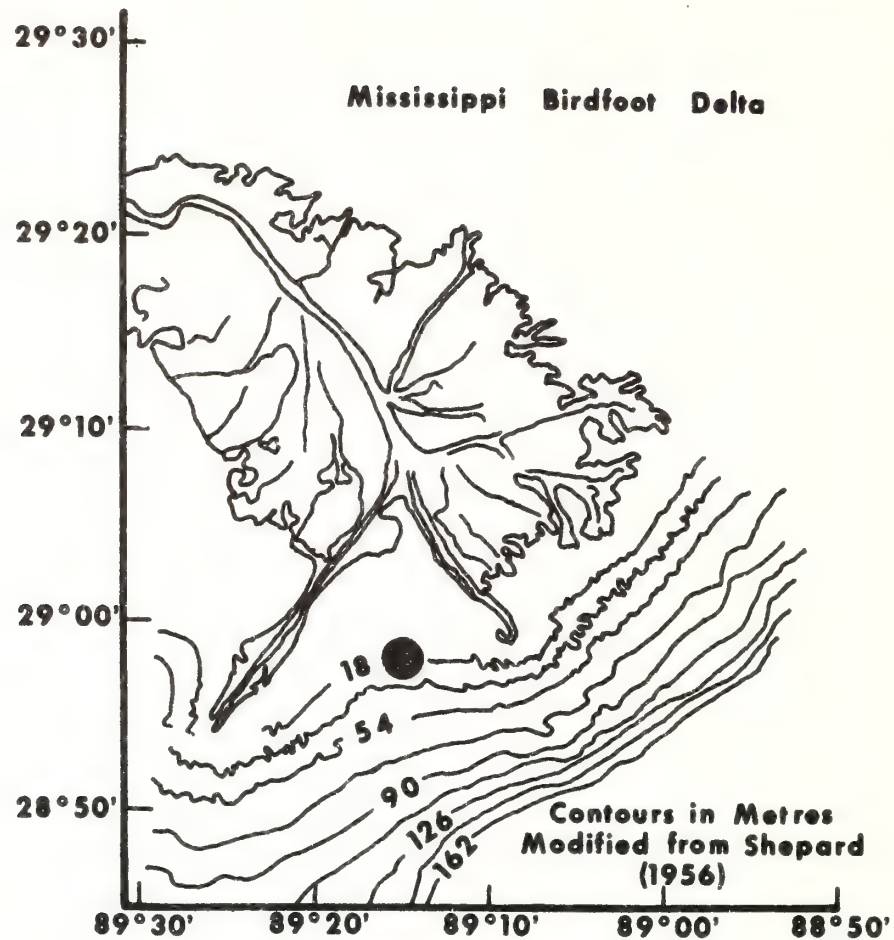
**Abstract** A pore-water pressure probe (piezometer) was implanted in Mississippi delta sediments at a preselected site (Block 28, South Pass area, 29°00'N, 89°15'W) 145 m from an offshore production platform (water depth approx. 19 m) in September 1975. Total pore-water pressures ( $u_w$ ) were monitored for extended periods of time at depths of approximately 15 and 8 m below the mudline concurrently with hydrostatic pressures ( $u_s$ ) measured at depths of 15 m and approximately 1 m below the mudline. Relatively high excess pore-water pressures,  $u_e = (u_w - u_s)$ , were recorded at the time of probe insertion measuring 99 kPa (14.4 psi) at 15 m and 50 kPa (7.3 psi) at 8 m. Six hours after the probe was implanted, excess pore pressures were still high at 81 kPa (11.8 psi, 15 m) and 37 kPa (5.4 psi, 8 m). Pore pressures appeared to become relatively constant at the 8-m depth after 7 h had elapsed, and at the 15 m depth after 10–12 h. Excess pore-water pressures averaged 72 kPa (10.4 psi, 15 m) and 32 kPa (4.6 psi, 8 m) prior to the initial effects of Hurricane Eloise, which passed in close proximity to the probe site. Significant variations in pressures were recorded during storm activity. As the effects of the storm subsided, excess pore-water pressures began to decline slightly at the 15-m depth; however, concurrently at the 8-m depth, pore pressures began to increase gradually. During the period of 21–25 days after the probe was implanted, excess pore pressures appeared to become more constant, averaging 24 kPa (3.5 psi) at 15 m and 43 kPa (6.2 psi) at the 8-m depth. The presence of methane, a common occurrence in these delta muds, may have influenced, or contributed to, the total pore-water pressures measured during this experiment.

\*NOAA-Atlantic Oceanographic and Meteorological Laboratories, Miami, Florida. (Received January 4, 1977; revised February 15, 1977; accepted February 21, 1977.)

*Marine Geotechnology*, Volume 2, Marine Slope Stability, 1977.

0360-8867/78/0100-0177/\$2.00/0

Copyright © 1978 Crane, Russak & Company, Inc.



### General Study Area.

**Figure 1.** General piezometer location in Block 28.

### Introduction

The nation's increasing demands for natural resources—particularly petroleum—have led to steadily increasing offshore activity. In response to the ever-increasing demands for energy, engineers are constantly faced



with the problems of placing structures on and within the seafloor, the safety of these structures in the environment, and the potential effects of offshore activities on the marine environment. Studies of the geological processes unique to a specific environment are prerequisite to the understanding of important engineering factors relative to seafloor sediment stability, specifically the assessment of potentially unstable areas and the potential forces related to mass movement. Once the geological processes have been elucidated for a given environment, and the important factors of sediment stability evaluated (potential stability-instability and forces), the engineer can design offshore structures with confidence and prepare for their emplacement in order to meet the predicted environmental conditions.

This study of Mississippi delta sediment pore-water pressures is directed toward the delineation and understanding of important processes related to submarine sediment stability. Engineers have known for decades that pore-water pressures are an important geotechnical consideration in assessing sedimentary deposits. The first reported attempt to measure pore pressure in submarine sediments was made by Lai et al. (1968) and Richards et al. (1975). Recently, Sangrey (1976) stressed the importance of obtaining sediment pore-pressure measurements in order to make accurate predictions of offshore soil conditions and to improve offshore geotechnical engineering significantly through the use of effective stress methods. Specifically, this investigation was designed to measure and continuously monitor not only pore water and hydrostatic pressures at selected depths below the mudline (Block 28, Figure 1), but to monitor significant pressure perturbations during active storm periods as well (Bennett et al., 1976).

The Mississippi delta is a very dynamic region characterized by the interaction of riverine and marine processes and the large discharge of bedload and suspended sediment. Large plumes of sediment extend considerable distances beyond the subaerially exposed delta, depositing vast quantities of silt and clay in the prodelta environment. This environment is characterized not only by the rapid deposition of fine-grained sediment having very high water content, but also by the accumulation of organic material (Coleman et al., 1974). Methane and carbon dioxide gases, intimately related to decomposition of the organic material, influence substantial portions of the Mississippi delta submarine sediments (Whelan et al., 1975).

Knowledge of the sediment geotechnical properties in this complex and dynamic environment is of great importance, not only to engineers faced with the design and construction of offshore structures, but also to geologists investigating sedimentological processes that relate to diagenesis, envi-

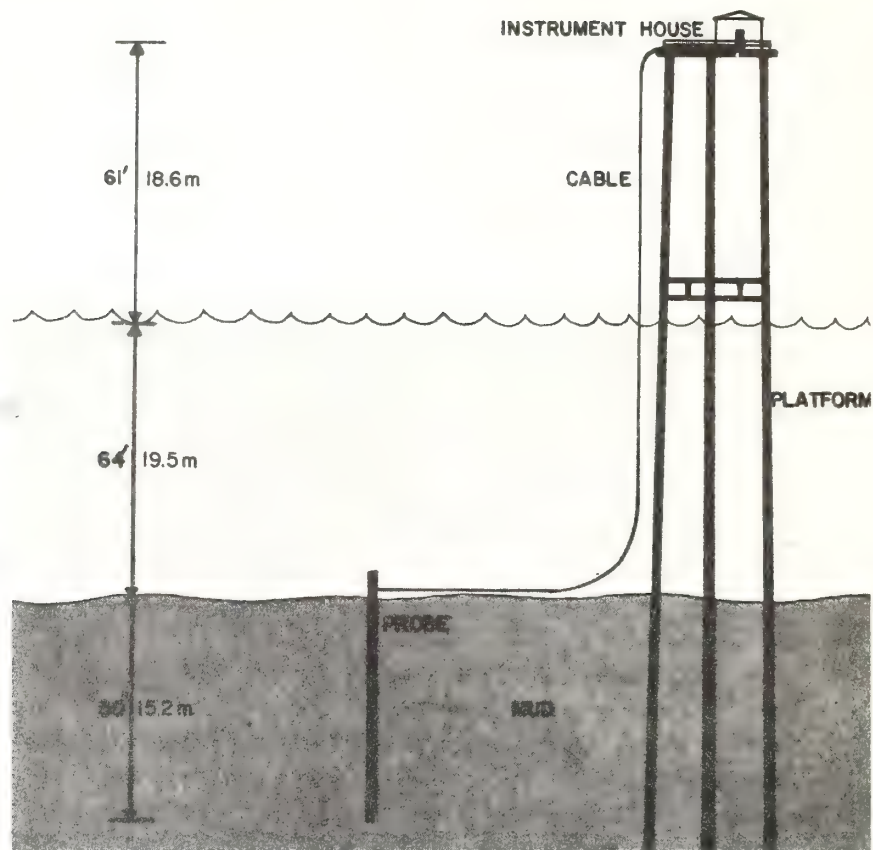


**Figure 2.** Diagrammatic sketch of relative positions of probe, platform, and instrument house.

ronments of deposition, mass movement, and sediment stability (Morelock and Bryant, 1966; Keller and Bennett, 1968; Bennett and Bryant, 1973; Bennett et al., 1977). Investigation of pore-water pressures in the Mississippi delta will provide valuable insight into sedimentological processes and aid in the understanding of other related geotechnical properties and the behavior of these prodelta fine-grained cohesive sediments in response to static and dynamic loads. Recently, Suhayda et al. (1976) made an important contribution to the understanding of hydrodynamic forces and bottom sediment interaction in a selected area of the Mississippi delta.

The pore-pressure data discussed in this article cover a period from September 19 to October 15, 1975, during which time Hurricane Eloise passed in close proximity to the probe site. Data gathered subsequent to October 15 until termination of the experiment in March 1976, are meager, and were recorded at irregular intervals. Instrument (primarily recorder) malfunctions and difficulties in maintaining the offshore electronics system, and data acquisition generally, increased the problems in obtaining long-term, continuous pore-pressure data.

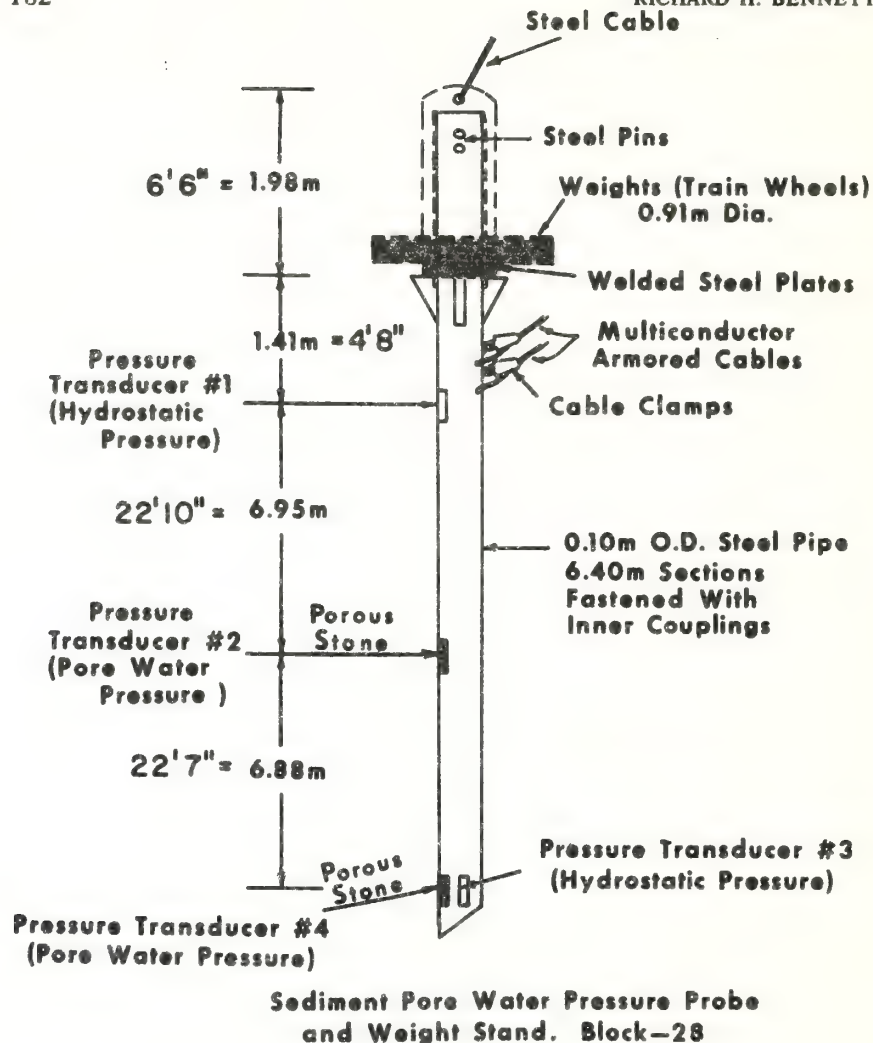
### **Instrumentation**

The NOAA piezometer and electronics system consisted of the following components:

1. Probe and sensing units (variable reluctance pressure transducers)
2. Signal conducting cables
3. Signal conditioners
4. Voltage and frequency regulator
5. Recorder (four-pen strip chart, ink type)

The probe was a 0.10-m O.D. steel pipe with a total length of 17.1 m. The pressure transducers were placed at selected distances in the pipe, enclosed within oil-filled capsules for protection. Transducers were connected to the appropriate pressure ports with short tubing within the capsules. A weight stand was mounted to the top of the probe on steel gusset plates and was fastened to the pipe with two steel pins. The probe assembly was lowered into the seafloor by a steel cable fastened to the top of the weight stand, which was removed immediately after the piezometer was implanted. Two pressure transducers placed in the probe at selected intervals measured pore-water pressure transmitted through porous corundum stones, and two pressure transducers measured hydrostatic pressure (Figure 2). Signals from each transducer were transmitted through a conducting cable to signal conditioners and electronic filtering systems prior to being recorded on a strip-chart recorder. Details of the system, field operations, and piezometer calibration are discussed by Bennett et al. (1976).

During probe deployment and prior to sediment penetration, a check on the system was made by observing virtually similar pressure readings recorded for transducers 3 and 4, located at the same position in the probe (Figure 2). Following stabilization of the electronic system, the difference in values recorded for transducers 1 and 3 (Figure 2) measuring hydro-



**Dwg. Not To Scale**

**Figure 3.** Sediment pore-water pressure probe and weight stand.

static pressures agreed well with theoretical values calculated from the density of seawater ( $1.024 \text{ Mg/m}^3$ ).

The probe was implanted in Block 28, South Pass area, slightly south of  $29^{\circ}00'N$ ,  $89^{\circ}15'W$  approximately 145 m from the platform where the recorder and signal conditioner units were installed in an instrument house



(Figure 1). Deployment was carried out aboard the Texas A&M University Ship R/V Gyre. During a 4-h period after the probe was implanted, no piezometer readings were recorded while the electronic instruments were being installed on the platform (Figure 3). The probe was implanted only a few days prior to the passage of Hurricane Eloise near the site.

### Discussion

Hydrostatic pressures ( $u_s$ ) were measured at depths of approximately 1 and 15 m (actual mudline difficult to determine) below the mudline concurrently with the measurement of pore-water pressures ( $u_w$ ) at depths of 8 and 15 m (Figure 2). When the sediment pore-water pressure exceeds the hydrostatic pressure ( $u_w > u_s$ ) at an equivalent depth below the mudline, the difference is expressed as excess pore-water pressure  $u_e = (u_w - u_s)$ . In order to compare the pore-water pressures measured at the 8-m depth with hydrostatic pressure, a value of 68.9 kPa (10 psi) was added to pressure transducer #1 values for direct comparison with #2 transducer readings. Pore-water pressure is considered in equilibrium with the hydrostatic pressure when the two are equal ( $u_s = u_w$ ). Factors responsible for pore-water disequilibrium in sediments under certain geological conditions

### MISSISSIPPI DELTA EXCESS PORE WATER PRESSURE

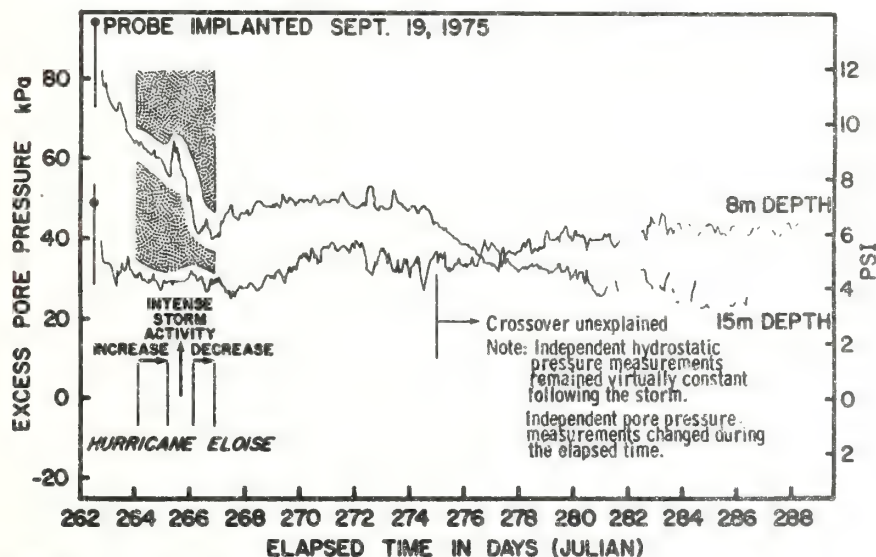


Figure 4. Excess pore-water pressure plotted against time.

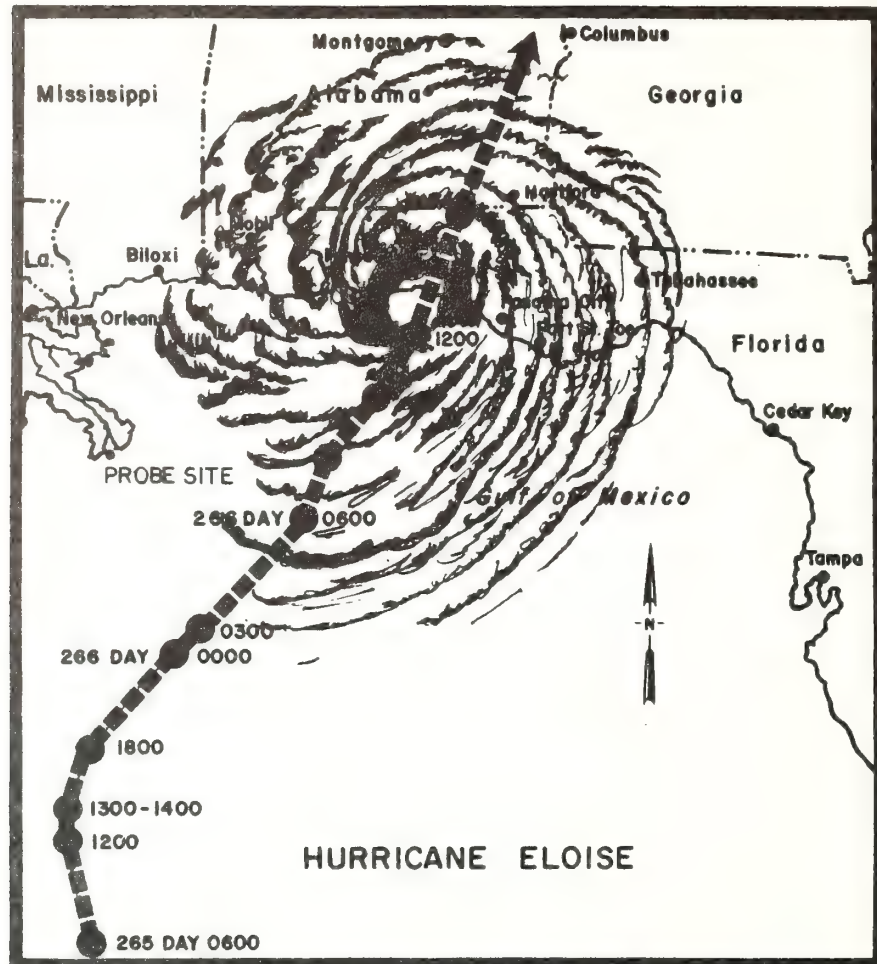


Figure 5. Track of Hurricane Eloise through the northern Gulf of Mexico and approximate lateral extent of the storm.

are discussed by Bennett et al. (1976). Piezometer data discussed in the remainder of this article are presented in terms of excess pore-water pressure ( $u_e$ ).

Relatively high excess pore-water pressures of 99 kPa (14.4 psi) and 50 kPa (7.3 psi) at depths of 15 and 8 m below the mudline, respectively, were measured at the time of probe insertion. As expected, these high pressures dissipated toward a static condition following a typical log-time consolidation relationship for the 8-m depth measurements, but were some-

what irregular for the 15-m readings. Minor significance can be attributed to the initial readings owing to the stabilization of the electronic system, including temperature equilibration of the pressure transducers. Six hours after the probe was implanted, excess pore pressures were still high at 81 kPa (11.8 psi, 15 m) and 37 kPa (5.4 psi, 8 m). They appeared to become relatively constant after approximately 7 h at 8 m and 10–12 h at 15 m. However, excess pore pressures began to decline again at the 15-m depth just prior to the initial effects of Hurricane Eloise. Examination of excess pore pressure versus time plots reveals that the decline in excess pore pressures was much more dramatic at the 15-m depth compared to the 8-m depth (Figure 4). Excess pore pressures averaged 72 kPa (10.4 psi, 15 m) and 32 kPa (4.6 psi, 8 m) prior to the initial effects of the hurricane, which passed in close proximity to the probe site (Figure 5).

Independently measured hydrostatic and pore-water pressures showed significant variations during storm activity. Figure 5 indicates the Julian Days in September during which time Hurricane Eloise passed through the Gulf of Mexico. Only a slight degree of activity attributable to the approaching storm was sensed by the hydrostatic transducers, #1 and #3, beginning about 0300 on day 264. Essentially no activity was indicated at this time in transducers #2 and #4, which measured pore-water pressures. Increased wave activity was recorded by the hydrostatic transducers following the time of about 0500–0600 on day 265, and maximum pressure variations ranged from 13.8 to 20.7 kPa (2.0–2.5 psi), equivalent to approximately 1.68 m (5.5 ft) of seawater at a density of 1.024 Mg/m<sup>3</sup>. At this time, the center of the hurricane was south of the probe site and moving northwesterly toward the delta (Figure 5). All four pressure sensors were responding to storm activity between 0800 and 0900 h on day 265, but only a minor response was indicated by transducer #2 intermittently until 2015 h, at which time transducer #2 became very active in response to wave activity. Very intense activity was recorded by all transducers between the period of 1200 to about 2300 on day 265, at which time the hurricane was sited south of the probe site and moving in a northeasterly direction (Figures 4 and 5). During this intense storm period, transducers 1 and 3 measured maximum pressure variations of 28 kPa (4.0 psi) and 24 kPa (3.5 psi), respectively, and transducers 2 and 4 measured maximum pressure variations of 14 kPa (2 psi).

It is important to note that maximum pore-pressure variations recorded by transducers 2 and 4 were approximately one-half the pressure variations recorded by the hydrostatic transducers 1 and 3. This may reflect a type

of "dampening" effect or energy loss through the sedimentary column, or a hydrostatic time lag in the transmission of the dynamic pore pressures. Of interest, too, is the apparent "lag" of transducer #2 recorded pressures behind the other transducers. This may be the result of differences in methane with sediment depth and the response of these gaseous sediments to dynamic loads.

Submarine sediments rich in methane exhibit considerable core expansion upon retrieval as a result of the change from *in situ* pressure to ambient pressure at sea level. Obviously, such important factors as the total amount of methane (gaseous or dissolved phases, or both) present *in situ*, and the total pressure, will affect the degree to which core expansion will occur. Borehole data and megascopic examination of cores demonstrated a significant increase in core expansion below 6 m, and considerable expansion was observed in cores retrieved below depths of about 15 m (Dunlap, personal communication, 1976). The relatively large perturbation in excess pore pressure observed during intense storm activity at the 15-m depth compared to the relatively low pore-pressure response at the 8-m depth

Table 1.  
Piezometer Response During Storm Activity

		Maximum Range Indicated and Equivalent Meters of Seawater <sup>a</sup>							
Days	Hours	Pore Pressure				Hydrostatic Pressure			
		Trans- ducer	kPa	psi	m	Trans- ducer	kPa	psi	m
264	0300	—	—	—	—	#1	6.9	1.0	0.7
						#3	6.9	1.0	0.7
265	0500–0600	—	—	—	—	#1	17.2	2.5	1.7
						#3	17.2	2.5	1.7
265	0800–0900	#2	Minor	Minor	—	#1	17.2	2.5	1.7
		#4	6.9	1.0	0.7	#3	17.2	2.5	1.7
265	0900–1200	Increasing activity				Increasing activity			
265	1200–2300	#4	13.8	2.0	1.4	#1	27.6	4.0	2.7
						#3	24.1	3.5	2.4
265	2015	#2	13.8	2.0	1.4				
265	2300	Storm began to subside between 2300 on day 265 and about 0300 on day 266, as indicated by the pressure sensors.							
266	—	Effects of the storm were essentially complete toward close of day 266.							

<sup>a</sup>Equivalent meters of seawater based on a density of 1.024 Mg/m<sup>3</sup> (63.9 lb/ft<sup>3</sup>).



may also be related to the methane concentration with depth in these sediments (Figure 4).

The effects of the storm activity, as recorded by the transducers implanted at the various depths below the mudline, began to diminish at about 2300 h on day 265, and pressure readings became relatively stable after 0300 h on day 266, at which time no significant rapid variations in pressures were observed (Table 1). Poststorm data indicate a general increase in excess pore pressure at both the 15- and 8-m depths between the period of days 267–273 (Figure 4). Approximately 6 days after the storm had passed, excess pore-water pressures began a gradual decline at the 15-m depth. However, excess pore pressure continued a general steady increase at the 8-m depth. Twenty-one days after the probe was implanted (16 days after the passage of the hurricane), pore pressures appeared to become more constant, and values averaged 24 kPa (3.5 psi) at 15 m and 43 kPa (6.2 psi) at 8 m (Figure 4).

Poststorm average rates of change of excess pore-water pressures are approximately the same for both the 15- and 8-m depth measurements. Calculated average rates of change are on the order of  $8.2 \times 10^{-6}$  kPa/s, increasing ( $1.2 \times 10^{-6}$  psi/s) at 8 m and  $10.3 \times 10^{-6}$  kPa/s, decreasing ( $1.5 \times 10^{-6}$  psi/s) at 15 m below the mudline. Although preliminary analysis of data (based on pore-water pressure measurements prior to Hurricane Eloise and wet unit weights obtained from borehole samples) indicate effective stress in these sediments close to zero, the pore-pressure measurements obtained for a period of 25 days strongly suggest a *time-dependent change* in effective stress over a considerable period of time.

Wet unit weights are lowest in the upper 9.1 m (30 ft) of sediment and average  $1.42 \text{ Mg/m}^3$  ( $88.7 \text{ lb/ft}^3$ ). An increase in wet unit weight occurs at about 9.1 m and averages  $1.44 \text{ Mg/m}^3$  ( $89.7 \text{ lb/ft}^3$ ) between this depth and 15.2 m (50 ft). Despite the measured increase in wet bulk density below 9.1 m, considerable core expansion was observed in samples recovered below this depth. Consequently, measured unit weights are probably somewhat lower than are *in situ* wet unit weights.

Data indicate not only long-term changes in *excess* pore pressures, but also short-term variations, particularly during storm activity, and likewise short-term variations in *total* pore-water pressure. Short-term variations and long-term changes in excess pore pressures appear to be the rule in these sediments at the probe site during the 25-day period for the data obtained before, during, and after Hurricane Eloise's passage through the northern Gulf of Mexico.

**Summary**

Piezometer measurements in Mississippi delta submarine sediments at a selected site (Block 28) have shown the presence of high excess pore-water pressures. Independently measured hydrostatic and pore-water pressures have indicated the presence not of only short-term rapid fluctuations in excess pore pressure during active storm conditions, but also long-term changes in excess pore pressure following the passage of Hurricane Eloise through the Gulf of Mexico. The long-term changes observed in excess pore pressure suggest a commensurate time-dependent change in effective stress in these submarine sediments, where the probe was implanted. Relatively rapid fluctuations were observed in hydrostatic and pore-water pressures during storm activity, and maximum pore-pressure variations measured approximately one-half the values observed for the hydrostatic pressure variations. This suggests an energy loss or "dampening" effect through the sediments of wave activity during the storm. Data collected following the 25 days reported here are presently being analyzed, although the data discussed in this article represent the most continuous set of measurements collected during the pore-pressure experiment.

**Acknowledgments**

This project was funded by the National Oceanic and Atmospheric Administration, Atlantic Oceanographic and Meteorological Laboratories. Funds for the field activities were provided by the U.S. Geological Survey. The writer wishes to acknowledge the assistance and support given by Dr. William R. Bryant, Dr. Wayne A. Dunlap, and Dr. George H. Keller, each of whom assisted in the field operations and discussed various aspects of the piezometer data. The writer appreciates the various contributions made by Dr. Louis Garrison, U.S. Geological Survey, Corpus Christi, Texas, who provided funds for the field activities and for the borehole made near the piezometer site. Michael Tubman assisted in the data collection and maintenance of the electronic equipment. John Burns assembled the electronic instrumentation and assisted in the field operations and in the calibration of the piezometer system. Charles Noble made possible the calibration of the pressure transducers and system. Field assistance provided by Shell Oil Company and employees is appreciated. The critical review of this manuscript and helpful suggestions by Dr. Wayne A. Dunlap are gratefully acknowledged.

## References

- Bennett, R. H., and W. R. Bryant, 1973. Submarine sediment microstructure, Clay and Clay Minerals Society 22nd Annual Clay Minerals Conference. Banff, Canada, Program Abstracts, p. 22.
- Bennett, R. H., W. R. Bryant, W. A. Dunlap, and G. H. Keller, 1976. Initial results and progress of the Mississippi Delta sediment pore water pressure experiment. *Marine Geotechnology*, vol. 1, no. 4, pp. 327-335.
- Bennett, R. H., W. R. Bryant, and G. H. Keller, 1977. Clay fabric and geotechnical properties of selected submarine sediment cores from the Mississippi Delta. NOAA Professional Paper #9, 87 pp.
- Bryant, W. R., W. Hottman, and P. Trabant, 1975. Permeability of unconsolidated and consolidated marine sediments. Gulf of Mexico, *Marine Geotechnology*, vol. 1, pp. 1-14.
- Coleman, J. M., J. N. Suhayda, T. Whelan III, and L. D. Wright, 1974. Mass movement of Mississippi Delta sediments. *Transactions Gulf Coast Association of Geological Societies*, vol. 24, pp. 49-68.
- Keller, G. H., and R. H. Bennett, 1968. Mass physical properties of submarine sediments in the Atlantic and Pacific Basins. *Proceedings International Geological Congress, 23rd, Prague*, vol. 8, pp. 33-50.
- Lai, J. Y., A. F. Richards, and G. H. Keller, 1968. In place measurement of excess pore water pressure of Gulf of Maine clays (abstract). *American Geophysical Union Transactions*, vol. 49, p. 221.
- Morelock, J., and W. R. Bryant, 1966. Physical properties and stability of continental slope deposits, northwest Gulf of Mexico. *Transactions Gulf Coast Association of Geological Societies*, vol. 16, pp. 279-295.
- Richards, A. F., K. Øien, G. H. Keller, and J. Y. Lai, 1975. Differential piezometer probe for an *in situ* measurement of sea-floor pore pressure. *Géotechnique*, vol. 25, pp. 229-238.
- Sangrey, D. A., 1976. Marine geotechniques—State of the art (abstract), Conference on Marine Slope Stability. Oct. 14-15, Louisiana State University, Baton Rouge, La., pp. 4-5.
- Shepard, F. P., 1956. Marginal sediments of the Mississippi Delta. *Bulletin American Association Petroleum Geologists*, vol. 40, pp. 2537-2623.
- Suhayda, J. N., T. Whelan III, J. M. Coleman, J. S. Booth, and L. E. Garrison, 1976. Marine instability: Interaction of hydrodynamic forces and bottom sediments. *Offshore Technology Conference Paper No. OTC 2426*, pp. 29-40.
- Whelan III, T., J. M. Coleman, and J. N. Suhayda, 1975. The geochemistry of Recent Mississippi River Delta sediment: Gas concentration and sediment stability. *Offshore Technology Conference Proceedings*, vol. 3, pp. 71-84.



## AOML PORE PRESSURE MEASUREMENTS

An improved shallow-water piezometer (pore water pressure probe) was fabricated at NOAA's Atlantic Oceanographic and Meteorological Laboratories (AOML) in Miami, and was deployed in March 1977 in the Delta near the mouth of the Mississippi River. This experiment is currently providing significant long-term measurements that will define the geotechnical properties (mechanical and mass physical) and the behavior of prodelta fine-grained cohesive sediments in response to static and dynamic loads. The role of pore pressures during dynamic (storm) as well as static (calm) conditions is considered to be significant in the ultimate stability of submarine sediments and in the safety of offshore structures.

The system is composed of the probe and pressure-sensing transducers, signal-conducting cables, signal conditioners, voltage and frequency regulators, and recorders. The probe shell enclosing the pressure transducers is a 0.10-meter OD steel pipe composed of several 3.05-meter segments with sealed couplings. The probe is 19.8 meters long, and includes a specially designed tip to control sediment disturbance during insertion. It contains six variable-reluctance pressure transducers: three to measure absolute pore water pressure, two to measure absolute hydrostatic pressure, and one to measure excess pore water pressure (differential pressure above hydrostatic). The separate measurement of pore water and hydrostatic pressures enables the determination of

storm wave effects on pore pressures, and the differential transducer provides more detailed information on the effect of probe installation on pore water pressures. Pore pressure is sensed through either porous corundum or high-air-entry ceramic discs inset in the pipe and connected to the transducers by short tubing. Hydrostatic pressure is transmitted to the sensor locations from the mud line through the seawater-filled interior of the pipe, thereby allowing comparison of hydrostatic versus pore water measurements at the desired elevations. Signals from each transducer are transmitted through an armored conducting cable to the signal conditioners and recorders on the surface at the nearby fixed platform.

To date, NOAA/AOML piezometer studies at three Mississippi Delta sites have revealed the presence of significant high excess pore pressures, and have indicated the presence of short-term rapid pore pressure fluctuations during active hurricane/storm periods to depths of 50 feet in the sediment and long-term changes over periods of many days. AOML plans to continue long-term tests in relatively shallow marine waters, to obtain additional data on pore pressure response during active storm periods. Also, AOML has plans to develop a self-contained deep-water piezometer for deployment in offshore areas of critical importance.

AOML CONTACTS: R. H. Bennett  
J. R. Faris



NOAA Professional Paper 9, 94 pages (pocket insert omitted).

**NOAA**

**Professional Paper 9**



# **Clay Fabric and Geotechnical Properties of Selected Submarine Sediment Cores from the Mississippi Delta**

Richard H. Bennett  
Environmental Research Laboratories  
Atlantic Oceanographic and Meteorological Laboratories  
Marine Geology and Geophysics Laboratory  
Miami, Florida 33149

William R. Bryant  
Department of Oceanography  
Texas A & M University  
College Station, Texas 77843

George H. Keller  
School of Oceanography  
Oregon State University  
Corvallis, Oregon 97331

July 1977

**U.S. DEPARTMENT OF COMMERCE**

Juanita M. Kreps, Secretary

**National Oceanic and Atmospheric Administration**

Robert M. White, Administrator

## Foreword

The field of "seafloor soil mechanics" or marine geotechnique, as it has come to be known, is still poorly explored and its practitioners still relatively few. However, the recent increases in continental shelf activities spearheaded by the offshore oil and gas industries, have focused increased attention on the need for a much better understanding of the mass physical properties of marine sediments.

This Professional Paper presents the results of some 4 years of geotechnical research by Richard H. Bennett of NOAA's Atlantic Oceanographic and Meteorological Laboratories, working with William R. Bryant at Texas A & M University and George H. Keller, formerly of NOAA and now with the School of Oceanography at Oregon State University.

The fabric of submarine clays as well as the mass physical properties and their changes during consolidation are characteristics important to the engineer concerned with implanting structures on the sea floor. This volume covers the history of the evolving theories in this field, the results of field and laboratory work, and new insights into the properties of submarine sediments.

Harris B. Stewart, Jr., Director  
NOAA Atlantic Oceanographic and  
Meteorological Laboratories  
Miami, Florida

## Acknowledgments

The authors are grateful to Harris B. Stewart, Jr., David Fahlquist, Richard Rezak, Christopher Mathewson, George Peter, and Robert Gallaway for their reviews of the manuscript and helpful suggestions; to Matthew H. Hulbert for contributing to the quality of the section on physiochemistry of clay fabrics and for critically reviewing the manuscript; to Frances Nastav for assistance in preparing the illustrations; to Charles W. Reeves for making possible the computer image enhancement analysis discussed in this paper; and to Shirlee Meola and Hilton H. Mollenhauer for use of the electron microscopy laboratory where most of the transmission electron microscopy work was carried out. The helpful contributions of these and other colleagues are greatly appreciated.

This research paper was prepared originally by Richard H. Bennett in partial fulfillment of the requirements for the Doctor of Philosophy degree in oceanography at Texas A&M University, College Station, Texas, in 1976, under the direction of William R. Bryant, Committee Chairman. The paper is published in the NOAA Professional Paper series with some editorial revision of content and format.

# Contents

	<i>Page</i>
Foreword .....	iii
Acknowledgments .....	iv
Abstract .....	1
INTRODUCTION .....	1
General statement .....	1
Clay soils and marine geotechnical properties .....	1
Soil, sediment, and clay minerals .....	1
Clay microstructure and clay fabric .....	2
Objectives .....	2
General purpose of the investigation .....	2
Specific objectives .....	3
LITERATURE REVIEW – CLAY FABRIC .....	3
Physiochemistry of clays .....	3
Physiochemistry of flocculation and dispersion .....	4
Concepts of clay fabric .....	4
Early concepts .....	4
Later concepts and observations .....	9
Current concepts and observations .....	11
Summary .....	17
GEOLOGIC SETTING AND SAMPLING .....	18
General geology .....	18
Prodelta depositional environments .....	19
Clay mineralogy .....	19
General core lithology .....	19
Field core sampling and testing .....	19
ANALYTICAL TECHNIQUES AND INSTRUMENTATION FOR CLAY FABRIC STUDIES .....	21
Selection of sediment samples .....	21
Subsampling techniques .....	21
Preparation of samples for electron microscopy .....	21
Early dehydration methods .....	21
Critical point drying .....	21
Techniques employed .....	22
Transmission electron microscopy .....	23
GEOTECHNICAL TESTS .....	25



	<i>Page</i>
EVALUATION OF SAMPLE QUALITY AND TECHNIQUES .....	25
Sediment shear strength .....	25
Consolidation tests .....	26
Testing and evaluation .....	27
Sample quality .....	29
Fabric of natural versus remolded clay samples .....	31
Deep Sea Drilling Project sample (undisturbed) .....	31
Deep Sea Drilling Project sample (remolded) .....	33
Mississippi Delta sample (undisturbed) .....	34
Mississippi Delta sample (remolded) .....	35
Image enhancement techniques .....	36
Instrumentation .....	38
Digital image processing of film transparency B-1 (1.4 m) ..	39
Data analysis .....	50
Discussion .....	52
Summary of sample quality and techniques .....	54
DISCUSSION OF CLAY FABRIC AND SELECTED GEOTECHNICAL	
PROPERTIES .....	54
Selected geotechnical properties .....	54
Identification and description of clay fabric by transmission electron	
microscopy .....	56
Terminology .....	56
Fabric of shallow versus deep core samples .....	57
High porosity clays .....	57
Low porosity clays .....	62
Summary of clay fabric versus depth of burial .....	63
Clay fabric versus selected mass physical properties .....	64
Void ratio versus particle orientation .....	64
Clay fabric notation and geotechnical properties .....	65
Comparison of natural and laboratory consolidation .....	66
Clay fabric of laboratory consolidated samples .....	67
Depth of burial versus fissility .....	73
Mississippi Delta clay fabric and depositional environment .....	74
Initial stage .....	75
Postdepositional stage .....	75
The principle of irreversibility of clay fabric: Discussion of concept .....	76
Tentative clay fabric models for submarine sediment .....	76
SUMMARY .....	77
A synopsis—literature review .....	77
A synopsis—evaluation of analytical techniques, instrumentation, and	
sample quality .....	80
A synopsis—clay fabric and selected geotechnical properties .....	81
REFERENCES .....	83

## Illustrations

Figure	Page
1. Honeycomb structure -----	5
2. Cardhouse structure, saltwater deposit -----	5
3. Cardhouse structure, freshwater deposit -----	5
4. Remolded structure -----	5
5. Three-dimensional representation of clay structure -----	6
6. Salt-flocculated cardhouse structure with stairstep configuration -----	7
7. Nonsalt-flocculated well-developed cardhouse structure -----	7
8. Dispersed structure with preferred grain orientation -----	7
9. Sedimentation from a peptized and a flocculated suspension -----	7
10. Various modes of particle association -----	8
11. "Turbostratic" structure -----	9
12. Perfect "stack" -----	9
13. Bookhouse or book structure -----	9
14. Domain structures -----	9
15. Fabric changes during consolidation in a clay -----	10
16. "Tactoid" structure -----	11
17. "Card-house" structure -----	11
18. Stairstep structure of kaolite minerals -----	12
19. Stairstep structure of illite minerals -----	12
20. Crumb structure and particle orientation under load -----	13
21. Structure of a marine quick clay depicting aggregates and links prior to compression (shear deformation) -----	14
22. Structure of a marine quick clay depicting breakdown of links result- ing in domain formation and orientation of linking grains (after shearing) -----	14
23. A proposed scheme of particle arrangement in clay sediments -----	15
24. General study area—Mississippi Birdfoot Delta -----	18
25. Generalized core lithology -----	20
26. Analytical techniques and instrumentation for clay fabric analysis: De- hydration techniques -----	23
27. Analytical techniques and instrumentation for clay fabric analysis: Impregnation, sectioning, and transmission electron microscopy ---	24
28. Typical consolidation test—void ratio versus logarithm of pressure curve -----	26
29. Void ratio versus logarithm of pressure, South Pass, core B-1, 1.37 m (4.5 ft), natural sample -----	27
30. Void ratio versus logarithm of pressure, South Pass, core B-1, 1.37 m (4.5 ft), remolded sample -----	27
31. Void ratio versus logarithm of pressure, South Pass, core B-1, 1.98 m (6.5 ft), natural sample -----	27
32. Void ratio versus logarithm of pressure, South Pass, core B-1, 1.98 m - (6.5 ft), remolded sample -----	27
33. Void ratio versus logarithm of pressure, South Pass, core B-2, 1.37 m - (4.5 ft), natural sample -----	28
34. Void ratio versus logarithm of pressure, South Pass, core B-2, 1.37 m (4.5 ft), remolded sample -----	28
35. Void ratio versus logarithm of pressure, South Pass, core B-1, 12.19 m (40 ft), natural sample -----	28
36. Void ratio versus logarithm of pressure, South Pass, core B-2, 27.58 m (90.5 ft), natural sample -----	28

Figure	Page
37. Void ratio versus logarithm of pressure, South Pass, core B-1, 120.55 m (395.5 ft), natural sample -----	28
38. Method for determining degree of disturbance from a typical $e$ -log $p$ curve -----	29
39. Degree of disturbance ( $I_D$ ) versus void ratio ( $e_0$ ) for Mississippi Delta samples -----	29
40. Plot of $I_D$ minimum versus $e_0$ for fixed values of $\Delta e$ -----	30
* 41. Clay fabric showing flocs, linking chains, and zeolitic aggregate, Deep Sea Drilling Project (D.S.D.P.) core 163A (143 m) undisturbed sample -----	32
* 42. Clay fabric showing zeolitic aggregate surrounded by domains, D.S.D.P. core 163A (143 m) remolded sample -----	32
* 43. Clay fabric showing clay flocs, floc intravoids, and linking chains, D.S.D.P. core 163A (143 m) undisturbed sample -----	33
* 44. Clay fabric showing (A) randomly oriented domains with high overall void ratio, and (B) local areas of strongly oriented, dense pseudo-aggregates and domains, D.S.D.P. core 163A (143 m) remolded sample -----	33
* 45. Clay fabric showing randomly oriented domains, core B-2 (1.4 m) undisturbed sample -----	34
* 46. Clay fabric depicting well-defined randomly oriented domains and high void ratio, core B-2 (1.4 m) undisturbed sample -----	34
* 47. Stereographic view of clay fabric depicting randomly oriented domains and high void ratio, core B-2 (1.4 m) undisturbed sample -----	35
* 48. Clay fabric depicting 'swirl' pattern and local areas of highly oriented clay particles, core B-2 (1.4 m) remolded sample -----	35
* 49. Clay fabric—depicted at high magnification—showing 'swirl' pattern and local area of highly oriented particles, core B-2 (1.4 m) remolded sample -----	36
* 50. Clay fabric of strongly oriented particles with high void ratio—depicted at high magnification for a local ultrathin section area, core B-2 (1.4 m) remolded sample -----	36
51. Digital Image Processing System (DIPS) components -----	37
* 52. Clay fabric photomicrograph selected for image enhancement through digital image processing, core B-1 (1.4 m) -----	39
* 53. DIPS subimage reproduction of photomicrograph, core B-1 (1.4 m) --	40
54. Histogram of gray scale density versus percent -----	41
55. Cumulative curve of gray scale density versus percent -----	42
56. DIPS/DGG gray zone 1 (level 3-63) -----	43
57. DIPS/DGG gray zone 2 (level 64-79) -----	44
58. DIPS/DGG gray zone 3 (level 80-95) -----	45
59. DIPS/DGG gray zone 4 (level 96-125) -----	46
60. DIPS/DGG gray zone 5 (level 126-175) -----	47
61. DIPS/DGG gray zone 6 (level 176-225) -----	48
62. DIPS/DGG gray zone 7 (level 226-250) -----	49
63. DIPS/DGG false color rendition for gray level zones 1-7 from transmission electron photomicrograph -----	50
64. Representation of various cross sections of clay sample thin sections from thick to ultrathin -----	53
65. Geotechnical properties, core B-1 -----	55
66. Porosity versus depth, core B-1 -----	56



Figure	Page
* 67. Clay fabric of randomly oriented domains, core B-1 (1.4 m) -----	57
* 68. Clay fabric of randomly oriented domains and a few short chains, core B-1 (1.4 m) -----	58
* 69. Clay fabric of randomly oriented domains showing numerous edge-to-face particle contacts, core B-1 (2.0 m) -----	58
* 70. Clay fabric showing randomly oriented domains, core B-1 (2.0 m) --	58
* 71. Clay fabric showing randomly oriented domains, with pronounced particle contacts and short chains, core B-1 (2.0 m) -----	59
* 72. Clay fabric showing short chains, arching, and particle contacts, core B-1 (2.0 m) -----	59
* 73. Clay fabric of randomly oriented domains, core B-2 (9.3 m) -----	59
* 74. Clay fabric of randomly oriented domains, core B-2 (9.3 m) -----	59
* 75. Clay fabric of well-defined domains, core B-1 (27.7 m) -----	60
* 76. Clay fabric of well-defined randomly oriented domains, core B-2 (27.6 m) -----	60
* 77. Clay fabric having relatively large domains, core B-1 (27.7 m) -----	60
* 78. Clay fabric of domains and chains, core B-1 (27.7 m) -----	61
* 79. Clay fabric of domains with pronounced particle contacts, core B-1 (27.7 m) -----	61
* 80. Clay fabric of randomly oriented domains with very fine "clusters" of particles around the domains, core B-1 (1.4 m) -----	61
* 81. Clay fabric of highly oriented domains that include obliquely oriented domains, core B-1 (120.4 m) -----	62
* 82. Clay fabric depicting highly oriented clay particles and bending around large electron dense particles, core B-1 (120.4 m) -----	62
* 83. Clay fabric of highly oriented domains, core B-1 (144.8 m) -----	63
* 84. Clay fabric of highly oriented domains in which not all particles are oriented preferentially, core B-1 (144.8 m) -----	63
85. Calculated cumulative stress with depth in core B-1 (buoyant overburden stress assuming no excess pore water pressure) -----	68
86. Void ratio core B-1 -----	69
87. Comparison of overburden stress determined by Hamilton (1959) method (based on consolidation data) and by laboratory-measured mass physical properties -----	70
* 88. Clay fabric of laboratory consolidated sample (load $61.29 \times 10^2$ kPa), core B-1 (1.4 m) -----	71
* 89. Clay fabric of laboratory consolidated sample (load $61.29 \times 10^2$ kPa), core B-1 (2.0 m) -----	71
* 90. Clay fabric of laboratory consolidated sample (load $61.29 \times 10^2$ kPa), core B-1 (12.2 m) -----	71
* 91. Clay fabric of laboratory consolidated sample (load $61.29 \times 10^2$ kPa), core B-1 (120.5 m) -----	72
* 92. Clay fabric of laboratory consolidated sample (load $15.32 \times 10^2$ kPa), core B-1 (27.7 m) -----	72
* 93. Clay fabric of laboratory consolidated sample (load $19.15 \times 10^2$ kPa), core B-1 (120.5 m) -----	72
94. Proposed tentative clay fabric models for submarine sediment -----	78

---

\* Transmission electron microscope photomicrograph.



# Clay Fabric and Geotechnical Properties of Selected Submarine Sediment Cores From the Mississippi Delta

*Richard H. Bennett, William R. Bryant, and George H. Keller*

**ABSTRACT.**—Results are reported of research on clay fabrics and selected geotechnical properties of submarine sediment samples—to core depths of 150 m—from the Mississippi prodelta depositional environment. The clay fabric of a Deep Sea Drilling Project sample is compared with the Delta samples because of its highly complex nature in the undisturbed versus the remolded states. Techniques of transmission electron microscopy, unique sample preparation, and quality control were used in the analyses. Three general areas of this investigation include: 1) A comprehensive literature review tracing the evolution of thought and development of concepts about clay fabrics; 2) a detailed study of analytical techniques, instrumentation, and sample quality as applied to clay fabrics; and 3) a study relating clay fabrics to selected geotechnical properties, depth of burial, and laboratory consolidation loads. Characteristics of clay fabrics in natural versus laboratory consolidated samples were evaluated. Tentative clay fabric models related to predicted void ratios were proposed for submarine sediments.

## INTRODUCTION

### *General Statement*

#### **Clay soils and marine geotechnical properties**

Soils engineers, soils scientists, and engineering geologists have been studying the physical and chemical properties of clay soils for several decades. Recently, marine geologists and engineers have been investigating the engineering behavior and fundamental nature of submarine sediments in terms of their geotechnical properties and sedimentological characteristics (Hamilton and Menard 1956; Hamilton 1959, 1960, 1964; Moore 1961; Richards 1961, 1962; Ingelman and Hamilton 1963; Richards and Hamilton 1967; McClelland 1967; Morgenstern 1967; Bryant and Wallin 1968; Keller and Bennett 1968). Study of marine sediment geotechnical properties includes all of the engineering and scientific aspects of the sedimentary material, specifically the chemical, mechanical, acoustical, biological, and physical properties of the electrolyte-gas-solid system and

its response to static and dynamic loads. The soils engineer, concerned with deposits on land or in the marine environment, determines the physical and mechanical properties of soils in order to accurately predict their behavior. Structures must be designed to meet specific conditions of soil strength, slope stability, and unique environmental conditions. On the other hand, the geologist is concerned with the relationships of the geotechnical properties of soils and their fundamental nature (i.e., texture, grain size and shape, fabric, and physicochemical properties) to the depositional history and diagenesis of sedimentary deposits in order to delineate complex geological processes.

#### **Soil, sediment, and clay minerals**

In a general engineering sense, soil is any unconsolidated material composed of discrete solid particles and interstitial gas and/or liquids (Sowers and Sowers 1961). More

specifically, soil has been described as a particulate, multiphase system; particulate refers to a system of soil particles (solids), and multiphase pertains to a system consisting of the mineral phase (solids) plus a fluid phase (Lambe and Whitman 1969). The mineral phase is often called the mineral skeleton and the fluid phase is the pore fluid. In some cases, soils include air or gas; however, soils below the water table and many deep-sea sediments may be totally saturated (the interparticle voids are completely filled with water). The pore fluid and its constituents, such as dissolved salts and organic compounds, will affect the nature of the clay mineral surfaces and therefore affect the processes of force transmission at the particle contacts. This type of interaction between the phases is referred to as chemical interaction (Lambe and Whitman 1969).

Sediment, to the geologist, is a deposit formed by the agents of water, wind, or ice and a product of chemical, biological, and physical weathering of solid material on the earth's surface. The term soil generally denotes those residual materials that accumulate during weathering (Krumbein and Sloss 1959). The terms soil and sediment are used interchangeably in this study depending upon the engineering or geological context of discussion. The most important and active constituents of a soil (sediment) are the clay minerals which are basically hydrous-aluminum silicates with unique layered or sheetlike structures. Technically, clay minerals are classified as phyllosilicates. Prior to 1923, however, clays were thought to be amorphous (Hadding 1923). Clays are generally less than 2  $\mu\text{m}$  in diameter although some clay minerals exceed this size. The most common clay minerals are kaolinite, montmorillonite (smectite), and illite. A few of the less common clays are allophane, halloysite, chlorite, and attapulgite. Clay mineralogy and clay classification can be found in Grim (1940, 1962, 1968) and in Grim and Johns (1958). An excellent review of chemical weathering of silicate minerals is given by Keller (1957). The reader is also referred to studies by Rateev and others (1969) and Lisitzen (1972) of clay mineral distribution in the world ocean basins.

### Clay microstructure and clay fabric

Clay microstructure refers to two important properties of a soil—the fabric and the physicochemistry (Mitchell 1956; Lambe 1958a; Foster and De 1971). Clay fabric, a geotechnical property of soil, is defined as the orientation and arrangement (spatial distribution) of the solid particles (generally  $<3.9 \mu\text{m}$  in size) and the particle-to-particle relationships. The physicochemistry pertains to the interparticle forces of the sediment. The clay minerals in most sedimentary deposits are not of the same size, shape, and mineralogy, and these characteristics coupled with the physicochemistry play a significant role in establishing the ultimate fabric at the time of deposition.

The geotechnical properties commonly studied include

shear strength, water content, unit weight, void ratio and porosity, permeability, and consolidation characteristics. These properties are strongly influenced and largely controlled in clay sediment by the fabric and physicochemistry, but very little is actually known of the microstructure in natural deposits (Lambe 1958a; Rosenqvist 1959, 1962). The understanding of clay microstructure (fabric and interparticle forces) and the related geotechnical properties is an important prerequisite to meaningful predictions of the engineering behavior of sedimentary deposits in response to static and dynamic loads, and to variations in environmental conditions (Lambe 1958a). Equally important, the study of clay microstructure is highly significant to the understanding of detailed changes in sedimentary deposits during diagenesis and sedimentary rock history.

Usually, the geotechnical properties of sedimentary material are easily determined by well established standard soil mechanics techniques, unlike the study of clay fabric which requires sophisticated techniques of transmission or scanning electron microscopy (T.E.M. and S.E.M., respectively) for the delineation of particle arrangements. This study was focused on a few significant aspects of submarine sediment clay fabric utilizing techniques of transmission electron microscopy.

## Objectives

### General purpose of the investigation

The purpose of this research was a detailed assessment of the clay fabric and selected geotechnical properties of submarine sediment from the Mississippi prodelta depositional environment sampling to depths of 150 m. Fabric analysis was carried out using techniques of transmission electron microscopy, unique sample preparation, and quality control. Relationships among the fabrics and selected geotechnical properties characteristic of Mississippi Delta sediments were investigated. The geotechnical properties of these Delta sediments, especially their variation with depth, play a critical role in the safe and proper design of offshore drilling platforms and manmade emplaced structures. An understanding of the changes that submarine sediments undergo during natural consolidation is a basic prerequisite in determining factors responsible for certain sediment properties.

Most previous studies of clay fabric have dealt with laboratory sedimented material, and a few investigations were concerned with marine quick clays. Although these studies provided an insight into the probable or possible nature of clay fabric in natural sedimentary deposits, studies by Bowles (1968a) and Bowles and others (1969) are the only detailed investigations of the clay particle relationships in submarine sediments. However, these studies were limited to sample depths of 10 m. No literature is known dealing with clay fabric and changes in particle orientation that oc-



cur during natural consolidation at significant depths of burial in submarine sediment. Clay orientation and particle rearrangement with increasing depth of burial are important factors in the development of shale. These factors were evaluated and formed an integral part of this research.

In order to clearly evaluate the fabric observed in the Mississippi Delta samples, a comprehensive review of the literature was made tracing the concepts and evolution of thought concerning clay fabric from early theories to recent findings. Several models of clay fabric have been proposed in the literature. These representations form a basis for comparison and evaluation with the fabric characteristic of the sediments studied.

### Specific objectives

The two major objectives of this study were to identify the "type" of fabric observed in the sediment core samples—such as single grain, domain, "turbostratic," floccule, dispersed, aggregated, etc.—and to delineate characteristic particle-to-particle arrangements with depth in cores to 150 m. To do this, photomicrographs of ultrathin sections of sediment samples were studied. The samples were extracted at selected depths in two cores from the same general Mississippi Delta location. Their observed fabric was compared with that of fabric models proposed in the literature and changes in fabric with increasing depth in the cores were assessed.

Other objectives—to learn more about development of fabric characteristics, their relation to depositional environments and geotechnical properties of the sediments, and analytical techniques and methods of investigation—were:

(1) To compare clay fabric for selected depths of burial and associated (estimated) overburden pressures with typical fabric characteristics of unconsolidated surficial sediment;

(2) To compare the fabric of naturally consolidated and laboratory-consolidated sediment samples, using transmission electron micrographs;

(3) To address the question of depth of burial versus fissility as related to the Mississippi Delta sediment and the environment of deposition, specifically to study the development of fissility in clay to form shales as a function of clay flake orientation in response to overburden pressure.

(4) To observe [possible] relationships between clay fabric characteristics and geotechnical properties of sediments;

(5) To determine changes in void ratio ( $e$ ) as a function of depth of burial, as determined from transmission electron micrographs and by standard geotechnical laboratory measurements;

(6) To demonstrate the usefulness and application of image enhancement techniques in the study of clay fabrics, using transmission electron micrographs; and

(7) To assess sample preparation techniques by using image enhancement techniques applied to transmission electron micrographs to determine void ratios (versus values obtained by standard laboratory techniques); and by observing (assessing) clay particle-to-particle integrity in response to sampling and transmission electron microscope preparatory techniques (by comparing undisturbed versus laboratory remolded sample fabrics).

## Literature Review—Clay Fabric

### *Physicochemistry of Clays*

The physicochemistry of clays is critical in determining the nature of clay fabric, especially in the early stage of formation. A brief discussion of its role is fundamental to the understanding of clay fabric. Detailed studies of this aspect of clay microstructure and its influence on the mechanical properties of soils are presented by Winterkorn (1948), Bolt (1965), Lambe (1958a), Rosenqvist (1959, 1962), Warner (1964), Buchanan (1964), and Ingles (1968). Excellent discussions concerning the physicochemistry of clays and colloids in general can be found in Kruyt (1952) and van Olphen (1963).

The physicochemical forces controlling clay mineral structure and the initial framework of clay fabric are essentially electrical in character. Suspended clay particles interact in response to the electrical nature of the particle surface and to the characteristics of the surrounding aqueous medium. The electrical forces can be classified as primary valence bonds, hydrogen bonds, van der Waals

forces, and simple electrostatic interactions (Lambe 1958a). Primary valence bonds hold atoms of individual clay particles together. These short-range powerful forces are highly directional and thus determine the crystal structure of the various clay minerals. Most clay minerals, specifically the phyllosilicates, are made up of sheets (tetrahedral and octahedral coordination polyhedra) generally in 1-to-1 or 1-to-2 layers such as one tetrahedral sheet plus one octahedral sheet (kaolinite), or two tetrahedral plus one octahedral sheet (smectite, illite, and chlorite). Thus most clay minerals are platy or sheetlike and for practical purposes can be considered as approximately two-dimensional. In addition, they possess an enormous surface area to mass ratio (specific surface,  $m^2/g$ ). Most clay particles are considered colloids which range in size from about  $1\ \mu m$  to as small as  $0.0001\ \mu m$ . However, some clay minerals are somewhat larger than colloid size. When a particle has a specific surface sufficient to have electrical forces which dominate mass forces, the particle is considered a colloid.



Hydrogen bonds hold hydrogen atoms to oxygen, nitrogen, or fluorine atoms. Although hydrogen atoms each have only one primary valence bond, each may be held to a second atom by a hydrogen bond. These hydrogen bonds are important only between hydrogen atoms and atoms of oxygen in clay-water systems. Hydrogen bonds are short range and directional much like primary valence bonds but they are only about one-tenth as strong. Van der Waals forces are somewhat weaker and less highly directional but of longer range than the primary valence forces and hydrogen bonds. Van der Waals forces and in some cases hydrogen bonds function in such a way as to hold the essentially two-dimensional clay mineral layers together to form relatively thin particles. During flocculation of suspended clay particles, deposition, and also during low pressure diagenesis, clay crystals are not generally broken (i.e., primary valence bonds are not broken) nor are the clay layers separated (Lambe 1958a). Although the absolute range of pressures may vary for different clay minerals, the breaking of interlayer bonds appears to be indicative of the onset of high pressure diagenesis as revealed through studies of consolidated kaolinite (Cabrera and Smalley 1971).

Electrostatic forces engender attraction between oppositely charged entities and repulsion between similarly charged ones. These forces are omnidirectional, somewhat weaker but of longer range than those forces previously discussed. Electrostatic interactions are critical in determining clay microstructure, particularly clay fabric, because clay particles carry a net negative charge which is large compared to the particle mass. The net charge varies with the clay mineral type and the charge is a function of isomorphous substitution in the crystal (lattice) structure. An additional complicating factor is introduced by the small positive charge carried by particle edges under certain conditions (Thiessen 1942; van Olphen 1963).

### *Physicochemistry of Flocculation and Dispersion*

The balance of the attractive van der Waals forces and the repulsive electrostatic forces active between particles determines whether the clay particles will flocculate (form aggregates) or disperse (remain in suspension as single particles during settling). The van der Waals forces are invariant and largely fixed by the specific clay minerals involved; however, the electrostatic interactions are easily modified by the physicochemical characteristics of the medium surrounding the particles. The electrostatic interaction in water is between the mobile atmospheres of hydrated positive ions (sometimes termed the double layers) that surround the negatively charged particles, rather than between the particles themselves. The total charge of the positive ions in the atmosphere of a clay particle is equal to the net charge of the particle, and it is thus approximately

invariant, but the density of the atmosphere of charge varies with the electrolyte concentration, ion valence, size of the hydrated ion, temperature, and dielectric constant.

Increasing electrolyte concentration and ion valence and decreasing hydrated ion size, temperature, and dielectric constant increases the density of the atmospheres of charge, and the atmospheres shrink in toward the particles. Thus the particles may approach each other more closely, and under the influence of thermal agitation, the shorter range attractive van der Waals forces come into play.

The combination of the physicochemical forces and changes in the variables of the clay colloid system determines whether the clay particles will flocculate or disperse. In natural systems, mixed electrolytes are the rule, and the variable of paramount importance which affects the ionic atmospheres is the electrolyte concentration (salinity). As an example, clay minerals are introduced to a relatively rapidly changing physicochemical environment in natural systems when rivers and streams discharge sediment into highly saline bodies of water such as coastal embayments, lagoons, and ocean basins in general or into estuaries and brackish waters high in organic compounds. Chemical reactions on the clay surfaces can alter the net charge of the particles and thus affect the physicochemistry of flocculation and dispersion. Important indicators for such chemical reactions in natural systems are the pH and the concentrations of organic anions and cations. Although the role of organic compounds in determining soil microstructure, and particularly clay fabric, has been shown to be significant, it is imperfectly understood (Meade 1964; O'Brien 1970a).

The electrical forces active among clay particles are important in determining the arrangement of clay minerals during deposition, whereas mechanical factors such as effective overburden pressures and in some cases lateral stresses are important in determining post depositional changes in fabric. Further changes in fabric subsequent to deposition can be brought about by migration of pore water solutions, living organisms, drying, and frost action (Gillott 1969).

### *Concepts of Clay Fabric*

#### *Early concepts*

Perhaps the earliest concept of clay fabric was presented by Terzaghi (1925a) in a discussion on arrangement of soil particles and the bonding of cohesive soils; although as early as 1908, Sorby (1908) alluded to the importance of clay particle arrangement during settling and consolidation. Terzaghi proposed that clay minerals stick to each other at points of contact with forces sufficiently strong to construct a type of honeycomb structure, permitting large amounts of water to be enclosed within the voids. Each unit or cell of the honeycomb was envisioned as being made up of numerous single grains held together by adhesion. Later, Casagrande (1932) presented an idea of the honeycomb struc-



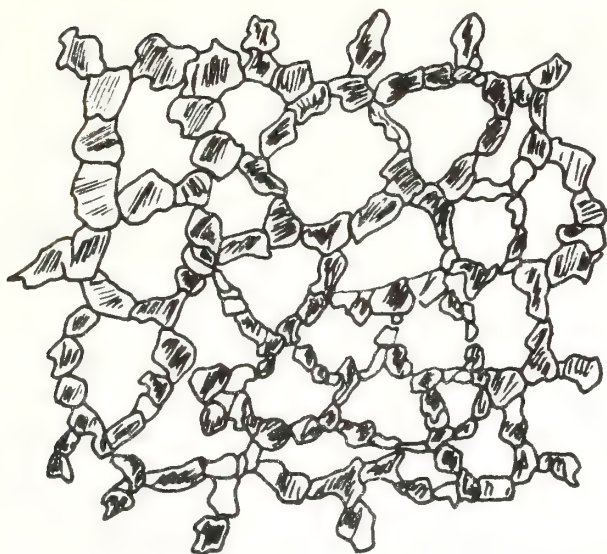


FIGURE 1.—Honeycomb structure. (Terzaghi-Casagrande 1925)

ture of sensitive soils very similar to Terzaghi's concept. This type of clay fabric is usually referred to as the Terzaghi-Casagrande honeycomb structure (fig. 1). Subsequent to Terzaghi's published work, Goldschmidt (1926) proposed that clay properties were due to crystalline minerals enclosed by a film of adsorbed water molecules. The water molecules were considered to stick to each other and to the mineral grains because of their dipolar moment. Goldschmidt proposed that the flaky minerals of highly sensitive clays were arranged in an unstable cardhouse structure. This structure was assumed to have a dominance of particle edge-to-face contacts. Over 20 years later, Lambe (1953) presented schematic diagrams of clay mineral arrangements similar to Goldschmidt's concept of clay fabric (fig. 2). Lambe proposed that undisturbed marine clays had an open structure similar to the cardhouse structure; however, the fabric of fresh water clays was thought to be somewhat denser (fig. 3). Remolded clay was assumed to have a high degree of parallelism between adjacent particles (fig. 4). The Goldschmidt-Lambe concept of cardhouse structure is clearly quite different from the Terzaghi-Casagrande honeycomb concept. Rosenqvist (1955) and Bjerrum and Rosenqvist (1956) presented similar views of the cardhouse fabric; however, their means of optical light microscopy were not completely satisfactory for definitive conclusions. The cardhouse fabric was also discussed and proposed by Hofmann as early as 1942, although his work was considerably later than Goldschmidt's initial studies.

Lambe (1953) considered that the random arrangement (cardhouse fabric) of the particles occurs when clay sediment enters salt water with a high electrolytic concentration. Flocculation of these particles causes them to settle simultaneously with silt particles and fine sand forming a loose porous structure. However, clay deposited in fresh

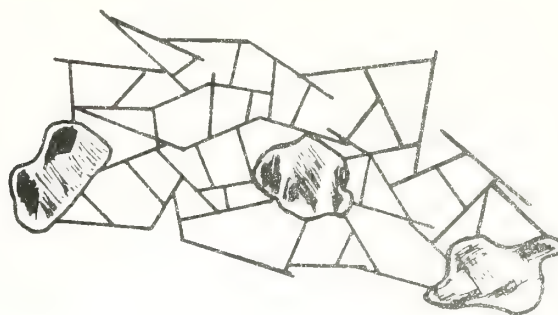


FIGURE 2.—Cardhouse structure. Saltwater deposit. (Goldschmidt-Lambe 1953)

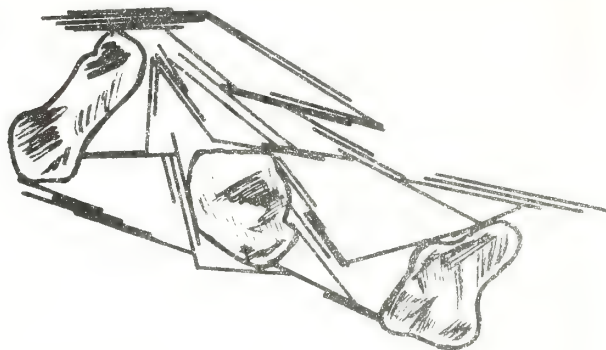


FIGURE 3.—Cardhouse structure. Freshwater deposit. (Lambe 1953)

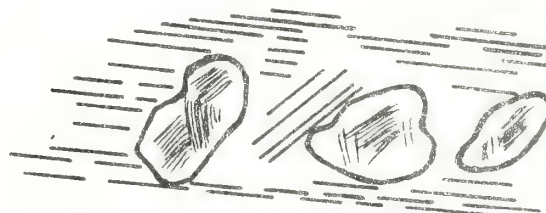


FIGURE 4.—Remolded structure. (Lambe 1953)

water remains dispersed and settles with a slower velocity than silt and forms a much greater degree of parallel particle orientation (oriented fabric). Thus, according to Lambe (1953), particle orientation in a dispersed system is a parallel arrangement (oriented fabric), whereas in a flocculated system it is a random arrangement (cardhouse fabric). Flocculation of a clay is thought to occur by electrostatic attraction of positively charged particle edges and negatively charged particle faces. Theissen (1942) has substantiated these electrostatic properties for some clays.

In an effort to reconstruct the environments of deposition for argillaceous rocks, Urbain (1937) used the optical microscope to delineate the microfabrics. He recognized the importance of the effects of electrolytes on the clay particle arrangements. Powers (1957) investigated clay floccules of suspended sediment from various estuaries. His studies indi-

ated a decrease in floccule size and a slight increase in crystal size in the downstream (estuary) direction. In the Chesapeake Bay area he found no size sorting or mineralogical sorting of clay minerals in the suspended sediment. In the Atchafalaya Bay area his studies showed that at 1 to 10 parts per thousand salinity (‰), rapid deposition of mud occurred due to flocculation.

Mitchell (1956) pointed out three important differences between dispersed and flocculated clays in relation to their geotechnical properties.

(1) For any given consolidation pressure, the weight of clay occupies a smaller volume in the dispersed or oriented state than in a flocculated condition.

(2) Dispersed clay particles are distributed more uniformly throughout a given volume than are particles distributed in a flocculated clay.

(3) For a given increment of stress, there is greater shifting of particles relative to one another in a flocculated clay than in a dispersed clay.

Fabric studies by Mitchell (1956) of undisturbed and remolded clays revealed that silt particles were not in contact with each other in either a remolded or undisturbed state. The silt appeared to "float" in a clay matrix, even in soils with greater than 75 percent of the particles larger than  $2\ \mu\text{m}$ . Remolding tended to homogenize the sample rendering the clay less variable. An improvement in the parallel orientation of clay platelets was greater in remolded samples than undisturbed samples when they were compressed one-dimensionally at natural water contents to loads of 196 kPa. Remolding caused preferred orientation over small areas such that oriented areas shifted smoothly from particle alignment in one direction to particle alignment in another direction. Over large areas, preferred particle orientation parallel to one direction was not strong; apparently kneading is responsible for this, because there is no force tending to orient particles in one direction. The illite-chlorite group of marine clays was observed to undergo the greatest change in grain orientation and engineering properties as a result of remolding when compared to the illite-montmorillonite fresh water clays and the Mexico City clay, which is described as a weathered volcanic glass. Mitchell (1956) also found that the clays deposited in marine or brackish water which had undergone natural precompression of up to 234 kPa (1 psi = 6.89 kPa) exhibited some degree of parallel particle orientation. Rosenqvist (1955) noted that the highly sensitive Norwegian marine clays showed almost complete random particle orientation, although they had never been consolidated to a great degree. Mitchell concluded that the concepts of Lambe (1953) were essentially correct for fresh water, marine, and remolded clays. However, deposition of clay in "fresh" water may not in every case produce an oriented fabric because impurities in the depositional water and the nature of the adsorbed cations

may affect the dispersion of the clay platelets during sedimentation. The reader is referred to early detailed studies of compaction, engineering properties, and clay fabric by Seed and Chan (1959), Trollope and Chan (1960), and Lambe (1960). Mechanical aspects of clay fabric have been studied also by ceramicists Weymouth and Williamson (1953), and Williamson (1947, 1960a, 1960b).

Early concepts of clay fabric were depicted as two-dimensional figures which actually represented three-dimensional arrangements of clay particles. Later, Tan (1957; 1959) presented a schematic picture of clay fabric with a three-dimensional configuration (fig. 5), showing a clay mineral network dominated by contacts between corners and planes of mineral particles. Rosenqvist (1959) using electron microscopy (carbon replication) confirmed the Goldschmidt-Lambe cardhouse concept of undisturbed clay. The mineral arrangement was dominated by contacts between corners and planes and was similar to the fabric proposed by Tan. This arrangement was found for all marine clays examined by Rosenqvist. Complete random orientation of illite and kaolinite particles in marine clay from the north-eastern area of the Black Sea was reported by Raitburd (1960). Different degrees of random and preferred orientation were reported by Wu (1958) for glacial-lake clays from the Great Lakes region. The arrangements could not be related, however, to the types and concentrations of ions.



FIGURE 5.—Three-dimensional representation of clay structure. (Tan 1957)

Lambe (1958a) described slightly different concepts of clay fabric than he had proposed in 1953 (figs. 6, 7, and 8). Salt type flocculation with grain orientation approaching parallelism and a somewhat open network indicative of moderately high void ratio was depicted (fig. 6). The non-salt type fabric exhibited a purely edge-to-face relationship among grains resulting in a high void ratio framework (fig. 7). The dispersed particle arrangement (fig. 8) is quite sim-



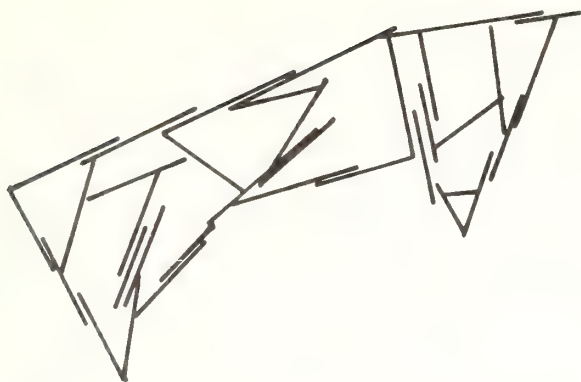


FIGURE 6.—Salt-flocculated cardhouse structure with a stair-step configuration. (Lambe 1958)

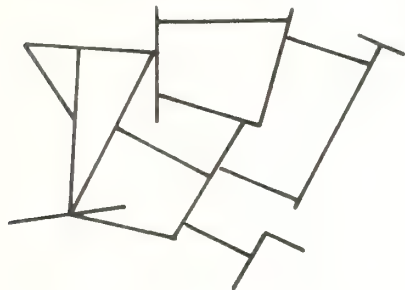


FIGURE 7.—Nonsalt-flocculated well-developed cardhouse structure. (Lambe 1958)



FIGURE 8.—Dispersed structure with preferred grain orientation. (Lambe 1958)

ilar to his earlier representation presented in 1953. An essential difference in the fabric concepts presented in 1958 was the absence of silt particles. Similar clay mineral arrangements were also shown by Schofield and Samson (1954). Other studies indicated that in sands permeated with clay suspensions, the clay plates orient parallel to the sand surfaces (Brewer and Haldans 1957). Clearly, the presence of silt and sand mixed with clays would influence the overall arrangements of the clay particles in close proximity to the larger grains.

Lambe's studies (1958a) with pure kaolinite indicated that the particles flocculate with an edge-to-face arrangement and that a small amount of salt results in dispersion. High concentrations of salt result in flocculation, but the increase in anions which gather at the particle edges results in a less effective positive charge over a smaller distance yielding a lower degree of flocculation (fig. 6). The reader is referred to a companion paper by Lambe (1958b) dis-

cussing the relationships between fabric and the engineering behavior of clay.

Van Olphen (1963) depicted in a descriptive sense the difference in particle arrangement of sedimentation from a peptized versus a flocculated suspension (fig. 9a, 9b). The main intent was to show that flocculated particles form a loose, voluminous sediment in contrast to a relatively dense sediment of closely packed particles formed from a peptized suspension. This would be equivalent to Lambe's flocculated versus dispersed fabrics respectively. Models were proposed by Von Engelhardt and Gaida (1963) depicting voluminous clay structure (large aggregates) indicative of high salinity water and a more dense small aggregate structure characteristic of low salinity water. Van Olphen (1963) further described various conceptual models of possible modes of particle association (figs. 10a–g). His basic difference in the scheme of particle associations was the “dispersed” single particle (fig. 10a) versus the “aggregated” compound particle (fig. 10b) interaction. Van Olphen points out that three modes of particle association

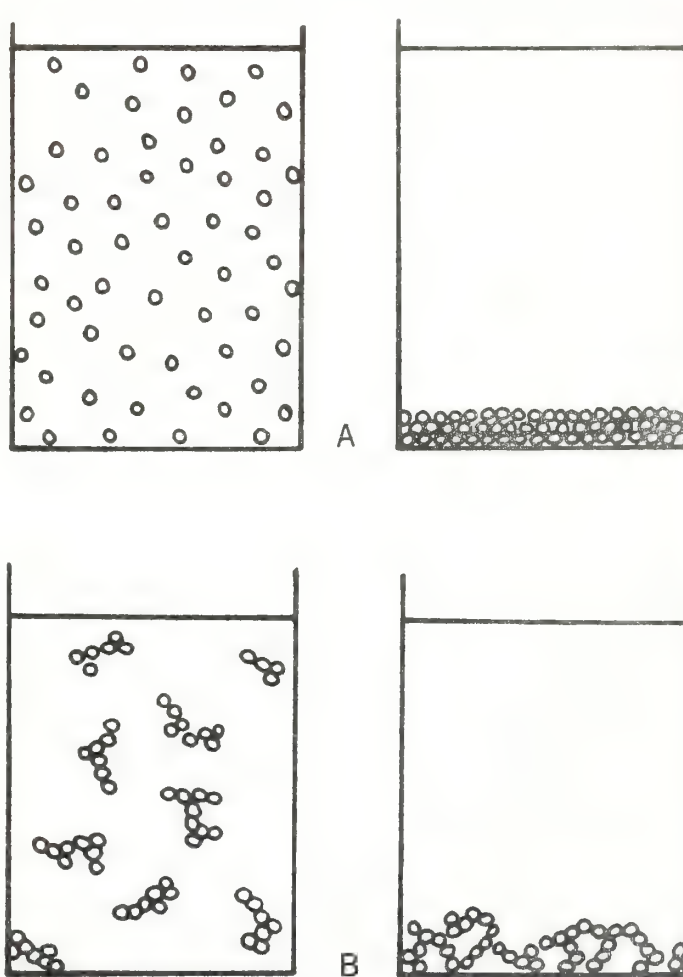


FIGURE 9.—Sedimentation from a peptized and a flocculated suspension (van Olphen 1963). (A) Peptized suspension; dense, close-packed sediment. (B) Flocculated suspension; loose voluminous sediment.

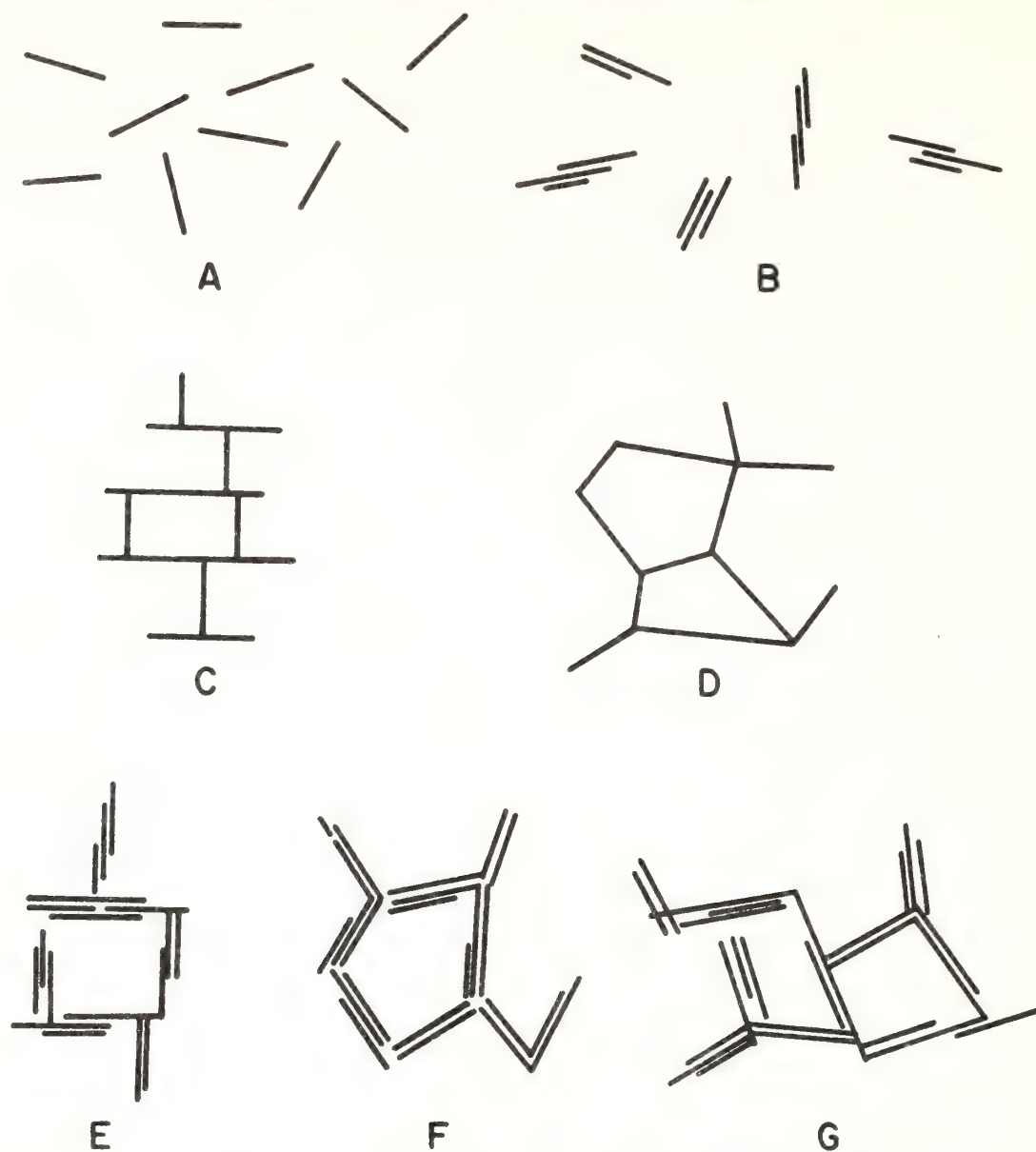


FIGURE 10.—Various modes of particle association (van Olphen 1963). (A) "Dispersed" and "deflocculated." (B) "Aggregated" but "deflocculated." (C) EF flocculated but "dispersed." (D) EE flocculated but "dispersed." (E) EF flocculated and "aggregated." (F) EE flocculated and "aggregated." (G) EF and EE flocculated and "aggregated."

are possible when platelike clay particles flocculate (FF, face-to-face; EF, edge-to-face; EE, edge-to-edge). Only EE and EF types of particle association produce agglomerates which he terms "flocs." The FF association is termed "aggregation" that refers not only to several FF multilayer particles but also to the degree of unit-layer stacking in a single particle. The type of particle association actually produced will depend strongly on the physicochemistry of the suspension during sedimentation. Apparently all of the models described by van Olphen have not been found for natural sediments (Moon 1972). The models, however, do afford a means of reference for the study of fabric in natural clay-water systems.

Prior to 1962, a few fabric studies of naturally consoli-

dated clayey sediments had been published (Grim and others 1957; Kaarsberg 1959; White 1961; Meade 1961). In an excellent review of particle arrangement during compaction (consolidation) of clayey sediment, Meade (1964) contended that there was meager evidence showing that preferred and turbostratic fabrics are formed readily and generally during natural compaction (consolidation) although these fabrics could be reproduced in laboratory tests.

Using X-ray diffraction techniques, Quigley and Thompson (1966) found that reorientation of clay platelets occurred during anisotropic consolidation of Leda marine clay and an abrupt increase in parallelism occurred at pressures exceeding the preconsolidation pressure. In undisturbed



samples, reorientation was in a plane perpendicular to the direction of the major principal consolidation pressure. Greater particle parallelism was produced at lower pressures in remolded samples relative to undisturbed clays, but the fabric-versus-void ratio relationship was the same for both undisturbed and remolded samples. Smart (1967), using artificially prepared kaolinite samples (mixed with distilled water) and techniques of electron microscopy, found that the unconsolidated samples exhibited random arrangements of particles or of small groups of particles. Failure zones in sheared samples showed preferred orientation of particles parallel to the zone of shear. Preferred orientation and turbostratic structure developed during consolidation testing. Smart also noted that nothing similar to a cardhouse structure or salt flocculated fabric was observed in any of the tested samples.

### Later concepts and observations

During the past 15 years, studies of clay fabric have been gaining momentum with the advent of the electron microscope (E.M.), and renewed interest has resulted in numerous investigations of clay particle arrangements in sediment by direct observation. Rosenqvist (1959) set the stage for E.M. studies of clay fabric which were to follow in the 1960s. Even as early as 1947, Hast employed the transmission electron microscope in the study of clays. Although his work primarily described techniques, the study pointed out that clay consisted of small plane crystals such as rounded plates and that these plates were placed one upon the other with a slight displacement of each.

Aylmore and Quirk (1960) proposed the term "turbostratic" arrangement for a fabric consisting of domains or "stacks" (Aylmore and Quirk 1959; Sides and Barden 1971)—also referred to as "tactoids," "packets," or "clusters" of clay platelets—among which the preferred orientation is nearly perfect (figs. 11, 12). Kell (1964) and Sloane and Kell (1966) described a clay fabric similar to the "turbostratic" arrangement but with more open structure, which they called bookhouse fabric or book structures (fig. 13). Ingles (1968) referred to this fabric as "card-house."

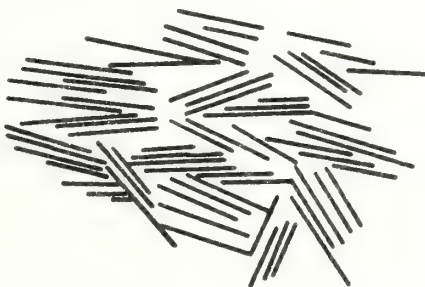


FIGURE 11.—"Turbostratic" structure. (Aylmore and Quirk 1960)



FIGURE 12.—Perfect "stack." (Sides and Barden 1970)

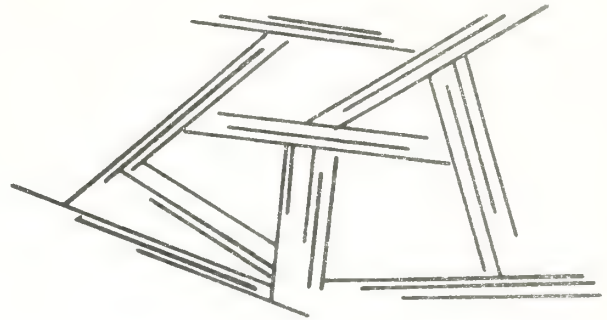


FIGURE 13.—Bookhouse or book structure. (Kell 1964 modified; Sloan and Kell 1966)

Evidence supporting this "turbostratic" type fabric was given by Rosenqvist (1959) although the term had not been proposed at that time. Types of domains were described by Sloane and Kell (1966) as "books" (fig. 14a) and by Smalley and Cabrera (1969) as "stepped face-to-face" (figs. 14b, 14c). In retrospect, the "stepped face-to-face" appears to have been alluded to by Hast (1947) and the "book" seems to be equivalent to the "aggregated" particle described by van Olphen (1963).



A



B



C

FIGURE 14.—Domain structures (from Moon 1972). A. "Book" (Sloan and Kell 1966). B and C. "Stepped face-to-face" (Smalley and Cabrera 1969).

O'Brien and Harrison (1967) investigated clay flake orientation in a sensitive illitic Pleistocene marine clay using electron microscopy. Carbon replicas were made of air-dried samples and examined by T.E.M. Random orientation of clay flakes was the most apparent feature, and the silt grains appeared to float in the clay matrix. They concluded that the random orientation of the clay flakes was probably caused by flocculation in a saline environment. The fabric of highly sensitive clays also has been studied by Karlsson and Pusch (1967).

The fabric of Ordovician shale and mudstone from Ontario was compared with post-Pleistocene marine deposited clay (Gillott 1969). The study was made using the petrographic microscope and scanning electron microscope (S.E.M.). Petrographic microscopic examination of the fissile shale indicated a strong but not perfect degree of preferred orientation of the micaceous particles. Observation of the mudstone showed little to no preferred orientation among platy minerals. At low S.E.M. magnification ( $\sim 300\times$ ) of the shale, preferred orientation was apparent; however, at higher magnifications ( $\sim 3,600\times$ ), preferred grain orientation was less apparent, and platy minerals were observed to be arranged at large angles to the fissility of the shale. Apparently, fissility in some shales does not require perfectly oriented particles but rather depends on a sufficiently large number of grains with parallel arrangement to establish the fissile property. Observations of the mudstone with the S.E.M. confirmed the light microscopic observations of random particle orientation. Scanning electron micrographs of Leda clay revealed random particle orientation in some samples and preferred orientation in others. The Leda clay samples had been subjected to a natural preconsolidation of about 490 kPa. These clays deposited under marine conditions would be expected to exhibit some degree of random arrangement of particles. However, some photographs showed that the orientation was far from perfect with many crystal faces and edges at oblique angles.

Strong preferred orientation of clay particles in argillaceous rocks has been reported by several investigators. White (1961) noted that random orientation of clay minerals in shales resulted in poor fissility, whereas fissile shales show clay minerals oriented with the longest dimensions parallel to the bedding. White attributed flocculation in saline environments to random orientation and concluded that in a sedimentary environment of low salt concentration the particles would settle as individual particles with parallel orientation ultimately producing a well developed fissile shale. Preferred orientation of clay particles associated with fissility and organic material in shales has been discussed by Gipson (1965, 1966), Odom (1967), and O'Brien (1968). Martin (1965, 1966) and Martin and Ladd (1970) have discussed techniques for determining clay particle orientation by X-ray measurement.

Electron micrographs of clayey submarine sediment showed that major reduction in void ratio was possible at low pressure during consolidation tests (Bowles and others 1969). At pressures of 49 kPa the fabric exhibited an open but random arrangement of particles, and at 392 kPa with a void ratio of 1.3 the fabric consisted of a denser packing of clumps and packets of particles with an overall random appearance. This would correspond, apparently, to a turbostratic type fabric. Samples consolidated to 3138 kPa and 6276 kPa revealed a high degree of parallelism among particles with some randomly arranged particles. In an earlier study of submarine sediments, Bowles (1968b) concluded that the clay particle arrangements of the undisturbed sediment closely resembled Terzaghi's (1925a) "honeycomb" structure.

Ingles (1968) showed schematically how the "card-house" fabric could change (particle reorientation) during the process of consolidation (fig. 15 and 15a). A reduction in the total volume of the voids occurs by an increase in the degree of particle orientation. Domains are considered to form and increase in size (fig. 15b) along the virgin consolidation curve and to orient wholly in a face-to-face relationship under high pressure (fig. 15c). During consolidation an edge-to-edge fabric (tactoid model, fig. 16) would experience an increase in the area and number of face-to-face bonds and an increase in tactoid links. Of significance here, his "cardhouse" fabric, spelled "card-house," consists of randomly arranged edge-to-face domains (exception—fig. 15a) rather than randomly arranged single particles as proposed in early concepts of clay fabric (fig. 17). This fabric is essentially the same as the "bookhouse" fabric

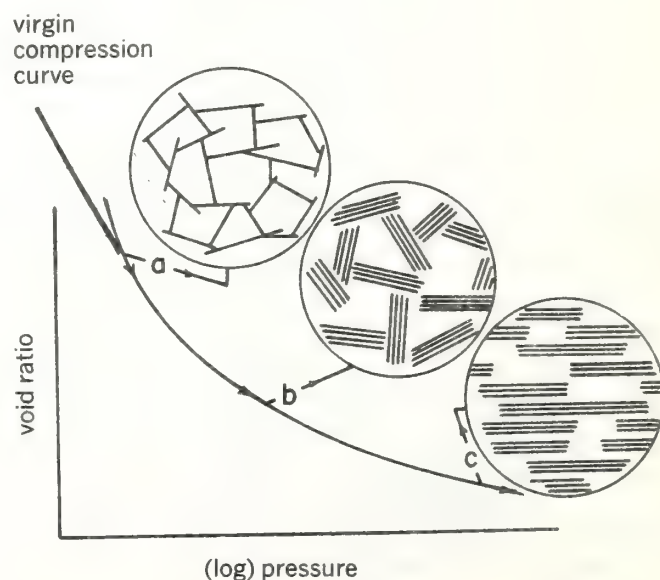


FIGURE 15.—Fabric changes during consolidation in a clay. (From Ingles 1968)



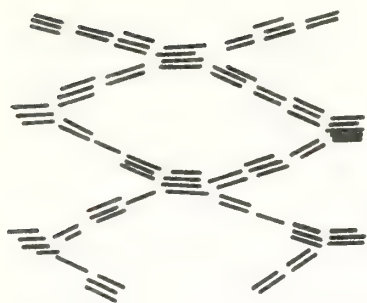


FIGURE 16.—“Tactoid” structure. (From Ingles 1968)

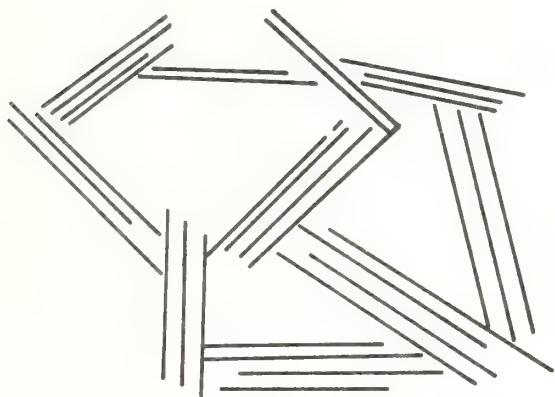


FIGURE 17.—“Card-house” structure. (From Ingles 1968)

of Kell (1964) and Sloane and Kell (1966). Ultrathin section photomicrographs of clayey submarine sediment have provided strong support to the concepts proposed by Ingles (1968) for consolidated clay sediment (Bowles and others 1969).

Barden and Sides (1970) investigated the engineering behavior and structure of selected compacted clay samples. Samples of kaolin compacted both wet and dry of optimum revealed no marked difference in structure but had the turbostratic structure evident at high magnifications (using S.E.M.). Low magnifications (visual assessment) revealed a homogeneous structure wet of optimum but pelletlike macropeds dry of optimum. Similar conclusions about compacted structure were made by Sloane and Kell (1966) and Smart (1967). Tovey (1970) made constructive criticism of the work of Barden and Sides (1970) and stated that particle associations in undisturbed kaolinite had stacks of particles in face-to-face arrangements.

Cabrera and Smalley (1971) pointed out that the characteristic domain structure or turbostratic structure formed in compacted kaolinite soils which they called stepped face-to-face was different from the structure of relatively undisturbed kaolinite systems. Cabrera and Smalley concluded that bookhouse stacks (large particles) are characteristic of undisturbed kaolinite deposits and that during the compaction processes of kaolinite soil from an undisturbed condition, several events occur:

(1) The bookhouse structure is disturbed with the large kaolinite particles successively broken, ultimately reaching the true particle size of  $0.001\ \mu\text{m}$ . The smaller the particle size, the greater the particle strength.

(2) Discrete domains reform; however, the initial regularity is not restored and stepped structures are formed.

(3) Stepped structure is predominant through compaction processes, and this structure becomes the form of particle association. The stepped structure is considered characteristic of compacted kaolinite soils, and the bookhouse stacks characteristic of undisturbed kaolinite deposits.

### Current concepts and observations

Intensified interest in clay microstructure and particularly clay fabric has been evident since about 1970. The acceleration of research has been due not only to the numerous findings and observations made using the electron microscope, but also more significantly to the general overall realization of the importance or influence of clay microstructure on the engineering behavior and the fundamental nature of clayey sediment. Meetings and symposia have been devoted almost entirely to the presentation of current research on clay microstructure, and other conferences have included microstructure with engineering discussions or with clay mineralogy studies in general. Excellent studies were presented at the Southeastern Asian Conferences on Soil Engineering, particularly in 1970 and 1971; the Roscoe Memorial Symposium, 1971, Cambridge University; the 3rd International Conference on Expansive Soils, 1973, Haifa, Israel; The Fourth International Working-Meeting on Soil Micromorphology, Kingston, Ontario, Canada, 1973; the Clays and Clay Minerals Conference, 1973, Banff, Canada; and the International Symposium on Soil Structure, 1973, Gotenburg, Sweden. The earliest studies using the electron microscope employed the transmission electron microscope exclusively. Recently, the scanning electron microscope has been employed frequently to study fractured surfaces of clay samples.

Scanning electron microscope studies of laboratory sedimented kaolinite and illite revealed little difference in the gross structure of either kaolinite or illite floccules formed in distilled water (high clay concentration) and in salt water (low clay concentration) with 1 g/l of NaCl (O'Brien 1970b, 1971). O'Brien suggested that under experimental conditions the double layer is compressed permitting the clay flakes to approach one another closely, resulting in significant van der Waals forces of attraction. Flat flakes of kaolinite would approach each other in a parallel position and the warped illite flakes would arrange in a sub-parallel position. The resulting structures would be an oriented arrangement of stepped clusters (figs. 18, 19). O'Brien considered the honeycomb concept of Terzaghi (1925a) to be more representative of the observed clay fabric than the cardhouse model of Casagrande (1932) and



FIGURE 18.—Stairstep fracture of kaolinite minerals. (O'Brien 1971)

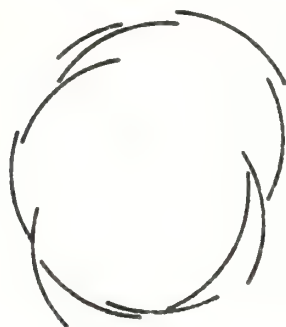


FIGURE 19.—Stairstep structure of illite minerals. (O'Brien 1971)

Tan (1957, 1959), but the fabric was found to be more complex than depicted by the early diagrams. Uncompressed flocculated kaolinite and illite was considered as consisting of a very porous network of randomly oriented flakes or clumps. A single floccule unit of kaolinite had numerous face-to-face flakes in a cluster with a stairstep arrangement. The domains may be oriented at any angle and attached in edge-to-face arrangements. This representation appears quite similar to Lambe's (1958) concept of salt flocculated clays, although he did not "coin" a term for this type of structure. Smalley and Cabrera (1969) also described a similar fabric called "stepped face-to-face." O'Brien's (1971) illite floccule unit consists of several stepped face-to-face oriented flakes.

During S.E.M. investigations of suspended sediments from the Brazos River, Texas, Mathewson and others (1973, and personal communication) observed an increase in floccule size in the downriver direction which corresponded to the increase in salinity. Clay particles were arranged predominantly in face-to-face contact forming a shingle type floc. Also, surficial submarine sediments were reported to be

characterized by a "shingle house" fabric of high porosity. The shingle is reported to become relatively large upon contact with water salinities of approximately 15‰ and while the large shingle is in suspension it behaves as a flexible sheet (similar to a two-dimensional form). When a large sheet experiences turbulence in the coastal environment, it is rolled and becomes a three dimensional thin shelled floccule (this would be similar to a crumpled sheet of paper). Mathewson (personal communication) also hypothesizes that the "shingle house" sedimentary fabric unit behaves, in an engineering sense, as a rigid, thin shelled structure. He suggests that this fabric would explain the apparent "overconsolidation" of numerous surficial submarine sediments and would be compatible with the engineering requirements discussed by Lambe (1953).

A study of shale and claystone fabric established a definite correlation between clay-flake orientation and fissility (O'Brien 1970a). Certain organic rich black shales revealed the best fissility and greatest degree of preferred grain orientation. Shales with poor to moderate fissility showed gross parallelism of flakes with areas of platelets dipping at angles to the bedding. Random clay flake orientation was observed only in nonfissile claystones.

O'Brien (1970a) proposed three possible means of producing parallel orientation of clay flakes in argillaceous rocks.

- (1) Original deposition in parallel arrangements.
- (2) Mechanical rearrangement and orientation during early stages of compaction.
- (3) Preferential growth of layer silicates under consolidation.

Geochemical factors affecting parallel orientation of clay grains could be caused by the presence of organic molecules which neutralize surface charges of the clays and result in sedimentation in a dispersed state (O'Brien 1970a). Also, low clay concentration and low rates of deposition may result in sedimentation in a dispersed state even in the presence of high salinities (Rosenqvist 1966). Thus well developed fissility in shales of marine origin indicate dilute clay concentration in seawater. Shales with poor fissility are interpreted as being formed by the collapse of a flocculated clay cardhouse structure through processes of consolidation following deposition of high clay concentrations in seawater during sedimentation (O'Brien 1970a). The reader is referred to a paper by Heling (1970) discussing the structure of shales and particle rearrangement during consolidation.

A noted change from the early ideas of clay fabric was realized by the pronounced increase in the observations, studies, and publications discussing and describing the presence of compound, multiplate particles such as domains, aggregates, and crumbs which contrasted sharply with the early concepts of single clay particle fabric. These observations were made by soils scientists as well as engineers and



geologists (Pusch 1970; Barden and others 1970; Burnham 1970; Green-Kelly and Mackney 1970; Yong 1972; Barden 1972; Smart 1972; Moon 1972; Rao 1972; Bennett and Bryant 1973; McConnachie 1974; Collins and McGown 1974). The importance of domains and compound multiplate particles in general, were clearly recognized as an important aspect of clay fabric. The influence of compound particles on the engineering behavior of sediment was studied by several of the above investigators. The majority of the current studies of clay fabric have not failed to recognize the presence of multiplate particles in various sediment types.

Yong (1972) discussed the concept of the mechanics of crumb-particle interaction and particle orientation under load. The crumb is considered equivalent to the aggregate having finite particle shape and structural integrity (fig. 20).

A sequence performance of particle-crumb interaction under load is given as follows:

(1) Rearrangement and reorientation of crumbs (aggregates) with no significant distortion within the crumbs.

(2) Further loading producing an accentuation of reorientation. Types of pseudoanisotropy effects may occur due to crumb alignment.

(3) Crumb distortion and volume change at high stresses.

Although Yong (1972) claimed that this sequential performance can be confirmed from fabric analysis, he did not assign specific stress conditions (specific loads) to the process during loading. The importance of this concept, however, is that crumbs or aggregates are considered to respond initially at low loads with essentially little or no single-particle reorientation, and at higher loads the crumbs distort and single particles begin to reorient in response to the imposed stress conditions.

The microstructure of artificially dispersed and flocculated kaolinite, illite, and montmorillonite was investigated (Sides and Barden 1971). Dispersed samples are prepared using sodium oxalate and consolidated with a uniaxial load of 29.4 kPa and air dried. Calcium hydroxide was used as the flocculating agent, and these samples were also consolidated under the same load as the dispersed samples. Dispersed kaolinite revealed a well-oriented structure, whereas flocculated kaolinite showed smaller domains and random orientation. Although the flocculated kaolinite showed orientation of grains, a tendency of horizontal bedding was observed, and the samples were described as having a turbostratic structure. Dispersed illite showed well-oriented grains, and some flakes were found to form a "skin" around silt particles. This "skin" was described earlier by Brewer (1964) and Burnham (1970). The flocculated illite structure was definitely random with some local areas of oriented particles. There was a marked scarcity of single edge-to-face contacts indicative of a cardhouse-type fabric. The overall structure was simply described as salt flocculated. Sides and Barden (1971) found that illite was more strongly affected by dispersing and flocculating agents than was kaolinite. The effects of chemical additives on montmorillonite were found to be similar to their effect on illite, but details of the structure were impossible to distinguish. Montmorillonite particles were observed to curl at their edges. This possibly was caused by preparation techniques. Yong (1972) has shown that if dehydration of the sample is not performed correctly, the fabric obtained is misleading and misrepresented. When montmorillonite or bentonite are air-dried, the fabric produced is the so-called "cornflake structure" of curled clay platelets. This effect was shown earlier also by Sloane and Diamond (1970).

Sides and Barden (1971) concluded that as clay particle size is reduced, the effect of chemical additives becomes more effective in producing dispersed or flocculated struc-

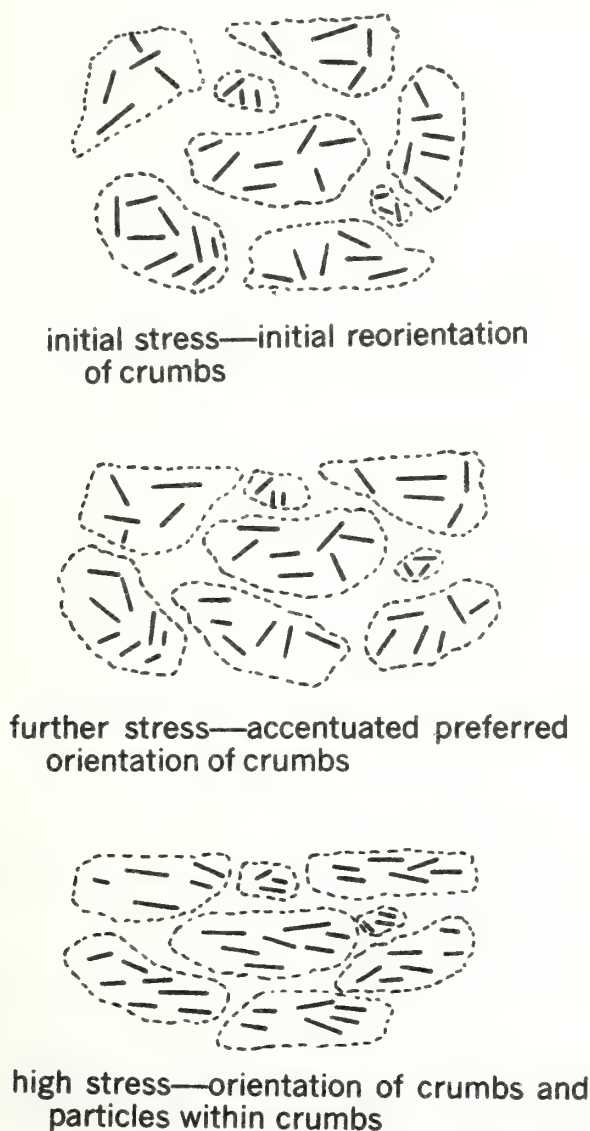


FIGURE 20.—Crumb structure and particle orientation under load (relative). (Yong 1972)

tures. Thus, illite showed greater effects due to chemical additives than did kaolinite, and no definite conclusions were reached for montmorillonite due to its extremely small size rendering interpretation difficult. Bhaskaran (1972) in a reply to Sides and Barden (1971) stated that the degree of orientation of clay particles is a function of the type of clay particles, percentage of chemical agent present, its influence on the clay, and the consolidation pressure. Kaolinite tends to align into parallel arrays with less resistance than other clays, and kaolinite may require a different quantity of flocculating agent to show significant effects.

Rao (1972), in a reply to Sides and Barden (1971), pointed out that calcium hydroxide was a very poor choice of flocculating agent to use in the study of clay fabric because its attack on certain clay minerals (kaolinite and montmorillonite) causes hydrolysis of Si-O-Si bonds in the silica tetrahedron with the formation of films of calcium-silicate compounds at the particle surfaces. Obviously, the use of strong chemicals in the treatment and preparation of clays for fabric studies of either natural or artificially prepared and sedimented material may produce unnatural physicochemical conditions and questionable fabrics if compared with naturally formed clay fabrics.

An excellent study was made of the microstructural changes in a marine quick clay at failure (Pusch 1970). Electron micrographs revealed that the clay was characterized by a very porous network of dense aggregates connected by links of particles (fig. 21). During initial failure (unconfined compression tests), link distortions were developed. Aggregates apparently moved as units in connection with deformation of their links. At high shear stresses, motion of the aggregates caused large deformations of connecting links. This resulted in parallel orientation of the linking particles (fig. 22). Remolding causes successive breakdown of aggregates and a decrease in shear strength. According to Pusch, the shear process is probably governed by the action of the aggregates, and their rigidity may be due to the small distance between individual particles. The high viscosity of water surrounding an aggregate relative to the viscosity of the free pore water together with the strong bonding of the closely spaced particles composing an aggregate result in considerable rigidity (Pusch 1970). A fabric characterized by a linkage of groups or chains of small particles between flocs and aggregates was found earlier by Pusch (1966) for a quick clay.

Studies of the New Liskeard varved clay from Ontario revealed a flocculated open soil structure atypical of deposits expected for cold, fresh melt waters of glacial lakes in which a dispersed condition would be most likely (Quigley and Ogunbadejo 1972). The clay was found to have a preconsolidation pressure in excess of the overburden pressure. Relatively slow sedimentation rates, bond development such as cementation by carbonates, and significant van der

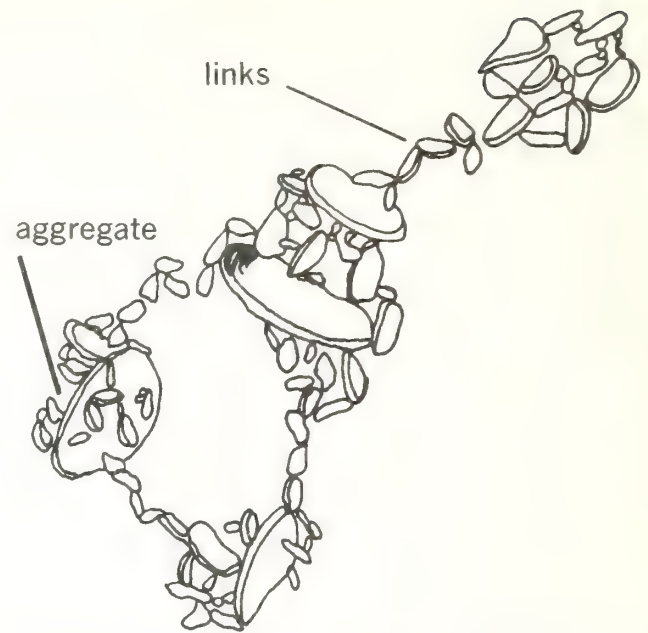


FIGURE 21.—Structure of a marine quick clay depicting aggregates and links prior to compression (shear deformation). (Pusch 1970)

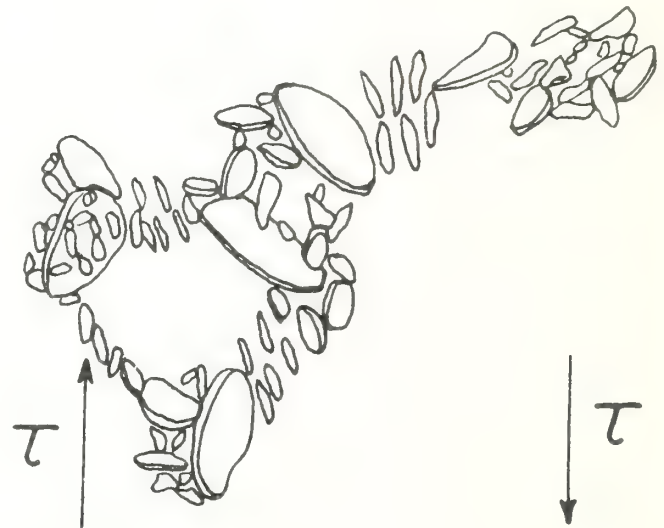


FIGURE 22.—Structure of a marine quick clay depicting breakdown of links resulting in domain formation and orientation of linking grains (same as fig. 21 after shearing). (Pusch 1970)

Waals forces were attributed to the overconsolidated characteristic. Comparison of the New Liskeard clay with soft stratified glacial sediments from Welland Ontario (similar composition) indicated that the New Liskeard clay had different properties. Platelet parallelism was considered to be due to faster sedimentation and compression rates together with an insignificant degree of bond development for the Welland clay.



Kirkpatrick and Rennie (1972) reported on the fabric of laboratory consolidated kaolin as observed by electron microscopy. Although the samples were air dried, the fabric was assumed to be representative of the wet samples. With these reservations in mind, the results indicated that kaolins consolidated under isotropic conditions had an isotropic structure with the clay particles oriented at random. Kaolin samples consolidated anisotropically were found to have a strongly oriented structure with the clay particles oriented at right angles to the direction of the principal stress.

The increasing observational evidence suggests that single clay particle fabric of sediment is not wholly tenable and that sediment fabric is more accurately represented by domain, aggregate and linking chain particle arrangements. Models of clay fabric are beginning to emerge with these more recent observations and concepts in mind (Moon 1972; Yong and Sheeran 1973; Collins and McGown 1974). A model of clay particle arrangement for unconsolidated versus consolidated sediment representing flocculated and dispersed conditions has been proposed by Moon (1972). Conceptually the model accounts for the basic domain particle interaction during consolidation with particle alignment of

domains toward preferred orientation (fig. 23). As consolidation proceeds, more particles are incorporated into each domain. Domains are of the "book" and "stepped face-to-face" type.

Fabric unit interaction and classification were recently discussed for the purpose of predicting response soil behavior and for the development of fabric models which more closely approach a physical description of real sedimentary material (Yong and Sheeran 1973). Fabric units were defined as groups of particles, the "fabric unit" which includes crumbs, aggregates, clusters, floccules, domains, and finally particles which are grouped into domains. Yong and Sheeran stressed the importance in recognizing the "fabric unit" as consisting of multiple particles in the majority of cases rather than single particle arrangements making up the basic structure of sediment.

Although specifics of each paper presented at the International Symposium on Soil Structure, Gothenburg, 1973, are too numerous to mention here, the meeting covered four basic themes of interest: (1) Techniques of observation and methods of quantification; (2) macro- and microstructure of soils; (3) physicochemical processes that affect soil struc-

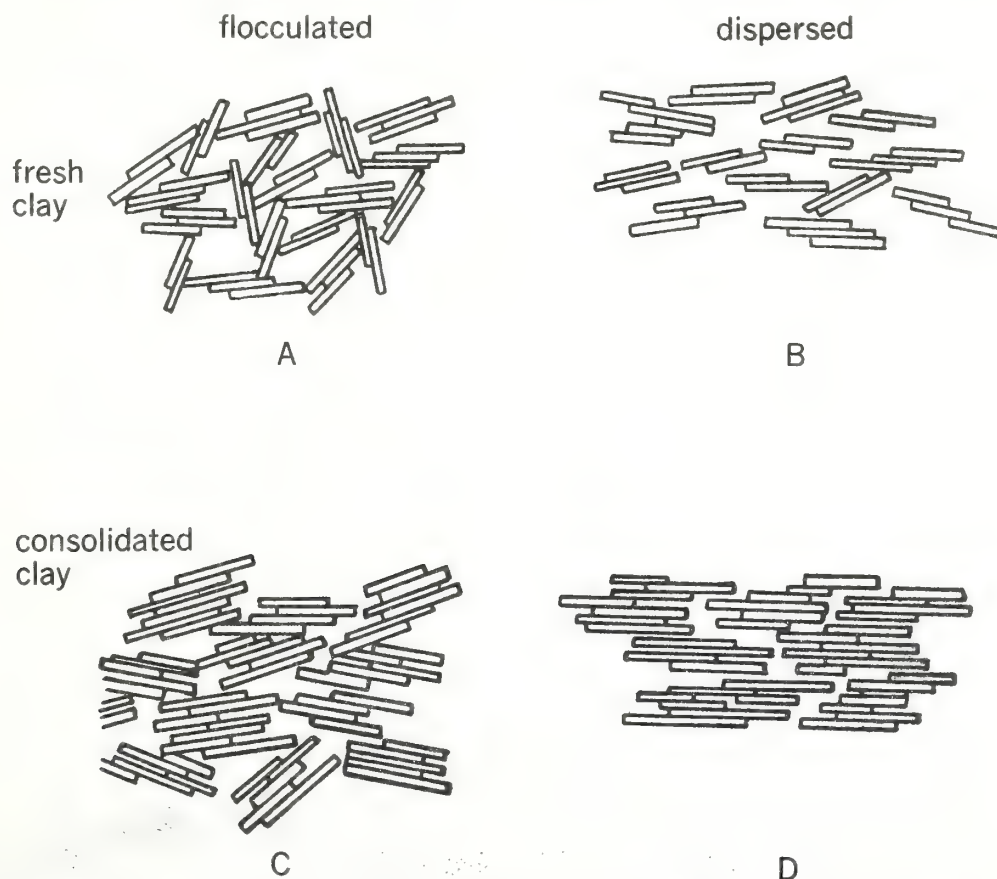


FIGURE 23.—A proposed scheme of particle arrangement in clay sediments (from Moon 1972). (A) Open, random arrangement of domains of two to three particles per packet. (B) Parallel or subparallel arrangement of domains of two to three particles per packet. (C) Increased parallelism and more particles incorporated into each domain than in A, i.e., mudstone. (D) Complete parallelism and more particles per packet than in B, i.e., shale.

ture and vice versa; and (4) mechanisms of deformation and failure.

Barden (1973) summarized the various factors important in the development of soil structure:

(1) The electrochemical environment at the time of deposition, as in hypersaline, marine, brackish, or fresh water. These factors are considered to have the dominant influence on the final structure.

(2) Changes in stress during loading and unloading which leads to the collapse of the initial structures and the development of preferred orientation of the fabric.

(3) In some cases, the effects of chemical and physical weathering may be strongly disruptive and remove effects of overconsolidation.

Barden also summarized the important general conclusions that have resulted from recent observations of sediment microstructure:

(1) The single particle behavior is very rare, and the "cardhouse" particle arrangements are a theoretical idealization of fabric rather than a common characteristic. Clay plates are usually aggregated in some fashion, and this observation confirms the suggestion by Yong that the single plate theory may be relevant to dilute colloid suspensions, but it does not apply generally to natural clays. This concept of multiple plates, according to Barden, may suggest some resemblance between clays and granular soils.

(2) Flocculated structure may result following sedimentation in marine, brackish, or fresh water, and the degree of openness of the fabric is influenced by the mineralogy, clay plate size, and amount and angularity of the silt particles present. Consolidation causes collapse of the bookhouse fabric into a turbostratic fabric which may result in horizontal orientation. Arching effects can maintain areas or pockets of open flocculated structures.

(3) The greatest single factor which influences the final structure of a clay is considered to be the electrochemical environment at sedimentation and its effect in establishing a flocculated or dispersed structure.

Although there are many factors involved in the development of soil structure, Barden claims that the study of microstructure is very important in understanding and linking the geological processes involved in the development or formation of the soil (sediment) and its geotechnical properties.

Smart (1973) has given a comprehensive review of the statistics of fabric analysis as observed by electron microscopy. He has discussed various methods for statistical analysis of particle size and orientation for both three-dimensional and two-dimensional cases for clay fabric.

A study was recently published on the microfabric features, their form and function, in various natural sediments (Collins and McGown 1974). The types of sediment studied included marine water, brackish water, fresh water, floodplain, lacustrine, aeolian, and glacial deposits. The ob-

jectives were to delineate the particular types of fabric, to establish if earlier concepts of particle arrangement were realistic, and to observe if the specific fabrics were associated with particular depositional environments. An additional objective was to determine if particular fabrics and particle arrangements were associated with specific engineering behavior of the sediment. Scanning electron microscopy was employed to investigate the fabric, and the samples were prepared using the air-dry-fracture-peel-coat technique described by Barden and Sides (1971). Although the air-dry technique is highly suspect in preserving the fabric of undisturbed sediment, the investigators apparently assumed that this factor was not critical.

Collins and McGown (1974) claim that the widespread assumptions of unique relationships between microfabric, mode of deposition, and depositional environment were not substantiated by their study; however, they found that there may be a dominant fabric feature or set of features characteristic of any one sediment. Commonly, different types of microfibrils were observed in any one type of sediment. The dominant microfabric features characteristic of particular sediments were associated with the engineering properties such as sensitivity, collapse and expansion. The medium sensitive to extra quick sediment was characterized by particle arrangements of the bookhouse and stepped flocculated fabrics, and a type called "partly discernable particle arrangements." Turbostratic arrangements were observed in the medium sensitive sediment. All sensitive material had clay matrices. The very sensitive quick clays from Norway often had connector and irregular aggregation assemblages. Linkages between aggregations were composed of a number of the connector assemblages. Other medium sensitive clays from various localities had interweaving bunches that tended to be oriented towards the horizontal. Aggregation assemblages were observed in some sediment of medium sensitivity. Connector assemblages were very infrequent in the low-medium sensitive sediment.

Collapsing sediment of usually silt, clay, sand, or till deposits contained elementary particle arrangements of fine silt and clay particles arranged in various configurations. The "partly discernable type fabric" was also present in these sediments, and the "onion skin" fabric which the investigators called the "clothed grain-grain" was observed. Connector assemblages were common in these sediments, and the granular particle matrices were predominant. Regular aggregations were observed in the collapsing sediments, but their occurrence was rare in the loess material.

Collins and McGown (1974) observed that in the expansive sediment studied, the predominant microfabric was the clay particle matrix assemblages, although fabric types included the connector and honeycomb fabric and the "clothed grain-grain" contact features.

Clearly, various types of fabric were observed by Collins



and McGown (1974) in the sediments studied, and specific types of fabric were present in numerous sediments; however, certain fabrics seemed to be characteristic (pre-dominant) of types of sedimentary material. The study points out that many of the particle arrangements and assemblages present in natural sediment have not been observed in laboratory prepared monomineralic clays and that laboratory test specimens may not possess the same fabric as occurs in natural sediment. The study also included description of the pore space of the sedimentary material following closely the classification of Brewer (1964) and Bochko (1973).

As an integral part of the study of microstructure in general, several investigators recently have been researching the characteristics of pores and pore systems in sediments and rocks (Diamond 1970; Timur and others 1971; Sarkisyan 1971; Bochko 1973). The scanning electron microscope has been the basic tool for much of the research on pores.

Recently, McConnachie (1974) reported on the fabric changes induced by laboratory consolidation of monomineralic kaolin prepared by mixing at a moisture content of 250 percent. The original void ratio (ratio of the volume of the voids to the volume of the solids) was about 5.5. The material was consolidated over a range of about 0.1 to 100,000 kPa. A strong inflection in the void ratio versus the logarithm of pressure occurred at 14.7 kPa creating two linear portions of the curve. The original clay fabric was characterized by edge-edge and edge-face contacts among domains. As the pressure was increased, the domains rotated and became more closely packed, and at approximately 14.7 kPa the domains became reduced in size. This change in domain size was attributed to a slippage of particles in face-to-face contact during rotation of the domains as consolidation proceeded. The change in behavior of the domains at the pressure of 14.7 kPa is attributed to the collapse of the clay fabric and is considered to correspond to the highest pressure at which inter-domain and interparticle physicochemical forces can be sustained. The fundamental change in the mechanism of consolidation occurred between 9.8 kPa and 98 kPa. Apparently, most of the increase in particle orientation was complete at about 9.8 kPa. The domains were observed to move closer together at higher pressures but with no significant change in orientation. At about 100,000 kPa the orientation of the domains showed a degree of orientation far from perfect with the mean angle of 22 degrees between domains. Apparently, the greatest degree of particle orientation occurred in the low pressure level, and little increase in orientation occurred even at very high loads. The sediment investigated, however, was relatively pure kaolinite, laboratory prepared at a specific water content, and thus the fabric and material engineering behavior may not be representative of naturally occurring sedimentary material.

## Summary

The early concepts and studies of clay fabric beginning with Terzaghi (1925a), and Goldschmidt (1926), Casagrande (1932), and Lambe (1953, 1958a) provided the impetus for a large number of clay fabric studies employing X-ray and high resolution electron microscopy techniques depicting the actual arrangements and orientation of clay particles (fabric); the "building blocks" of soil structure. The importance of physicochemical factors on particle arrangements in soils has been discussed by Winterkorn (1948), Bolt (1956), Lambe (1958a), Rosenqvist (1959, 1962), and Buchanan (1964). They have clearly shown that the physicochemical factors involved in the formation of sedimentary deposits cannot be divorced from the physical and mechanical aspects for a complete assessment of soil formation, diagenesis, engineering properties, and fabric analysis.

The importance of fabric in determining the physical properties and engineering behavior of sediments has been clearly established. For further discussions concerning sediment structure interrelationships with the physical properties, the reader is referred to papers by Mitchell and Houston (1969), Houston and Mitchell (1969), and Torrance (1970). A detailed study on bonding and effective stress and strength of soil (Mitchell and others 1969) followed by later studies (Andersland and others 1970; Singh 1970; Mitchell and others 1971) has clearly revealed the importance of these factors on the microstructure of soils. Olson and Mesri (1970) discussed the influences of both the mechanical and physicochemical mechanisms important in the compressibility of clays.

A few typical fabric types have been classified as honeycomb, cardhouse, turbostratic, bookhouse, and stairstepped. Recently, studies have revealed that the single plate concepts of fabric are not wholly tenable and that the multiple unit, domain-type fabrics are the rule for most sediments. The unlimited variation in particle size, shape, and composition coupled with the depositional environment, physicochemistry, and transportation of sedimentary detritus through changing environmental conditions, all increase the complexity and the ultimate nature of the sediment fabric of a particular sedimentary deposit. A paucity of data and information on clay fabric of submarine sediment exists, and only a few studies of the fabric of natural sedimentary material have been made. Numerous studies have dealt with the fabric and engineering behavior of laboratory prepared material. Qualitative and ultimately quantitative assessment of sediment fabric and microstructure of naturally occurring sediments could result in predictions of the engineering behavior of clay sediments, a clearer understanding of the geotechnical properties, and a much better understanding of complex sedimentological processes.

## Geologic Setting and Sampling

This study of clay fabric and geotechnical properties of submarine sediment is confined to a selected area of the Mississippi Birdfoot prodelta depositional environment (fig. 24). The sediment cores investigated were recovered from water depths ranging from 67 to 73 m with a lateral separation of approximately 610 m. The cores are referred to as B-1, B-2, and B-3 in this study. Detailed analyses were restricted to cores B-1 and B-2; core B-3 was used for supplemental mass physical properties data. The Birdfoot Delta is the most modern depositional area of the Mississippi Delta complex. Sediments are prograding seaward depositing clays and silty clays in the prodelta environment.

### General Geology

Sediments of the Mississippi Delta, particularly the prodelta and adjacent shelf area sediments, are dominantly clay. The Mississippi River discharges approximately  $4.54 \times 10^{11}$  kg of sediment annually into the Gulf of Mexico with a contribution of about 30% sand, 30% silt, and 40% clay size material (Coleman and Wright 1974). Sand that reaches the Mississippi Birdfoot Delta consists of fine to very fine material which is deposited largely on the distributary-mouth bars. Silts and clays are deposited largely in the prodelta and deeper Gulf floor environments. The Mis-

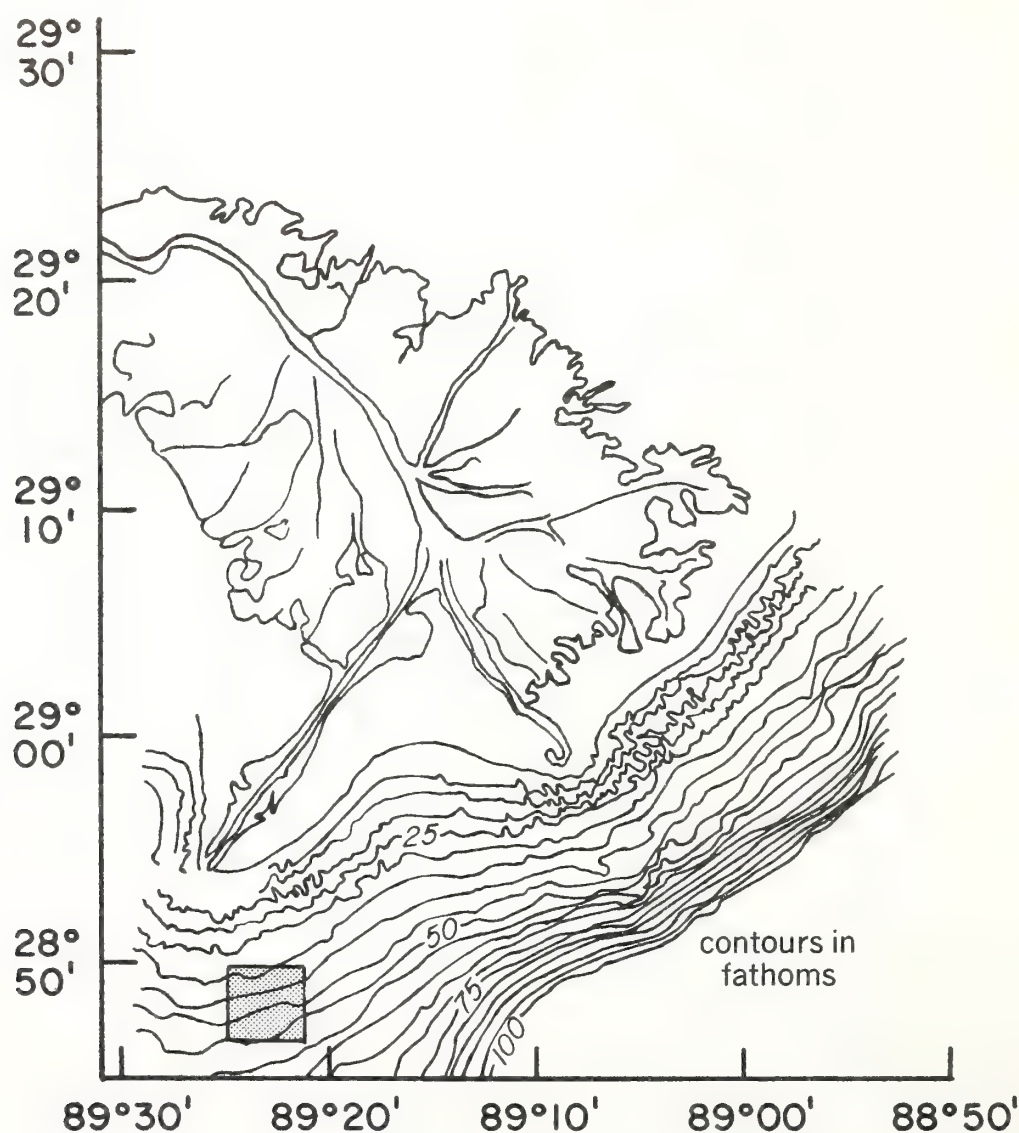


FIGURE 24.—General study area—Mississippi Birdfoot Delta. (From Shepard 1956)



Mississippi River has changed course several times, and in doing so it has constructed and abandoned several deltas which form the broad Mississippi Deltaic Plain. The last major course change occurred approximately 450 years ago and resulted in the modern Birdfoot Delta which is the only delta within the Deltaic Plain that was constructed in deep water (Fisk and McClelland 1959). Sediments of the modern Delta have prograded across a thick section of older shelf and prodelta clays.

### Prodelta depositional environments

Fisk and McClelland (1959) delineated three general facies of the prodelta depositional zone that appear to be indicative of subenvironments of the more general prodelta depositional environment. These sediment facies are characterized as follows:

- (1) Delta front facies, shallow inner-neritic zone. Deposition in less than 18 m of water; dominantly massive silty clays.
- (2) Mid-neritic prodelta zone facies, deeper water. Deposition in the water depths ranging between 18 and 76 m; more massive clays than in delta front facies deposits; characterized by delicate laminations.
- (3) Outer-neritic zone prodelta facies. Deposition in water depths greater than 76 m; sediments consist of massive clays with only faint laminations.

The prodelta deposits of the subenvironments are characterized also by specific faunal remains and the presence or general absence of plant debris. Sediments collected for this study were cored near the seaward edge of the mid-neritic prodelta zone.

### Clay mineralogy

The clay mineral composition of recent sediments from the Mississippi River Delta and adjacent offshore areas has been reported by Johns and Grim (1958). The study was restricted primarily to the area bordering the Mississippi Birdfoot Delta on the east. Studies were made of a few samples farther offshore. Montmorillonite was reported as the dominant clay mineral in the Delta region, and it was suggested that this mineral represented sediment contribution from the drainage basin of the Missouri River system. Small amounts of illite and chlorite were considered as the approximate contribution of the drainage from the Ohio River system.

Fisk and McClelland (1959) discussed the clay-sized mineral assemblage carried by the Mississippi River. Montmorillonite was reported to dominate and kaolinite, illite, quartz, and feldspar were present in smaller quantities. Although quartz and feldspar are not clay minerals, they were reported as being present in the clay size fraction of the sediment transported by the river. Fine-grained sedi-

ments, particularly clays, are not only deposited in the near-shore environments but are also carried many kilometers offshore in large plumes of turbid water.

### General core lithology

The general lithology of the cores investigated during this study is characterized by a massive, relatively hard, gray, old submarine clay which occurs at depths of approximately 85 m below the mudline to depths greater than 152 m (fig. 25). This gray clay is overlain by 26 m of fine sand between 85 and 59 m below the mudline. The sand forms the broad and extensive strand plain deposit of Pleistocene age. The strand plain sands form the base of the overlying fine-grained clays of the premodern and modern deposits of the Mississippi River (Coleman and Wright 1974). The section of premodern and modern gray submarine clay is 59 m thick ranging in depth from the mudline to the top of the sand.

The premodern clays overlying the strand plain sands were deposited in a thick onlap sequence in response to rising sea level during the last climatic cycle of the late Quaternary Period (Gould 1970). At the end of the onlap depositional period and approximately 5,000 years before present, the Mississippi River began to build the broad Mississippi Deltaic Plain prograding seaward. Subsequently, 450 years ago, the Mississippi River began to construct the modern Birdfoot Delta which is prograding into deeper water (Fisk and McClelland 1959; Gould 1970).

### Field Core Sampling and Testing

Core samples from the South Pass area of the Mississippi Delta were provided by McClelland Engineers, Houston, Texas, through William R. Bryant, Department of Oceanography, Texas A&M University. Sediments were drilled with 0.089-m drill pipe rotary rigs mounted on the decks of the *MV State Point* and the *MV Livingston*. Four 0.127-m long liner segments with a 0.064-m O.D. (outside diameter) and a 0.054-m I.D. (inside diameter) were used to obtain samples. At boring B-1, a 0.057-m O.D. and 0.054-m I.D. thin-wall tube sampler was used below a penetration depth of 35.2 m. After the drill pipe was advanced to the desired sampling depth, it was then raised a short distance above the bottom of the hole. A wireline sampler was then lowered through the drill pipe to secure the sediment samples. Details of the wire-line sampler have been discussed by Emrich (1971). Core segments were sealed to prevent moisture loss and stored in a high humidity refrigerator. Core B-1 was drilled to a depth of 154 m, and cores B-2 and B-3 were drilled to depths of 38 and 40 m, respectively.

Field testing was confined to shear strength measurements. Tests were made using a wire-line vane probe, a miniature vane, and a Torvane. These data were provided by McClelland Engineers. Miniature vane tests were als



performed on samples which were sent to the laboratory for routine geotechnical measurements. Shear strength data were used for two general purposes in this investigation of clay

fabric: (1) assessment of sediment sample quality, and (2) general strength profiles with depth in cores as related to selected mass physical properties and clay fabric.

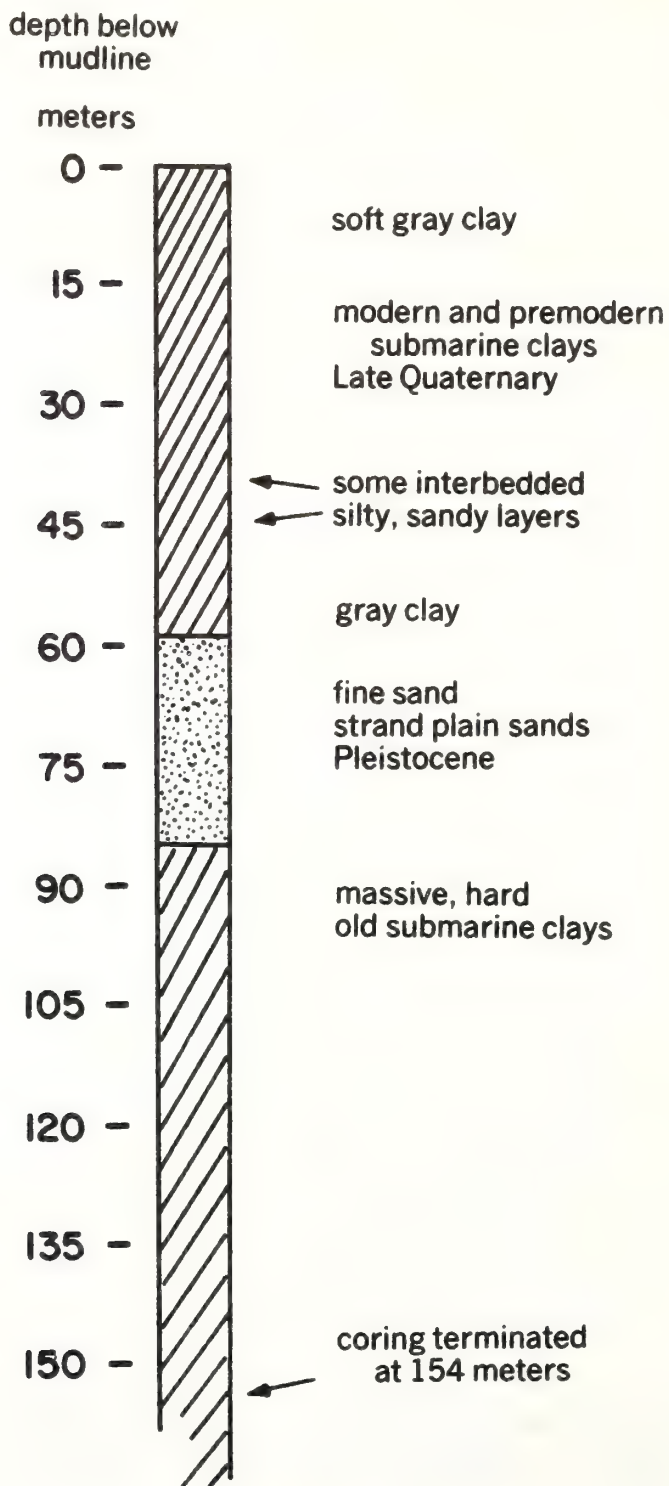


FIGURE 25.—Generalized core lithology.

# Analytical Techniques and Instrumentation for Clay Fabric Studies

## *Selection of Sediment Samples*

Samples were selected on the basis of sample quality and availability from core depths of 1.4 to 151 m in core B-1. Supplemental samples were selected from core B-2 for comparison with the fabric studies carried out on core B-1. The B-2 samples were obtained from core depths of 1.4 to 27.6 m.

In addition to the Mississippi Delta samples, a clay sample from Leg 16 of the Deep Sea Drilling Project (D.S.D.P.), Site 163A, 11°14.7'N, 150°17.5'W, was analyzed for fabric with two major objectives in mind (collected by R. Bennett, 1971; permission of Tj. H. van Andel and G. Ross Heath, Chief Scientists). The first objective was to delineate the diagnostic characteristics of the fabric of sample 163A which may be related to the depositional environment and to relate its features to the selected geotechnical properties. The second objective was to use this sample as part of the evaluation of sample preparation techniques employed during this study because of its highly complex fabric in the undisturbed versus the remolded state. D.S.D.P. 163A was sampled from a depth of 144 m below the sediment-water interface in 5,330 m of water and is Cretaceous in age. The D.S.D.P. sample afforded an excellent opportunity to compare the clay fabric of two submarine sediments (D.S.D.P. versus Mississippi Delta) from different depositional environments. The fabric of a few selected laboratory consolidated samples was investigated for comparison with the fabric of the naturally consolidated sediment.

## *Subsampling Techniques*

Selected sediment samples were carefully subsampled from the centers of core segments using a thin wire knife and trimmed into small blocks a few millimeters in size. The initial size of a subsample was generally less than 5 mm on a side. Later the sides were trimmed to 2 to 3 mm. Subsamples were cut with two faces of the block lying generally parallel with the plane of bedding, that is, normal to the core length. The remaining four faces of the blocks were then normal to the bedding plane. After careful trimming, the samples were ready for further processing.

## *Preparation of Samples for Electron Microscopy*

The most critical steps in preparing samples for electron microscopy (E. M.) studies are the techniques employed in the dehydration of water-saturated specimens and the techniques for embedding a sample with an appropriate medium, a necessary prerequisite to ultrathin sectioning that must be

accomplished with care. These factors were given paramount importance during this study of clay fabric. Techniques were carefully employed to ensure high-quality comparable results—to minimize sample disturbance and maintain the structural integrity (particle-to-particle orientations) of the clay samples. Clay specimens for this study were critical-point dried and embedded with a low-viscosity epoxy resin (SPURR).

## **Early dehydration methods**

Studies have clearly shown that air drying and/or oven drying of clay specimens can cause severe distortion to the fabric, thus rendering the structure of the sample unlike its natural state. (Yong 1972; Naymik 1974). Yong (1972) has shown that dehydration of montmorillonite clays by air drying can create the so-called "cornflake structure" commonly observed in photomicrographs. Curled and warped clay plates, which are characteristic of the "cornflake" effect, are caused by strong surface tension forces during drying. Naymik (1974) has clearly shown that the critical point drying technique is far superior to either air-drying or freeze-drying of clayrich specimens. He found that a large reduction in pore space volume occurred during air-drying and that drying artifacts were formed during freeze-drying. He also reported an absence of desiccation shrinkage in samples critical point dried.

Gillott (1969) has discussed the details of freeze-drying and critical-point drying of clay samples. He has noted the strong likelihood that fabric is affected by shrinkage during air-drying as revealed by the large volume decrease when dried under ambient conditions. This is attributed to the strong force of surface tension during air-drying that causes clay plates to roll up and become tubular and seriously modifies the arrangement of the particles of weak clay sediments. Gillott (1969) also considers that artifacts may be formed by ice crystallization during freeze-drying, causing damage to the original fabric. Detailed studies of the freezing of physical systems have revealed that some amorphous portions, or bound water, do not freeze but are merely dried at low temperature which constitutes a type of "pseudo freeze-drying" (Luyet 1961). Luyet alludes to the fact that ice crystallization generally forms to some degree during the freeze-drying process. Undoubtedly, prior to the development of the critical-point drying technique, the freeze-drying method was the most satisfactory dehydration technique for preparing clay samples for electron microscopy.

## **Critical point drying**

Critical point drying has not been used extensively in studies of clay fabric, but its importance is becoming recog-



nized as a necessary dehydration method in order to maintain the particle-to-particle integrity of a clay sample. The critical-point method has been used extensively for biological applications in order to preserve delicate membrane tissues for electron microscopy studies (Hayat and Zirkin 1973). The technique involves a series replacement from water to alcohol or liquid CO<sub>2</sub> and has been described thoroughly for biological specimens by Anderson (1951) and Cohen and others (1968). Gillott (1969) has successfully applied the technique to clay sediment using both alcohol and CO<sub>2</sub> for critical-point drying. Gillott claims that the appearance of the fabric was identical in both cases. Liquid CO<sub>2</sub> has a lower temperature at the critical point (31°C at 7,391 kPa) than alcohol (243°C at 6,526 kPa), and thus the CO<sub>2</sub> is more convenient for routine laboratory use. Other fluids also have been used for critical-point drying (Cohen and others 1968). Unfortunately, water does not have favorable critical characteristics (374°C at 9,542 kPa). This makes it impractical for most standard laboratory applications.

The critical point (C.P.) technique is a marked improvement over other dehydration methods because surface tension forces are avoided. At the critical temperature and pressure of a liquid, no boundary exists between the liquid and the gas phase; and when the temperature is held above the critical point, the gas may be released until atmospheric pressure is reached. Thus the sample can be dried without surface tension effects that are extremely deleterious to clay fabric. Intermediate fluids, such as acetone, alcohol, and amyl acetate, are often used at transition media as it is usually necessary to interpose one of these liquids between the aqueous phase of the sample and the liquid CO<sub>2</sub> or other critical point fluid. The liquid CO<sub>2</sub> or other critical point fluid is introduced into the sample chamber "bomb" in the critical point apparatus, and the specimen is purged until the intermediate fluid is removed. The sample chamber is closed at the purge valve and then raised to a temperature above the critical point of the fluid for drying.

### Techniques employed

The series of techniques used for sample preparation of the clay specimens for the transmission electron microscopy (T.E.M.) fabric studies are as follows:

- (1) Subsampling of sediment from core segments.
- (2) Replacement of saline interstitial water by a series of miscible fluids (ethyl alcohol-amyl acetate). Complete removal of interstitial water checked by the silver nitrate test (precipitation of silver chloride).
- (3) Careful wrapping of small specimens in thin lens paper.
- (4) Further soaking of lens paper and specimen in amyl acetate.
- (5) Placement of wrapped specimens into the critical point chamber.
- (6) Purging of the specimen with liquid CO<sub>2</sub> replacing amyl acetate.
- (7) Critical point drying with CO<sub>2</sub>.
- (8) Placement of dried, wrapped specimens into small individual desiccators.
- (9) Placement of individual specimens (wrapping paper removed) into small containers and placed in a large desiccator under vacuum.
- (10) Embedding of individual specimens under vacuum with a very low viscosity epoxy resin (SPURR).
- (11) Removal of specimens from the vacuum and subsequent curing of the epoxy resin at 60° to 70°C.
- (12) Trimming of the specimens with glass knives prior to ultrathin sectioning. Larger specimens were trimmed with a jeweler's saw prior to trimming with a glass knife.
- (13) Ultrathin sectioning with a diamond knife (sections cut approximately  $5 \times 10^{-8}$  to  $1 \times 10^{-7}$  m thick [500 to 1000Å] on a microtome).
- (14) Placement of ultrathin sections on copper grids.
- (15) Very light carbon "sputtering" of ultrathin sections and grids in a vacuum evaporator.

The specimens were then ready for examination of the clay fabric in the transmission electron microscope (figs. 26 and 27).

SPURR epoxy resin was used to increase sample impregnation efficiency because of its very low viscosity (60 cps). It has an impregnating advantage over ordinary epoxies that have high viscosities (approx. 2,000 cps). The usefulness and advantages of this epoxy have been determined by experiments on various Mississippi Delta and D.S.D.P. samples during this study. Samples with a high water content (low cohesive strength) were found to remain intact if impregnated while under a vacuum, but similar samples were found to completely collapse if they were impregnated at ambient pressure (without vacuum). Samples having a very complex fabric were found to retain their particle-to-particle structural integrity.

The embedding techniques used during this study were similar to the methods described by Brewer (1964) for impregnating soil samples under a vacuum. The specimens were placed in a vacuum desiccator over silica gel desiccant in order to maintain a low humidity condition throughout the process. Other embedding techniques for the study of soils by electron microscopy have been described by Pusch (1966, 1967, 1968), Smart (1967a, 1967b), O'Brien (1971a), and Foster and De (1971). A detailed investigation of impregnating techniques was carried out by Foster and De (1971), and their results showed that the observed strains in the original fabric were minimal in "soft" ma-



terial. Their techniques, however, did not involve drying, but rather followed a series replacement of the interstitial water by diffusion processes to a final hardened resin. The technique is apparently very time consuming and laborious. Photomicrographs of submarine sediment—prepared by freeze-drying, embedded with Maraglas Epoxy, and subjected to ultrathin sectioning—has clearly revealed detailed, complex fabrics that appear to be unaffected significantly by sample preparatory techniques (Bowles 1968a, 1968b). The freeze-drying technique also is time consuming, and there is danger of ice crystallization during the process.

### Transmission Electron Microscopy

Photomicroscopy of the clay fabric for all of the Mississippi Delta samples was carried out using a Philips Transmission Electron Microscope, Model 300, at 80 kV. The work was carried out at the Veterinary, Toxicology, and Entomology Research Laboratory, U.S. Department of Agriculture, College Station, Texas. Under routine research conditions, the Philips Model 300 has a resolution of about  $8 \times 10^{-10}$  m (8 Å) which can be improved for specific requirements (personal communication, Hilton H. Mollen-

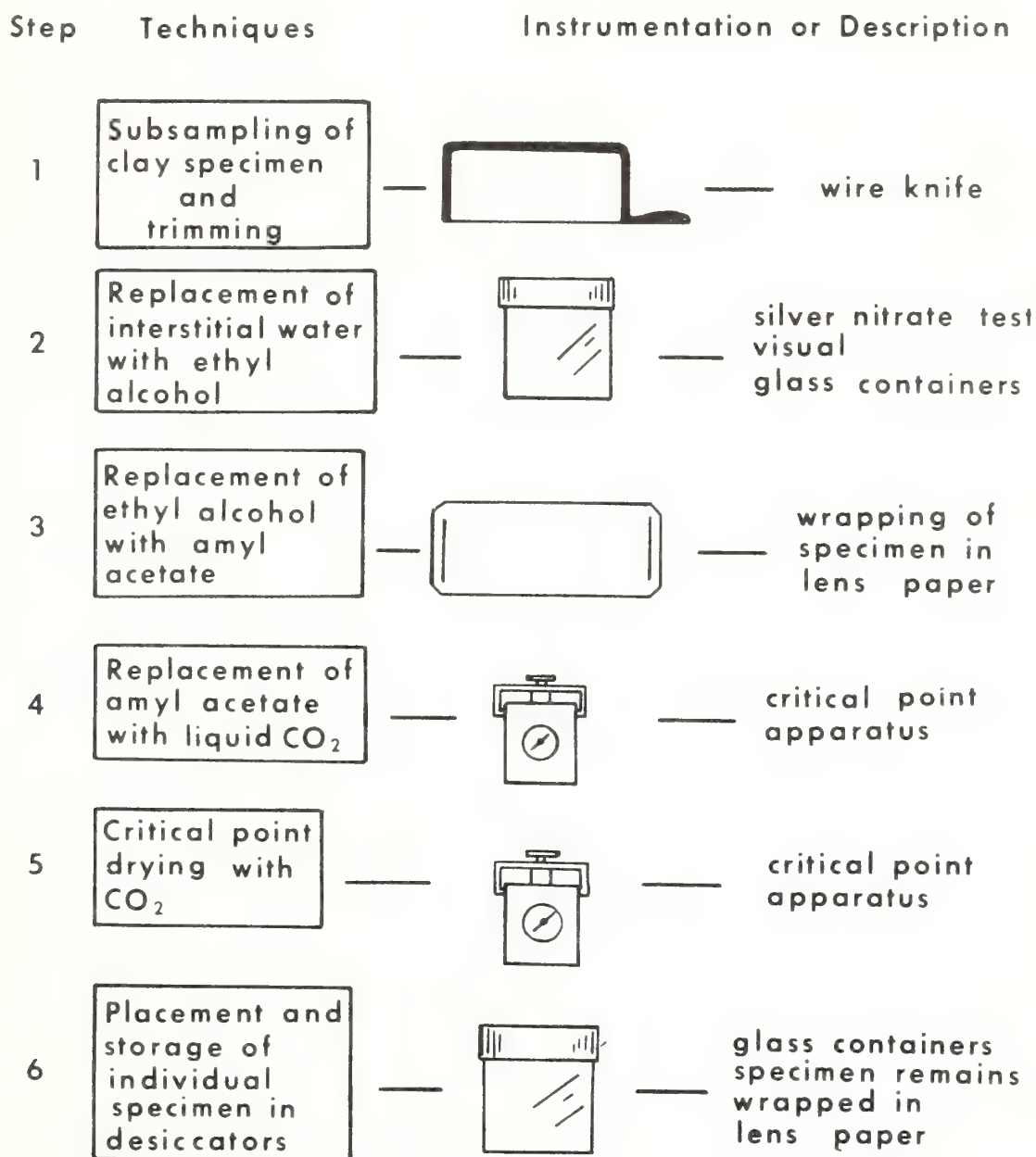


FIGURE 26.—Analytical techniques and instrumentation for clay fabric analysis: Dehydration techniques.

hauer, U.S.D.A.). The D.S.D.P. clay fabric samples were analyzed with an Hitachi Model HS-8A Transmission Electron Microscope at 50 kV, which is considered to have considerably less resolving potential than the Philips 300. Both instruments, however, proved to be adequate for this study. The photomicroscopy with the Hitachi E. M. and all of the ultramicrotomy were carried out at the Electron Microscopy Center, Texas A&M University, College Station, Texas.

A total of 426 transmission electron photomicrographs were taken and examined during this study. Typical examples of the characteristic fabric for each specimen examined have been used in this investigation. Although different magnifications were made of the fabric periodically, a magnification of 16,000 times was found to be the most useful in terms of overall delineation of the general fabric characteristics, clarity, and particle size.

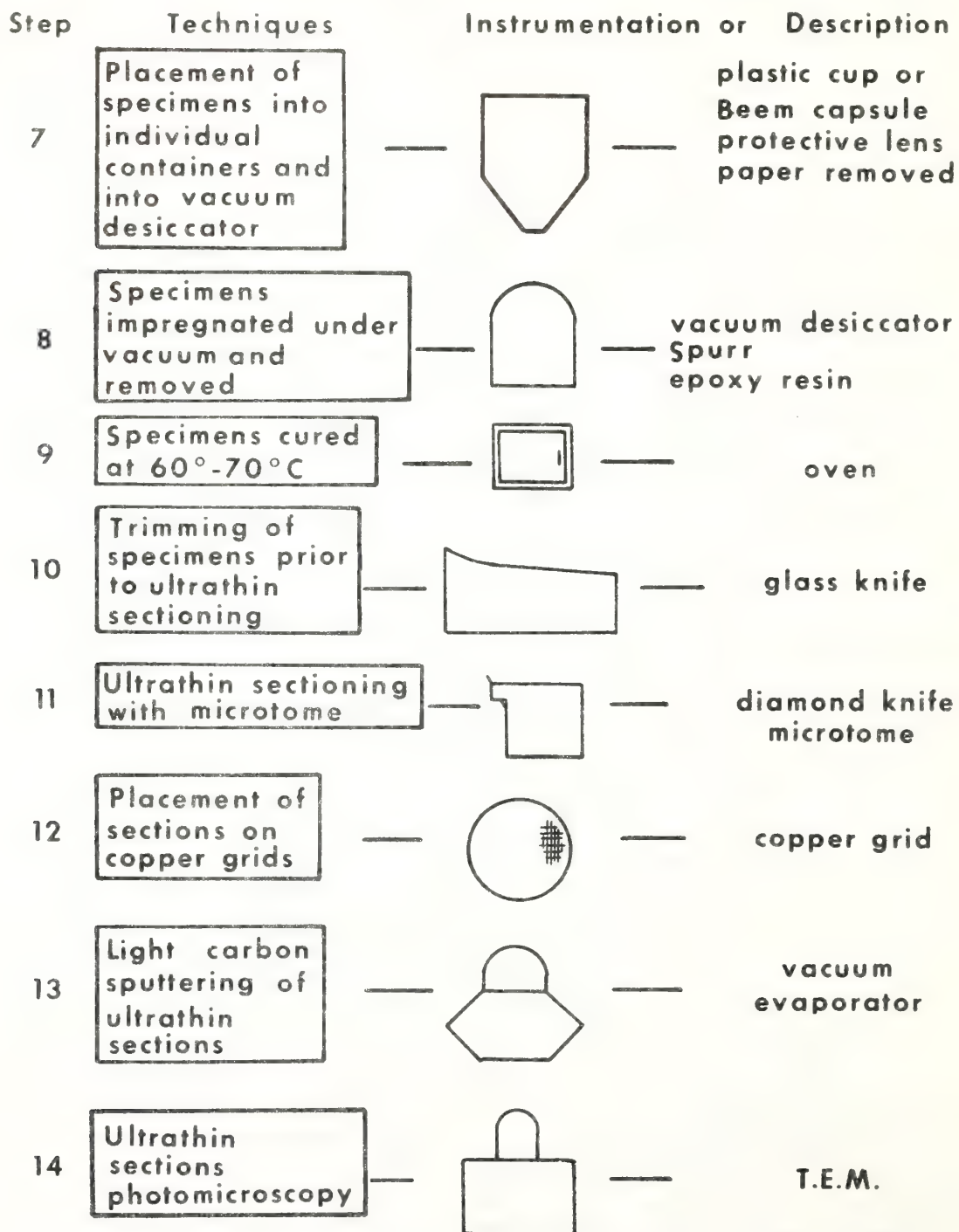


FIGURE 27.—Analytical techniques and instrumentation for clay fabric analysis: Impregnation, sectioning, and transmission electron microscopy (T.E.M.).

## Geotechnical Tests

The mass physical properties investigated in this study were determined by standard geotechnical tests which are described in numerous text books on soil mechanics (Scott 1963; Wu 1966; Terzaghi and Peck 1967; Lambe and Whitman 1969). Lambe (1951) has presented an excellent detailed account of the standard laboratory soils tests, particularly techniques for determining water content, grain specific gravity (grain density), grain size, Atterberg limits, shear strength, and consolidation. Richards (1961, 1962) has discussed the specifics of the geotechnical tests, including the miniature vane test, water content, porosity, wet unit weight (bulk density), as applied to submarine sediments. Bennett and others (1970) and Bennett and Lambert (1971) have discussed techniques and the reproducibility for many of the common mass physical properties tests as applied to submarine sediments. Lowe and others (1964) and Bryant and others (1967) have reviewed the use and applications of the Anteus Back Pressure Consolidometer which was the instrument used to determine the consolidation characteristics of the sediment samples. Void ratio versus logarithm of pressure curves ( $e$ -log  $p$ ) are derived from these tests. In function, the basic difference between the Anteus Consolidometers and other standard consolidometers is that back pressure (a hydrostatic pressure) is applied to the sediment sample surrounded with water (in this case, seawater). This technique insures nearly 100% saturation of the sediment prior to loading at back pressures of 686 kPa to 1079 kPa (Bryant and others 1975).

bility for many of the common mass physical properties tests as applied to submarine sediments. Lowe and others (1964) and Bryant and others (1967) have reviewed the use and applications of the Anteus Back Pressure Consolidometer which was the instrument used to determine the consolidation characteristics of the sediment samples. Void ratio versus logarithm of pressure curves ( $e$ -log  $p$ ) are derived from these tests. In function, the basic difference between the Anteus Consolidometers and other standard consolidometers is that back pressure (a hydrostatic pressure) is applied to the sediment sample surrounded with water (in this case, seawater). This technique insures nearly 100% saturation of the sediment prior to loading at back pressures of 686 kPa to 1079 kPa (Bryant and others 1975).

## Evaluation of Sample Quality and Techniques

Sediment core quality and subsample preparation techniques for clay fabric analysis were evaluated during this study. The quality of sediment cores was assessed in terms of shear strength test both in situ and in the laboratory by miniature vane and Torvane, and the results from void ratio versus log of pressure curves ( $e$ -log  $p$ ). Clay fabric particle-to-particle integrity as depicted in T.E.M. photomicrographs was evaluated in terms of fabrics of natural (undisturbed) versus remolded samples, image enhancement techniques applied to clay fabric, and visual assessment of subsample integrity during sample preparation and analyses. Standard techniques as well as new methods were developed and used in this study throughout the entire analytical procedure in order to maintain the particle-to-particle integrity and characteristic features of the clay fabrics. Image enhancement techniques developed in this study offer a new approach to the evaluation of transmission electron photomicrographs of clay fabrics.

### *Sediment Shear Strength*

Natural (undisturbed) shear strength measurements with the in-situ wire line vane for B-1 yielded values ranging from about 4.8 kPa to slightly greater than 9.6 kPa between the mudline and 23 m. A general steady increase in shear strength occurs between 23 and 37 m with the highest values of approximately 23.9 kPa. Residual shear strength (vane rotated 360 degrees after initial strength measurement followed by the residual strength test) and cyclic shear strength tests (vane rotated 10 times through 90 degrees after the initial failure and then tested for shear strength) yielded values of up to one half the undisturbed values giving sensitivities (ratio of the natural shear strength to the remolded or disturbed shear strength) of 2 but commonly less

than 2 between the mudline and 23 m. Generally higher sensitivities of only slightly over 2 occur between the mudline and 23 m. Sensitivity values of 2 and less are considered indicative of insensitive clays, and values ranging between 2 and 4 are characteristic of normal clays. Values of 4 to 8 are considered characteristic of sensitive clays. Sensitivities of 8 to 16 are diagnostic of many of the well known quick clays (Terzaghi and Peck 1967).

Miniature vane and Torvane tests of the cored sediment show strikingly similar results when compared to the in situ wire-line vane test. Values average 4.8 kPa between the mudline and 23 m, and steadily increase between 23 and 37 m to values of 23.9 kPa as observed for the wireline measurements. With the exception of an anomalous high shear strength zone at approximately 7.5 m below the mudline in both B-2 and B-3, similar shear strength values and relationships are found among the in situ, and miniature vane and Torvane measurements. This close agreement between in-situ shear strength measurements and strength tests on cored material indicates relatively high-quality sediment cores with minimal disturbance due to coring technique. The similarity in sensitivities, by the wire-line vane measurement and those determined on the cored material also corroborates this conclusion.

Wire-line vane measurements at B-1 were not made in the hard, stiff, clay cored between 85 and 154 m; however, miniature vane shear test values ranged from 23.9 kPa in the upper stiff clay to values of 192.5 kPa in the hard deep clays. Sensitivities for this Pleistocene clay averaged 2.3 with a range of 1.4 to 3.2, essentially the same as the sensitivities found for the soft clays between the mudline and 37 m.



### Consolidation Tests

Laboratory tests with the Anteus Back Pressure Consolidometer were performed on selected sediment samples from cores B-1 and B-2 following standard procedures discussed by Lowe (1964) and Bryant and others (1967). Consolidation test data from these cores were used to evaluate sediment core quality. Principles of consolidation testing have been treated in detail by Terzaghi (1925b), Terzaghi and Peck (1948, 1967), and by Lambe (1951). A typical diagrammatic void ratio versus logarithm of pressure curve ( $e$ -log  $p$ ) and the standard graphical construction of the

preconsolidation pressure is depicted in figure 28, representing a typical, "normal" sediment commonly encountered in testing terrestrial soils. The preconsolidation pressure,  $\bar{P}_c$ , is defined as the greatest stress to which a sediment has ever been subjected. The graphical construction as proposed by Casagrande (1936), using the  $e$ -log  $p$  curve, theoretically, determines the preconsolidation pressure.

Extensive back pressure consolidation testing has been carried out on submarine sediment from various depositional environments in the Gulf of Mexico. These surficial submarine clays tested are characterized by an atypical  $e$ -log

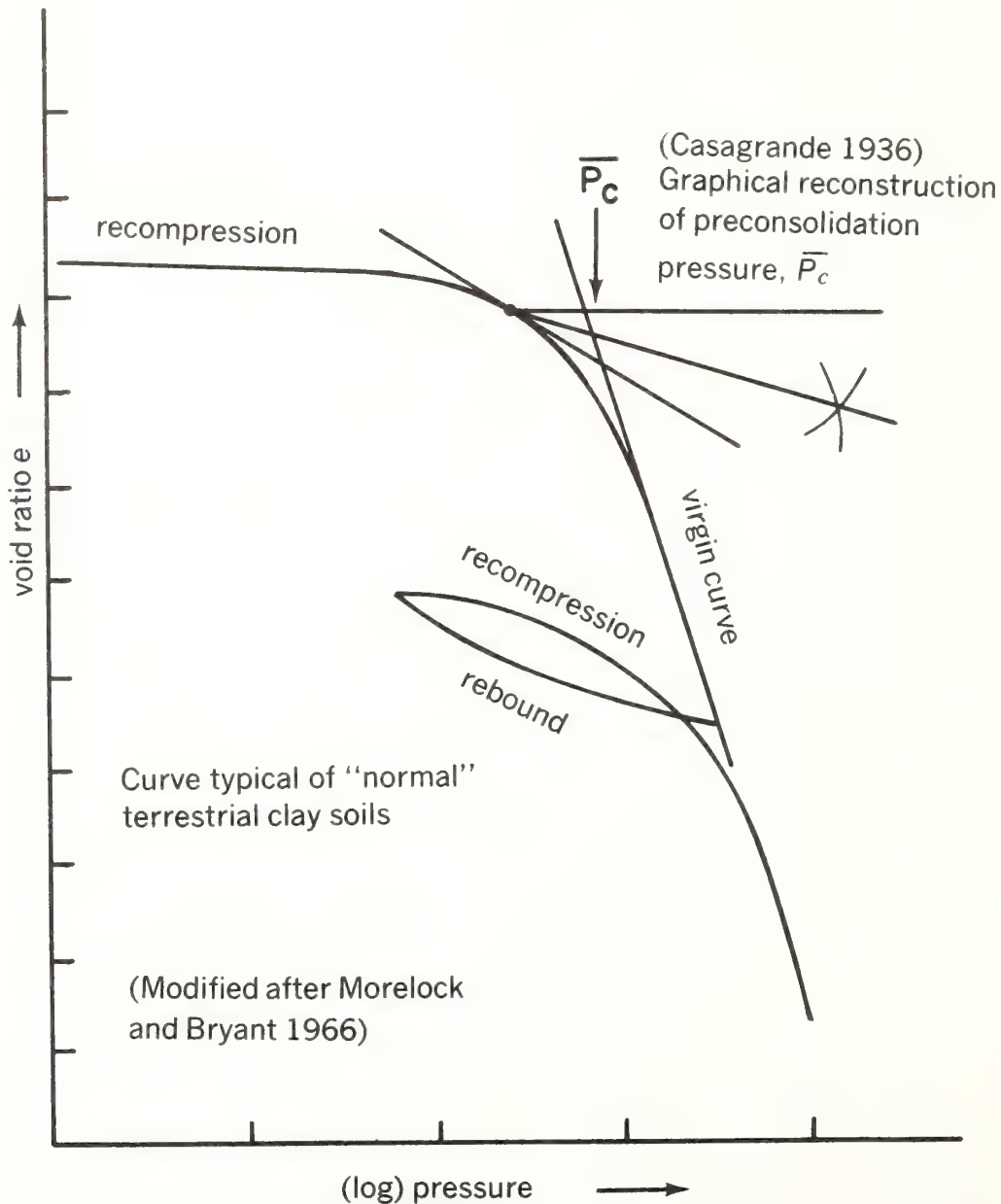


FIGURE 28.—Typical consolidation test—void ratio versus logarithm of pressure curve.

terial. Their techniques, however, did not involve drying, but rather followed a series replacement of the interstitial water by diffusion processes to a final hardened resin. The technique is apparently very time consuming and laborious. Photomicrographs of submarine sediment—prepared by freeze-drying, embedded with Maraglas Epoxy, and subjected to ultrathin sectioning—has clearly revealed detailed, complex fabrics that appear to be unaffected significantly by sample preparatory techniques (Bowles 1968a, 1968b). The freeze-drying technique also is time consuming, and there is danger of ice crystallization during the process.

### Transmission Electron Microscopy

Photomicroscopy of the clay fabric for all of the Mississippi Delta samples was carried out using a Philips Transmission Electron Microscope, Model 300, at 80 kV. The work was carried out at the Veterinary, Toxicology, and Entomology Research Laboratory, U.S. Department of Agriculture, College Station, Texas. Under routine research conditions, the Philips Model 300 has a resolution of about  $8 \times 10^{-10}$  m (8 Å) which can be improved for specific requirements (personal communication, Hilton H. Mollen-

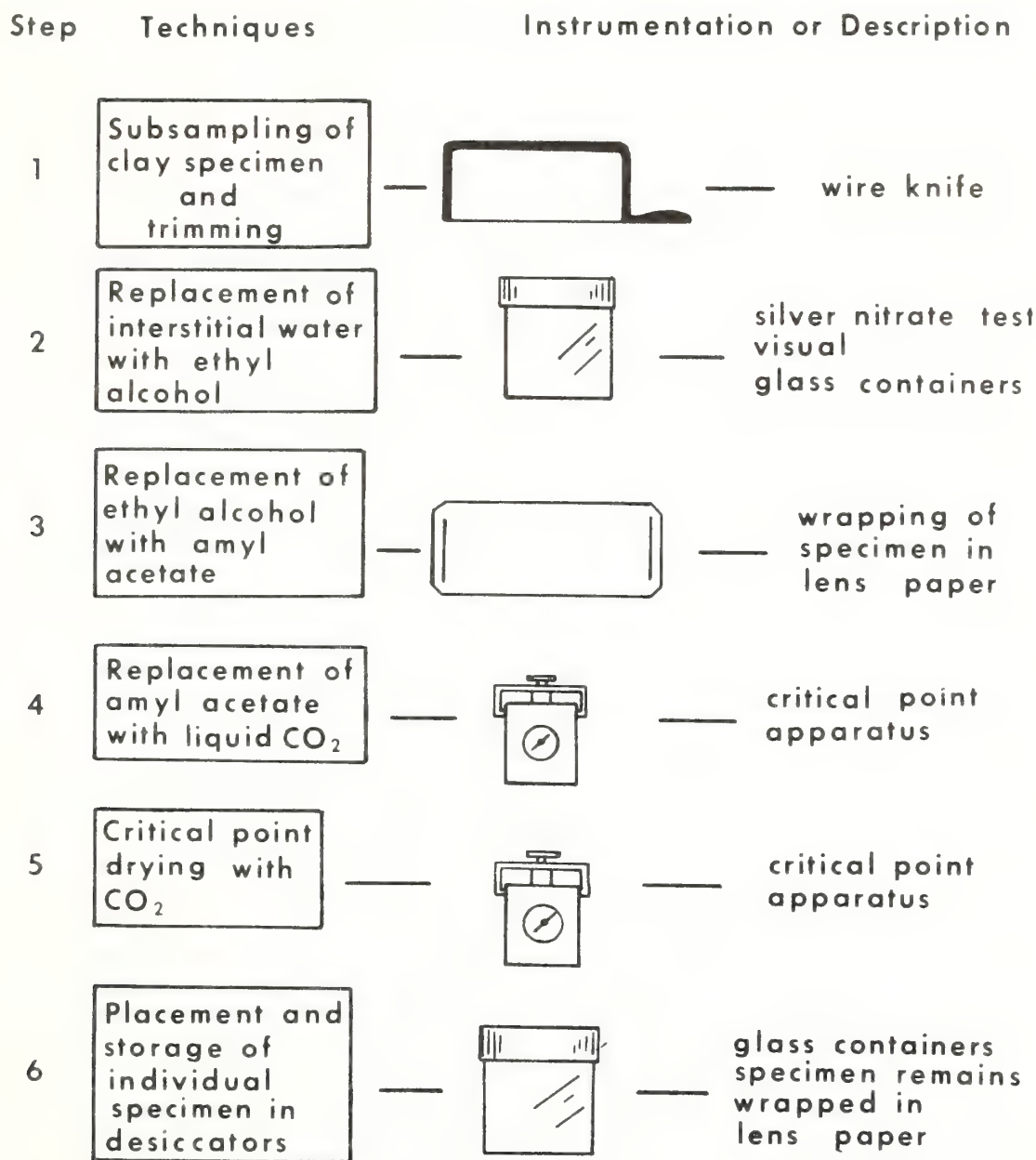


FIGURE 26.—Analytical techniques and instrumentation for clay fabric analysis: Dehydration techniques.

hauer, U.S.D.A.). The D.S.D.P. clay fabric samples were analyzed with an Hitachi Model HS-8A Transmission Electron Microscope at 50 kV, which is considered to have considerably less resolving potential than the Philips 300. Both instruments, however, proved to be adequate for this study. The photomicroscopy with the Hitachi E. M. and all of the ultramicrotomy were carried out at the Electron Microscopy Center, Texas A&M University, College Station, Texas.

A total of 426 transmission electron photomicrographs were taken and examined during this study. Typical examples of the characteristic fabric for each specimen examined have been used in this investigation. Although different magnifications were made of the fabric periodically, a magnification of 16,000 times was found to be the most useful in terms of overall delineation of the general fabric characteristics, clarity, and particle size.

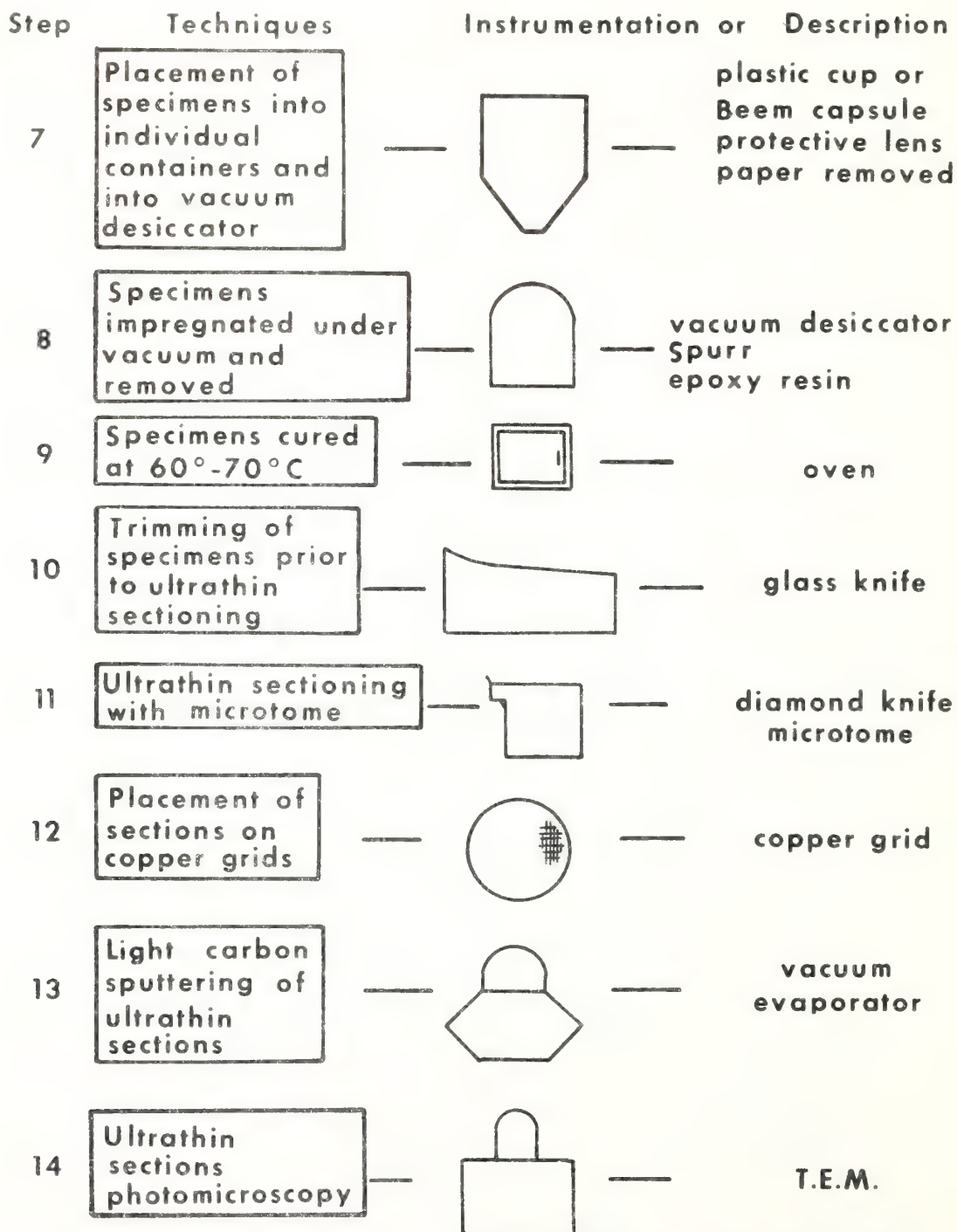


FIGURE 27.—Analytical techniques and instrumentation for clay fabric analysis: Impregnation, sectioning, and transmission electron microscopy (T.E.M.).



## Geotechnical Tests

The mass physical properties investigated in this study were determined by standard geotechnical tests which are described in numerous text books on soil mechanics (Scott 1963; Wu 1966; Terzaghi and Peck 1967; Lambe and Whitman 1969). Lambe (1951) has presented an excellent detailed account of the standard laboratory soils tests, particularly techniques for determining water content, grain specific gravity (grain density), grain size, Atterberg limits, shear strength, and consolidation. Richards (1961, 1962) has discussed the specifics of the geotechnical tests, including the miniature vane test, water content, porosity, wet unit weight (bulk density), as applied to submarine sediments. Bennett and others (1970) and Bennett and Lambert (1971) have discussed techniques and the reproducibility for many of the common mass physical properties tests as applied to submarine sediments. Lowe and others (1964) and Bryant and others (1967) have reviewed the use and applications of the Anteus Back Pressure Consolidometer which was the instrument used to determine the consolidation characteristics of the sediment samples. Void ratio versus logarithm of pressure curves ( $e$ -log  $p$ ) are derived from these tests. In function, the basic difference between the Anteus Consolidometers and other standard consolidometers is that back pressure (a hydrostatic pressure) is applied to the sediment sample surrounded with water (in this case, seawater). This technique insures nearly 100% saturation of the sediment prior to loading at back pressures of 686 kPa to 1079 kPa (Bryant and others 1975).

bility for many of the common mass physical properties tests as applied to submarine sediments. Lowe and others (1964) and Bryant and others (1967) have reviewed the use and applications of the Anteus Back Pressure Consolidometer which was the instrument used to determine the consolidation characteristics of the sediment samples. Void ratio versus logarithm of pressure curves ( $e$ -log  $p$ ) are derived from these tests. In function, the basic difference between the Anteus Consolidometers and other standard consolidometers is that back pressure (a hydrostatic pressure) is applied to the sediment sample surrounded with water (in this case, seawater). This technique insures nearly 100% saturation of the sediment prior to loading at back pressures of 686 kPa to 1079 kPa (Bryant and others 1975).

## Evaluation of Sample Quality and Techniques

Sediment core quality and subsample preparation techniques for clay fabric analysis were evaluated during this study. The quality of sediment cores was assessed in terms of shear strength test both in situ and in the laboratory by miniature vane and Torvane, and the results from void ratio versus log of pressure curves ( $e$ -log  $p$ ). Clay fabric particle-to-particle integrity as depicted in T.E.M. photomicrographs was evaluated in terms of fabrics of natural (undisturbed) versus remolded samples, image enhancement techniques applied to clay fabric, and visual assessment of subsample integrity during sample preparation and analyses. Standard techniques as well as new methods were developed and used in this study throughout the entire analytical procedure in order to maintain the particle-to-particle integrity and characteristic features of the clay fabrics. Image enhancement techniques developed in this study offer a new approach to the evaluation of transmission electron photomicrographs of clay fabrics.

### *Sediment Shear Strength*

Natural (undisturbed) shear strength measurements with the in-situ wire line vane for B-1 yielded values ranging from about 4.8 kPa to slightly greater than 9.6 kPa between the mudline and 23 m. A general steady increase in shear strength occurs between 23 and 37 m with the highest values of approximately 23.9 kPa. Residual shear strength (vane rotated 360 degrees after initial strength measurement followed by the residual strength test) and cyclic shear strength tests (vane rotated 10 times through 90 degrees after the initial failure and then tested for shear strength) yielded values of up to one half the undisturbed values giving sensitivities (ratio of the natural shear strength to the remolded or disturbed shear strength) of 2 but commonly less

than 2 between the mudline and 23 m. Generally higher sensitivities of only slightly over 2 occur between the mudline and 23 m. Sensitivity values of 2 and less are considered indicative of insensitive clays, and values ranging between 2 and 4 are characteristic of normal clays. Values of 4 to 8 are considered characteristic of sensitive clays. Sensitivities of 8 to 16 are diagnostic of many of the well known quick clays (Terzaghi and Peck 1967).

Miniature vane and Torvane tests of the cored sediment show strikingly similar results when compared to the in situ wire-line vane test. Values average 4.8 kPa between the mudline and 23 m, and steadily increase between 23 and 37 m to values of 23.9 kPa as observed for the wireline measurements. With the exception of an anomalous high shear strength zone at approximately 7.5 m below the mudline in both B-2 and B-3, similar shear strength values and relationships are found among the in situ, and miniature vane and Torvane measurements. This close agreement between in-situ shear strength measurements and strength tests on cored material indicates relatively high-quality sediment cores with minimal disturbance due to coring technique. The similarity in sensitivities, by the wire-line vane measurement and those determined on the cored material also corroborates this conclusion.

Wire-line vane measurements at B-1 were not made in the hard, stiff, clay cored between 85 and 154 m; however, miniature vane shear test values ranged from 23.9 kPa in the upper stiff clay to values of 192.5 kPa in the hard deep clays. Sensitivities for this Pleistocene clay averaged 2.3 with a range of 1.4 to 3.2, essentially the same as the sensitivities found for the soft clays between the mudline and 37 m.

### Consolidation Tests

Laboratory tests with the Anteus Back Pressure Consolidometer were performed on selected sediment samples from cores B-1 and B-2 following standard procedures discussed by Lowe (1964) and Bryant and others (1967). Consolidation test data from these cores were used to evaluate sediment core quality. Principles of consolidation testing have been treated in detail by Terzaghi (1925b), Terzaghi and Peck (1948, 1967), and by Lambe (1951). A typical diagrammatic void ratio versus logarithm of pressure curve ( $e$ -log  $p$ ) and the standard graphical construction of the

preconsolidation pressure is depicted in figure 28, representing a typical, "normal" sediment commonly encountered in testing terrestrial soils. The preconsolidation pressure,  $\bar{P}_c$ , is defined as the greatest stress to which a sediment has ever been subjected. The graphical construction as proposed by Casagrande (1936), using the  $e$ -log  $p$  curve, theoretically, determines the preconsolidation pressure.

Extensive back pressure consolidation testing has been carried out on submarine sediment from various depositional environments in the Gulf of Mexico. These surficial submarine clays tested are characterized by an atypical  $e$ -log

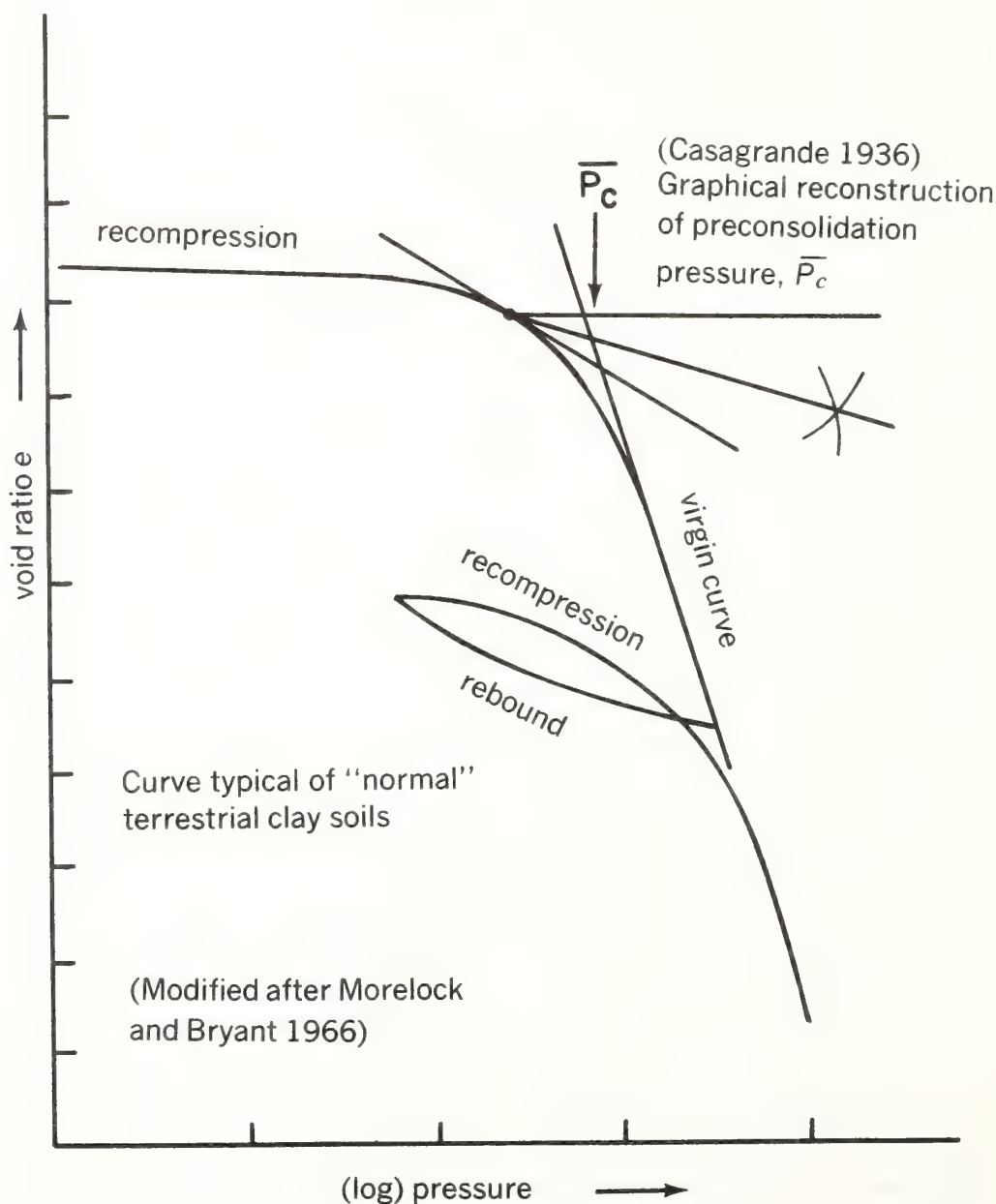


FIGURE 28.—Typical consolidation test—void ratio versus logarithm of pressure curve.



*p* virgin curve which is concave upward and to the right as compared to the usual straight-line virgin curve typical of many terrestrial clay soils (Morelock and Bryant 1966; Bryant and others 1967; Delfache and Bryant 1970; Bryant and Delfache 1971; Bryant and others 1974). The atypical characteristic of the virgin *e-log p* curves have been found to be generally ubiquitous for the Gulf of Mexico surficial submarine sediment, and this feature of the curves also has been found to be diagnostic of sensitive and highly sensitive clays. These studies have clearly pointed out that the high sensitivity indicated by the void ratio versus log of pressure curves strongly reflects the relatively undisturbed nature of the sediment samples tested (Morelock and Bryant 1966; Bryant and others 1967). Similarly shaped *e-log p* curves were reported for highly sensitive, subaerially exposed, marine clay (Jarrett 1967). Sensitive clays typically are characterized by essentially two straight-line portions comprising the virgin line of the *e-log p* curves. Sensitive clays with values of 4 to 8, typically lose 75 to 87.5 percent of their strength when remolded or severely disturbed. Although sensitivities as high as 57 were reported for submarine sediment, average values of only 4 are the most common (Keller and Bennett 1970). Values of 4 border on being slightly sensitive to sensitive.

### Testing and evaluation

Selected sediment core samples from B-1 and B-2 were consolidated in the laboratory. Sampling depths ranged from 1.4 to 120.6 m including not only the young, recent, "soft" clays, but also the deeply buried Pleistocene clays. Core sample B-1 (1.3 m depth) was consolidated in the "undisturbed" natural condition to a load of  $61 \times 10^2$  kPa, and a remolded sample was also consolidated to the same load. The natural, "undisturbed" sample clearly shows a strong virgin curve which is concave up and to the right (fig. 29). The remolded sample (fig. 30) does not reflect the strong inflection in the virgin curve but rather shows a more typical *e-log p* curve indicative of a disturbed condition as compared to the *e-log p* curve of the undisturbed sample (fig. 29). Likewise, samples B-1 (2 m depth), B-2 (1.4 m depth), and B-2 (27.9 m depth) show the typical "sensitive-like" nature as reflected in the *e-log p* curves of the "undisturbed" natural sediment (figs. 31, 32, 33, 34, 36). The remolded samples do not show this characteristic in the consolidation curves.

Sample B-1 (12.2-m depth) is suspect owing to the straight line portion of the virgin curve and also to the considerably lower initial void ratio, *e*, of the sample (fig. 35). This sample, however, serves as a good example of

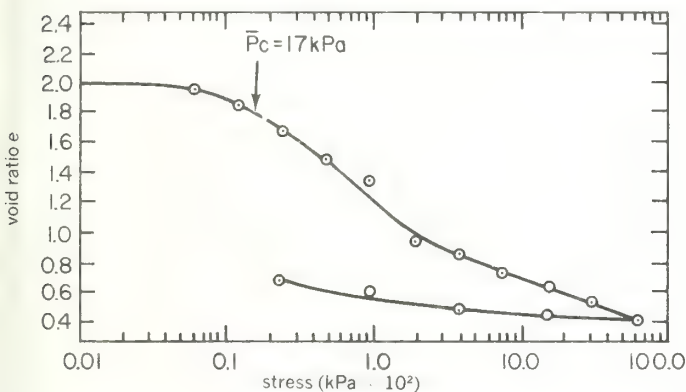


FIGURE 29.—Void ratio versus logarithm of pressure. South Pass, core B-1, 1.37 m (4.5 ft), natural.

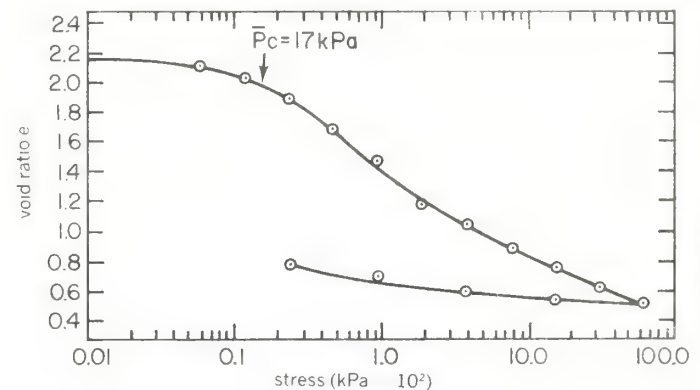


FIGURE 31.—Void ratio versus logarithm of pressure. South Pass, core B-1, 1.98 m (6.5 ft), natural.

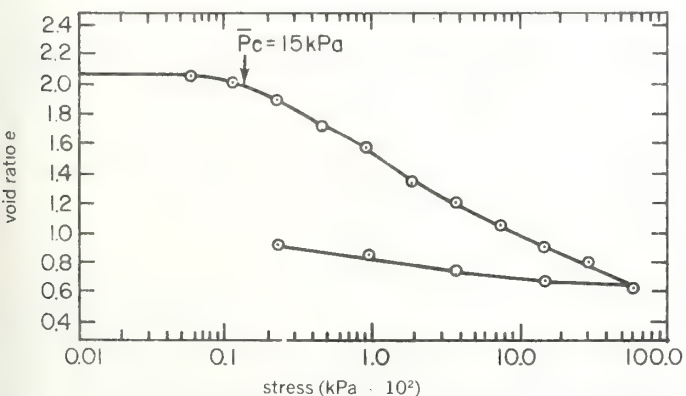


FIGURE 30.—Void ratio versus logarithm of pressure. South Pass, core B-1, 1.37 m (4.5 ft), remolded.

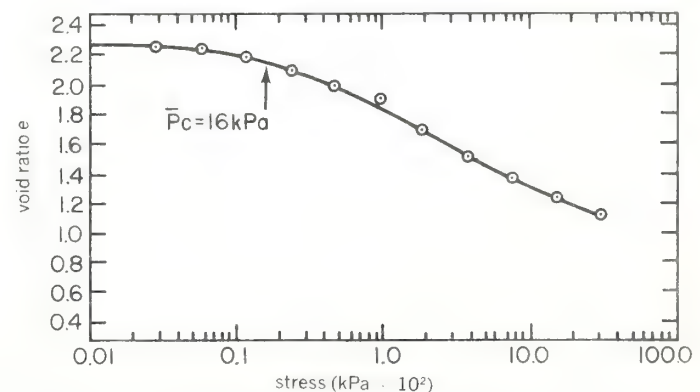


FIGURE 32.—Void ratio versus logarithm of pressure. South Pass, core B-1, 1.98 m (6.5 ft), remolded.



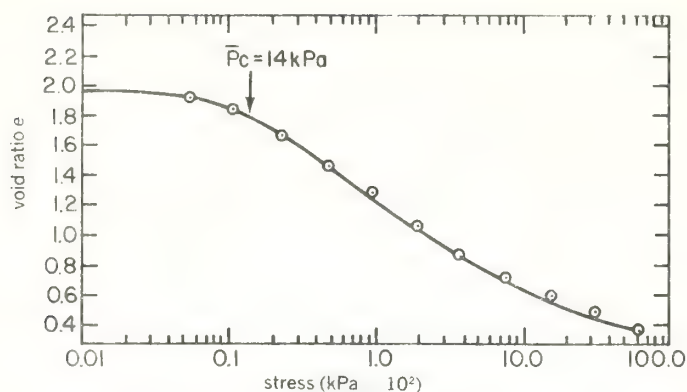


FIGURE 33.—Void ratio versus logarithm of pressure. South Pass, core B-2, 1.37 m (4.5 ft), natural.

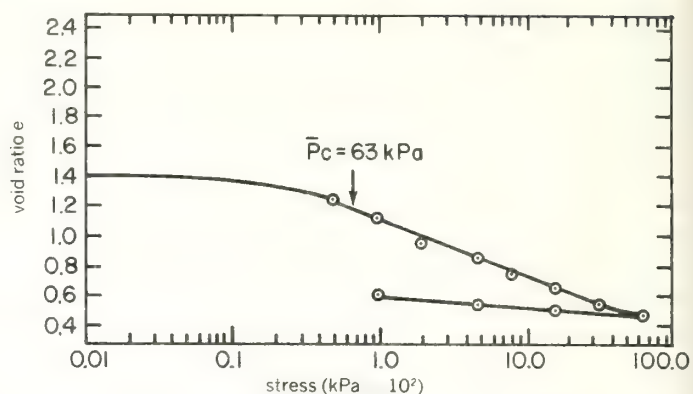


FIGURE 35.—Void ratio versus logarithm of pressure. South Pass, core B-1, 12.19 m (40 ft), natural.

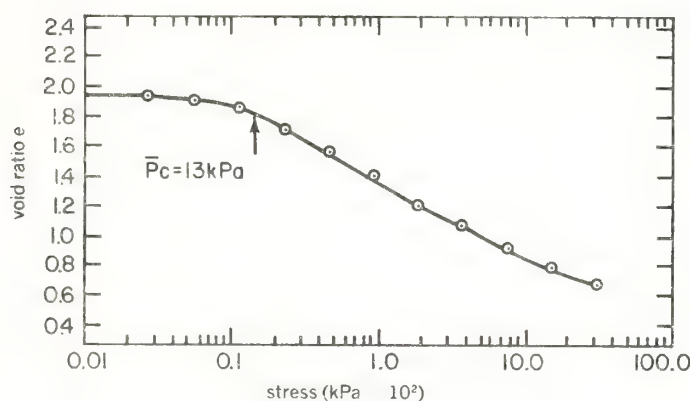


FIGURE 34.—Void ratio versus logarithm of pressure. South Pass, core B-2, 1.37 m (4.5 ft), remolded.

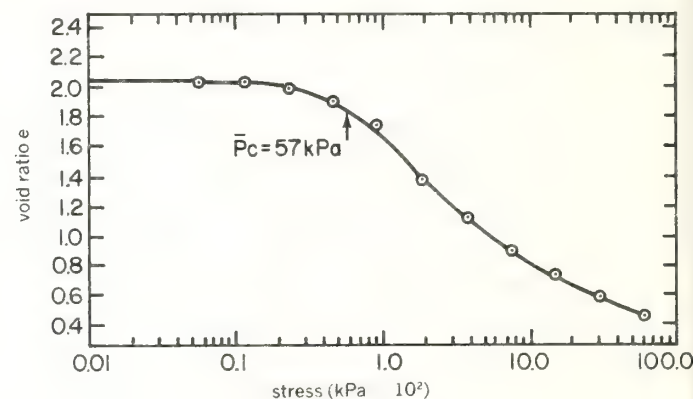


FIGURE 36.—Void ratio versus logarithm of pressure. South Pass, core B-2, 27.58 m (90.5 ft), natural.

sediment possibly disturbed (or a poor laboratory test, i.e. malfunctioning of the consolidometer) but *not* remolded in the laboratory by standard testing procedures. Void ratio determinations on samples from the same approximate depths yielded values of 1.9, considerably closer to the void ratio values found for the sediment to depths of 35 m below the mudline. Bryant and others (1974) have attributed the "sensitive-like" nature of the  $e$ -log  $p$  curves (virgin curve which is concave up) to be characteristic of the Gulf of Mexico submarine sediments with void ratios greater than about 1.0.

A sample from a depth of 120.6 m (core B-1) with an initial void ratio of less than 1.0 was consolidated to a load of  $19.15 \times 10^2$  kPa. The  $e$ -log  $p$  curve shows a broad recompression curve up to a preconsolidation pressure of  $10.73 \times 10^2$  kPa which is quite unlike the  $e$ -log  $p$  curves of the much higher void ratio (high porosity) overlying sediment (fig. 37). Clearly this material represents a considerably greater degree of natural consolidation than the high void ratio sediment. Noteworthy, however, is the fact that sensitivities, determined by shear strength tests to depths of approximately 150 m, ranged from slightly less than 2 to

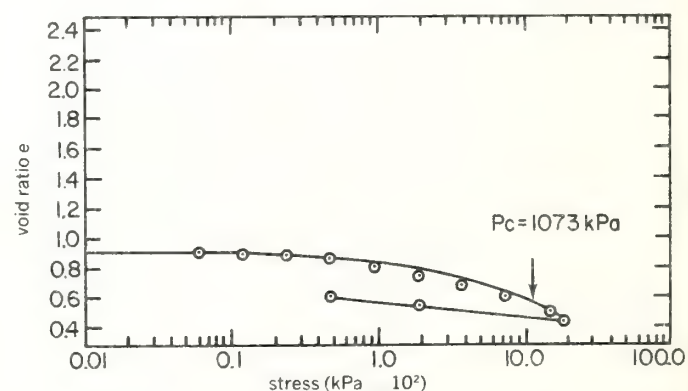


FIGURE 37.—Void ratio versus logarithm of pressure. South Pass, core B-1, 120.55 m (395.5 ft), natural.

slightly greater than 3 (characteristic of "nonsensitive" normal clays), and yet the  $e$ -log  $p$  curves of the high void ratio sediment indicate a sensitive nature unlike the deeper (void ratio of from slightly greater than 1.0 to less than 1.0) naturally consolidated clay. A possible explanation for this behavior will be discussed later.

### Sample quality

Schmertman (1955) and Silva (1974) have discussed methods of assessing the degree of sample disturbance and quality through the analysis of laboratory void ratio versus logarithm of pressure curves. Based on quite similar reasoning as that of Schmertman, Silva has proposed a quantitative method of determining the relative degree of sediment sample disturbance in terms of an index parameter. Silva (1974) defines a disturbance index,  $I_D = \frac{\Delta e}{\Delta e_0}$ , with  $\Delta e$  equal to the change in void ratio from the initial value to the void ratio at the preconsolidation pressure ( $\bar{P}_c$ ). Silva uses a value of  $\bar{P}_c$  determined on a corrected field compression line. The change in void ratio,  $\Delta e_0$ , is equal to the difference in void ratio between the initial value and the value at the theoretical void ratio on an idealized remolded base line directly at the preconsolidation pressure,  $\bar{P}_c$ . The idealized base line is constructed as a straight line between  $e_0$  and a void ratio of 42 percent of  $e_0$  over two log cycles (fig. 38). Schmertman (1953) found that straight line extensions on the initial virgin slope of consolidation tests, on most clays (disturbed to varying degrees), intersect at approximately 42 percent of the initial void ratio. The intersection of field initial virgin slopes and laboratory virgin slopes generally also were found to agree within a few percent, and therefore the value of 42 percent  $e_0$  was chosen as a good estimate for most clays (nonsubmarine). The classification (Silva 1974) based on the disturbance index is as follows:

Disturbance  
index,  $I_D$

Degree of  
disturbance

-0.15	Very little disturbance ("undisturbed")
0.15-0.30	Small amount of disturbance
0.30-0.50	Moderate disturbance
0.50-0.70	Much disturbance
-0.70	Extreme disturbance (remolded)

The disturbance index,  $I_D$ , was calculated for the relatively soft, "undisturbed"  $e$ -log  $p$  samples from the upper 91 m of high void ratio sediment. In addition,  $I_D$  was also determined for the stiff, hard, clay sampled from a depth of 120.6 m. For graphical presentation (fig. 39), these data ( $I_D = \Delta e / \Delta e_0$ ) are plotted against initial void ratio,  $e_0$ , with the major divisions for the degree of disturbance depicted according to Silva (1974). The disturbance index was calculated for these samples using the standard techniques for determining the preconsolidation pressure developed by Casagrande (1936). Clearly, the disturbance index for all of the high void ratio samples falls within the division of "small amount of disturbance" to the middle and lower end of the "moderate disturbance" division. Important to note is the fact that of the high void ratio sediment tested, sample B-1 (12.2-m depth) showed the highest degree of disturbance based on  $I_D$ . This sample was suspected to be somewhat disturbed due to the initial low void ratio and poorly shaped  $e$ -log  $p$  curve as compared to the other samples tested.

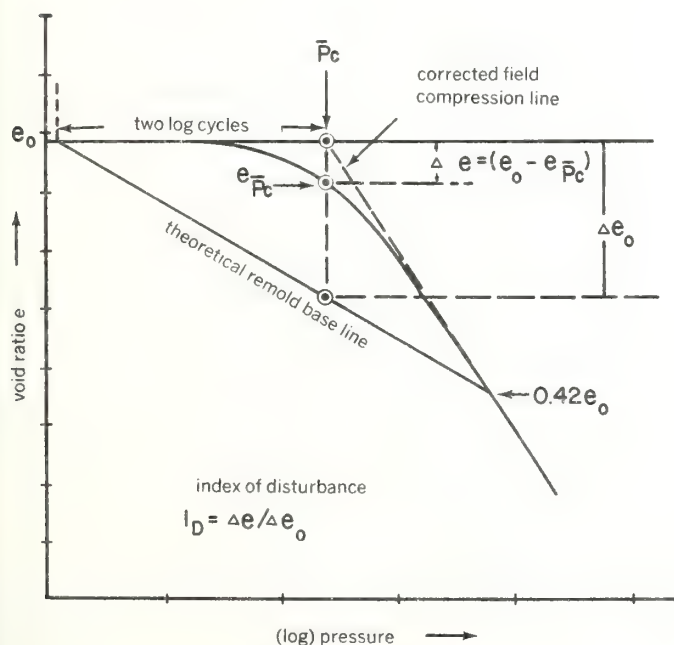


FIGURE 38.—Method for determining degree of disturbance from a typical  $e$ -log  $p$  curve. (Modified after Silva 1974)

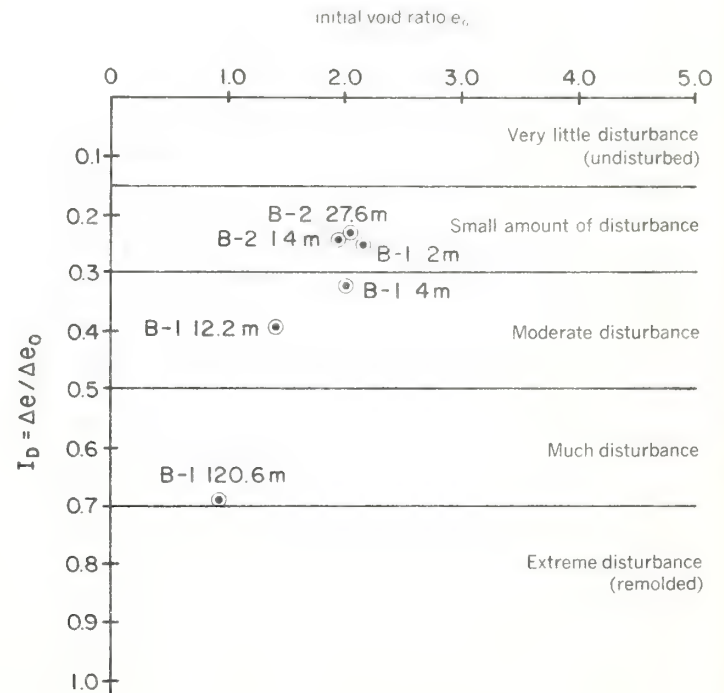
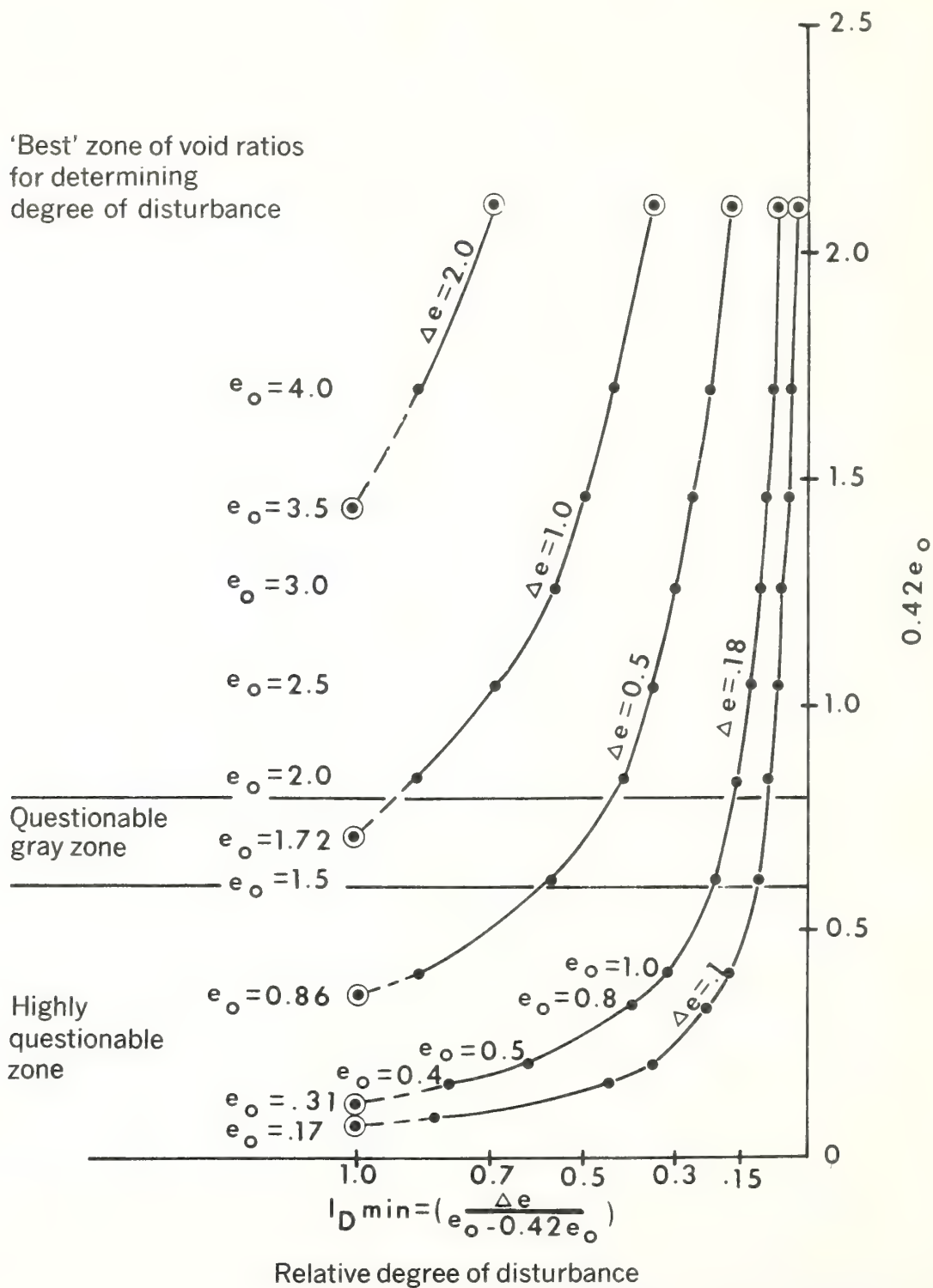


FIGURE 39.—Degree of disturbance ( $I_D$ ) versus void ratio ( $e_0$ ) for Mississippi Delta samples.

FIGURE 40.—Plot of  $I_D$  minimum versus  $e_o$  for fixed values of  $\Delta e$ .



The peculiar disturbance index for sample B-1 (120.1 m) indicating "much disturbance" requires explanation. This sediment, a stiff, low-porosity, relatively hard clay, would be considerably less subject to coring and sampling disturbance than the soft, high-porosity sediment. With respect to the disturbance index,  $I_D$ , the ratio  $\Delta e/\Delta e_0$  is a function of the actual departure of the void ratio,  $e\bar{P}_c$ , at the preconsolidation pressure from the initial void ratio,  $e_0$ , such that  $\Delta e = (e_0 - e\bar{P}_c)$ . The index  $I_D$  is strongly influenced by  $\Delta e$  disproportionately with a decrease in initial void ratio,  $e_0$ .

As an example, given a fixed value for  $\Delta e$  and calculating  $I_D$ , with decreasing values for the initial void ratio,  $e_0$ , one can observe that the disturbance index increases sharply with decreasing initial void ratio. This relationship can be depicted by plotting  $e_0$  or  $0.42e_0$  as a function of  $I_D$ ,  $\min. = \frac{\Delta e}{e_0 - 0.42e_0}$  (fig. 40). A minimum index of disturbance,  $I_D \min.$ , differs from  $I_D$  by the substitution of  $(e_0 - 0.42e_0)$  for the value  $\Delta e_0 = e_0 - e\bar{P}_c$  which varies from sample to sample depending on the slope of the virgin curve. Since  $I_D \min.$  is slightly smaller in value than  $I_D$ , the index would indicate a minimum degree of disturbance for a given sample following the classification of Silva (1974). In practice,  $0.42e_0$  is a larger value than  $e\bar{P}_c$  which occurs on the theoretical remold curve at the preconsolidation pressure and  $I_D \min.$  would not reach a critical value of 1 but could approach the value of 1 as the degree of disturbance increased. Nevertheless, for graphical presentation, the plots of  $I_D \min.$  versus  $0.42e_0$  illustrates the *nonlinear* relationship between  $\Delta e$  and  $e_0$  and indicates the probability that the disturbance index classification is not valid for relatively low void ratio (low-porosity) sediment. The index of disturbance,  $I_D \min.$ , is strongly influenced by the value of  $e_0$  between 1.5 to 2.0 void ratio, and the index increases rapidly below values of  $e_0 = 1.5$ . Apparently sediment samples showing initial void ratios,  $e_0$ , much less than 2.0 should not be assessed in terms of disturbance by the index of disturbance classification. Considerably more study is required to arrive at a workable, unbiased classification of disturbance applicable to a wide range of void ratios.

In review, the void ratio versus logarithm of pressure curves indicates in general that the cores tested were relatively high-quality samples showing minimal degree of disturbance with the exception of sample B-1 (12.2-m depth) which is suspect.

### *Fabric of Natural Versus Remolded Clay Samples*

Clay fabric particle-to-particle integrity and characteristic features of natural (undisturbed) samples were compared with the clay fabric of remolded (disturbed) subsamples of contiguous material. Essentially identical tech-

niques were employed for both the remolded and the undisturbed material. Subsamples of undisturbed material were remolded in the laboratory by standard techniques commonly used for preparing samples for sensitivity determinations by vane shear measurement. Technically, remolding is carried out in the laboratory by mixing and working a clay sample into a plastic mass, usually with a spatula, at the same water content as the undisturbed sample. The fabrics of undisturbed and remolded samples were compared in order to determine the relative degree of disturbance and the particle-to-particle integrity of the sediment, to determine sample quality, and to assess the analytical techniques of sample preparation for clay fabric analysis employing the transmission electron microscope.

Two samples were selected for remolding and comparison with an undisturbed counterpart subsample. Mississippi Delta sample B-2, 1.4 m below mudline, and sample D.S.D.P. 163A, 143 m below mudline, were selected for the evaluation. Because "soft," low shear strength sediments having relatively high void ratios are commonly much more susceptible to disturbance than low void ratio stiff material, sample B-2 (void ratio  $e = 1.94$ , porosity  $n = 66\%$ ) from a depth of 1.4 m below the mudline was selected as representative of the "soft" sediment encountered during this study. B-2 (1.4 m) is a silty clay (approximately 30% silt, approximately 69% clay) with essentially little or no sand (less than 1%). The clay size fraction is composed of approximately 57% smectite (montmorillonite), 33% illite (mica), and about 10% kaolinite and/or chlorite. Sample 163A (143 m below mudline) is a yellow brown zeolitic clay, late Cretaceous in age, and was retrieved from a water depth of 5,330 m in the equatorial Pacific. The sample is a silty clay (approximately 81% clay, approximately 18% silt) with less than 2% sand. Smectite is the dominant clay mineral with trace amounts of illite, clinoptilolite, and quartz in the clay size fraction (approximately  $<2 \mu\text{m}$ ). Clinoptilolite, smectite, and quartz are the major minerals of the silt size fraction, and a minor trace of illite is present. Phillipsite has been reported as a constituent of the zeolitic clay sampled at D.S.D.P. site 163A at 140 to 144 m (van Andel, Health, and others 1973). The sample is characterized by a very high void ratio of 3.5 and a porosity of 78 percent. Clearly, this deep-sea, high void ratio, clay sample represents a strong contrast to the Mississippi Delta clays particularly in terms of depositional environment. The D.S.D.P. sample was selected for the natural versus remolded comparison because of its uniquely different nature (deep-sea), high void ratio, clay mineralogy, and highly complex clay fabric in the "undisturbed" state.

### **D.S.D.P. sample (undisturbed)**

The highly complex clay fabric of the "undisturbed" D.S.D.P. 163A sample is revealed in fig. 41EM, an electron microscope photomicrograph (hereafter electron micro-



FIGURE 41.—Clay fabric showing flocs, linking chains, and zeolitic aggregate, Deep Sea Drilling Project (D.S.D.P.) core 163A (143 m) undisturbed sample.

scope photomicrographs will be indicated by the figure number followed by the notation EM, i.e. fig. 41EM). The fabric is characterized by clay flocs connected by linking chains with relatively large intervoids. Occasionally "high density" aggregates were observed as revealed in the far left edge of fig. 41EM. The high density aggregates are tentatively interpreted as being composed of essentially clinoptilolite and possibly some phillipsite as revealed by their needle-like, lath-shaped crystals (fig. 42EM). Mumpton (1960) has

presented a detailed treatment of the mineral clinoptilolite, and Deer and others (1963) have discussed zeolites in general. Linking chains between flocs appear to be built primarily in an edge-to-edge (EE) association of clay particles; however, some face-to-face (FF), stair-stepped associations appear to be present but to a lesser degree. An important feature of the flocs is the relatively large intervoids which are clearly revealed at high magnifications (fig. 43EM). The large floc in figure 43EM is approximately

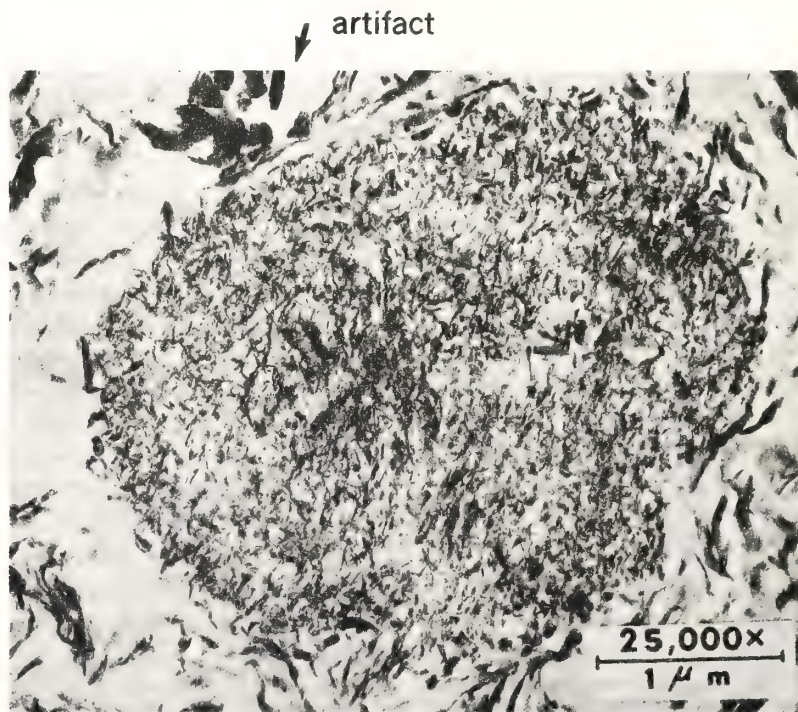


FIGURE 42.—Clay fabric showing zeolitic aggregate surrounded by domains, D.S.D.P. core 163A (143 m) remolded sample.



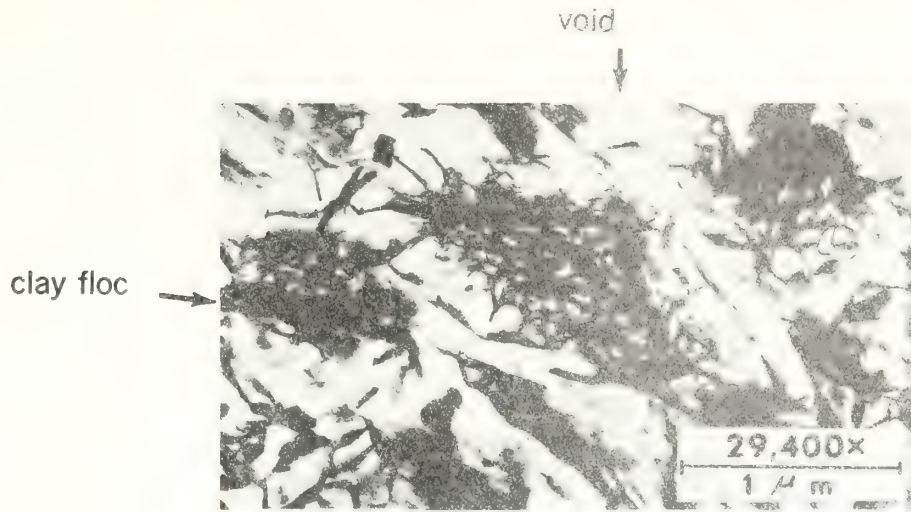


FIGURE 43.—Clay fabric showing clay flocs, floc intravoids, and linking chains, D.S.D.P. core 163A (143 m) undisturbed sample.

$1.6 \times 10^{-6}$  m (1.6 microns) in maximum length, and about  $0.7 \times 10^{-6}$  m in width as revealed in the ultrathin section photomicrograph. Because of the very small size of the floc, the numerous clay particles which build the floc are extremely small. The flocs appear to be built of numerous clay particles arranged in an edge-to-face structure at oblique angles resulting in the relatively high intravoids (fig. 43EM). Close examination of the photomicrographs indicates that the flocs appear to be somewhat compressed possibly due to the process of consolidation and in situ overburden pressure. The important features of sample D.S.D.P. 163A, however, is the highly complex fabric of flocs, linking chains, and zeolitic aggregates structured to form a high

void ratio (high-porosity) clay sediment in the relatively undisturbed state. These features show a strong contrast to the fabrics observed in the remolded (disturbed) samples.

#### D.S.D.P. sample (remolded)

The remolded D.S.D.P. 163A sample reveals a strikingly different fabric than observed in the photomicrographs of the undisturbed sample. Clearly, the highly complex fabric characteristic of the undisturbed sediment is completely destroyed in the remolded material (fig. 44EM-A). Flocs and linking chains are broken down to form well identifiable domains of essentially face-to-face platelets arranged in a random orientation. The overall high void ratio is main-

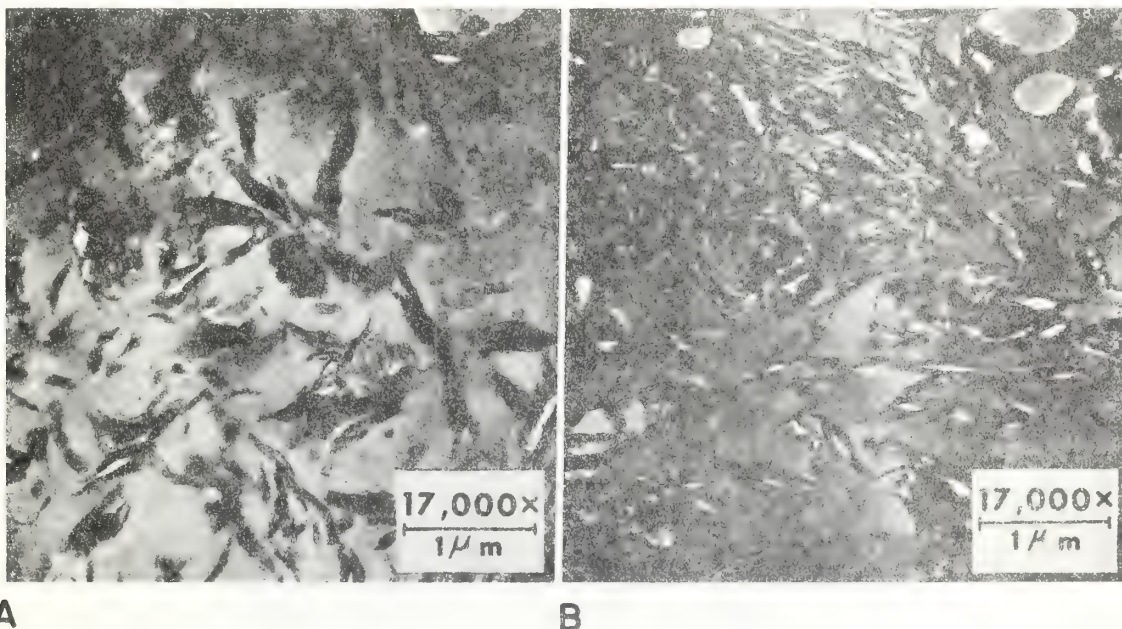


FIGURE 44.—Clay fabric showing (A) randomly oriented domains with high overall void ratio, and (B) local areas of strongly oriented, dense pseudoaggregates and domains, D.S.D.P. core 163A (143 m) remolded sample.



tained, and the intravoids of the preexisting floes are destroyed. A few rather dense "aggregates" comprised of strongly oriented particles over local areas were observed in some of the remolded samples (fig. 44EM-B). These "aggregates" are collapsed, highly disturbed floes combined with other adjacent clay particles brought about by remolding and kneading. Interesting to note is that many of the "zeolitic" aggregates found in the undisturbed samples were also present in the remolded material indicating a strong structural integrity for these aggregates despite the remolding action. Figure 42EM is a photomicrograph of a typical

"zeolitic" aggregate from the remolded D.S.D.P. 163A sample. The remolded sample is characterized by randomly oriented domains as observed in the previous photomicrograph (fig. 44EM), but the "zeolitic" aggregate appears to have remained structurally intact. Intravoids are also present in the aggregate even though the aggregate has an overall appearance of being quite dense.

#### Mississippi Delta Sample (undisturbed)

Mississippi Delta sample B-2 (1.4 m) was selected for comparison of the undisturbed versus the remolded material.

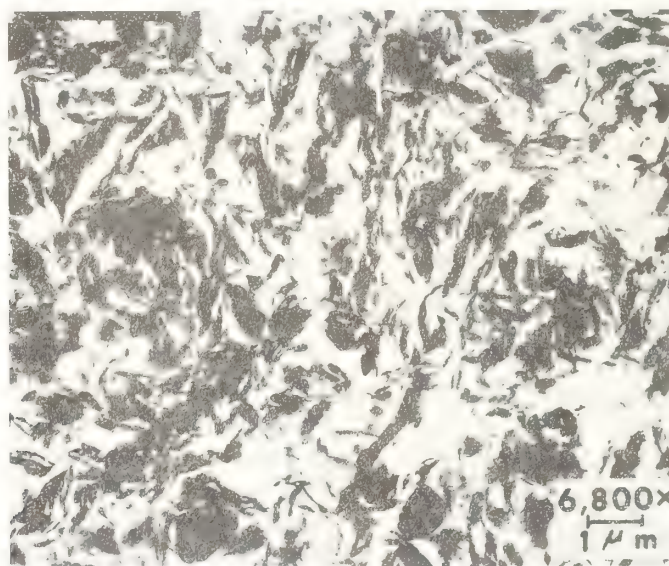


FIGURE 45.—Clay fabric showing randomly oriented domains, core B-2 (1.4 m) undisturbed sample.

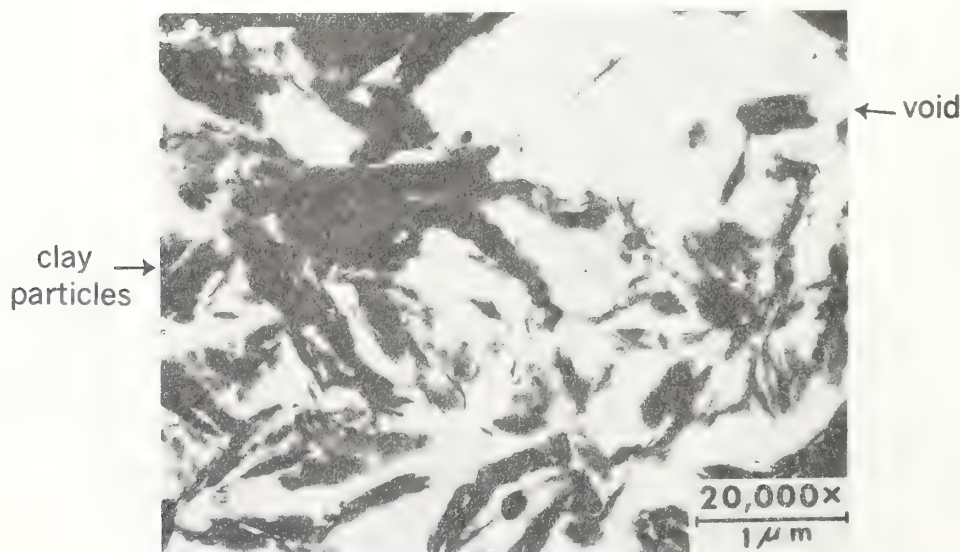


FIGURE 46.—Clay fabric depicting well-defined randomly oriented domains and high void ratio, core B-2 (1.4 m) undisturbed sample.



FIGURE 47.—Stereographic view of clay fabric depicting randomly oriented domains and high void ratio, core B-2 (1.4 m) undisturbed sample.

A general view of the undisturbed clay fabric at low magnification is observed in figure 45EM. The details of the fabric are rather difficult to interpret at low magnifications because of the very fine grained nature of these clays. However, the figure reveals an overall random orientation of the clay particles, generally domains. Much clearer details of the clay fabric are discernible at relatively high magnifications of 16,000 $\times$  to 20,000 $\times$  as revealed in figure 46EM. This photomicrograph also depicts the characteristic random fabric with large voids structured by numerous edge-to-face particle contacts. The clay fabric appears to be

predominantly domains (particles in face-to-face arrangement) oriented randomly; however, some rather continuous "chains" and edge-to-edge arrangements are observed (fig. 47EM). These characteristics are clearly evident in the stereographic view of photomicrograph 47EM.

#### Mississippi Delta sample (remolded)

A rather strong contrast is evident between the remolded and undisturbed fabric of sample B-2 (1.4 m). At low magnification the fabric is characterized by a typical "swirl" pattern (fig. 48EM) recognizable even at higher magnifica-

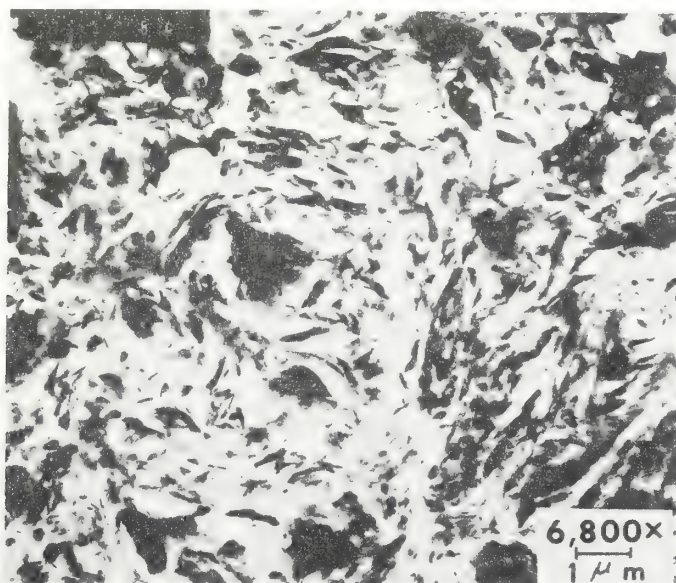


FIGURE 48.—Clay fabric depicting 'swirl' pattern and local areas of highly oriented clay particles, core B-2 (1.4 m) remolded sample.



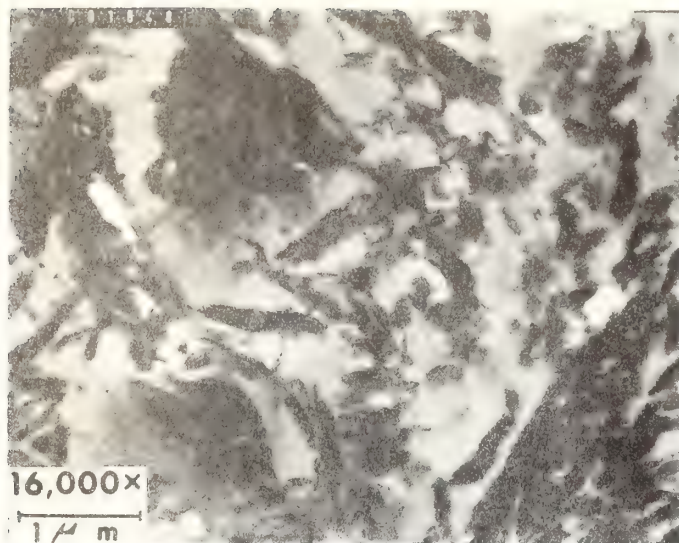


FIGURE 49.—Clay fabric—depicted at high magnification—showing 'swirl' pattern and local area of highly oriented particles, core B-2 (1.4 m) remolded sample.

tions (fig. 49EM). The overall remolded fabric is characterized by large areas of highly oriented particles (domains) forming the "swirl" pattern over extensive areas. The general high void ratio is maintained by remolding at the original water content. Although some small areas show randomly oriented clay particles or domains, the common features of the remolded fabric are the highly oriented clay particles as observed in the photomicrographs of figure 50EM. Lambe (1953) proposed that remolded clay was

characterized by a high degree of parallelism between adjacent particles (fig. 4), and Mitchell (1956) claimed that remolding tended to homogenize the sediment sample rendering the clay less variable. Lambe and Whitman (1969) claim that physically working or remolding of an element of soil until it becomes homogeneous tends to align adjacent particles and thus destroys the bonds between particles. Pusch (1970) also reported that remolding causes successive breakdown of aggregates and a decrease in shear strength. The electron photomicrographs of both D.S.D.P. 163A and B-2 samples contrasting the undisturbed and remolded sediments reveal the characteristic features of the clay fabric described by the above researchers. In addition, these comparisons of undisturbed versus remolded fabrics give strong evidence that the samples have not been severely disturbed, and the fabric of the undisturbed samples have maintained a high degree of structural integrity.

### *Image Enhancement Techniques*

Clay fabric particle-to-particle integrity and sample quality as influenced by sample preparation were evaluated by image enhancement techniques. A representative clay fabric sample T.E.M. photomicrograph of the low shear strength, high-porosity sediment (B-1, 1.4 m) was assessed with a Digital Image Processing System (DIPS), figure 51, for the primary purpose of detecting possible microstructural damage (i.e., a major change in clay fabric) caused by sample preparation techniques. The secondary purpose for using the DIPS was to investigate other possible potentials of the system for clay fabric analysis through image en-

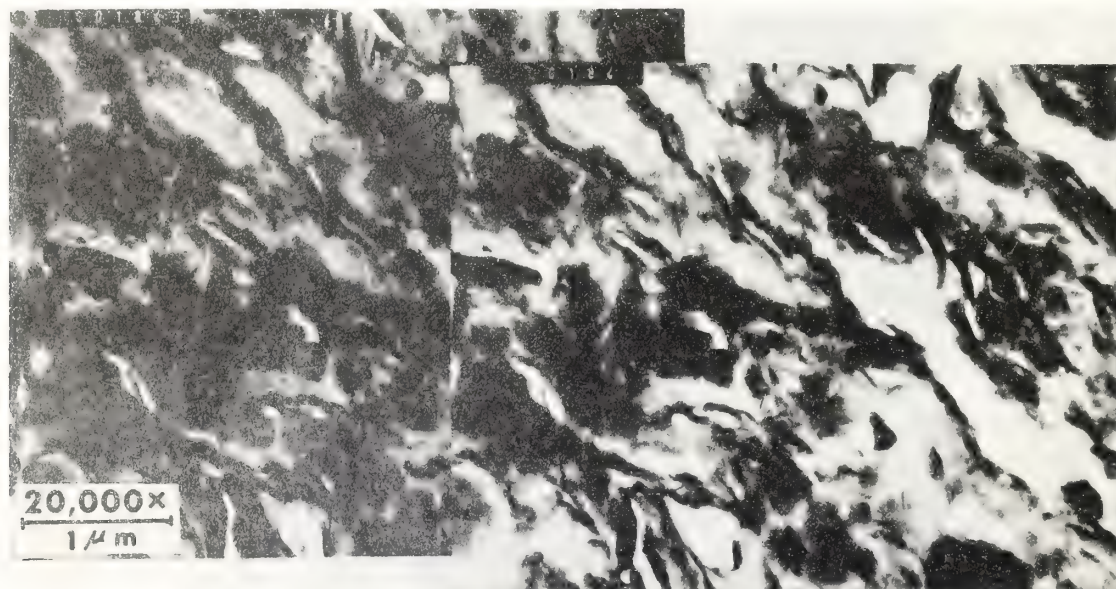


FIGURE 50.—Clay fabric of strongly oriented particles with high void ratio—depicted at high magnification for a local ultrathin section area, core B-2 (1.4 m) remolded sample.



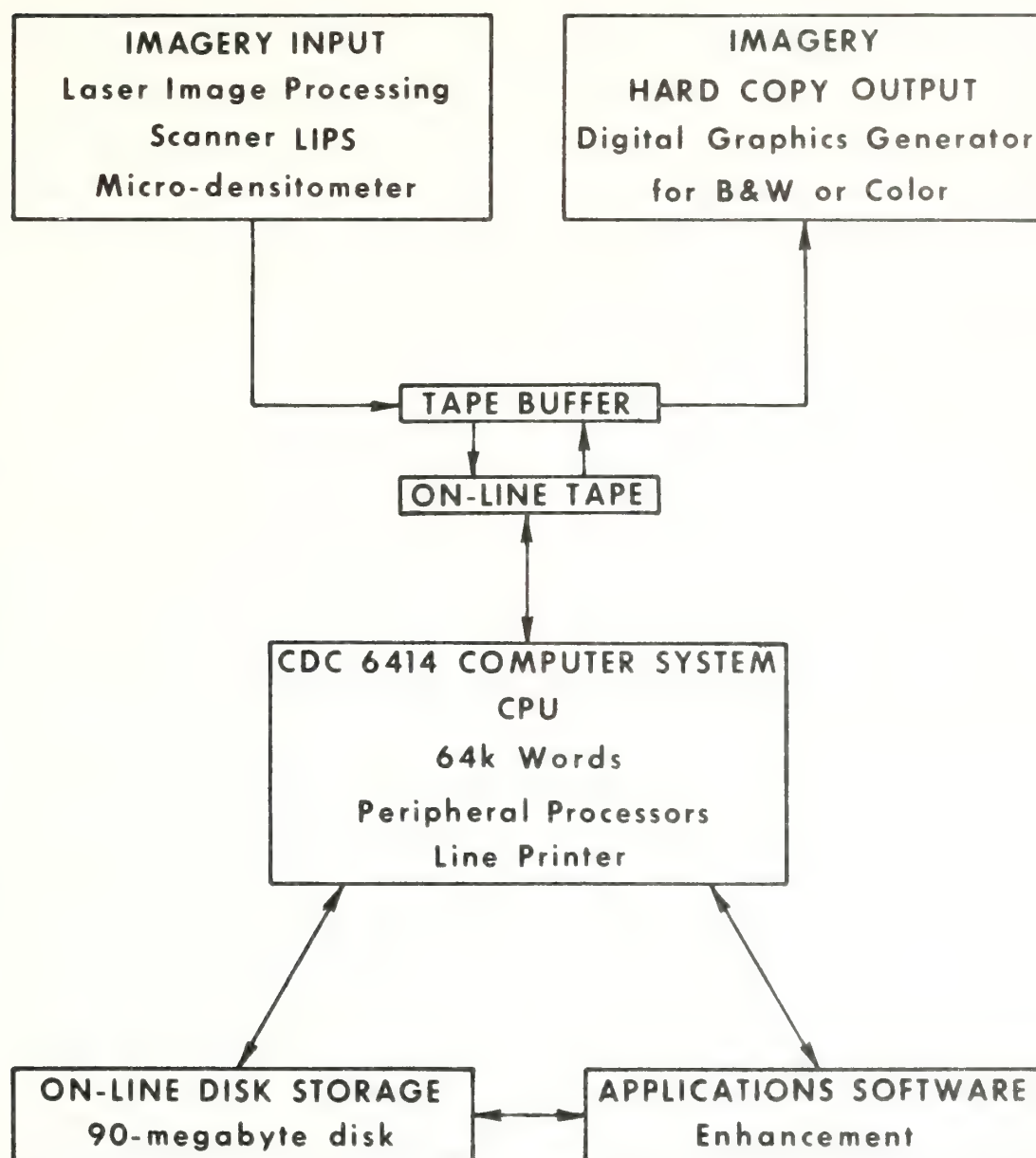


FIGURE 51.—Digital Image Processing System (DIPS) components.

hancement. The basic premise is that microstructural damage to a sample would be exemplified by a significant change in porosity (void ratio) and borne out by image enhancement techniques applied to transmission electron photomicrographs.

Research in image analysis of clay fabric using the Quantimet instrument for ultrathin sections of soil and kaolin samples was pioneered by Foster and Evans (1971) and Foster (1973). The early study dealt with electronic characteristics of the Quantimet and the application of image analysis by computer to clay fabric. The later study investigated the use of the imaging instrument for determining degree of particle preferred orientation and specific surface per unit volume, but the study was concerned with labora-

tory resedimented and fractionated kaolin and not natural soils. Although theoretical and practical work was carried out for the "clean" silt size kaolin fabrics by Foster (1973), the study by Foster and Evans (1971) clearly pointed out that natural soils were not amenable to evaluation by the Quantimet because of the poor instrument discrimination capabilities between particles and voids. Smart (1973) has also investigated the use of the Quantimet image analyzing instrument for ultrathin sections of soils and found that the computer will scan all voids measuring all the cords along the scanning lines in a certain direction producing a different distribution for various directions. Smart also points out, however, that it is difficult to discriminate between particles and voids using the Quantimet. Certain limitations of

the Quantimet as applied to natural soils have been pointed out, but these studies have recognized possible potentials of computer image analysis to the study of clay fabric.

### Instrumentation

Image enhancement of photomicrograph 52EM, sample B-1 (1.4 m), was carried out with a Digital Image Processing System consisting of a combination of hardware devices and software subsystems which was developed by Mead Technology Laboratories for the U.S. Navy. The computer Processing was made possible through the consideration of Charles W. Reeves, Naval Intelligence Support Center Suitland, Maryland. The hardware devices consisted of a Laser Image Processing Scanner (Imagery Input), a CDC 6414 Computer System (Central Processing Unit), a 90-megabyte disk (On Line Disk Storage), and a Digital Graphics Generator (Imagery Output). The software included the enhancement and control systems programs (Applications Software). These devices and software subsystems were integrated into a total processing system through tape buffer and on-line tape functions (fig. 51). A short summary of the hardware processes and components of the Digital Image Processing System is given as follows:

**IMAGERY INPUT:** Laser Image Processing Scanner (LIPS).—The device utilizes a rotating-drum laser scanner/printer which can be used for either input or output. The LIPS is off-line equipment using 9-track magnetic tape for communication of data to and from DIPS. The LIPS operates on input, digitizing a selected area on a film transparency to one of 256 levels. A given density range can be compressed or expanded into the 256 levels. A sampling aperture and interval of  $40.0\text{ }\mu\text{m}$  on  $40\text{ }\mu\text{m}$  centers was selected for analysis of the photomicrograph used in this study. The scanning area depends upon the sampling interval and can range from  $0.005\text{ m}^2$  to  $0.040\text{ m}^2$ . Because of equipment limitations, the original  $0.08\text{-m}$  by  $0.10\text{-m}$  negative was cut to a size of  $0.072\text{ m}$  by  $0.092\text{ m}$ . The negative was scanned with the LIPS microdensitometer resulting in a matrix of 2,000 picture elements by 1,750 rows for a total of 3,500,000 picture elements.

**CDC 6414 COMPUTER SYSTEM:** Central Processing Unit.—The 6414 is a general purpose high speed computer which is programmed to perform the computations involved in DIPS applications. The main memory consists of 65,536 words each of 60 bits. There are an additional 10 identical support processors each with 4,096 words of 12 bits, and these execute simple instructions. Peripheral devices include an operator console, card reader, card punch, line printer, tape drives, and access disc drives containing 360 million 8-bit bytes of storage for specific applications.

**IMAGERY HARD COPY OUTPUT:** Digital Graphics Generator.—The Digital Graphics Generator (DGG) is an output device that produces a hard-copy ink-on-paper dis-

play of the image type data in either black and white or color. Each picture element of the display may consist of one of 39 shades of gray or a number of colors specified by the control systems software. The device places selected inkdrops from up to four orifices onto paper mounted on a rotating drum. The digital input to the DGG is from magnetic tape which has been formatted by the digital image processing system. The tape specifies the locations on the paper where the drops of ink are to be placed. Highly repeatable shades of gray can be produced by a pseudohalf-tone process which creates a given shade using a combination of printed dots in a 4 by 4 matrix. The image elements are  $14/1000$  of an inch ( $3.56 \times 10^{-4}\text{ m}$ ) apart resulting in approximately 72 elements to an inch ( $.0254\text{ m}$ ). Distance is the same in both directions of the paper providing about 5,000 image elements to a square inch ( $6.451 \times 10^{-1}\text{ sq. m}$ ).

The drum rotates, making one revolution in  $\frac{1}{2}$  second. Four revolutions are required to complete an image element scan line of about 4,000 elements. After each revolution the printing jets step  $3.5/1000$  inch ( $8.89 \times 10^{-5}\text{ m}$ ) down the drum axis. Approximately 2,800 lines of image elements can be printed in a single run resulting in a picture about 57 inches ( $1.448\text{ m}$ ) wide and 40 inches ( $1.016\text{ m}$ ) long, which would contain approximately 11 million picture elements. Only the jet of black ink is active for the black-and-white operation, whereas color operation is produced by jets of cyan, magenta, and yellow, the proportions of which are controlled by the software-generated bit patterns on the magnetic tape. False color imaging can be thus produced representing selected shades of the gray scale as recorded by the LIPS and processed by the computer.

**GRADIENT:** The gradient process operates on a digital image in order to produce an estimate of the rate of change of density at each location in the input image and it is used to emphasize edges in the input image.

**DENSITY CONTOUR MAP GENERATION:** The contour process operates on a digital image to produce an output image from which isodensity contour lines can be drawn on the Digital Graphics Generator. When false color DGG output is used, each contour level can be represented by a unique color. The contour process provides a means for better locating and defining specific objects of interest.

**HISTOGRAM:** The histogram process operates on a digital image to produce a density histogram image depicting gray level versus percent. An additional graph can be generated based on the histogram data plotting the gray densities against their cumulative percent.

**DENSITY IMAGE TO BIKINI IMAGE AND HARD COPY (GRAY SHADE/FALSE COLOR):** The Density Image to Bikini Image and the DGG/FCDDG operate on a digital image to produce a digital image with a density range of 1 to 39 and to produce a magnetic tape to provide either a gray or color rendition of the digital data.



Basically, the Digital Image Processing System operates on an image such as a film transparency or photograph using a Laser Processing Scanner (microdensitometer) for input. The system digitizes the film (or photo) densities or gray levels present over an arbitrary scale from zero to 256. These data are fed into the CDC 6414 Computer System for processing and instructions from the Enhancement and Control Systems Programs. The final data are output through the Digital Graphics Generator in either black and white or false color renditions representing selected gray level steps. Each gray level represents a specific area or percentage of the total image scanned.

*Digital image processing of film transparency B-1 (1.4 m).* Image enhancement through digital image processing was carried out on transmission electron photomicrograph 52EM for the purpose of determining the total area of the

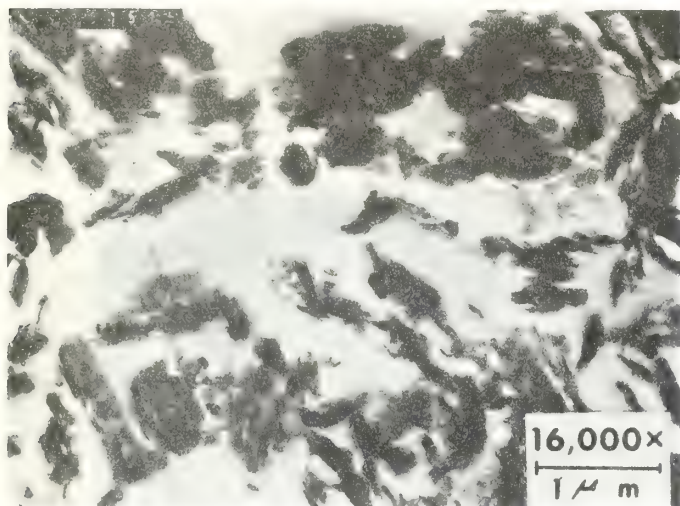


FIGURE 52.—Clay fabric T.E.M. photomicrograph selected for image enhancement through digital image processing, core B-1 (1.4 m).

clay particles and total area of the voids depicted in the film transparency. Given the total area of the voids and solids, the void ratio could be calculated and this value compared to the void ratio as determined on the bulk sample by standard laboratory techniques. These comparisons were made in order to assess any significant disturbance caused by T.E.M. preparation techniques from the first subsampling and dehydration steps through the final steps of ultrathin sectioning and transmission electron photomicroscopy. A collapse of the clay fabric would produce a lower porosity (lower void ratio) than the original bulk sample porosity, and conversely a swelling of the sample during preparation would cause an increase in the porosity. These analyses were intended as an experimental test for void ratio comparisons and additionally to investigate the possible applications of image enhancement techniques as applied to the study of clay fabric.

Examination of photomicrograph 52EM reveals the clay particles which are indicated by the dark areas. The voids are represented by the light areas which were impregnated with SPURR epoxy resin. The photomicrograph reveals a clay fabric of randomly oriented domains and high porosity (void ratio). A wide range of gray levels is apparent in the photomicrograph with very light, nearly white areas to black, electron dense areas representing clay particles. Due to equipment limitations, the original 0.08 m by 0.10 m negative was trimmed to 0.064 m by 0.080 m and the negative scanned on the LIPS microdensitometer using a 40 micron ( $40 \times 10^{-6}$  m) spot size. The resultant matrix was 2,000 picture elements by 1,750 rows for a total of 3,500,000 picture elements. Since this picture area contained information alien to the clay sample—a thin dark edge on the bottom of the picture area and the area containing the T.E.M. picture frame number (001515)—the extraneous information was removed from the processing by creating a subimage (fig. 53). This subimage was used for all processing and analyses resulting in a 1,600 by 2,000 matrix for a total of 3,200,000 picture elements. This subimage (fig. 53) represents a strikingly accurate representation of the actual negative or photomicrograph processed by the DIPS (figs. 52EM and 53).

The basic problem was to delineate the different densities of gray in the negative as processed by the LIPS and the DIPS and the area represented by each gray level. Subsequent to scanning by the LIPS and processing of the digitized information, a histogram was generated to depict the number of elements containing the different shades of gray (fig. 54). A second graph was also generated based on the histogram data depicting the gray densities versus cumulative percent (fig. 55). These graphics, cumulative curve and histogram, were used to evaluate and distinguish the well defined general shades of gray densities present in the negative.

Examination of the histogram and cumulative curves, representing the gray scale densities versus percent of total area, reveals seven major zones of gray scale density. The boundaries of these zones were selected on the basis of major changes in the film densities as depicted by the histograms. The zones also are represented well by the cumulative curve. The reasonably well-defined zones of gray (seven) were isolated as a density slice and graphically displayed by the DGG as black on white, the black being represented as that specific zone of gray levels. The actual gray levels scanned in this photomicrograph (52EM) ranged from a value of 1 to 250 (fig. 54). Each gray level, density step, was recorded by the line printer giving frequency, percent between 1 and 250, and cumulative percent. Each major zone is depicted on a separate graphic and registered to the graphic display of the original image (figs. 56, 57, 58, 59, 60, 61, 62). The separate graphic display of each major zone represents the total area of the gray levels present within the boundaries of



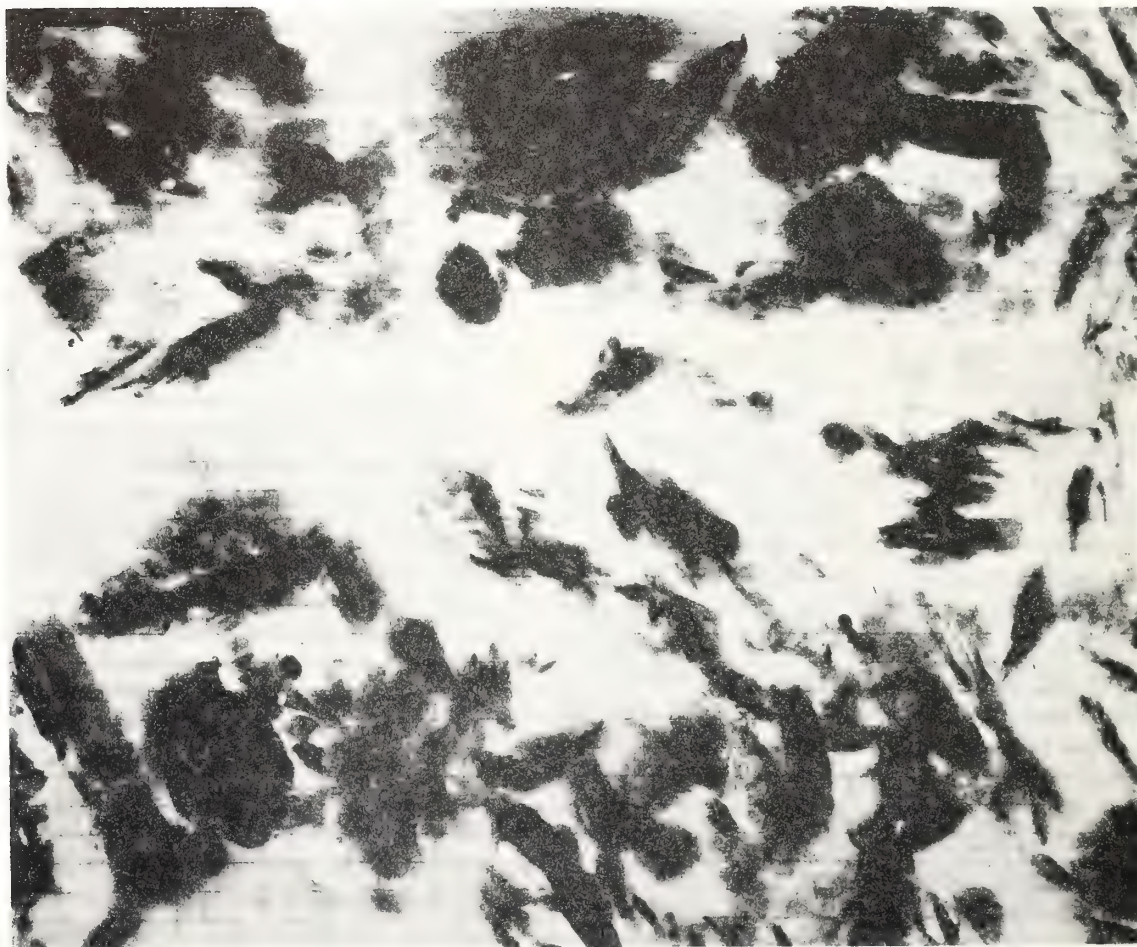


FIGURE 53.—DIPS subimage reproduction of photomicrograph, core B-1 (1.4 m).

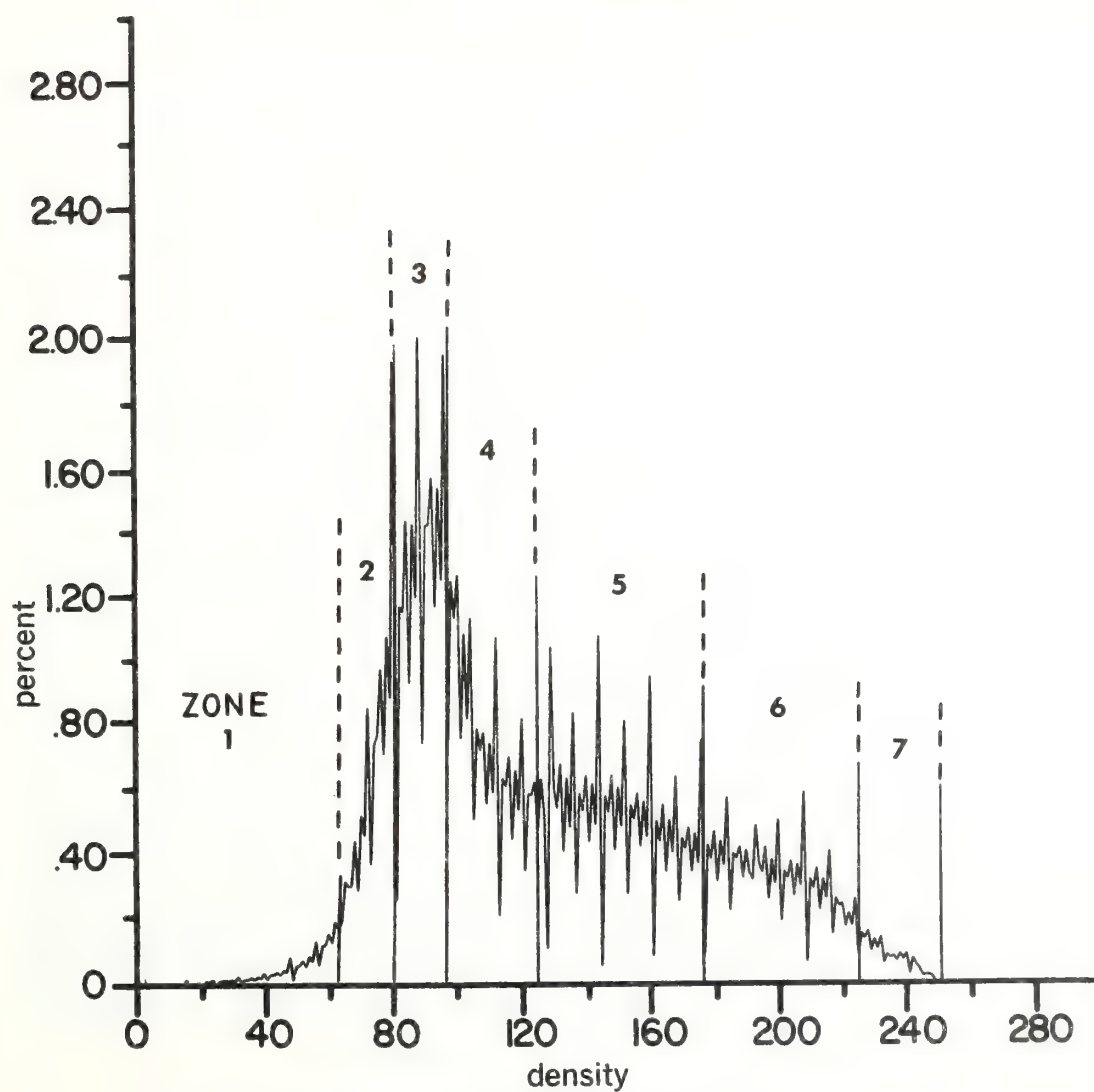


FIGURE 54.—Histogram of gray scale density versus percent.

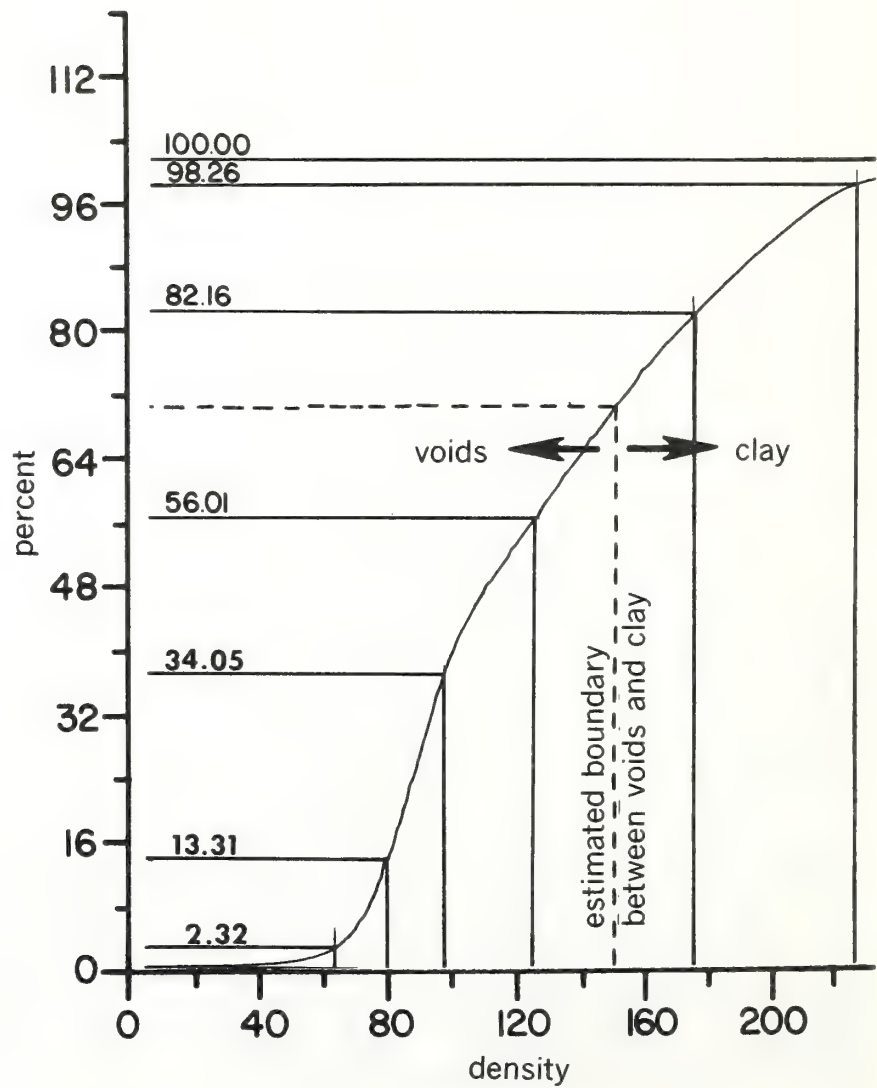


FIGURE 55.—Cumulative curve of gray scale density versus percent.





FIGURE 56. DIPS/DGG gray zone 1 (level 3-63).

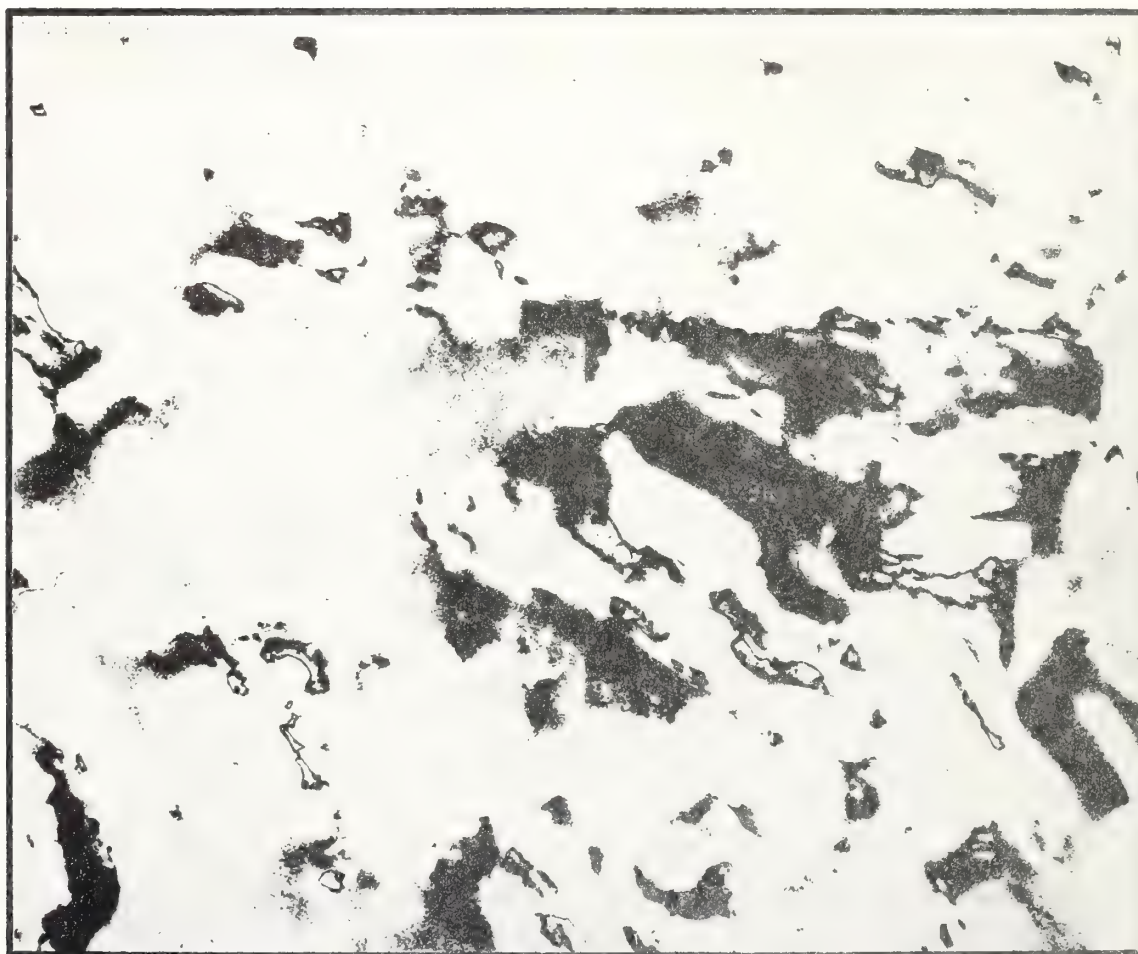


FIGURE 57.—DIPS/DGC gray zone 2 (level 64-79).

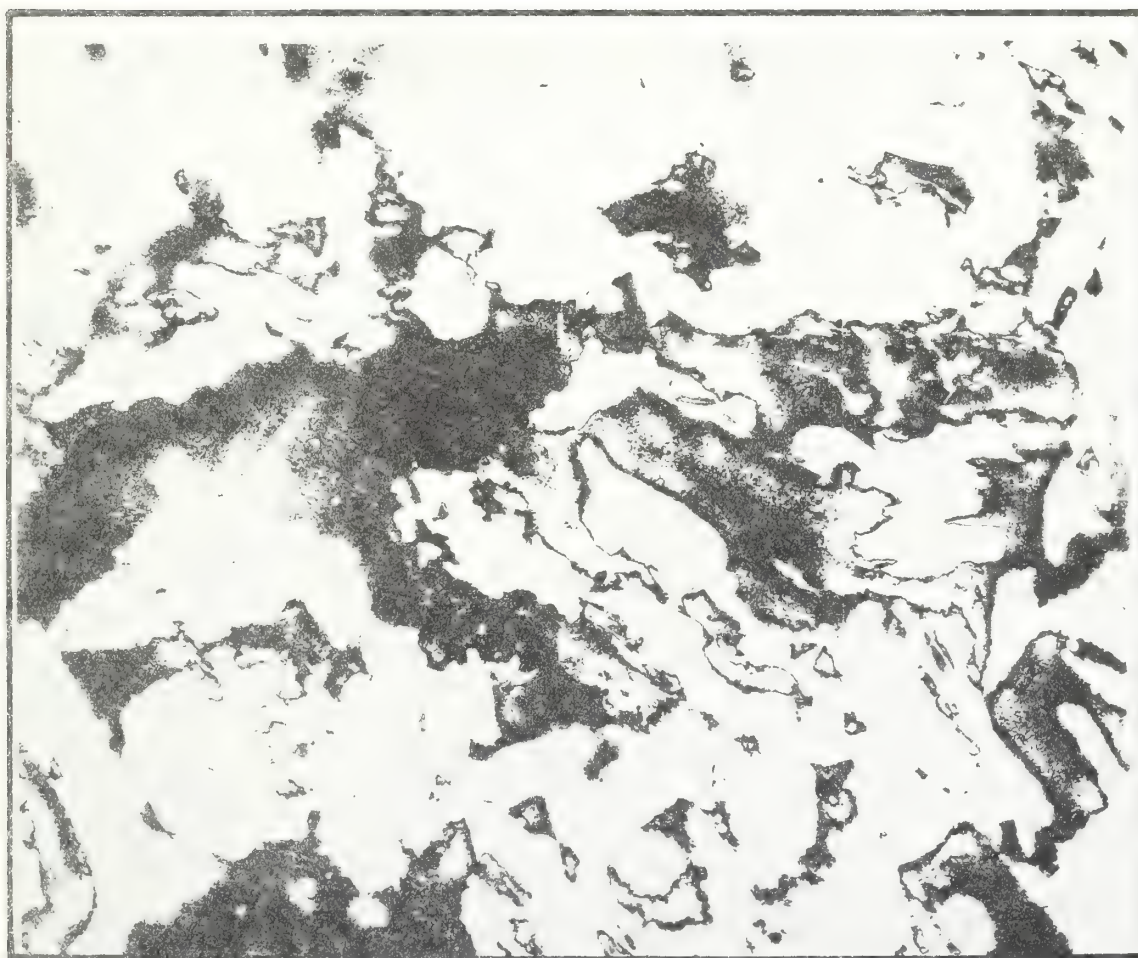


FIGURE 58.—DIPS/DGG gray zone 3 (level 80-95).



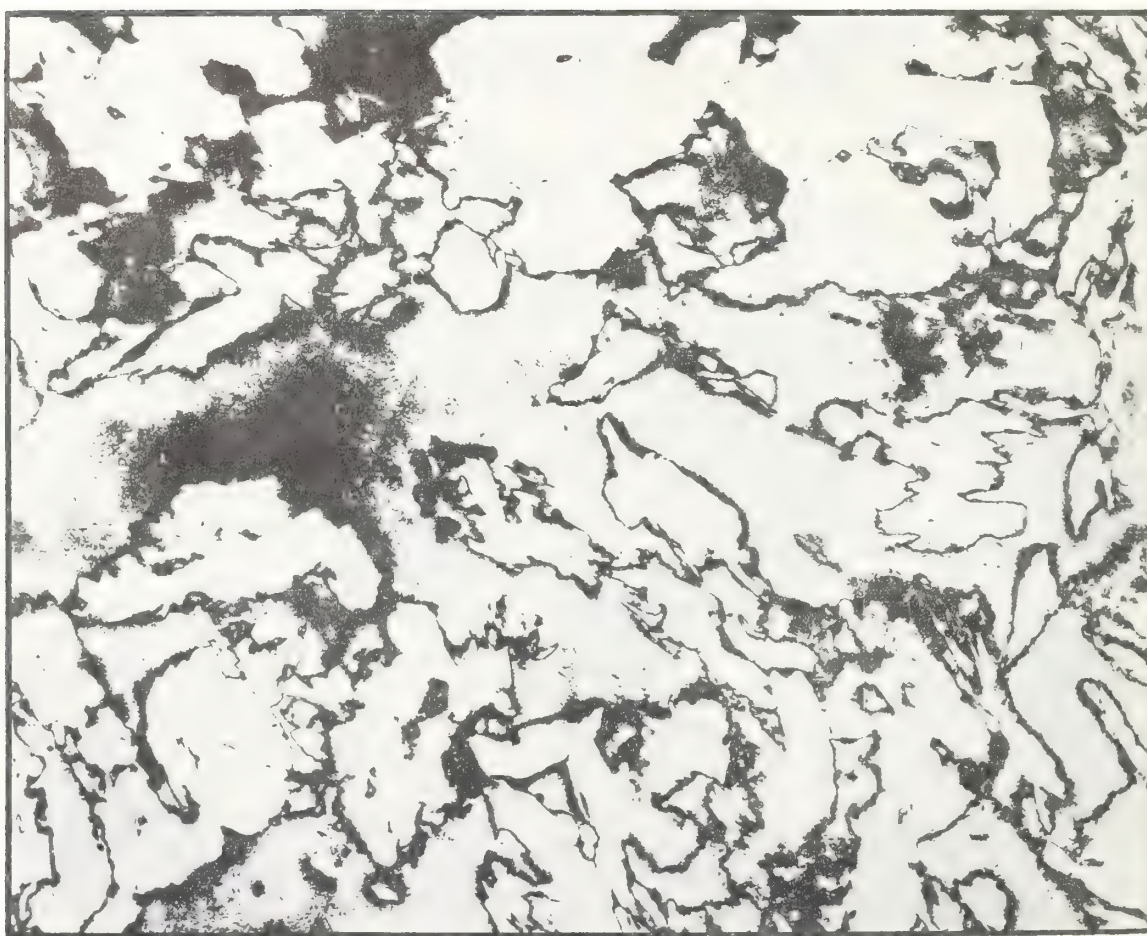


FIGURE 59.—DIPS/DGG gray zone 4 (level 96-125).

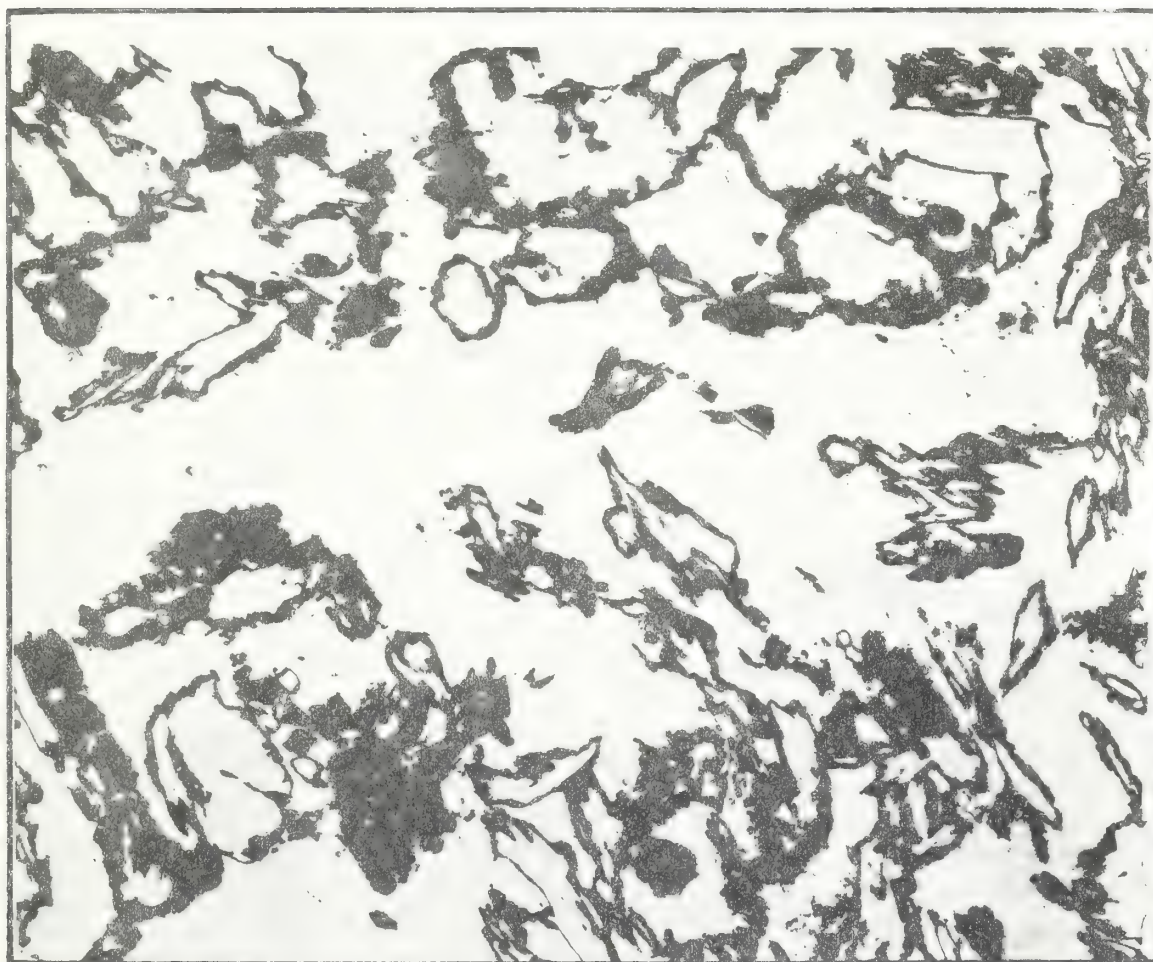


FIGURE 60.—DIPS/DGG gray zone 5 (level 126-175).

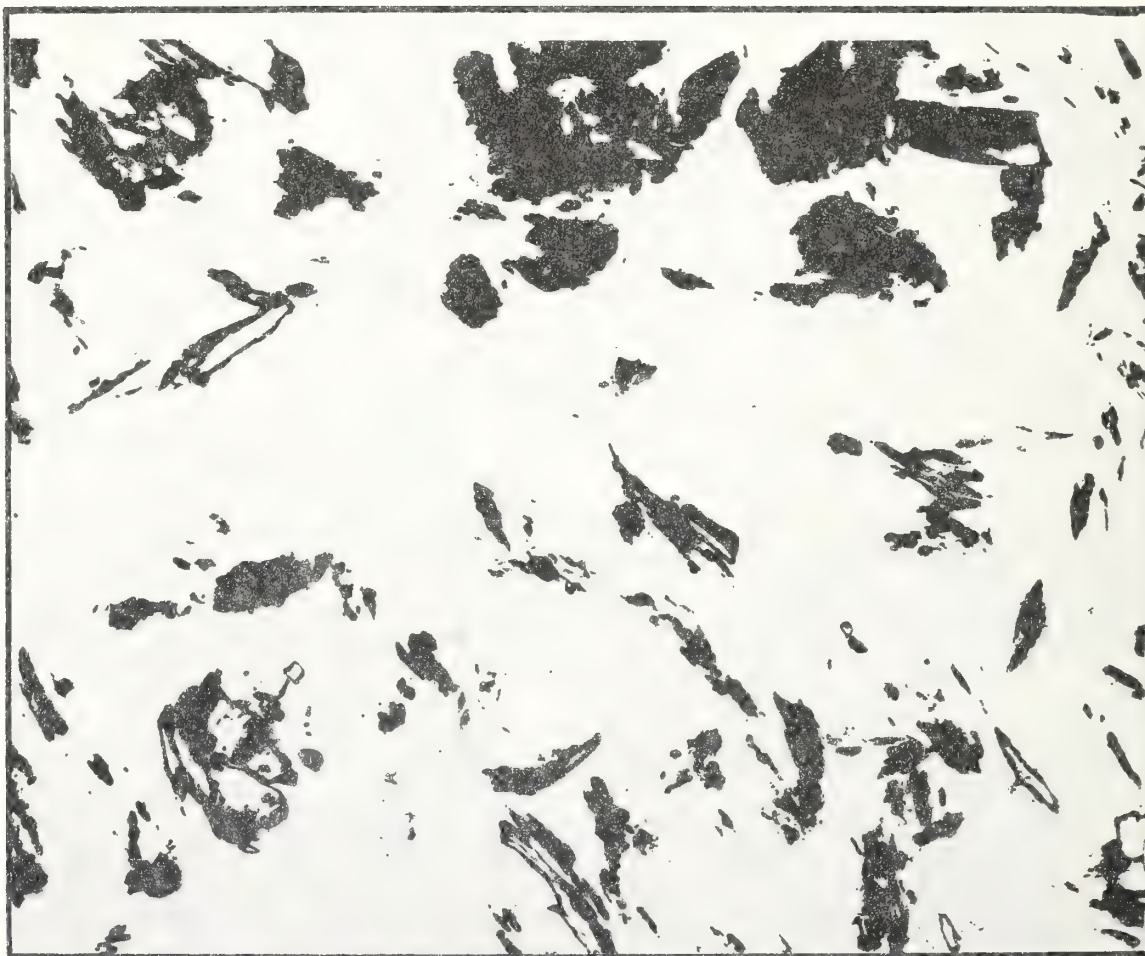


FIGURE 61.—DIPS/DCG gray zone 6 (level 176–225).



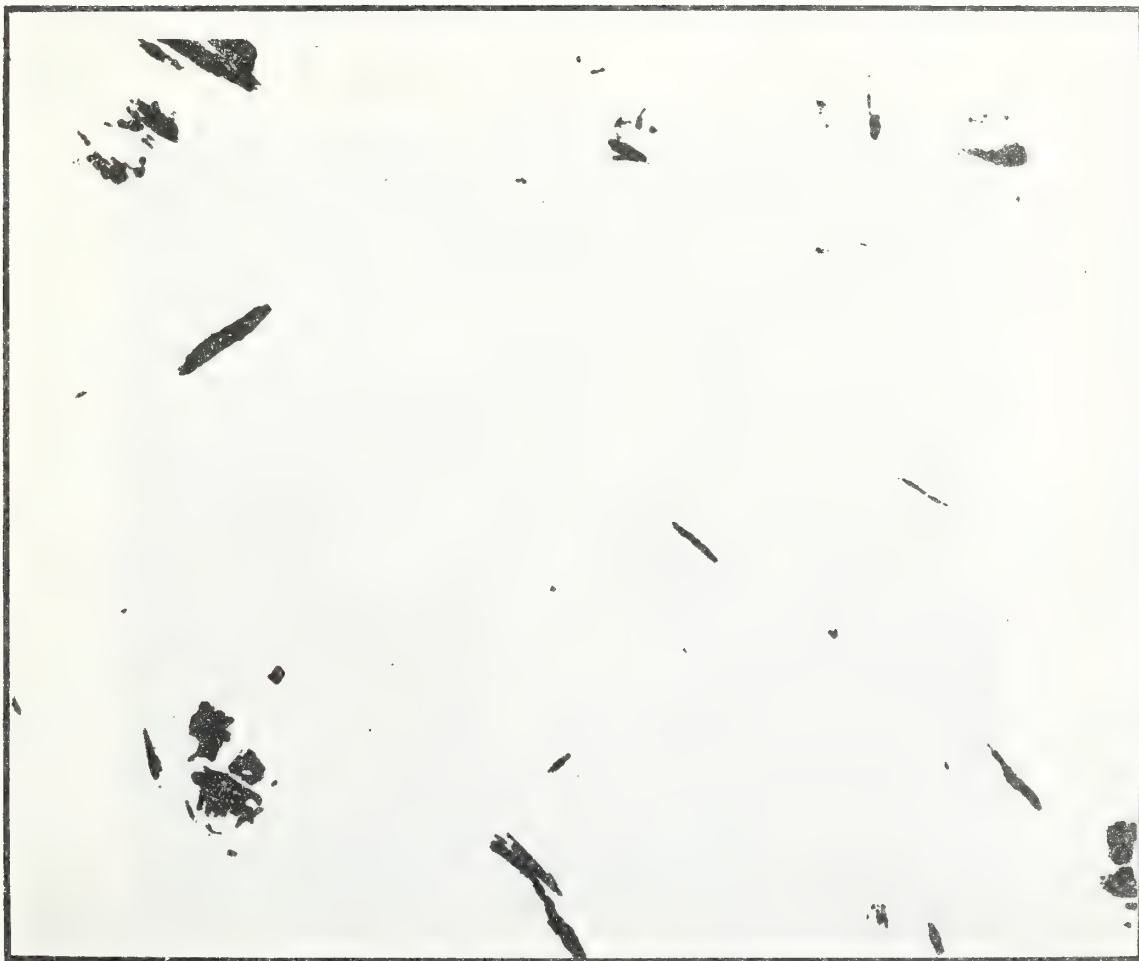


FIGURE 62.—DIPS/DGG gray zone 7 (level 226-250).

the selected zone and depicts the positions where the specific gray level occurs. The selected gray levels are indicated in figure 54 and span the following intervals: 3–63, 64–79, 80–95, 96–125, 126–175, 176–225, and 226–250. Gray levels 1 and 2 and those above 250 were recorded as essentially zero percent and therefore not included in the computations (see fig. 54). A total of 3,200,000 picture elements are contained in the image. Each gray level span contains a given number of picture elements and represents a specific percentage of the total image (picture) area. Each of the seven gray zones was assigned a separate color (false color image), and all colors were printed by the Digital Graphics Generator as a composite picture for comparison with each graphic display density slice and for comparison with the original photomicrograph and DIPS image (figs. 52EM, 53, and 63).

*Data analysis.* Two independent analyses were made to determine the total area of the voids and total area of the clay particles as recorded by the DIPS. The first analysis (Case 1) was made by Naval Intelligence Support Center (NISC) personnel using the computer data and estimating the percentage of clay present in each gray level (table 1).

The original photomicrograph was compared with each of the selected gray zones (density slice) to estimate the percentage of clay present. The cumulative curve (fig. 55) was used to determine the percentage of picture elements in each of the selected gray zones. The percentage of clay present in the sample was calculated from the data as follows:

The total number of picture elements = 3,200,000 = Total Area of Picture (TAP).

The total number of clay elements = 1,035,994 = Total Area of the Clay (TAC).

$$\text{Thus: } \frac{\text{TAC}}{\text{TAP}} = \frac{1,035,994 \times 100}{3,200,000}$$

$$= 32.375\% \text{ of the sample is clay. (1)}$$

And:  $100\% - 32.375\% = 67.625\%$  voids (porosity).

For example: By definition, porosity,  $n$ , is equal to the ratio of the total volume of the voids to the total sample volume, and void ratio,  $e$ , is equal to the ratio of the total volume of the voids to the total volume of the solids.

Then:  $\text{Area of the Voids} \times \text{Height} = \text{Volume of Voids}$   
 $\text{Total Area} \times \text{Height} = \text{Total Volume}$

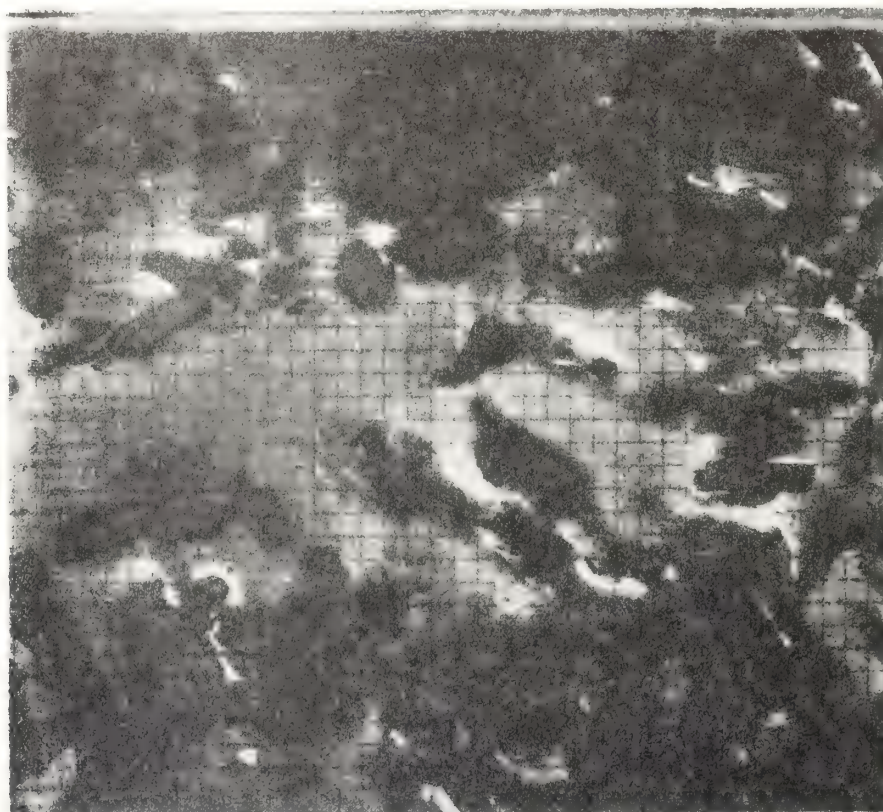


FIGURE 63.—DIPS/DGG false color rendition for gray level zones 1–7 from transmission electron photomicrograph.

Since the height appears in both the numerator and denominator, then:

Area of Voids  $\times$  Height

—————

$$\frac{\text{Total Area} \times \text{Height}}{\text{Area of Voids}} = A_V/A_T \quad (2a)$$

Porosity  $n = A_V/A_T$

$$= \frac{3,200,000 \text{ (total area)} - 1,035,994 \text{ (total clay area)}}{3,200,000 \text{ (total area)}}$$

$$\text{Porosity } n = A_V/A_T = \frac{2,164,006}{3,200,000} = 0.67625 \quad (2b)$$

$$\text{And: Void Ratio } e = A_V/A_S = \frac{2,164,006}{1,035,994} = 2.0888 \quad (3)$$

The calculations for Case 1 were made by an unbiased, "nonclay" specialist trained in photo interpretations. They represent analysis based on estimates of clay percentages present in the selected gray level zones.

TABLE 1.—CASE 1 picture elements and percentage of clay in gray zones

Gray zone	Gray level span	% clay (est.)	% picture elements	Picture elements contained in zone	Amount clay (clay %) $\times$ (number of picture elements)
1	3-63	0	2.32	74,240	0
2	64-79	10	10.99	351,680	35,168
3	80-95	15	20.74	663,680	99,552
4	96-125	20	21.96	702,720	140,544
5	126-175	35	26.15	836,800	292,880
6	176-225	80	16.1	515,200	412,160
7	226-250	100	1.74	55,680	55,680
Totals				3,200,000	1,035,994

The second analysis (Case 2) was made by the writer with a similar use of the DIPS data, but using a different approach to the evaluation of clay and voids present in the electron photomicrograph. Examination of each gray zone (density slice) display from gray zone 1 through zone 7, particularly in sequence from the lowest gray level to the highest gray level, reveals that zone 5 shows a closure on essentially all of the major clay particles present (compare figs. 52EM, 53, and 61). Density slice 5 represents a boundary between major clay particles, represented by the electron photomicrograph, and the voids (area impregnated with SPURR epoxy resin). As a first approximation, since gray zone 5 covers a span between 126 and 175, or 50 gray level steps, a value of 150 was selected as the approximate gray level step representing the actual boundary between

TABLE 2.—CASE 2 picture elements in gray zones

Gray zone	Gray level span	Picture elements contained in zone
1	3-63	74,240
2	64-79	351,680
3	80-95	663,680
4	96-125	702,720
5	126-150	439,360
Total		2,231,680 (voids)

the clay particles and the voids. Summing the number of picture elements contained in zones 1 through 4 and the number of picture elements contained in density levels 126 through 150 inclusive, the total number is equal to 2,231,680 (table 2). The calculations are as follows:

The porosity is calculated by:

$$\text{porosity } n = \frac{2,231,680}{3,200,000} = 0.6974 \quad (4)$$

The void ratio is calculated by:

$$\text{void ratio } e = \frac{2,231,680}{3,200,000 - 2,231,680} = 2.305 \quad (5)$$

The value for porosity can be approximated also by using the cumulative curve of gray scale density versus percent of the total area (fig. 55). A line is extended from the density level of 150 on the abscissa to intersect the cumulative percent curve, and the total percent of the void (porosity) area can be read directly on the ordinate (see dashed line of fig. 55). These calculations of Case 2 are based on the approximation that the boundary of the clay particles lies within the zone 5 gray level step at a value of 150.

An important point to note is that a much more well-defined boundary between clay particles and voids could be determined by taking a series of small gray level slices (gray level span) within zone 5 and registering each slice with the graphic display of the original image as was done with each major zone. Using this suggested method, the major density slice such as zone 5 would define the approximate gray level where the boundary occurred, and the finer, thin slices, would closely approximate the boundary within a very narrow limit by finding a very thin density slice where closure occurred on the clay particles. Unfortunately, the refinement was not possible for this study. The method of using finer density slices to determine the clay particle boundary might possibly change the initial calculated values for porosity and void ratio slightly as compared to the first approximation based on the boundary taken at the density level of 150. However, with the methods and limitations in mind, the values for porosity and void ratio determined in Cases 1 and 2 are compared with the values determined by standard laboratory techniques.



	Case 1	Case 2	Laboratory method	
			(uncor- rected)	(cor- rected)
Void ratio	2.09	2.30	2.08	2.16
Porosity	67.6%	69.7%	67.5%	68.3%

The tabulation of values for void ratio and porosity indicates very close agreement among the methods. Case 2 is slightly higher than the laboratory method (corrected for salt content), which also is slightly higher than Case 1. Generally, for most practical purposes uncorrected values for salt content are reported and commonly used in calculations; however, corrections have been made here for comparison since the corrected values would be expected to more closely approximate the actual properties of the sample studied. An acceptable correction for porosity of 1.2 percent of the water volume (interstitial water) for dissolved salts (salinities of 35‰) is generally applied (Bennett and Lambert 1971). Both Case 1 and Case 2 calculations agree well with the laboratory values, particularly for a first approximation, and refinements in methods and techniques would undoubtedly improve the reliability of the estimates of void ratio and porosity through image enhancement techniques.

*Discussion.* The confidence placed on the interpretation of clay fabric employing the use of the transmission electron microscope and image enhancement system depends not only on the quality of sample preparation and techniques but also on the degree to which the electron photomicrographs represent the actual spatial arrangements of the clay particles and associated voids. The limitations and factors important in T.E.M. clay fabric studies can be summarized briefly. If one can consider that uniform exposure in the electron microscope is achieved and that processing is also uniform, then the apparent image density is dependent on the type of material present in the ultrathin section, its thickness, and the angle of incidence of the electron beam on a particular particle (Foster and Evans 1971).

Three cases can be established for particles lying wholly or partially within an ultrathin section. Each case can affect the degree and variation in the particular image density.

- (1) Particle is cut by both boundaries of the section.
- (2) Particle is cut by only one section boundary.
- (3) Whole particle is lying within both boundaries of the section; i.e., particle is nearly parallel with boundary section planes.

Case 1 would be reflected in the photomicrograph as a relatively high density area (fig. 64-[3] particles a and b). Cases 2 and 3 would be represented by relatively low density images of varying degrees (fig. 64-[3] particles c and d, Case 2 and particle e, Case 3). Also four types of particle fabric can affect image density.

- (1) Edge-to-face contact (fig. 64-[3] particles e-f).

- (2) Edge-to-edge contact (fig. 64-[3] particles d-g).
- (3) Overlap or stepped face-to-face contact (fig. 64-[3] particles c-h-i).
- (4) Apparent "isolated" particle (fig. 64-[3] particle b).

The condition of the particles lying within the ultrathin section, each of the three cases, and the type of fabric can affect image density. Other factors that affect the apparent image density include particle thickness, particle orientation, irregular particle edges, and the "wedge effect." The "wedge effect" occurs when particles are inclined at an angle to the plane(s) of the section. Relatively thick particles inclined at an angle to the section plane show a maximum apparent density in the central portion of the particle and a grading of density (apparent gray level or gray density decrease) towards the edge of the particle. Zone A of particle b would show a relatively high image density compared to zones B which would produce a grading of gray levels (fig. 64-[1] particle b). Important to note, however, is the fact that the "wedge effect" becomes minimal as the thickness of the section or the thickness of the particle decrease (compare figs 64-[1], [2]). Zone B substantially decreases relative to zone A as the section becomes ultrathin (fig. 64-[3]). Clay particles lying normal to the section boundaries and those particles with clay surfaces lying essentially parallel with the plane of the section will effectively show no "wedge effect" (fig. 64-[1] and [3] particles a and j). The "wedge effect", however, becomes larger as the particle orientation changes from a vertical to a horizontal position (compare particles b and k, 64-[1] and [2]). Examination of figure 64 clearly reveals that the "wedge effect" approaches an insignificant portion of the total particle image as the section becomes ultrathin when the clay particle thickness is effectively larger than the section thickness.

Another important feature to recognize in the study of clay particles sectioned to various thicknesses is the fact that thick sections as depicted in figure 64-[1], when projected onto a film transparency would show a very low void area and a rather distorted representation of particle size. The projected length of an inclined particle would be shorter in overall length than the actual particle length represented in the section. Both of these effects become less and less important as the thickness of the section decreases, and they become relatively insignificant in ultrathin sections (compare particles and voids in figs. 64-[1] and 64-[3]). An essentially well represented void-to-solid ratio is realized in the ultrathin section representation as depicted in two dimensions (plan view). A simplistic plan view of ultrathin section [3] is depicted in figure 64-[4]. A plan view of the thick section [1] would obviously be represented by a very large area of solid particles with voids represented only at points V (fig. 64-[1]) and would be quite unlike plan view [4].

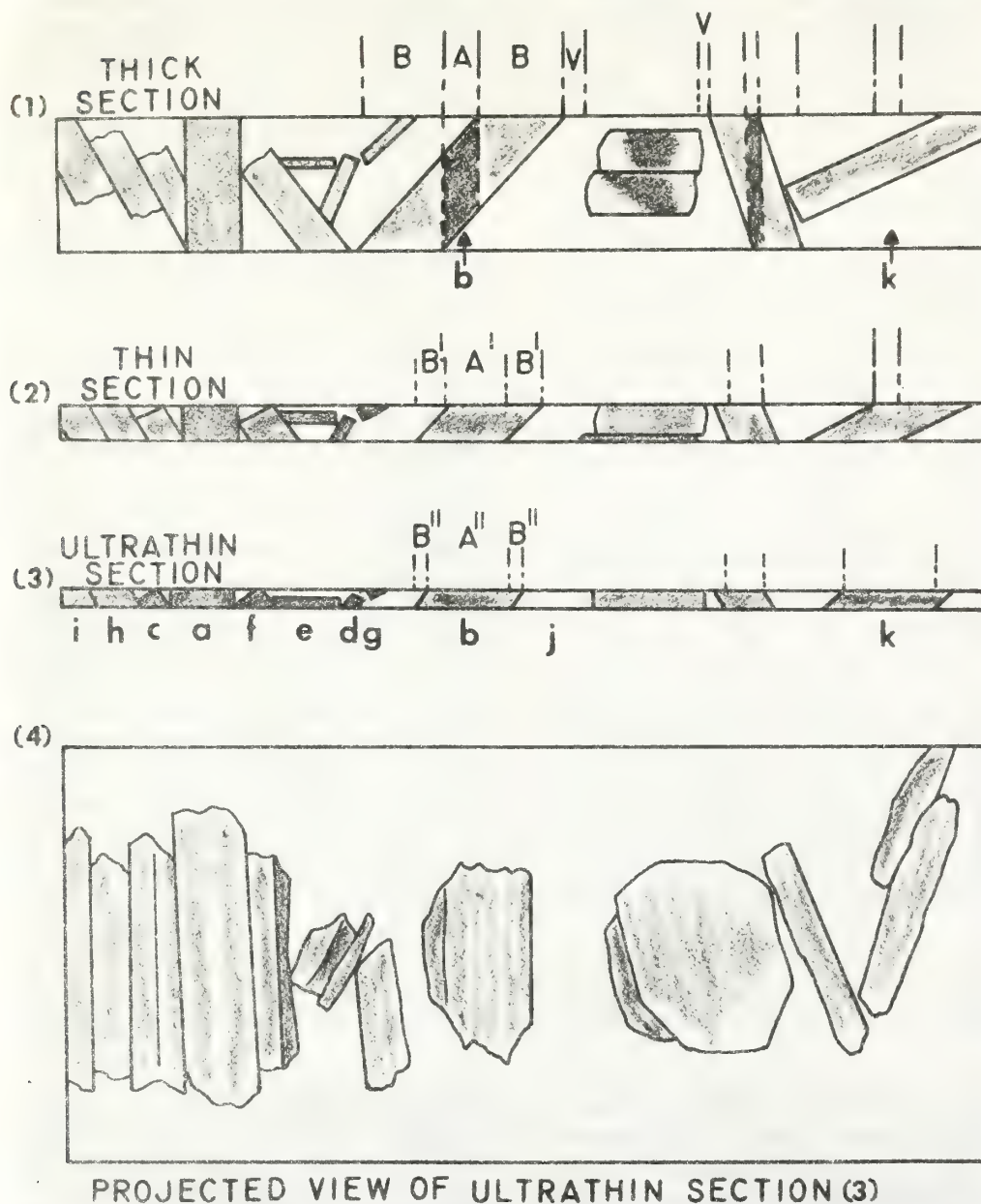


FIGURE 64.—Representation of various cross sections of clay sample thin sections from thick to ultrathin.

The above discussion points out the obvious, important factors one should consider when interpreting electron photomicrographs and image enhancement data and graphics of clay fabrics. However, through the study and examination of hundreds of ultrathin sections and photomicrographs of clay fabric, it became clear to the writer that the various factors adversely affecting gray level variations of particle images were virtually insignificant in the final analyses. Obviously clay particles are considerably more electron dense than the SPURR embedding medium which also can vary slightly in thickness rendering a range of low gray

level densities. Particle boundaries are clearly discernable despite the various factors that can affect the final gray level densities. Again, the various factors that affect the gray level density of the particles are significantly minimized when sections are made ultrathin and solid-to-void ratios appear to be well represented in ultrathin sections.

The initial study of image enhancement techniques as applied to the analysis of clay fabric has revealed a unique means of evaluating various aspects of clay particle and particle-voids relationships. The technique indicates that the sediment investigated has remained essentially "micro-



structurally" intact, maintaining its particle-to-particle integrity. This is borne out by the apparent constant void ratio (porosity) maintained throughout the entire analytical procedures of sample preparation. In addition, by finding a relatively thin density slice which represents the boundary between clay particles and voids, the DIPS and DGG systems could produce a total "black" representation for the particles and total "white" image for the voids creating a very simple rendition for interpretation by virtually eliminating confusing gray levels, particularly in the regions of particle-void boundaries. Through this proposed technique, studies could be made of void geometry, size and shape, and intravoid geometry of flocs; particle contacts, size and shape, and the relationships of interconnected voids and particle-particle links (all two-dimensional relationships). Although such studies can presently be made with electron photomicrographs, the image enhancement techniques and digital image processing would undoubtedly simplify the various tasks considerably.

Investigation of other imaging systems applied to numerous electron photomicrographs of clay fabric would be a suggested means of further testing and evaluation of the proposed techniques and studies. Other selected image enhancement systems are presently being investigated by the writer, and, as pointed out above, various applications of computer analysis as applied to the study of clay fabric appear to be feasible.

## Discussion of Clay Fabric and Selected Geotechnical Properties

### *Selected Geotechnical Properties*

The Mississippi Delta submarine sediment investigated is classified as a silty clay consisting of essentially little or no sand. A few exceptions occur with core depth, particularly between 6 to 21 m below the mudline, where the percentage of sand size particles reaches 2 to 3 percent by weight. The actual percentages of silt and clay size particles vary somewhat throughout the cored sediment.

A fine-grained sand occurs between 59 and 85 m below the mudline, and physical properties measurements were not available for this material. Selected geotechnical properties were measured, however, for the silty clay sediment to depths of 152 m below the mudline in core B-1 and to shallower depths in cores B-2 and B-3. The clay fabrics and mass physical properties of core B-1 were selected and studied in detail because of the long continuous recovery of cored sediment compared to cores B-2 and B-3. These two cores were included in this study for supplemental material (selected cored depths) and for additional related mass

### *Summary of Sample Quality and Techniques*

The evaluation of core sample quality and subsample preparation techniques has revealed that standard soil mechanics tests, transmission electron microscopy, and computer digital image processing and image enhancement can be integrated and used effectively to assess the quality of clay sediment cores, the preparation of samples (techniques), and the electron photomicrographs for clay fabric studies. Vane shear test, both in situ and laboratory (miniature vane), revealed that the sediment cores of this study were high-quality samples. Consolidation tests also corroborated this conclusion. Examination of transmission electron photomicrographs of "undisturbed" and remolded samples strongly indicated that the subsamples had been prepared effectively and that the undisturbed samples had maintained their particle-to-particle structural integrity. Digital image processing and image enhancement of a selected T.E.M. photomicrograph (low shear strength, high-porosity sample) revealed that the fabric had not been significantly affected by preparatory techniques, and the particle-to-particle integrity had been maintained by virtue of the close agreement in measured porosities between standard laboratory technique and computer analysis.

The evaluation of sample quality and techniques described in this study appears to be applicable to other studies of clay fabric employing the T.E.M., particularly as applied to the study of submarine clay sediment. The use of digital image processing and image enhancement appears to offer unique techniques to evaluate various attributes of clay fabric, particle-to-particle relationships, and clay voids.

physical properties data. The clay minerals composing the fine-grained sediment consisted primarily of smectite and illite and secondarily, in minor proportions, of kaolinite and/or chlorite. These platy minerals constitute the "building blocks" of clay fabric.

General trends in the sediment geotechnical properties discussed here are quite similar among the three cores with core depth (except where noted). Since this study was concerned primarily with core B-1 and for the sake of simplicity, the discussion of the mass physical properties will be confined to data from this core. Examination of data (plots of physical properties versus depth) from each of the three cores revealed not only similar grain size characteristics (general trends) but also similar trends in water content and wet bulk density. Average values of wet bulk density, water content, and porosity were determined for 3-m intervals for core B-1.

The highest water contents, averaging greater than 80 percent (percent dry weight), occur in the upper few meters



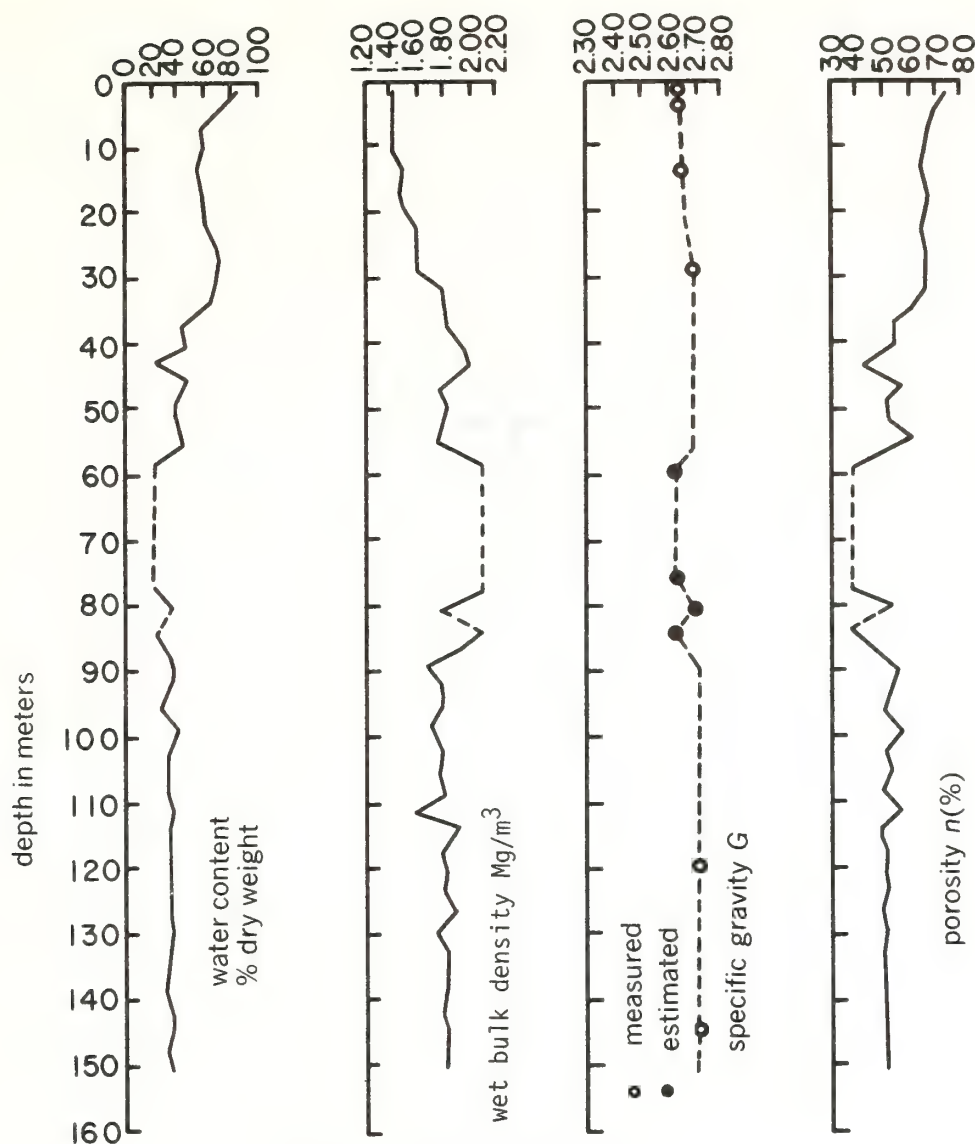


FIGURE 65.—Geotechnical properties, core B-1.

of sediment. Water content decreases slightly to values of 66 percent between 3 and 6 m. At depths between 6 and 21 m, the average values decrease to 54 to 60 percent in response to a significant decrease in clay size material with an increase in silt and a slight increase in sand. Water content again increases to values as high as 70 percent between 21 and 37 m, reflecting an increase in clay size material. Below 37 m the water content decreases to values of 40 to 46 percent in this silty clay sediment which overlies the fine sand at approximately 59 m. These lower water contents occurring between 37 and 59 m apparently are caused not only by a slight decrease in clay size material and increase in silt within this interval as compared to the overlying sediment, but also by dewatering and consolidation processes commensurate with increasing overburden stress. The lowest water contents averaging 35 percent occur in the old, hard, Pleistocene clays below 85 m depth (fig. 65).

Wet bulk density (wet unit weight,  $\text{Mg}/\text{m}^3$ ) increases rather steadily from low values of 1.41  $\text{Mg}/\text{m}^3$  in the upper few meters of sediment to values of 1.78  $\text{Mg}/\text{m}^3$  at 37 m. Wet bulk density values average 1.82  $\text{Mg}/\text{m}^3$  between 37 and about 58 m which are slightly higher than those of the overlying sediment. The clays between 85 and 152 m have wet bulk densities which average about 1.81  $\text{Mg}/\text{m}^3$ , essentially the same as the values for the younger clay between 37 and 58 m. Only a very slight overall increase in bulk density appears to occur with increasing depth in this old Pleistocene clay (fig. 65).

The rather homogenous mineralogy of the sediment throughout the length of the cored material is reflected in the average grain specific gravities (average grain densities). Specific gravities of the solids show a slight increase from a low 2.64 in the upper few meters of sediment to a high of 2.71 in the deep Pleistocene clays between 85 and 152 m.

A value of 2.65 was estimated for the fine sands at 59 and 85 m depth and was used for computation purposes in deriving other physical properties of the sands (i.e. porosity, void ratio, buoyant weight, and overburden stress—Lambe and Whitman 1969, pp. 30–31).

As expected, the changes in porosity (ratio of volume of voids to total unit volume) with core depth follow closely the same general trends as the water content profile (fig. 65). Porosities range from as high as 71 percent in the upper few meters of cored sediment to as low as 49 percent in the deeply buried Pleistocene clays. Porosity or void ratio (volume of the voids to the volume of solids) is a good indicator of the dewatering which sediments undergo during natural consolidation as a function of increasing overburden stress with sediment depth. Void ratio and porosity are related not only to water content but also to basic mass physical properties such as grain specific gravity and wet bulk density (Bennett and Lambert 1971) which in turn normally vary with increasing depth of burial. Thus the porosity of a sediment core of relatively uniform grain specific gravity and grain size would reflect significant changes in bulk density and water content with increasing core depth in response to sediment dewatering.

Based on the physical properties of core B-1 discussed above, five general porosity zones can be delineated which reflect relative degrees of increasing natural consolidation and dewatering of the silty clay sediment (fig. 66). These porosity zones form a framework for discussion and description of the clay fabrics and related physical properties of the cored sediment investigated during this study. The most directly apparent mass physical properties that can be related to clay fabric for a given naturally deposited sediment having relatively uniform grain specific gravity, mineralogy, and grain size, are porosity and void ratio. For this reason, void ratio,  $e$ , and porosity,  $n$ , are discussed in terms of clay fabrics in this investigation, and they are related by:

$$\text{porosity } n = \frac{e}{1+e} \text{ and: } n = V_v/V_T \text{ and}$$

$$e = V_v/V_s \text{ and } V_T = V_v + V_s \quad (6a)$$

$$\text{then: } V_v/V_T = \frac{V_v/V_s}{V_s/V_s + V_v/V_s} = \frac{V_v/V_s}{V_s + V_v} \quad (6b)$$

$$\text{and: } \frac{V_v}{V_v + V_s} = \frac{V_v}{V_v + V_s}, \text{ where} \quad (6c)$$

$V_v$  = volume of voids

$V_s$  = volume of solids

$V_T$  = total volume of sediment mass

The void ratio profile follows the same trends as the porosity profile with increasing depth below the mudline.

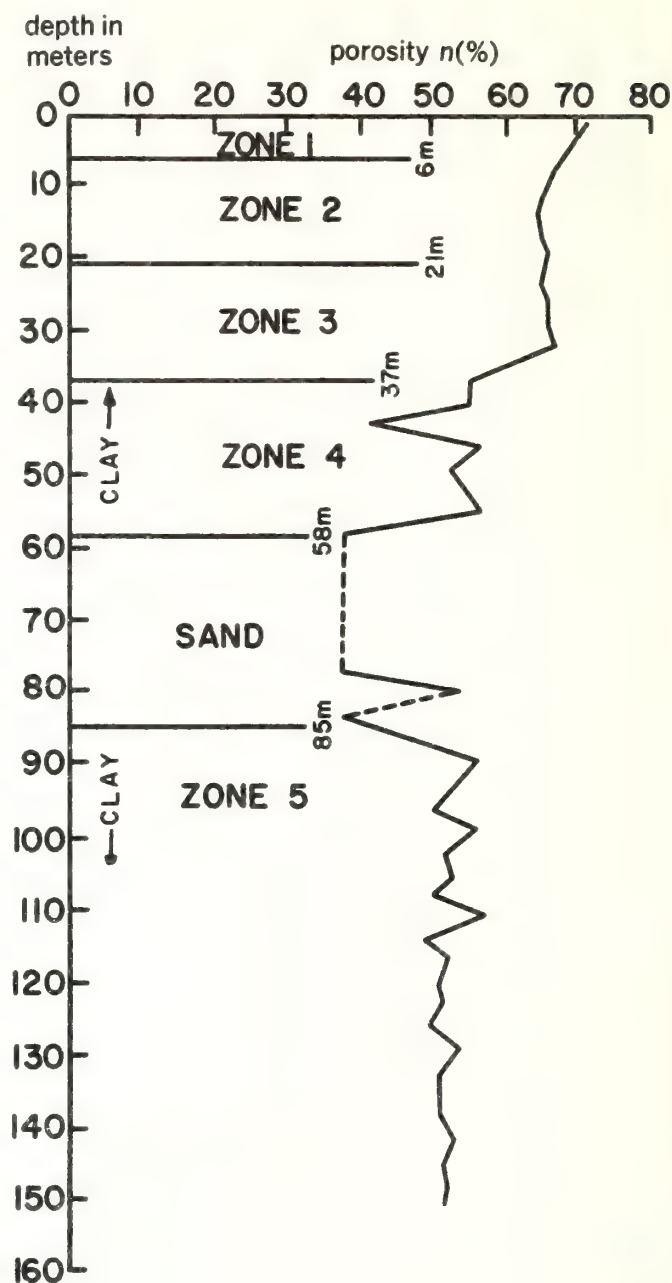


FIGURE 66.—Porosity versus depth, clay porosity zones core B-1.

## Identification and Description of Clay Fabric by Transmission Electron Microscopy

### Terminology

The review of previous research on clay fabric and clay microstructure in general has revealed a rather broad use of terminology and in some cases an overlap in meaning of terms. A few key terms will be defined here as used in the context, description, and discussion of the clay fabric of cores B-1 and B-2 and in the remainder of this paper.



**DOMAIN:** A perfect or nearly perfect stack of face-to-face clay plates with some slight stepped face-to-face association possible. No genetic connotation is implied in the use of this term, although it is realized that the domain may have formed through processes of flocculation, consolidation, formed authigenically, or developed as such from a parent mineral prior to its erosion and subsequent deposition as a detrital particle.

**FLOCCULE or FLOC:** A well defined clay unit of several particles having spatial arrangements and particle contacts which produce relatively large intravoids relative to the thickness of an individual particle of which the floc is composed. No meaning is implied as to the origin of the floccule whether in the water column, at the sediment-water interface, or otherwise.

**CHAIN or LINKING CHAIN:** A series of particles in stepped face-to-face and/or edge-to-edge contact which may terminate in contact between larger units such as flocs or larger particles. Some chains appear to be long and rather continuous. The mode of origin is not implied in the use of these terms.

**PARTICLE:** The particle as used in this paper is a well defined and identifiable unit. It can be a single clay platelet (as resolved by the electron microscope), and it can also be used in reference to a domain. The particle can be thought of as the fundamental "building block" of clay fabric. Although the single clay platelet may be more a figment of theory than a significant component of natural clay sediments, the clay platelet terminology is used here to differentiate between the relatively thick well identifiable domains and the very thin "single platelike" clay particles.

The clay particle as defined here is the fundamental unit upon which a particular sediment fabric is built. Domains and/or single clay platelets are deposited as sediment to form various arrays, spatial arrangements, and larger fabric units. Flocs and/or chains, and domains whether formed in the water column, or at the sediment-water interface, in turn play a significant role in constructing different types of sediment fabric.

### Fabric of shallow versus deep core samples

**High porosity clays.** The relatively high porosity sediment of the upper few meters of cores B-1 and B-2 is characterized by randomly arranged particles. The particles are for the most part domains, and their presence can be verified not only by megascopic examination of the photomicrographs but also by the graphic displays depicted by the image enhancement DIPS/DGC system. Domains are clearly borne out in the density slice renditions of figures 61 and 62. Particles are composed of face-to-face clay platelets forming an essentially nearly perfect "stack." Thus the DIPS was capable of delineating at least some of the components of the domain particles. Photomicrographs 45EM, 46EM, and

52EM depict the clay fabric which is characteristic of the upper few meters of high porosity sediment of cores B-1 and B-2 (zone 1, fig. 66). Photomicrograph 67EM (1.4 m) reveals numerous randomly arranged domains in edge-to-edge and edge-to-face contact producing a relatively high porosity sediment. The domains appear to vary over a considerable range of sizes. Large voids and particle contacts are clearly apparent in the stereographic view of figure 68EM (1.4 m), and a few short chains appear to be present.

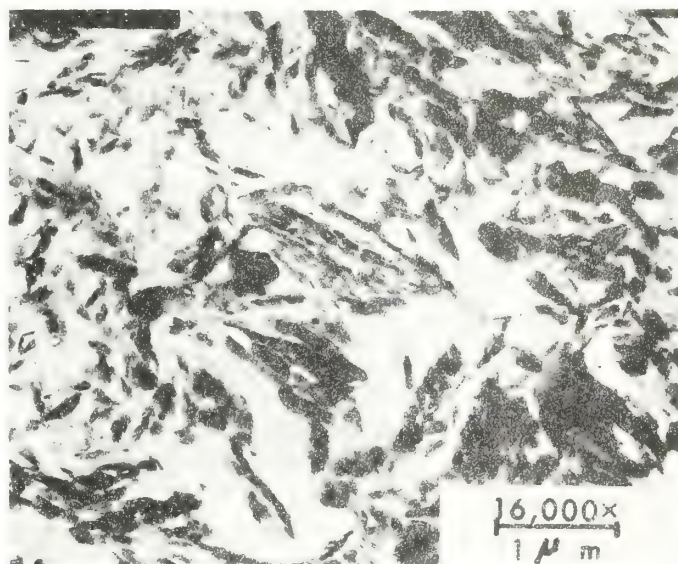


FIGURE 67.—Clay fabric of randomly oriented domains, core B-1 (1.4 m).

Sediment sampled from 2 m below the mudline reveals the same general fabric as the overlying clay. The fabric also is characterized by well defined domains oriented in a random arrangement with numerous edge-to-face particle contacts (figs. 69EM and 70EM). High magnifications of this clay (B-1, 2 m) reveal the nature and details of the fabric particle contacts (figs. 71EM and 72EM). Very small particle chains and "arching" are readily apparent, and edge-to-face contacts are clearly visible. Even at these relatively high magnifications, the linking chains (although short) and oblique particle contacts reveal the nature of large voids relative to the clay and thus provide a reasonable explanation for the high porosity of these shallow, zone 1, clays.

Clay samples from 9.3 m below the mudline reveal a slight increase in density and decrease in porosity within zone 2; however, the fabric characteristics are essentially a random arrangement of domains as revealed by the electron photomicrographs (figs. 73EM and 74EM). Important





FIGURE 68.—Clay fabric of randomly oriented domains and a few short chains, core B-1 (1.4 m).

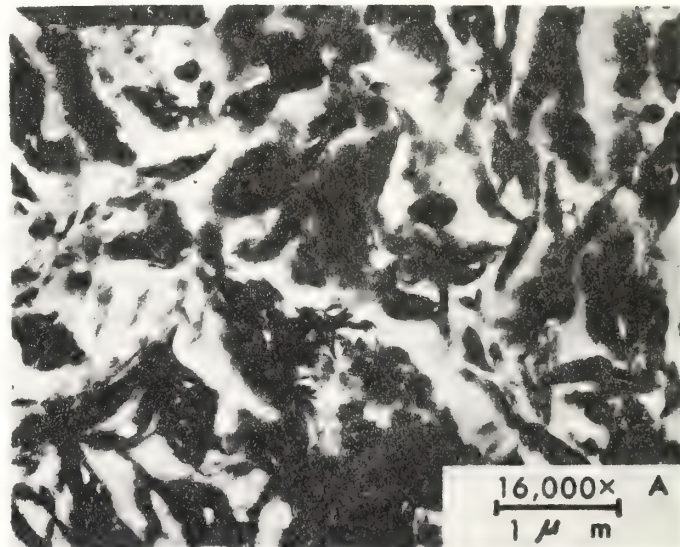
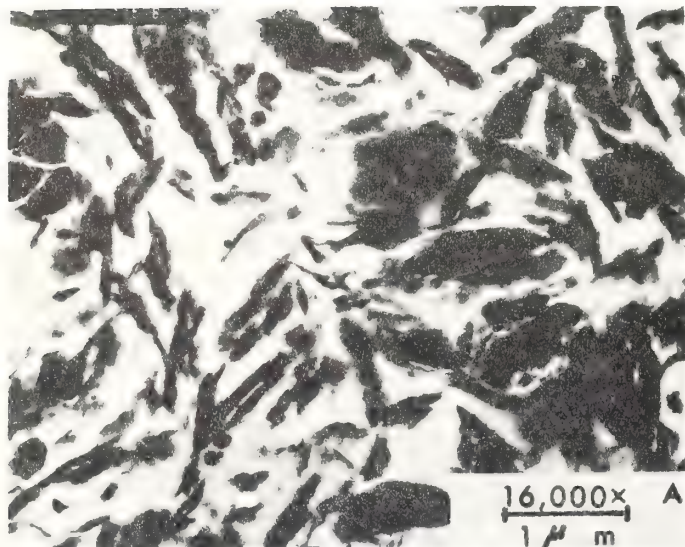


FIGURE 69.—Clay fabric of randomly oriented domains showing numerous edge-to-face particle contacts, core B-1 (2.0 m).



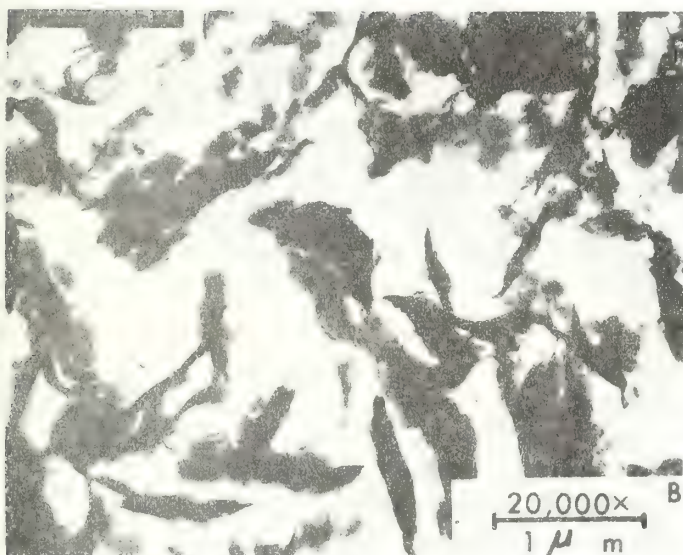


FIGURE 71.—Clay fabric showing randomly oriented domains, with pronounced particle contacts and short chains, core B-1 (2.0 m).

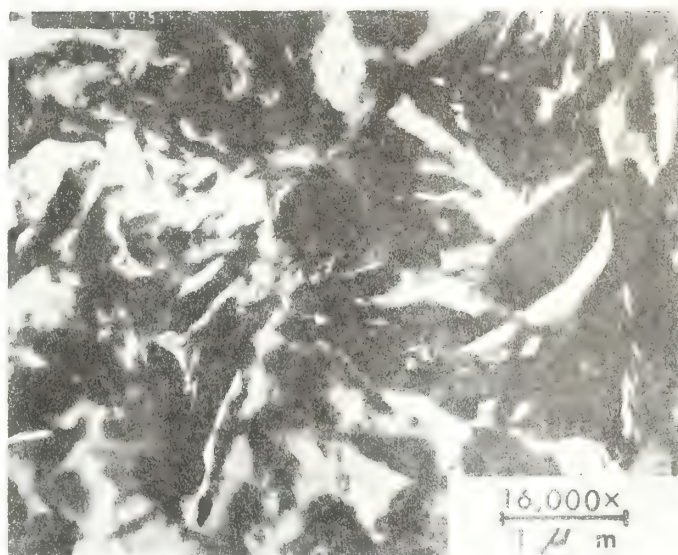


FIGURE 73.—Clay fabric of randomly oriented domains, core B-2 (9.3 m).

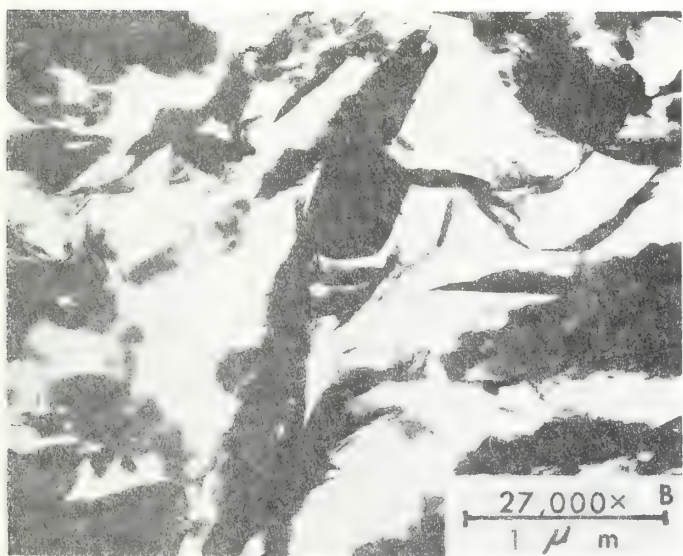


FIGURE 72.—Clay fabric showing short chains, arching, and particle contacts, core B-1 (2.0 m).

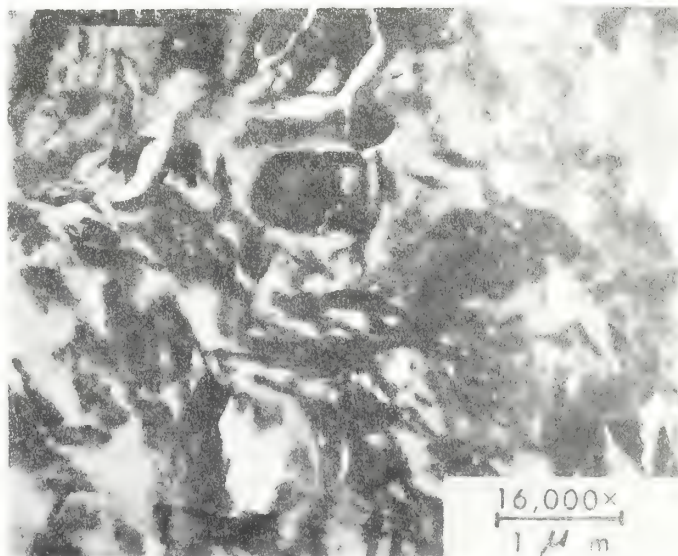


FIGURE 74.—Clay fabric of randomly oriented domains, core B-2 (9.3 m).



to note is the fact that the decrease in porosity in zone 2 is due not only to the slight dewatering commensurate with the process of consolidation but also, possibly more important in this case, to the significant overall decrease in clay content and corresponding increase in silt size particles within this interval.

Clay samples from 27.6 and 27.7 m in porosity zone 3 are characterized by relatively high water contents and correspondingly high porosities (figs. 65 and 66). Despite the fact that porosity zone 3 is deeper (below the mudline) than zone 2, the porosities are high due to the significant increase in clay size material in this zone and corresponding decrease in silt and sand size particles. The clay fabric photomicrographs clearly depict the relatively high porous nature of these zone-3 sediments (figs. 75EM and 76EM).



FIGURE 75.—Clay fabric of well-defined domains, core B-1 (27.7 m).

The clay particles, predominately domains, are oriented randomly; however, the photomicrographs reveal a slight tendency of some of the particles toward common alignment, but it appears to be a very minor degree. Of significance to note are the large voids (depths of 27 to 28 m below the mudline), the presence of some fairly large domains, and a few relatively long chains as compared to the fabric characteristics of the overlying sediment (figs. 77EM and 78EM). Numerous edge-to-face particle contacts are depicted in the photomicrographs. These particle contacts and the large voids, relative to the thickness of the clay particles, are evident at high magnification (fig. 79EM). Although a few chains are observed in the photomicrographs, the fabric of zone 3, in general, appears to be quite similar and essentially the same as the overlying sediment clay fabric. The differences appear to be the slight decrease in porosity with

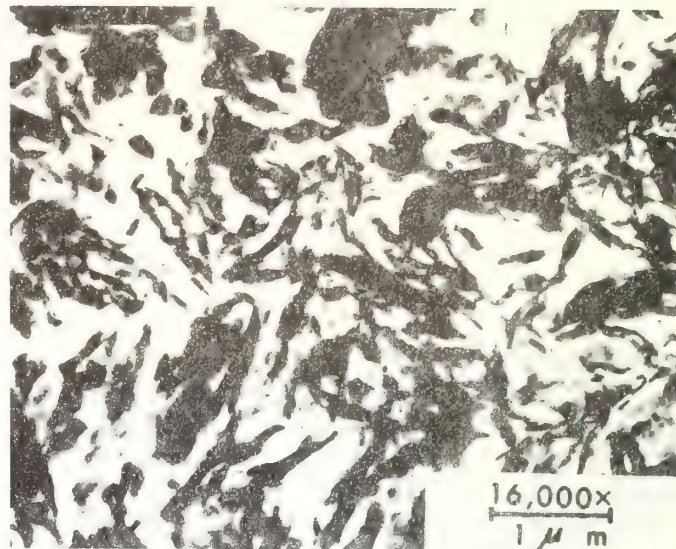


FIGURE 76.—Clay fabric of well-defined randomly oriented domains, core B-2 (27.6 m).

depth of burial and a slight increase in packing of the clay particles as compared with zone 1. Sediments from zones 1 through 3 have the highest porosities and void ratios as compared to the remainder of the cored material.

The clay fabric characteristics of the high porosity sediment can be summarized prior to proceeding to a description of the deeper, underlying, lower-porosity clays. Examination of the clay fabric has revealed a relatively high void ratio sediment with randomly oriented domains forming the dominant clay structure. An important feature to note, particularly visible in the stereographic photomicrographs, is

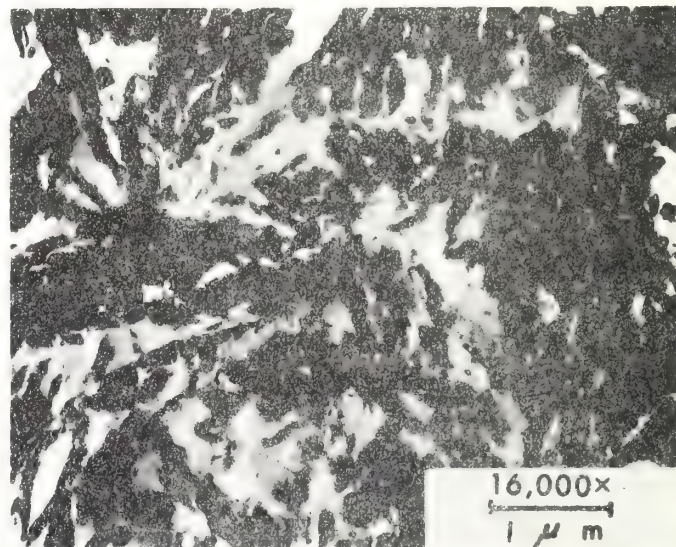


FIGURE 77.—Clay fabric having relatively large domains, core B-1 (27.7 m).





FIGURE 78.—Clay fabric of domains and chains, core B-1 (27.7 m).

the extremely fine (thin), small clay particles that appear to cluster in close proximity to the relatively large domains which form the dominant characteristic of the clay fabric. These fine particles appear to have a strong affinity to the large domains and also seem to cluster between the larger particles (figs. 68EM and 78EM). These particles are recognized by their light gray, thin, "halo-like" appearance around the large particles in contrast to the electron-dense domains. They are observed fairly well also at high magnifications (figs. 79EM and 80EM).

The randomly oriented domain fabric is structured to form the moderately high-porosity, high void ratio, clay sediment characteristic of the 37 m of cores B-1 and B-2 (fig. 66). This type of fabric does not, however, have the highly structured floe and linking chain features characteristic of the D.S.D.P. clay sample, and thus the intravoid features are not present to the same degree in these delta clay samples. Expressed in another sense, the relatively high-porosity Mississippi Delta samples of this study are characterized by a rather wide distribution of void sizes as ob-

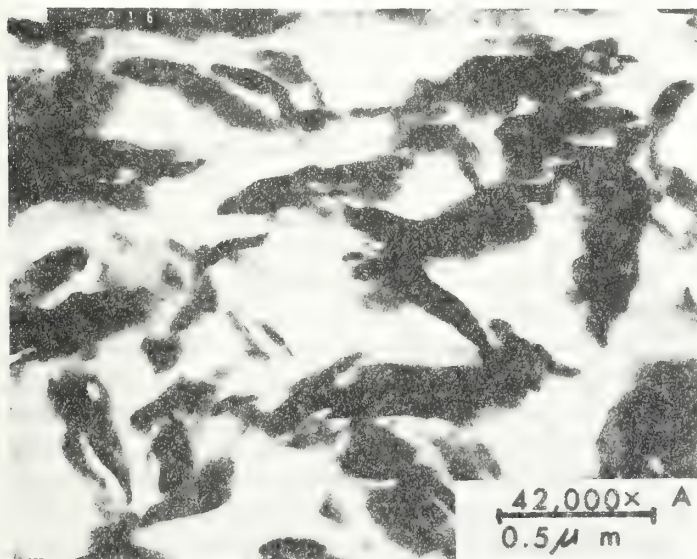


FIGURE 79.—Clay fabric of domains with pronounced particle contacts, core B-1 (27.7 m).

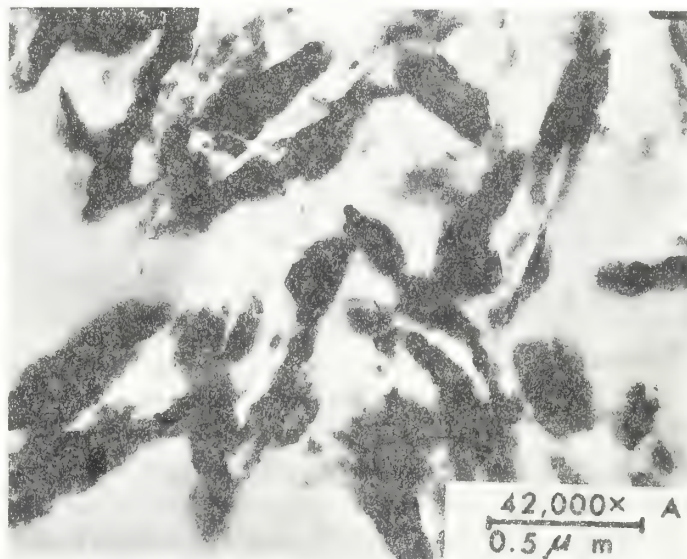


FIGURE 80.—Clay fabric of randomly oriented domains with very fine "clusters" of particles around the domains, core B-1 (1.4 m).



served in the electron photomicrographs as compared to the apparent bimodal-like distribution of void sizes (intra-voids versus intervoids) observed in the D.S.D.P. clay fabric (figs. 41EM and 43EM). Although obliquely oriented edge-to-face particle contacts enclose and develop pore space in the Mississippi Delta clays, well defined floc entities are not readily apparent. Well developed multiplate domains are the dominant particle "building blocks" of the relatively high-porosity clay fabric of cores B-1 and B-2 in contrast to the more "single platelike" nature of the flocs and linking chains of the D.S.D.P. clay fabric.

*Low-porosity clays.* The lowest-porosity clays encountered in this study occurred at core depths in excess of 85 m (Fig. 66). Samples from zone 4 with porosities only slightly higher than zone 5 were not available for electron microscopy studies. However, the samples studied from zone 5 have indeed revealed significant clay fabric characteristics quite different from the overlying moderately high-porosity clays (zones 1-3).

Electron photomicrographs of the clay fabric sampled at a depth of 120.4 m below the mudline (core B-1) reveal a remarkable increase in overall density of particle packing, the presence of small, thin voids, low porosity and strong particle-to-particle alignment (fig. 81EM) as compared with

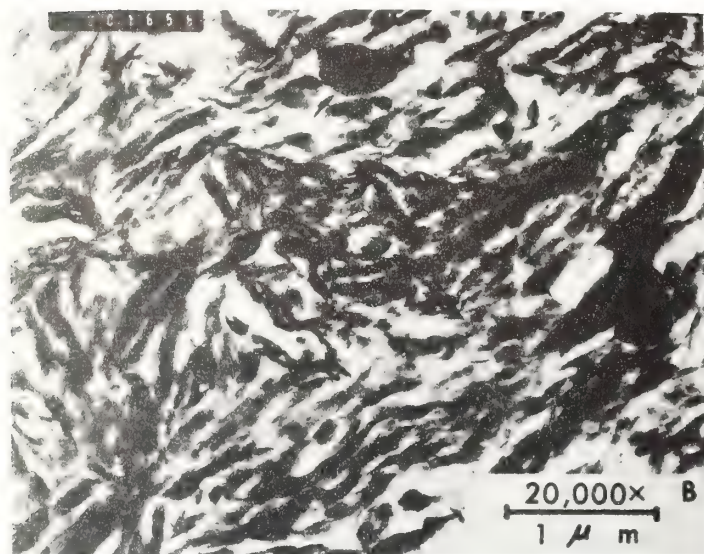


FIGURE 81.—Clay fabric of highly oriented domains that include obliquely oriented domains, core B-1 (120.4 m).

the higher porosity clays. Very strong overall preferred particle orientation is observed; however, local areas also are observed with some particles aligned at oblique angles to the general trend of the preferred particle orientation. Considerably long continuous chains of particles are depicted which form the bulk of the preferred orientation.

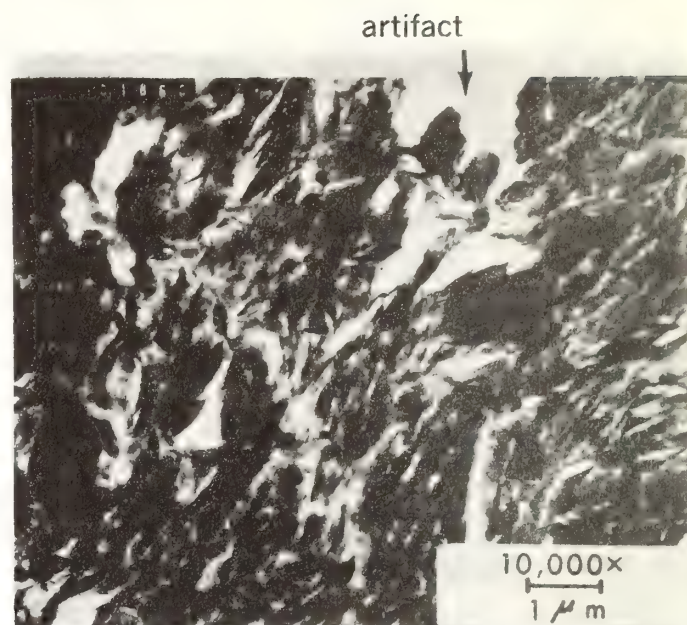


FIGURE 82.—Clay fabric depicting highly oriented clay particles and bending around large electron dense particles, core B-1 (120.4 m).

These chains undoubtedly developed in response to the process of natural consolidation and dewatering commensurate with increasing sedimentation and overburden stress. Some of the chains and particles are seen to bend and distort around relatively large electron dense particles (fig. 82EM). The white area observed in photomicrograph 82EM is artifact and due to slight tearing and/or incomplete impregnation of the embedding medium during sample preparation. Strong preferred orientation of the clay particles is apparent; however, numerous clay particles (domains) are aligned at large angles to the preferred orientation.

Photomicrographs depicting the clay fabric of the sediment sampled at a depth of 144.8 m reveal a quite similar fabric compared with the clays sampled at 120.4 m (core B-1) below the mudline. The clay fabric is characterized by very strong preferred particle orientation of domains and rather continuous, long chains (figs. 83EM and 84EM). The clay particles are efficiently packed in close proximity, giving rise to the development of preferred particle orientation; however, as observed in the photomicrographs of the clay fabric of the sediment from 120.4 m, not all of the particles are aligned parallel with one another and with the general trend of the preferred particle orientation of the sample. Likewise, these photomicrographs depict several areas where chains and particles wrap and bend around adjacent, larger particles and groups of particles. A few particles are oriented not only at oblique angles to the preferred particle orientation but are observed to lie virtually normal to the preferred direction (fig. 84EM). Gillott (1969) also observed a strong but not perfect degree of particle preferred orientation of clay minerals in a well developed fissile shale. He observed



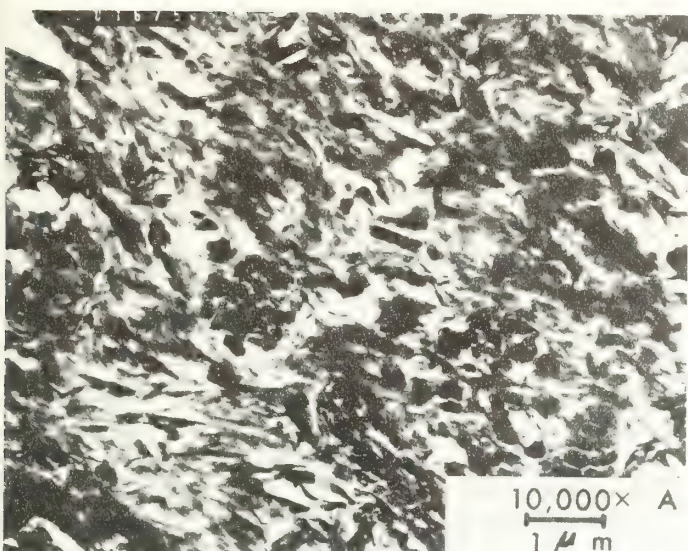


FIGURE 83.—Clay fabric of highly oriented domains, core B-1 (144.8 m).

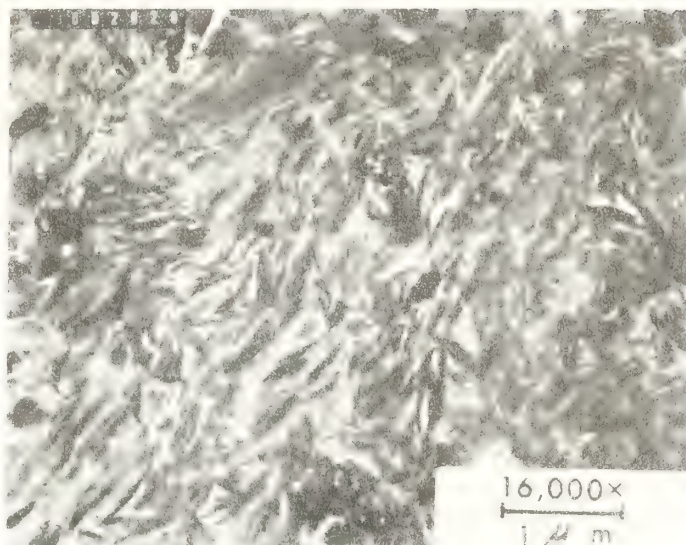


FIGURE 84.—Clay fabric of highly oriented domains in which not all particles are oriented preferentially, core B-1 (144.8).

that numerous platy minerals were arranged at large angles to the general fissility of the shale. Gipson (1965) observed a similar fabric relationship during the study of fissility in shale. Strong preferred particle orientation but not perfect particle alignment is necessary to develop a relatively fissile sediment.

Noteworthy also is the fact that these rather deeply buried submarine clays of porosity zone 5 are characterized by a preponderance of "thin," long, narrow voids which are produced by the particle-to-particle alignment and development of chains.

The void geometry of the deeply buried clays is quite unlike the voids of the overlying high-porosity sediment, which is characterized by very irregular shape. In general descriptive terms, the voids of the shallow, high-porosity clays could be expressed by a length to width ratio which approaches a value of unity, whereas the lower, deeply buried clays would be characterized by a void geometry with the length to width ratio approaching infinity. Apparently a number of the obliquely trending particles and particles lying normal to the overall general preferred orientation of the clay fabric are associated with a few of the larger irregular shaped voids of the deeply buried clays. Clearly, despite the considerable strong degree of preferred clay particle orientation observed in these low-porosity clays, significant numbers of particles usually in the form of domains, deviate from the preferred general direction. This influences the overall fabric characteristics and thus produces few irregularly shaped voids and folding and bending of particles and chains. These characteristic features were not observed in the overlying high-porosity clays. These features are interpreted here as being formed and thus developed from the process of natural consolidation

and imposed stress conditions given the fabric type and related geochemical conditions amenable to the development of strong preferred particle orientation at depths of burial within zone 5.

*Summary of clay fabric versus depth of burial.* In retrospect, the electron photomicrographs have clearly revealed a clay fabric of randomly oriented domains characteristic of the moderately high porosities to depths of approximately 37 m below the mudline. Domains are the predominant clay particle type present with some recognizable thin "single platelike" particles associated particularly in close proximity to the large particles. The voids of the high-porosity clays range in size from "small" to relatively "large," and they are irregularly shaped. The deeply buried, relatively low-porosity clays are characterized by a strongly oriented clay fabric with associated "thin" long voids. A dominant preferred particle orientation but *not* complete preferential arrangement is the rule for these clay sediments.

In reference to various fabric models proposed in the literature, the most important feature characteristic of the Mississippi Delta clays (cores B-1 and B-2) investigated during this study, is the presence of domains as the basic framework of the fabric. The fabric characteristic of these clay sediments appears to agree reasonably well with the model of particle arrangement in flocculated clay proposed by Moon (1972) with the following exceptions (fig. 23):

(1) The Mississippi Delta clays are characterized by a wide range of clay particle sizes not depicted in the model proposed by Moon. Thus the natural fabric is more varied and complex.

(2) Moon proposed a considerably lower degree of preferred particle orientation for consolidated clay than was observed in the low-porosity Delta clays.



(3) The Delta low-porosity consolidated clays revealed the "thin" long voids associated with the high degree of preferred particle orientation not shown by Moon.

Noteworthy also is the fact that the clay fabric of the relatively high-porosity (zones 1 through 3) sediment rather closely resembles the "turbostratic" arrangement proposed by Aylmore and Quirk (1960, fig. 11). This type of fabric was questioned strongly by Meade (1964) as being a significant component of natural sediments. Meade (1964) stated that there was little or no evidence to support the formation of either oriented fabrics, preferred or turbostratic arrangements during natural consolidation. Bowles and others (1969) found that the clay fabric of most undisturbed submarine sediment from selected areas of the Gulf of Mexico was characterized by a loose, open, random arrangement of particles. They suggested that clay particles, observed in samples subjected to low normal stresses, were packets of parallel oriented particles that may have been an original feature of the fabric prior to loading. The evidence was not conclusive for the presence of domains but it was certainly suggestive.

Through the application of image enhancement and digital image processing of the high porosity, zone 1, clay fabric photomicrograph 52EM, evidence clearly indicates the presence of multiplate particles or domains. This particular clay sample was under only 1.4 m of relatively recently deposited sediment with obviously minimal overburden stress ( $<0.12 \times 10^2$  kPa) imposed on the material.

The D.S.D.P. clay fabric sample characterized by flocs and linking chains contrasts sharply with the fabrics of the Mississippi Delta samples. In addition, the void ratio of 3.5 and porosity of 78 percent determined for the D.S.D.P. sample differed markedly from the Delta samples. The clay fabric of the D.S.D.P. sample, however, closely resembles the observations and model depicted by Pusch (1966, 1970) by virtue of the flocs and linking chains observed in his T.E.M. studies (fig. 21). This conclusion was corroborated by Pusch (personal communication).

The significant conclusion regarding the clay fabric observed for the Mississippi Delta samples is that domain particles do exist in these moderately high porosity, only slightly consolidated, submarine clay sediments and that strong preferred particle orientation is achieved at depths of not greater than 120 m and probably somewhat less. The D.S.D.P. high-porosity, high void ratio, deep-sea clay fabric is characterized by flocs (with large intravoids) connected by linking chains thus producing a sediment of high water content even at depths of 140 to 144 m below the mudline. The difference in the fabrics of the two sediment types is clearly due to the significant difference in depositional environment, sediment source, and related environmental conditions. Rates of sediment deposition and source of supply are quite likely important contributing factors responsible

for the differences in the ultimate clay fabrics of the two sediment types.

### Clay fabric versus selected mass physical properties

Void ratio and porosity are fundamental properties of sediment that readily reflect changes in water content with increasing depth of burial through the processes of dewatering and consolidation. Important to note is that changes in void ratio of a given sedimentary deposit of relatively uniform grain size distribution and uniform grain density clearly reflect corresponding changes in the basic mass physical properties such as wet bulk density and water content. Void ratio is an excellent property for comparing samples of a given sediment particularly with reference to consolidation, dewatering, and depth of burial, because the voids decrease in size with increasing overburden stress in contrast to the solids which maintain a constant volume acting as a "common denominator" for comparison purposes. Thus void ratio indicates a direct relationship between the solids and the voids of a given sediment mass.

Decreasing water content, void ratio, and porosity and increasing bulk density as a function of depth below mudline is an accepted axiom of marine geology and sedimentology. Although exceptions and variation to the rule do occur, the basic principle of decreasing water content with increasing sediment depth, particularly for a specific sediment type, has been observed to be essentially ubiquitous for submarine sediments in general. This raises fundamental questions as to what changes a sediment undergoes during consolidation with increasing overburden stress in terms of 1) changes in particle orientation relative to the fabric of the freshly deposited high porosity material, 2) how the fabric is related to fundamental physical properties of the particular sediment mass, and 3) whether the laboratory consolidation of a given sediment sample accurately simulates the natural consolidation process of the sedimentary deposit from which it was sampled. The purpose here is to examine these questions in light of the observed clay fabrics and laboratory data. The first of these questions has been examined in the previous section of this paper with the exception that the clay fabric was discussed in terms of depth of burial rather than in terms of imposed load or overburden stress.

*Void ratio versus particle orientation.* Examination of the numerous electron photomicrographs of the clay fabric from cores B-1 and B-2, particularly with reference to depth of burial, has clearly revealed a decrease in void ratio and change in general voids shape. As with porosity versus depth, void ratio can be summarized for each zone depicting a range of values and a characteristic average value for each zone as follows:



Depth in meters	Zone	Void ratio ( $e$ ) range	Average value
0–6	1	2.21–2.45	2.33
6–21	2	1.86–2.10	1.96
21–37	3	1.51–1.94	1.81
37–58	4	1.09–1.28	1.21
85–152	5	0.94–1.29	1.07

These data show a significant decrease in void ratio with increasing depth of burial that is reflected particularly well in the average values. Due to a common degree of variability observed in most sediment cores, a slight overlap occurs in the range of void ratio values between some zones. The clay fabric characteristic of each selected zone can be related in general to the observed void ratios by the following diagnostic features:

**Zone 1 (0–6 m, average void ratio  $e=2.33$ ):** The moderately high void ratio sediment is characterized generally by randomly oriented domains in edge-to-face contact, large irregularly shaped voids, a few short chains, and some edge-to-edge contacts. “Clusters” of fine small clay particles appear as “halos” around larger domains.

**Zones 2–3 (6–37 m, average void ratios  $e=1.96$ – $1.81$ ):** The void ratios within these two zones are observed to decrease slightly with depth, and are significantly lower than observed in zone 1. The clay fabric characteristics are in general common for both zones 2 and 3. The clay fabric is dominated by randomly oriented domains, a lower void to solid ratio as compared to zone 1, an apparent slight increase in the size of some domains, a slight increase in particle-to-particle packing as compared to zone 1, and the presence of a few chains. “Clusters” of small, fine particles around larger domains are observed also in these zones.

**Zone 4 (37–58 m, average void ratio  $e=1.21$ ):** No clay fabric data are available, but the void ratios indicate that the fabric characteristics would probably lie between those observed in zones 2 to 3 and zone 5.

**Zone 5 (85–152 m, average void ratio  $e=1.07$ ):** Low void ratios are common to these clays, and the corresponding fabric is dominated by a high degree of preferred particle orientation. Long continuous chains of particles are arranged preferentially, separated by small, thin voids. A few particles are oriented obliquely to the overall preferred orientation of the particles. The “clusters” of fine particles appear to generally lose identity in this zone.

**Clay fabric notation and geotechnical properties.** A very clear and intelligible picture of the clay fabric of the Mississippi Delta sediment is realized when the void ratio is given with the characteristic features of the fabric. To a first approximation, the clay fabric observed during this study of the Delta sediment can be described as randomly oriented domains (relatively high void ratio, high porosity sediment) and preferentially oriented domains (low void ratio, low po-

rosity sediment). Other descriptive terms can be applied to the characteristics of the clay fabric, such as long or short linking chains (regardless of their nature, i.e. EE, stepped FF, or a combination of EE and stepped FF). For example, a fabric can be described as randomly oriented domains with short or long linking chains. Further, the presence of floccules with linking chains (D.S.D.P. sample), domains, or with relatively thin “single platelike” particles can be described. Short, simple notations can be applied to these rather long descriptive phrases for clarity, simplicity, and for comparison of fabric samples. The suggested clay fabric notation can be summarized as follows:

D	Domains
T	Thin “single platelike” particles
C	Chains
F	Floccule or Floc
R	Random (randomly)
P	Preferred (preferential)
O	Oriented
S	Short
L	Long
<u>L</u>	Linking

A few possible combinations are as follows:

ROD	Randomly Oriented Domains
POD	Preferentially Oriented Domains
<u>LLC</u>	Long Linking Chains
<u>SLC</u>	Short Linking Chains
ROT	Randomly Oriented Thin “single platelike” particles
POT	Preferentially Oriented Thin “single platelike” particles
F/D	Floccules with Domains
F/C	Floccules with Chains

Many other combinations for describing clay fabric are possible with these notations. With these simple notations and a given void ratio, a clear picture of the clay fabric can be described. For example, the clay fabric of the upper 6 m of the Delta clay can be easily described as ROD/SLC (2.33) or randomly oriented domains with short linking chains having a void ratio of 2.33. The fabric characteristic of the sediment between 6 and 37 m can be described as ROD/SLC (1.96–1.81) which is a similar fabric compared to the overlying fabric but slightly consolidated. The deeply buried clays can be described by the notation POD/LC (1.07). Obviously this denotes a relatively highly consolidated clay with strong preferred particle orientation and long chains. The D.S.D.P. clay fabric sample can be easily described as ROTF/LLTC (3.5) or randomly oriented “thin platelike” particle flocs with long linking “thin platelike” particle chains.

Using the proposed simple clay fabric notations, the characteristic features of the clay fabric of the Mississippi Delta of cores B-1 and B-2 can be compared easily with the associated geotechnical properties as follows:

Zone	Fabric	Wet unit weight (ave.) Mg/m <sup>3</sup>	Shear strength kPa
1	ROD/SLC (2.33)	1.42	from 4.8 (low)
2	ROD/SLC (1.96)	1.45	to 9.6 (high)
3	ROD/SLC (1.81)	1.63	9.6 - 23.9
4	unknown but probably ROD (1.21)	1.82	18.7 - 38.3 (27.1 ave.)
5	POD/LC (1.07)	1.81	23.9 - 192.5 (111.6 ave.)

The low shear strength values are associated with void ratios greater than 1.5 and a fabric of randomly oriented domains with short linking chains. High shear strengths are associated with clays of low void ratio less than 1.3 and preferentially oriented domains with long chains. Interesting to note is the fact that the D.S.D.P. sample not only differed in clay fabric characteristics but also, as might be expected, in the overall mass physical properties. The D.S.D.P. clay fabric and selected geotechnical properties can be described as follows:

Depth below mudline	Fabric	Void ratio	Wet unit weight Mg/m <sup>3</sup>	Solid grain density Mg/m <sup>3</sup>
144 m	ROTF/LLTC	3.5	1.38	2.71

The basic mass physical properties of the D.S.D.P. clay sample can be related to the dominant fabric characteristics. The low wet unit weight and high void ratio are a function of not only the presence of very thin platelets but also more importantly to the presence of the long linking chains between floccules with large intravoids, which in harmony build a very high-porosity clay sediment. This sample contrasts with the Mississippi Delta high porosity clay samples investigated during this study. The Delta clay fabric built of randomly oriented domains would, however, be expected to have much lower void ratios than observed for the D.S.D.P. submarine clay sediment by virtue of greater particle packing and short chains.

A high void ratio sample from the Mississippi Fan studied by Bowles and others (1969) can likewise be described as a fabric of randomly oriented domains with long linking chains (ROD/LLC [2.80]), which is clearly intermediate in void ratio and in fabric characteristics between the Delta high void ratio samples and the D.S.D.P. clay. This high void ratio (2.80) is developed through the presence of the *long linking chains* as observed by Bowles and others (1969). The above relationships between void ratio and fabric are quite reasonable by recognizing that in order to have a high void ratio (high-porosity) sediment, the ratio of void to solids must likewise increase. In order to develop in-

creasingly *higher void ratio* sediment with *structural integrity* and particle-to-particle contact, the number of solid particles per unit volume of sediment must decrease. This characteristic can be accomplished efficiently with long, rather continuous chains. These features and characteristics were observed in the clay fabric samples investigated during this study.

The change in void ratio with increasing depth of burial for the sediment investigated can be related to the characteristic clay fabrics. Relatively high void ratio sediment is characterized by a fabric of randomly oriented domains and short chains with particles in edge-to-face and some face-to-face contact. Lower intermediate void ratio sediment shows greater particle-to-particle packing but a consistent predominance of randomly arranged particles with a few chains and perhaps a slight development of larger domains than observed in the high void ratio sediment. The low void ratio of the sediment is strongly influenced by the highly oriented clay particles and thin, long, narrow development of voids brought about by high density packing of the particles into long chains.

*Comparison of natural and laboratory consolidation.* Three important factors were examined in order to gain an insight into the possible degree to which laboratory consolidation of the selected Mississippi Delta samples simulates the natural consolidation of its parent sedimentary deposit. The factors examined are:

- (1) Void ratio versus depth of burial in:
  - a. actual physical properties—laboratory measurements (calculated).
  - b. predictions based on consolidation test (Hamilton method 1959).
- (2) Overburden stress in:
  - a. calculations based on measured physical properties.
  - b. predictions based on consolidation test (Hamilton method 1959).
- (3) Delineation of the clay fabric of consolidated samples and comparison with naturally consolidated samples.

The void ratios were calculated for core B-1 based on the measured mass physical properties such as water content, wet bulk density, and average grain density which were determined by standard laboratory techniques. Average values were determined for 3-meter intervals, and the void ratios were calculated by

$$\text{void ratio, } e = \left( \frac{1+w}{\gamma_t} \right) [G\gamma_w] - 1 \quad (7)$$

where

$w$  = water content by dry weight  
 $G$  = grain density



$\gamma_w$  = density of seawater (typical average value)  
= 1.024

$\gamma_t$  = wet bulk density or wet unit weight

These relationships can be found in Lambe and Whitman (1969).

The predicted void ratios versus depth of burial were determined by the method described by Hamilton (1959) which he used for the purpose of predicting the consolidation behavior of submarine clay sediment. The method is based on data determined from typical consolidation,  $e$ -log  $p$  curves from laboratory tests. The details of the method can be found in Hamilton's (1959) paper. The technique can be summarized as follows:

(1) The weight of a column of sediment is computed for the first few meters of sediment, such as zero to 3 m, based on the submerged unit weight of the surface sediment.

(2) Using the cumulative stress for the given column of sediment, which is the same as the interval stress for the first increment, the void ratio corresponding to the calculated stress is taken from the laboratory  $e$ -log  $p$  curve typical of the upper sediment.

(3) Porosity is computed from the void ratio by

$$\text{porosity}, n = e / (1 + e) \quad (8)$$

and the new in situ wet bulk density,  $\gamma_{\text{sed}}$ , of the sediment is computed using the equation

$$\gamma_{\text{sed}} = n(\gamma_w) + (1 - n)G \quad (9)$$

(4) The interval stress is calculated based on the new wet bulk density (submerged unit weight) and the total cumulative stress determined to the selected depth.

(5) Total stress and void ratios at successively deeper intervals are calculated and determined by repeated use of the  $e$ -log  $p$  curve and the above techniques.

As can be readily observed, the predicted void ratios and predicted stress versus sediment depth below mudline can be determined using this method.

The consolidation data,  $e$ -log  $p$  curve, from core B-1, 1.4 m depth, was used to calculate the predicted void ratios and overburden stress for comparison with the actual measured properties (fig. 29). An initial void ratio of 2.17 and a grain density of 2.66 Mg/m<sup>3</sup> was used in the calculations. These were typical values characteristic of the upper few meters of sediment (fig. 65). Overburden stress versus depth of burial was determined for core B-1 from laboratory mass physical properties data. Data were not available, however, for the fine sand between 59 and 85 m below the mudline. Consequently, values for bulk densities of highly compacted and lightly compacted fine sand were taken from Lambe and Whitman (1969) in order to determine a reasonable range of densities possible for such material. These data were entered into the calculations of overburden stress, and plots were drawn depicting the possible range of values for cumulative stress versus depth of burial using maximum and minimum bulk densities for the fine sand (fig. 85). An intermediate

value was considered most reasonable for comparison with the data of overburden stress determined by the Hamilton (1959) technique based on the laboratory  $e$ -log  $p$  consolidation data. As readily depicted (fig. 85), the maximum difference between the overburden stress using maximum and minimum values for bulk density is only  $1 \times 10^2$  kPa. Using an intermediate value the possible variation in actual overburden stress would be approximately  $\pm 0.5 \times 10^2$  kPa.

Plots of void ratio versus depth of burial for both measured and predicted cases clearly depict a very close similarity in curve shape and change in void ratio with depth (fig. 86). The slight offset of the lower void ratio curve is due to the fact that the predicted values represent void ratios determined under a loaded condition and the measured values are those characteristic of the sediment after slight rebound due to the removal of overlying material. Examination of the consolidation curves (figs. 29, 30, and 31) depicts rebounds with changes in void ratios of approximately 0.2 to 0.3 under high loads. Rebounds for sediment under lower loads characteristic of the depths cored in B-1 would probably be somewhat less. With these conditions in mind, the two void ratio curves appear to agree very well. The deviation of the curve for the measured values for depths between approximately 15 and 35 m is due to the significant increase in clay and water content within this interval relative to the overlying sediment.

Comparison of the overburden stress determined by the Hamilton (1959) method (determined from the consolidation data) and the laboratory data (measured mass physical properties) clearly reveals a strong similarity between the two methods as revealed by the two plots (fig. 87). The difference between the curves apparently is caused, at least in part, by the laboratory samples having slightly lower wet bulk densities than the actual in-situ bulk densities. This correction would actually shift the curves closer together giving an even better agreement. Even so, the similarity between the two curves depicting overburden stress versus depth is quite remarkable. Noteworthy is the fact that the calculations of the overburden stress conditions give a maximum possible overburden with depth of burial and do not take into account possible reduction in stress due to factors such as excess pore water pressure which, if it exists, would be expected to effectively reduce the actual overburden stress. However, data are not available on the pore water pressures in these sediments. Since both the calculated overburden stress based on the laboratory data and the predicted overburden stress from consolidation data consider the maximum possible stress conditions in each case, the two curves offer a reasonable means of comparing the two methods.

*Clay fabric of laboratory consolidated samples.* Selected sediment samples from core B-1 were consolidated in the laboratory using an Anteus Back Pressure Consolidometer. Maximum loads ranged from as high as  $61.29 \times 10^2$  kPa to as low as  $15.32 \times 10^2$  kPa for the different samples. Subse-

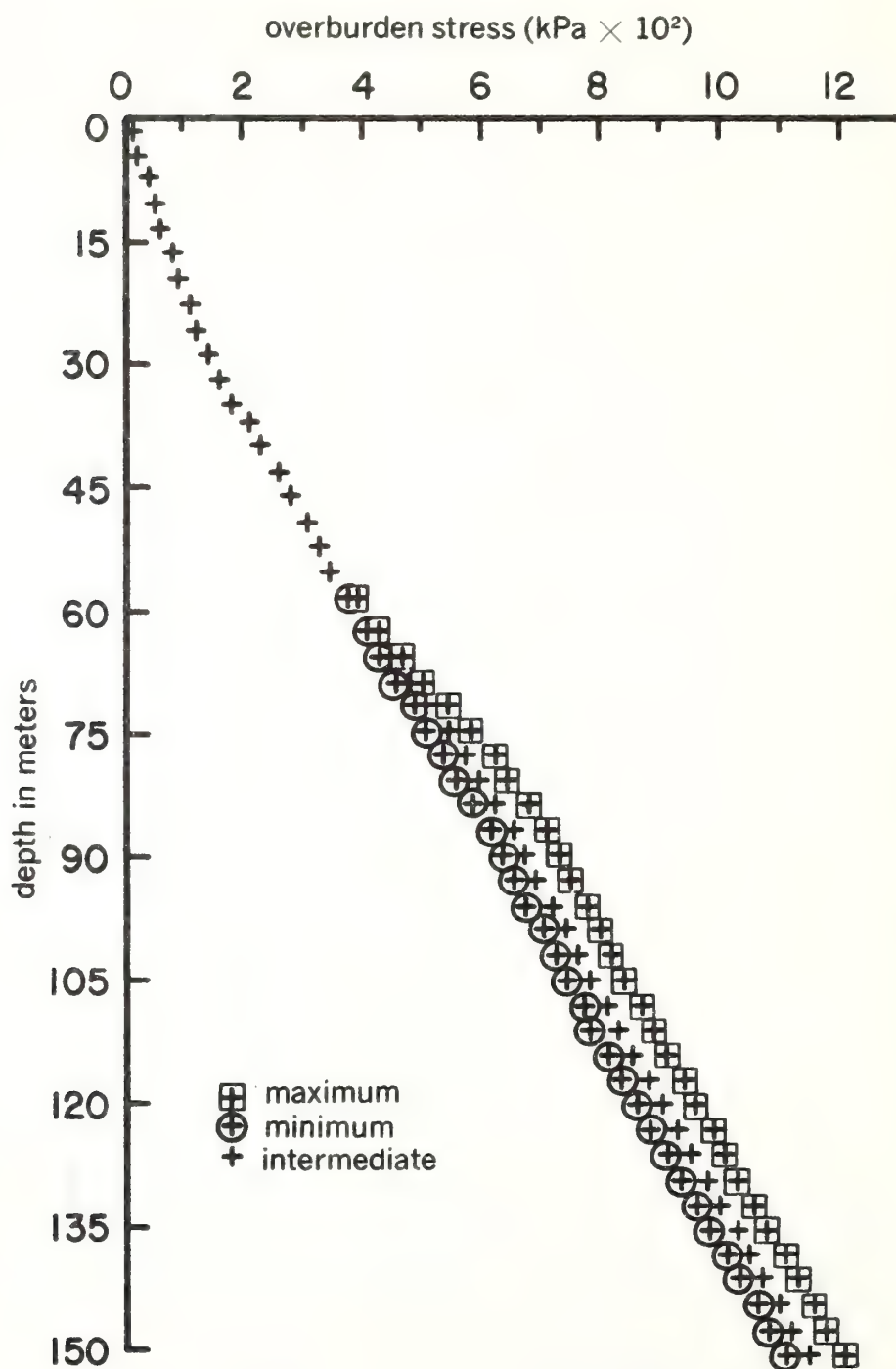


FIGURE 85.—Calculated cumulative stress with depth in core B-1 (bouyant overburden stress assuming no excess pore water pressure).





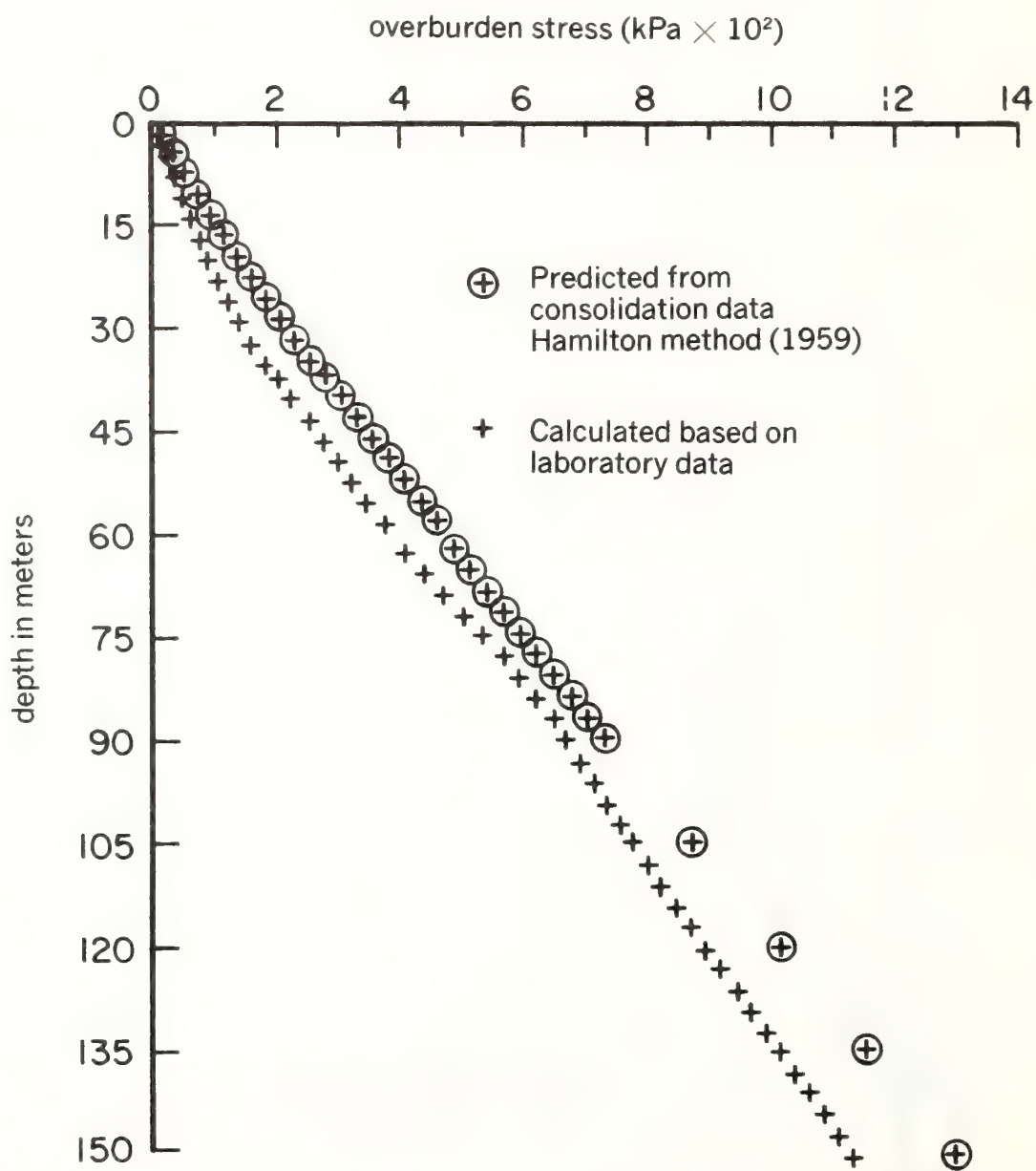


FIGURE 87.—Comparison of overburden stress determined by 1) Hamilton (1959) method based on consolidation data and by 2) laboratory-measured mass physical properties.

quent to laboratory consolidation of each sample, the clay fabric was examined by T.E.M. for comparison with the fabric of the naturally consolidated sediment.

An overburden stress of approximately  $10.9 \times 10^2$  kPa was calculated for the deep samples examined for clay fabric which were sampled from depths of 144.8 m below the mudline (fig. 87). Sediment from depths of 1.4, 1.98, 12.2, and 120.5 m below the mudline were consolidated in the laboratory to loads of  $61.29 \times 10^2$  kPa or approximately five and one half times the maximum load calculated for sediment at depths of about 144.8 m. Electron photomicrographs of the clay fabric clearly reveal a similar appearance among the laboratory consolidated samples regardless of the original sampling depths. The photomicrographs depict a highly oriented clay fabric with a close packing of clay particles (figs. 88EM, 89EM, 90EM, and 91EM). Figure 89EM in-

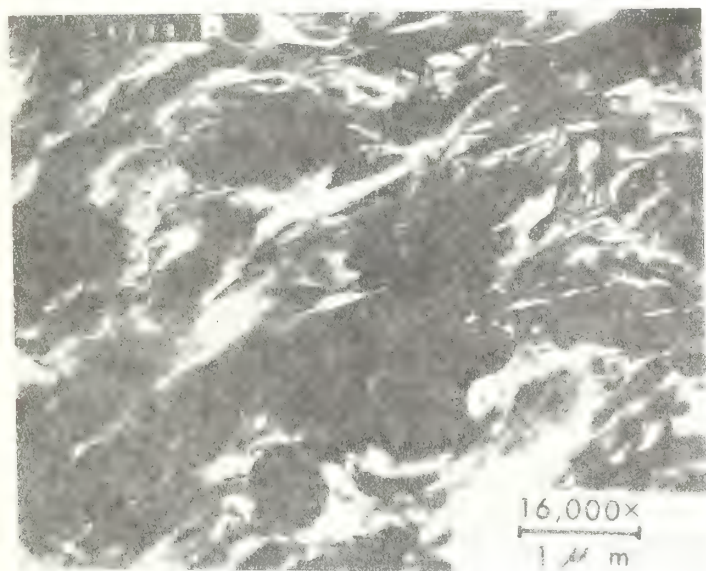


FIGURE 88.—Clay fabric of laboratory consolidated sample (load  $61.29 \times 10^2$  kPa), core B-1 (1.4 m).

icates a somewhat less organized, but highly oriented, clay fabric as compared to the other samples consolidated to the same maximum loads. This may be caused by the presence of slightly larger particles in the sample that effectively inhibited the degree to which the particles could be efficiently oriented under the imposed load (fig. 89EM). Folding and bending of particles around larger particles were observed in these samples as were observed in the deep naturally consolidated samples (figs. 89EM, 90EM, 81EM, 82EM, and 84EM).

Sediment samples from 27.7 and 120.5 m below the mudline were consolidated to loads of  $15.32 \times 10^2$  kPa and  $19.15 \times 10^2$  kPa, respectively. Likewise, these samples are characterized by a clay fabric of highly oriented particles with strong particle-to-particle packing, essentially the same

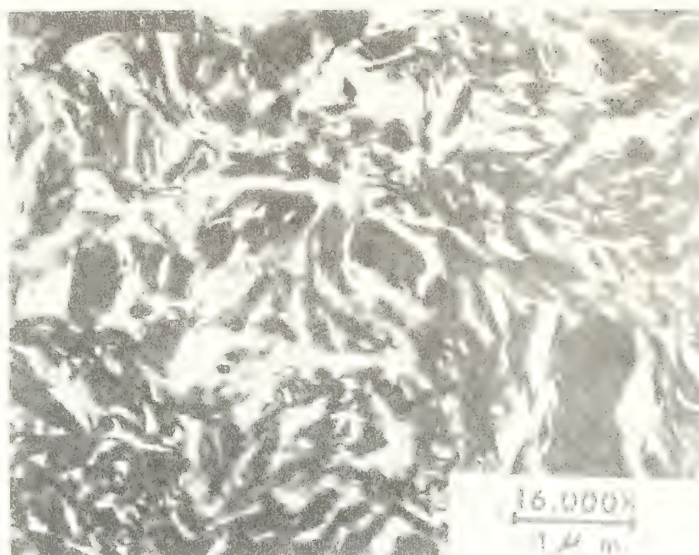


FIGURE 89.—Clay fabric of laboratory consolidated sample (load  $61.29 \times 10^2$  kPa), core B-1 (2.0 m).

as the clay fabric observed for the deeply buried samples from depths of 120.4 and 144.8 m (figs. 92EM, 93EM, 81EM, 82EM, 83EM, and 84EM). An important point to note is that Bowles and others (1969) found that submarine clay samples subjected to normal laboratory consolidation loads in excess of  $31.38 \times 10^2$  kPa displayed a very strong degree of preferred particle orientation. They observed that at loads of  $3.92 \times 10^2$  kPa the clay fabric was characterized by a dense packing of the particles which apparently were forced into clumps (particles randomly arranged) and packets (particles preferentially arranged). Still at this load of

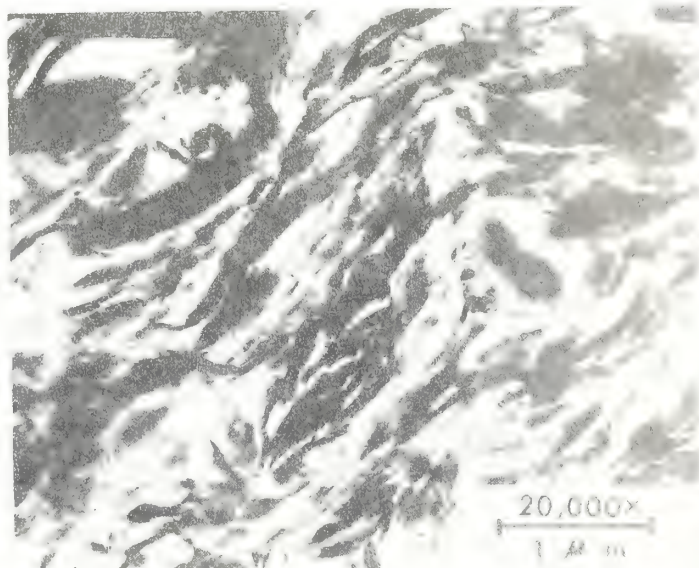


FIGURE 90.—Clay fabric of laboratory consolidated sample (load  $61.29 \times 10^2$  kPa), core B-1 (12.2 m).



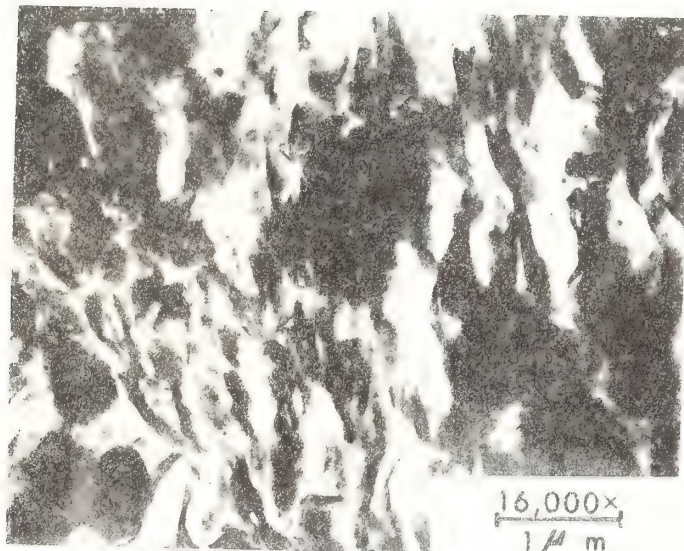


FIGURE 91.—Clay fabric of laboratory consolidated sample (load  $61.29 \times 10^2$  kPa), core B-1 (120.5 m).

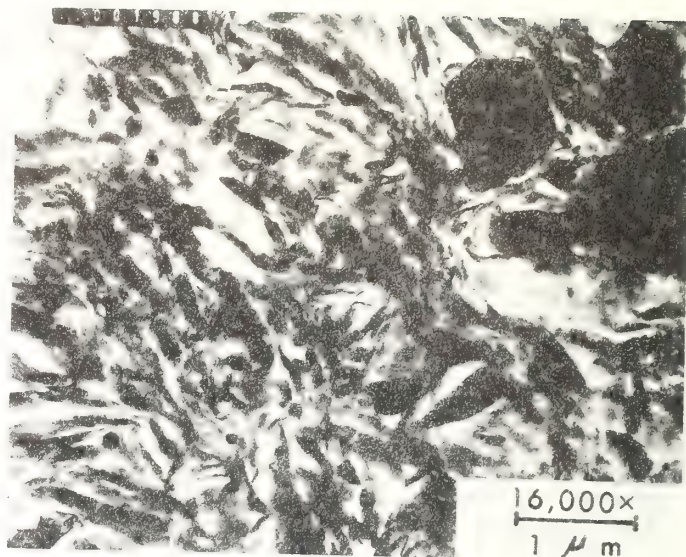


FIGURE 93.—Clay fabric of laboratory consolidated sample (load  $19.15 \times 10^2$  kPa), core B-1 (120.5 m).



FIGURE 92.—Clay fabric of laboratory consolidated sample (load  $15.32 \times 10^2$  kPa), core B-1 (27.7 m).



nearly  $4 \times 10^2$  kPa, the particles were reported to be essentially randomly arranged but closely packed to a void ratio of 1.3. A load of  $3.92 \times 10^2$  kPa is very close to the calculated load for the lower limit of zone 4 at approximately 58 to 60 m depth (figs. 66 and 85). The clay fabric observed by Bowles and others (1969) at this load corresponds very closely to the fabric characteristics predicted for zone 4 of this study. In addition, the void ratio of 1.3 is quite similar to the measured void ratios of the zone 4 clays (fig. 86). Further, Bowles and others (1969) noted that at laboratory consolidation loads of  $0.49 \times 10^2$  kPa, the fabric was characterized by an open, essentially random, arrangement of clay particles with some minor degree of preferred orientation in the form of packets of parallel particles. These packets were suspected of being an original feature of the clay and probably more correctly should be referred to as domains.

Apparently, according to the data and features of the clay fabric observed by Bowles and others (1969), structural collapse of the *high void ratio* submarine clay fabric occurs above or near the preconsolidation stress developing a much more dense, closely packed sediment, but not developing a strong preferred particle orientation until high loads in excess of  $3.92 \times 10^2$  kPa are achieved. Although the sediment studied by Bowles and others (1969) was characterized by higher void ratios than the clay sediment investigated during this study, the clay fabric and related consolidation characteristics of the submarine sediment of both studies appear to agree well. In summary, based on the data by Bowles and others (1969), the observed clay fabric, consolidation, and related data presented in this study, the high degree of preferred particle orientation of a consolidating high void ratio submarine clay sediment (Mississippi Delta and Gulf of Mexico sediment studied by Bowles and others, 1969) is achieved probably at loads in excess of  $3.92 \times 10^2$  kPa but at loads less than  $8.95 \times 10^2$  kPa. In retrospect, with regard to the consolidation  $e$ -log  $p$  curves examined earlier in this paper, the very broad  $e$ -log  $p$  curve with a high  $\bar{P}_c$  (preconsolidation pressure) observed for the sediment sampled at a depth of 120.5 m below the mudline, deserves special note. This  $e$ -log  $p$  curve contrasts with the sharply inflected, steep virgin curves concave up and to the right that are characteristic of the higher-porosity clays. The deep low-porosity clay sampled at 120.5 m had obviously been consolidated to a high degree through natural processes, and the clay particles had become well aligned, thus inhibiting further consolidation during laboratory testing, particularly at low loads. Obviously very little compression could ensue following the rather strong preferred particle orientation of the clay particles. Apparently the above range of loads or overburden stresses required to achieve strong preferred particle orientation of a submarine clay sediment is not ubiquitous and applicable to all types of clayey submarine sediment. This is borne out by the typical clay fabric characteristics ob-

served for the deeply buried D.S.D.P., high void ratio, clay which displayed no preferred particle orientation despite its depth of 144 m below the mudline (figs. 41EM and 43EM). Factors responsible for the apparent high degree of structural strength under relatively high overburden stresses and particle-to-particle integrity of certain submarine clay sediments have not yet been determined.

*Depth of burial versus fissility.* To the geologist, the term compaction refers to a decrease in the volume of sediment as a result of compressive stress usually considered in terms of overburden caused by continued deposition of sediment. This term is essentially equivalent to the term consolidation as used by the soils engineer with reference to a gradual decrease in water content and decrease in total sample volume as a function of an imposed load (usually a vertical load) on a sediment or soil sample. Perhaps the earliest serious study of clay sediment compaction was made by Sorby (1908), who recognized that the compaction of sediments was due primarily to a change in porosity. He carried out both field and laboratory investigations of sediment porosity. Numerous subsequent studies have been concerned with the deciphering of relationships among porosity (changes), depth of burial, overburden stress, the presence and degree of fissility in certain shales, stages of compaction, and relationship with organic materials and depositional environment (Hedberg 1936; Weller 1959; White 1961; Meade 1964, 1966; Gipson 1965, 1966; Odom 1967; Gillott 1969; Rieke and Chilingarian 1974). Although the details of these studies are too numerous to mention here, a few of the more important aspects can be summarized.

Hedberg (1936) recognized four intergradational stages of compaction of a fluid mud to a dense shale or slate and related these stages to changes in porosity as a function of compressive stress. He recognized the importance of the mechanical rearrangement of particles during the early stages of compaction. Weller (1959) was concerned with a quantitative approach to the evaluation of overburden stress with depth of burial, and he developed numerous data curves relating these factors to porosity. Meade (1966) pointed out the important inverse relationship between particle size and porosity particularly within the range of stress of up to about  $100 \times 10^2$  kPa. He recognized that the effect of particle size may be strong enough to obscure the expected decrease in porosity with increasing depth of burial.

White (1961) and Gipson (1965, 1966) found that a high degree of clay mineral preferred particle orientation was associated with fissile shales and that random orientation was characteristic of the more massive argillaceous rocks. Similar conclusions were drawn by Gillott (1969) during a study of the fabric of argillaceous rocks and soils. Likewise, in an excellent study by Odom (1967), a strong correlation was found between the degree of clay mineral preferred particle orientation and fissility and the presence of organic mate-



rial. Massive shales showed essentially random orientation of clay particles. The direct correlation of fissility and organic material was noted also by Gipson (1965). Numerous investigators have speculated that the presence of organic material tends effectively to reduce the net negative charge of clay particles, thus allowing them more efficiently to move closer together in a face-to-face arrangement. Both Gipson (1966) and Odom (1967) found no correlation between depth of burial and preferred clay mineral orientation.

Although there has been considerable conjecture concerning changes in porosity with increasing depth of burial and development of fissility in shale, the most conclusive evidence to date indicates that preferred particle orientation is related to fissility, but the degree of preferred clay mineral orientation is not directly related in most cases to depth of burial. The general decrease in porosity with increasing depth of burial and overburden stress varies considerably from sediment to sediment.

Evidence pointed out and alluded to by the numerous investigators studying clay fabric, compaction (consolidation) of muds, and the fabric of shales, has indicated the importance of understanding the geochemical conditions, environments of deposition, and related geological factors that set the stage for the initial formation of clay fabric and development of fabric characteristics at the time of deposition. Apparently, the fabric at the time of deposition plays an important role in determining the ultimate response of the clay particles to overburden stress and degree to which consolidation will ensue. Detailed studies are required, focused on the delineation of geochemical conditions that influence the formation of clay floccules in the water column, such as flocculation and/or sustained dispersion of clay particles from freshwater to saline water under varying natural geochemical conditions (such as the influence of organics and peptizers on flocculation and dispersion). Very little is actually known of these factors as they influence the development of clay fabric in the natural environment. Virtually nothing has been published concerning the effects of biological activity on the depositional and postdepositional clay fabric. The effects of the energy environment such as currents, waves, turbulence, and mechanical energy in general are virtually unknown as they influence the development of clay fabric in the water column and at the sediment-water interface. Essentially all of the previous studies have been concerned with the postdepositional sediment and rock fabrics. Considerable knowledge is lacking in regard to the initial stages of fabric formation particularly with regard to natural environments and environmental conditions.

This study of Mississippi Delta sediments has been confined to the delineation of the postdepositional clay fabrics of selected cores from the prodelta depositional environment. Although recognizing that very little is actually known of the initial stages of fabric formation in marine environments,

and keeping in mind the above brief review of a few studies of compaction, changes in porosity, and preferred particle orientation versus fissility, this study has recognized a high degree of preferred clay particle orientation characteristic of the sediment buried to depths of not more than 120.5 m below the mudline corresponding to an overburden stress of *not greater* than  $8.95 \times 10^2$  kPa. These clays contrast sharply with the overlying high-porosity sediments which show essentially no strong preferred particle orientation to depths of at least 37 m below the mudline corresponding to an overburden stress of not greater than  $2.02 \times 10^2$  kPa. These Delta sediments with highly oriented clay particles are obviously developing the high degree of fissility commonly observed in shales despite the rather limited depth of burial and corresponding relatively low overburden stress. They also contrast sharply with the D.S.D.P. deep-sea submarine clay sample with its very high void ratio (3.5) and high porosity although sampled from a depth of 144 m below the mudline. Clearly, factors other than increasing depth of burial and corresponding overburden stress influence the degree of preferred clay particle orientation, the development of fissility, and degree of compaction (consolidation) of a particular submarine sedimentary deposit.

### *Mississippi Delta Clay Fabric and Depositional Environment*

The Mississippi Delta is a very dynamic region characterized by the interaction of riverine and marine processes and the extremely large discharge of bedload and suspended sediment. Coarse sediment carried down the river is deposited at the distributary mouths, and the finer silts and clays are transported far out beyond the immediate mouths of the river as suspended sediment (Coleman and others 1974). Large plumes of suspended sediment extend considerable distances beyond the subaerially exposed Delta and deposit vast quantities of silt and clay in the prodelta environment.

The prodelta environment is characterized not only by rapid deposition of fine-grained sediment having very high water contents but also by the abundant accumulation of organic material (Coleman and others 1974). The Mississippi Delta is clearly a unique geological sedimentary environment quite unlike other nondeltaic shelf regions. The Delta also differs markedly from those deep-sea depositional environments that receive sediment at extremely slow rates, an example of which is the pelagic clays where rates of deposition are in terms of millimeters of sediment per thousand years.

This discussion points out that the clay fabric of Mississippi prodelta sediment would be expected to differ somewhat from the clay fabric of other nondeltaic depositional environments. The characteristics of Delta fabrics should not be arbitrarily extrapolated as diagnostic of other submarine sediment, but rather, the observations can be used as a guide

for further studies of various submarine sediment fabric. Although features similar to the Delta fabrics were observed by Bowles and others (1969) for other Gulf of Mexico sediments, observations clearly point out significant differences that can account for the variations in certain measured mass physical properties. An example of this is the relationships of fabric and void ratio. A striking difference in the clay fabric was observed in the deep-sea pelagic clay sample from the Pacific Basin as compared to the Mississippi Delta fabrics, and, again, selected mass physical properties were related to the observed fabrics.

The relative degree to which various factors interact and affect the ultimate nature of the clay fabric particle-to-particle relationships, particularly during initial stages of development, is virtually unknown. However, the obvious environmental factors that play a role in the formation and development of the clay fabrics of the Mississippi Delta can be summarized as follows.

### Initial stage

(1) Clay particles undergo a transition in the chemical environment as sediment is carried from the riverine fresh water to the saline marine environment. Flocculation or some form of clay particle aggregation would be expected on contact with seawater. Whitehouse and others (1960) have reported minimum concentrations of major cations (sodium, magnesium, calcium, and potassium) required to initiate flocculation of montmorillonite, illite, chlorite, and kaolinite. Montmorillonite required the highest concentration of cations to cause flocculation as compared to the other clay minerals. Concentrations of sodium and magnesium equivalent to approximately 20 percent of the open ocean water salinities were found to cause flocculation of montmorillonite, whereas calcium and potassium were found to cause flocculation at concentrations equivalent to approximately normal seawater salinities. Bouma and others (1971) have reported relatively high salinities in close proximity to the channel mouths and over extensive areas of the prodelta environment despite the vast influx of fresh water through the distributary channels of the Mississippi Delta.

(2) The effects of organic and inorganic compounds on the development of clay fabric carried by the Mississippi River are virtually unknown. As an example, various phosphates present in the river waters may act as peptizers that tend to disperse the fine particulate clays, while other chemical compounds may tend to cause flocculation. As mentioned earlier, certain organic materials of undetermined composition are considered to affect the clay mineral surface charges allowing them to approach one another more closely. These factors undoubtedly play a significant role in the initial formation of clay fabric; however, the degree to which these and other chemical aspects influence the particle-to-particle interaction is virtually unknown. Future research concerning

these chemical effects would substantially increase the understanding concerning the importance of the chemistry on the initial stages of clay fabric development.

(3) Turbulence, particularly in the nearshore and riverine environments, undoubtedly plays a role in the development of clay fabric. Turbulence as a form of mechanical energy would tend to disperse and disaggregate flocculated particles in the water column. Currents and turbulence on the other hand would tend to modify and/or disturb freshly deposited clays and in some cases cause resuspension. Studies addressing these questions and processes as related to clay fabric are unknown but would seem to offer worthwhile areas of research.

### Postdepositional stage

(1) The effect of benthic biological processes on freshly deposited sediment undoubtedly influences the nature and characteristics of clay fabric particularly in areas of high faunal activity. The influence of biological activity on the mass physical properties of submarine sediment has been studied to a limited extent (Moore 1931; Piper and Marshall 1969; Rhoads and Young 1970). Nevertheless little is known regarding the changes in clay fabric as a result of biological processes and activity. Bioturbation would be expected to influence freshly deposited clay sediments, but this would be relatively insignificant in the Mississippi Delta sediments investigated during this study owing to the rapid rates of sediment deposition which usually inhibit a substantial degree of biological activity.

(2) Postdepositional cementation would be expected to influence clay particle rearrangement during dewatering and natural consolidation of fine grained sediment. These factors have been alluded to by Nacci and others (1974); but considerably more research is required in order to assess the importance of the chemical cementation processes as related to their influence on clay fabric. Evidence of cementation was not observed in the clay fabrics for either the Mississippi Delta clays or the D.S.D.P. clay sample. Apparently other factors, yet undefined, are likewise important in influencing the force transmission and particle-to-particle interaction during natural consolidation as a function of overburden stress.

Numerous processes and environmental factors play a role in the development of clay fabric both during initial stages and during post depositional stages. Other possible factors yet unknown may be important in determining and thus influencing the formation and ultimate fabric characteristics of other submarine sedimentary deposits. The purpose of this discussion was to summarize and trace some of the more important aspects concerning the development of clay fabric beginning with particulate sediment in a riverine environment, through its further development in a marine environment, and finally to the influences of postdepositional factors. This hopefully sets a framework for future investigations in



order to gain a clearer insight into the nature of clay fabric as related to the sediment mass physical properties and the behavior of clays to dynamic processes.

### *The Principle of Irreversibility of Clay Fabric: Discussion of Concept*

Previous sections of this manuscript have discussed the importance of the physicochemistry and chemical environment in general on the development of clay fabric, particularly with regard to the initial stages of fabric formation. As pointed out earlier, the chemical nature of the fluid medium of both fresh and saline waters strongly affects the electrostatic interactions among suspended clay particles and thus determines the fabric characteristics of flocculation or dispersion prior to sediment deposition. During natural processes of weathering, transport, and subsequent deposition of detrital particles, an *increasing* electrolytic chemical environment is the rule. This is particularly significant in the case of terrestrial sediments which are transported from riverine environments to the marine environment as is the case for a substantial quantity of weathered sedimentary particles.

Considerable evidence indicates that clay particles that flocculate in the marine environment and those clay particles that mutually contact at the sediment-water interface, attract particle-to-particle with sufficient resultant physicochemical force to be chemically irreversible. This is particularly evident with regard to further chemical changes that may ensue during natural processes. The chemically irreversible nature of marine flocculated clay particles has been alluded to by Whitehouse and others (1960). These researchers stated that clay materials exposed to marine waters exhibit a dispersal resistance to ultimate deflocculation that is quite different from the resistance to dispersal of similar material not so exposed.

Convincing evidence indicating the chemically irreversible nature of marine flocculated clays was revealed during the analysis of the clay fabric techniques employed in this study of the Mississippi Delta and D.S.D.P. samples. In retrospect, these sediment subsamples were prepared for T.E.M. clay fabric analysis through the replacement of the interstitial water by a series of miscible fluids for critical point drying. The dry samples were then embedded with SPURR low-viscosity resin. The miscible fluids included the series ethyl alcohol to amyl acetate and then to liquid carbon dioxide for critical point drying. This type of treatment is considered to be rather vigorous in terms of the chemical changes that the interstitial (intermediate) fluids and the surrounding chemical atmosphere of clay particles of a sediment undergo and such treatment is much more rigorous than would be experienced by marine suspended sediment or submarine sedimentary deposits in nature (Matthew H. Hulbert, personal communication). As an example, an important factor of the chemical changes that

the interstitial fluids undergo is the virtually complete stripping away of the ambient saline interstitial water that is high in electrolyte content. In addition, the original interstitial saline water having a bulk dielectric constant of approximately 78 to 80 is replaced by fluids having considerably lower dielectric constants of approximately 24 (ethyl alcohol), 5 (amyl acetate), and 1.6 (liquid CO<sub>2</sub>).

Clearly, despite the rather vigorous chemical changes and subsequent embedding of the dry samples with resin, the clay fabric samples retained their particle-to-particle integrity indicating the existence of strong attractive forces between clay particles sufficient to overcome microstructural degradation. This suggests that chemical changes in the marine environment following the flocculation and sedimentation of particles will not significantly alter the fabric of sedimentary material and that subsequent changes in the "original" character of the fabric require some form of mechanical energy such as turbulence (in the water column), shearing of sediment or flocs, overburden stress, and in some cases possibly biological activity (bioturbation).

The significance of the principle of clay fabric irreversibility for marine sediment is that the chemical environment surrounding the clay particles plays a critical role in the *initial stages* of fabric development in the water column and at the sediment-water interface. Subsequent to the initial flocculation of particles and deposition, the chemistry of the interstitial water and ambient water chemistry probably play very passive roles in the postdepositional changes in the clay fabric and in the postflocculated states. Flocculation in the water column would not be a significant process without a sufficient concentration of suspended sediment providing close particle-to-particle proximity for particle contact. This does not rule out the fact that postdepositional cementation and authigenic mineralization may in some cases influence the ultimate response of the clay particles to physical forces. Mechanical energy rather than chemical energy plays the dominant role in *postflocculation* and *postdepositional stages* of clay fabric development.

### *Tentative Clay Fabric Models for Submarine Sediment*

This clay fabric study of selected Mississippi Delta and D.S.D.P. submarine sediments and also the fabric studies by Bowles (1968) and Mathewson and others (1972) have revealed a few characteristic features of clay fabric that appear to be diagnostic of material composed largely of smectite and illite. Based on the observations of these studies, a tentative fabric model can be developed integrating the basic characteristics of the clay fabric. First, a few fundamentals of submarine sediment clay fabric can be established.

- (1) The basic "building blocks" of clay fabric are domains and/or "single platelike" particles.
- (2) The basic particles can form flocs or chains. Because



T.E.M. photomicrographs represent two-dimensional features of the clay fabrics, some chains observed may actually be composed of numerous face-to-face particles oriented in approximately the "third dimension" of the field of view (a "shingle" type particle chain).

(3) The framework of clay fabric can be developed by predominantly domains, "single platelike" particles, flocs, chains, or a combination of these basic fabric entities.

(4) High-porosity submarine sediment having microstructural integrity, as borne out by the property of significant natural shear strength, requires well established particle-to-particle contacts.

(5) In order to build a high-porosity (high void ratio) sediment having microstructural integrity, particle-to-particle contacts must be maintained commensurate with an increase in the ratio of the volume of the voids to the volume of the solids.

(6) The most efficient method of building a high-porosity sediment is through the development of long chains (edge-to-edge or stepped face-to-face particle contacts or a combination of these features). Very high-porosity sediment is achieved by combining these features with a decrease in particle thickness such as "single platelike" particles rather than domains.

(7) Very low-porosity sediment can be achieved efficiently by face-to-face particle packing resulting in a high degree of particle preferred orientation.

These basic characteristics of clay fabric have been observed during this study. They form a basis for the development of various models considered to be diagnostic of submarine sediment composed predominantly of smectite and illite. Submarine sediment composed chiefly of other types of clay minerals may develop somewhat different particle-to-particle clay fabric relationships. Further studies of submarine clay fabric may require some modification and/or additions to the proposed fabric models. With the above fundamentals in mind, the various models were developed relating fabric characteristics to void ratio as depicted in figure 94. Based on the observations made during this study and through the examination of the fabric presented by Bowles (1968), approximate tentative values for void ratios characteristic of the various fabric models are suggested.

The models reveal that the void ratio can be efficiently increased simply by increasing the lengths of the chains. Low void ratios conversely are characterized by essentially no chains but a relatively high density packing of clay particles with a tendency toward preferential particle orientation. Clay sediment having very low void ratios, on the other hand, can be efficiently developed by close particle-to-particle packing with strong preferred overall particle orientation.

The proposed models of submarine sediment clay fabric can be used as a guide to further investigations of sediments, particularly studies focused on various depositional environ-

ments. These models should *not* be considered as characteristic of all submarine clays. They are, however, useful in gaining an insight into the particle-to-particle characteristics related to selected mass physical properties such as void ratio, porosity, and wet bulk density. In addition, the clay fabric representations establish a framework for further studies relating diagnostic features of the fabric (particle-to-particle associations) to the behavior of clay sediments under static and dynamic loads. Some of the obvious clay particle-to-particle associations with reference to selected geotechnical test data were discussed in earlier sections of this paper. Further detailed studies would increase our understanding of the relationships among clay fabric characteristics and submarine sediment geotechnical properties.

## Summary

This research was concerned with the clay fabric and selected geotechnical properties of submarine sediment from the Mississippi prodelta depositional environment sampled to depths of 150 m below the mudline. Fabric analysis was carried out using techniques of transmission electron microscopy, unique sample preparation, and quality control. Relationships among the clay fabrics and selected geotechnical properties characteristic of the Mississippi Delta submarine sediments and of a selected D.S.D.P. clay sample were investigated. This study was organized and pursued under three general areas of investigation.

(1) A comprehensive review of the literature was made, tracing the early concepts of clay fabric and evolution of ideas to the recent observations. This study found a basis for comparison and evaluation of previous ideas and observations with the fabric characteristics of the sediments investigated. The review revealed major areas where important research and new clay fabric techniques were needed.

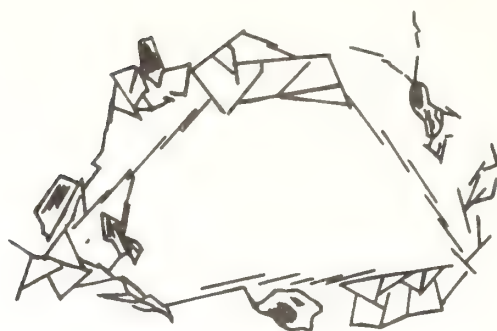
(2) A detailed study was given to the evaluation of analytical techniques, instrumentation, and sample quality as applied to the study of clay fabric. Sediment core sample quality was assessed by various techniques, and special methods were used to maintain the clay particle-to-particle integrity during sample preparation for T.E.M.

(3) A detailed investigation was made of submarine sediment clay fabrics from Mississippi Delta and D.S.D.P. core samples. The clay fabrics were related to selected geotechnical properties, depth of burial, and laboratory consolidation loads. Tentative clay fabric models for submarine sediment were proposed and related to characteristic void ratios. The significance and evidence of the principle of clay fabric irreversibility for marine sediments were discussed.

## A Synopsis—Literature Review

Review of the literature revealed that as early as the first part of the 1900s engineers and geologists recognized the importance of clay particle arrangements in sediments as





single platelike  
particles and chains

very high void ratio

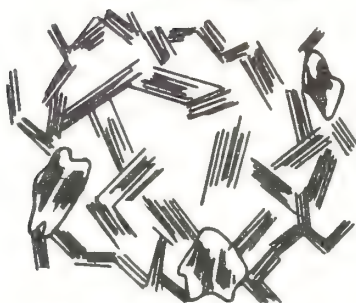
$> 3.0$



domain particles  
and chains

high void ratio

$> 2.5$



medium to high void ratio

$\sim 1.5-2.5$



low void ratio

$< 1.5$



very low void ratio

$< 1.2$

FIGURE 94.—Proposed tentative clay fabric models for submarine sediment.

fundamental to the understanding of the behavior of clay materials to natural and artificial loads. Sorby (1908) alluded to the importance of clay particle arrangements during settling and during consolidation processes. Perhaps the most well-known and earliest concept of clay fabric was presented by Terzaghi (1925) in a discussion on particle arrangement and bonding of cohesive soils. He proposed a honeycomb type structure conceived as being made up of numerous single grain clay particles held together by adhesion. Later Casagrande (1932) presented a similar idea of the honeycomb structure as an explanation for the nature of sensitive soils. Goldschmidt (1926) and Lambe (1953) proposed the classical cardhouse structure to explain the highly sensitive nature of some clays and the nature of clay particle-to-particle arrangements as a function of the electrolytic environment during flocculation in a marine environment. The importance of the physicochemistry in determining clay fabric characteristics was clearly pointed out by Lambe (1953, 1958a). A schematic picture of clay fabric showing a three-dimensional configuration was presented by Tan (1957). This contrasted with the two-dimensional representation by earlier investigators.

Mitchell (1956) pointed out important differences between dispersed and flocculated clays in relation to their geotechnical properties. Rosenqvist (1955) described the random particle orientation of highly sensitive Norwegian marine clays that had never been consolidated to a great degree. Somewhat later, van Olphen (1963) depicted in a descriptive sense the difference in particle arrangements of sediment in a peptized versus a flocculated suspension and described various conceptual models of possible modes of particle association such as dispersed, flocculated, deflocculated, and aggregated. Many of the earlier studies discussed clay fabric in terms of single particle associations and interaction. Meade (1964) contended that there was meager evidence showing that preferred and turbostratic fabrics (composed of multiplate particles) formed readily and generally during natural consolidation, although they were observed in laboratory tests. Quigley and Thompson (1966) found that reorientation of clay particles occurred during laboratory consolidation of a marine clay and that abrupt increases in parallelism occurred at pressures exceeding the preconsolidation pressure. Smart (1967) also found that laboratory prepared clay samples (kaolinite) exhibited a random arrangement of particles or small groups of particles and that during consolidation testing preferred particle orientation occurred and turbostratic structure developed. These early studies set the stage for later observations of clay fabric made with the electron microscope.

With the advent of the electron microscope (E.M.), renewed interest in clay fabric developed. This resulted in numerous direct observations of clay particle arrangements in natural and artificially prepared sediments. A very early E.M. study vaguely described clay particles (plates) arranged one upon

the other with a slight displacement of each (Hast 1947). Later Rosenqvist (1959), giving evidence supporting the "turbostratic" type fabric, set the stage for E.M. studies to follow in the "sixties." Numerous electron microscopy studies of clay fabric followed these initial E.M. investigations. Aylmore and Quirk (1959, 1960) proposed the term "turbostratic" arrangement for a fabric consisting of domains or "stacks." Kell (1964) and Sloane and Kell (1966) described a clay fabric similar to the "turbostratic" arrangements but with a more open structure which they called bookhouse or book structures. Types of domains were described by Sloane and Kell (1966) as "books" and by Smalley and Cabrera (1969) as stepped face-to-face. T.E.M. and S.E.M. studies have advanced the understanding of sediment clay fabrics considerably. Several studies were concerned with clay particle arrangements in shales (White 1961; Gipson 1965, 1966; Odom 1967; O'Brien 1968). The first reported fabric studies of submarine sediments were made by Bowles (1969) for various Gulf of Mexico clays. His studies strongly suggested the presence of domains in lightly (naturally) consolidated submarine sediments and the development of strong preferred particle orientation in laboratory consolidated samples at loads of 3,128 kPa and higher.

An acceleration of clay fabric research since about 1970 was evident by the numerous meetings and symposia devoted almost entirely to the presentation of research on clay microstructure. The increasing interest has been due not only to the numerous findings and observations made using the electron microscope as a tool to study clay fabric, but also more significantly to the general realization of the importance of clay microstructure on the engineering behavior and the fundamental nature of clayey sediments. Excellent studies were presented at the Southeastern Asian Conferences on Soil Engineering, 1970, 1971; the Roscoe Memorial Symposium, 1971, Cambridge University; the 3rd International Conference on Expansive Soils, 1973, Haifa, Israel; The Fourth International Working-Meeting on Soil Micro-morphology, Kingston, Ontario, Canada, 1973; the Clays and Clay Minerals Conference, 1973, Banff, Canada; and the International Symposium on Soil Structure, 1973, Gothenburg, Sweden. The earliest studies using the electron microscope used the transmission electron microscope exclusively. Recently, however, the scanning electron microscope has been frequently used to study fractured surfaces of clay samples.

O'Brien (1971) described staircase structures characteristic of laboratory sedimented kaolinite and illite clays. The representations appeared quite similar to the structure presented by Lambe (1958a) for salt-flocculated sediment and similar to the fabric called stepped face-to-face described by Smalley and Cabrera (1969). O'Brien (1970) found a strong relationship between clay-flake orientation and fissility



during a study of shale and claystone fabrics. He found that certain organic-rich black shales revealed the best fissility and greatest degree of preferred grain orientation. An excellent study was made of the microstructural changes in a marine quick clay at failure (Pusch 1970). Electron photomicrographs revealed that the clay was characterized by a very porous network of dense aggregates connected by links of particles (linking chains).

A noted change from the early ideas of clay fabric was realized by the pronounced increase in the observations, studies, and publications discussing the presence of compound, multiplate particles such as domains, aggregates, and crumbs—which contrasted sharply with the early concepts of single clay particle fabrics. These observations were made by soil scientists as well as by engineers and geologists (Pusch 1970; Barden and others 1970; Yong 1971; Barden 1972; Smart 1972; Moon 1972; Bennett and Bryant 1973; McConnachie 1974; Collins and McGown 1974). The importance of domains, and compound multiplate particles in general, were clearly recognized as an important aspect of clay fabrics. The influence of compound particles on the engineering behavior of sediment was studied by several of the above mentioned investigators. The majority of current studies of clay fabric have not failed to recognize the presence of multiplate particles in various sediment types; however, it has been pointed out that their presence in freshly deposited sediment, rather than formed as a function of consolidation, has been difficult to establish (Moon 1972).

Fabric unit interaction and classification were recently discussed for the purpose of prediction of soil behavior response and for the development of fabric models which more closely approach a physical description of real sedimentary material (Yong and Sheeran 1973). Yong and Sheeran stressed the importance in recognizing the "fabric unit" (groups of particles including crumbs, aggregates, clusters, floccules, and domains) as consisting of multiple particles in the majority of cases rather than single particle arrangements making up the basic structure of sediment. Collins and McGown (1974) attempted to delineate relationships among clay fabrics, mode of deposition, and depositional environment but were not entirely successful. They found, however, fabric features or sets of features characteristic of any one sediment type.

Review of the literature on clay fabric clearly pointed out that, although numerous studies have been made, a paucity of data and information exists in various areas of clay fabric research. Only a few studies dealing with the fabric of natural sedimentary material have been reported in contrast to numerous studies of laboratory prepared sedimentary material. With the exception of the research of Bowles (1968) and Bowles and others (1969), studies of submarine sediment clay fabrics are virtually nil. Very scant information exists on the initial stages of fabric formation in natural sys-

tems and the affects of organic and inorganic compounds on the development of clay fabrics. Unfortunately, clay fabric samples of many T.E.M. and S.E.M. studies were not carefully prepared, rendering the final observations highly suspect in terms of original features characteristic of the sediment investigated. Standards for 1) clay fabric analysis, 2) sample preparation, 3) assessing bulk sample quality, and 4) electron microscopy techniques in general were found to be virtually nonexistent. A few studies recognized the need for careful laboratory techniques applied to the study of clay fabric; however, no basic standards were established.

Although a few typical fabric types have been classified as honeycomb, cardhouse, turbostratic, bookhouse, and stairstepped, recent studies have clearly revealed that domain type particles rather than single plate particles are the rule for most natural sedimentary clayey materials. The unlimited variation in particle size, shape, and composition, coupled with the depositional environment, physicochemistry and transportation of sedimentary detritus through changing environmental conditions, all increase the complexity and ultimate nature of the sediment fabrics of a particular deposit.

### *A Synopsis—Evaluation of Analytical Techniques, Instrumentation, and Sample Quality*

The most critical steps in preparing samples for electron microscopy studies are the techniques employed in the dehydration of water-saturated specimens. Likewise, the techniques for embedding a sample with an appropriate medium, a necessary prerequisite to ultrathin sectioning, must be accomplished with care. These factors were given paramount importance during this study of clay fabric. Careful techniques were employed in order to insure high quality comparable results by maintaining the structural integrity and particle-to-particle relationships of the clay samples. Clay specimens for this study were critical point dried following careful removal of interstitial water and replacement with intermediate fluids, embedded with a low-viscosity epoxy resin, and sectioned with a microtome. Ultrathin sections were examined by transmission electron microscopy.

Sediment core quality and subsample preparation techniques for clay fabric analysis were evaluated during this study. The quality of the sediment cores was assessed by means of shear strength tests, both in situ and laboratory miniature vane and Torvane, and by results from consolidation test ( $e$ -log  $p$  curves). Clay fabric particle-to-particle integrity as depicted in T.E.M. photomicrographs was evaluated in terms of fabrics of natural (undisturbed) versus remolded samples, image enhancement techniques applied to clay fabric, and visual assessment of subsample integrity during preparation and analysis. Close agreement between in-situ shear strength measurements and strength tests on cored material indicated relatively high quality sediment



cores with minimal disturbance caused by coring. Similarities between sensitivities by the in-situ vane measurements and those determined on the cored sediment also corroborated this conclusion. Consolidation tests of natural and remolded samples as well as evaluation by the index of disturbance classification (Silva 1974) indicated that the cored sediment was of relatively high quality showing a minimal degree of disturbance.

Examination of transmission electron photomicrographs of undisturbed and remolded samples clearly indicated that the subsamples had been prepared effectively and that the undisturbed samples had maintained their particle-to-particle structural integrity. Remolding revealed complete structural breakdown and a rearrangement of particles into local areas of strong preferred orientation. Remolding caused flocs of the D.S.D.P. sample to reform into domains, causing complete collapse of the flocs and linking chain structure of the undisturbed samples. Undisturbed samples revealed unique particle-to-particle contacts and structural complexity quite different from the remolded sample fabrics.

Clay fabric integrity and sample quality as influenced by sample preparation were evaluated by image enhancement techniques. A representative clay fabric sample T.E.M. photomicrograph of low shear strength, high-porosity sediment was assessed with a Digital Image Processing System for the primary purpose of detecting possible microstructural degradation due to sample preparation techniques. The basic problem was to delineate the different film densities or gray levels present in the negative as processed by the Laser Image Processing Scanner and the Digital Image Processing System and to determine the area represented by each gray level. Given the total area of the film transparency and the area of the solids and the voids, the void ratio and porosity for the sample was calculated and compared with the values determined by standard laboratory techniques. Close agreement between techniques indicated that the sediment subsample investigated had remained essentially microstructurally intact, maintaining its particle-to-particle integrity. This was borne out by the apparent constant void ratio (porosity) maintained throughout the entire analytical procedures of sample preparation.

The evaluation of core sample quality and subsample preparation techniques has clearly revealed that standard soil mechanics tests, transmission electron microscopy analysis, and computer digital image processing and image enhancement can be integrated and used effectively to assess the quality of clay sediment cores, the preparation of samples (techniques), and the electron photomicrographs of clay fabrics.

### *A Synopsis—Clay Fabric and Selected Geotechnical Properties*

The electron photomicrographs have revealed a clay fabric of randomly oriented domains characteristic of the

moderately high-porosity sediment to depths of approximately 37 m below the mudline. Domains were the predominant clay particle type present with some recognizable thin "single platelike" particles associated particularly in close proximity with the larger particles (domains). The voids of the high-porosity clays ranged in size from "small" to relatively "large", and they were irregularly shaped. The deeply buried low-porosity clays in excess of 85 m were characterized by a strong preferred particle orientation with associated "thin" long voids. Dominant preferred particle orientation but *not* complete preferential arrangement was the rule for these clay sediments. With a few exceptions, the fabric characteristics of the Mississippi Delta sediments investigated during this study agreed reasonably well with the model of particle arrangement in flocculated clay proposed by Moon (1972). The clay fabric of the relatively high porosity sediment closely resembled the "turbostratic" arrangement proposed by Aylmore and Quirk (1960) but questioned by Meade (1964) as being a significant component of natural sediments. Image enhancement and digital image processing of the high-porosity clay fabric photomicrograph clearly revealed the presence of multiplate particles or domains.

The D.S.D.P. clay fabric sample characterized by flocs and linking chains contrasted sharply with the Mississippi Delta samples. The fabric, however, closely resembled the observations and model depicted by Pusch (1966, 1970) by virtue of the flocs and linking chains. The differences in the fabrics of the two sediment types undoubtedly were due to significant differences in depositional environment, sediment source, and related environmental conditions. Different rates of sediment deposition were quite likely an important contributing factor for the differences in the ultimate clay fabrics of the Mississippi Delta and D.S.D.P. (deep-sea) samples.

Geotechnical properties were related to the clay fabrics observed for the Mississippi Delta sediment, and particular reference was given to changes in the properties with depth of burial. The change in void ratio with increasing depth of burial was related to the clay fabrics. Relatively high void ratio sediment was found to be characterized by a fabric of randomly oriented domains and short chains with particles in edge-to-face and some face-to-face contacts. Lower intermediate void ratio sediment showed greater particle-to-particle packing but a consistent predominance of randomly arranged particles with a few chains and perhaps a slight development of larger domains than observed in the high void ratio sediment. The low void ratio sediment was strongly influenced by the highly oriented clay particles and thin, long, narrow voids brought about by high density packing of the particles into long chains. Five general porosity zones with depth below the mudline were delineated and re-



lated to the clay fabrics, wet unit weights (wet bulk densities), and shear strengths.

Three important factors were examined to gain an insight into the possible degree and similarity to which laboratory consolidation of selected Mississippi Delta samples simulated the actual natural consolidation of the parent sedimentary deposit. The three factors examined and studied in the analysis were:

- (1) Void ratio versus depth of burial:
  - a. actual physical properties laboratory measurements (calculated).
  - b. predicted based on consolidation tests (Hamilton method, 1959).
- (2) Overburden stress based on measured physical properties:
  - a. calculated based on actual physical properties.
  - b. predicted based on consolidation tests (Hamilton method, 1959).
- (3) Delineation of the clay fabrics of consolidation samples and comparison with the fabrics of naturally consolidated sediment.

Plots of void ratio versus depth of burial as well as overburden stress versus depth of burial for both predicted and calculated (measured) cases revealed a very close similarity in the curves for the artificial (laboratory) and natural cases. Examination of the clay fabrics from laboratory consolidated samples revealed a striking similarity with the deeply buried naturally consolidated sediment. Based on the data presented in this study, the observed clay fabrics, consolidation data, and the data presented by Bowles and others (1969), the high degree of preferred particle orientation of a consolidating high void ratio submarine clay sediment (Mississippi Delta and some Gulf of Mexico sediment) is achieved probably at loads in excess of  $3.92 \times 10^2$  kPa, but at loads less than  $8.95 \times 10^2$  kPa. Evaluation and analysis of the data strongly suggest and indicate a striking similarity between natural and laboratory consolidated Mississippi Delta sediments.

There has been considerable conjecture concerning changes in porosity with increasing depth of burial and development of fissility in shale. The most conclusive evidence from other studies to date indicated that preferred particle orientation is related to fissility, but the degree of preferred clay mineral orientation is not generally directly related in most cases to depth of burial. The general decrease in porosity with increasing depth of burial and overburden stress varies considerably from sediment to sediment. These relationships were investigated during this study. The Delta sediments with highly oriented clay particles were observed to be "well on the way" to developing the high degree of fissility commonly found in shales despite the rather limited depth of burial and corresponding relatively low overburden

stress. Apparently, the fabric at the time of sediment deposition plays an important role in determining the ultimate response of the clay particles to overburden stress and the degree to which consolidation will ensue. Low rates of sedimentation and loading commensurate with diagenetic cementation and particle-to-particle bonding would be expected to substantially inhibit realignment of clay particles and the development of fissility in clayey sediments. Factors other than increasing depth of burial and corresponding overburden stress influence the degree of consolidation of a particular sedimentary deposit.

Convincing evidence indicating the chemically irreversible nature of marine flocculated clays was revealed during the analysis of the clay fabric techniques used in this study. The present evidence indicates that clay particles which flocculate in the marine environment and those clay particles that mutually contact at the sediment-water interface, attract particle-to-particle with sufficient resultant physico-chemical force to be chemically irreversible. This is particularly evident with regard to further chemical changes that may ensue during natural processes. The significance of the principle of clay fabric irreversibility for marine sediment is that the chemical environment of clay particles plays a critical role in the *initial stages* of fabric formation (development) in the water column and at the sediment-water interface. Subsequent to the initial flocculation of particles and deposition, the chemistry plays a very passive role in the postdepositional changes in the clay fabric and the post-flocculated states. Mechanical energy rather than chemical energy plays the dominant role in *postflocculation* and *post-depositional stages* of clay fabric development.

Based on a few fundamentals of submarine sediment clay fabric delineated during this study, tentative fabric models were developed and considered to be characteristic of material composed predominately of smectite and illite. These models were associated with void ratios and based on fundamental characteristics of the clay fabrics. The models reveal that the void ratio can be efficiently increased simply by increasing the lengths of the chains. Low void ratios, conversely, can be characterized by essentially no chains but relatively high density packing of clay particles with a tendency toward preferential particle orientation. Clay sediment having very low void ratios can be efficiently developed by close particle-to-particle packing with strong preferred overall particle orientation. The proposed models of submarine sediment clay fabric can be used as a guide to further investigations of sediment fabrics, particularly studies focused on various marine depositional environments. This research pointed out numerous areas of clay fabric studies that require further investigation, particularly those aspects concerned with the initial stages of fabric formation and the effects of the surrounding chemical environment on clay particles in natural systems.

## References

- Andersland, O. B., and A. G. Douglas, 1970. Bonding, effective stresses, and strength of soils, *J. Soil Mech. and Found. Div., Proc. ASCE* 96: 1073-1077.
- Anderson, T. F., 1951. Techniques for the preservation of three-dimensional structure in preparing specimens for the electron microscope, *Trans. N.Y. Acad. Sci.* 13:130-133.
- Aylmore, L. A. G., and J. P. Quirk, 1959. Swelling of clay-water systems, *Nature* 183:1752-1753.
- Aylmore, L.A.G., and J. P. Quirk, 1960. Domain or turbostratic structure of clays, *Nature* 187:1046-1048.
- Barden, L., 1972. The influence of structure on deformation and failure in clay soil, *Geotechnique* 22:159-163.
- Barden, L., 1973. Theme 2, Macro- and microstructure of soils, in *Int. Symp. on Soil Structure*, Gothenburg, Sweden, pp. 22-26.
- Barden, L., and G. R. Sides, 1970. Engineering behavior and structure of compacted clay, *J. Soil Mech. and Found. Div., Proc. ASCE* 96:1171-1200.
- Barden, L., and G. R. Sides, 1971. Sample disturbance in the investigation of clay structure, *Geotechnique* 21:211-222.
- Barden, L., G. R. Sides, and J. P. Karunaratne, 1970. A microscopic examination of aspects of clay structure, *Proc. Second Southeast Asian Conf. on Soil Eng.*, Singapore, pp. 67-72.
- Bennett, R. H., and W. R. Bryant, 1973. Submarine sediment microstructure (abstract), in *Clays and Clay Minerals Conference*, Banff, Canada, 22 p.
- Bennett, R. H., G. H. Keller, and R. F. Busby, 1970. Mass property variability in three closely spaced deep-sea sediment cores, *J. Sed. Pet.* 40:1038-1043.
- Bennett, R. H., and D. N. Lambert, 1971. Rapid and reliable technique for determining unit weight and porosity of deep-sea sediments, *Mar. Geol.* 11:201-207.
- Bhaskaran, R., 1972. The microstructure of dispersed and flocculated samples of kaolinite, illite, and montmorillonite: Discussion, *Canadian Geotech. J.* 9:233-234.
- Bjerrum, L., and I. Th. Rosenqvist, 1956. Some experiments with artificially sedimented clays, *Geotechnique* 6:124-136.
- Bochko, R., 1973. Types of microstructural elements and microporosity in clays (based on scanning electron microscopy studies), in *Int. Symp. on Soil Structure*, Gothenburg, Sweden, pp. 97-101.
- Bolt, G. H., 1956. Physico-chemical analysis of the compressibility of pure clays, *Geotechnique* 6:86-93.
- Bouma, A. H., F. B. Chmelik, and R. Rezak, 1971. East Bay Mississippi River Delta, *Gulf Coast Assoc. Geol. Soc.* 21:273-289.
- Bowles, F. A., 1968a. Electron microscopy investigation of the microstructure in sediment samples from the Gulf of Mexico, Ph.D. dissertation, Texas A&M University.
- Bowles, F. A., 1968b. Microstructure of sediments: Investigation with ultrathin section, *Science* 159:1236-1237.
- Bowles, F. A., W. R. Bryant, and C. Wallin, 1969. Microstructure of unconsolidated and consolidated marine sediments, *J. Sed. Pet.* 39:1546-1551.
- Brewer, R., 1964. *Fabric and Mineral Analysis of Soils*, John Wiley and Sons, New York, 470 p.
- Brewer, R., and A. D. Haldane, 1957. Preliminary experiments in the development of clay orientation in soils, *Soil Sci.* 84:301-309.
- Bryant, W. R., P. Cernock, and J. Morelock, 1967. Shear strength and consolidation characteristics of marine sediments from the western Gulf of Mexico, in *Marine Geotechnique*, A. F. Richards (ed.), Univ. of Illinois Press, pp. 41-62.
- Bryant, W. R., and A. P. Delfache, 1971. Geotechnical charts of the deep water portion of the Gulf of Mexico, *Offshore Tech. Conf. Paper*, No. OTC 1468, pp. 493-502.
- Bryant, W. R., A. P. Delfache, and P. K. Trabant, 1974. Consolidation of marine clays and carbonates, in *Deep-Sea Sediments: Physical and Mechanical Properties*, A. L. Inderbitzen (ed.), Plenum Press, New York, pp. 209-244.
- Bryant, W. R., W. Hottman, and P. Trabant, 1975. Permeability of unconsolidated and consolidated marine sediments, Gulf of Mexico, *Mar. Geotech.* 1:1-14.
- Bryant, W. R., and C. S. Wallin, 1968. Stability and geotechnical characteristics of marine sediments, Gulf of Mexico, *Trans. Gulf Coast Assoc. Geol. Soc.* 18:334-356.
- Buchanan, P. N., 1964. Effect of temperature and adsorbed water on permeability and consolidation characteristics of sodium and calcium montmorillonite, Ph.D. dissertation, Texas A&M University.
- Burnham, C. P., 1970. The micromorphology of argillaceous sediments: particularly calcareous clay and siltstones, in *Micromorphological Techniques and Applications*, D. A. Osmond, and P. Bullock (eds.), *Agr. Res. Council Soil Survey Tech. Mono.* No. 2, pp. 83-96.
- Cabrera, J. G., and I. J. Smalley, 1971. Engineering behavior and structure of compacted clay, discussion and reply, *J. Soil Mech. and Found. Div., Proc. ASCE* pp. 802-803.
- Casagrande, A., 1932. The structure of clay and its importance in foundation engineering, *Contrib. Soil Mech., Boston Soc. C.E.* (1940) p. 72, and *J. Boston Soc. C.E.* vol. 19 (April, 1932).
- Casagrande, A., 1936. The determination of the preconsolidation load and its practical significance, *Proc. 1st Int. Conf. Soil Mech. and Found. Eng.*, Cambridge, 3:60-64.
- Clays and Clay Minerals Society, 1973. *22nd Annual Clay Minerals Conference*, Banff, Canada.
- Cohen, A. L., D. P. Marlow, and G. E. Garner, 1968. A rapid critical point method using fluorocarbons ("Freons") as intermediate and transitional fluids, *J. Microscopic.* 7:331-342.
- Coleman, J. M., J. N. Suhayda, T. Whelan, and L. D. Wright, 1974. Mass movement of Mississippi River Delta sediments, *Trans. Gulf Coast Assoc. Geol. Soc.* 24:49-68.
- Coleman, J. M., and L. D. Wright, 1974. Formative mechanisms in a modern depocenter, in *Stratigraphy and petroleum potential of northern Gulf of Mexico (Part II)*, *New Orleans Geol. Soc. Seminar*, Jan. 22-24, 1974, pp. 90-139.
- Collins, K., and A. McGown, 1974. The form and function of microfabric features in a variety of natural soils, *Geotechnique* 24: 223-254.
- Deer, W. A., R. A. Howie, and J. Zussman, 1963. *Rock-Forming Minerals*, Vol. 4, Framework Silicates, John Wiley and Sons, New York, 435 p.
- Delfache, A. P., and W. R. Bryant, 1970. Compressional behavior of high void ratio marine sediments, *Offshore Tech. Conf. Paper* No. OTC 1148, pp. 1147-1150.
- Diamond, S., 1970. Pore size distributions in clays, *Clays and Clay Minerals*, 18:7-23.
- Emrich, W. J., 1971. Performance study of soil sampler for deep-penetration marine borings, in *Sampling of Soil and Rock, ASTM Special Tech. Pub.* 483, pp. 30-50.
- Fisk, H. N., and B. McClelland, 1959. Geology of continental shelf, Louisiana: its influence on offshore foundation design, *Bull. Geol. Soc. Amer.* 70:1369-1394.
- Foster, R. H., 1973. Analysis of soil microstructure, in *Proc. Int. Symp. on Soil Structure*, Gothenburg, Sweden, p. 5-12.



- Foster, R. H., and P. K. De, 1971. Optical and electron microscopic investigation of shear induced structures in lightly consolidated (soft) and heavily consolidated (hard) kaolinite, *Clays and Clay Minerals* 19:31-47.
- Foster, R. H., and J. S. Evans, 1971. Image analysis of clay fabric by Quantimet, *Microscopy* 19:377-401.
- Gillott, J. E., 1969. Study of the fabric of fine-grained sediment with the scanning electron microscope, *J. Sed. Pet.* 39:90-105.
- Gipson, M., Jr., 1965. Application of the electron microscope to the study of particle orientation and fissility in shale, *J. Sed. Pet.* 35:408-414.
- Gipson, M. R., 1966. A study of the relations of depth, porosity and clay mineral orientation in Pennsylvanian shales, *J. Sed. Pet.* 36:888-903.
- Goldschmidt, V. M. 1926. Undersøkelser over lersedimenter, *Nordisk jordbrugsforskning*, No. 4-7, pp. 434-445.
- Gould, H. R., 1970. The Mississippi Delta complex, in Deltaic Sedimentation, Modern and Ancient, J. P. Morgan (ed.), *SEPM Special Pub.* No. 15, pp. 3-30.
- Green-Kelly, R., and D. Mackney, 1970. Preferred orientation of clays in soils: the effect of drying and wetting, in Micromorphological Techniques and Applications, D. A. Osmond, and P. Bullock (eds), *Agr. Res. Council Soil Surv. Tech. Mono.* No. 2, pp. 43-52.
- Grim, R. E., 1940. The clay minerals in soils and their significance, *Proc. Purdue Conf. Soil Mech.* pp. 216-223.
- Grim, R. E., 1962. Clay mineralogy, *Science* 135:890-898.
- Grim, R. E., 1968. *Clay Mineralogy*, 2nd Ed., McGraw-Hill Co., New York, N.Y., 596 p.
- Grim, R. E., W. F. Bradley, and W. A. White, 1957. Petrology of the Paleozoic shales of Illinois, *Illinois Geol. Survey Rpt. Inv.* 203, 35 p.
- Grim, R. E., and W. D. Johns, 1958. Clay mineral composition of recent sediments from the Mississippi River Delta, *J. Sed. Pet.* 28:186-199.
- Hadding, A., 1923. Eine röntgenographische methode, kristalline und kryptokristalline substanzen zu identifizieren, *Zeitschrift für kristallographie, mineralogie und petrographie*, 58:108-112.
- Hamilton, E. L., 1959. Thickness and consolidation of deep-sea sediments, *Bull. Geol. Soc. Amer.* 70:1399-1424.
- Hamilton, E. L., 1960. Ocean basin ages and amounts of original sediments, *J. Sed. Pet.* 30:370-377.
- Hamilton, E. L., 1964. Consolidation characteristics and related properties of sediments from experimental Mohole (Guadeloupe site), *J. Geophys. Res.* 69:4257-4269.
- Hamilton, E. L., and H. W. Menard, 1956. Density and porosity of sea-floor surface sediments off San Diego, California, *Bull. Amer. Assoc. Pet. Geol.* 40:754-761.
- Hast, N., 1947. Structure of clay, *Nature* 159:354-357.
- Hayat, M. A., and B. R. Zirk, 1973. Critical point drying method, in Principles and Techniques of Electron Microscopy, Biological Applications, M. A. Hayat, ed., pp. 307-312.
- Holmes, H. C., 1966. Experimental consolidation of clays and shales, *Amer. J. Sci.* 31:241-287.
- Holmes, H. C., 1968. Mechanical behavior of clays and shales, in *Clay Mineralogy*, R. E. Grim, ed., pp. 217-230.
- Holmes, H. C., 1969. Experimental consolidation of clays and shales, *Geology* 55:283-289.
- Holmes, H. C., and T. E. Mitchell, 1969. Pressure interrelation with in situ stress, *J. Soil Mech. and Found. Div., Proc. ASCE* 95:1017-1022.
- Holmes, H. C., and R. E. Mitchell, 1970. Bulk density of mineral grains from Mohole samples (Guadeloupe Site), *J. Sed. Pet.* 40:461-470.
- Ingles, O. G., 1968. Soil chemistry relevant to the engineering behavior of soils, in *Soil Mechanics—Selected Topics*, I. K. Lee (ed.), Butterworth's, London, pp. 1-57.
- Int. Symp. on Soil Structure, 1973. Gothenburg, Sweden.
- Jarrett, P. M., 1967. Time-dependent consolidation of a sensitive clay, *Materials Res. and Standards* 7:300-304.
- Johns, W. D., and R. E. Grim, 1958. Clay mineral composition of recent sediments from the Mississippi Delta, *J. Sed. Pet.* 28:186-199.
- Kaarsberg, E. A., 1959. Introductory studies of natural and artificial argillaceous aggregates by sound-propagation and X-ray diffraction methods, *J. Geol.* 67:447-472.
- Karlsson, R., and R. Pusch, 1967. Shear strength parameters and microstructure characteristics of a quick clay of extremely high water content, in *Proc. Geotech. Conf. on Shear Strength Properties of Natural Soils and Rocks*, Oslo, Volume I, and, in Statens Geotekniska Inst., Swedish Geotechnical Institute, Report No. 23, 1968, pp. 35-42.
- Kell, T. R., 1964. The influence of compaction method on fabric of compacted clay, unpublished M.S. thesis, University of Arizona, Department of Civil Engineering.
- Keller, G. H., and R. H. Bennett, 1968. Mass physical properties of submarine sediments in the Atlantic and Pacific basins, *23rd Int. Geol. Cong.* 8:33-50.
- Keller, G. H., and R. H. Bennett, 1970. Variations in the mass physical properties of selected submarine sediments, *Mar. Geol.* 9:215-223.
- Keller, W. D., 1957. *The Principles of Chemical Weathering*, Lucas Brothers Publishers, Columbia, Missouri, 111 pp.
- Kirkpatrick, W. M., and I. A. Rennie, 1972. Directional properties of consolidated kaolin, *Geotechnique* 22:166-169.
- Krumbein, W. C., and L. L. Sloss, 1959. *Stratigraphy and Sedimentation*, W. H. Freeman and Company, San Francisco, California, 497 p.
- Kruyt, H. O. (ed.), 1952. *Colloid Science* Vol. 1, Irreversible Systems, Elsevier Pub. Co., Amsterdam, 554 p.
- Lambe, T. W., 1951. *Soil Testing for Engineers*, John Wiley and Sons, New York, N.Y., 165 p.
- Lambe, T. W., 1953. The structure of inorganic soil, *ASCE Proc.* 79:1-49, Separate 315, October.
- Lambe, T. W., 1958a. The structure of compacted clay, *ASCE Proc.* Separate 1654, and *J. Soil Mech. and Found. Div.*, 84:1-34.
- Lambe, T. W., 1958b. The engineering behavior of compacted clay, *J. Soil Mech. and Found. Div., Proc. ASCE* 84:1-35.
- Lambe, T. W., 1960. Compacted clay, a symposium, structure and engineering behavior, *ASCE Trans.* 25:682-717.
- Lambe, T. W., and R. V. Whitman, 1969. *Soil Mechanics*, John Wiley and Sons, New York, N.Y., 553 p.
- Lisitzin, A. P., 1972. Sedimentation in the World Ocean, *SEPM. Special Pub. No. 17*, 218 p.
- Lisitzin, A. P., P. E. Sloss, and H. C. Holmes, 1964. Clay consolidation testing with two specimens, *J. Soil Mech. and Found. Div., Proc. ASCE* 90:69-86.
- Lisitzin, A. P., 1965. Recent developments in consolidation and shear behavior of the study of fine-grained and fine-grained soils, in *Proc. Eng. Transactions, Minneapolis, Minn.*, pp. 64-87.
- Martin, R. T., 1965. Quantitative Fabric of Consolidated Kaolinite, *Mineralogical Magazine and Transactions*, 29, 6:64-74 p.
- Martin, R. T., 1966. Quantitative fabric of wet kaolinite, *Proc. 14th Conf. Clays and Clay Minerals* pp. 271-296.
- Martin, R. T., and C. C. Ladd, 1970. Fabric of consolidated kaolinite, *Mineralogical Magazine and Transactions*, 34, 6:64-74 p.

- 95-27-53



- Rosenqvist, I. Th., 1962. The influence of physico-chemical factors upon the mechanical properties of clays, *Ninth National Conf. on Clays and Clay Minerals* 9:12-27.
- Rosenqvist, I. Th., 1966. Norwegian research into the properties of quick clay—a review, *Eng. Geol.* 1:445-450.
- Sarkisyan, S. G., 1971. Application of the scanning electron microscope in the investigation of oil and gas reservoir rocks, *J. Sed. Pet.* 41:289-292.
- Schmertmann, J. H., 1953. Estimating the true consolidation behavior of clay from laboratory test results, *J. Soil Mech. and Found. Div., Proc. ASCE* 79:1-26, Separate 311.
- Schmertmann, J. H., 1955. The undisturbed consolidation behavior of clay, *J. Soil Mech. and Found. Div., Proc. ASCE Paper #2775*, pp. 1201-1233.
- Schofield, R. K., and H. R. Samson, 1954. Flocculation of kaolinite due to the attraction of oppositely charged crystal faces, *Faraday Soc., London*, pp. 135-145.
- Scott, R. F., 1963. *Principles of Soil Mechanics*, Addison-Wesley, 550 p.
- Seed, H. B., and C. K. Chan, 1959. Structure and strength characteristics of compacted clays, *J. Soil Mech. and Found. Div., Proc. ASCE* 85:87-128.
- Shepard, F. P., 1956. Marginal sediments of the Mississippi Delta, *Bull. Amer. Assoc. Pet. Geol.* 40:2537-2623.
- Sides, G., and L. Barden, 1971. The microstructure of dispersed and flocculated samples of kaolinite, illite, and montmorillonite, *Canadian Geotech. J.* 8:291-399.
- Silva, A. J., 1974. Marine geomechanics: Overview and projections, in *Deep-Sea Sediments, Physical and Mechanical Properties*, A. L. Inderbitzen (ed.), Plenum Press, p. 45-76.
- Singh, S., 1970. Bonding, effective stresses, and strengths of solids, *J. Soil Mech. and Found. Div., Proc. ASCE* 96:1469-1473.
- Sloane, R. L., and S. Diamond, 1970. Effects of predessication on the texture of some scanning electron microscopy clay mineral specimens, *Nineteenth Annual Clay Minerals Conf.*, Miami, Beach, Florida, 34 p.
- Sloane, R. L., and T. R. Kell, 1966. The fabric of mechanically compacted kaolin, *Fourteenth Nat. Conf. on Clays and Clay Minerals* 14:289-296.
- Smalley, I. J., and J. G. Cabrera, 1969. Particle association in compacted kaolin, *Nature* 22:80-81.
- Smart, P., 1967a. Soil structure, mechanical properties and electron microscopy, Ph.D. thesis, University of Cambridge.
- Smart, P., 1967b. Particle arrangements in kaolin, *Fifteenth Conf. on Clays and Clay Minerals* 15:241-254.
- Smart, P., 1972. A discussion to: A microstructural view of the mechanical properties of saturated clay, by Calladine, C. R., 1971, *Geotechnique* 21:391-415; *Geotechnique* 22:368-371.
- Smart, P., 1973. Statistics of soil structure in electron microscopy, in *Proc., Int. Symp. on Soil Structure*, Gothenburg, Sweden, pp. 69-76.
- Sorby, H. C., 1908. On the application of quantitative methods to the study of the structure and history of rocks, *The Quarterly J. Geol. Soc. London* 64:171-233.
- Sowers, G. B., and G. F. Sowers, 1961. *Introductory Soil Mechanics and Foundations*, 2nd Ed., The Macmillan Company, 386 p.
- Tan, T. K., 1957. Discussion on: Soil properties and their measurement, *Fourth Int. Conf. on Soil Mech. and Found. Div.*, Vol. III, London, pp. 87-89.
- Tan, T. K., 1959. Structure mechanics of clays, *Sci. Sinica*, 8:83-96.
- Terzaghi, K., 1925a. *Erdbaumechanik auf Bodenphysikalischer Grundlage*, Leipzig und Wien, Franz Duetz, 399 p.
- Terzaghi, K., 1925b. Principles of soil mechanics settlement and consolidation of clay, *Eng. News-Record*, pp. 874-878.
- Terzaghi, K., and R. B. Peck, 1948. *Soil Mechanics in Engineering Practice*, John Wiley, 566 p.
- Terzaghi, K., and R. B. Peck, 1967. *Soil Mechanics in Engineering Practice*, 2nd Ed., John Wiley, 729 p.
- Theissen, D. A., 1942. Wechelseitige adsorption von kolloiden, *Z. Electrochem.* 48:675.
- Timur, A., W. B. Hemphkins, and R. M. Weinbrandt, 1971. Scanning electron microscope study of pore systems in rocks, *J. Geophys. Res.* 76:4932-4948.
- Torrance, K. J., 1970. Causes of clay sensitivity, *J. Soil Mech. and Found. Div., Proc. ASCE* 96:360-361.
- Tovey, N. K., 1970. Electron microscopy of clays, Ph.D. thesis, Cambridge University, Cambridge, England.
- Trollope, D. H., and C. K. Chan, 1960. Soil structure and the step-strain phenomenon, *J. Soil Mech. and Found. Div., Proc. ASCE* 86: part 1, pp. 1-39.
- Urbain, P., 1937. Texture microscopique des roches argileuses, *Bull. Societe Geologique de France*, pp. 341-348.
- van Andel, T. H., G. R. Heath et al., 1973. Initial Reports of the Deep Sea Drilling Project. Vol. 16, U.S. Govt. Printing Office, 949 p.
- van Olphen, H., 1963. *An Introduction to Clay Colloid Chemistry*, Interscience Publishers, John Wiley and Sons, 301 p.
- Von Engelhardt, W., and K. H. Gaida, 1963. Concentration changes of pore solution during the compaction of clay sediments, *J. Sed. Pet.* 33:919-930.
- Warner, D. L., 1964. An analysis of the influence of physical-chemical factors upon the consolidation of fine-grained clastic sediments, Ph.D. dissertation, University of California at Berkeley.
- Weller, J. M., 1959. Compaction of sediments, *Bull. Amer. Assoc. Pet. Geol.* 43:273-310.
- Weymouth, J. H., and W. O. Williamson, 1953. The effects of extrusion and some other processes on the microstructure of clay, *Amer. J. Sci.* 251:89-108.
- White, W. A., 1961. Colloid phenomena in the sedimentation of argillaceous rock, *J. Sed. Pet.* 31:560-570.
- Whitehouse, U. G., L. M. Jeffrey, and J. D. Debbrecht, 1960. Differential settling tendencies of clay minerals in saline waters, *Seventh Nat. Conf. on Clays and Clay Minerals*, pp. 1-79.
- Williamson, W. O., 1974. The fabric, water-distribution, drying-shrinkage, and porosity of some shaped discs of clay, *Amer. J. Sci.* 245:645-662.
- Williamson, W. O., 1960a. Particle orientation in a kaolinite-illite clay caused by deposition and deformation. Some shrinkage and mechanical properties of the oriented aggregates so formed, *Paper—Interparticle forces in clay-water electrolyte systems*, Melbourne, Div. 2, pp. 40-65.
- Williamson, W. O., 1960b. Some effects of deformation on the structure and properties of clay, *Mineral Industries* 29:1-8.
- Winterkorn, H. F., 1948. Physico-chemical properties of soils, *Proc. 2nd Int. Conf. on Soil Mech. and Found. Eng.*, Rotterdam, pp. 23-29.
- Wu, T. H., 1958. Geotechnical properties of glacial lake clays, *Amer. Soc. Civ. Eng. Proc.*, vol. 84, Paper 1732, *J. Soil Mech. and Found. Div.*, pp. 1-34.
- Wu, T. H., 1966. *Soil Mechanics*, Allyn and Bacon, 431 p.
- Yong, R. N., 1972. Soil technology and stabilization, in *Proc. Fourth Asian Regional Conf. on Soil Mech. and Found. Eng.*, F. C. Moh (ed.), vol. 2, pp. 111-124.
- Yong, R. N., and D. E. Sheeran, 1973. Fabric unit interaction and soil behavior, in *Int. Symp. on Soil Structure*, Gothenburg, Sweden, pp. 176-183.

## Geotechnical Properties of a Submarine Slide Area on the U.S. Continental Slope Northeast of Wilmington Canyon

RICHARD H. BENNETT,\* DOUGLAS N. LAMBERT,\*  
AND MATTHEW H. HULBERT†

**Abstract** A relatively large submarine slide (slump block) and apparent unstable surficial sediments undergoing creep have been delineated in bathymetric and seismic reflection profiles along the U.S. Atlantic continental margin northeast of Wilmington Canyon. A downslope core transect was made over selected areas to assess the geotechnical properties of the sediments associated with the slide. Sediments are predominantly silty clays and clayey silts rich in illite, with lesser quantities of feldspar, kaolinite, chlorite, quartz, and smectite minerals. Surficial sediments (cored up to 12 m) upslope from the slump block reveal typical variations in the mass physical properties with core depth. Shear strength and wet unit weight show a steady increase with depth below the mudline commensurate with a decrease in water content. In contrast, surficial sediments downslope overlying the slump block generally have low shear strength and relatively high variability in other mass physical properties with core depth. Chemical evidence of slumping (as defined by the sulfate ion content) is not apparent in the pore waters collected from the upper 10 m of sediment. No important relationships are obvious among the physical and chemical properties, specifically the carbonates or complex solids of iron and manganese oxides or hydroxides. Sediment failure in the form of a major submarine slide appears to have been a significant deformational process during the geological past (late Pleistocene). Creep and associated deformational features recorded in the surficial sediments are presumably a result of recent geological processes.

\*NOAA-Atlantic Oceanographic and Meteorological Laboratories, Miami, Florida 33149

†Department of Chemistry, Connecticut College, New London, Connecticut 06320

(Received January 4, 1977; revised February 15, 1977; accepted February 21, 1977.)

*Marine Geotechnology*, Volume 2, Marine Slope Stability, 1977.

0360-8867/78/0100-0245/\$2.00/0

Copyright © 1978 Crane, Russak & Company, Inc.



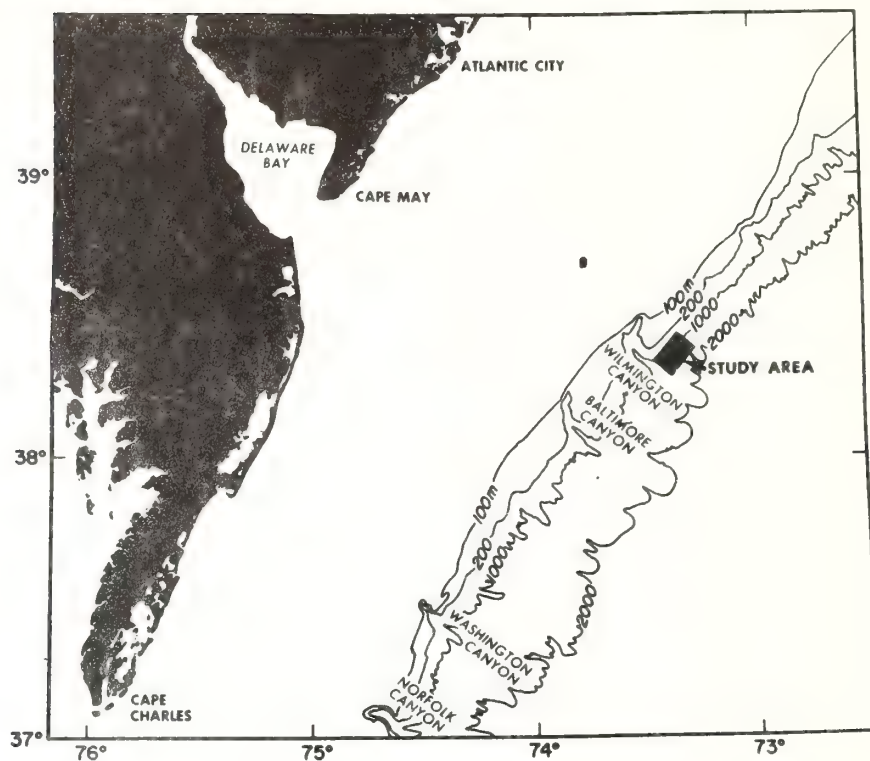


**Figure 1.** Study area northeast of Wilmington Canyon.

### Introduction

Numerous geological and geophysical studies have been concerned with regional and local offshore areas of the shelf, slope, and rise of the U.S. Atlantic continental margin in recent years (Emery, 1966; Stanley and Kelling, 1968; Uchupi, 1968, 1970; Kelling and Stanley, 1970; Lyall et al., 1971; Emery and Uchupi, 1972; Schlee, 1973; Doyle et al., 1975; Fritz and Pilkey, 1975; Knebel and Folger, 1976). Available detailed geotechnical studies of the U.S. Atlantic continental margin are virtually nonexistent; however, a few investigations of the North Atlantic Basin sediments have been carried out (Richards, 1961, 1962; Keller and Bennett, 1968, 1970; Silva et al., 1976). This article discusses the geotechnical

characteristics, specifically the mass physical and chemical properties and the sedimentological nature of surficial sediments associated with a major submarine slide on the U.S. continental slope northeast of Wilmington Canyon (Figure 1).

Examination of bathymetric charts of the continental slope demonstrated that the area northeast of Wilmington Canyon was characterized by unique morphological features, highly suspect as an area of instability and slumping. Stanley (personal communication, 1974) suggested that the area northeast of Wilmington Canyon was a likely area to investigate for submarine slides. A detailed bathymetric and seismic reflection survey of the selected slope area has revealed a major submarine slide with an estimated sediment volume of approximately  $11 \text{ km}^3$  comprising the slump block proper. Details of the geophysical nature, slump block, stratigraphic column, and geologic history of the slide area are discussed in

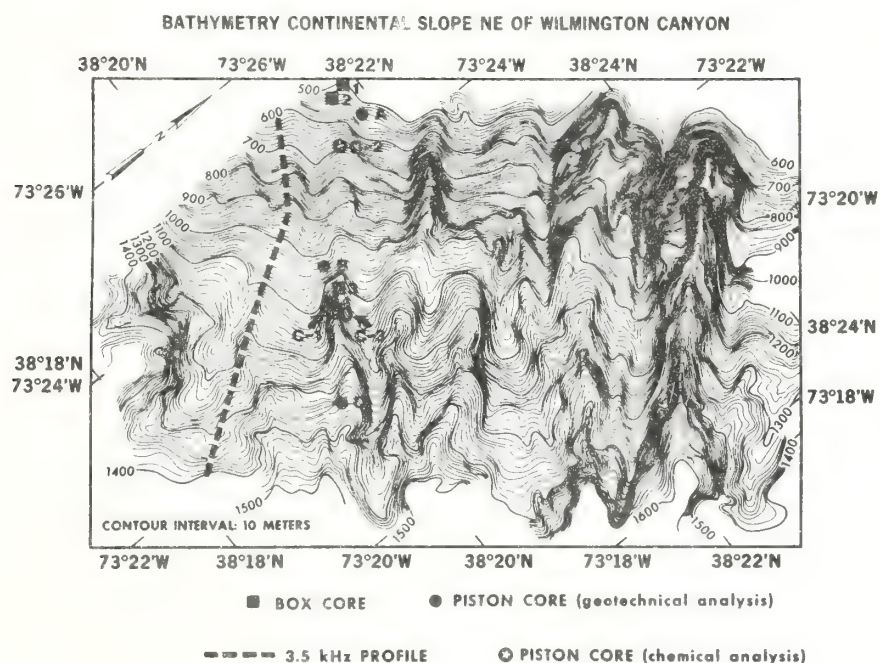


**Figure 2.** Detailed bathymetric map of study area depicting core locations and location of 3.5-kHz profile.



detail by both McGregor and Bennett (1977) and McGregor (1977). Sediment failure is considered to have occurred along a late Tertiary erosion surface during the late Pleistocene.

#### Site Survey and Coring

A detailed narrow-beam (half-angle beam width approximately  $7^\circ$ ) echo sounding (NBES), 3.5-kHz seismic reflection profile (SRP) was made

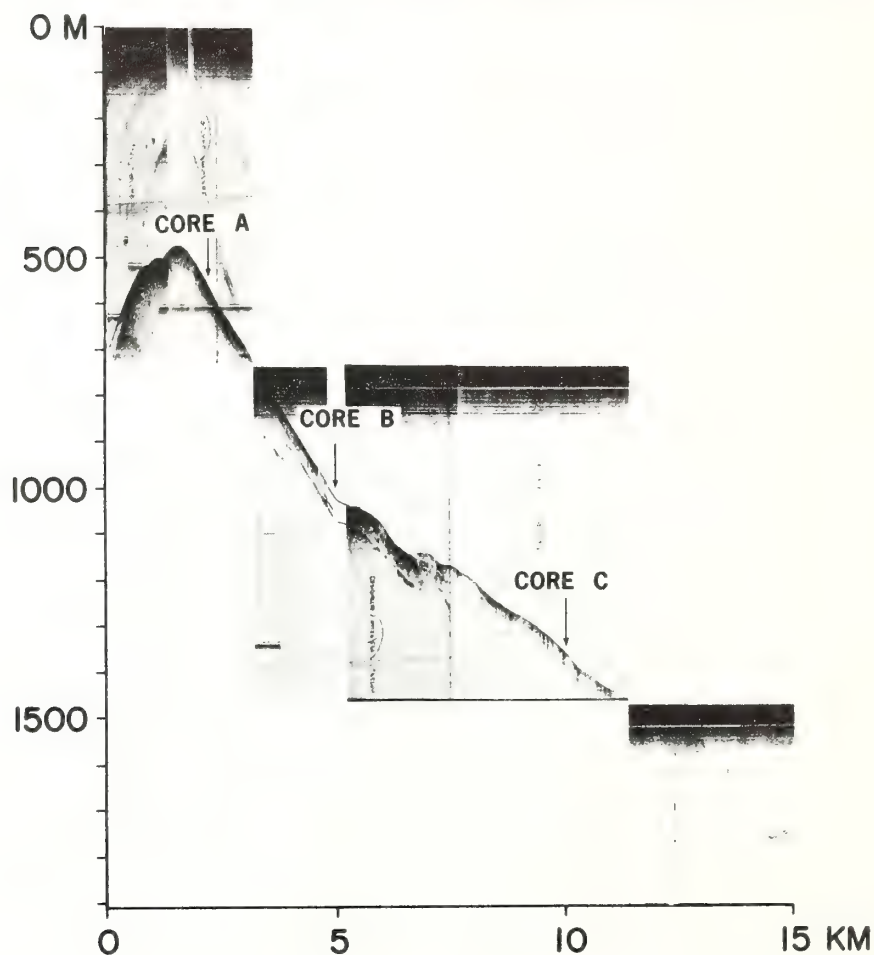


Figure 3. Core positions relative to 3.5-kHz profile depicting submarine slide.

in the selected area of the submarine slide. The survey was carried out using Loran C and satellite navigation with approximately 0.5-km track line spacing. The NBES data were used to develop the detailed bathymetric map of the study area. Examination of the detailed map shows dissection of the slope by numerous small valleys, which are incised above the slump block in some cases and extend to the lower slope (Figure 2), suggesting postslump erosional processes in this area of the continental slope. Surface expression of the slump block is clearly shown in the bathymetric map as a broadening of the contours at depths of 1000–1100 m, which represents the head of the block. The toe of the block was delineated by SRP and NBES records to occur approximately in the 1500–1600-m isobath range. Although a wide range occurs in the degree of slope over small areas, particularly in and around the incised valleys, the average bottom slope or gradient above the slump block is  $9^{\circ}$ – $14^{\circ}$ , whereas the slope averages  $3.5^{\circ}$ – $5^{\circ}$  in water depths exceeding 950 m over the slump block proper (Figure 2).

A sediment core transect was made over selected areas of the slope identified by seismic reflection profiles as both slumped and unslumped. A total of 13 Ewing-type piston cores, one Boomerang, and four Bouma box cores were collected in the study area. A few hydroplastic pilot cores were recovered during the piston coring operation, but are not presented here. This article discusses in detail a few representative (from the suite of cores collected) box and piston cores recovered from upper slope sediment above the slump block and from the slump block proper (Figure 2). Figure 3 depicts the relative positions of the three Ewing piston cores (A–C), plotted on a typical 3.5-kHz profile run slightly southwest of the core transect and normal to the continental slope. Core A was collected above the slump block on the upper slope, and cores B and C were collected from the head and downslope area of the slump block, respectively. The box and piston cores used for chemical analyses were collected from similar locations (Figure 2).

### Core Handling and Analyses

Immediately following shipboard recovery, the piston core liners were cut into 1.4-m sections, sealed, and labeled. Within a few hours after retrieval, the cores were radiographed and stored vertically in a refrigerator maintained at  $4^{\circ}\text{C}$ . The box cores were placed immediately in individually sealed wooden boxes and surrounded with seawater to prevent desiccation of the sediment. Unfortunately, during shipboard storage and subsequent



transfer to the shore-based laboratory, the wooden boxes lost considerable water, resulting in the slight desiccation of the sediment box cores. Consequently, these cores were useful only for descriptive purposes and for textural analyses, and they were not used for geotechnical testing. The box cores, however, were useful in indicating significant information regarding sediment type and structures, as discussed later in this article.

Piston cores taken for chemical analyses (other than core A, which was stored under refrigeration for several months prior to processing) were subsampled immediately after retrieval on board ship, and the samples were squeezed to expel approximately 5 ml interstitial water. These subsamples were handled with minimum exposure to air and were collected and processed in less than 45 min after core recovery. The salinity and pH of the pore-water samples were determined without delay, and a portion of this sample was preserved by acidification with nitric acid and refrigerated. The preserved pore-water samples were analyzed at the shore-based laboratory for sulfate ion content and for iron, manganese, calcium, and magnesium. Sulfate was determined gravimetrically, and the metal ions in the pore-water samples were analyzed by atomic absorption spectrophotometry.

Hulbert and Brindle (1975) have discussed the importance of expeditions subsampling and chemical preparations for submarine sediment interstitial water analyses. Samples for sediment chemistry and mineralogy were prepared following closely the procedures of Jackson (1956). Carbonates, iron, and organics were removed from the sediment samples prior to carrying out X-ray diffraction analyses. Approximately 8 g (wet weight) of each sediment sample was sieved without prior drying to remove particles larger than 2000  $\mu\text{m}$ . Carbonates and soluble manganese compounds were extracted with pH 5 sodium acetate buffer and with hydrogen peroxide. The carbonate mineral content was determined by weight loss on treatment in acidic medium. Iron compounds were extracted by gentle treatment with sodium dithionate-citrate solution. Manganese was determined in the hydrogen peroxide extractate from a dried sample weighing approximately 0.5 g. The iron and manganese were analyzed using an atomic absorption spectrophotometer.

The radiographs of the cores were used to assess any disturbance that may have occurred during coring operations, to delineate the presence or absence of sedimentary structures, and to describe the cores initially, prior to laboratory analysis. Using the initial core descriptions, a general

sampling pattern was established for geotechnical testing and subsampling before the cores were opened. This procedure permits the best selection of the core sections and intervals for geotechnical analyses.

Core processing was accomplished by extruding short core sections (10–20 cm) and by performing miniature vane shear and water content (% dry weight, uncorrected for salt content) tests. Sediments were sheared with a 1.27×2.54-cm miniature vane at a rotation rate of 60°/min ( $1.7 \times 10^{-2}$  rad/s). Techniques for testing cohesive submarine sediments are described by Richards (1961). Wet unit weights and porosities were determined using methods described by Bennett and Lambert (1971). Cores were subsampled for size analyses, average grain density, Atterberg limits, X-ray diffraction measurements, and microfossil examination. A detailed written description was made combining visual and radiographic techniques followed by close-up color photography of the total core lengths.

### Discussion of Sediments and Selected Geotechnical Properties

#### *Sediments*

Surficial sediments of the study area are predominantly silty clay and clayey silts rich in illite with lesser quantities of feldspar, chlorite, kaolinite, quartz, and smectite minerals. A few types of heavy minerals are also present in the  $> 5\text{-}\mu\text{m}$  fraction of upslope sediments examined by X-ray diffraction. Authigenic pyrite (X-ray dense) is common and occurs as burrow replacements and globular masses, and often shows up in radiographs as “white” flecks. The presence of calcium carbonate occurs predominantly in the form of calcareous tests scattered throughout the muds. Similar mineralogical and textural characteristics of U.S. continental slope sediments have been reported by Doyle et al. (1975). Texture and mineralogy of suspended sediments in the Wilmington Canyon area, at the shelf break and on the slope, have been discussed by Lyall et al. (1971). These workers reported a downslope transport of fines and a predominance of illite, kaolinite, and chlorite with lesser quantities of smectite in the clay-size suspended sediment fractions.

Upper slope cores, above the slide, consistently have several centimeters of topmost sand and coarse sandy silts overlying the muds. These topmost sandy sediments were not present in the cores recovered downslope on the slide proper. The quantity of sand throughout the silty clays and clayey silts is generally much less than 10% both for upper slope and downslope



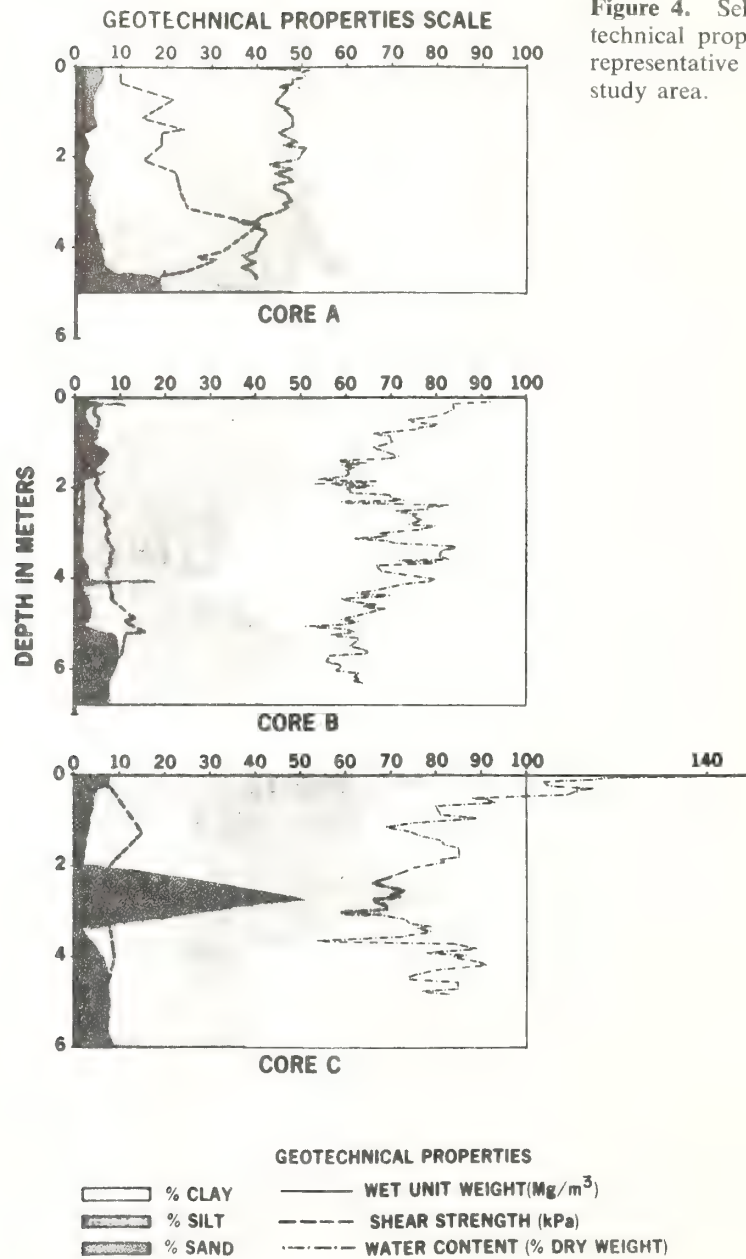


**Figure 4.** Selected geotechnical properties of representative cores from study area.

sediments. The top 4–5 m of upper slope sediment are characterized by a slight increase in silt content relative to clay with increasing depth below the mudline. In contrast, profiles of silt and clay in cores associated with the slide indicate a general decrease in silt and increase in clay-size particles with increasing core depth (Figure 4, cores A–C).

Examination of sedimentary structures in box cores and piston cores suggests that gravity-induced sediment failure of surficial seafloor deposits is an important deformational process active on the continental slope northeast of Wilmington Canyon. Box cores 1 and 2 (Figure 2) taken on the upper slope above the slide are characterized by a soft dark olive-gray silty clay composed of 10–12% sand and 88–90% silt and clay overlaid by approximately 20 cm of brownish silty clay sand made up of approximately 38% sand and the remainder silt and clay (Figure 5). Large “sand balls” or clasts within the underlying silty clays appear to be composed of the same overlying clastic sediment by virtue of similar grain size and contorted bedding (megascopic observations of the sedimentary structures) and indicate downslope creep and apparent foundering of the upper slope surficial sediments. Numerous fine-grained, relatively stiff, “clay balls” are present in the overlying coarse-grained material. These “clay balls” are probably formed as a result of erosion of clay beds from the upper slope or outer continental shelf. Box cores 3 and 4 taken downslope within the slide are composed entirely of silty clay containing less than 5% sand.

The apparent load structures present in the upper slope cores represent unstable conditions; they probably develop contemporaneously with slow creep of sediments down the continental slope. The upper slope coarse-grained sediments and underlying muds occur on slopes (gradients) averaging about  $9^{\circ}$ – $14^{\circ}$  in water depths less than 950 m. The downslope muds, having a conspicuous absence of topmost coarse clastics, occur on slopes (gradients) averaging  $3^{\circ}$ – $5^{\circ}$  in water depths exceeding 950 m in this study area.

#### *Mass Physical Properties*

Surficial sediments upslope from the slump block are characterized by typical variations in the mass physical properties with core depth. Undrained shear strength, determined with a miniature vane shear apparatus, and wet unit weight (wet bulk density) steadily increase with depth below the mudline commensurate with a decrease in water content (Figure 4, core A). Richards (1961, 1962) and Keller and Bennett (1968, 1970)



# WILMINGTON CANYON SLUMP AREA BOX CORE 1 (UPPER SLOPE)

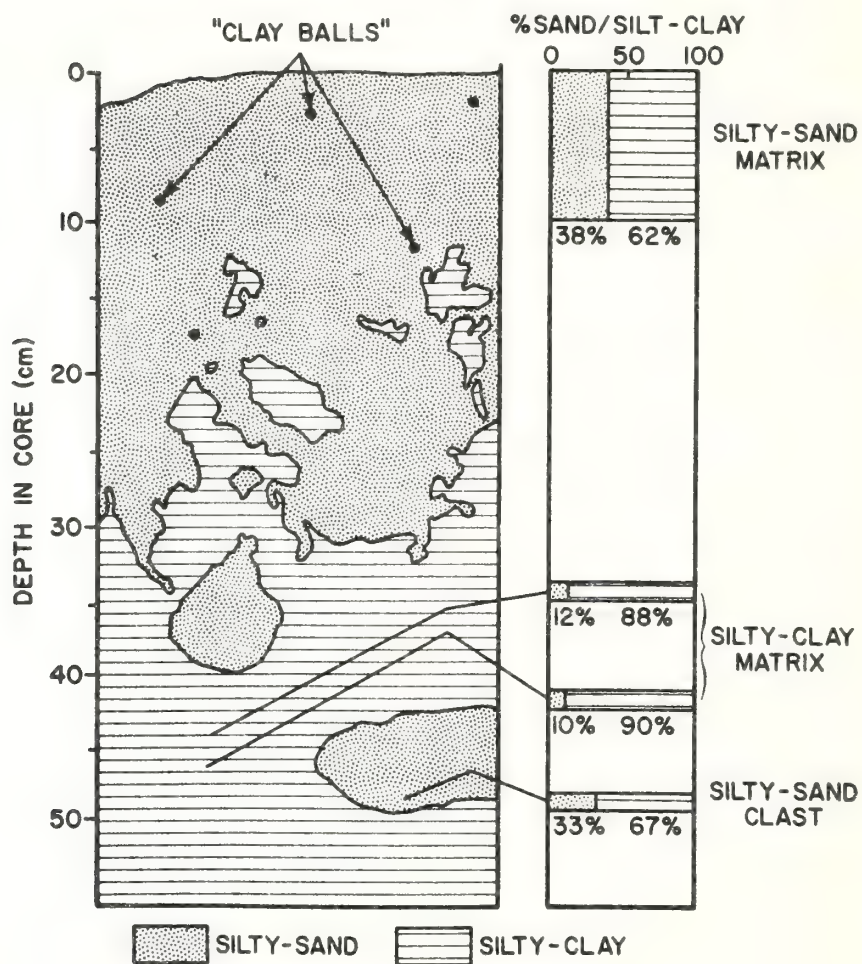


**Figure 5.** Sketch of box core sedimentary structures typical of upper slope surficial sediments.

have discussed typical geotechnical properties of submarine sediments and their variation with core depth. In contrast to the upper slope sediments, surficial sediments downslope overlying the slump block generally have *low* shear strengths and relatively high-mass physical properties variability with core depth. This variability is demonstrated particularly well in the profiles of water content, wet unit weight, and texture (Figure 4, cores B and C). Wet unit weight is considerably less sensitive to variations in other related physical properties than is water content alone (Bennett and Lambert, 1971). Wet unit weights average 1.79, 1.61, and 1.52 mg/m<sup>3</sup> in cores A, B, and C, respectively, reflecting a general decrease in average value in the downslope direction. This agrees with the overall increase in the water content values in the downslope direction. Profiles of the mass physical properties clearly show that sediment grain size is considerably more variable with core depth in sediments recovered from the slump proper as compared to the textures of upper slope sediments (Figure 4, cores A-C).

Numerous Atterberg limits were determined on cores from along the entire slope transect. Although a few exceptions occur, the plasticity index ( $I_p < 20\%$ ) and liquid limit ( $W_L < 45\%$ ) are lowest in the upper slope sediment samples, and these properties increase significantly in the downslope direction ( $I_p = 54\%$  and  $W_L = 91\%$ ). These data generally fall slightly above the A line on the plasticity chart (Casagrande, 1932, 1948). On the basis of this classification, the continental slope sediments investigated during this study are inorganic clays ranging from relatively low plasticity to high plasticity increasing generally in the downslope direction. It is interesting to note that the initial evaluation of X-ray diffraction and grain-size analyses of these sediment cores indicates an apparent subtle increase in the presence of smectite and clay-sized material in the downslope direction.

Preliminary evaluation of the cores collected in the submarine slide area has demonstrated significant differences not only in the magnitude of the upper slope as compared with downslope selected geotechnical properties, but differences in their variation with core depth as well. Further detailed mass physical property data analyses are presently being carried out on a suite of cores collected in the study area.

#### *Chemical Properties*

The chemical definition of the limits of physically disturbed (slumped) material and the determination of the importance of potential cementing



agents were the specific goals of the chemical analyses and studies of this research project. The sulfate ion was expected to be a particularly suitable indicator of sediment disturbance after deposition. Sediments deposited under open ocean water may be expected to have approximately the same sulfate content profile with increasing depth below the mudline over local areas of undisturbed sediment. Sulfate ion content in the pore water of the topmost sediment would also be expected to be approximately the same as in the immediately adjacent overlying seawater. With increasing depth in the sediment, the sulfate ion content of the pore water would be expected to decrease as a function of the loss of sulfate as a result of its use by the microbial population in metabolizing organic matter. The particular shape of the sulfate concentration profile with depth of burial would vary from area to area depending on the particular microbial population, the rate of sedimentation, the quantity of organic matter, and other less significant geochemical characteristics. But these factors would not be expected to vary significantly within a local area.

The sulfate ion profile would be expected to become relatively complex in sediments that had undergone disturbance. Removal of overlying sediment would lead to pore-water sulfate contents abnormally low at depth below the mudline for the particular locality. Movement of sediment blocks would lead to juxtaposition of differing sulfate concentrations. Mixing of sediment with seawater through physical or biological disturbance would lead to the incorporation of a large amount of sulfate relative to organic carbon. These anomalies of the sulfate-depth profile would be expected to remain detectable, provided that a significant portion of the sulfate ion remains in the pore water.

Cementing agents may be expected to strengthen and stabilize the open structure of surficial fine-grained submarine sediments. Important aspects of cementation and its role in influencing the mass physical properties of submarine sediments have been discussed by Nacci et al. (1974). Particularly attractive candidates for such a role in cementation are the carbonates and the hydrous oxides of iron and manganese. These potential cementing agents were studied in order to relate characteristic chemical properties to the observed variations in the mass physical properties of the sediments associated with the submarine slide.

Cores C-1, C-2, and C-3 collected from the Wilmington Canyon study area and examined for chemical evidence of slumping demonstrated by analyses of the pore water, showed no obvious indication of sediment disturbance, or mass movement. Chemistry (cores) samples above the

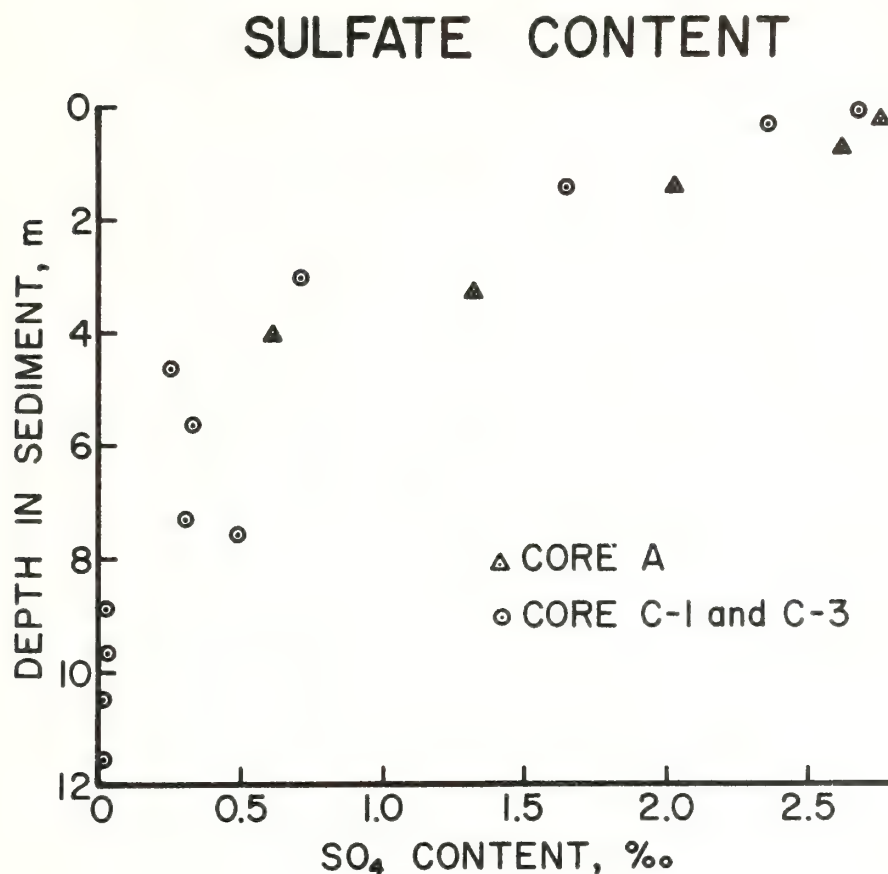


Figure 6. Sulfate ion content versus depth in cores A, C-1, and C-3.

slump block (cores C-2 and A) and sampled in the slump block proper (cores C-1 and C-3) showed no significant abnormalities in the sulfate ion content with depth below the mudline (Figure 2 core locations). Sulfate ion content in the upper few centimeters was typical of open ocean water; values decreased to less than half this concentration at 3 m below the mudline, and continued the decrease to very low sulfate values with depth. In general, the sulfate ion profiles decreased smoothly with depth and were atypical of what would be expected for highly disturbed sediment (Figure 6). One exception was in the upper 30 cm of core C-2, in which



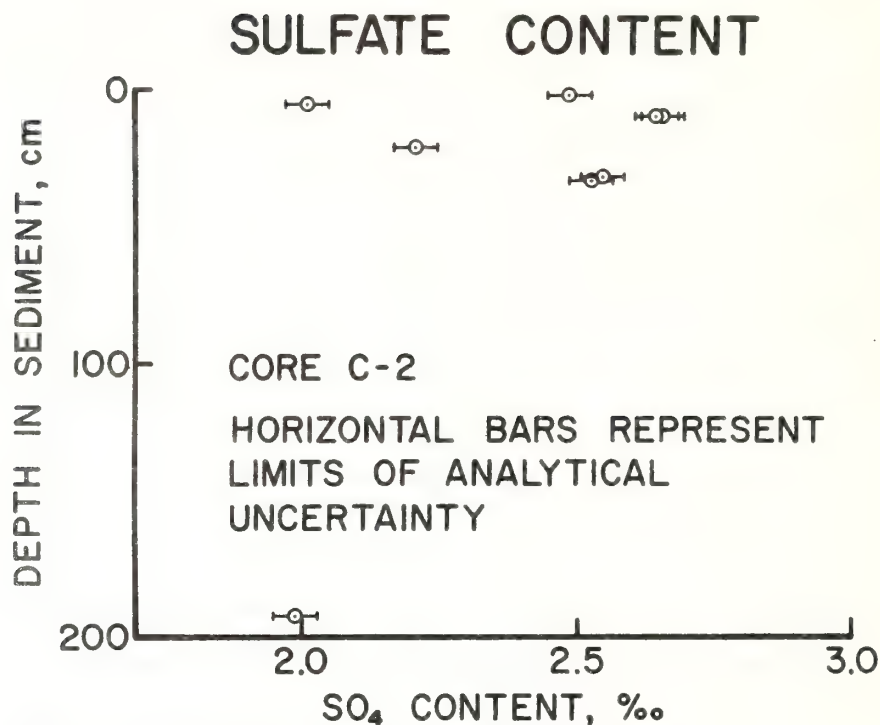


Figure 7. Sulfate ion content versus depth in core C-2.

the sulfate content varied markedly over small intervals (Figure 7). This variation in the sulfate content may be the result of movement in the upper few centimeters of sediment. The calcium content decreases from a concentration of about that of seawater in the upper few centimeters to one-fifth this value at 10 m and is in accord with the sulfate in all cores. Hence, calcium is not as suitable an indicator for disturbance as sulfate, as the relative analytical uncertainty in its determination is greater.

The sediment cores contained about 10% carbonate minerals (by weight), which occurred predominantly in the form of calcareous shells and shell fragments. Preliminary analyses of the carbonates and complex solids containing iron and manganese oxides and hydroxides exhibited no obvious or significant relationships with the mass physical properties of the sediment cores under investigation.

### Summary

A large submarine slide (slump block with a sediment volume of approximately 11 km<sup>3</sup>) has been delineated in bathymetric and seismic reflection profiles along the U.S. Atlantic continental margin northeast of Wilmington Canyon. Unstable surficial fine-grained sediment appears to be undergoing creep. Sediments are predominantly silty clays and clayey silts rich in illite with lesser quantities of feldspar, kaolinite, chlorite, quartz, and smectite with calcareous shells and shell fragments scattered throughout the muds.

Gravity-induced sediment failure has been identified by the recognition of sedimentary structures characteristic of past and present deformational processes on the continental slope northeast of Wilmington Canyon. The geological processes and related features are summarized as follows:

1. A slide (slump block) demonstrated by geophysical techniques depicts a prominent slip circle, large slide block, contorted and truncated sedimentary beds.
2. Surface expressions of the slide are clearly shown in a detailed bathymetric map and slope map compiled for the area. Within the study area, slopes range from less than 5% to greater than 100%.
3. Creep and apparent foundering of surficial sediment are indicated by contorted bedding and the presence of "sand balls" within the silty clays and clayey silts. Load structures of the topmost sands and sandy silts overlying the muds are characteristic of box cores sampled in the sediment above the slide. Numerous "clay balls" were scattered throughout the topmost sands and sandy silts in cores sampled above the slide. The apparent load structures represent unstable conditions and probably develop contemporaneously with slow creep of sediments down the continental slope.

Surficial sediments cored upslope from the slump block show typical variations in the mass physical properties with core depth. Shear strength and wet unit weight show a steady increase with depth below the mudline commensurate with a decrease in water content. In contrast, surficial sediments downslope overlying the slump block generally have low shear strengths and relatively high variability in other mass properties with core depth.



Chemical evidence of slumping is not apparent in the pore waters collected from the upper 10 m of sediment. No evidence was found to indicate changes in the mass physical properties related to changes in the carbonate mineral content or to the content of hydrous iron or manganese oxides.

Sediment failure in the form of a major submarine slide appears to have been a significant deformational process during the geological past (late Pleistocene). Creep and associated deformational features recorded in the surficial sediments are presumably a result of Recent geological processes.

### Acknowledgments

This research was supported by the National Oceanic and Atmospheric Administration (NOAA), Atlantic Oceanographic and Meteorological Laboratories (AOML). The authors acknowledge the support given by the officers and crew of the NOAA Ocean Survey Ship *Researcher* in carrying out the surveys and coring operations for this project. George Lapiene assisted in all phases of the data collection, coring, and SRP operations. William Sawyer, Ms. Pamela Bates, and Joseph Stinus contributed in the data reduction and various phases of the laboratory analyses. Dr. Matthew Hulbert acknowledges the support of AOML and the National Research Council during his tenure as an associate in 1974-1975 while at AOML, during which time a large part of this research was completed. The writers appreciated the critical reviews of this manuscript by Dr. William R. Bryant, Dr. George H. Keller, and Dr. Harris B. Stewart, Jr. Support and encouragement throughout this project by Jack Kofoed is appreciated.

### References

- Bennett, R. H., and D. N. Lambert, 1971. Rapid and reliable technique for determining unit weight and porosity of deep-sea sediments. *Marine Geology*, vol. 11, pp. 201-207.
- Casagrande, A., 1932. Research on the Atterberg Limits of soils. *Public Roads*, vol. 13, pp. 121-135.
- Casagrande, A., 1948. Classification and identification of soils. *American Society of Civil Engineers Transactions*, vol. 113, pp. 901-931.
- Doyle, L. J., O. H. Pilkey, G. L. Hayward, and J. S. Arbogast, 1975. Sedimentation of the northeastern continental slope of the United States. IX Congress International de Sedimentologie, Nice, pp. 51-56.
- Emery, K. O., 1966. Atlantic continental shelf and slope of the United States: Geologic background. U.S. Geological Survey Professional Paper 529-A, 23 pp.
- Emery, K. O., and E. Uchupi, 1972. Western North Atlantic Ocean: Topography, rocks, structure, water, life, and sediments. *American Association of Petroleum Geologists, Memoir 17*, 532 pp.

- Fritz, S. J., and O. H. Pilkey, 1975. Distinguishing bottom and turbidity current coarse layers on the continental rise. *Journal of Sedimentary Petrology*, vol. 45, pp. 57-62.
- Hulbert, M. H., and M. P. Brindle, 1975. Effects of sample handling on the composition of marine sedimentary pore water. *Geological Society of America Bulletin*, vol. 86, pp. 109-110.
- Jackson, M. L., 1956. Soil chemical analysis: Advanced course. University of Wisconsin, Madison, Wisconsin, 894 pp.
- Keller, G. H., and R. H. Bennett, 1968. Mass physical properties of submarine sediments in the Atlantic and Pacific basins. *Proceedings of the 23rd International Geological Congress, Prague*, vol. 8, pp. 33-50.
- Keller, G. H., and R. H. Bennett, 1970. Variations in the mass physical properties of selected submarine sediments. *Marine Geology*, vol. 9, pp. 215-223.
- Kelling, G., and D. J. Stanley, 1970. Morphology and structure of Wilmington and Baltimore submarine canyons, eastern United States. *Journal of Geology*, vol. 78, pp. 637-660.
- Knebel, H. J., and D. W. Folger, 1976. Large sand waves on the outer shelf near Wilmington Canyon. *EOS, Transactions of the American Geophysical Union*, vol. 57, p. 268.
- Lyall, A. K., D. J. Stanley, H. N. Giles, and A. Fisher, Jr., 1971. Suspended sediment and transport at the shelf-break and on the slope Wilmington Canyon area, eastern U.S.A. *Marine Technology Journal*, vol. 5, pp. 15-27.
- McGregor, B. A., and R. H. Bennett, 1977. Continental slope sediment instability northeast of Wilmington Canyon. *American Association of Petroleum Geologists*, vol. 61, pp. 918-928.
- Nacci, V. A., W. E. Kelly, M. C. Wang, and K. R. Demars, 1974. Strength and stress-strain characteristics of cemented deep-sea sediments. *In Deep-Sea Sediments, Physical and Mechanical Properties*, A. L. Inderbitzen, ed., Marine Sciences, vol. 2, New York, Plenum Press, pp. 129-150.
- Richards, A. F., 1961. Investigation of deep-sea sediment cores I. Shear strength, bearing capacity, and consolidation. Technical Report TR-63, U.S. Navy Hydrographic Office, Washington, D.C., 70 pp.
- Richards, A. F., 1962. Investigations of deep-sea sediment cores II. Mass physical properties. Technical Report TR-106, U.S. Navy Hydrographic Office, Washington, D.C., 146 pp.
- Schlee, J., 1973. Atlantic continental shelf and slope of the United States: Sediment texture of the northeastern part. U.S. Geological Survey Professional Paper 529-I, 64 pp.
- Silva, A. J., C. D. Hollister, E. P. Laine, and B. E. Beverly, 1976. Geotechnical properties of deep sea sediments: Bermuda Rise. *Marine Geotechnology*, vol. 1, pp. 195-232.
- Stanley, D. J., and G. Kelling, 1968. Sedimentation patterns in the Wilmington Submarine Canyon area. *In National Symposium on Oceanographic Science and Engineering, Atlantic Shelf Transactions*, Marine Technology Society, Philadelphia, pp. 127-142.
- Uchupi, E., 1968. Sedimentary framework of the continental terrace off the east coast of the United States. *Southeastern Geology*, vol. 9, no. 4, pp. 269-271.
- Uchupi, E., 1970. Atlantic continental shelf and slope of the United States: Shallow structure. U.S. Geological Survey Professional Paper 529-I, 44 pp.





## FET pair and op amp linearize voltage-controlled resistor

by Thomas L. Clarke

*Atlantic Oceanographic and Meteorological Laboratory, Miami, Fla.*

A matched field-effect transistor pair can be combined with an operational amplifier and a few resistors to form a circuit in which one FET's drain-to-source resistance ( $R_{ds}$ ) bears a precisely linear relationship to a control voltage ( $V_c$ ). Though a single FET can serve as a voltage-controlled resistor, the relationship of  $R_{ds}$  to the gate-to-source voltage ( $V_{gs}$ ) is nonlinear.

The basic idea in this circuit is to control  $V_{gs}$  through a feedback loop that senses if the amount of current flowing through the FET, and hence its  $R_{ds}$ , is of the proper value. As shown in Fig. 1, this is accomplished by deriving a signal from half of the FET and applying it to a "summing" node at the inverting port of an op amp.

The output of the op amp is connected to the gate of the FET, thus forming a closed loop. The resulting change in  $V_c$  causes a proportional change in  $R_{ds}$  because the op amp is a linear device, and because input voltages are compared to a fixed voltage ( $V_{ref}$ ) at the noninverting terminal. Depending on the configuration,  $R_{ds}$  can be made proportional to  $V_c$  or its reciprocal.

In the circuit to be seen at the left of Fig. 1,  $R_{ds}$  varies in proportion to the reciprocal of the control voltage, as

is indicated by the following equation:

$$R_{ds} = |V_{ref}|R_c / (|V_d| - |V_{ref}|)$$

where  $V_{ref}$  is assumed to be between 0 and  $V_c$ . A voltage divider may be used to derive  $V_{ref}$ . Moving  $V_{ref}$  to the drain of the FET, as in the circuit to the right, the following equation holds:

$$R_{ds} = |V_{ref}|R_c / |V_d|$$

where  $V_{ref}$  should be a well-regulated source, since it may have to supply considerable current. These equations are based on the facts that  $V_c$  draws current from the negative input of the op amp through  $R_c$  and that this voltage drop results in current flow into the terminal by the FET. The application of Kirchhoff's law then yields the above relationships.

As shown in the circuit at the left of Fig. 2,  $R_{ds}$  may also vary in direct proportion to the control voltage. Therefore, the relationship becomes:

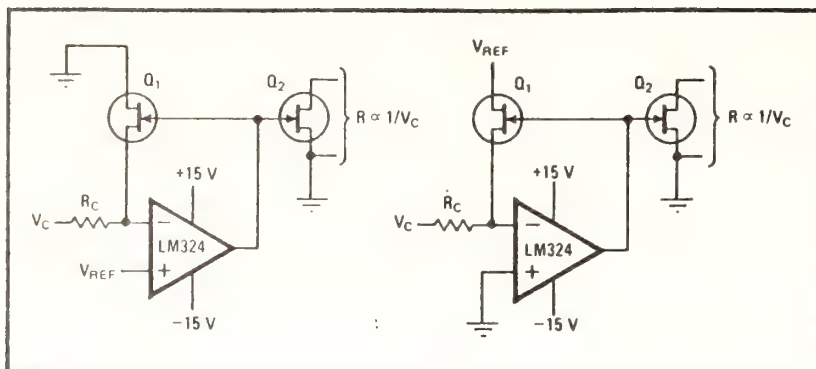
$$R_{ds} = R_d |V_d| / (V - |V_d|)$$

where  $V_c$  is greater than  $-V_p$  but less than 0 v. This circuit, while not as linear as those of Fig. 1, can be improved significantly by replacing  $R_c$  with a current source,  $I$ , as shown at the right of Fig. 2. The relationship then simply becomes:

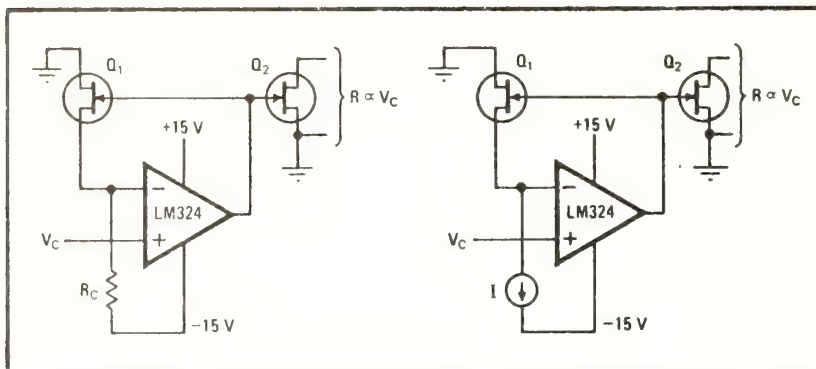
$$R_{ds} = |V_d| / I$$

The circuits are built with Siliconix 285 dual FET chips and LM324 op amps. Use of high-speed op amps such as the LM318 would permit more rapid variations of resis-





**1. Voltage-controlled resistance.** Unused half of FET  $Q_2$  can function as voltage-controlled resistor in external circuits.  $R_{ds}$  is inversely proportional to control voltage in both circuits.  $V_C$  values are negative for n-channel FETs, positive for p-channel FETs.



**2. Direct proportional control.**  $R_{ds}$  varies linearly with  $V_C$  in both circuits. If  $V_C$  exceeds  $V_{ref}$  or breakdown voltages of FET in either figure, a resistor should be inserted between output of operational amplifier and gate of FET to prevent burnout.

tance. No stability problems are encountered because the FET introduces negligible phase shift in bandpass frequencies of the op amp. Optimal results are obtained,

of course, with FETs formed on a common substrate, and if desired, p-channel devices may be used for positive control voltages. □

## PLATE TECTONICS: A REVOLUTION IN GEOLOGY AND GEOPHYSICS

ROBERT S. DIETZ

*National Oceanic and Atmospheric Administration, Atlantic Oceanographic and Meteorological Laboratories, Miami, Florida 33149 (U.S.A.)*

(Manuscript received March 4, 1976; revised version received June 25, 1976)

### ABSTRACT

Dietz, R.S., 1977. Plate tectonics: a revolution in geology and geophysics. In: J. Bonnin and R.S. Dietz (editors), *Present State of Plate Tectonics*. Tectonophysics, 38 (1-2): 1-6.

This symposium concerns *The Present State of Plate Tectonics*. By any measure, plate tectonics can be described as "alive and well" and, in fact, a "healthy, burgeoning concept", although only eight years have passed since (in 1967) plate tectonics suddenly won general acceptance, at least among western scientists, as the proper model for global tectonics. This concept is, of course, an integration of, and a follow-on to, sea-floor spreading, transform faulting, trench subduction and continental drift. Although some criticism has arisen, this revolution in geology and geophysics has provoked remarkably little cogent dissent. Of late, plate tectonics has bridged the gap from basic to applied science in the search for natural resources; e.g. petroleum accumulations on continental margins, porphyry copper deposits associated with subduction zones, base metal sulfides associated with pillow lavas at fossil rifts, etc. Perhaps the largest gap that remains is in a definitive understanding of plate driving forces. The viability of plate tectonics is emphasized by the several symposia at this IUGG meeting which concern, either directly or peripherally, plate tectonics. In this symposium, we have asked the organizers of such symposia, or their nominees, to present a synthesis concerning the implications of their particular specialty for plate tectonics. These include plate tectonics aspects of seismology, heat flow, plate accretion processes at ridges, paleo-oceanography, etc.

### INTRODUCTION

These remarks were prepared as an introduction to the symposium organized by J. Bonnin and myself on "The Present State of Plate Tectonics" convened in Grenoble, France, on 5 September 1975 at the meeting of the International Union of Geodesy and Geophysics. I suppose that it is significant to note that we did not propose to inquire into the validity of this new concept but simply accepted plate tectonics as the proper geotectonic model of the Earth. There have been, and still are, some critics of plate tectonics, but they are few and have been virtually overwhelmed by wide general acceptance by the opinion makers or "invisible college" within our scientific



discipline. Undoubtedly advocates of plate tectonics, in their enthusiasm, have overapplied this new paradigm. Doubtless, also, in view of remaining unanswered aspects, such as the driving mechanism of the lithospheric plates, plate tectonics has yet to achieve the status of a definitive theory. Nonetheless, this new integrated view of global tectonics seems destined to remain, while still evolving, the Rosetta Stone of modern geology.

Ours is a "topping off" or summary symposium. About eight other earlier symposia within this IUGG meeting have been involved either wholly, or in part, with plate tectonics. We, therefore, regarded it appropriate to ask the convenors of these other symposia, or their nominees, to relate in a summary manner the input from their scientific sub-discipline, into the present state of this revolutionary concept. Over the past decade, plate tectonics (and its predecessors — sea-floor spreading and continental drift) has generated a virtual blizzard of papers. Much ink has been spilled with associated acrimonious debate. It seems now appropriate to review the impact of plate tectonics.

#### PROJECT FAMOUS

There is naturally an intense interest in plate boundaries as these are the locus of major tectonic activity on Earth. This is especially true for the accreting boundaries which are marked by the mid-ocean ridges. We were fortunate to have included in this symposium two summary papers by leaders of both the American team (James Heirtzler) and the French team (Xavier Le Pichon) of Project FAMOUS (French-American Mid-Ocean Undersea Study). (However, in view of extensive publication of these results elsewhere only extended summaries are included among the papers published here.) Never before has any segment of the mid-ocean ridge and rift been so intensively studied. A great variety of geophysical sensors have been brought to this task as well as visual observations from three deep-sea research vehicles (DRV's). Perhaps never before have DRV's been so effectively applied toward the solving of a deep-sea floor problem. In the past such vehicles have captured an inordinate share of the publicity of oceanography as well as much of the funding while contributing little to the data of this science. On FAMOUS, however, they amply demonstrated that their usefulness has come of age. While the mechanism of sea-floor spreading and plate accretion at the mid-ocean rifts is firmly established, the details of this process remain elusive. The FAMOUS Project has done much to clarify this process. A rather curious result is that dike injection presently seems to be somewhat asymmetrical; however, over the past two hundred million years in the Atlantic Ocean the process seems to have averaged out as symmetrical, as indicated by the median position of the rift. This curiosity remains to be resolved. Also, while the rift is obviously a steady-state feature, the nature of the faulting, whether normal or reversed, or a combination of the two, remains unsettled. In this symposium, Harrison and Stieltjes have addressed themselves to this subject.

## A NEW PARADIGM

Science, does, of course, advance brick-by-brick as new information is added to the pyramid of knowledge. But from time to time a great breakthrough occurs when an entirely new concept or model is demonstrated to be true. Such a new concept generates a revolution — i.e. “a complete change, a turning upside down, and fundamental reconstruction”. These revolutions apparently occur by the replacement of one general conceptual view, or paradigm, by another. Beginning in 1967, the old fixist Earth was supplanted by the new mobilistic Earth. In these early years plate tectonics was virtually a UK—USA monopoly. This timing is true for the USA although the revolution may have been won a bit earlier in the UK. At this point in time the revolution is more or less complete and we seem to be involved in mopping-up operations.

Plate tectonics has, of course, not been without its critics. Also, there have been some super-enthusiasts who would describe all structures on Earth as due to plate tectonics excepting meteorite craters and astroblemes. More striking is the alacrity with which this new paradigm has been almost universally accepted. This quick acceptance stands in marked contrast, for example, to Darwin's theory of biologic evolution through natural selection. Perhaps this is because no one's ancestry is being impuned, but more likely it is the result of the vast numbers of competent scientists at work today and the sharpness of our modern tools of research. A vast, almost overwhelming, number of publications on plate tectonics have come off the press in the past decade.

Although plate tectonics offers a great clarifying principle, in some ways it increases the difficulty of finding a unique solution to any geotectonic problem because it adds a new dimension — in fact a fourth dimension. Formerly, fixistic geology was concerned with up, down and time, but now we must add sideways. For example, the Bahama Platform since its birth, presumably in the Triassic has undergone a remarkable subsidence of about 6 km; but during the same interval we now learn that it has drifted probably about 6,000 km. The evidence for subsidence is derived, of course, from the classical stratigraphy of layered sedimentary rocks, but the quantitative evidence for drift comes from the new stratigraphy provided by the magnetic-anomaly stripes.

In anthropomorphic terms it has been pointed out that North America, for example, drifts about the length of one's body in a lifetime while the more rapidly drifting Pacific Plate drifts nearly as fast as one of the coconut palms grows on one of the atolls. I have told my own students that North America is drifting or rotating generally westward at the rate one's fingernail grows, which is 0.10 mm/day. This would amount to 3.65 cm/year which is perhaps too fast relative to the mid-ocean rift in the Atlantic but a reasonable approximation of absolute drift with respect to the Earth's fixed (?) deep mantle if the clockwise rotation of Eurasia has no westward compo-



nent. Kevin Burke, however, has pointed out to me that the growth of one's toe nails provides a more accurate figure as their rate of growth is only one-half that of a fingernail or 0.05 mm/day (Edwards and Schott, 1937).

#### A CURIOUS PROCESS

We may wonder why earth scientists were so slow in discovering the plate-tectonic Earth. Two reasons seem likely. Firstly, nearly all of the evidence was hidden beneath the ocean floor — out of sight and beyond knowing until the advent of marine geology and geophysics in the post World War II years. Nearly all plate boundaries are hidden beneath the sea with but a few exceptions. The trenches, where subduction occurs, are wholly submarine although one can possibly regard the Himalayan arc in this light. The mid-ocean ridge is exposed only at Iceland and even there it is anomalous being overprinted by a "hot spot" — an ascending magma plume from beneath the asthenosphere. The Afar triangle is our only subaerial triple junction — now a new Mecca for plate tectonicists. Among transform faults we can cite only the San Andreas of California, the Alpine Fault of New Zealand, plus some segments along the Alpine—Himalayan collision front. These few examples only serve to emphasize that nearly all of the evidence for this new Earth model lies beneath the waves. We can now understand why marine geologists of the 1950's were constantly confronted with surprises — the apparent youth of the ocean floor, thinness of sedimentary cover, etc. One cannot be surprised unless one has a preconceived model — and a preconceived model or paradigm which is wrong!

Secondly, we were tardy in discovering the new geotectonic model because the Earth's crust behaves in such a curious and almost unbelievable fashion. Once again Earth has proven to be unique among the planets. It is certainly much easier to conceive of a rigid crust like that of the Moon; or to understand a convecting and turbulent surface like that of Jupiter or the Sun itself. But to accept continuous and steady shifting of crustal plates of but a few centimeters per year comes close to defying imagination.

The recent major earthquake in Guatemala of January 1976 emphasizes once again that plate boundaries are where tectonic action occurs. This quake was apparently due, according to early reports, to abrupt slippage along the Motaqua fault which is the southern splay of two major faults which comprise the North Caribbean Shear Zone (a transform fault) marking the boundary of the Caribbean Plate with the North America Plate. Although mantle ultrabasic rocks occur squeezed up into this fault marking it as a geosuture, the fault apparently has been inactive for at least two centuries. The strike-slip offset along this fault occurred in the left-lateral sense indicating a relative westward drift of the North America Plate with respect to the Caribbean Plate. This is in accordance with plate-tectonic expectations. The Polochic fault, the northern splay, was regarded as the active plate-boundary fault which warns us once again that inactive faults may only

be "sleeping" and, if no creep is observed, they may be stick-slip faults which accumulate strain and then yield by abruptly.

## GLOBAL PROCESS

A significant aspect of plate tectonics is that our center of interest has shifted from local phenomena to an integrated global process. The wide-angle view is emphasized in the term "new global tectonics". It follows, from the concept of rigid lithospheric caps forming an earth-covering mosaic, that plate boundaries do not terminate. Instead, they transform from one type of boundary to another, and continue around the world until they close on their own tail. In his attempt to understand the Earth, the plight of the geologist was akin to that of an ant attempting to understand an elephant by crawling around its skin. With plate tectonics we now believe we are beginning to understand how the Earth really works.

Among Earth phenomena for which plate tectonics seems to offer a reasonable explanation are mountain building, volcanism, the geosynclinal cycle (by a new version), and the origin of ocean basins and continents, and the nature of the continental slopes with respect to subduction zones, transform faults or rift scarps. This list could easily be greatly extended for there is virtually no aspect of regional geology which has not been revised by plate-tectonic interpretations.

## THE WILSON CYCLE

Any successful revolution is followed by an effort to identify the heroes. Such searches always are limited to the generals, although it is well known that soldiers, and not generals, win wars. Many persons have been identified usually on the basis of some single important contribution. Alfred Wegener, with his espousal of continental drift, clearly stands alone as the classic hero in this revolution. But what about modern heroes? I find it difficult to identify any single person, but, if forced to do so, I would name J. Tuzo Wilson for his several basic contributions to plate tectonics. These include the concept of transform faulting, the early version of magmatic plumes and the drift of oceanic islands over a relatively fixed mantle, and, most importantly, the concept of collapsing and re-opening ocean basins — the grand theme of Earth evolution. Kevin Burke has aptly termed this the Wilson cycle.

## SOME UNSOLVED PROBLEMS

Among the problems which need further detailed study according to Gastil (1975) are the following:

(1) The relationship of spreading-center chemistry to island-arc geochemistry; e.g. are there systematic variations in rock chemistry related to spreading velocity?

- (2) The relationship of sea-floor sediments to island arc chemistry.
- (3) The relationship of metallogenic provinces to spreading and subduction; e.g. are the copper porphyries of the Andes and southwestern USA related to magmas arising from subduction zones and were these originally emplaced in pillow basalts at spreading axes?
- (4) Balancing the spreading—subduction budget. Magnetic anomalies indicate that about  $2.0 \text{ km}^2$  of new ocean floor are generated annually, but can we demonstrate an equal amount of lithospheric consumption at trenches?
- (5) Plate response rates; e.g. what was the global effect of India colliding with Asia and did this cause a re-ordering of plate motion vectors?
- (6) Passive versus directed spreading; e.g. can the response to collision be used as a test of the cause of spreading and the driving mechanisms of plate tectonics?

#### CONCLUSION

Kenneth Deffeyes of Princeton remarked in 1973, "Plate tectonics has caught us with our textbooks down. They must now all be rewritten." This updating, in fact, is now rapidly being done as most new textbooks include a chapter on plate tectonics as the unifying concept of earth evolution. Although we now have this new Rosetta Stone, the workings of the Earth still remain far from being fully elucidated. For example, we believe that it is now feasible to predict earthquakes, but we remain far from reaching that goal. We hope that this symposium will add a significant increment to our growing inverted pyramid of knowledge, of which the pivotal stone is the paradigm of plate tectonics. We trust it will not crumble. And we can observe that the principal corollary of plate tectonics, that is continental drift, appears in a few short years to have bridged the gap from heresy to orthodoxy.

#### REFERENCES

- Edwards, L. and Schott, R., 1937. Daily rate of growth of toe nails. *Ohio J. Sci.*, 27 (2): 91—98.
- Gastil, G., 1975. Working document (unpublished) of Working Group 10, submitted to U.S. Geodynamics Committee.



NOAA Technical Memorandum ERL MESA-19, 22 pages.

NOAA Technical Memorandum ERL MESA-19

THE 1973 BATHYMETRIC SURVEY IN THE NEW YORK BIGHT APEX:  
MAPS AND GEOLOGICAL IMPLICATIONS

George L. Freeland  
George F. Merrill

Marine Geology and Geophysics Laboratory  
Atlantic Oceanographic and Meteorological Laboratories  
Miami, Florida

Marine Ecosystems Analysis Program  
Boulder, Colorado  
December 1977



UNITED STATES  
DEPARTMENT OF COMMERCE  
Juanita M. Krops, Secretary

NATIONAL OCEANIC AND  
ATMOSPHERIC ADMINISTRATION  
Richard A. Frank, Administrator

Environmental Research  
Laboratories  
Wilmot N. Hess, Director

## CONTENTS

	Page
Abstract.....	1
1. INTRODUCTION.....	1
2. THE 1973 SURVEY.....	2
3. NET BATHYMETRIC CHANGES.....	5
4. DISCUSSION.....	7
4.1 Anthropogenic Sediments.....	7
4.2 Natural Sediments.....	9
5. ACKNOWLEDGMENTS.....	10
6. REFERENCES.....	11

# THE 1973 BATHYMETRIC SURVEY IN THE NEW YORK BIGHT APEX: MAPS AND GEOLOGICAL IMPLICATIONS

George L. Freeland  
George F. Merrill

## ABSTRACT

A hydrographic survey of the New York Bight Apex was undertaken by the New York District of the Corps of Engineers under contract to NOAA as part of the MESA Program. A bathymetric map was prepared and a comparison was made between the 1973 data and hydrographic data from the most recent previous survey of the area, H-6190, done in 1936 by the U.S. Coast and Geodetic Survey. A resulting contoured net bathymetric change map shows that the most significant change has occurred in the dredge-spoil dumpsite, where there has been up to 10 m of shoaling. Calculations of volumes of eroded and deposited sediment indicate that the area has generally eroded and that, except at the dredge-spoil dumpsite and the now abandoned dumpsites near Ambrose and Sandy Hook Channels, dumping is not causing significant changes in water depths.

## 1. INTRODUCTION

The disposal of solid wastes from the New York-New Jersey metropolitan area causes considerable environmental concern, as large volumes of these wastes are dumped in waters outside of the harbor mouth (Table 1 gives the source of Bight wastes). Dredge spoil and sewage sludge constitute 89% by weight of the solids dumped; their disposition is an important part of related environmental studies.



The U.S. Coast and Geodetic Survey (now the National Ocean Survey [NOS], NOAA) has made hydrographic surveys in the New York Bight since 1845. The last C.&G.S. survey to cover the Bight Apex, which is the area immediately adjacent to the harbor mouth where dumping is most intense, was in 1936 (survey H-6190). In 1973 the NOAA Marine EcoSystems Analysis (MESA) Program initiated research to determine recent effects of dumping in the New York Bight. A new hydrographic survey of the Bight Apex was conducted to determine what changes had occurred in bottom topography since 1936. The contract for the survey was let by NOAA to the U.S. Army Corps of Engineers, New York District. In turn, the New York District subcontracted the area south of 40°26'N latitude to the Philadelphia District to use the high-speed, 65-ft, survey catamaran *Shuman* because of the longer distances to the nearest port at Atlantic Highlands, New Jersey. Work north of 40°26'N was done with the New York District's 58-ft survey vessel *Hatton*. Changes in water depths reported in this study were calculated from the 1936 and 1973 surveys. Original data and calculations of net changes have been converted from English to metric units. Comparison between the 1845 and 1936 surveys (Williams and Duane, 1974) revealed the development of several knolls due to early dumping.

## 2. THE 1973 SURVEY

Location. The area covered by the survey was the Bight Apex from 40°18'N latitude northward to as close to the Long Island shoreline as was practical (generally from the 5 to 7 m isobath) and from 73°40'W longitude westward to equivalent New Jersey isobaths. This area included all of the Apex dumpsites, the upper part of the Hudson

Shelf Valley and its northward terminus (the Christiaensen Basin), the western part of Cholera Bank, and the entrance to New York Harbor between Rockaway Beach and Sandy Hook (see Fig. 1). The Christiaensen Basin was defined on the basis of topography as the area between 26 and 37 m depths north of 40°24'N. The Hudson Shelf Valley area lies north of 40°19.22'N at depths greater than 37 m.

Survey Lines. Survey lines were laid out approximately perpendicular to the average shoreline in three sub-areas (Fig. 2). Line spacing was established at 305 m (1000 ft) as a compromise between the desire for close line spacing and the time and cost involved. Soundings were taken on all lines. On alternate lines, at 610 m (2000 ft) spacing, other geophysical data (side-scan sonar and 3.5 kHz seismic reflection profiling) were taken. Lines with the added geophysical data were run first in each sub-area, with NOAA personnel and geophysical equipment on board. Then the survey vessels ran soundings-only lines without NOAA assistance. Field work was accomplished from June 19 to September 1, 1973.

Navigation. Navigation for the entire area was provided by the New York District using a Cubic Autotape DM40A system, accurate to  $\pm 0.5$  m at 5 km range and  $\pm 1.0$  m at maximum range of 50 km. Shore stations were set up at an old lighthouse at Highlands, New Jersey, and atop a 17-story apartment house at Far Rockaway Beach, New York, for most of the southern area. The Highlands station was moved to an abandoned lighthouse on Sandy Hook for middle and northeastern lines. For northwestern lines, stations were established at Ft. Tilden on Rockaway Beach, and at the Sandy Hook lighthouse.

Both survey vessels were equipped with fathometer, timer, and readout of the two navigation ranges. Data from all three were recorded on magnetic tape every 10 sec and printed on paper tape every minute.

Positions were plotted every minute on boat sheets (1:20,000 scale) provided by the New York District. The fathometer on the *Hatton* printed a paper record in addition to the magnetic tape recordings. Bar checks for fathometer accuracy were made at the beginning and end of each day's work.

Vessel speeds were about 9 km/hr (5 kn) during the running of geophysical tracklines. Soundings-only tracklines were run at about 22 km/hr (12 kn) on the *Shuman* and 11 km/hr (6 kn) on the *Hatton*.

Data Processing. A total of 2438 km (1317 nmi) of soundings trackline were run, including three tie lines, of which 1043 km (563 nmi) were run to take the added geophysical data. Soundings and navigation data taken by the *Shuman* were computer processed by the Philadelphia District using tidal corrections from the Sandy Hook tide gage station. The final products were computer-printed boat sheets at 1:20,000 scale with soundings to the nearest 0.03 m (0.1 ft ) printed at 101-m (333-ft ) intervals along tracklines.

Paper fathometer records from the *Hatton* were processed by drawing an average depth line through wave tracings on the record and plotting the tidal corrections from the Sandy Hook station. Corrected depths were then hand plotted at the same accuracy and spacing as the *Shuman* data on boat sheets (1:20,000 scale), which were checked for positional accuracy against the original plotting sheets.

Six boat sheets, which summarized the data for the entire survey, were delivered to NOAA. Copies of each sheet were contoured at 1-m and 1/2-fathom intervals, reduced to a scale of 1:40,000 and then spliced to assemble the complete map. Maps were further reduced to page-size for publication.



### 3. NET BATHYMETRIC CHANGE

The primary objective of the 1973 survey was to calculate the changes in bottom topography in the Bight Apex for geological studies of the nature of sediment transport.

Map Construction and Contouring. Examination of the boat sheets from survey H-6190 (1936) revealed trackline spacing of approximately 900 m (3038 ft) compared with 305 m (1000 ft) spacing for the 1973 survey; trackline directions between the two also diverged. In order to compare surveys, boat sheets from both surveys were contoured by NOAA at 0.9 m (3 ft) intervals at a common scale of 1:20,000. Boat sheets and contour maps were then sent to the Marine Sciences Institute, University of Connecticut, where net change values were calculated. Hydrographic profiles of the 1936 data were constructed for lines that coincided with tracklines of the 1973 survey. Depths along these profiles were determined by linear interpolation at every fourth 1973 posted depth (every 305 m [1000 ft]). The 1936 interpolated depth was then subtracted from the 1973 depth. The differences (net change values) were checked for sign and magnitude consistency by plotting them as profiles and were then plotted on a map at a scale of 1:40,000. After correction for a sea level rise of 0.189 m (0.62 ft) calculated from NOS mean monthly sea levels at Sandy Hook, New Jersey, values were then contoured at 0.6-m (2-ft) intervals from 0 to 1.83 m (6 ft) and at 1.52-m (5-ft) intervals for values higher than 3.05 m (10 ft) for both deposition and erosion. However, isopleths of 1.83 m for deposition and 0.6 m for erosion were used for the maps reduced to page size.

Determination of Areas of Deposition and Erosion. Five sub-areas were defined on the basis of anthropogenic net bottom change and natural topography (Table 2): 1) the Ambrose and Sandy Hook Channels area to the northwest of a zero deposition contour enclosing the peninsula-shaped area of mapped data (Fig. 3). Up to 14 m (45 ft) of bottom sediment "erosion" is due to dredging of navigation channels and for construction sand; lesser amounts of deposition are from spoil dumping; 2) the dredge-spoil dumpsite (also referred to as the mud dump), within a surrounding zero-deposition contour but excluding the cellar-dirt dumpsite and a contiguous area of 0-1.8 m deposition to the northeast. Up to 10 m (34 ft) of deposition was mapped; 3) the cellar-dirt dumpsite, within a zero-deposition contour to the southeast of the dredge-spoil dumpsite; 4) the Christiaensen Basin; and 5) the Hudson Shelf Valley.

Volume Calculations. Volumes of erosion and deposition were calculated by repetitive measuring of the areas within all contours by planimeter and multiplying the mean by the appropriate contour interval. Volumes for sediment in the slope between contours were calculated and added.

The net change map (Fig. 3) consists of enclosed contours for deposition greater than 0 m net change, and for erosion greater than 0.6 m. The volume of material eroded between the 0 and 0.6-m erosion isopleths was calculated by adding the areas inside the 0 deposition contours to the areas inside the over-0.6-m erosion contours, then subtracting that sum from the total area considered. This was done for each of the five sub-areas mentioned above and for the remainder of the

Apex outside the sub-areas. The data thus obtained were multiplied by 0.204 m (0.67 ft) (the average depth of erosion after sea-level correction) between the 0- and 0.6-m erosional contours to obtain the volume of sediment eroded in this interval. This figure was then added to data from erosion contours greater than 0.6 m to obtain total volume of erosion for each area.

Areas, volumes of erosion and deposition, and net changes for Bight Apex features are listed in Table 2.

Sources of Error. Accuracy of the net change map is dependent upon the accuracy of the two surveys, the net change calculations, the contouring of these values, and the area and volume calculations. Of these, the accuracy of the 1936 survey is probably the greatest source of error. On relatively even bottoms or in critical depths less than 20 m (66 ft), soundings were accurate to 0.15 m (0.5 ft), and to within 1% of greater depths (Adams, 1942). In rapidly changing depths and over irregular bottoms, errors could be twice the above limits. The Corps of Engineers estimated that the accuracy of the 1973 soundings was 0.03 m (0.1 ft). The soundings picked for each survey for net change calculations were estimated to have an accuracy of 0.06 m (0.2 ft). If the errors are assumed to be random, and the total error  $E = \sqrt{e_1^2 + e_2^2 + e_3^2 + e_4^2}$ , where  $e_1$ ,  $e_2$ ,  $e_3$ , and  $e_4$  are the mapped-soundings and net-change-soundings errors mentioned above, the net change error is  $\pm 0.18$  m (0.58 ft).

## 4. DISCUSSION

### 4.1 Anthropogenic Sediments

Sediments are introduced into the Bight Apex almost entirely in the form of fine-grained sand (0.25-0.0625 mm) and mud-sized (less than



0.0625 mm) particles. Dredge spoil is the greatest source of solids brought in by man (see Table 1). Estimates of the total amount of dredgings from 1936 to 1973 using Corps of Engineers data (records are questionable for years prior to 1954) indicate that about  $142 \times 10^6 \text{ m}^3$  ( $186 \times 10^6 \text{ yd}^3$ ) of material was dumped. Our calculations of net bottom change indicate that  $124 \times 10^6 \text{ m}^3$  ( $162 \times 10^6 \text{ yd}^3$ ) has accumulated on the bottom at the dredge-spoil dumpsite and at the dumping areas near Ambrose and Sandy Hook Channels (Table 2). This indicates that approximately 87% of the dredge spoil dumped is still in place on the bottom. Detailed mapping of the dredge-spoil dumpsite shows that shoaling of up to 10.4 m (34 ft) has occurred over an area of  $36 \text{ km}^2$  ( $10.4 \text{ nmi}^2$ ) south of a knoll which was formed by earlier dumping (see Figs. 4-6).

Sewage sludge, on the other hand, is a much smaller source of Bight sediment by weight: it contains an average of 2.6% solids, has a mean bulk density of 1.0090 (less than that of sea water, 1.019-1.025; Callaway et al., 1976) and contains 80% to 100% organic matter (Hatcher, 1977). Mean particle sizes vary from 0.025 mm to 0.065 mm, but due to flocculation and low particle densities (a mean of 1.50 g/cc dry), settling velocities vary from 0.5 cm/s (equivalent to 0.074 mm, very fine sand) to less than 0.001 cm/s (equivalent to clay particles less than 0.004 mm; Callaway et al., 1976). Larger particles settle to the bottom (24 m at the dumpsite) in about 5 min, but many particles often remain in the water column after 4 h (Prioni et al., 1976). Spreading the entire annual volume of sludge ( $3.3 \times 10^6 \text{ m}^3$ ; see Table 1) over the area of the Christiaensen Basin and the upper Hudson Shelf Valley ( $106 \text{ km}^2$ ) would result in a layer 3 cm thick (sediment was assumed to have compacted to a

bulk density of 1.052 at which water content would be 600% and dry grain density 1.50; from Bennett et al., 1971). If the total volume of sludge dumped since 1924 (approx.  $107 \times 10^6 \text{ m}^3$ ; Mueller et al., 1976) accumulated in these areas, the layer would be 1 m thick. Since currents carry some of the suspended matter out of the Christiaensen Basin and Hudson Shelf Valley areas, and since storms resuspend, mix, and disperse natural and anthropogenic particles already on the bottom, it is not surprising that sludge cannot be found on the bottom as a discrete layer. At present it is possible to distinguish sludge-derived material from natural organic mud only by the interpretation of a number of complex organic chemical analyses now ongoing (Harvey, 1977).

While sludge is being mixed with natural muds in the topographically low areas, there is a close balance of deposition versus erosion during the 37 years prior to 1973 (see below).

Cellar dirt, the third anthropogenic sediment, consists of construction rubble from demolition, foundation rock and dirt, and slag. Brick, metamorphic rocks, and red sandstone are commonly recovered in grab samples. Cellar dirt, although making a recognizable spoil mound, is not considered an important input because of its comparatively low volume.

#### 4.2 Natural Sediments

Natural sediment input from land sources comes mainly from stream runoff (mostly from the Hudson River drainage basin) and urban runoff (mostly from the New York metropolitan area; Table 1). These sources are relatively easy to measure compared with sediment transported from other areas of the shelf. Various estimates of sediment transport indicate that, for the continental margin of the eastern U.S., three con-

clusions can be reached: 1) 90% of the sediment from land sources is deposited in estuaries and wetlands; 2) net suspended fine sediment transport on the shelf is probably landward, with possibly much of the material finally settling in estuaries; and 3) recycling (resuspension and settling) of sediment on the shelf may transport amounts of sediment that are greater by orders of magnitude than either enter or leave the shelf (Meade et al., 1975; Milliman et al., 1972).

From our net change map (Fig. 3), volumes of natural sediment deposited and eroded in the Bight Apex over the 37 year period between surveys have been calculated (Table 2). After the anthropogenic material in the Ambrose-Sandy Hook Channels area and the dredge spoil and cellar dirt dumpsites are subtracted, the volume of material eroded exceeds deposition by  $79 \times 10^6 \text{ m}^3$  ( $103 \times 10^6 \text{ yd}^3$ ), equivalent to a layer 13.5 cm (5.3 in) thick over the non-anthropogenic areas. This is an average of 3.6 mm (0.14 in) per year. It is also less than the calculated error estimate of  $\pm 18 \text{ cm}$  for the net change map, representing  $106 \times 10^6 \text{ m}^3$  ( $138 \times 10^6 \text{ yd}^3$ ) over the non-anthropogenic areas. Therefore, within the error estimate, the net change could be from  $185 \times 10^6 \text{ m}^3$  ( $242 \times 10^6 \text{ yd}^3$ ) of erosion (31 cm or 12 in) over the non-anthropogenic areas to  $27 \times 10^6 \text{ m}^3$  ( $35 \times 10^6 \text{ yd}^3$ ) of deposition (4.5 cm or 1.8 in) over the non-anthropogenic areas for the 37 years. Thus the system appears to be nearly in balance, requiring periodic removal of bottom sediment. From other ongoing studies, this erosion apparently occurs primarily during storms that occur most frequently in winter months.

## 5. ACKNOWLEDGMENTS

Field operational aspects of this program were carried out by the Survey Branches, New York and Philadelphia Districts, U.S. Army Corps of



Engineers. John J. Dowling of the University of Connecticut made the net change calculation. NOS, Rockville, Md., and R.L. Swanson, MESA, Stony Brook, N.Y., supplied sea level and tidal correction data. H.B. Stewart, Jr., D.J.P. Swift, and H. Stanford reviewed the manuscript. This work was supported by the Environmental Research Laboratories' Marine EcoSystems Analysis Program of the National Oceanic and Atmospheric Administration.

## 6. REFERENCES

- Adams, K.T. (1942): Hydrographic Manual, U.S. Coast and Geodetic Survey, Spec. Pub. 143.
- Bennett, R.H., D.N. Lambert, and P.J. Grim (1971): Tables for Determining Unit Weight of Deep-Sea Sediments from Water Content and Average Grain Density Measurements, NOAA Tech. Memo. ERL AOML-13.
- Callaway, R.J., A.M. Teeter, D.W. Browne, and G.R. Ditsworth (1976): Preliminary Analysis of the Dispersion of Sewage Sludge Discharge from Vessels to New York Bight Waters, Environmental Protection Agency, Corvallis, Oregon, draft manuscript.
- Harvey, G. (1977): Personal communication based on ongoing chemical analyses, AOML, Miami, Fla.
- Hatcher, P.G. (1977): Personal communication based on ongoing chemical analyses, AOML, Miami, Fla.
- Lavelle, J.W., P.E. Gadd, G.C. Han, D.A. Mayer, W.L. Stubblefield, and D.J.P. Swift (1976): Preliminary results of coincident current meter and sediment transport observations for wintertime conditions on the Long Island Inner Shelf, Geophysical Res. Letters, 3:97-100.
- Meade, R.H., P.L. Sachs, F.T. Manheim, J.C. Hathaway, and D.W. Spencer (1975): Sources of suspended matter in waters of the Middle Atlantic Bight, Jour. Sed. Pet., 45:171-188.
- Milliman, J.D., O.H. Pilkey, and D.A. Ross (1972): Sediments of the continental margin of the eastern U.S., Bull. Geol. Soc. Amer., 83:1315-1334.
- Mueller, J.A., J.S. Jeris, A.R. Anderson, and C.F. Hughes (1976): Contaminant Inputs to the New York Bight, NOAA Tech. Memo. ERL MESA-6.

Proni, J.R., F.C. Newman, R.H. Sellers, and C. Parker (1976): Acoustic tracking of ocean-dumped sewage, Science, 193:1005-1007.

Williams, S.J., and D.B. Duane (1974): Geomorphology and Sediments of the Inner New York Bight Continental Shelf, Tech. Memo 45, U.S. Army, Corps of Engineers, Coastal Eng. Res. Center.

TABLE 1

Source of Solids Transported Annually into Marine Waters  
of the New York Bight

SOURCE	VOLUME		WEIGHT		
	$10^6 \text{ m}^3$	% of barged	$10^6$ metric tons	% of barged	% of total input
Dredge spoil	8.8	53	4.7	85.3	53.4
Sewage sludge	4.3	26	0.165	3	1.9
Cellar dirt	0.5	3	0.6	10.9	6.8
Acid waste	2.5	15	0.04	0.73	0.5
Chemical waste	0.5	3	0.003	0.05	0.03
Total barged	16.6	100	5.51	100.00	62.6
Atmospheric fallout			0.427		4.8
Wastewater*					
Municipal			0.35		4.0
Industrial			0.02		0.2
Runoff*					
Gaged			1.4		15.9
Urban			1.1		12.5
Total input			8.81		100.00

From Mueller et al. (1976)

\*98% of these coastal zone inputs come through the Rockaway-Sandy Hook transect. Figures do not include shelf-derived sediment from outside the Bight.



TABLE 2

Volumes of Erosion and Deposition in the New York Bight Apex  
Between 1936 and 1973

	Area (km <sup>2</sup> )	Volume (10 <sup>6</sup> m <sup>3</sup> )		
		Erosion(E)	Deposition(D)	Net Change
1. Entire Apex	718	161	162	1 D
2. Dredge Spoil Dumpsite	36		93	93 D
3. Cellar Dirt Dumpsite	9		5	5 D
4. Ambrose and Sandy Hook Channel Areas	86	49	31	18 E
5. Total Anthropogenic (2-4)	131	49	129	80 D
6. Christiaensen Basin <sup>1</sup>	83	13	6	7 E
7. Hudson Shelf Valley <sup>2</sup>	23	10	2	8 E
8. Other Non-Anthropogenic	397	89		} 64 E
	84		25	
9. Total Non-Anthropogenic(6-8)	587			79 E <sup>3</sup>
Total Erosion	477	112		
Total Deposition	110		33	

<sup>1</sup>Area between 26 and 37 m depths north of 40°24'N.

<sup>2</sup>Area deeper than 37 m north of 40°19.22'N.

<sup>3</sup>Equal to a layer 13.5 cm thick (3.6 mm/yr).



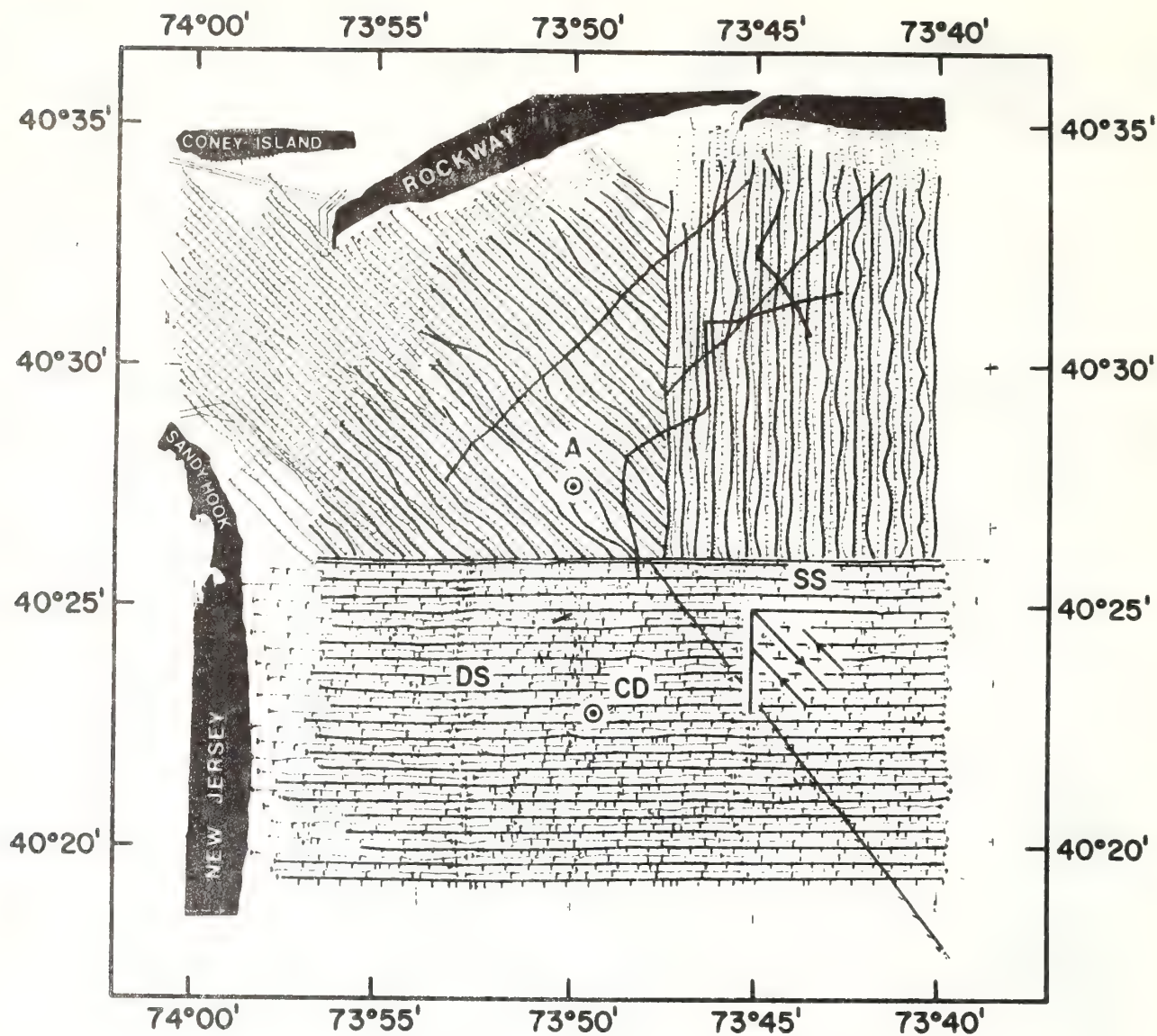


Figure 2. Tracklines of the 1973 bathymetric survey. Light lines show tracklines for bathymetry only. On heavy lines both bathymetric and geophysical data were collected. A: Ambrose Light Tower; SS: Sewage-sludge dumpsite; DS: Dredge-spoil dumpsite; CD: Cellar-dirt dumpsite.



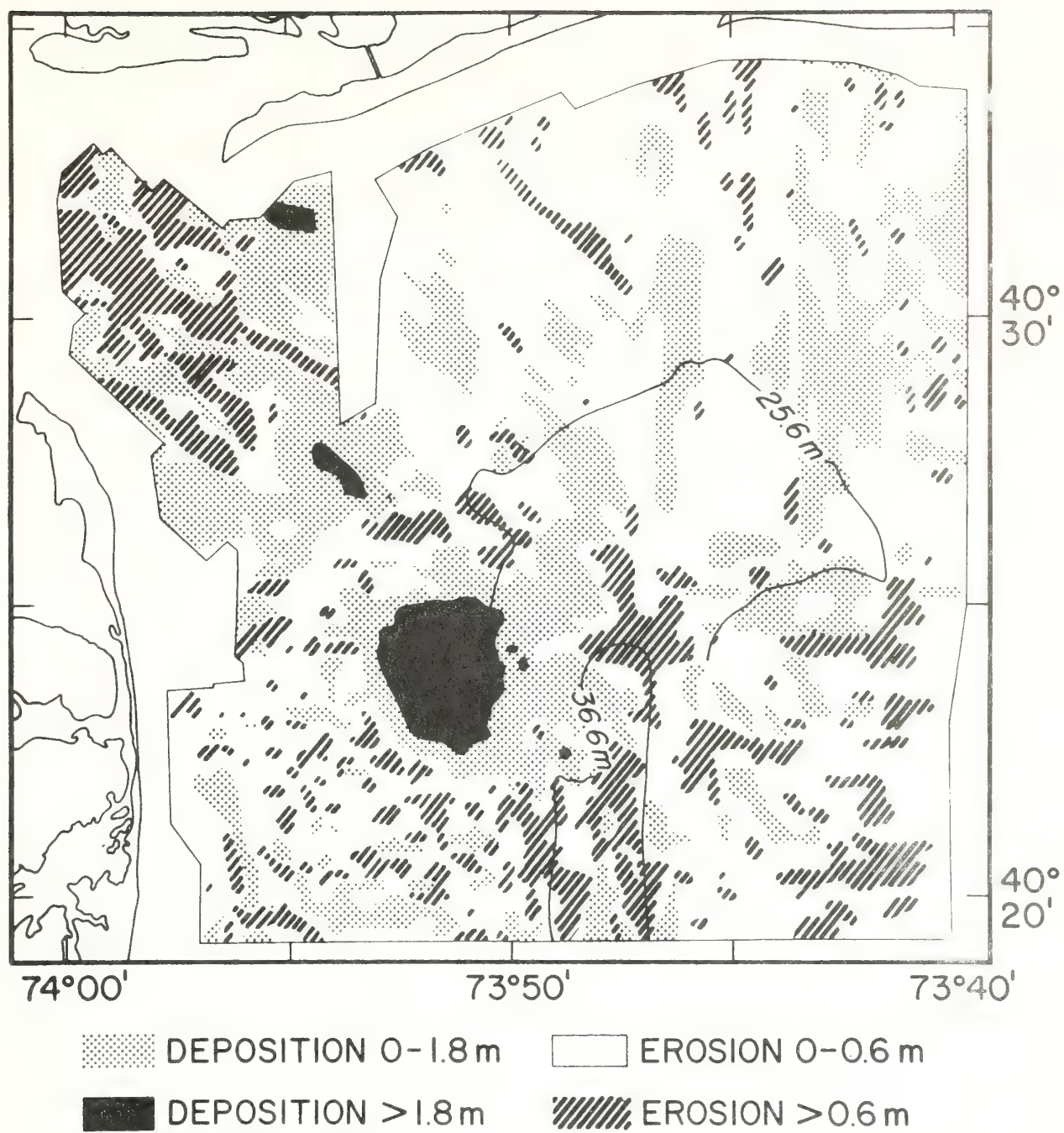


Figure 3. Net bathymetric change, New York Bight Apex, from 1936 to 1973.

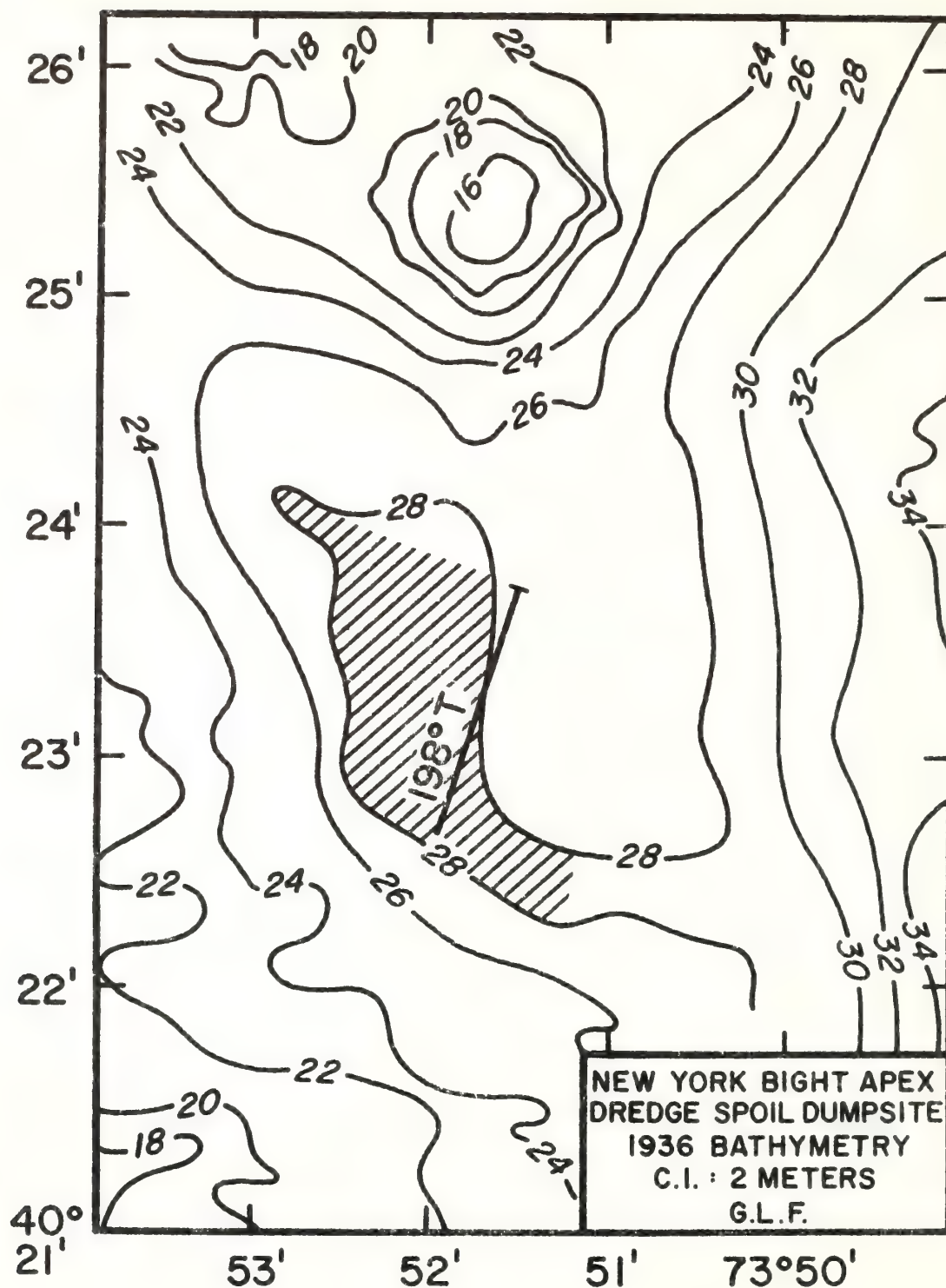


Figure 4. New York Bight dredge-spoil dumpsite. 1936 bathymetry. Line marked 198°T and hachured area show the dumpsite designated prior to 1977 based on 1936 soundings to lie within the 27.4-m (90-ft) isobath.

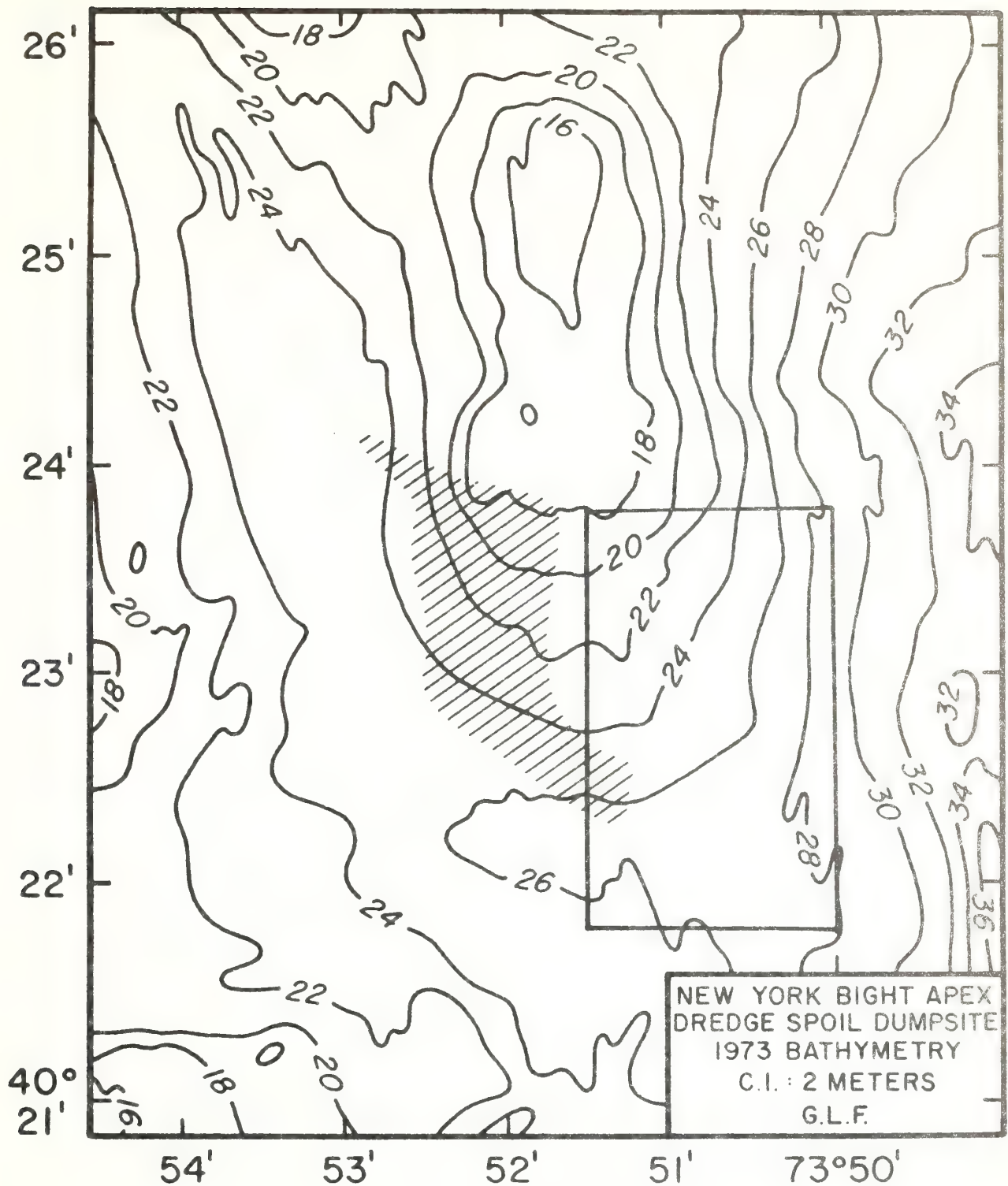


Figure 5. New York Bight dredge-spoil dumpsite, 1973 bathymetry. The rectangular area to the southeast of the mound is the dumpsite designated by the Environmental Protection Agency starting January 1977.



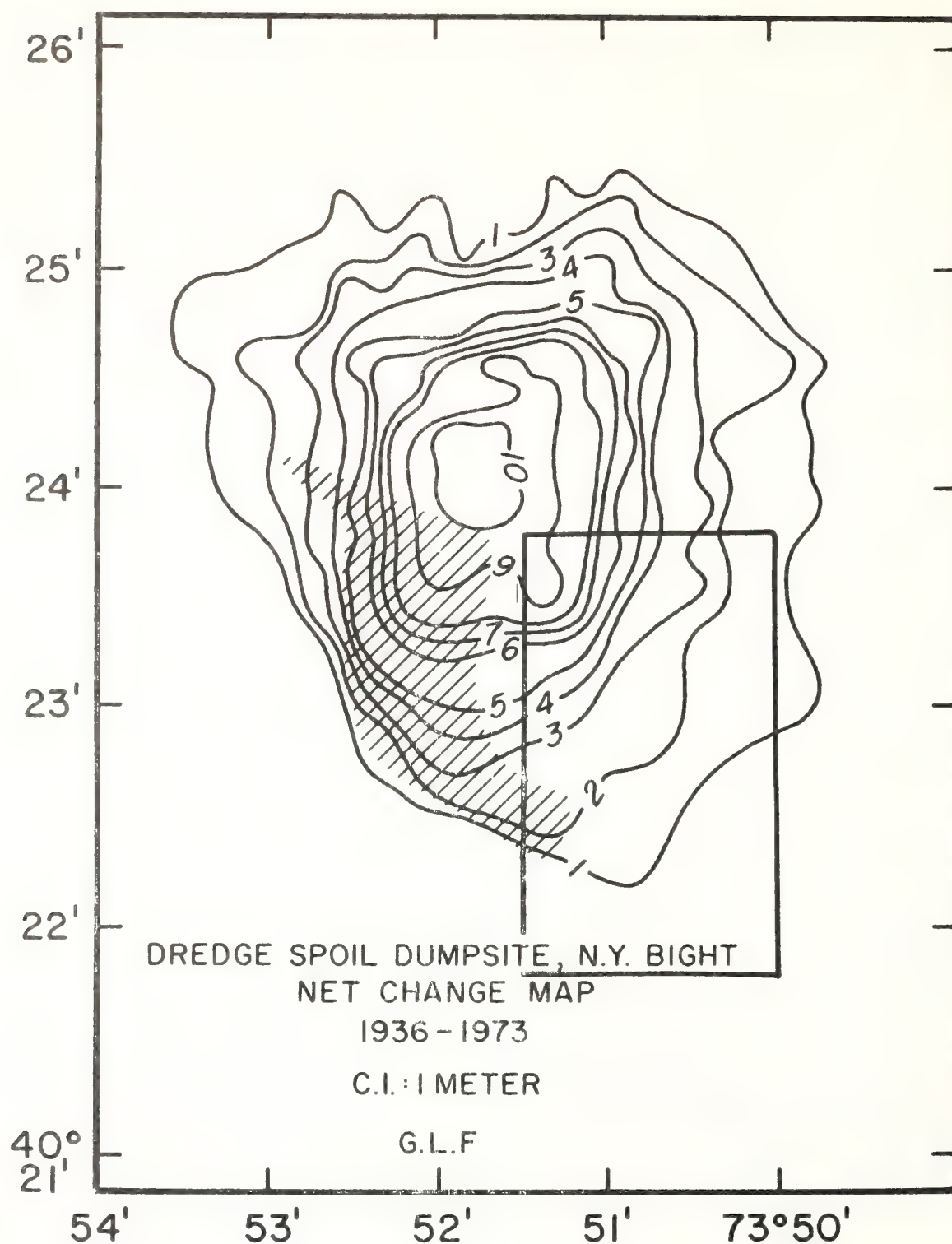


Figure 6. New York Bight dredge-spoil dumpsite. Net change in depth from 1936 to 1973. Note that the 14.3-m (47-ft) knoll in the 1936 map is essentially unchanged and that a large volume of material has been dumped north and east of the dumpsite designated from the 1936 map (hachured area). The rectangular area is the same as shown on Figure 5.

Middle Atlantic Continental Shelf and the New York Bight, Special Symposia 2, 1976, M.G. Gross, ed. (the American Society of Limnology and Oceanography, Inc.) 90-101.

## Surficial sediments of the NOAA-MESA study areas in the New York Bight

*George L. Freeland, Donald J. P. Swift, and William L. Stubblefield*

Atlantic Oceanographic and Meteorological Laboratories, NOAA, 15 Rickenbacker Causeway, Miami, Florida 33149

*Anthony E. Cok*

Department of Earth Sciences, Adelphi University, Garden City, New York 11530

### *Abstract*

In the New York Bight apex, extensive sedimentological studies and a 1973 bathymetric survey reveal that the only significant change in bottom topography since 1936 occurred at the dredge spoil dumpsite where the dumping of  $98 \times 10^6 \text{ m}^3$  of dredged material has caused up to 10 m of shoaling. The center of the Christiaensen Basin, a natural collecting area for fine-grained sediment, is no doubt contaminated with sludge but shows no apparent sediment buildup during the intervening 37 years. The apex outside of the Christiaensen Basin is floored primarily by sand ranging from silty fine to coarse, with small areas of sandy gravel, artifact (anthropogenic) gravel, and mud. Nearshore mud patches appear to be covered at times with sand and occasionally scoured out. Sidescan sonar records show linear bedforms, indicative of sand movement, over most of the apex area.

Two midshelf areas have been proposed as interim alternative dumping areas. The northern area is in a tributary valley of the ancestral Long Island river system. Fine sands cover the northeast part and medium sands predominate to the west and south. Bottom photographs show a smooth, slightly undulatory, mounded or rippled sea floor.

In the southern alternative dumping area coarse sand and gravel deposits lie on the crest and east flank of the Hudson divide, while medium and fine sand occurs in the ridge and swale topography to the west. These distributions suggest fine sediment is winnowed from the crest and east flank of the divide and deposited to the west. Veatch and Smith Trough contains a veneer of shelly, pebble sand with large, angular clay pebbles and occasional oyster shells derived from exposed early Holocene lagoonal clay. These studies suggest that if sewage sludge were dumped, widespread dispersion, mostly to the southwest, could be expected, with winter resuspension and transport of fine material on the bottom. Possible permanent buildup on the bottom could be expected if dredged material were dumped.

The nature of bottom sediments and sediment particles suspended in the water column becomes of interest to environmental managers when man's activities in the ocean disturb the sea floor or the near-bottom water column. In addition to the immediate results, one must also consider the effect on long term natural phenomena. How are these processes affected by what man has done, or perhaps more importantly, how do natural processes modify what man has done to disturb the natural environment?

Here we report work done at the Atlantic Oceanographic and Meteorological Laboratory as part of the NOAA-MESA New York Bight Project.

Hydrographic surveys of the New York Bight were initiated in 1936 by the Coast and Geodetic Survey (now the National Ocean Survey) in nearshore areas and have been repeated periodically. Bathymetric

maps at 1-fathom (Stearns and Garrison 1967) and 4-m intervals on the shelf and 200-m intervals on the continental slope (Fig. 1; Uchupi 1970) were made from 1936 survey data. A new survey of the bight was made in 1975; results should be available in 1977.

Surficial morphology of the New York Bight, and sediment distribution across this surface, may be explained by sea level fluctuations caused by continental glaciation during the past several million years. The last glacial stage ended 15,000 years ago (Milliman and Emery 1968) when the eastern North American ice sheet extended as far as Long Island and northern New Jersey. During maximum glacial advance sea level was lowered about 160 m (Veatch and Smith 1939) so that the shoreline of the bight was in the vicinity of Hudson Canyon (see Fig. 1). Since the ice melted, the shore-

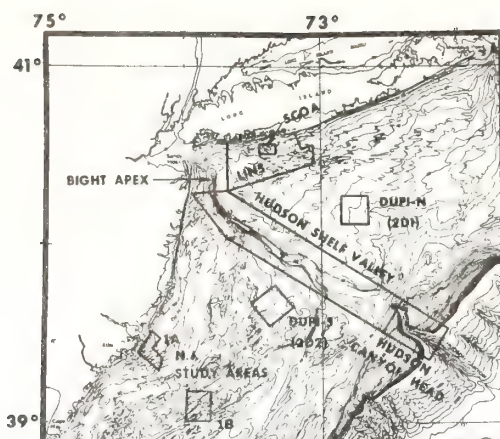


Fig. 1. Index to detailed study areas and topographic features in the New York Bight. (Bathymetry from Uchupi 1970.) Contour intervals 4 and 200 m. 1A—New Jersey nearshore ridge and swale study area and the Atlantic generating station site; 1B—New Jersey central shelf ridge and swale study area; LINS—Long Island nearshore study area; SCOA—Suffolk County outfall area; 2D1, 2D2—proposed interim alternative dumpsites.

line advanced to its present position; many features of the shelf are the result of several sea level fluctuations. Morphologic features are discussed in our companion paper in this volume (Swift et al. 1976) and elsewhere (e.g. McKinney and Friedman 1970; McKinney et al. 1974; Stubblefield et al. 1974, 1975; Knott and Hoskins 1968; Duane et al. 1972; Williams 1976).

### Surficial sediments

A comprehensive sampling program for the outer shelf was conducted by the Woods Hole Oceanographic Institution and the U.S. Geological Survey, who sampled on an 18-km spacing. The Corps of Engineers Coastal Engineering Research Center has collected about 4,200 km of geophysical data and over 300 cores as a part of its studies on the inner shelf of the bight (Duane 1969; Williams and Duane 1974; Williams 1976). MESA work had been conducted primarily in New Jersey nearshore and central shelf areas, the bight apex, the nearshore of Long Island eastward to Fire Island, two central shelf alternative dumping areas, and the Hudson Shelf Valley (Fig.

1). Emphasis here is on the bight apex and the central shelf alternative dumping areas.

**Source and age of sediments**—Sediments covering the floor of the bight were mostly deposited during lowered sea level and were reworked during the landward-seaward migrations of the shoreline. As transgression progressed, fluvial and older sediments were covered by estuarine and lagoonal sediments behind barrier islands or directly reworked by littoral processes associated with the advancing shoreline. During a transgression, bottom currents of the inner shelf interact with the shelf floor to form a concave surface whose profile resembles an exponential curve, with the steep limb comprising the shoreface (Swift et al. 1972). With a loose, sandy substrate, the inner shelf shoreface tends to extend itself laterally across the mouths of bays, closing them, except for inlets, by the deposition of sand in the form of spits and barrier islands. Estuaries and lagoons behind these spits and islands then trap suspended fine sediment (mud), while the barrier islands are nourished by littoral drift from eroding headlands and by sand moving landward from the shelf.

As sea level rose during the Holocene transgression, the inner shelf profile moved shoreward by means of shoreface erosion. Some eroded sand was swept onto the barrier islands by storm overwash and buried, only to be re-exposed again at the eroding shoreface. Most material from shoreface erosion, has, however, been washed down-coast and seaward to form a discontinuous sand blanket 0 to 10 m thick (Stahl et al. 1974). Thus, the New York Bight shelf floor is dominantly sand-sized sediment (Schlee 1973). Fine-grained sediments are generally absent, having been transported either into the Hudson-Raritan estuary, behind barrier islands, or off the shelf edge. Locally, underlying strata of transgressed lagoonal and estuarine semiconsolidated mud deposits or resistant coastal plain strata are exposed on the sea floor (Swift et al. 1972; Stahl et al. 1974; Sheridan et al. 1974).

**Sediment types**—Sediment types have been mapped in the New York Bight primarily by dominant grain size (Fig. 2).



Generally, the shelf is covered by sand-sized sediment with isolated gravel patches (Schlee 1973, 1975; Williams and Duane 1974; Williams 1976). In deeper water, generally seaward of the 60-m isobath, in the Hudson Shelf Valley, and in lagoons and estuaries where wave action is less pronounced, silt is the dominant sediment (Freeland and Swift in press). In the Long Island nearshore zone west of Fire Island, small mud patches, some of which are seasonal, are of considerable environmental concern owing to contamination of the fines by pollutants.

*Suspended sediments*—Meade (1972a, b) noted the following: Pleistocene glaciations and sea level fluctuations drastically altered the composition and distribution of sediments on continental margins; it is not always immediately evident whether present shelf deposits reflect modern or Pleistocene conditions. Fine sediment transport studies are hindered by the fact that deposited sediments may reflect processes acting over thousands of years, whereas our

Table 1. Source of suspended solids in the New York Bight.\*

	×10 <sup>6</sup> tonnes/yr
Direct bight (68%)	
Dredged (54%)	4.73
Sludge (2.1%)	0.18
Cellar dirt (6.8%)	0.60
Total barged (62.9%)	5.51
Atmospheric (5%)	0.45
Coastal zone (32%)	
(98% of coastal zone input is through the Rockaway-Sandy Hook transect)	
Municipal wastewater (4%)	0.35
Industrial wastewater (0.2%)	0.02
Gauged runoff (16%)	1.4
Urban runoff (12%)	1.1
Total coastal zone	2.87
Total input	8.83

\* From Mueller et al. 1976.

studies of suspended sediment are commonly limited to a few days or months of observations. Natural processes may be impossible to separate from the changes produced by human activities, particularly in estuaries (and at the present dumpsites).

*Fine sediment sources to estuaries and the shelf*—Fine sediment discharged into the bight is shown in Table 1 (Mueller et al. 1976). Fluvial sediment is comprised of roughly 85% inorganic and 15% combustible organic material (Table 2). The fine inorganic fraction is mostly illite, chlorite, feldspar, and hornblende from the Hudson River (Hathaway 1972).

Shelf erosion and coast-parallel transport appear to be significant but unmeasured sources of suspended material and were probably major sources during the Holocene transgression. Hathaway (1972) showed that fine sediments near the mouths

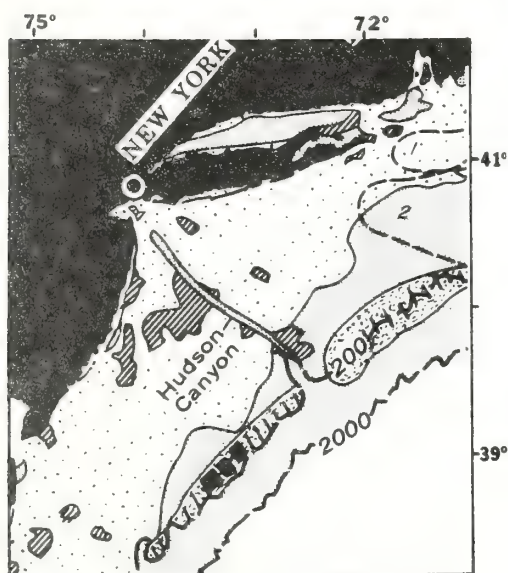


Fig. 2. Sediment types in the bight area (depth in meters). Hatching—gravel, sandy gravel, and gravelly sand; speckling—sand; stippling—silty sand, sandy silt, and clayey silt; dappling—glauconitic sand, silty sand, and sandy silt. ■■■—Pyrite-filled foraminiferal tests. 1—Zone of rounded quartz grains; 2—zone of limonitic pellets. (From Uchupi 1963.)

Table 2. Composition of suspended matter.

Rivers	80–90% minerals	10–20% combustible organics
Estuaries	60–80% minerals + biogenic shells	20–40% combustible organics
Shelf	10–70% minerals + biogenic shells	30–90% combustible organics

of coastal plain estuaries differ significantly from the composition of riverborne sediments. It is probable that much estuary-mouth sediment is being eroded from shelf deposits and returned to and trapped in estuaries (Meade 1969). The fact that the sediments from modern rivers have not obscured this conclusion implies that either the modern sediment is bypassing the lower portions of the estuary, or it is trapped almost completely near the river mouths. Along the east coast, the heads of the Chesapeake and Delaware estuaries are far upstream from the estuary mouth, therefore, most river sediment is deposited far inland from the sea. Although saline tidal water is present in the Hudson River up to Albany, fine fluvial sediment is carried by low-salinity surface water to Upper and Lower New York Bays where some fines settle out (Folger 1972*b*) and the remainder is carried with estuarine sediment into the bight apex and mixed with recirculated shelf sediment. In the northeast United States, most of the fluvial suspended sediment is effectively trapped in estuaries and coastal wetlands (Milliman 1972).

At the present, the annual suspended sediment discharge of Atlantic coastal rivers is about equal to the annual deposition on marsh surfaces (Meade 1972*a*). However, much of the deposited material re-enters the shelf water column after the shoreline has passed over the marsh, through the process of shoreface erosion (Fischer 1961).

Particles derived from biologic processes are also a significant component of suspended matter in estuaries and on the shelf (Table 2), ranging from 20–90% in surface waters (Manheim et al. 1970). However, concentrations of combustible biogenic matter decrease rapidly with depth, and little of this material is preserved in sediment deposits (Folger 1972*a*; Gross 1972).

Atmospheric fallout over the New York Bight is small relative to other sediment sources (Table 1), but it may be a significant transport path for specific pollutants (e.g. lead from vehicular exhaust emissions).

Highest concentrations of organic and inorganic suspended materials in the water

occur within 10 km of the coastline and decrease nearly exponentially seaward (Manheim et al. 1970). Mineral grains larger than 4  $\mu\text{m}$  (silt-size) comprise 10–25% of near-shore suspended sediment and only 2–5% of offshore samples; the remainder is organic matter. The zone of strong terrigenous influence is restricted to nearshore waters and, specifically, to the inner shelf zone of turbid water drifting away from the estuary mouth. The coarser grains in this zone are effectively trapped in the “estuarine” circulation (which serves to reinforce the surface concentrations) and are transferred from one estuary to the next along the path of the longshore current.

Studies of other areas (Postma 1967) suggest that volumes of suspended sediment transported on the many feedback loops in the bight are probably orders of magnitude greater than both the net volume from the Hudson River that is transported across the shelf and the much larger amounts introduced by dumping.

Although the factors which influence suspended sediment dispersal can be readily defined, many large gaps in our knowledge must be closed before quantitative sediment transport budgets can be constructed on a regional scale. The most important of these are: shelf circulation patterns and mechanisms, particularly during storms; hydraulic properties of suspended sediments, particularly resuspension and settling properties; and the influence of flocculation and biologic aggregation on settling.

#### *Detailed studies in the New York Bight apex*

A 1973 bathymetric map (Fig. 3) of the bight apex was made as the result of a NOAA-Corps of Engineers survey. The principal topographic features are the northern end of the Hudson Shelf Valley, Cholera Bank, and the Christiaensen Basin, an amphitheaterlike feature terminating the Hudson Shelf Valley (Veatch and Smith 1939). Dumpsites for dredge spoils (the mud dump), cellar dirt, sewage sludge, and acid wastes are shown. Knolls immediately northwest of Ambrose Light and north and northwest of the dredge spoil dumpsite



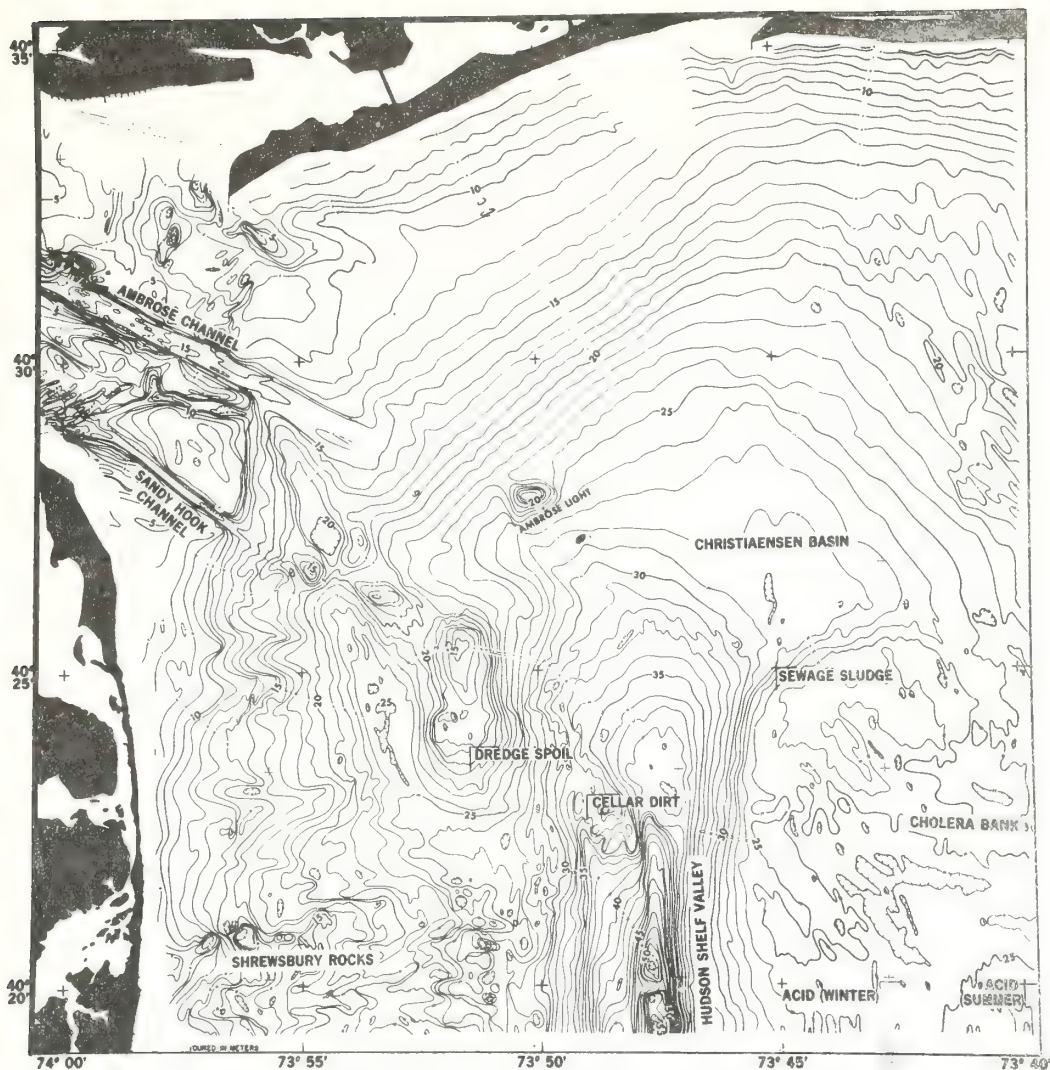


Fig. 3. Bathymetric map of the New York Bight apex. Contour interval, 1 m. Data (in meters) from 1973 NOAA-Corps of Engineers survey.

were formed from early 20th century dumping of assorted building excavation material and sand and gravel from the dredging of Ambrose and Sandy Hook Channels (Williams 1975).

Comparison of the 1973 bathymetric survey results with data from the 1936 survey reveals that only the anthropogenic areas have changed significantly. Figure 4 shows the 1973 and 1936 bathymetry of the dredge spoil site, as well as the net change between the two surveys. The 50-ft knoll on the 1936 map (relatively unchanged in 1973) is itself

the result of earlier dumping (Williams 1975). The amount of anthropogenic material accumulated during these years (1936–1973) has been calculated to be about  $124 \times 10^6 \text{ m}^3$ . This compares with about  $142 \times 10^6 \text{ m}^3$  dumped. The difference easily can be accounted for by settling alone.

Surficial sediments have been mapped by analyzing over 700 bottom grab samples collected at 1-km spacing (Fig. 5). The topographically low Hudson Shelf Valley and the Christiaensen Basin are flooded



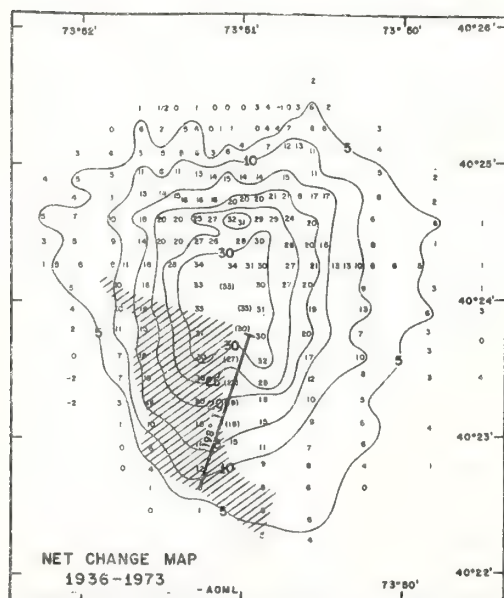
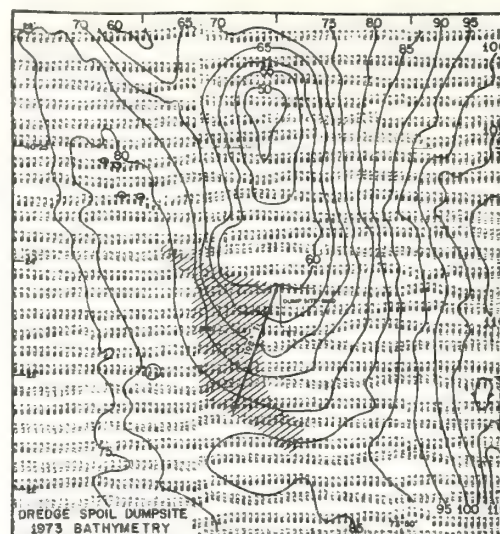
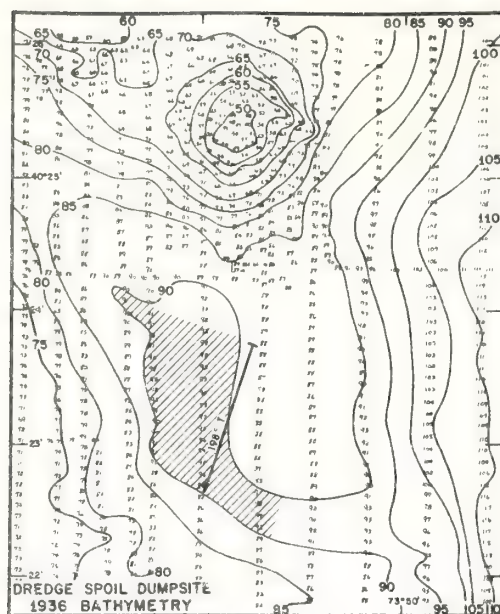


Fig. 4. Bathymetric maps (5-ft contour intervals) of the dredge spoil dumpsite, New York Bight apex. The 198°T azimuth (minimum distance 4 nmi from Ambrose Light) and the 90-ft isobath define the designated site (hatched). Upper left—1936; upper right—1973; left—net change from 1936–1973.

with fine-grained sediment, whereas the rest of the area contains assorted sizes of sand and both anthropogenic (artifact) and natural gravel deposits. Artifact gravels consist of recognizable construction rubble—brick, schist, concrete, etc.

Geophysical data taken during the 1973 survey consisted of 3.5-kHz shallow-penetration seismic reflection records and side-

scan sonar records with 150-m range on each side of 610-m-spaced tracklines. Although data interpretation is incomplete, bottom roughness patterns and trends of linear bedforms (sand ribbons and de-graded sand waves) have been mapped from sidescan data (Fig. 6). These bedforms appear as alternating light and dark bands corresponding to fine- and coarse-

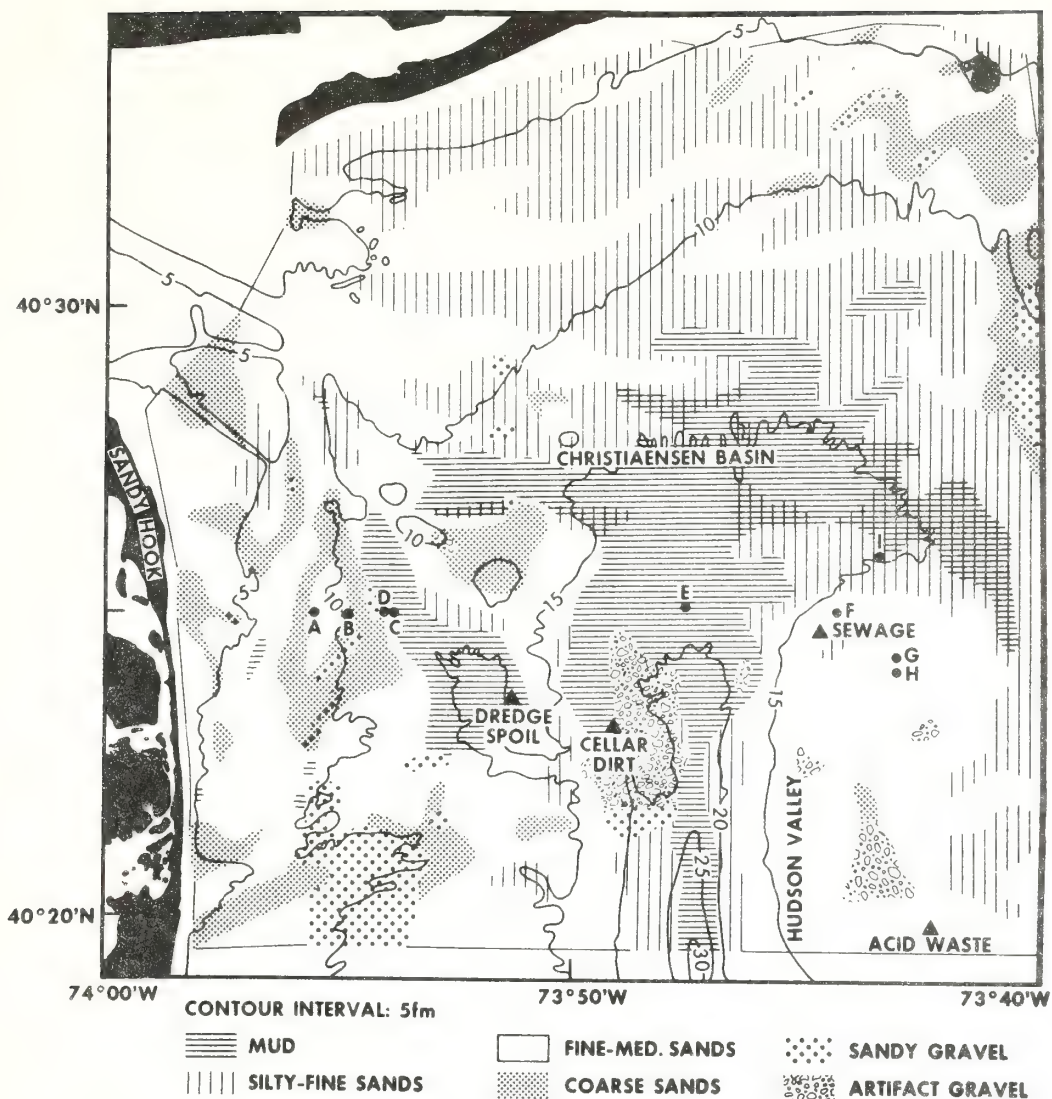


Fig. 5. Distribution of surficial sediment based on visual sample examination. Bathymetry from 1936 data.

grained sediment or as isolated dark bands. Streaky, patchy, and rough textures are associated with the dredge spoil and cellar dirt dumpsites and may be related to individual dumps.

Preliminary analysis of seismic data shows filling of the Hudson Shelf Valley from Cholera Bank.

Suspended sediment studies are particularly important in the bight apex because of the large amounts of fine particles dispersed in the water by waste disposal operations.

These particles are in addition to the fine sediments discharged from the Hudson River, other river mouths, and tidal inlets connected to coastal wetlands. Fine-grained sediment is also eroded from the sea floor during storms. Of immediate concern is sewage sludge which contains bacterial, viral, and heavy metal contaminants that adhere to fine sediment particles in the water column. The suspended fraction of dredge spoils is also probably similarly contaminated. All of these fines are largely re-

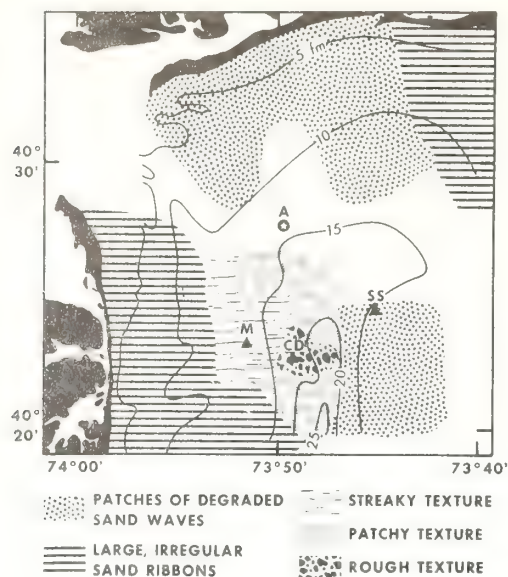


Fig. 6. Distribution of bottom roughness patterns from sidescan sonographs. Blank area NW and SE of Ambrose Light (A) shows no bedforms. M—Dredge spoil dumpsite; CD—cellar dirt site; SS—sewage sludge site.

tained in the nearshore water column as a consequence of the bight circulation pattern.

Suspended sediment studies were initiated in the bight apex during 1973 when sample stations were occupied to collect chemical and physical oceanographic data. Water samples were collected, filtered, and examined from the surface, 10-m depth, and the bottom at 25 stations. Preliminary

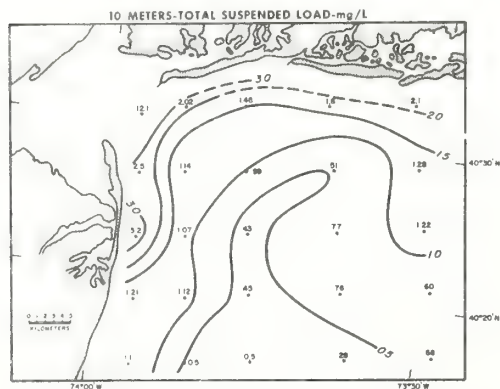


Fig. 7. Total suspended sediment load in waters at 10-m depth, late November 1973. (From Drake 1974.)

results for data taken in fall 1973 (Drake 1974; Figs. 7–10) indicate the existence of a fair-weather, clockwise current-circulation gyre, driven in part by the southwest drift of offshore shelf water. This has been verified by current meter studies in the

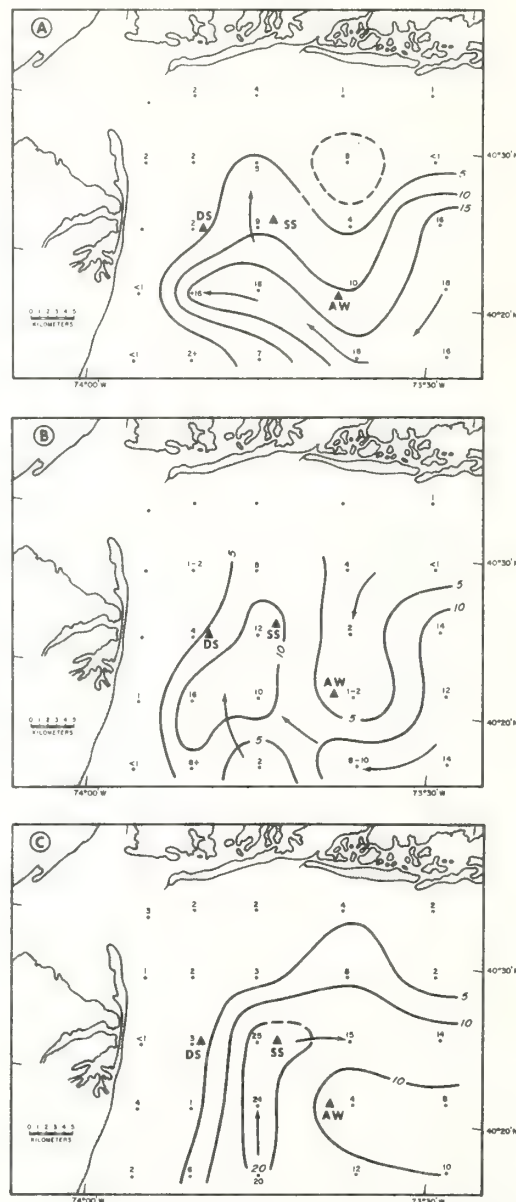


Fig. 8. Distribution of ferric hydroxide particles in the water column in late November 1973 (grains  $\times 10^3$ /liter). A—Surface; B—midwater; C—bottom water. (From Drake 1974.)



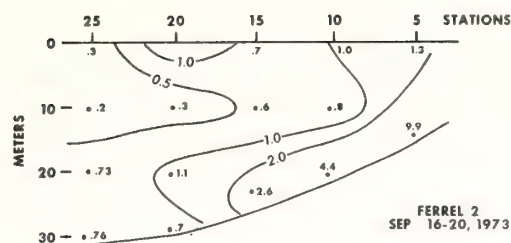


Fig. 9. Vertical distribution of total suspended load (in mg/liter) seaward of Long Beach, Long Island. (From D. E. Drake unpublished.)

apex (Charnell and Hansen 1974). Part of the total suspended load in the bight apex is easily identifiable, red-orange ferric hydroxide particles. These particles are formed by precipitation of iron in seawater as the result of acid waste dumping. They constitute an excellent tracer of suspended sediment circulation. The vertical distribution of suspended sediment shows high values (1.0 mg/liter) near the surface, and 2.0 mg/liter in the near-bottom "nepheloid" layer, typical of shelf areas (Fig. 9). It is expected that this layer will transport much of the suspended particulate matter and its associated contaminants.

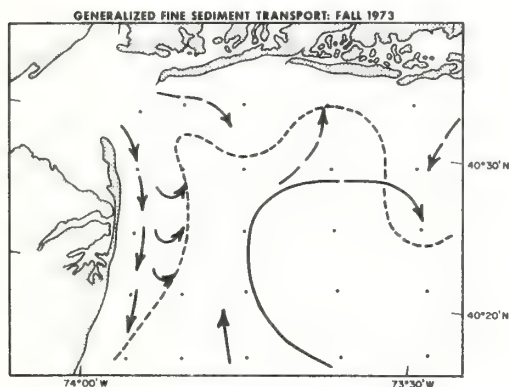


Fig. 10. Fine sediment transport system as inferred from distribution of suspended sediments during fall 1973. Dashed line is mean position of boundary between more turbid coastal water and less turbid offshore water. Clockwise gyre is apparently driven by southwesterly drift of offshore shelf water, and, on the bottom, by influx of saline water into New York Harbor. Regional currents which appear to be persistent are indicated by solid arrows. (From Drake 1974.)

Preliminary results show there is a concentration of fine-grained sediment in enclosed lows in the Hudson Valley axis, sandy mud in the remainder of the valley axis, and coarser sediment up the flanks of the valley and onto the shelf.

#### *Alternative dumping area studies*

Two midshelf areas have been designated as possible interim alternative dumping areas for sewage sludge and dredge spoils from the New York metropolitan area (see Fig. 1). The northern area is to be a minimum of 46 km from the Long Island shoreline, 18 km from the axis of the Hudson Shelf Valley, and 120 km from the entrance to New York Harbor. The southern area is seaward of the 36-m isobath and the same distances from the Hudson Valley axis and the New York Harbor entrance as the northern area (areas 2D1 and 2D2 on Fig. 1). Each area is 18.5×18.5 km.

**Northern area**—In the northern area (Fig. 1, 2D1), the sampling grid was placed seaward of the center of the location-criteria triangle to investigate, in part, a shallow tributary valley of the ancestral Long Island drainage system. The surficial sediments consist of sand with some areas of over 5% gravel (Fig. 11). Fine sands lie in the north-eastern part of the area, medium sands cover the western and southern parts, with a gravel deposit ( $\leq 39\%$  gravel) at one station associated with an area of coarser medium sand in the southern part of the area. Only two stations contained  $>5\%$  mud. Bottom photographs indicate that the area is characterized by a smooth, slightly undulatory, mounded or rippled bottom. Side-scan sonar records reveal elongate dark areas which may be erosional windows in the Holocene sand sheet that expose the basal Holocene pebbly sand or may be areas of abundant large shell fragments. Grab samples were spaced too far apart to be definitive. Bottom photo and submersible-observation data support the existence of windrows of shell fragments.

**Southern area**—The southern study area in Fig. 1 (2D2) is centered over the broad, flat high of the Hudson divide (Fig. 12). To

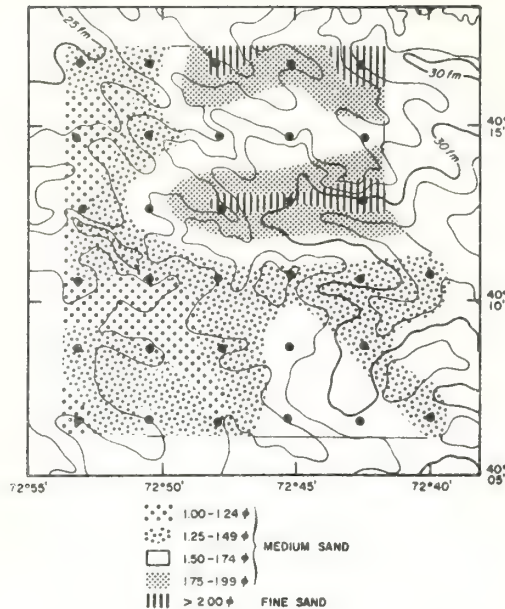


Fig. 11. Northern proposed interim alternative dumping area (2D1 on Fig. 1). Grain-size distribution of sand-sized fraction. Large dots—sample stations. (Bathymetry from Stearns and Garrison 1967; 1-fm contour intervals.)

the northeast the bottom grades gently into the Hudson Shelf Valley, while the western section is characterized by northeast-trend-



Fig. 12. Southern proposed interim alternative dumping area (2D2 on Fig. 1). (Bathymetry from Stearns and Garrison 1967, 1-fm contour intervals.) Solid lines—geophysical tracklines; bars—sites of dives by submersibles.

ing ridge and swale topography. Geophysical data, sediment samples, and two dives in submersibles showed that grain-size patterns appear to be related to bottom topography; coarser sand and gravel deposits lie on the crest and east flank of the Hudson divide, while medium- and fine-grained sand occur in the ridge and swale topography (Fig. 13). These distributions suggest that fine sediment is winnowed from the crest and east flank of the divide and deposited to the west. Observations from a submersible in Veatch and Smith Trough reveal a veneer of shelly, pebbly sand with large, angular clay pebbles and occasional oyster shells derived from the underlying early Holocene lagoonal clay. Seismic data also reveal that the reflector associated with this surface outcrops on the ridge flank. It appears that storm-generated currents from the northeast have winnowed the east flank of the Hudson divide and formed or maintained the ridge and swale topography on the west side of the divide.

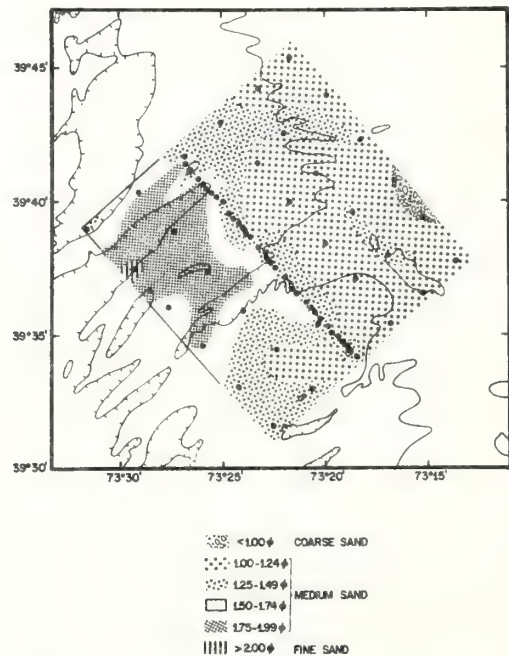


Fig. 13. Southern proposed interim alternative dumping area, (2D2 on Fig. 1). Grain-size distribution of sand-sized fraction. Large dots—sample stations. (Only the 20-fm isobath is shown.)



**Suspended sediment**—As previously mentioned, most fluvial suspended sediment is effectively trapped in estuaries and coastal wetlands. Consequently, the terrigenous fraction of the suspended matter decreases rapidly seaward. Suspended solids throughout the water column in the alternative dumping areas were predominately plankton and their noncombustible remains. Total suspended matter concentration in surface water is from 100–500  $\mu\text{g/liter}$ , comprised of 5% or less terrigenous matter, 80% combustible matter, and 15% siliceous and calcareous noncombustible planktonic remains (D. E. Drake personal communication). Subsurface water-suspended matter concentration is similar or somewhat less, except in the nepheloid layer 5–10 m above bottom. There, suspended matter concentrations are 500–2,000  $\mu\text{g/liter}$ , consisting of 30–60% combustible matter and 50–80% noncombustible matter which includes 10–20% terrigenous matter. Textural properties of sediment deposits in the alternative dumping areas show that very little sediment finer than 62 microns is present.

## References

- CHARNELL, R. L., AND D. V. HANSEN. 1974. Summary and analysis of physical oceanography data collected in the New York Bight apex during 1969–1970. NOAA-MESA Rep. 74–3. 74 p.
- DRAKE, D. E. 1974. Suspended particulate matter in the New York Bight apex: September–November 1973. NOAA Tech. Rep. ERL 318-MESA 1.
- DUANE, D. B. 1969. Sand inventory program. A study of New Jersey and northern New England coastal waters. Shore Beach October.
- , M. E. FIELD, E. P. MEISBURGER, D. J. SWIFT, AND S. J. WILLIAMS. 1972. Linear shoals on the Atlantic inner continental shelf, Florida to Long Island, p. 447–498. In D. J. Swift et al. [eds.], Shelf sediment transport: Process and pattern. Dowden, Hutchinson & Ross.
- FISCHER, A. G. 1961. Stratigraphic record of transgressing seas in light of sedimentation on Atlantic coast of New Jersey. Bull. Am. Assoc. Pet. Geol. 45: 1656–1666.
- FOLGER, D. W. 1972a. Texture and organic carbon content of bottom sediment in some estuaries of the United States, p. 391–408. In B. W. Nelson [ed.], Environmental framework of coastal plain estuaries. Geol. Soc. Am. Mem. 133.
- . 1972b. Characteristics of estuarine sediments of the United States. U.S. Geol. Surv. Prof. Pap. 742. 94 p.
- FREELAND, G. L., AND D. J. SWIFT. In press. Surficial sediments. NOAA-MESA New York Bight Atlas Monogr. 10.
- GROSS, M. G. 1972. Geologic aspects of waste solids and marine waste deposits, New York metropolitan region. Geol. Soc. Am. Bull. 83: 3163–3176.
- HATHAWAY, J. C. 1972. Regional clay mineral facies in estuaries and continental margin of the U.S. East Coast, p. 293–316. In B. W. Nelson [ed.], Environmental framework of coastal plain estuaries. Geol. Soc. Am. Mem. 133.
- KNOTT, S. T., AND H. HOSKINS. 1968. Evidence of Pleistocene events in the structure of the continental shelf of the northeastern U.S. Mar. Geol. 6: 5–43.
- McKINNEY, T. F., AND G. M. FRIEDMAN. 1970. Continental shelf sediments of Long Island, N.Y. J. Sediment. Petrol. 40: 213–218.
- , W. L. STUBBLEFIELD, AND D. J. SWIFT. 1974. Large-scale current lineations on the central New Jersey shelf: Investigations by side-scan sonar. Mar. Geol. 17: 79–102.
- MANHEIM, F. T., R. H. MEADE, AND G. C. BOND. 1970. Suspended matter in surface waters of the Atlantic continental margin from Cape Cod to the Florida Keys. Science 167: 371–376.
- MEADE, R. H. 1969. Landward transport of bottom sediments in estuaries of the Atlantic Coastal plain. J. Sediment. Petrol. 39: 222–234.
- . 1972a. Transport and deposition of sediments in estuaries, p. 91–120. In B. W. Nelson [ed.], Environmental framework of coastal plain estuaries. Geol. Soc. Am. Mem. 133.
- . 1972b. Sources and sinks of suspended matter on continental shelves, p. 249–262. In D. J. Swift et al. [eds.], Shelf sediment transport: Process and pattern. Dowden, Hutchinson & Ross.
- MILLIMAN, J. D. 1972. Marine geology, p. 10–1 to 10–91. In Coastal and offshore environmental inventory, Cape Hatteras to Nantucket Shoals. Mar. Publ. Ser. 6. Univ. R.I.
- , AND K. O. EMERY. 1968. Sea levels during the past 35,000 years. Science 162: 1121–1123.
- MUELLER, J. A., A. R. ANDERSON, AND J. S. JERIS. 1976. Contaminants entering the New York Bight: Sources, mass loads, significance. Am. Soc. Limnol. Oceanogr. Spec. Symp. 2: 162–170.
- POSTMA, H. 1967. Sediment transport and sedimentation in the estuarine environment, p. 158–179. In C. H. Lauff [ed.], Estuaries. Publ. Am. Assoc. Adv. Sci. 83.
- SCHLEE, J. 1973. Atlantic continental shelf and slope of the U.S. Sediment texture of the



- northeast part. U.S. Geol. Surv. Prof. Pap. 529-L. 64 p.
- . 1975. Sand and gravel. MESA New York Bight Atlas Monogr. 21. 26 p.
- SHERIDAN, R. E., C. E. DILL, JR., AND J. C. KRAFT. 1974. Holocene sedimentary environment of the Atlantic inner shelf off Delaware. *Geol. Soc. Am. Bull.* **85**: 1319–1328.
- STAHL, L., J. KOCZAN, AND D. J. SWIFT. 1974. Anatomy of a shoreface-connected sand ridge on the New Jersey shelf: Implications for the genesis of the surficial sand sheet. *Geology* **2**: 117–120.
- STEARNS, F., AND L. E. GARRISON. 1967. Bathymetric maps, middle Atlantic U.S. continental shelf, 1:125,000. NOAA, Natl. Ocean Surv.
- STUBBLEFIELD, W. L., M. DICKEN, AND D. J. SWIFT. 1974. Reconnaissance of bottom sediment on the inner and central New Jersey shelf. NOAA-MESA Rep. 1.
- , J. W. Lavelle, T. F. MCKINNEY, AND D. J. SWIFT. 1975. Sediment response to the present hydraulic regime on the central New Jersey shelf. *J. Sediment. Petrol.* **45**: 337–358.
- SWIFT, D. J., G. L. FREELAND, P. E. GADD, C. HAN, J. W. LAVELLE, AND W. L. STUBBLEFIELD. 1976. Morphologic evolution and coastal sand transport, New York–New Jersey shelf. *Am. Soc. Limnol. Oceanogr. Spec. Symp.* **2**: 69–89.
- , J. W. KOFOED, F. P. SAULSBURY, AND P. SEARS. 1972. Holocene evolution of the shelf surface, central and southern Atlantic shelf of North America, p. 499–574. *In* D. J. Swift et al. [eds.], *Shelf sediment transport: Process and pattern*. Dowden, Hutchinson & Ross.
- UCHUPI, E. 1963. Sediments on the continental margin off eastern U.S. U.S. Geol. Surv. Prof. Pap. 475-C, p. C132–C137.
- . 1970. Atlantic continental shelf and slope of the U.S.—shallow structure. U.S. Geol. Surv. Prof. Pap. 529-I.
- VEATCH, A. C., AND P. A. SMITH. 1939. Atlantic submarine valleys of the United States and the Congo Submarine Valley. *Geol. Soc. Am. Spec. Pap.* 7.
- WILLIAMS, S. J. 1975. Anthropogenic filling of the Hudson River shelf channel. *Geology* **10**: 597–600.
- . 1976. Geomorphology, shallow subbottom structure, and sediments of the Atlantic intercontinental shelf off Long Island, New York. U.S. Army Corps Eng. Coastal Eng. Res. Center Tech. Pap. 76–2. 123 p.
- , AND D. B. DUANE. 1974. Geomorphology and sediments of the inner New York Bight continental shelf. *Tech. Memo.* 45. U.S. Army Corps Eng. Coastal Eng. Res. Center. 81 p.

Virginia Institute of Marine Science, SRAMSOE, No. 143, June 10-11, 1977,  
23-1 - 23-17.

BEACH RESPONSE IN THE VICINITY OF A  
SHOREFACE RIDGE SYSTEM: FALSE CAPE, VIRGINIA

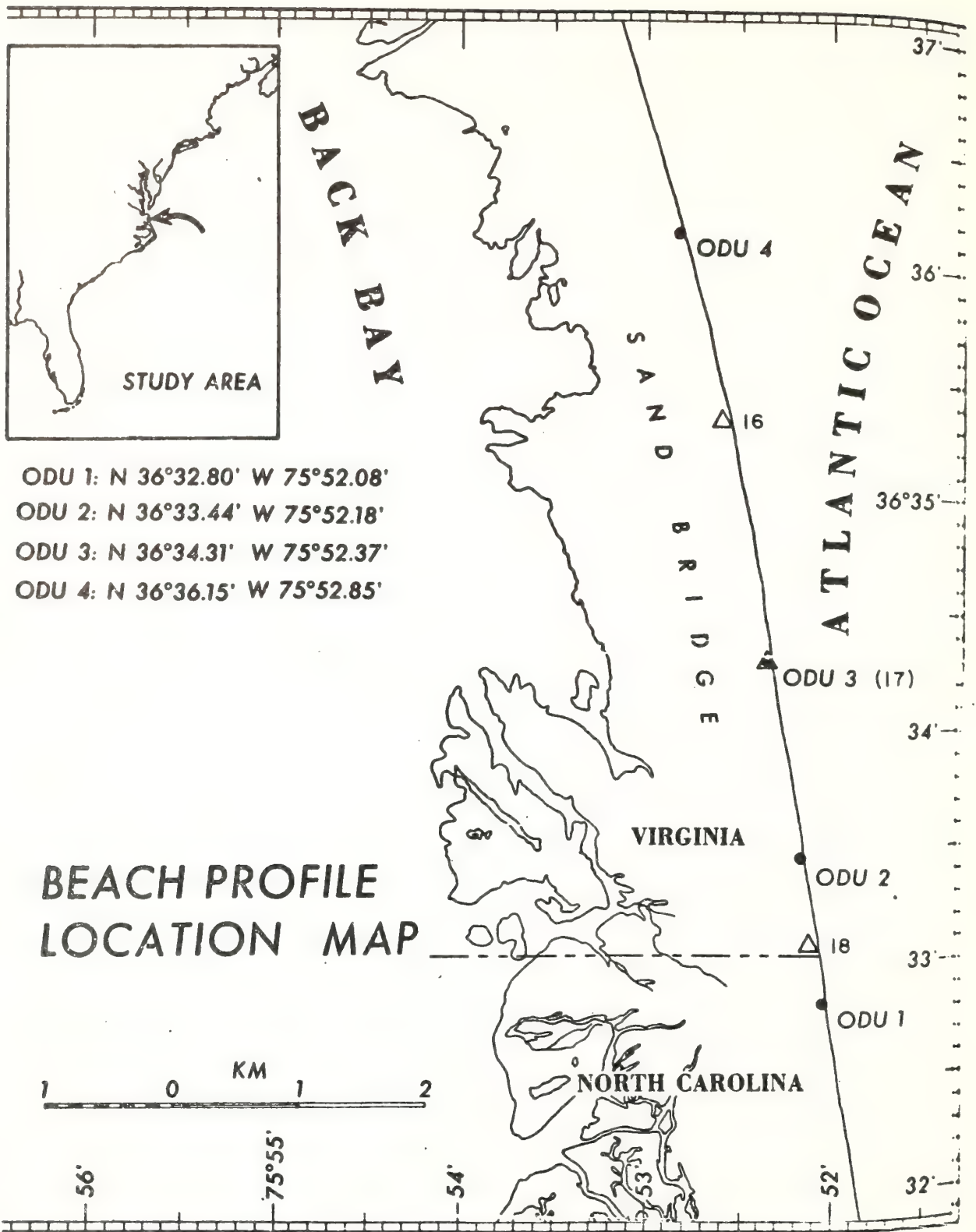
Victor Goldsmith, Gerald L. Shideler<sup>1</sup>,  
John F. McHone<sup>1</sup> and D.J.P. Swift<sup>1</sup>

INTRODUCTION

Submarine ridge and swale systems constitute a conspicuous topographic element of the Middle Atlantic shelf. These ridge systems are morphologically diversified, and have been extensively described by several investigators (e.g., Shepard, 1963; Uchupi, 1968; Duane, et al., 1972; Swift, et al., 1972b). One of the most interesting and perplexing varieties of submarine ridges are the oblique-trending, shoreface-connected ridges, such as ideally exemplified at False Cape, Virginia (Fig. 1). The genetic significance of the False Cape Ridge System has been an issue of controversy. Sanders (1962) has suggested that the ridges are relict Pleistocene beach ridges. However, more recent studies of the system suggest that they represent large-scale modern hydraulic bedforms that are maintained by southward flowing coast-parallel storm currents (Swift, et al., 1972a, 1973; McHone, 1972). Even more recently, Swift (1976a and b) suggested that the ridges form in response to southward moving coastal jet currents formed on the shelf in response to winter northeaster storms. Additional studies by Hunt, et al. (1977) and Swift, et al. (1977) indicate that large bedforms are associated with the linear ridges.

---

<sup>1</sup>A draft of this paper was jointly prepared in 1972 using beach profile data collected by the last three authors while at Old Dominion University, Norfolk. It was revised for this volume by the first author, who added the VIMS-CERC profile data and who accepts full responsibility for all conclusions and shortcomings.





In an attempt to explain the sediment source for ridge construction, a conceptual model has been hypothesized (Swift, et al., 1970); the model employs the Bruun coastal retreat concept (Bruun, 1962; Schwartz, 1965), whereby shoreface erosion along a retrograding coast during rising sea level results in equal-volume aggradation along the adjacent sea floor. The aggraded sediment may then be subsequently molded into a shoreface-connected ridge by the modern hydraulic regime. After development, the ridge would function as a feedback element by influencing coastal currents and impinging wave characteristics. In turn, this feedback influence could exert control over erosional and accretionary processes along the adjacent beach sector, as manifested in beach morphology. The False Cape Ridge illustrated in Figure 1 shoals and closes toward the south; consequently, differential influences might be anticipated along the beach sector adjacent to the ridge. Such differential effects have been noted along the adjacent subaqueous shoreface during the 1922-1969 interval, where erosion occurred along the central and northern portions of the sector, while the southern portion was characterized by accretion (Swift, et al., 1972). Similar differential effects were also noted along the adjacent beach of this sector for the same time interval (Felton, unpublished manuscript, Norfolk District Corps of Engineers), with retrogression toward the north, and progradation toward the south.<sup>2</sup>

The purpose of the present paper was to gain greater insight into the influences exerted by the False Cape submarine ridge on beach processes along the adjacent coastal sector. This was accomplished by conducting a time series study of beach morphology during the 1969-1972 interval. Beach topographic profiles were obtained periodically at four selected stations along the coastal sector adjacent to the False Cape Ridge (Fig. 1), employing the leveling technique described by Emery (1961). The comparative profile data were processed with an IBM 360 computer, employing a curve plotting program which permitted direct volumetric comparisons of morphological variations occurring during sequential time intervals (Colonell and Goldsmith, 1972). It was believed that a study of this nature might be helpful in predicting the response characteristics of similar beach sectors throughout the world which are flanked by shoreface-connected ridge systems.

---

<sup>2</sup>See Sutton, this volume.

## 1969-1971 BEACH PROFILE DATA (O.D.U.)

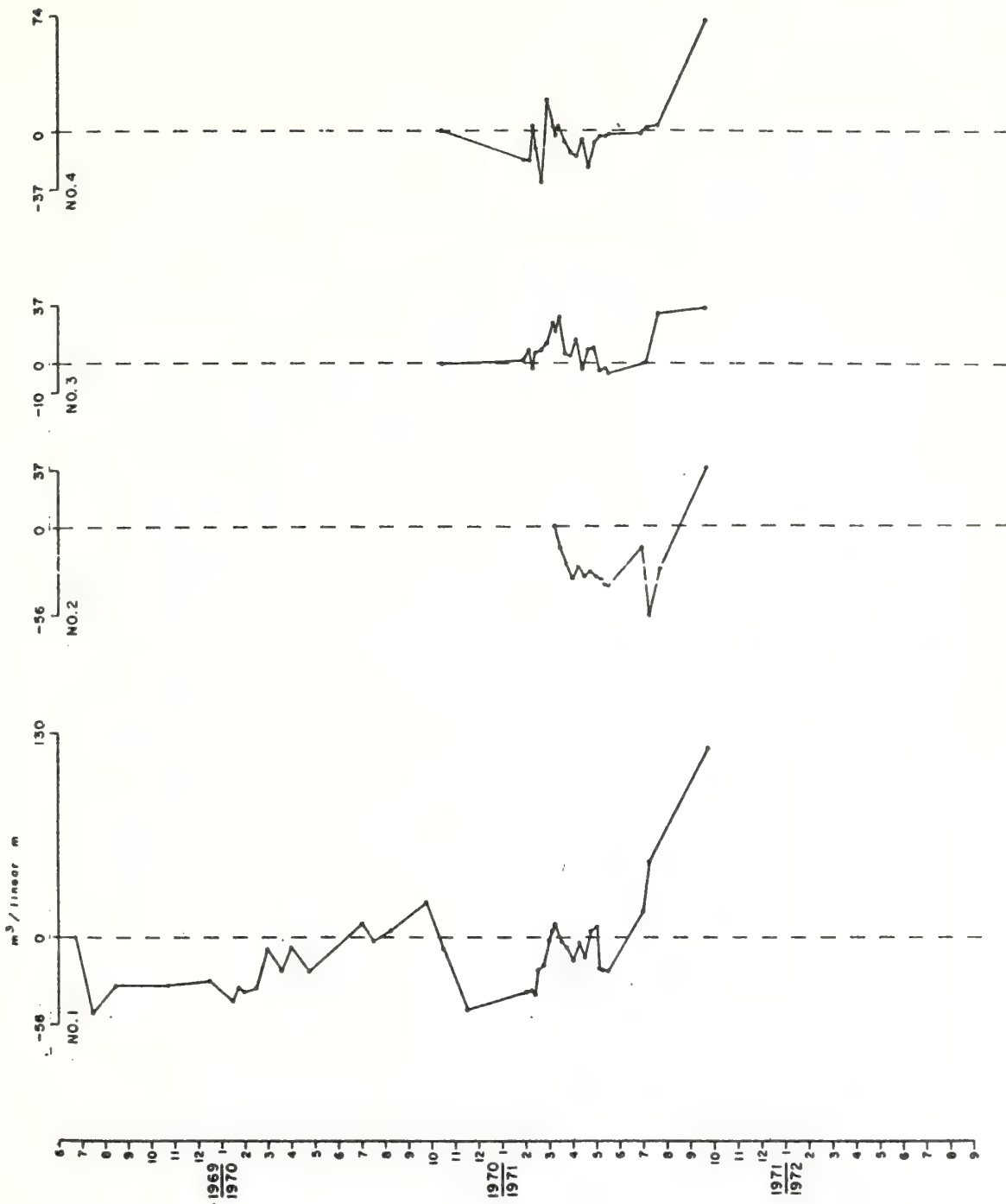
ODU-1 at the south end of the studied sector illustrates the most extensive coverage, ranging from June, 1969 to September, 1971 (Fig. 2). This 27-month curve nicely illustrates two distinct sources of variability: (1) Long-period trend - this trend consists of a cyclic component that appears to generally reflect seasonal variations in the hydraulic regime, though not in every season. The fall and winter months can be generally characterized as an erosional or destructive phase. In contrast, the spring and summer months are generally characterized as accretionary phases.

On an annual basis, this particular beach section appears to approach a condition of dynamic equilibrium over the monitored 27-month interval. If mid-June is used as a reference point, the cumulative curve illustrates a nearly constant annual transfer of sand, with very little net loss or gain from this specific locality. However, on a longer term secular basis (e.g., 1922-1969), this may be a prograding locality. Progradation is suggested by what appears to be an accretionary linear component of the long-term trend. This would be compatible with other data (e.g., Swift, et al. 1972) suggesting progradation in the southern end of the False Cape sector. This station exhibits a total net change consisting of 120 m<sup>2</sup> of accretion over the monitored time interval.<sup>3</sup> (2) Short-period variations - relatively short period variations superimposed on the long-period trend reflect highly transient events, such as storm erosion and subsequent beach rebuilding episodes. The most prominent events, which involved volumetric changes exceeding 28 m<sup>2</sup>/linear meter occurred during the following comparison intervals: 6/30/69-7/18/69 (49 m<sup>2</sup> erosion), 4/26/70-7/8/70 (30 m<sup>2</sup> accretion), 9/25/70-10/20/70 (29 m<sup>2</sup> erosion), 10/20/70-11/17/70 (31 m<sup>2</sup> erosion), 5/22/71-7/4/71 (38 m<sup>2</sup> accretion), 7/4/71-7/14/71 (31 m<sup>2</sup> accretion), and 7/14/71-9/26/71 (73 m<sup>2</sup> accretion).

The cumulative curve from ODU-2 provides only a 7-month coverage from March, 1971 to September, 1971. The curve

---

<sup>3</sup>Profile changes are presented here in area change between two successive beach profiles (ODU data) or in volume change/linear meter of beach (VIMS-CERC data). Since the volume is for one linear meter of beach, the numbers are actually the same for volume and area.



23-5



is of insufficient length to delineate a long-term trend, but it does illustrate a total net change consisting of  $37 \text{ m}^2$  of accretion. The curve illustrates short period transient events. The most prominent events ( $> 28 \text{ m}^2$ ) occur in succession during the latter three comparison intervals: 7/4/71-7/14/71 ( $43 \text{ m}^2$  erosion), 7/14/71-7/28/71 ( $31 \text{ m}^2$  accretion), and 7/28/71-9/26/71 ( $63 \text{ m}^2$  accretion). This sequence appears to reflect a major storm, followed by an extensive rebuilding phase.

The cumulative curve from ODU-3 provides an eleven-month coverage from October, 1970 to September, 1971. The curve is of insufficient length to delineate a well-developed long-period trend, but it does illustrate a total net change consisting of  $34 \text{ m}^2$  of accretion. Short-period transient variations are readily apparent; the most prominent transient event occurred during the 7/14/71-7/28/71 comparison interval, resulting in  $31 \text{ m}^2$  of accretion.

The cumulative curve from ODU-4 also provides an eleven-month coverage from October, 1970 to September, 1971. The curve's short length does not adequately delineate a long-term trend, but it does illustrate a total net change consisting of  $71 \text{ m}^2$  of accretion. The curve also illustrates some short-period transient events, with the most prominent ones occurring during the 2/27/71-3/5/71 interval ( $52 \text{ m}^2$  accretion), and the 7/28/71-9/26/71 ( $68 \text{ m}^2$  accretion) interval.

In comparing the time series response characteristics of the four beach stations, the only available comparison interval is from March, 1971 to September, 1971. During this interval, the cumulative curves of the four stations do illustrate differences in magnitude, but not in occurrence of net erosion and accretion. This indicates differential beach response characteristics in a north-south direction, possibly induced by the southward shoaling False Cape Ridge, since the most accretional profile is ODU-1. There are two features which correlate well among the four curves. One feature is the brief two-cycle sequence of minor erosion and accretion which occurred during April, 1971. The second feature is a major accretionary phase which commenced during July, 1971, and continued into September, 1971. In general, erosion and accretion occur simultaneously at all four locations, but differ in magnitude. This suggests that the False Cape Ridge is only partially effective in inducing differential beach response characteristics along the studied sector over the short term.

## 1969-1976 BEACH PROFILE DATA (VIMS-CERC)

These data include the reoccupied profile locations of ODU-3 (VIMS No. 17) and Harrison and Bullock, 1972 (VIMS Nos. 15, 16 and 18) (Figs. 1 and 3). The tape and level surveying methods employed in the 1974-1976 VIMS-CERC study, and other pertinent aspects are discussed in Goldsmith, et al., 1977, and in this volume. Net longshore transport is concluded to be to the south in the False Cape area (Goldsmith, et al., 1977).

Figure 3 illustrates the relation between the beach profile locations and the adjacent offshore bathymetry (from Sutton, et al., 1976). Note that profile locations 17 (ODU-3), ODU-2, 18 and ODU-1 are opposite the portion of the relatively shallow False Cape Ridge System which abuts against the shore; and that profile locations 15, 16 and ODU-4 are opposite a steeper portion of the nearshore where the 30' depth contour (9.1 m) is much closer to shore.

Figures 4 through 7 show the volume changes at profile locations 15, 16, 17 (ODU-3) and 18, respectively, between 1969 and 1976. Profile locations 17 and 18 show very dramatic accretional trends. Whereas profile locations 15 and 16 show large volume fluctuations, the net accretional trend at 16 is quite subdued relative to locations 17 and 18, and 15 shows no trend. Table 1 gives the linear regression lines fitted to the volume trends, and the statistical tests for the goodness of fit (i.e., significance) of the linear regression lines.

It is interesting to note that a similar trend exists to the north, in that profile locations 12, 13, and 14, which are opposite a relatively wider shoreface, as delineated by the 30 ft (9.1 m) contour, are also characterized by larger net accretion.

This may be explained, simply, as due to the wider shoreface acting as a wave buffer, causing the frictional loss in wave energy as the waves pass over the shallower area. More complexly, the shoreface ridge systems may provide a conduit for longshore sediment transport, resulting in larger accumulations at the shorelines where the obliquely oriented ridge systems are attached to shore.

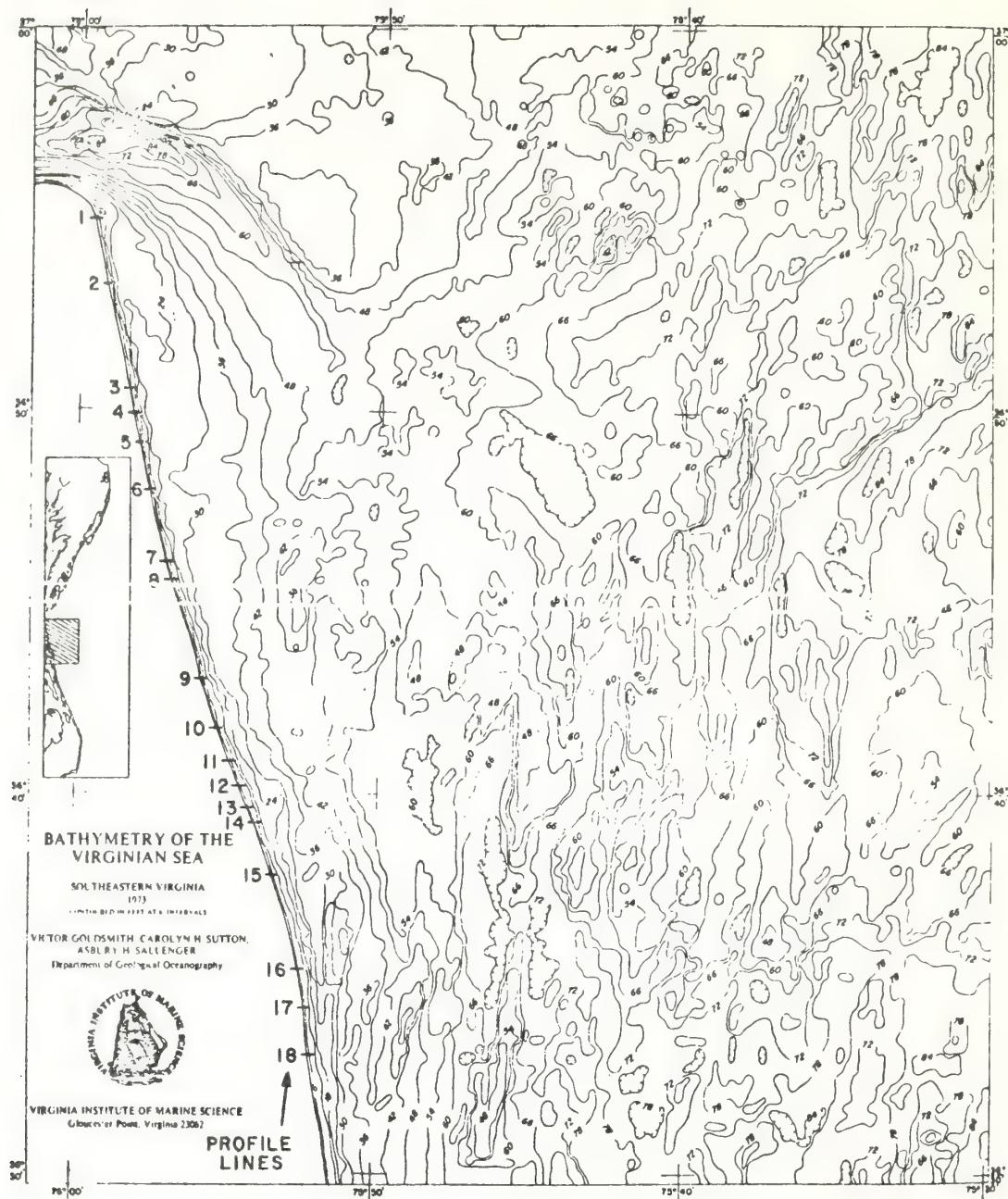


Figure 3. Bathymetry of southeast Virginia shelf; contours in feet (1 foot = 0.305 meter).



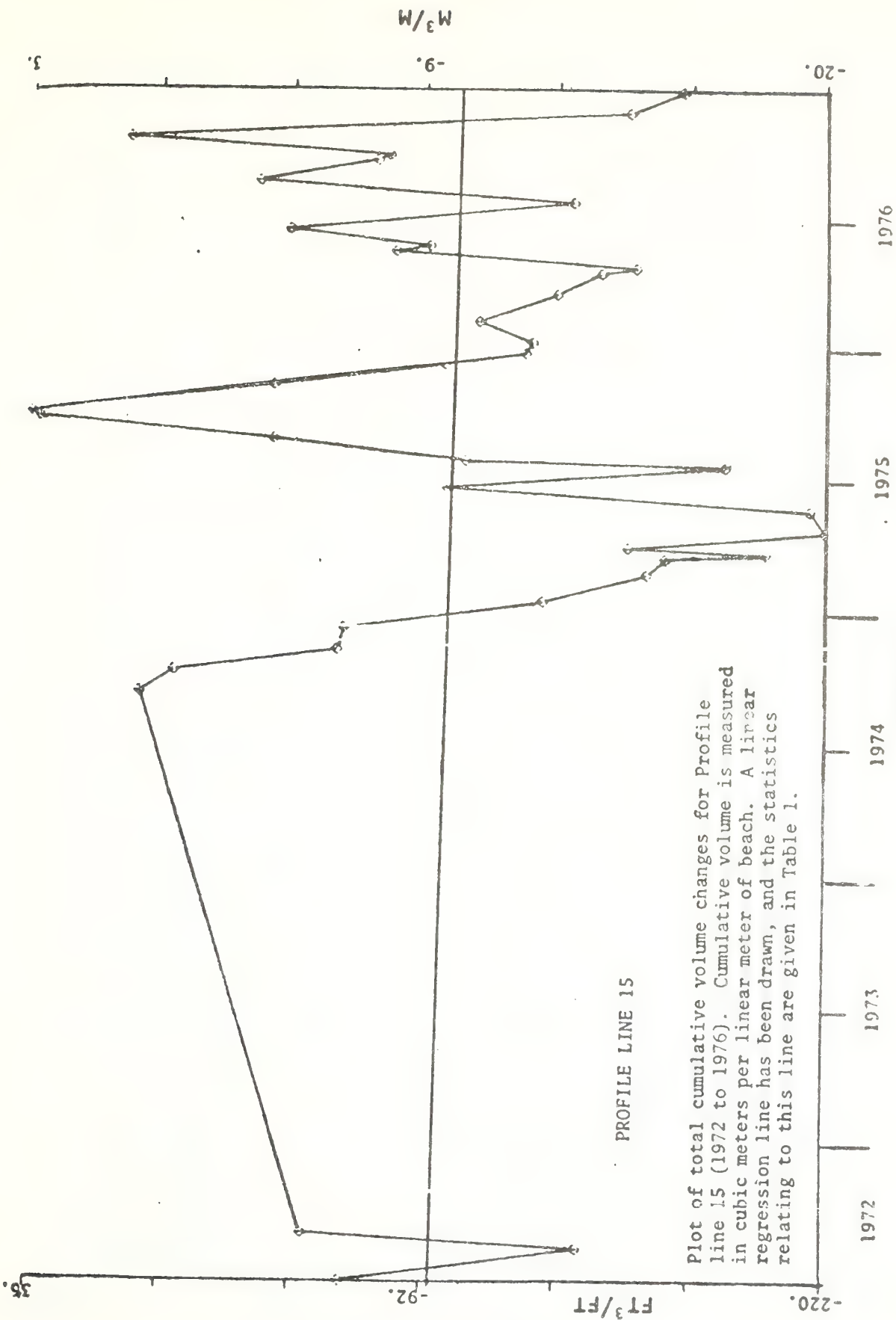
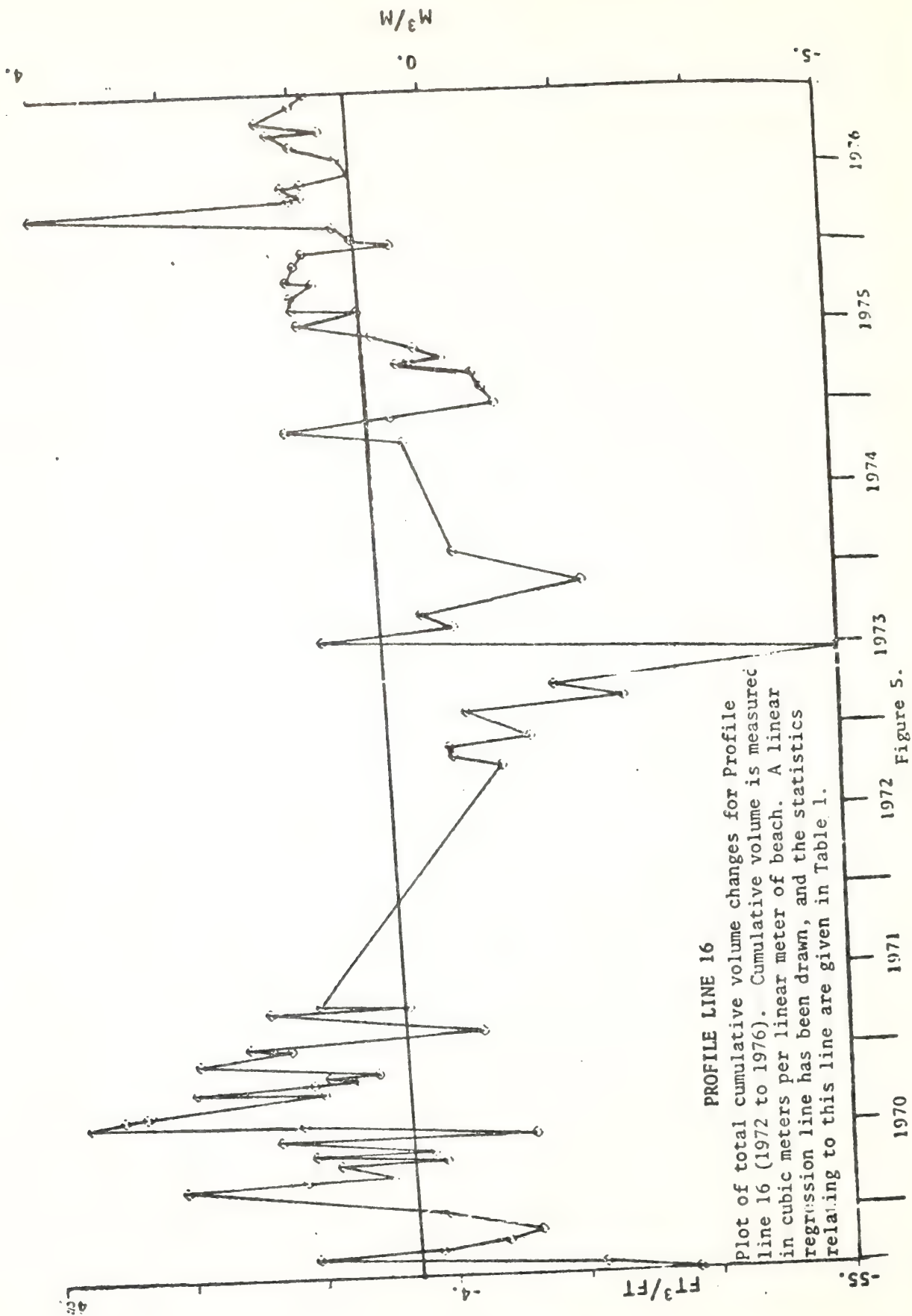


Figure 4.



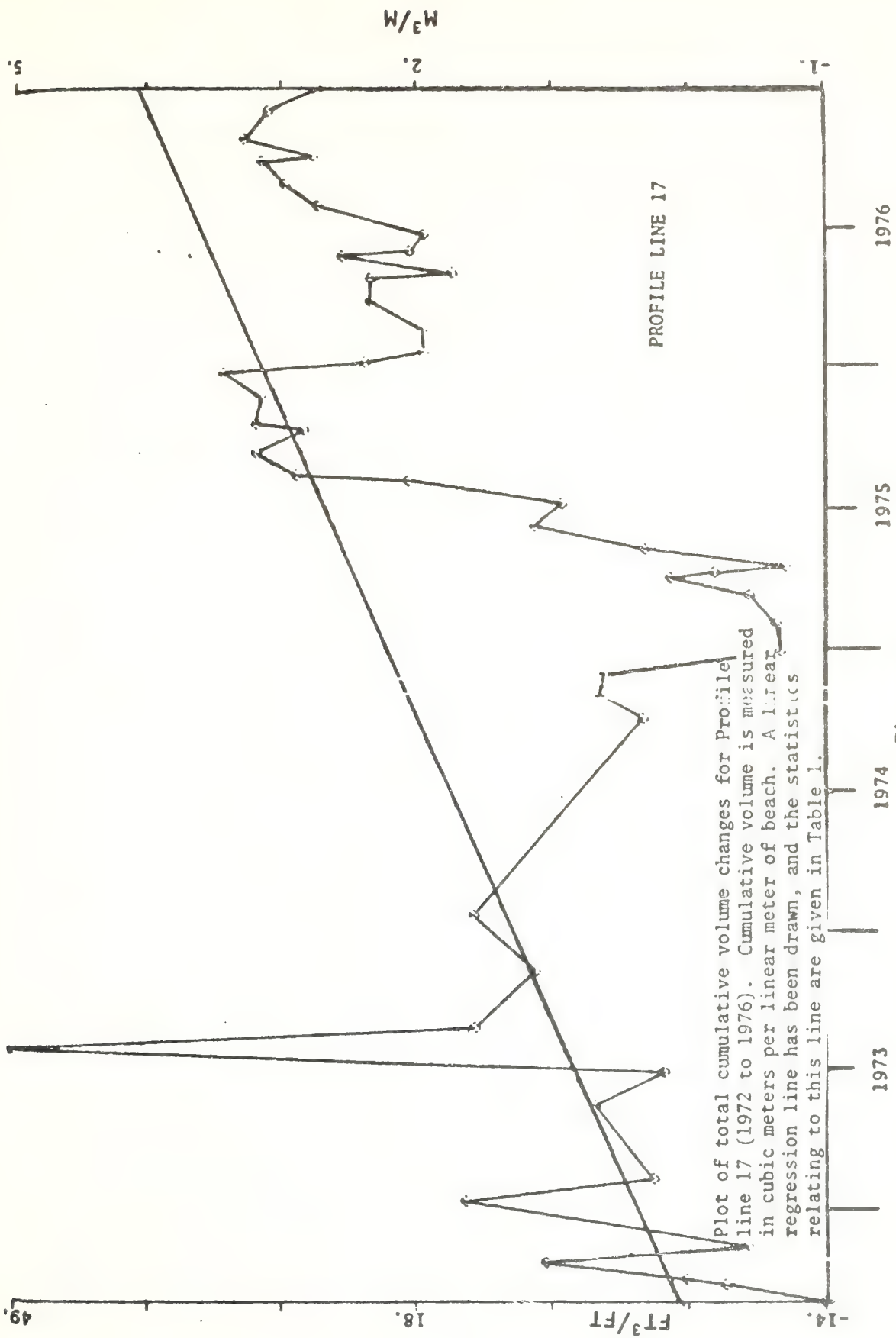


Figure 6.



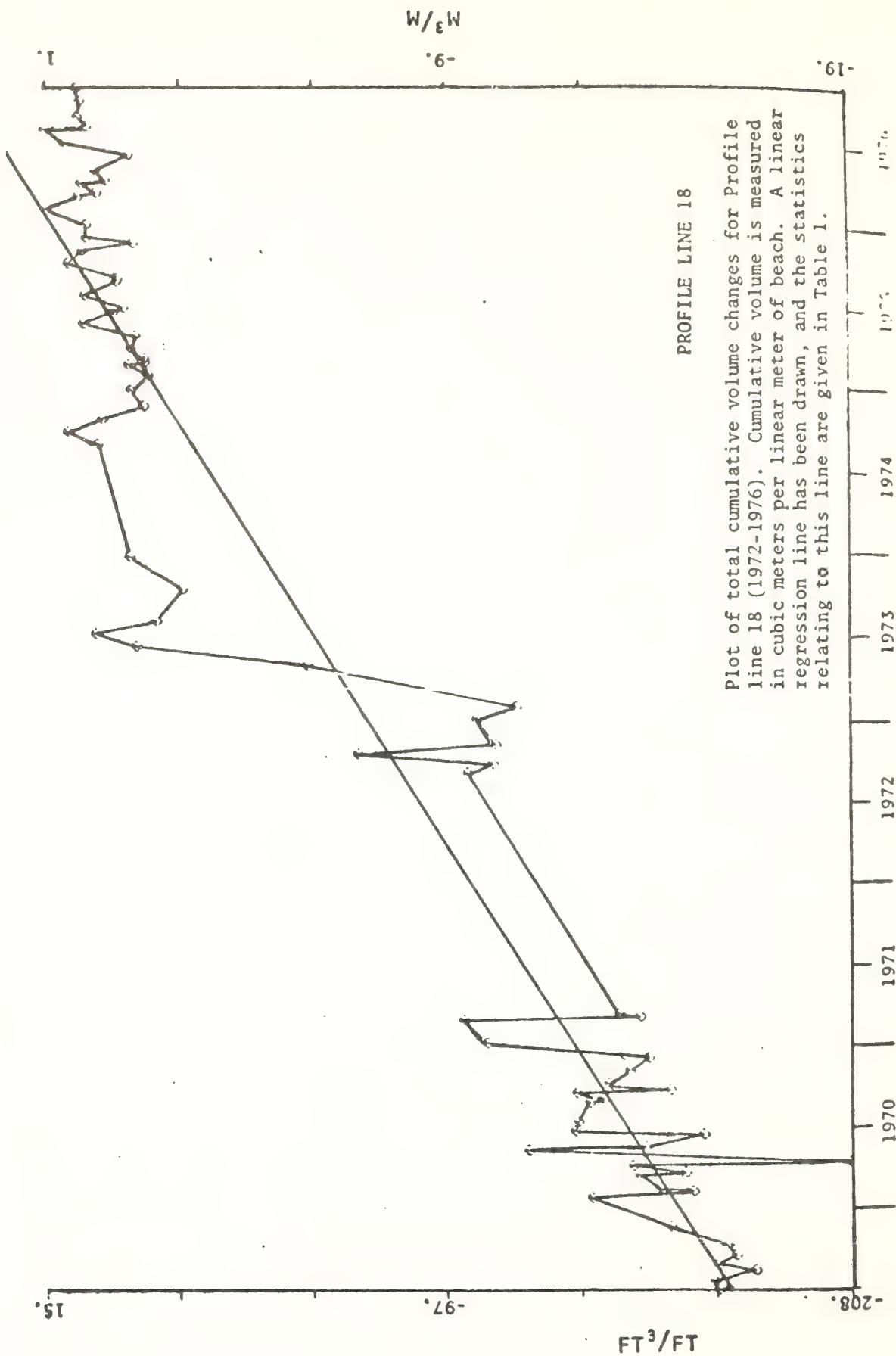


Figure 7.

Table 1 Linear regression lines fitted to the beach volume trends and statistical significance of the long-term trends.

<u>Profile line</u>	<u>Estimated coefficient</u>	<u>Y Intercept</u>	<u>R<sup>2</sup></u>	<u>Significance<sup>1</sup></u>	<u>Trend<sup>2</sup></u>
12	6.74	-2203.28	0.68	0.001	+
13	1.09	- 489.12	0.06	0.10	+
14	4.08	-1399.52	0.88	0.001	+
15	-0.05	- 85.93	0.001	0.90	=
16	0.04	46.60	0.001	0.001	+
17	1.26	- 232.90	0.31	0.001	+
18	5.47	-1741.74	0.92	0.001	+

<sup>1</sup>The lower the number, the higher the significance; e.g., 0.001 indicates that the erosion or accretion trend is not due to chance at the 99.9 percent level.

<sup>2</sup>+, accretion; -, erosion.

<sup>3</sup>Data does not meet basic assumptions.

## SUMMARY

Long-term beach trends (1969-1976) in the vicinity of the False Cape Ridge System show variations in the magnitude but not in the general concurrent occurrence of erosion and accretion. The most accretional beach profile locations (17 and 18) are opposite the area of attachment of the ridge system, and the least accretional profile locations are opposite the narrowest portion of the shoreface, as delineated by the 30 ft (9.1 m) contour.

These trends are not apparent in the short-term (1970-1971) beach profile data.

It is hypothesized that the larger accretional trends may be due to the obliquely-oriented ridges acting as conduit for longshore transport resulting in additional accretion at the profile locations opposite the area of ridge attachment to the shoreline. Since profile locations 15 and 16 are also the most active with respect to daily and weekly wave events, the ridge at shoreline attachment may also "dampen" these daily and weekly wave events.



## REFERENCES

- Bruun, P., 1962. Sea Level Rise as a Cause of Shore Erosion: Jour. Waterways Harbors Div., Amer. Soc. Civil Eng., V. 88, p. 117-130.
- Bullock, P.A., 1972. The Feasibility of Developing Forecast Systems to Predict Changes in Beach Sand Volume on Ocean Beaches During Storms: Masters Thesis, Virginia Institute of Marine Science, Gloucester Point, Va.
- Duane, D.B., Field, M.E., Meisburger, E.P., Swift, D.J.P., and Williams, S.J., 1972. Linear Shoals on the Atlantic Inner Continental Shelf, Florida to Long Island: in Processes and Patterns of Continental Shelf Sediment Transport: Swift, Duane, and Pilkey (editors), Dowden, Hutchinson and Ross Co., Stroudsburg, Pa.
- Emery, K.O., 1961. A Simple Method of Measuring Beach Profiles: Limn. and Ocean., V. 6, p. 90-92.
- Goldsmith, V., Sturm, S., Thomas, G., 1977. Variations in Beach Erosion and Accretion Trends at Virginia Beach, Virginia, and Vicinity: Final Report CERC Contract DACW-72-74-C-0008 and CERC Tech. Memo (in press), C.E.R.C., U.S. Army Corps of Engs., Ft. Belvoir, Virginia, VIMS SRAMSOE No. 122.
- Goldsmith, V., Sutton, C.H., and Davis, J.S. 1973. Bathymetry of the Virginian Sea-Continental Shelf and Upper Slope, Cape Henlopen to Cape Hatteras: Bathymetric Map, Virginia Institute of Marine Science, SRAMSOE No. 39.
- Hunt, R.E., Swift, D.J.P., Palmer, H., 1977. Construction Shelf Topography, Diamond Shoals, North Carolina: Geol. Soc. of Amer. Bull., Vol. 88, p. 299-311, 16 figs.
- McHone, J.F., Jr., 1972. Morphological Time Series From a Submarine Sand Ridge on the South Virginia coast: Unpublished M.S. Thesis, Old Dominion Univ., 59 p.

- Sanders, J.E., 1962. North-South Trending Submarine Ridge Composed of Coarse Sand Off False Cape, Virginia (abst): Amer. Assoc. Pet. Geol., Bull., Vol. 46, p. 278.
- Schwartz, M.L., 1965. Laboratory Study of Sea Level Rise as a Cause of Shore Erosion: Jour. Geology, Vol. 75, p. 76-92.
- Shepard, F.P., 1963. Submarine Geology: Harper and Row, N.Y., 567 p.
- Swift, D.J.P., 1976a. Coastal Sedimentation: Chapter 14, p. 255-310, In Marine Sediment Transport and Environmental Management, Stanley and Swift (eds.), Wiley, N.Y., 602 p.
- Swift, D.J.P., 1976b. Continental Shelf Sedimentation: Chapter 15, p. 311-350, In Marine Sediment Transport and Environmental Management, Stanley and Swift (eds.), Wiley, N.Y., 602 p.
- Swift, D.J.P., Holliday, B., Avignone, N., and Shideler, G., 1972a. Anatomy of a Shoreface Ridge System, False Cape, Virginia: Marine Geology, Vol. 12, p. 59-84.
- Swift, D.J.P., Kofoed, J.W., Saulsbury, F.P., and Sears, P., 1972b. Holocene Evolution of the Shelf Surface, Central and Southern Atlantic Shelf of North America: in Processes and Patterns of Continental Shelf Sediment Transport: Swift, Duane, Pilkey (editors), Douden, Hutchinson, and Ross Co., Stroudsburg, Pa.
- Swift, D.J.P., Lavelle, J.W., Ludwick, J.C., McHone, J.F., Shideler, G.L., McFall, J.C., Holliday, B.W., 1973. Ridge Fields of the Inner Virginia Shelf: Substrate Response to Wind and Wave Currents During Storms (abst.): Amer. Geophy. Union, Transactions, Vol. 54, p. 334.
- Swift, D.J.P., Sears, P.C., Bohlke, B., and Hunt, R., 1977. Evolution of a Shoal Retreat Massif, North Carolina: Inferences from Areal Geology: Marine Geology (in press).

- Swift, D.J.P., Shideler, G.L., Avignone, N.F., and Holliday, B.W., 1970. Holocene Transgressive Sand Sheet of the Middle Atlantic Bight - A Model for Generation by Shoreface Erosion (discussion paper): Geol. Soc. America, Abstracts with Programs, Vol. 2, p. 757-759.
- Uchupi, Elazar, 1968. The Atlantic Continental Shelf and Slope of the United States: Physiography: U.S. Geol. Survey Prof. Paper, 529-C, 30 p.



# Constructional shelf topography, Diamond Shoals, North Carolina

ROBERT E. HUNT  
DONALD J. P. SWIFT  
HAROLD PALMER

*Atlantic Oceanographic and Meteorological Laboratories, 15 Rickenbacker Causeway, Miami, Florida 33149*

*Dames and Moore, Inc., 7101 Wisconsin Avenue, Washington, D.C., 20014*

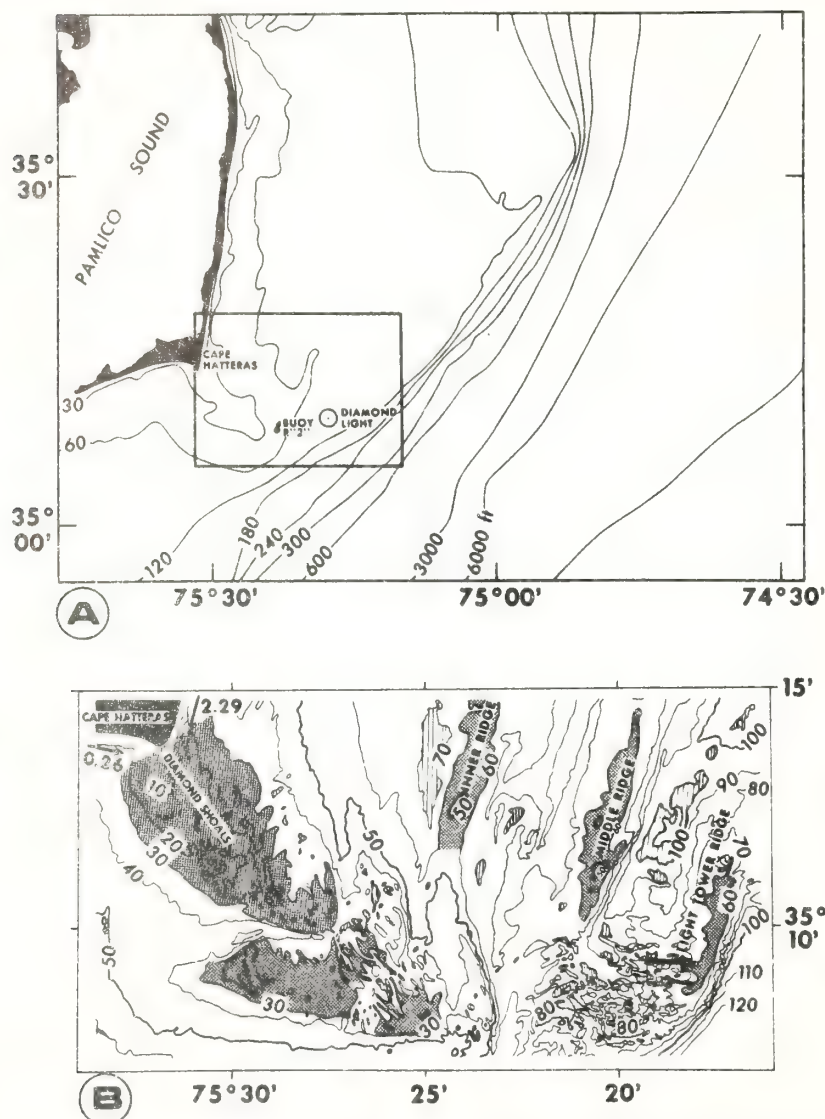


Figure 1. A. Regional bathymetry of North Carolina coast, indicating study area. Contours in feet. B. Relationship of outer shelf ridge topography to Diamond Shoals. Arrows indicate mean annual littoral drift in millions of cubic yards per year. Ridges are stippled; lows are ruled. Contours in feet. From Swift and others (1972).

## ABSTRACT

The surficial sand sheet seaward of Diamond Shoals on the North Carolina shelf is molded into a series of coast-parallel ridges as much as 10 m high and 5 km apart. An older cohesive substrate is exposed in the troughs. Fields of sand waves as much as 7 m high occur on the ridges and in the troughs. Their crests are normal to the ridges. Sand size varies across the sea floor in sympathy with the ridge topography. The gently inclined landward flanks are coarser grained; the steeper seaward flanks are finer grained.

There is evidence to indicate that the sand ridges, like the sand waves with which they are associated, are responses to flow. However, it is not possible to demonstrate the nature of coupling between fluid motion and substrate morphology on the basis of the existing data.

The landward part of the study area is subjected to a southward water drift that during winter is punctuated by intense southward pulses associated with storms. The seaward part experiences a strong, predominantly northward flow throughout most of the year, and the zone of shear appears to migrate back and forth across the study area. Regional considerations suggest a southward sand transport. However, during the period of observation, water flow and bedform asymmetry indicated northward transport. It seems probably that the transport direction reverses with time.

## INTRODUCTION

The sandy shelf floor north of Cape Hatteras on the Atlantic coast of North America (Figs. 1, 2) has impressed upon it a complex topography of large-scale north-trending sand ridges, smaller north-trending sand ribbons, and fields of sand waves whose crests trend east. We describe here the topographic patterns and distribution of surficial sediments and attempt to assess the extent to which these characteristics are responses to the prevailing hydraulic regime.

A variety of techniques was used to map

the substrate and determine the character of flow. A sand-wave field was mapped by means of precision bathymetric data supplied by the National Ocean Survey. Vibracores and grab samples were taken to define shallow stratigraphy and sediment parameters. Sidescan sonar and seismic reflection profiling were employed to observe the bottom in plan and cross section, and bottom photography was used to examine small-scale bottom features. Earth Resources Technology Satellite (ERTS) images were used to indicate the distribution of suspended sediment and to deduce directions of flow in the surface layers. A near-bottom current meter was deployed for 19 days. Through these methods, the character of the sea floor has been observed, and the nature of its response to flow has been inferred.

In the following discussion, depths and distances will be presented in metric units. However, the contour maps are based on National Ocean Survey data obtained before the beginning of this study, and the contours therefore are presented in feet.

#### Bathymetry

The Virginia-North Carolina shelf narrows to the south from almost 100 km at Cape Henry to about 37 km at Cape Hat-

teras. It widens below Hatteras to nearly 100 km (Fig. 1). At Cape Hatteras, Diamond Shoals extends 20 km seaward across two-thirds of the shelf, with water depths of less than 15 m for most of that distance. It has been suggested that Diamond Shoals was deposited by the littoral drift convergence at Cape Hatteras as the cape retreated from its position at the shelf edge to its present position in response to postglacial sea-level rise (Swift and others, 1972; Swift and Sears, 1974). The shoal is deeply incised by arcuate channels, presumably eroded by pulses of Virginia Shelf Water pumped across the shoal during storms (Swift and others, 1972). These channels are apparently modified by wave refraction into arcuate forms, with the outer ends deflected landward.

Seaward of the main shoal, a series of ridges and swales trends north-northeast, with crests at 18 m and troughs at 25 to 30 m (Figs. 1, 2). Seaward flanks tend to be steeper than landward flanks. Inshore of Light Tower Ridge, a broad swale narrows and shallows to the south, ending in a sand-wave field seaward of the tip of Diamond Shoals. Small sand-wave patches also occur on the crests of the inner ridges. Another field of sand waves occurs on the shelf edge northeast of Diamond Light.

Seaward of Light Tower Ridge and the

outer sand-wave field, the shelf drops off steeply to a terrace, at about 80 m, that has been equated with a former low stand of sea level, the Franklin Shore (Swift and others, 1972, Fig. 229). Beyond this terrace, the continental slope begins.

#### Regional Circulation

The Middle Atlantic Bight is characterized by a south-trending fair-weather drift, whose basic driving mechanism may be the nearshore elevation of the sea surface as a consequence of fresh-water runoff, resulting in southward geostrophic flow (Bumpus, 1973). During the summer, southward flow on the North Carolina-Virginia shelf north of Cape Hatteras is weak and may be reversed by southerly winds (Harrison and others, 1967; Miller, 1952). This south-trending drift tends to turn seaward at Cape Hatteras and to be entrained by the north-flowing Gulf Stream (Miller, 1952; Harrison and others, 1967; Stefansson and others, 1971; Bumpus, 1973).

Stratification breaks down in the Middle Atlantic Bight during the months of November and December as a consequence of cooling of the water column and of turbulent mixing by more frequent storms. A general southward drift continues, punctuated by reversals due to southerly storm winds and by intensifications of southward flow due to northerly storm winds. Beardsley and Butman (1974) and Boicourt and Hacker (1976) have noted that strong coupling between wind and water flow and appreciable net excursion of the water mass tend to be associated with storms whose trajectories result in periods of northerly winds parallel to the regional isobaths of the Middle Atlantic Bight. Such winds result in coastward Ekman transport of water and a coastal setup on the order of 40 to 60 cm (Beardsley and Butman, 1974). In the ensuing southward geostrophic flow, mid-depth velocities of 30 to 45 cm/sec and net water excursions of 40 to 70 km occur. During these periods, massive pulses of Virginia Shelf Water flow over Diamond Shoals into Raleigh Bay (Stefansson and others, 1971).

#### Current Patterns from ERTS Imagery

Interaction of the shelf flow field with the Gulf Stream over the shelf edge is vividly illustrated by computer-enhanced ERTS imagery (Charnell and others, 1974; Charnell and Maul, 1973; Maul, 1975; Fig. 3). Shelf water is marked by high turbidity that decreases seaward. Successive ebb-tidal plumes from tidal inlets may be seen drifting along the coast. Most notable is a zone of shear on the shelf edge seaward of

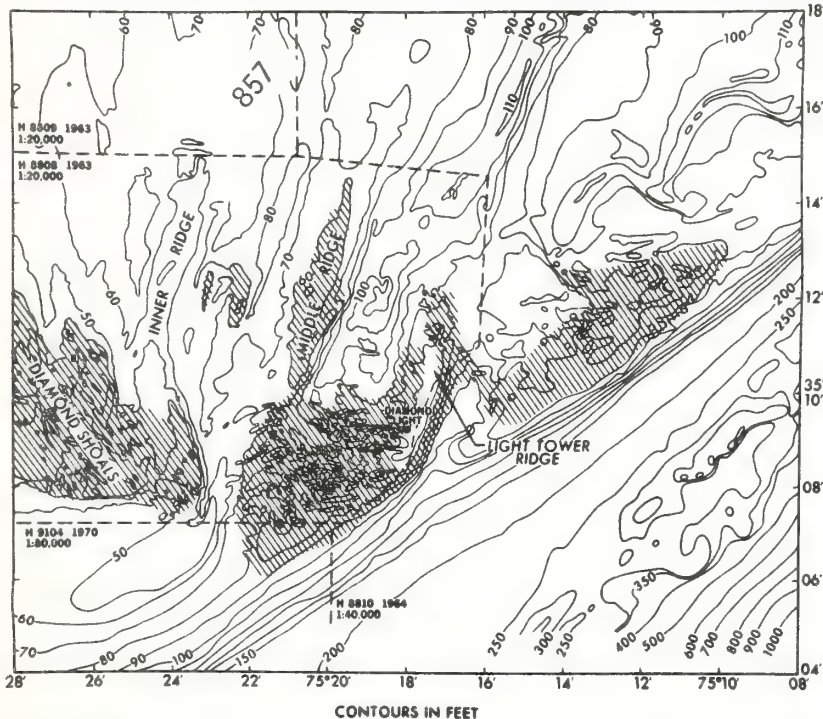


Figure 2. Bathymetry of outer study area, showing relationship of ridge field to shelf-edge terrace. Contoured from U.S. Coast and Geodetic Survey smooth sheets dated 1963-1964 and 1970. Areas of sand waves are diagonally ruled.



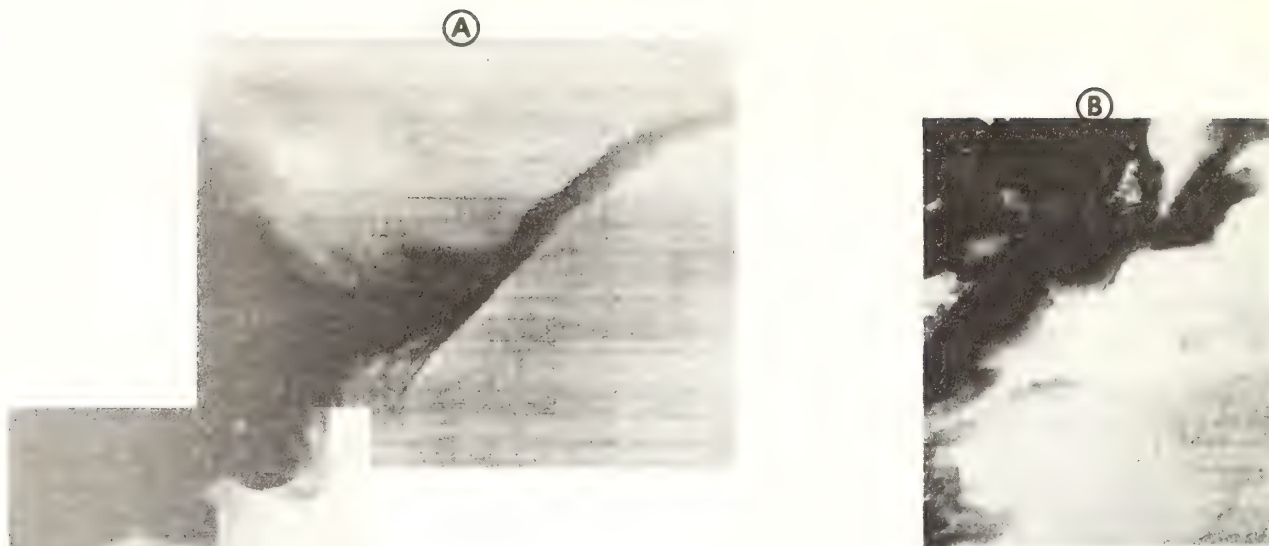
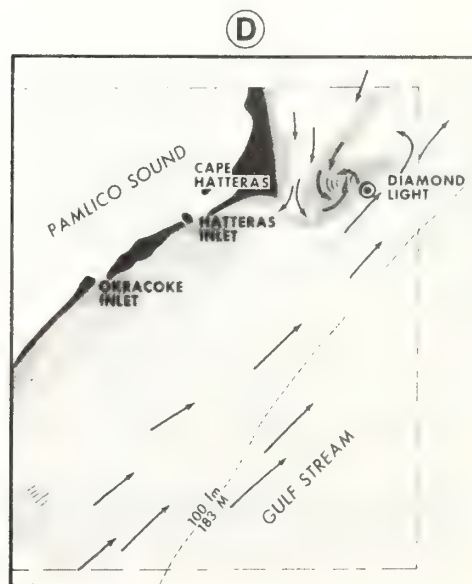
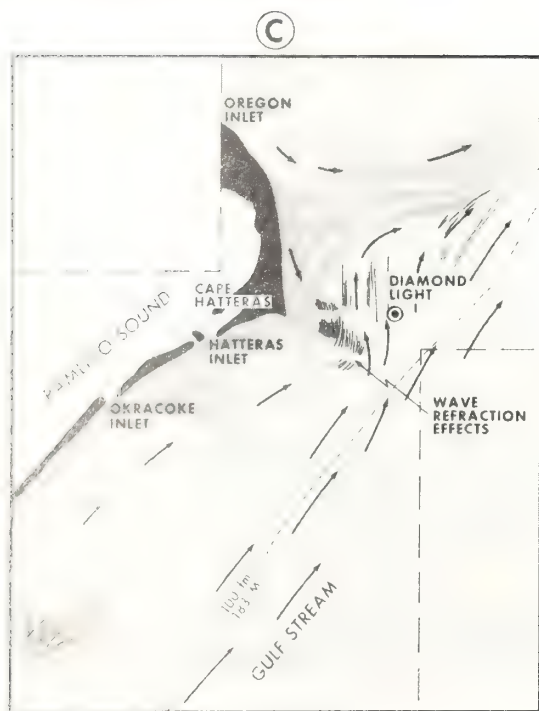


Figure 3. Computer enhancement of ERTS-I satellite imagery by stretching contrast within water part of scene. A. Scenes 113215092 and 113215094 MSS5 ( $0.60.7 \mu\text{m}$ ) were taken December 2, 1972, at 1509Z. Suspended sediments show motion of inshore water. Wind was a constant 5m/sec from west for several days. B. Scene 118616093 was taken at 1509Z on January 25, 1973, in MSS4 ( $0.50.6 \mu\text{m}$ ). Wind had been blowing from north at 5m/sec for several hours prior to this image time. C and D are interpretations of A and B, respectively.





Diamond Shoals, where turbid shelf water from north of the shoals is drawn seaward over the shoals and is entrained into the northward flow of the Gulf Stream. The position and configuration of the shear zone varies in the two illustrations. In Figure 3A winds were from the southwest, and the zone of shelf-water entrainment has been pushed north of the shoals by the Gulf Stream. In Figure 3B the wind has been blowing from the north at 5 m/sec. A tongue of Virginia Shelf Water is beginning to cross Diamond Shoals, and the shear zone has been displaced seaward. A cyclonic eddy is forming where the Virginia Shelf Water meets the Gulf Stream, and part of the Virginia Shelf Water can be seen crossing Diamond Shoals into Raleigh Bay.

#### Direct Current Measurements

The Atlanta office of the engineering firm of Dames and Moore has recently completed a one-year current station on Light Tower Ridge at the request of the U.S. Coast Guard, which maintains the light tower. A Hydrometrics current meter was installed 2 m off the sea floor, in 18 m of water, 4 m southwest of the tower. The

meter was connected to a Rustrak recorder on the light tower.

Dames and Moore personnel reported that during the year of observation, flows were directed toward the north or northeast more than 80 percent of the time (William Smith, 1975, personal commun.). Speeds averaged 50 to 100 cm sec<sup>-1</sup>, occasionally dropping to 10 cm sec<sup>-1</sup> and occasionally exceeding 100 cm sec<sup>-1</sup>. Scuba divers noted that the southerly flows consisted of "green water" that tended to be noticeably colder than the "blue-water" northerly flows.

Atlantic Oceanographic and Meteorological Laboratories positioned a Geodyne 102-C current meter on the landward flank of Light Tower Ridge from October 22, 1973, to November 9, 1973, in 27 m of water (Fig. 4). Flow was consistently to the north-northeast for the first 14 days, except for a reversal that lasted five hours. There was little correlation between the National Weather Service wind records from Cape Hatteras and current velocity during that period. On the 14th day, however, a cold front moved across the Middle Atlantic Bight, exposing it to northeasterly winds. The current at the light tower decelerated, reversed, and accelerated to a southwesterly

velocity of 50 cm sec<sup>-1</sup>. Observations by the vessel retrieving the meter suggested that this current reversal was associated with an offshore shift of the shear zone between the shelf flow and the Gulf Stream as described above.

#### Wave Climate

Wave-and-swell conditions were among the observations recorded at three-hour intervals at the Diamond Light 12 n mi (approximately 22 km) east of Cape Hatteras. The water depth at this site is 16.5 m. Quantification of these data suffers from a random bias inherent in watch schedules and crew rotation. Under these circumstances, various individuals enter height and directional data. However, the summary presented in Figure 5 is the result of 4,586 observations during the period March 1973 through September 1974. Without doubt, the trends shown are close approximations of actual conditions. These data reveal a strong tendency for both waves and swell to transit the tower site from north to south. It should be noted that the tower is evacuated when intense storms threaten the site, so extreme values for wave height cannot be recorded. One entry of a 13-m wave (February 11, 1973) from the north has been noted, but the critical periods during intense storms remain unobserved.

#### SUBSTRATE RESPONSE TO FLOW

##### Surficial Sediment Pattern

Grab samples were collected by Shipek sampler in a radial pattern extending 6 km from Diamond Light. Position was determined by radar range and bearing from the light tower. Navigational error varied from 20 to 200 m. The samples were washed, dried, split, dry sieved through  $-1\phi$  and  $0\phi$  sieves, and finally wet sieved through a  $4\phi$  sieve. Coarse fractions,  $> -1\phi$  and  $-1\phi$  to  $0\phi$  were weighed, and their percentage of the total sample was calculated. The  $0$  to  $4\phi$  fraction was analyzed with a settling tube, and Inman parameters were calculated for each sample (Inman, 1952).

Sidescan sonar and seismic records were collected along north-south, east-west, and northeast-southwest tracklines. Sidescan data were obtained partly by means of an EG&G 120-kHz unit and partly by means of a Westinghouse 150- to 160-kHz sidescan unit. The seismic profiling system was a towed Edo Western 3.5-kHz unit. A total of 520 km of trackline was examined.

Grab samples of bottom sediment, bottom photographs, and sidescan sonar records indicate that the distribution of bot-

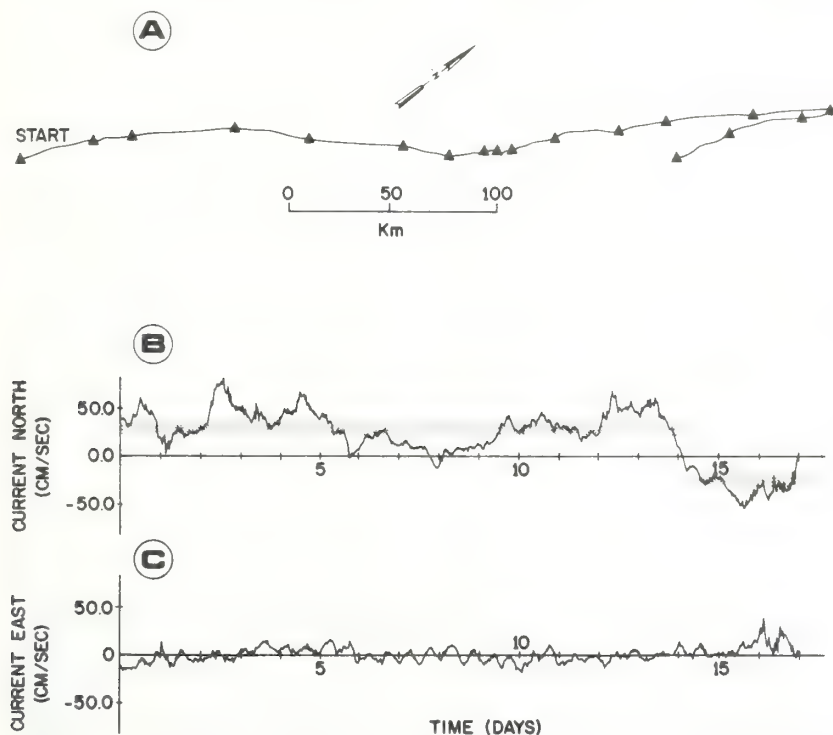


Figure 4. A. Progressive vector diagram from Geodyne 102-C current meter mounted 100 cm off sea floor between Light Tower Ridge and Middle Ridge. B. Time-velocity record for velocity component in flow direction. Stippled band is envelope of threshold velocities based on Shields criterion for unidirectional flow. C. Time-velocity plot for velocity component transverse to main flow direction.

tom sediment reflects the distribution of first-order topographic elements. The map of mean sand size (Fig. 6) indicates that seaward flanks of sand ridges tend to be composed of fine-grained sand; crests and landward flanks tend to be composed of medium-grained sand. Swales are more variable, containing fine to very coarse sand. Bottom photographs (C and D in Fig. 7) indicate that outcrops of stiff clay, or clay veneered with fine gravel, also occur in the swales. Sidescan records (Figs. 8, 9B) indicate that sand in swales tends to occur in elongate ribbons, separated by strips of coarser sand, gravel, or clay outcrop. These coarse strips strongly reflect sound and appear as dark bands on the sidescan records. In the inner part of the study area, zones of mottled bottom occur (Figs. 8, 9A). The "mottles" appear to be patches of coarser sand several metres in diameter. In some areas they appear to be degraded megaripples. Elsewhere their origin is uncertain.

A plot of graphic standard deviation against graphic mean (Inman parameters — Inman, 1952) reveals a crudely sinusoidal

scatter (Fig. 10); see Folk and Ward (1957) and Inman (1949) for discussions of the origin of such a pattern. Three grain-size provinces may be distinguished in Figure 10A. Poorly sorted, fine and very fine sands occur on the Franklin Terrace. Fine sand occurs south of the ridges, whereas medium- and coarse-grained sand occurs on the shelf edge to the northeast of the ridges.

Sand in the ridge-and-swale topography forms a scatter that overlaps with the coarse- and fine-grained shelf provinces. When plotted by themselves, coarse, poorly sorted landward flank sands are clearly distinguished from fine, well-sorted seaward flank sands (Fig. 10B). Trough samples are both coarse and fine grained and overlap both of the other ridge provinces.

### Transverse Bed Forms

The surface of the study area comprises a hierarchical association of bed forms (Allen, 1968) — an association in the sense that two basic species are present (current-

parallel and current-transverse forms), and hierarchical in that the bed forms and the flow perturbations responsible for them occur at several scales.

Current-transverse bed forms occur at three scales. *Ripples* exhibit a characteristic spacing of 10 to 60 cm (A and B in Fig. 7). They are identified as current-transverse bed forms because they commonly have well-developed north-facing avalanche slopes, although symmetrical forms also occur (Fig. 7F). Ripples are commonly of the linguoid variety, but they occasionally form interference patterns or ladderlike patterns in the troughs of larger transverse bed forms (B and F in Fig. 7). Larger scale transverse bed forms (3- to 6-m spacing, Fig. 7B) will be referred to in this report as *megaripples*. They have well-developed avalanche slopes and bear on their upcurrent sides linguoid ripples with the same northward sense of asymmetry. Ripples and megaripples appear to compose two distinct populations with little overlap in bed-form spacing. Sidescan records indicate sinuous megaripple crest lines. Ladderlike arrays of ripples occur in troughs with ripple crest lines normal to megaripple crests.

A third scale of transverse bed forms will be referred to as *dunes*. Dune spacings range from 100 to 300 m. Dune spacing does not overlap with megaripple spacing. However, for convenience, the term *sand wave* will be used as a generic name for these apparently related larger transverse bed forms. Dunes tend to have slip faces, but these commonly occupy only part of the downcurrent slope (Figs. 11A, 12). Dunes tend to bear megaripples on both slopes, with the megaripples of the downcurrent side distinctly larger than those of the upcurrent side (Figs. 11A, 12). Megaripples on both faces have the same northward sense of asymmetry as do the dunes. Megaripples are locally aligned at oblique angles to dune crests (Fig. 11A). This angle tends to disappear near the dune crest, a phenomenon attributed by Terwindt (1971) to acceleration of the transverse component of a flow moving obliquely over the crest of the dune.

Fathograms obtained during the 1963 and 1964 U.S. Coast and Geodetic Survey *Explorer* cruises reveal a field of dunes ranging in height from 2 to 8 m (Fig. 13). *Shoran*, a range-range electronic navigation system, provided an accuracy of  $\pm 50$  m over the inner shelf for this survey. The average line spacing is 100 m, with greater line spacing farther seaward. We have plotted crest-line positions from the fathograms (see Fig. 13B); they are shown in Figure 14A.

In the area of maximum sand-wave amplitude (Fig. 14B), there is a suggestion

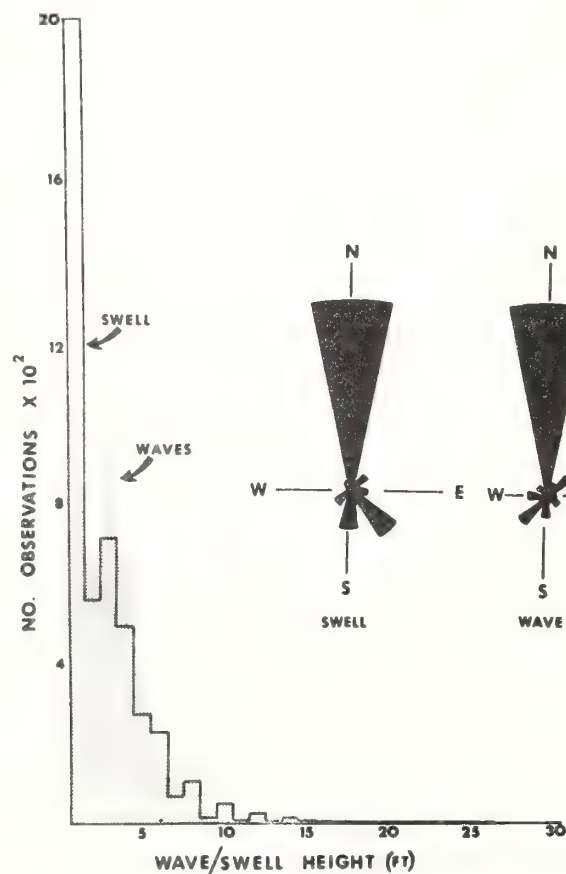


Figure 5. Histogram of wave-and-swell frequency and height derived from visual observations at Diamond Light Tower off Cape Hatteras. Data summarized from U.S. Coast Guard observations, March 1973 through September 1974.



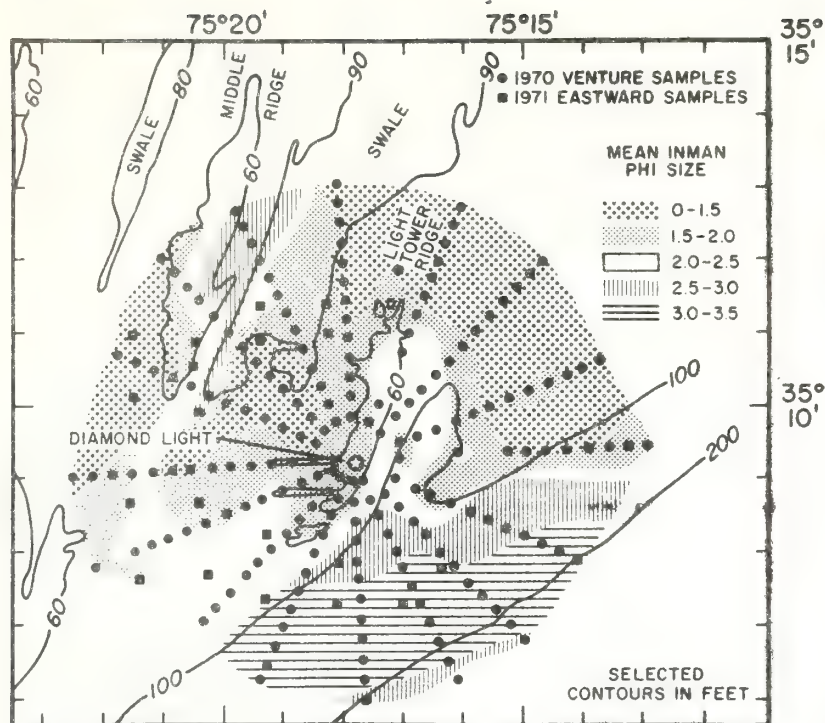


Figure 6. Mean Inman  $\phi$  grain-size map based on analysis of the sand fraction. Sample locations are shown for a sample net including 1970 samples and samples from Philip Sears taken from R/V *Eastward*, 1971.

of a fourth order of transverse bed form in the fact that large dunes tend to occur in distinct sets of two to four dunes per set (Fig. 13A). In the bathymetric map of Figure 14A, two dune sets are shown as single ridges, perturbing the outline of Light Tower Ridge as defined by the 18-m (60-ft) contour.

**Significance of Transverse Bed Forms.** Allen (1968, p. 68) suggested that the features we describe as ripples are the consequence of transverse flow perturbations within the logarithmic boundary layer, whereas the large sand waves are responses to transverse perturbations of much or all of the entire flow. McCave (1971) observed smaller sand waves (our megaripples) climbing the backs of larger sand waves (our dunes) in the tidal sand-wave field of the Dutch coast. He cited Kennedy's (1969) interpretation for the dual pattern, wherein the megaripples are primarily responses to bed-load transport characterized by relatively short particle trajectories, whereas the dunes are the response of the substrate to suspensive sand transport and have longer particle trajectories. This explanation is in harmony with our observation of differing sizes of megaripples on the upcurrent and lee sides of the dunes. The dunes, composed of finer sand carried mainly in suspension from the upstream dune, would develop small megaripples on their backs in response to the increase in bottom shear

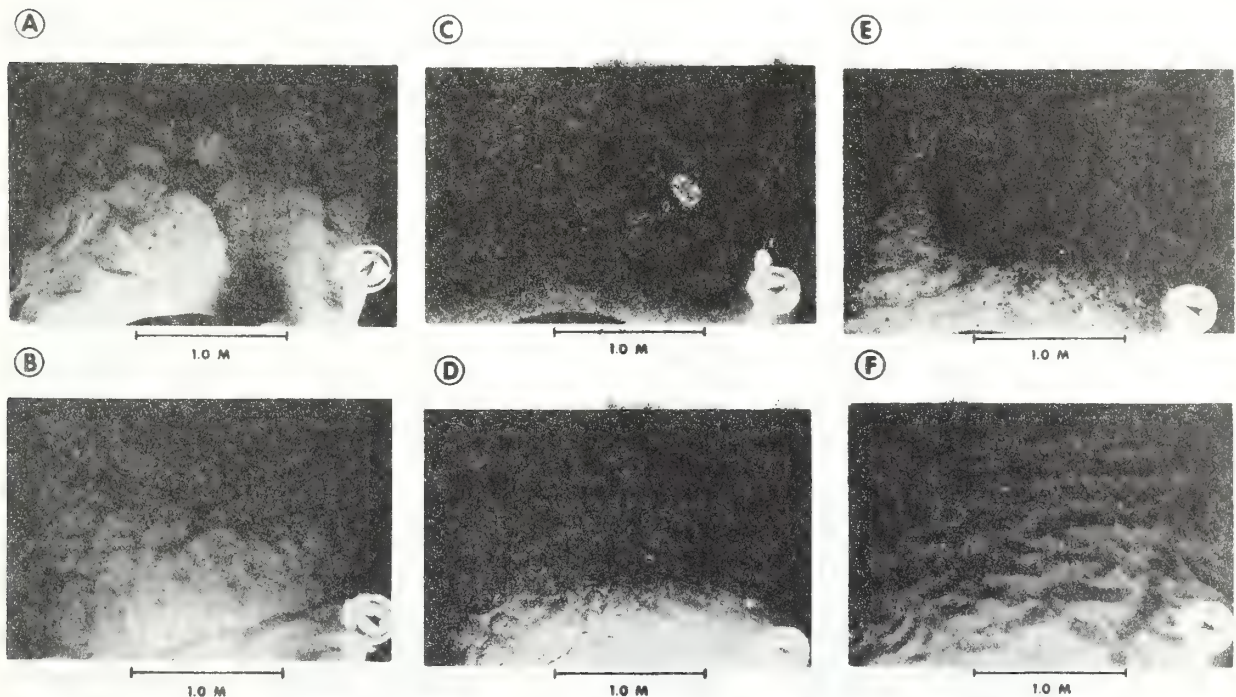


Figure 7. Photographs taken from the R/V *Eastward*, 1973. A. Typical ripples within sand-wave field. Ripples are about 60 cm long and 10 cm high. B. Small ripples superimposed on larger megaripples (see Figs. 14, 16). C. Section of main swale floored by coarse gravel and shell hash. D. Exposure of clay substrate beneath sand sheet. E. Gravel street exposed between sheets of fine sand. F. Small symmetrical north-trending oscillation ripples on crest of Light Tower Ridge. There is also indication of east-trending current ripples showing as secondary feature. For photograph key, see Figure 8.



toward the dune crest. Fine sand would be stored in these megaripples until it is swept on to the next dune. Megaripples below the dune slip face, in the zone of highly turbulent flow reattachment, would consist of coarser sand and would be larger in scale, since grain size is a primary control of ripple size (Allen, 1968, p. 68).<sup>1</sup>

Sand waves occur primarily on ridge crests and flanks and also at the head of the main trough. Our data are not adequate to explain their distribution, but the constraints probably include (1) sand sufficiently deep for their construction, as determined by the primary ridge topography, (2) sand sufficiently coarse that an appreciable portion will travel as bed load, and (3) a sufficient frequency of flows above a critical threshold. In the main sand-wave field, the dunes attain heights greater than 7 m. McCave (1971) used an equation of Kennedy (1969) to indicate that dunes of similar height in similar water depth are at the equilibrium height relative to a reversing tidal flow field.

We note that Light Tower Ridge, unlike Middle Ridge, is devoid of sand waves (Fig. 14A). At a depth of 16 m, the crest of this shelf-edge ridge may become a breaker zone for oceanic waves during major storms, and breaking waves have in fact been reported by the Light Tower crew during storms, although the tower is usually evacuated before storms become that intense. Recent wave data from the Light Tower include a period of 12-sec waves during February 1973 in which wave heights were on the order of 13 m. Such waves would create surf or near-surf conditions on Light Tower Ridge and would probably destroy all sand waves. Middle Ridge is screened by Light Tower Ridge from the full force of oceanic waves, but we note that sand waves, although observed there by the 1963 survey, were absent in the 1973 survey. The wave climate probably sets an upper limit on both sand-wave and sand-ridge amplitudes.

#### Longitudinal Bed Forms

**Sand Ribbons.** Strips of sand as much as 200 m wide occur between Light Tower Ridge and Middle Ridge, parallel to the axis of the trough (Figs. 8, 9B). They exhibit relief only to the extent that they bear megaripples on their backs. These features are inferred to be sand ribbons, analogous to the current-parallel sand ribbons described by Kenyon (1970) from the tidal shelf around Great Britain.

**Sand Ridges.** The regional pattern of ridges and swales in the study area has been described in the Introduction. The internal structure of this topography has been observed by means of seismic profiling (Fig. 15). The records show that the surficial sand sheet with its ridge-and-swale topography rests on a reflecting surface that is locally exposed in the floor of the trough.

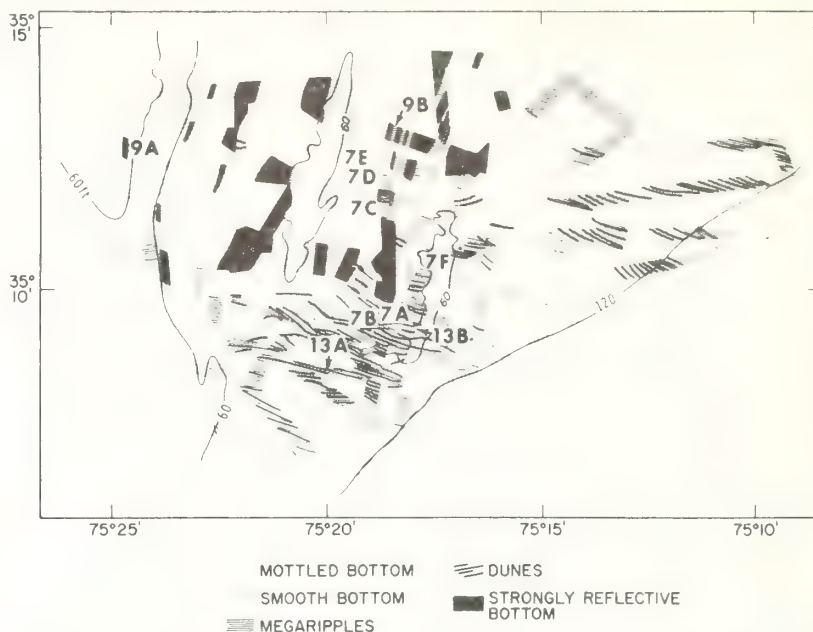


Figure 8. Composite of sidescan records and locations of other illustrations. Lateral width of track lines exaggerated four times for clarity. Positions of other illustrations are indicated.

Photographs of these exposures reveal a gravelly sea floor (Fig. 7C), and samples of the gravel commonly contain clay clasts. One photo reveals an outcropping ledge of clay (Fig. 7D). A single vibracore in the trough between Light Tower Ridge and Middle Ridge revealed a few decimetres of fine gravel over more than 2 m of silty clay (H. Palmer, 1975, unpub. data).

North of the study area, a similar gravel-veneered, clayey stratum underlies the surficial sand sheet of which the ridge-and-swale topography is composed. Radiocarbon dates and vibracores indicate that it is an inner shelf deposit associated with the withdrawal of the sea at the onset of the late Wisconsin ice advance of 20,000 to 30,000 B.P. (Sears, 1973; Shideler and others, 1972).

**Significance of Longitudinal Bed Forms.** Analytical models for the genesis of transverse bed forms are available (for example, Smith, 1970), and their behavior is reasonably well understood. The genesis and behavior of longitudinal bed forms is not as well understood. Current-parallel bed forms may represent zones of near-bottom flow convergence, or at least zones of reduced flow competence. Theoretical investigations into fluid dynamics suggest that strong geostrophic currents associated with winter storms may indeed experience structured flow, in which current-parallel zones of upwelling alternate with zones of downwelling so that the flow is partitioned into current-parallel helical flow cells of alternating right- and left-hand sense of rotation (Faller, 1963, 1971; Faller and Kaylor, 1966). More recently, Gammelsrod (1975)

has shown that Couette-like currents such as those of the inner shelf, which do not have a significant Coriolis term in their equation of motion, may also experience cellular flow structure.

Experiments have not yet been designed to observe such flow in the field, and it is by no means clear that the bed forms of the study area are responses to structured flow of this type. The thin, well-defined character of the sand ribbons suggests that they are the most likely to have been formed by the helical flow mechanism. The response time of a bed form is a function of the volume of sand it contains, and the thin sand ribbons may be responses to a single storm, or season of storms.

The sand ridges are more difficult to assess. It has been argued elsewhere (Swift and others, 1973) that the ridge topography of the Middle Atlantic Bight is a very long term response to flow, in that ridges were initiated after passage of the shoreline at the onset of the Holocene transgression and have continued to grow as the shoreline receded and the water column deepened. The sand ridges in this scheme are responses to many thousands of storm seasons, in which the flow pattern, either of the kind described above or of some unknown kind, has shaped the ridges. The ridges would in turn have determined the pattern of flow during major flow events.

The Hatteras ridges compose the southernmost part of the central Atlantic shelf ridge topography for which this hypothesis has been proposed (see map of Goldsmith and others, 1974). However, they exhibit some characteristics that shed new light on

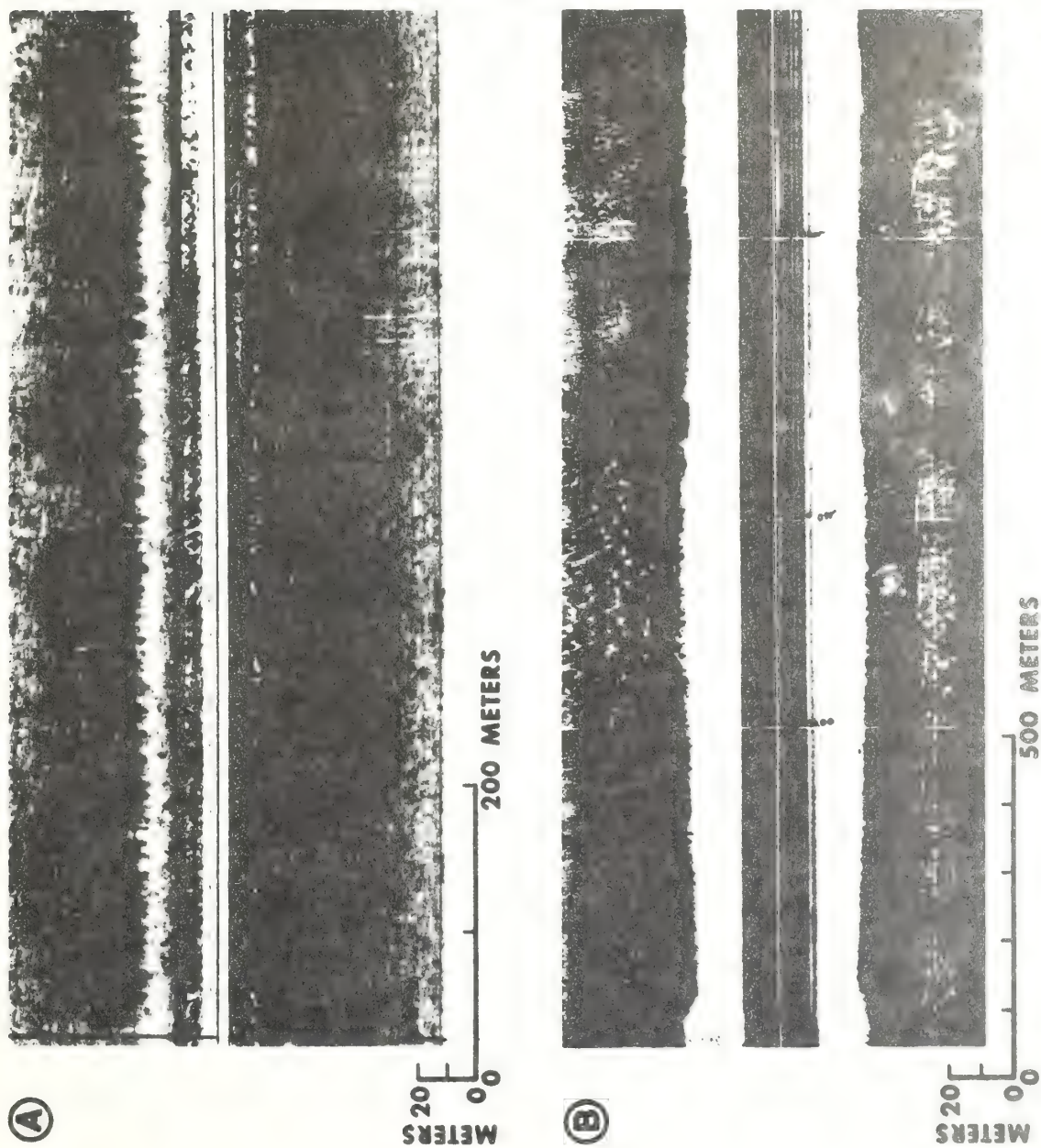


Figure 9. Sidescan sonar profiles keyed to Figure 8. A. Mottled facies. B. Profile across main swale showing megarippled sand ribbons separated by lanes of gravel or coarse sand.

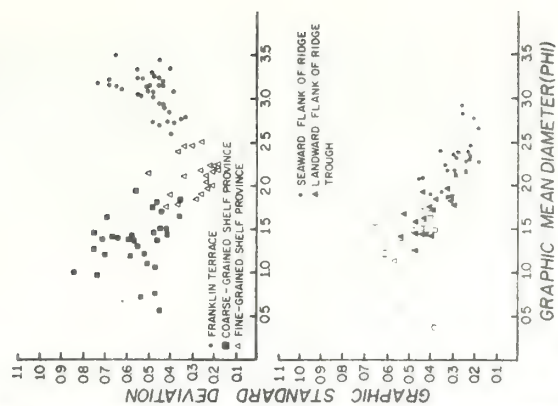


Figure 10. Scatter plots of standard deviation versus mean diameter in sand fraction (Inman parameters).



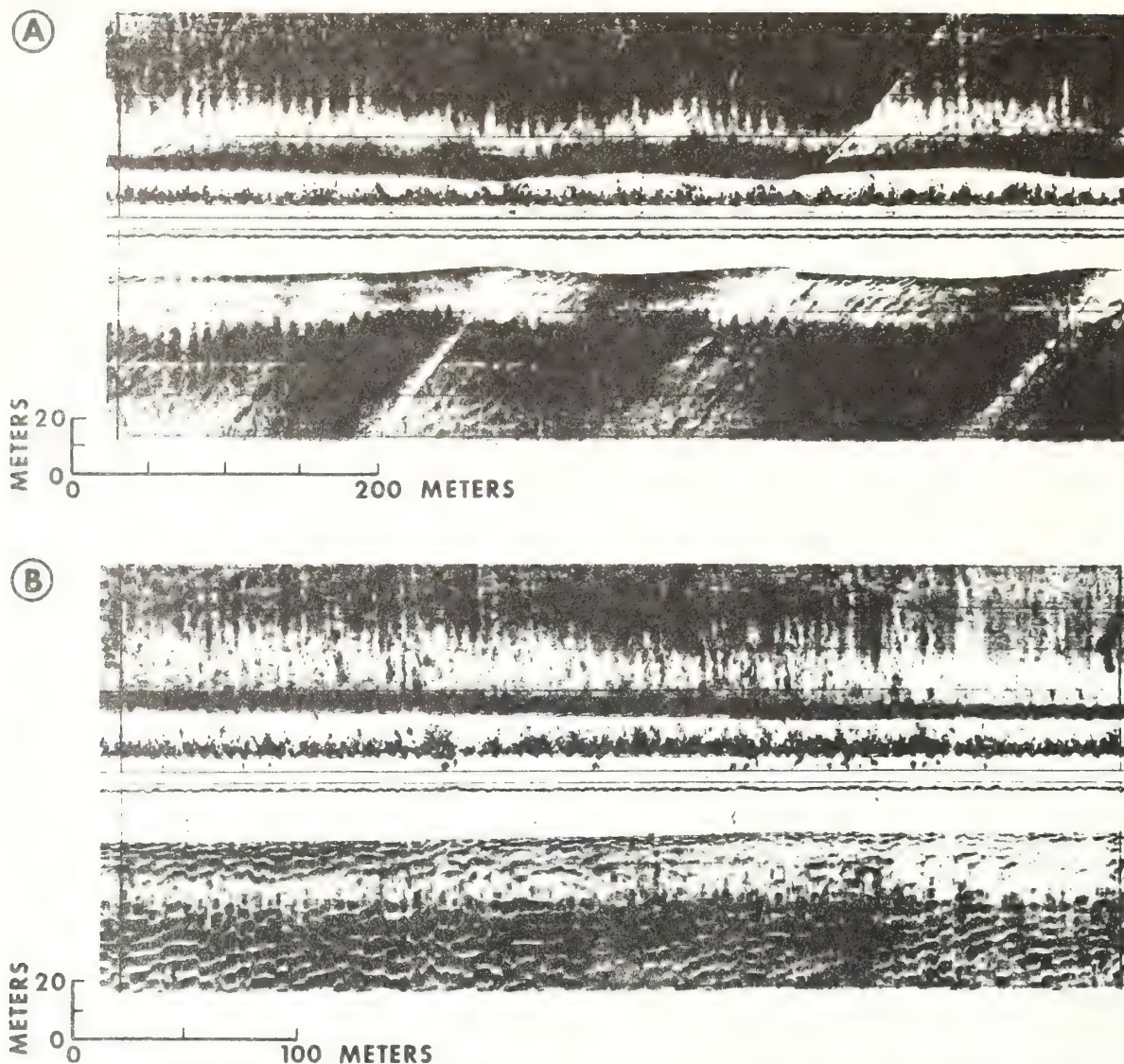


Figure 11. Sidescan sonar profiles keyed to Figure 8. A. Three wave forms detectable with sidescan — dunes, stoss-side megaripples, and lee-side megaripples (see Figs. 15B, 16). B. Megaripples without dunes.

the problem of ridge genesis. They retain the asymmetry noted in nearshore ridges; the seaward flanks are steeper and finer grained than the landward flanks, despite the fact that they have been isolated on the outer shelf for many thousands of years since the passage of the shoreline. The asymmetry suggests that the ridges are responding as sand waves to a cross-ridge component of flow (Smith, 1969, 1970), with greater shear stress being experienced on the upcurrent (northwestern) than downcurrent (southeastern) slope. Such behavior is compatible with the cellular flow hypothesis, if the flow cells are skewed with respect to the mean flow direction (Faller, 1963; Lilly, 1966; Gammelsrod, 1975).

The question arises whether this asym-

metry is maintained by the modern hydraulic regime or is an inheritance from a period when the ridges were forming on the inner shelf. It can be completely answered only by a program of sustained hydraulic observa-

tion. However, the character of the sea floor provides some clues. The ridges have not been flattened in the millenia since transgression, nor have the troughs been filled; ridges rise as much as 10 m beside

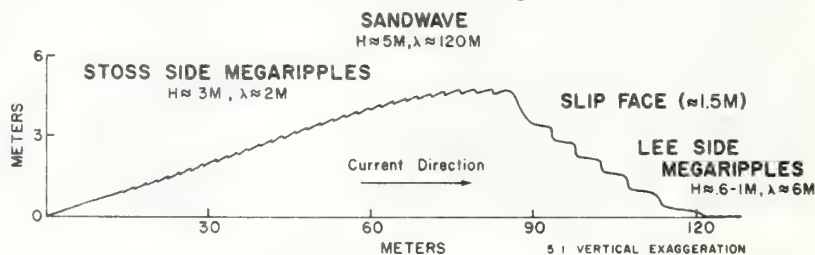


Figure 12. Generalized profile of sand wave from Light Tower sand-wave field (compare with Fig. 10A).



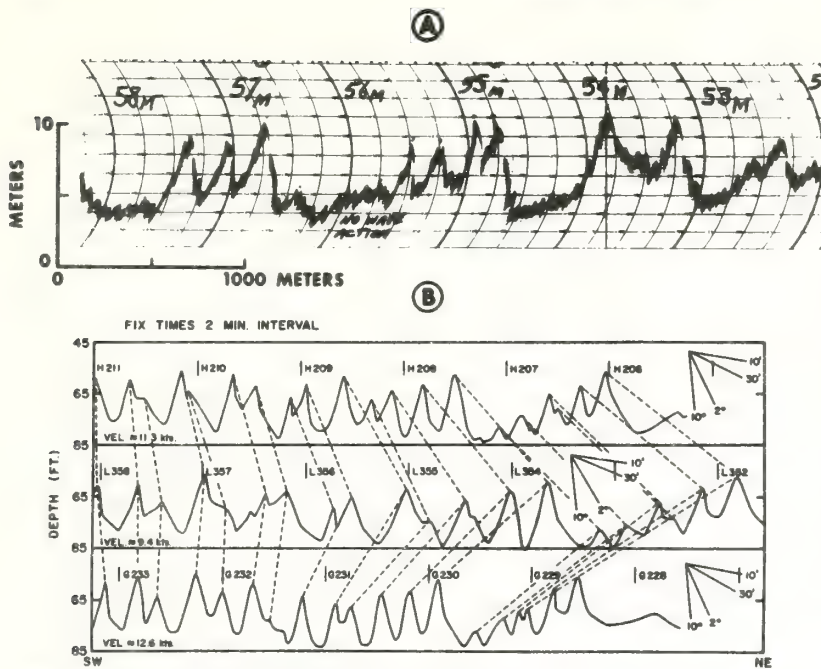


Figure 13. Northeast-southwest bathymetric profile normal to crest lines across Light Tower sand-wave field. Note sand-wave groups that appear as single shoals on contour maps. B. Example of correlation of three successive profiles across wave field. Wave forms have been rectified, and individual crests are correlated between track lines at 100-m spacing. Variation in profile lengths is due to differences in speed. From U.S. Coast and Geodetic Survey records, 1963, smooth sheet H-8808.

troughs, exposing bare or gravel-armored cohesive substrate.

The orthogonal relationship of sand ridges to sand waves implies that they are products of the same flow. The sand waves, with their well-defined slip faces, are clearly responses to modern flow, and they are almost as high as the ridges. This suggests that the power expended during peak-flow events is adequate to build and maintain flow-parallel ridges as well as flow-transverse sand waves.

#### CHARACTER OF SEDIMENT TRANSPORT, HATTERAS OUTER SHELF

##### Direction of Sand Transport

The direction of sand transport through the study area is problematic. Published studies indicate that southward water and sand transport is characteristic of the Middle Atlantic Bight (see next section). Some of our observations in the study area suggest that the southerly transport prevails here also. Erosion of north-facing slopes and deposition on south-facing slopes of Diamond Shoals suggests southward sand transport (Swift and others, 1972; Fig. 16).

The sequence of facies down the main trough in north to south order, from bare gravel and sand ribbons to sand waves to smooth fine sand, is the characteristic downstream facies succession reported from the sand transport paths around the British Isles by Belderson and others (1971). Both ridge crest lines and trough thalwegs tend to shoal toward the south, as they do in areas where southerly sand transport prevails (Swift and others, 1972). Because of the rotating stylus used in the 1963 surveys, dune asymmetries cannot be reliably determined (Fig. 13), but we note that dune crest lines in the main trough are slightly convex to the south (Fig. 14A). The looping pattern suggests southward flow, with the most intense flow occurring in the trough axis. The prevailing northerly wave-and-swell regime indicates that the wave-driven component of sand transport must be from north to south. However, current-ripple and sand-wave asymmetries observed on our two cruises and current-meter observations on our second cruise clearly indicate northward flow.

Until further long-term current measurements can resolve this dilemma, we tentatively conclude that the flows responsible for the topography are reversing. The re-

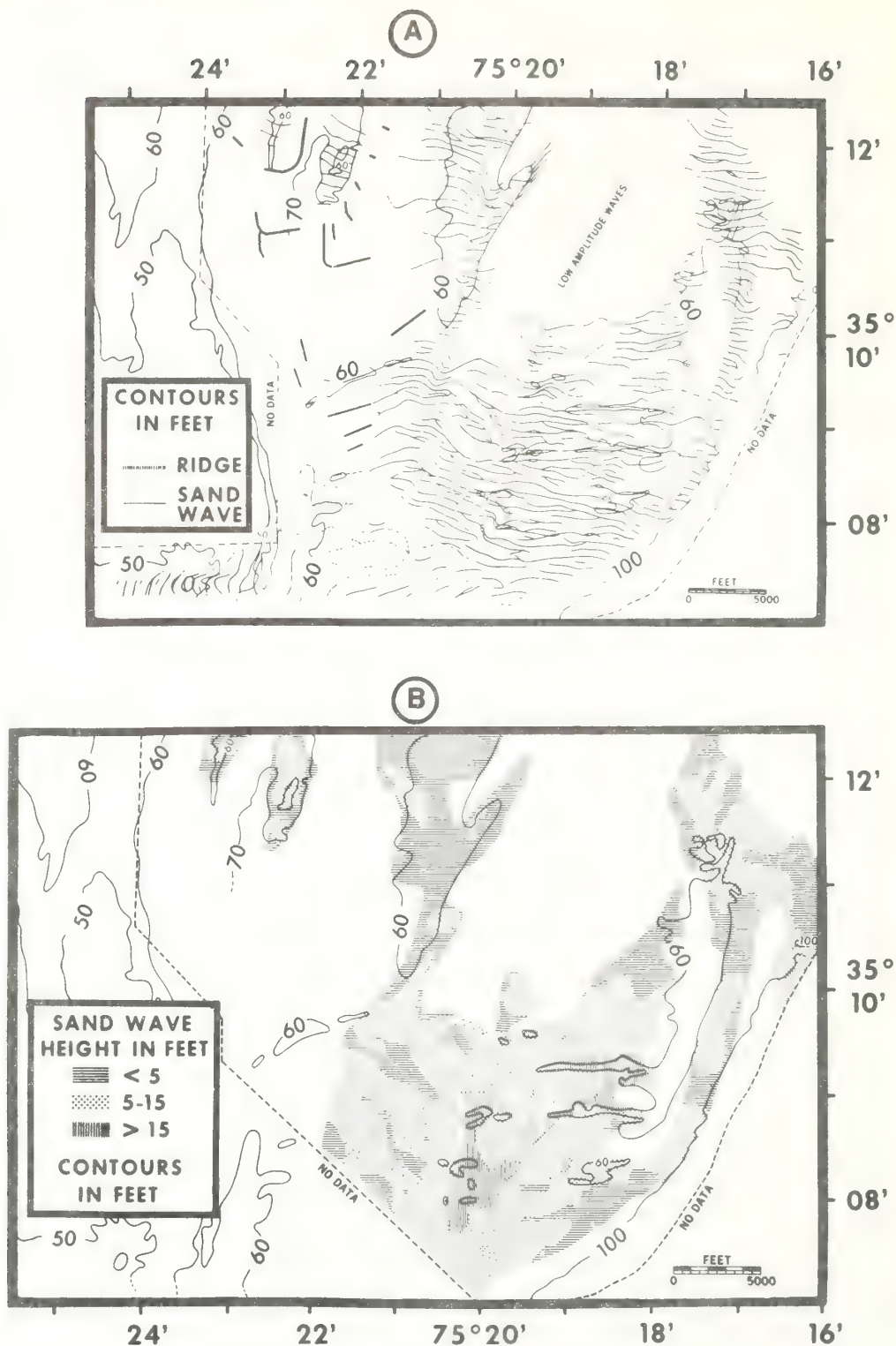
gional morphologic pattern and flow observations elsewhere in the Middle Atlantic Bight lead us to infer that the dominant flows are southward geostrophic storm flows. We note, however, that the main shear zone between the Gulf Stream and the shelf water tends to move in over the study area when the southerly shelf flow is not strong enough to keep it out (Fig. 3). The sharp nature of asymmetrical current ripples in our bottom photographs suggests that such a Gulf Stream transgression had just transpired, although it apparently was no longer in progress; we see no indication of grain movement in the photos. Reversing flows may explain the limited slip face development on the dunes (Figs. 11A, 12); such forms would presumably have their sense of asymmetry reversed by each sustained flow. Sidescan sonar data from a November 1974 cruise indicate that dunes in the Light Tower Ridge field did attain at that time the classic "sawtooth" form in which the slip face reaches the trough.

##### Regional Sand Transport Pattern

Our observations suggest to us that our study area is a key sector in the regional pattern of sand transport. Inferential evidence for southward sand transport in the Middle Atlantic Bight occurs as far northward as Long Island (Swift and others, 1972, p. 561-565). The study of Beardsley and Butman (1974) suggests that strong geostrophic coupling of water flow with wind flow results in southward water transport in the Middle Atlantic Bight. Measurements of water and sand transport off the coasts of Long Island (Lavelle and others, 1976), New Jersey (DeAlteris and others, 1976), and on the Maryland coast (Moody, 1964; Palmer and Wilson, 1975) suggest a southerly transport direction. However, the floor of the Middle Atlantic Bight is partitioned by transverse shelf valleys that would serve as sand traps, and it appears unlikely that any single grain has traversed an appreciable part of this distance since the Holocene transgression began.

The shelf shoals and narrows toward Cape Hatteras, and the bed-form pattern of Figures 2 and 14A suggests that the dominant direction of sand transport obliquely intersects the shelf edge within the study area. According to the recent study by Horn and others (1971), the sediments of abyssal plains west of the Mid-Atlantic Ridge are derived from only two sources, the Hudson and Hatteras Canyons systems. The ancestral Hudson River unquestionably discharged directly into the Hudson Canyon during Pleistocene low stands of the sea, and the Pamlico-Albemarle River systems

Fig. 14. Sand-wave maps from U.S. Coast and Geodetic Survey smooth sheet H-8808, 1963. Light Tower Ridge is enclosed 60-ft contour to right. A. Crest lines of major sand waves correlated from original fathograms as demonstrated in Figure 4B. Lines have been smoothed for small navigational errors. Solid lines are definite correlations, and dotted lines are possible correlations in areas of poor data. Note general southward convexity of crest lines and absence of sand waves on Light Tower Ridge. B. Average sand-wave heights within sand-wave field. Arbitrary limits occur where bottom relief cannot be filtered from wave noise.





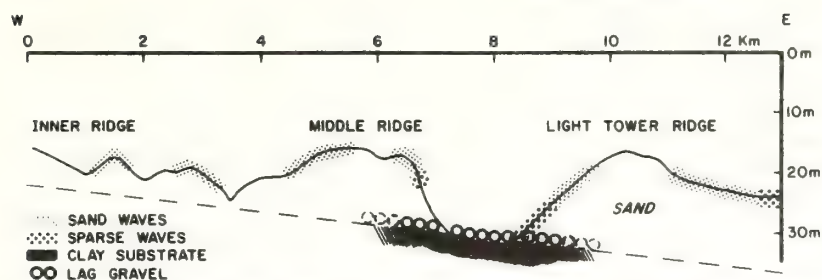


Figure 15. Cross-shelf profile north of main sand-wave field based on 3.5-kHz seismic profiles, grab samples, and photographs. Areas of sandwaves are shown on surficial sand sheet as well as relation of ridges to pre-Holocene substrate. Bathymetry is from the U.S. Coast and Geodetic Survey smooth sheet H-8808, 1963.

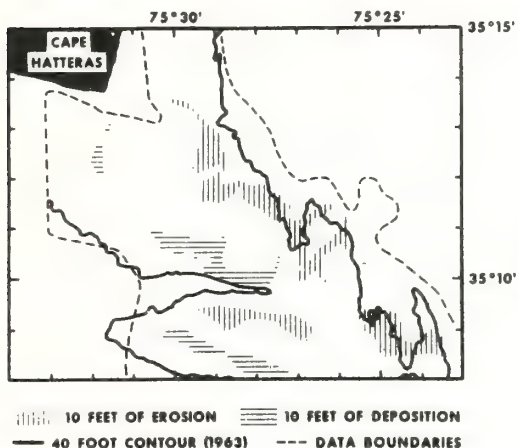


Figure 16. Net-change map of Diamond Shoals, 1953 to 1963. After Swift and other (1972). Note erosion on north slope and deposition on south slope.

may likewise have discharged into the Hatteras Canyon system during low stands. Diamond Shoals in fact may have been initiated as a low-stand cusped delta ancestral to Cape Hatteras, although it has since clearly led an independent existence as a cape extension shoal, focusing wave energy on and being nourished by its associated cusped foreland (Swift and Sears, 1974).

However, our observations lead us to suggest that since the beginning of the Holocene transgression, a significant part of the surficial sand sheet of the shelf to the north has been delivered to the shelf edge of the study area. Rona (1970) noted that the heads of the Hatteras and tributary canyons on the upper slope off Cape Hatteras are buried beneath a cap of foraminifera-rich silt raining out of the Gulf Stream. Sand delivered to the zone of reversing flow at shelf edge does not therefore bypass directly into the canyons at present; it must instead mix with the fine, relatively "sticky" pelagic material and cause the slope to prograde. Such shelf-edge progradation has been inferred for the northern North Carolina-Virginia

shelf from seismic records by Shideler and Swift (1972) and by McIntyre and Milliman (1970).

#### ACKNOWLEDGMENTS

This study is part of the Continental Shelf Sedimentation Project (CONSED) of Atlantic Oceanographic and Meteorological Laboratories (AOML), National Oceanic and Atmospheric Administration (NOAA). It incorporates data collected by AOML and Westinghouse Ocean Research Laboratory, part of which was collected during cruise E-5-73 of Duke's R/V *Eastward*. The cooperative oceanographic program of Duke Marine Laboratory is supported by National Science Foundation Grant GB-17545. The early hydrographic data were collected and provided by the National Ocean Survey. The enhancement of ERTS-I scenes was done by G. Maul and R. Qualset of AOML. Data on wave-and-swell observations were kindly provided by the United States Coast Guard Group, Cape Hatteras, Buxton, North Carolina. The current-meter

data of Figure 3 were collected by W. Stubblefield and G. Lapiene of AOML on board the NOAA ship *Peirce*.

#### REFERENCES CITED

- Allen, J.R.L., 1968, Current ripples: Amsterdam, North Holland Pub. Co., 433 p.
- Beardsley, R. C., and Butman, B., 1974, Circulation on the New England continental shelf: A response to winter storms: *Geophys. Research Letters*, v. 1, p. 181-184.
- Belderson, R. H., Kenyon, N. H., and Stride, A. H., 1971, Holocene sediments of the continental shelf west of the British Isles, in Delany, F. M., ed., *The geology of the East Atlantic Continental Margin*: London, Inst. Geol. Sciences, Rept. 70/14, p. 160-170.
- Boicourt, W. C., and Hacker, P. W., 1976, Circulation on the Atlantic continental shelf of the United States, Cape May to Cape Hatteras: *Mémoires Société Royale des Sciences de Liège*, 7th, Liège, Belgium, 1975, Colloquium Proc., v. 10, p. 187-200.
- Bumpus, D. F., 1973, A description of the circulation on the continental shelf of the east coast of the United States: *Progress in Oceanography*, v. 6, p. 117-157.
- Charnell, R. L., and Maul, G. A., 1973, Oceanic observation of New York Bight by ERTS-I: *Nature*, v. 242, p. 451-452.
- Charnell, R. L., Apel, J. R., Manning, W., III, and Qualset, R. H., 1974, Utility of ERTS-I for coastal ocean observation: The New York Bight example: *Marine Technol. Soc. Jour.*, v. 8, p. 42-47.
- DeAlteris, J. T., Roney, J. R., Stahl, L. E., and Carr, C., 1976, A sediment transport study, offshore, New Jersey: *Am. Soc. Civil Engineers Specialty Conf., Ocean Engineering III*, Newark, Del., 1975, Proc. (in press).
- Faller, A. J., 1963, An experimental study of the instability of the laminar Ekman boundary layer: *Jour. Atmos. Phys. Sci.*, v. 23, p. 466-480.
- 1971, Oceanic turbulence and the Langmuir circulations: *Ann. Rev. Ecology and Systematics*, v. 2, p. 201-236.
- Faller, A. J., and Kaylor, R. E., 1966, A numerical study of the instability of the laminar Ekman boundary layer: *Jour. Atmos. Sci.*, v. 23, p. 466-480.
- Folk, R. L., and Ward, W. C., 1957, Brazos River Bar: A study in the significance of grain size parameters: *Jour. Sed. Petrology*, v. 27, p. 3-26.
- Gammelsrod, T., 1975, Instability of Couette flow in a rotating fluid and origin of Langmuir circulations: *Geophys. Research*, v. 80, p. 5069-5075.
- Goldsmith, V., Sutton, C. H., and Davis, J. S., 1974, Bathymetry of the Virginian Sea (map): Gloucester Point, Va., Virginia Inst. Marine Sci.
- Harrison, W., Norcross, J. J., Pore, N. A., and Stanley, E. M., 1967, Circulation of shelf waters off the Chesapeake Bight: Surface and bottom drift of continental shelf waters between Cape Henlopen, Delaware, and Cape Hatteras, North Carolina, June 1963-December, 1964: *Environmental Sci.*



- Services Adm. Prof. Paper 3, 82 p.
- Horn, D. R., Ewing, M., Horn, B. M., and Delach, M. N., 1971, Turbidities of the Hatteras and Sohm abyssal plains, western North Atlantic: *Marine Geology*, v. 11, p. 287-323.
- Inman, D. L., 1949, Sorting of sediments in the light of fluid mechanics: *Jour. Sed. Petrology*, v. 19, p. 51-70.
- , 1952, Measures for describing the size distribution of sediments: *Jour. Sed. Petrology*, v. 22, p. 125-145.
- Kennedy, J. F., 1969, The formation of sediment ripples, dunes, and antidunes: *Ann. Rev. Fluid Mechanics*, v. 1, p. 147-168.
- Kenyon, N. H., 1970, Sand ribbons of European tidal seas: *Marine Geology*, v. 9, p. 25-39.
- Lavelle, J. W., Brashear, H. R., Case, F. N., Chamell, R. L., Gadd, P. E., Haff, K. W., Han, G. A., Kunselman, C. A., Mayer, D. A., Stubblefield, W. L., and Swift, D. J. P., 1976, Preliminary results of coincident current meter and sediment transport observations for wintertime conditions, Long Island Inner Shelf: *Geophys. Research Letters*, v. 3, p. 97-100.
- Lilly, D. K., 1966, On the instability of Ekman boundary flow: *Jour. Atmos. Sci.*, v. 23, p. 481-494.
- Maul, G. A., 1975, An evaluation of the use of the Earth Resources Technology Satellite for observing ocean current boundaries in the Gulf Stream system: *Natl. Oceanic and Atmos. Adm. Tech. Rept. ERL-335-AOML-18*, 125 p.
- McCave, I. N., 1971, Sandwaves in the North Sea off the coast of Holland: *Marine Geology*, v. 10, p. 199-225.
- McIntyre, I. G., and Milliman, J. D., 1970, Physiographic features on the outer shelf and upper slope, Atlantic continental margin, southeastern United States: *Geol. Soc. America Bull.*, v. 81, p. 2577-2598.
- Miller, A. R., 1952, A pattern of coastal circulation inferred from surface salinity-temperature data and drift bottle recoveries: *Woods Hole Oceanog. Inst. Ref. 52-28*, Office Naval Research Tech. Rept., 14 p.
- Moody, D. W., 1964, Coastal morphology and processes in relation to the development of submarine sand ridges off Bethany Beach, Delaware [Ph.D. dissert.]: Baltimore, Johns Hopkins Univ., 167 p.
- Palmer, H., and Wilson, D. G., 1975, Nearshore current regimes in a linear shoal field, Middle Atlantic Bight, USA: *Internat. Sedimentology Cong.*, 9th, Nice, France 1975, thème 6, proc., p. 137-140.
- Rona, P. A., 1970, Submarine canyon origin on upper continental slope off Cape Hatteras: *Jour. Geology*, v. 78, p. 141-152.
- Sears, P. C., 1973, Evolution of Platt Shoals, northern North Carolina shelf: Inferences from areal geology [M.S. thesis]: Norfolk, Va., Old Dominion Univ., 82 p.
- Shideler, G. L., and Swift, D. J. P., 1972, Seismic reconnaissance of post-Miocene deposits, middle Atlantic continental shelf, Cape Henry, Va., to Cape Hatteras, North Carolina: *Marine Geology*, v. 12, p. 165-185.
- Shideler, G. L., Swift, D. J. P., Johnson, G. H., and Holliday, B. W., 1972, Late Quaternary stratigraphy of the inner Virginia continental shelf: A proposed standard section: *Geol. Soc. America Bull.*, v. 83, p. 1787-1804.
- Smith, J. P., 1969, Geomorphology of a sand ridge: *Jour. Geology*, v. 77, p. 39-55.
- , 1970, Stability of a sand bed subject to shear flow of low Froude number: *Jour. Geophys. Research*, v. 30, p. 5918-5940.
- Stefansson, U., Atkinson, L. P., and Bumpus, D. F., 1971, Hydrographic properties and circulation of the North Carolina shelf and slope waters: *Deep-Sea Research*, v. 18, p. 383-420.
- Swift, D. J. P., and Sears, P., 1974, Estuarine and littoral depositional patterns in the superficial sand sheet, central and southern Atlantic shelf of North America: *Internat. Symp. Interrelationships of Estuarine and Continental Shelf Sedimentation*, Inst. Géol. du Bassin d'Aquitaine, Bordeaux, France, Mém. 7, p. 171-181.
- Swift, D. J. P., Kofoed, J. W., Saulsbury, F. P., and Sears, P., 1972, Holocene evolution of the shelf surface, central and southern Atlantic shelf of North America, in: Swift, D. J. P., Duane, D. B., and Pilkey, O. H., eds., *Shelf sediment transport: Process and pattern*: Stroudsburg, Pa., Dowden, Hutchinson & Ross, Inc., p. 499-574.
- Swift, D. J. P., Duane, D. B., and McKinney, T. F., 1973, Ridge and swale topography of the Middle Atlantic Bight, North America: Secular response to the Holocene hydraulic regime: *Marine Geology*, v. 15, p. 227-247.
- Terwindt, J. H. J., 1971, Sandwaves in the Southern Bight of the North Sea: *Marine Geology*, v. 10, p. 51-67.

MANUSCRIPT RECEIVED BY THE SOCIETY SEPTEMBER 10, 1975.

REVISED MANUSCRIPT RECEIVED JUNE 10, 1976  
MANUSCRIPT ACCEPTED JULY 17, 1976

## Geophysical Assessment of Submarine Slide Northeast of Wilmington Canyon

BONNIE A. MCGREGOR\*

**Abstract** As part of a National Oceanic and Atmospheric Administration (NOAA) program to understand bottom and near-bottom processes on the continental margin, the continental slope seaward of the coast of Delaware, just east of the Baltimore Canyon Trough, and northeast of Wilmington Canyon was studied in detail. With a suite of geophysical data, a  $7.5 \times 13.0$ -km portion of the continental slope was surveyed and found to be composed of a large submarine slide, approximately  $11 \text{ km}^3$  in volume. The slide varies from 50 to 300 m in thickness and is believed to be composed of Pleistocene Age sediments. The internal structure of the continental slope can be seen on the seismic reflection profiles, as well as the readily identifiable continuous slip surface. Pliocene to Cretaceous horizons comprise the continental margin with Pliocene to Eocene horizons truncated at the slip surface. Sediment failure occurred on the slope between the late Tertiary erosion surface, which shaped the continental margin, and the overlying Quaternary sediments. A mechanism suggested to have contributed to the sediment failure is a late Pleistocene lower stand of sea level. Creep of surficial sediments is believed to be active on the surface of the submarine slide, indicating present-day instability.

### Introduction

The NOAA program on Rational Use of the Seafloor (RUSEF) of the AOML Marine Geology and Geophysics Laboratory is designed to study bottom and nearbottom processes active on the continental margin. Our understanding of the continental margin has been based historically on seismic reflection profiles oriented perpendicular to the continental margin,

\*Atlantic Oceanographic and Meteorological Laboratories, National Oceanic and Atmospheric Administration, Miami, Florida 33149.

(Received November 29, 1976; accepted December 23, 1976.)

*Marine Geotechnology*, Volume 2, Marine Slope Stability, 1977.

0360-8867/78/0100-0229/\$2.00/0

Copyright © 1978 Crane, Russak & Company, Inc.

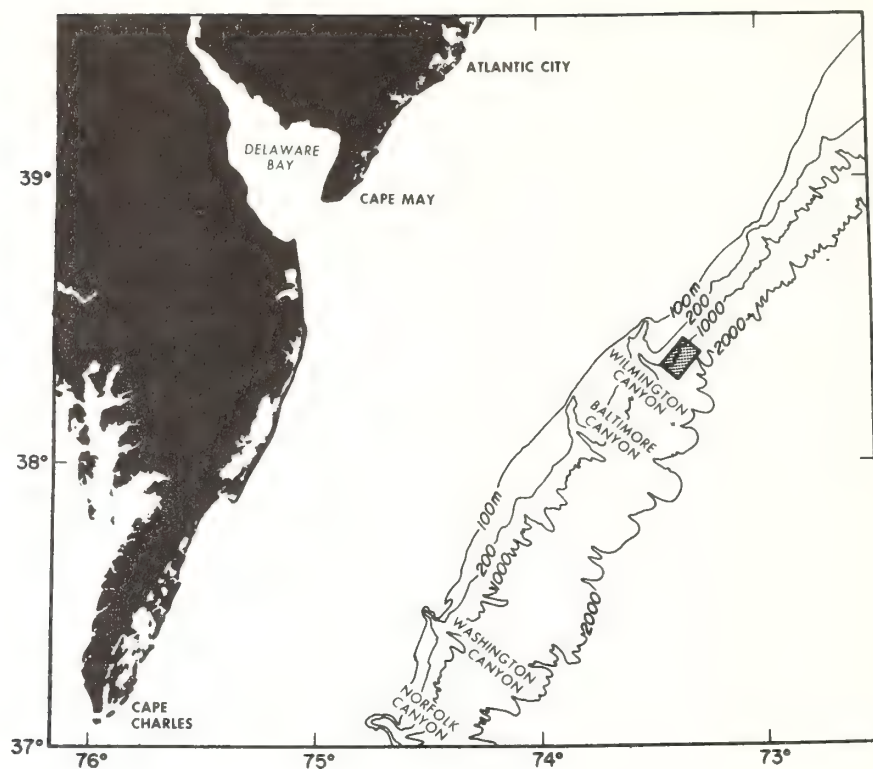


**Figure 1.** Index map of the study area. Bathymetric contours are from Uchupi (1970).

such as the work of Uchupi and Emery (1967). The RUSEF program has collected seismic reflection data on five lines parallel to the continental margin on the outer shelf, upper and lower slope, and rise, with about a 20-km separation between the lines, extending from Hydrographer Canyon, Georges Bank area, to Cape Canaveral, Florida (McGregor et al., 1975, 1976). Transects consisting of four piston cores sampling the outer shelf, slope, and rise, were spaced 80–100 km apart along the margin. The piston cores are currently being analyzed by Dr. Larry Doyle of the University of South Florida and Dr. Orrin Pilkey of Duke University (Doyle et al., 1975). The laboratory analyses of the pilot cores are being made



at AOML. From the seismic data, the mineralogy of the piston cores, and the geotechnical properties of the pilot cores, variations in the sedimentation pattern parallel to the margin are assessed. Areas in which bottom processes have affected the sedimentation pattern are studied in more detail.

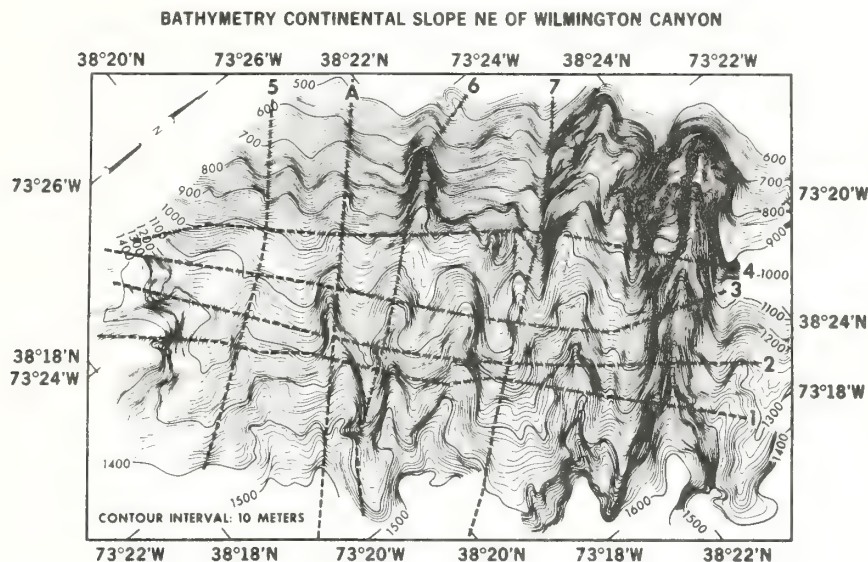


**Figure 2.** Bathymetry of the continental slope. Data in corrected meters (Matthews, 1939) with a 10-m contour interval (McGregor and Bennett, 1977).

The continental margin seaward of New Jersey and Delaware in the vicinity of Wilmington Canyon is a region of dynamic bottom processes (Figure 1). The continental slope northeast of Wilmington Canyon has been dissected by many small valleys (Figure 2) and, judging from a contour map (Wear et al., 1974), many areas of the slope have been affected by small-scale slumping. This portion of the slope (Figure 1) was studied in detail using narrow-beam echo sounding (NBES), 3.5 kHz, and air-gun reflection data. The NBES survey using Loran C and satellite navigation with 0.5-km track line spacing (Figure 3) was conducted to

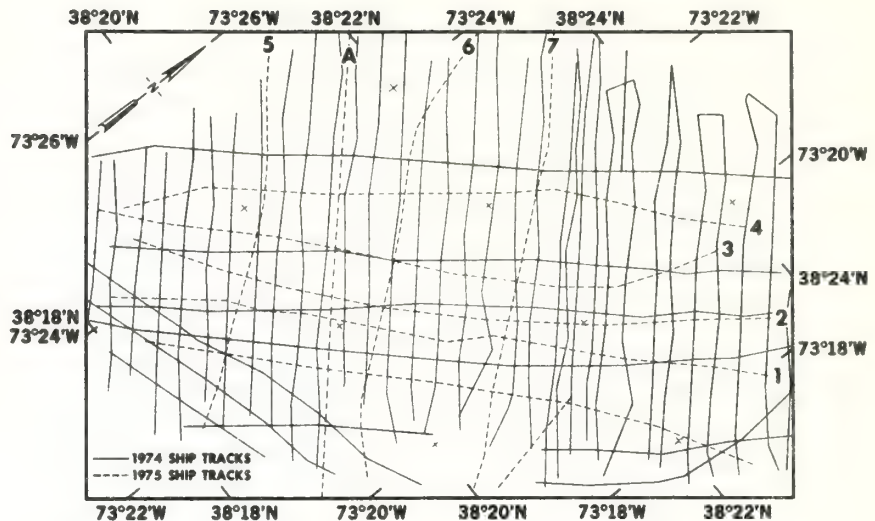
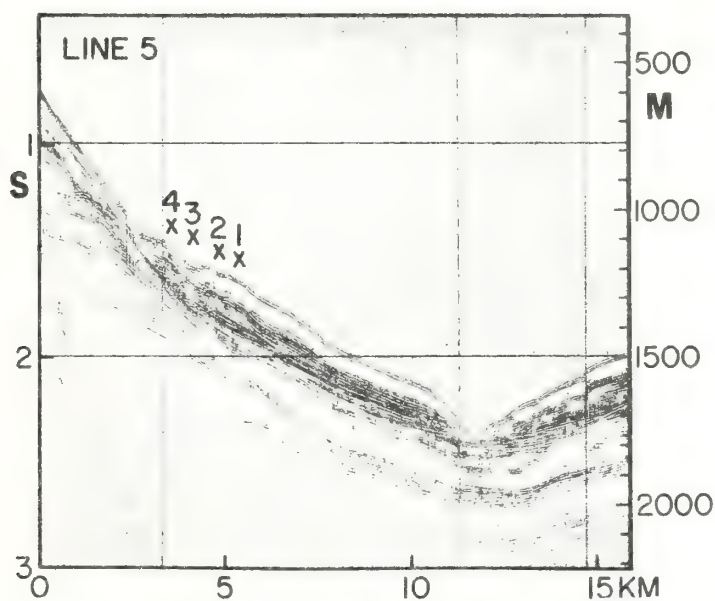
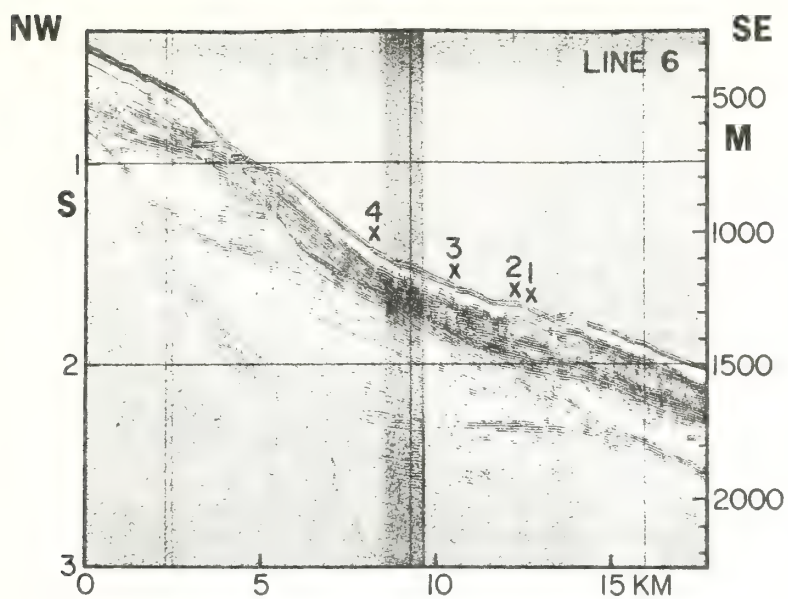


Figure 3. Track chart showing location of data.

delineate the morphology of the slope in this region. The dashed track lines (Figure 3) are locations of seismic reflection profiles. An air gun with a 40-in<sup>3</sup> chamber was used as a sound source with a Teledyne 50-element hydrophone receiver. On line A, the sound source consisted of two air guns with chambers 10 and 120 in<sup>3</sup>. The returning signal was filtered at 80–205-Hz frequency. Bottom samples in this integrated study are discussed by Bennett et al. (1976).

The bathymetry (Figure 2) of the continental slope northeast of Wilmington Canyon between 500 and 1600 m has been contoured with water depths in corrected meters (Matthews, 1939). The slope has been dissected by a large valley on the northeast, as well as by several smaller valleys which, in some cases, extend down across the slope. Wilmington Canyon is just to the southwest of the survey area. The average seafloor slope is approximately 8°; however, the slope is considerably greater in the vicinity of the valleys. The broadening of the area between the 1000- and 1100-m contour is suggestive of slumping and represents the head of a large submarine slide, which is present on the slope extending as far as the valley on the northeast. From the seismic reflection profiles, the areal extent of the sediment failure as well as the internal characteristics of the slide can be determined.



**Figure 4.** Photographs of original seismic reflection records perpendicular to the slope. See Figure 2 for locations. X's refer to the location of line crossings. Depths measured in meters and two-way travel time in seconds.



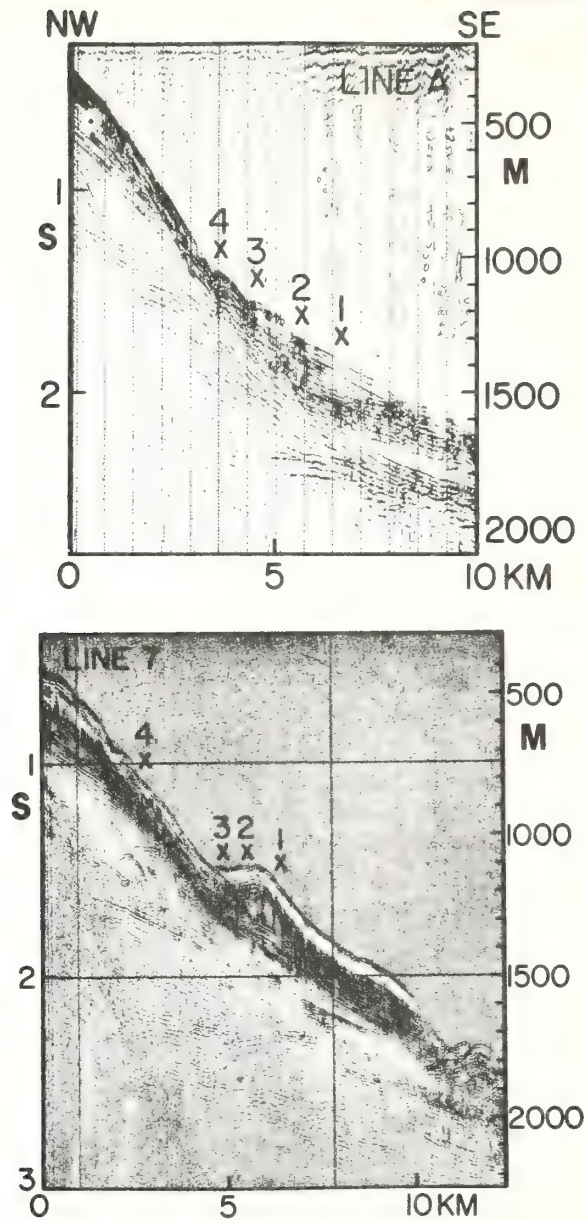


**Figure 5.** Photographs of original seismic reflection records perpendicular to the slope. See Figure 2 for locations. X's refer to the location of line crossings. Depths are in meters and two-way travel time in seconds.

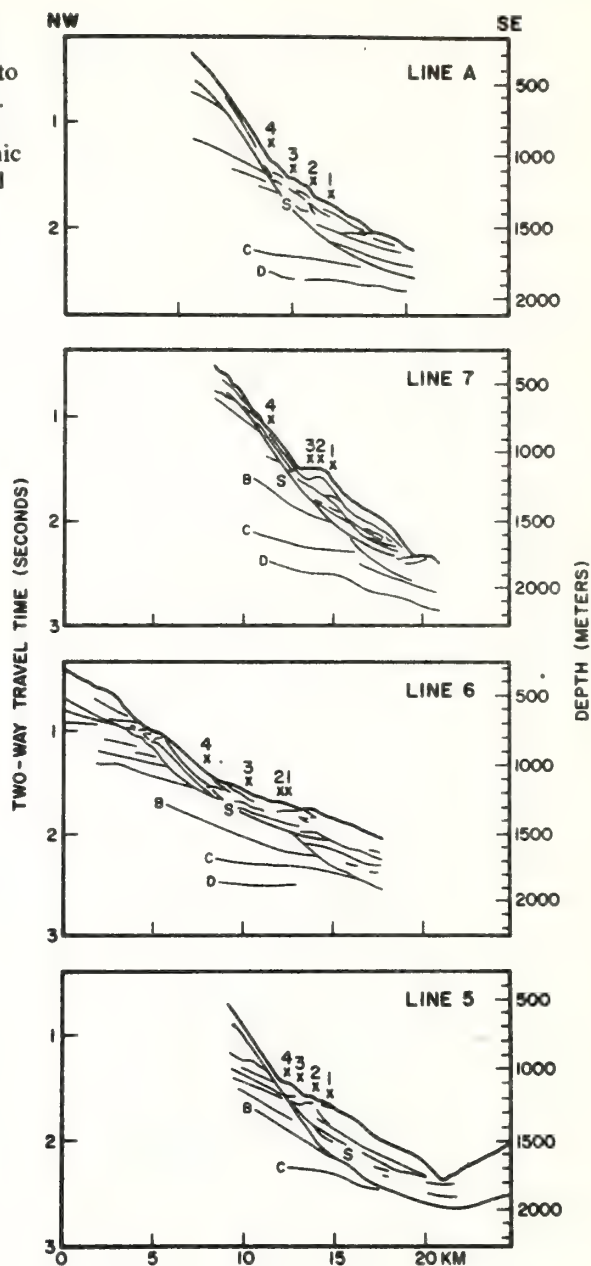
### Seismic Reflection Data

A series of seismic reflection profiles parallel and perpendicular to the continental margin (Figure 2) shows the sedimentary sequence and internal structure of the continental slope. Figures 4 and 5 present the profiles perpendicular to the slope, showing the internal structure of the margin and the submarine slide. Depth in meters and two-way travel time in seconds are shown for each line. The slump block varies in thickness from 50 to 300 m between 800 and 1500 m water depth. The slip surface labeled S (Figure 6) can be seen on all the profiles. The lateral extent of the slide can be determined on the profiles parallel to the slope (Figures 7 and 8). The slip surface (S) is continuous on each of the profiles across a portion of the slope (Figure 9). Numbers and X's refer to the crossing location of the profiles.

Reflecting horizons are present within the slump block above the slip surface (S), but are not continuous over long distances (Figure 9). Horizons (labeled B, C, D) are more continuous and slope seaward truncating at the slip surface (Figure 6). These are part of the older stratigraphic sequence, which forms the framework of the continental margin. The internal structure of the submarine slide can be seen in Figures 4 and 5. A zone of acoustically transparent material approximately 100 m thick is present at the base of the slump block. Lines 5 and 6 in Figure 4 show patchy reflectors in this zone. Stratified sediments are present above the transparent zone. As mentioned previously, these horizons are discontinuous and have an irregular surface in some cases (Figures 6 and 9). The surface of the slide itself is irregular, cut by small valleys (Figure 9), and deformed as a result of the mass movement (Figure 6). Near the head of the slump block toward the base of the scar, interpreted as such from the thinning of sediments and change in the angle of the slope, the sediments are jumbled and the surface irregular, suggestive of tensional forces and rotation of the sediments (Figures 4 and 5). Similarly, on line 7 in Figure 4 the sediments are pushed up near the toe of the slide thereby suggesting compressional forces. The contorted beds at the head and toe of the slide are similar to those shown by Lewis (1971), characterizing the Kidnapper Slump off New Zealand.

Shallow penetration, high-resolution 3.5-kHz data show the structures in the upper 100 m of the submarine slide. Figure 10 is a photograph of the original record along line 5. Distorted sediments at the head of the slump are present. A thin veneer of sediments is located on the slope above the slide. Stratigraphic horizons within the continental margin can

**Figure 6.** Line drawing of profiles perpendicular to the margin. X's refer to location of line crossings. S (slip surface); B,C,D are identifiable stratigraphic horizons (McGregor and Bennett, 1977).





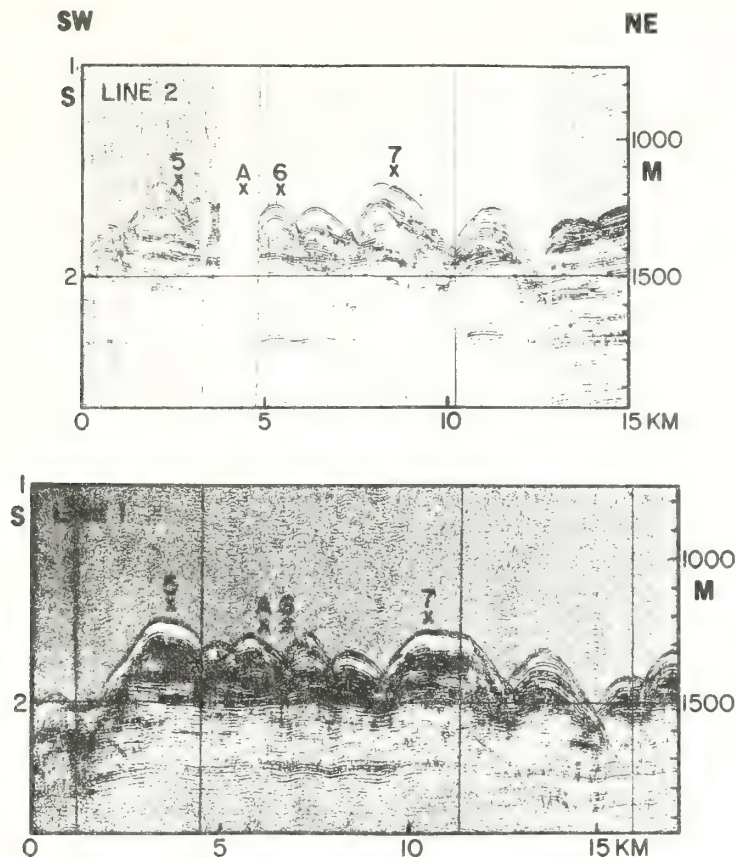


**Figure 7.** Photographs of original seismic reflection records parallel to the slope. See Figure 2 for location. X's refer to the location of line crossings. Depths are in meters and two-way travel time in seconds.

be seen truncating very close to or at the seafloor. A change in slope of the seafloor occurs between the steeper scar and the lower angle of the top of the slide. The shallow penetration data, as well as the seismic reflection data, define the geophysical character of this submarine slide.

### Discussion

This study provides very detailed seismic reflection information of a submarine slide. From the data, the area and the volume of the slump block can be calculated as approximately 68 km<sup>2</sup> and 11 km<sup>3</sup>, respectively.

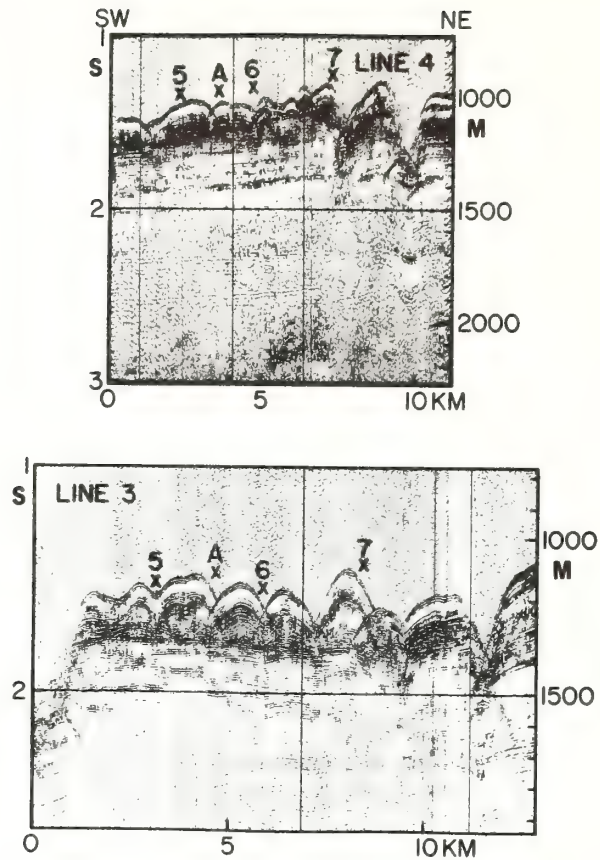


**Figure 8.** Photographs of original seismic reflection records parallel to the slope. See Figure 2 for location. X's refer to the location of line crossings. Depths are in meters and two-way travel time in seconds.

This is a large slide comparable to the Ranger Submarine Slide off Baja, California (Normark, 1974), and to massive slides found in the stratigraphic record on land (Rupke, 1976).

The profiles permit determination of the seafloor slope for different portions of the slide. The present surface of the slide has a generalized

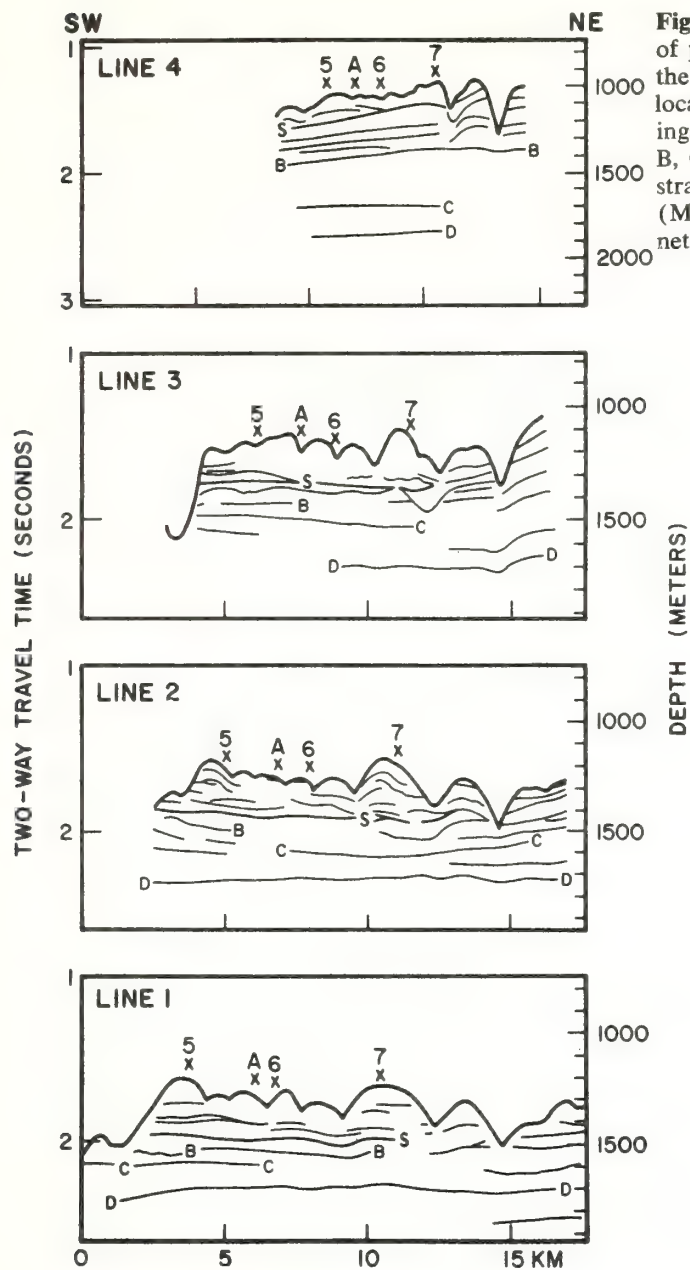


**Figure 9.** Line drawing of profiles parallel to the margin. X's refer to location of line crossings. S (slip surface), B, C, D are identifiable stratigraphic horizons (McGregor and Bennett, 1977).



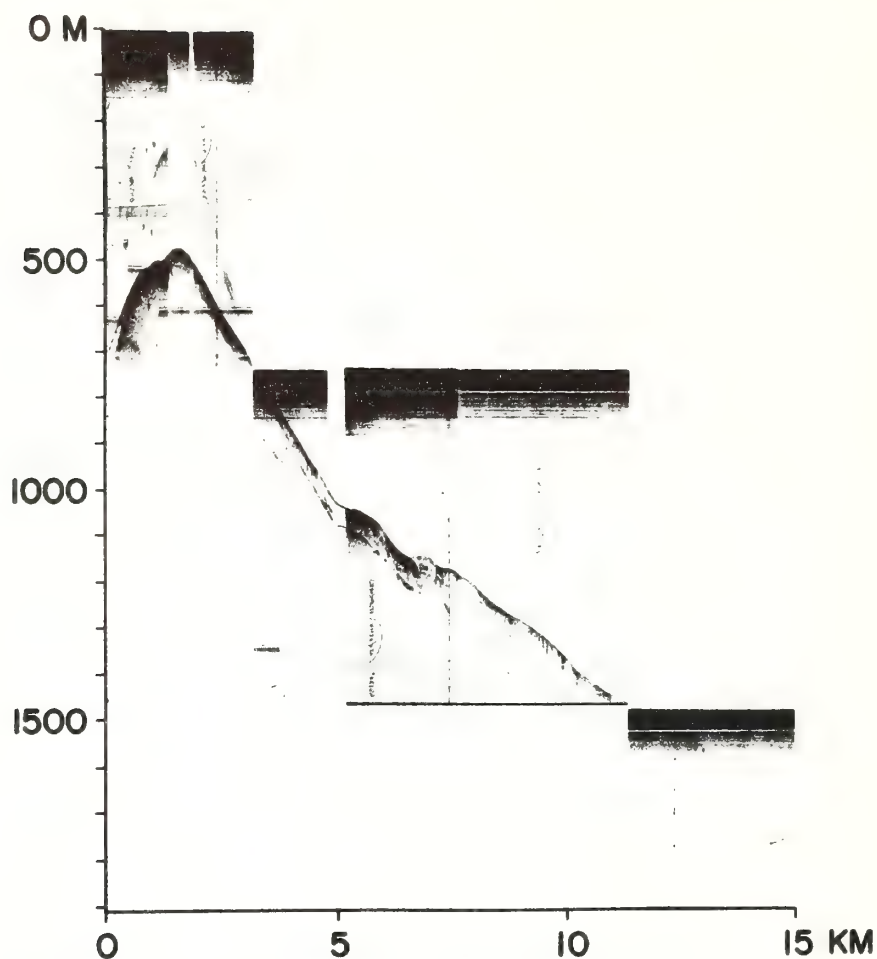


**Figure 10.** Photograph of original 3.5-kHz record along line 5.

slope of  $3^{\circ}$  to  $5^{\circ}$ , and the scar above the slide has a slightly steeper angle of  $9^{\circ}$  to  $14^{\circ}$ . Steeper seafloor slopes are present in localized areas on the bathymetric map (Figure 2). The angle of the surface forming the sole of the slide is about  $7^{\circ}$  (Figures 4 and 5).

The acoustically transparent sediments directly above the slip surface (Figures 4 and 5) may be attributable to the homogenization of sediments,

destroying any preexisting stratification. Rupke (1976) reported deformed and homogenized sediments in slump sheets studied in the southwestern Pyrenees. Another possible origin of the nonstratified zone is a mudflow associated with the slide. In the Sunda Arc region, Moore et al. (1976) interpret a basal nonstratified zone as representative of a mudflow. Material downslope and continuous with the zone was found to bury channels and contain mud volcanoes. Available data in the Wilmington Canyon area do not indicate that the unstratified basal zone of the slide is a mudflow; however, this possibility should not be ruled out.

The age of sediments is important in establishing the time the sediment failure occurred. To the north of this area reflecting horizons within the continental slope truncate at the seafloor, indicating that the continental slope represents a late Tertiary erosion surface (Uchupi and Emery, 1967). Correlation of reflecting horizons with Heezen et al. (1959), Kelling and Stanley (1970), and Sheridan (1975) suggests that horizon B represents the base of the Miocene, C the Eocene, and D the top of the Cretaceous (Figures 6 and 9). The age of a truncated reflecting horizon near the top of the slope (Figures 6, 9, and 10) is interpreted to be Pliocene. The age of the slip surface is believed to be late Pliocene or Quaternary, as it is superimposed on truncated horizons interpreted to be Tertiary. Late Pleistocene material was recovered in 40' piston cores in the surface of the slide (Stefan Gartner, personal communication, 1975). On the basis of the age of the slip surface and the cored material, the slump block is believed to be Pleistocene.

Sediment failure on the slope northeast of Wilmington Canyon occurred between the late Tertiary erosion surface that shapes most of the continental slope and the overlying Quaternary sediments. This failure occurred along a preexisting discontinuity, an erosion surface, as opposed to failure within the stratigraphic column.

Although the main mass sedimentation movement occurred in the Pleistocene, activity is presently occurring near the surface of the slide. Figure 10 shows the thin veneer, and lack of sedimentary accumulation on the slide scar in places. This lack of surficial sediment suggests low sedimentation or a continuing movement of material downslope. The lack of a conformable layer of sediments blanketing the irregular surface of the head of the slide also suggests recent activity. Sedimentological characteristics and the geotechnical properties of sediments also support the occurrence of creep (Bennett et al., 1976).

Possible trigger mechanisms for sediment failure include rapid sediment accumulation, faulting with possibly related earthquake activity, and increased energy input to the seafloor by waves during low sea-level stands in the Pleistocene. Although the head of Wilmington Canyon is interpreted by Kelling and Stanley (1970) to be underlain by a fault, there is no indication of its activity. Faults are present in the Tertiary sequence in the area (Sheridan, 1975), but their activity during the Pleistocene is not known. An increase in rate of sediment accumulation probably occurred on the slope during the Pleistocene; however, profiles to the north and south of this area show a 200-m blanket of Pleistocene material on the slope with no sediment failure. The likely trigger mechanism is increased energy input to the shelf break and upper slope during a low stand of sea level in the late Pleistocene. Terraces believed to have been cut during Pleistocene-lowered sea level are present on the upper slope (Wear et al., 1974). The shape of the shelf edge on the north side of Wilmington Canyon (Figure 1) would focus wave energy on this headland-like area, and would account for sediment failure here as opposed to universal failure along the slope. The surface morphology of the slump block was probably also formed at a lower stand of sea level with the dissection of the upper continental slope. The valleys cut the scar as well as the top of the slide (Figure 2), indicating that dissection is postsediment failure. Also, on line 4 (Figures 8 and 9), the valley northeast of the crossing of line 7 appears to cut through the slip surface. Although faulting cannot be ruled out as contributing to the sediment failure, the Pleistocene and coincident sediment failures around the Atlantic, such as those reported by Roberts (1972), Seibold and Hinz (1974), and Embley (1976), suggest that increased energy input to the seafloor during a Pleistocene low stand of sea level may be an important part of the trigger mechanism for sediment failure on the slope northeast of Wilmington Canyon.

### Conclusions

A submarine slide has been defined through the use of geophysical techniques. From the bathymetry, the morphology of the slide and its setting were determined. The seismic reflection data identified the slip surface, the internal structure of the slide and the continental slope, and the volume of the slide (approximately 11 km<sup>3</sup>). Sediment failure occurred along the late Tertiary erosion surface, which shapes most of the continental slope. Sediments comprising the slide are interpreted to be Pleistocene. A composite mechanism may have triggered the failure; however,



increased energy input to the seafloor during a late Pleistocene lower stand of sea level is believed to have played an important role. Lack of sediments on the slide scar is suggestive of present-day instability.

### Acknowledgments

Special thanks are due to Richard H. Bennett for his assistance and discussions during all aspects of this study and to Mahlon M. Ball and William R. Bryant for critically reviewing the manuscript. I would like to express my appreciation to Douglas Lambert, William Sawyer, George Lapiene, Evan Forde, and Frances Nastav of AOML, and to Matthew Hulbert of Connecticut College for assisting in the data collection and processing. The bathymetry was contoured by Evan Forde and Douglas Lambert. Appreciation is also extended to the officers and crew of the NOAA Ship Researcher for diligence and excellence in executing the survey. Funds for this work were provided by the National Oceanic and Atmospheric Administration.

### References

- Doyle, L. J., Pilkey, O. H., Hayward, G. L., and Arbogast, J. S., 1975. Sedimentation on the northeastern continental slope of the United States. IX Congress International de Sedimentologie, Nice, pp. 51-56.
- Embley, R. W., 1976. New evidence for occurrence of debris flow deposits in the deep sea. *Geology*, vol. 4, pp. 371-374.
- Heezen, B. C., Tharp, M., and Ewing, M., 1959. The floors of the oceans 1. North Atlantic. *Geological Society of America Special Paper*, vol. 65, 122 pp.
- Kelling, G., and Stanley, D. J., 1970. Morphology and structure of Wilmington and Baltimore submarine canyons, eastern United States. *Journal of Geology*, vol. 78, pp. 637-660.
- Lewis, K. B., 1971. Slumping on a continental slope inclined 1°-4°. *Sedimentology*, vol. 16, pp. 97-100.
- McGregor, B. A., and Bennett, R. H., 1977. Continental slope sediment instability NE of Wilmington Canyon. *American Association of Petroleum Geologists Bulletin*, vol. 61, pp. 918-928.
- McGregor, B. A., Keller, G. H., and Bennett, R. H., 1975. Seismic profiles along the U.S. northeast coast continental margin. *EOS, Transactions of the American Geophysical Union*, vol. 56, p. 382.
- McGregor, B. A., Keller, G. H., and Bennett, R. H., 1976. Seismic reflection profiles along the Middle Atlantic U.S. continental margin. *Geological Society of America NE-SE Meeting Abstracts*, vol. 8, p. 227.
- Matthews, D. J., 1939. Tables of the velocity of sound in pure water and sea water for use in echo-sounding and sound ranging. Admiralty Hydrographic Department, London, Publication H.D. 282, 52 pp.
- Moore, D. G., Curray, J. R., and Emmel, F. J., 1976. Large submarine slide (olistostrome) associated with Sunda Arc subduction zone, northeast Indian Ocean. *Marine Geology*, vol. 21, pp. 211-226.

- Normark, W. R., 1974. Ranger submarine slide, northern Sebastian Vizcaino Bay, Baja California, Mexico. *Geological Society of America Bulletin*, vol. 85, pp. 781-784.
- Roberts, D. G., 1972. Slumping on the eastern margin of the Rockall Bank, North Atlantic Ocean. *Marine Geology*, vol. 13, pp. 225-237.
- Rupke, N. A., 1976. Large-scale slumping in a flysch basin southwestern Pyrenees. *Journal of the Geological Society of London*, vol. 132, pp. 121-130.
- Seibold, E., and Hinz, K., 1974. Continental slope construction and destruction, West Africa, in C. A. Burke, and C. L. Drake, (eds.) *Geology of Continental Margins*, New York, Springer-Verlag, pp. 179-196.
- Sheridan, R. E., 1975. Dome structure, Atlantic continental shelf east of Delaware: Preliminary geophysical report. *American Association of Petroleum Geologists Bulletin*, vol. 59, p. 1203-1211.
- Uchupi, E., 1970. Atlantic continental shelf and slope of the United States—Shallow structure. U.S. Geological Survey Professional Paper 529I, pp. 1-43.
- Uchupi, E., and Emery, K. O., 1967. Structure of continental margin off Atlantic coast of United States. *American Association of Petroleum Geologists Bulletin*, vol. 51, pp. 223-234.
- Wear, C. M., Stanley, D. J., and Boula, J. E., 1974. Shelfbreak physiography between Wilmington and Norfolk Canyons. *Marine Technological Society Journal*, vol. 8, pp. 37-48.

## Continental Slope Sediment Instability Northeast of Wilmington Canyon<sup>1</sup>

BONNIE A. MCGREGOR<sup>2</sup> and RICHARD H. BENNETT<sup>2</sup>

**Abstract** A region on the U.S. East Coast exhibiting sediment instability is present on the continental margin seaward of the coast of Delaware and the Baltimore Canyon Trough area. A detailed bathymetric and seismic-reflection survey of a 7.5 by 13.0-km area, together with box, hydroplastic, and piston cores, affords an integrated study of a large submarine slide with a volume of 11 cu km on the continental slope northeast of Wilmington Canyon. The geotechnical properties and sedimentologic characteristics of the seafloor show variations that are associated with the slide. The slump block is believed to be composed of Pleistocene sediment with sediment failure occurring on the slope along a late Tertiary erosion surface which formed the gross morphology of the continental margin. The suggested mechanism for triggering the sediment failure is increased wave energy associated with a lower stand of sea level during the late Pleistocene. Mass wasting of material downslope by creep is a process which apparently still is occurring.

### INTRODUCTION

Seaward of New Jersey and Delaware, in the vicinity of Wilmington Canyon (Fig. 1), dynamic processes are operating on the continental slope. Wilmington Canyon actively channels material from the continental shelf to the rise (Kelling and Stanley, 1970). The continental slope northeast of Wilmington Canyon has been dissected by many small valleys, and many areas show small-scale slumping (Wear et al, 1974).

One such location with suspected slumping was studied in detail using narrow-beam echo sounding (NBES), 3.5-kHz seismic-reflection data, and bottom samples. This paper is concerned with the initial results of a major geotechnical program designed to investigate the mass physical and chemical properties and related geologic and geophysical characteristics of a well-defined submarine slide.

### METHODS

An NBES survey, using Loran C and satellite navigation with 0.5-km track-line spacing was conducted to delineate the morphology of the slope between the water depths 500 and 1,600 m in a 7.5 × 13-km area. A transect of box and piston cores normal to the slope was taken to determine the kind, distribution, and geotechnical properties of the sediment. A series of eight seismic-reflection profiles was made across the slope. The seismic system used consisted of an airgun with a 640 × 10<sup>-6</sup> cu m (40 cu in.) chamber as a

sound source with a Teledyne 50-element hydrophone receiver. On line A the sound source consisted of two air guns with chambers 160 × 10<sup>-6</sup> cu m and 1,920 × 10<sup>-6</sup> cu m (10 and 120 cu in.). The returning signal was filtered at 80 to 205-Hz frequency. Five 3.5-kHz profiles were made.

### SLOPE MORPHOLOGY

The study area is the upper to lower continental slope adjacent to Wilmington Canyon that encompasses a water-depth range of 500 to 1,600 m. This part of the slope is flanked on the southwest by Wilmington Canyon and on the northeast by another relatively large, well-defined valley (Figs. 1, 2). The slope in this area is dissected by several small valleys, some of which extend all the way down the slope. The average seafloor gradient is about 8°, but in the vicinity of the valleys, it is considerably steeper. A detailed slope map following techniques described by Schmoll and Dobrovolsky (1972) for the area will be presented elsewhere (Bennett et al, in prep.). The whole portion of the slope, as far as the valley at the northeast side, is a large submarine slide with small-scale features superimposed. The broadening of the area between contours 1,000 and 1,100 m suggests the presence of small slumps and was found to represent deformation at the head of the slide (Fig. 2).

### SEISMIC-REFLECTION PROFILES

Seismic-reflection profiles collected parallel with and perpendicular to the margin (Fig. 2) outline the sedimentary sequence and internal structure of the continental slope. The profiles that

© Copyright 1977. The American Association of Petroleum Geologists. All rights reserved.

<sup>1</sup>Manuscript received, September 17, 1976; accepted, November 29, 1976.

<sup>2</sup>Atlantic Oceanographic and Meteorological Laboratories, Marine Geology and Geophysics Laboratory, NOAA, 15 Rickenbacker Causeway, Miami, Florida 33149.

We would like to thank Douglas Lambert, William Sawyer, George Lapiene, Evan Forde, and Frances Nastav of AOML, and Matthew Hulbert of Connecticut College for assisting in the data collection and processing of data and bottom samples. The bathymetry was contoured by Evan Forde and Douglas Lambert. Appreciation also is extended to the officers and crew of the NOAA Ship *Researcher* for diligence and excellence in executing the survey. Funds for this work were provided by the National Oceanic and Atmospheric Administration.



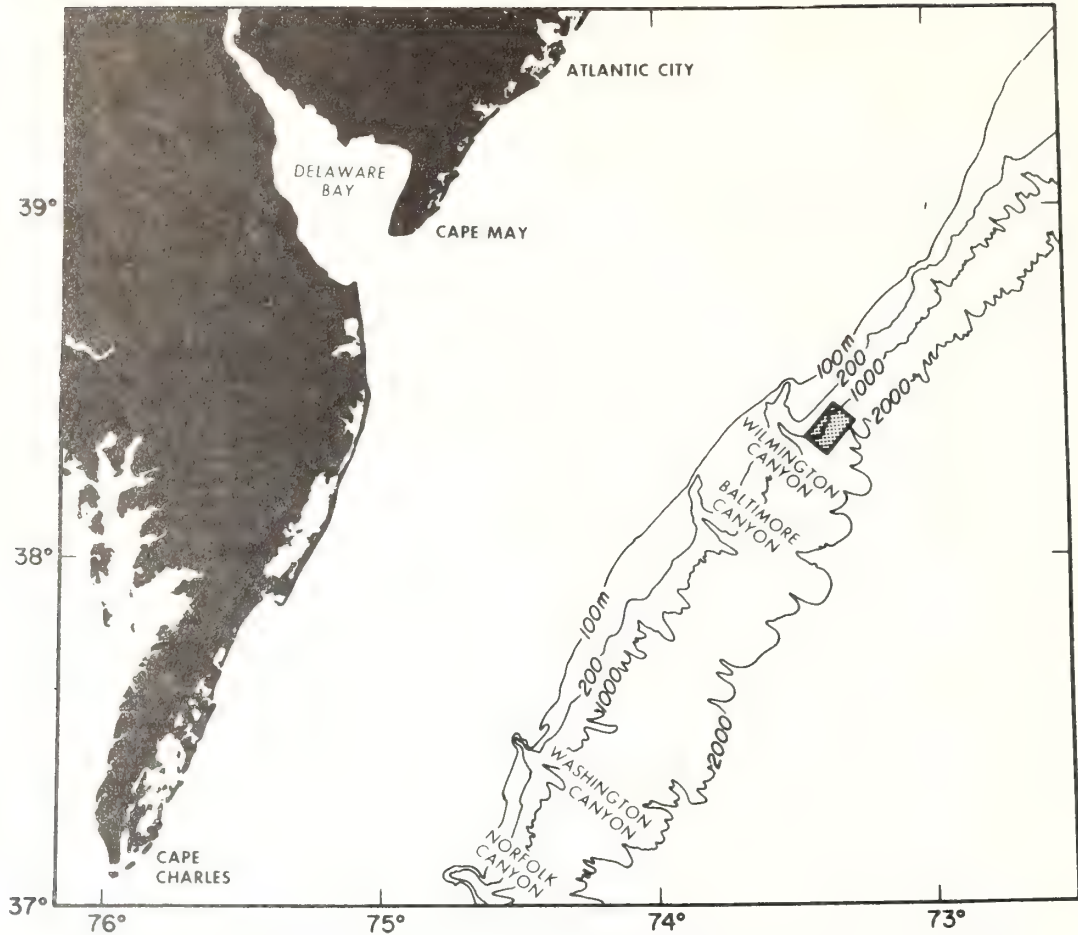


FIG. 1—Index map showing detail study area. Bathymetric contours in meters from Uchupi (1970).

were obtained perpendicular to the slope (Figs. 3, 4) show a well-defined submarine slide between 800- and 1,500-m water depth. The thickness of this block ranges from 50 to 300 m, assuming 1,500 m/sec sound velocity in the sediments. On the profiles parallel with the strike of the slope (Figs. 5, 6), we determined the lateral extent of the block to be 10 km.

The slip surface, labeled A, of the slide is present on all profiles and is traceable across most of the slope. Without the profiles normal to the slope, A could be misinterpreted as a stratigraphic horizon rather than a deformational zone. The slip surface appears to slope up to the northeast (Fig. 6, line 4). Reflecting horizons are present within the slump block above the slip surface A, but these are not continuous over long distances. Below the slip surface the reflecting horizons are more continuous (labeled B, C, D; Figs.

5, 6). Figures 3 and 4 show these horizons to slope seaward, to be truncated at the slip surface, and to represent the older stratigraphic sequence comprising the continental margin.

The sediments composing the slump block have different acoustic properties. A zone of acoustically transparent material approximately 100 m thick is present at the base of the slump block on lines 5 through 7 (Fig. 4). Patchy reflectors in the transparent zone on line 6 suggest that homogenization of the sediments may have occurred in this zone adjacent to the slip surface. Moore et al (1976) reported a similar nonstratified zone at the base of a submarine slide in the Sunda Arc region. They interpret this zone as a mudflow, on the basis of the burial of channels downslope and on the presence of mud volcanoes. In the Wilmington Canyon area there is at present no evidence that the unstratified basal

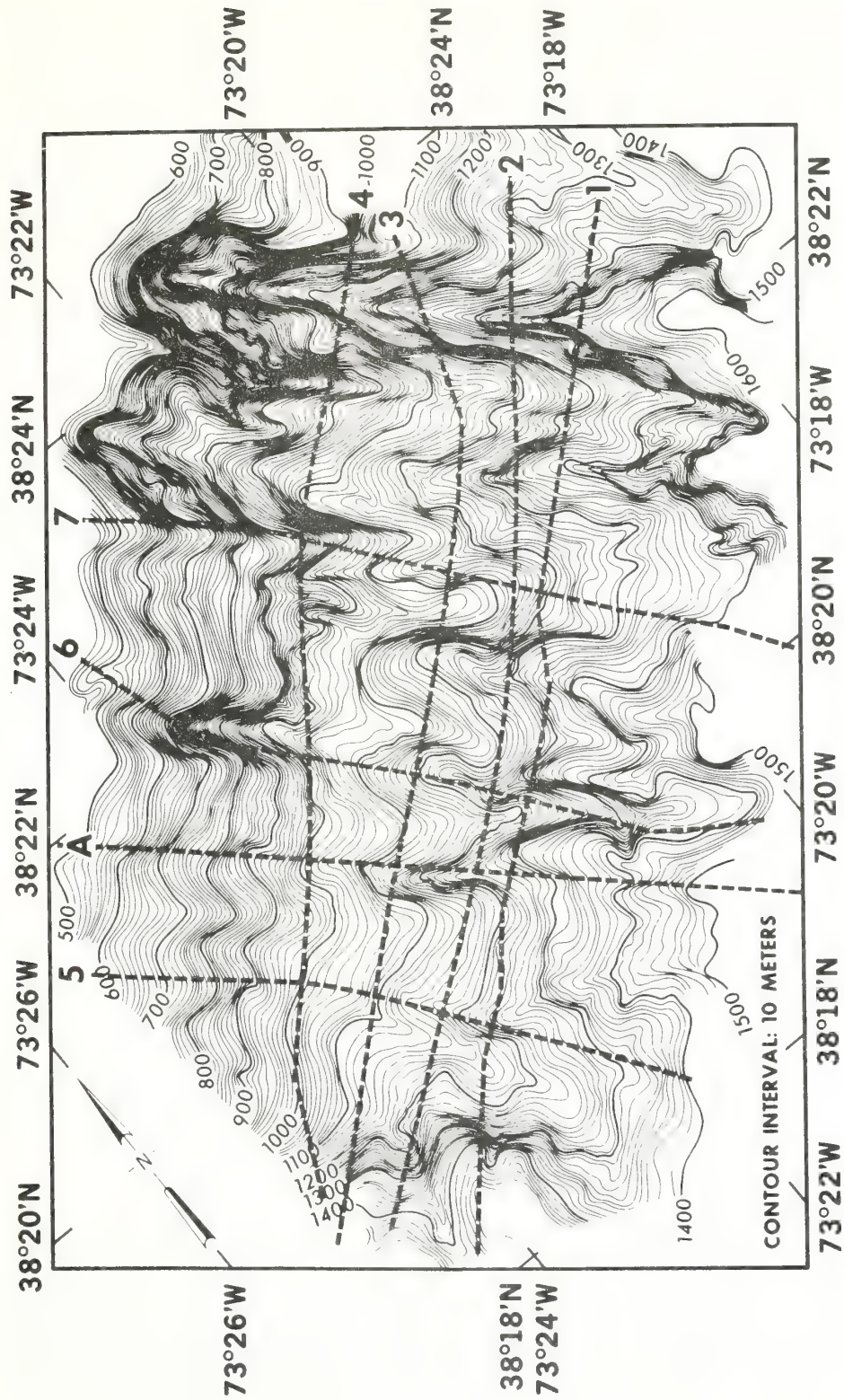


FIG. 2.—Bathymetric contour map in corrected meters of continental slope northeast of Wilmington Canyon (Matthews, 1939). Numbered lines are location of seismic-reflection profiles.



unit of the slide represents a mudflow, although this interpretation cannot be ruled out. The remainder of the slump block is composed of stratified sediments. Near the head of the slump block in the vicinity of what is interpreted to be the scar on the basis of thinning of the sediments and change in angle of the slope, the sediments are jumbled and the surface is irregular, suggesting tensional forces and rotation of the sediments. On line 7 (Figs. 3, 4) near the toe of the slump the sediments are pushed up and the surface also is irregular, suggesting compressional forces. Hyperbolic echoes and contorted beds on line 6 downslope from the crossing of profile 1 also indicate activity of the surface material of the slide. The contorted beds at the head of the slide on all lines (Figs. 3, 4) and at the toe on line 7 are similar to those found by Lewis (1971) characterizing the Kidnapper Slump off New Zealand.

Shallow-penetration 3.5-kHz records were collected on some of the seismic lines, and Figure 6 is the record along line 5. Locations of the cores discussed in this paper are projected onto this line to show the morphology and acoustic reflectors where the cores were taken. The maximum sediment penetration is about 100 m. The top of the slide and the upper slope are shown on the profile. Horizons comprising the continental margin are truncated at the slip surface on the slope above the slide and the veneer of sediments is thin. In the vicinity of core A, horizons appear to be truncated at the seafloor. The irregular topography of the head of the slump block has reflecting horizons cropping out at the seafloor. The thin veneer and in places apparent lack of surficial sediment on the slide scar suggest low sedimentation or movement of sediment downslope by creep. Also the lack of postslump sediment accumulation draping over the head of the slide suggests creep.

From the seismic-reflection profiles, the area and also the volume of the slide block can be calculated as 68 sq km and 11 cu km respectively. Thus, the slide is large, comparable in size to the Ranger submarine slide off Baja California (Normark, 1974), and to massive slides in the stratigraphic record on land (Rupke, 1976). The thickness of the sediment in the slump block ranges from 50 to 300 m.

The gradient of the slope on which the block slid (angle of the slip surface) is about 7° (Fig. 3). The angle of the present surface of the slump varies depending on morphology, but in general is between 3 and 5°. The upper part of the continental slope that represents the slide scar has a slightly steeper angle between 9 and 14°. The break in slope between the present surface of the slump block and the scar is at about 950-m depth.

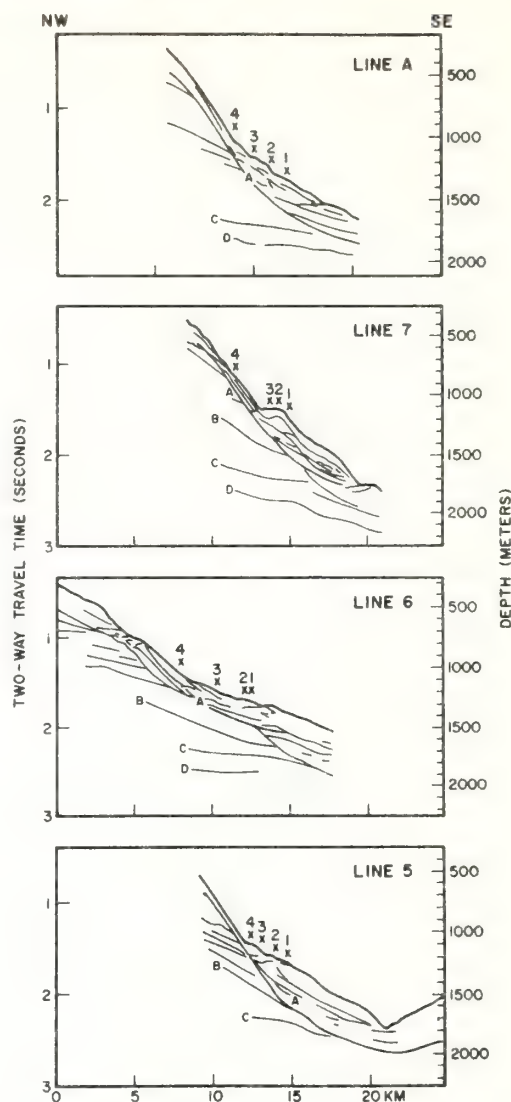


FIG. 3—Line drawings of seismic-reflection profiles perpendicular to continental slope. Number with X refers to crossing location of profile of Figure 5. Slip surface is labeled A; B, C, and D are identifiable horizons. Vertical exaggeration is 7.5× (assuming velocity of 1,500 m/sec).

A profile just north of this area shows reflecting horizons within the continental slope truncated at the seafloor, with the continental slope in the area representing a late Tertiary erosion surface (Uchupi and Emery, 1967). The age of reflecting horizons B, C, D shown here (Figs. 3, 5) can be estimated by correlation with those found by Heezen et al (1959), Kelling and Stanley (1970),



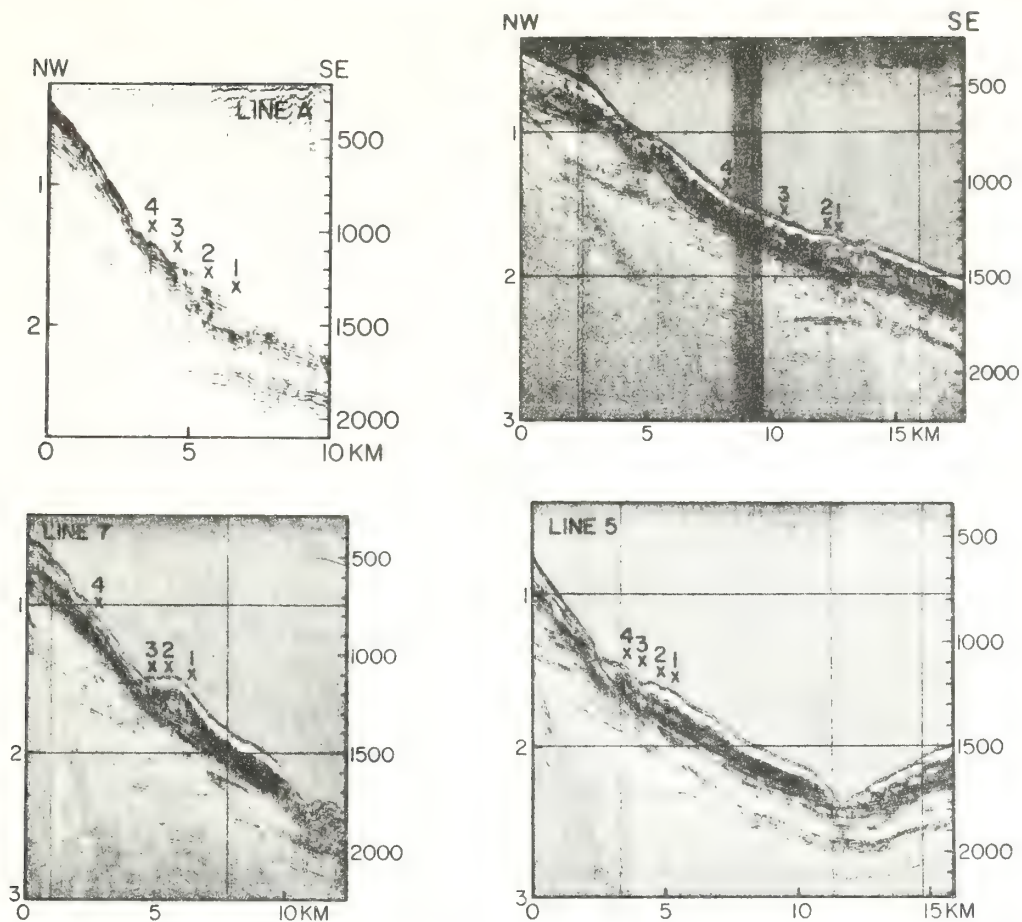


FIG. 4—Photographs of original seismic-reflection records. Number with X refers to crossing location of profile of Fig. 6 (see Fig. 2 for line locations). Vertical exaggeration is  $7.5\times$  (assuming velocity of 1,500 m/sec).

and Sheridan (1975). Reflecting horizon B is interpreted to represent the base of the Miocene, C Eocene, and D the Eocene-Cretaceous boundary; a truncated reflecting horizon near the top of the slope (Figs. 3, 4) is interpreted to be Pliocene in age. Because the slip surface is superimposed on this truncated Pliocene horizon, its age is younger, therefore Quaternary in age. Dredged samples from the edge of the survey area contain Pleistocene material (Gibson et al, 1968). An age of late Pleistocene approximately  $250 \times 10^3$  years B.P. was obtained from microfossils piston cored at a depth of 40 ft (12 m) and  $100 \times 10^3$  years B.P. near the surface of the slide (Stefan Gartner, 1975, personal commun.). The slump block appears to be composed primarily of Pleistocene material. The triggering mechanism for the sediment failure can only be suggested. Kelling and Stanley (1970) indicated that the head of Wil-

lington Canyon is underlain by a fault, although its history of activity was not reported. A more likely mechanism is increased energy input to the shelf break and upper slope during a lower stand of sea level in the late Pleistocene. The surface morphology of the slump block probably was formed during a lower stand of sea level about 180 m lower than at the present (Wear et al, 1974) when the upper continental slope was dissected. The valleys cut the scar as well as the top of the slide, indicating that dissection was after sediment failure. However, in some slope regions submarine valleys and gullies are believed to represent slump scars (Moore, 1969). This is unlikely here, for the region is a slide and the valleys are superimposed.

On the continental slope northeast of Wilmington Canyon, sediment instability on a large scale has occurred. The gravitational induced shear

stress exceeded the shear strength of the sediments with failure occurring between the late Tertiary erosion surface of the continental slope and the overlying Quaternary sediments. It is important to note that sediment failure was along a preexisting discontinuity, an erosion surface, as opposed to failure within the stratigraphic column. The failure is believed to have occurred during a late Pleistocene lower stand of sea level. Profiles north and south of this area show approximately 200 m of Pleistocene material blanketing the continental slope.

That activity is occurring now near the surface of the slump is suggested by the shallow-penetration 3.5-kHz data (Fig. 7) which show lack of sediment accumulation on the slide scar and lack of a conformable sedimentary layer blanketing the irregular surface of the head of the slump. Creep may be occurring on the slide scar. The age data of  $100 \times 10^3$  years B.P. on sediment near the surface of the slump also indicate little deposition or mixing of the sediments. Sedimentologic characteristics and the geotechnical properties of the sediments, as will be shown, also suggest the creep-process concept.

#### SEDIMENTS AND SELECTED GEOTECHNICAL PROPERTIES

A sediment-core transect was made over selected areas of the slope identified by seismic-reflection profiles as both slumped and unslumped (Fig. 7). Piston, box, Boomerang, and hydroplastic cores were collected to assess the geotechnical properties and sedimentologic characteristics of the seafloor deposits associated with the submarine slide. Three cores have been selected as examples for the detailed discussion here.

Surficial sediments are predominantly silty clay and clayey silts rich in illite with lesser quantities of feldspar, chlorite, kaolinite, quartz, and smectite minerals. A few types of heavy minerals are also present in the  $>5\text{-}\mu$  fraction of upslope sediments, on the slide scar, examined by X-ray diffraction. Authigenic pyrite is common as burrows and as globular masses and often shows up in radiographs as dense, "white" flecks. Calcium carbonate is present predominantly in the form of calcareous tests scattered throughout the muds. Similar mineralogic and textural characteristics of U.S. continental-slope sediments have been reported by Doyle et al (1975). Texture and mineralogy of suspended sediments in the Wilmington Canyon area, at the shelf break, and on the slope have been discussed by Lyall et al (1971).

Upper slope cores, above the slide, consistently have several centimeters of sand and coarse shaly silts at the sediment-water interface overlying the muds. These topmost sandy sediments were not

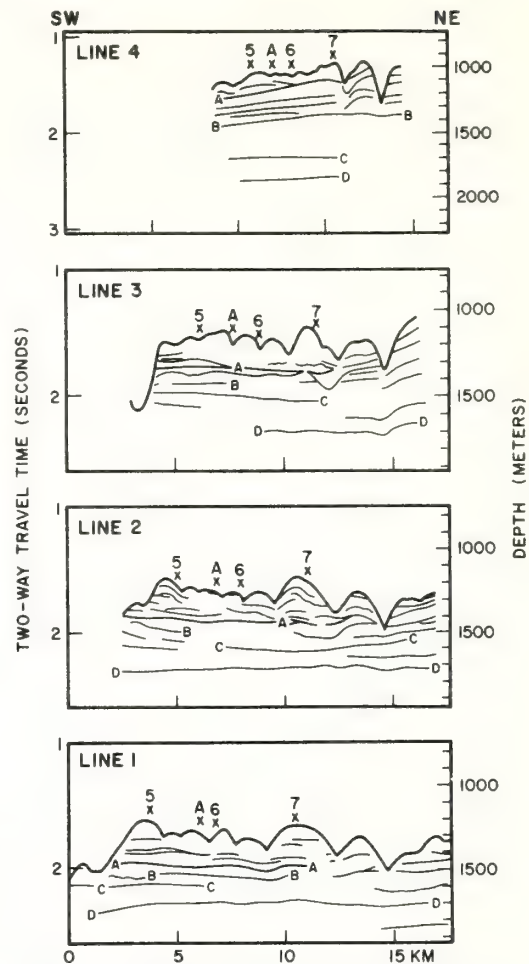


FIG. 5—Line drawings of seismic-reflection profiles parallel with continental slope. Number with X refers to crossing location of Figure 3. Slip surface is labeled A; B, C, and D are identifiable horizons. Vertical exaggeration is  $7.5\times$  (assuming velocity of 1,500 m/sec).

present in the cores recovered from the surficial sediments downslope on the slump block proper. The presence of sand throughout the silty clays and clayey silts is generally much less than 10% for both upslope (scar) and downslope (slump block proper) sediments. The top 4 to 5 m of upslope sediment is characterized by a slight increase in silt content relative to clay with increasing depth below the mud line. In contrast, profiles of silt and clay in cores associated with the slump block reveal a general decrease in silt and increase in clay-size particles with increasing core depth (Fig. 8A, B, C).

Examination of sedimentary structures in box cores and piston cores suggests that gravity-induced sediment failure of surficial seafloor depos-

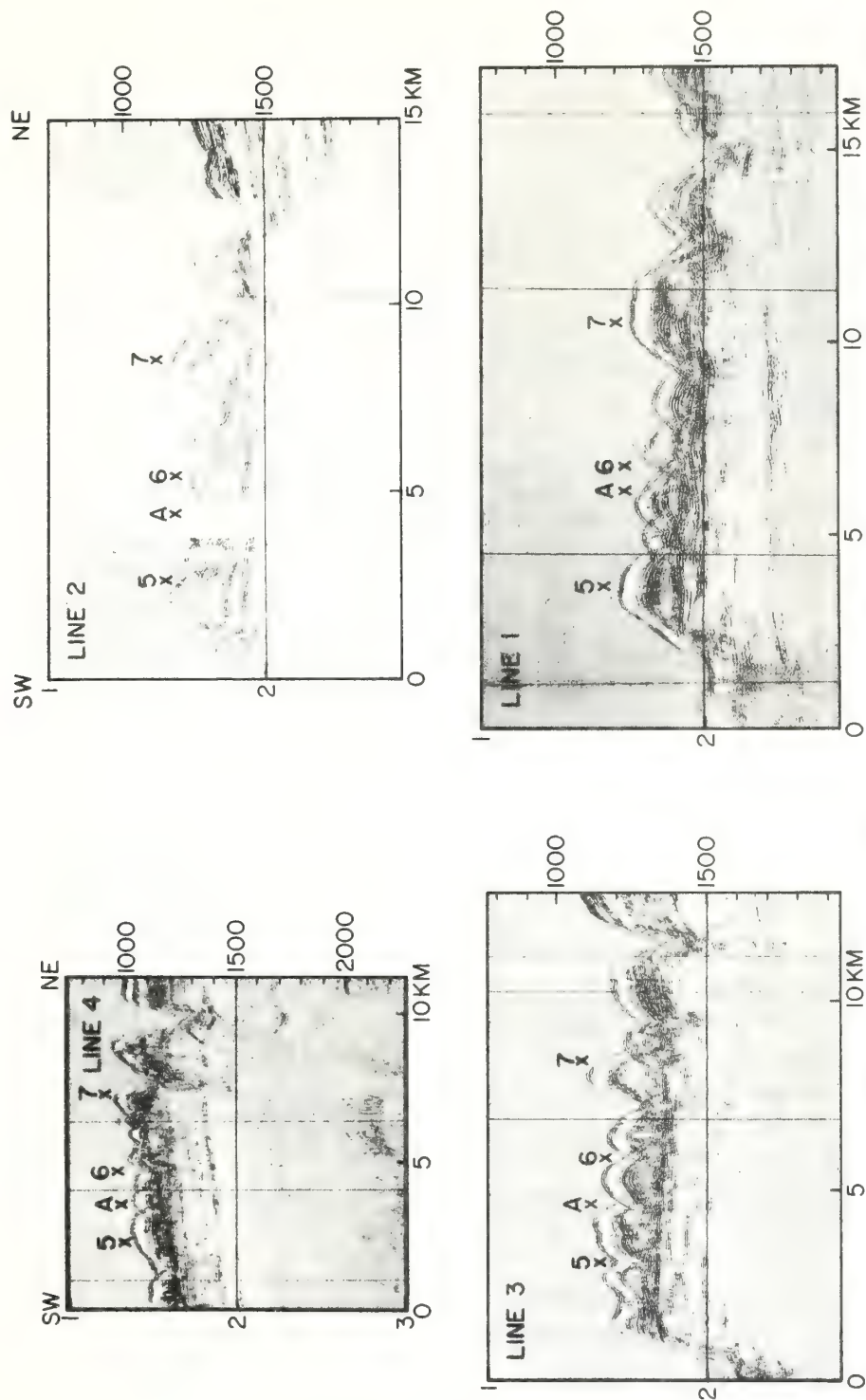


FIG. 6—Photographs of original seismic-reflection records. Number with  $x$  refers to crossing location of profile of Figure 4 (see Figure 2 for line locations). Vertical exaggeration is  $7.5\times$  (assuming velocity of 1,500 m/sec).



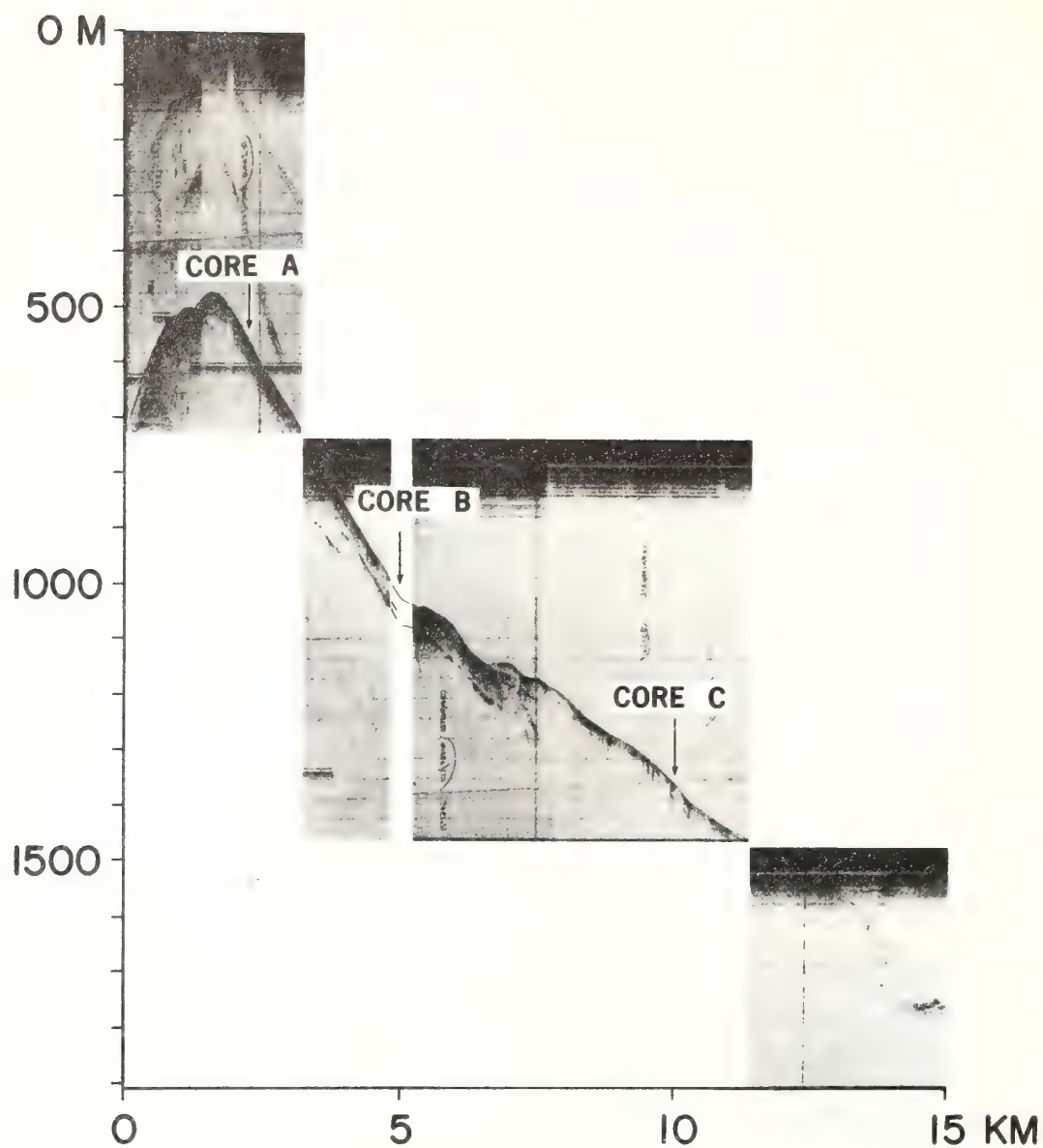


FIG. 7—Photograph of original 3.5-kHz record along line 5 (Figs. 2, 4). Piston-core locations have been projected onto profile to show morphology and stratigraphic setting of core site.

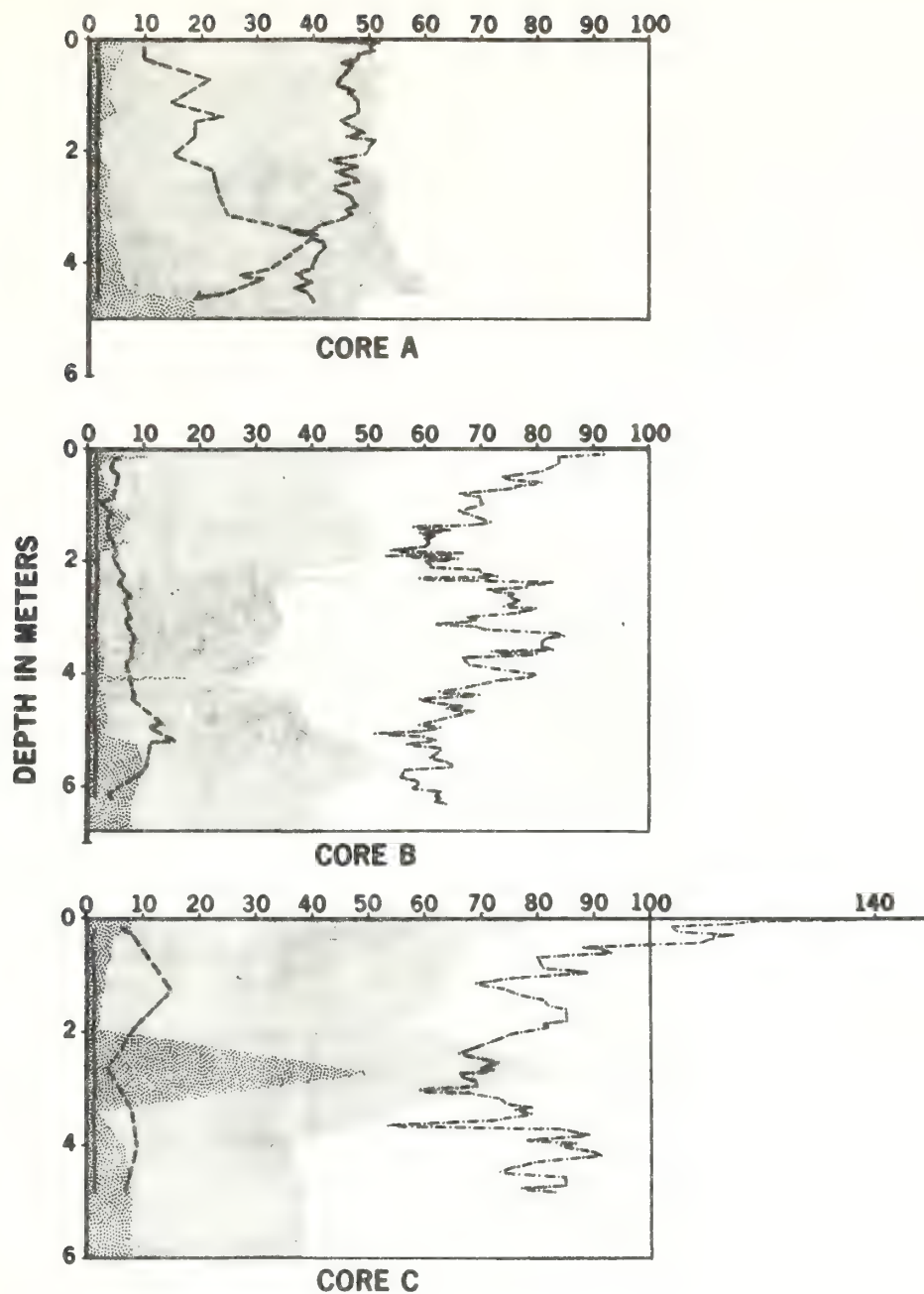


FIG. 8—Selected geotechnical properties of slope cores A, B, and C, locations of which are shown in Figure 7. See key for units on horizontal scale.

its is an important deformational process active on the continental slope northeast of Wilmington Canyon. Creep and apparent foundering of surficial sediments are revealed by contorted bedding and the presence of "sand balls" or clasts within the silty clays and clayey silts. Apparent load structures of the topmost sands and sandy silts overlying the muds are characteristic of the box cores from the sediment on the slope above the slide. Numerous "clay balls" are scattered throughout these topmost coarse-grained clastic sediments. The apparent load structures represent unstable conditions and probably develop contemporaneously with slow creep of sediments down the continental slope. The upslope coarse-grained sediments and underlying muds are on slopes averaging about 9 to 14° in water depths less than 950 m. The downslope muds, having a conspicuous absence of topmost coarse clastics, are on slopes averaging 3 to 5° in water depths exceeding 950 m in the study area.

Surficial sediments upslope from the slump block are characterized by typical variations in the mass physical properties with core depth. Undrained shear strength, determined with a miniature vane-shear apparatus, and wet unit weight (wet bulk density) steadily increase with depth below the mud line commensurate with a decrease in water content (Fig. 8A). Richards (1961, 1962) and Keller and Bennett (1968, 1970) have discussed typical geotechnical properties of submarine sediments and their variation with core depth. In contrast to the upslope sediments, surficial sediments downslope overlying the slump block generally have low shear strengths and relatively high variability of mass physical properties with core depth. This variability is revealed particularly well in the profiles of water content and sediment texture (Fig. 8B, C). Wet unit weight is considerably less sensitive to variation in other related physical properties than is water content alone (Bennett and Lambert, 1971). Profiles of the mass physical properties clearly reveal that sediment grain size is considerably more variable with core depth in sediments recovered from the slump block proper in comparison to the textures of upslope sediments (Fig. 8A, B, C).

Many Atterberg limits were determined on cores from along the entire slope transect. Although there are a few exceptions, the plasticity index ( $I_p < 20\%$ ) and liquid limit ( $W_L < 45\%$ ) are lowest in the upslope sediment samples and these properties increase significantly in the downslope direction ( $I_p = 54\%$  and  $W_L = 91\%$ ). These data generally fall slightly above the A line on the plasticity chart (Casagrande, 1932, 1948). On the basis of this classification, the continental-slope sediments investigated during this study belong

to the category of inorganic clays ranging from relatively low plasticity to high plasticity trending generally in the downslope direction. It is interesting to note that the initial evaluation of X-ray diffraction and grain-size analyses of these sediment cores indicates an apparent subtle increase in the presence of smectite and clay-sized material in the downslope direction.

The preliminary evaluation of the cores collected in the submarine-slide area has revealed significant differences not only in the magnitude of the upslope versus downslope geotechnical properties, but also differences in the variation of the sediment-mass physical properties with core depth. Further detailed analyses of the geotechnical properties of a suite of cores collected in the study area are being carried out, a part of which is presented in Bennett et al (in press).

## CONCLUSIONS

Integration of the geophysical, sedimentologic, and geotechnical data provides a unique study of the characteristics of a submarine slide. From the geophysical data, the volume, shape, and internal structure of the slide have been determined. Identification of the slip surface as a late Tertiary erosion surface which shaped the continental slope is important in assessing the processes responsible for the sediment failure. The seafloor environment was affected by a change in the sedimentation regime and the variable energy input associated with sea-level changes during the Pleistocene. From the sediment cores, variations in the geotechnical properties occur between the sediments of the slump block and sediments upslope. The sediments of the slump block have less strength than sediments on the slope above. The restriction of surficial sand to the steeper upslope region as opposed to the surface of the slump block suggests differing sedimentation patterns. This sand may be transported over the shelf edge from the sand-wave field on the continental shelf around the head of Wilmington Canyon described by Knebel and Folger (1976) with the fines deposited further downslope. Although the major sediment failure occurred in the past, creep and deformation of the surface sediments appear to be occurring today.

## REFERENCES CITED

- Bennett, R. H., and D. N. Lambert, 1971, Rapid and reliable technique for determining unit weight and porosity of deep-sea sediments: *Marine Geology*, v. 11, p. 201-207.
- , D. N. Lambert, and M. H. Hulbert, in press, Geotechnical properties of a submarine slide area on the U.S. continental slope northeast of Wilmington Canyon: *Marine Geotechnology*.



- Casagrande, A., 1932, Research on the Atterberg limits of soils: Public Roads, v. 13, p. 121-136.
- 1948, Classification and identification of soils: Am. Soc. Civil Engineers Trans., v. 113, p. 901-931.
- Doyle, L. J., et al, 1975, Sedimentation on the north-eastern continental slope of the United States: 9th Cong. Internat. Sedimentologie, Nice, p. 51-56.
- Gibson, T. G., J. E. Hazel, and J. F. Mello, 1968, Fossiliferous rocks from submarine canyons off the north-eastern United States: U.S. Geol. Survey Prof. Paper 600D, p. 222-230.
- Heezen, B. C., M. Tharp, and M. Ewing, 1959, The floors of the oceans, I, North Atlantic: Geol. Soc. America Spec. Paper, v. 65, 122 p.
- Keller, G. H., and R. H. Bennett, 1968, Mass physical properties of submarine sediments in the Atlantic and Pacific basins: 23d Internat. Geol. Cong. Czech., Rept., sec. 8, Proc., p. 33-50.
- 1970, Variations in the mass physical properties of selected submarine sediments: Marine Geology, v. 9, p. 215-223.
- Kelling, G., and D. J. Stanley, 1970, Morphology and structure of Wilmington and Baltimore submarine canyons, eastern United States: Jour. Geology, v. 78, p. 637-660.
- Knebel, H. J., and D. W. Folger, 1976, Large sand waves on the outer shelf near Wilmington Canyon: EOS, v. 57, p. 268.
- Lewis, K. B., 1971, Slumping on a continental slope inclined at 1°-4°: Sedimentology, v. 16, p. 97-110.
- Lyall, A. K., et al, 1971, Suspended sediment and transport at the shelf-break and on the slope, Wilmington Canyon area, eastern U.S.A.: Marine Technology Jour., v. 5, p. 15-27.
- Matthews, D. J., 1939, Tables of the velocity of sound in pure water and sea water for use in echo-sounding and sound ranging: Admiralty Hydrog. Dept., Pub., H.D. 282, 52 p.
- Moore, D. G., 1969, Submarine slumps: Jour. Sed. Petrology, v. 31, p. 343-357.
- J. R. Curray, and F. J. Emmel, 1976, Large submarine slide (olistostrome) associated with Sunda Arc subduction zone, northeast Indian Ocean: Marine Geology, v. 21, p. 211-226.
- Normark, W. R., 1974, Ranger submarine slide, northern Sebastian Vizcaino Bay, Baja California, Mexico: Geol. Soc. America Bull., v. 85, p. 781-784.
- Richards, A. F., 1961, Investigation of deep-sea sediment cores; I, Shear strength, bearing capacity, and consolidation: U.S. Navy Hydrog. Office Tech. Rept. TR-63, p. 70.
- 1962, Investigation of deep-sea sediment cores; II, Mass physical properties: U.S. Navy Hydrog. Office Tech. Rept. TR-106, p. 146.
- Rupke, N. A., 1976, Large-scale slumping in a flysch basin, southwestern Pyrenees: Geol. Soc. London Jour., v. 132, p. 121-130.
- Schmoll, H. R., and E. Dobrovolny, 1972, Slope map of Anchorage, Alaska: U.S. Geol. Survey Map I-787-B, scale 1:24,000.
- Sheridan, R. E., 1975, Dome structure, Atlantic continental shelf east of Delaware: preliminary geophysical report: AAPG Bull., v. 59, p. 1203-1211.
- Uchupi, E., 1970, Atlantic continental shelf and slope of the United States—shallow structure: U.S. Geol. Survey Prof. Paper 529-I, p. 11-144.
- and K. O. Emery, 1967, Structure of continental margin off Atlantic Coast of United States: AAPG Bull., v. 51, p. 223-234.
- Wear, C. M., D. J. Stanley, and J. E. Boula, 1974, Shelf-break physiography between Wilmington and Norfolk Canyons: Marine Tech. Soc. Jour., v. 8, p. 37-48.

## MAGNETIC ANOMALY PATTERNS ON MID-ATLANTIC RIDGE CREST AT 26°N

Bonnie A. McGregor

Atlantic Oceanographic and Meteorological Laboratories, NOAA, Miami, Florida 33149

C. G. A. Harrison

Rosenstiel School of Marine and Atmospheric Science, Miami, Florida 33149

J. William Lavelle and Peter A. Rona

Atlantic Oceanographic and Meteorological Laboratories, NOAA, Miami, Florida 33149

**Abstract.** Magnetic anomalies over ocean crust with ages between 0 and 3.5 m.y. B.P. have been identified on the Mid-Atlantic Ridge crest at 26°N. These anomalies indicate a spreading rate of 1.1 cm/yr on the west flank of the ridge and 1.3 cm/yr on the east flank. Computer modeling of the anomalies has shown that simple blocks of uniform thickness, whose width and direction of magnetization are obtained from the reversal time scale and whose intensities are chosen for best visual fit of the anomaly, are not capable of explaining the details of the observed magnetic anomalies. Shorter-wavelength variation in the intensity of magnetization parallel to the ridge crest can, however, explain the observed anomalies. A possible degradation of the intensity of magnetization within the axial anomaly is associated with large faulted blocks in the wall of the rift, which is the site of the Trans-Atlantic Geotraverse (TAG) hydrothermal field. Magnetic anomaly data suggest that extensive rotation of blocks within the rift valley is not likely.

## Introduction

In the fall of 1973 as part of the Trans-Atlantic Geotraverse (TAG) program of NOAA's Atlantic Oceanographic and Meteorological Laboratories [Rona, 1973] a detailed study of the magnetic anomaly pattern of the Mid-Atlantic Ridge crest was made using 2-km-spaced track lines. The objective of the study was to analyze the variations in the magnetic anomaly pattern, perpendicular and parallel to the ridge crest. Determination of the origin of the anomaly pattern is of significance in establishing the relationship of this pattern to tectonic processes active on the Mid-Atlantic Ridge crest. A hydrothermal mineral deposit, the TAG hydrothermal field, has been identified in the study area on the east wall of the rift valley [M. Scott et al., 1974; R. Scott et al., 1974; Rona et al., 1976]. Coincident with this region is a local low in the axial magnetic anomaly.

The study was conducted between 25.75°N and 26.50°N over an area of 75 x 55 km (Figure 1). Continuous magnetic field measurements were collected aboard the NOAA ship *Researcher* along the track lines shown in Figure 2 with a Varian proton precession magnetometer. The International Geomagnetic Reference Field 1965 coefficients [IAGA Commission 2 Working Group 4,

1969] were used to reduce the data with a 400-yr adjustment to the reference field based on the American World Chart 1970 model [Hurwitz, 1970]. No correction for diurnal variation was made, and no magnetic storms were recorded during the period of data collection.

A contour map of the residual field shows a large positive anomaly in the center of the area. This is the axial anomaly and is displaced slightly to the southeast in relation to the topographic rift valley (Figure 3). The topographic axis of the rift valley is indicated by the dashed line (Figure 3), and the two shaded negative anomalies on either side of the axial anomaly represent the Matuyama reversed period. They in turn are flanked by the beginning of the Gauss normal. The oldest sea floor in the area is slightly older than 3.5 m.y. if a 1.2-cm/yr spreading rate is assumed [Lattimore et al., 1974]. A low within the axial anomaly is present over the southeast wall of the rift valley (26°07'N, 44°47'W).

A sequence of bathymetric and magnetic profiles across the area is shown in Figure 4; computed magnetizations, to be discussed below, are also included. The magnetic low over the east wall can be seen in profiles 10 through 18 (see arrows), gradually decreasing to the north and south of the hydrothermal area (profile 14). The anomalies are smooth with little indication of minor polarity events. The topographic axis of the rift valley is indicated by the line down the center of the profiles. The axis was positioned by the deepest portion of the rift valley or by the medial ridge, where it was present, which Moore et al. [1974] identified between 36° and 37°N as the most active region geologically. Steps in the east wall of the rift interpreted to be fault blocks [McGregor and Rona, 1975] are indicated by the shaded portions of profiles 8 through 20. The hydrothermal area is associated with these faulted blocks. Computer modeling studies have been done in order to determine the origin of the magnetic anomalies and their relationship to topography and ridge crest processes.

## Computer Modeling: Forward Method

The Talwani and Heirtzler [1964] computer program for the computation of magnetic anomalies caused by two-dimensional structures was used for the initial model studies. An axial dipole field was assumed with a 44° inclination based on the



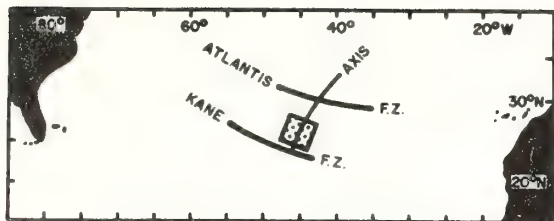


Fig. 1. Index map showing general location of study area.

present latitude. The thickness of the magnetized layer is assumed to be a uniform 500 m, since this is the generally accepted thickness, with the top of the layer at the sea floor. Periods of normal and reversed field are based on the Talwani et al. [1971] revised magnetic chronology from the Reykjanes Ridge crest. Figure 5 shows the parameters used to calculate the anomaly for profile 20. The axial anomaly is displaced 5 km to the east of the bathymetry axis. A similar offset was found in the FAMOUS area between 36° and 37°N [Needham and Francheteau, 1974]. The intensity of remanent magnetization of 30 A/m is the same intensity of remanent magnetization used for the axial block in model studies of the Reykjanes Ridge [Talwani et al., 1971], while de Boer [1975] measured intensities from 15 to 65 A/m on dredged samples from the Reykjanes Ridge. The remanent magnetization of 50 A/m is based on Klitgord's [1974] identification of high magnetization within the central anomaly over slow spreading Pacific ridges. This area of higher magnetization coincides with a topographic high in the floor of the rift that is presumed to be the site of recent volcanism [McGregor and Rona, 1975]. However, this small region of high magnetization has no expression in surface magnetism, as we shall see later. The 12-A/m block reduced the axial anomaly in amplitude and peakedness. A similarly reduced block was used as one solution for the magnetic anomaly associated with the TAG hydrothermal field. The presence of extensive faulting affords avenues for the migration of hydrothermal solutions in portions of the ridge [McGregor and Rona, 1975; R. Scott et al., 1974; Rona et al., 1976]. Hydrothermal alteration of basalts has been shown to reduce the magnetic susceptibility and remanent magnetization [Luyendyk and Melson, 1967; Watkins and Paster, 1971]. No dredge stations were made along profile 20, but to the south near profile 14, hydrothermal manganese, greenstones, altered basalt, and zeolitized rocks were dredged [R. Scott, 1973]. These are the same rock types found by the previously mentioned authors to have low intensities of remanent magnetization. The Reykjanes peninsula of Iceland, a hydrothermal area, also has a conspicuous magnetic low attributed to the hydrothermal alteration of basalt [Bjornsson et al., 1972].

The magnetic parameters of block width and magnetization intensity from profile 20 were used with the bathymetry from profile 14 to simulate the anomaly over the hydrothermal area (Figure 6). The match between the computed and observed magnetic anomalies was not as good as the match for profile 20. The axis of the magnetic symmetry

is about 2 km east of the bathymetric axis. The large amplitude of the axial anomaly indicates that the magnetic intensity of 30 A/m is too large. A block with degraded intensity of remanent magnetization (5 A/m) over the east wall reduces the amplitude of the axial anomaly and changes its shape.

This type of modeling indicates the complexity that exists in the simple model of magnetic anomalies generated by sea floor spreading. Difficulty in anomaly correlations from profile to profile in the Atlantic may result from this complexity. The two-dimensional block model forward method does not provide a unique solution for the source of magnetic anomalies. This time-consuming trial-and-error matching of the anomaly limited the number of profiles analyzed. In order to overcome some of the arbitrariness and increase the number of profiles analyzed an inversion technique was used [Parker and Huestis, 1974].

#### Computer Modeling: Inverse Method

On the basis of Parker's [1973] work for the inversion of magnetic anomalies, Parker and Huestis [1974] have developed a fast Fourier transform method for the deconvolution of crustal magnetization. Several assumptions are made in the modeling: magnetization is assumed to be confined to a relatively thin layer of the sea floor approximately 500 m thick, with the upper surface coincident with the basement topography; the magnetization varies only horizontally, not vertically, in the layer; and the direction of magnetization is assumed to be either parallel or antiparallel to a centered axial dipole. Another possible source of the anomaly pattern is variation in thickness of the magnetized layer, but we consider it less likely on a local scale. Although Wilson [1970] has suggested that the time average field may more closely resemble an off-centered axial dipole than a centered dipole, the angular deviation of field direction produced by the two is so close that we may assume

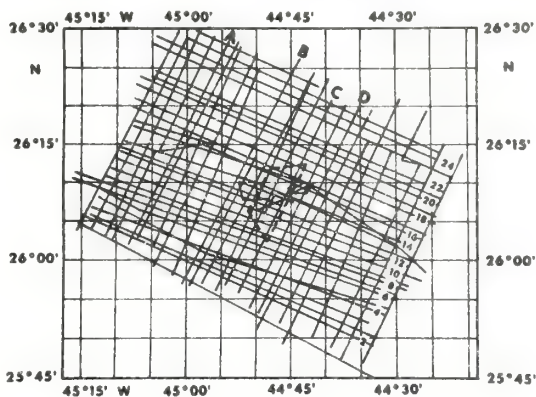


Fig. 2. Track lines from the Trans-Atlantic Geotraverse of 1973. Track lines are data control for Figure 3, and index numbers are track locations for Figure 4. Dashed lines outline the TAG hydrothermal field [R. Scott et al., 1974; Rona et al., 1976].



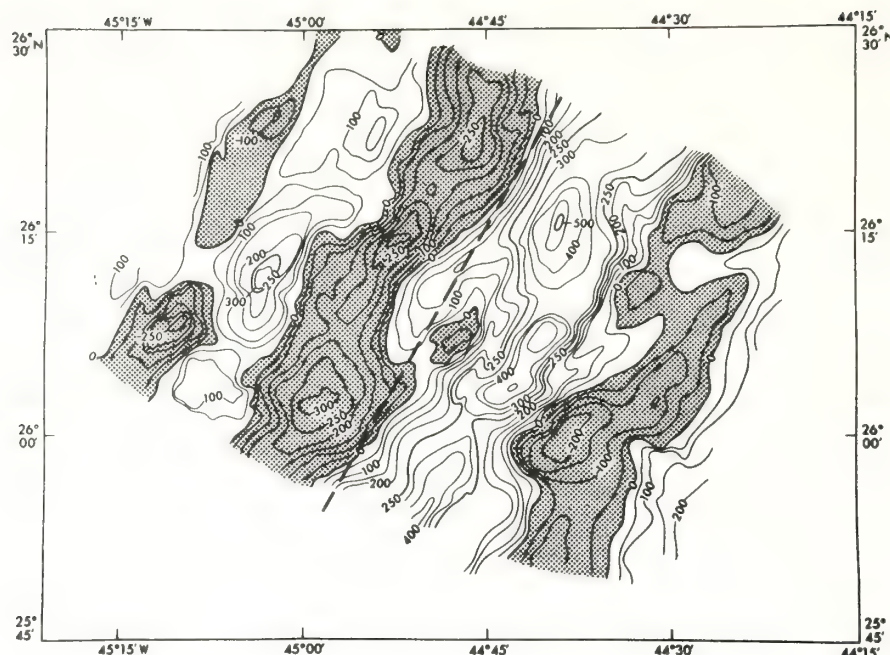


Fig. 3. Residual magnetic anomalies with a 50- $\gamma$  contour interval. Shaded areas are negative. Dashed line is topographic axis of the rift valley.

an average magnetization along an axial dipole field direction. Over the last 3 m.y. the sea floor in this study area has not moved appreciably, so that constant direction of magnetization is a reasonable assumption. Recent Deep-Sea Drilling Project analyses of 3.5-m.y. lavas from west of the Azores Plateau, however, showed that the magnetic intensity and polarity of the volcanic sequence varied greatly with depth in the sequence [Ade-Hall et al., 1975]. Simplifying assumptions for the model may introduce some departures from reality, but as more drilled samples become available, the model can be adjusted.

Ten profiles across the ridge crest approximately 4 km apart (Figure 2) were analyzed with a computer program written by R. L. Parker and S. P. Huestis of the Institute of Geophysics and Planetary Physics, University of California at San Diego (Figure 4). Bathymetry and magnetic anomaly values were selected every 0.5 km. The sloping line at the end of each profile represents artificial data to reduce the contamination of the computed magnetization by replications introduced by the Fourier transform [Parker, 1973]. The measured magnetic anomaly, the calculated magnetization, and the bathymetry are plotted for each profile. The solution of the inverse problem given the set of assumptions outlined above is still nonunique. To the solution of the equation which gives the observed magnetic anomaly, one may add any amount of the solution which causes no external field [Parker and Huestis, 1974]; the latter magnetization function is called the annihilator. In each of the profiles of Figure 4 the amount of annihilator that was added was chosen so that positive and negative magnetic material appeared

in the appropriate places along the profile. The alternative method of choosing the annihilator such that the positive and negative magnetizations are about equal was not used because of the shortness of the record and also because of problems concerning the intensity of magnetization in the axial region.

High wave number components in the raw anomaly data not caused by the local magnetization or caused by very irregular topography as on a ridge crest can, as a result of magnification in downward continuation, dominate the inversion scheme unless filtered. The origin of these components can be inhomogeneities in the magnetization, instrument limitations, digitizing errors [Schouten and McCamy, 1972], or time varying ionospheric currents [Parker, 1974]. Klitgord [1974] found in deep tow experiments that crust younger than 3 m.y. had high wave number variations and attributed the variations to topography or vertical inhomogeneities in the magnetic layer, but such high wave number variations cannot be observed in surface tow observations like those reported here.

Parker [1974] showed that the logarithm of the power spectrum of the raw anomaly data can be used as a means of determining at which wave number noise overcomes the magnetization signal. We have used this procedure to choose our anomaly filter parameters. The magnetic data were filtered, completely suppressing wavelengths less than 2.56 km and greater than 128 km and cosine tapering wavelengths from 2.56 to 5.1 km and from 42 to 128 km. The short wavelengths which were suppressed or partially suppressed varied slightly with each profile. An 11-point triangular data window covering 5 km which was

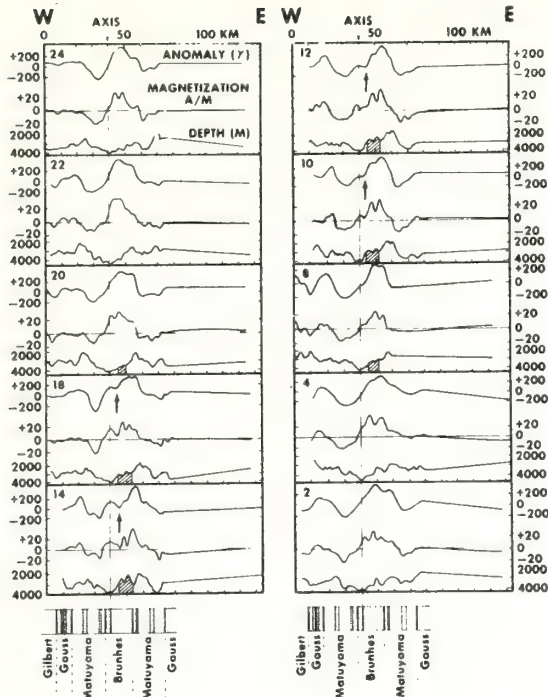


Fig. 4. Profiles of bathymetry, magnetization, and magnetic anomaly (see Figure 2 for location). Magnetic reversal chronology is from Talwani et al. [1971]. Axis line represents present-day location of spreading. Hatched area under bathymetry indicates region of faulted blocks which can be traced from profile to profile. Arrows indicate low in axial anomaly.

initially used to smooth the data prior to profiling was left in the analysis sequence prior to filtering, amounting to some modulation of the band-pass filter described above. This combined smoothing technique did not appreciably change the appearance of the magnetic anomaly. The depth-to-block  $D$  versus the width-of-block  $w$  ratio has been shown by Bott and Hutton [1970] and Blakely and Schouten [1974] to be important in the separation of noise from data, when the short-period behavior of the earth's magnetic field is studied. Their criterion of  $D/2w \leq 1$  is essentially met in our treatment in that the short-wavelength cutoff of the filter  $\lambda_{sm1}$ , which is twice the effective sampling interval  $w_{eff}$ , is such that  $D/\lambda_{sm1} = D/2w_{eff} \approx 1$ . The magnetic anomaly pattern on this portion of the Mid-Atlantic Ridge (Figure 4) does not show the short-period events in the magnetic reversal chronology. Therefore we wish to focus attention on the general trends of the magnetization pattern.

In Figure 4 the line down the center of each profile represents the present axis of spreading in the rift valley. The axis was positioned by the medial ridge where it was present and otherwise by the deepest part of the rift valley. The positive zone of magnetization, approximately 25 km wide in the center of each profile, and the associated positive anomaly represent the axial

anomaly. On either side of this zone is a section of negative magnetizations that represent the Matuyama reversed epoch, which in turn is flanked by the Gauss normal and on the west side of the rift in some profiles the beginning of the Gilbert reversed epoch.

The short-term magnetic events (such as the Jaramillo and Olduvai) do not stand out above the high wave number background fluctuations for surface measured magnetics. The transition zone between normal and reversed material necessarily appears to be several kilometers wide. In order for a magnetic excursion of the earth's field to be visible its duration would have to be greater than 0.3 m.y. when a spreading rate of 1.2 cm/yr is assumed. Random injection of dikes adding new material to the rift area apparently has taken place over a zone several kilometers wide [Matthews and Bath, 1967; Harrison, 1968; Atwater and Mudie, 1973].

The intensity of magnetization is dependent on the thickness of the magnetized layer and on the annihilator used. The layer thickness was assumed to be 500 m. Increasing the layer thickness to 1000 m would decrease the magnetization an average of 45%. The maximum magnetization value on this portion of the ridge crest is 35 A/m and associated with the axial anomaly. Away from the axial anomaly the intensity drops to about 20 and then to about 5 A/m by 2.5 m.y.

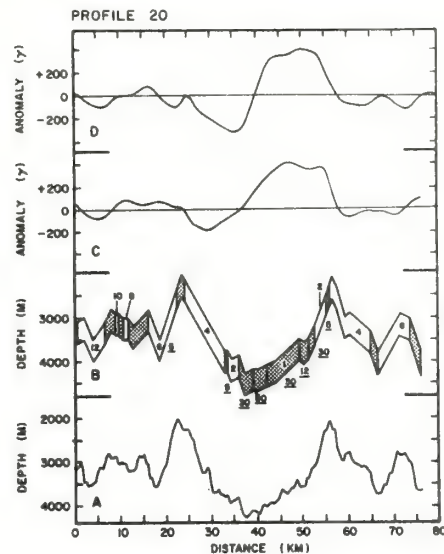


Fig. 5. Profile 20 (see Figure 2 for location). (a) Measured bathymetry. (b) Computer-simulated bathymetry. (c) Measured magnetic anomaly. (d) Computer-generated magnetic anomaly. A 500-m magnetized layer is assumed (b) with numbered unshaded blocks representing reversed material. Shaded blocks have normally magnetized material with 1 representing the axial anomaly. Width of blocks is based on a 1.2-cm/yr spreading rate and the Talwani et al. [1971] magnetic chronology. Underlined values are intensities of remanent magnetization in amperes per meter. (For conversion to SI units, 1  $\gamma$  = 1 nT; 0.001 emu/cm<sup>3</sup> = 1 A/m.)



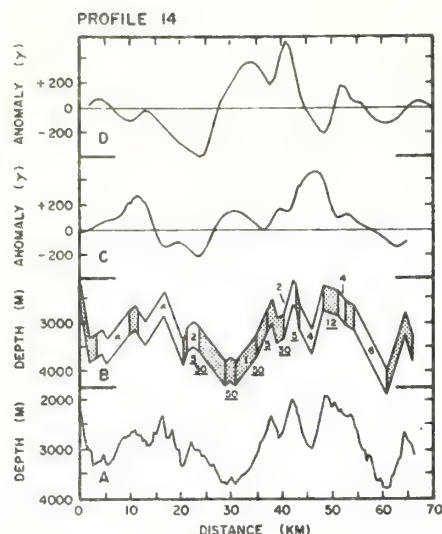


Fig. 6. Profile 14 over TAG hydrothermal field (see Figure 2 for location). (a) Measured bathymetry. (b) Computer-simulated bathymetry. (c) Measured magnetic anomaly. (d) Computer-generated magnetic anomaly. A 500-m magnetized layer is assumed (b) with numbered unshaded blocks representing reversed material. Shaded blocks are normally magnetized, with 1 representing the axial anomaly. Width of blocks is based on a 1.2-cm/yr spreading rate and the Talwani et al. [1971] magnetic chronology. Underlined values are intensities of remanent magnetization in amperes per meter. Bathymetric peak between 35 and 40 km is the region where hydrothermal manganese is present.

The axial block can be seen to be composed of a series of blocks with different intensities of magnetization. A pronounced local low in the magnetic intensity occurs in profiles 10 through 18 with a value between 2 and 10 A/m. This low is associated with inferred faulted blocks which can be traced from profile 8 through profile 20 (shaded area in the bathymetry) [McGregor and Rona, 1975]. The elevation of these blocks is believed to be a function of the fault displacement. The TAG hydrothermal field is associated with these faulted blocks. Migrating hydrothermal solutions or other forms of alteration along the fault zones may have degraded the magnetization. The median ridge in the forward method was modeled with very high intensity of magnetization (50 A/m) on the basis of Moore et al.'s [1974] interpretation that it is the site of active dike emplacement at 36°N. This high magnetization was subsequently confirmed by Macdonald et al. [1975] with deep tow data over the median ridge. Klitgord [1974] also reported regions of high magnetization in the central anomaly over the Gorda Rise, Galapagos Spreading Center, and the Pacific-Antarctic Ridge. By following the axis line through the profiles (Figure 4) it can be seen from the inverse method using surface magnetic data that large magnetizations are not consistently seen associated

with the median ridge, but occasionally a slight increase occurs, such as in profiles 2, 4, and 10.

The median ridge and the axis line indicate that the present-day active zone of spreading is not centered in the Brunhes normal epoch but is much closer to the western boundary. Although asymmetric spreading appears to be occurring in the area of the Atlantic at 26°N, the degree of asymmetry implied by the position of this axis is not supported by the spreading rates. This large asymmetry supports the suggestion that injection of new material occurs over an area in the rift zone that is several kilometers wide. From the magnetization it can be seen that the west wall of the rift is slightly older than the east wall. A spreading rate of 1.1 cm/yr for the west side and 1.3 cm/yr for the east side fits the data from 0 to 2.4 m.y. The spreading rates were determined by measuring the width of the Matuyama epoch on each side of the ridge. Matching of anomaly wavelengths in the forward method supports these asymmetric spreading rates. Averaging to 10 m.y., Lattimore et al. [1974] found a similar spreading rate asymmetry.

To the north on the Mid-Atlantic Ridge crest between 36° and 37°N an asymmetry in spreading rate was also found with 0.9–1.0 cm/yr on the west side and 1.3 cm/yr on the east [Needham and Francheteau, 1974; Greenewalt and Taylor, 1974]. Between 6° and 8°S, van Andel and Heath [1970] found faster spreading to the east from 0 to 10 m.y. At 45°N, asymmetric spreading occurs but with the faster 1.28 cm/yr on the west and 1.1 cm/yr on the east [Loncarevic and Parker, 1971]. Therefore the pattern of differential spreading rates for the North Atlantic apparently changes north of the Azores triple junction.

#### Test of Rift Model

By using the magnetic anomaly pattern and shape, models for processes and origin of the rift valley can be tested. Moore et al. [1974] presented a model for the origin of the rift valley topography at 36°N. The floor of the rift valley contains linear medial ridge segments separated by central troughs. The ridge is believed to mark the locus of active volcanism, and the troughs periods of quiescence accompanied by spreading. In Moore et al.'s model the medial ridge is split by spreading and subsides with tilting toward the rift valley axis during the post-eruptive stage; the total amount of tilting is about 45° about an axis parallel to the rift valley. As the basalt comprising the median ridge cools, a direction of remanent magnetization is acquired. At a later time when the ridge splits and tilts toward the rift valley axis, the direction of remanent magnetization rotates, an action which alters the shape of the resulting magnetic anomaly.

With the use of the Talwani et al. [1971] reversal chronology and the Talwani and Heirtzler [1964] computer program previously discussed, the effect on the shape of the anomaly of rotating the direction of magnetization can be assessed. Figure 7a shows the anomaly generated at 36°N when an axial dipole and no rotation (declination 0°, inclination 56°) are assumed. Figure 7b



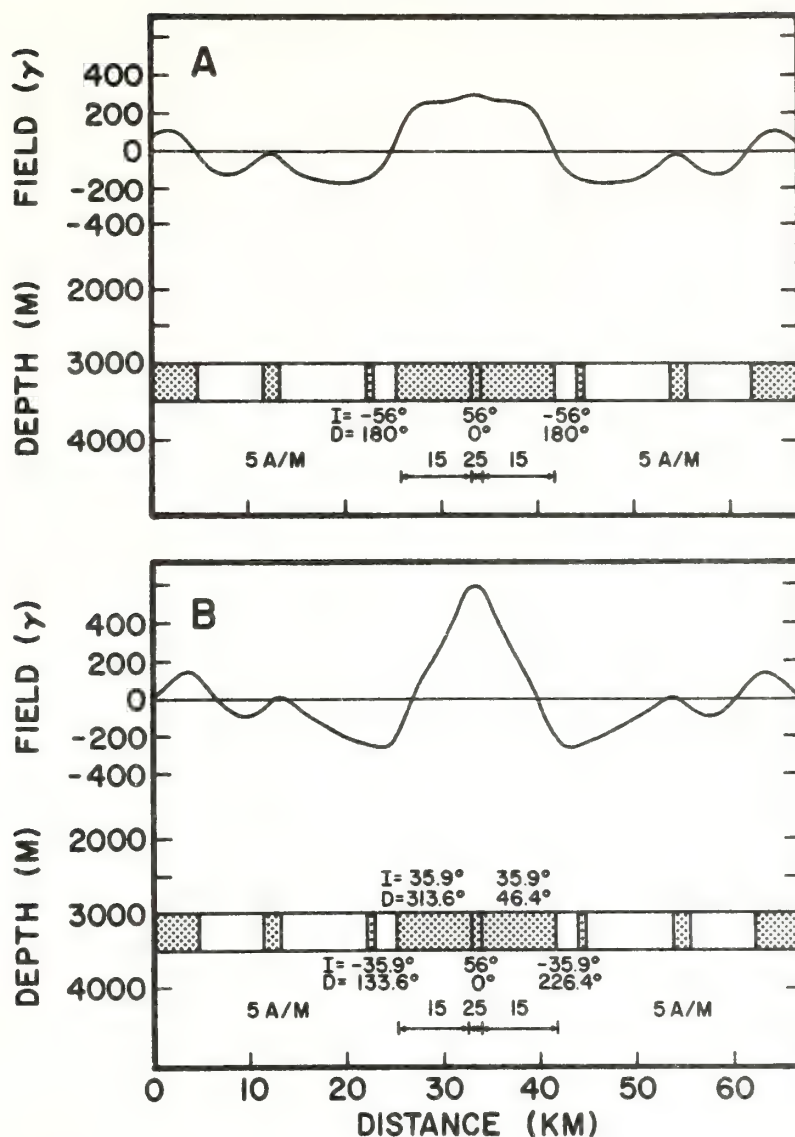


Fig. 7. Models using the forward method with idealized blocks of sea floor to show the effect of (a) normal direction of magnetization and (b) direction of magnetization rotated  $45^\circ$ . Blocks are numbered sequentially away from the axis of spreading, with normally magnetized blocks shaded. Directions and intensities of magnetization used are shown.

shows the anomaly generated by tilting the blocks  $45^\circ$  as suggested by Moore et al. [1974] (declination  $46.4^\circ$ , inclination  $35.9^\circ$  for the east side of the ridge and declination  $-46.4^\circ$ , inclination  $35.9^\circ$  for the west side). The intensities of magnetization used are shown and are in agreement with those reported by Macdonald et al. [1975], which were determined by inverting deep tow magnetic field data. The shape of the axial anomaly and the shapes of the flanking lows differ considerably (Figures 7a and 7b). From the shape of the axial anomaly measured at  $26^\circ\text{N}$  (Figures 4 and 5) it does not appear that tilting

of the blocks in the rift valley has occurred as Moore et al. [1974] suggested for  $36^\circ\text{N}$ . Further confirmation of rotation as suggested by Moore et al. [1974] must await analysis of magnetic anomalies which are less variable in shape than the ones discussed here. It seems unlikely that rotation by  $45^\circ$  is a general feature of the magnetic blocks, because then the paleomagnetic pole positions obtained from the shapes of the anomalies [Larson and Chase, 1972] would not agree with paleomagnetic pole positions determined from the magnetic anomalies over seamounts in the Pacific [Harrison et al., 1975].

## Summary

The magnetic anomaly pattern along the Mid-Atlantic Ridge crest is very smooth, suggesting that the zone of dike injection is several kilometers wide. The topographic axis of symmetry is offset to the west of the magnetic axis, with a slight asymmetry in spreading rate, faster spreading to the east occurring over the past 3 m.y. and probably over the last 10 m.y. Variations in intensity of magnetization parallel to the ridge crest are present. One such variation is a low in the magnetic anomaly and in the intensity of magnetization of the axial anomaly associated with large faulted blocks and the TAG hydrothermal field on the east wall of the rift valley. Degradation of the intensity of magnetization along fault zones possibly by hydrothermal activity is suggested as the origin of this low, although variations in block thickness cannot be ruled out. From magnetic anomaly model studies it appears that extensive rotation of blocks in the rift valley has not occurred as part of the spreading process.

**Acknowledgments.** We gratefully acknowledge Dale C. Krause for his invaluable assistance in establishing the objectives of the NOAA-TAG 1973 field work. We thank Mahlon M. Ball and George H. Keller for enlightening discussions and review of the manuscript. We are indebted to Robert L. Parker and Steven Huestis for making available a computer program for the inversion of magnetic anomalies. We express appreciation to Sam A. Bush and Frances W. Nastav for assisting in data reduction, to R. K. Lattimore for making available computer program documentation, and to Martin R. Fisk for calculating magnetic field values. L. L. Posey and W. S. Simmons and the officers and crew of the NOAA ship *Researcher*, provided cooperation and diligence in executing the survey. Funds for this study were provided by NOAA's Atlantic Oceanographic and Meteorological Laboratories and by the Oceanography Section of the National Science Foundation, grant GA-42979. Contribution from the Rosenstiel School of Marine and Atmospheric Science of the University of Miami.

## References

- Ade-Hall, J. M., F. Aumento, R. D. Hyndman, W. G. Melson, H. Bougault, L. Dmitriev, J. F. Fischer, P. T. Robinson, T. L. Wright, G. A. Miles, M. Flower, and R. C. Howe, Sources of magnetic anomalies on the Mid-Atlantic Ridge, *Nature*, **255**, 389-390, 1975.
- Atwater, T., and J. D. Mudie, Detailed near-bottom geophysical study of the Gorda Rise, *J. Geophys. Res.*, **78**, 8665-8686, 1973.
- Bjornsson, S., S. Arnorsson, and J. Tomasson, Economic evaluation of Reykjanes thermal brine area, Iceland, *Amer. Ass. Petrol. Geol. Bull.*, **56**, 2380-2391, 1972.
- Blakely, R. J., and H. Schouten, Comments on "Filtering Marine Magnetic Anomalies" by Hans Schouten and Keith McCamy, *J. Geophys. Res.*, **79**, 773-774, 1974.
- Bott, M. H. P., and M. S. Hutton, Limitations on the resolution possible in the direct interpretation of marine magnetic anomalies, *Earth Planet. Sci. Lett.*, **8**, 317-319, 1970.
- de Boer, J., Variations of the magnetic properties of postglacial pillow lavas along the Reykjanes Ridge, *J. Geophys. Res.*, **80**, 3769-3776, 1975.
- Greenewalt, D., and P. Taylor, Deep-tow magnetic measurements across the axial valley of the Mid-Atlantic Ridge, *J. Geophys. Res.*, **79**, 4401-4406, 1974.
- Harrison, C. G. A., Formation of magnetic anomaly patterns by dike injections, *J. Geophys. Res.*, **73**, 2137-2142, 1968.
- Harrison, C. G. A., R. Jarrard, V. Vacquier, and R. Larson, Paleomagnetism of Cretaceous Pacific seamounts, *Geophys. J. Roy. Astron. Soc.*, **42**, 859-882, 1975.
- Hurwitz, L., Mathematical model of the 1970 geomagnetic field (abstract), *Eos Trans. AGU*, **51**, 269, 1970.
- IAGA Commission 2 Working Group 4, International geomagnetic reference field 1965.0, *J. Geophys. Res.*, **74**, 4407-4408, 1969.
- Klitgord, K. D., Near-bottom geophysical surveys and their implications on the crustal generation process, sea-floor spreading history of the Pacific and the geomagnetic time scale 0 to 6 my BP, Ph.D. dissertation, 177 pp., Univ. of Calif. at San Diego, La Jolla, 1974.
- Larson, R. L., and C. G. Chase, Late Mesozoic evolution of the western Pacific Ocean, *Geol. Soc. Amer. Bull.*, **83**, 3626-3644, 1972.
- Lattimore, R. K., P. A. Rona, and O. E. Dewald, Magnetic anomaly sequence in the central North Atlantic, *J. Geophys. Res.*, **79**, 1207-1209, 1974.
- Loncarevic, B. D., and R. L. Parker, The Mid-Atlantic Ridge near 45°N, 17, Magnetic anomalies and ocean floor spreading, *Can. J. Earth Sci.*, **8**, 883-898, 1971.
- Luyendyk, B. P., and W. G. Melson, Magnetic properties and petrology of rocks near the crest of the Mid-Atlantic Ridge, *Nature*, **215**, 147-149, 1967.
- Macdonald, K., B. L. Luyendyk, J. D. Mudie, and F. N. Speiss, Near-bottom geophysical study of the Mid-Atlantic Ridge median valley near 37°N: Preliminary observations, *Geology*, **3**, 211-215, 1975.
- Matthews, D. H., and J. Bath, Formation of magnetic anomaly pattern of Mid-Atlantic Ridge, *Geophys. J. Roy. Astron. Soc.*, **13**, 349-357, 1967.
- McGregor, B. A., and P. A. Rona, Crest of the Mid-Atlantic Ridge at 26°N, *J. Geophys. Res.*, **80**, 3307-3314, 1975.
- Moore, J. G., H. S. Fleming, and J. D. Phillips, Preliminary model for extrusion and rifting at the axis of the Mid-Atlantic Ridge, 36°48' north, *Geology*, **2**, 437-440, 1974.
- Needham, H. D., and J. Francheteau, Some characteristics of the rift valley in the Atlantic Ocean near 36°48' north, *Earth Planet. Sci. Lett.*, **22**, 29-43, 1974.
- Parker, R. L., The rapid calculation of potential anomalies, *Geophys. J. Roy. Astron. Soc.*, **31**, 447-455, 1973.
- Parker, R. L., Stacking marine magnetic anomalies: A critique, *Geophys. Res. Lett.*, **1**, 259-260, 1974.
- Parker, R. L., and S. P. Huestis, The inversion

- of magnetic anomalies in the presence of topography, J. Geophys. Res., **79**, 1587-1593, 1974.
- Rona, P. A., Marine geology: The Trans-Atlantic Geotraverse, in 1973 McGraw-Hill Yearbook of Science and Technology, pp. 252-256, McGraw-Hill, New York, 1973.
- Rona, P. A., R. H. Harbison, B. G. Bassinger, R. B. Scott, and A. J. Nalwalk, Tectonic fabric and hydrothermal activity of Mid-Atlantic Ridge crest (26°N), Geol. Soc. Amer. Bull., **87**, 661-674, 1976.
- Schouten, H., and K. McCamy, Filtering marine magnetic anomalies, J. Geophys. Res., **77**, 7089-7100, 1972.
- Scott, M. R., R. B. Scott, A. J. Nalwalk, P. A. Rona, and L. B. Butler, Rapidly accumulating manganese deposit from the median valley of the Mid-Atlantic Ridge, Geophys. Res. Lett., **1**, 355-358, 1974.
- Scott, R. B., Trans-Atlantic Geotraverse leg 4, cruise report, Atl. Oceanogr. and Meteorol. Lab., NOAA, Miami, Florida, 1973.
- Scott, R. B., P. A. Rona, B. A. McGregor, and M. R. Scott, The TAG hydrothermal field, Nature, **251**, 301-302, 1974.
- Talwani, M., and J. R. Heirtzler, Computation of magnetic anomalies caused by two-dimensional structures of arbitrary shape, Stanford Univ. Publ. Geol. Sci., **9**, 464-480, 1964.
- Talwani, M., C. C. Windish, and M. G. Langseth, Jr., Reykjanes Ridge crest: A detailed geophysical study, J. Geophys. Res., **76**, 473-517, 1971.
- van Andel, T. H., and G. R. Heath, Tectonics of the Mid-Atlantic Ridge 6-8° south latitude, Mar. Geophys. Res., **1**, 5-36, 1970.
- Watkins, N. D., and T. P. Paster, The magnetic properties of igneous rocks from the ocean floor, Phil. Trans. Roy. Soc. London, Ser. A, **268**, 507-550, 1971.
- Wilson, R. L., Permanent aspects of the earth's non-dipole magnetic field over upper Tertiary time, Geophys. J. Roy. Astron. Soc., **19**, 417-438, 1970.

(Received July 7, 1975;  
revised July 6, 1976;  
accepted July 21, 1976.)



## **New England Offshore Mining Environmental Study: the Character of Particle Dispersion and Water Movement in Massachusetts Bay and Adjacent Waters**

**Terry A. Nelsen<sup>a</sup>, Dennis A. Mayer<sup>a</sup>,  
Patrick G. Hatcher<sup>a</sup>, and Wilmot N. Hess<sup>b</sup>**

*Received 16 December 1975 and in revised form 8 August 1976*

---

**Keywords:** dredge spoil, dispersion, experiment, current meters, drogues, temperature profiles, salinity, Massachusetts coast

The New England Offshore Mining Environmental Study (NOMES) was conducted in Massachusetts Bay during June 1973. The project was designed to study the dispersal of fine particles during proposed sand and gravel dredging operations.

Current meter and drogue measurements revealed a strong north-south current shear zone. The mean motion within 10 km of the beach was predominantly northward, while seaward of this limit the mean flow was mostly southward.

Silt-size glass spheres and synthetic sphalerite (ZnS) particles were used as tracers to determine the behavior of suspended particles. The sphalerite data showed particle dispersion toward Boston Harbor, eastward toward Stellwagen Bank and the Atlantic, and southward hugging the Massachusetts shore and following a counter-clockwise gyre in Cape Cod Bay.

### **Introduction**

The New England Offshore Mining Environmental Study (NOMES) was conducted by the National Oceanic and Atmospheric Administration and the Commonwealth of Massachusetts in June 1973, to help determine the environmental effects of offshore sand and gravel dredging.

The study was designed around a proposed dredging operation in which 764 000 m<sup>3</sup> of sand and gravel were to be removed from a site 12.9 km east of Boston (Figure 1). It was estimated that approximately 3% (22 900 m<sup>3</sup>) of the dredged material (particle diameter <62.5  $\mu$ ) would be pumped over the side of the dredge as dredging waste.

Significant problems can be caused by the rain of fine material from overboard pumping of dredge spoil. These include:

- (a) effects on metabolism and survival of organisms confronted with high concentrations of fine particulate matter;
- (b) effects on the benthic habitat caused by sediment removal and redeposition; and
- (c) types, amounts, and methods of chemical constituents transfer to the water column or sediments, and their amplification by organisms through the marine food web.

<sup>a</sup>NOAA, Atlantic Oceanographic and Meteorological Laboratories, Miami, Florida.

<sup>b</sup>NOAA, Environmental Research Laboratories, Boulder, Colorado.

The tracer experiment began on 11 June 1973 and terminated on 21 June 1973. The day of the tracer drop, 11 June, will hereafter be termed 'D-day', while days prior to the drop will be 'D-1', 'D-2', etc., and the days following the drop will be 'D+1', 'D+2', etc. Meteorological, current, and tide data were collected for a 30-day period beginning approximately 2 weeks prior to D-day.



Figure 1. NOMES dispersion study site, showing the proposed dredging site (stippled box) where test particles were released, sampling area (line portion), generalized path of drogues, current meter locations (black dots numbered 1-6 and A and B) and comparative sample stations (stars), where D3-6 represents D+3 sample 6, etc.

## Experimental procedure

### Tracer particles

Fluorescent dyes such as rhodamine B were deemed inadequate for a dredge plume simulation, since dye does not exhibit the settling characteristics of natural sedimentary particles. Thus a tracer was used composed of particles which exhibited settling characteristics similar

to those of natural silt and clay-size sediments, but were easily identifiable from particles indigenous to the local water column and substrate.

Two types of particles were used as tracers. The first were small spherical glass beads, selected because their specific gravity of 2.5 approximated that of quartz (2.65) and other natural sediments. Nine hundred kilograms of glass beads were used in the experiment. With an average particle size of  $13.8 \mu$  an estimated  $2.6 \times 10^{14}$  beads were released into the water column. Unforeseen difficulties in sizing and counting of glass bead samples prevented meaningful analysis of that data. Therefore, interpretations and conclusions in this paper are based on data from the sphalerite counts made in the shore laboratory and onboard the tracking vessel.

Atmospheric diffusion studies have made use of sphalerite (ZnS) particles with fluorescent inclusions which are counted with a specially designed fluorometer (Nickola *et al.*, 1966). It was decided that this same method could be utilized in water to provide real-time data for the plume tracking. Therefore, as a supplementary tracer, laboratory-grown sphalerite (ZnS) crystals with fluorescent inclusions were also used (ZnS; Hellecon 2210, U.S. Radium Corp.; P-22 Green, GTE Sylvania Corp.). Their fluorescent property made them easily identifiable under a microscope in ultraviolet light. Five hundred and forty kilograms of sphalerite crystals were used in the experiment. Since the specific gravity of sphalerite (4.1) is greater than that of glass beads (2.5), a finer grain size was chosen so that the hydraulic settling characteristics of the two types of particles would be roughly equivalent. With an average particle diameter of  $2.8 \mu\text{m}$ , an estimated  $3.8 \times 10^{15}$  sphalerite particles were used.

#### *Particle collection and analysis*

In order to track the plume, it was necessary to have real-time information about the concentration of fluorescent tracer particles in the water column. Water samples were collected in 5-l Niskin bottles, 100 ml aliquots of the samples were filtered on board the vessel through  $1 \mu$  filter paper, and total fluorescence was measured using the Turner fluorometer.

#### *Laboratory procedure*

The entire 5-l sample was filtered through  $8 \mu$  millipore filter paper. After the sample was filtered, 5 l of fresh seawater were run through the filtering system to pick up any tracer particles adhering to it. Particles on the filter were then examined with a binocular microscope using an ultraviolet light to identify the sphalerite particles.

#### *Current meters*

Twenty-eight current meters were deployed at eight stations on 24 and 25 May 1973, for 1 month. Of the 28 meters, 10 were Aandaraa and 18 were photogeodynes deployed by EG & G International, Inc. Current meter stations are shown in Figure 1. No data were recorded from station 3. Detailed current observations are discussed below.

#### *Drogues*

Drogues consisted of two  $91 \times 122$  cm aluminium plates connected by a variable length cord to a  $4.1$  cm diameter aluminium pipe, 4.9 m long. Above the center of the pipe a float with a number was attached. On the top of the pipe a flag and a radar reflector were placed, while inside the upper part of the pipe a radio transmitter was secured. For each drogue, the signal transmitted was of a different frequency, so that direction and identity of each drogue was known.



Commencing on D-day, a continuous 3-day drogue study was carried out. One drogue each was deployed at depths of 7, 12 and 22 m on D-day. On D+2 a fourth drogue was added at 17 m. In the evening of D+3, a deep 32-m drogue was deployed and was followed for 3 days. The track of general drogue movement is shown in Figure 1.

### *Temperature*

Temperature data were taken at all particle sampling stations and at each sample depth. A laboratory thermometer was immersed into each sample immediately upon its arrival on deck and temperatures read to the nearest 0.1 °C.

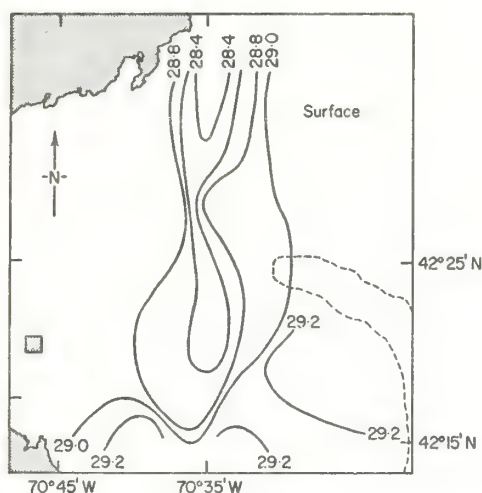


Figure 2. Salinity data (‰) taken on Days 'D+2' and 'D+3' in Massachusetts Bay by Manohar-Maharaj and Beardsley (1973). The proposed dredging site is shown by the stippled square.

### *Salinity*

Salinity data were collected (Manohar-Maharaj & Beardsley, 1973) on days D+2 and D+3 in the same areas as the water samples for bead counts (Figure 2).

## **Experimental results and discussion**

### *Drogue and current meter data*

The track of the 12-m drogue is shown in Figure 3 as well as the locations of all current meters. Figure 3 shows sequences of current vector fields for a selected subset of drogue observations. There are a total of 29 observations for the 12-m drogue as shown in Figure 3(d). Each drogue position and associated vector field shows the drogue position at the observed time in relation to past drogue positions. The current vector fields were constructed from data subjected to a 3-h low pass filter. Thus the raw data were smoothed such that fluctuations with periods of less than 3 h were rejected. The data were then resampled hourly. Raw data time intervals were 5 min for the photogeodynes and 10 min for the Aandaraa meters.

Drogue movement was consistent with the observed current fields and was in phase with the vector at station A while it was near A. As the drogue advanced along its track, it fluctuated east and then west [Figure 3(a)] and then east again in phase with the tidal currents relative to the fixed-point (Eulerian) measurements at A. Figure 3(b) shows the drogue in a region of transition where flows near station 5 begin to influence its motion. Eventually the drogue was transported through a sharp shear zone into a southerly flowing current regime where it remained [Figure 3(c)].

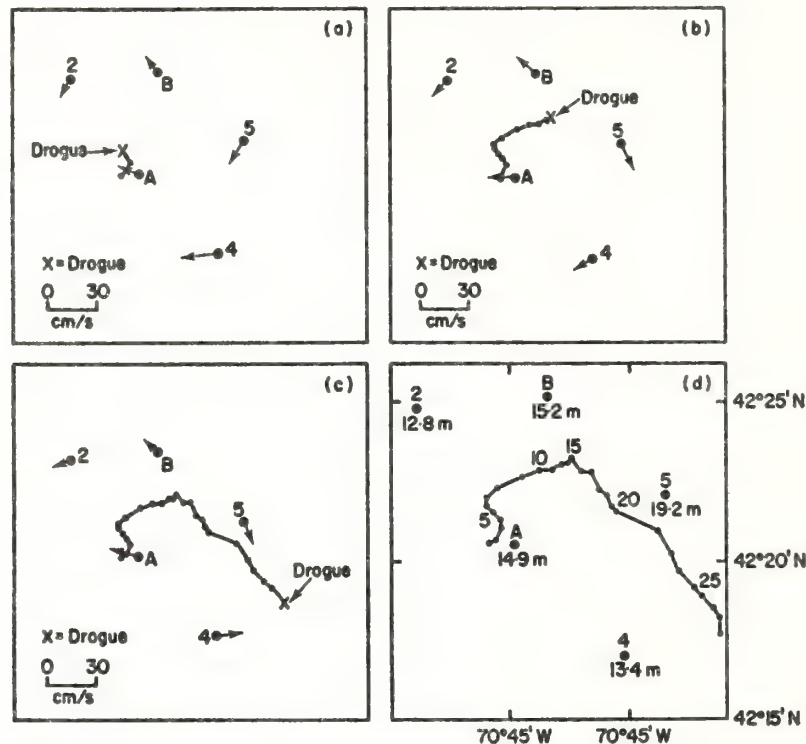


Figure 3. Twelve-meter drogue track, (a) while under the influence of currents near A (D-day, 16.00 hours); (b) approaching the shear zone (D+1, 05.00 hours); (c) while under the influence of currents near 4 and 5 (D+2, 04.00 hours); and (d) current meter depths and total drogue track to D+2, 06.00 hours.

### *Sphalerite*

The daily sphalerite counts are plotted in sequence of successive days and depths (Figures 4–6). It should be noted here that only one vessel was available for water sampling, therefore, the data were collected over periods of up to 12 h. Although a biasing of the data by tidal influences is probably present, a coherent pattern of observations seems to emerge.

On D-day all samples were obtained by pumping from the various depths. Later, it was discovered that sphalerite particles adhered to the pump hose walls, and therefore no sphalerite data were plotted for D-day.

Figure 4 shows the sphalerite dispersion on day D+1. The 5-m plot shows little dispersion northward, but high concentrations moving eastward from the dumpsite. The 10-m depth cloud seemed to be broken into two major sections, one with a high of 11 640 particles  $l^{-1}$  and the other with a high of 21 175 particles  $l^{-1}$ . It is interesting to note that the former high

drifted northward in a direction compatible with the current vectors of station A [Figure 3(a)]. The major high of 21 175 particles  $l^{-1}$  was roughly in the same position as the 7-m drogue at that time. The 15- and 20-m isopleth maps seem to exhibit the same partitioning of the plume into northwest and southeast portions. Settling was apparently taking place as evidenced by an increase in magnitude with depth of concentration highs. The general eastward motion of the higher concentrations seem to agree with the previously discussed displacement of the drogues under tidally dominated eastward flow.

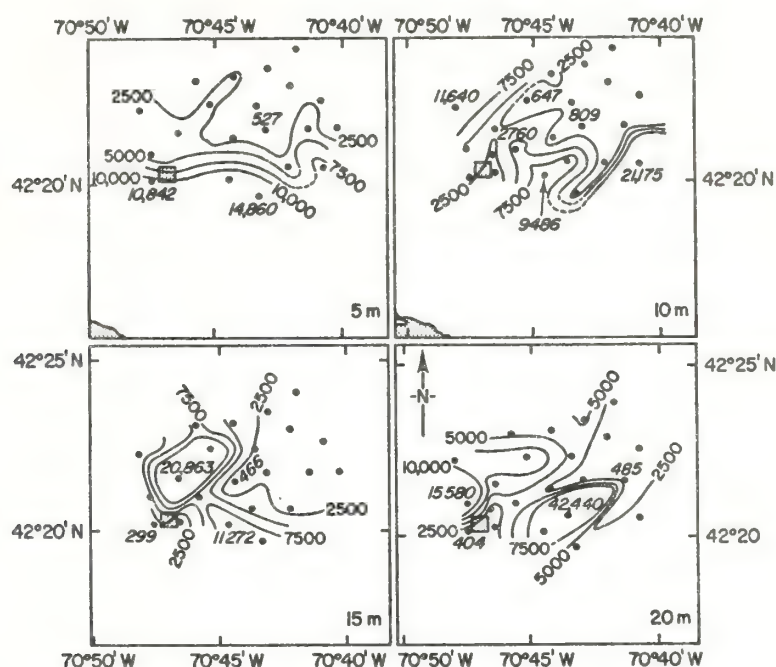


Figure 4. Sphalerite isopleth data (particles/l) for day 'D+1' at depths of 5, 10, 15 and 20 m. Some isopleths in high concentration areas have been deleted for simplicity. The particle dumpsite is shown as a stippled square.

D+2 data found in Figure 5 sustain the previous day's observation that the particle cloud was partitioned into at least two segments. Relatively high counts increased in magnitude toward the Boston Harbor mouth at depths of 15 and 20 m. This sense of particle motion is consistent with the general concept of landward bottom transport of sediments in estuarine areas (Meade, 1969). It should also be noted that the count maximum at each datum plane was at least an order of magnitude smaller than on the previous day.

Figure 6 illustrates the plots for day D+3. On that day there were inadequate data for a plot of the 10-m level. The 5-m plot shows concentrations increasing rapidly to the south and landward, a distribution in harmony with the general flow at current meter station 4 [Figure 3(a), (b)]. A similar trend was observed at 15 m in addition to apparent plume partitioning similar to the data at 15 m for the previous day. Plots at 20 and 30 m also show partitioning with a concentration increase to the south.

A storm cancelled all sampling activities for the latter half of D+5 and all of D+6. By D+7 and after, the concentrations of sphalerite particles in the water were so low that, in using the microscope, the contamination 'noise' and the count 'signal' were roughly of the



same magnitude. Therefore, any plots of sphalerite data would be questionable at best. However, it was possible to make Turner fluorometer measurements on D+7 and D+8. Figure 7 is a composite of Turner fluorometer data at 20 m for D+7 and D+8. Data from 42°05'N and to the south are for D+7 and to the north of 42°05'N for D+8. Two noteworthy features are present in this figure. Although based on one sample point at the 'toe' of the '40' isopleth, D+7 data to the south suggest a counterclockwise motion of the particles in central and southern Cape Cod Bay. D+8 data to the north show relatively high values in apparent motion to the southeast. The isopleths over Stellwagen Bank are more closely spaced and somewhat aligned with the bathymetry of the eastern side of the Bank.

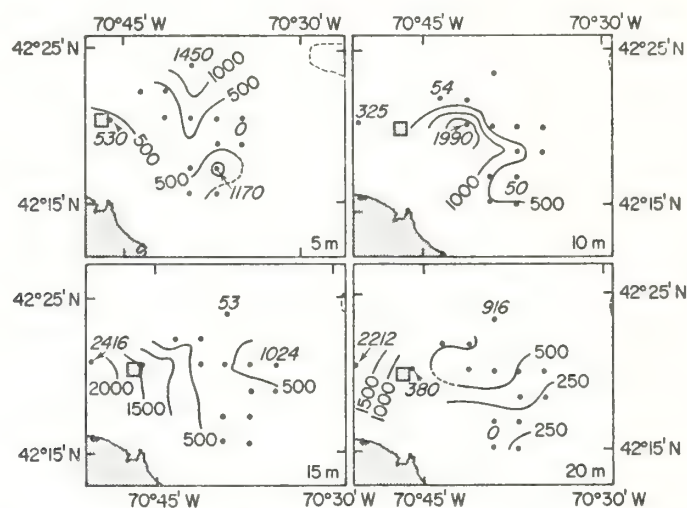


Figure 5. Sphalerite isopleth data for Day 'D+2' as in Figure 4.

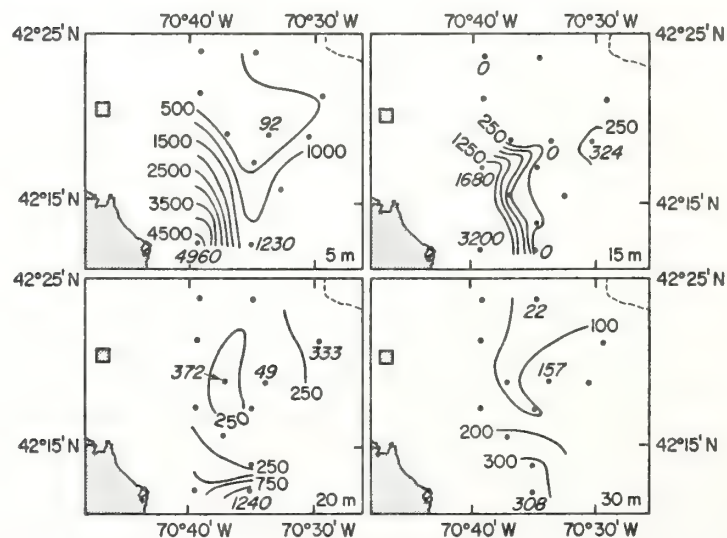


Figure 6. Sphalerite isopleth data for day 'D+3' as in Figure 4.

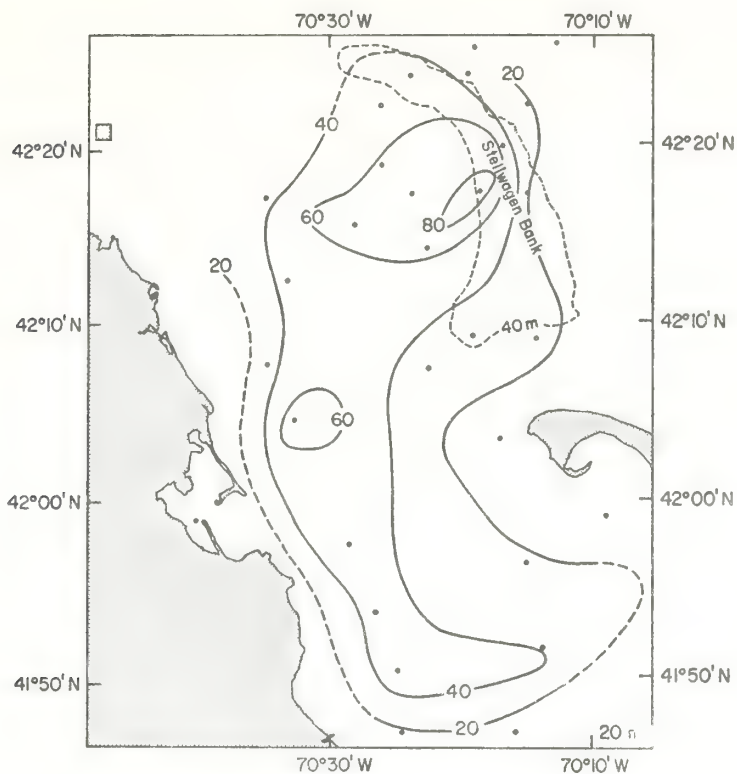


Figure 7. Composite of Turner fluorometer data for days 'D+7' and 'D+8'. Isopleths in relative intensity units.

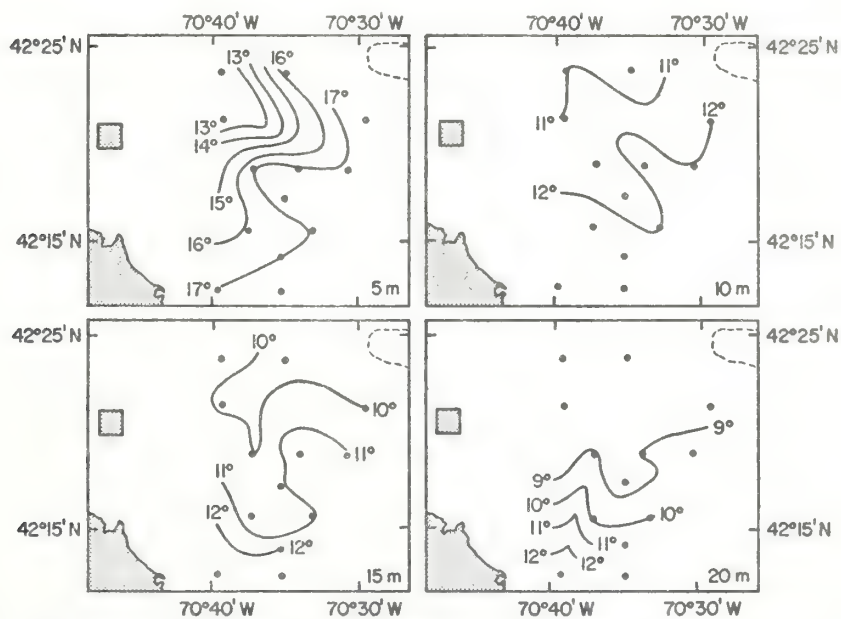


Figure 8. Temperature data ( $^{\circ}\text{C}$ ) for day 'D+3'. The particle dumpsite is shown as a stippled square.

### Temperature data

Temperature data were collected at most particle sampling stations during the experiment. Figure 8 is a plot of the horizontal temperature distributions at four depths on D+3.

In Figure 6 the lowest concentration isopleth, at the 5-m level, (500 particles  $l^{-1}$ ) occupied the same position as the coolest lobe of the isotherm plot and has a similar geometry. To the southwest, both the temperature and the concentration values increase. At the 15-m level, the relatively cool lobes occupying the central area of the isotherm plot correspond to the lowest concentrations in the isopleth map. As in the 5-m data, the temperatures and concentrations increase to the southwest. Although less obvious, this relationship appears to hold true for the 20-m level also.

These data seemingly indicate the boundary between two dissimilar water types, one rich in test particles and relatively warm, the other deficient in test particles and relatively cool. Lack of supporting data prohibits speculation for the cause of this phenomenon beyond suggesting a low salinity cool water plume intruding from the north.

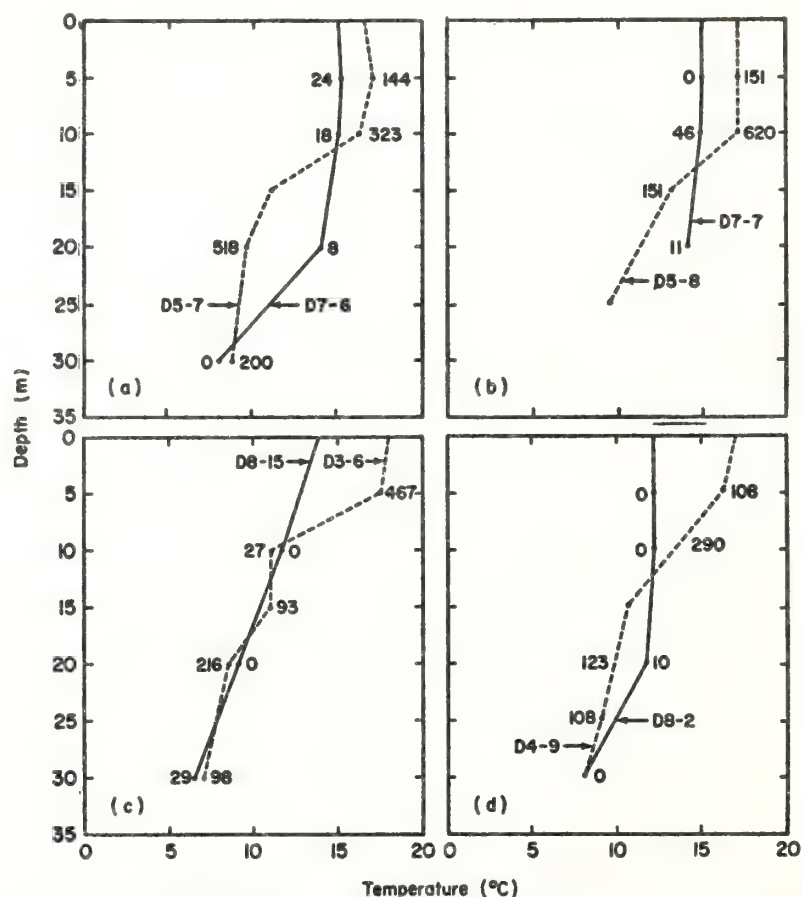


Figure 9. Temperature-depth profiles for pre-storm (-----) and post-storm (—) stations. Profiles within each illustration (such as D5-7, and D7-6 in 'A') are from nearly identical station locations as shown in Figure 1. Sphalerite concentrations (particles/l) are shown at various depths next to each profile.



Figure 9(a)–(d) show water sample stations taken before and after the storm. As seen in Figure 1, stations within each frame of Figure 9 are in nearly identical locations but at different times. The dashed lines represent data collected before the storm and the solid lines represent data taken after the storm. The numbers next to the temperature-depth profiles are values of the sphalerite concentrations at that level. Those stations which represent pre-storm conditions all have pronounced seasonal thermoclines. The storm's effects which extended to depths of 30 m induced vertical mixing and modified or destroyed the pre-storm thermoclines. In pre-storm observations the sphalerite concentrations maxima appear at or above the base of the seasonal thermocline. The pre-storm conditions of this stratified two-layer system strongly suggest particles 'hanging up' on or about the thermocline. This phenomenon has been observed elsewhere in the world oceans (Jerlov, 1958; Costing, 1970; Drake, 1971).

### Mathematical modeling

Mathematical models were developed at M.I.T. to predict the dispersion of particles in coastal waters. A two-dimensional finite element circulation model (Connor & Wang, 1973) and a compatible finite element dispersion model (Leimkuhler, 1974; Christodoulou & Pearce, 1975) were developed. The dispersion model was applied specifically to this experiment and the results compared in a favorable manner (Christodoulou & Pearce, 1975). By comparing several dispersion coefficients,  $30 \text{ m}^2 \text{ s}^{-1}$  appears to be closest to reality, yielding better agreement than other values ( $50 \text{ m}^2 \text{ s}^{-1}$  and  $100 \text{ m}^2 \text{ s}^{-1}$ ).

### Conclusions

Drogue and particle concentration data show that net water and particle movement during the study were tidally dominated and in an easterly direction until a current shear zone east of the proposed dredging site was reached. Eastward of this shear zone a strong south flowing current predominated and was responsible for the southward displacement for those drogues and portions of the particle plume entrained by the current.

A relatively low salinity intrusion (Figure 2) moving down from the north through central Massachusetts Bay may be associated with the consistent southward current flow at the easternmost current meter stations (Figure 3) as well as the 'lobed' nature of some high gradient isotherms (Figure 8).

Although sphalerite isopleth maps indicate progressive settling with time, particle settling was apparently impeded by the presence of a strong vertical gradient of temperature and salinity (pycnocline) which existed before the storm. This pycnocline may have caused greater lateral dispersion in the upper water layer than might otherwise have been the case. Although the experimental particles may not have behaved exactly as a real dredge plume, they were a more reasonable indicator of dredge plume dispersal and behavior than dissolved dye traces which do not exhibit the sedimentary characteristics of particles, but rather the movement of the water alone.

Caution should be used in the interpretation of the dispersal data, and conclusions should not be extended to other times of the year. From evidence presented above, it is reasonable to conclude that the dispersion of the particle plume was contingent upon the stage of the tidal cycle at introduction, the seasonal structure of the water column, and the effect of the storm which mixed the water column down to 30 m in some places [Figure 9(a)].

The observed dispersion of the particle plume was toward Boston Harbor (Figure 5), eastward toward Stellwagen Bank (Figure 7), and then southward along the coast into Cape Cod Bay where a counterclockwise gyre was suggested (Figure 7).

### Acknowledgements

We gratefully acknowledge the assistance of: Charles S. Yentsch (Bigelow Laboratory for Ocean Sciences, Booth Bay Harbor, Maine) and his former staff at the University of Massachusetts Marine Laboratory for the fluorometry; Bryan R. Pierce, George C. Christodoulou and others at R.M. Parsons Laboratory for Water Resources and Hydrodynamics, Massachusetts Institute of Technology, Department of Civil Engineering, for drogue data and plots and mathematical modeling; Loren W. Setlow (The Commonwealth of Massachusetts, Department of Natural Resources) for setting up and running a good laboratory; and the U.S. Coast Guard which provided ship time and manpower for current meter work and drogue tracking, and many others.

Helpful suggestions throughout the project planning and critical review of the manuscript were graciously provided by George Keller and Donald J. P. Swift.

This paper presents in final form the results of this study of which a presentation of preliminary data and initial results was given by Hess & Nelsen (1975).

### References

- Christodoulou, G. & Pearce, B. R. 1975 Mathematical modeling relevant to the glass bead study: technical report to be published by R. M. Parsons Laboratory for Water Resources and Hydrodynamics, M.I.T.
- Connor, J. & Wang, J. 1975 Mathematical models of the Massachusetts Bay. Part I. Finite element modeling of two-dimensional hydrodynamic circulation. *R. M. Parsons Laboratory for Water Resources and Hydrodynamics, M.I.T., Technical Report No. 172.*
- Costing, J. M. 1970 Visual observations of suspended-particle distributions at three sites in the Caribbean Sea. *Journal of Geophysics Research* **75**, 4144-4150.
- Drake, D. E. 1971 Suspended sediment and thermal stratification in Santa Barbara Channel, California. *Deep Sea Research* **18**, 763-769.
- Hess, W. H. & Nelsen, T. A. 1975 A test particle dispersion study in Massachusetts Bay. *Offshore Technical Conference, Dallas, Texas, paper No. OTC 2160.*
- Jerlov, N. G. 1958 Maxima in the vertical distribution of particles in the sea. *Deep Sea Research* **5**, 173-184.
- Leimkuhler, W. 1974 A two-dimensional finite element dispersion model: thesis submitted to M.I.T. in partial fulfillment of requirements for degree of Civil Engineer.
- Manohar-Maharaj, V. & Beardsley, R. C. 1973 Spring run-off and nutrient-seawater density correlations in the Massachusetts Bay. *M.I.T. Report No. MITSG-74-9 Part I*, pp. 2-103.
- Meade, R. H. 1969 Landward transport of bottom sediments in estuaries of the Atlantic coastal plain. *Journal of Sedimentary Petrology* **39**, 222-234.
- Nickola, P. W., Rankin, M. O., Scoggins, M. F. & Sheen, E. M. 1966 A system for recording air concentrations of zinc sulfide fluorescent pigment on a real-time scale. *Journal of Applied Meteorology* **6**, 430-433.

Geology 5, No. 1, 4-10.

# Lithoherms in the Straits of Florida

A. C. Neumann

Marine Sciences Program  
University of North Carolina  
Chapel Hill, North Carolina 27514

J. W. Kofoed

Atlantic Oceanographic and Meteorological Labs  
National Oceanic and Atmospheric Administration  
15 Rickenbacker Causeway  
Miami, Florida 33149

G. H. Keller

School of Oceanography  
Oregon State University  
Corvallis, Oregon 97331

## ABSTRACT

Along the base of Little Bahama Bank and out into the northeastern Straits of Florida in depths of 600 to 700 m, the research submersible *Alvin* encountered an extensive area of rocky mounds that are hundreds of metres long and as high as 50 m. The larger mounds are elongated in the direction of northerly bottom flow. They are composed of surface-hardened concentric crusts of submarine-lithified muddy to sandy carbonate sediment upon which a dense and diverse community of benthic organisms such as crinoids, corals, and sponges attach. Many of the organisms grow oriented into the prevailing northward current. The crusts are cemented in varying degree by micritic magnesian calcite and are intensively bored by endolithic organisms. Excavation of the softer undercrust by currents and (or) organisms can produce stromatolite voids. It appears that these deep mounds are biohermal in nature and constructed in situ by the subsea lithification of successive layers of trapped sediment and deposited skeletal debris. The term "lithoherm" is proposed to describe the mounds. These and the hardgrounds between them indicate that subsea lithification aids in the accretion of the flanks of carbonate platforms. Micritic carbonate build-ups similar to lithoherms have been recognized in the geologic record. The mounds of the Waulsortian bank margin offer one possible ancient analog.

## BACKGROUND

Deep-water biohermal build-ups and foreslope mud mounds have been noted in the deep flank and basinal facies associated with ancient carbonate platforms (Evans and others, 1974; Wilson, 1975), but they are rarely encountered in recent facies. A broad band of topographic irregularities with as much as 50 m of relief has been mapped in the northeastern Straits of Florida from south of Bimini northward to the Blake Plateau, in depths of 600 to 800 m, 10 to 150 km from the margin of the Bahama Banks. Although contoured as closely spaced east-west valleys and

ridges (Malloy and Hurley, 1970), Hurley and others (1962) had earlier noted the possibility that they may be individual mounds, likened to "haystacks." Other interpretations of the bottom irregularities in this general area have included outcropping bed rock and (or) slump blocks (Hurley and others, 1962), erosional features carved by present (Pratt, 1966) or Pleistocene bottom currents, deposition of sand waves (Uchupi, 1969), and the growth of unconsolidated deep-sea coral mounds (Stetson and others, 1962).

In 1971, the research submersible *Alvin* made a series of reconnaissance dives in the northeastern Straits of Florida at the base and lower slope of Little Bahama Bank in order to examine these features mapped as east-west valley and ridge (Fig. 1). Encountered instead were numerous rocky mounds, the largest of which are 30 to 50 m high, elongate, and oriented in a north-south direction. Some samples were obtained during the dives, and more were dredged in follow-up surface cruises between 1973 and 1976. During these later cruises, the area was extensively surveyed by subbottom seismic profiling with small chamber guns (1 to 40 in.<sup>3</sup>). On the basis of our in situ observations using *Alvin*, analyses of rock and sediment samples, and the seismic reflection profiles, we have concluded that these mounds are the product of in situ accumulation and lithification of pelagic and bank-derived carbonate sediments. The term "lithoherm" has been applied to the mounds in order to emphasize the role that subsea cementation plays in their formation. The color photographs presented here convey the critical observations, made through the viewing ports of *Alvin*, that have led to these conclusions. Later papers will deal with the petrographic, geochemical, and geophysical results in more detail.

## OBSERVATIONS AND INTERPRETATIONS

Of the five dives made in the northeastern Straits of Florida between Memory Rock and Matanilla Buoy off Little Bahama



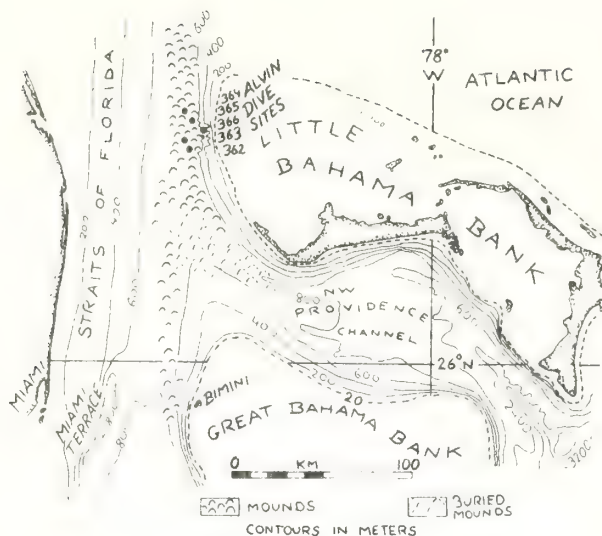


Figure 1. Index map of study area.

Bank, four were in the region of the mounds at depths between 639 and 675 m and 13 to 22 km from the bank edge. One dive, only 6 km from the bank edge at 504-m depth, encountered a steep-walled canyon complex floored with bank-derived sand and blocks of float (Fig. 1).

The elongate, steep-sided mounds are separated by smooth, flat or imperceptibly sloping areas where dark-colored hard-rock bottom (hardgrounds) crops out in patches beneath a thin veneer of cream-colored muddy sand and light-brown streaked or rippled sand. The patches of hardground surface are made apparent by localized clusters of organisms that preferentially attach to this solid substrate. Much of the surface of the muddy sand has diffuse, dark-colored parallel streaks, like windrows, which are oriented north-south and spaced about 10 cm apart (Fig. 2). Observed at close range (0.5 m), the streaks appear to be thin bands of mobile, centimetre-sized aggregates of foram-pteropod debris loosely held together by fibrous organic material. They are moved easily by weak currents. Nicknamed "bedfluff transport," this process appears to be the significant mode of sediment transport along the streaked, flat areas between the mounds. There were also occasional patches of rippled sand, and in the area of dive 364 rippled sand was dominant.

The orientation of the streaks and the observed sediment transport were parallel to the predominantly northward bottom current in the area of the dives. Several bottom-current measurements, made by a meter mounted on the submersible, ranged from 2 to 7 cm/s to the north on dive 364. Regardless of directional variations, the sedimentary features—that is, current crescents, streaks, and ripples—all indicated formation by a north-moving current.

Small, irregular mounds often dot the flat sediment or hardground surfaces between the larger mounds. Figure 3 shows a small mound formed by a low half-dome of lithified crust. Edges of individual crusts seen on both large and small mounds are about 10 to 30 cm thick. Crust surfaces are often smooth,

flat, and dense, and they are more cemented at the exposed upper surface and become progressively less cemented and more irregular toward the base. This was confirmed by studies of dredged samples (Wilber, 1976). The edge of a crust in the foreground of Figure 3 has been excavated by the action of currents and (or) organisms. The intercrust voids produced by excavation would be expected to have flat bases and irregular roofs. Later infilling by sediment or spar could produce stromatolite structure.

Attached organisms must preferentially select the hard substrate, because the lithoherm, as well as local patches of hardgrounds, exhibit a dense cover of benthic growth relative to the intervening flats of unconsolidated sediment. Stalked crinoids are common on the soft sediment, whereas sponges, unstalked crinoids, ahermatypic coral, and a wide variety of alcyonarians are the most obvious fauna of the rocky mounds (Figs. 3, 4). Figure 4, from the crest of a larger mound, reveals the superposition of four crusts as well as an excavated intercrust opening.

The sides of the larger mounds are abrupt and steep, at least 20° to 30°, and are sometimes only thinly veneered with sediment, as evidenced by alcyonarian attachment to the rock beneath (Fig. 5). The sides at the long ends do not seem as steep as the flanks; thus, in general form, the mounds appear to resemble an inverted boat. Aprons of sand, often rippled, were observed at the base of some of the mounds in areas of stronger currents. At one place, part of the side of a large mound had fallen away, or was otherwise eroded, revealing a series of overlapping, concentric crusts about 10 to 30 cm thick which appear to conform to the shape of the lithoherm (Fig. 6). This suggests that the mounds have an onion-skin-like inner structure and are the product of layer-by-layer construction in place, rather than being slump blocks.

Both the microtopography of the mound crest and the fauna of observed mounds seemed to exhibit considerable variation from mound to mound within a small area, yet no single mound appeared to exhibit any obvious ecologic zonation upon it. Some lithohermes are very narrow and rocky at the crest (Fig. 7); others are broad and rounded (Figs. 5, 8, 9). Some are veneered with sediment (Fig. 5), and some are thickly encrusted with branching, deep-water ahermatypic coral (Fig. 8). Others have a rocky surface of low local relief (Fig. 9).

The crests of several lithohermes were observed to be partly or entirely topped by an extremely rugged microtopography of crescentic embayments 10 to 30 cm in relief and dimension. On the sides of these curved scarps, a crude bedding is revealed that is parallel to the mound surface (Fig. 10). Sectioned samples are seen to be intensively bored by a variety of endolithic organisms (Wilber, 1976), and it is suggested that the irregular microtopography is also the result of active bioerosion. Burrow excavation of the less well-cemented undercrust is another process contributing to the irregular microtopography of many mounds (Figs. 3, 4, 10). Figure 11 shows a large eel emerging from an excavation beneath a crust. Local piles of debris at the doorstep of these openings also indicate that organisms excavate burrows in the softer interarea between successive crusts (see foreground of Fig. 8).

Deep-water, branching ahermatypic corals (*Lophelia* sp. and *Enallopsammia* sp.) are an often obvious component of the mound-top fauna (Figs. 3, 8, 10) and are also a common fossil component of sampled rocks. At a few localities the coral exhibited an oriented fabric by branching mostly with or into the northward-flowing current. The large white cup- or fan-shaped sponges on the mound tops and hardgrounds grow with their concave





Figure 2. Dive 36; depth, 675 m. North-south streaks of foraminiferous sand on thin veneer of more cohesive muddy sand, beneath which hardgrounds with attached organisms are exposed.

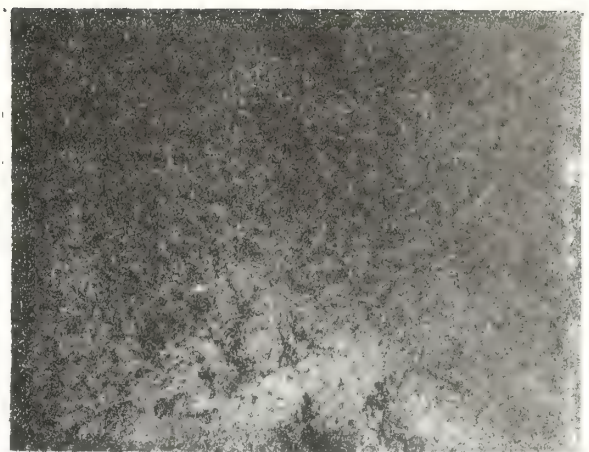


Figure 5. Dive 363; depth, about 655 m. Rounded crest of 20-m lithoherm is thinly veneered with sand.



Figure 3. Dive 364; depth, 668 m. Organisms attach to exposure of subsea cemented crust. Sand shadow (background) accumulates in lee of an obstacle. Current is from south (left).

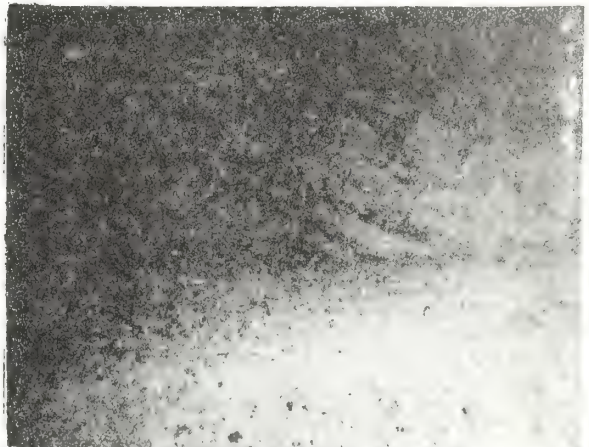
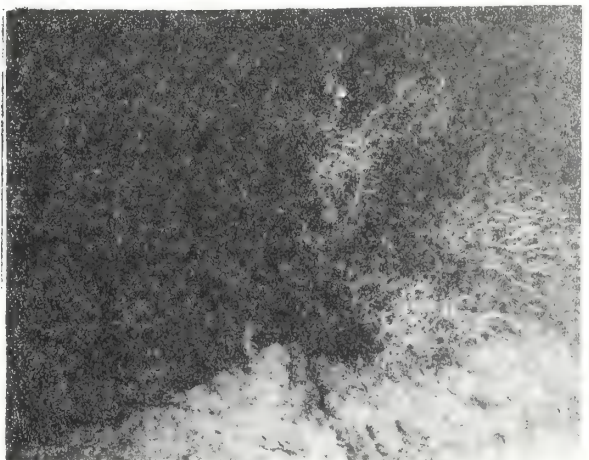


Figure 6. Dive 365; depth, 639 m. Exposed base of lithoherm reveals series of crusts about 10 to 30 cm thick.

Figure 4. Dive 362; depth, 666 m. Comatulids, sponges, and alcyonarians attached to rocky crest of lithoherm face into northward current (to right).



Figure 7. Dive 364; depth, about 640 m. Black coral, >1 m high, attached to sharp, rocky crest of a lithoherm.





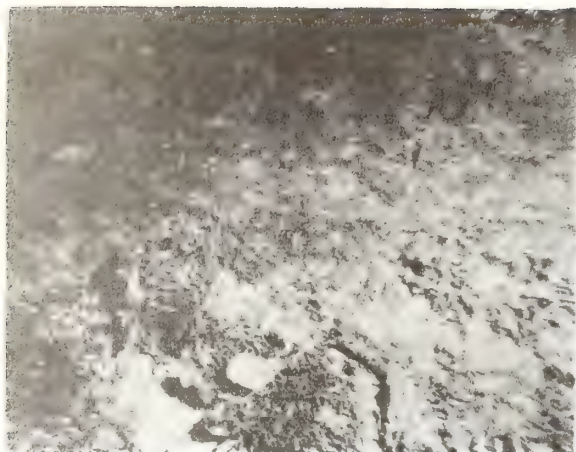


Figure 8. Dive 364; depth, about 640 m. Broad rounded crest of lithoherm densely covered by sponges and branching, ahermatypic coral.

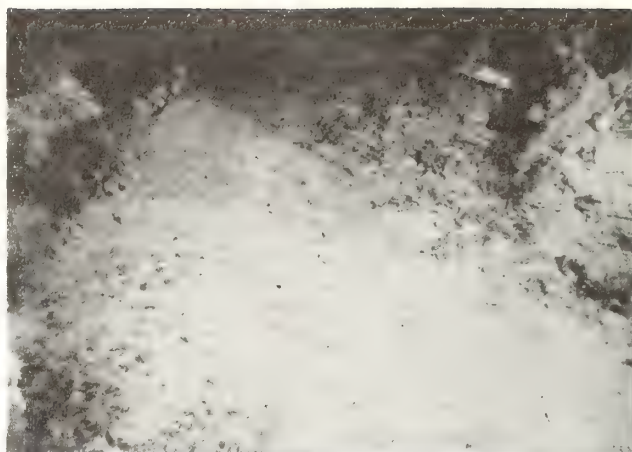


Figure 11. Dive 362; depth, 666 m. Eel emerges from opening excavated beneath lithified crust on top of lithoherm.



Figure 9. Dive 362; depth, about 666 m. Rocky crest of lithoherm showing attached organisms and low local relief.



Figure 12. Dive 362; depth, about 650 m. Filtering organisms respond to gentle current by bending with it like the sponge (foreground), or by leaning and (or) cupping into it, as sea pen and stalked crinoid do (background). Bottom here is unconsolidated.

Figure 10. Dive 363; depth, about 650 m. Crescentic scarps create rugged microtopography on this rocky mound crest. Note layering and dense cover of attached organisms.

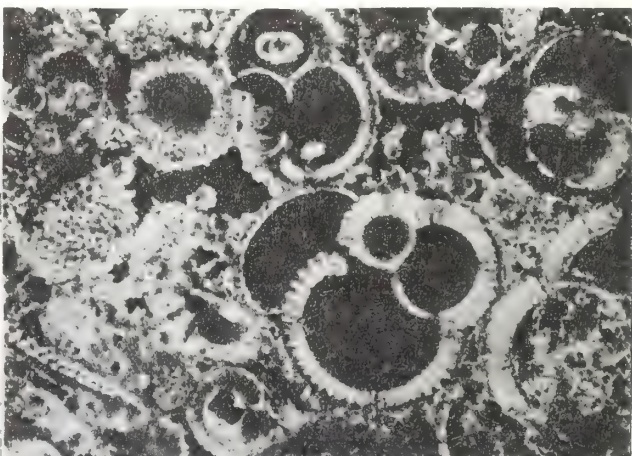
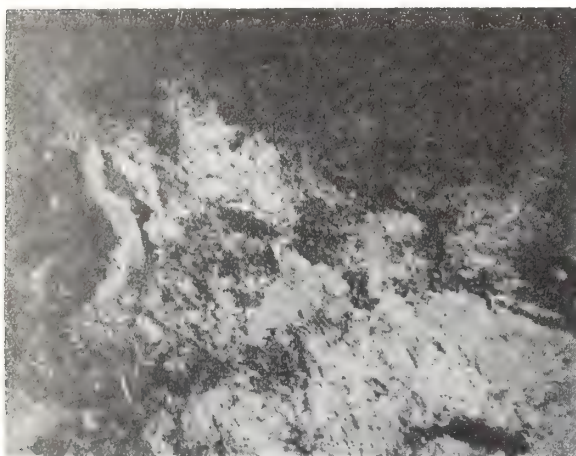


Figure 13. Dive 365; depth, about 640 m. Thin section in polarized light shows foram-pteropod sand lightly cemented by microspar and micritic magnesian calcite. Foram in center is 0.47 mm in diameter.



surfaces facing into the current (Figs. 3, 4, 9). Comatulid (unstalked) crinoids, often positioned on the rim of sponges on the hardgrounds and mound tops, also cup into the current (Fig. 4). Sea pens (Pennatulids) and stalked crinoids on the inter-mound areas of unconsolidated sediment also lean and cup into the current (Fig. 12). The current-oriented behavior of the deep crinoids has been discussed in more detail by Macurda and Meyer (1974). The alcyonarians of planar form are almost always oriented perpendicular to the current. Thus, the filtering organisms observed appear to establish an orientation and spacing that allows each one maximal cross-sectional exposure to unobstructed current flow. Under proper conditions, evidence of this faunal orientation and spacing, especially of the fixed sponges and corals, should be carried into the fossil record and provide a paleoecologic indication of current presence and direction. Certainly, the sedimentary structures as well as the overall elongate geometry of the larger lithoherms preserve a current-oriented fabric.

The process of initiation of the mounds is not apparent. They could begin by lithification within localized accumulations of sediment, such as that trapped by a cluster of organisms on a flat hardground, or accumulated as a "sand shadow" in the lee of attached organisms (see background of Fig. 3). Mound nucleation could also be triggered by hardground deformation due to lateral gravitational forces (Lindström, 1963) or the "force of crystallization" (Shinn, 1969). Growth of the mound is believed to result as the benthic community that has selectively attached itself to a lithified substrate (1) sheds its skeletal debris by death or growth, (2) adds fecal matter filtered from the water column, and (3) perhaps of most importance, collects detritus by the baffling effect of the dense cover of benthic growth. Holes and pits produced by bioerosion and burrowing in and under rock surfaces also become infilled with sediment that later lithifies, and this too serves as a process of mound maintenance.

Pelagic and bank-derived sediment must be accumulating at present, and yet the bank tops and hardgrounds are only thinly veneered with sediment. This suggests that the lithifying process responsible for the mounds and hardgrounds has recently been or is now active; otherwise, a thicker sediment mantle and fewer attached organisms might be expected.

Some analyses of rock and sediment samples have been made. The rock is a dense, hard, fossiliferous, muddy to sandy, heavily bored limestone, which breaks into slablike fragments with a smooth upper surface and a more irregular undersurface. The sediments range from mud to sand. The sand fraction is mostly planktonic foram and pteropod tests, with occasional contributions of obviously shallow-water detritus, such as *Halimeda* fragments and oolitic grains (Wilber, 1976). The mineralogy of the unconsolidated sediment varies, but it is largely aragonite with lesser amounts of largely low-magnesium calcite. In contrast, the rock is mostly magnesian calcite of about 14 mol percent  $MgCO_3$ , with aragonite common only where unaltered fossil ahermatypic coral and pteropods are present. Some concentrations of aragonitic micrite are observed, however (Wilber, 1976). Electron microprobe analysis shows that the magnesium is concentrated within the micritic matrix. The abundant macroborings appear to be produced mainly by endolithic sponges, living examples of which are occasionally found (Wilber, 1976). Microborers include sponges and fungi (R. Perkins, personal commun.). Commonly, there has been more than one generation of boring, infilling, cementation, and reboring. The macrofossils in the rock

appear to be the same ahermatypic corals living on the mound tops today. The rock type ranges from mud-supported to grain-supported coral biomicrudites, foram-pteropod biomicrites, and biopelmicrites, with many local variations. Figure 13 shows a poorly cemented biopelmicrite; other rocks range from moderately to densely cemented biomicrites. Occasional rock constituents include fragments of echinoderms and calcareous algae, siliceous sponge spicules, oolitically coated grains, composite grains, and micritized grains. Micropelleting of the micritic matrix is observed, as are pseudostylolitic contacts, geopetal fills, micritic rinds, manganic stains, and dentate fringes of microspar in sheltered voids (Wilber, 1976). Many of these features have been noted and associated with subsea cementation (Shinn, 1969; Bricker, 1971). The bioerosional and (or) solutional stylolitic contacts, the manganic staining, the common presence of multi-generation boring and infilling, and the gradation from well-lithified to poorly lithified rock downward within a crust all indicate that the lithifying process is a near-interface phenomenon and is probably now active within the bank-margin and basin environment.

Some preliminary geochemical data are available and are helpful. Oxygen isotope analyses of bulk biomicritic rock yield ratios that correspond to paleotemperatures of 5.6° and 8.4°C, and these are within the 5.5° to 10°C range of bottom temperatures recorded in the Straits of Florida today (Moore, 1965). The only radiocarbon dates done so far are on a bulk rock sample and a cleaned fossil coral and are 26,000 and 28,170 ± 500 C<sup>14</sup> yr B.P., respectively. This could mean a Pleistocene age for the cementation, but more dates are needed, and other observations already discussed suggest that lithification continues to the present.

## DISCUSSION

The exact nature of the mechanism of subsea lithification is as much of a mystery to us as to most. Certainly, the supply of potentially reactive aragonite fines to the deep marginal environment (Neumann and Land, 1975) could play a part; yet these fines are also supplied to the south Florida margin as well as the deeper parts of northwest Providence Channel, where modern products of subsea cementation are not common. Submarine-lithified hardgrounds and lithoherms are common in northern northwest Providence Channel and on the east side of the northern Straits of Florida and not common on the west side of the straits or in the deeper parts of northwest Providence Channel. This association suggests that a certain type of oceanographic control may be associated with subsea cementation in this area. The floors of both these seaways slope upward to the north (Fig. 1), and because of the direction of bottom flow, the area of lithification at the base of the Bahaman platform here is also one of ascending bottom flow. In contrast, the bottom flow on the Florida side of the straits has recently been seen to be a periodic southward-flowing countercurrent under the northward-coursing Florida Current above (Düing and Johnson, 1972). As such, the bottom flow on the west is more often descending than that on the eastern, or Bahama, side. On the Florida side, products of modern lithification occur less commonly; instead, older Tertiary rocks of the Miami terrace escarpment are exposed and are encrusted with phosphatic and manganic deposits. They exhibit smooth surfaces of apparent solutional erosion. The low sandy coral banks at the base of the terrace are unconsolidated

(Neumann and Ball, 1970). The contrast in rock types and mound types on either side of the straits begs for an explanation. It is tempting to suggest that in the ascending bottom water on the eastern side, the effects of reduced pressure and increased temperature upon the  $\text{CO}_2$  system promote an increase of supersaturation that does not occur on the western, descending, side. This manifests itself in precipitation of cements and in diagenetic alteration of sediment at or just below the sediment-water interface, transforming the sediments into lithified crusts that become either mounds of micritic rock (lithohermes) or hardgrounds. Rate of deposition of sediment and sediment texture and mineralogy must also play a part, and these controls are influenced in turn by the oceanographic regime.

Which controls act to produce which topographic form—mound or hardground—is most likely a function of local effects, such as organism attachment, microtopography, rate of deposition, and bottom sediment transport. Once a mound starts to grow, the attachment of organisms creates something of a positive-feedback system, because the organisms, in selecting the hard substrate, concentrate sedimentation there, and, when lithified, this adds another layer of crust for more attachment; and so the process goes, creating densely clustered topographic forms with as much as 50 m of relief. Shinn (1969) described a similar process to explain formation of hardgrounds in the Persian Gulf.

## SUMMARY

The submersible, with its 10- to 20-m range of effective viewing, provides the observer with a series of glimpses taken close up, from which he must construct, piecemeal, a unified impression. Such is the idealized "lithoherm" presented in Figure 14. The northward current transports sediment along the



Figure 14. Idealized lithoherm constructed from observations accumulated in four dives on research submersible *Alvin*. Hardground is exposed (foreground) beneath veneer of muddy carbonate sand. Attached organisms cluster on rocky mound composed of a sequence of concentric crusts of submarine lithified sediment, 600 to 700 m deep, in northeastern Straits of Florida.

bottom, as indicated by the streaks and ripples. Sand shadows accumulate in the lee of irregularities. Submarine cementation by processes as yet poorly known follows deposition. Hardgrounds form as flat surfaces of cementation. A mound begins if a locus of deposition is established by one of several suggested means. Organisms preferentially attach to the cemented substrate, bore into it, and burrow under it. The organisms provide a baffle that further localizes deposition. Corals provide coarse skeletal debris. Deposition of fecal pellets may further enhance the local accumulation. Renewed cementation follows deposition in a mode that may be either continuous or episodic. The result is a local build-up of roughly concentric, fossiliferous, surface-hardened lithified crusts. The development of this build-up in a regime of bottom-current flow elongates the overall moundlike form parallel to the dominant flow direction and may also result in oriented fossils and sedimentary structures. The presence of these features in a distinct belt or band within the interbank seaways suggests that they form as the result of a certain chemical oceanographic regime or of the interaction of such a regime with a bank-derived supply of reactive (aragonitic) carbonate fines.

The term "lithoherm" is proposed here to describe these deep, muddy carbonate build-ups formed by the constructive interaction of penecontemporaneous submarine lithification and organism attachment below the photic zone. As more is learned about these deep, lithified biohermal features, the term "lithoherm" can be better defined. Its utility at present is to call attention to the presence of these features, to signify a morphological expression of subsea lithification, and to emphasize the primary role of this chemical process in a biological build-up.

## GEOLOGIC SIGNIFICANCE

The presence of hardgrounds and lithohermes on the flanks and at the base of modern carbonate banks indicates that sub-sea lithified sequences may be a significant component of the lateral accretion of these platforms. Our preliminary seismic data suggest that this is so. The simple atoll model of carbonate platform development wherein lagoonal facies are contained within talus-flanked reef walls should be re-examined. The flanking deposits may be volumetrically important, not necessarily talus, and through lithification, play a major role in bank-margin maintenance. Our present indication that these mounds and hardgrounds are associated with an oceanographic regime of ascending bottom water may yield a paleoceanographic indicator useful in the reconstruction of paleocirculation systems.

Teichert (1958) and other workers have warned that certain types of low, unconsolidated ahermatypic coral banks develop below the photic zone, yet ancient bioherms so often have been associated with patch reefs, lagoonal build-ups, and other carbonate platform top- or shallow-marginal environments as to make the general term one with shallow-water affinity.

In the geologic record, flanking deposits of carbonate platforms and associated lithohermes could readily be mistaken for shallower bank-margin or bank-top facies and features. As far as ancient limestones are concerned, we should be suspicious of what we view as indicators of depth, especially if we are using biohermal build-ups for our criteria. Through *Alvin*'s viewing ports, 600 to 700 m down, we have been able to observe biohermal structures growing at the base of the carbonate platform flank and also well out into the adjacent seaway. If the porous mound-bearing facies are destined to be reservoirs, hydrocarbon exploration



tion could be extended beyond the "rim of the bucket" and into the flanking and even basin-floor deposits beyond.

Are there examples of deep-water lithoherms in ancient limestones? Evans and others (1974) reported 800-m-thick sequences of stacked lithoherms in Mesozoic marginal facies in Morocco. Our seismic profiles also reveal stacked sequences of lithoherms buried beneath the floor of the northeastern Straits of Florida. Wilson (1975) recognized deep foreslope mud mounds as a characteristic of one of his bank-margin types. He cited our observations of lithoherms as a possible modern analog of the lower Carboniferous Waulsortian mound-bearing facies seen in Europe and North America (Wilson, 1975, p. 168). Some of the mounds Wilson has cited, like those in New Mexico, are oriented (p. 156), most are not. In our modern example, this characteristic is a result of geostrophic currents associated with the oceanic setting. In ancient seaways the current patterns and velocities might have been more variable. Crinoids are components common to both ancient and recent examples, but stalked crinoids characteristic of the Waulsortian mounds are found associated more often in our area with the unconsolidated sediment than with the rocky mounds or hardgrounds. Bryozoans, common in the ancient mounds, are not common in our case. Certainly the micritic, crudely layered mound rocks are very similar, and the bank-margin locale is the same. Even stromatolite structures, so common in ancient mud mounds, could be accounted for in our case by infilling of excavations made between layers of surface-hardened crust. Clotted texture in the ancient mud-mound rocks could result on the macroscale from infilled borings, so common in our modern examples, and on the microscale from textures of micritic cements (Wilber, 1971).

A lithoherm origin has been considered in some detail for an Ordovician mud mound in southern Nevada by Ross and others (1975), but they stopped short of concluding this, even though many aspects of the two are similar. Stromatolite is an important component of this Ordovician mound, as it is in many ancient mud mounds. Burrow structures have been likened to stromatolites (Shinn, 1968), and burrows modified by surface-hardened hardgrounds such as those described here and in the Persian Gulf by Shinn (1969) are possible sources of stromatolite cavities.

We concur with Wilson (1975, p. 168) that it is tempting to cite lithoherms as a partial analog in many ancient cases. Both the similarities and differences between the lithoherms and the Waulsortian mounds in particular, and mud mounds in general, are interesting and productive to consider. Our initial observations from *Alvin* and some possible geologic ramifications are presented here in order to stimulate consideration of past and present biohermal analogs.

## REFERENCES CITED

- Bricker, O. P., ed., 1971, Carbonate cements: Baltimore, M.J., The Johns Hopkins Press, p. 47-120.
- Duing, W., and Johnson, D., 1972, Southward flow under the Florida Current: *Science*, v. 173, p. 428-430.
- Evans, J., Kendall, D. G., St. C., and Warme, J. F., 1974, Jurassic sedimentation in the High Atlas Mountains of Morocco during early rifting of Africa and North America: *Geology*, v. 2, p. 295-296.
- Hurley, R. J., Siegler, V. B., and Fink, L. K., Jr., 1962, Bathymetry of the Straits of Florida and the Bahama Islands. Pt. I. Northern Straits of Florida: *Bull. Marine Sci. Gulf and Caribbean*, v. 12, p. 313-321.
- Lindstrom, M., 1963, Sedimentary folds and the development of limestone in an Early Ordovician sea: *Sedimentology*, v. 2, p. 243-276.
- Macurda, D. B., and Meyer, D. L., 1974, Feeding posture of modern stalked crinoids: *Nature*, v. 247, p. 394-396.
- Malloy, R. J., and Hurley, R. J., 1970, Geomorphology and geologic structure: Straits of Florida: *Geol. Soc. America Bull.*, v. 81, p. 1947-1972.
- Moore, H. B., 1965, Bottom temperatures between Miami and Bimini: Miami Univ. Inst. Marine Sci. Tech. Rept., July.
- Neumann, A. C., and Ball, M. M., 1970, Submersible observations in the Straits of Florida: *Geology and bottom currents*: *Geol. Soc. America Bull.*, v. 81, p. 2861-2874.
- Neumann, A. C., and Land, L. S., 1975, Lime mud deposition and calcareous algae in the Bight of Abaco, Bahamas: A budget: *Jour. Sed. Petrology*, v. 45, p. 763-786.
- Pratt, R. M., 1966, The Gulf Stream as a graded river: *Limnology and Oceanography*, v. 11, p. 60-67.
- Ross, R. J., Jr., Jaanusson, V., and Friedman, I., 1975, Lithology and origin of Middle Ordovician calcareous mudmound at Meiklejohn Peak, southern Nevada: U.S. Geol. Survey Prof. Paper 871, 48 p.
- Shinn, F. A., 1968, Burrowing in recent lime sediments of Florida and the Bahamas: *Jour. Paleontology*, v. 42, p. 879-894.
- , 1969, Submarine lithification of Holocene carbonate sediments in the Persian Gulf: *Sedimentology*, v. 12, p. 109-144.
- Stetson, T. R., Squires, D. F., and Pratt, R. M., 1962, Coral banks occurring in deep water on the Blake Plateau: *Am. Mus. Novitates*, no. 2114, p. 1-39.
- Teichert, C., 1958, Cold- and deep-water coral banks: *Am. Assoc. Petroleum Geologists Bull.*, v. 42, p. 1064-1082.
- Uchupi, E., 1969, Morphology of the continental margin of southeastern Florida: *Southeastern Geology*, v. 11, p. 129-134.
- Wilber, R. J., 1976, Petrology of submarine-lithified hardgrounds and lithoherms from the deep flank environment of Little Bahama Bank (northeastern Straits of Florida) [M.S. thesis]: Durham, N.C., Duke Univ., 241 p.
- Wilson, J. L., 1975, Carbonate facies in geologic history: New York, Springer-Verlag, 471 p.

## ACKNOWLEDGMENTS

Reviewed by E. A. Shinn, H. B. Stewart, and H. R. Wanless. The National Oceanic and Atmospheric Administration, Atlantic Oceanographic and Meteorological Laboratories, sponsored the dive series. Research supported by National Science Foundation Grants GA-36674 and OCE 76-04330. We thank L. S. Land for geochemical data and discussion, G. Ostlund for radiocarbon dates, and the support crews of the *Alvin* and the *Fastward* for valuable assistance in the field.

MANUSCRIPT RECEIVED SEPTEMBER 13, 1976

MANUSCRIPT ACCEPTED OCTOBER 26, 1976



# PALEOBATHYMETRY OF THE CREST OF SPREADING RIDGES RELATED TO THE AGE OF OCEAN BASINS – COMMENT

PETER A. RONA

*NOAA – Atlantic Oceanographic and Meteorological Laboratories, Miami, Fla. (USA)*

Received April 7, 1977

J.J. Veever's paper [1] and prior work based on the age-depth relation of oceanic crust [2-4] treat the mean crestral depth of oceanic ridges. In treating the depth of an oceanic ridge simply as variation about a mean, they overlook a systematic variation in depth that exists along the axes of oceanic ridges. Crestal depth along the axis of an oceanic ridge varies as a function of geographic latitude, generally increasing from the pole to the equator of rotation of the lithospheric plates bounding the oceanic ridge [5].

When this systematic variation in crestral depth along the axes of oceanic ridges was noted [5], it was unclear whether the depth variation was related to pole of plate rotation or geographic pole, because the present poles of plate rotation tend to lie close to the geographic poles (Table 1). Menard and Dorman [6] have recently shown that the depth variation is related to geographic latitude. For example, the crestral depth of the Mid-Atlantic Ridge increases as the cosine of the latitude from about 1 km below sea level at 60°N to 3 km below sea level at 10°N (Fig. 1); the depth of the ridge crest is irregular in an equatorial transition zone between about 10°N and 5°S; the depth of the ridge crest then decreases from about 3 km below sea level at 5°S to 2 km below sea level at 52°S (Table 1). A compilation of crestral depths along the axes of other oceanic ridges (Table 1) based on the data of Anderson et al. [4], indicates that a latitude-depth relation also holds for the Southwest Indian Ridge, the Carlsberg-Central Indian Ridge, a segment of the Southeast Indian Ridge (segment 1 in Table 1), the Pacific-Antarctic Ridge, and a segment of the East Pacific Rise (segment 4 in Table 1).

Exceptions to the depth-latitude relation include segments of the Southeast Indian Ridge (segments 2, 3, in Table 1), and of the East Pacific Rise (segments 1, 2, 3, in Table 1).

The latitude-depth relation, the systematic increase in crestral depth of oceanic ridges toward the equator, is obviously independent of the age-depth relation, because age is supposed to be the same along the axis of a given oceanic ridge. The latitude-depth relation appears to be maintained as oceanic crust subsides about an oceanic ridge according to the age-depth relation. For example, the inclination of the axes of maximum depth of the eastern and western basins of the North Atlantic and of the axis of the crest of the Mid-Atlantic Ridge are sub-parallel (Fig. 1) [5], evidencing the independent and simultaneous operation of the latitude-depth and age-depth relations. The observation of the systematic variation of crestral depth, along the axes of oceanic ridges does not conflict with the work of Veever's [1] and others [2-4] based on the age-depth relation, but indicates that processes other than thermal contraction of the lithosphere as a function of age are required to explain the latitude-depth relation [6], as well as exceptions to that relation.

## References

- 1 J.J. Veever's, Paleobathymetry of the crest of spreading ridges related to the age of ocean basins, *Earth Planet. Sci. Lett.* 34 (1977) 100-106.
- 2 H.W. Menard, Elevation and subsidence of oceanic crust, *Earth Planet. Sci. Lett.* 6 (1969) 275-284.

TABLE 1  
Variation in crestal depth of oceanic ridges with geographic and plate parameters

Oceanic ridge	Bounding plates [7]	Pole of plate rotation [7]		Latitude span	Longitude span	Depth change [4] (km)	Direction of deepening of oceanic ridge crest
		lat.	long.				
Mid-Atlantic Ridge 1	EU/NAM	69°N	128°E	60°N–39°N	30°W–30°W	1.0–1.8	south
Mid-Atlantic Ridge 2	AF/NAM	80°N	23°E	39°N–10°N	30°W–40°W	1.8–3.0	south
Mid-Atlantic Ridge 3	AF/NAM	57°N	37°W	10°N–5°S	40°W–12°W	irregular	irregular
Mid-Atlantic Ridge 4	AF/SAM	57°N	37°W	5°S–52°S	12°W–5°E	3.0–2.0	north
Southwest Indian Ridge 1	AF/AN	19°S	13°W	52°S–51°S	5°E–30°E	2.0–2.2	east
Southwest Indian Ridge 2	AF/AN	19°S	13°W	51°S–25°S	30°E–70°E	2.2–2.8	northeast
Carlsberg-Central Indian Ridge	IN/AF	19°N	45°E	10°N–25°S	57°E–70°E	2.5–2.8	south
Southeast Indian Ridge 1	IN/AN	11°N	32°E	25°S–49°S	70°E–110°E	2.8–3.0	southeast
Southeast Indian Ridge 2	IN/AN	11°N	32°E	49°S–50°S	110°E–140°E	3.0–2.5	west
Southeast Indian Ridge 3	IN/AN	11°N	32°E	50°S–60°S	140°E–150°E	irregular	irregular
Pacific-Antarctic Ridge 1	PA/AN	69°S	100°E	60°S–62°S	155°E–168°E	2.0–2.0	horizontal
Pacific-Antarctic Ridge 2	PA/AN	69°S	100°E	65°S–60°S	170°E–150°W	2.0–2.8	northeast
East Pacific Rise 1	PA/AN	69°S	100°E	60°S–33°S	150°W–112°W	2.8–2.8	horizontal
East Pacific Rise 2	NZ/PA	57°N	86°W	33°S–23°S	112°W–114°W	2.8–2.8	horizontal
East Pacific Rise 3	NZ/PA	57°N	86°W	20°S–2°N	114°W–102°W	2.9–2.9	horizontal
East Pacific Rise 4	CO/PA	41°N	108°W	2°N–20°N	102°W–105°W	2.9–2.7	south

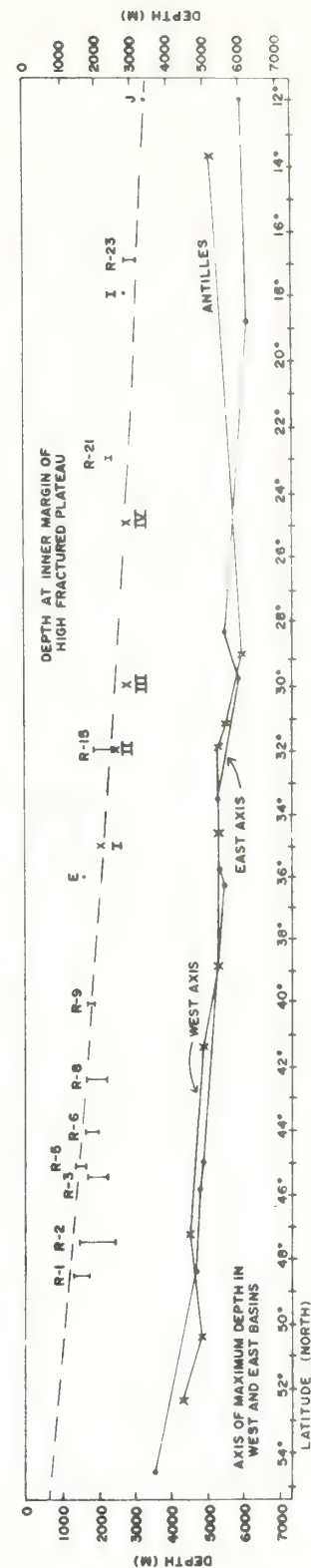


Fig. 1. Curves through data points along the axis of the crest of the Mid-Atlantic Ridge (dashed line) and along the axes of maximum depth of the eastern and western basins (solid lines) of the North Atlantic [5].

- 3 J.G. Sclater, R.N. Anderson and M.L. Bell, Elevation of ridges and evolution of the Central Eastern Pacific, *J. Geophys. Res.* 76 (1971) 7888–7915.
- 4 R.N. Anderson, D. McKenzie and J.G. Sclater, Gravity, bathymetry and convection in the earth, *Earth Planet. Sci. Lett.* 18 (1973) 391–407.
- 5 P.A. Rona, Depth distribution in ocean basins and plate tectonics, *Nature* 231 (1971) 179–180.
- 6 H.W. Menard and L.M. Dorman, On the variation of ocean depth with latitude, *EOS, Trans. Am. Geophys. Union* 57 (1976) 933.
- 7 J.B. Minster, T.H. Jordan, P. Molnar and E. Haines, Numerical modelling of instantaneous plate tectonics, *Geophys. J.R. Astron. Soc.* 36 (1974) 541–576.



# Plate Tectonics, Energy and Mineral Resources: Basic Research Leading to Payoff

Peter A. Rona

We like to believe that basic research ultimately pays off in practical benefits. Yet when the theory of plate tectonics was developed during the 1960's, the prognosis for its impact on mineral prospects was generally negative. The conceptual changes of plate tectonics from old to young ocean basins and from deterministic to indeterministic geotectonic cycles were initially considered to be unfavorable to the occurrence of energy and mineral resources, including hydrocarbons and metals. The prognosis has changed. The kinematic model provided by plate tectonics of the earth's outer layer or lithosphere, involving the interaction of a small number of large plates the boundaries of which are global seismic belts (Figures 1 and 2), not only is helping to explain the distribution and genesis of known mineral deposits, but also is

revealing new prospects [Rona, 1973a].

The earth model prior to plate tectonics was essentially static in that continents were fixed and ocean basins were permanent. Geotectonic cycles of mountain building were considered to follow a predetermined sequence of events involving a finite number of variations on the theme of sediment accumulation in elongate belts (geosynclines) and subsequent crustal accretion involving relatively small horizontal movements and vertical uplift. Under this static and deterministic earth model, only the most accessible energy and mineral occurrences were discovered, largely by trial and error, with limited understanding of why and where the resources might occur. The earth model of plate tectonics is dynamic, allowing continents to drift and ocean

basins to open and close. Geotectonic cycles follow a random rather than a predetermined sequence of events involving an infinite number of variations depending on continually changing plate interactions. Most energy expended at the surface of the earth occurs at plate boundaries, including submarine regions that were not adequately considered prior to plate tectonics. The dynamic and indeterministic plate tectonic model presents both problems and prospects for the occurrence of energy and mineral resources.

The occurrence of energy and mineral resources is related to plate tectonics in three ways:

1. Geological processes driven by energy expended at plate boundaries control to varying degrees the formation of energy and mineral resources.
2. Plate motions create tectonic

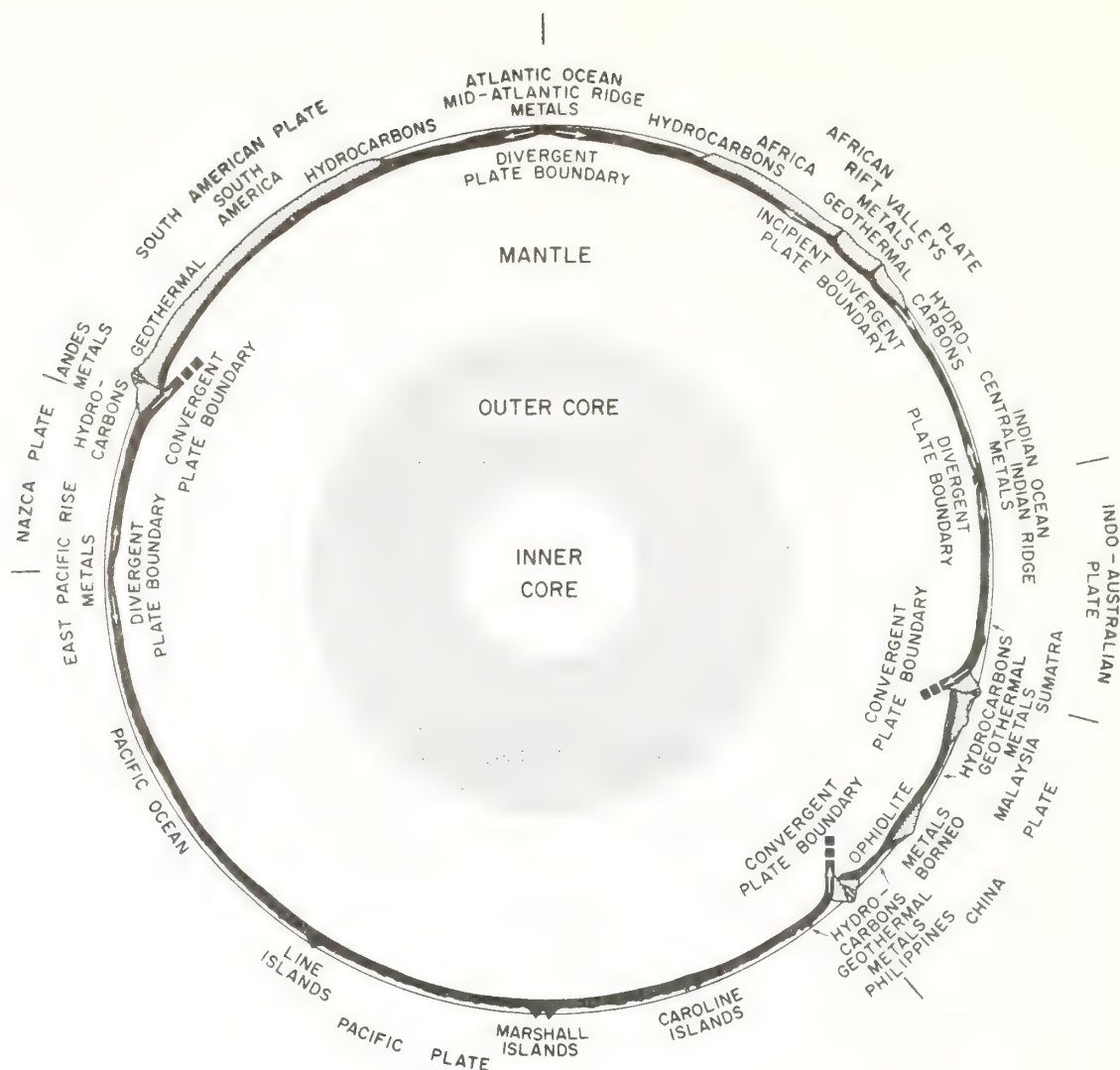


Fig. 1. Schematic great circle section through the equator of the earth, showing lithospheric plates, plate boundaries, and occurrences of energy and mineral resources. The thickness of the lithosphere is expanded by a factor of approximately 3 for clarity.

settings that influence the formation of energy and mineral resources. The two fundamental tectonic settings are opening ocean basins created by divergent plate motions and closing ocean basins created by convergent plate motions.

3. Observed relations between the formation of energy and mineral resources, geological processes at plate boundaries, and tectonic settings can be used to decipher their past relations by interpretive reconstruction of former plate configurations, following the uniformitarian principle of geology, which states that the present is the key to the past.

### Resources and Opening Ocean Basins

The opening of an ocean basin about a divergent plate boundary is accompanied by a characteristic sequence of mineral deposits. The sequence begins when development of a divergent plate boundary rifts a continent apart, and the continental fragments separate in response to creation of oceanic lithosphere by sea floor spreading to either side of the boundary at rates of centimeters per year (Figure 1). The sequence of mineral deposits as the continents separate is related to the

changing basin configuration from a sea enclosed by the surrounding land-masses to an open ocean basin. The sequence may be interrupted at any stage in its development by a reorganization of plate motion.

### Hydrocarbons

The preservation of organic matter as the progenitor of hydrocarbons in the marine environment requires a restriction on water circulation to create oxygen deficient toxic near-bottom conditions that inhibit decomposition and consumption of the organic

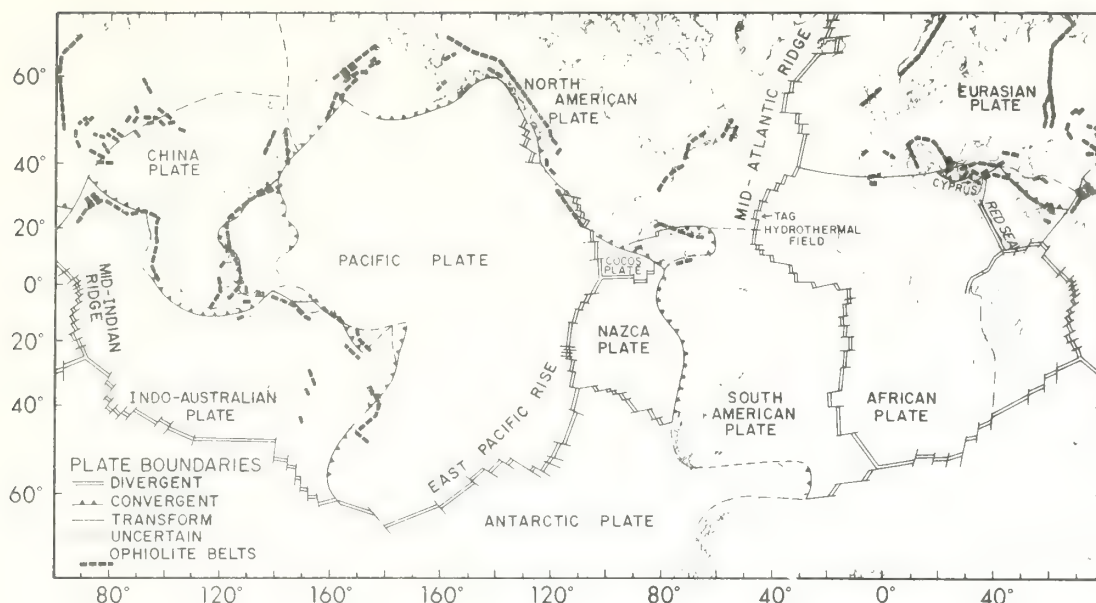


Fig. 2. World map showing principal plates, plate boundaries, and belts of oceanic crust exposed on land (ophiolites; after Coleman [1971]).

matter. According to the static earth model, a buried basement ridge, present beneath the seaward edge of many continental shelves, served as the barrier required to restrict water circulation. Consequently, hydrocarbon accumulations were assumed to terminate at the seaward edge of the continental shelf at depths of up to about 100 m below sea level. According to the plate tectonic model, the surrounding landmasses constitute the barrier required to restrict water circulation during the sea stage of opening of an ocean basin about a divergent plate boundary. Consequently, hydrocarbon accumulations do not terminate at the shelf edge but may extend seaward beneath the continental slope and continental rise in the deep ocean basin at depths of up to 6 km below sea level.

When evaporation of seawater within the sea exceeds inflow from exterior oceans restricted by the surrounding landmasses, salinity of the sea increases until rock salt is deposited in layers that may form beds kilometers thick. As a consequence of continued separation of the surrounding landmasses by sea floor spreading accompanied by subsidence of the adjacent continental margins the barrier to water circulation is breached.

Water circulation switches from restricted to unrestricted and the accumulation of organic matter and rock salt ceases. High geothermal gradients associated with rifting and increasing pressure due to progressive burial beneath continental margin sediment of several kilometers' thickness facilitate conversion of the organic matter to oil and gas. The buried salt beds, inherently unstable due to density differential with surrounding sediments, may eventually rise through overlying sedimentary strata as domes that trap any oil and gas present beneath opposite margins of the opening ocean basin.

Proposed on the basis of limited data [Rona, 1969, 1970], the relation between the sea stage in the opening of an ocean basin and the accumulation of hydrocarbons and rock salt has received support from subsequent findings in the Red Sea and the Atlantic Ocean. In the Red Sea, representing the sea stage of opening, wells have encountered hydrocarbons associated with high geothermal gradients and rock salt up to 5 km thick; seismic reflection profiles reveal that the salt extends beneath a large area of the sea [Lowell and Genik, 1972]. In the Atlantic, representing the ocean basin stage of opening, Deep-Sea Drilling

Project holes and seismic reflection profiles have confirmed that rock salt beds, domes, and hydrocarbons present in certain sedimentary basins beneath continental shelves extend seaward beneath continental slopes and continental rises on both sides of the ocean basin (Figure 3; see also McIver [1975] and Roberts and Caston [1975]). The distribution of Atlantic hydrocarbon and salt accumulations in space and time is consistent with the independently determined history of opening of the North Atlantic (Late Triassic and Jurassic periods; see Rona [1970], Schneider and Johnson [1970], Pautot et al. [1970], and Olson and Leyden [1973]) and the South Atlantic (Early Cretaceous period; see Belmonte et al. [1965], Campos et al. [1974], and Scientific Party [1975]). From preliminary sampling it is estimated that 10 times the amount of reduced carbon exists in sediments deposited during the sea stage of opening of ocean basins than is present in known reserves of coal and petroleum [Ryan and Cita, 1977].

Many of the world's most productive hydrocarbon accumulations exist in sedimentary basins on continents away from either present or former plate boundaries. Despite geographic separation these hydrocarbon accu-



mulations may be related to geologic processes at divergent plate boundaries (Figures 1 and 2) through control of global sea level primarily by reversible volume changes of oceanic ridges. The volume of an oceanic ridge (divergent plate boundary) varies directly with rates of sea floor spreading during opening of an ocean basin [Roma, 1973b; Hays and Pitman, 1973; Flemming and Roberts, 1973]. A net volume increase in the world oceanic ridge system during relatively fast sea floor spreading reduces the cubic capacity of ocean basins, resulting in transgressions of shallow seas onto continents and deposition of a marine sedimentary sequence that may contain organic source material and reservoir rocks for hydrocarbons [Roma, 1973b]. Conversely, a net volume decrease in the oceanic ridge system during relatively slow sea floor spreading increases the cubic capacity of ocean basins, resulting in marine regression and the worldwide development of unconformities on the sedimentary sequences due to erosion and/or nondeposition [Roma, 1973b]. The marine regression may create restricted conditions that favor the preservation of organic matter, and the unconformities may act as traps for hydrocarbon accumulations. Reversible volume changes of the world oceanic ridge system, evidenced by worldwide unconformities between sedimentary sequences accumulated during the past 600 million years, have operated in cycles of tens of millions of years, the time scale of geologic periods [Sloss, 1963]. The surfaces of unconformities between sedimentary sequences constitute reflecting and refracting interfaces that are correlatable on a worldwide basis by seismic methods [Vail and Mitchum, 1977]. The inferred relation between global sea level and stratigraphy is proving useful in exploration for hydrocarbons associated with stratigraphic traps and also provides globally synchronous time references applicable to many geologic problems.

#### Geothermal Energy

The components necessary for geothermal systems are present at divergent plate boundaries (Figures 1 and 2; also see Elder [1965]), including heat supplied by creation of oceanic

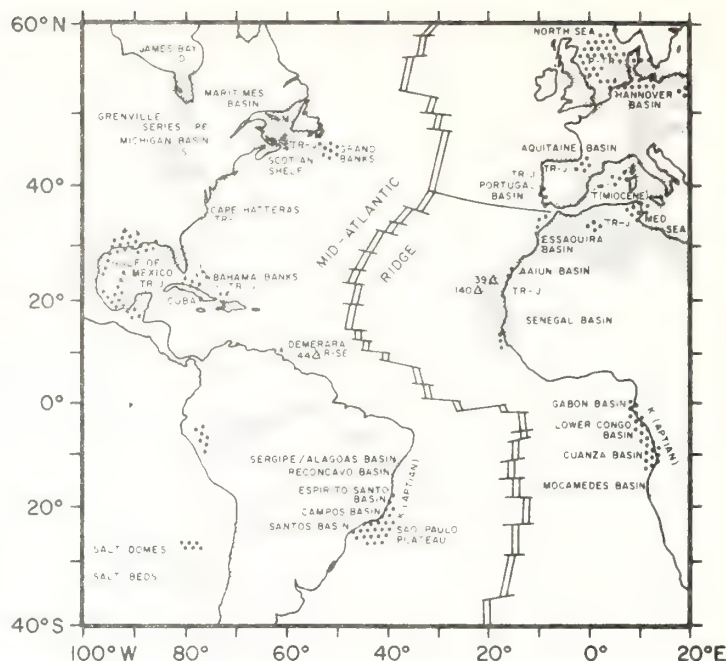


Fig. 3. Atlantic salt deposits [from Roma, 1976a]. The distribution of salt in time and space around the Atlantic is consistent with deposition during sea stages in the opening of the North and South Atlantic ocean basins. Areas of hydrocarbon potential correspond to the salt deposits. Deep-Sea Drilling Project sites 139, 140, 144 are shown. (T, Tertiary; K, Cretaceous; J, Jurassic; TR, Triassic; P, Permian; M, Mississippian; D, Devonian; S, Silurian; PC, Precambrian.)

lithosphere that accounts for 20% of the earth's estimated total rate of heat loss of  $10.2 \times 10^{12}$  cal/sec [Williams and Von Herzen, 1974], a recharge system involving sea or meteoritic water, a circulation system through fractures in volcanic rocks emplaced at the plate boundary, and a submarine or subaerial discharge system. Geothermal energy was utilized in Iceland long before the island was interpreted as part of the divergent plate boundary that forms the Mid-Atlantic Ridge. Other regions where divergent plate boundaries intersect land offer potential for geothermal development, including the rift valleys of Africa (Figure 1), the Gulf of California, Salton Sea, and Rio Grande Rift of southwestern North America. Geothermal energy is inaccessible as an energy resource along most of the 54,000-km-long divergent plate boundary system submerged beneath the oceans (Figure 2). Geothermal energy is the driving force of hydrothermal processes that concentrate metal-

lic minerals at divergent plate boundaries.

#### Metals

When the concept of creation of oceanic lithosphere by sea floor spreading about oceanic ridges (divergent plate boundaries) was proposed [Dietz, 1961; Hess, 1962], the prospect for metal deposits in oceanic crust (the brittle upper several kilometers of oceanic lithosphere) was considered negligible. The homogenous composition and young age of oceanic crust were thought to preclude the kind of crustal differentiation that has concentrated metal deposits in older continental crust [Dietz, 1969]. Contrary to this prognosis, a series of discoveries has demonstrated that metallic mineral deposits do form in oceanic crust at sites along divergent plate boundaries during both the sea stage and the ocean stage in the opening of an ocean basin.

A cruise of the HMS *Challenger*

discovered metalliferous sediment on the East Pacific Rise [Murray and Renard, 1891]. It was later inferred that the metalliferous sediments were formed by hydrothermal processes related to volcanism at the East Pacific Rise [Revelle *et al.*, 1955; Skorogov, 1964; Arrhenius and Bonatti, 1965; Boström and Peterson, 1966]. Subsequent work has better defined the distribution and geochemistry of these deposits and has established their genetic association with divergent plate boundaries. The Deep-Sea Drilling Project has found that as a consequence of sea floor spreading, metalliferous sediments occur in a layer several meters thick overlying basalt of oceanic crust both at and away from oceanic ridges in all the major ocean basins.

Another discovery demonstrating that metallic mineral deposits form in oceanic crust at sites along divergent plate boundaries was that of the metalliferous sediments of the Red Sea, which was made by scientists participating in the International Indian Ocean Expedition (1963–1965). The metalliferous sediments are concentrated in basins along the divergent plate boundary at the axis of the Red Sea (Figure 2) and are overlain by hot aqueous (hydrothermal) solutions from which the sediments precipitated under conditions of restricted oceanic circulation [Degens and Ross, 1969]. The hydrothermal solutions are further stabilized by high salinities acquired by flow through adjacent rock salt beds characteristic of the sea stage of opening. Sampling of the upper 10 m of metalliferous sediment in the largest ( $56 \times 10^6 \text{ m}^2$ ) of the 16 basins containing hydrothermal solutions and/or metalliferous sediments known in the Red Sea revealed a total dry weight of about  $80 \times 10^6$  tons containing 29% Fe, 3.4% Zn, 1.3% Cu, 0.1% Pb, 54 ppm Ag, and 0.5 ppm Au, with an estimated market value of \$2.5 thousand million exclusive of recovery and refining costs which exceed present technology [Bischoff and Manheim, 1969; Backer and Schoell, 1972]. The metal content of metalliferous sediments in the Red Sea is generally higher than that of metalliferous sediments in ocean basins due to dilution of the latter with other types of sediment. The distribution of metalliferous sediments indicates formation primarily by hydrothermal processes

at divergent plate boundaries where the sediments are deposited under conditions of restricted water circulation during the sea stage and from where they are dispersed by unrestricted water circulation during the ocean stage of opening of an ocean basin.

The TAG Hydrothermal Field, discovered by the NOAA Trans-Atlantic Geotraverse (TAG) project on the Mid-Atlantic Ridge crest in the central North Atlantic (Figure 2), exemplifies the ocean stage in the sequence of metal deposition in an opening ocean basin [Rona *et al.*, 1976]. In place of the Red Sea basins, filled with metalliferous sediments overlain by hydrothermal solutions, the current-swept basalt wall of the rift valley at the TAG Hydrothermal Field is encrusted with manganese oxide centimeters thick. The purity (40% Mn) and the rapid accumulation rate (200 mm/ $10^6$  yr) evidence a hydrothermal origin for the manganese oxide [Scott *et al.*, 1974], similar to metalliferous sediments of the Red Sea but different from hydrogenous manganese nodules of mixed metal composition that slowly (1–10 mm/ $10^6$  yr) precipitate from sea water. It is infeasible at present to drill through the manganese oxide of the TAG Hydrothermal Field into the underlying basalt. However, observations of oceanic crust exposed on land (Figure 2) suggest that the manganese oxide may be underlain by metallic sulfide bodies, which constitute an economically important class of metal deposits to be considered with reference to closing ocean basins. The thermal output calculated from a measured near-bottom water temperature anomaly attributed to hydrothermal discharge at the TAG Hydrothermal Field is several megawatts per kilometer of ridge axis, which is the same order of magnitude as that of major continental geothermal systems [Rona *et al.*, 1975; Lowell and Rona, 1976]. The metalliferous deposits of the Red Sea basins and the TAG Hydrothermal Field indicate that hydrothermal processes of metal concentration in oceanic crust can act continuously from the sea stage through the ocean stage in the opening of an ocean basin about a divergent plate boundary.

The major role of hydrothermal activity at divergent plate boundaries is indicated by the occurrence of metal-

liferous sediments, metalliferous encrustations, and metallic sulfide bodies of hydrothermal origin in oceanic crust, along with other lines of evidence from surrounding rocks including heat flow patterns, hydration, and isotopic composition [Sillitoe, 1972a; Spooner and Fyfe, 1973; Hutchinson, 1973; Lister, 1974]. Hydrothermal convection constitutes about 80% of the estimated  $2 \times 10^{12}$  cal/s rate of heat loss from lithospheric cooling at divergent plate boundaries; the balance of 20% is due to heat conduction through the rocks [Williams and Von Herzen, 1974]. Sub-sea floor hydrothermal convection systems involving the circulation of seawater through oceanic crust and upper mantle driven by volcanic heat sources are hypothesized to concentrate metallic ores at divergent plate boundaries as follows: cold dense seawater penetrates fractures in newly created basalt, is heated by hot volcanic rocks at depth, rises in response to decreased density, dissolves metals disseminated in low concentrations in the basalt, transports the metals as chloride complexes, and precipitates metals during ascent through chemical and physical gradients, beginning with precipitation of metallic sulfide bodies under reducing conditions within the basalt, continuing with precipitation of metallic oxide encrustations under oxidizing conditions at the basalt-seawater interface, and ending with precipitation of metal-rich suspended particulate matter from discharge into the overlying water column, which settles out as metalliferous sediments [Krauskopf, 1956; Helgeson, 1964; Corliss, 1971; Boström, 1973; Bonatti, 1975].

The intensity of hydrothermal metal concentrating processes compensates for the homogeneous composition and relatively young age of oceanic crust. Hydrothermal metal deposits do not form continuously along divergent plate boundaries but are localized where structural and thermal conditions favor exceptionally intense hydrothermal circulation. To date, only a few active hydrothermal mineral fields, including the Red Sea basins and the TAG Hydrothermal Field, are known along the worldwide divergent plate boundary system (Figure 2). A small inactive hydrothermal deposit was found on the Mid-Atlantic Ridge crest 1000 km north of

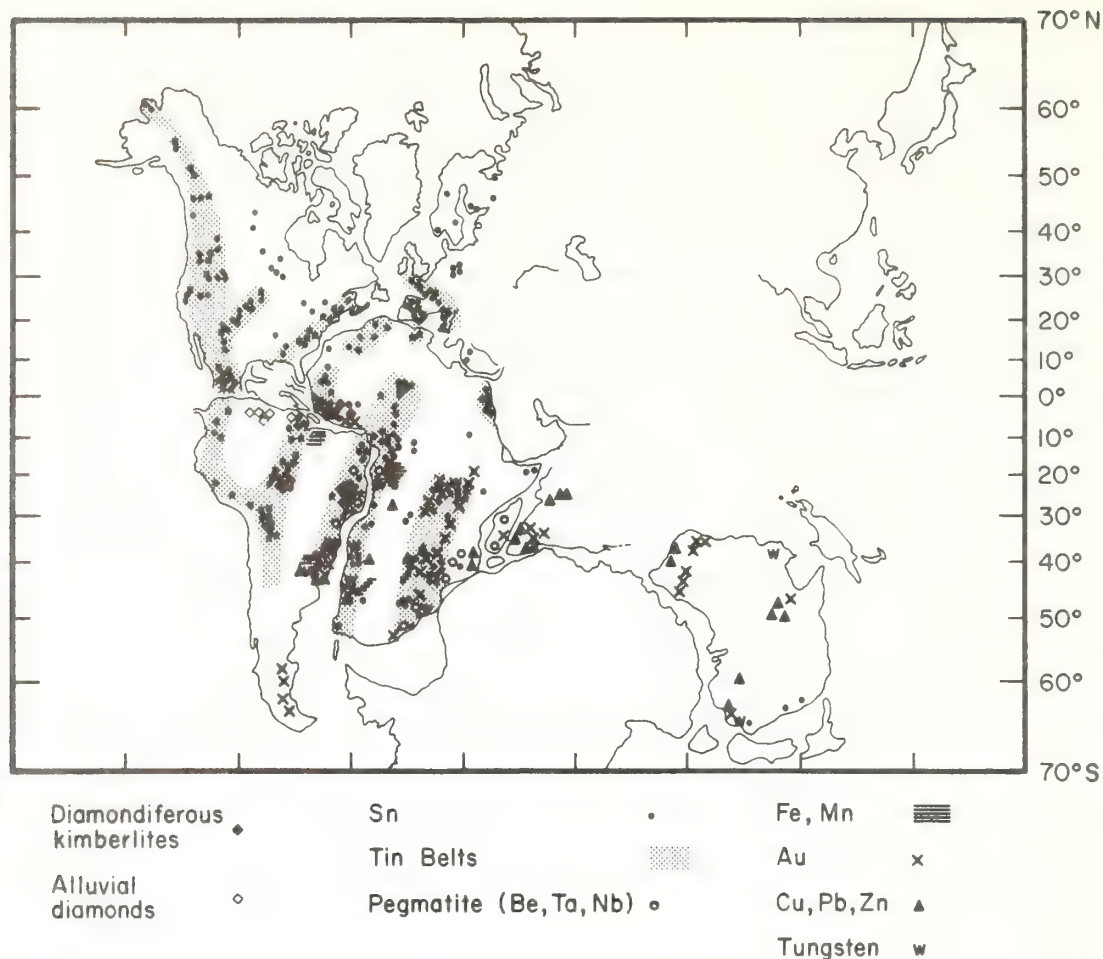


Fig. 4. Mineral provinces shown on the continents [Schuiling, 1967; Petrascheck, 1973] in reconstructed positions during the Triassic period ( $220 \pm 20$  m.y. B.P.; see Smith et al. [1973]) prior to continental separation.

the TAG Hydrothermal Field by the Famous project (Figure 2; see also Areyana [1975]). An active hydrothermal field at the Galapagos spreading center in the eastern equatorial Pacific was investigated in recent dives by the deep submergence research vehicle *Alvin* [Corliss et al., 1976; Weiss et al., 1976].

Once formed at a divergent plate boundary, the hydrothermal metal deposits are moved away from the boundary by sea floor spreading. The distribution of hydrothermal mineral deposits in oceanic crust is presently unknown. Knowledge of hydrothermal ore forming processes at divergent plate boundaries is helping to guide exploration for metal deposits in oceanic crust exposed on land where

accessible to immediate exploitation (Figure 2, to be considered with reference to closing ocean basins) and in oceanic crust submerged beneath ocean basins where some deposits may eventually become exploitable. Evaluation of the metallic mineral potential of oceanic crust which covers two thirds of the earth is contingent on the results of this exploration on land and at sea.

#### *Rifted Continental Mineral Provinces*

Two distinct situations relevant to the occurrence of mineral resources exist when a continent rifts apart and an intervening ocean basin opens in response to sea floor spreading about

a divergent plate boundary. In the first situation, already considered, metal deposits are concentrated in oceanic crust by hydrothermal processes at the divergent plate boundary. In the second situation, preexisting mineral provinces of the continent are rifted apart and separate as the ocean basin grows between the continental fragments. Knowledge of the location of a mineral province that trends transverse to the margin of one continental fragment can lead to the continuation of that mineral province in the other fragment when the fragments are reconstructed to their pre-rift configuration by morphologic and paleomagnetic techniques. Mineral provinces that may have been separated (Figure 4) include tin, gold, and



diamond deposits of western Africa and eastern South America, as well as tin deposits of North America, Europe, Australia, and southeast Africa [Schubert, 1967; Raymond, 1970; Petrascheck, 1973; Reid, 1974]. The southward trend of certain prerift mineral provinces in the southern continents suggests interesting mineral potential for Antarctica (Figure 4; see also Rønnov [1970]). The mineral potential of microcontinents such as Madagascar and the Seychelles of the Indian Ocean may also be related to their prerift positions. Prerift mineral provinces must be distinguished from postrift provinces, such as the metal provinces along the western margins of the Americas formed at convergent plate boundaries during closing of the Pacific (Figures 4 and 5).

### Resources and Closing Ocean Basins

When a great circle section of the earth is viewed (Figure 1), it is apparent that the opening of ocean basins by crustal creation at divergent plate boundaries requires the closing of other ocean basins by crustal destruction at convergent plate boundaries, if the diameter of the earth remains essentially constant. Like all ocean basins the oceanic lithosphere of the Pacific is being created at divergent plate boundaries. Unlike opening ocean basins the oceanic lithosphere is being consumed at convergent plate boundaries around the Pacific faster than it is being created. The closing of an ocean basin is accompanied by the formation of characteristic energy and mineral resources at the convergent plate boundaries around its perimeter. From a resource point of view, the name 'ring of fire' for the circum-Pacific region could well be changed to 'ring of resources' [Rona and Newman, 1976a, b].

The nature of interactions between converging plates continually changes in space and time, creating different tectonic settings that influence the occurrence of energy and mineral resources. Certain broad patterns emerge in the relation between tectonic settings and resources, apparently related to rate and direction of plate convergence. When oceanic lithosphere and continental litho-

sphere converge, in the general (stable) case an oceanic trench forms, and the heavier oceanic lithosphere descends beneath the lighter continental lithosphere (subduction). The oceanic lithosphere is subducted along an inclined plane, identified by earthquakes of the Benioff seismic zone (Figure 1). The inclination of the Benioff zone along a convergent plate boundary is inversely proportional to the relative rate of plate convergence [Luyendyk, 1970]. Where relative rates of plate convergence are slow, such as along sections of the western Pacific (about 5 cm/yr), the inclination of the upper portion of the Benioff zone is high (about 40°), and volcanic island arcs are present. Where relative rates of plate convergence are fast (about 9 cm/yr), such as along sections of the eastern Pacific, the inclination of the upper portion of the Benioff zone is low (about 15°), and volcanic island arcs are absent [Mitchell, 1973]. In place of offshore island arcs a volcanic mountain chain forms on the adjacent continent which is in effect an island arc superposed on the continent, like the Andes of western South America (Figure 1). In the special (unstable) case of plate convergence the upper portion of the oceanic lithosphere comprising oceanic crust and upper mantle is thrust onto continental lithosphere (obduction). The occurrence of mineral resources at convergent plate boundaries of a closing ocean basin is controlled by geological processes at the boundaries and influenced by the different tectonic settings described.

### Hydrocarbons

Oceanic trenches and volcanic island arcs that form at convergent plate boundaries where oceanic lithosphere is being subducted around a closing ocean basin create a habitat that favors accumulation of hydrocarbons [Dickinson, 1974; Curran, 1975; Bally, 1975]. The island arcs divide the ocean basin into marginal basins. The marginal basins and the oceanic trenches catch organic matter and sediment and restrict water circulation, so that the organic matter may be preserved. Additional deep-sea sediment with variable organic matter content is continuously transported

into the oceanic trenches during subduction of the oceanic lithosphere [Sorokhtin *et al.*, 1974]. Geothermal heat in the trenches and marginal basins facilitates conversion of the organic matter to oil and gas [Klemme, 1975]. Deformation of the sediment in the trenches and marginal basins by tectonic forces associated with plate convergence forms traps for the accumulation of hydrocarbons. For example, the marginal basins enclosed by the volcanic island arcs of the western Pacific, including the South China Sea, the East China Sea, the Yellow Sea, the Sea of Japan, the Sea of Okhotsk, and the Bering Sea, are being explored as some of the most promising areas in the world for hydrocarbons. The oceanic trenches of the Pacific are potential targets for future exploration, because drilling would not be economic at present owing to their great water depth.

### Geothermal Energy

Geothermal phenomena including active volcanoes, hot springs, fumaroles, and geysers are distributed along convergent plate boundaries where oceanic lithosphere is being subducted around a closing ocean basin (Figure 1). The geothermal phenomena result from heating due to mechanical factors (friction), chemical reactions (dehydration), and internal heat of the earth associated with descent of the oceanic lithosphere. Despite their spectacular manifestation as the 'ring of fire' around the Pacific the estimated rate of heat loss from these surficial geothermal phenomena at convergent plate boundaries is  $5 \times 10^{10}$  cal/s [Elder, 1965], less than 1% of the estimated total rate of heat loss from the earth. Considerable potential exists for utilization of geothermal energy at subducting convergent plate boundaries. The geothermal energy also plays an important role in hydrothermal ore forming processes.

### Metals

Unlike metal deposits at divergent plate boundaries in opening ocean basins that are difficult to explore and presently inaccessible to exploit, metal deposits at convergent plate

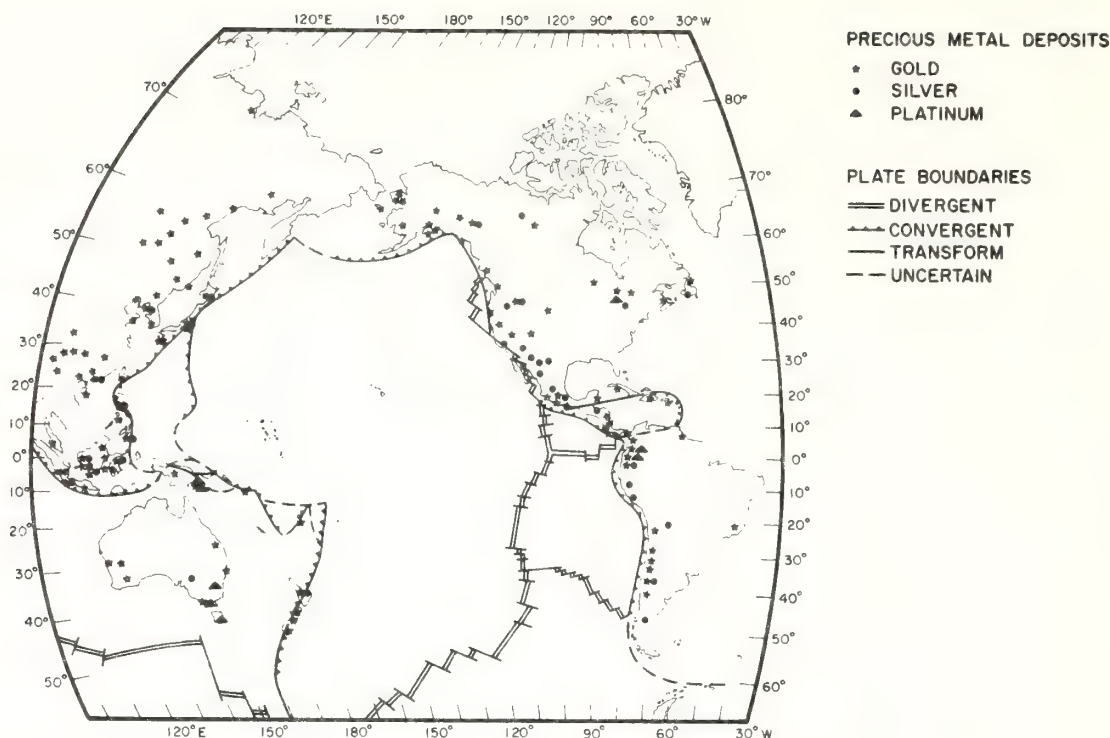


Fig. 5. Map of precious metal deposits and plate boundaries of the Pacific region [Rona and Neuman, 1976a, b].

boundaries are exposed on land accessible to exploration and exploitation (Figure 1). The metal deposits at convergent plate boundaries are concentrated in two fundamentally different ways related to the general case of subduction and the special case of obduction. A major portion of base, precious, iron, and ferroalloy metals are distributed along present and former convergent plate boundaries where oceanic lithosphere has been subducted around a closing ocean basin. For example, in the eastern Pacific, precious metal deposits occur along convergent plate boundaries at the western margins of North America and South America (Figure 5). In the western Pacific, precious metal deposits occur on volcanic island arcs including Japan, the Philippines, and Indonesia at present convergent plate boundaries and in eastern Asia and Australia at former convergent plate boundaries (Figure 5). More than half of the western world's copper production (about 45% of world copper production) comes from porphyry copper deposits, large-volume low-grade de-

posits of disseminated copper sulfide minerals associated with volcanic rocks, that occur at present or former convergent plate boundaries (average size deposit  $150 \times 10^6$  tons; average copper content 0.8%). Porphyry copper deposits frequently contain economically significant quantities of molybdenum and gold.

According to the static earth model, the source for circum-Pacific metal deposits was generally considered to be anomalous metal concentrations in underlying continental crust and mantle [Krauskopf, 1967; Noble, 1970]. The dynamic earth model of plate tectonics has identified subducted oceanic lithosphere as an additional source for the metal deposits. The 'geostill concept' attempts to explain how metals may be distilled from one plate (oceanic lithosphere) and transferred to another plate (continental lithosphere) during subduction. The geostill concept envisages extraction of metals from seawater-saturated oceanic crust by partial melting under conditions of increasing temperature and pressure during descent of oceanic

lithosphere along a Benioff zone, upward transport of the metals in fluid and gaseous phases, addition of other metals during flow through overlying mantle and continental lithosphere, and concentration of the metals as deposits in volcanic island arcs and mountain chains by primary processes at the time of solidification of the volcanic rocks and by secondary processes following their solidification [Sawkins, 1972; Sillitoe, 1972b; Guild, 1972].

Models of metallogenesis associated with subduction at convergent plate boundaries are becoming increasingly complex in order to differentiate multiple interacting processes and to explain the characteristics of actual deposits. With regard to subcrustal processes, the models are incorporating variations in sources of metals, magmatic processes, seismicity, nature of lithospheric descent, and structure of the subducted plate [Krauskopf, 1967; James, 1971; Mitchell and Garson, 1972, 1976; Stern and Wylie, 1973; Oyarzun and Frutos, 1974; Sillitoe, 1974]. The pro-

portion of metals derived from oceanic lithosphere, mantle, and continental crust is being traced, by using sulfur, lead, and strontium isotopes, as part of a study of metallogenesis in the southeastern Pacific by the Nazca Plate project (Figures 1 and 2; see also *Dasch* [1974], *Field et al.* [1976], and *Heath and Dymond* [1977]). With regard to crustal processes, the models are incorporating variations in regional and local volcanism, magmatic processes, hydrothermal activity, and geologic structure of volcanic island arcs and mountain chains, resulting in the merger of plate tectonics with traditional field geology [Mitchell and Bell, 1973].

The special case of obduction, when slices of oceanic crust and upper mantle perhaps 10 km thick by tens of kilometers long are uprooted from ocean basins or marginal basins and emplaced on land at convergent plate boundaries (ophiolites; for example, Borneo in Figure 1; see *Coleman* [1971]), provides remarkable opportunities for study and exploitation of metal deposits in oceanic crust. As a consequence of obduction the metal deposits formed in oceanic crust by hydrothermal processes at divergent plate boundaries (metalliferous sediments, metallic encrustations, metallic sulfide bodies) may be exposed on land.

The copper sulfide ore bodies of the Troodos Massif of Cyprus in the eastern Mediterranean (Figure 2) exemplify economically important deposits formed in oceanic crust by hydrothermal processes during sea floor spreading, similar to the formation of deposits of the Red Sea basins and the TAG Hydrothermal Field. Subsequent to formation of the Troodos deposits the oceanic crust was emplaced on land as an ophiolite during a former closing of a section of the Mediterranean [Gass and Masson-Smith, 1963; Moores and Vine, 1971]. One of several copper sulfide ore bodies of the Troodos Massif (Mavrovouni) contains an estimated mass greater than  $15 \times 10^6$  tons with average composition of 4.2% copper, 48% sulfur, 43% iron, 0.4% zinc, 8 ppm gold, and 8 ppm silver [Constantinou and Govett, 1973]. Having been mined since preclassical times, the mineral products exported from Cyprus had an

estimated value amounting to \$30 million in the year 1970.

Ophiolites have become prospective as a consequence of the realization that hydrothermal processes concentrate metallic mineral deposits in oceanic crust at divergent plate boundaries and that economic mineral deposits occur in oceanic crust obducted at convergent plate boundaries. Other ophiolites exist along present and former convergent plate boundaries where ocean basins or marginal basins have closed, including regions within major mountain ranges such as the Alpine-Himalayan mountain belt, the Urals, the marginal ranges of eastern and western North America, volcanic island chains along the western margin of the Pacific, and regions along former convergent plate boundaries within Asia (Figure 2). Copper sulfide bodies in ophiolites, exemplified by the Troodos deposits, are smaller but of higher grade than the porphyry copper deposits described in conjunction with subduction at convergent plate boundaries around closing ocean basins. The implications of the size differential of such deposits for the economic mineral potential of oceanic crust will remain unclear until more is known about the distribution of copper sulfide bodies in oceanic crust.

The observation that a major portion of known base, precious, iron, and ferroalloy deposits is situated along either present or former convergent plate boundaries around closing ocean basins establishes trends of mineralization that can be used to steer mineral exploration. The developing understanding of how the metal deposits are concentrated at convergent plate boundaries, involving the geostill concept associated with subduction and emplacement of ophiolites by obduction, is being used to identify those tectonic settings where geologic conditions favor the occurrence of metal deposits.

## Summary

Geological processes driven by energy expended at plate boundaries control to varying degrees the formation of energy and mineral resources. Reversible volume changes of oceanic ridges (divergent plate boundaries)

may control the development of sedimentary sequences and stratigraphic traps for hydrocarbons. Metalliferous sediments, metallic oxide encrustations, and metallic sulfide bodies are concentrated in oceanic crust by hydrothermal processes at divergent plate boundaries and may be emplaced on land accessible to exploitation by obduction of the oceanic crust at convergent plate boundaries (Figures 1 and 2). Many base, precious, iron, and ferroalloy metal ores including porphyry deposits are concentrated by processes related to subduction of oceanic crust at convergent plate boundaries (Figure 5). Geothermal energy resources occur at both divergent and convergent plate boundaries.

Plate motions create tectonic settings that influence the formation of energy and mineral resources. The sea stage of opening of ocean basins favors the accumulation of hydrocarbons and thick layers of rock salt (Figure 3). Oceanic trenches and marginal basins bounded by volcanic island arcs around closing ocean basins also create habitats that favor the accumulation of hydrocarbons. Tectonic settings of the sea stage and ocean stage of opening ocean basins favor the formation of hydrothermal metal deposits. Volcanic island arcs and volcanic mountain chains at convergent plate boundaries provide the tectonic settings for metallic sulfide bodies and porphyry deposits. Plate motions also act to rift apart preexisting mineral provinces of continents and microcontinents (Figure 4).

Current research on the formation of energy and mineral resources, geological processes at plate boundaries, plate motions, and tectonic settings is establishing the basis for judicious use of the present as the key to discovering resources formed during past plate tectonic regimes. Industry is applying the relations between plate tectonics and energy and mineral resources to guide exploration for hydrocarbons and metals [Rona, 1976b].

## References

- Arceyana, Transform fault and rift valley from bathyscap and diving saucer. *Science*, 190, 108, 1975.
- Arrhenius, G., and E. Bonatti, Neptunism and volcanism in the ocean. *Progr. Oceanogr.*, 3, 7, 1965.
- Bäcker, H., and M. Schoell, New depths with



- brines and metalliferous sediments in the Red Sea, *Nature Phys. Sci.*, 240, 153, 1972.
- Bally, A. W., A geodynamic scenario for hydrocarbon occurrences, *World Petrol Congr. Proc.* 9th, 1(1), 1975.
- Belmonte, Y., P. Hirtz, and R. Wenger, The salt basins of the Gabon and the Congo (Brazzaville): A tentative paleogeographic interpretation, in *Salt Basins Around Africa*, p. 55, Institute of Petroleum, London, 1965.
- Bischoff, J. L., and F. T. Manheim, Economic potential of the Red Sea heavy metal deposits, in *Hot Brines and Recent Heavy Metal Deposits in the Red Sea*, edited by E. T. Degens and D. A. Ross, p. 535, Springer, New York, 1969.
- Bonatti, E., Metallogenesis at oceanic spreading centers, *Annu. Rev. Earth Planet. Sci.*, 4, 401, 1975.
- Boström, K., The origin and fate of ferromanganese active ridge sediments, *Stockholm Contrib. Geol.*, 24, 149, 1973.
- Boström, K., and M. N. A. Peterson, Precipitates from hydrothermal exhalations on the East Pacific Rise, *Econ. Geol.*, 61, 1258, 1966.
- Campes, C. W. M., F. C. Ponte, and K. Miura, Geology of the Brazilian continental margin, in *The Geology of Continental Margins*, edited by C. A. Burk and C. L. Drake, p. 447, Springer, New York, 1974.
- Coleman, R. G., Plate tectonic emplacement of upper mantle peridotites along continental edges, *J. Geophys. Res.*, 76, 1212, 1971.
- Constantinou, G., and G. J. S. Govett, Geology, geochemistry, and genesis of Cyprus sulfide deposits, *Econ. Geol.*, 68, 843, 1973.
- Corliss, J. B., The origin of metal-bearing submarine hydrothermal solutions, *J. Geophys. Res.*, 76, 8128, 1971.
- Corliss, J. B., J. Dymond, M. Lyle, T. Doerge, K. Crane, P. Lonsdale, R. P. Von Herzen, and D. Williams, Sediment mound ridges of hydrothermal (?) origin along the Galapagos Rift (abstract), *Eos Trans. AGU*, 57, 935, 1976.
- Curry, J. R., Marine sediments, geosynclines, and orogeny, in *Petroleum and Global Tectonics*, edited by A. G. Fischer and S. Judson, p. 157, Princeton University Press, Princeton, N. J., 1975.
- Dasch, E. J., Metallogenesis in the southeastern Pacific: A progress report on the IDOE Nazca Plate project, *Phys. Earth Planet. Interiors*, 9, 249, 1974.
- Degens, E. T., and D. A. Ross (Eds.), *Hot Brines and Recent Heavy Metal Deposits in the Red Sea*, 600 pp., Springer, New York, 1969.
- Dickinson, W. R., Plate tectonics and sedimentation, in *Tectonics and Sedimentation*, *Spec. Publ.* 22, edited by W. R. Dickinson, p. 1, Soc. Econ. Paleontol. and Mineral., Tulsa, Okla., 1974.
- Dietz, R. S., Continent and ocean basin evolution by spreading of the sea floor, *Nature*, 190, 854, 1961.
- Dietz, R. S., Ocean floor in the decade ahead, *Mar. Technol. Soc. J.*, 3(5), 68, 1969.
- Elder, J. W., Physical processes in geothermal areas, in *Terrestrial Heat Flow*, *Geophys. Monogr. Ser.*, vol. 8, edited by W. H. K. Lee, p. 211, AGU, Washington, D. C., 1965.
- Field, C. W., J. R. Dymond, J. B. Corliss, E. J. Dasch, G. R. Heath, R. G. Senchal, and H. H. Veeh, Metallogenesis in southeast Pacific Ocean: Nazca Plate Project, Circum-Pacific Energy and Mineral Resources, *Mem.* 25, p. 539, Amer. Ass. Petrol. Geol., Tulsa, Okla., 1976.
- Flemming, N. C., and D. G. Roberts, Tectono-eustatic changes in sea level and sea floor spreading, *Nature*, 243, 19, 1973.
- Gass, I. G., and D. Masson-Smith, The geology and gravity anomalies of the Troodos Massif, Cyprus, *Phil. Trans. Roy. Soc. London, Ser. A*, 255, 417, 1963.
- Guild, P. W., Distribution of metallogenic provinces in relation to major earth features, in *Metallogenetic and Geochemical Provinces*, edited by W. E. Petrascheck, p. 10, Springer, New York, 1972.
- Hays, J. D., and W. C. Pitman III, Lithospheric plate motion, sea level changes and climatic and ecological consequences, *Nature*, 246, 18, 1973.
- Heath, G. R., and J. Dymond, Genesis and transformation of metalliferous sediments from the East Pacific Rise, Bauer Deep, and Central Basin, northwest Nazca plate, *Geol. Soc. Amer. Bull.*, 88, 723, 1977.
- Helgeson, H. C., *Complexing and Hydrothermal Ore Deposition*, Pergamon, New York, 1964.
- Hess, H. H., History of ocean basins, in *Petrologic Studies*, edited by A. E. J. Engel, p. 599, Geological Society of America, Boulder, Colo., 1962.
- Hutchinson, R. W., Volcanogenic sulfide deposits and their metallogenic significance, *Econ. Geol.*, 68, 1223, 1973.
- James, D. E., Plate tectonic model for the evolution of the Central Andes, *Geol. Soc. Amer. Bull.*, 82, 3325, 1971.
- Klemme, H. D., Geothermal gradients, heat flow, and hydrocarbon recovery, in *Petroleum and Global Tectonics*, edited by A. G. Fischer and S. Judson, p. 251, Princeton University Press, Princeton, N. J., 1975.
- Krauskopf, K. B., Factors controlling the concentrations of thirteen rare metals in seawater, *Geochem. Cosmochim. Acta*, 9, 1, 1956.
- Krauskopf, K. B., Source rocks for metal-bearing fluids, in *Geochemistry of Hydrothermal Ore Deposits*, edited by H. L. Barnes, p. 1, Holt, Rinehart, and Winston, New York, 1967.
- Lister, C. R. B., Water percolation in the oceanic crust, *Eos Trans. AGU*, 55, 740, 1974.
- Lowell, J. D., and G. J. Genik, Sea-floor spreading and structural evolution of southern Red Sea, *Amer. Ass. Petrol. Geol. Bull.*, 56, 247, 1972.
- Lowell, R. P., and P. A. Rona, On the interpretation of near-bottom water temperature anomalies, *Earth Planet. Sci. Lett.*, 32, 18, 1976.
- Luyendyk, B. P., Dips of downgoing lithospheric plates beneath island arcs, *Geol. Soc. Amer. Bull.*, 81, 3411, 1970.
- McIver, R. D., Hydrocarbon occurrences from Joides Deep Sea Drilling Project, *World Petrol. Congr. Proc.* 9th, 5(1), 1, 1975.
- Mitchell, A. H. G., Metallogenic belts and angle of dip of Benioff zones, *Nature Phys. Sci.*, 245, 49, 1973.
- Mitchell, A. H., and J. D. Bell, Island-arc evolution and related mineral deposits, *J. Geol.*, 81, 381, 1973.
- Mitchell, A. H. G., and M. S. Garson, Relationship of porphyry copper and circum-Pacific tin deposits to palaeo-Benioff zones, *Inst. Mining Met. Trans., Sect. B*, 81, B10, 1972.
- Mitchell, A. H. G., and M. S. Garson, Mineralization at plate boundaries, *Miner. Sci. Eng.*, 8(2), 129, 1976.
- Moore, E. M., and F. J. Vine, The Troodos Massif, Cyprus and other ophiolites as oceanic crust: Evaluation and implications, *Phil. Trans. Roy. Soc. London, Ser. A*, 268, 443, 1971.
- Murray, J., and A. F. Renard, Report on deep sea deposits based on the specimens collected during the voyage of the H.M.S. Challenger in the years 1872 to 1876, in *Report of the Scientific Results of the Voyage of H.M.S. Challenger During the Years 1873-1876*, edited by C. W. Thompson and J. Murray, p. 190, Her Majesty's Stationery Office, London, 1891.
- Noble, J. A., Metal provinces of the western United States, *Geol. Soc. Amer. Bull.*, 81, 1607, 1970.
- Olson, W. S., and R. J. Leyden, North Atlantic rifting in relation to Permian-Triassic salt deposition, The Permian and Triassic Systems and Their Mutual Boundary, *Mem.* 2, Can. Soc. Petrol. Geol., 720, Calgary, Alta., 1973.
- Oyarzun, J. M., and J. J. Frutos, Porphyry copper and tin-bearing porphyries: A discussion of genetic models, *Phys. Earth Planet. Interiors*, 9, 259, 1974.
- Pautot, G., J. M. Auzende, and X. Le Pichon, Continuous deep salt layer along North Atlantic margins related to early phase of rifting, *Nature*, 227, 351, 1970.
- Petrasccheck, W. E., Some aspects of the relations between continental drift and metallogenic provinces, in *Implications of Continental Drift to the Earth Sciences*, vol. 1, edited by D. H. Tarling and S. K. Runcorn, p. 567, Academic, N. Y., 1973.
- Raymond, A. R., Continental drift and uncontinental thinking, *Econ. Geol.*, 65, 11, 1970.
- Reid, A. R., Proposed origin for Guianian diamonds, *Geology*, 2, 67, 1974.
- Revelle, R., M. Bramlette, G. Arrhenius, and E. D. Goldberg, Pelagic sediments of the Pacific, *Spec. Pap.* 62, edited by A. Poldervaart, p. 221, Geol. Soc. Amer., Boulder, Colo., 1955.
- Roberts, D. G., and V. N. D. Caston, Petroleum potential of the deep Atlantic Ocean, *World Petrol. Congr. Proc.* 9th, 5(2), 1, 1975.
- Rona, P. A., Possible salt domes in the deep Atlantic off northwest Africa, *Nature*, 224, 141, 1969.

- Rona, P. A., Comparison of continental margins of eastern North America at Cape Hatteras and northwestern Africa at Cap Blanc, *Amer. Ass. Petrol. Geol. Bull.*, 54, 129, 1970.
- Rona, P. A., Plate tectonics and mineral resources, *Sci. Amer.*, 229(1), 86, 1973a.
- Rona, P. A., Relations between rates of sediment accumulation on continental shelves, sea-floor spreading, and eustasy inferred from the central North Atlantic, *Geol. Soc. Amer. Bull.*, 84, 2851, 1973b.
- Rona, P. A., Worldwide unconformities in marine sediments related to eustatic changes of sea level, *Nature Phys. Sci.*, 244, 25, 1973c.
- Rona, P. A., Salt deposits of the Atlantic, *Anais Acad. Bras. Cienc.*, 48, suppl., 265, 1976a.
- Rona, P. A., Plate tectonics and mineral exploration, *Nat. Resour. Forum*, 1, 17, 1976b.
- Rona, P. A., and L. D. Neuman, Plate tectonics and mineral resources of circum-Pacific region, Circum-Pacific Energy and Mineral Resources, *Mem.* 25, p. 48, Amer. Ass. Petrol. Geol., Tulsa, Okla., 1976a.
- Rona, P. A., and L. D. Neuman, Energy and mineral resources of the Pacific region in light of plate tectonics, *Ocean Manage.*, 3, 57, 1976b.
- Rona, P. A., R. N. Harbison, B. G. Bassinger, R. B. Scott, and A. J. Nalwalk, Tectonic fabric and hydrothermal activity of Mid-Atlantic Ridge crest (lat. 26°N), *Geol. Soc. Amer. Bull.*, 87, 661, 1976.
- Rona, P. A., B. A. McGregor, P. R. Betzer, G. W. Bolger, and D. C. Krause, Anomalous water temperature over Mid-Atlantic Ridge crest at 26° north latitude, *Deep Sea Res.*, 22, 611, 1975.
- Runnells, D. D., Continental drift and economic minerals in Antarctica, *Earth Planet. Sci. Lett.*, 8, 400, 1970.
- Ryan, W. B. F., and M. Cita, Ignorance concerning episodes of ocean-wide stagnation, *Mar. Geol.*, 23, 197, 1977.
- Sawkins, F. J., Sulfide ore deposits in relation to plate tectonics, *J. Geol.*, 80, 377, 1972.
- Schneider, E. D., and G. L. Johnson, Deep-ocean diapir occurrences, *Amer. Ass. Petrol. Geol. Bull.*, 54, 2152, 1970.
- Schuiling, R. D., Tin belts on the continents around the Atlantic Ocean, *Econ. Geol.*, 62, 540, 1967.
- Scientific Party, Basins and margins of the eastern South Atlantic, *Geotimes*, 20(6), 22, 1975.
- Scott, M. R., R. B. Scott, P. A. Rona, L. W. Butler, and A. J. Nalwalk, Rapidly accumulating manganese deposit from the median valley of the Mid-Atlantic Ridge, *Geophys. Res. Lett.*, 1, 355, 1974.
- Sillitoe, R. H., Formation of certain massive sulfide deposits at sites of sea floor spreading, *Inst. Mining Met. Trans., Sect. B*, 81, B141, 1972a.
- Sillitoe, R. H., A plate tectonic model for the origin of porphyry copper deposits, *Econ. Geol.*, 67, 184, 1972b.
- Sillitoe, R. H., Tectonic segmentation of the Andes: Implications for magmatism and metallogeny, *Nature*, 250, 542, 1974.
- Skornyakova, I. S., Dispersed iron and manganese in Pacific Ocean sediments, *Int. Geol. Rev.*, 7, 2161, 1964.
- Sloss, L. L., Sequences in the cratonic interior of North America, *Geol. Soc. Amer. Bull.*, 74, 93, 1963.
- Smith, A. G., J. C. Briden, and G. E. Dreyer, Phanerozoic world maps, in *Organisms and Continents Through Time: A Symposium, Spec. Pap. Palaeontol.*, vol. 12, edited by N. F. Hughes, p. 1, Paleontological Association, London, 1973.
- Sorokhtin, O. G., S. A. Ushakov, and V. V. Fedynskiy, Dynamics of crustal plates and origin of petroleum deposits (in Russian), *Dokl. Akad. Nauk SSSR*, 214, 1407, 1974.
- Spooner, E. T. C., and W. S. Fyfe, Sub-sea floor metamorphism, heat and mass transfer, *Contrib. Mineral. Petrol.*, 42, 287, 1973.
- Stern, C. R., and P. J. Wylie, Water-saturated and undersaturated melting relations of a granite to 35 kilobars, *Earth Planet. Sci. Lett.*, 18, 163, 1973.
- Vail, P. R., and R. M. Mitchum, Jr., Stratigraphic interpretation of seismic data, *Mem.* 26, Amer. Ass. Petrol. Geol., Tulsa, Okla., 1977.
- Weiss, R. F., J. E. Lupton, P. F. Lonsdale, A. E. Bainbridge, and H. Craig, Hydrothermal plumes on the Galapagos spreading center (abstract), *Eos Trans. AGU*, 47, 935, 1976.
- Williams, D. L., and R. P. Von Herzen, Heat loss from the Earth: New estimate, *Geology*, 2(7), 327, 1974.

*Dr. Rona replies:*

Sir,

I am pleased to answer Mr. A. A. Archer's comments on my paper (Plate Tectonics and Mineral Exploration, *Natural Resources Forum*, **1**, No. 1). Mr. Archer's comments pertain to the development of the theory of plate tectonics, the status of understanding of mineral deposits prior to plate tectonics, and the economic mineral potential of oceanic crust.

The subject of my paper is application of plate tectonics to mineral exploration. This application is linked to the change in the prevalent theoretical vision from that of a static to a dynamic earth, when the theory of plate tectonics places the dynamic earth vision on a solid quantitative base. This does not deny either the contributions of early workers or the recognition of a limited amount of earth movement, pointed out by Mr. Archer, under the old theoretical vision of a static earth. It emphasizes the conceptual breakthrough of plate tectonics relevant to application, rather than the development relegated to history.

An aim of mineral exploration is to achieve an understanding that can be used to predict the locations of undiscovered deposits. A groundwork for this understanding was laid prior to the advent of plate tectonics by study of deposits that had already been discovered and grouping of similar known deposits into mineral provinces. That the grouping was more descriptive than predictive is suggested by the observation that discovery has generally followed a trend of diminishing size and accessibility of ore deposit. As stated by Mr. Archer, "The theory of plate tectonics now underlies theories on minerali-



zation and the distribution of many mineral deposits, and provides a satisfactory fundamental basis for further studies.”

With regard to economic mineral potential of oceanic crust, I do not share Mr. Archer's disappointment that only a small proportion of holes of the Deep Sea Drilling Project ('Glomar Challenger') have found abnormal concentration of metals far from divergent plate boundaries (oceanic ridges). On the contrary, it is remarkable how many indications of metal concentrations, if not actual deposits, have been found in light of the fact that only about 400 holes have been drilled to date in ocean basins comprising an area of 362 000 000 square kilometers with no special placement of holes to test for mineral deposits. A comparable number of holes may be required to delineate a single major ore body on land. The economic prospect for recovering metallic ores, other than manganese nodules, from the deep ocean basin is, of course, long term. However, knowledge of metal deposits formed in oceanic crust at divergent plate boundaries can be immediately applied to guide exploration for metal deposits in oceanic crust where accessible to exploitation along present and former convergent plate boundaries, as emphasized in my paper.

*Yours faithfully,*  
PETER A. RONA

National Oceanic and Atmospheric Administration  
Miami, Florida  
USA  
18 November 1976

## Time and Space Variation in the Surficial Sediments of the New York Bight Apex

**W. L. Stubblefield, R. W. Permenter and  
D. J. P. Swift**

*Atlantic Oceanographic and Meteorological Laboratories, 15 Rickenbacker Causeway, Miami, Florida 33149, U.S.A.*

*Received 18 August 1976 and in revised form*

---

**Keywords:** sediment patterns, sidescan sonar, band waves, sewage disposal, dumping, annual variations, New York Bight

Sidescan sonar records, grab samples, and bottom photographs were collected along two transects in the New York Bight apex, on a quarterly basis for six quarters. Sampling was designed to determine the natural variability of bottom deposits in time and space, and the effect of ocean dumping on these patterns.

The Hudson Shelf Valley and the Christiaensen Basin at its head are floored by fine muddy sand and mud, while the high areas on either side are covered by medium grained sand. Bottom sands on the seaward side are relatively uniform. On the New Jersey side, and near the Long Island coast, sand ribbon-like patterns with spacings of 10-200 m appear. Separate dumpsites for sewage sludge, dredge spoil, cellar dirt, and acid waste occur within the area.

The distribution of grain sizes and bedform patterns are stable over time, indicating that the bottom is in a state of textural near-equilibrium with the hydraulic climate. The effects of ocean dumping are most obvious in the vicinity of the dredge spoil dumpsite, which has shoaled 15 m within the last years. Here an aureole of anomalously fine sediment is spreading over a bottom locally composed of artificial rubble. Cholera Bank, the area where the highly mobile sewage sludge is dumped, is floored by sand; no permanent sludge deposits form. The bottom muds of the adjacent Christiaensen Basin may, however, be contaminated with this material.

### Introduction

Most continental shelves are veneered with a mosaic of sediment patches of contrasting grain size. The pattern is in part inherited from the passage of nearshore depositional environments during the Holocene transgression, and in part to reworking of bottom materials by the modern hydraulic climate (Swift *et al.*, 1971).

Our need to understand these patterns and their time behavior has increased greatly as a consequence of the mounting concern with marine environmental management. In the New York Bight, our study area, the problem is the simultaneous use of the sea floor for food resources (finfish and shellfish), recreational pursuits, and for waste disposal. Sewage sludge, dredge spoil, acid wastes and cellar dirt are all dumped in the New York Bight apex within 40 km radius of New York Harbor mouth (Figure 1).

We have undertaken to determine the physical character of the surficial sediments in the New York Bight apex as part of the Marine Ecosystems Analysis (MESA) Program of the National Oceanic and Atmospheric Administration. We are concerned with the pattern of

sediment distribution from two points of view. The natural pattern must be resolved because it is a major control of the distribution of benthic fauna. For the sake of ongoing ecological studies it is necessary to determine the time and space scale of sediment distribution, and the degree to which these patterns are systematic or random. Secondly, it is necessary to distinguish between natural aspects of the sediment distribution pattern and changes that have been wrought in the pattern by ocean dumping.

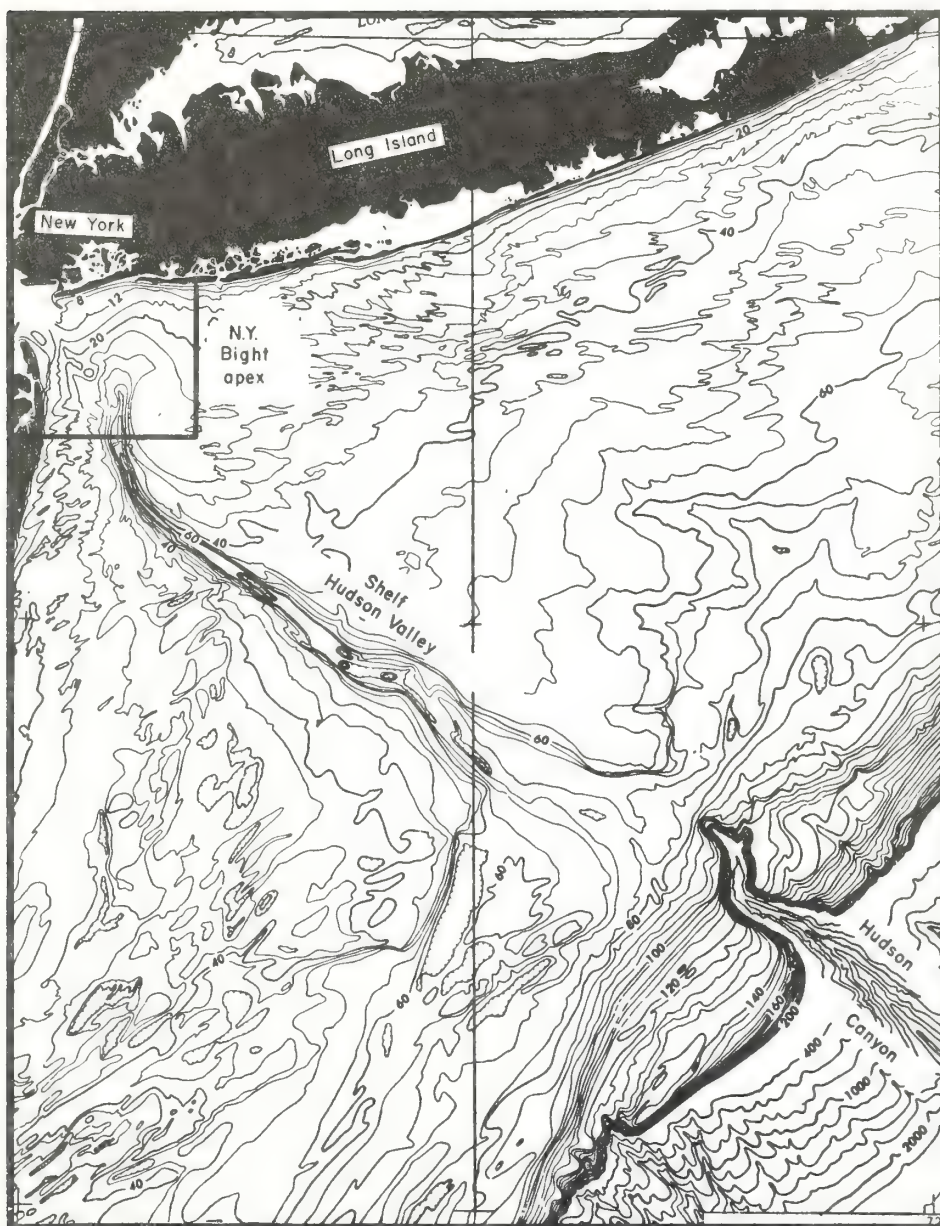


Figure 1. Bathymetric map of the New York Bight, showing location of Bight Apex. Depth in metres. After Uchupi, 1970.



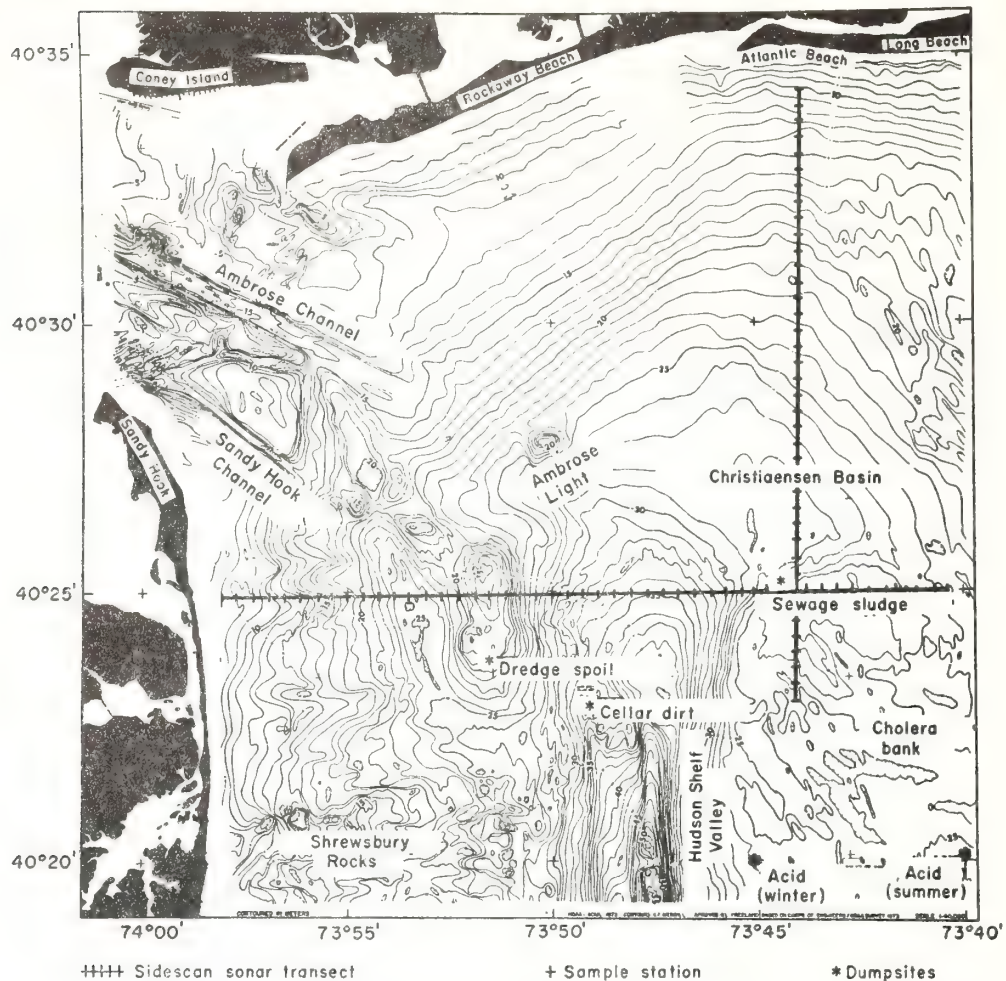


Figure 2. Bathymetric map of the New York Bight Apex, showing sampling transect and sampling stations. From unpublished data of G. Freeland. Depth in metres.

## Methods

### Field methods

Samples were taken along two transects in the New York Bight apex on a quarterly schedule for a year and a half (Figure 2). Precision navigation was achieved by use of Raydist, which afforded accuracy to within  $\pm 5$  m. Confidence in the accuracy was substantiated when a sunken vessel, located by sidescan sonar, plotted in the same position on the respective cruises.

For the six cruises, five different research vessels were used. Consequently, accurate positioning required compensating for the size of the different ships and the winch positions on the vessel during sampling of finer-grained material. By comparing the complete sidescan sonar records and using grain size values plotted at respective points on these records for calibration with returned intensity, an estimate of grain size over the complete transect is possible. In many respects the sidescan is preferred over the grab samples since a continuous record is possible. This is especially important in the New York Bight where pronounced local variability exists as evidenced by Figure 3.

The EG&G sidescan unit was towed approximately 9 m above the bottom at speeds of 3–4 knots. Each channel recorded a strip of the bottom 75 m wide. A time mark, which was subsequently correlated to a position, was annotated on the record every five minutes.

#### Laboratory methods

Grab sample aliquots were processed for grain size distribution in accordance with standard sedimentological laboratory procedures. The sand fraction ( $-1.0 \phi > x > 4.0 \phi$ ) was analyzed by a rapid sediment analyzer (RSA) which measures the fall velocity of the sand through 132 cm of water. An assumption was made that the material was of uniform density, that of quartz (2.65). The fine fraction ( $<4.0 \phi$ ) was examined with a Coulter counter which operates on the principle of varying voltage pulses across an aperture opening. Data from

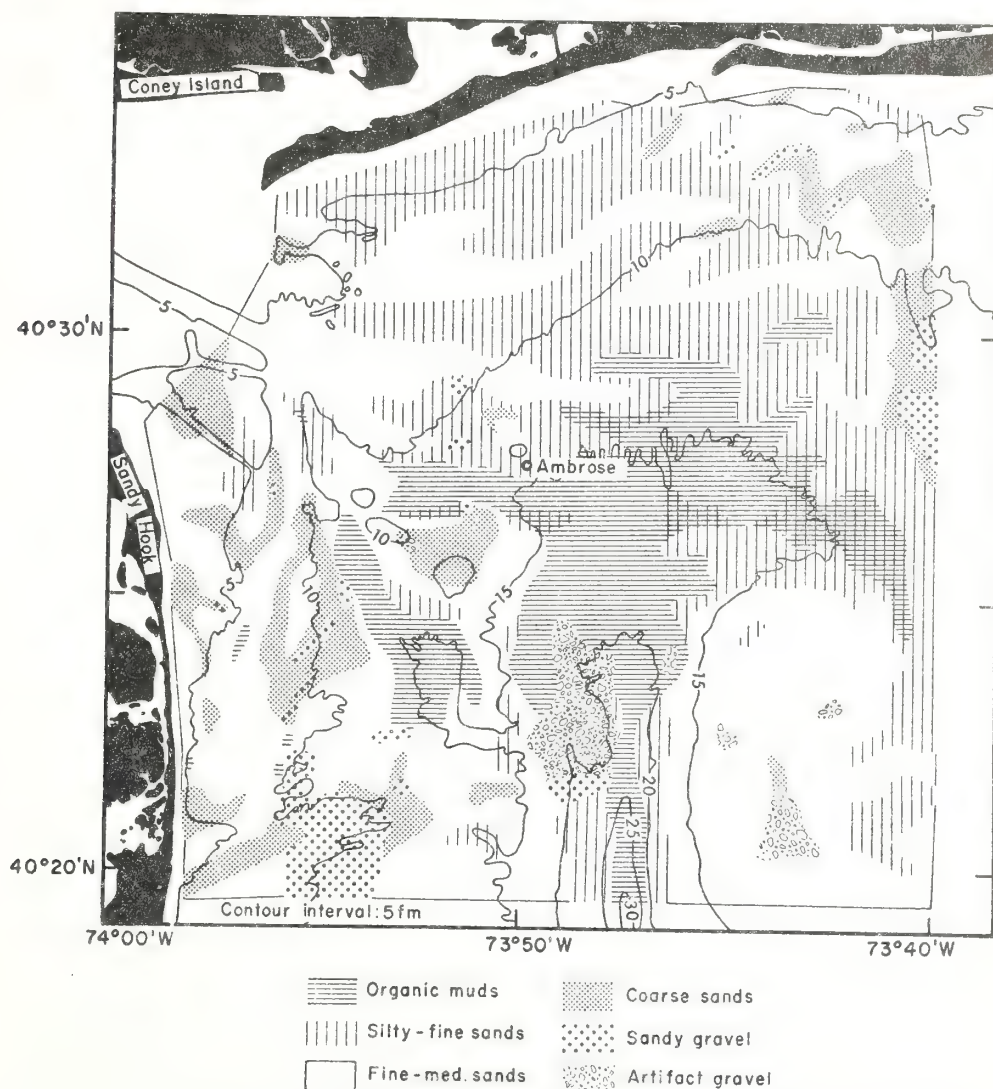


Figure 3. Surficial sediment distribution in the New York Bight Apex, based on macroscopic, ship-borne observation of samples. From unpublished data of A. Cok and G. Freeland. Depths in fathoms.

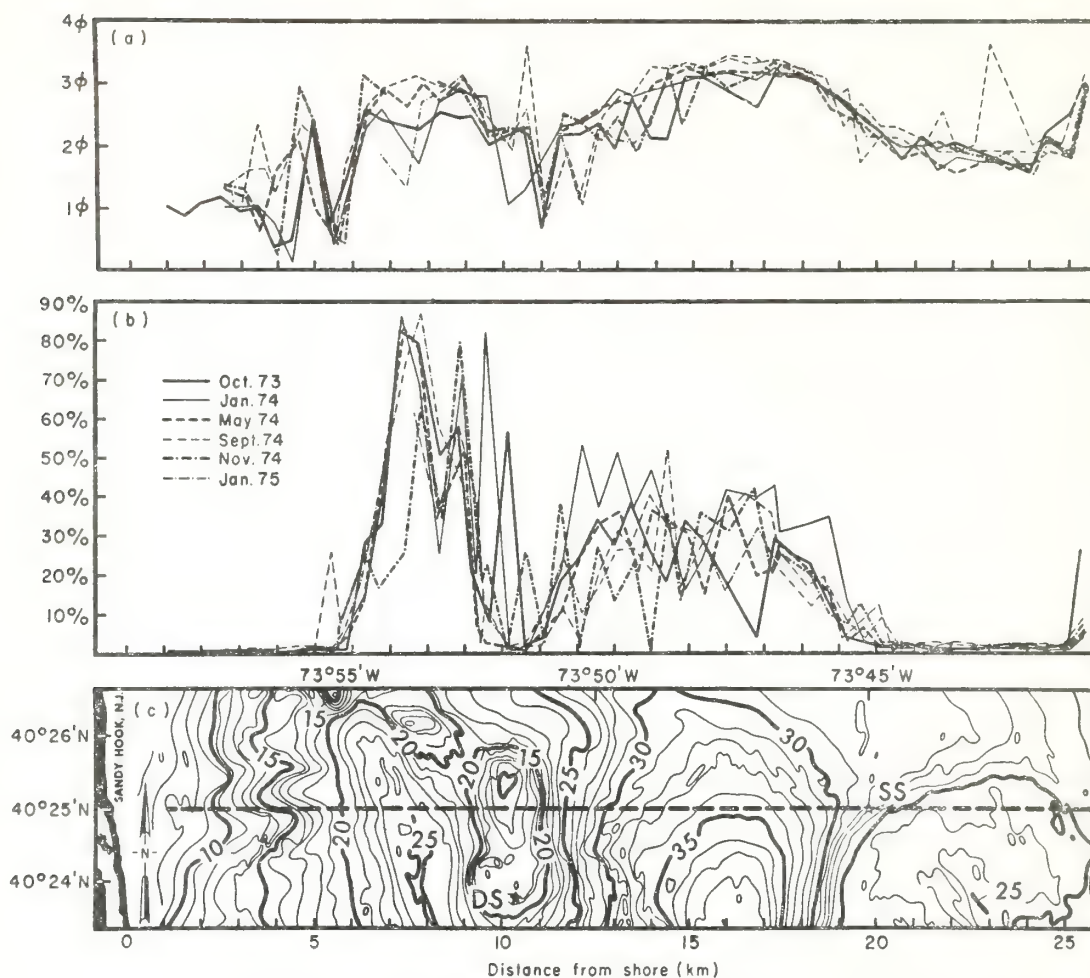


Figure 4. Median diameter and per cent of clay and silt along east-west transect. (a), Median sand  $\phi$ -size; (b), per cent of fine fraction (<4.0  $\phi$ ); (c) bathymetry in metres.

both the RSA and Coulter counter were used to compute mean grain size, standard deviation, skewness, and kurtosis, by using moment parameters.

### Geological setting

The surface of the New York Bight apex was shaped by the succession of fluvial, estuarine, and nearshore marine regimes during later Quaternary time. During the last glacial maximum (around 15 000 BP, Milliman & Emery, 1968) the ice margin trended along the crest of Long Island, and westward, across New Jersey, and the Bight apex constituted an outwash plain. Sea level was at least 125 m lower than at present, and the shoreline lay seaward of the shelf break, over 170 km southeast of the study area. At this time, the Hudson River discharged through the Hudson Shelf Valley, into the Hudson Canyon. At some time during the subsequent period of glacial retreat and sea level rise, the Hudson River may have received the entire drainage of the Great Lakes area and the anomalously great relief of the shelf valley may be due to scour during this period (Veatch & Smith, 1939).



During the period of post-glacial sea level rise, the floor of the Bight apex was modified by two processes. The erosional retreat of the Long Island and New Jersey shorefaces beveled the surface of the glacial outwash plain, and much of the resulting debris was left as a discontinuous sheet of relatively clean, well-sorted, coarse sand 0–8 m in thickness (Swift *et al.*, 1972). The sand sheet grades downwards into a thin basal unit of coarse sand, gravel, and shell hash which is exposed at the surface where the sheet is thinnest.

As the shoreface retreated landwards, some of the eroded material was transported by wave-driven littoral currents toward the Ancestral Hudson Estuary from both sides. As a result, the subaerial river valley was partly filled. On the northeast side of the retreating estuary, the intense discharge of the ancestral Long Island littoral drift system was deposited as a series of tide-molded sand shoals on the shelf valley's northeast flank. As a consequence the north rim of the shelf valley is presently a poorly defined levee-like feature (Cholera Bank) that tends to rise above the level of the adjacent shelf.

As the shoreline approached its present position, the rate of sea level rise decreased from 16 mm year<sup>-1</sup> to 0.8 mm year<sup>-1</sup> (Emery & Uchupi, 1972, pp. 242–244). The mouth of New York Harbor became largely filled by the littoral drift of the adjacent coastal compartment. The amphitheater-like head of the present shelf valley, the Christiaensen Basin, may have been formed at this time by strong, topographically-controlled shelf currents that develop in the shelf valley in response to storms (Charnell & Mayer, 1975).

## Surficial sediment

### *Spatial distribution*

Sediments along the sampling transects consist of two main depth-controlled provinces; a fine muddy sand and mud province at depths greater than 24 fathoms, and a sand province at depths shoaler than this (Figures 3, 4 and 5).

The fine muddy sand—mud province occurs in the Hudson Shelf Valley, in the Christiaensen Basin, and in the tributary channel that extends northeastward toward the harbor mouth (Figures 3, 4 and 5). True muds (50% > 4  $\phi$ ) occur only in the tributary channel and on the western side of the Christiaensen Basin, on either side of the dredge spoil dumpsite; the ridge on which the dumpsite occurs is surfaced by relatively mud-free and coarse sands (Figures 3 and 4). The Christiaensen Basin is floored by fine (2–3  $\phi$ ) muddy (10–40% silt and clay) sands, which become coarser and less muddy in the direction of shoaling (Figure 6 and Plate I).

Two major sand provinces are apparent on the east-west transect; the New Jersey Platform and Cholera Bank. Both are floored by medium-grained sand (1–2  $\phi$ ). However, the character of the bottom is quite different in the two areas. On the New Jersey Platform, sidescan sonar records reveal a north- to northwest-trending banded pattern of lighter and darker tones, representing finer and coarser sand (Plate II). The bands are generally 10–30 m apart. On Cholera Bank, however, sidescan sonar records reveal a uniform bottom (Plate III). A banded pattern appears again on the north-south transect very near the Long Island Shore. These grain-size variations associated with these banded patterns are reflected in the median diameter profiles of Figures 4 and 5. Direct evidence of dumping occurs on the west side of the ridge on which the dredge spoil dumpsite occurs. Here sidescan sonar reveals a patchy pattern of dark areas with a rubbly texture, surrounded by a lighter toned substrate (Plate IV). Bottom photographs reveal deposits of rubble (Plate V), frequently of artificial origin (brick, concrete, etc.). Freeland & Merrill (in press) report that the adjacent dredge spoil dumpsite has shoaled over 10 m in the last 37 years.

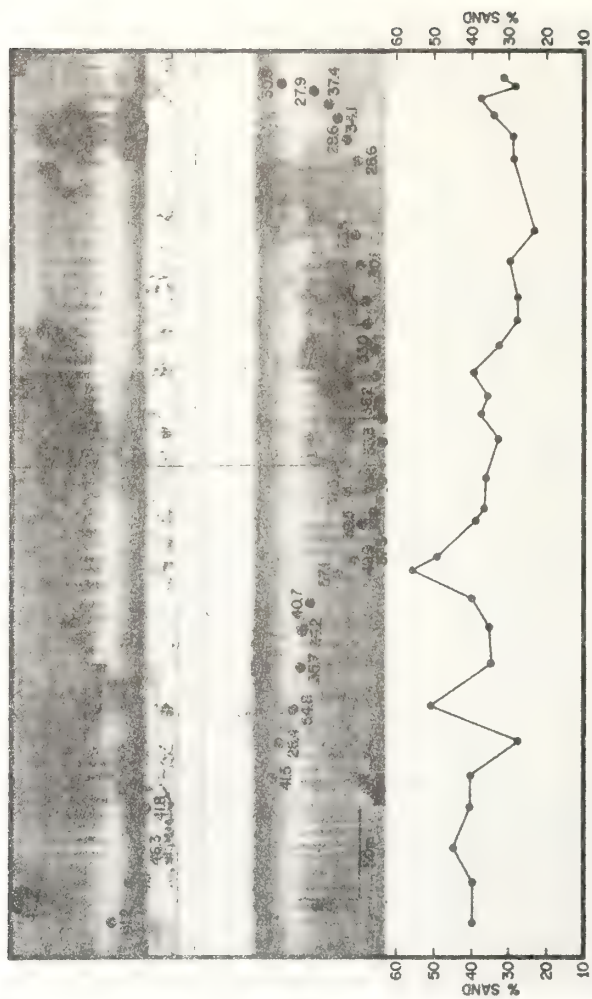


Plate 1. Sidescan sonar record and grab sample data from the fine muddy sand and mud province of the Bight apex. Positioning of grab samples relative to sidescan record is  $\pm 7$  m. From unpublished data of R. Permenter. See Figure 6 for location.

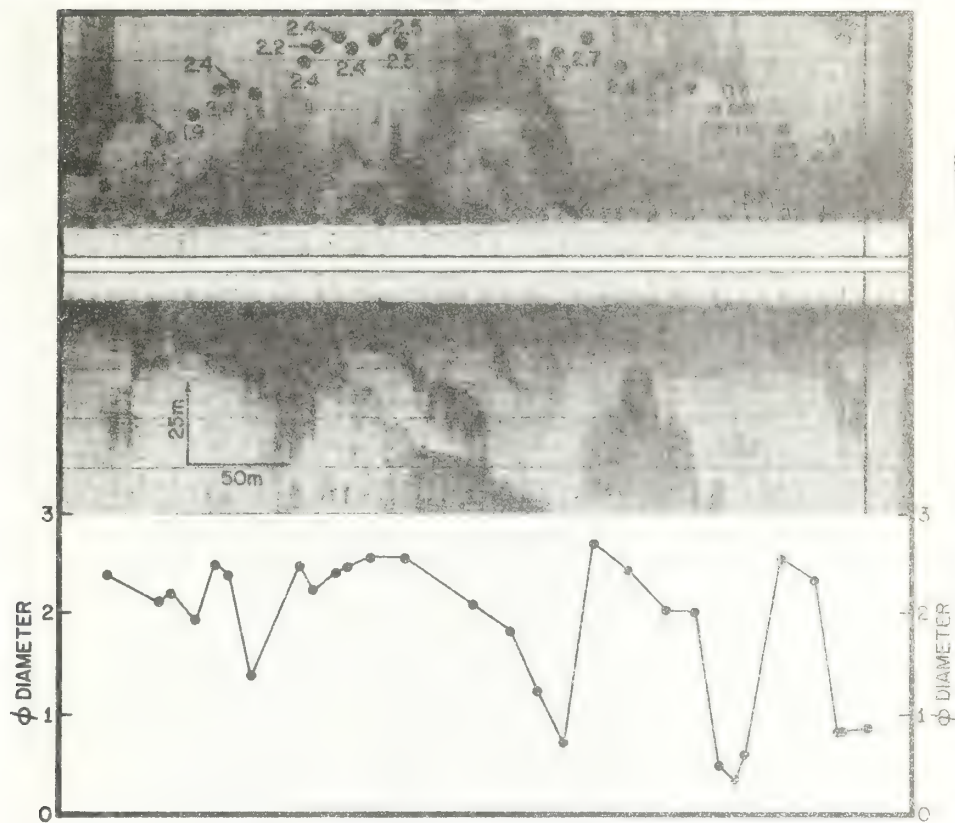


Plate II. Sidescan sonar record and grab sample data from the banded sand province on the New Jersey platform. Positioning of grab samples relative to side-scan record is  $\pm 7$  m. From unpublished data of R. Permenter. See Figure 6 for location.



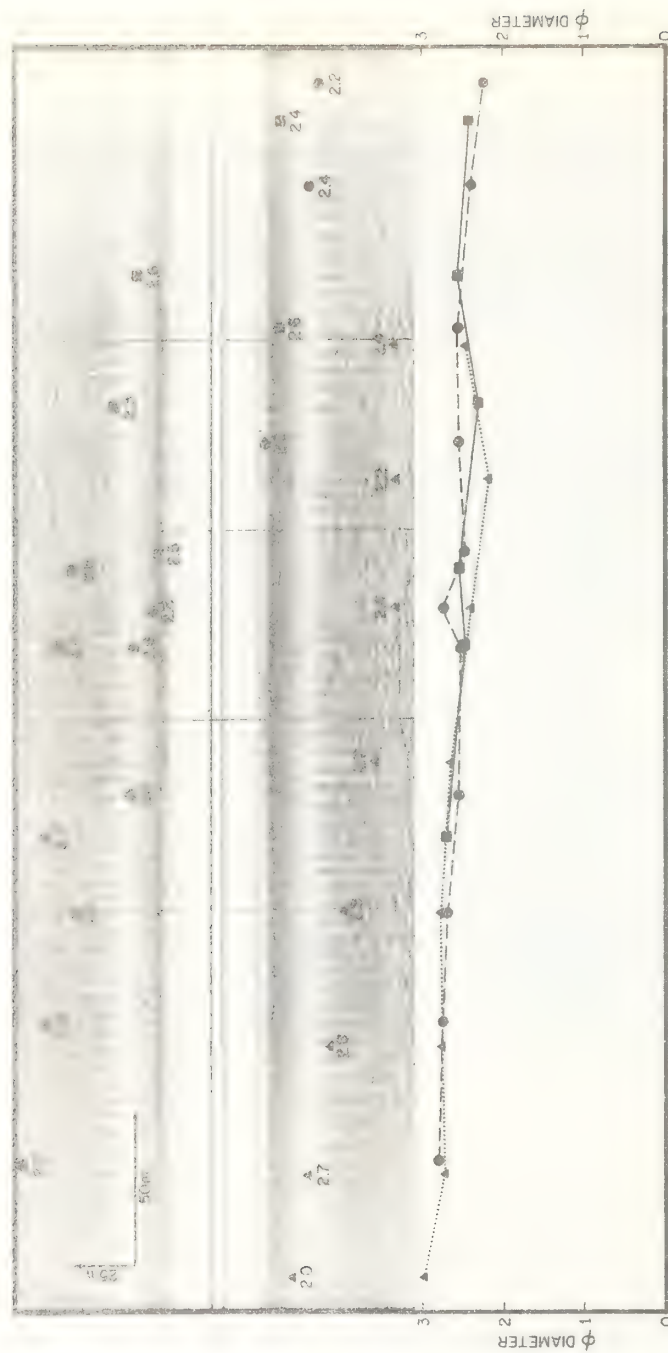


Plate III. Sidescan sonar record and grab sample data from the smooth sand province on Choleta Bank. Positioning of grab samples relative to sidescan record is  $\pm 7$  m. From unpublished data of R. Permenter. See Figure 6 for location.

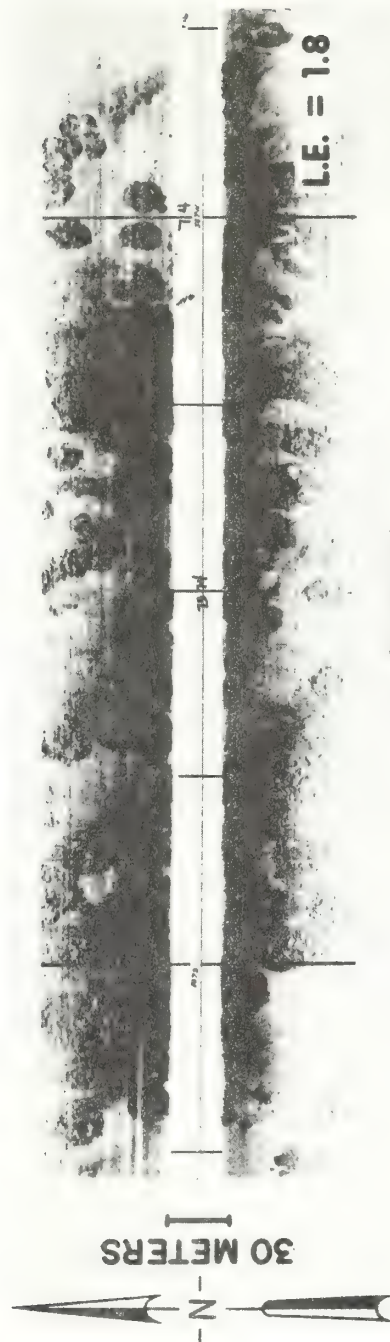


Plate IV. Sidescan sonar record of rubble 'islands' surrounded by fine sand. From western margin of Christiaensen Basin. See Figure 6 for location.

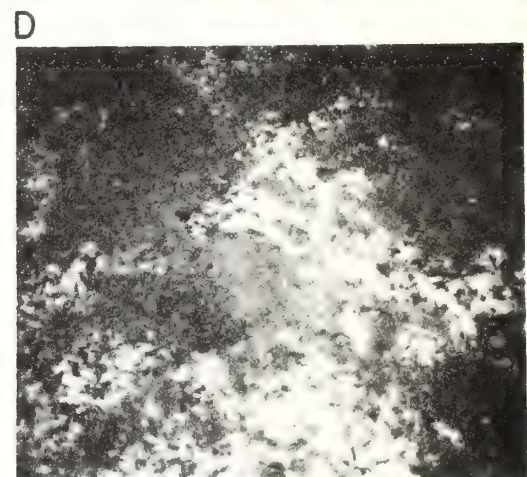
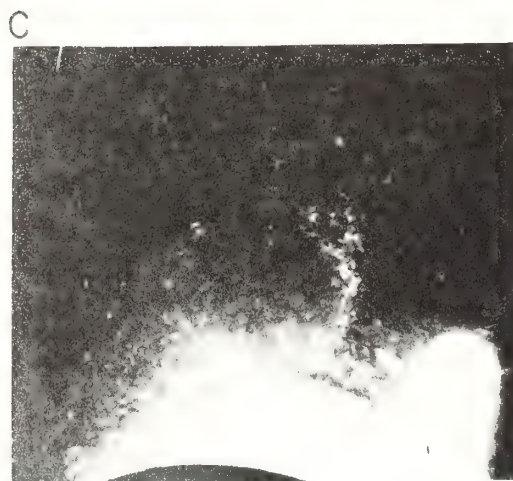
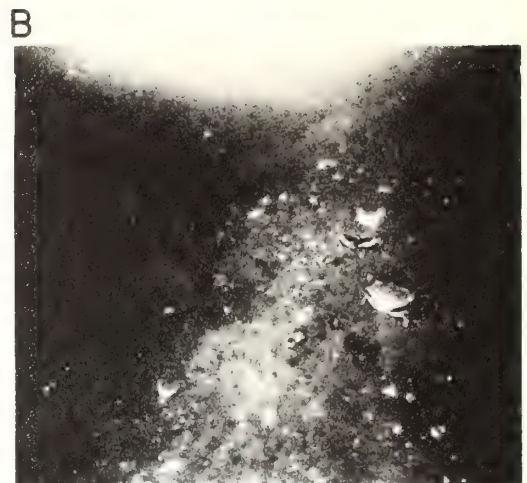


Plate V. Representative bottom photographs from the New York Bight Apex. (a), rippled bottom of median sand from Cholera Bank. (b), Contact between two contrasting sediment bands on New Jersey Platform. (c), Rubble on western margin of Christiaensen Basin. (d), 'Fluff' of finely comminuted organic matter on eastern margin of Christiaensen Basin. See Figure 6 for locations.



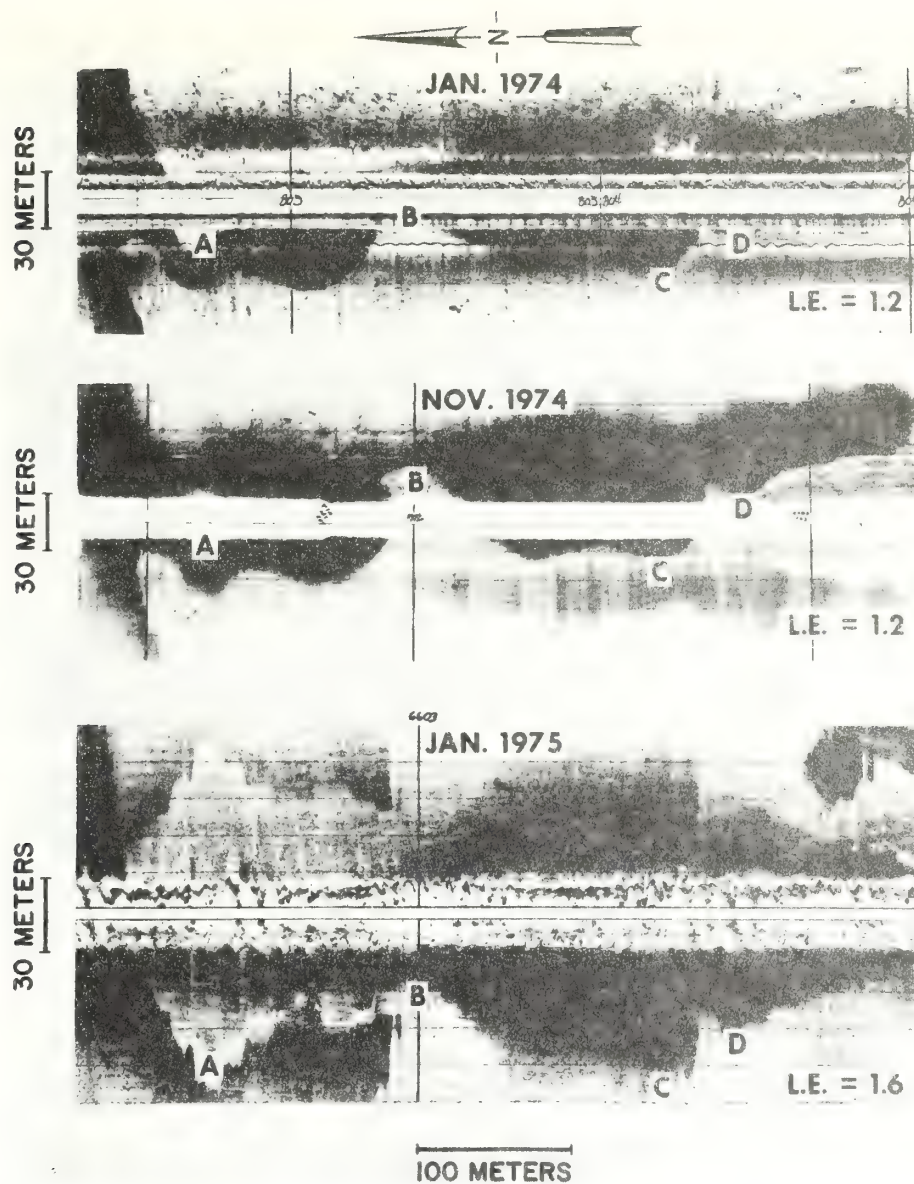


Plate VI. Repeated observations of a broad coarse band on the north western margin of the Christiaensen Basin. Points A through I are common in each record. The shape of the band is constant throughout the observation period. The diffused nature of the January, 1975 record is due to the greater height of the transducer off the bottom during recording.

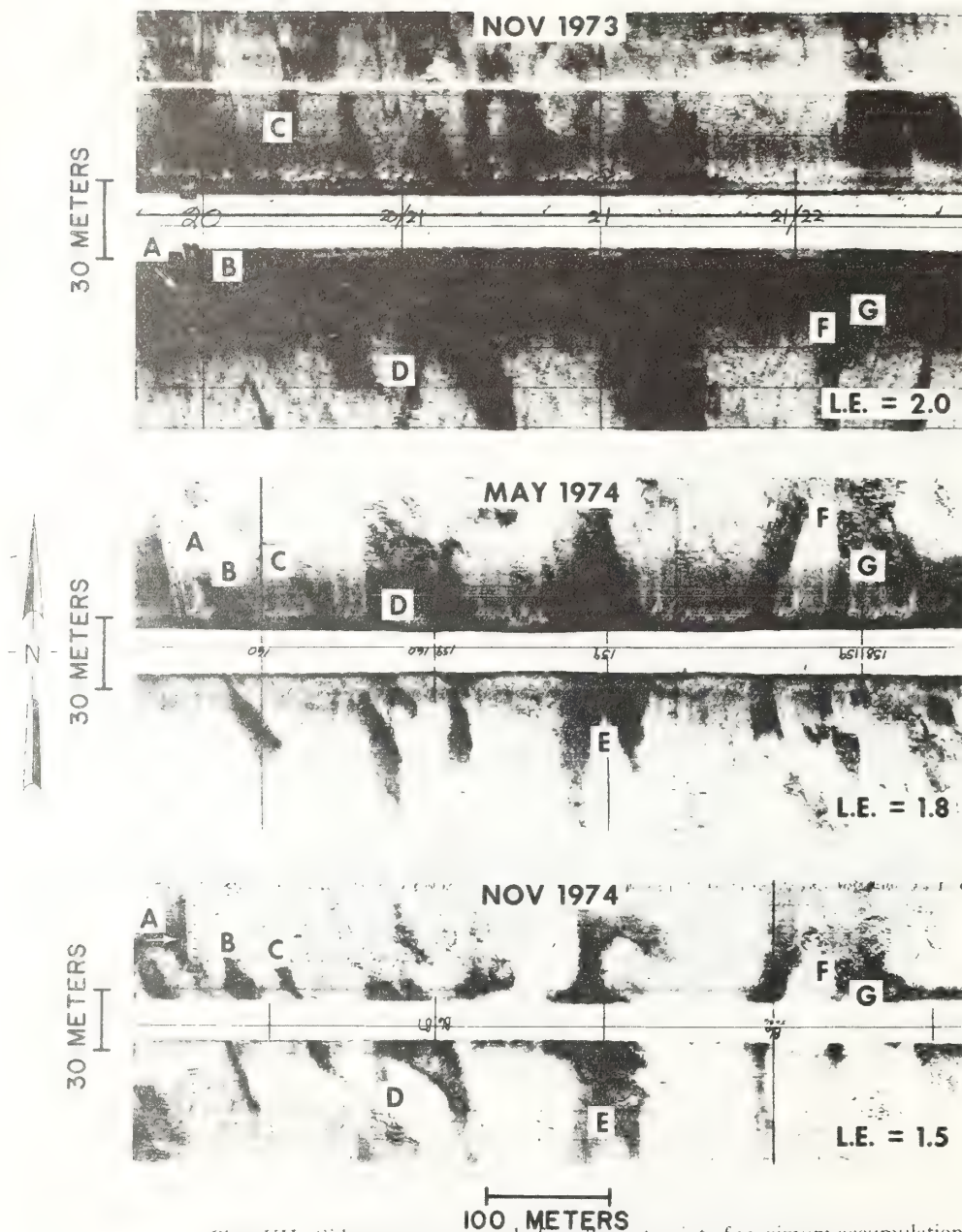


Plate VII. Sidescan sonar record of sea floor at point of maximum accumulation of dredge spoil material. Points A through G are common in each record. Point A is a sunken vessel which was used as a reference point. Lighter areas are fine muddy sand, darker areas are medium sand.

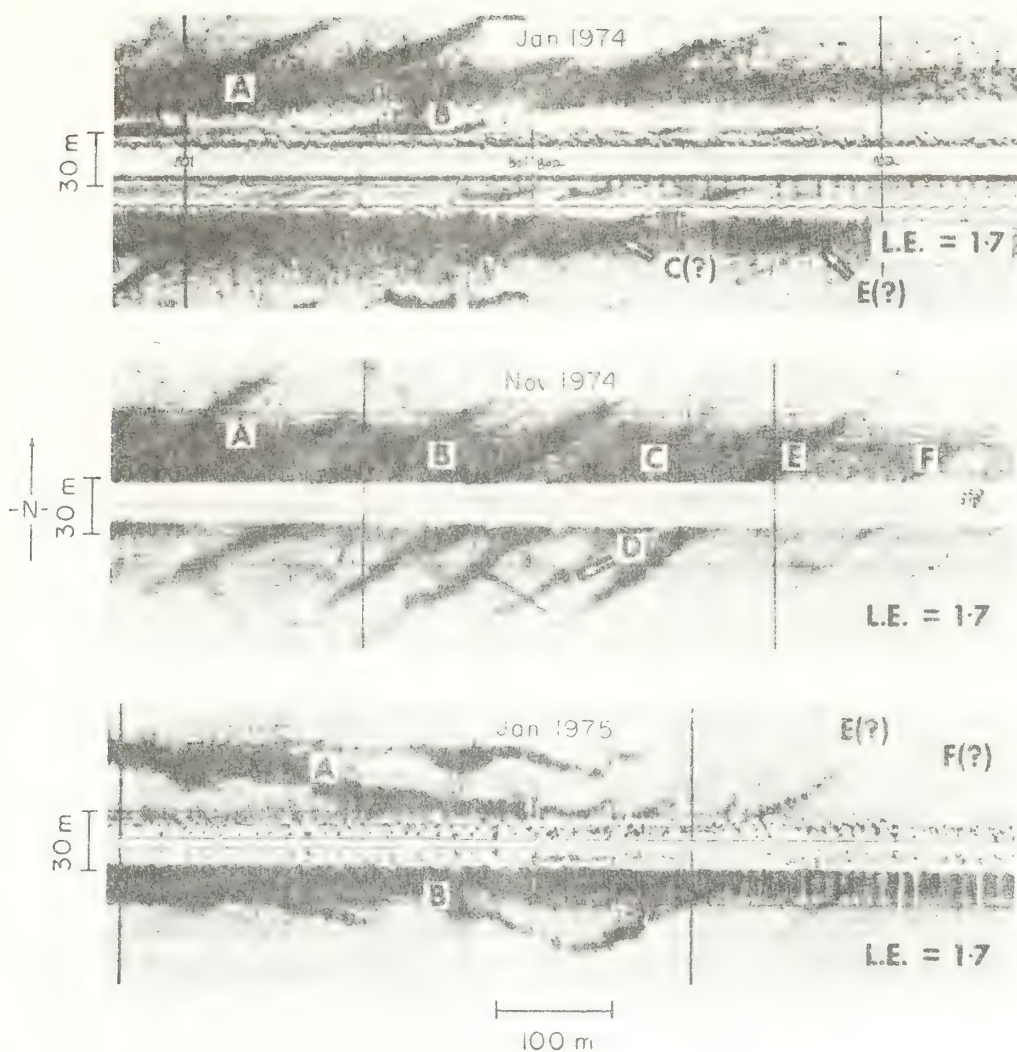


Plate VIII. Sidescan sonar record on the north-western margin of the Christiaensen Basin. Dark bands are coarser sand; light intervening zones are finer sand. Pattern extends to south with time. Curved pattern for January 1975 is due to ships maneuvering, not to change in shape of features.



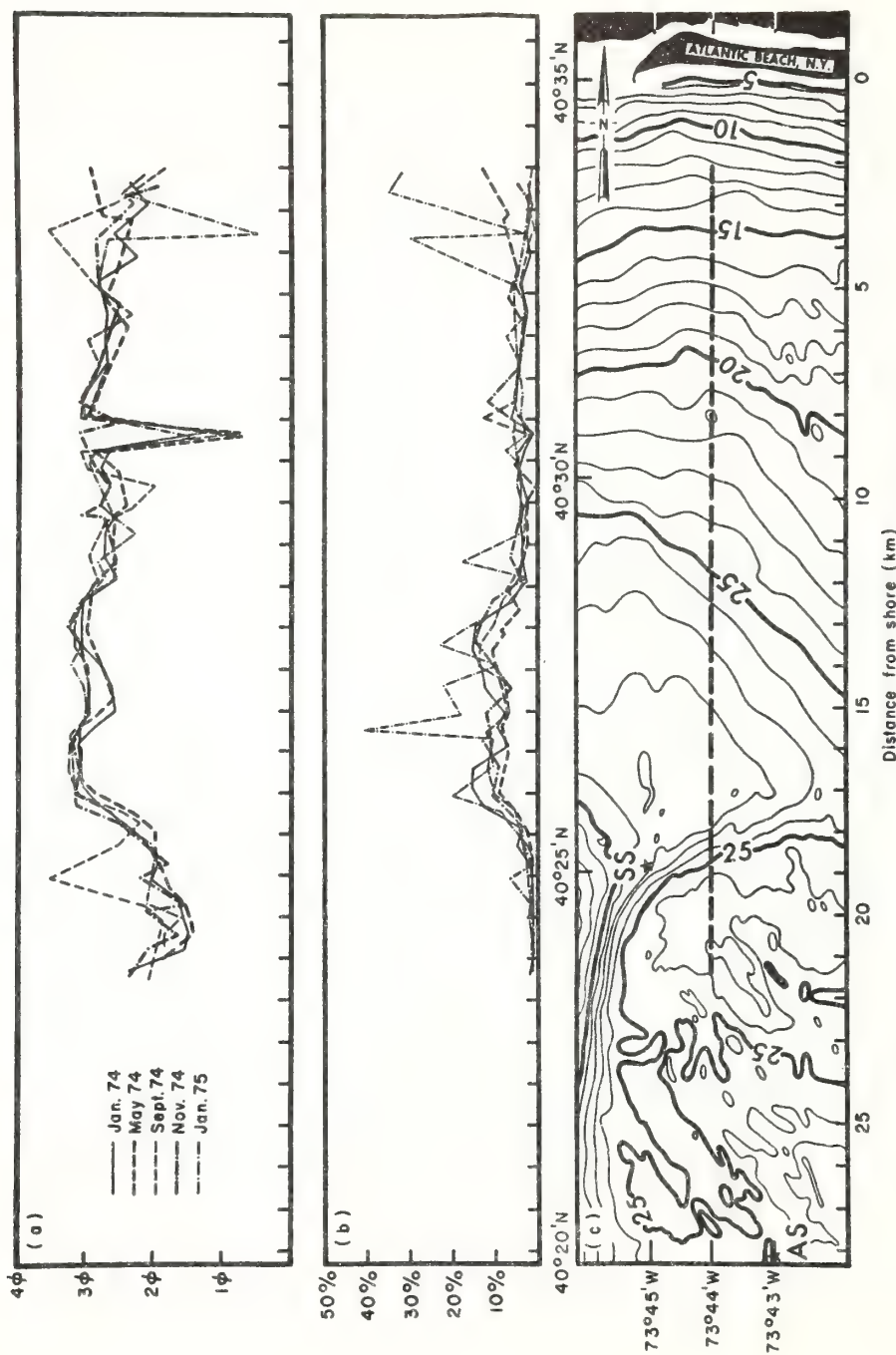


Figure 5. Median diameter and per cent of clay and silt along north-south transect. (a), Median sand  $\phi$ -size; (b), per cent of fine fraction ( $<4.0 \phi$ ); (c), bathymetry in metres.

Grab sampling in the vicinity of the sewage sludge dumpsite reveals only clean sand. Bottom photographs taken in the adjacent Christiaensen Basin [Plate V (d)] reveal in some areas a 'fluff' of comminuted organic material resting on the bottom. Such a 'fluff' would escape the grab sampler. The material may consist of the coarser portion of sewage sludge. However, such dark organic fluffs may occur naturally on quiet bottoms.

#### *Temporal distribution*

Repeated grab sampling and sidescan sonar examination of the two transects reveals a remarkable degree of bottom stability. In general, it appears that the bottom is in a state of textural equilibrium with the hydraulic climate. The envelopes of grain size transects in Figures 4 and

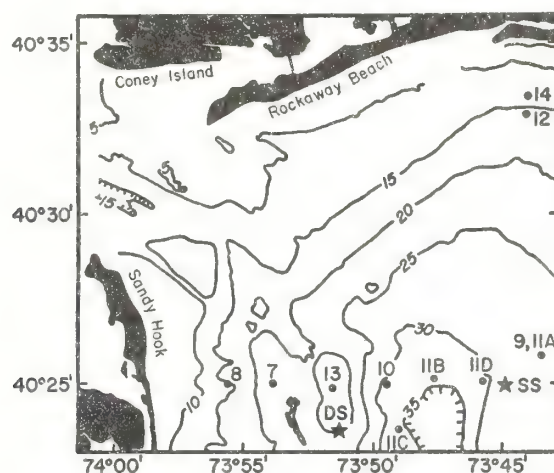


Figure 6. Location map for figures presented in this paper.

5 show no systematic seasonal variation, and their spread appears to be due primarily to small positioning areas. The banded bottoms revealed by sidescan sonar are in general quite stable. A broad band of coarse sand or sandy gravel near the Long Island shore underwent no visible change during the year of observation (Plate VI; Figure 5, 8.5 km).

Other areas have undergone minor change. We have particularly good control of bottom changes in the patchy texture east of the dredge spoil dumpsite because the transect passes over a wreck which appears in successive sidescan records. Changes in the shape of bottom sediment patches were observed in the year of observation (Plate VII). At the very northern end of the north-south transect a series of light and dark bands increased in number (Plate VIII).

W. Harris of Brooklyn College has independently sampled nearshore portions of the north-south transect during 1974 and 1975 (personal communication). He reports the presence of mud patches up to 500 m wide at two localities, which appear to correspond with the gravel band of Plate VI and the narrower bands of Plate VIII. In these areas, mud and gravel were sampled in close proximity in topographic lows. When resampled at intervals on the order of a year, most of localities that had yielded mud samples were found to be mud free. In Figure 5, our January 1975 cruise appears to have sampled muddy gravel at 3-4 km from the shore, corresponding with the locality presented in Plate VIII.

### Discussion

The New York Bight apex is characterized by a large-scale, depth-controlled pattern of sediment distribution, whereby the Hudson Shelf Valley and its extensions are occupied by mud and fine muddy sand, and the plateau-like areas on either side are veneered with sand.

McCave (1972) has pointed out that the distribution of fine sediments on the wave-agitated continental shelf is controlled by the balance between the near bottom hydraulic climate on one hand, and the near bottom concentration of suspended sediment on the other. If bottom wave agitation is intense, then the suspended sediment concentration must be quite high if muddy bottom deposits are to form. Drake (1974) has reported near-bottom suspended sediment concentrations in the Bight apex on the order of  $4 \text{ mg l}^{-1}$ . Under these conditions, it seems that only the areas deeper than 24 m have a regime of bottom wave surge that is sufficiently damped to allow fine sediments to accumulate. In the Bight apex, only the

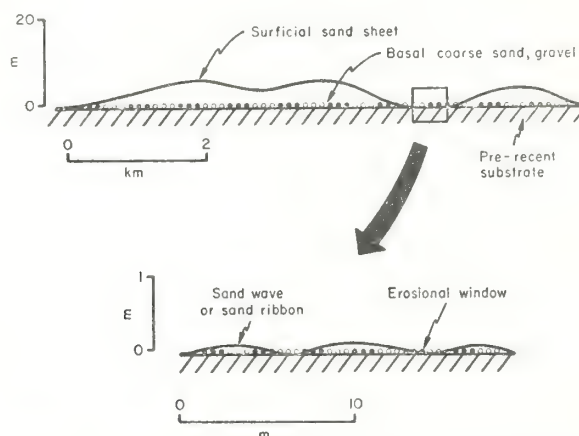


Figure 7. Schematic stratigraphy in areas of banded bottom.

Hudson Shelf Valley and its extensions exceed this critical depth. Further seaward, this isobath is again encountered on the central shelf, but here the near bottom suspended sediment concentration is much lower, and mud deposits do not form.

The banded sand bottoms on the New Jersey platform, and on the Long Island south shore appear to be the result of two circumstances; water movements during storms that are sufficiently intense to transport sand (Lavelle *et al.*, in press) and a sand cover so thin that short term erosion during storms is sufficient to bare the coarse lag veneer that separates the surficial sand sheet from the older strata underneath (Figure 7).

The banded bottoms are best understood as bedform sequences, where secondary flow components in the bottom boundary layer have swept sand in a layer a few decimeters thick in flow-parallel or flow-transverse ribbons of negligible relief, separated by zones in which the underlying lag pavement of coarse sand, or pebbly or shelly sand is exposed (Allen, 1968, pp. 37-38). The absence of such features on Cholera Bank is more probably due to the greater thickness of the sand bed rather than to a lack of strong currents. If the coarse substrate is not exposed between sand ribbons and patches, then the acoustic contrast is not sufficient to reveal the presence of such bedforms on sidescan sonar records.

The significance of the banded patterns is not easy to interpret without fairly detailed information on the hydraulic climate. The banding on the New Jersey platform is generally



parallel to the New Jersey shore. Since nearshore flows must generally parallel the coast in order to satisfy continuity requirements, the banding in this area may be flow-parallel, formed in response to divergences and convergences in the bottom boundary layer.

The continuity requirement for coastal flows suggests that the banded bottom on the north end of the north-south transect is comprised of low amplitude, flow-transverse sand waves, rather than of flow-parallel current lineations, since the features are within  $8^\circ$  of a right angle relationship with the shoreline. If so, the features may be responses to west-trending coastal currents generated by intense northeast storms, such as the 30 November–3 December flow event reported by Lavelle *et al.* (in press) from the Long Island coast. This flow had a near-bottom offshore component, so that flow-transverse bedforms would be skewed some few degrees from a coast-normal orientation.

The intermittent presence of mud deposits associated with coarse bands on the north-south transect has been reported from other localities on the Middle Atlantic Bight. Gravel-floored topographic lows appear to be maintained by intense bottom scour during storms, but may accumulate up to a decimeter of mud during the quiet summer months, particularly in nearshore areas. The mud may be scoured out during the following period of winter storms, or may survive into the next summer (Swift *et al.*, 1971; Stubblefield *et al.*, 1974).

The impact of dumping is most clearly seen on the east-west transect in the vicinity of the dredge spoil dumpsite; the adjacent portion of the Christiaensen Basin east of the dumpsite, and the tributary valley to the west contain anomalously fine sediments. Per cent analysis of current meter records indicates that during periods of strong west winds, the Hudson Shelf Valley experiences a strong up-channel bottom flow (Gadd *et al.*, in press). These flows may be part of a clockwise gyral circulation pattern repeatedly observed in the Bight apex (Charnell & Mayer, 1975). These currents occasionally exceed  $50 \text{ cm s}^{-1}$ , and are competent to carry the finer fraction of the dredge spoil to the north. It is presumably such currents that have caused the more mobile dredge spoil to drift into the lows of the irregular surface of dumped rubble seen in Plate IV.

Neither the north-south nor the east-west transects reveal any permanent effects of sewage sludge dumping on the flank of Cholera Bank, where fine sand bottoms occur. Apparently, the sewage sludge is so mobile that it is widely diffused through the Bight apex. It seems reasonable to suppose that the fine muddy sands of the Christiaensen Basin may be contaminated with sewage sludge, but resolution of such contamination is beyond the primarily physical observations undertaken during the course of this study.

### References

- Allen, J. R. L. 1968 *Current Ripples*. North Holland Publishing Co., Amsterdam. 432 pp.
- Charnell, R. L. & Mayer, D. A. 1975 Water movement within the apex of the New York Bight during summer and fall of 1973. *NOAA Technical Memorandum*. Boulder, Colorado (in press).
- Drake, D. E. 1974 Suspended particulate matter in the New York Bight apex: September–November, 1973. *NOAA Technical Report ERL 318-MESA 1*, Boulder, Colorado, 53 pp.
- Emery, K. O. & Uchupi, E. 1972 Western North Atlantic Ocean; topography, rocks, structure; water, life, and sediments. *American Association of Petroleum Geologists Bulletin*, Memoir 17, 532 pp.
- Freeland, G. L. & Merrill, G. Deposition and erosion in the dredge spoil and other New York Bight dumping areas. *Proceedings of the ASCE Speciality Conference on Dredging* Mobile, Ala., 1976. (In press).
- Gadd, P. E., Lavelle, J. W. & Swift, D. J. P. Calculations of sand transport on the New York Shelf using near-bottom current meter observations. *Journal of Sedimentary Petrology* (in press).
- Lavelle, J. W., Brashear, H. R., Case, F. N., Charnell, R. L., Gadd, P. E., Haff, K. W., Han, G. A., Kunselman, C. A., Mayer, D. A., Stubblefield, W. L. & Swift, D. J. P. 1976 Preliminary results of coincident current meter and sediment transport observations for wintertime conditions on the Long Island inner shelf. *Geophysical Research Letters* (in press).

- McCave, I. N. 1972 Transport and escape of fine-grain sediment from shelf areas. In *Shelf Sediment Transport: Process and Pattern*. (Swift, D. J. P., Duane, D. B. & Pilkey, O. H., eds.); Dowden, Hutchinson and Ross, Inc., Stroudsburg, Pa. pp. 225-248.
- Milliman, J. D. & Emery, K. O. 1968 Sea levels during the past 35,000 years. *Science* **162**, 1121-1123.
- Stubblefield, W. L., Lavelle, J. W., McKinney, T. F. & Swift, D. J. P. 1974 Sediment response to the present hydraulic regime on the Central New Jersey Shelf. *Journal of Sedimentary Petrology* **45**, 337-358.
- Swift, D. J. P., Stanley, D. J. & Curray, J. R. 1971 Relect sediments on continental shelves; a reconsideration. *Journal of Geology* **79**, 322-346.
- Swift, D. J. P., Kofoed, J. W., Saulsbury, F. P. & Sears, P. 1972 Holocene evolution of the shelf surface, south and central Atlantic Shelf of North America. In *Shelf sediment transport: process and pattern*. (Swift, D. J. P., Duane, D. B. & Pilkey, O. H., eds.). Dowden, Hutchinson and Ross, Stroudsburg, Pa. pp. 499-574.
- Uchupi, E. 1970 Atlantic continental shelf and slope of the United States: shallow structure. *United States Geological Survey Professional Papers* 529-1, 44 pp.
- Veatch, A. C. & Smith, P. A. 1939 Atlantic submarine valleys of the United States and the Congo submarine valleys. *Geological Society of America Special Papers* no. 7, 101 pp.

## shelf-sediment dynamics

**N**ov. 2-6, 64 geological oceanographers, physical oceanographers, and geologists attended a workshop on shelf-sediment dynamics at Vail, Colo., sponsored by NSF's International Decade of Ocean Exploration. Sponsoring federal agencies included NOAA, the U.S. Geological Survey, and ERDA. The workshop, convened by Donn Gorsline of the University of Southern California and Don Swift of NOAA, surveyed the present state of shelf research and laid plans for future progress.

**The first day** was devoted to a review of ongoing research. In a preliminary session on boundaries on the shelf system, Douglas Inman (Scripps Institution of Oceanography) described both applied and basic aspects of beach and nearshore sedimentation. Donn Gorsline presented his group's studies of modern and ancient canyons and fans.

A second session dealt with studies of fluid motion and sediment en-

trainment. Gabriel Csanadv (Woods Hole Oceanographic Institution) outlines the approach of physical oceanographers to problems of shelf circulation. Many of his examples were drawn from his work in the Great Lakes, from the preliminary results of the Coastal Boundary Layer Transect project on the Long Island inner shelf, and from the Shelf Edge Exchange Processes project. Paul Komar (Oregon State University) presented recent advances in the understanding of sediment entrainment by wave action, including his recent studies with Martin Miller (Oregon State University).

John Southard (Massachusetts Institute of Technology) talked about bedforms and flow regimes. Some of his material was extracted from his own flume research, but he also summarized recent studies of marine bedforms of greater scale than can be produced in the laboratory, and remarked on the apparent genetic distinction between 'megaripples' and

the larger 'sand waves'. J.D. Smith (University of Washington) described a new analytical model for boundary flow and bedload sediment transport, and David Drake (U.S. Geological Survey) discussed the transport of suspended fine sediment across the continental shelf.

A final session presented studies of regional patterns of shelf sedimentation. I.N. McCave (University of East Anglia) summarized recent studies of the 'tide-swept' shelves around Great Britain. George Allen of CNEXO (Centre Nationale pour L'Exploitation des Oceans, France) described work that he and his colleagues had accomplished on the Aquitaine Shelf and in the Gironde Estuary. Don Swift of NOAA reviewed earlier studies in the Middle Atlantic Bight. He also described recent attempts by J.C. Ludwick (Old Dominion University) to estimate sediment transport quantitatively at the mouth of the Chesapeake Bay, and similar work by J.W. Lavelle (NOAA) on the Long Island inner shelf. Finally, L.D. Kulm (Oregon State University) described work that he and his colleagues have carried out on the Northwest Pacific shelf.

**The second day** was devoted to a review of the programs of U.S. Federal agencies in shelf-sediment transport. R. Roland described the Office of Marine Geology, U.S. Geological Survey, which has 98 professionals di-



vided between the Pacific-Arctic Branch based in Menlo Park, Calif., (63 professionals) and the Atlantic Branch based in Woods Hole, Mass., and Corpus Christi, Tex. (35). Most of the work comes under the heading of resource assessment, and much of it is paid for by another Interior agency, the Bureau of Land Management, which is responsible for determining the potential impact of exploitation of the continental margin for oil and gas.

R. Beauchamp of the Bureau of Land Management gave a more detailed explanation of BLM's activities. BLM, with no field capability of its own, has been given \$50 million to make its environmental-impact studies. The money is divided equally between Alaska, where it is administered by NOAA, and the lower 48 states. NOAA-administered studies in Alaska are made by NOAA, USGS, and academic scientists. Studies in the southern California coast are made by a consortium of universities. Studies in the Northwest Gulf of Mexico are made in part by the Survey's Office of Marine Geology at Corpus Christi. Studies on the Atlantic Shelf (Georges Bank, Baltimore Canyon trough area, Georgia Bight) are made by universities (University of Miami, University of Georgia in the Georgia Bight), the USGS, private companies (ERCO and EG&G on Georges Bank), and state institutions (Skidaway Institute of Oceanography, Georgia Bight; Virginia Institute of Marine Science, Baltimore Canyon trough area).

NOAA presented its program in 2 parts. David Duane described the Sea Grant program, now a part of NOAA: Sea Grant's role in the shelf has been limited, but the number of proposals received is increasing as a result of increasing federal, state, local government and industrial interest in the shelf. For this reason, and because new legislation permits Sea Grant to fund ship activities, Sea Grant's role will probably increase. George Peter described the programs administered by NOAA's Environmental Research Laboratories. They include the Outer Continental Shelf Environmental Assessment Program, in which NOAA administers BLM flow-through money in an Alaskan-shelf program. The program's field personnel are NOAA, USGS, and university scientists.

**A second major NOAA program** is Marine Ecosystems Analysis, whose goal is to assess human impact on some of our most heavily stressed marine areas. The oldest ongoing MESA field study is the New York Bight Project, which started in 1973. Its primary concern is the impact of

sewage sludge, dredge spoil, cellar dirt, and industrial waste disposal on the inner shelf off New York City. The study is being made by federal laboratories, such as Atlantic Oceanographic & Meteorological Laboratories, Miami, and the National Marine Fisheries Service Laboratory at Sandy Hook, N.J., and by universities under contract. A similar MESA project is starting in Puget Sound, staffed by the Pacific Marine Environmental Laboratory and by universities under contract. Other MESA projects include the Deep Water Ocean Mining Experimental Study and research into the effect of ocean dumping on the marine environment.

William Forster of ERDA's Environmental Programs Office described its support for shelf-dynamics research. ERDA is interested in the impact of all energy-related activities on human use of the continental shelf. ERDA's policy is to stress intermediate and long-term research ('basic' research) rather than studies that seek short-term solutions ('applied' research). In this respect, its fund-granting policy is more nearly like that of NSF than are the policies of 'mission-oriented' agencies.

Workshop sessions began on the third day. Their purpose was 1, to inventory existing facilities for shelf-dynamics research; 2, to define research directions; and 3, to make recommendations for stimulating and coordinating research in shelf-sediment dynamics. These topics were identified as of primary importance: 1, Bottom boundary-layer flow, sediment entrainment, and sediment bed-load transport; 2, Mechanics of suspended-sediment transport; 3, The shelf flow fields generated by winds, tides, and density differences; 4, Flow at the coastal and shelf-edge boundaries; 5, The role of bedforms in sediment transport; 6, The role of organisms in sediment transport and accumulation; 7, Techniques for developing accurate mass budgets for various shelf systems; 8, Engineering properties of the shelf substrate; 9, The role of large-scale topographic features such as estuary mouths, shelf valleys, submarine canyons, and shoal areas in modifying regional patterns of fluid motion and sediment transport.

**Recommendations for stimulating research** included the formation of an informal society and the formation of a research steering committee. The society is SANDS (Shelf & Nearshore Dynamics & Sedimentation). It is open to anyone who submits his name to the secretary, O.S. Madsen, Department of Civil Engineering, M.I.T. and \$1 for a subscription to a

newsletter. The society will meet in odd-numbered years with the American Geophysical Union in Washington, D.C., and in even-numbered years with AGU in San Francisco. This year's spring meeting in Washington will piggyback on a session already initiated by R. Young of the Atlantic Oceanographic & Meteorological Laboratories. SANDS members are invited to listen to keynote speakers, present a poster at a poster session, and take part in a business meeting during which the San Francisco meeting will be planned. They should submit poster abstracts to AGU in the normal fashion, but specify that the poster be part of the SANDS session.

14 members have been nominated to a steering committee for research in shelf sedimentation, with Don Swift of the Atlantic Oceanographic & Meteorological Laboratories as acting chairman.

One of the most stimulating aspects of the workshop was the evening poster sessions in which attendees exchanged notes about recent research activities. These sessions indicated that the number of people studying shelf-sediment dynamics has increased manifold since the GSA workshop on shelf-sediment transport, in 1971.

The level of technical sophistication has also increased. One of the notable presentations at the 1971 symposium was R. Sternberg's analysis of data obtained by his tripod-mounted boundary-layer measurement system. If there was a theme in the evening poster session, it was 'son of tripod'; Drake and Cacchione, (USGS, Menlo Park), Butman and Beardsley, (USGS, Woods Hole), and Lavelle, Swift, Young, and Freeland (NOAA, Miami), and Lesht (University of Chicago) all described data from shelf boundary-layer monitoring systems.

The level of conceptual sophistication has likewise increased. In the 1971 Geological Society of America symposium only J.D. Smith seemed to be fully using both geological and hydrodynamical concepts. At the Vail poster sessions, physical oceanographers as well as geologists made presentations, and each group seems reasonably fluent in the other's language. In the words of one of the attendees of the Vail workshop, the meeting took a major step in overcoming the centripetal forces that have long afflicted marine scientists studying water-substrate interaction.

**Donald J.P. Swift**  
Marine Geology & Geophysics  
Laboratory  
15 Rickenbacker Causeway  
Miami, 33149

Middle Atlantic Continental Shelf and the New York Bight, Special Symposia 2, 1976, M.G. Gross, ed. (the American Society of Limnology and Oceanography, Inc.) 69-89.

## Morphologic evolution and coastal sand transport, New York—New Jersey shelf<sup>1</sup>

Donald J. P. Swift, George L. Freeland, Peter E. Gadd, Gregory Han, J. William Lavelle, and William L. Stubblefield

Atlantic Oceanographic and Meteorological Laboratories, NOAA, Virginia Key, Miami, Florida

### Abstract

The surface of the New York—New Jersey shelf has been extensively modified by landward passage of nearshore sedimentary environments during the postglacial rise of sea level. The retreat of estuary mouths across the shelf surface has resulted in shelf valley complexes. Constituent elements include shelf valleys largely molded by estuary mouth scour, shoal retreat massifs left by the retreat of estuary mouth shoals, and midshelf or shelf-edge deltas.

The erosional retreat of the straight coast between estuary mouths has left a discontinuous sheet of clean sand 0–10 m thick. During the retreat process, a sequence of oblique-trending, shoreface-connected sand ridges formed at the foot of the shoreface. As a consequence, the surficial sand sheet of the shelf floor bears a ridge and swale topography of sand ridges up to 10 m high and 2–4 m apart.

The mechanics of sedimentation in these two nearshore environments (estuary mouth and interestuarine coast) are now being investigated for purposes of environmental management as well as for further understanding of shelf history. In late fall and winter 1974, current meters were deployed on the Long Island coast and a radioisotope tracer dispersal pattern was traced over an 11-week period. Eastward or westward pulses of water were generated during this period of successive weather systems. Flows in excess of the computed threshold velocity of substrate materials were sustained for hours or days and were separated by days and weeks of subthreshold velocities, and the sand tracer pattern expanded accordingly. A single intense westward flow transported more sand than all the other events combined. The storm was anomalous with respect to the short term observation period, but it may in fact have been representative of the type of peak flow event that shapes the inner shelf surface.

Systematic observations of sedimentation in New York Harbor mouth have not yet been initiated. However, reconnaissance data reveal a complex pattern of ebb- and flood-dominated zones that control the pattern of sand storage.

We review in this paper our knowledge of the surface of the continental shelf off New York and New Jersey by considering two distinct topics: the geological history of this surface and the nature of sand transport across it. Our knowledge of the New York—

New Jersey shelf surface is primarily the result of a decade of work by K. O. Emery and his colleagues at the Woods Hole Oceanographic Institution. A summary of this information and much more has recently been provided by Emery and Uchupi (1972). As the work of the Woods Hole group drew to a close, we attempted to consider in greater detail some aspects of the morphologic evolution of the Middle At-

<sup>1</sup> Contribution of the New York Bight Project of the NOAA Marine EcoSystems Analysis (MESA) Program.



lantic Bight surface (Swift et al. 1972, 1974; Swift 1973; Swift and Sears 1974; Stubblefield et al. 1974). A summary of this work constitutes the first section of this paper.

As participants in NOAA's MESA (Marine EcoSystems Analysis) program, we have been asked not only to evaluate the geological history of the New York Bight, but also to provide quantitative estimates of sediment transport that will be of direct use to environmental managers. It turns out that these two goals are closely related. Our surveys of the shelf surface have led us to infer that it has been shaped by the landward retreat of two basic sedimentary regimes during the Holocene transgression: tide-dominated sedimentation at estuary mouths, and the sand transport pattern of the adjacent shoreface and adjacent inner shelf. Environmental engineers and managers must deal with these same regimes.

To satisfy their needs, we have initiated real-time studies of fluid motion and substrate response. State-of-the-art techniques for such studies are inadequate and progress has been slow. We report in the second portion of this paper fragments of our studies

of sand transport to encourage colleagues engaged in similar studies. Our own initial experiments have raised more questions than they have answered.

#### *Evolution of the continental shelf surface*

*Evolution of shelf valley complexes*—The New York Bight is a pentagonal sector of the North American Atlantic shelf, extending 800 km from Cape May, New Jersey, to Montauk Point, Long Island. Off New York, the shelf is 180 km wide (Fig. 1).

The sandy shelf floor is divided into compartments by shelf valley complexes extending from the shoreline toward shelf edge canyons (Fig. 1). The most obvious elements of these complexes are the shelf valleys themselves which may appear as narrow, well defined channels (Delaware Shelf Valley; Hudson Shelf Valley) or as broad, shallow depressions which barely perturb the isobaths defining the shelf surface (Block Shelf Valley, Long Island Shelf Valley, North New Jersey Shelf Valley, Great Egg Shelf Valley). Shelf valley complexes generally contain other morphologic elements. The north rims of the shelf valleys

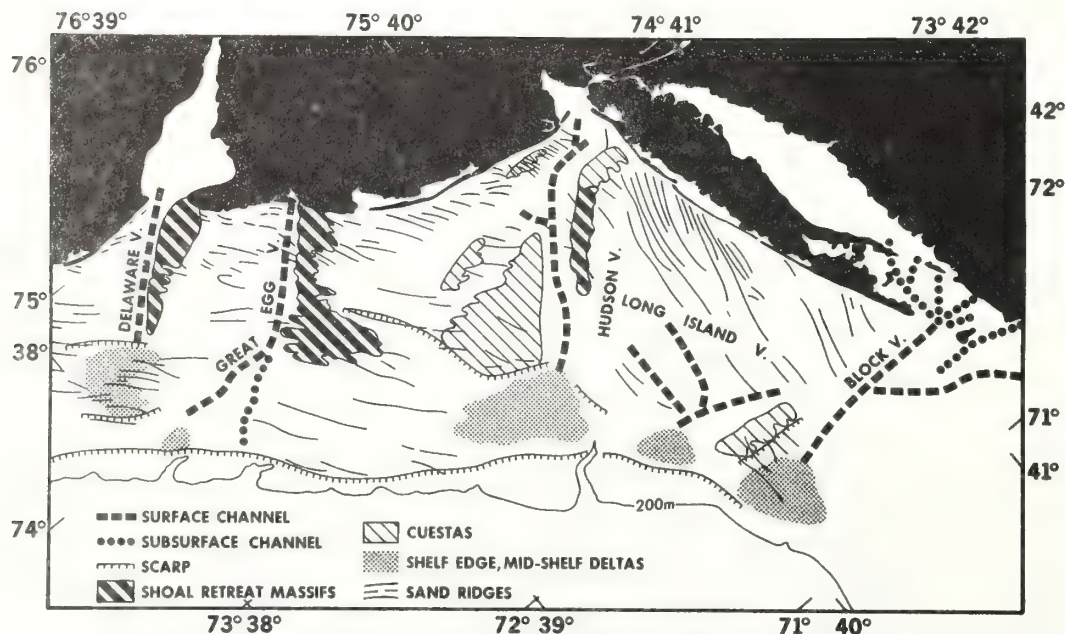


Fig. 1. Morphologic framework of the New York-New Jersey shelf. (Modified from Swift et al. 1972.)



tend to be elevated like levees above the adjacent shelf. Seaward ends of shelf valleys often terminate in delta terraces. Shelf valley complexes tend to be broken into segments by coast-parallel scarps, which may have been formed by temporary stillstands of the returning Holocene sea.

The origin of the shelf valley complexes is best inferred from the configuration of the Delaware Shelf Valley (Fig. 2), which can be traced without interruption into its modern estuary. The Delaware estuary mouth has a sill of sand nourished by littoral drift from the New Jersey coast (Swift 1973). The sill is stabilized by an interdigitating system of ebb- and flood-dominated channels, whose discharge inequalities are a consequence of the phase lag of the tidal wave in its passage across the sill (Swift and Ludwick in press). The Delaware Shelf Valley may be traced directly into the flood channel of the main ebb channel-flood channel couplet. Its leveelike north rim may be traced directly into the complex of smaller ebb channels, flood channels, and sand banks on the north side of the estuary mouth. This shoal area serves as the depositional center for the littoral sand discharge of the New Jersey coast.

The shelf valley complex, then, is not a drowned river valley, but is rather the track left by the retreat of the Delaware estuary mouth across the shelf during the Holocene sea-level rise. The shelf valley is the retreat path of a flood channel. The north flank levee is the retreat path of the estuary mouth shoal or is a shoal retreat massif—massif in the sense of a compound topographic high consisting of smaller scale highs (Swift 1973). The surface channel does not directly overlie the buried river-cut channel but is offset to the south (Sheridan et al. 1974). As the estuary retreated up the river valley, it not only tended to fill the river valley but in the final, estuary-mouth stage decoupled from it altogether by migrating to the south.

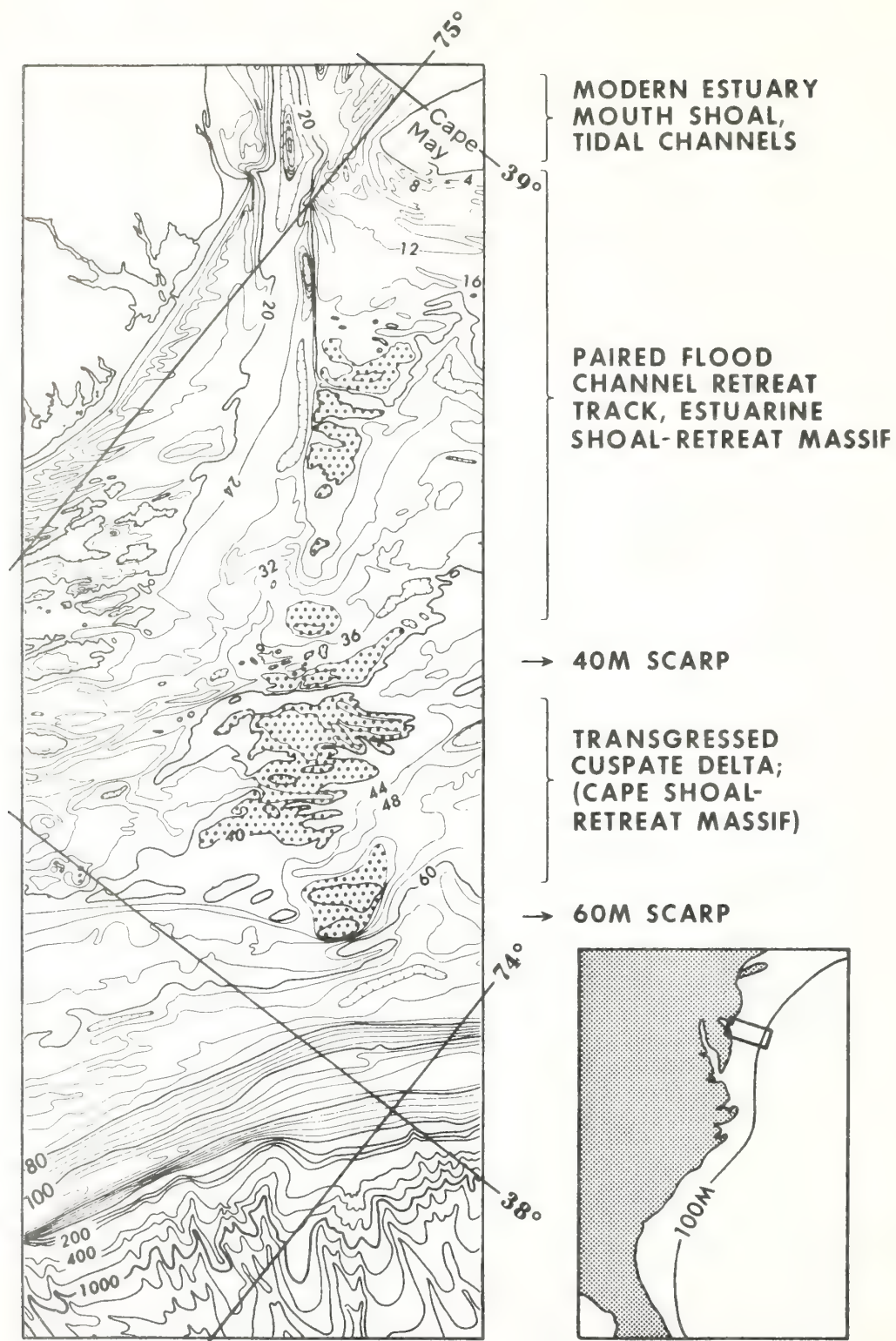
The largely constructional nature of the Delaware Shelf Valley complex is also characteristic of the Great Egg Shelf Valley complex (Fig. 1), although the associated massif has been heavily dissected by the

posttransgressional regime of southerly storm flows. To the north, however, the Hudson and Block Shelf Valleys occur on a terrain of innately greater relief. There are cuestaslike highs, and the estuarine deposits only partly fill the shelf valleys. The deeply incised nature of the Hudson Shelf Valley may reflect the era when it received Great Lakes meltwater (Veatch and Smith 1939).

*Evolution of interfluves*—Plateaulike interfluves between the shelf valleys have likewise been intensively modified by passage of the shoreline. Interfluve surfaces range from exceedingly flat plains (slopes of 1:2,000) to irregularly undulating sand ridge topography (Fig. 3). Sand ridges exhibit up to 10 m of relief, are spaced 2 to 4 km apart, and their crestlines may be traced for tens of kilometers. Side slopes are generally less than a degree. Crestlines are not quite parallel to the regional trend of the isobaths but tend to converge to the southwest with the shoreline (Fig. 1). Ridges attain their maximum development on the northeast sides of shoal retreat massifs.

The ridges are molded into a surficial sheet of relatively homogeneous, well sorted sand, 0–10 m thick. In trough axes the sheet thins to a basal shelly, gravelly sand several decimeters or less thick, and a more heterogeneous older substrate is locally exposed (Donahue et al. 1966; Stubblefield et al. 1974). This is commonly a muddy sand or mud deposited behind the retreating Holocene barrier system (Stahl et al. 1974; Sheridan et al. 1974), but it is locally absent due to erosion or nondeposition, so that the Holocene sands rest directly on older Pleistocene sands.

To understand the genesis of this postglacial stratigraphy, it is necessary to consider the dynamics of a transgressing shoreline. We are indebted in this regard to Bruun (1962) and Fischer (1961) who appear to have independently appreciated the role of the landward translation of the wave- and current-maintained coastal profile in generating transgressive stratigraphy. In the New York Bight, as along most low, unconsolidated coasts, the coastal profile consists of a steeply sloping nearshore sector (the shoreface) and a gently dipping in-





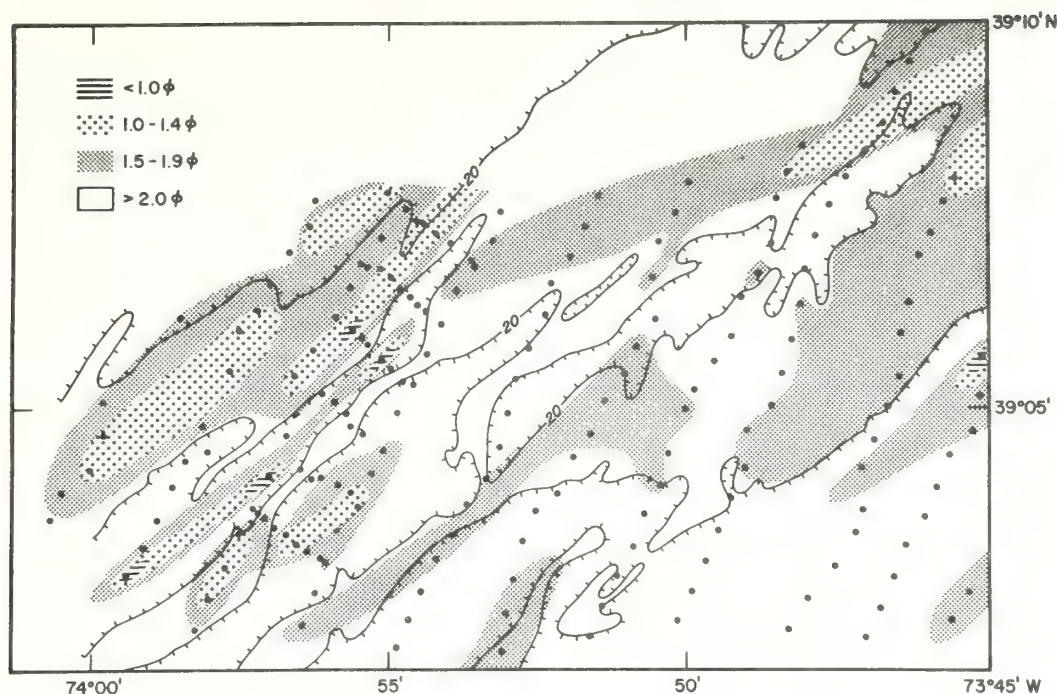


Fig. 3. Simplified bathymetry and distribution of grain sizes on a portion of the central New Jersey shelf. Medium to fine sand occurs on ridge crests. Fine to very fine sand occurs on ridge flanks and in troughs. Locally, erosion in troughs has exposed a thin lag of coarse, shelly, pebbly sand over lagoonal clay. (Reprinted from Stubblefield et al. 1974 by permission of the *Journal of Sedimentary Petrology*.)

ner shelf floor. The break in slope, which may be well defined or gently rounded, generally occurs at depths of 12 to 18 m, some few kilometers from the shoreline.

Bruun (1962) pointed out that if this profile is in fact an equilibrium response of the seafloor to the coastal hydraulic climate, then a rise in sea level must result in a landward and upward translation of the profile (Fig. 4A). Such a translation necessitates erosion of the shoreface. Much of the resulting debris will presumably be entrained in the littoral current and move downcoast, but during periods of onshore storm winds, the littoral drift may leak sea-

ward, due to an offshore component of bottom flow, to be deposited beneath the rising seaward limb of the equilibrium profile on the adjacent inner shelf floor.

Evidence for such seaward bottom transport is varied. Murray (1975) described periods of offshore bottom flow on the gulf coast, when winds are onshore and the water column is not stratified. Sonu and Van Beek (1971) noted that sand loss from North Carolina beaches correlates poorly with periods of high waves but correlates well with high waves generated by onshore northeast winds. On the Long Island inner shelf, we used sidescan sonar to map inner

←

Fig. 2. Delaware Shelf Valley complex. Southward littoral drift along the New Jersey coast is injected into the reversing tidal stream of Delaware Bay mouth. The resulting sand shoal is stabilized as a system of interdigitating ebb- and flood-dominated channels. The shelf valley complex seaward of the bay mouth was formed by the retreat of the coastal sedimentary regime through Holocene time. Retreat of the main flood channel has excavated the Delaware Shelf Valley; retreat of the bay mouth shoal has left a levee-like high on the shelf valley's north flank. (Reprinted from Swift 1973 by permission of the *Geological Society of America Bulletin*.)



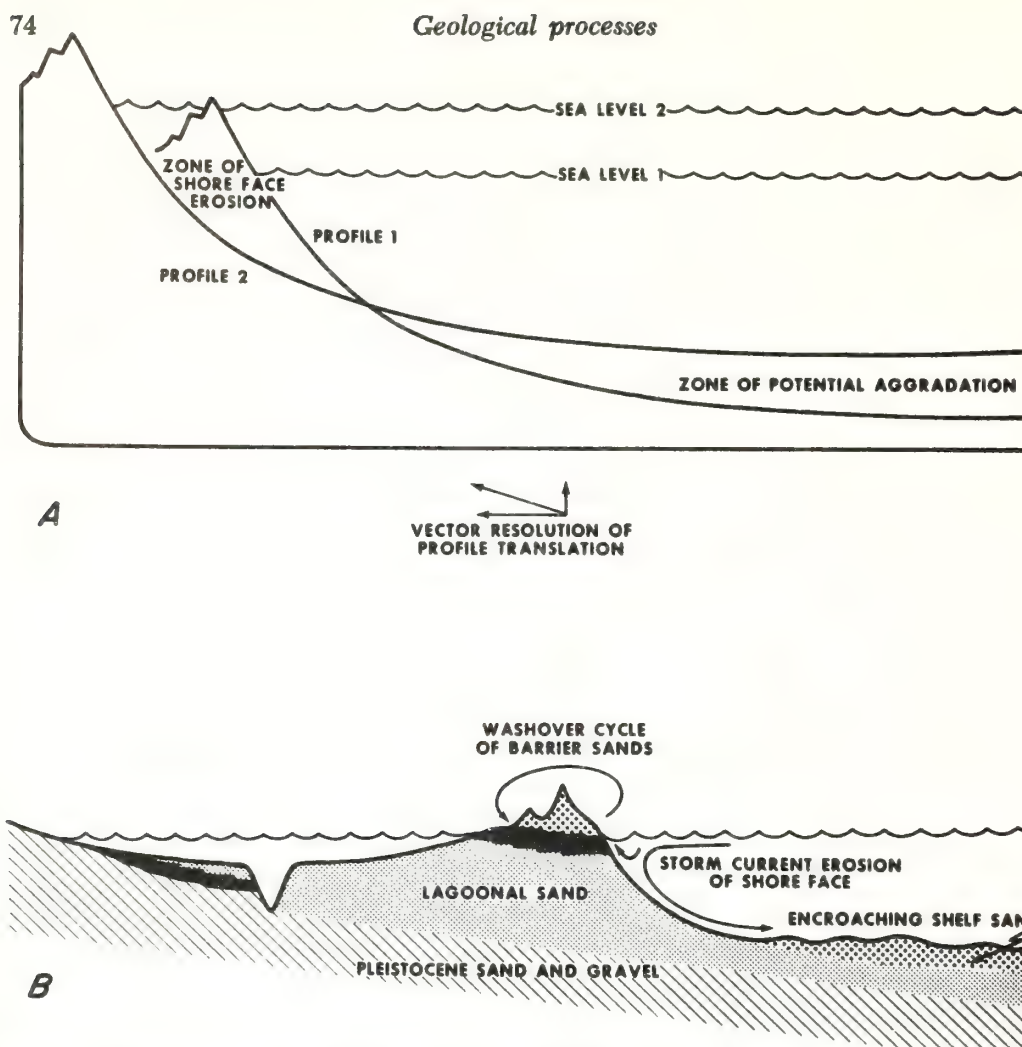


Fig. 4. Models for a coast undergoing erosional shoreface retreat during a rise in sea level. A—Rise in sea level results in landward and upward translation of coastal profile (Bruun 1962). B—Translation is accomplished. Wind and storm washover transport on the barrier surface and erosion of the shoreface and seaward transport of the resulting debris (Fischer 1961).

shelf current lineations that form an eastward-opening angle with the beach (Fig. 5). A poorly defined asymmetry is apparent: the western sides of the lineations are gradational, whereas the eastern sides are sharply defined. The origin of this pattern is not clear. The dark bands are strips of coarse or gravelly sand that may either be troughs between low amplitude, current-transverse sand waves or troughs between current-parallel sand ribbons. However, considering the angle that the lineations make with the beach, sand ribbons seem unlikely for reasons of flow continuity. If

sand waves, the lineations are responses to strong bottom flows trending westerly and offshore.

Fischer (1961), Stahl et al. (1974), and Sanders and Kumar (1975) described the stratigraphic consequences of erosional shoreface retreat, based on their observations of the New Jersey and New York coasts. The barrier superstructure will retreat over the lagoonal deposits by a cyclic process of storm washover, burial, and re-emergence at the shoreface (Fig. 4B). Lower shoreface sands will tend to be transported seaward to accumulate over the

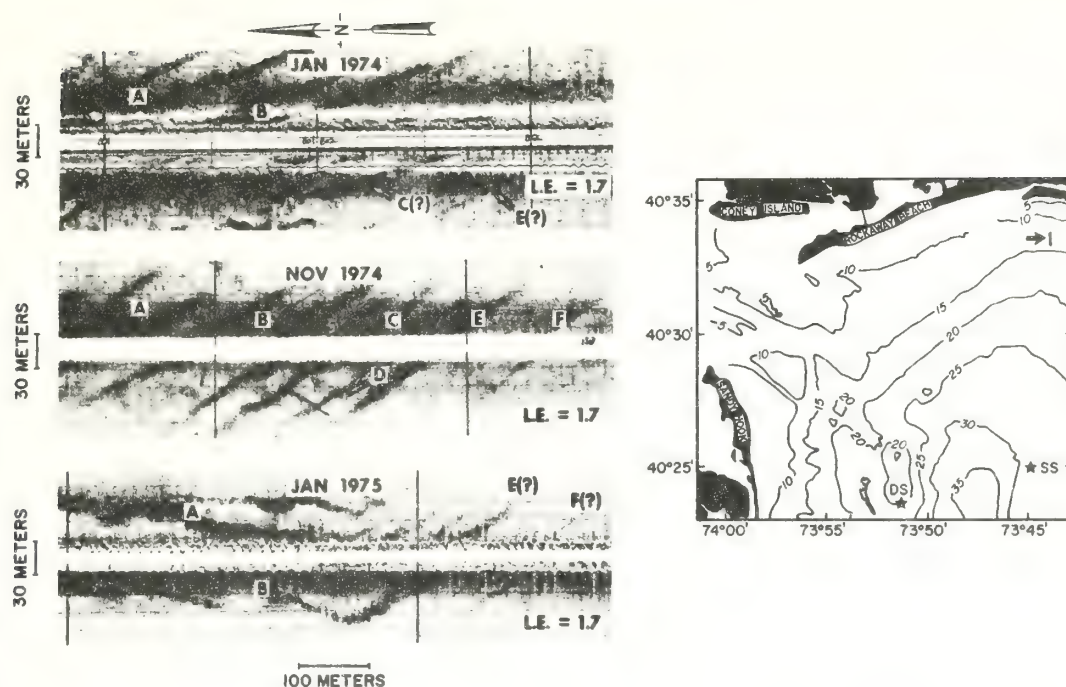


Fig. 5. Sidescan sonar records of current lineations on the Long Island coast, collected at three different periods. Positioning by Raydist. Current lineation pattern (bands A–F) expands to south during observation period. Apparent change in orientation in last panel is due to ship maneuvering. (From Stubblefield et al. in prep.)

eroded surface of the lagoonal deposits as the leading edge of a marine sand sheet. Bruun's hypothesis is compatible with the stratigraphic evidence and with our limited knowledge of coastal hydraulics. A more rigorous test requires bathymetric time series to document changes in the coastal profile. Limited data of this sort are becoming available. Harris (1954) undertook a study of the Long Branch, New Jersey, dredge spoil dumpsite to determine if dumping was nourishing the beach (Fig. 6). In fact, during a 4-year period, the shoreface underwent between 5 and 26 cm of erosion, while an irregular pattern of deposition prevailed on the inner shelf floor. A somewhat longer time series has been prepared by Kim and Gardner (Woodward-Clyde Assoc.) during study of proposed sewage outfall routes for the Ocean County, New Jersey, sewerage authority (Fig. 7). Two out of three profiles taken indicate 1.5–2.0 m of erosion over 20 years. The third profile is immediately south of a shoreface-connected sand ridge; here

comparable aggradation has occurred as a consequence of southward ridge migration.

*Growth of ridges*—Erosional shoreface retreat on the Atlantic cannot be adequately described by a two-dimensional model such as Fig. 4 because the shoreface appears to be the formative zone for sand ridge topography as well as for the sand sheet into which it is impressed. Clusters of shoreface-sand ridges occur on the New Jersey coast between Brigantine and Barnegat Inlets, on the north New Jersey coast between Manasquan and Sea Bright, and on the Long Island coast from Long Beach to the shoreface of eastern Fire Island.

The shoreface-connected ridges are named for their oblique, fingerlike extensions of the shoreface, causing seaward deflections of isobaths as shoal as 5 m. The ridges tend to be asymmetric in cross-section, with steep seaward flanks, although this relationship may be reversed at the base of the ridge where it joins the shoreface. Seaward flanks tend to be notably

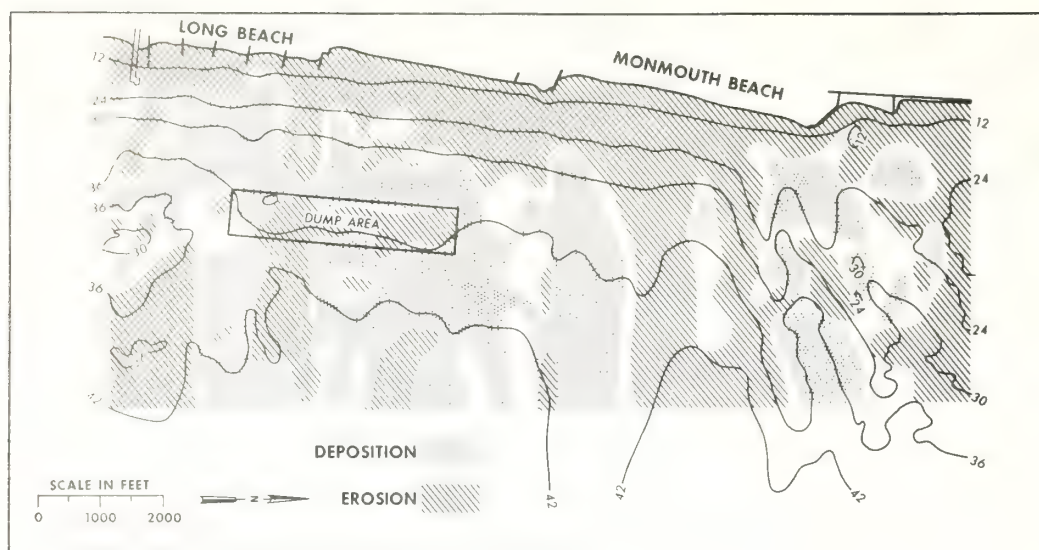


Fig. 6. Erosion and deposition near Long Branch, New Jersey, dredge spoil dumpsite during a 4-yr period. Recorded changes are 0.4–1.4 ft. Shoreface has undergone erosion; adjacent seafloor primarily has undergone aggradation. (From Harris 1954.)

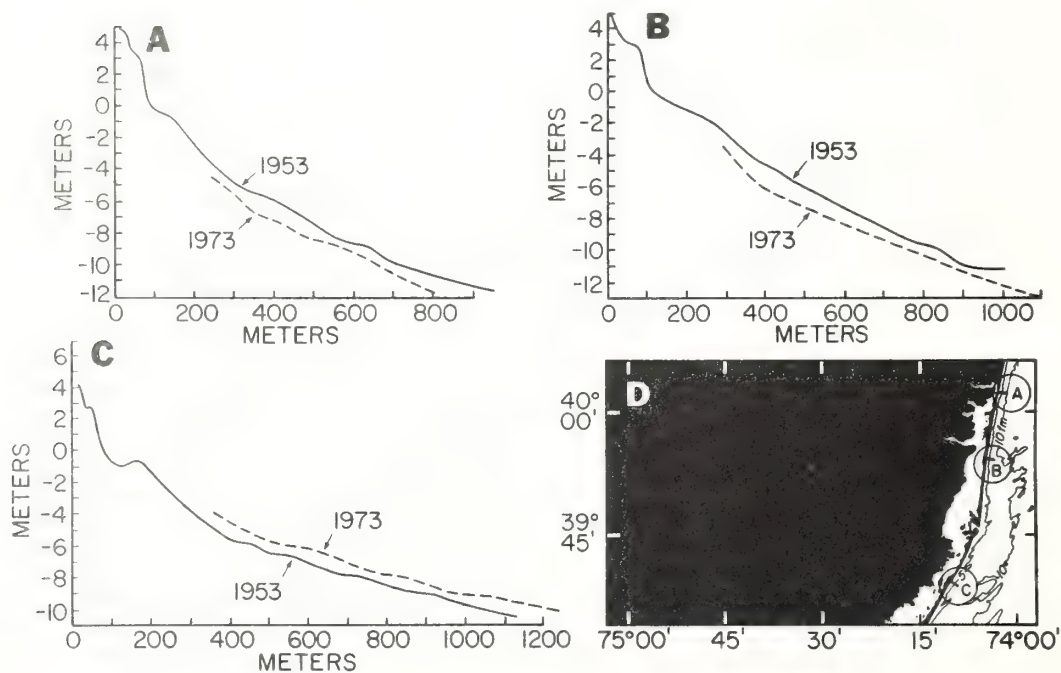


Fig. 7. Profiles of proposed sewage outfall sites on the New Jersey coast. Sites A and B have eroded over a 20-yr period. Site C, immediately downcoast of a shoreface-connected sand ridge, has aggraded. (Reprinted from Kim and Gardner 1974 with permission of Woodward-Clyde Assoc.)



finer than landward flanks. Off Brigantine Inlet and off the New Jersey coast, shoreface-connected ridges are associated with free-standing inner shelf ridges that can be traced seaward for tens of kilometers in apparent genetic sequence. The ridges form on the shoreface in response to south-trending coastal storm currents (Duane et al. 1972) and become detached from the shoreface as it retreats. They tend to migrate downcoast (to the south or west) and offshore, extending their crestlines so as to maintain contact with the shoreline (Fig. 8). Eventually, however, contact is broken, and they are stranded on the deepening shelf floor. Downcoast ridge migration is part of a general pattern of southwesterly sand transport on the Atlantic shelf. In the offshore ridge topography, this pattern is indicated by the tendency of both ridge crests and trough talwegs to rise toward the southwest. Locally, it is indicated by patterns of erosion and deposition near wrecks (Fig. 9).

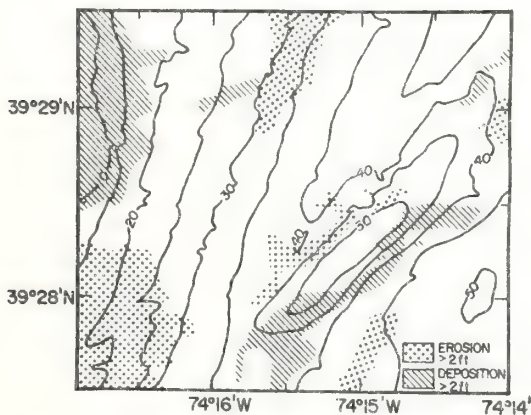
#### *Sand transport on the inner shelf*

The preceding description of the morphologic evolution of the New York shelf surface is based primarily on the interpretation of bathymetric maps, aided by local substrate inventories in which the bottom is

examined by grab sampling, photography, Vibracoring, and seismic profiling. The conclusions are qualitative but nonetheless valid. However, fuller understanding of the behavior of the shelf surface requires a different approach.

We must directly measure fluid and sediment transports involved in the two basic mechanisms that have shaped the shelf surface: tidal flow and sand storage at estuary mouths, and erosional retreat of the shoreface between estuary mouths. Environmental managers who must make decisions about dredged channels, sewage outfalls, sewage and dredge spoil dumpsites, deep-water tanker terminals, and offshore power plants need to understand these processes before they can evaluate the stability of the inner shelf surface.

The nature of coastal sand transport during storms is the first major problem we will consider. Fluid motions in the surf zone have been studied for decades, and the role of longshore currents driven by shoaling and breaking waves has been described (e.g. Bowen 1969). In the New York area,



massive discharges of sand in the surf zones of the Long Island and New Jersey coasts move toward the New York harbor mouth; these discharges have built Sandy Hook and Rockaway spits within subhistoric to historic times. However, we know almost nothing about fluid motions over the adjacent inner shelf, although the geologic data presented above show that currents seaward of the surf play a major role in the coastal sand budget. We must specifically ask what time and space scales of inner shelf flows are intense enough to entrain sand? Is their velocity field so structured that there are periods of significant offshore bottom flow and sand transport?

Equally important is the problem of the inner shelf sand ridges, which seem to occur wherever a sewage outfall or power plant is to be located. If we wish to predict the probable behavior of these features through the design life of the structure, we must understand their genesis and how they are maintained by flow. It is a truism of loose boundary hydraulics that sheared boundary flows are innately unstable, and that these instabilities tend to interact with the substrate to generate sand ripples, sand ribbons, sand waves, and sand dunes. The circumstantial evidence that inner shelf sand ridges are similarly responses to flow is strong. How are they formed and maintained?

As a first attempt to investigate these questions, Lavelle et al. (in press) placed 40 Aandaraa current meters at 19 stations over the Tobay Beach sand ridges of the Long Island inner shelf (Figs. 10 and 11). The meters were in place for 6 weeks during late November and December 1974; a single meter recorded for an additional 5 weeks. All meters averaged speed over 10 min and took an instantaneous direction reading during each sampling period.

During the observation period, a series of moderate storms induced easterly and westerly flows parallel to the coast. A final storm on 1-4 December was very intense, causing more beach erosion than any storm since the Ash Wednesday storm of 1962 (C. Galvin personal communication).

In Fig. 12, vector averages for all near-bottom, middepth, and near-surface meters

are presented for periods of both westward and eastward flows. A wind-controlled pattern of coastal flow emerges. There is a top to bottom speed shear as well as a directional shear. Prevailing fall and winter winds blow out of the northwest, across the east-west Long Island shoreline; the result is a tendency toward coastal upwelling. Surface flows have an offshore component for both eastward and westward flow directions. The response is less symmetrical at depth; westward bottom flows parallel the isobaths, whereas eastward bottom flows have an onshore component. Net water transport during the observation period was eastward.

During the early December storm there was a small offshore component to the water flow near the bottom. Figure 13 shows the winds during the storm and the associated current velocities from a near-bottom current meter, which have been filtered with a 40-h and a 3-h low-pass filter. The 40-h low-pass filtered record, which is a segment

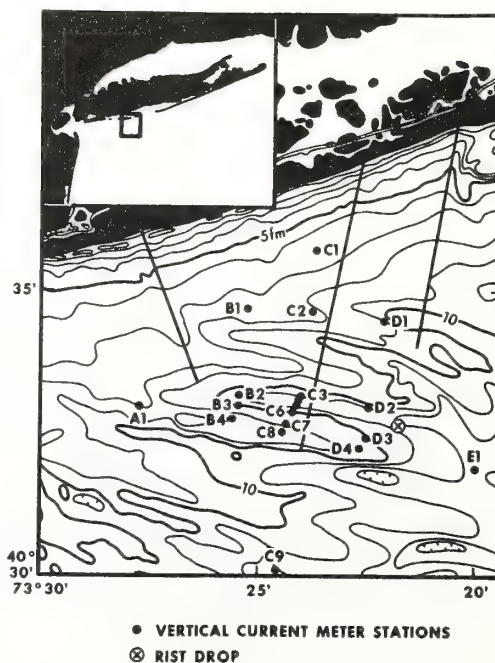


Fig. 10. Bathymetry, current meter stations, and tracer release point (RIST drop) for the Long Island nearshore (LINS) experiment. (From Lavelle et al. in press.)



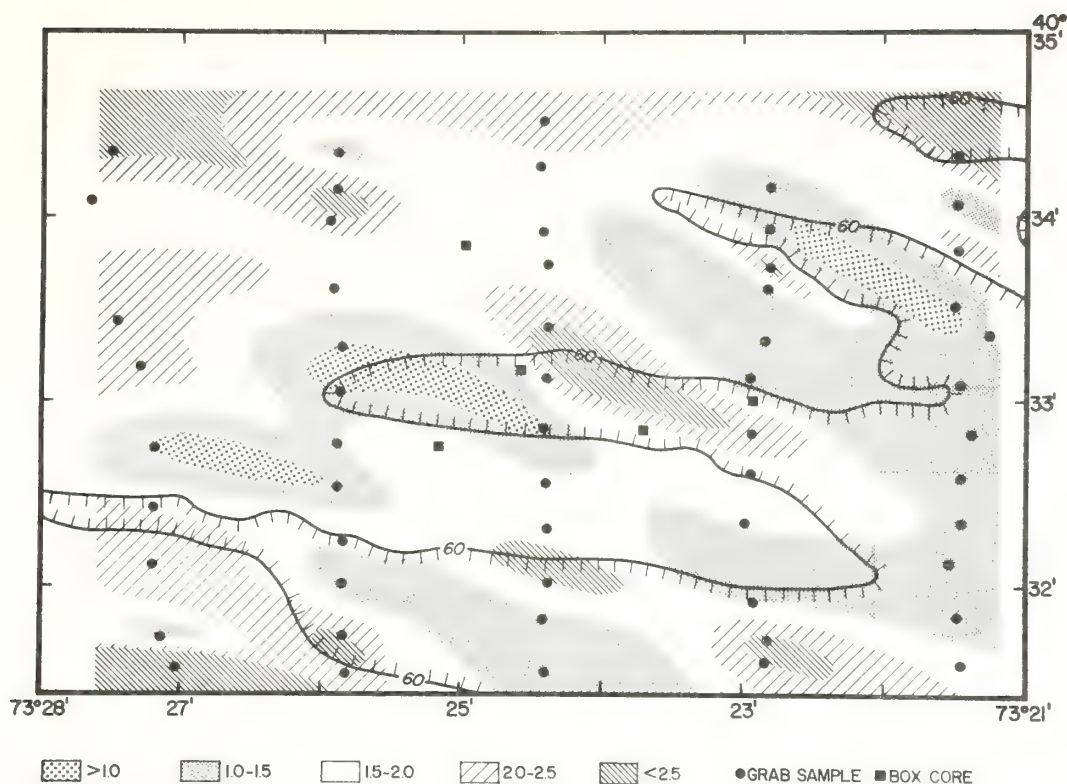


Fig. 11. Distribution of grain sizes over the Tobay Beach ridges, LINS area. Size classes in phi units.

taken from Fig. 12, obscures the brief time-scale flow associated with the storm. The 3-h low-pass record, which is only slightly smoothed and still contains the tidal signal, shows a period of offshore flow more clearly. These results must be viewed cautiously. The Aandaraa current meters which were used have large direction and speed errors when used in shallow water with surface wave amplitudes as large as were present during the event described here.

During the November–December experiment on the Long Island inner shelf, estimates of sand transport were made from calculations from current meter records (Lavelle et al. in press) and also from radioisotope tracer dispersal patterns (Lavelle et al. unpublished data). To generate the patterns, about 500 cm<sup>3</sup> of indigenous fine to very fine sand was surface-coated with 10 Ci of <sup>103</sup>Ru (half-life, 39.6 d). On 12 November, equal portions of tagged sand were released in water soluble bags at three

points at the east end of the main trough (Fig. 14). The injection points formed an equilateral triangle with sides roughly 100 m long. The developing dispersal pattern of labeled sand was surveyed at intervals by scintillation detectors mounted in a cylinder towed across the bottom. Navigation was by a Raydist system with 10-m resolution. Four postinjection surveys were made during the 11-week tracer experiment. Dispersal patterns mapped 2 and 8 weeks after injection are shown in Fig. 14. After 2 weeks (25 November) roughly ellipsoidal smears trended east from each of the three injection points (Fig. 14A). Each smear could be traced for about 200 m before the signal was lost in the background radiation. After 8 weeks (10 January) the three eastward smears had been replaced by a single, more extensive pattern extending 700 m to the west (Fig. 14B). Partially processed data from an intermediate survey (17–19 December) indicate that the reversal in fact had



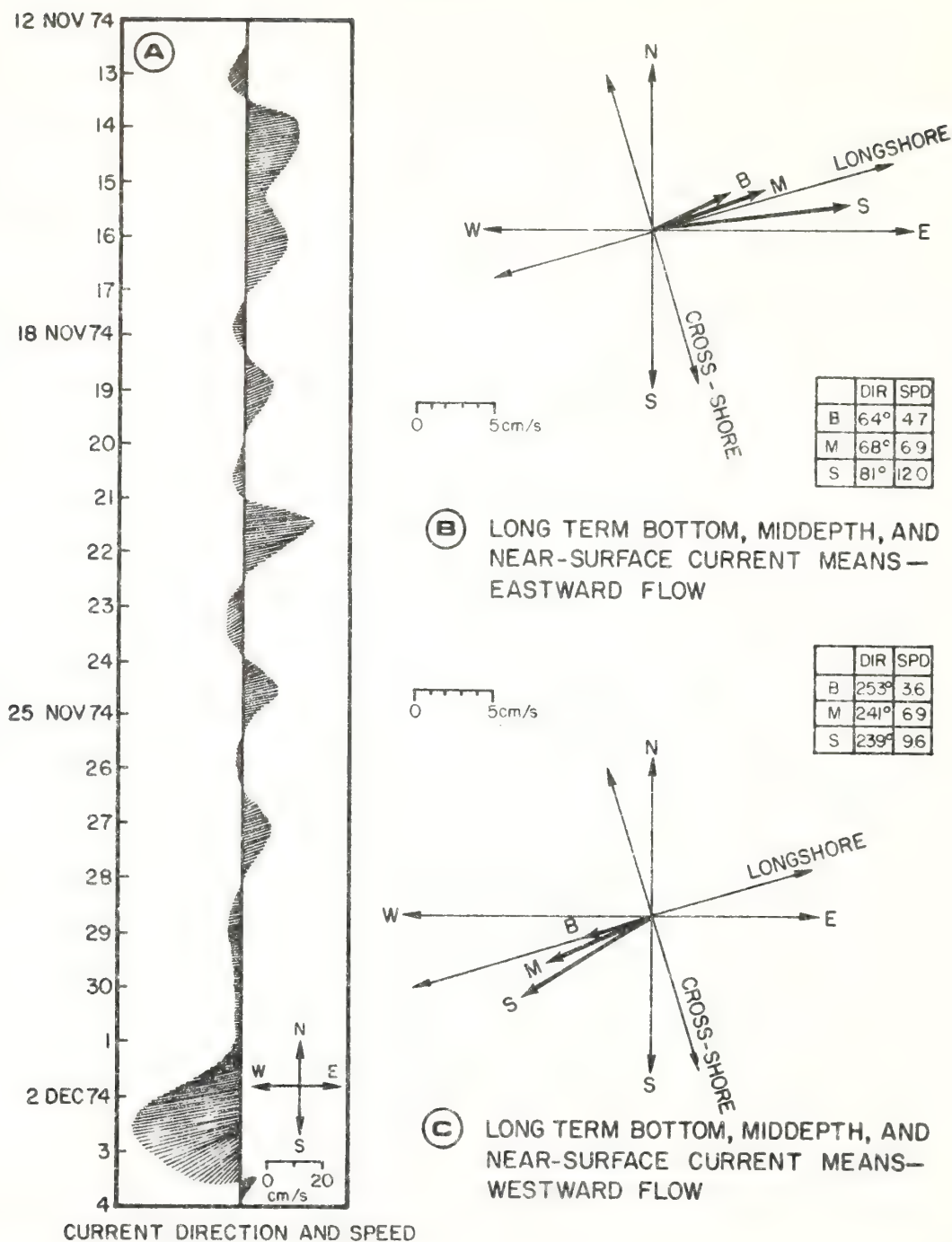


Fig. 12. Summary of flow data for the LINS experiment. A—Vector time series of representative near-bottom flow. Data have been subjected to a 40-h low-pass filter. B, C—Long term velocity averages of eastward and westward flow for meters grouped by depth in water column. Bottom, middepth, and near-surface groupings are labeled B, M, and S. (From Lavelle et al. in press.)

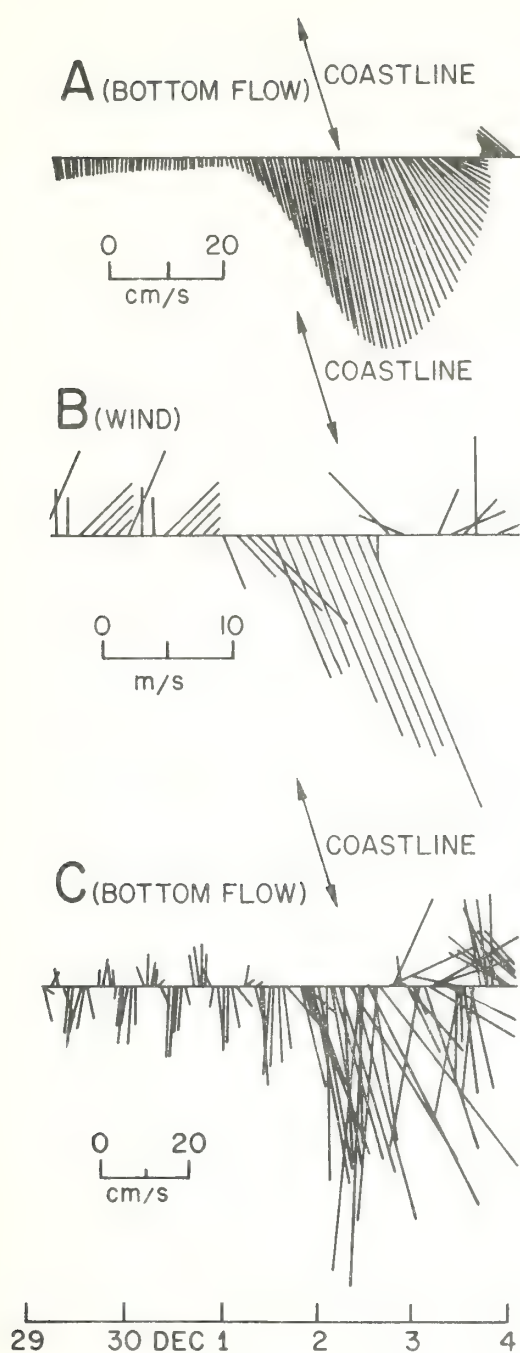


Fig. 13. Vector time series for bottom current and wind velocities during the 1-4 December storm. A—40-h low-pass filtered record (Lanczos filter with response,  $-6$  db at 36 h and  $-20$  db at 40 h). B—Wind record from Ambrose Tower. C—3-h low-pass filtered record (Lanczos filter with response,  $-6$  db at 2.5 h and  $-20$  db at 3 h).

occurred before this and that it initially had been at least 1,200 m long.

The temporal pattern of sediment transport over 60 days may be inferred from Fig. 14C. Current speed, measured 1.5 m from the bed, is plotted against time. The horizontal line at 18 cm/s is an estimated threshold for the fine to very fine sand (mean diameter,  $3.0 \phi$ ) found at the site. It is based on the work of Shields and subsequent workers (Graf 1971: p. 90) and on a choice of  $3.0 \times 10^{-3}$  for the drag coefficient (Sternberg 1972). This choice of threshold velocity was supported by empirical evidence obtained during the course of the experiment (Lavelle et al. in press). Estimates have been prepared for the relative role each transport event played in the overall transport record, based on the concept of frictional energy expenditure proportional to the transport volume (Bagnold 1963). For each event where velocities exceeding threshold were recorded, a transport volume was calculated:

$$Q_i = \alpha \int_i (|u| - |u_{th}|)^3 dt,$$

where  $|u|$  is measured current speed,  $|u_{th}|$  is threshold speed,  $\alpha$  is a constant of proportionality, and  $t_i$  is the duration of the transport event (Lavelle et al. in press).

Expression of sand transport as a power of the difference of measured and threshold velocity is supported by Kennedy's (1969) analysis of stream transport data. Without assigning a value to  $\alpha$ , we can calculate the rate of transport of one flow event relative to the next or in relation to the sand discharge that occurred over the entire duration of the current meter record. The second of these options has been used in Fig. 14C, where relative sand transport as percent of total transport has been represented as solid bars superimposed on the current meter record. Bar height is a measure of volume percent of transport; bar width is a measure of duration of the transport event. Despite the exceedence of the sediment transport threshold at many points in the record, only the solid bars centered on 2 and 16-17 December are visible in the figure. Thus sand transport during observation

consisted of periods of quiescence separated by brief, intense transport events. Furthermore, since discharge is calculated as a power function of excess velocity, intense storms are far more efficient transporters of sand than mild ones. Although the transport index calculated for the 1-4 December storm may be biased by the choice of threshold speed as well as by the functional dependence on velocity, it seems probable that any reasonable parameterization would lead to the same general conclusion: the storm event of 1-4 December moved more sand at 20-m water depth than the combination of all other transport events.

Attempts have also been made to calculate sediment transport indices over longer

periods of time in the New York Bight apex. The following computation is based on 30-80-day Aandaraa current meter records (Fig. 15). Data in each current meter record consist of an average speed,  $u$ , and an instantaneous direction,  $\theta$ , taken for each 10-min sampling interval. For each interval in which an assigned threshold speed,  $|u_{th}|$ , is exceeded, a sediment transport index,  $Q$ , has been computed, as follows:

$$Q = (|u| - |u_{th}|)^3, (|u| - |u_{th}|) > 0.$$

For each current meter, the set of vectors of flow direction,  $\theta$  ( $0^\circ \leq \theta \leq 359^\circ$ ), and of sediment transport index,  $Q$ , is sorted into 10-degree classes. The results are plotted as

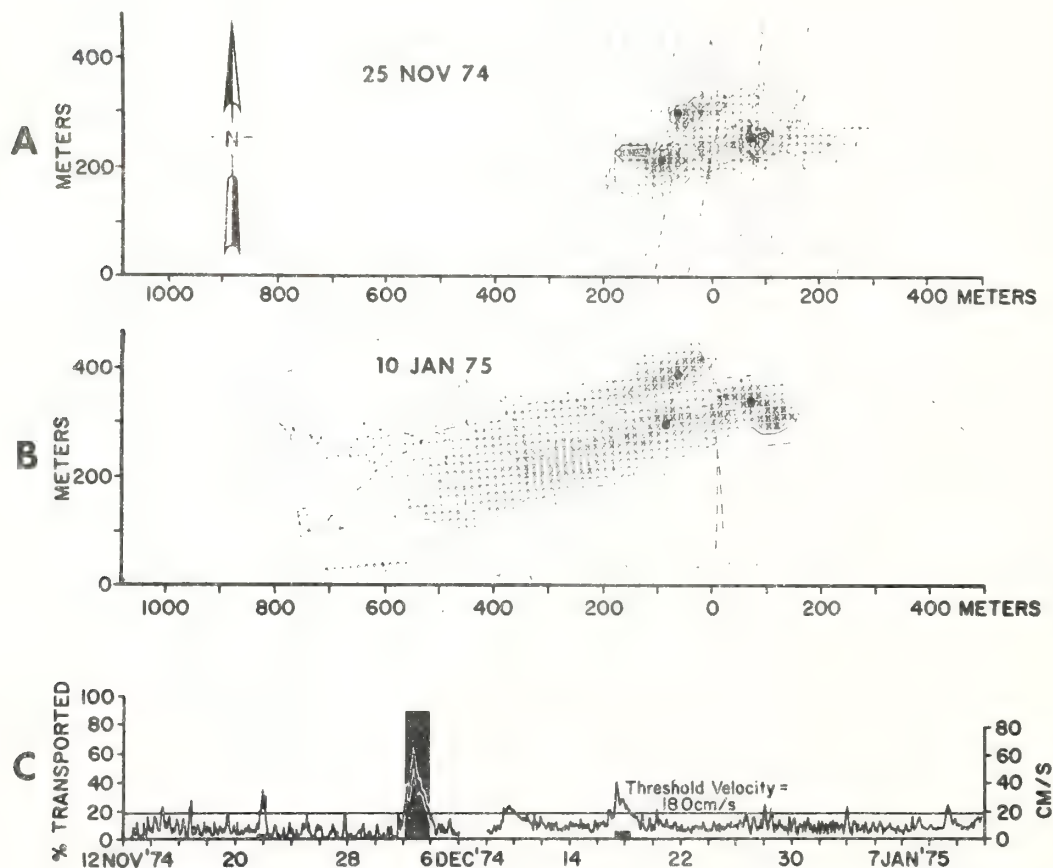


Fig. 14. Sand transport data. A, B—Dispersion patterns measured 13 and 59 days after injection of tagged sand. Point sources are represented by dots. Broken line is the survey trackline. Dots, coarse dots, and Xs indicate increasing intensity of radiation. C—Near-bottom current speed record over the duration of the experiment and calculated sediment transport information. (From Lavelle et al. in press.)



APRIL - JUNE 1974

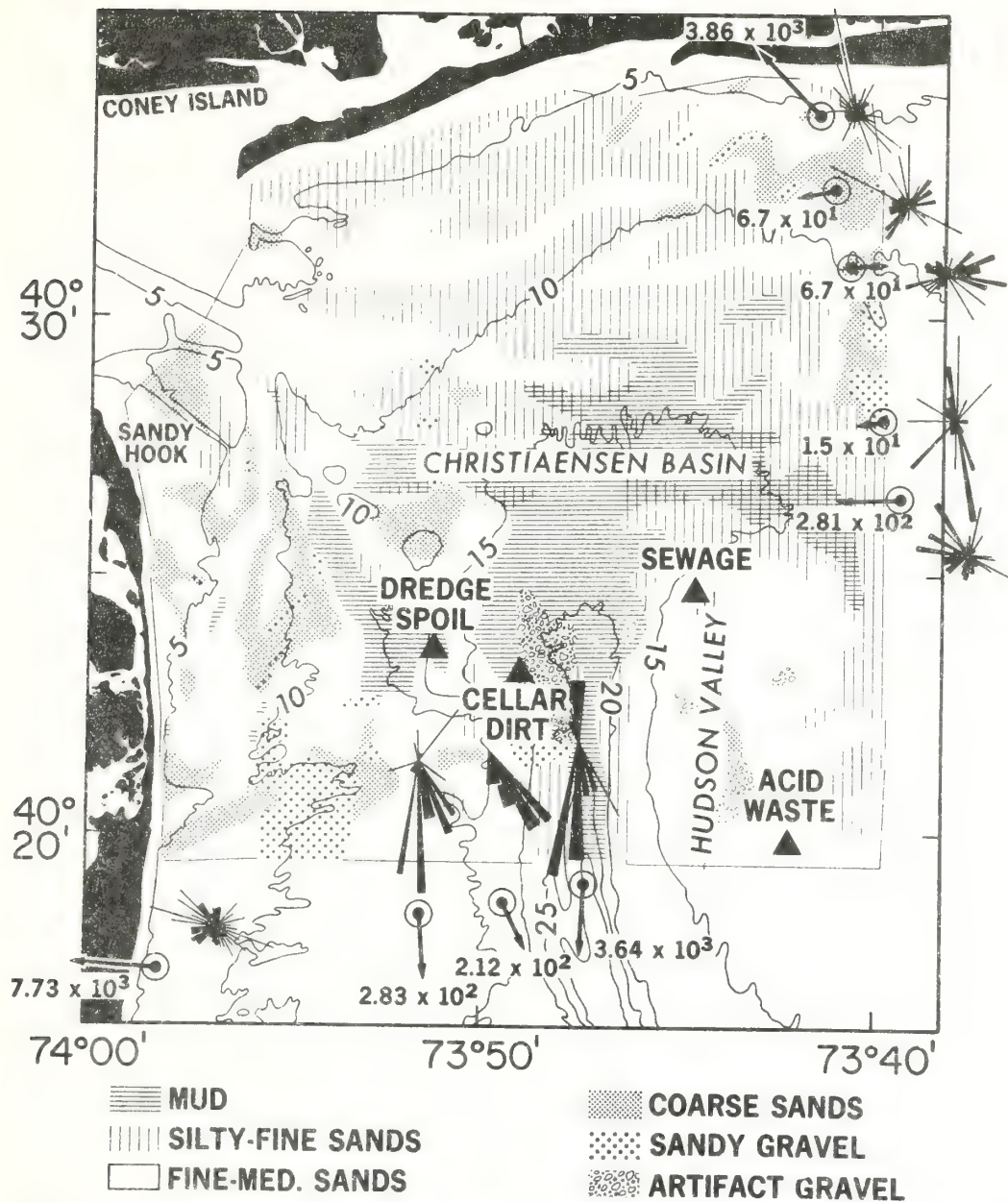


Fig. 15. Bathymetry, bottom sediment character, and calculated patterns of sediment transport for April-June 1974 in the New York Bight apex (see text). Depth in fathoms.

rose diagrams in Fig. 15. The length of each radial bar is proportional to the mean sediment transport index, while the width is proportional to the duration of flow above threshold, hence the bars may overlap.

For each current meter station in Fig. 15, the normalized resultant of all sediment transport vectors is indicated by a single arrow. The resulting magnitude has been divided by the total number of days that the

current meter was in operation ( $T_p$ ) to derive a daily average,  $\bar{Q}_D$ :

$$\bar{Q}_D = \frac{1}{T_p} \int_0^T (|u| - |u_{th}|)^3 \mathbf{u} dt,$$

where  $\mathbf{u}$  is a unit vector with direction  $\theta$ , and  $T$  is the total number of days. The integrand is zero when the velocity is less than threshold.

Figure 15 suggests that during April–June 1974, sand transport was westward off the Long Island shore and southward off the New Jersey shore. Nearshore stations reveal a strong onshore component of the sand transport index, perhaps because of wind-induced upwelling or because of the landward directed asymmetry of bottom wave surge, or both. The magnitude of the sand transport index generally decreases seaward but is anomalously large within the Hudson Shelf Valley. The easterly transport revealed by a single station off the Long Island coast is probably due to instrument problems.

#### *Some unsolved problems*

*The inner shelf sand budget*—Our studies of sand transport on the New York inner shelf have resolved some questions but raised others. It is clear that sand transport occurs seaward of the surf zone. Transport is episodic in nature. Sand is entrained and transported by brief, intense, wind-driven coast-parallel flows lasting for hours or days and separated by days or weeks of quiescence. Our measurements suggest that inner shelf bottom flows are more likely to transport shelf sands shoreward than seaward. This appears to be due to intermittent coastal upwelling induced by northwesterly winds and perhaps also to the landward-oriented asymmetry of near-bottom wave surge. Baylor (1973) has also noted this pattern of wind-induced coastal upwelling off Long Island, and R. Scarlet (EG&G, Waltham, Mass., unpublished) reported a similar regime of coastal upwelling for the Beach Haven Ridge site (Fig. 16).

However, our observations indicate that the 1–4 December storm was the only event

that caused massive sand transport. It stands out within our two periods of current monitoring not only in its duration, intensity, and westward direction of net transport but in the offshore component of bottom flow. We must consider the hypothesis that the 1–4 December storm, anomalous within the context of our short term winter observation period, is in fact the kind of peak flow event that shapes the inner shelf surface and controls its sand budget. We have noted that Atlantic shelf stratigraphy is best explained by erosional shoreface retreat and seaward transport of the eroded material. We have described the southwest migration of shoreface-connected ridges off New Jersey and have cited evidence for the net southwest transport of sand (Fig. 8). We note that the Tobay Beach ridges (Fig. 11) are, like other Atlantic Bight ridge fields, asymmetrical in both grain-size distribution and morphology; the seaward-facing southwest slopes are steeper and finer grained, implying that westward flows scour the upcurrent flanks and deposit fine sand on the seaward-facing downcurrent flanks.

Recent studies by physical oceanographers also suggest that southwestward currents generated by “northeaster” storms have the greatest potential for shaping the shelf surface. Beardsley and Butman (1974) have described a scale-matching phenomenon, in which the Middle Atlantic Bight tends to interact with “northeasters” of the appropriate size and trajectory so that intensive southwestward flows result (Fig. 17). Their observations indicate that if low pressure cells cross the bight on a trajectory such that the isobars of atmospheric pressure cross the isobaths of the shelf surface at a high angle, then oscillations of the water column may result, but there is little net displacement of water. However, when the trajectory and scale of the storm are such that for a period it rests in the Middle Atlantic Bight so that the isobars parallel the isobaths, then strong sustained coupling of wind and water flow results. The winds blow along the isobars, down the arc of the Middle Atlantic Bight. Landward Ekman transport of surface water causes 40 to 60 cm of coastal setup and results in a south-

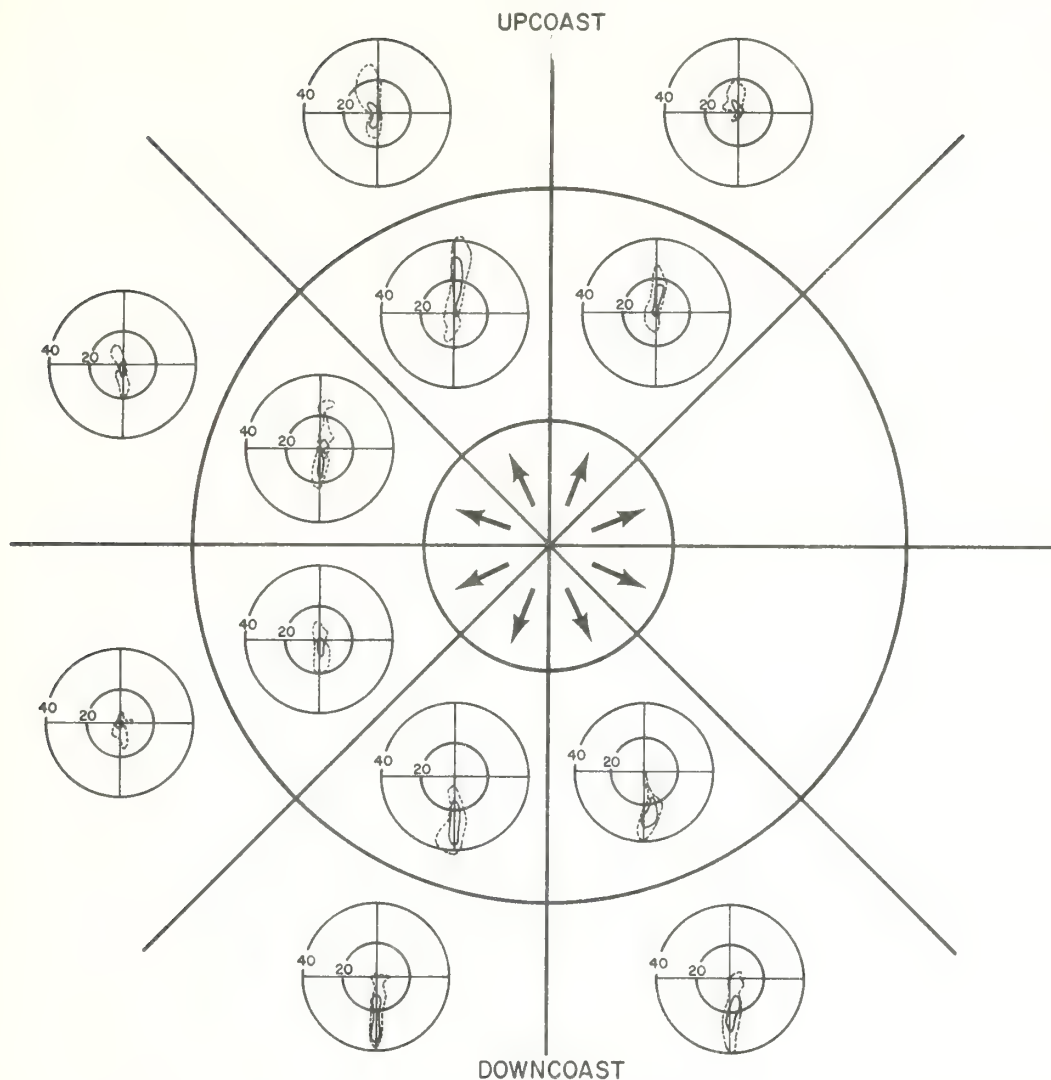


Fig. 16. Polar histograms of hourly averaged, de-tided summer currents in cm/s in the vicinity of Beach Haven Ridge, New Jersey. Only flows associated with winds over 5 m/s are shown. Prevailing wind is indicated by location of histogram on page with wind direction shown in center. Inner ring of histograms is for near-surface measurements, outer ring is for near-bottom measurements. Directions of winds and currents are indicated with top of page representing upcoast motion ( $036^\circ$  true). Histograms are omitted if fewer than 35 h of data were found for specified wind condition. Solid contours enclose 50% and dashed contours enclose 90% of data. (Adapted from EG&G Environ. Consult. 1975.)

ward geostrophic transport of the shelf water column that is coherent and slablike. Boicourt and Hacker (1976) described a similar period of southward storm flow on the Virginia coast with sustained middepth velocities of 30–50 cm/s. Both sets of investigators noted a marked asymmetry in the hydraulic climate, whereby southwest storm

flows tend to be noticeably more intense than northeast flows.

It is clear from the preceding discussion that the role of storm-driven currents in mediating the coastal sand budget requires additional study. We need to know more about the frequency of southwestward storm flows and their velocity structure. We



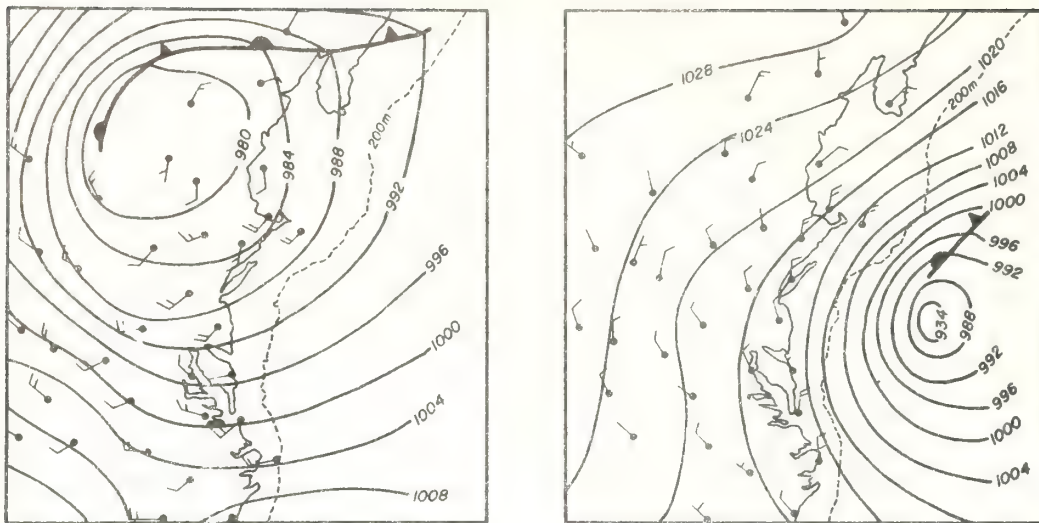


Fig. 17. Surface weather maps for 18 and 22 March 1974. Only the second storm produced sustained coupling between wind and water flow. (From Beardsley and Butman 1974.)

must also learn to design experiments that will resolve perturbations of flow that build and maintain ridge systems.

**Sand transport and storage at New York Harbor mouth**—Major sections of the New York–New Jersey shelf have been shaped by the tidal regimes associated with estuary mouths during the postglacial rise of sea level. Sand budgets of estuary mouths are also of great interest to environmental managers; the Atlantic coast estuaries are the approaches to the major coast ports and require repeated costly dredging. At present, the only estuary mouth subjected to systematic study is that of Chesapeake Bay (Ludwick 1972, 1974, in press). However, reconnaissance data are available for the Hudson estuary mouth, which suggest directions for further study.

New York Harbor mouth is clearly a sink for the littoral drift of the Long Island and New Jersey coasts. Within the past century, much of the deposition has occurred on the ends of Rockaway and Sandy Hook spits; these features have grown rapidly, nearly closing off the harbor mouth within historic times (Shepard and Wanless 1971). However, it appears that much sand has bypassed the spits; a complex system of sand banks separated by interdigitating ebb

and flood channels lies between them (Fig. 18). A profile of velocity residual to the semidiurnal tidal cycle gives some indication of the flow structure responsible for

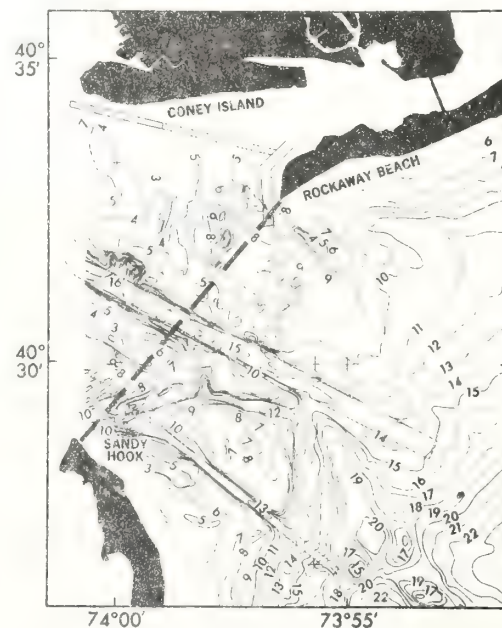


Fig. 18. Bathymetry of the New York Harbor mouth, from a 1973 NOAA/AOML survey. Depth in meters. Dashed line indicates profile of Fig. 19.

bank-channel topography (Fig. 19). The characteristic estuarine two-layer flow is present as indicated schematically in Fig. 19B. The less saline upper water has a residual seaward flow, and the more saline lower water has a residual landward flow. As a consequence of the Coriolis effect, the interface is tilted so that the east side of the harbor mouth is flood dominated while the upper level of the west side is ebb dominated. The distribution of isovels in Fig. 19A suggests that this basic pattern has been modified by the frictional retardation of the tidal wave in the shallow estuary and the resulting phase lag (Swift and Ludwick

in press). Because of retardation, there is a brief period during the tidal cycle when the estuary tide is still ebbing through the central channel while the shelf tide has already turned and is flooding on either side of the ebb tidal jet. This flow pattern, integrated over the tidal cycle, results in greater ebb than flood discharge in the central channel (ebb dominance) and greater flood than ebb discharge in the marginal zones (flood dominance; Fig. 19C). It is probably because of this lag-induced flow interpenetration that the Sandy Hook Channel is not completely ebb dominated as required by the two-layer,

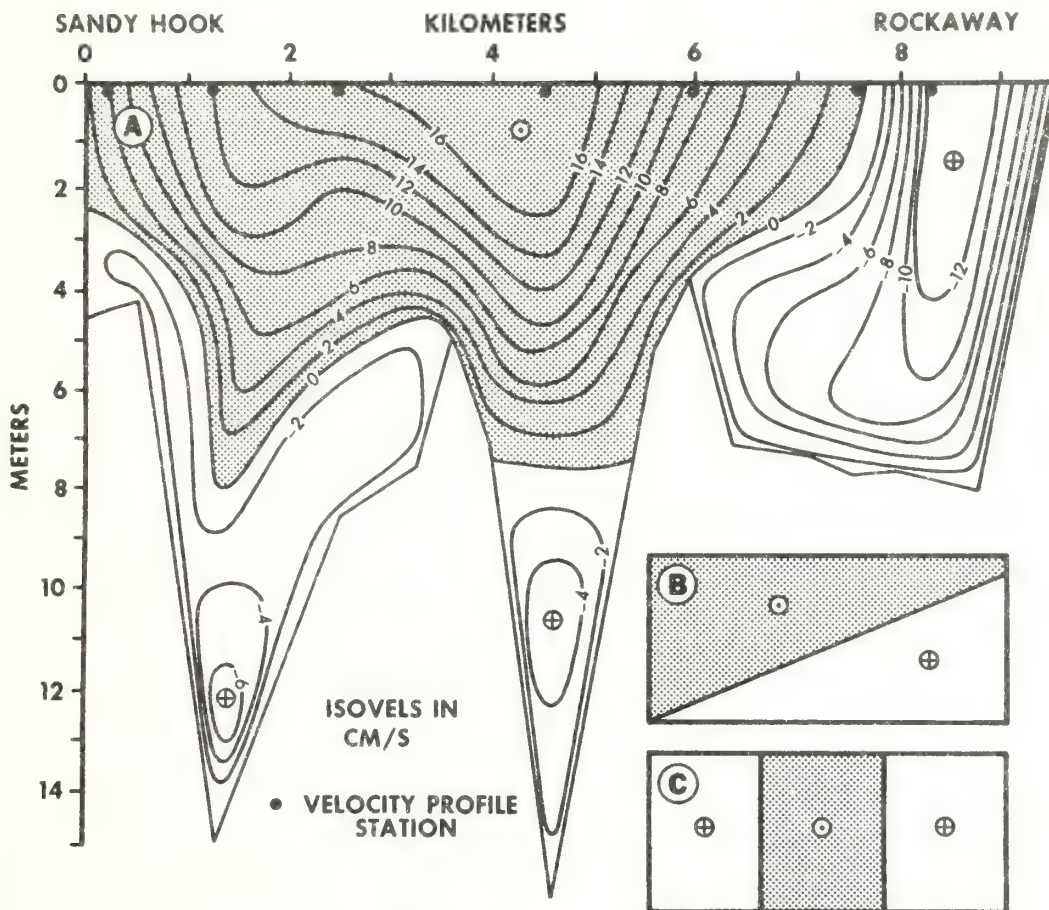


Fig. 19. A—Profile across the Hudson estuary mouth (mouth of New York Harbor), contoured for velocity residual to the semidiurnal cycle. Pattern is interpreted as a resultant response to component patterns shown in B and C. B—Schematic diagram of two-layered, density-driven estuary flow. C—Schematic diagram of pattern resulting from phase lag of the tidal wave. (Modified from data of Kao 1975; reprinted from Duedall et al. in press by permission of *Estuarine and Coastal Marine Science*.)



estuarine component of flow but is flood dominated near the channel floor (Fig. 19A). The two sand ridges that separate the three channels are presumably built by this pattern of flow dominance. Residual flow on the opposite sides of a given sand ridge will have the opposite sense; each ridge is therefore a sand circulation cell or closed loop in the sand transport pattern.

Here perhaps are the ultimate sinks in the littoral sand transport pattern of the New York Bight. Efficient maintenance of the dredged shipping channels demands verification of this inferred pattern of flow dominance and careful analysis of the resulting sand budget.

### References

- BAGNOLD, R. A. 1963. Mechanism of marine sedimentation, p. 507-528. *In* M. N. Hill [ed.], *The sea*, v. 3. Interscience.
- BAYLOR, E. R. 1973. Final report of the oceanographic and biological study for Southwest Sever District No. 3, Suffolk County, New York. Rep. for Bowe Walsh Assoc. by Mar. Sci. Res. Center. SUNY, Stony Brook.
- BEARDSLEY, R. C., AND B. BUTMAN. 1974. Circulation on the New England continental shelf: Response to strong winter storms. *Geophys. Res. Lett.* 1: 181-184.
- BOICOURT, W. C., AND P. W. HACKER. 1976. Circulation on the Atlantic continental shelf of the United States, Cape May to Cape Hatteras. *Mem. Soc. R. Sci. Liege Ser. 6* 10: 187-200.
- BOWEN, A. J. 1969. The generation of longshore currents on a plane beach. *J. Mar. Res.* 27: 206-215.
- BRUNN, P. 1962. Sealevel rise as a cause of shore erosion. *J. Waterways Harbors Div. Am. Soc. Civ. Eng. Proc.* 88: 117-130.
- DEALTERIS, J. T., J. R. RONEY, L. E. STAHL, AND C. CARR. *In press*. A sediment transport study, offshore New Jersey. *Am. Soc. Civ. Eng. Spec. Conf.*, Jun 1975.
- DONAHUE, J. G., R. C. ALLEN, AND B. C. HEEZEN. 1966. Sediment size distribution profile on the continental shelf off New Jersey. *Sedimentology* 7: 155-159.
- DUANE, D. B., M. E. FIELD, E. P. MIESBERGER, D. J. SWIFT, AND S. J. WILLIAMS. 1972. Linear shoals on the Atlantic continental shelf, Florida to Long Island, p. 447-498. *In* D. J. Swift et al. [eds.], *Shelf sediment transport: Process and pattern*. Dowden, Hutchinson & Ross.
- DUEDALL, I., H. B. O'CONNORS, J. B. PARKER, R. WILSON, W. MILOSKI, AND G. HULSE. *In press*. The abundance, distribution, and flux of nutrients and chlorophyll *a* in the New York Bight apex. *Estuarine Coastal Mar. Sci.*
- EG&G ENVIRONMENTAL CONSULTANTS. 1975. Forecasting power plant effects on the coastal zone. EG&G, Waltham, Mass. 335 p.
- EMERY, K. O., AND E. UCHUPI. 1972. Western North Atlantic Ocean: Topography, rocks, structure, water, life, and sediments. *Am. Assoc. Pet. Geol. Mem.* 17.
- FISCHER, A. G. 1961. Stratigraphic record of transgressing seas in the light of sedimentation on the Atlantic coast of New Jersey. *Am. Assoc. Pet. Geol. Bull.* 45: 1656-1660.
- GRAF, W. H. 1971. *Hydraulics of sediment transport*. McGraw-Hill.
- HARRIS, R. L. 1954. Restudy of test shore nourishment by offshore deposition of sand, Long Branch, New Jersey. Beach Erosion Board Tech. Memo. 62.
- KAO, A. 1975. A study of the current structure in the Sandy Hook-Rockaway Point transect. M.S. Res. Pap., Mar. Sci. Res. Center. SUNY, Stony Brook.
- KENNEDY, J. F. 1969. The formation of sediment ripples, dunes, and antidunes. *Annu. Rev. Fluid Mech.* 1: 147-168.
- KIM, J. H., AND W. S. GARDNER. 1974. Geomarine investigation. Final design study wastewater ocean outfalls. Ocean Co. Sewerage Authority, Ocean Co., N.J.
- LAVELLE, J. W., AND OTHERS. *In press*. Preliminary results of coincident current meter and sediment transport observations for wintertime conditions on the Long Island inner shelf. *Geophys. Res. Lett.*
- LUDWICK, J. C. 1972. Migration of tidal sandwaves in Chesapeake Bay entrance, p. 377-410. *In* D. J. Swift et al. [eds.], *Shelf sediment transport: Process and pattern*. Dowden, Hutchinson & Ross.
- . 1974. Tidal currents and zig-zag sand shoals in a wide estuary entrance. *Geol. Soc. Am. Bull.* 85: 717-726.
- . *In press*. Tidal currents, sediment transport, and sandbanks in Chesapeake Bay entrance, Virginia. *Proc. Int. Estuarine Conf.*, 2nd, Myrtle Beach, S.C., Oct 1973.
- MURRAY, S. P. 1975. Trajectories and speeds of wind-driven currents near the coast. *J. Phys. Oceanogr.* 5: 347-360.
- SANDERS, J. E., AND N. KUMAR. 1975. Evidence of shoreface retreat and in-place "drowning" during Holocene submergence of barriers, shelf off Fire Island, New York. *Geol. Soc. Am. Bull.* 86: 65-76.
- SHEPARD, F. P., AND H. R. WANLESS. 1971. *Our changing shorelines*. McGraw-Hill.
- SHERIDAN, R. E., C. E. DILL, JR., AND J. C. KRAFT. 1974. Holocene sedimentary environment of the Atlantic inner shelf off Delaware. *Geol. Soc. Am. Bull.* 85: 1319-1328.
- SONU, C. J., AND J. L. VAN BEEK. 1971. System-



- atic beach changes on the Outer Banks, North Carolina. *J. Geol.* **79**: 416-425.
- STAHL, L., J. KOCZAN, AND D. J. SWIFT. 1974. Anatomy of a shoreface-connected sand ridge on the New Jersey shelf: Implications for the genesis of the shelf surficial sand sheet. *Geology* **2**: 117-120.
- STERNBERG, R. W. 1972. Predicting initial motion and bedload transport of sediment in the marine environment, p. 61-82. *In* D. J. Swift et al. [eds.], *Shelf sediment transport: Process and pattern*. Dowden, Hutchinson & Ross.
- STUBBLEFIELD, W. L., J. W. LAVELLE, T. F. MCKINNEY, AND D. J. SWIFT. 1974. Sediment response to the present hydraulic regime on the central New Jersey shelf. *J. Sediment. Petrol.* **45**: 337-358.
- SWIFT, D. J. 1973. Delaware Shelf Valley: Estuary retreat path, not drowned river valley. *Geol. Soc. Am. Bull.* **84**: 2743-2748.
- , D. B. DUANE, AND T. F. MCKINNEY. 1974. Ridge and swale topography of the Middle Atlantic Bight: Secular response to Holocene hydraulic regime. *Mar. Geol.* **15**: 227-247.
- , J. W. KOFOED, F. P. SAULSBURY, AND P. SEARS. 1972. Holocene evolution of the shelf surface, central and southern shelf of North America, p. 499-574. *In* D. J. Swift et al. [eds.], *Shelf sediment transport: Process and pattern*. Dowden, Hutchinson & Ross.
- , AND J. C. LUDWICK. *In press*. Substrate response to hydraulic process: Grain size frequency distributions and bedforms. *In* D. J. Stanley and D. J. Swift [eds.], *Marine sediment transport and environmental management*. Wiley-Interscience.
- , AND P. SEARS. 1974. Estuarine and littoral depositional patterns in the surficial sand sheet, central and southern Atlantic shelf of North America. *Inst. Geol. Bassin Aquitaine Mem.* **7**, p. 171-189.
- VEATCH, A. G., AND P. A. SMITH. 1939. Atlantic submarine valleys of the United States and the Congo submarine valley. *Geol. Soc. Am. Spec. Pap.* **7**. 101 p.

## HOLOCENE EVOLUTION OF THE INNER SHELF OF SOUTHERN VIRGINIA<sup>1</sup>

DONALD J. P. SWIFT AND TERRY NELSEN

Atlantic Oceanographic and Meteorological Laboratories, NOAA, Miami, FL 33149

JOHN MCHONE

Department of Geology, University of Illinois, Urbana, IL 61801

BARRY HOLLIDAY

Waterways Experimental Station, U.S. Army Corps of Engineers, Vicksburg, MS 39180

HAROLD PALMER

Dames and Moore, Inc., Suite 700, 7101 Wisconsin Avenue, Washington, DC 20014

GERALD SHIDELER

U.S. Geological Survey, Box 6732, Corpus Christi, TX 78411

**ABSTRACT:** The southern Virginia shelf is traversed by a shelf valley which may constitute the retreat path of the ancestral James River during the late Holocene sea level rise. It is flanked by levee-like margins (shoal-retreat massifs) which are the retreat paths of littoral drift depositional centers that were maintained on the sides of the retreating estuary mouth.

This transgressive nearshore marine topography has been heavily modified as Holocene sea level rise has continued; the water column has deepened, and the shoreline has receded. Strong south-trending currents associated with "northeaster" storms have redistributed the surficial sand. They have impressed patterns of transverse sand waves, current-parallel lineations, and large-scale, nearly current-parallel sand ridges.

The sand ridges are a variety of large-scale bedform whose genesis is still not adequately understood. The ridges on the Virginia Beach Massif appear to have been incised into the massif as successive segments became exposed to open shelf flows, while the False Cape ridges appear to have formed by a somewhat different scheme of ridge growth and detachment during erosional retreat of the shoreface. However, both ridge sets have a number of significant characteristics in common. Trough talwegs and crestlines climb to the south in both sets. Both sets make northward-opening angles of 20-35° with the shoreline. For both sets the landward flanks are more coarse grained and more gently inclined than the seaward flanks, perhaps as a consequence of a cross-ridge component of flow. The same or very similar hydraulic mechanisms appear to have been involved in their respective schemes of formation.

### INTRODUCTION

The floor of the inner continental shelf of Virginia (Fig. 1) contains classic examples of the morphologic patterns seen at many other places in the Middle Atlantic Bight (Swift et al., 1972b), including a shelf valley, shoal retreat massif, and a set of shoreface-connected ridges. We present observations on the character of the substrate, gained by bathymetric measurements, grab sampling, vibracoring, sidescan sonar profiling, and limited flow observations. We infer from these observations the mode of formation of these morphologic elements during the Holocene transgression

and their subsequent modification in response to the Holocene hydraulic regime.

Metric units will be used in this report except in maps based on National Ocean Survey data. The manpower requirement for recontouring the smooth sheets for these maps in metric units is prohibitive. When these maps are discussed in the text, both metric and English units will be reported.

### BATHYMETRY

The Virginia Inner Shelf south of Cape Henry is a gently undulating sand plain characterized by north-south-trending sand ridges with up to 10 m of relief. This topography extends 15 km seaward from the beach toward a well-defined, southwest-trending

<sup>1</sup> Manuscript received October 22, 1976; revised March 16, 1977.

scarp whose toe lies at 43 m (141 ft); see Figs. 1 and 2. A more steeply dipping shoreface lies between the beach and the inner shelf proper, from which it is separated by the 21-m (70-ft) isobath. In the south, the shoreface bears a series of sand ridges which trend obliquely across it, converging with the beach toward the south. Toward the north the shoreface becomes wider and more gently inclined as the mouth of Chesapeake Bay is approached. The most prominent feature of the shelf floor is a broad, poorly defined shelf valley (Virginia Beach Valley) that trends west across the southern margin of the study area, then northwest. The valley is bordered on the north by an east-west-trending topographic high, which is segmented into north-south-trending ridges and swales (Figs. 2, 3). This feature will be referred to as the Virginia Beach Massif (massif in the sense of a compound topographic high consisting of smaller scale highs; Swift, 1972, 1973).

Ridge crests on the massif climb toward the south. Trough axes also climb toward the south, passing through low saddles before dropping abruptly into the shelf valley (the reverse trough in the "Z"-shaped ridge of Fig. 3 is an exception). The ridges tend to have the outline of isosceles triangles with northward-facing apices. As a consequence, the massif has a comblike pattern in plan view, with "teeth" generally extending from the spine of the massif toward the north. South of the shelf valley at False Cape, a series of sand ridges trends obliquely northeast across the shoreface (Swift et al., 1972). Ridge crestlines and trough axes of the False Cape ridges also rise to the south, and the shelf valley between the two massifs therefore does not constitute an axis of symmetry (Swift et al., 1972b, p. 534-537).

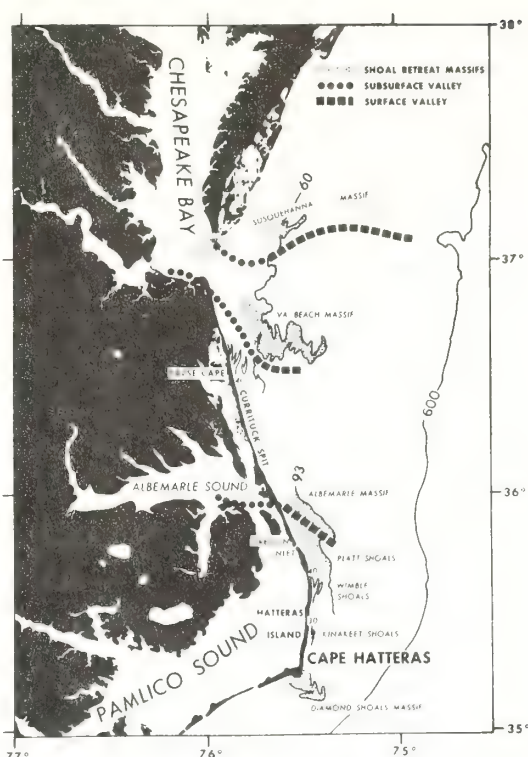


FIG. 1.—Chesapeake Bight of the Atlantic continental shelf showing major morphologic elements. Data for subsurface channels on the inner Virginia shelf from Harrison et al., 1965; Meisburger, 1972. From Swift, 1975. Depths in feet.

#### STRATIGRAPHY

The stratigraphy of this region has been interpreted by means of vibracores, seismic profiles, and radiocarbon dates (see also Swift et al., 1972a; Shideler et al., 1972). The results are presented as Figs. 4 and 5. An early Wisconsinan unit (unit B, Fig. 5) has a radiocarbon age of greater than 37,000 yr (Table 1).

TABLE 1.—Radiocarbon dates from the inner Virginia shelf (Geochron Laboratories)

Number	Locality	Location		Depth (m)	Age	Unit
		N	W			
RCZ1	Z Ridge	36°38.5'	75°39.6'	27	29,800 ± 3,000 — 2,000	C
RCZ2	Z Ridge	36°38.5'	75°39.6'	22	495 ± 100	D1
RCZ5	Z Ridge	36°38.5'	75°39.6'	23	1,595 ± 115	D1
RCZ7	Z Ridge	36°38.5'	75°38.1'	24	2,300 ± 160	D1
RCF1	False Cape	36°32.8'	75°44.8'	15	20,400 ± 840	C?
RCF2	False Cape	36°32.8'	75°48.0'	19	4,220 ± 140	D
RCF3	False Cape	36°32.8'	75°45.5'	21	25,700 ± 800	C



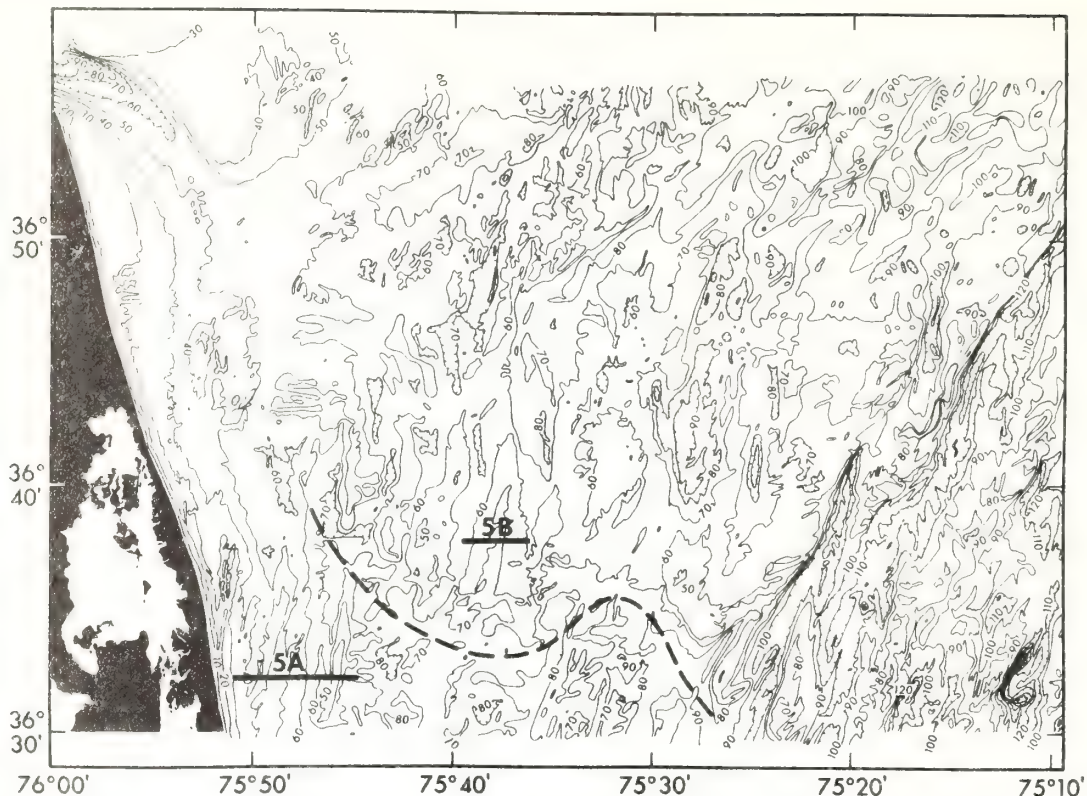


FIG. 2.—Bathymetry of the inner shelf of southern Virginia with locations for Figs. 5, 6, and 7. From Payne, 1970. Contours in feet. Dots and bars are locations of other figures. Dashed line indicates axis of Virginia Shelf Valley.

Vibracores reveal a fine-grained muddy sand; seismic profiles indicate that its stratification tends to be lenticular with prominent channeling. The unit appears to consist of both fluvial and nearshore deposits.

The overlying unit (unit C) has a radiocarbon age ranging from  $29,800 \pm 800$  yr to possibly as young as  $20,400 \pm 850$  yr (Table 1). Vibracores penetrating this unit reveal laminae and thin beds of muddy sand and sandy mud. Seismic profiles indicate a relatively uniform, continuous stratification. The unit appears to represent a regressive nearshore sequence deposited at the end of the mid-Wisconsinan interstadial.

The youngest unit (unit D, Fig. 5) is a discontinuous sheet of fine to coarse-grained sand that is molded into the sand ridge topography seen in Figs. 2 and 3. Locally, in the axis of some troughs, it thins to a few centimeters of shelly gravel overlying unit C (Swift et al., 1971, fig. 9; Shideler et al., 1972, fig. 9).

Numerous cores have been collected from this basal gravel by Powers and Kinsman, 1953. They have interpreted it as a product of the liquefaction and size sorting of seafloor sediment by storm waves. However, the regional stratigraphic relationships outlined in this paper suggest that the basal gravel is more reasonably explained as a lag deposit, formed during the erosional retreat of the shoreface (Swift, 1976, p. 265–268).

This three-fold stratigraphy may be intermittently resolved on the margins of the Virginia Beach Shelf Valley (Shideler et al., 1972; see Fig. 5B). Within the shelf valley proper, however, multiple, strong, upward-concave reflectors indicate a complex history of scour, channeling, and fill, which is not easily correlated with the deposits on either side (Fig. 4). The Shelf Valley continues to the north as a subsurface channel that passes beneath Cape Henry (Meisburger, 1972) and the Chesapeake Bay Bridge (Harrison et al., 1965).

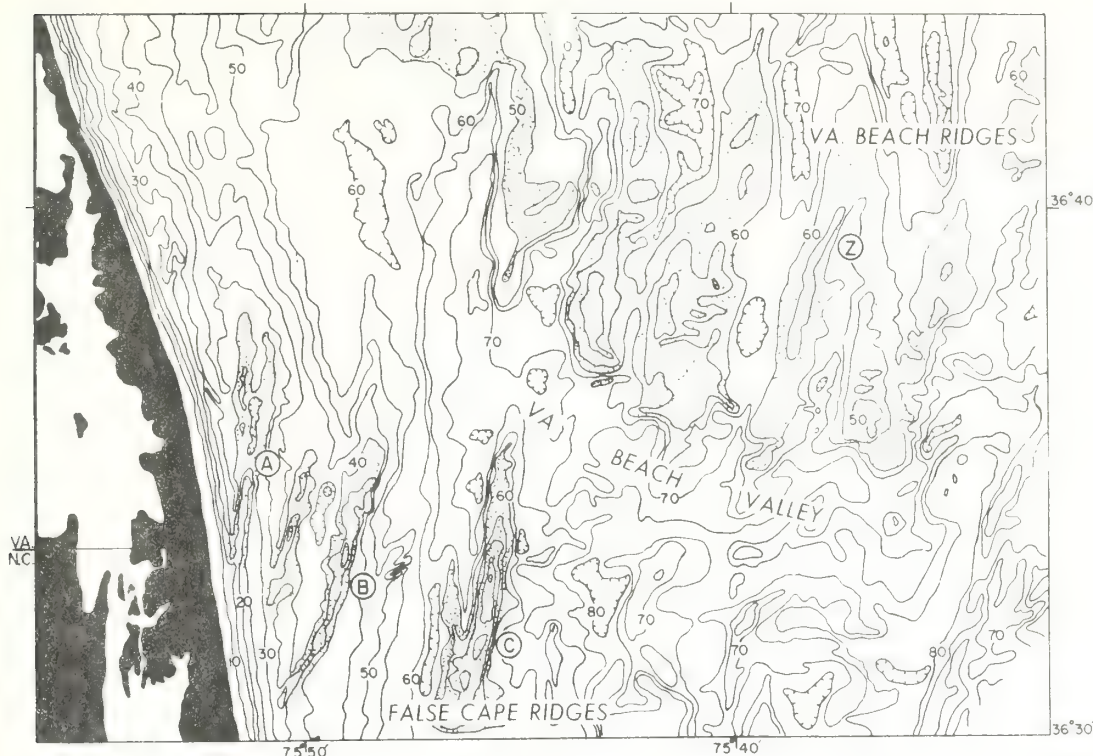


FIG. 3.—Bathymetry of the Virginia Beach Shelf Valley. From Payne, 1970. Contours in feet. Important topographic highs are stippled. Letters refer to ridges discussed in the text.

The data presented above indicate that the Virginia Beach Shelf Valley existed as a landward-transgressing-estuary during the period of Holocene sealevel rise between 20,000 and 4,000 yr ago (Table 1). The Virginia Beach Massif would appear to be a shoal-retreat massif (Swift et al., 1972; Swift, 1973) an elongated cross-shelf high marking the retreat path of the littoral drift depositional center on the northern side of the estuary. The position of the False Cape Massif is appropriate for a shoal-retreat origin; littoral drift on the south sides of modern middle Atlantic estuaries also moves toward the estuary mouth, although not as strongly as does drift on the north side. However, the False Cape Massif can also be explained as a series of shoreface-connected sand ridges whose presence is entirely the consequence of open coast, non-estuarine processes (see later discussion).

The Virginia Beach Shelf Valley complex is morphologically very similar to the Albemarle Shelf Valley complex 110 km to the south (Swift et al., in press).

#### SURFICIAL SEDIMENTS

The distribution of size grades of surficial sediment over the study area is presented in Figs. 6–10. The distribution is complex but may be resolved into two topographically controlled components, a large-scale pattern that reflects the disposition of shelf valley and massifs, and a small-scale pattern that varies with the ridge and swale topography.

In Fig. 6, the large-scale pattern appears as a series of east-west-trending bands; a band of gravel and coarse and medium sand across the top of the map, a band of medium sand along the crest of the Virginia Beach Massif, and a band of fine to very fine sand on the southern slope of the massif and in the shelf valley.

The grab sample net on which Fig. 6 is based is inadequate to resolve fine structure in this pattern of east-west banding. A denser grab sample net from the "Z"-ridge sector of the Virginia Beach Massif (Fig. 7) reveals a uniform grain-size decrease from the medium sand of the massif crest to the fine sand of the shelf valley floor; see also Fig. 8. A denser



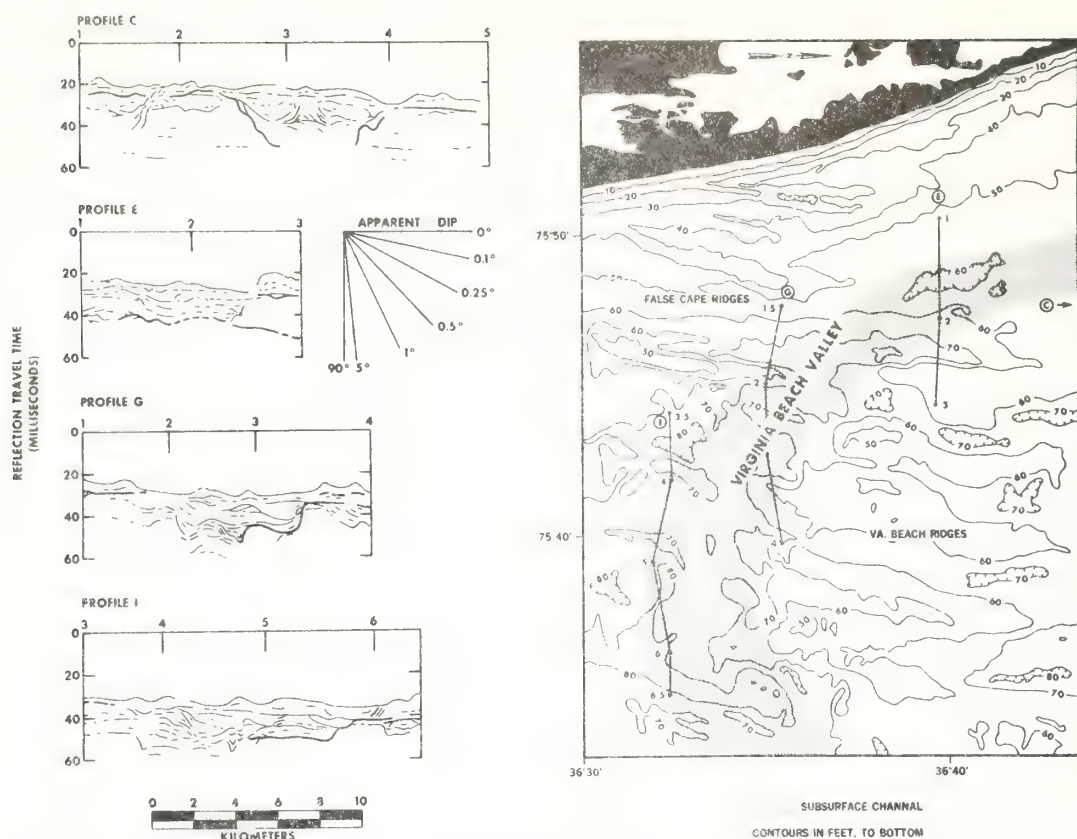


FIG. 4.—Stratigraphy of the Virginia Beach Shelf Valley. Seismic profile data modified from Shideler et al., 1972. North is to the right of the map. Depth is one way travel time.

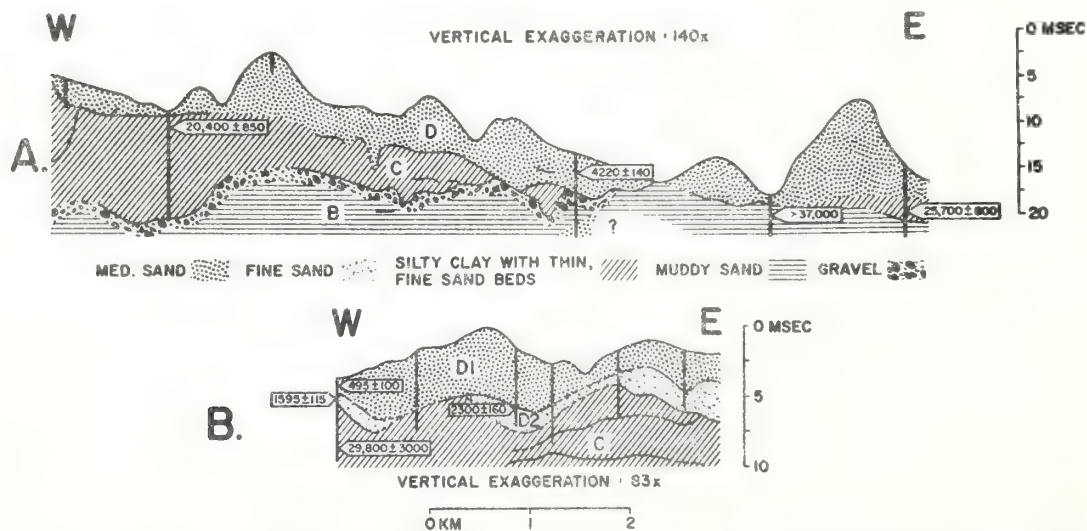


FIG. 5.—Vibracore and seismic profile transects of the False Cape and Virginia Beach ridges. See Fig. 2, positions 5A and 5B, for locations of profiles.



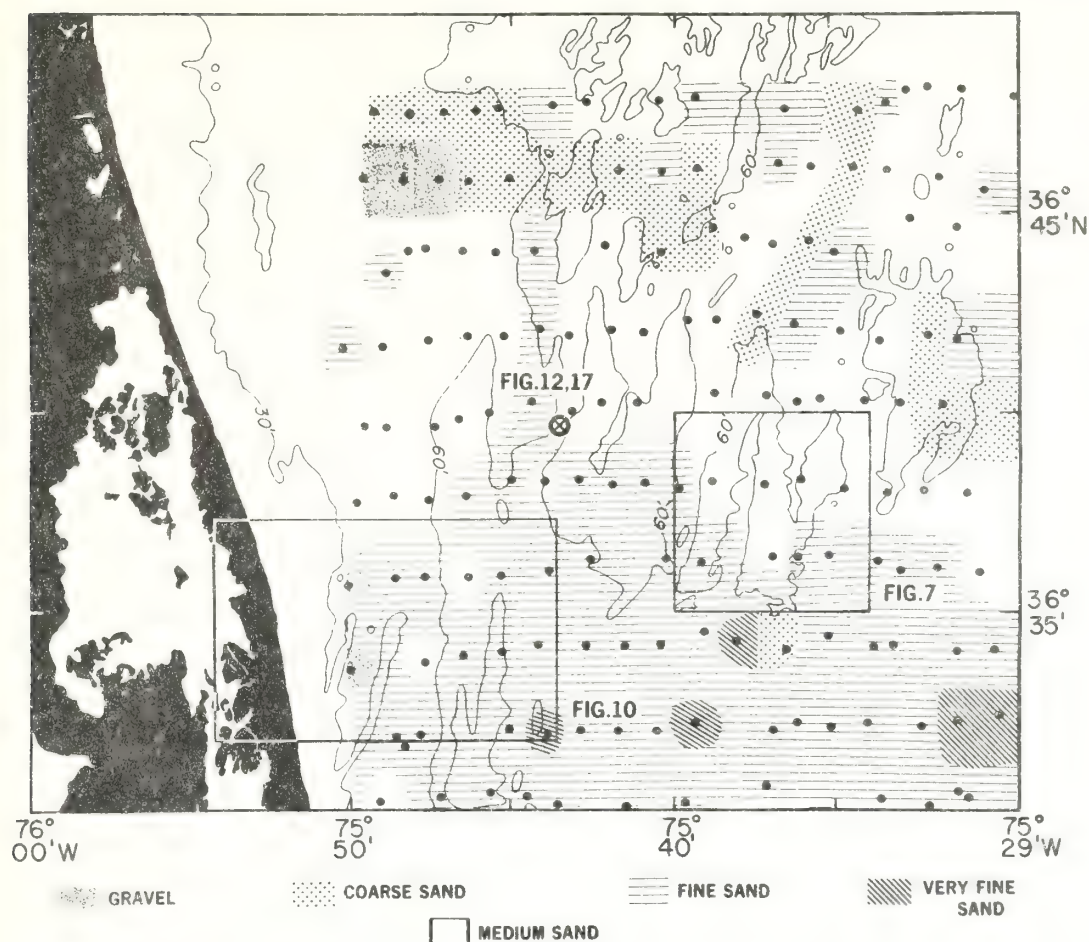


FIG. 6.—Distribution of median diameter of the sand fraction over the study area. Modified from Shideler et al., 1972. Size analyses performed by an automated rapid sediment analyzer (Nelsen, 1974). Boxes indicate locations of Figs. 7 and 10. The locations of Figs. 12 and 17 are also indicated.

grab sample net from the False Cape Massif (Fig. 10) reveals a similar grain-size gradient. Here it occurs mainly in the troughs, which grade from fine to very fine sand toward the south.

The detailed grain-size maps also reveal a smaller scale, north-south banding, superimposed on the coarser pattern of east-west-trending bands. The north-south-trending pattern is controlled by topography; lenses of coarser sand and pebbly, shelly sand lie on trough floors, whereas ridge crests and flanks are composed of medium and fine sand. Some grab samples and cores of this coarser sand contain numerous clay clasts apparently eroded from the underlying substrate. Comparisons of grain size and topographic profiles

across "Z" ridge indicate that even this denser sample net does not fully resolve the pattern of grain-size variation; grain-size values fluctuate erratically from east to west through a range of one phi unit. Smoothing of the grain size profiles by means of a three-point running average (Fig. 9) suggests that coarser sand tends to occur in the trough and on the landward flank of the ridge, and that the finest sand occurs on the seaward flanks. Trough and landward flank sands also appear coarser than seaward flank sands in a profile across "A" ridge in the False Cape sector (Fig. 11), and in sidescan sonar records (see later discussion).

The coarsest sand occurs as elongate patches and ribbons in the troughs near the base of the landward flanks of ridges and lo-

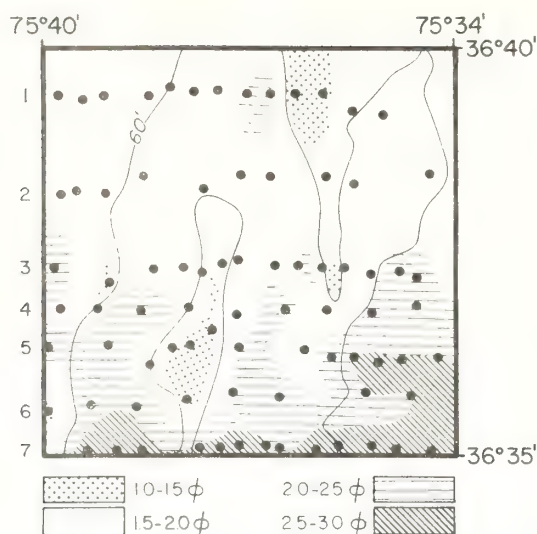


FIG. 7.—Distribution of mean diameter in the "Z"-ridge sector. See Fig. 6 for location. Numbers on left hand margin are transect numbers.

cally extends up the landward flanks (Figs. 10, 11). Scuba dives reveal that in trough axes these coarse patches are centimeters to decimeters thick and are underlaid by a stiff clay surface. Scuba dives also indicate that during the quiet summer months mud lenses may accumulate in the troughs, but these are swept away during the winter months. These elongate coarse patches, observed by scuba divers and by means of grab sampling, are probably the same as the coarse-grained current lineations observed by sidescan sonar (see next section).

#### BEDFORM PATTERNS

Both flow-transverse and flow-parallel bedforms occur in the study area at several scales.

The ubiquitous small-scale flow-transverse bedform in the study area is the wave-generated ripple. Ripple spacings vary from 6 to 100 cm with larger spacings occurring in coarser sands. Scuba dives reveal that during fair weather, rippled surfaces deeper than 15 m may be partially or fully stabilized by the growth of interstitial reddish-brown algae ("rusty bottoms"). In the partially stabilized case, "striped bottoms" occur, in which wave-activated ripple crests appear yellowish-white, while ripple troughs are pigmented by red-brown algae.

Fair-weather ripples at 10 m on the crests of

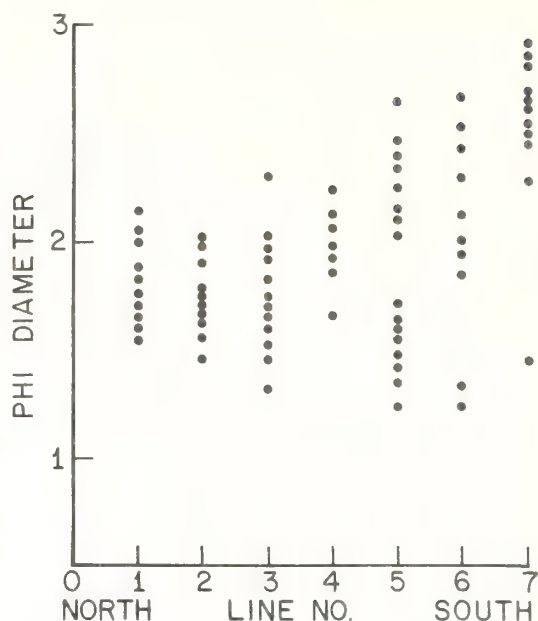


FIG. 8.—Plot of mean diameter of the sand fraction against transect line down the length of "Z" ridge. See Fig. 7 for location of transects.

the False Cape ridges were observed by divers to migrate to the northwest under the impetus of landward-asymmetric wave surge and a northerly near-bottom mean flow of 15 cm/sec. Jackson (1975) has summarized studies indicating that small-scale ripples are responses to flow in the inner boundary layer.

Sand waves with south-facing steeper slopes occur on ridge flanks and in troughs. Sand wave spacings vary from 10 m to 200 m, and sand wave heights vary from 20 cm to 2 m. Several much larger solitary sand waves were observed, one over 5 m high. Two distinct sand-wave populations appear to be present, one with a mean spacing of 10–15 m, and one with a mean spacing of 50 to 200 m. Jackson's (1975) analysis would suggest that the mesoscale sand waves are responses to flow in the turbulent outer boundary layer, while the large-scale features are due to interaction of the whole depth of flow with the bottom.

Mesoscale sand waves (10-m spacing) were observed primarily by divers (Fig. 12). The mesoscale features had rounded crests, and southward-facing, steeper slopes that were inclined at less than the angle of repose. Dark mud 10-cm thick lay in the troughs. The observation was made in July 1971; the sand

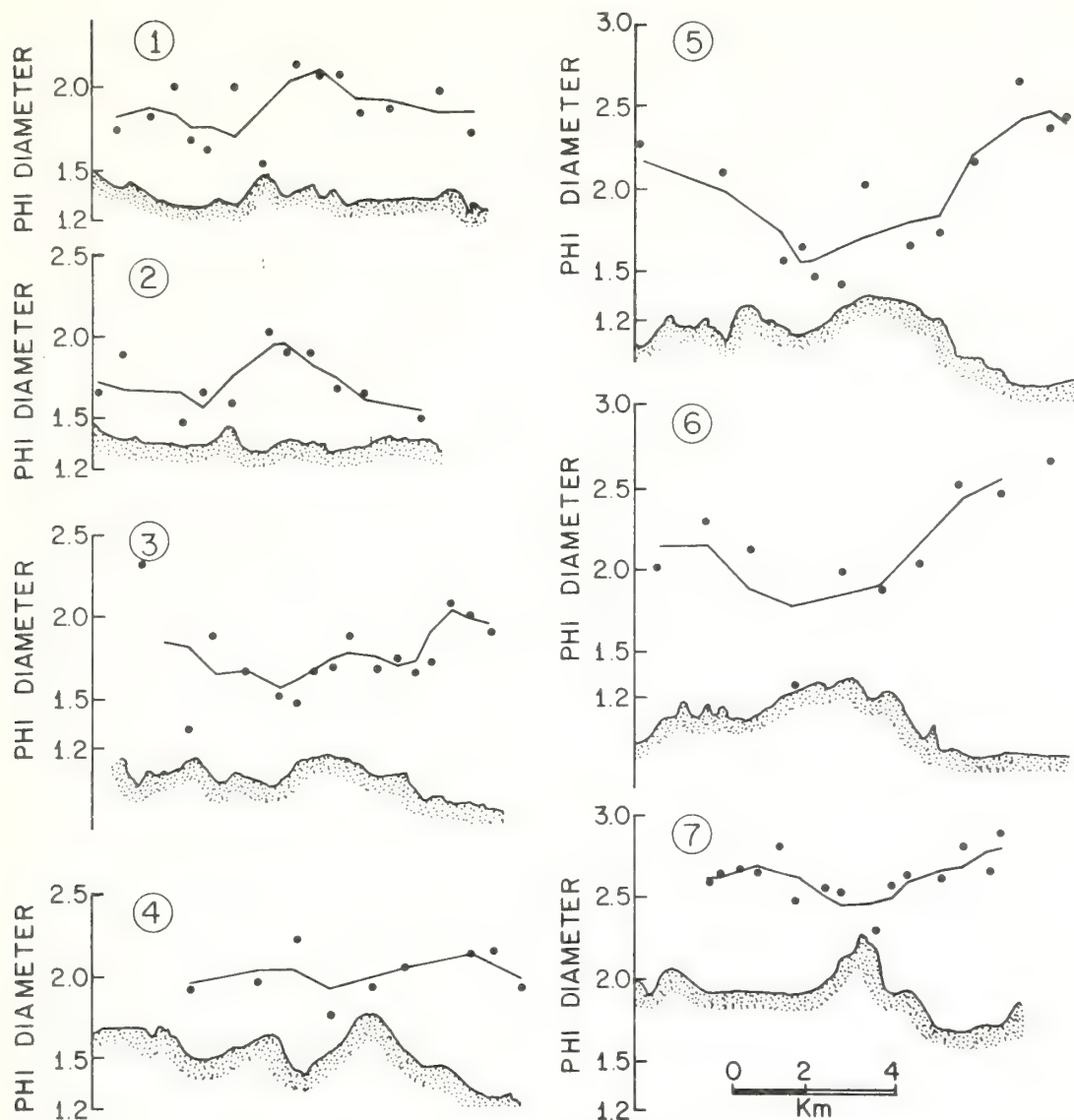


FIG. 9.—Topography and mean diameter across “Z”-ridge transects. Dots are raw data; zig-zag lines are 3-point running averages. See Fig. 7 for location of transects.

waves may have been formed in the intense storm of March 21, 1971. They appeared to have undergone a prolonged period of quiescence after formation, in which crests were rounded by bioturbation and troughs filled with mud.

The large-scale sand waves were observed primarily by means of sidescan sonar and acoustic depth recorder (Figs. 13, 14). Steeper slopes were often inclined at less than the angle of repose. Some of the larger sand

waves appear as perturbations of the 60-ft contour that outlines the “Z”-shaped ridge in the Virginia Beach Massif. Sand waves were oriented with steeper west slopes facing southwest, except in the extreme southwest of the study area where steeper slopes face southeast (Fig. 13). Sand wave orientation suggests a strong southward flow component during peak flow events and in most of the area a weaker offshore component.

Low amplitude, “tongue-like” sand wave



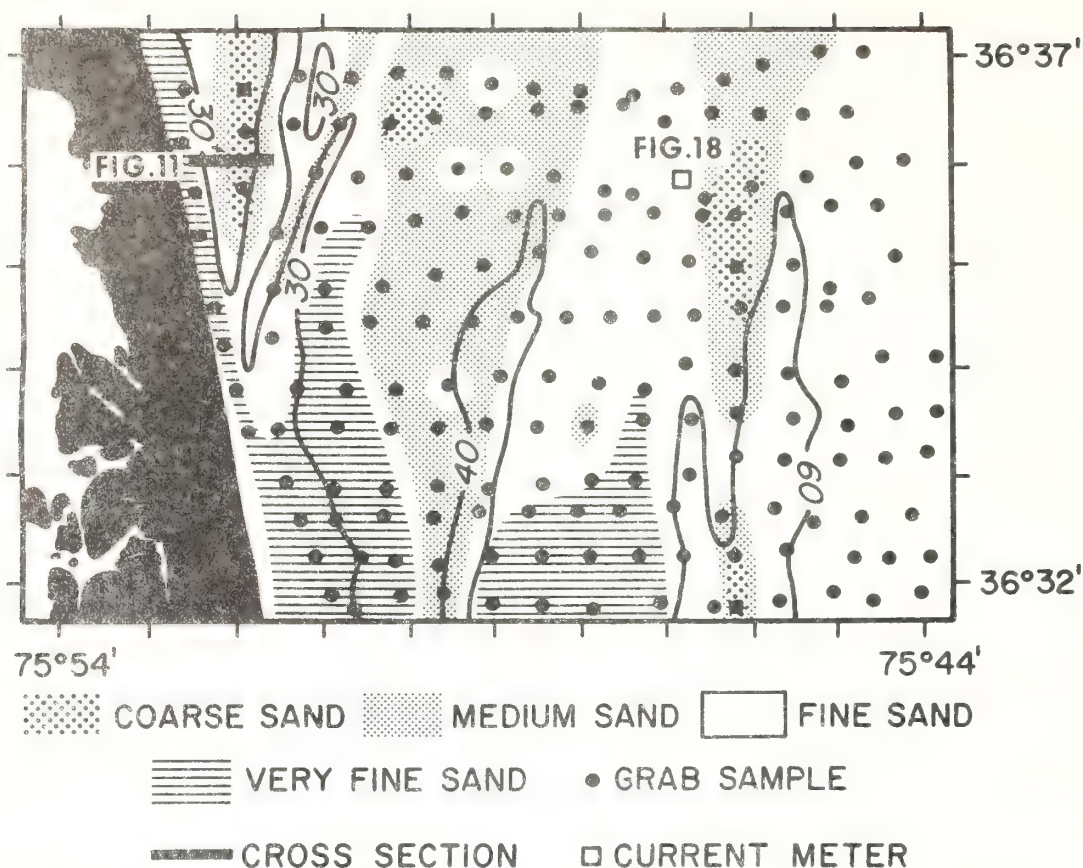


FIG. 10.—Distribution of median diameter of the sand fraction across the False Cape sector. Modified from Swift et al., 1972. Size analyses performed by rapid sediment analyzer (Sanford et al., 1971). Depth in fathoms.

patterns also appear on ridge flanks and crests (Figs. 13, 15B).

Flow-parallel bedforms appear on sidescan sonar records as dark (highly reflective) north-south bands of coarse gravelly sands, fine gravel, or shell hash. The sidescan sonar

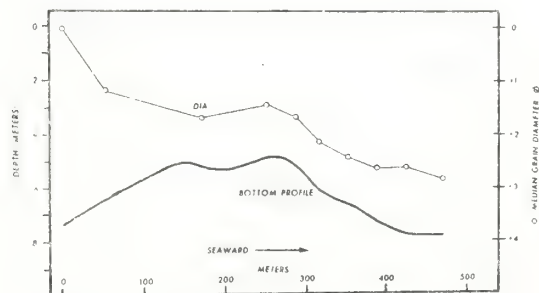


FIG. 11.—Profile of median diameter across "A" ridge. See Fig. 10 for location of profile. Data collected by Leonard Nero. From McHone, 1972.

records suggest that several different kinds of such "current lineations" (McKinney et al., 1974) are present. Sharp, well-defined bands of gravel or gravelly sand are 10 to 400 m wide and up to several km long (Fig. 16). They occur in the troughs between sand ridges. They appear to be linear windows in the Holocene sand sheet, exposing the basal gravel that locally underlies it. These well-defined linear features may be responses to specific near-bottom flow patterns (see later discussion).

Broader, more poorly defined coarse zones are also found in troughs. They tend to occur primarily on the seaward sides of the troughs and may extend up the landward flank of the adjacent ridge (Fig. 15A). Broad zones on the trough floor may be deflation zones where repeated intense flows have removed the surficial sand layer and exposed the basal gravel.

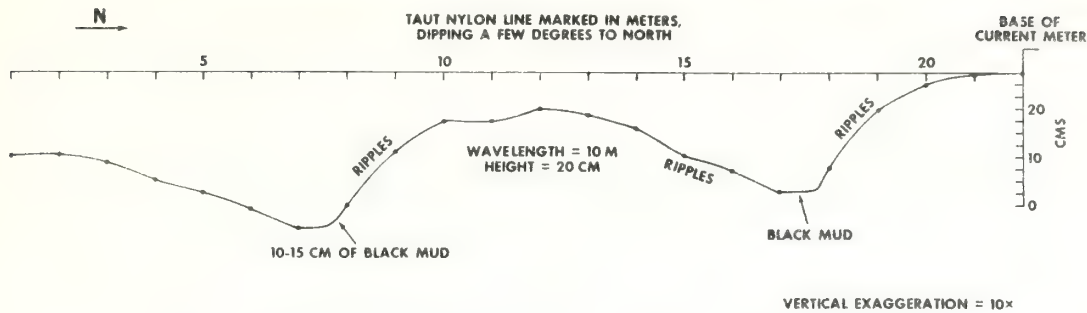


FIG. 12.—Profile of sand waves measured by divers. See Fig. 6 for location.

On the side of a ridge, however, such a zone must be a “perched” deflation zone of fine gravel or coarse sand armoring fine sand, or simply the surface of a relatively thick deposit of coarse material. The tendency for such coarse zones to occur on the landward flank of ridges was observed in grain-size transects (Figs. 9, 11). The relatively erratic fluctuation of mean diameter in the transects of Fig. 9 becomes understandable when the complexity of small-scale grain-size patterns is observed on sidescan sonar (e.g., Fig. 15A).

#### HYDRAULIC CLIMATE AND SUBSTRATE RESPONSE TO FLOW

##### *Offshore Flow*

Flow in the study area tends to be a slow northward drift. Our bottom-mounted Geodyne current meters revealed a mean flow of 10–15 cm/sec as measured within 37 cm of the bottom during two ten-day periods in July and August 1971 (see also Holliday, 1971). The flow was modulated by, but not generally reversed by, the semidiurnal tide. The north-

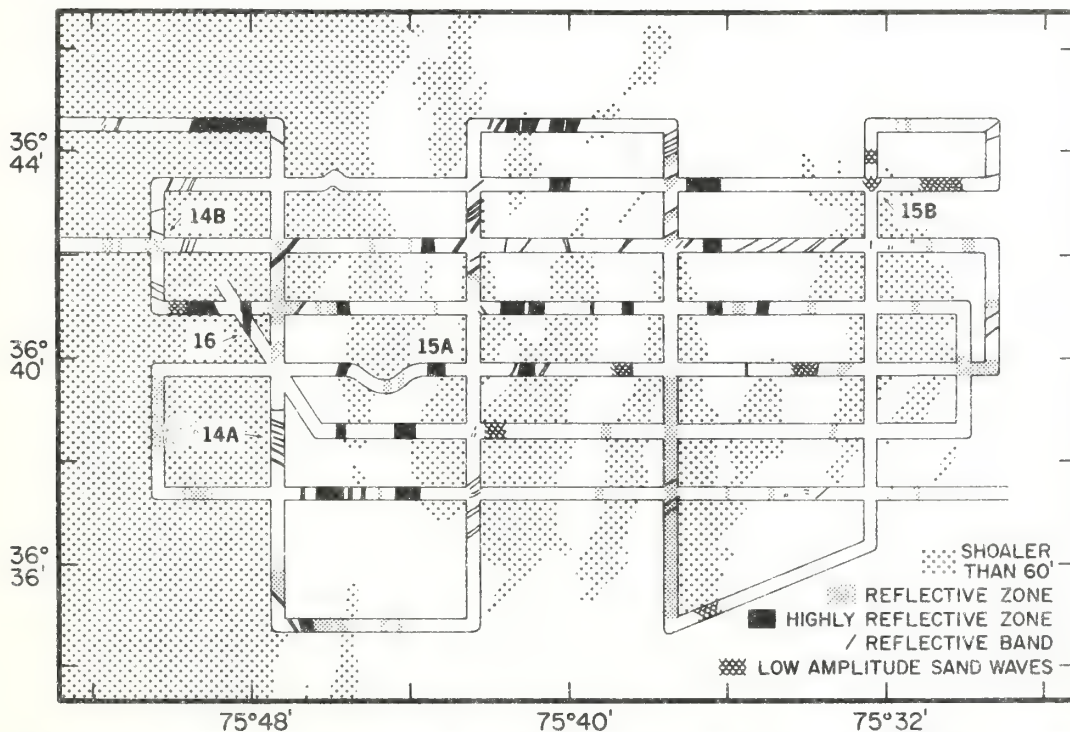


FIG. 13.—Schematic representation of sidescan sonar tracklines across study area. Tracklines are shown 4× actual width for clarity. Navigation was conducted by means of Raydist. Locations of other figures are indicated.

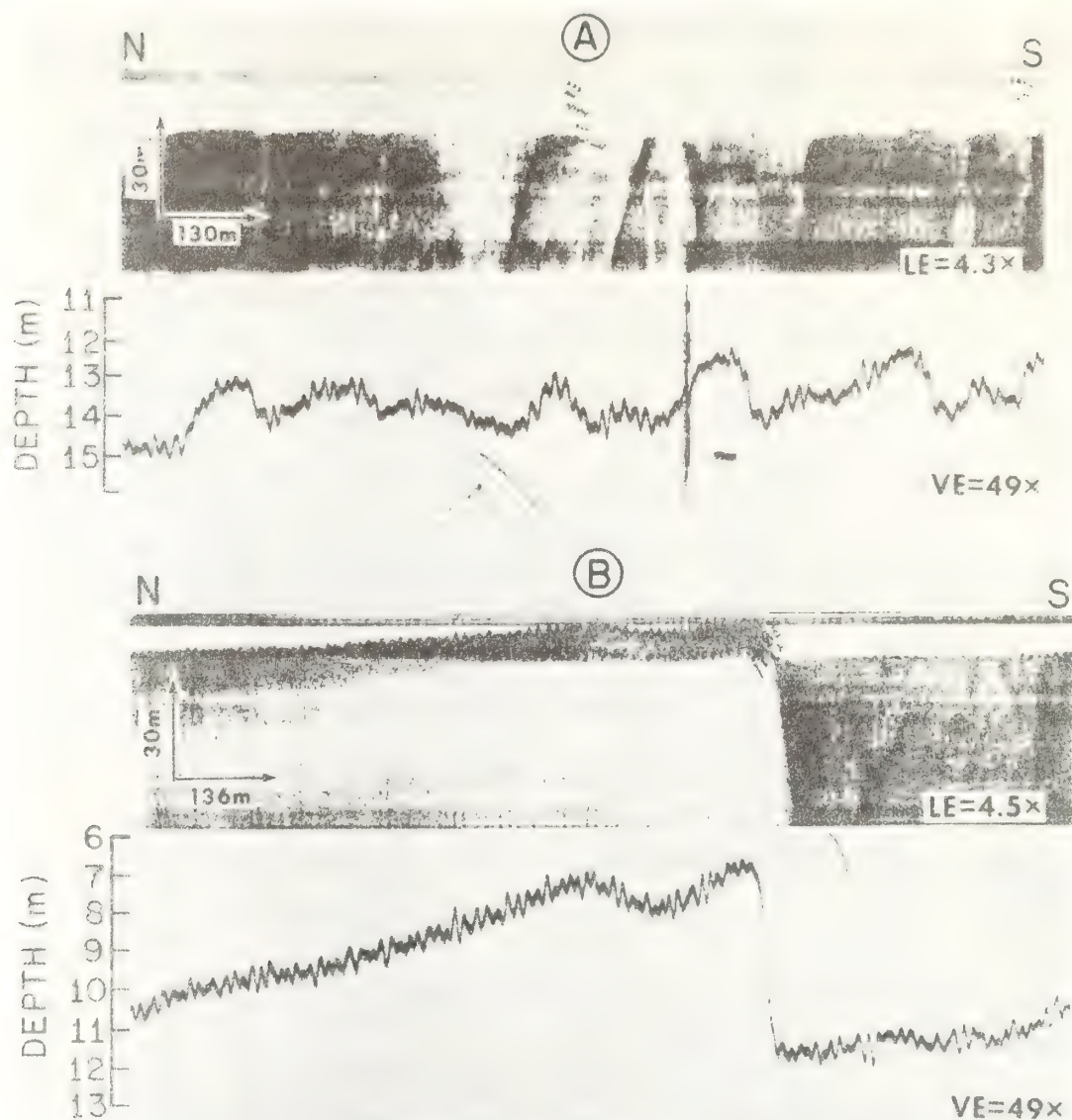


FIG. 14.—Sidescan and bathymetric records of sand waves from study area. See Fig. 13 for location.

ward flow is anomalous with respect to the generally southward flow of the Middle Atlantic Bight and may be part of a density driven circulation associated with the mouth of Chesapeake Bay (Norcross and Stanley, 1967; Bumpus, 1969, 1973). However, during our observations, water motions correlated well in this friction-dominated nearshore regime with southerly winds, lagging (or occasionally leading) wind by up to 6 h (Fig. 17).

During periods of strong winds, more intense flows result. Beardsley and Butman (1974) have noted that the geometry of the Middle Atlantic Bight tends to interact with the geometry of mid-latitude low-pressure systems that move obliquely across it. If the trajectory of the storm is such that the Bight experiences mainly the westerly winds of the storm's southern half, then there may be strong short-term water movements, but little net transport of water.



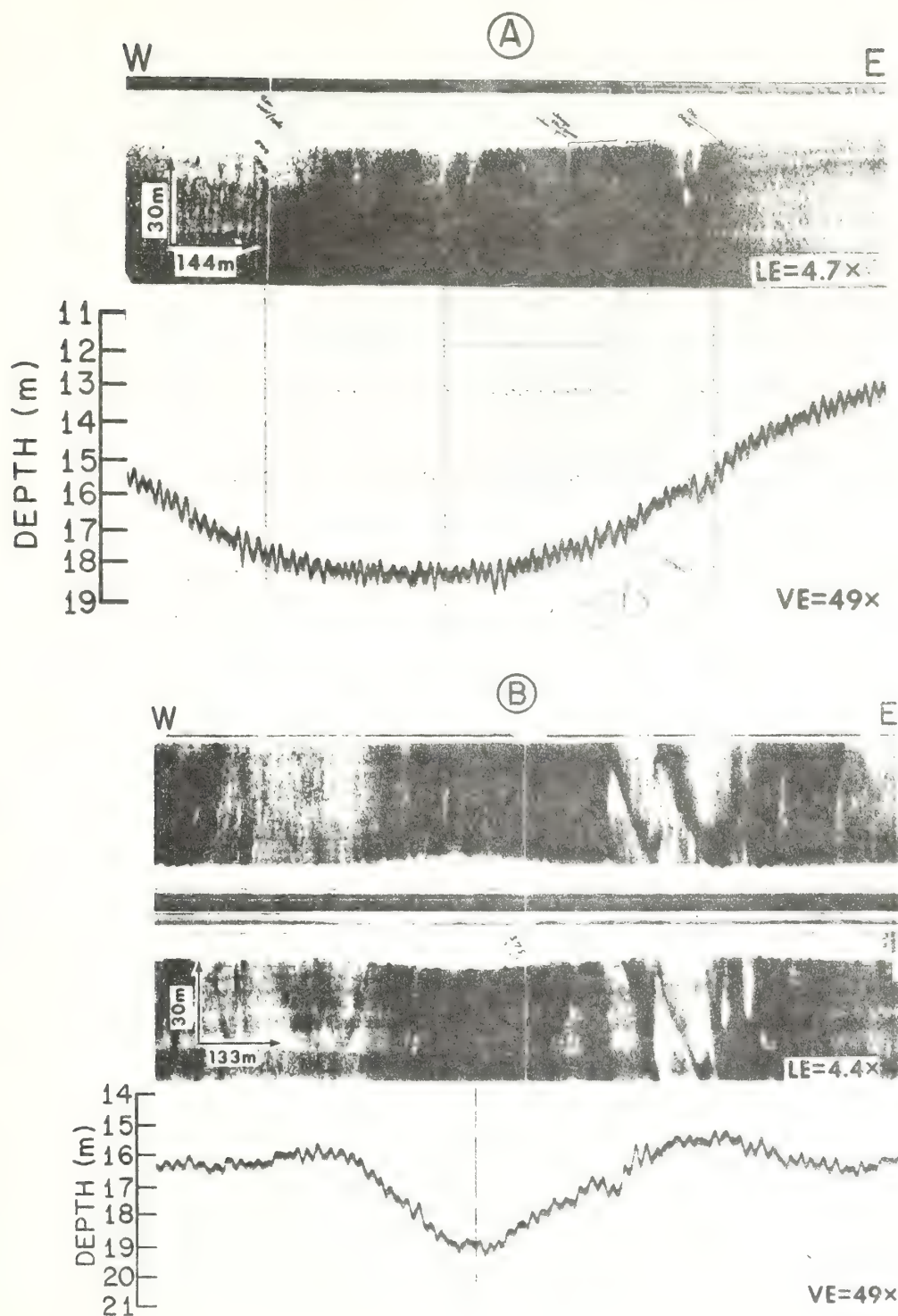


FIG. 15.—A: Sidescan record of deflation zone extending up landward flank of ridge. See Fig. 13 for locations. B: Sidescan and bathymetric records of low amplitude sand-wave-like features from ridge crest.

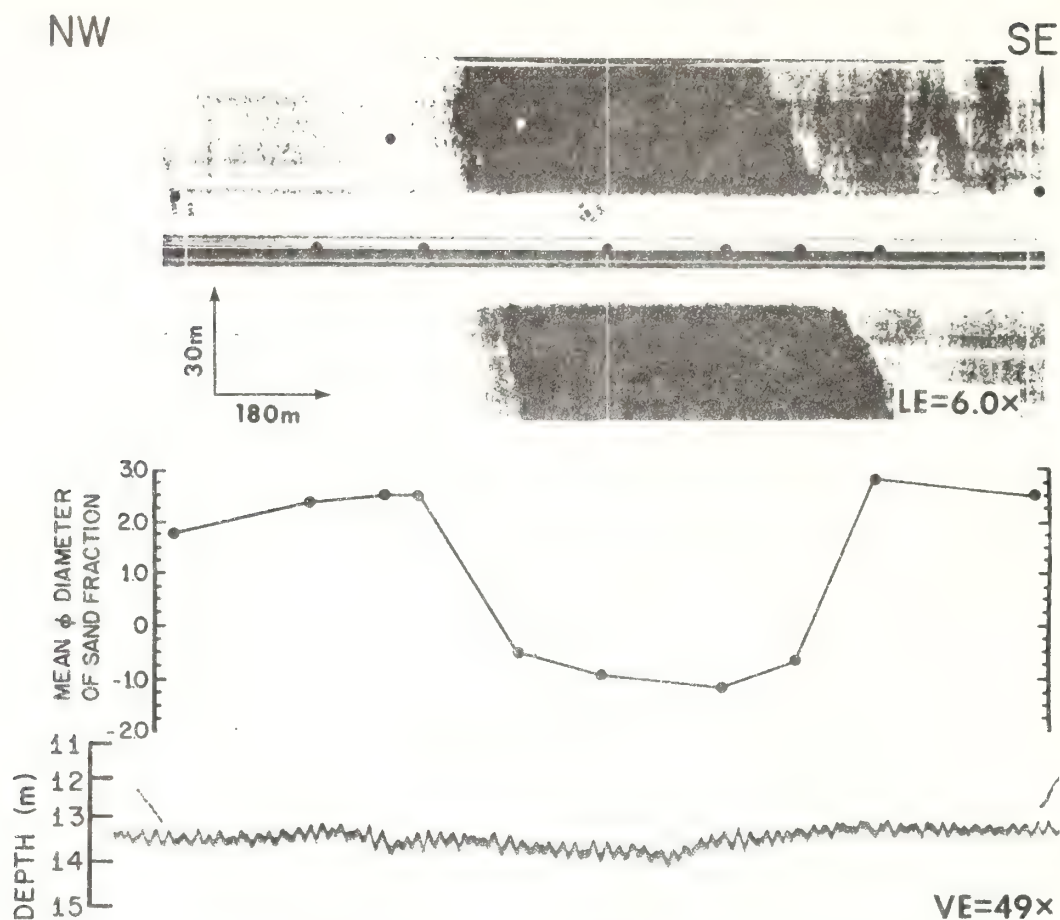


FIG. 16.—Sidescan and bathymetric record and grain size profile of current lineation with plot of mean diameter of sand fraction of grab samples. Samples from dark area consisted of 65% fine shelly gravel. See Fig. 13 for location.

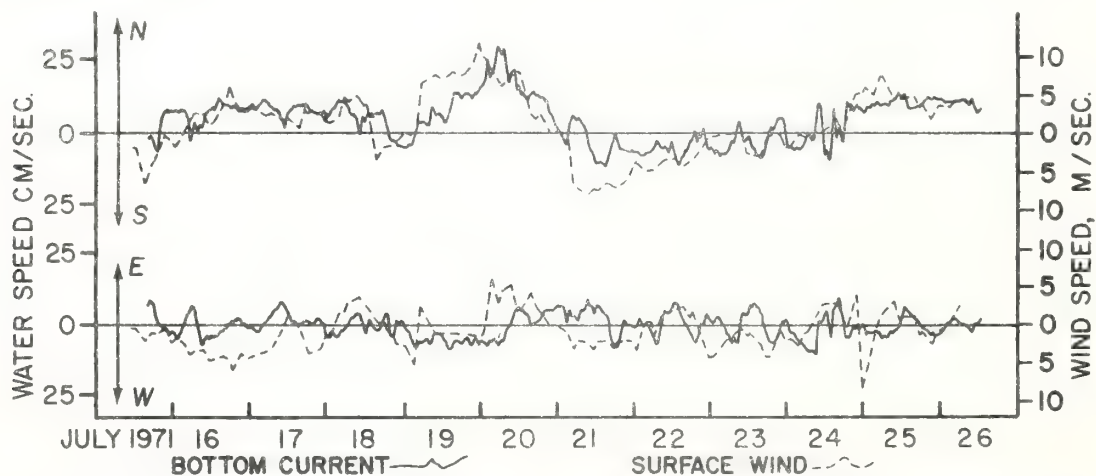


FIG. 17.—North-south and east-west components of bottom currents and winds at "Z" ridge, measured with a Geodyne (Savonius rotor) meter with impeller 37 cm off seafloor, July 1971. Surface wind data collected at Chesapeake Light Tower. See Fig. 6 for location. From McHone, 1972.

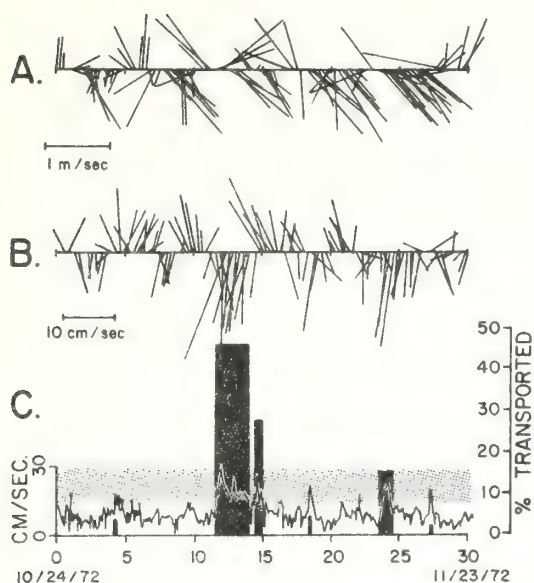


FIG. 18.—A: 6-h vectors of winds at the Chesapeake Light during November 1972. B: 6-h vectors of current measured 37 cm off the seafloor at False Cape by a Geodyne (Savonius rotor) meter. See Fig. 10 for location. C: Speed-time plot of current meter record. Height of vertical bars indicates percent of fine sand transport occurred during this particular threshold exceedence event; width of vertical bars indicates duration of threshold exceedence as compared with total transport during duration of record. Transport is taken as proportional to the cube of the velocity in excess of threshold. See text.

However, if the storm nests in the Middle Atlantic Bight for an appreciable period of time so that isobars of atmospheric pressure parallel the isobaths of the shelf surface (scale-matching storm), then the winds blow down the arc of the shelf. Landward Ekman transport of surface water results in 40 to 60 cm of coastal setup, and strong geostrophic coupling between wind and water results. Coherent southward water transport with mid-depth velocities in excess of 35 cm/sec may be sustained for hours or days. Boicourt and Hacker (1976) have examined in some detail the barotropic response of the water column in the study area to strong northerly wind forcing during the storm of February 3–5, 1974. The most notable feature is a “wind-driven outflow surge of low salinity water from Chesapeake Bay which forms a southward flowing, high velocity jet along the Virginia and North Carolina Coast.”

In addition to the strong downshelf flow, Boicourt and Hacker observed cross-shelf components of velocity up to 13 cm/sec. These are larger than necessary to account for setup against the coast, and suggest a return flow “perhaps in a bottom Ekman layer.” However, Boicourt and Hacker’s current meter array was not sufficiently dense to show whether or not such a bottom flow did in fact exist.

Boicourt and Hacker further report that periods of strong southerly wind result in a reversal of this pattern with somewhat weaker northward flow with an offshore component at the surface and mid-depth, and intrusion of cold slope water along the bottom near the shelf edge.

Wintertime observations in the False Cape ridges have allowed us to calculate the response of the shelf floor to strong wind events (Fig. 18). No true scale-matching storms, as described above, occurred during this period. However, the study area was repeatedly subject to strong northwest winds resulting in southward and slightly onshore bottom currents. Periods of peak wind speed resulted in exceedence of the band of velocities of which successive sand classes became entrained (under shallow shelf conditions 16–35 cms/sec; see Gadd et al., in press). Sediment was entrained for 10% of the 30-day observation period.

Fluid power applied to the sea floor during threshold exceedence and the resulting sediment discharge ( $\bar{q}$ ) may be calculated according to the relationship:

$$\bar{q} = \frac{3.46 \times 10^{-5}}{t} \int_0^t (U_{100} - U_{Th})^3 \hat{u}_{100} dt$$

where  $U_{100}$  is the speed (cm/sec) at 100 cm off the bottom,  $U_{Th}$  is threshold speed,  $\hat{u}_{100}$  is a unit vector, and  $T$  is the duration of threshold exceedence (Gadd et al., in press). Application of this equation to the data of Fig. 18 indicates an average rate of sediment transport of  $4.17 \times 10^{-3}$  gm/cm/sec towards the southwest (200°).

#### *Inshore Region*

The hydraulic regime and substrate response in the vicinity of the innermost False Cape ridge (“A” ridge, Fig. 3) is of particular interest. The floor of the Virginia inner shelf has been created by the process of erosional



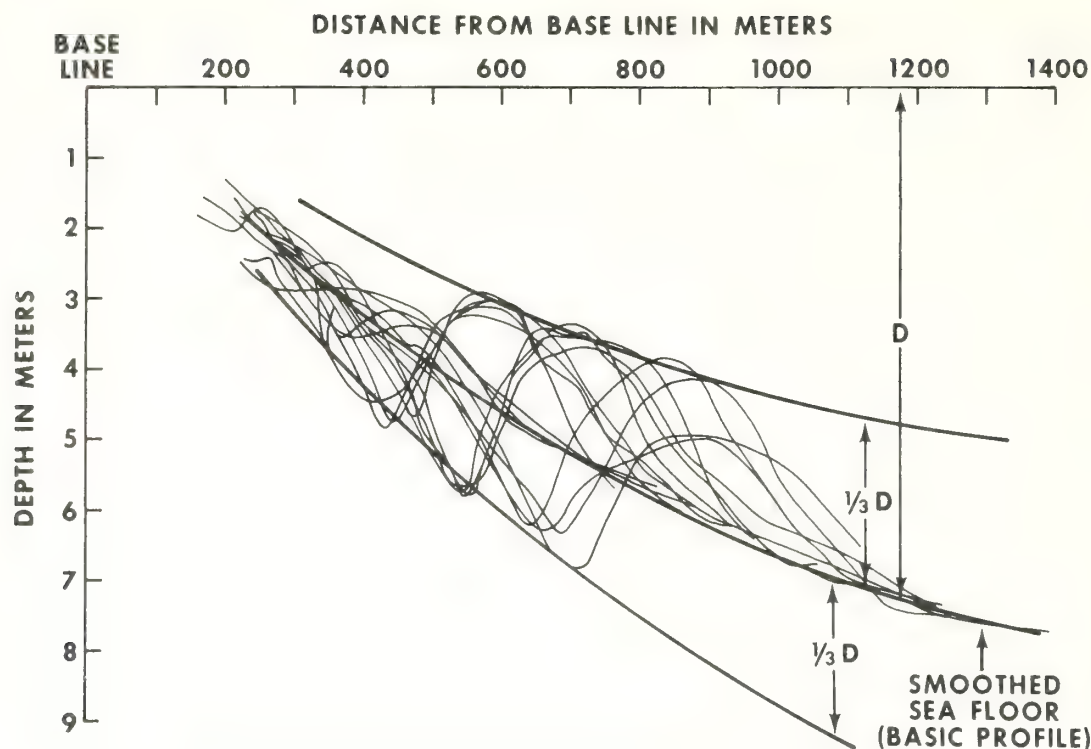


FIG. 19.—Superimposed profiles of the nearshore end of "A" ridge. From McHone, 1972.

shoreface retreat (see Swift, 1976) during the Holocene transgression, and is a progressively younger surface as the shoreline is approached. The innermost sand ridges are therefore most probably in a state of active formation, or are the ridges that have most recently been in such a state. "A" ridge may be traced as far as the 3 m contour over most of its length and maintains 3 to 4 m of relief in water less than 12 m deep. It is difficult to see how such a pile of loose sand would survive in the energetic nearshore environment unless the pattern of coastal flow is serving to actively maintain it.

In this shallow water, it becomes necessary to consider the role of shoaling and breaking waves in ridge formation. Wave-built submarine sand bars similar in height to the nearshore southern end of "A" ridge may occur in similar depths of water (see discussions in Schwartz, 1972). Such bars form at the breakpoint where oscillatory wave surge is downgraded to turbulence, and sand is no longer moved landward in response to the more intense landward stroke.

The wave climate of the Virginia coast is appropriate for a response of this scale since breaking waves occur at the depth of the inner crest of "A" ridge between 1 and 10% of the time (McHone, 1973). The inner ridge has in fact the morphologic characteristics of a wave-built bar, in that the inner side slopes more steeply than the outer side (Fig. 19). Also, the ridge extends a distance of one-third water depth above the smooth profile, and the trough extends a distance of one-third water depth below it. King and Williams (1949) and King (1972), who have modeled breakpoint bars, have reported that as bars build to equilibrium (condition in which bars display imperceptible motion; Keulegan, 1948), their crests approach a height of one-third water depth above the original profile. The nearshore portion of "A" ridge thus has the response characteristics of a breakpoint bar. The implication is that "A" ridge is at least partly wave-built from material excavated from troughs. This hypothesis would require that the building process continues until the water column over the bar is so thin and the turbulence of breaking waves is

so intense that no further growth can occur, and that this equilibrium occurs when the original depth is decreased by one-third.

However, "A" ridge cannot be completely explained as a wave-built bar. Its orientation is wrong; wave-built bars parallel the beach, or if oblique to it, are oriented so that they parallel the wave fronts of waves from the predominant direction. (Sonu et al., 1967). At False Cape waves from the northeast predominate. "A" ridge is also too large; if its seaward northern end is included, it is larger than the breakpoint bars of even the Pacific Coast of the United States with its more rigorous wave climate.

A second major mechanism for the construction and maintenance of "A" ridge appears to be the storm-generated coastal flow field. A current meter station was occupied on September 10 and 11, 1970 for 28 h in 10 m of water in the innermost False Cape trough between the "A" ridge and the beach (Fig. 20). The instrument used was a Bendix Q-18 current meter in which two low-mass impellers were mounted at right angles to each other in a horizontal plane so that current velocity is sensed by the impellers from 0 to 15 cm above the seafloor. Bottom currents were averaged over 3 min at half-hour intervals.

Initially, the winds were out of the southwest at 10–30 m/sec. Bottom currents were 6 cm/sec or less and were nearly random in orientation. Halfway through the observation period, a cold front crossed. The wind shifted and approached from the northeast at 12 m/sec with stronger gusts. Within a few hours, a steady, southeast-trending (obliquely offshore) bottom current had attained a mean velocity of 15–20 cm/sec and persisted through the turn of the tide. After passage of the front, seas built to 2 m height and peak bottom surge velocities were many times the mean current. Divers observed the coarse sand of the bottom molded into current ripples which migrated towards the southeast. There was considerable shear between the bottom and upper water column; the wake from the moored observation boat streamed down coast and onshore, rather than offshore as the bottom current was trending.

Aerial photography during a similar period of northeast winds has revealed intense turbidity on the inshore side of the inner trough and also over "A" ridge, with a tongue of darker,

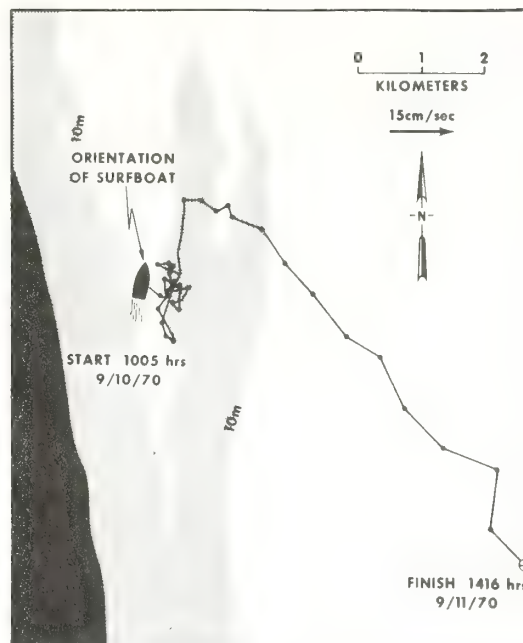


FIG. 20.—Progressive vector diagram from a station between "A" ridge and the beach, September 10–11, 1970. See text for explanation.

clean water between (McHone, 1973). Down coast from the ridge, a rip-current-like "head" of turbid water lay parallel to the beach, apparently fed by water flowing over the base of "A" ridge. Detailed maps of the base of "A" ridge during four successive months reveal the presence of a shifting saddle between the ridge and the shoreface, presumably cut by such flows (Fig. 21). Comparison of the 1922 and 1969 bathymetric maps reveals that 2 to 3 m of erosion have occurred in the trough, while 2 to 3 m of aggradation has occurred in the zone of fine sand south of the ridge base (Swift et al., 1972b). It seems possible that the intense flow observed in the trough between "A" ridge and the beach may be related to the coastal jet described by Boicourt and Hacker (1976; see discussion in previous section).

## DISCUSSION

### *Formation and Modification of Massifs*

A preceding section has described the first order morphology of shelf valley and flanking massifs as constructed by the landward displacement of the ancestral James Estuary during a period of rising sea level between 4,000

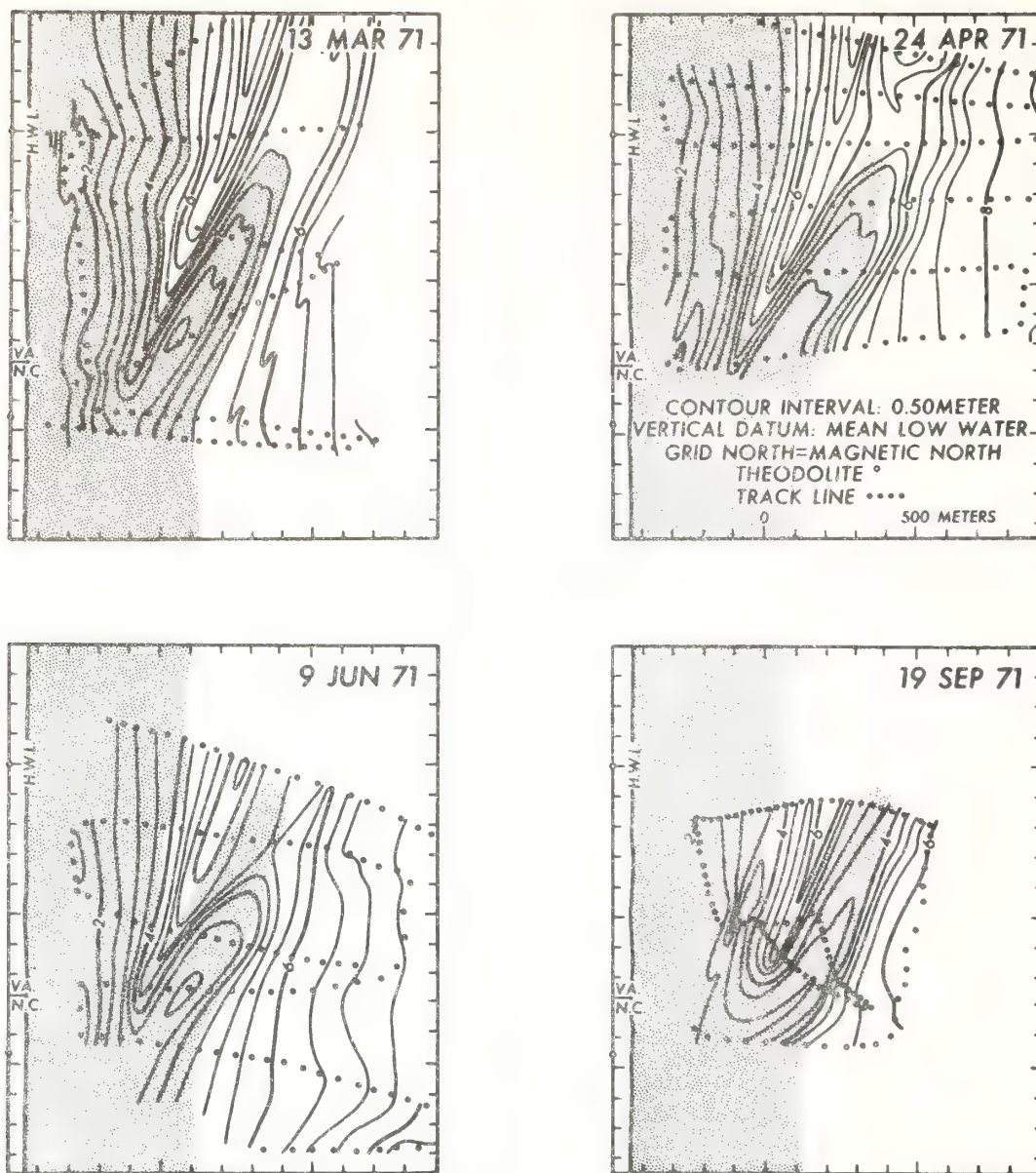


FIG. 21.—Bathymetry at the landward end of "A" ridge, False Cape, over successive months. Stippled area is the area shallower than 5 m on 13 March 1971. Navigation by shore-based theodolite. Contours in meters. From McHone, 1972.

and 20,000 yr ago. We are concerned here with the extent to which this first order morphology is being modified by the modern hydraulic regime, and the process by which such adjustment occurs.

Our current meter observations indicate that current velocities capable of entraining sand are repeatedly attained during a typical

winter month, and the orthogonal bedform pattern of flow-parallel current lineations and flow-transverse sand waves suggests that the substrate is systematically reworked to a depth equal to the height of the more common bedforms (2 m).

The north to south grain-size gradient characteristic of the massifs (Figs. 7, 8, 11)



indicates the regional pattern of sand redistribution during the reworking process. Acceleration of southward bottom flow over the northern slopes of the massifs during peak flow events has resulted in erosion of the finer sand fraction and the generation of a coarser residue; deceleration over the southern slopes has resulted in the deposition of fine and very fine sand on the southern slopes and in the shelf valley. The pervasive southward asymmetry in the ridge patterns north and south of the shelf valley (trough axes and crest lines climb toward the south on both sides) suggests that these features are also responses to southward flow, with troughs cut through the upcurrent sides of the massifs into Pleistocene strata.

However, the processes operating on the north (Virginia Beach) massif must have differed considerably in detail from those operating on the south (False Cape) massif. The origin of the ridges and troughs of the Virginia Beach Massif on the north side of the shelf valley may be sought by analogy with the Delaware Massif on the north side of the Delaware Shelf Valley (Swift, 1973). Unlike the Virginia Beach Massif, the Delaware Massif may be traced directly into a modern, active estuary mouth shoal, and its origin deduced from uniformitarian principles. Troughs have been incised into the north side of the Delaware Massif. On the offshore sector they are shore-parallel, presumably reflecting the orientation of the shore-parallel currents that cut them. On the shoal within the mouth of Delaware Bay, however, the troughs and ridges are responses to the reversing tide, and are oriented normal to the regional trend of the shoreline. Apparently as each segment of estuary shoal entered the shelf environment during the Holocene transgression and became part of the Delaware Massif, the tidal channels rotated to the new orientation or were filled in and replaced by others.

The ridges and troughs of the Virginia Beach Massif may have been formed according to this scenario. However, the shoreface-connected ridges of the False Cape sector are more nearly analogous to the shoreface-connected ridges of the Delaware-Maryland coast, where there appears to be no close relationship between ridge groups and former estuary mouths (Duane et al., 1972; Swift et al., 1974). On the Delaware-Maryland coast,

ridges appear to be forming at the foot of a shoreface undergoing erosional retreat in response to periods of intense flow during "northeaster" storms. The ridges may be seen in all stages of formation and detachment from the retreating shoreface. An array of parallel, free-standing ridges extends seaward for 30 km across the Delaware-Maryland shelf and appears to represent a history of shoreface retreat and ridge detachment over several millennia. The False Cape ridges would similarly appear to be an evolutionary sequence of ridges, with "A" ridge the newest and "C" ridge the oldest (Fig. 3).

The mechanics of ridge formation are poorly understood. While the False Cape ridges and the Virginia Beach ridges have arisen under different sets of circumstances, they are very similar in terms of morphology and grain-size patterns, and it seems probable that they are responses to the same or to very similar hydraulic mechanisms. Any theory which undertakes to explain their formation must account for the following aspects:

1. Shoreward flanks are coarser grained than seaward flanks and tend to have gentler slopes.
2. Sand waves on their crests are not truly orthogonal, but are inclined, indicating that during the responsible flow events there is an offshore, cross-ridge component of flow as well as a stronger southward, ridge-parallel component of flow.
3. Trough and crest axes shoal to the south at angles of 20–35° with the beach and the regional trend of the isobaths.

Bedforms are responses to patterns of rhythmic boundary instability that arise in sheared flow (Allen, 1968, p. 50; Wilson, 1972, p. 209; Jackson, 1975). An analytical model for the generation and maintenance of small-scale (current ripples) and medium- and large-scale (sand waves) current-transverse bedforms has been presented, in which the bedforms are maintained by a phase lag between bottom shear stress and bottom topography (Smith, 1970). No such analytical model exists at present for the medium-scale (current lineations) and large-scale (sand ridges) current-parallel bedforms. Numerical and experimental studies (Faller and Kaylor, 1966; Faller, 1962, 1971; Gammelsrod, 1975) suggest that the shelf flows of the scale and

character described by Boicourt and Hacker (1976; see previous discussion) may be subject to a flow structure in which flow-parallel zones of downwelling and bottom current divergence alternate with flow-parallel zones of upwelling and bottom current convergence. The result is a series of flow-parallel helical cells of alternating right- and left-hand sense of rotation. If such flow structure does occur on the Virginia Shelf, then deflation zones such as those in Fig. 15A may be formed by zones of downwelling and bottom divergence, and may localize such zones through successive storms.

Both the sand wave and the helical flow models appear to have some value in accounting for the observed characteristics of sand ridges. The texture and morphologic asymmetry of a typical sand ridge cross section is also characteristic of the cross section of a flow-transverse sand wave and indicates that the ridges are reacting as sand waves to the cross-ridge component of flow. Sand waves experience maximum flow acceleration and shear stress on the upcurrent flanks; wave crests and downcurrent flanks experience decelerating flow. As a consequence, upcurrent flanks are coarse-grained eroding surfaces, while crests and downcurrent flanks are successively finer grained, depositional surfaces (Smith, 1970).

Flow appears to trend obliquely across the sand ridges, while in sand wave theory, flow is normal to sand waves. However, recent studies by Furness (1976) have shown that sand waves may be oriented obliquely to flow if there is a cross-flow speed gradient. The sand wave becomes sheared out with the crest further downstream on the faster side of the flow. Thus the seaward decrease in velocity observed by Boicourt and Hacker (1976, see previous discussion) on the seaward side of the storm-induced coastal jet might result in the observed skew of sand ridges with respect to the characteristically southward storm flow over the centuries required for the formation of a shoreface-connected sand ridge (J. C. Ludwick, personal communication). If this model is applicable, the ridges are induced in the nearshore zone by the jetlike flows that occur during storms and are left behind as the water column deepens and the shoreline recedes in response to the post-Pleistocene rise in sea level. The sand waves on the crests and flanks of ridges that now lie kilometers sea-

ward of the formative zone would constitute the response of the ridge surface to the present flow regime.

The skew of sand ridge orientation with respect to flow is also compatible with helical flow theory; flow cell orientation may be inclined across the mean flow direction (Faller, 1962; Gammelsrod, 1975). If this model is applicable, then the sand ridges may result from the interaction of a broad cross section of the shelf floor with cellular storm flow over many thousands of years. Sand ridges and the sand waves superimposed on them would be responses to the same flow regime, although at different temporal and spatial scales.

At present neither scheme provides an entirely satisfactory model for ridge formation. The problem will only be solved by a program of detailed hydraulic observation coupled with a more advanced understanding of geophysical boundary layers.

Our observations allow us to conclude that the old estuary mouth topography of the southern Virginia shelf has been modified during later stages of the Holocene transgression, primarily by the incision of a ridge and swale topography on the Virginia Beach Massif, and by the serial growth of a sequence of shoreface-connected ridges at False Cape. Ridge morphology and grain size distribution suggest that both sets of ridges are responses to the same or similar hydraulic mechanisms. Our observations provide constraints that this mechanism must comply with, but are not sufficient to lead us to a complete and unique solution. Such a solution will require a program of direct measurement of flow in which boundary flow patterns are resolved.

#### ACKNOWLEDGMENTS

We thank Mr. Leonard Nero, who presented us with the data for Fig. 11, and Mr. Jeff Nolder, who aided in the field work. We thank the officers and men of the NOAA Ship WHITING for their support during field operations.

#### REFERENCES

- ALLEN J. R. L., 1968, *Current ripples*: North Holland Publishing Co., Amsterdam, 433 p.
- BEARDSLEY, R. C., AND B. BUTMAN, 1974, Circulation on the New England continental shelf: response to strong winter storms: *Geophys. Res. Letters*, v. 1, p. 181-184.



- BOICOURT, W. C., AND D. W. HACKER, 1976, Circulation of the Atlantic continental shelf of the United States, Cape May to Cape Hatteras: *Mem. Soc. Royale des Sciences de Liege*, v. 10, p. 187-200.
- BUMPUS, D. F., 1969, Reversals in the surface drift in the Middle Atlantic Bight area: *Deep-Sea Res. Suppl.*, v. 16, p. 17-23.
- , 1973, A description of circulation on the continental shelf of the east coast of the United States: *Progress in Oceanography*, v. 6, p. 117-157.
- CSANADY, G. T., 1976, Wind driven and thermohaline circulation over the continental shelves: in Manowitz, B. (ed.), *Effects of energy related activities on the Atlantic continental shelf: Conference at Brookhaven National Laboratory*, Nov. 10-12, 1975, p. 31-47.
- DUANE, D. B., M. E. FIELD, E. P. MEISBURGER, D. J. P. SWIFT, AND S. J. WILLIAMS, 1972, Linear shoals on the Atlantic continental shelf, Florida to Long Island: in Swift, D. J. P., D. B. Duane, and O. H. Pilkey (eds.), *Shelf sediment transport: Process and pattern*: Dowden, Hutchinson and Ross, Stroudsburg, Pa., p. 447-495.
- FALLER, A. J., 1962, An experimental study of the instability of the laminar Ekman boundary layer: *Jour. Fluid Mech.*, v. 15, p. 560-576.
- , 1971, Oceanic turbulence and the Langmuir circulations: *Ann. Rev. Ecology and Systematics*, v. 2, p. 201-236.
- , AND R. E. KAYLOR, 1966, A numerical study of the instability of the laminar Ekman boundary layer: *Jour. Atmos. Sci.*, v. 23, p. 466-480.
- FURNESS, G. K., 1976, Formation of oblique dunes: Danish Center for Applied Mathematics and Mechanics, Technical University of Denmark, Report 105, 34 p.
- GADD, P. E., J. W. LAVELLE, AND D. J. P. SWIFT, in press, Calculations of sand transport on the New York shelf using near bottom current meter observations: *Jour. Sed. Petrology*.
- GAMMELSDOD, T., 1975, Instability of Couette flow in a rotating fluid and origin of Langmuir circulations: *Jour. Geophys. Res.*, v. 80, p. 5069-5075.
- HARRISON, W., R. J. MALLOY, G. A. RUSNAK, AND J. TERASMAL, 1965, Possible late Pleistocene uplift, Chesapeake Bay entrance: *Jour. Geol.*, v. 75, p. 201-229.
- HOLLIDAY, B. W., 1971, Observations on the hydraulic regime of the ridge and swale topography of the Inner Virginia Shelf: unpublished M.S. Thesis, 84 p.
- HUNT, R. E., D. J. P. SWIFT, AND H. PALMER, 1977, Constructional shelf topography, Diamond Shoals, North Carolina: *Geol. Soc. Amer. Bull.*, v. 88, p. 299-311.
- HUTHNANCE, J. M., 1972, Tidal current asymmetries over the Norfolk sandbanks: *Estuarine and Coastal Mar. Sci.*, v. 1, p. 89-99.
- JACKSON, R. A., 1975, Hierarchical attributes and a unifying model of bedforms composed of cohesionless material and produced by shearing flow: *Geol. Soc. Amer. Bull.*, v. 86, p. 1523-1533.
- KEULEGAN, G. H., 1948, An experimental study of submarine sand bars: *Beach Erosion Board Tech. Rept.* 3, 42 p.
- KING, C. A. M., 1972, Beaches and coasts: St. Martin's Press, New York, 570 p.
- , AND W. W. WILLIAMS, 1949, The formation and movement of sand bars by wave action: *Geographical Jour.*, v. 113, p. 70-85.
- McHONE, J. F., JR., 1973, Morphologic time series from a submarine sand ridge on the south Virginia coast: unpublished M.S. Thesis, Old Dominion Univ., Norfolk, Va., 59 p.
- McKINNEY, T. F., W. L. STUBBLEFIELD, AND D. J. P. SWIFT, 1974, Large scale current lineations on the Great Egg Shoal retreat massif: investigations by sidescan sonar: *Mar. Geol.*, v. 17, p. 79-102.
- MEISBURGER, E. P., 1972, Geomorphology and sediments of the Chesapeake Bay entrance: *Coastal Eng. Res. Ctr. Tech. Memo.* 38, 61 p.
- NELSEN, T. A., 1976, An automated rapid sediment analyzer (ARSA): *Sedimentology*, v. 23, p. 867-872.
- NORCROSS, J. J., AND E. M. STANLEY, 1967, Inferred surface and bottom drift, June 1963 through October 1964: in Harrison, W., J. J. Norcross, N. A. Pore, and E. M. Stanley (eds.), *Circulation of shelf water off the Chesapeake Bight: ESSA Prof. Paper* 3, 82 p.
- PAYNE, L. H., 1970, Sediments and morphology of the continental shelf off southeast Virginia: unpublished Ph.D. Thesis, Columbia Univ., New York, 70 p.
- POWERS, M. C., AND B. KINSMAN, 1953, Shell accumulations in underwater sediments and their relationship to the thickness of the traction zone: *Jour. Sed. Petrology*, v. 23, p. 229-234.
- SCHWARTZ, M. L., 1972, Spits and bars: Dowden, Hutchinson and Ross, Stroudsburg, Pa., 452 p.
- SHIDELER, G. L., D. J. P. SWIFT, G. H. JOHNSON, AND B. W. HOLLIDAY, 1972, Late Quaternary stratigraphy of the Virginia inner shelf: *Geol. Soc. Amer. Bull.*, v. 83, p. 1787-1804.
- SMITH, J. D., 1969, Geomorphology of a sand ridge: *Jour. Geol.*, v. 77, p. 39-55.
- , 1970, Stability of a sand bed subjected to a shear flow of low Froude number: *Jour. Geophys. Res.*, v. 75, p. 5928-5940.
- SONU, C. J., J. M. MCCLOY, AND D. S. ARTHUR, 1967, Longshore currents and nearshore topographies: *Proc. 10th Conf. Coastal Eng.*, p. 525-549.
- SWIFT, D. J. P., 1973, Delaware Shelf Valley: estuary retreat path, not drowned river valley: *Geol. Soc. Amer. Bull.*, v. 84, p. 2743-2748.
- , 1975, Barrier island genesis: evidence from the central Atlantic shelf, eastern USA: *Sedimentary Geol.*, v. 14, p. 1-43.
- , 1976, Coastal sedimentation: in Stanley, D.



- J., and D. J. P. Swift (*eds.*), Marine sediment transport and environmental management: John Wiley and Sons, New York, p. 255-309.
- , AND P. SEARS, 1974, Estuarine and littoral depositional patterns in the surficial sand sheet, central and southern Atlantic shelf of North America: Mem. 7, Inst. Geol. Bassin Aquitaine, 1974, p. 171-189.
- , D. B. DUANE, AND T. F. MCKINNEY, 1974, Ridge and swale topography of the Middle Atlantic Bight: secular response to Holocene hydraulic regime: *Mar. Geol.*, v. 15, p. 227-247.
- , D. J. STANLEY, AND J. R. CURRAY, 1971, Relict sediments on continental shelves: a reconsideration: *Jour. Geol.*, v. 79, p. 322-346.
- , B. HOLLIDAY, N. AVIGNONE, AND G. SHIDELER, 1972a, Anatomy of a shoreface ridge system, False Cape, Virginia: *Mar. Geol.*, v. 12, p. 59-84.
- , J. W. KOFOED, F. P. SAULSBURY, AND P. SEARS, 1972b, Holocene evolution of the shelf surface, central and southern shelf of North America: in Swift, D. J. P., D. B. Duane, and O. H. Pilkey (*eds.*), Shelf sediment transport, process and pattern: Dowden, Hutchinson and Ross, Stroudsburg, Pa., p. 499-574.
- , P. C. SEARS, B. BOHLKE, AND R. E. HUNT, in press, Evolution of a shoal retreat massif, North Carolina shelf: inferences from areal geology: *Mar. Geol.*
- WILSON, I. G., 1972, Aeolian bedforms—their development and origins: *Sedimentology*, v. 19, p. 173-210.

# Eastern Atlantic Fracture Zones as Potential Disposal Sites for Radioactive Waste

Karl K. Turekian

Department of Geology and Geophysics  
Yale University  
New Haven, Connecticut 06520

Peter A. Rona

National Oceanic and Atmospheric Administration  
Atlantic Oceanographic and Meteorological Laboratories  
Miami, Florida 33149

**ABSTRACT** / Disposal of radioactive waste in the sea floor of fracture zones associated with the flanks of the Mid-Atlantic Ridge may be a satisfactory alternative to land disposal. Effective physiographic, sedimentary, chemical, and oceanographic barriers exist in these aseismic deep canyons, especially in the eastern Atlantic. In addition, the major producers of radioactive wastes are likely to be near the Atlantic Ocean. If such a disposal strategy is adopted, intensive study of the sedimentologic and oceanographic properties of oceanic fracture zones will be necessary.

## Environmental Viewpoint

Occasionally we receive a short paper in which an author expresses a controversial opinion or hypothesis which has both scientific merit and important environmental implications, but for which adequate data may not exist to prove or disprove validity. We believe that such views should be presented for scientific examination and discussion. Therefore, we will publish a few of these papers as part of a new section entitled *Environmental Viewpoint*. Well-documented rebuttals to these viewpoints will be reviewed by the editorial board and published at the editor's discretion. All articles and opinions published in this section represent the views of the authors and are not necessarily those of *Environmental Geology* or of Springer-Verlag.

The growing use of nuclear power as an energy source is causing accumulation of radioactive nuclear wastes in temporary repositories (Bethe 1976). Permanent disposal of these waste materials awaits the designation of storage areas where the wastes will have the least effect upon the environment while the longest lived radionuclides (specifically plutonium) decay to acceptable levels. The suitability of an area for permanent storage depends upon the effectiveness of physical, chemical, and biologic barriers in restraining the migration of the nuclides into the biosphere for about 250,000 years.

Several geologic environments on the continents and in the ocean basins have been suggested as potential permanent disposal sites. These include bedded salt deposits underlying certain continental areas and the marginal deep-sea trenches that partially surround the Pacific Ocean basin. Recently, the regions receiving the most attention have been the abyssal hills submarine physiographic provinces in the mid-crustal plate, mid-oceanic circulation gyre regions of the North Atlantic and North Pacific ocean basins (Bishop and Hollister 1974). The purpose of this paper is to demonstrate that oceanic fracture zones provide an effective combination of physiographic, sedimentary, biologic, and oceanographic barriers to nuclear waste dispersal.

Fracture zones of the Atlantic Ocean basin are physiographically well developed and have been better studied than those in the other oceans. They are also closest to the major producers of radioactive waste. The arguments we use for the use of fracture zones in the Atlantic may apply as well to those areas of the Pacific Ocean and Indian Ocean where similar features exist.

## The Barriers

### Physiographic barriers

Fracture zones are the major transverse structures of ocean basins and may extend across the entire width of an ocean basin. The effectiveness of fracture zones as physiographic barriers to nuclear waste dispersal derives from their topographic relief, degree of topographic closure, and tectonic stability. Major fracture zones like the Atlantis Fracture Zone (Fig. 1) transect the Mid-Atlantic Ridge at spacings of about 100 km in the North Atlantic and South Atlantic ocean basins. The major fracture zones exhibit a canyon-like profile attaining floor widths of about 10 km and wall relief up to several kilometers where they transect the Mid-Atlantic Ridge crest in the central third of the Atlantic. The topographic relief of a typical fracture zone progressively decreases away from the crustal region of the Mid-Atlantic Ridge. This is thought to be due to crustal subsidence as a function of increasing crustal age and consequent burial beneath sediments of the continental margin. Although fracture zones may form linear structures apparently continuous for hundreds to thousands of kilometers across an ocean basin, they are actually segmented along their lengths both by *en echelon* offsets, as

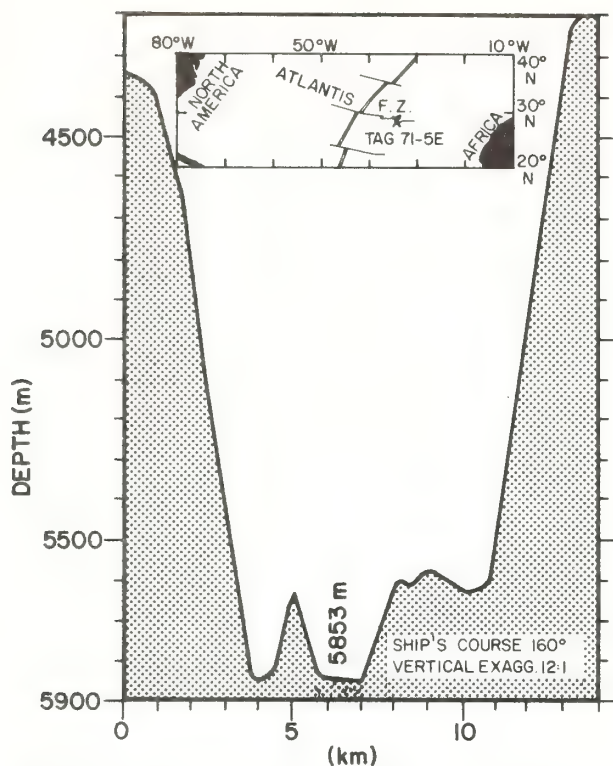


**Figure 1.** Location of the Atlantic Fracture Zone. The dated core showing slumping is marked, TAG 71-SE, and the topographic cross section is at right angles to the trend of the fracture zone at this site.

shown by the Atlantis Fracture Zone (Fig. 1) and by transverse structures that breach the walls of the fracture zones.

The tectonic stability of fracture zones varies along their lengths. Evidence from earthquake seismology indicates that fracture zones are seismically active along that small fraction of their length that offsets the axis of an oceanic ridge and otherwise are almost inactive outside the zone of ridge-ridge offset (Sykes 1967). The distribution of seismic activity indicates that fracture zones are tectonically active within the zone of ridge-ridge offset, usually a length less than 100 km, and are tectonically inactive along the greater portion of their length outside this zone. Exceptions to tectonic stability may exist where fracture zones lie along lithospheric plate boundaries, such as in the Equatorial Atlantic (Harrison and Ball 1973), or where they intersect active fault systems at continental margins.

Various physiographic features of fracture zones, including topographic relief, degree of topographic closure, and tectonic stability provide partial physical barriers to the dispersion of radioactive waste. In addition, these physiographic features influence sedimentary, oceanographic, and chemical conditions that further enhance the effectiveness of fracture zones as disposal sites.

### Sedimentary barriers

Oceanic fracture zones provide a sedimentary framework for relatively rapid burial of waste materials. The fracture zones progressively fill with sediment from both particle-by-particle deposition and slumping as they proceed away from the crest of an oceanic ridge. On the flanks, sediment fill is probably dominated by episodic input of sediment by slumping from the fracture zone walls. As demonstrated by van Andel and Komar (1969), the high walls of fracture zones on the Mid-Atlantic Ridge form catchment areas for sediment accumulation while the steepness of the walls favors episodic slumping resulting in ponding of sediment within the confines of the fracture zones. Closer to the continental margin, bottom transport of sediment will be the major means of filling in the remaining topographic features.

The role of episodic accumulation of sediment by slumping in oceanic fracture zones is supported by evidence from the Atlantis Fracture Zone where a piston core sampled a sediment pile of virtually pure calcareous lutite of biogenic origin with constant excess  $^{230}\text{Th}$  more than 11 m down its length (Fig. 1, core TAG 71-5E; Turekian and others 1972). There was no evidence of burrowing by organisms in the core. The inferred slumping event, which provided at least 11 m of sediment, may have occurred in the last 50,000 years (based on estimates of total excess  $^{230}\text{Th}$  and radiocarbon age).

Slumping frequency in fracture zone regions could be determined by assaying cores for natural radionuclides with different half-lives. In addition to  $^{230}\text{Th}$  (75,000 yr half-life) and  $^{14}\text{C}$  (5,700 yr half-life),  $^{210}\text{Pb}$  (22 yr half-life) and  $^{228}\text{Th}$  (1.9 yr half-life) could be used. The presence of excesses above secular equilibrium for all of the short-lived nuclides, for example, would indicate that slumping occurred less than 10 years ago. Equilibrium for  $^{228}\text{Th}$  and  $^{210}\text{Pb}$  but disequilibrium for  $^{230}\text{Th}$  would indicate the slump occurred more than 100 years ago. This kind of study would reveal the rate of burial of the radioactive waste by natural means in particular basins.

Nozaki and others (1977) have shown that in a fracture zone site near the crest of the Mid-Atlantic Ridge the depth of bioturbation is about 8 cm. The radiocarbon and  $^{210}\text{Pb}$  data require that the rate of biological mixing below that depth is virtually zero. This means that a layer of sediment more than 8 cm thick deposited on a completely buried capsule will essentially isolate the material from contact by purely particulate transport with the ocean-sediment surface. It does not, of course, speak to the question of chemical migration through molecular diffusion in pore waters.

### Chemical barriers

If the adsorption of plutonium can be modeled roughly after that of thorium, lead, and other heavy metals, then our knowledge of the geochemistries of these analog nuclides indicates that the sediment-water interface (up to several tens of meters into the water column) should be an effective trap for plutonium. The reasons are as follows:



1. Manganese and iron are released from the ocean floor in this environment either by direct hydrothermal emanations from the oceanic crust (Scott and others 1974; Rona and others 1976) or by bioturbation and release from reduced sediments (Ku and Glasby 1972). Under either condition the reduced manganese and iron are precipitated upon oxidation, carrying metals scavenged from the oceans with them to the ocean floor. The ubiquitous presence of ferromanganese oxide coatings on a variety of materials of the ocean floor (for example basaltic rocks, calcareous tests, man-made materials) indicates the general nature of this scavenging.

2. Studies of  $^{210}\text{Pb}$  (22 yr half-life) disequilibrium in the deep ocean water column relative to its parent  $^{226}\text{Ra}$  (1,620 yr half-life) indicate that it is the most pronounced in areas of high productivity and that generally the disequilibrium in any part of the ocean increases near the bottom (Craig and others 1973; Bruland and others 1974; Nozaki and Tsunogai 1976; Thomson and Turekian 1976; Krishnaswami and others 1975; Bacon and others 1976; Benninger 1976; Somayajulu and Craig 1976). The latter observation implies that bottom processes are even more effective in  $^{210}\text{Pb}$  removal from the ocean than the remarkably effective water column. If this observation is applicable to plutonium it reaffirms the fact that the water column as a whole tends to be scavenged of reactive nuclides by particles; the particles near the bottom are quantitatively even more effective as scavengers. Since the ocean bottom is the source of nuclides from radioactive waste deposits, all processes act as a restraint to their upward migration in solution.

3. Evidence exists that the plutonium inventory in deep-sea sediments in general is as predicted from anticipated fallout, irrespective of type of sediment (Noshkin and Bowen 1975). It thus appears that sediment rich in calcium carbonate is as effective a trap for plutonium as any other type. The reason may well be that ferromanganese coatings on calcareous deposits are ubiquitous and act as effective traps for other metals.

#### Oceanographic barriers

The eastern Atlantic Ocean is dominated by North Atlantic Deep Water admixed with Antarctic Bottom Water. The exact mechanism of formation is not well worked out. On the basis of non-conservative chemical property distributions in the eastern and western basins it is evident that the residence time of water in the eastern is longer than in the western basin. As eastern basin waters are returned to the western basin they begin their major journey around the deep oceans. Thus on the average, the length of time between release of a substance to the ocean bottom in the eastern Atlantic and its arrival at the surface will be one of the longest in the ocean system, perhaps a thousand years.

The time required for the wandering of a water parcel from the deep ocean bottom to the ocean surface provides a barrier to the release of plutonium to the surface where it would be a concern to man. The travel time for the water parcel provides an addition-

al barrier should any radioactive substance escape from a container, from the sediment, and from the sediment-water interface (all events of low probability).

#### A Strategy for Radioactive Waste Disposal in the Deep Ocean

If the oceans are to be considered as a repository for the growing burden of radioactive wastes that will accompany increasing dependence on nuclear reactors, then oceanic fracture zones, and particularly those of the eastern Atlantic, should be considered as potential disposal sites. The particular properties that make them effective as potential radioactive waste disposal sites include the combination of physiographic, sedimentary, chemical, and oceanographic barriers described above. In addition, the proximity of the sites to the major power users is a convenience.

The following strategy is proposed for radioactive waste disposal in the fracture zones of the eastern Atlantic Ocean:

1. The major producers of radioactive wastes in the near future are likely to be from countries around the Atlantic Ocean basin. Therefore, on proximity principles the Atlantic Ocean basin rates high as a repository.

2. The eastern Atlantic is free from strong western boundary currents that would tend to disperse and erode sediment piles. It is also the closest thing to a young *cul de sac* for deep ocean waste. Leakage from the deep to the ocean surface requires the longest mean time of all deep oceanic areas. For example, the deep water in the North Pacific (being the "oldest" water) can be expected to return to the shallower parts of the ocean more quickly than the deep water in the northeast Atlantic Ocean.

3. The fracture zones outside the ridge-ridge offset of the Mid-Atlantic Ridge are almost inactive seismically. Thus, materials deposited in the sediments are not likely to be disrupted by tectonic instability. Indeed, if disruptions should occur they are more likely to add more sediment cover.

4. Slumping from adjacent highlands is known to provide a great deal of sediment to the deeper parts of the fracture zones. Most of this material is biogenic calcium carbonate.

5. Manganese and iron in reduced form from biogenic or hydrothermal sources are oxidized and flocculate near the ocean bottom to form ferromanganese oxide concretions and coatings. This process acts to scavenge  $^{210}\text{Pb}$ , the thorium isotopes, and some heavy metals, and can be expected to prevent the escape of any plutonium that has managed to reach the sediment-water boundary in solution.

6. Thus containers of solid radioactive wastes that are encapsulated to survive mechanical or corrosive rupture for several hundred years can be completely buried in the sediments of a fracture zone (such as the eastern end of the Atlantis Fracture Zone). Any plutonium released to interstitial solution on later disruption of the container would be constrained by the geochemical barriers of the sediment-water interface. Should any plutonium escape through this severe barrier it could spend as much as

a thousand years in the deep ocean during its ineluctable transfer from ocean to ocean.

This strategy requires more intensive study of the sedimentologic and oceanographic properties of fracture zones. Such studies should include the stochastics of sediment slumping processes, the leakage of deep water out of the "box canyons" of the fracture zones through unmapped sills, and the special geochemical processes at the sediment-water interface which cause the distribution and precipitation of iron and manganese as heavy metal scavengers.

#### ACKNOWLEDGMENTS

The studies of the Atlantis Fracture Zone were done as part of the NOAA Trans-Atlantic Geotraverse project. Support was received from NOAA, the U.S. National Science Foundation, and the U.S. Energy Research and Development Administration.

#### REFERENCES

- Bacon, M. P., D. W. Spencer, and P. G. Brewer, 1976,  $^{210}\text{Pb}$ - $^{226}\text{Ra}$  and  $^{210}\text{Po}$ / $^{210}\text{Pb}$  disequilibrium in seawater and suspended particulate matter: *Earth Planet. Sci. Letters*, v. 32, p. 277-296.
- Benninger, L. K., 1976, The uranium-series radionuclides as tracers of geochemical processes in Long Island Sound: Yale University, Ph.D. dissert.
- Bethe, H. A., 1976, The necessity of fission power: *Scientific American*, v. 234, no. 1, p. 21-31.
- Bishop, W. P., and C. D. Hollister, 1974, Seabed disposal—where to look: *Nuclear Technology*, v. 34, p. 425-443.
- Bruland, K. W., M. Koide, and E. D. Goldberg, 1974, The comparative marine geochemistries of lead 210 and radium 226: *Jour. Geophys. Res.*, v. 79, p. 3083-3086.
- Craig, H., S. Krishnaswami, and B. L. K. Somayajulu, 1973,  $\text{Pb}^{210}$ - $\text{Ra}^{226}$  radioactive disequilibrium in the deep sea: *Earth Planet. Sci. Letters*, v. 17, p. 295-305.
- Harrison, C. G. A., and M. M. Ball, 1973, The role of fracture zones in sea floor spreading: *Jour. Geophys. Res.*, v. 78, p. 7776-7785.
- Krishnaswami, S., B. L. K. Somayajulu, and Y. Chung, 1975,  $^{210}\text{Pb}$ / $^{226}\text{Ra}$  disequilibrium in the Santa Barbara Basin: *Earth Planet. Sci. Letters*, v. 27, p. 388-392.
- Ku, T.-L., and G. P. Glasby, 1972, Radiometric evidence for rapid growth rate of shallow-water continental margin manganese nodules: *Geochim. et Cosmochim. Acta*, v. 36, p. 699-704.
- Noshkin, V. E., and V. T. Bowen, 1975, Concentration and distributions of long-lived fallout radionuclides in open ocean sediments: *Internat. Atomic Energy Agency Symposium*, Seattle, Wash.
- Nozaki, Y., J. K. Cochran, K. K. Turekian, and G. Keller, 1977, Radiocarbon and  $^{210}\text{Pb}$  distribution in submersible-taken deepsea cores from Project FAMOUS: *Earth Planet. Sci. Letters*, v. 34, p. 167-173.
- Nozaki, Y., and S. Tsunogai, 1976,  $^{226}\text{Ra}$ ,  $^{210}\text{Pb}$  and  $^{210}\text{Po}$  disequilibria in the western North Pacific: *Earth Planet. Sci. Letters*, v. 32, p. 313-321.
- Rona, P. A., R. H. Harbison, B. G. Bassinger, R. B. Scott, and A. J. Nalwalk, 1976, Tectonic fabric and hydrothermal activity of Mid-Atlantic Ridge crest (lat.  $26^\circ\text{N}$ ): *Geol. Soc. America Bull.*, v. 87, p. 661-674.
- Scott, M. R., R. B. Scott, P. A. Rona, L. B. Butler, and A. J. Nalwalk, 1974, Rapidly accumulating manganese deposit from the median valley of the Mid-Atlantic Ridge: *Geophys. Research Letters*, v. 1, p. 355-358.
- Somayajulu, B. L. K., and H. Craig, 1976, Particulate and soluble lead 210 activities in the deep sea: *Earth Planet. Sci. Letters*, v. 32, p. 268-276.
- Sykes, L. R., 1967, Mechanism of earthquakes and nature of faulting on the mid-ocean ridges: *Jour. Geophys. Res.*, v. 72, p. 2131-2153.
- Thomson, J., and K. K. Turekian, 1976,  $^{210}\text{Po}$  and  $^{210}\text{Pb}$  distributions in ocean water profiles from the eastern South Pacific: *Earth Planet. Sci. Letters*, v. 32, p. 297-303.
- Turekian, K. K., J. Thomson, S. Leighton, N. D. Watkins, T.-C. Huang, J. P. Kennett, P. A. Rona, G. H. Keller, and L. W. Butler, 1972, Sources of sediments and rates of accumulation in the Canary Basin: *Geol. Soc. Amer., Abs. with programs*, v. 4, no. 7, p. 694-695.
- van Andel, Tj. H., and P. D. Komar, 1969, Ponded sediments of the Mid-Atlantic Ridge between  $22^\circ$  and  $23^\circ$  North latitude: *Geol. Soc. America Bull.*, v. 80, p. 1163-1190.

## Letter Section

### SEAFUME: A DEVICE FOR IN-SITU STUDIES OF THRESHOLD EROSION VELOCITY AND EROSIONAL BEHAVIOR OF UNDISTURBED MARINE MUDS

ROBERT A. YOUNG\*

*Massachusetts Institute of Technology—Woods Hole Oceanographic Institution Joint Program in Oceanography, Woods Hole, Mass. 02543 (U.S.A.)*

(Received November 11, 1976)

#### ABSTRACT

Young, R.A., 1977. Seaflume: a device for in-situ studies of threshold erosion velocity and erosional behavior of undisturbed marine muds. *Mar. Geol.*, 23: M11—M18

A self-contained sea-going flume has been designed for use in sediment transport studies on the sea floor. Bottom sediment behavior and flow velocity resulting from water pumped through the flume are recorded photographically to obtain estimates of threshold erosion velocity and modes of erosion. Precision and accuracy of estimated threshold velocities for muddy marine sediments are found to be as good or better than those previously obtained by other field or laboratory techniques.

#### INTRODUCTION

A problem encountered by many marine geologists is the sparcity of reliable estimates of threshold erosion velocities for muddy marine sediments. Laboratory studies alone cannot provide reliable estimates because the field sampling process itself may change the erosion resistance of the sediment through small alterations in those physical properties related to erosion resistance. This effect was alluded to in the laboratory experiments of Postma (1962, 1967) where changes of 5% or less in water content of an estuarine mud caused the threshold erosion velocity to increase by a factor of 1.5—2.0. In addition, the highly complex electrochemical nature of the interparticle bonds and organic binding which are mainly responsible for erosion resistance in muddy sediments (Van Olphen, 1966) makes theoretical calculations of threshold velocity impossible for nearly all cases of practical importance. Therefore, it appears that the most reliable estimates of threshold velocities for marine muds will be obtained from direct observations of erosion processes and bottom currents on the sea floor.

\*Present address: National Oceanic and Atmospheric Administration, Atlantic Oceanographic and Meteorological Laboratories, Marine Geology and Geophysics Laboratory, 15 Rickenbacker Causeway, Miami, Fla. 33149 (U.S.A.).



In both shallow and deep environments, natural erosion processes can be aperiodic thereby necessitating long observation periods, and flow structure in the bottom boundary layer can be complex and highly variable. For example, Sternberg (1970) determined that a uniform semilogarithmic velocity distribution was present in less than half of the measurements made by him in both deep and shallow marine boundary layers. During other times, Sternberg noted that the velocity distribution was irregular and could not be described by known flow laws. Thus, in many instances, estimation of a characteristic threshold erosional velocity could require long observation times to ensure sufficient observations of the infrequently well-behaved boundary layer. For some studies a long time series encompassing several erosional events at a single location is desirable, but for many studies a single rapid, but reliable, measurement of threshold velocity made under the control of the observer would be more desirable.

#### THE SEAFLUME

The SEAFLUME is a sea-floor flume designed to study erosion of undisturbed muddy sediments under controlled flow conditions. Sea-going flumes of other designs have been used previously but primarily for experimentation in shallow waters. Neumann et al. (1970) used a 2 m long, hand-operated sea-going flume (described by Scoffin, 1968) in 2–4 m of water in Abaco Sound, Bahama, to investigate the binding effects of algal mats on carbonate sediments. Sedimentary environments which could be studied using their flume were limited, since flow velocity and the criteria for sediment entrainment were obtained from visual observations made by SCUBA divers. A much smaller sea-going flume was used by SCCWRP (1975) to estimate erosion velocities of coastal muds off southern California. Apparently only very crude estimates of threshold velocities can be made with this instrument, since the channel length of this flume does not appear sufficient to allow damping of turbulent entrance effects or full development of the boundary layer.

#### *Channel*

The SEAFLUME is basically an open-bottomed rectangular duct with a sloping, open-mouthed entrance section, and a straight observation section (Fig.1). The channel is 4 m long and has a 15 cm by 61 cm cross-section. The sloping entrance section is designed so that when flow reaches the threshold for erosion in the observation section, it is still sub-threshold in the entrance section. This minimizes the possibly confusing effects of erosion and transport of sediments from the entrance section into the observation section during the critical time when erosion is just beginning.

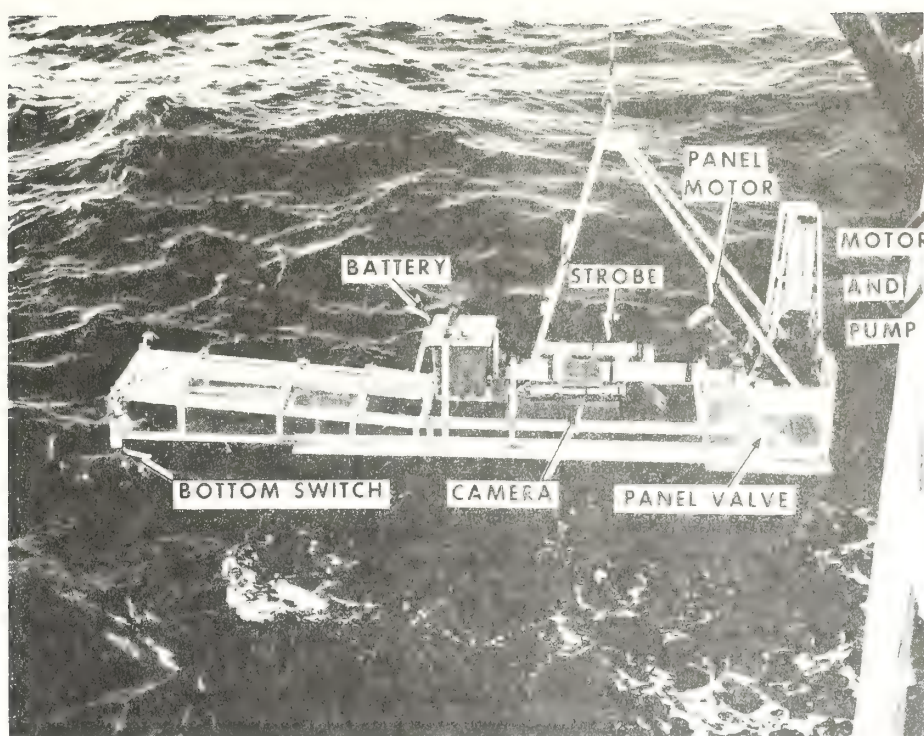


Fig.1. A photograph of SEAFLUME being deployed at sea. The flanges along the duct wall and plywood sheet under the pump chamber provide sufficient bearing surface to allow penetration of the channel to a design depth of 1 cm.

#### *Pump, panel-valve and batteries*

A by-pass panel valve on the bulkhead between the pump chamber and the observation section controls discharge inside the duct. A sliding panel, slowly slides off the opening on the bulkhead between the duct and the pump chamber while simultaneously closing an opening in the bulkhead leading to the exterior of the pump chamber. The panel is driven by a slow-speed DC stepping motor enclosed in an oil-filled pressure-compensated housing. This design allows the pump to achieve its most efficient discharge potential. A cast-iron propeller pump with bronze bearings is used which produces a discharge of approximately 900 gal/min (3,400 l/min) at 1150 rpm (Byron-Jackson, Model 8 DL). A separate oil-filled housing encloses a 0.75 HP DC motor which drives the pump. This case is vented to allow escape of gases produced by brush arcing and is connected to an oil-filled flexible bladder for pressure compensation.

Power for the pump and panel motors is provided by a pair of 6-volt DC batteries connected in series and enclosed in an oil-filled pressure-compensated fiberglass box.

### *Camera system*

Close-up photography is the principal means of observing the erosional behavior of the sediments. A portion of the sea floor of approximately 15 cm<sup>2</sup> is photographed every 5–15 sec by an E.G. & G. 35-mm deep-sea camera. The camera is mounted parallel to the duct top, and the sediments are photographed through the transparent top by means of a 45° mirror mounted on the lens port of the camera (see Fig.1). Light is provided by an E.G. & G. 100 watt-sec strobe reflected by a mirror through the side wall of the duct to produce low-angle side-lighting. Although light distribution is somewhat uneven, apparent relief of the sea floor is enhanced by side lighting and modifications of features as small as 500  $\mu$ m can be discerned. Approximately 400 frames can be taken during each experiment with standard 100-foot film rolls.

### FIELD METHODS

The SEAFUME is presently configured horizontally for lowering. A tripod is used for this purpose (Fig.1). The standard procedure is to wind a length equal to 1.5 times the water depth of 5/8 inch (1.6 cm) nylon rope onto the winch, attach and slowly lower the flume to the bottom, then quickly unwind the remaining rope, attach a small surface float, and cast it free. This ensures complete uncoupling of ship's motion from the flume. The reliability of this procedure was verified by the direct observation of divers during testing and the initial field experiments.

A mercury tilt switch senses bottom contact and, after a 15 sec time delay, two relays are actuated which turn on the pump and panel-valve motors and start the camera system. The panel-valve motor turns off automatically after completely opening the panel-valve, but the pump motor and camera turn off only when the flume is raised off the bottom. Battery voltage, rate of panel-valve opening, and interval between film frames determine maximum length of each run which ranges from 30 to 45 minutes.

### FLOW VELOCITY

A ballasted nylon sphere (diameter = 1.6 cm) suspended on a thin nylon line in the field of view of the camera was used to measure flow velocity inside the duct. Such simple devices previously have been used with success to measure currents in the deep sea (Bruce and Thorndike, 1967). Horizontal deflection of the sphere from its resting position was measured photographically and compared to a laboratory calibration curve (Fig.2). Calibrations were carried out by suspending the sphere in an enclosed, recirculating laboratory flume at a number of different flow velocities. Generally, current velocity could be estimated from sphere deflection to within  $\pm 10\%$ .

The velocity distribution in a smooth or rough-walled duct can be closely approximated by the power-law velocity distribution given by Prandtl and



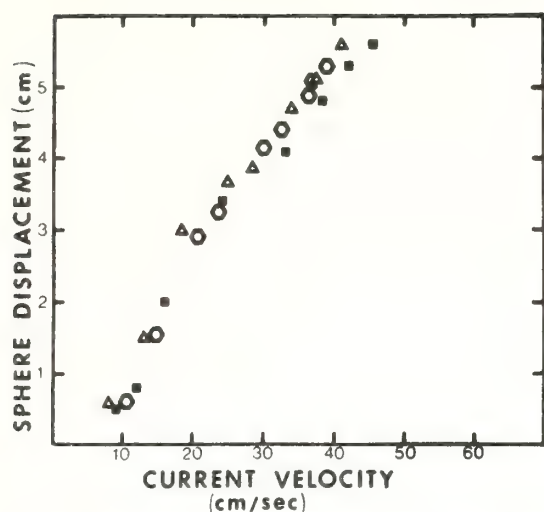


Fig. 2. Calibration curve for sphere flow meter. Sphere deflection was plotted against the average flow velocity (total discharge/cross-sectional area) in an enclosed recirculating laboratory flume (4 cm × 17 cm flow cross-section) during three separate runs. Velocities of less than about 5 cm/sec and velocities above about 45–50 cm/sec did not produce noticeable changes in sphere deflection. Two linear ranges above and below about 20 cm/sec are observed in the plot.

Tietjens (1934, p. 71) as:

$$u_z = u_{\max} \left( \frac{z}{d} \right)^{1/7}$$

where  $u_z$  is velocity at a distance  $z$  from the wall,  $u_{\max}$  is maximum velocity, and  $d$  is flow depth (Fig. 3). If we assume that the velocity profile follows the power-law distribution given above, then for turbulent flows in smooth or rough ducts average wall shear stress,  $\tau_0$ , can be closely approximated by (Prandtl and Tietjens, 1934, p. 71–75):

$$\tau_0 = 0.0228 \rho \left( \frac{u_z^7 \nu}{z} \right)^{1/4}$$

where  $\rho$  is fluid density and  $\nu$  is kinematic water viscosity. From this estimate of  $\tau_0$ , the shear velocity,  $u_* = (\tau_0/\rho)^{1/2}$ , may be calculated.

Since the plastic top and sides are smoother than the sediments comprising the bottom of the closed duct, it is worthwhile considering the probable partitioning of total  $u_*$  between the plastic walls and sedimentary bottom. To do so, we must rely on pipe flow theory. Shear velocity in pipe flows can be estimated from:

$$u_* = V \left( \frac{f}{8} \right)^{1/2}$$

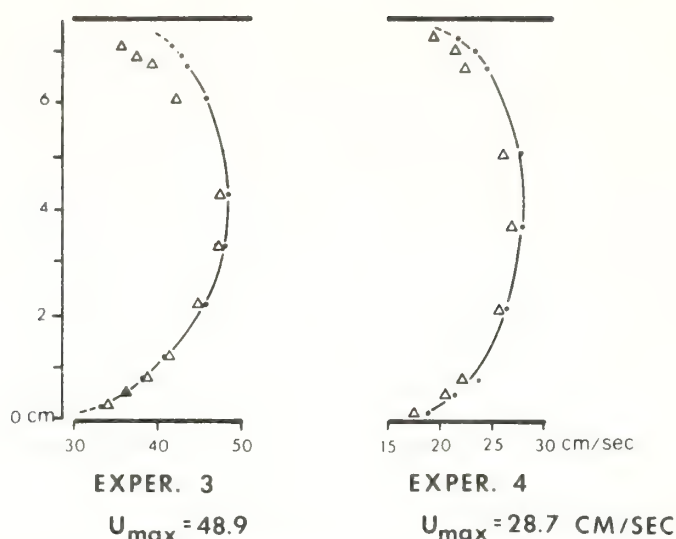


Fig. 3. Vertical velocity profiles at two flow rates measured with a pitot tube. Profiles were made at a position along the axis of a half-scale model of the SEAFUME equivalent in location to the position of the sphere flow meter and camera in the prototype. Dots and solid line (—) are observed velocity and triangles ( $\Delta$ ) are velocity calculated from the one-seventh power law (Prandtl and Tietjens, 1934).

where  $V$  is average velocity, and  $f$  is the Darcy friction factor which is dependent on pipe Reynolds number,  $R_N = DV/\nu$ , where  $D$  is pipe diameter, and relative roughness of the wall. These values have been tabulated graphically for a variety of pipes (Daley and Harleman, 1966, p. 274). In non-circular pipes, the diameter can be approximated by the hydraulic radius (wetted flow perimeter/flow cross-sectional area). Assuming that flow in the flume duct is roughly similar to pipe flow, using the values given for plastic and concrete to approximate the roughness of the flume walls and sediment surface, respectively, and letting  $V = 10$  cm/sec,  $D = 6.5$  cm and  $\nu(15^\circ) = 1.14 \cdot 10^{-2}$  cm<sup>2</sup>/sec (which gives  $R_N = 5.4 \cdot 10^3$ ), we obtain  $f^{1/2}$  (plastic) = 0.190, and  $f^{1/2}$  (sediment) = 0.217. This is equivalent to stating that for flows in a totally plastic duct or a totally sediment duct:

$$\frac{u_* \text{ (plastic)}}{u_* \text{ (sediment)}} = 0.88$$

This crude comparison between flow resistance in smooth and rough ducts allows us to infer that a relatively small error is introduced by using total  $u_*$ , rather than attempting a more complex analysis of partitioning of flow resistance in the duct.

To achieve better estimates of threshold  $u_*$  from the SEAFUME would require either better definition of the vertical velocity profile or a means of establishing the roughness of the sediments. In the laboratory, several instru-

mental techniques are available by which more detailed velocity profiles may be obtained, (i.e. hot wire anemometry, pitot tube) but these techniques are not easily adaptable for field use. On the other hand, for future use, an improved means of measuring mean flow in the SEAFUME can be achieved through the use of small propellor or electromagnetic current meters.

#### INITIAL RESULTS

A discussion of erosion experiments using SEAFUME on a clayey silt in water depths of 16 m in Buzzards Bay, Mass., is given in Young and Southard

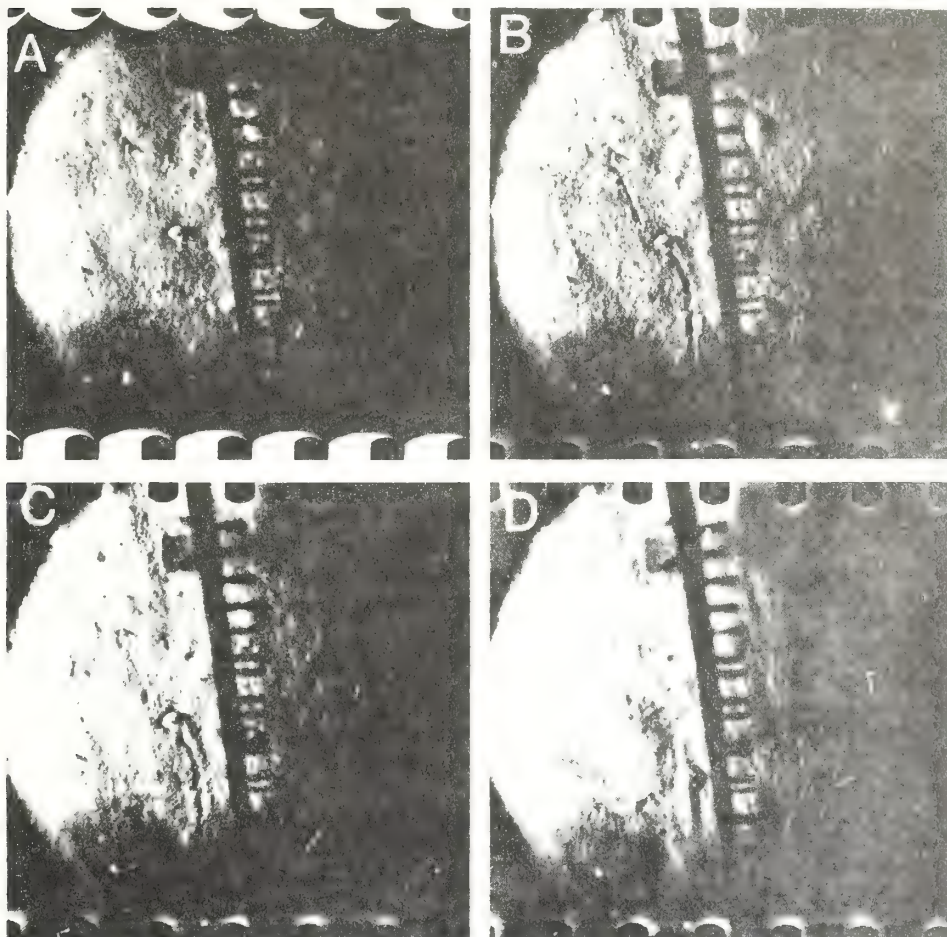


Fig. 4. Photographs taken during SEAFUME experiments on the clayey silts in the central region of Buzzards Bay, Massachusetts. Water depth is about 13 m. The upper photographs (A, B) show the initial condition of the bed. Note the organic mounds, tracks, and burrows, some of which are created by deposit-feeding benthic organisms during the experiments. Photograph C shows initiation of erosion at  $u_* = 0.35$  cm/sec. Photo D shows the bed after about 15 min of erosion at  $u_* > 0.35$  cm/sec.



(1976). Other experiments have since been carried out in water depths to 35 m. Examples of photographs obtained during some of these experiments are shown in Fig. 4. Comparison between threshold  $u_*$  in tidal flows in Buzzards Bay and in erosion experiments on the same sediment carried out in a laboratory flume shows that estimates of  $u_*$  obtained with SEAFUME are representative of those produced by tidal bottom currents, while  $u_*$  values obtained in the laboratory overestimate critical  $u_*$  obtained with SEAFUME by a factor of two or more. It is suggested that the precision and accuracy of threshold  $u_*$  estimates obtained with the SEAFUME are as good or better than estimates of  $u_*$  obtained with other instrument systems in situ, and are significantly better than laboratory measurements. The short time required to complete an erosion experiment in situ and the undisturbed nature of the sediments are additional advantages. An improved version of SEAFUME is being readied for use in the deep sea as well as in other shallow water environments.

#### ACKNOWLEDGEMENTS

Thanks are due to J.B. Southard and D.A. Ross for support and advice throughout development of SEAFUME. W. Gardner, S. Briggs, B. Allen, M. McCanus, and R. Nowak assisted in construction and engineering. H. Clifford and T. Stetson assisted during diving operations. Construction and salary support were initially given through the Education Office and Ocean Industries Program at the Woods Hole Oceanographic Institution and Office of Naval Research contract Nonr 4029 (00) NR 260-101 to W.H.O.I. Later support was through O.N.R. contract N00014-75-C-0291 and National Oceanographic and Atmospheric Administration contract 04-5-022-7 to M.I.T.

#### REFERENCES

- Bruce Jr., J.G. and Thorndike, E.W., 1967. Photographic measurements of bottom currents. In: J.B. Hersey (Editor), *Deep-Sea Photography*. Johns Hopkins Press, Baltimore, Md., pp. 107-111.
- Daley, J.W. and Harleman, D.R.F., 1966. *Fluid Dynamics*. Addison-Wesley, Reading, Mass., 454 pp.
- Neumann, A.C., Gebelein, C.D. and Scoffin, T.P., 1970. The composition, structure and erodibility of subtidal mats, Abaco, Bahama. *J. Sediment. Petrol.*, 40: 274-297.
- Postma, H., 1962. Sediment. In: *Demerara Coastal Investigation*. Hydraulics Lab., Delft, pp. 105-164.
- Postma, H., 1967. Sediment transport and sedimentation in the estuarine environment. In: G.H. Lauff (Editor), *Estuaries*. Am. Assoc. Adv. Sci. Publ., 83: 158-179.
- Prandtl, L. and Tietjens, O.G., 1934. *Applied Hydro- and Aero-mechanics*. Dover, New York, N.Y., 311 pp.
- SCCWRP, 1975. Progress Report 15: November, 1975. Southern California Coastal Water Res. Proj., 1500 E. Imperial Hwy., El Segundo, Calif.
- Scoffin, T.P., 1968. An underwater flume. *J. Sediment. Petrol.*, 38: 244-247.
- Sternberg, R.W., 1970. Field measurements of the hydrodynamic roughness of the deep-sea boundary. *Deep-Sea Res.*, 17: 415-442.
- Van Olphen, H., 1966. *An Introduction to Clay Colloid Chemistry*. Interscience, New York, N.Y., 301 pp.
- Young, R.A. and Southard, J.B., 1976. Erosion of fine-grained marine sediments: sea floor and laboratory experiments. *Geol. Soc. Am. Bull.*, in press.

Proceedings 11th Technical Conference on Hurricanes and Tropical Meteorology of the American Meteorological Society, Miami Beach, Florida, December 13-16, 1977, 688-695.

## AN EXPERIMENT IN FORECASTING HURRICANE GENERATED SEA STATES

Vincent J. Cardone

Oceanweather, Inc.  
White Plains, New York, 10601

Duncan B. Ross and Merlin R. Ahrens

National Oceanic and Atmospheric Administration  
Atlantic Oceanographic and Meteorological Laboratories  
Miami, Florida, 33149

### 1. INTRODUCTION

The need for better design surface wind and wave data in oceanic regions affected by tropical cyclones has stimulated measurement and modelling programs directed specifically towards describing surface environmental conditions. For example, a cooperative oil industry sponsored program known as the Ocean Data Gathering Program (Ward, 1974) resulted in the acquisition of a unique set of surface wave measurements in severe Gulf of Mexico hurricane Camille, 1969. The data were then used to calibrate numerical wind and surface wave specification models developed in a study described by Cardone, Pierson, and Ward (1976). They found the models to be capable of accurately specifying the anemometer level wind and directional wave spectrum for a variety of storm types if given an accurate description of certain meteorological characteristics of the storm and its track.

Recently new measurement capabilities have made possible the study of the hurricane surface environment from aircraft. Ross (1975) describes a NOAA research aircraft mission into severe Pacific hurricane Ava, which obtained boundary layer wind measurements and surface wave height and frequency spectral information.

In addition, NOAA data buoys positioned off the U. S. East and Gulf coasts have acquired interesting meteorological and oceanographic data sets, including wave spectra, in hurricanes Eloise, 1975 (Withee and Johnson, 1975), Belle, 1976, and Anita, 1977. Ross (1976) combined forty measured hurricane wave spectra from these rig, aircraft, and buoy (Eloise, 1975) sources and developed an empirically based parametric model of the wave characteristics in tropical cyclones.

Hurricane wave specification models are most often applied in a hindcast mode to simulate severe historical storms for climatological or design studies, or to validate model physics in well documented storms (cf. Cardone and Ross, 1977). The models, however, may be applied in real time to forecast winds and waves associated with hurricanes and typhoons (cf. Brand et al., 1977). The model outputs can

therefore provide objective guidance for the marine forecaster.

In the study reported here, the numerical spectral model of Cardone et al. (1976) and the parametric model of Ross (1976) were used experimentally to make wave forecasts in real time. The models were installed on the NOAA/AOML 1108 computer facility along with the numerical wind model described by Cardone et al., which was used to calculate hurricane surface winds from available National Hurricane Center hurricane advisory products.

Since the program began, real time forecasts have been made experimentally in hurricane Belle, 1976, in the pre-landfall period and in hurricane Anita, 1977, in the central and western Gulf of Mexico. This paper describes briefly the models used and presents verification of the forecasts against wind and wave measurements obtained as the storms passed near and over NOAA data buoys.

### 2. WAVE PREDICTION MODELS

This section summarizes the spectral and parametric wave prediction models. Only a brief review is attempted here - readers interested in the spectral model should refer to Cardone et al. (1976) while those interested in the basic approach followed by Ross (1976) should refer to Hasselmann et al. (1976).

#### 2.1 Spectral Model

The approach taken in this model is based upon the numerical integration of the wave energy-balance equation:

$$\frac{\partial S(f, \theta)}{\partial t} = -v_g(f, \theta) \cdot \nabla S(f, \theta) - F \quad (1)$$

where  $S$  is the directional wave spectrum,  $f$  is wave frequency,  $\theta$  wave propagation direction,  $v_g$  is group velocity, and  $F$ , the so-called source function, represents all processes that can transfer energy to or from the spectrum. In the model, equation (1) is solved by the successive simulation at each time step and on a regular grid array of points covering the spatial domain of

interest of the processes of wave propagation (the first term on the r.h.s. of (1)) and wave growth and dissipation (in the source function, F).

In the model the grid system is hexagonal and consists of 1521 points nominally spaced 20 n. mi. apart, laid out on a gnomonic map projection. At each grid point, the directional spectrum is resolved into fourteen frequency bands and twenty-four directional bands. Thus at each grid point there are 336 numbers, each of which represents the contribution to the variance spectrum of wave components in a finite frequency and directional band. At each model time step, which simulates one hour, equation (1) is solved, effectively, for each of the 336 spectral elements. The growth calculation uses a form for F which is applied only to spectral components propagating within  $\pm 90^\circ$  of the local wind direction and is consistent with models of the physical mechanisms that are believed to be responsible for the transfer of energy from the wind to surface waves.

Spectral components travelling against the wind are attenuated at a rate that depends on wave frequency and the energy of the local wind sea. The weak non-linear wave interactions of the type discussed by Hasselmann et al. (1976) are not modelled explicitly in the source function, but non-linear effects are certainly modelled implicitly by the form of F used.

Propagation of spectral components in deep water is accomplished by a Lagrangian scheme whereby spectral components simply translate (jump) to adjacent grid points in the appropriate direction after a sufficient number of time steps have elapsed to account for the displacement according to that component's deep water group velocity.

A version of the model includes a shallow water algorithm that accounts for wave refraction, shoaling and bottom friction, but this effect was not modelled in the experimental forecast in order to reduce costs.

The execution of the model starts with the calculation of the hurricane wind field and the mapping of hourly wind fields onto the model grid system. The ocean surface is taken initially as calm. Then, for each subsequent time step, the program updates the wind field, computes the changes in the spectrum at each grid point caused by growth and dissipative processes, and then propagates spectral components across the grid. The spectral field is at first unrealistic because of the initial conditions, but after a short spin-up period, usually 6-12 hours or so, it becomes indicative of the storm environment and responds thereafter to changes in storm size, intensity, and track.

It takes about eight minutes of central processor time on a Univac 1108 computer to execute one time step of the model for the full grid. For typical hurricanes, parts of the full grid can be made inactive, and a 24-hour storm period can thus be simulated in about two hours

of computer time (including the calculation of the wind field).

## 2.2 The Parametric Model

The model proposed by Ross (1976) is a simplification of the parametric approach to wave prediction proposed by Hasselmann et al. (1976). The method follows from the data collected in the JONSWAP study, the analysis of which suggested that fetch-limited wave spectra can be normalized in a way such that there is an approximate invariance of normalized spectral shape with fetch. The spectra can therefore be parameterized in terms of a small (2-5) number of parameters, for which forecast equations can be derived.

The original analysis of JONSWAP data followed the procedure proposed by Kitaigorodskii (1961) that for ideal fetch-limited wind seas, all wave variables, when non-dimensionalized in terms of g, gravity, and the wind speed U, should be functions only of the single non-dimensional fetch,  $\xi = gX/U^2$ , where X is the fetch. In JONSWAP, the non-dimensional peak frequency  $\nu = Uf_m/g$ , where  $f_m$  is the peak frequency, was found to be described well by the relation

$$\nu = 2.84 \xi^{-0.3} \quad (2)$$

Similarly, the non-dimensional total energy  $\epsilon = E^2 g/U^4$  where  $E = \int S(f, \theta) d\theta df$  showed a linear fetch dependence

$$\epsilon = 1.6 \times 10^{-7} \xi \quad (3)$$

In the Ross (1976) model, the fetch, X, is replaced by R, the radial distance to the eye of the hurricane, which represents a parameterization of fetch or duration. The data set from hurricanes Ava, Camille, and Eloise were then combined to produce the following power law fits:

$$\left. \begin{aligned} \nu &= .97 \xi'^{-.21} \\ \epsilon &= 2.25 \times 10^{-5} \xi'^{.45} \end{aligned} \right\} \xi' \leq 3.0 \times 10^4 \quad (4)$$

where  $\xi' = gR/U^2$ . It is noted, however, that the above mentioned hurricanes were relatively slow moving ( $v_f < 15$  knots), and therefore the power law fits could be appreciably different for fast moving storms or significantly smaller storms.

The application of the parametric model is, of course, much simpler and computationally more efficient than the spectral model. Given a specification of the average surface (10 m) wind field on an arbitrary set of grid points and the location of the storm center,  $\xi'$ ,  $\epsilon$ , and  $\nu$  can quickly be computed, and E, or significant wave height ( $4\sqrt{E}$ ), and  $f_m$  can then be easily displayed.

## 3. THE WIND SPECIFICATION

The hurricane wind-field model used in this study is an application of the theoretical model of the horizontal air flow in the boundary



layer of a moving vortex, as originally derived by Chow (1971). This model is based on the numerical integration of the vertically averaged (over the depth of the boundary layer) equations of motion that govern a boundary layer subject to horizontal and vertical shear stresses on the rotating earth. In vector form, the equation of motion is written in coordinates fixed to the earth:

$$\frac{d\vec{v}}{dt} + \psi \vec{k} \times \vec{v} = -\frac{1}{\rho} \nabla p + \nabla(K_H \nabla \cdot \vec{v}) - \frac{K_d}{h} |\vec{v}| \vec{v} \dots \quad (5)$$

where  $\vec{v}$  is the vertically averaged horizontal velocity,  $\psi$  is the Coriolis parameter,  $\rho$  is air pressure,  $h$  is the depth of the boundary layer,  $K_H$  is the horizontal eddy viscosity coefficient, and  $K_d$  is the drag coefficient. The equation is resolved in a Cartesian coordinate system the origin of which is allowed to translate at constant velocity ( $\vec{v}_f$ ) with the center of the pressure field associated with the vortex (in this case, the hurricane pressure eye). The variations in storm intensity and motion are represented by a series of quasi-steady states. With this representation, the pressure gradient becomes independent of time and may be simply prescribed. This nonlinear system of equations is solved numerically on a fine-mesh nested grid system as an initial value problem for the steady-state solution of the horizontal component of the vertically averaged velocity; that is, until the wind field on the moving grid becomes approximately steady. A simple transformation then yields the wind field with respect to the fixed-earth coordinate system. The calibration of the model involved the development of a scaling relationship between the anemometer level wind speed and the integrated boundary layer wind speed. This scaling law was developed mainly on the basis of wind data from a rig in the path of Camille, 1969, but it appears to be valid rather generally.

The adoption of the pressure specification technique originally suggested by Chow satisfied the constraint that the model be capable of initialization with the type of data available for historical storms. That is, the hurricane pressure field could be prescribed as the sum of an axially symmetric part ( $\bar{p}$ ) and a large-scale pressure field ( $\bar{p}$ ) of a constant gradient. The latter could be interpreted as a mean surface geostrophic flow ( $\vec{v}_g$ ) in which the storm is embedded, as determined from

$$\psi \vec{k} \times \vec{v}_g = -\frac{1}{\rho} \nabla \bar{p} \quad (6)$$

The symmetric variation of pressure with radius away from the storm's central pressure ( $p_0$ ) is described as

$$\bar{p} = p_0 + \Delta p e^{-r_a/r} \quad (7)$$

where  $r$  is the radial distance from the center of the hurricane,  $r_a$  is the scale radius (at approximately the radius of maximum wind) of the radial pressure profile, and  $\Delta p$  is the storm pressure anomaly. In this form, the theoretical model can be initialized from the parameters that are available or that can be determined

from historical meteorological records; i.e.,  $\Delta p$  (which also determines  $p_0$ ),  $r_a$ ,  $\vec{v}_g$ ,  $\vec{v}_f$ , and the location (latitude and longitude) of the hurricane center. The wind-field history for a storm then can be computed from knowledge of the variation of these parameters along the storm track.

A forecast wind field can be specified similarly from forecast track information and forecasts of storm central pressure, scale, and forward velocity.

Figure 1, is an example of the solution of the model for a typical storm; that is, one which is moving in the direction of the surface steering gradient. The parameters applicable to that representation are those of hurricane Belle actually observed when it was off the mid-Atlantic coast.

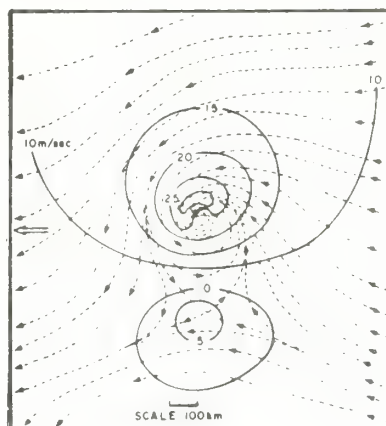


Figure 1. Typical solution of vortex boundary layer model for "steering flow" pressure specification. Streamlines and isotachs of 20 meter level wind shown.

#### 4. HURRICANE BELLE FORECAST

The first opportunity to run the forecast program in real time was provided by Hurricane Belle, which formed east of Florida on August 6, 1976. By the morning of August 9, it was apparent that Belle would likely move up the east coast of the U. S. passing near Buoys EB 15 and EB 41 and enter New England within 24 hours. A forecast run was initiated from 10 GMT August 9 inputs. The forecast track and wind model input parameters were extracted wherever possible from official NHC advisories and products, but were supplemented with information obtained in personal communication with the NHC forecaster on duty.

The forecast track used for the Belle forecast is compared to the actual track in Figure 2 which also depicts the relative location of the NOAA data buoy EB 41. The forecast parameters of storm intensity and scale are compared to observed data in Figure 3. Clearly, errors in the forecast track, at least up to the approximate locations of EB 41, are small, but

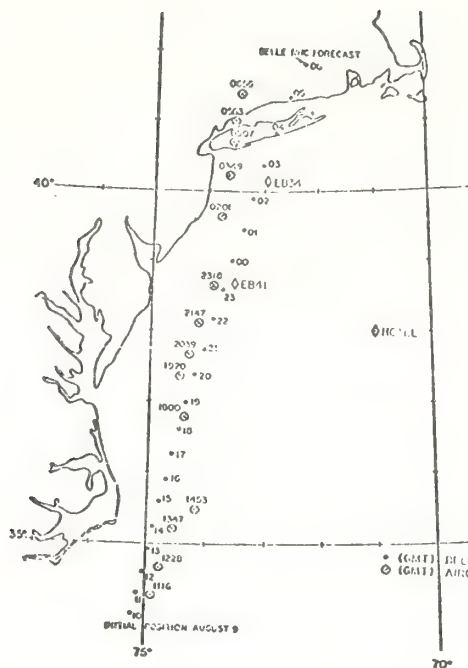


Figure 2. Forecast and observed track in Hurricane Belle 8/9-8/10.

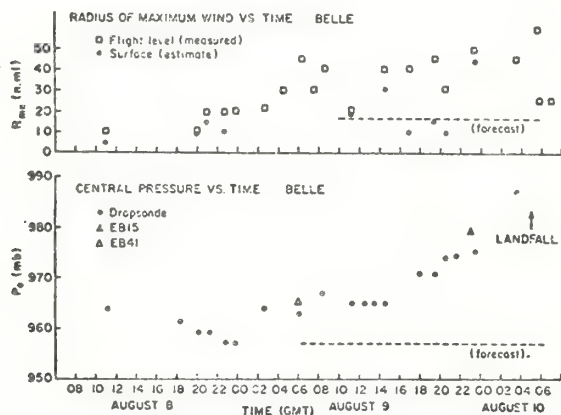


Figure 3. Observed and forecast storm parameters in Hurricane Belle.

but errors in forecast storm characteristics are large.

Since the forecast track moved Belle almost directly over EB 41, the maximum storm sea states were forecast by both models to pass just to the right of the buoy. EB 41 recorded a 15-minute sample of wave height every three hours. The data are processed on board, and spectra and derived quantities are transmitted to a shore facility for dissemination on the standard synoptic communications network. The

buoy also measured wind speed and direction over an 8.5-minute interval once per hour. The vortex shedder anemometer is mounted at a height of five meters. Data from EB 34 are considered unreliable as the buoy broke loose from its mooring during the storm.

Figure 4 compares the model forecasts of average wind speed at an anemometer height of 20 meters, wind direction, and Figure 5 the significant wave height, at EB 41 to the buoy measurements. For this comparison, wind speeds

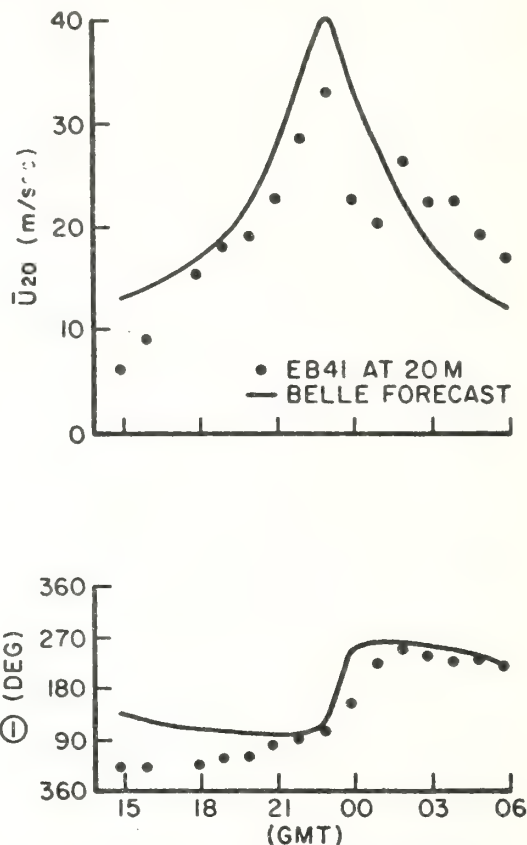


Figure 4. Comparison of measured (adjusted to 20 meter height) and forecast wind speed and direction in Belle at EB 41.

measured by the buoy were adjusted to a height of 20 meters using the method of Cardone (1969).

The "errors" in the forecast time-histories shown in Figures 4 and 5 require very cautious interpretation, as they represent a complicated mix of errors from the forecast of storm track, intensity, and size and errors due to model deficiencies. In addition there is some indication that the buoy vortex shedder winds may be degraded by rain, which surely was present for most of the period of interest. Finally, the wave measurements are available only once per three hours, which in a hurricane environment is

insufficient to sample and resolve the true evolution of the wave history at the site. It is quite possible that maximum sea states at the buoy site were higher than the highest measured value.

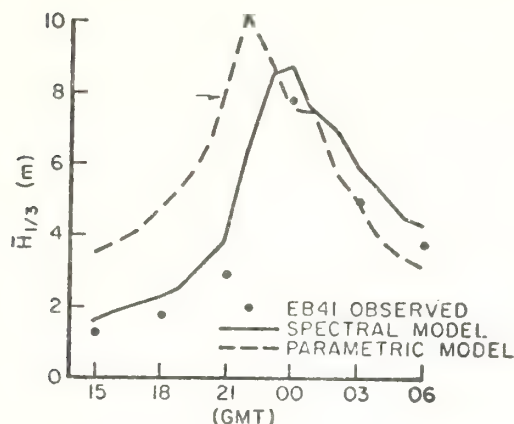


Figure 5. Verification of significant wave height time history forecast from spectral and parametric wave models at EB 41 in Belle.

Nevertheless, it may be said that both wave forecast models do a creditable job of specifying the maximum sea states likely experienced at the buoy, while the spectral model appears to better forecast the overall time history. At least part of the overall positive bias in the forecasts of both models is due to the unforecast rapid weakening of Belle in the pre-landfall period.

The forecast wind errors in the Belle wave forecast has been investigated by performing a detailed post analysis and hindcast of the winds and waves in this storm. Using post analysis values for storm input parameters, the wind model calculated winds at EB 41 that compared very well with those measured (Figure 6).

The wave height predictions from hindcast winds are compared to the EB 41 measurements in Figure 7. As expected, the hindcast time histories are closer to the observations than those forecast, but infra-model differences remain. For example, the parametric model hindcast positive bias early in the EB 41 time history implies that the model is overpredicting wave heights in Belle's forward quadrants. This is believed to be a consequence of the calibration of the model against data from slow moving storms and the more wind duration limited characteristics of waves in the forward quadrants of fast moving storms.

As an example of the more detailed forecast products potentially available from wave models, Figure 8 compares maximum hindcast one-dimensional frequency spectra specified directly by the spectral model, computed from the forecast parameters of the parametric model, and observed at EB 41.

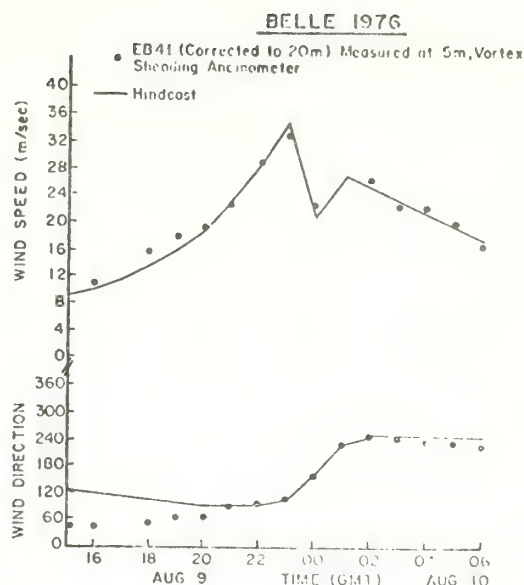


Figure 6. Hindcast wind speed and direction at EB 41 in Belle (Cardone and Ross, 1977).

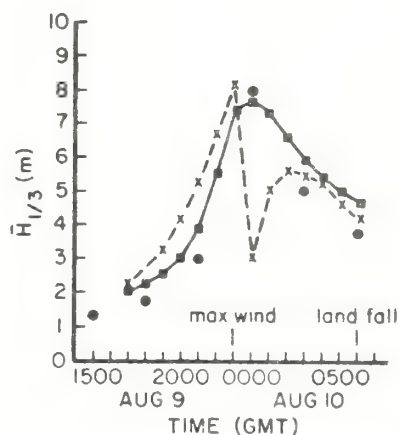


Figure 7. Hindcast significant wave height time history at EB 41 in Belle (Ross and Cardone, 1977): • - measured; x - parametric model; ■ - spectral model.



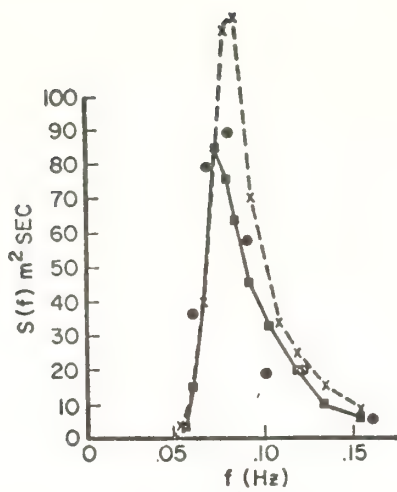


Figure 8. Maximum hindcast spectra for Hurricane Belle at EB 41 (Ross and Cardone, 1977): x - parametric model,  $H_{1/3}=8.2$  m; ■ - spectral model,  $H_{1/3}=7.8$  m. Also shown is maximum observed spectrum (●)  $H_{1/3}=7.8$  m.

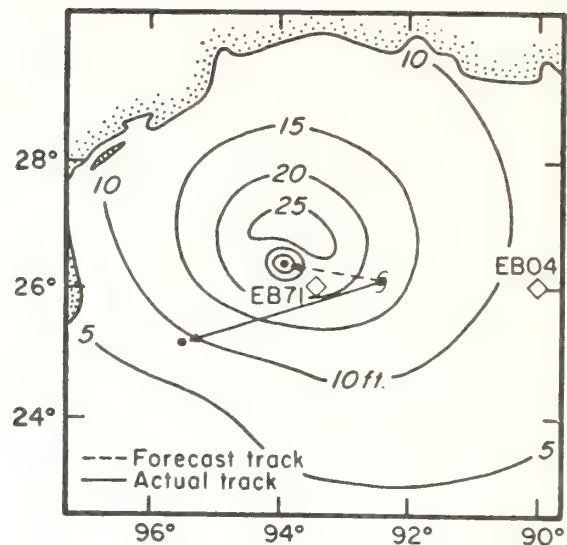


Figure 9. Parametric model derived forecast of significant wave height around Anita. Forecast made at 22 GMT 8/31/77, valid at 18 GMT 9/1/77. Buoy positions, forecast track, and actual track also are shown.

## 5. HURRICANE ANITA FORECAST

A series of forecasts were prepared in real time during Hurricane Anita and made available as guidance for the National Hurricane Center forecasters. Only a brief preliminary evaluation of one of the series is presented here as the forecast data sets are presently under study. The forecast described here was prepared from 2200 GMT 8/31/77 inputs and covered the 21 hour period ending 1800 GMT 9/1/77.

During the forecast period, Hurricane Anita passed very near buoy EB 71, at which hourly wind and 3-hourly wave measurements were made. Similar measurements were made at EB 04, which was on the periphery of the storm during the period of the forecast. Figure 9 shows the forecast wave height distribution around Anita produced by the parametric model, the forecast track used, the actual track, and the locations of the data buoys. Figures 10 and 11 compare the forecast parameters of intensity,  $p_0$ , and scale,  $r_p$ , used as input to the wind model, and the characteristics actually observed. As in Belle, the scatter in  $r_p$  is large. The most significant error in Anita's forecast, however, is the forecast position error.

In view of the large error in forecast track, especially with respect to the location of EB 71, the track error, which would have overwhelmed the comparisons at the buoy, was removed completely before "forecast" wind and wave time histories at EB 71 and EB 04 were compared to measurements. Figures 10 through 15 pre-

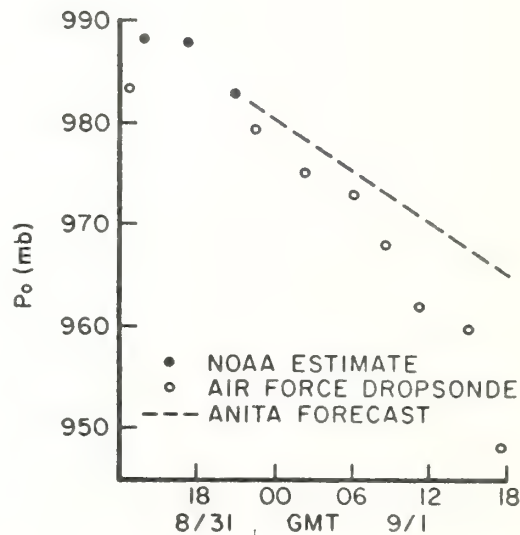


Figure 10. Observed and forecast central pressure in Hurricane Anita.

sent those "best track" forecast wind and wave time histories. The forecast wind time histories compare favorably with those observed. The mean and rms differences between forecasts and measured significant wave heights are  $-.75 \pm .54$  m (spectral) and  $.21 \pm .83$  m (parametric) at EB 71, and  $-.64 \pm .23$  m (spectral), and  $-.48 \pm .64$  m (parametric) at EB 04.

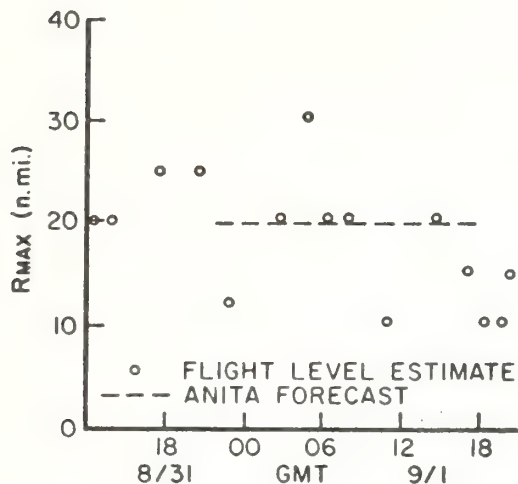


Figure 11. Observed and forecast radius of maximum wind in Anita.

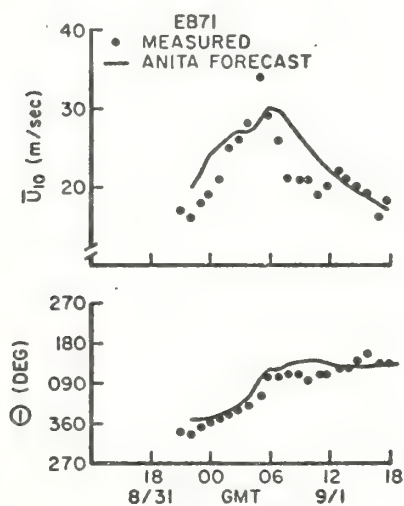


Figure 12. Measured and forecast wind speed and direction in Hurricane Anita at EB 71.

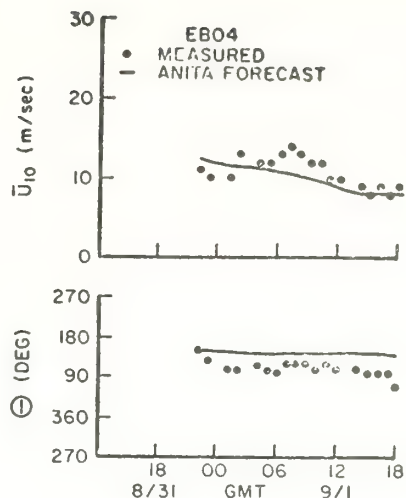


Figure 13. Measured and forecast wind speed and direction in Hurricane Anita at EB 04.

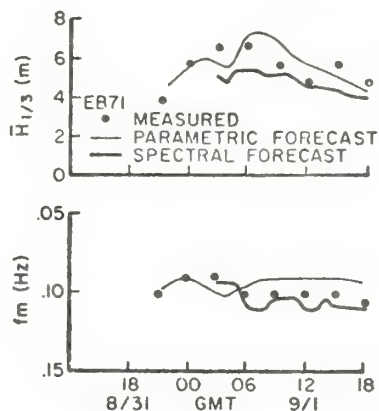


Figure 14. Measured and forecast significant wave height and peak frequency in Hurricane Anita at EB 71.

## 6. CONCLUSIONS

This study demonstrates feasibility of obtaining useful forecasts of sea state in hurricanes with existing model capabilities. However, it must be remembered that the models are critically dependent upon a proper specification of the wind field which in turn depends upon accurate forecasts of storm track, intensity, and size. The errors seen in the forecast wave conditions of Belle and Anita are typical of the current state of the art.

In view of those errors, it is appropriate that the computationally efficient parametric model be employed in operational

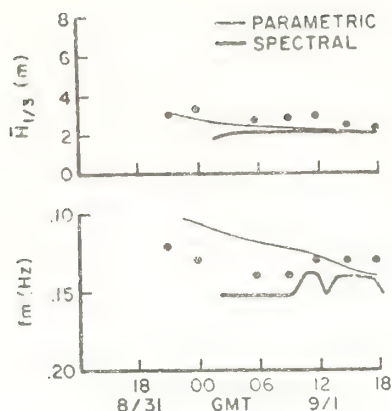


Figure 15. Measured and forecast significant wave height and peak frequency in Hurricane Anita at EB04.

forecasting, as it can be quickly updated as changes in storm intensity and track occur.

A particularly important parameter in the wind specification model is the radius of maximum wind. This parameter is not routinely forecast nor is it reliably measured to the desired accuracy. The scatter in the estimates of this parameter, strongly suggests the need for improvements in the monitoring of this storm characteristic, possibly through consistent low altitude eye penetration by reconnaissance aircraft and use of enhanced satellite imagery.

Finally, this study begins to reveal the tremendous potential of the NOAA data buoy system. The data buoys not only are important elements of the operational marine observing system but can provide unique measurements in extreme conditions for use in research programs concerned with the development of improved environmental prediction models. The outstanding performance of the prototype buoys in hurricanes Eloise, Belle, and Anita has resulted in unique data that will be particularly valuable in the further development of hurricane wind and wave models.

## 7. ACKNOWLEDGEMENTS

We thank Shell Development Company, for supporting jointly with NOAA, the adaptation of the Ocean Data Gathering Program hurricane wind and spectral models to the NOAA, AOML computer facility.

Dr. Cardone's participation in this study was supported by NOAA under Grant 04-7-022-44014.

## 8. REFERENCES

- Brand, S., K. Rabe, and T. Laevastu, 1977: Parameterization characteristics of a wind-wave tropical cyclone model for the Western North Pacific Ocean. *J. of Phys. Oceanogr.*, Vol. 7, 5, 739-746.
- Cardone, V. J., 1969: Specification of the wind distribution in the marine boundary layer for wave forecasting. TR69-1 Geophysical Sciences Laboratory, New York University. (NTIS No. AD702490).
- Cardone, V. J., W. J. Pierson, and E. G. Ward, 1976: Hindcasting the directional spectra of hurricane generated waves. *J. Pet. Tech.*, April, pp. 385-394.
- Cardone, V. J. and D. B. Ross, 1977: State of art wave prediction methods and data requirements. Prepared for the NOAA Ocean Wave Climate Symposium, July 12-14, 1977, Washington, D. C. Proceedings to be published by Plenum Company, 1978.
- Chow, S., 1971: A study of the wind field in the planetary boundary layer of a moving tropical cyclone. MS thesis, Dept. of Meteorology and Oceanography, New York University.
- Hasselmann, K., D. B. Ross, P. Muller, and W. Sell 1976: A parametric wave prediction model. *J. Phys. Oceanogr.*, 6, pp. 200-228.
- Kitaigorodskii, S. A., 1961: Applications of the theory of similarity to the analysis of wind-generated wave motion as a stochastic process. 1 zu. Akad. Nauk. SSSR, Ser. Geophys., No. 1, 73-80.
- Ross, D. B., 1975: A comparison of SKYLAB S-193 and aircraft views of surface roughness and a look toward Seasat. Proceedings of the NASA Earth Resources Survey Symposium, L. B. Johnson Space Center, Houston, Texas, June, 1975, 1911-1920.
- Ross, D. B., 1976: A simplified model for forecasting hurricane generated waves (Abstract). B. Amer. Met. Soc., January, p. 113. Presented at Conference on Atmospheric and Oceanic Waves, Seattle, Washington, March 29-April 2.
- Ross, D. B., and V. J. Cardone, 1977: A comparison of parametric and spectral hurricane wave prediction products. To be published in the Proceedings of "NATO Symposium on Turbulent Fluxes through the Sea Surface, Wave Dynamics and Prediction", Marseille, France, 12-16 September 1977 (Plenum Publishing Corporation, New York, New York).
- Ward, E. C.: Ocean Data Gathering Program - An overview. Paper OTC 2108-B presented at Sixth Annual Offshore Technology Conference, Houston, May 6-8, 1974.
- Withee, G. W., and A. Johnson, Jr., 1975: Buoy observations during hurricane Eloise. Data Buoy Office National Oceanic and Atmospheric Administration, Bay St. Louis, Mississippi.



Final Report to: NOAA Sea-Air Interaction Laboratory and Shell Development Company, December 1976, 45 pages (Abstract only).

FORECASTING HURRICANE WINDS AND WAVES  
A PILOT STUDY

V. J. Cardone<sup>1</sup>, D. Ross<sup>2</sup>, M. Ahrens<sup>2</sup>, J. A. Greenwood<sup>1</sup>,  
C. Greenwood<sup>1</sup>, R. E. Salfi<sup>1</sup>

ABSTRACT

A directional spectral wave hindcast model developed at the City University of New York Institute of Marine and Atmospheric Sciences for application to Gulf of Mexico hurricanes is modified for implementation on the NOAA Atlantic Oceanographic and Meteorological Laboratories' computer facility for application in real time to forecasting of Gulf and East Coast hurricanes. The results of this model are compared to results from a simpler parametric model developed at the AOML Sea-Air Interaction Laboratory for several severe historical storms that have affected the Gulf and East Coast. The intercomparison indicates that the models produce similar results for slow moving ( $\leq 15$  knots) storms and increasingly divergent results for faster moving storms. A real time forecast of Hurricane Belle is described. The forecast sea states verified at a NOAA data buoy suggest that both models are limited mainly by errors in operational forecasts of hurricane track, intensity, and scale.

---

<sup>1</sup>CUNY Institute of Marine and Atmospheric Sciences at the City College  
New York, N.Y. 10031

<sup>2</sup>NOAA Sea-Air Interaction Laboratory, Miami, Florida

### Reply

K. HASSELMANN,<sup>1</sup> D. B. ROSS,<sup>2</sup> P. MÜLLER<sup>3</sup> AND W. SELL<sup>1</sup>

26 August 1976

#### 1. Introduction

In his comments Pierson has raised a number of interesting questions. To place the discussion in proper perspective, we should perhaps first point out that the

purpose of our paper was not to experiment with various parametrical representations of the wave spectrum—as interesting as these are—but to apply recent results on the energy balance of the wave spectrum to the practical task of wave prediction. These results, summarized in Hasselmann *et al.* (1973, hereafter called J), have changed the structure of the wave prediction problem.

On the one hand, the problem has apparently be-

---

<sup>1</sup> Max-Planck-Institute für Meteorologie, Hamburg.

<sup>2</sup> Sea-Air Interaction Laboratory, NOAA, Miami, Fla.

<sup>3</sup> Sonderforschungsbereich 94, Meeresforschung, University of Hamburg, and Max-Planck-Institut für Meteorologie.

come more complicated through the dominant role of the nonlinear resonant energy transfer mechanism in determining the form of the spectrum and the rate of shift of the spectral peak in a growing wind sea. With present day (and foreseeable) computers the rigorous Boltzmann integral expression for the energy transfer cannot be integrated numerically, even approximately, for an arbitrary wave spectrum within the framework of a numerical wave prediction scheme. In another respect, however, the problem has in fact become simpler, because the nonlinear energy transfer continually readjusts the energy distribution within the spectrum to a selfstabilizing, quasi-universal form in which the individual geometric signatures of the generating wind fields are largely lost. Both factors point to the need for simplified parametrical representations in which the usual discretization of the wave spectrum in terms of several hundred degrees of freedom is replaced by far simpler representations containing only a few free parameters.

Although parametrical representations clearly have their specific problems, as Pierson points out, we feel this is not the principal difficulty confronting the development of wave-prediction models. For this reason, many of the valid points raised by Pierson were not discussed in detail in the paper. For example, it is clear that since the wave spectrum is a statistical quantity, the parameters describing the wave spectrum will also be statistical variabiles. Thus, whenever presenting a spectral parameter one should also indicate its statistical sampling variability; in the same way that plots of power spectra are normally presented with error bars denoting their confidence limits. This was not done in our paper, as it is obvious from a cursory inspection of our data that the natural geophysical variability of the parameters shown by far exceeds the sampling variability associated with the statistical uncertainty of the spectra to which the parametrical forms were fitted (see also J, § 2.4). The understanding of this large natural variability, which is apparent even in the highly selected JONSWAP data, is one of the important problems which must be faced in assessing the ultimate limitations of numerical wave prediction models.

After these general comments we turn to the specific points raised by Pierson, following his subdivision into four groups of questions.

## 2. The parameters $\alpha$ and $\gamma$

It is not claimed that our method of fitting parameters to fetch-limited and fully developed spectra is unique. After experimenting with a number of different functions, we chose the five-parameter function (H 2.1) as a manageable but sufficiently flexible form simply because 1) it gave a good fit to essentially all the spectra

we encountered, and 2) it was conceptually rather simple, being derived from the well-known Pierson-Moskowitz spectral shape by multiplying with a narrow band "peak-enhancement" function, effective only near the peak, to model the observed variations in the width and amplitude of the peak. We agree with Pierson that Salfi's (1974) method of representing fetch-limited spectra in which the fully developed PM spectrum is replaced by a low-frequency cutoff function  $G$  below some fetch-dependent peak frequency also yields a spectrum rather similar in shape to the mean JONSWAP spectrum, with an equivalent peak enhancement factor  $\gamma$  near 3 for small fetches. However, it should be noted that Salfi's form contains only one free parameter, the peak frequency, which then determines the peak enhancement factor and the equivalent left- and right-sided peak widths. Thus Salfi's form is not general enough to investigate the observed variability of spectral shapes, which was the principal reason we introduced a parametrical representation of the spectrum containing three free-shape parameters, in addition to the peak frequency and energy-scale parameter  $\alpha$ . However, when considering only the *mean* evolution of a growing wind sea as a function of fetch, where we found  $\gamma$ ,  $\sigma_a$  and  $\sigma_b$  in our representation to be essentially constant until one comes very close to the fully developed state, any one of the different empirical formulas quoted in J and H are probably acceptable within the scatter of the observations. Our only criticism of Salfi's representation is that it fails to reproduce the decrease of  $\alpha$  with fetch found in J and by a number of other workers (cf. J, Fig. 2.7). (The minor differences—less than 20%—in computing  $\alpha$  according to Salfi's or our procedure are negligible in this context.)

As pointed out in J, however, the reason for introducing a parametrical representation of our fetch-limited data was not to present yet another empirical formula for the growth of wind waves for the ideal case of a uniform wind blowing orthogonally off a straight shore, but rather to clarify the physics responsible for the observed wave growth in order to develop a wave prediction model applicable for *arbitrary* wind fields and boundaries. As a result of our dynamical analysis, we believe that wave prediction models which ignore the nonlinear energy transfer and are based solely on the combination of a Miles-Phillips generation mechanism and a limiting equilibrium range characterized by a universal Phillips constant  $\alpha$  are physically incorrect. While these models can be tuned to give similar results to our model for the ideal fetch-limited situation (except for the fetch-dependence of  $\alpha$ ), we believe they will produce incorrect predictions when applied to other wind fields. These conclusions are based on rigorous calculations of the nonlinear energy transfer for observed spectra, rather



than actual comparisons of the performance of different models for complex wind fields. Such experiments are clearly needed.

### 3. Sampling variability and bias

Since the observed spectra to which our parametrical form (2.1) is fitted is a statistical estimate of the "true" spectrum, the fitted parameters  $f_m$ ,  $\alpha$ ,  $\gamma$ ,  $\sigma_a$  and  $\sigma_b$  also represent statistical variables. If the parameters depend linearly on the spectrum, their statistical properties can readily be evaluated from the standard Tukey statistics of spectral estimates. Unfortunately, it is a characteristic of most parametrical fits, including ours, that the fitting algorithm represents a rather complex nonlinear functional dependence of the parameters on the spectrum. Thus it is possible to give only rather crude estimates of the statistical variability of the parameters. For a typical JONSWAP spectrum computed with 36 degrees of freedom, the standard deviations of the individual spectral estimates are approximately 24% of the spectral values. We estimate the standard deviations of our parameters, expressed as percentages of the variables themselves, to be of the following orders:  $f_m$ : 5–10%;  $\alpha$ : 4–6%;  $\gamma$ : 20–40%;  $\sigma_a$ ,  $\sigma_b$ : 20–50%. These variations are relatively insignificant compared with the much larger natural variability of the parameters found even for the highly selected, "ideal" JONSWAP cases.

Pierson has further suggested that our  $\gamma$  estimates are biased toward too high values through our rejection of multiple-peaked spectra. Multiple-peaked spectra were rejected only for the Moskowitz (1963) set of fully-developed spectra. The rejections were limited to cases where the deviation of the spectrum from a single-peaked Pierson-Moskowitz form were considerably greater than could be explained by the variability of spectral estimates. Multiple-peaked spectra which were consistent with the estimated statistical variability were retained. Similarly, all multiple-peak spectra of the other data sets were retained. We believe our rejection of these multiple-peaked spectra to be fully justified and certainly as rigorous a procedure as that of Pierson and Moskowitz when they rejected the averaged 18.01 m s<sup>-1</sup> spectrum in the development of their model because it "seems to be distorted in shape compared to the other four" (Pierson and Moskowitz, 1964, p. 5183).

However, this point need hardly be argued. We reanalyzed Moskowitz' fully developed spectra, because it was clear that Moskowitz' method of averaging all spectra within a 5 kt wind band would necessarily yield a flatter average spectrum than the technique we used, in which the spectral shape parameters were first fitted to each spectrum separately and then the shape parameters averaged afterward. We suspected

that this may be the reason the JONSWAP data indicated no systematic decrease of  $\gamma$  relative to its mean value of 3.3 with increasing fetch, although the fully developed Pierson-Moskowitz spectrum corresponds to a value of  $\gamma=1$ . Contrary to our suspicions, however, our reanalysis of Moskowitz' data *did* indicate a significantly lower value of  $\gamma=1.4$  for fully developed spectra, and our conclusion was that the Pierson-Moskowitz spectrum was indeed a fair description of a fully developed sea, despite the ambiguities in defining an average spectrum. In view of the standard deviation of 62% in the  $\gamma$ -values of the Moskowitz set of fully developed spectra (cf. H, Table 1) it appears a rather fine point to debate whether the residual difference between our value of  $\gamma=1.4$  and the Pierson-Moskowitz value  $\gamma=1$  is due to the genuine difference in averaging techniques or the rejection of multiple-peaked spectra which were considered—correctly or incorrectly—to be swell contaminated.

### 4. The use of winds at 10 m

We have used 10 m winds consistently throughout our analysis except at one point, where we have mistakenly substituted the 10 m wind instead of the 19.5 m wind into the expression for the peak frequency of the fully developed PM spectrum. We are grateful to Pierson for drawing attention to this error. It can be corrected, as he points out, by setting  $\nu=0.13$  instead of  $\nu=0.14$  as the transition point from a fetch-limited to a fully developed sea. Fortunately, the error is such that it led only to the exclusion of some marginal cases of almost fully developed seas from our fetch-limited data sets, rather than the incorrect inclusion of fully-developed cases. Thus our results are not materially affected.

### 5. The equilibrium range

Throughout J and H, the  $f^{-5}$  "equilibrium" range referred for field data always to frequencies in the gravity-wave region between the peak frequency and the natural cutoff of most of the instruments used, around 0.5 Hz. Within this range, the data could be scaled quite well using Kitaigorodskii's scaling relations.

The  $\alpha$ - $\bar{x}$  relation (2.44) in J, from which the  $\alpha$ - $\nu$  relation (6.1) in H was derived, was based not only on field data but also on laboratory results. These were included because they were still within the gravity-wave range and scaled quite well with the field data in accordance with Kitaigorodskii's relations. However, it was pointed out in J that the JONSWAP data alone would have produced a steeper  $\alpha$ - $\bar{x}$  relation (as evidence in the steeper  $\alpha$ - $\nu$  relation in H, Fig. 9a), so that Kitaigorodskii's relations apparently do not apply exactly.

The relation (6.1) was nevertheless retained in H as it was found to give good agreement again with the composite data set (cf. H, Fig. 9j). We agree with Pierson that one must expect Kitaigorodskii's scaling laws to break down in the capillary-wave range, but large systematic discrepancies were not evident in the field data for gravity-wave frequencies below 0.5 Hz.

## REFERENCES

- Hasselmann, K., T. P. Barnett, E. Bouws, H. Carlson, E. E. Cartwright, K. Enke, J. A. Ewing, H. Gienapp, D. E. Hasselmann, P. Kruseman, A. Meerburg, P. Müller, D. J. Olbers, K. Richter, W. Sell, and H. Walden, 1973: Measurements of wind-wave growth and swell decay during the Joint North Sea Wave Project (JONSWAP). *Deut. Hydrogr. Z.*, A8, No. 12.

# Quantitative mapping of suspended solids in wastewater sludge plumes in the New York Bight Apex

R. W. Johnson  
National Aeronautics and Space Administration,  
Hampton, Va.

I. W. Duedall  
State University of New York, Stony Brook

R. M. Glasgow  
Vought Corporation, Hampton, Va.

J. R. Proni, T. A. Nelsen  
National Oceanic and Atmospheric Administration,  
Miami, Fla.

Large quantities of wastewater sludge, dredge spoils, industrial wastes, and cellar dirt are dumped<sup>1, 2</sup> in the apex of the New York Bight (Figure 1). Little is known about the local dispersion of these wastes in coastal waters. Previous preliminary investigations of the dispersion of wastewater sludge plumes and suspended materials include studies on the fate of sludge-derived ammonium in the water column,<sup>3</sup> the fate of wastewater sludge as measured by carbon and nitrogen in sediment samples collected from the wastewater sludge disposal site,<sup>4</sup> and the distribution of suspended material in the water column as measured by an acoustical system.<sup>5</sup> These studies have provided valuable information about both long- and short-term aspects of wastewater disposal at sea, but they are limited by the number of stations that can be sampled in a short time.

Synoptic surface distributions of features such as suspended solids (ss) associated with ocean dumping and the resultant surface plumes may be studied by remote sensing from aircraft and satellite platforms. Spectral anomalies have been used to locate and qualitatively map readily identifiable features such as suspended sediment associated with river discharges.<sup>6</sup> Quantitative mapping of the distribution of water quality properties using remotely sensed data has been reported by

Johnson,<sup>7-9</sup> who used a statistical stepwise regression analysis to calibrate remotely sensed data.

The purpose of this investigation was to apply the previously reported methodology<sup>7-9</sup> to remotely sensed data that were collected over wastewater sludge plumes in the New York Bight apex on September 22, 1975. Spectral signatures were also determined during this study. These signatures may be useful in the specific identification of sludge plumes, as opposed to other plumes such as those created by the disposal of industrial acid wastes. The work described here was conducted jointly by the National Aeronautics and Space Administration (NASA), the National Oceanic and Atmospheric Administration (NOAA), and the State University of New York (SUNY).

## TEST SITE

The area selected by NOAA for this experiment was in the apex of the New York Bight (Figure 1). Within the apex, wastewater sludge is dumped on a daily schedule in an Environmental Protection Agency (EPA) designated area about 18 km (9.7 nautical miles) south of Long Island. Prior to the experiment, a 2-day moratorium on sludge dumping in the Bight apex was in effect.



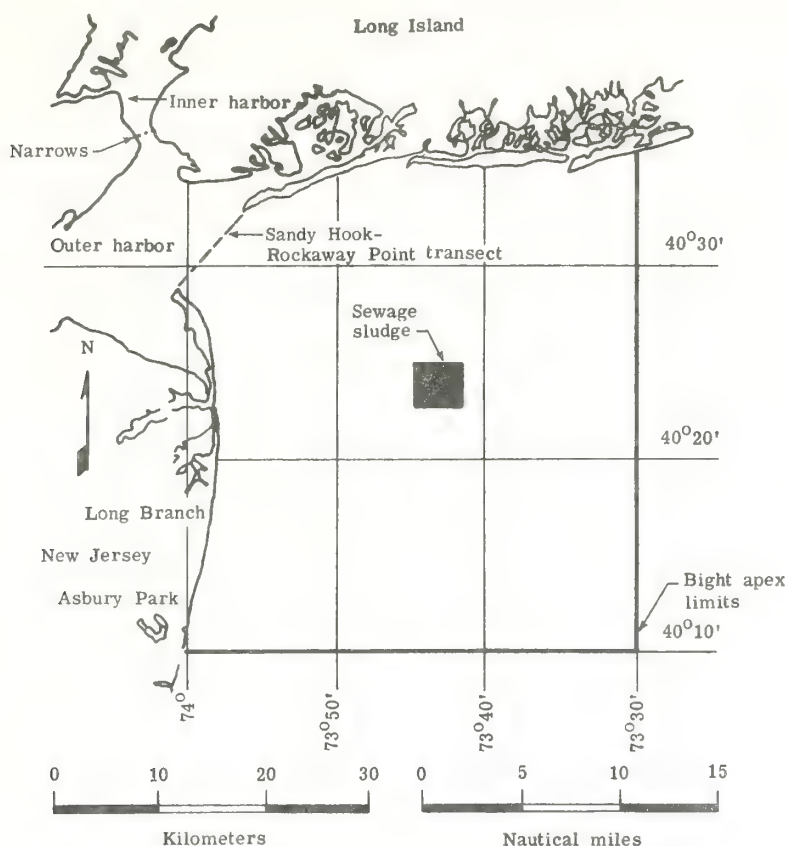


FIGURE 1. Wastewater sludge dump area in the New York Bight apex.

#### EXPERIMENTAL METHOD

On September 22, 1975, three wastewater sludge dumps and their plumes were monitored by aircraft remote sensing and by the surface vessels *Kelez* (NOAA) and the *Onrust* (SUNY). Data from the aircraft platform were collected by a multispectral scanner, multispectral photography, and a mapping camera. The sea-truth data were obtained by water sampling and acoustic profiling (from the *Kelez* only) in and around the sludge plumes. In this paper, only the multispectral scanner data are considered, using the mapping camera photography for visual location and identification of the surface features and the sea-truth measurements consisting of the concentrations of ss and chlorophyll *a*. The water column distributions of properties and results from acoustic investigations are presented in other reports.<sup>10, 11</sup>

Two dumps were made in the morning: A line dump from a moving barge, starting at about 10:46 AM eastern daylight time (EDT) and ending about 11:16 AM, and a spot dump from a stationary barge, which began at 11:00

AM and ended at 11:05 AM (EDT). A third spot dump took place from about 2:53 PM to 2:58 (EDT). The sea-truth measurements reported here were made during and following the morning dumps. No sea-truth measurements were made during the afternoon dump.

**Sea-truth measurements.** Sea-truth measurements made by the *Kelez* in the morning line dump plume consisted of 10 sets of water samples, five taken in the plume and five taken in water adjacent to the plume. These samples were subsequently analyzed in the laboratory for ss and chlorophyll *a* concentrations. Particle size distributions (by Coulter Counter) were made onboard the *Kelez* within 2 hours of sampling. Locations of the sea-truth stations were determined from a plot of the ship's path during the sampling period, overlaid on the essentially instantaneous location of the plume from the remote sensors and taking into account the apparent plume drift. Sea-truth stations and the ship's path (*Kelez*) are shown in Figure 2. The ss and chlorophyll *a* concentrations determined for the 10 sea-truth

stations are listed in Table I, along with corresponding radiance values obtained by the remote sensor, which will be described in the following section. Typical particle size distributions for stations in and out of the plume area are shown in Figure 3.

The *Onrust* was stationed in the spot dump where samples for ss, chlorophyll *a*, and other analyses were collected. The samples for ss analysis were collected in 500-ml glass bottles and taken back to the laboratory for vacuum filtration onto preweighed 0.8- $\mu\text{m}$  (pore size) filters. The results from the *Onrust* are also given in Table I.

**Remotely sensed data.** Remote sensors that measure electromagnetic radiation in the visible and near-infrared (IR) wavelengths were flown over the test site. The NASA NP-3A aircraft flew at a nominal altitude of

3.0 km (10 000 ft) and a speed of 444 km/h (240 knots). Two onboard remote sensor systems collected data for these analyses: an 11-band M2S multispectral scanner, which consisted of 10 bands in the visible and near-infrared and one thermal band; and a Zeiss mapping camera. Spectral and spatial characteristics of the M2S scanner and mapping camera are listed in Table II. Because of instrumentation problems, the M2S unit recorded useable data only in Bands 2, 3, 4, 7 and 9. These bands seem to provide adequate coverage of the visible and near infrared spectral range.

Digital data from the M2S scanner were recorded inflight on magnetic tape in a high density format. Inflight calibration was also provided for each line of data. Screening imagery in conjunction with the mapping

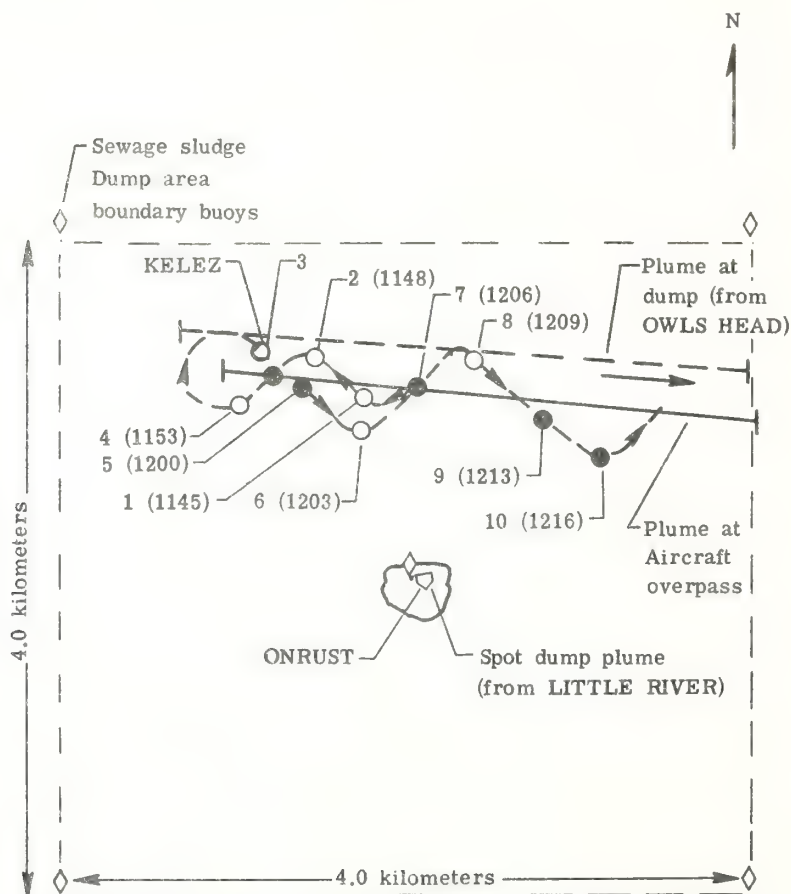


**FIGURE 2.** Wastewater sludge plumes from moving and stationary dumping barges at the time of the NP-3A aircraft flight at 11:59 EDT. NOAA ship Kelez path is shown during water sampling (sample numbers are indicated with time of sample in parentheses). Solid circles indicate samples in the plume and open circles samples in adjacent water.

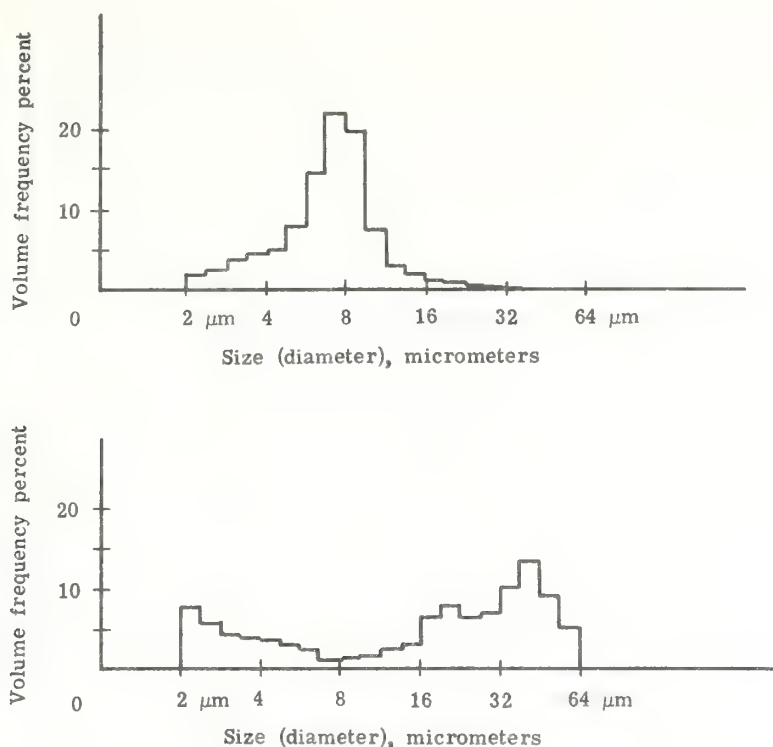


FIGURE 3. Particle size distribution (determined by Coulter Counter) in plume and adjacent water (2  $\mu\text{m}$  and 64  $\mu\text{m}$  are instrument lower and upper limits). Top graph is in plume at Station 9 (Figure 10), bottom is out of plume at Station 8 (Figure 11).

camera products were used to locate areas of interest in the scanner data. Digital data (measured in counts) in these areas were

transferred to computer compatible tapes (cct) with a typical format of nine-track, 800 bytes per inch. Inflight calibration pro-

TABLE I. Sea-truth measurements and remotely sensed data.

Station	Sea Truth		Remotely Sensed Radiances, $\text{mW}/\text{cm}^2 \cdot \text{steradian} \cdot \mu\text{m}$ M2S Band				
	Suspended Solids (mg/l)	Chlorophyll <i>a</i> (mg/m <sup>3</sup> )	2	3	4	7	9
1	1.53	1.0	3.00	3.05	2.22	0.93	0.37
2	1.26	1.0	2.88	2.81	1.98	0.75	0.30
3	27.00	1.5	3.04	2.96	2.07	1.08	0.49
4	1.60	1.2	2.59	2.99	2.16	0.85	0.34
5	30.10	1.9	2.99	2.92	2.02	1.04	0.46
6	1.70	1.1	2.96	2.99	2.16	0.88	0.34
7	32.20	1.8	3.10	3.07	2.16	1.16	0.53
8	1.11	1.2	3.12	3.14	2.24	0.95	0.39
9	13.26	1.5	3.26	3.24	2.29	1.20	0.49
10	13.36	1.5	3.30	3.30	2.30	1.05	0.41
SPOT*	12.0†	—	3.30	3.45	2.51	1.36	0.52

\* Average radiances near SUNY ship *Onrust*.

† Interpolated value.



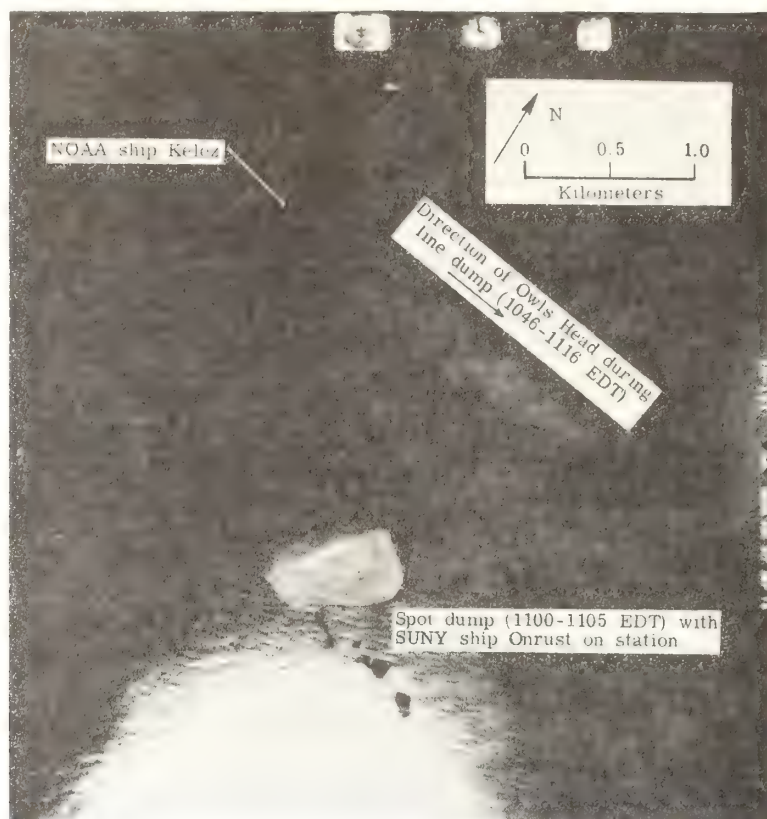


FIGURE 4. Photograph taken at 11:59 AM EDT over sludge dump area (see Figure 2).

vided information to convert instrument count data to average radiances in each band.

Figure 4 is a photograph taken at 11:59 AM (EDT) (about 1 hour after the dumping events) showing the plumes of the morning line and spot dumps. The *Kelez* is shown near the line dump plume and the *Onrust* is shown in the spot dump plume. Figures 5 and 6 are from aircraft flights at about 3:00 PM and 3:52 PM (EDT), respectively, or about 4 hours and 4.87 hours after the morning dumps. The afternoon spot dump plume is also shown in Figures 5 and 6. NASA operations during the experiment are described elsewhere.<sup>12</sup>

**Preprocessing of remotely sensed data.** Data preprocessing included locating the sample points in the imagery and determining radiance values in the M2S bands to be compared to the sea-truth measurements obtained from the *Kelez* and *Onrust*. In the analysis, representative radiance values were determined by taking a  $7 \times 7$  pixel field centered at the best estimate of the sea-truth measurement.

This pixel field was determined empirically as the minimum size that compensated for uncontrollable spectral and spatial errors. The average count in the  $7 \times 7$  field was multiplied by a radiance conversion value obtained from calibrating the inflight system to known radiance sources. Evaluation of inflight calibration data indicates less than 2 percent, or negligible, instrument drift. Average radiances in individual band ranges have the units  $\text{mW}/\text{cm}^2 \cdot \text{sr} \cdot \mu\text{m}$ , or an average radiance per unit band width. Representative radiance values in each of the bands for the sea-truth stations are listed in Table I. The time interval between remote sensor overpass and sea-truth measurements was less than 20 minutes.

**Data analysis.** Multiple regression techniques, specifically stepwise regression analysis, previously have been used to quantitatively relate remotely sensed data to sea-truth measurements.<sup>7-9</sup> The resulting calibrated regression equations were used to map synoptic quantitative distributions of water quality parameters in the remotely sensed area. The

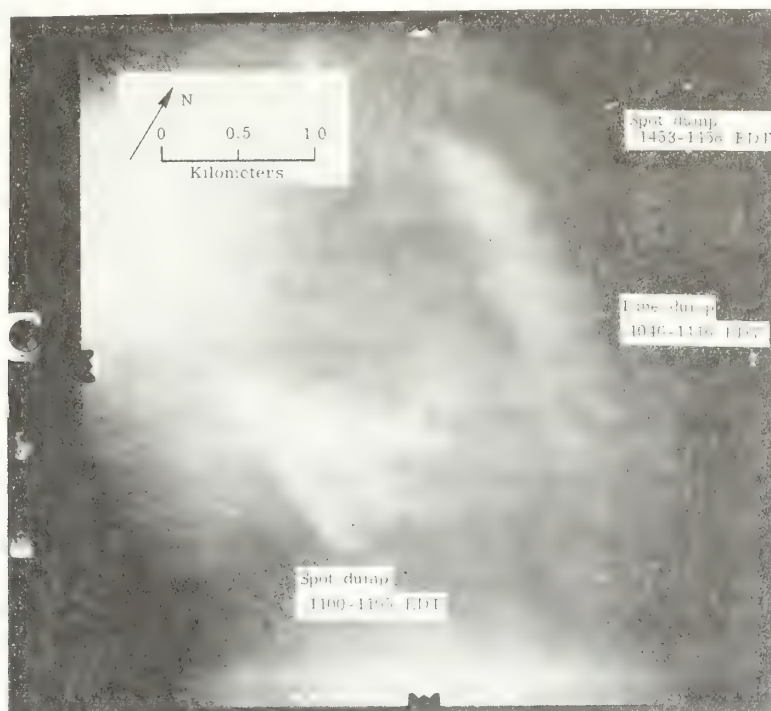


FIGURE 5. Photograph taken at 3:00 PM EDT over sludge dump area.

TABLE II. Spectral and spatial characteristics of remote sensors.\*

Modular Multispectral Scanner (M2S)			
Band		Band width	
1		380-440 nm	
2†		440-490 nm	
3†		495-535 nm	
4†		540-580 nm	
5		580-620 nm	
6		620-660 nm	
7†		660-700 nm	
8		700-740 nm	
9†		760-860 nm	
10		970-1 060 nm	
Thermal		8 000-13 000 nm	
Scan width, m		8 500	
Resolution, m		8	
Zeiss Mapping Camera			
Spectral Range, nm	Film	Resolution, m	Footprint, m
300-700	2 402 (black and white)	1.3	4 550 × 4 550

\* Measurements made at 3.0 km altitude.

† Radiance data are available in these bands.

methodology reported by Johnson<sup>7</sup> was used in the data analysis for this experiment, with ss and chlorophyll *a* as the dependent variables and average radiances of the five M2S bands as the independent variables. In a stepwise regression analysis the program selects the independent variable (radiance for an M2S band) that has the highest correlation with the dependent variable (ss concentration). In subsequent steps, the stepwise regression analysis then adds variables to the regression based on *F*-ratio values, a statistical measure of significance, until all of the independent variables that make significant contributions to determining the dependent variable are in the regression, and the others outside the regression.<sup>13</sup> Limiting the regression equation to significant variables reduces the analysis time and improves the accuracy of the results. A 95-percent confidence level is used to determine variables that are included in the regression equation. The resultant regression equation is a calibrated relation between remotely sensed data and sea-truth measurements.

## RESULTS AND DISCUSSION

Results of the stepwise regression analysis for ss are shown following for the 10 sets of



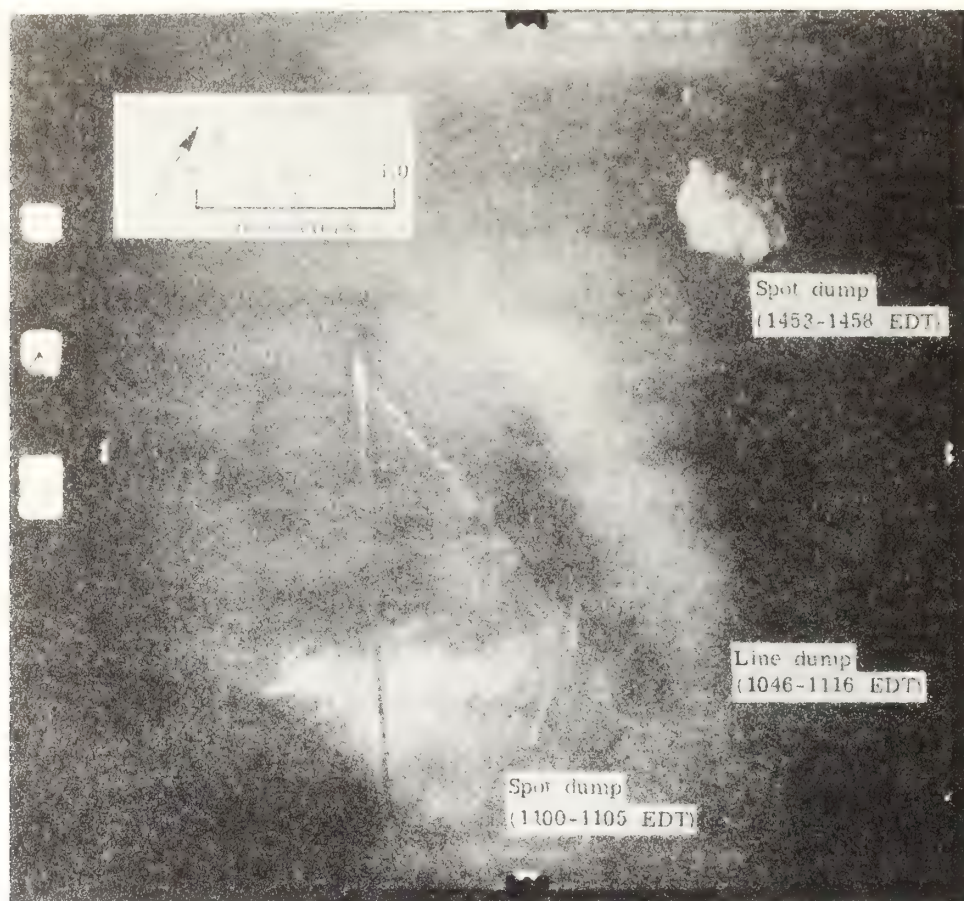


FIGURE 6. Photograph taken at 3:52 PM EDT over sludge dump area.

observations from the line dump plume:

Step	Regression Variables	Correlation Coefficient	Standard Error of Estimate	Measurement Range
1	$R_9$	0.88	6.47 mg/l	1.11-32.20 mg/l
2	$R_4, R_9$	0.96	4.11 mg/l	1.11-32.20 mg/l

Where  $R_N$  is the average radiance in M2S band  $N$  (that is,  $R_9$  is the average radiance in Band 9); the correlation coefficient is a measure of the relative responses of variables, with a maximum value of unity; the standard error of estimate is a measure of the deviation from the fitted regression line; and the measurement range is the range of sea-truth measurements. The calibrated regression equation is:

$$ss \text{ (mg/l)} = 45.29 - 45.67 R_4 + 159.69 R_9$$

Comparison of the remotely sensed  $ss$  (calculated from the regression equation) with the measured values of  $ss$  is shown in Figure 7. Deviations about the fitted regression are approximately random; thus, the linear model is

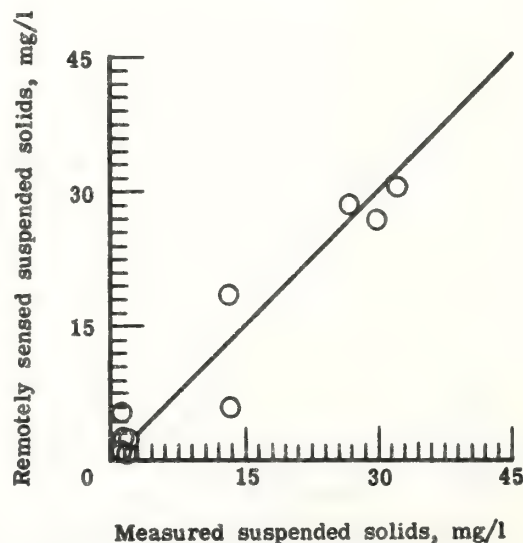


FIGURE 7. Remotely sensed and measured values for  $ss$  concentrations in sludge line dump.



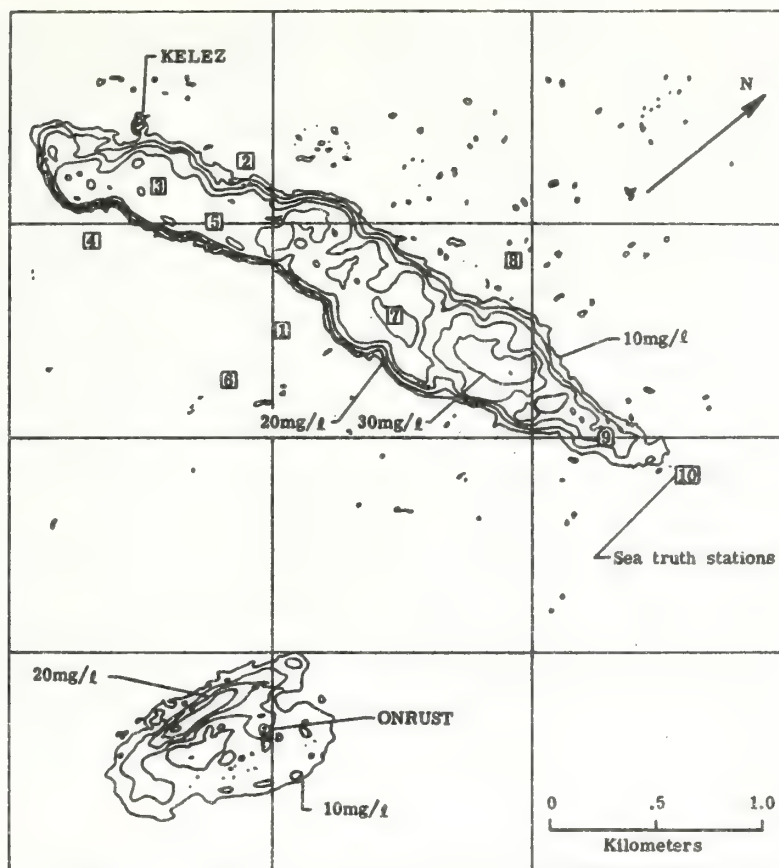


FIGURE 8. Quantitative distribution of ss in plumes at 11:59 AM EDT, about 1 hour after dumps (see Figures 2 and 4).

adequate. Johnson<sup>6,7</sup> have previously indicated a linear variation for the present range of ss data.

With chlorophyll *a* as the dependent vari-

able, one band of M2S data (Band 9) indicated a significant correlation. As shown above, Band 9 also had the highest individual correlation between ss and remotely sensed

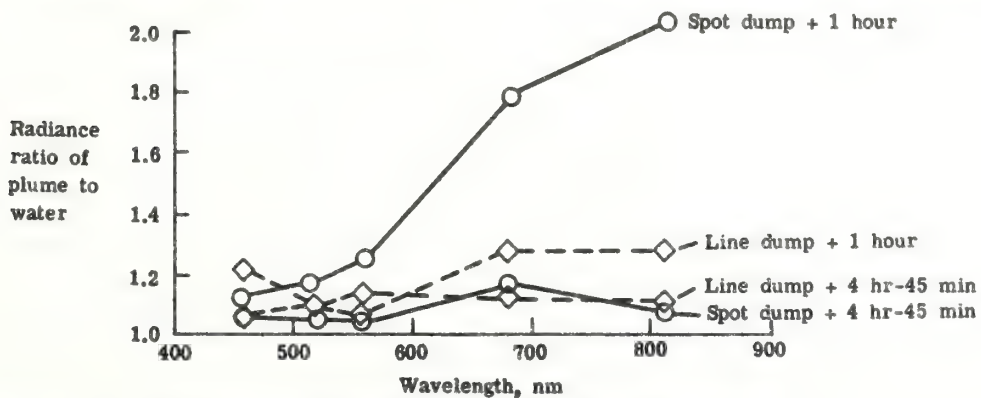


FIGURE 9. Normalized (to ocean water) radiances of sludge plumes.

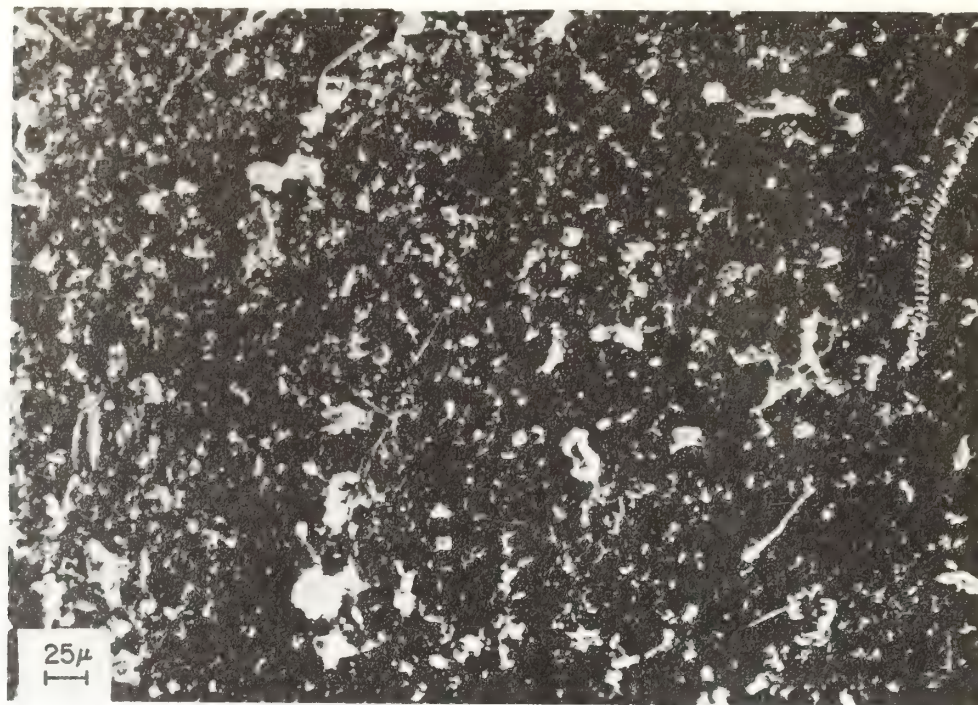


FIGURE 10. Scanning electron microscope image of particles in sludge plume (200 $\times$ ).

data. In addition, as observed by Duedall *et al.*,<sup>10</sup> there may be some fluorescent characteristics of the wastewater dump material that interfere with the chlorophyll *a* analysis. Thus, it seems that the indicated chlorophyll *a* correlation is a "false positive" indication.

**Quantitative mapping of ss.** Quantitative mapping of the distribution of water quality parameters may be determined from the regression equation. For the water quality parameter, concentrations are determined at each pixel (or equal spacings of lines or columns). This field of data is typically smoothed to remove local spectral and spatial noise features, and a contour map is developed by a computerized plotting routine. The smoothing routine used in this analysis is an averaging on a line-by-line and column-by-column basis in the data field, where the middle value is replaced by the mean of it and the two adjacent values. Edge values remain the same. In this analysis each pixel in each line of data was used to generate the field of data for mapping. Two smoothing passes were made for the ss concentrations.

Quantitative distributions of ss in the wastewater sludge plumes are mapped in Figure 8.

Sea-truth station locations are indicated on the map. The single ss concentration value determined (by interpolation) for the spot dump plume was not included in the regression equation. However, the comparison is good (12 mg/l measured value, 14 mg/l as mapped value), indicating that the line and spot dump plumes have similar spectral characteristics even though total radiance levels are higher in the spot dump plume (Table I).

**Spectral signatures.** Spectral signatures may be used to identify particular types of features in a body of water. The ocean disposal of wastewater sludge is regulated by the EPA permit system. Because of its wide area and synoptic coverage, remote sensing may be useful in enforcement of ocean dumping regulations if the type and location of these dumps can be unambiguously defined. One means of applying spectral characteristics for identification is to normalize to ocean water in each of the spectral bands (that is, using the water for an in-scene calibration). Normalized spectral characteristics of the morning spot and line dumps are shown in Figure 9. The dumps are shown also in the photography of Figure 4. The higher radiances in the spot





**FIGURE 11.** Scanning electron microscope image of particles in background water (200 $\times$ ).

dump are probably caused by greater concentrations of organic and other floatable materials.

The morning line and spot dumps, which occurred about 4 hours before they were remotely sensed in the afternoon, are still distinguishable in the photography Figures 5 and 6. However, the normalized spectral responses are weak and dispersed in the radiometric data of Figure 9.

**Particle characteristics.** Particle characteristics in and out of the line dump plume are shown in Figures 10 and 11. As indicated in the particle size distributions obtained from the Coulter counter (see Figure 3), there is a large concentration of uniformly sized particles (about 8  $\mu\text{m}$  in diameter) in the plume. Outside of the plume, both large phytoplanktonic and very small particles were observed.

The scanning electron microscope images seen in Figures 10 and 11 represent typical suites of particles collected in and out of the dumped wastewater plume. Both images were taken at 200 $\times$  magnification. Figure 10 shows the wastewater-laden particulate matter in the plume. The helical shaped organism at

the right edge of the micrograph is a ciliated protozoan typically associated with wastewater. Figure 11 shows particulate matter and planktonic organisms representative of background suspended particulate matter in the water samples outside of the wastewater sludge plume.

#### CONCLUDING REMARKS

Calibrated regression equations that relate remotely sensed data to sea-truth measurements may be used to provide maps of the synoptic distributions of water quality parameters associated with ocean disposal of wastewater sludge. These maps provide information for location and quantitative assessment of dispersion characteristics of plumes resulting from ocean dumping of wastewater sludge. Spectral responses, or signatures, from the plume may be used to identify the type of plume, without concurrent water sampling. This would provide a basis for enforcement of dumping regulations by local, state, and federal agencies.

Sea-truth measurements indicate that particle size distributions associated with this



pollutant plume are different from those of natural water in the same area. Specifically, there is a peak in the smaller particle sizes in the plume, while natural ocean water has a more even distribution of both large and small particles.

Results of this experiment are encouraging for the use of remote sensing techniques for locating, identifying, and mapping spectral anomalies that may be related to pollutant plumes. Additional experiments should be performed in different environmental settings in order to more accurately establish the role of remote sensing in monitoring and studying pollution.

## REFERENCES

1. Pararas-Carayannis, G., "Ocean Dumping in the New York Bight: An Assessment of Environmental Studies." Tech. Memorandum No. 39, Coastal Eng. Res. Center, U. S. Army Corps of Engineers, Fort Belvoir, Virginia (1973).
2. Mueller, J. A., *et al.*, "Contaminant Inputs to the New York Bight." NOAA Tech. Memorandum ERL MESA-6, National Oceanic and Atmospheric Administration, Environmental Research Laboratories, Marine Ecosystems Analysis Program, New York Bight Project, Boulder, Colo. (1976).
3. Duedall, I. W., *et al.*, "Sewage Sludge and Ammonia Concentrations in the New York Bight Apex." *Estuarine and Coastal Mar. Sci.*, 3, 457 (1975).
4. Duedall, I. W., *et al.*, "Fate of Wastewater Sludge in the New York Bight Apex." *Jour. Water Poll. Control Fed.*, 47, 2702 (1975).
5. Proni, J. R., *et al.*, "On the use of acoustics for studying suspended oceanic sediment and for determining the onset of the shallow thermocline." *Deep-Sea Res.*, Pergamon Press, 23, 831 (1976).
6. Johnson, R. W., "Quantitative Sediment Mapping From Remotely Sensed Multispectral Data." *Proc. Fourth Annual Remote Sensing of Earth Resources Conf.*, Tullahoma, Tenn. (March 24-26, 1975).
7. Johnson, R. W., "Quantitative Suspended Sediment Mapping Using Aircraft Remotely Sensed Data." *Proc. Earth Resources Survey Symposium*, Houston, Tex. (June 8-13, 1975).
8. Johnson, R. W., "Application of Aircraft Multispectral Scanners to Quantitative Analysis and Mapping of Water Quality Parameters in the James River, Virginia." *Proc. XIXth Meeting of COSPAR*, Philadelphia, Pa. (June 14-19, 1976).
9. Johnson, R. W., "Quantitative Mapping of Chlorophyll *a* Distribution in Coastal Zones by Remote Sensing." *Proc. 43rd Annual Meeting Amer. Soc. of Photogrammetry*, Washington, D. C. (Feb. 27-March 5, 1977).
10. Duedall, I. W., *et al.*, "Short-Term Water Column Perturbations due to Sewage Sludge Dumping in the New York Bight Apex." *Jour. Water Poll. Control Fed.* (In Press).
11. Proni, R., *et al.*, "Acoustic Tracking of Ocean-Dumped Sewage Sludge." *Science*, 193, 1005 (1976).
12. Johnson, R. W., and Hall, J. B., Jr., "Remote Sensing Operations (Multispectral Scanner and Photographic) in the New York Bight September 22, 1975." NASA TM X 73993, Langley Research Center, Hampton, Va.
13. Draper, N. R., and Smith, H., "Applied Regression Analysis." John Wiley & Sons, Inc., N. Y. (1966).

## Acoustic imaging of the New England shelf-slope water mass interfaces

PULSED high frequency acoustics has been shown to have unique applications in the detection and measurement of oceanic phenomena such as internal waves<sup>1-3</sup> and dispersion of ocean-dumped sewage sludge<sup>4,5</sup> or dredge material<sup>6</sup>. With moderate to high pulse repetition rates, a virtually continuous record of water column scattering strength is available to depths of the order of 500 m from a ship travelling at speeds of 4 or 5 knots. We used this feature to detect acoustically the interfaces associated with an intrusion of cold New England shelf water into the warmer slope water during a 9-d period in June 1976.

From 15 to 23 June 1976 measurements of effects of internal waves were made from the National Oceanic and Atmospheric Administration (NOAA) ship *George B. Kelez* in an area on the New England continental shelf partly shown in Fig. 1. Although measurements were made on three tracklines shown, most of the work concentrated on the centre trackline. A 1-kW 20-kHz pulsed acoustic system, specially modified for detection of weak signals scattered from the water column, was operated continuously throughout the cruise. Field operation of this system has been described previously<sup>4,7</sup>. Profiles using expendable bathythermographs (XBT) and a conductivity-temperature-depth probe (CTD) were obtained at regular intervals.

Throughout the cruise, the acoustic record revealed a reflecting layer (Fig. 2) of limited horizontal extent and rather variable location. Some observations of the offshore boundary of this layer are indicated in Fig. 1. The layer was observed in all cases (18 observations) to have a slope opposite to that of the bottom. As shown along the ship's trackline, the layer displayed apparent widths of 2.8-7.4 km. The last few records (for example, Fig. 2) of the scattering layer also show a second layer higher in the water column and parallel to the surface, but apparently descending to join the ascending lower layer at their offshore boundary. This made a sufficiently dramatic feature to finally get our attention. We then obtained XBT and CTD profiles through the feature when the cruise plan permitted.

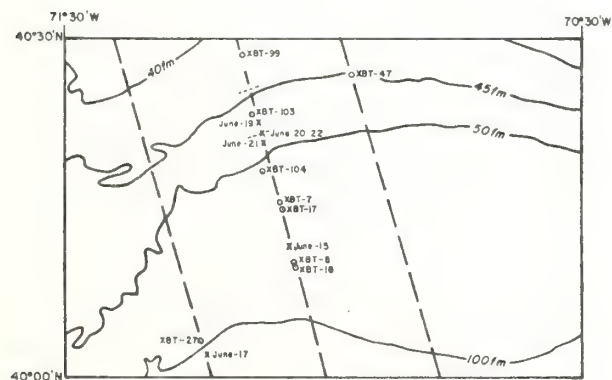


**Fig. 1** Region of New England continental shelf where water mass interfaces were observed. Contours are in fathoms, dashed lines are tracklines along which most work was performed. X with a date denotes an observation of the intersection of the scattering layer offshore boundary and the ship's trackline. The light dashed lines represent the width of the intrusion observed on 22 June.

A series of three XBT profiles (Fig. 3) across the layers revealed that they occur in a region of transition between two distinct water masses. XBT 99 shows the bottom shelf water to have a temperature of about 7 °C while XBT 104 shows the minimum temperature of the deeper slope water to be about 10 °C. XBT 103, taken in the region where the layers were present shows interleaving of 7 °C water with 10 °C water. The depths of the upper and lower steep temperature gradients in XBT 103 coincide with the depths of the acoustically reflecting layers measured at the moment the XBT 103 profile was taken. The gradient depths of XBT 103 (taken at 0729 GMT, 22 June) may be compared with the depths of the reflecting layers in Fig. 2, observed at 1325 GMT, 22 June. The slightly later acoustic image was chosen for its higher quality and clearer manifestation of the layers joining at the offshore boundary. In the right hand portion of Fig. 3 (the region of lighter background), the *Kelez* took station and a CTD profile was made and can be seen falling and then rising through the layers. The CTD temperature profile was similar to XBT 103 but showed very much steeper temperature gradients at the top and bottom of the 7 °C intrusion.

The horizontal transition from 7 to 10 °C water is a familiar feature. It is well known<sup>8</sup> that by June the surface shelf water has warmed due to increased net solar radiation while the bottom shelf water remains cold, typically about 7 °C. The slope water is not cooled as much during winter mixing and has a minimum temperature of about 10 °C. During winter the shelf-slope water front is a well formed feature<sup>9</sup>, but spring surface warming over the shelf and slope removes the horizontal temperature contrast except in the lower water column. The reflecting layers manifested in the acoustic image are associated with nearly horizontal interfaces formed by interleaving of the shelf and slope water masses during spring and summer.

The location of the shelf-slope water interface on the centre trackline migrated about 18 km northwards during the nine-day span of observations. Reflecting layers observed on 15 and 16 June were confirmed to be shelf-slope water interfaces by XBT pairs (7, 8, and 17, 18 respectively) taken north and south of the observed layers. On 17 June a layer observation on the western trackline, confirmed by XBT 26 (not shown on map) and XBT 27, showed the shelf-slope water interface to be further south. We observed no reflecting layer associated with the water-mass interface on the eastern trackline but found the transition took place between XBT 46 42° 32'N and XBT 47 on 18 June. It would seem, then, that the shelf-slope water transition zone was in a

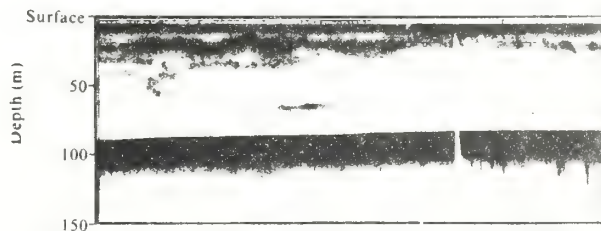


**Fig. 2** A portion of the acoustic image showing the scattering layers associated with the intrusion interfaces (frequency 20 kHz). The left portion of the image, with darker background, represents a distance of 5.6 km. The portion to the right of the interrupted bottom signal was made with the ship on station for a CTD profile. The CTD echo signal is visible on the image.

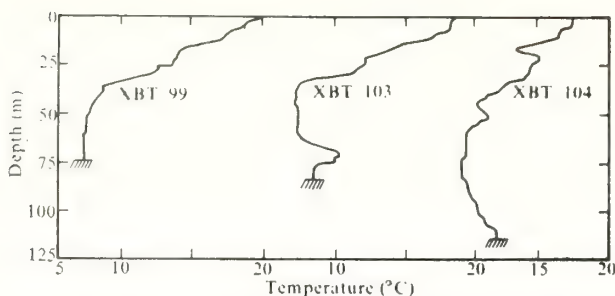


Fig. 3 Three XBT profiles (locations shown in Fig. 1) showing the changing make-up of the water column across the region in which acoustic scattering layers were identified as shelf-slope water mass interfaces. The temperature scale is actually three scales joined at the 20 °C points.

north east-south west direction in the vicinity of this experiment. Curiously, from 19 through 22 June the deep water boundary of the transition zone was roughly stationary as shown in Fig. 1. Thus the boundary moved 18 km along the centre trackline from 16 to 19 June and moved very little in the next four days.

The shelf-slope water transition zone apparently fluctuates significantly in location on a time scale of a few days. Also, Cresswell<sup>10</sup> has observed distinct parcels of shelf water in the deeper slope water indicative of a mixing process. If the conditions for scattering at these water mass interfaces are often suitable for acoustic scattering, it may be possible to observe acoustically the shelf-slope water exchange process occurring in the summer on the New England continental shelf. XBT and CTD profiles would be needed only

occasionally to confirm that the scattering layers are the interfaces of interest. Most of the ship time would then be spent covering the area of interest in a regular fashion with sufficient frequency to resolve water mass movements as they occur.

FRED C. NEWMAN  
JOHN R. PRONI  
DONALD J. WALTER

Sea-Air Interaction Laboratory,  
Atlantic Oceanographic and Meteorological Laboratories,  
Environmental Research Laboratories,  
National Oceanic and Atmospheric Administration,  
Miami, Florida, 33149

H. MICHAEL BYRNE

Pacific Marine Environmental Laboratory,  
Environmental Research Laboratories,  
National Oceanic and Atmospheric Administration,  
Seattle, Washington, 98105

Received 26 July; accepted 14 September 1977.

1. Weston, D. E., Review, J., Jones, F. R., & Ranster, J. W. *Rep. ARL/L/R88* (Admiralty Res. Lab., Teddington, 1970).
2. Proni, J. R., & Apel, J. R. *J. geophys. Res.* **80**, 1147-1151 (1975).
3. Fischer, F. H., & Squier, E. D. *J. acoust. Soc. Am.* **58**, 1315-1317 (1975).
4. Proni, J. R., Newman, F. C., Sellers, R. L., & Parker, C. *Science* **193**, 1005-1007 (1976).
5. Proni, J. R. *et al. J. geophys. Res.* (submitted).
6. Proni, J. R., Rona, D. C., Lauter, C. A. Jr & Sellers, R. L. *Nature* **254**, 413-415 (1975).
7. Proni, J. R. *et al. Deep Sea Res.* **23**, 831-837 (1976).
8. Beardsley, R. C. & Flagg, C. N. *Mem. Soc. R. Sci. Liège* **6**, 209-225 (1976).
9. Wright, W. R. *J. mar. Res.* **34**, 1-14 (1976).
10. Cresswell, G. M. *Rep.* 67-35 (Woods Hole Oceanogr. Inst., Massachusetts, 1967).



NOAA Technical Memorandum ERL AOML-25, 129 pages.

NOAA Technical Memorandum ERL AOML-25

SURFACE METEOROLOGICAL OBSERVATIONS  
ON R/V COLUMBUS ISELIN  
DURING PHASE III OF GATE

Feodor Ostapoff  
Sylvia Worthem  
William Everard

Sea-Air Interaction Laboratory

Atlantic Oceanographic and Meteorological Laboratories  
Miami, Florida  
January 1977

UNITED STATES  
DEPARTMENT OF COMMERCE  
Elliot L. Richardson, Secretary

NATIONAL OCEANIC AND  
ATMOSPHERIC ADMINISTRATION  
Robert M. White, Administrator

Environmental Research  
Laboratories  
Wilmot N. Hess, Director



## DISCLAIMER

The Environmental Research Laboratories do not approve, recommend, or endorse any proprietary product or proprietary material mentioned in this publication. No reference shall be made to the Environmental Research Laboratories, or to this publication furnished by the Environmental Research Laboratories, in any advertising or sales promotion which would indicate or imply that the Environmental Research Laboratories approve, recommend, or endorse any proprietary product or proprietary material mentioned herein, or which has as its purpose an intent to cause directly or indirectly the advertised product to be used or purchased because of this Environmental Research Laboratories publication.

## TABLE OF CONTENTS

	Page
ABSTRACT	1
1. INTRODUCTION	1
2. SHIP TRACK	3
3. INSTRUMENTATION	19
3.1 Sensor Description	19
3.2 Sensor Exposure	21
4. DATA PRESENTATION	25
5. CALCULATION OF MOMENTUM AND HEAT FLUXES	54
5.1 Near-Neutral Stratification	54
5.2 Non-Neutral Stability Conditions	58
5.3 Longwave Back Radiation from the Sea Surface	69
6. MOMENTUM, HEAT AND RADIATIVE FLUXES IN THE VICINITY OF THE R/V C. ISELIN IN THE C-SCALE AREA	71
7. REFERENCES	108

## APPENDIX

### LIST OF FIGURES

Figure		
1.	R/V C. ISELIN and R/V DISCOVERY tracks 2000 GMT 5 Sept. to 0050 GMT 6 Sept. 1974.	4
2.	R/V C. ISELIN and R/V DISCOVERY tracks 2030 GMT 6 Sept. to 1220 GMT 7 Sept. 1974.	5
3.	R/V C. ISELIN and R/V DISCOVERY tracks 1620 to 2200 GMT 7 Sept. 1974.	6
4.	R/V C. ISELIN track 8 Sept. 1974.	7
5.	R/V C. ISELIN and R/V DISCOVERY tracks 1947 to 2150 GMT 14 Sept. 1974.	8
6.	R/V C. ISELIN and R/V DISCOVERY tracks 0032 to 0210 GMT 15 Sept. 1974.	9
7.	R/V C. ISELIN and R/V DISCOVERY tracks 0200 to 0410 GMT 15 Sept. 1974.	10



# TABLE OF CONTENTS (Continued)

Page

## LIST OF FIGURES (Continued)

Figure		
8.	R/V C. ISELIN track 0440 to 0745 GMT 15 Sept. 1974.	11
9.	R/V C. ISELIN track 0810 to 1200 GMT 15 Sept. 1974.	12
10.	R/V C. ISELIN track 1200 to 1440 GMT 15 Sept. 1974.	13
11.	R/V C. ISELIN track 1410 to 1740 GMT 15 Sept. 1974.	14
12.	R/V C. ISELIN track 1820 to 2220 GMT 15 Sept. 1974.	15
13.	R/V C. ISELIN track 2300 GMT 15 Sept. to 0100 GMT 16 Sept. 1974.	16
14.	R/V C. ISELIN track 0100 to 0345 GMT 16 Sept. 1974.	17
15.	R/V C. ISELIN and R/V DISCOVERY tracks 0640 to 2000 GMT 16 Sept. 1974.	18
16.	Schematic diagram of R/V C. ISELIN showing sensor exposures.	23
17.	Radiation, air temperature, and wind speed.	47
18.	Sensible and latent heat fluxes and long- wave back radiation.	94
19.	Wind stress, daily net radiation, and daily net heat flux.	101

## LIST OF TABLES

Table		
1	Hourly meteorological observations	26
2	Momentum and heat fluxes	72

SURFACE METEOROLOGICAL OBSERVATIONS ON  
R/V COLUMBUS ISELIN DURING PHASE III OF GATE

Feodor Ostapoff, Sylvia Worthem, and William Everard

This report describes the surface meteorological instrumentation used during the third phase of GATE aboard the R/V COLUMBUS ISELIN. The ship track, surface meteorological observations, and the calculated momentum and heat fluxes are presented. The procedure for calculating the fluxes is described.

1. INTRODUCTION

The R/V COLUMBUS ISELIN of the University of Miami participated in GATE during the second phase in the Equatorial Experiment and the third phase in the C-scale Experiment. This report describes and presents the surface meteorological observations for the third phase only.

The primary function of the R/V COLUMBUS ISELIN in the third phase was to deploy and service the cyclesonde buoys D1, D2, and D3. Secondary objectives were joint roving operations with the R/V DISCOVERY of the U.K. to map the upper ocean on a horizontal scale of 20 km.

The R/V COLUMBUS ISELIN was, nevertheless, instrumented to obtain surface meteorological observations, including radiation data, cloud photography, and sea surface temperature data. As much as possible, all data recording was done automatically, because of limited personnel. Only one man was available for carrying out this program.

## 2. SHIP TRACK

In as much as the R/V COLUMBUS ISELIN was a roving ship and a great deal of her time was spent servicing the cyclesonde buoys, the navigational smooth plotting presented no major problems. The ship was equipped with a satellite navigation system which functioned continuously with the exception of a brief period during a power failure.

Although the hourly positions are tabulated together with the meteorological data, some tracklines are presented in Figures 1 through 15. These will be useful in the interpretation of other than the meteorological data. The presented tracklines cover the cases when the R/V COLUMBUS ISELIN was roving jointly with the R/V DISCOVERY on September 5-7, September 8, and September 14-15, and with the R/V DISCOVERY and R/V QUADRA on September 16. During these exercises, the absolute navigation (by satellite) was performed by the R/V DISCOVERY. The R/V COLUMBUS ISELIN took a radar range and bearing on the DISCOVERY every ten minutes. In many cases, the DISCOVERY also took ranges and bearings on the ISELIN. With the data from both ships, smooth plotting was performed by Lt. R. Sellers (NOAA).



This report describes the instrumentation and sensor exposure. The data and derived flux quantities are presented. Also, all available navigational data are provided.

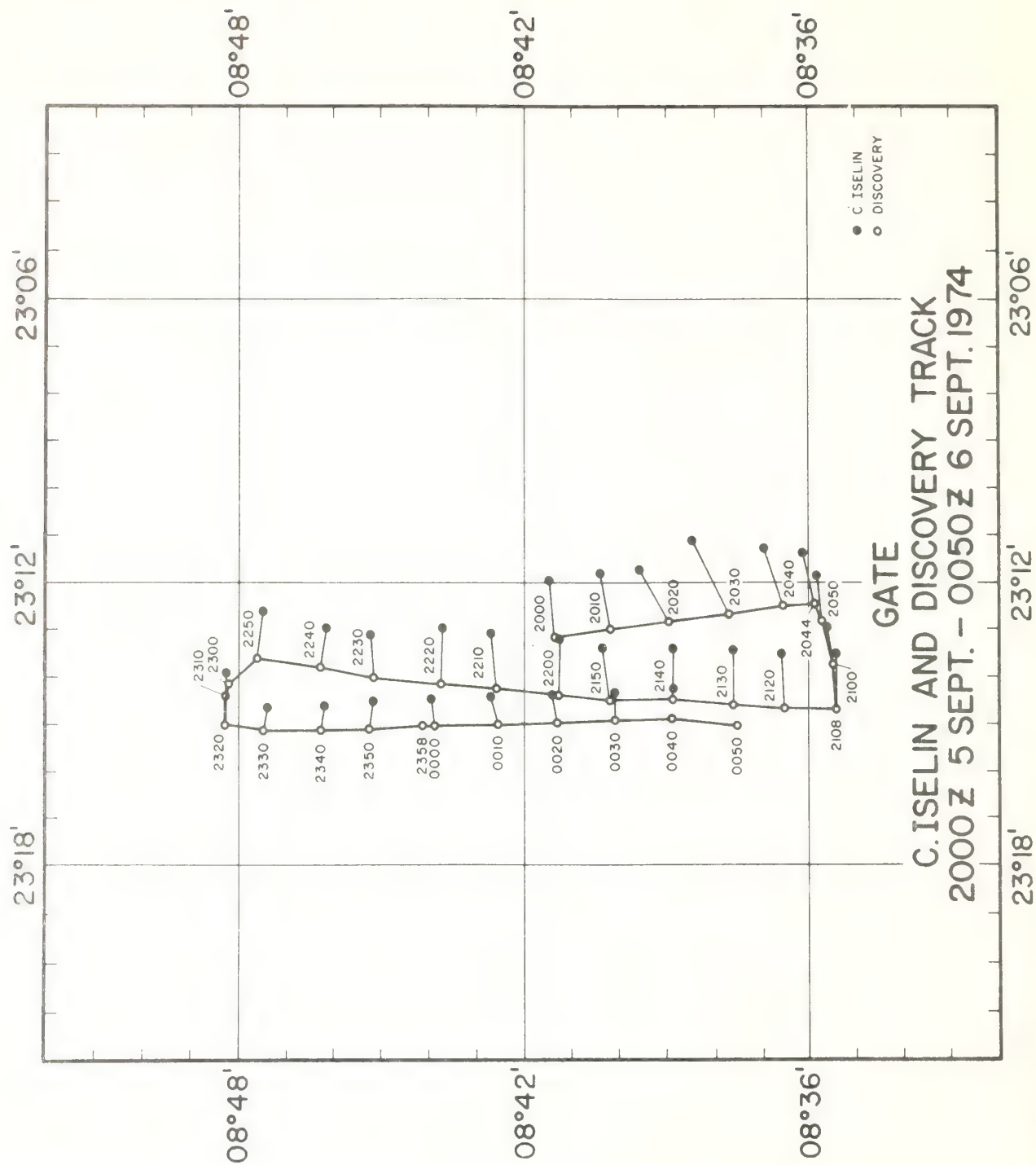


Figure 1. R/V C. ISELIN and R/V DISCOVERY tracks 2000 GMT 5 Sept. to 0050 GMT 6 Sept. 1974.

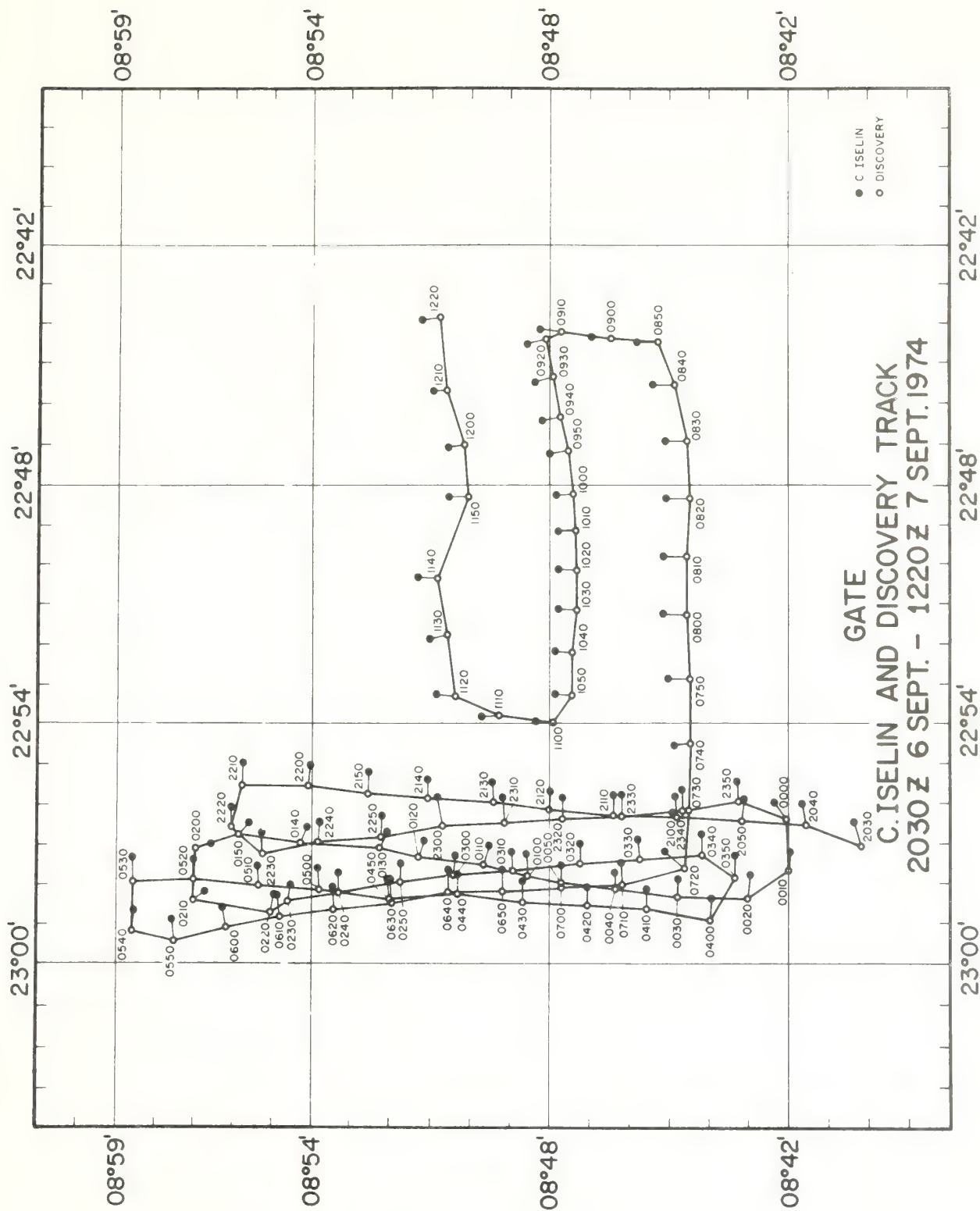


Figure 2. R/V C. ISELIN and R/V DISCOVERY tracks 2030 GMT 6 Sept. to 1220 GMT 7 Sept. 1974.



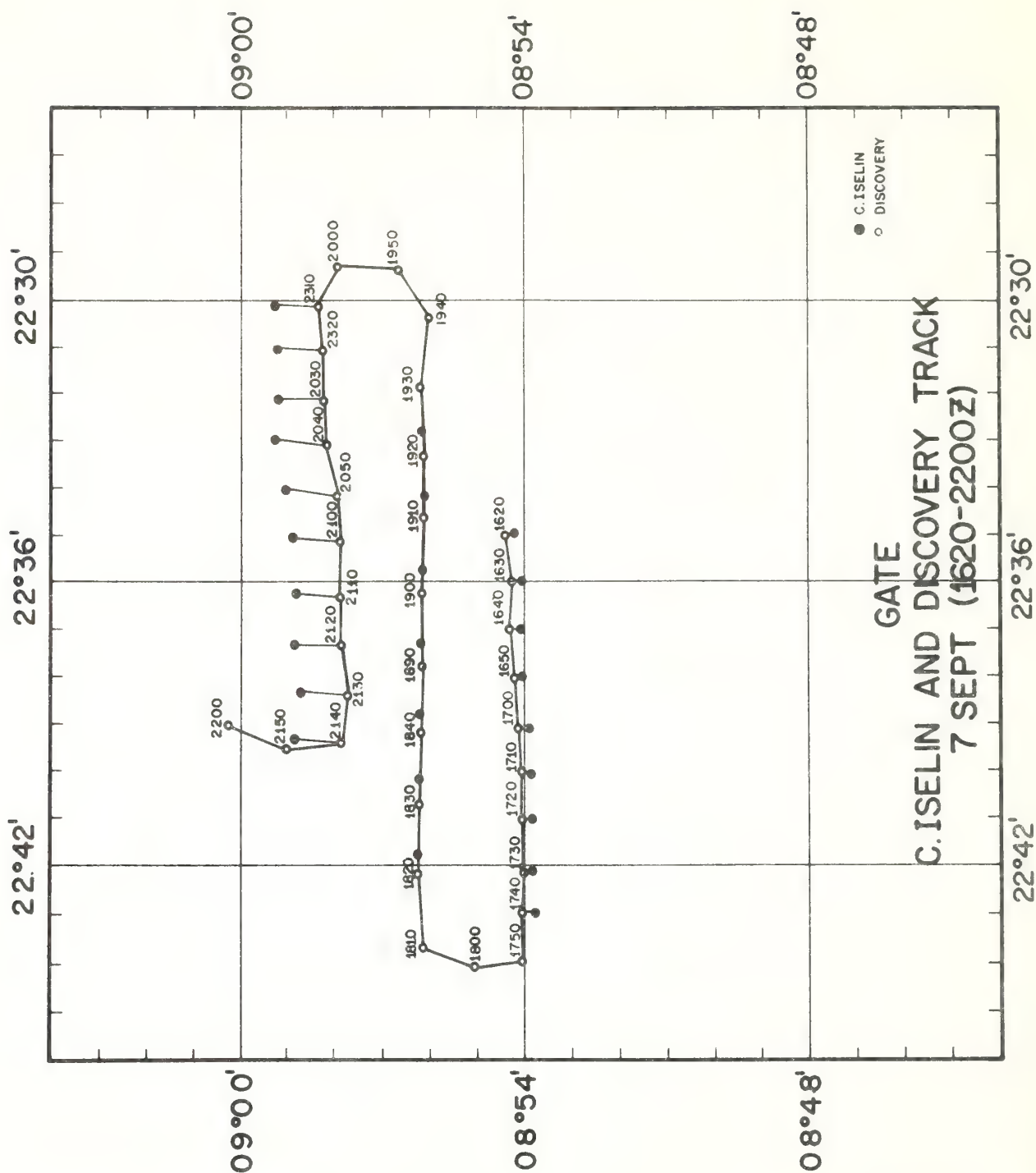


Figure 3. R/V C. ISELIN and R/V DISCOVERY tracks 1620 to 2200 GMT 7 Sept. 1974.

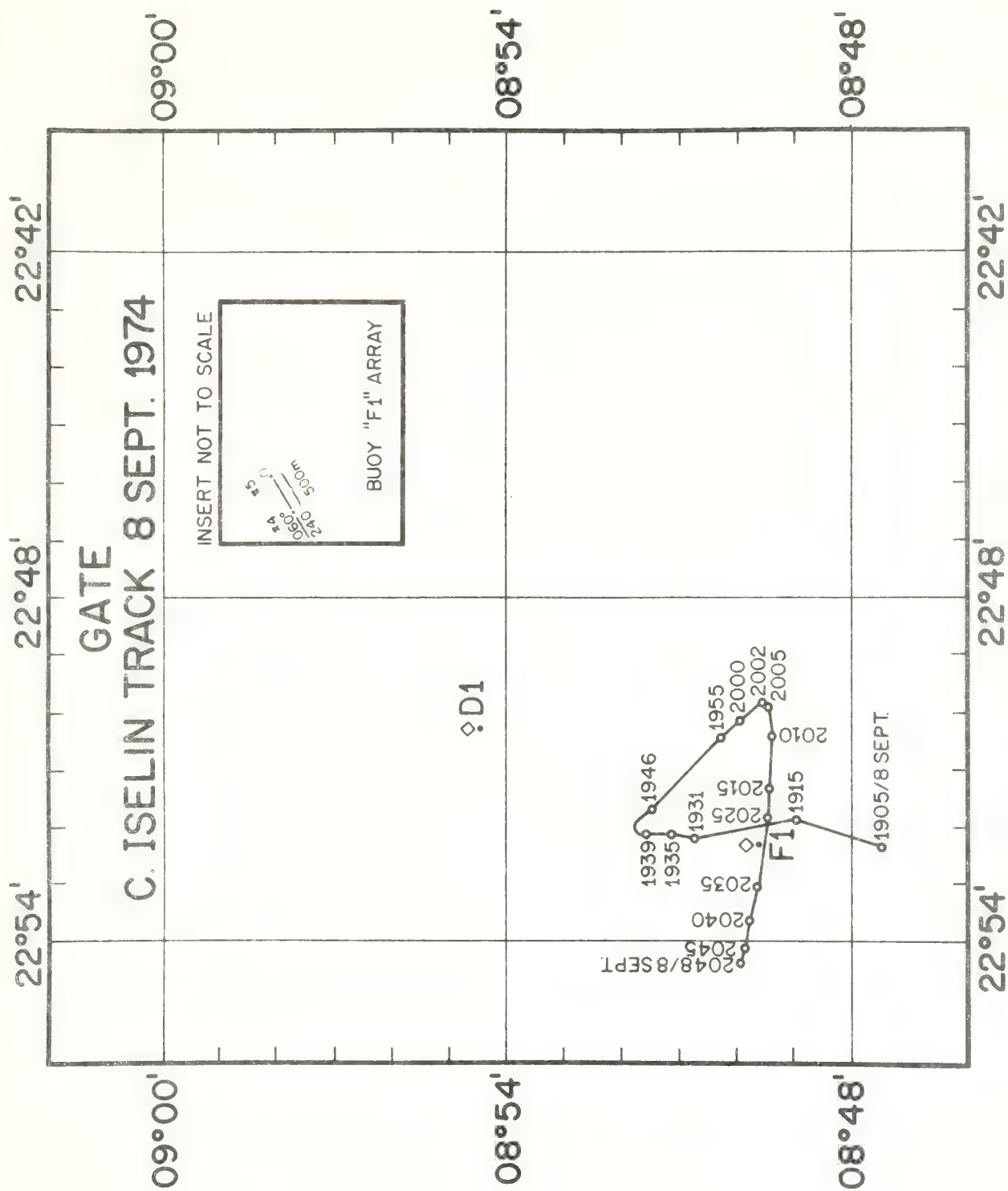


Figure 4. R/V C. ISELIN track 8 Sept. 1974.

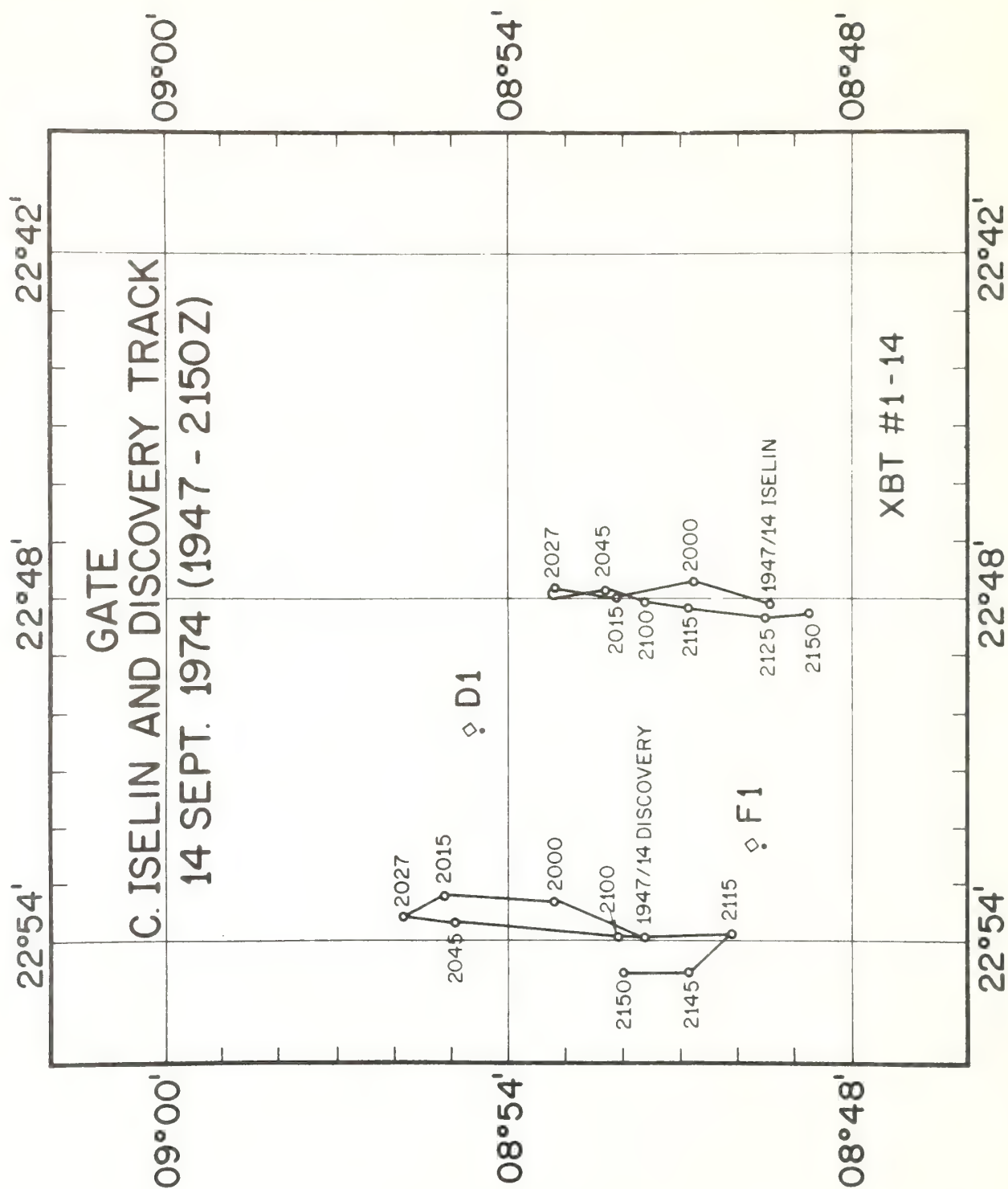


Figure 5. R/V C. ISELIN and R/V DISCOVERY tracks 1974 to 2150 GMT 14 Sept. 1974.



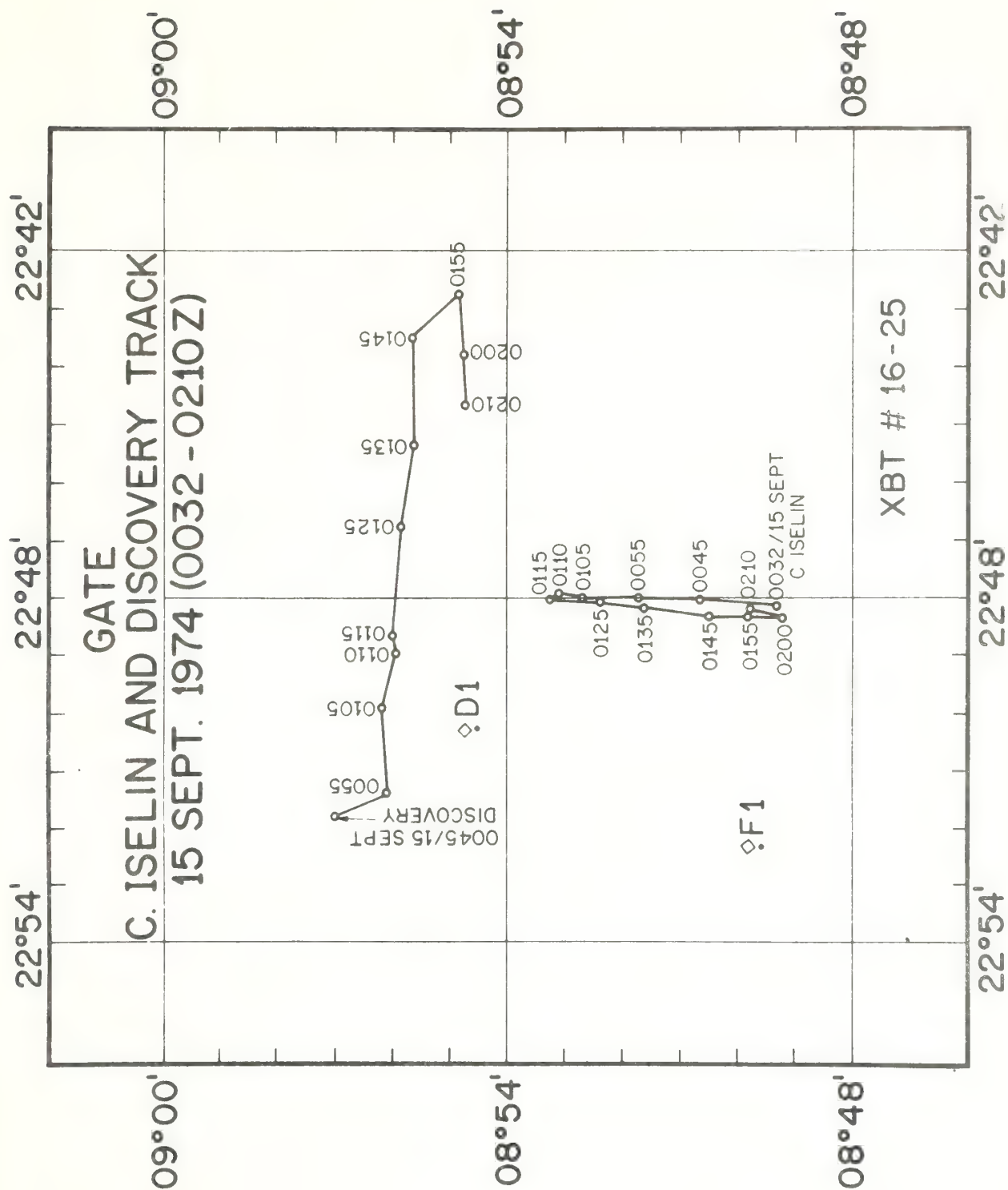


Figure 6. R/V C. ISELIN and R/V DISCOVERY tracks 0032 to 0210 GMT 15 Sept. 1974.

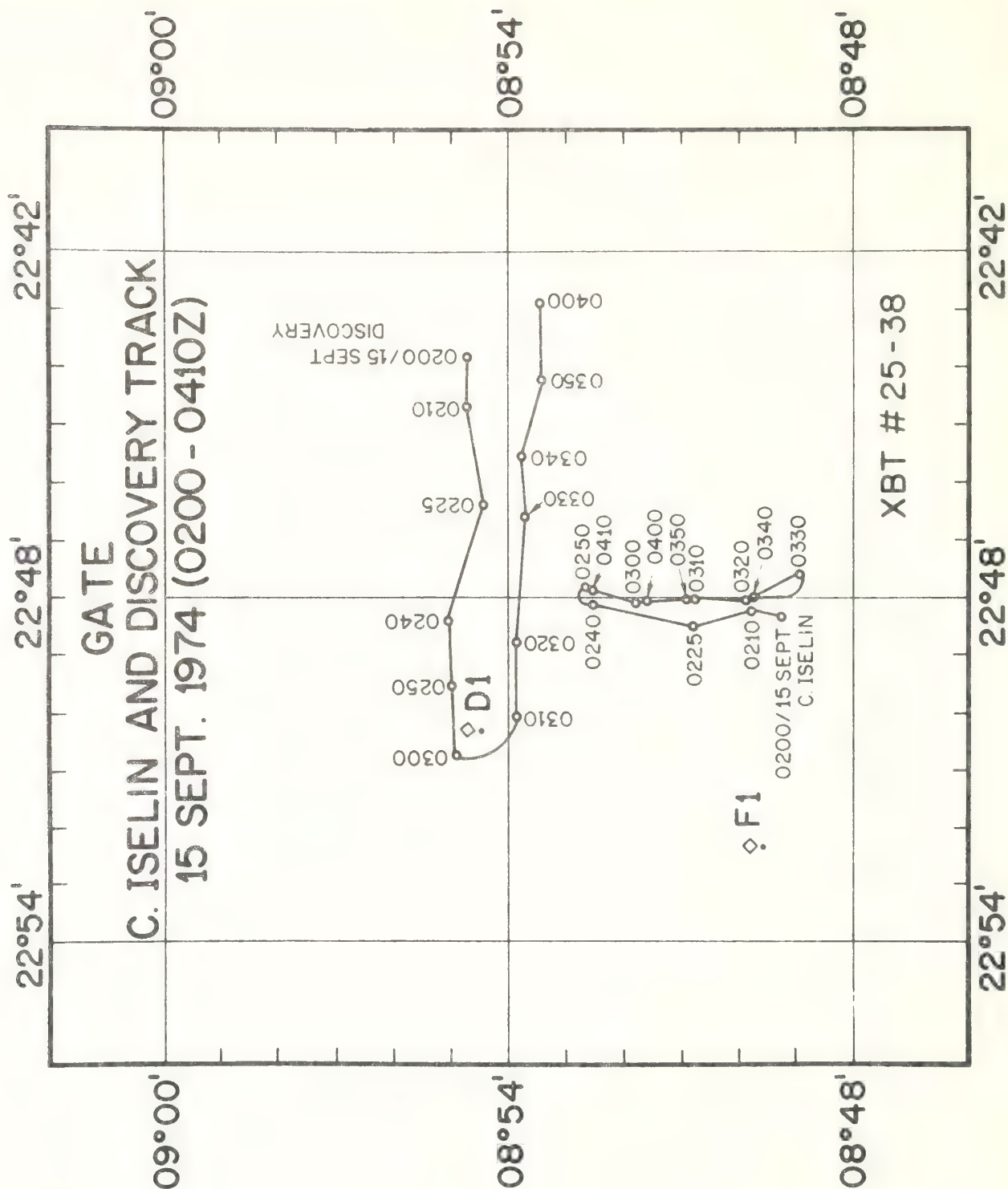


Figure 7. R/V C. ISELIN and R/V DISCOVERY tracks 0200 to 0410 GMT 15 Sept. 1974.

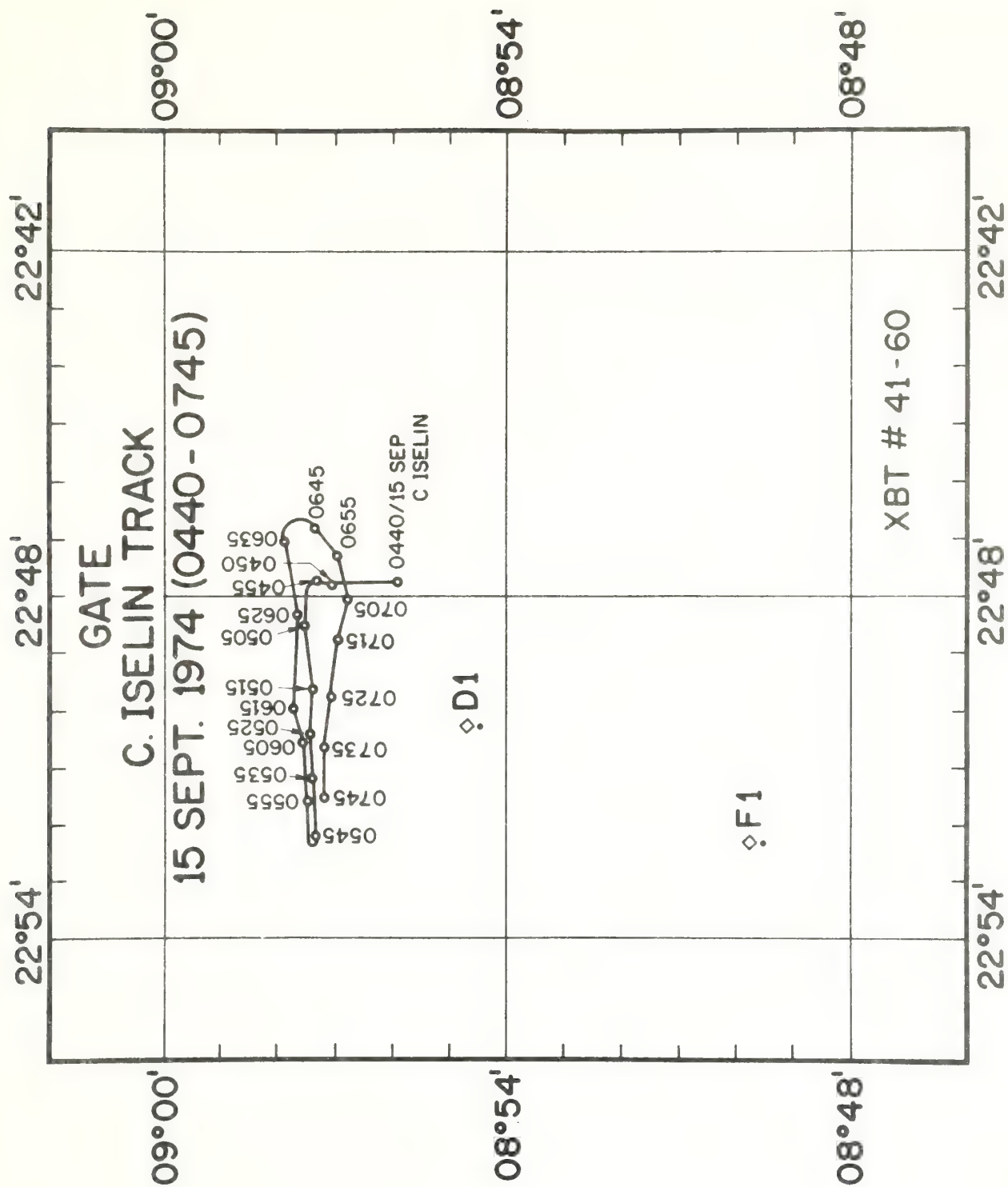


Figure 8. R/V C. ISELIN track 0440 to 0745 GMT 15 Sept. 1974.



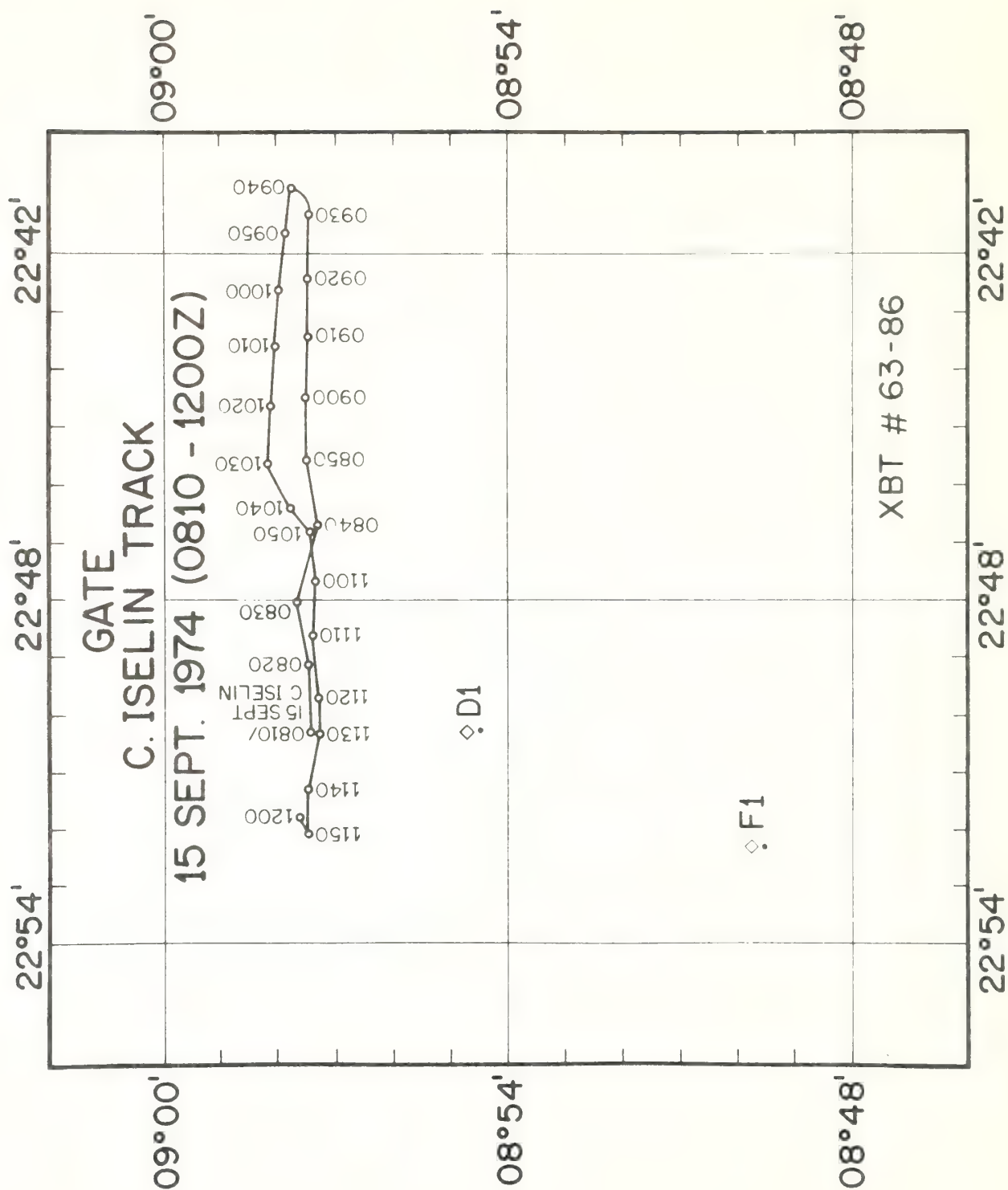


Figure 9. R/V C. ISELIN track 0810 to 1200 GMT 15 Sept. 1974.

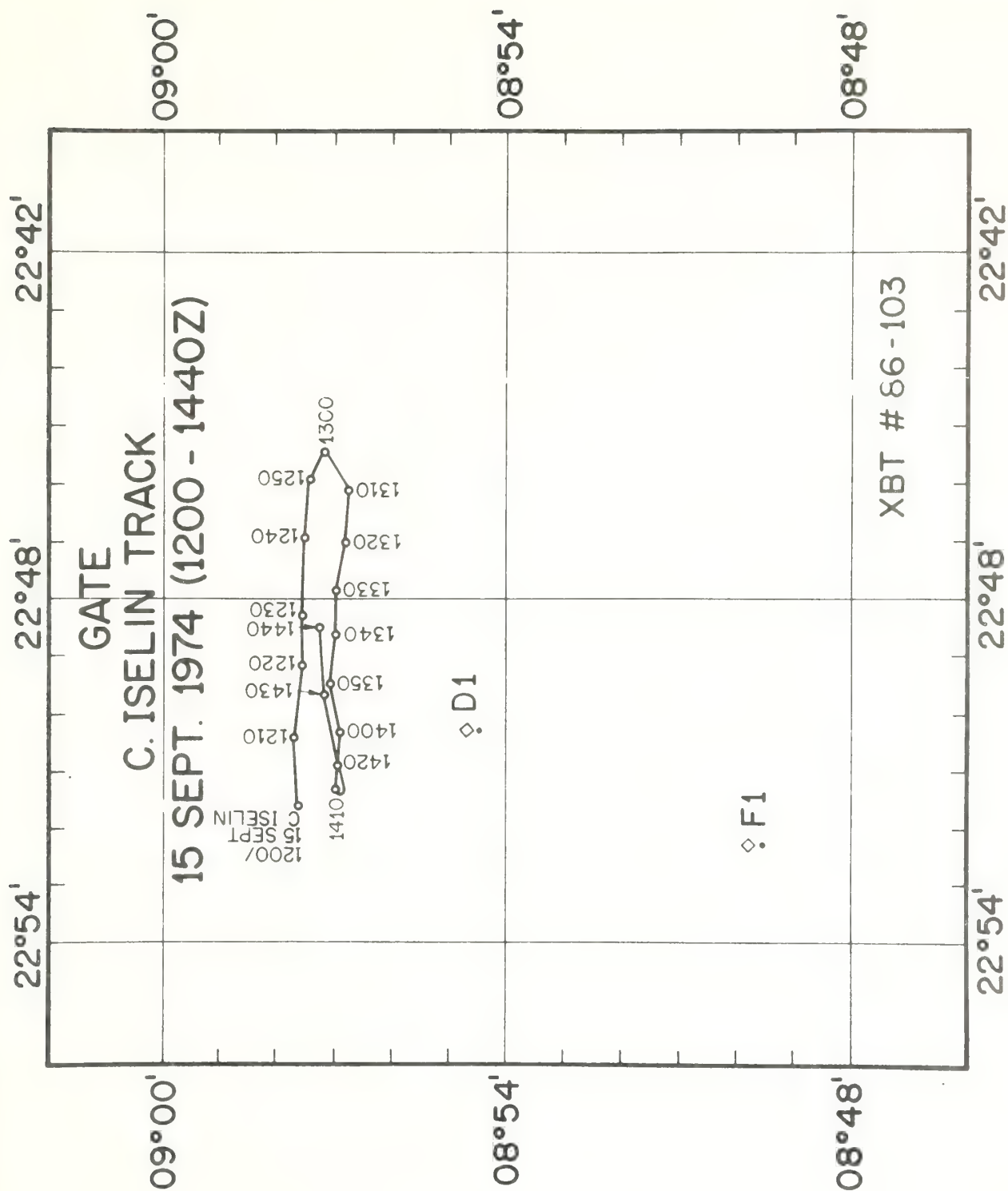


Figure 10. R/V C. ISELIN track 1200 to 1440 GMT 15 Sept. 1974.

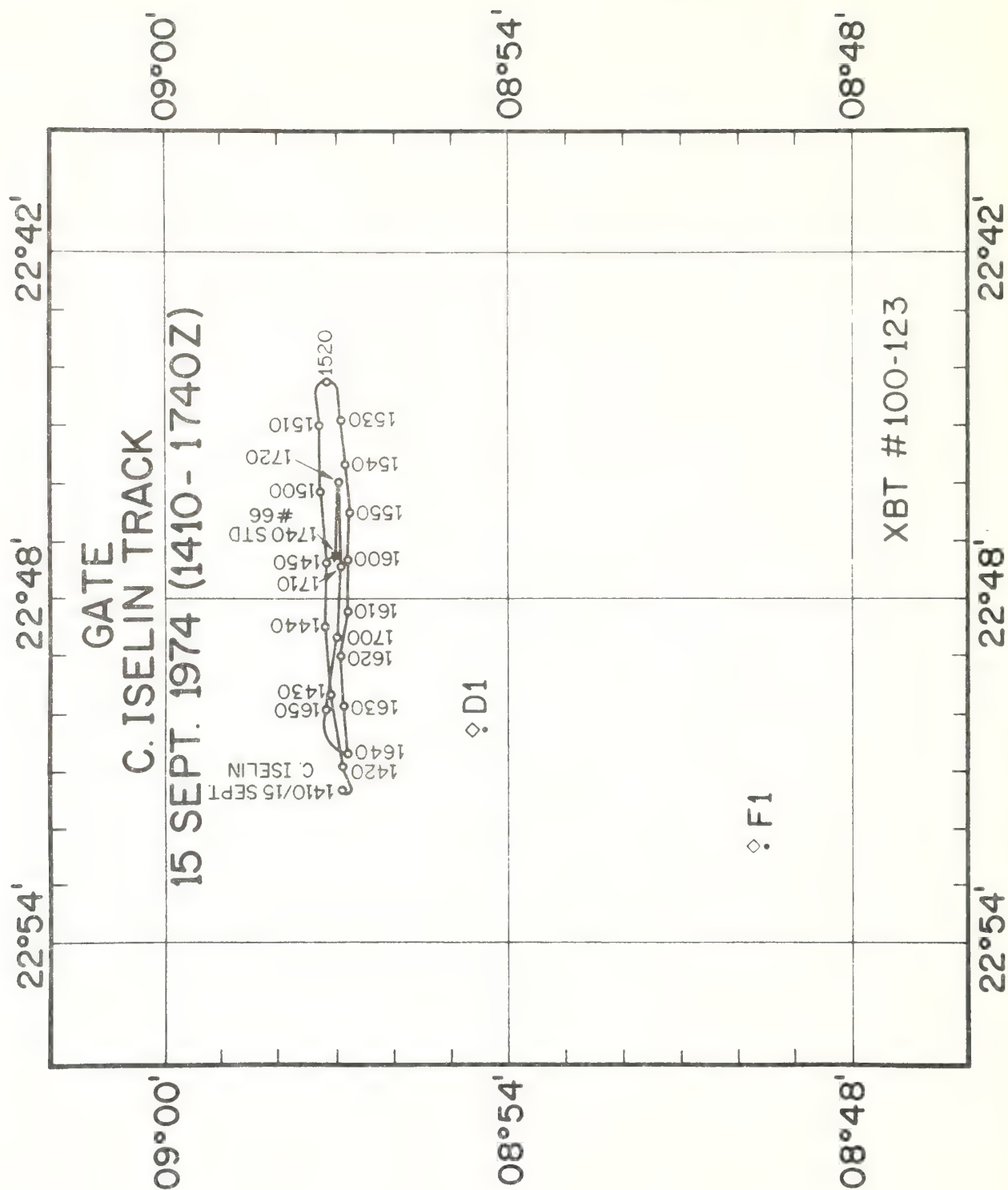


Figure 11. R/V C. ISELIN track 1410 to 1740 GMT 15 Sept. 1974.



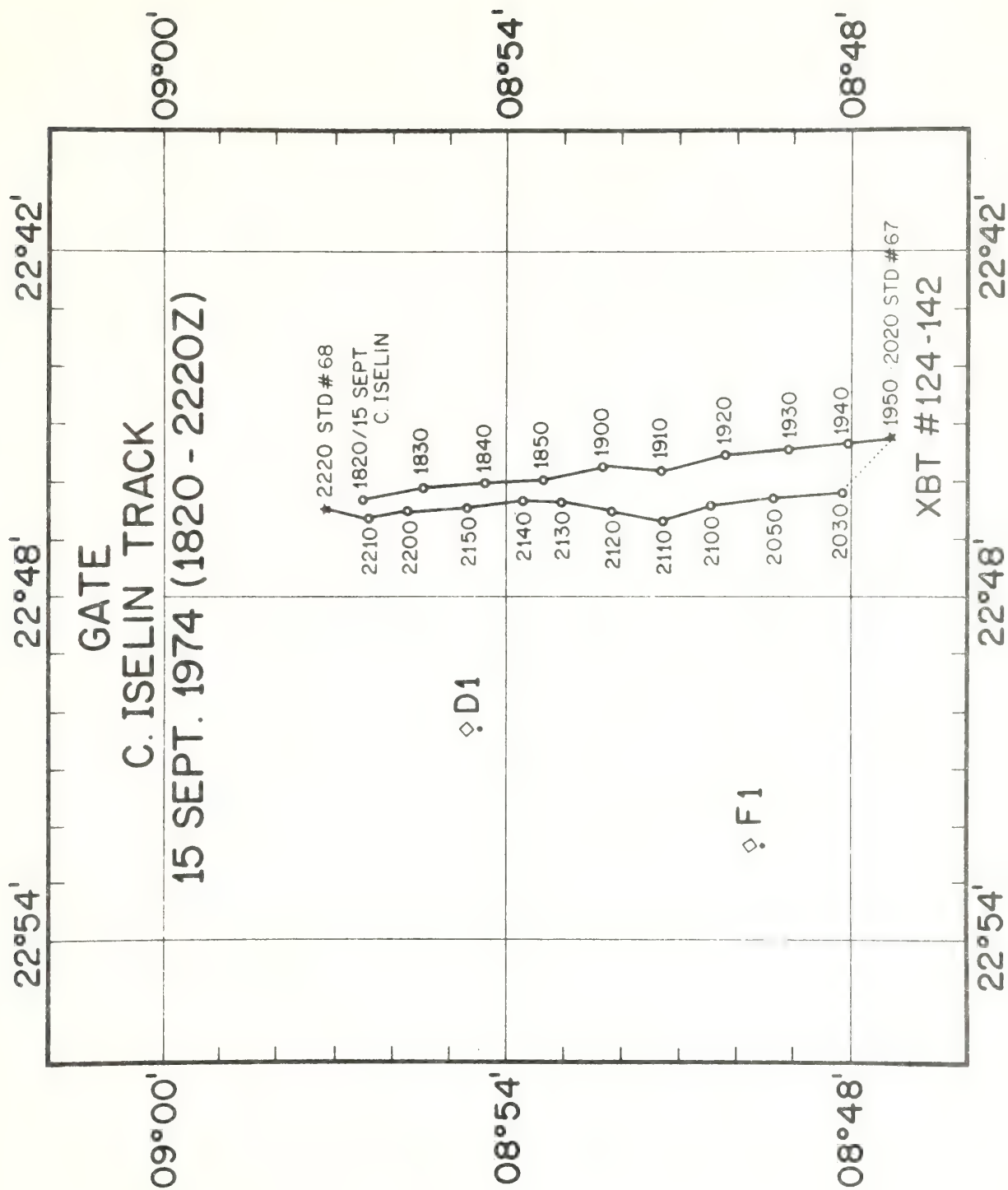


Figure 12. R/V C. ISELIN track 1820 to 2220 GMT 15 Sept. 1974.

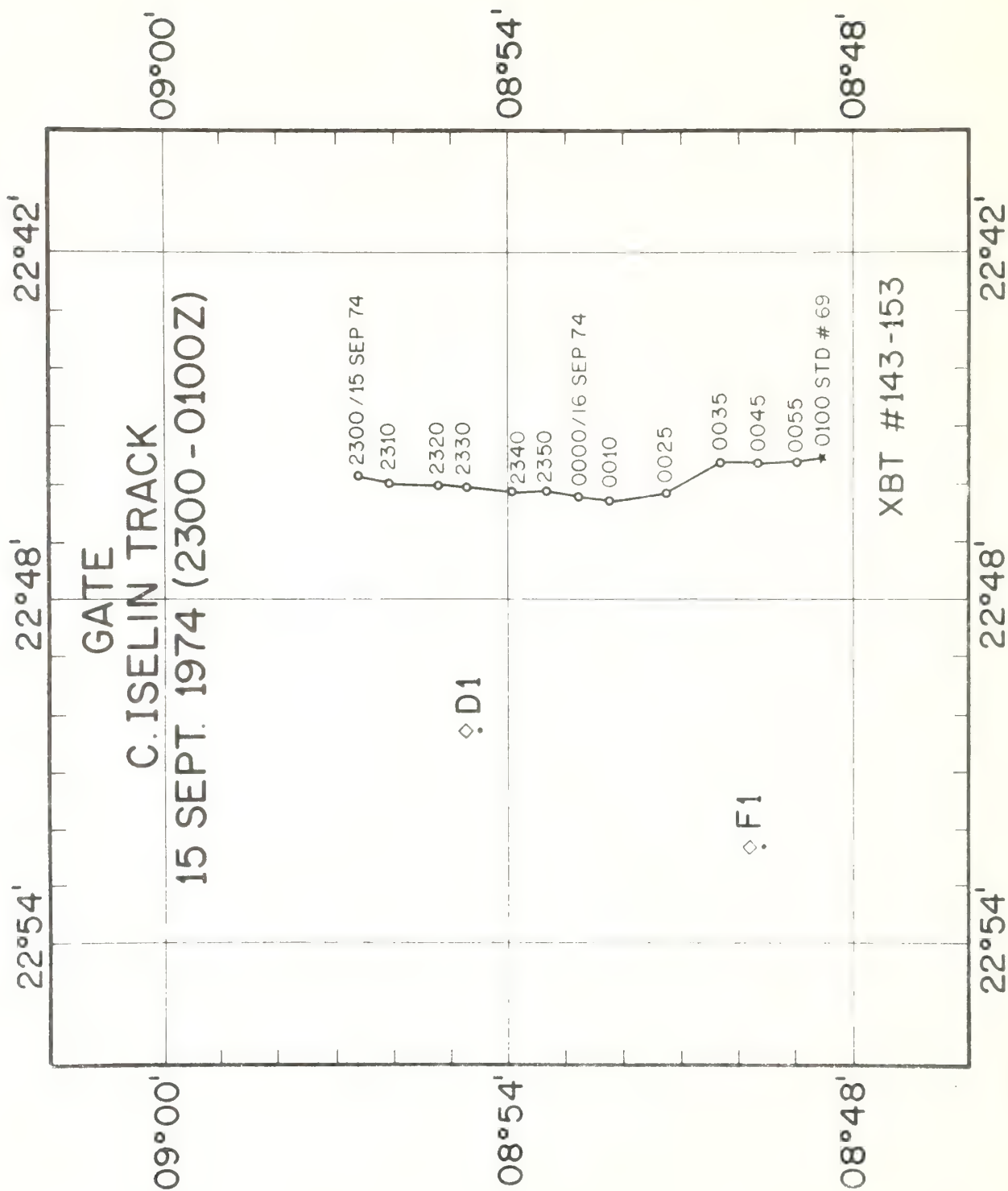


Figure 13. R/V C. ISELIN track 2300 GMT 15 Sept. to 0100 GMT 16 Sept. 1974.

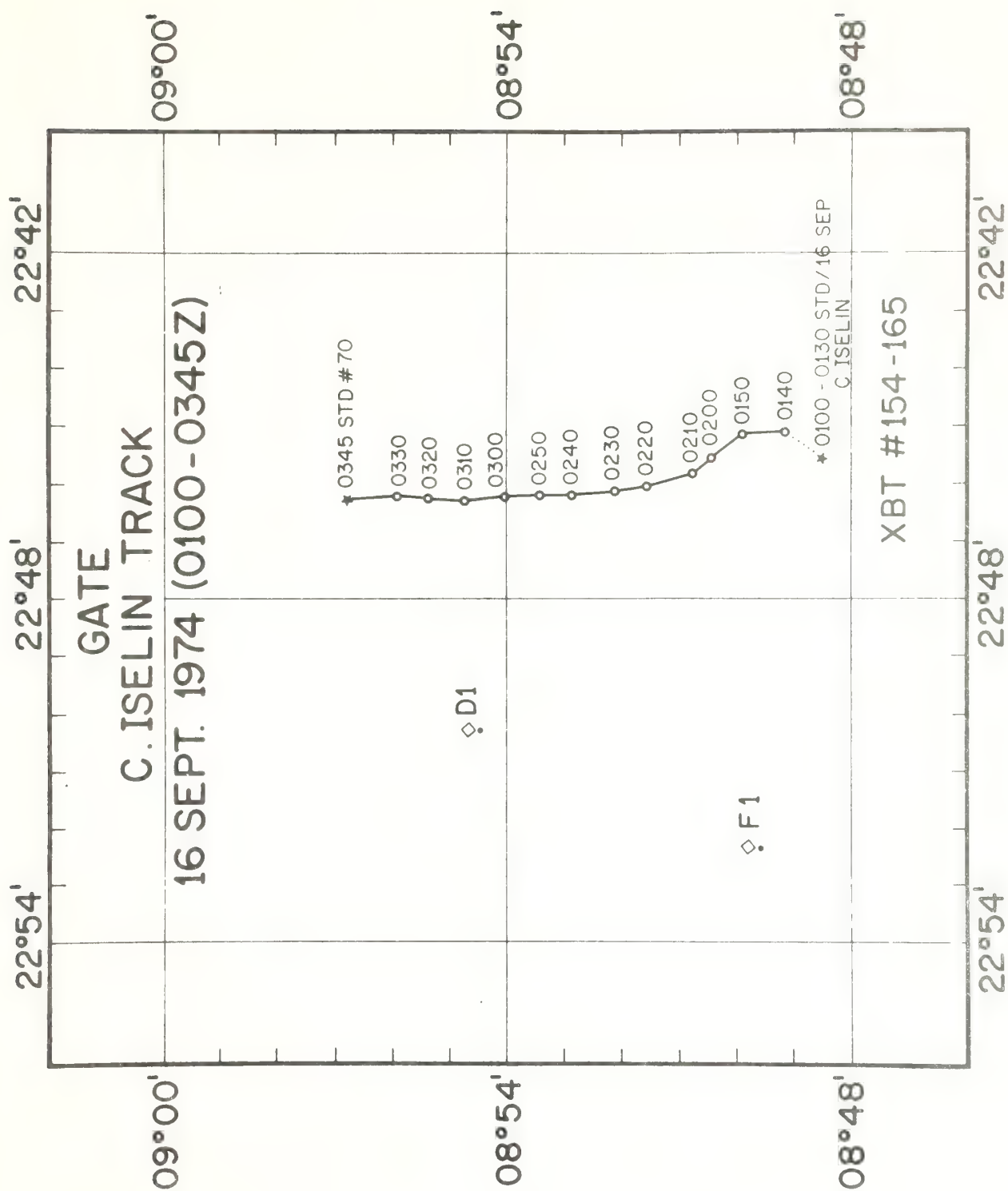


Figure 14. R/V C. ISELIN track 0100 to 0345 GMT 16 Sept. 1974.



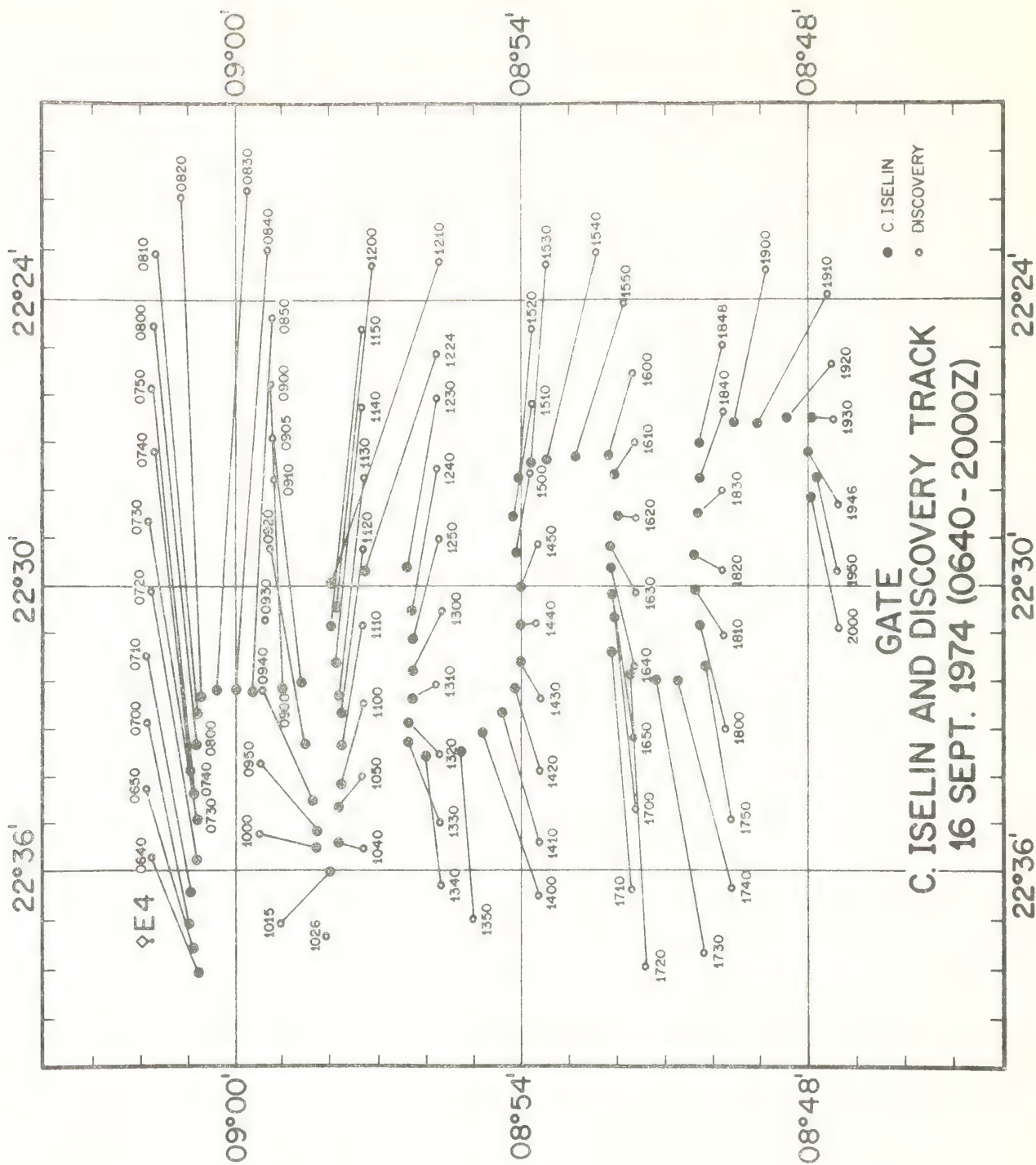


Figure 15. R/V C. ISELIN and R/V DISCOVERY tracks 0640 to 2000 GMT  
16 Sept. 1974.

### 3. INSTRUMENTATION

Although the R/V COLUMBUS ISELIN performed her functions during the third phase of GATE as a roving ship within the C-scale array, she was equipped to observe the following basic meteorological parameters: sea surface temperature, air temperature, relative humidity, atmospheric pressure, wind speed, wind direction relative to the ship's direction, solar radiation, rainfall, and cloud photographs.

#### 3.1 Sensor Description

The sea surface temperature and the air temperature were measured by means of platinum resistance thermometers from Minco Products, Model S31-20A. They were used in a three-wire bridge circuit with signal conditioning providing 0-10 VDC output. This corresponds to a temperature range of 15-35°C.

A Hygrodynamics humidity sensor, Model 15-7012, was used to measure the relative humidity. Its operation is based on adsorption of moisture in lithium cells, which changes the electrical resistance. Signal conditioning provided an output of 0-10 VDC corresponding to 0-100% relative humidity with a stated accuracy of  $\pm 3\%$ .

The atmospheric pressure was measured with a Hamilton Standard pressure transducer. The output is frequency. It was read on a frequency counter (in Hertz) and logged once every hour.

For wind speed and direction measurements, a Gill three-cup anemometer and microvane were used.

After signal conditioning, 0-10 VDC corresponded to 0-20  $\text{ms}^{-1}$  wind speed. The direction was sensed by a potentiometer with the following output relative to the ship's direction:

0.0V =  $180^{\circ}$  (stern)  
2.5V =  $270^{\circ}$  (port)  
5.0V =  $000^{\circ}$  (bow)  
7.5V =  $090^{\circ}$  (starboard).

Solar radiation was measured by an Eppley pyranometer (Model 15) with a calibrated sensitivity of  $7.37 \mu\text{V}/\text{watt m}^{-2}$ . Signal conditioning provided a 0-10 VDC range corresponding to an input of 0-1360  $\text{watt m}^{-2}$ .

All of these parameters, except the atmospheric pressure, were recorded on an Esterline Angus 24-point strip chart re-



corder, and each of the recorded parameters was sampled once every minute.

In addition to these parameters, rainfall was estimated using a standard NWS 8-inch collector and measuring cup system. This gauge was read on a 12-hourly basis or more often when dictated by weather events.

Finally, cloud pictures were taken with a hand-held Pentax camera with data pack, pointing to the four principal sky directions and using Kodak color films. Usually, pictures were taken with the sea surface in the frame for wave documentation. It was attempted to photograph the sky condition on an hourly basis. This was not always possible because of a personnel shortage. However, cloud cover and convective codes were estimated from these photographs, of which some 600 were made. They were also helpful in validating the wind data in the few cases when small scale disturbances were documented to be present, resulting in very local wind conditions. The Appendix lists the cloud photographs available at SAIL.

### 3.2 Sensor Exposure

The R/V C. ISELIN was not equipped with a meteorological boom system as were the dedicated ships. Therefore, the

sensors were placed on the ship with the goal of obtaining the best possible exposures.

Figure 16 shows the outline of the R/V COLUMBUS ISELIN and the sensor exposures. The air temperature and relative humidity sensors were mounted in a thermal shield with forced air aspiration on the starboard rail of the flying bridge, about 11 meters above the sea surface (see Figure 16, location 1). The pyranometer was also mounted at the starboard rail of the flying bridge, about 10.4 meters above the sea surface (see Figure 16, location 2). The wind speed and direction sensors were positioned as high as possible on the main mast (see Figure 16, location 3) in order to obtain wind measurements which were least affected by the ship. This placed the wind sensors at about 16.2 meters above the sea surface. Since the efficiency of rain collection in rain gauges depends to some degree on the air flow, the rain collector was also placed high on the mast (see Figure 16, location 4) next to the wind sensors. The measuring cup was placed at the deck level of the mast and was connected to the rain collector by 1/4 inch tygon tubing.

The atmospheric pressure sensor was located in the scientific plotting room and was connected to a pressure head

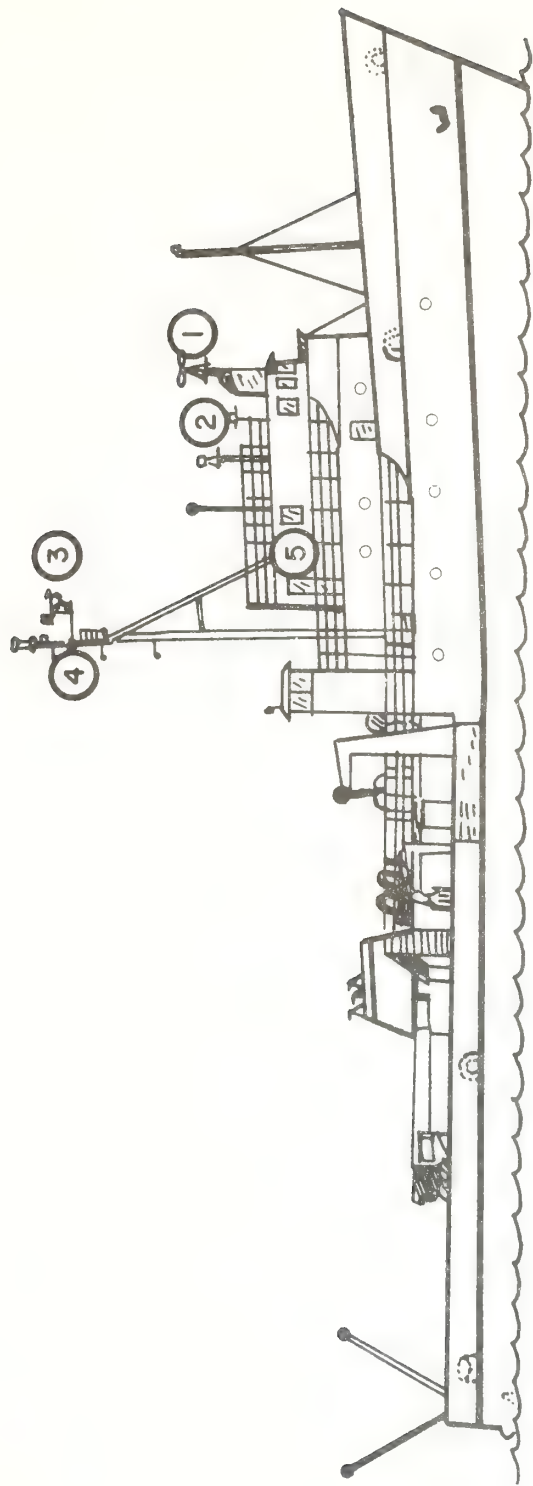


Figure 12. Schematic diagram of H/V C. ISELIN showing sensor exposures.



mounted on a rail at about 7.3 meters above the sea surface (see Figure 16, location 5).

The sea surface temperature was measured at a depth of about 10 centimeters from a towed float. The float was suspended from a 6-meter long fiberglass pole on the starboard side.

#### 4. DATA PRESENTATION

Hourly meteorological observations obtained aboard the R/V COLUMBUS ISELIN from 2 to 20 September, 1974, are given in Table 1. The hourly ship positions were obtained either by the on-board satellite navigation system, navigational radar range and bearing from moored buoys, or as described in Section 2 during joint roving exercises with the R/V DISCOVERY.

As discussed in Section 3, the sea surface temperature, air temperature, relative humidity, and solar radiation were sampled and recorded once a minute. To obtain the hourly data (and half-hourly data for radiation) presented in Table 1, average values for the fifteen minutes prior to the stated time were used. In Table 1, values of sea surface temperature marked with "\$" are bucket temperatures. It is estimated that such data are accurate to within  $0.3^{\circ}\text{C}$ . The other data are accurate to the precision indicated in the table. The relative humidity was converted to mixing ratio using the measured atmospheric pressure and (5.1.4) and (5.1.5). Both the mixing ratio and air temperature given in Table 1 have been reduced to 10 m values using (5.2.25).

The atmospheric pressure transducer had a digital output which was logged hourly. Since the pressure was measured

TABLE 1

HOURLY METEOROLOGICAL OBSERVATIONS



# ATLANTIC OCEANOGRAPHIC AND ATMOSPHERIC ADMINISTRATION SFA AIR INTERACTION LABORATORIES

COLUMBUS ISLEIN (GATE) HOURLY METEOROLOGICAL OBSERVATIONS  
SEPTEMBER 2, 1974

JULIAN DAY	GMT HOUR	LATITUDE DEG MIN	LONGITUDE DEG MIN	SEA	TEMPERATURE DEG.C AIR	SPECIFIC HUMIDITY (G/M <sup>3</sup> )	RADIATION WATTS/M <sup>2</sup> HOURLY 1/2-HR	PRESSURE MB	WIND SPEED M/S	WIND DIREC DEG	SHIP SPEED KNOTS	SHIP DIREC DEG	CONVECTIVE CODE	CLOUD COVER
245	0	8 54.4	22 50.3		26.5	18	0	0	.0*	0*				
245	1	8 54.4	22 50.3		26.6	17	0	0	.0*	0*				
245	2	8 54.4	22 50.3		26.4	17	0	0	.0*	0*				
245	3	8 54.4	22 50.3		26.1	17	0	0	3.0*	300*				
245	4	8 54.4	22 50.3		26.3	17	0	0	2.0*	300*				
245	5	8 54.4	22 50.3		26.8	17	0	0	2.0*	300*				
245	6	8 54.4	22 50.3		26.3	18	0	0	2.0*	300*				
245	7	8 49.0	22 52.8		26.4	18	0	0	1.4*	180*				
245	8	8 42.2	22 55.3		26.5	18	69	62	3.4*	280*				
245	9	8 35.2	22 55.8		26.3	17	104	111	3.9*	320*				
245	10	8 29.5	22 2.6		24.4	17	355	677	3.9*	320*				
245	11	8 29.5	22 2.6		25.7	17	760	844	3.9*	310*				
245	12	8 29.5	22 2.6		26.1	18	914	746	3.9*	310*				
245	13	8 29.5	22 2.6		27.5	17	474	516	3.0*	275*				
245	14	8 29.5	22 2.6		25.7	18	781	404	.0*	0*				
245	15	8 29.5	22 2.6		26.2	16	656	544	.0*	0*				
245	16	8 29.5	22 2.6		26.5	16	348	328	.0*	0*				
245	17	8 29.5	22 2.6		26.5	16	104	76	3.0*	180*				
245	18	8 29.5	22 2.6		25.1	18	48		4.9*	180*				
245	19	8 29.5	22 2.6		24.4	16			3.9*	180*				
245	20	8 29.5	22 2.6		24.4	17			3.0*	180*				
245	21	8 29.5	22 2.6		24.3	17	0	0	3.9*	210*				
245	22	8 29.5	22 2.6		25.0	17	0	0	5.9*	210*				
245	23	8 29.5	22 2.6				0	0	5.9*	190*				

\* INDICATES VALUES FROM SHIP LOG  
\$ UNCALIBRATED SEA TEMPERATURE - BELIEVED TO BE WITHIN 0.3 DEG.C

NATIONAL OCEANIC & ATMOSPHERIC ADMINISTRATION  
ATLANTIC OCEANOGRAPHIC & METEOROLOGICAL LABORATORIES  
SEA AIR INTERACTION LABORATORY

COLUMBUS ISLEIN (GATF) HOURLY METEOROLOGICAL OBSERVATIONS  
SEPTEMBER 3, 1974

JULIAN DAY	GMT HOUR	LATITUDE		LONGITUDE		TEMPERATURE DEG.C		SPECIFIC HUMIDITY (G"/KGW)	RADIATION WATTS/M2 HOURLY 1/2-HR	PRESSURE MB	WIND		SHIP SPEED KNOTS	SHIP DIREC DEG		SHIP CONVECTIVE CODE	CLOUD COVER
		DEG	MIN	DEG	MIN	SEA	AIR				M/S	DIREC		DIREC	DEG		
246	0	8	29.5	23	2.3												
246	1	8	29.5	23	2.3								4.4*			180*	
246	2	8	29.5	23	2.3								5.4*			175*	
246	3	8	29.5	23	2.3								5.9*			195*	
246	4	8	29.5	23	2.3								4.9*			240*	
246	5	8	29.5	23	2.3								3.0*			255*	
246	6	8	29.5	23	2.3								3.0*			180*	
246	7	8	29.5	23	2.3								4.9*			230*	
246	8	8	29.5	23	2.3		25.8*	17*	34	104			5.4*			230*	
246	9	8	29.5	23	2.5		25.5	17	209	293			5.9*			230*	
246	10	8	29.6	23	6.0		26.2	17	272	404			4.9*			230*	
246	11	8	29.5	23	0.5		26.0	17	509	460			5.9*			230*	
246	12	8	29.5	23	13.0		26.6	18	607				5.4*			230*	
246	13	8	29.5	23	13.1								4.9*			180*	
246	14	8	29.5	23	13.1								5.9*			190*	
246	15	8	29.5	23	13.1								5.9*			205*	
246	16	8	29.5	23	13.1		26.6	17	404	348			5.9*			205*	
246	17	8	29.5	23	13.1								5.9*			204*	
246	18	8	29.5	23	13.1								4.9*			220*	
246	19	8	29.5	23	13.1		26.4	17	55				4.4*			220*	
246	20	8	29.5	23	13.1		26.4	17					4.4*			235*	
246	21	8	29.5	23	13.1		26.5	18	0	0			3.9*			225*	
246	22	8	29.5	23	13.1				0	0			3.9*			225*	
246	23	8	29.5	23	13.1				0	0			3.4*			225*	

\* INDICATES VALUES FROM SHIP LOG  
\$ UNCALIBRATED SEA TEMPERATURE - RELIEVED TO BE WITHIN 0.3 DEG.C

NATIONAL OCEANIC & ATMOSPHERIC ADMINISTRATION  
ATLANTIC OCEANOGRAPHIC & METEOROLOGICAL LABORATORIES  
SFA AIR INTERACTION LABORATORY

COLUMBUS TSELIN (GATF) HOURLY METEOROLOGICAL OBSERVATIONS  
SEPTEMBER 4, 1974

JULIAN DAY	GAT HOUR	LATITUDE DEG	LONGITUDE MIN	TEMPERATURE DEG.C	SPECIFIC HUMIDITY (G/KGM)	RADIATION WATTS/M2 HOURLY 1/2-HR	PRESSURE MB	WIND SPEED M/S	WIND DIRECTION DEG	SHIP SPEED KNOTS	SHIP DIRECTION DEG	SHIP CONVECTIVE CODE	CLOUD COVER
247	0	8 54.1	23 13.1	26.4	17	0	0	3.9*	230*				
247	1	8 54.1	23 13.1	26.3	18	0	0	3.9*	225*				
247	2	8 54.1	23 13.1	26.2	17	0	0	3.4*	235*				
247	3	8 54.1	23 13.1	26.2	17	0	0	3.0*	245*				
247	4	8 54.1	23 13.1	26.3	17	0	0	2.0*	260*				
247	5	8 54.1	23 13.1	26.3	17	0	0	2.0*	260*				
247	6	8 54.1	23 13.1	26.1	17	0	0	3.0*	260*				
247	7	8 54.1	23 13.1	25.9	17	0	0	3.0*	260*				
247	8	8 54.1	23 13.1	25.8	17	41	132	2.5*	260*				
247	9	8 54.1	23 13.1	26.1	18	146	307	2.5*	260*				
247	10	8 54.1	23 13.1	26.8	18	460	586	3.0*	250*				
247	11	8 52.1	23 11.1	26.8	18	725	816	3.9*	250*				
247	12	8 41.2	23 9.7	26.7	18	697		3.0*	305*				
247	13	8 41.2	23 9.7					3.0*	305*				
247	14	8 41.2	23 9.7	26.6	17		488	.0*	0*				
247	15	8 41.2	23 9.7	27.0	18		328	1.4*	300*				
247	16	8 41.2	23 9.7	26.9	18		132	3.9*	300*				
247	17	8 41.2	23 9.7	26.9	18			4.9*	300*				
247	18	8 29.5	23 2.3	27.8	18	27		5.9*	300*				
247	19	8 29.5	23 2.3	27.3	18			5.9*	310*				
247	20	8 29.5	23 2.3	27.5	18	0	0	6.9*	305*				
247	21	8 29.5	23 2.3	27.5	17	0	0	6.4*	305*				
247	22	8 29.5	23 2.3	27.1	18	0	0	7.3*	305*				
247	23	8 29.5	23 2.3	27.1	18	0	0						

\* INDICATES VALUES FROM SHIP LOG  
% UNCALIBRATED SEA TEMPERATURE - RELIEVED TO BE WITHIN 0.3 DEG.C

Table 1. (continued).



NATIONAL OCEANIC AND ATMOSPHERIC ADMINISTRATION  
ATLANTIC OCEANOGRAPHIC METEOROLOGICAL LABORATORIES  
SEA AIR INTERACTION LABORATORY

COLUMBUS ISELIN (GATF) HOURLY METEOROLOGICAL OBSERVATIONS  
SEPTEMBER 5, 1974

JULIAN DAY	G-T HOUR	LATITUDE		LONGITUDE DEG MIN SEC W	TEMPERATURE		SPECIFIC HUMIDITY (G/KG)	RADIATION WATTS/M2 HOURLY 1/2-HR	PRESSURE MB	WIND		SHIP SPEED KNOTS	SHIP DIREC		CLOUD COVER
		DEG	MIN		SEA	AIR				M/S	DEG		DIREC	DEG	
248	0	8 29.5	23	2.3	27.95	26.5	18	0	0	5.0*	280*				
248	1	8 41.2	23	0.7	27.85	26.8	18	0	0	4.9*	285*				
248	2	8 41.2	23	0.7	27.85	24.6	17	0	0	9.9*	215*				
248	3	8 41.2	23	0.7	27.75	24.7	17	0	0	9.8*	230*				
248	4	8 41.2	23	9.7	25.1	25.1	17	0	0	6.9*	230*				
248	5	8 41.2	23	0.7	25.1	25.1	18	0	0	6.9*	230*				
248	6	8 41.2	23	0.7	25.0	25.0	17	0	0	7.8*	230*				
248	7	8 47.1	23	11.3	24.8	24.8	17	0	0	7.8*	230*				
248	8	8 54.1	23	11.2	25.0	25.0	17	0	0	6.9*	210*				
248	9	8 54.1	23	11.2	22.9	22.9	17	27	279	5.0*	245*				10
248	10	8 54.1	23	11.2	23.2	23.2	17	425	453	5.9*	240*				10
248	11	8 54.1	23	11.2	24.0	24.0	17	439	258	3.4*	240*				2
248	12	8 54.1	23	11.2	25.1	25.1	17	230	125	3.4*	240*				10
248	13	8 54.1	23	11.2	25.1	25.1	17	125	1013.7	5.9*	240*				10
248	14	8 54.1	23	11.2	22.7	22.7	17	202	258	3.4*	230*				10
248	15	8 54.1	23	11.2	23.7	23.7	16	300	230	3.4*	215*				2
248	16	8 54.1	23	11.2	24.9	24.9	17	209	181	3.9*	30*				2
248	17	8 54.1	23	11.2	25.5	25.5	17	139	34	3.9*	230*				2
248	18	8 52.1	23	11.2	27.65	25.7	17			1012.7					
248	19	8 52.1	23	11.2	27.75	23.4	17			1012.8					
248	20	8 41.4	23	12.0	27.65	23.4	17			1012.8					
248	21	8 35.6	23	11.0	27.75	24.0				1013.3					
248	22	8 41.1	23	11.2						1013.6					
248	23	8 47.8	23	11.2	27.45	25.0	16	0	0	1014.2					

\* INDICATES VALUES FROM SHIP LOG

\$ UNCALIBRATED SEA TEMPERATURE - RELIEVED TO BE WITHIN 0.3 DEG.C

Table 1. (continued).

NATIONAL OCEANIC & ATMOSPHERIC ADMINISTRATION  
ATLANTIC OCEANOGRAPHIC & METEOROLOGICAL LABORATORIES  
SFA AIR INTRODUCTION LABORATORY

COLUMBUS ISLAND (GATE) HOURLY METEOROLOGICAL OBSERVATIONS  
SEPTEMBER 6, 1974

JULIAN DAY	GMT HOUR	LATITUDE DEG MIN	LONGITUDE DEG MIN	TEMPERATURE DEG.C	SPECIFIC HUMIDITY (G"/KG)	RADIATION WATTS/M2 HOURLY 1/2-HR	PRESSURE MB	WIND SPEED W/S	WIND DIREC DEG	SHIP SPEED KNOTS	SHIP DIREC DEG	SHIP CONVECTIVE CODE	CLOUD COVER
249	0	8 44.1	23 14.5	27.5\$	16	0	1014.2	4.9*	285*				
249	1	8 43.2	23 13.5	27.6\$	16	0		.0*	0*				
249	2	8 42.6	23 12.5	27.6\$	16	0		.0*	0*				
249	3	8 41.0	23 11.5	27.6\$	16	0		3.4*	240*				
249	4	8 40.8	23 9.7	27.6\$	16	0		3.4*	200*				
249	5	8 34.1	23 5.7	27.5\$	17	0		3.0*	200*				
249	6	8 29.5	23 2.3	27.6\$	17	0		3.0*	200*				
249	7	8 29.5	23 2.3	27.7\$	17	0		3.0*	200*				
249	8	8 35.0	23 0.0	27.7\$	17	63	1013.0	3.0*	200*			1	
249	9	8 42.0	23 9.5	27.9\$	17	355	1013.4	.0*	0*				
249	10	8 47.0	23 11.0	27.9\$	17	586	1013.7	2.0*	260*			2	
249	11	8 54.1	23 13.0	27.7\$	16	789	1013.7	2.5*	270*				
249	12	8 54.2	23 13.0	27.7\$	17	753	1013.9	3.4*	275*				
249	13	8 54.1	23 13.1	27.7\$	16	942	1013.9	3.4*	270*				
249	14	8 53.0	23 12.1	26.6	16		1012.5	3.4*	270*			2	
249	15	8 47.7	23 5.7	26.6	16	579	1011.7	3.4*	288*			3	
249	16	8 42.4	23 5.0	26.6	16	125	1011.7	3.4*	230*			3	10
249	17	8 40.6	22 57.7	26.6	16	293	1011.7	4.9*	230*			2	9
249	18	8 40.6	22 57.7	26.6	16		1011.7	2.5*	230*			1	9
249	19	8 40.4	22 57.7	26.6	16		1011.7	3.4*	230*			1	9
249	20	8 40.3	22 57.7	26.6	17			3.4*	230*				
249	21	8 44.3	22 55.8	27.1	18	0	1013.0	5.4*	230*				
249	22	8 54.0	22 55.1	27.2	17	0	1013.1	7.4*	235*				
249	23	8 50.1	22 55.8	27.1	17	0	1013.9	5.9*	230*				

\* INDICATES VALUES FROM SHIP LOG

\$ UNCALIBRATED SEA TEMPERATURE - RELIEVED TO BE WITHIN 0.3 DEG.C

Table 1. (continued).

# NATIONAL OCEANIC & ATMOSPHERIC ADMINISTRATION ATLANTIC OCEANOGRAPHIC & METEOROLOGICAL LABORATORIES SEA AIR INTERACTION LABORATORY

COLUMBUS ISLAND (GATE) HOURLY METEOROLOGICAL OBSERVATIONS  
SEPTEMBER 7, 1974

JULIAN DAY	GWT HOUR	LATITUDE DEG	LONGITUDE MIN	TEMPERATURE SEA	TEMPERATURE AIR	SPECIFIC HUMIDITY (G"/KGM)	RADIATION WATTS/M2 HOURLY 1/2-HR	PRESSURE MR	WIND SPEED M/S	WIND DIREC DEG	SHIP SPEED KNOTS	SHIP DIREC DEG	SHIP CONVECTIVE CODE	CLOUD COVER
250	0	8 42.1	22 57.8	27.1	24.0	15	0	1013.7	8.0	206	9.0	265		
250	1	8 44.0	22 57.3	27.2	26.0	17	0	1013.6	5.9*	230*				
250	2	8 57.0	22 57.0	27.2	26.2	17	0	1012.2	7.8	223	9.0	270		
250	3	8 50.1	22 57.3	27.2	24.8	17	0	1012.1	6.8	212	9.0	180		
250	4	8 44.0	22 59.3	27.2	26.4	17	0	1011.9	7.7	235	9.0	360		
250	5	8 51.0	22 57.7	27.2	26.2	17	0	1011.7	7.9	226	9.0	360		
250	6	8 56.2	22 58.6	27.1	26.5	17	0	1011.7	7.4	212	9.0	180		
250	7	8 47.7	22 58.1	27.1	26.7	17	0	1012.1	8.6	209	9.0	187		
250	8	8 45.0	22 51.3	27.2	26.4	17	41	1012.4	5.6	216	8.0	88	1	A
250	9	8 47.0	22 44.1	27.2	26.9	16	230	1012.7	6.7	231	7.0	357	1	A
250	10	8 47.0	22 48.2	27.1	26.7	16	348	1012.8	8.0	213	7.0	270		A
250	11	8 48.0	22 51.9	27.1	27.0	17	495	1014.0	6.5	220	7.0	360	1	A
250	12	8 50.5	22 47.0	27.2	27.0	17	802	1013.4	6.5*	220*				
250	13	8 50.6	22 47.0	27.1	27.5	17	942	1012.8	6.5*	240*				
250	14	8 50.6	22 47.0	27.1	26.6	17	928	1011.9	6.5*	245*				
250	15	8 50.6	22 47.0	27.2	26.0	17	823	1011.2	6.7	223	8.0	154		A
250	16	8 50.6	22 47.0	27.1	28.1	18	872	1011.2	5.1	204	3.0	290	2	A
250	17	8 50.6	22 47.0	27.2	26.9	17	530	1011.1	6.7	223	8.0	270	1	A
250	18	8 50.0	22 47.0	27.1	27.1	17	153	1011.7	6.8	230	8.0	5	3	6
250	19	8 50.6	22 47.0	27.1	27.2	17	90	1012.1	5.3	222	8.0	90		
250	20	8 50.6	22 47.0	27.2	26.8	17	0	1011.9	7.5	212	7.0	270		
250	21	8 50.6	22 47.0	27.2	26.1	17	0	1013.0	6.9	222	8.0	215		
250	22	8 50.6	22 47.0	27.2	26.8	17	0	1012.5	6.1	223	7.0	270		
250	23	8 50.6	22 47.0	27.1	26.6	17	0	1013.4	6.0	203	8.0	220		

\* INDICATES VALUES FROM SHIP LOG

§ UNCALIBRATED SEA TEMPERATURE - RELIEVED TO BE WITHIN 0.3 DEG.C

Table 1. (continued).



NATIONAL OCEANIC & ATMOSPHERIC ADMINISTRATION  
ATLANTIC OCEANOGRAPHIC & METEOROLOGICAL LABORATORIES  
SEA AIR TELEACTION LABORATORY

COLUMBUS TSELIN (GATE) HOURLY METEOROLOGICAL OBSERVATIONS  
SEPTEMBER 8, 1974

JULIAN DAY	GMT HOUR	LATITUDE		LONGITUDE		TEMPERATURE		SPECIFIC HUMIDITY (G"/KGW)	RADIATION WATTS/M2 HOURLY 1/2-HK	PRESSURE MB	WIND SPEED M/S	WIND DIREC DEG	SHIP SPEED KNOTS	SHIP DIREC DEG	CONVECTIVE CODE	CLOUD COVER
		DEG	MIN	DEG	MIN	SFA	AIR									
251	0	8 50.7	22 47.0	27.5	26.6	14	0	0	0	1013.3	7.3	199	3.0	270		
251	1	8 50.2	22 47.0	27.4	26.2	17	0	0	0	1012.7	7.3	182	2.0	270		
251	2	8 50.2	22 47.0	27.5	26.8	18	0	0	0	1012.4	8.4	197	3.0	197		
251	3	8 50.6	22 47.0	27.3	26.8	17	0	0	0	1012.1	7.0	197	3.0	337		
251	4	8 50.1	22 47.0	27.1	26.9	18	0	0	0	1011.8	7.5	204	4.0	337		
251	5	8 50.5	22 47.0	27.1	26.7	17	0	0	0	1012.2	7.8*	195*	2.0	324		
251	6	8 50.5	22 47.0	27.2	26.7	18	0	0	0	1013.1	6.9	186	2.0	175		
251	7	8 50.3	22 47.0	27.1	26.4	18	0	0	0	1013.6	7.8	195	2.0	185		2
251	8	8 54.4	22 50.3	27.1	26.6	17	104	188	104	1014.3	6.4	195	2.0	185		1
251	9	8 54.4	22 50.3	27.1	26.6	17	223	376	223	1014.6	7.4	198	2.0	213		1
251	10	8 54.4	22 50.3	27.2	27.0	17	677	691	677	1014.3	7.1	206	2.0	240		1
251	11	8 54.4	22 50.3	27.2	27.0	17	865	572	865	1013.3	5.1	215	1.0	110		0
251	12	8 54.4	22 50.3	27.2	27.1	17	481	495	481	1013.3	5.9	225	1.0	255		0
251	13	8 54.4	22 50.3	27.2	27.1	17	474	446	474	1013.1	5.5	216	1.0	260		0
251	14	8 54.4	22 50.3	27.2	27.2	17	369	369	481	1013.1	4.9	210	1.0	270		0
251	15	8 54.4	22 50.3	27.1	27.1	17	335	272	335	1012.8	4.9	225	1.0	275		0
251	16	8 54.4	22 50.3	27.1	27.1	17	181	153	181	1013.4	4.1	232	7.0	205		0
251	17	8 51.7	22 50.7	27.1	27.0	17	49	27	49	1013.7	5.1	225	8.0	355		1
251	18	8 49.3	22 50.4	27.2	27.1	17	20	13	20	1014.3	4.2	246	8.0	160		
251	19	8 48.5	22 51.5	27.2	27.0	17	0	0	0	1015.2	3.0	205	8.0	220		
251	20	8 43.7	22 54.3	27.1	27.1	17	0	0	0	1015.9	3.1	197	8.0	220		
251	21	8 39.2	22 57.0	27.1	27.0	17	0	0	0	1016.4	2.6	196	7.0	220		
251	22															
251	23															

\* INDICATES VALUES FROM SHIP LOG  
\$ UNCALIBRATED SEA TEMPERATURE - BELIEVED TO BE WITHIN 0.3 DEG.C

Table 1. (continued).

# NATIONAL OCEANIC & ATMOSPHERIC ADMINISTRATION ATLANTIC OCEANOGRAPHIC & METEOROLOGICAL LABORATORIES SEA AIR INTERACTION LABORATORY

COLUMBUS ISLEIN (GATE) HOURLY METEOROLOGICAL OBSERVATIONS  
SEPTEMBER 9, 1974

JULIAN DAY	GAT HOUR	LATITUDE DEG	LONGITUDE DEG	TEMPERATURE SEA	TEMPERATURE AIR	SPECIFIC HUMIDITY (G"/KG)	RADIATION WATTS/M2 HOURLY 1/2-HR	PRESSURE MR	WIND SPEED M/S	WIND DIREC DEG	SHIP SPEED KNOTS	SHIP DIRFC DEG	SHIP CONVECTIVE CODE	CLOUD COVER
252	0	8 34.4	22 50.7	27.1	27.0	17	0	1016.7	2.6	196	7.0	220		
252	1	8 29.5	23 2.3	27.1	26.9	17	0		2.0*	189*				
252	2	8 29.5	23 2.3	27.1	26.9	17	0		.0*	0*				
252	3	8 29.5	23 2.3	27.0	26.6	17	0		.0*	0*				
252	4	8 29.5	23 2.3	27.1	26.2	17	0		3.0*	240*				
252	5	8 29.5	23 2.3	27.0	26.1	17	0		3.0*	240*				
252	6	8 29.5	23 2.3	26.9	25.6	17	0	1014.2	4.9	205	.0	105		
252	7	8 29.5	23 2.3	27.0	26.6	18	0	1014.6	4.9	205	.0	115		
252	8	8 29.5	23 2.3	27.0	26.8	17	6	1014.7	5.9	215	.0	115		
252	9	8 29.5	23 2.3	26.9	26.8	17	34	1015.3	6.9	228	.0	118		
252	10	8 29.5	23 2.3	27.1	27.0	17	27	1016.4	5.4	224	.0	114		
252	11	8 29.5	23 2.3	26.9	26.4	17	13	1016.4	4.9	198	.0	108		
252	12	8 29.5	23 2.3	27.1	25.9	17	223	1016.1	5.4	185	.0	90		
252	13	8 29.5	23 2.3	27.1	26.2	17	551	1015.8	4.4	223	2.0	101		
252	14	8 29.5	23 2.3		25.8	16	272	1014.9	7.3	279	1.0	285		
252	15	8 29.5	23 2.3		25.3	16	732	1014.4	5.9	285	.0	270		
252	16	8 29.5	23 2.3		25.4	17	390	1014.9	4.9	235	.0	305		
252	17	8 29.5	23 2.3	27.1	25.5	17	62	1015.2	5.9	255	.0	265		
252	18	8 29.5	23 2.3	27.2	25.4	16		1015.3	4.9	262	.0	212		
252	19	8 29.5	23 2.3	27.1	25.4	16		1015.9	5.9	294	.0	204		
252	20	8 29.5	23 2.3		25.2	17		1016.4	6.3	306	2.0	250		
252	21	8 29.5	23 2.3		25.6	17	6	1016.8	3.9	295	.0	235		
252	22	8 29.5	23 2.3		24.6	16	0		6.3	324	1.2	335		
252	23	8 36.5	23 6.7		25.2	17	0							

\* INDICATES VALUES FROM SHIP LOG  
\$ UNCALIBRATED SEA TEMPERATURE - RELIEVED TO BE WITHIN 0.3 DEG.C

Table 1. (continued).

NATIONAL OCEANIC & ATMOSPHERIC ADMINISTRATION  
ATLANTIC OCEANOGRAPHIC & METEOROLOGICAL LABORATORIES  
SEA AIR INTERACTION LABORATORY

COLUMBUS ISLIN (GATE) HOURLY METEOROLOGICAL OBSERVATIONS  
SEPTEMBER 10, 1974

JULIAN DAY	GUT HOUR	LATITUDE DEG	LONGITUDE DEG	TIME MIN	TEMPERATURE		SPECIFIC HUMIDITY (G./KG.)	RADIATION WATTS/M2 HOURLY 1/2-HR	PRESSURE MB	WIND		SHIP SPEED KNOTS	SHIP DIREC DEG	CONVECTIVE CODE	CLOUD COVER
					SEA	AIR				SPEED M/S	DIREC DEG				
253	0	8 45.3	23 11.8			24.4	16	0	1016.7	1.5	271	12.0	325		
253	1	8 54.1	23 11.1	27.2	27.2	25.0	16	0	1015.5	2.0	300	.0	230		
253	2	8 54.1	23 11.1	27.2	27.2	25.1	17	0	1014.6	3.0	305	.0	245		
253	3	8 54.1	23 11.1	27.1	27.1	25.1	16	0	1014.3	1.0	308	.0	248		
253	4	8 54.1	23 11.1	27.1	27.1	25.2	17	0	1014.0	1.0	260	.0	260		
253	5	8 54.1	23 11.1	27.1	27.1	25.3	16	0	1014.6	.5	260	.0	260		
253	6	8 54.1	23 11.1	27.1	27.1	25.4	17	0		.0*	0*				
253	7	8 54.1	23 11.1	27.1	27.1	25.6	17	0	1015.5	2.0	340	.0	350	1	4
253	8	8 54.1	23 11.1	27.1	27.1	25.6	16	76	1016.1	3.0	240	.0	250	1	1
253	9	8 54.1	23 11.1	27.1	27.1	26.2	17	223	1016.2	3.0	238	.0	248	2	3
253	10	8 54.1	23 11.1	27.2	27.2	26.4	17	432	1016.9	2.0	238	.0	248	1	3
253	11	8 54.1	23 11.1			27.0	16	746		.0*	0*			1	5
253	12	8 54.1	23 11.1			27.4	17	949	1017.1	.0*	0*			1	
253	13	8 54.1	23 11.1			27.8	17	900	1016.8	.0*	0*			1	
253	14	8 54.1	23 11.1			28.0	16	1026	1016.2	.0	193	4.0	295	1	
253	15	8 54.1	23 11.1			28.0	17	956	1015.2	.5	260	.0	270	4	
253	16	8 54.1	23 11.1			27.7	16	774	1014.9	1.0	290	.0	260	4	
253	17	8 54.1	23 11.1			27.6	16	509		2.5	269	1.0	275	4	
253	18	8 54.1	23 11.1			27.2	16	132	1015.3	2.0	260	.0	265	1	
253	19	8 54.1	23 11.1			27.3	16	62	1015.6	2.0	295	.0	265	1	
253	20	8 54.1	23 11.1			27.0	16		1016.1	3.9	300	.0	265	4	
253	21	8 54.1	23 11.1			27.1	15	0	1016.4	2.0	255	.0	255		
253	22	8 54.1	23 11.1			26.9	15	0	1016.5	2.0	265	.0	255		
253	23	8 54.1	23 11.1			26.8	16	0	1016.8	3.0	260	.0	270		

\* INDICATES VALUES FROM SHIP LOG  
\$ UNCALIBRATED SEA TEMPERATURE - RELIEVED TO BE WITHIN 0.3 DEG.C

Table 1. (continued).



# NATIONAL OCEANIC & ATMOSPHERIC ADMINISTRATION ATLANTIC OCEANOGRAPHIC & METEOROLOGICAL LABORATORIES SEA AIR INTERACTION LABORATORY

COLUMBUS ISLEIN (GATE) HOURLY METEOROLOGICAL OBSERVATIONS  
SEPTEMBER 11, 1974

JULIAN DAY	GPT HOUR	LATITUDE DEG	LONGITUDE DEG	TIME MIN	TEMPERATURE DEG.C	SPECIFIC HUMIDITY (G"/KGW)	RADIATION WATTS/M2 HOURLY 1/2-HR	PRESSURE MB	WIND SPEED M/S	WIND DIREC DEG	SHIP SPEED KNOTS	SHIP DIREC DEG	CONVECTIVE CODE	CLOUD COVER
254	0	8 54.1	23 17.1	26.2	18	0	0	1016.7	3.0	325	.0	280		
254	1	8 54.1	23 17.1	26.2	17	0	0	1015.9	3.9	280	.0	280		
254	2	8 54.1	23 17.1	26.2	17	0	0	1015.2	3.9	205	.0	205		
254	3	8 54.1	23 17.1	26.1	17	0	0	1014.2						
254	4	8 54.1	23 17.1	26.1	18	0	0	1013.7	3.6	284	1.0	340		
254	5	8 54.1	23 17.1	26.0	17	0	0	1013.7	5.4	302	1.0	270		
254	6	8 54.1	23 17.1	26.1	17	0	0		3.8*	290*				
254	7	8 54.1	23 17.2	26.2	16	0	0		3.9*	344	2.0	93	1	6
254	8	8 54.1	23 17.2	26.2	17	62	132	1014.9	3.1	327	7.0	93	1	6
254	9	8 54.1	23 17.7	27.4	17	286	223	1015.2	4.8	342	7.0	78	1	6
254	10	8 54.1	22 54.5	27.5	16	307	537	1015.9	3.1	300	.0	210	1	6
254	11	8 54.1	22 50.3	27.7	17	621	774	1015.9	2.5	300	.0	193	1	6
254	12	8 54.1	22 50.3	27.7	17	886	970	1015.9	2.0	303	.0	200		6
254	13	8 54.1	22 50.3	28.0	17	935	970	1015.5	2.0	300	.0	195		
254	14	8 54.1	22 50.3	28.0	17	865	900	1014.6	1.0	285	.0	200		
254	15	8 54.1	22 50.3	28.0	17	872	823	1013.7	1.4	295	.0	270		
254	16	8 54.1	22 50.3	28.0	17	628	558	1013.3	3.9	300	.0	270		
254	17	8 54.1	22 50.3	28.1	18	439		1013.1	4.9	295	.0	270		
254	18	8 54.1	22 50.3	28.1	17	266	244	1013.7	2.8	327	4.0	35		4
254	19	8 54.1	22 50.3	27.1	17	83	13	1013.9	3.4	315	.0	270		
254	20	8 54.1	22 50.3	26.9	17	0	0	1014.0	3.0	303	.0	303		
254	21	8 54.1	22 50.3	26.9	17	0	0	1014.6	2.5	298	.0	303		
254	22	8 54.1	22 50.3	26.8	17	0	0	1014.9	1.4	280	.0	310		
254	23	8 54.1	22 50.3	26.8	17	0	0	1015.2	2.0	295	.0	295		

\* INDICATES VALUES FROM SHIP LOG

§ UNCALIBRATED SEA TEMPERATURE - BELIEVED TO BE WITHIN 0.3 DEG.C

# NATIONAL OCEANIC & ATMOSPHERIC ADMINISTRATION ATLANTIC OCEANOGRAPHIC & METEOROLOGICAL LABORATORIES SEA AIR INTERACTION LABORATORY

COLUMBUS ISFLIN (GATF) HOURLY METEOROLOGICAL OBSERVATIONS  
SEPTEMBER 12, 1974

JULIAN DAY	GMT HOUR	LATITUDE DEG MIN	LONGITUDE DEG MIN	TEMPERATURE DEG.C SEA AIR	SPECIFIC HUMIDITY (G"/KGW)	RADIATION WATTS/M2 HOURLY 1/2-HR	PRESSURE MB	WIND SPEED M/S DIREC DEG	SHIP SPEED KNOTS DIREC DEG	SHIP CONVECTIVE CODE	CLOUD COVER
255	0	8 54.4	22 50.3	26.7	18	0	1014.6	3.0 325	.0 275		
255	1	8 54.4	22 50.3	26.6	18	0	1013.7	4.9 325	.0 230		
255	2	8 54.4	22 50.3	26.5	18	0	1012.7	4.9 305	.0 200		
255	3	8 54.4	22 50.3	26.4	17	0	1012.2	3.9 300	.0 195		
255	4	8 54.4	22 50.3	26.5	18	0	1011.7	5.9 310	.0 285		
255	5	8 54.4	22 50.3	26.6	18	0	1011.8	4.9 325	.0 295		
255	6	8 54.4	22 50.3	26.6	17	0	1012.1	4.9 325	.0 300		
255	7	8 54.4	22 50.3	27.4	17	0	1012.2	3.4 323	.0 313	2	8
255	8	8 54.4	22 50.3	26.7	18	111	1012.7	2.5 339	.0 304	2	2
255	9	8 54.4	22 50.3	26.8	18	111	1012.7	5.9 315	.0 285	2	7
255	10	8 54.4	22 50.3	26.8	18	181	1013.6	4.9 330	.0 240	2	7
255	11	8 54.4	22 50.3	27.4	18	314	1013.7	5.9 348	.0 288	2	7
255	12	8 54.4	22 50.3	26.8	18	132	1013.7	6.9 330	.0 270	2	10
255	13	8 54.4	22 50.3	27.4	17	27	1013.7	5.9* 345*		2	9
255	14	8 54.4	22 50.3	27.4	17	34		7.3* 150*			
255	15	8 54.4	22 50.3	24.4	17	83		7.8* 150*			
255	16	8 57.4	23 54.0	24.5	17	146		8.4* 160*			
255	17	9 0	23 0	24.4	17			5.8 190	8.0 300		
255	18	9 6.0	23 6.0	25.5	16		1011.2	5.0 192	4.0 295	1	
255	19	9 11.4	23 12.0	25.7	16	13	1011.7	5.4 210	.0 200		
255	20	9 11.4	23 12.0	26.1	15		1011.8	4.9 250	.0 125		
255	21	9 3.4	23 11.5	25.9	17	0	1012.4	4.9 250	.0 240		
255	22	9 5.5	23 10.0	25.8	18	0	1012.5	4.9 255	.0 190		
255	23	8 53.0	23 11.5	26.0	17	0	1013.4	5.1 245	8.0 175		

\* INDICATES VALUES FROM SHIP LOG  
\$ UNCALIBRATED SEA TEMPERATURE - BELIEVED TO BE WITHIN 0.3 DEG.C

Table 1. (continued).

NATIONAL OCEANOGRAPHIC & ATMOSPHERIC ADMINISTRATION  
ATLANTIC OCEANOGRAPHIC & METEOROLOGICAL LABORATORIES  
SEA AIR & TELEACTION LABORATORY

COLUMBUS ISLE IN (GATE) HOURLY METEOROLOGICAL OBSERVATIONS  
SEPTEMBER 13, 1974

JULIAN DAY HOUR	LATITUDE DEG MIN SEC	LONGITUDE MIN SEC	TEMPERATURE SEA	TEMPERATURE AIR	SPECIFIC HUMIDITY (G"/KGW)	RADIATION WATTS/M2 HOURLY 1/2-HR	PRESSURE MB	WIND SPEED M/S	WIND DIREC DEG	SHIP SPEED KNOTS	SHIP DIREC DEG	SHIP CONVECTIVE CODE	CLOUD COVER
256 0	8 47.0	23 12.2	27.3	26.1	17	0	1013.6	3.0	235	.0	160		
256 1	8 41.0	23 12.2	27.3	26.4	17	0	1013.4	4.0	215	.0	155		
256 2	8 36.5	23 12.2	27.4	26.1	16	0	1012.5	3.0	245	.0	165		
256 3	8 34.5	23 12.0	27.4	26.1	17	0	1011.5	5.4	225	.0	125		
256 4	8 28.3	23 12.0	27.4	25.8	17	0	1010.9	4.3*	214*	1.0	188		
256 5	8 25.4	23 11.8	27.4	26.0	17	0	1011.1	7.3	235	.0	215		
256 6	8 26.6	23 7.7	27.4	25.0	19	0	1011.2	1.4	214	1.0	55		
256 7	8 29.5	23 2.3	27.3	26.2	19	0	1011.4	7.3	240	.0	230		
256 8	8 29.0	23 2.3	27.3	26.4	17	41	1011.8	6.0	225	.0	242	3	0
256 9	8 28.6	23 2.6	27.3	26.4	17	62	1012.5	6.0	237	.0	225	3	0
256 10	8 28.5	23 2.3	27.3	26.6	17	90		6.0*	225*			2	0
256 11	8 27.3	23 5.7	27.2	26.7	17	140		7.3*	225*			2	10
256 12	8 40.0	23 0.9	27.2	25.0	19	188	1012.8	5.3*	240*			2	10
256 13	8 52.0	23 12.3	27.1	26.0	17	293	1012.4	6.4	235	.0	145		
256 14	8 54.1	23 13.1	27.2	25.0	17	362	1012.1	5.4	245	.0	250		
256 15	8 54.1	23 13.1	27.2	25.8	17	344	1011.5	5.4	258	.0	258		
256 16	8 54.1	23 13.1	27.2	25.7	18	272	1010.9	5.4	270	.0	280		
256 17	8 54.1	23 13.1	27.1	25.8	17	139	1010.8	6.4	270	.0	250		
256 18	8 54.1	23 13.1	27.1	25.6	17	48	1011.7	6.4	290	.0	250		
256 19	8 54.1	23 13.1	27.1	25.1	16	13	1011.7	3.9	295	.0	255		
256 20	8 54.1	23 13.1	27.1	24.1	16		1012.7	1.0	350	.0	260		
256 21	8 54.1	23 13.1	27.1	24.1	17	0	1012.7	3.0	360	.0	270		
256 22	8 54.1	23 13.1	27.1	24.4	15	0	1013.4	2.0	325	.0	145		
256 23	8 54.1	23 13.1	27.1	24.6	16	0	1014.0	1.4	340	.0	40		

\* INDICATES VALUES FROM SHIP LOG  
§ UNCALIBRATED SEA TEMPERATURE - BELIEVED TO BE WITHIN 0.3 DEG.C

Table 1. (continued).



# ATLANTIC OCEANOGRAPHIC METEOROLOGICAL LABORATORIES NATIONAL CCEANIC A ATMOSPHERIC ADMINISTRATION SEA AIR INTERACTION LABORATORY

COLUMBUS ISLEIN (CATF) HOURLY METEOROLOGICAL OBSERVATIONS  
 SEPTEMBER 14, 1974

JULIAN DAY	GVT HOUR	LATITUDE DEG	LONGITUDE DEG	MIN	TEMPERATURE SEA	TEMPERATURE AIR	SPECIFIC HUMIDITY (G"/KG)	RADIATION WATTS/M2 HOURLY 1/2-HR	PRESSURE MR	WIND SPEED M/S	WIND DIREC DEG	SHIP SPEED KNOTS	SHIP DIREC DEG	CONVECTIVE CODE	CLOUD COVER
257	0	8 54.1	23 13.1			24.8	16	0	1014.0	3.9	165	.0	35		
257	1	8 54.1	23 13.1			25.3	17	0	1013.0	4.9	180	.0	260		
257	2	8 54.1	23 13.1			24.8	17	0	1012.5	2.5	210	.0	250		
257	3	8 54.1	23 13.1			24.2		0	1012.1	8.9	185	.0	255		
257	4	8 54.1	23 13.1			24.3	17	0	1011.7	7.3	173	.0	248		
257	5	8 54.1	23 13.1			24.0	17	0	1011.4	9.5	152	1.0	90		
257	6	8 54.1	23 13.1			24.2	17	0	1011.7	7.2	153	1.0	90		
257	7	8 54.1	22 50.3			24.1	16	0	1011.7	5.3	180	1.0	95		
257	8	8 54.1	22 50.3		27.0	24.6	17	62	1012.1	5.9	175	.0	190	2	9
257	9	8 54.1	22 50.3		27.0	25.2	16	216	1013.3	6.0	193	.0	23A	2	8
257	10	8 54.1	22 50.3		27.0	25.7	17	453	1013.9	5.9	190	.0	265	2	8
257	11	8 54.1	22 50.3		27.1	25.4	17	809	1014.0	3.9	208	.0	228	2	9
257	12	8 54.1	22 50.3		27.1	26.8	17	1005	1014.0	7.4*	200*			2	10
257	13	8 54.1	22 50.3			24.0		188		7.8*	215*	1.0	235	2	10
257	14	8 54.1	22 50.3			24.7	17	460	1013.3	6.9	235	.0	266	2	9
257	15	8 54.1	22 50.3			23.4		244	1012.7	5.9	206	.0	237	2	9
257	16	8 54.1	22 50.3			23.2		139	1011.9	3.9	207	.0	225	2	9
257	17	8 54.1	22 50.3			25.1	18	265	1011.7	4.9	195	.0	220	2	9
257	18	8 54.4	22 50.3			26.1	17	279	1011.7	7.4	175	.0		2	9
257	19	8 50.7	22 50.8		27.0	25.6	18	62		4.9*	180*	.0	355		
257	20	8 49.5	22 52.3		26.0	26.2	17	0	1013.3	3.9	175	.0	200		
257	21	8 49.5	22 52.3		26.0	25.2	17	0	1013.9	7.3	138	4.0	145		
257	22	8 49.5	22 52.3		27.0	24.6	17	0	1014.6	8.4	160	.0	145		
257	23	8 49.5	22 52.3		26.0	23.6	16	0	1014.7	3.9	155	4.0	330		

\* INDICATES VALUES FROM SHIP LOG  
 \$ UNCALIBRATED SEA TEMPERATURE - RELIEVED TO BE WITHIN 0.3 DEG.C

Table 1. (continued).

# ATLANTIC OCEANOGRAPHIC & ATMOSPHERIC ADMINISTRATIONS SEA AIR TEMPERATURE LABORATORIES

COLUMBUS ISLAND (CAT) HOURLY METEOROLOGICAL OBSERVATIONS  
 SEPTEMBER 15, 1974

JULIAN DAY	GMT HOUR	LATITUDE DEG N	LONGITUDE DEG W	SEA TEMP	AIR TEMP	SPECIFIC HUMIDITY (G"/KG)	RADIATION WATTS/M2 HOURLY 1/2-HR	PRESSURE MB	WIND SPEED KTS	WIND DIRECTION DEG	SHIP SPEED KTS	SHIP DIRECTION DEG	CONVECTIVE CODE	CLOUD COVER
258	0	8 40.0	22 50.3	26.9	25.0	16	0	1014.9	1.7	200	4.0	350		
258	1	8 42.0	22 48.0	26.9	27.2	20	0	1014.6	2.1	227	4.0	350		
258	2	8 40.0	22 48.4	26.9	25.0	18	0	1013.7	2.0	175	4.0	355		
258	3	8 51.0	22 48.1	26.9	26.0	19	0	1012.8	3.1	165	4.0	190		
258	4	8 51.0	22 48.1	26.9	26.5	16	0	1012.5	4.4	165	5.0	350		
258	5	8 56.0	22 48.0	26.9	26.5	16	0	1012.5	4.4	200	4.0	270		
258	6	8 57.0	22 51.1	26.9	26.6	16	0	1012.5	4.1	168	4.0	90		
258	7	8 56.0	22 47.6	26.9	26.6	16	0	1012.5	3.8	208	4.0	275	1	8
258	8	8 57.0	22 50.8	26.9	26.6	17	41	1013.3	3.8	159	4.0	93	2	8
258	9	8 57.0	22 48.5	26.9	26.6	16		1014.0	3.8	160	4.0	94		
258	10	8 58.0	22 46.6	26.9	27.0	17	474	1014.9	2.5*	195*	4.0	270	2	6
258	11	8 57.0	22 47.7	27.0	27.2	17	816	1015.2	2.9	196			2	8
258	12	8 56.0	22 51.7	27.0	26.5	17	809	1014.4	2.5*	180*	4.0	270	1	8
258	13	8 56.0	22 48.4	27.0	26.7	17	830		3.5	254				
258	14	8 57.0	22 50.3	27.0	26.5	17	907		3.9*	240*				
258	15	8 57.0	22 48.2	27.0	26.5	17	900	1012.7	.7	313	4.0	90	1	2
258	16	8 56.0	22 47.4	27.0	27.0	17			2.5*	225*			1	3
258	17	8 57.0	22 48.7	27.0	27.0	17	453	1011.9	1.6	158	4.0	90	1	5
258	18	8 56.0	22 46.3	27.0	27.0	17	272	1013.1	1.0	310	4.0	205	1	4
258	19	8 49.0	22 45.7	27.0	26.7	17	418		2.0*	200*			2	
258	20	8 49.0	22 46.3	27.5	26.8	17		1012.7	1.4	210	.0	120		0
258	21	8 50.0	22 46.4	27.6	26.8	17	0	1013.3	1.0	216	4.0	245		
258	22	8 55.0	22 46.5	27.6	26.7	17	0	1013.9	1.3	303	4.0	355		
258	23	8 56.0	22 45.8	27.7	26.7	17	0	1014.3	1.4*	330*				

\* INDICATES VALUES FROM SHIP LOG  
 \$ UNCALIBRATED SEA TEMPERATURE - RELIEVED TO BE WITHIN 0.3 DEG.C

Table 1. (continued).

ATLANTIC OCEANIC & ATMOSPHERIC ADMINISTRATION  
SEA AIR INTERACTION LABORATORIES

COLUMBUS ISLEIN (GATE) HOURLY METEOROLOGICAL OBSERVATIONS  
SEPTEMBER 16, 1974

JULIAN DAY HOUR	G-T	LATITUDE DEG MIN SEC	LONGITUDE DEG MIN	TEMPERATURE SEA	TEMPERATURE DEG.C AIR	SPECIFIC HUMIDITY (G/KG)	RADIATION WATTS/M2 HOURLY 1/2-HR	PRESSURE MB	WIND SPEED M/S	WIND DIREC DEG	SHIP SPEED KNOTS	SHIP DIREC DEG	CONVECTIVE CODE	CLOUD COVER
259	0	6 52.7	22 44.2	27.3	26.4	17	0	1014.0	1.5	359	4.0	190		
259	1	6 48.6	22 44.6	27.2	25.8	17	0	1013.3	3.4	235	.0	175		
259	2	8 50.4	22 44.5	27.1	25.6	17	0	1012.4	4.3	246	4.0	330		
259	3	8 54.1	22 44.3	27.0	25.4	17	0	1011.4	4.1	241	4.0	350		
259	4	8 56.7	22 44.3	26.9	25.1	13	0	1010.9	4.9	275	.0	225		
259	5	8 59.1	22 41.7	26.9	26.0	16	0	1010.8	3.9	355	.0	55		
259	6	9 1.	22 37.5	26.9	25.6	17	0	1010.9	1.7	333	3.0	55		
259	7	9 1.1	22 37.2	26.8	25.3	17	0	1011.1	2.4	281	3.0	90		
259	8	9 1.7	22 33.4	26.7	24.2	17	41	1011.5	.5	270	4.0	90	1	10
259	9	6 59.3	22 32.2	26.9	24.8	17	111	1012.1	.0	282	4.0	180	1	10
259	10	8 58.3	22 35.5	26.9	25.2	17	160	1012.8	2.1	187	4.0	274	3	0
259	11	8 57.7	22 30.2	26.9	25.5	17	453	1012.7	3.5	213	4.0	90	3	0
259	12	8 57.0	22 30.6	27.0	26.7	17	600	1012.7	3.0	279	4.0	185	3	10
259	13	8 56.3	22 32.4	26.9	25.4	17	502	1012.2	7.3	231	4.0	275		10
259	14	8 54.7	22 33.1	26.7	23.2	17	153	1011.7	5.7	259	4.0	100		
259	15	8 54.2	22 28.7	26.9	23.5	17	293	1010.6	5.3	260	4.0	87		
259	16	8 52.2	22 27.4	27.1	24.4	17	404	1009.7	4.9*	225*				
259	17	8 52.2	22 30.7	27.0	24.7	17	286	1010.0	8.4	174	4.0	274	1	0
259	18	8 50.3	22 30.9	27.0	25.5	17	146	1010.6	6.2	253	4.0	94		
259	19	8 49.6	22 26.6	27.0	25.7	17		1010.6	8.4	360	4.0	180	1	10
259	20	8 49.6	22 28.3	27.0	25.6	17		1010.6	6.5	237	1.0	270		
259	21	8 48.0	22 29.3		23.9		0	1011.8	5.9	245	2.0	245		
259	22	8 48.1	22 29.3		24.3	17	0	1012.4	6.0	238	5.0	260		
259	23	8 49.0	22 35.7		25.0	17	0	1012.4	6.4	221	8.0	285		

\* INDICATES VALUES FROM SHIP LOG  
% UNCALIBRATED SEA TEMPERATURE - RELIEVED TO BE WITHIN 0.3 DEG.C

Table 1. (continued).



# NAVY NATIONAL OCEANOGRAPHIC AND METEOROLOGICAL LABORATORIES ATLANTIC OCEANOGRAPHIC AND METEOROLOGICAL LABORATORIES SEA AIR INTERACTION LABORATORY

COAST GUARD (GAT) HOURLY METEOROLOGICAL OBSERVATIONS  
SEPTEMBER 17, 1974

JULIAN DAY	GUT HOUR	LATITUDE DEG	LONGITUDE MIN	TEMPERATURE SEA	TEMPERATURE AIR	SPECIFIC HUMIDITY (G/KG)	RADIATION WATTS/M2 HOURLY 1/2-HR	PRESSURE MB	WIND SPEED KTS	WIND DIREC DEG	SHIP SPEED KTS	SHIP DIREC DEG	SHIP CONVECTIVE CODE	CLOUD COVER
260	0	8 50.0	22 48.3	25.7	17	0	0	1012.5	8.4	248	1.0	280		
260	1	8 52.0	23 1.8	25.7	17	0	0		5.4*	214*				
260	2	8 54.1	23 1.1	25.7	13	0	0	1011.4	4.3	200	2.0	255		
260	3	8 54.1	23 1.1	23.4		0	0		7.3*	235*				
260	4	8 54.1	23 1.1	23.0		0	0		4.9*	215*				
260	5	8 54.1	23 1.1	23.4		0	0		6.0*	230*				
260	6	8 54.1	23 1.1	23.6	16	0	0		4.0*	230*				
260	7	8 54.1	23 1.1	23.6		0	0		5.0*	230*				
260	8	8 54.1	23 1.1	23.0	17	41	104	1010.2	4.9	228	.0	278	1	10
260	9	8 54.1	23 1.1	23.7	16	130	237		0.8*	250*				
260	10	8 54.1	23 1.1	24.3		425	118	1011.8	7.8	210	.0	210		
260	11	8 54.1	23 1.1	24.0	10	48	202		6.9*	235*				
260	12	8 53.0	23 3.5	24.4	17	481	495	1012.1	3.0	113	1.0	00		
260	13	8 54.0	22 50.3	24.9	18	000	656		7.8*	230*				
260	14	8 54.0	22 50.3	25.3	18				7.3*	225*				
260	15	8 54.0	22 50.3	24.2	17	202	355	1010.2	2.5*	225*				
260	16	8 54.4	22 50.3	24.6	16	551	383	1010.5	4.9	250	5.1	250		
260	17	8 54.0	22 50.3	24.4	18	328			3.0	225	3.1	225	1	8
260	18	8 51.0	22 52.2						2.5*	213*				
260	19	8 41.5	22 56.7	25.3	17			1011.1	2.5*	213*				
260	20	8 32.0	23 1.0	25.4	17	0	0		3.0*	210*				
260	21	8 20.5	23 2.3	25.8	17	0	0	1012.1	3.9	225	4.1	225		
260	22	8 20.5	23 2.3	25.7	17	0	0	1012.7	6.4	220	6.7	220		
260	23	8 20.5	23 2.3	25.7	18	0	0	1013.1	6.4	200	6.7	200		

\* INDICATES VALUES FROM SHIP LOG  
\$ UNCALIBRATED SEA TEMPERATURE - REFERENCE TO BE WITHIN 0.3 DEG.C

Table 1. (continued).

ATLANTIC OCEANIC ATMOSPHERIC AERONAUTICAL LABORATORIES  
SEA AIR INTERACTION LABORATORY

COLUMBUS TIFLIN (GATF) HOURLY METEOROLOGICAL OBSERVATIONS  
SEPTEMBER 18, 1974

JULIAN DAY	GAT HOUR	LATITUDE DEG	LONGITUDE MIN	TEMPERATURE SEA	TEMPERATURE AIR	SPECIFIC HUMIDITY (G/KG)	RADIATION WATTS/M2 HOURLY 1/2-HR	PRESSURE MB	WIND SPEED KNOTS	WIND DIRECTION DEG	SHIP SPEED KNOTS	SHIP DIRECTION DEG	CONVECTIVE CODE	CLOUD COVER
261	0	9 29.5	23 2.3		26.1	18	0	1013.0	6.9	165	.0	205		
261	1	9 29.5	23 2.3		26.0	17	0	1012.8	7.3	190	.0	205		
261	2	9 29.5	23 2.3		26.0	17	0	1012.1	6.3	205	.0	305		
261	3	9 29.5	23 2.3		25.8	17	0	1011.8	6.0	200	.0	250		
261	4	9 29.5	23 2.3		25.8	17	0	1011.5	5.9	195	.0	275		
261	5	9 29.5	23 2.3		25.9	18	0	1011.5	6.4	195	.0	205		
261	6	9 29.5	23 2.3		26.0	17	0	1011.7	5.9	205	.0	265		
261	7	9 29.5	23 2.3		25.9	18	0	1011.8	5.4	195	.0	275		
261	8	9 29.5	23 2.3		26.2	17	118	1012.1	5.9	210	.0	300	2	6
261	9	9 29.5	23 2.3		26.8	17	363	1012.8	5.8	200	1.0	285		
261	10	9 29.5	23 2.3		26.5	17	411	1013.4	6.4	165	.0	20	1	6
261	11	8 29.5	23 2.3		26.7	18	593	1013.7	5.9	185	.0	215		
261	12	8 29.5	23 2.3		27.4	18	725	1013.9	4.3	193	12.0	360	1	7
261	13	8 40.8	23 1.9		27.4	18	865	1013.6	3.5	182	12.0	355		
261	14	8 1.7	23 2.5		27.6	18	928	1011.9	4.9	178*	12.0	355		3
261	15	9 13.5	23 2.9		27.6	18	928	1011.9	5.2	199	12.0	90	1	
261	16	9 24.1	22 5.0		27.6	17	272	1011.7	4.2	214	12.0	90		
261	17	9 24.2	22 4.1		27.1	18	565	1011.9	3.9*	190*				
261	18	9 24.4	22 3.4		27.2	18	111	1011.9	4.2	196	12.0	93	2	8
261	19	9 24.5	22 10.4		25.0	17	83	1012.1	5.4	169	11.0	90		
261	20	9 24.7	22 6.9		26.8	18	34	1012.7	4.4	181	11.0	90		
261	21	9 24.3	21 56.0		26.5	17	0	1013.3	3.0	193	11.0	90		
261	22	9 24.3	21 44.3		25.3	17	0	1014.0	2.8	171	11.0	90		
261	23	9 24.9	21 32.3		25.8	18	0	1014.6	1.5	169	11.0	90		

\* INDICATES VALUES FROM SHIP LOG

§ UNCALIBRATED SEA TEMPERATURE - RELIEVED TO BE WITHIN 0.3 DEGREE

Table 1. (continued).

# ATLANTIC OCEANOGRAPHIC & METEOROLOGICAL LABORATORIES NAUTICAL, OCEANOGRAPHIC & METEOROLOGICAL ADMINISTRATIONS SEA AIR TEMPERATURE OBSERVATIONS

COLUMBUS ISLAND (GATE) HOURLY METEOROLOGICAL OBSERVATIONS  
 SEPTEMBER 19, 1974

JULIAN DAY	GAT HOUR	LATITUDE DEG	LONGITUDE MIN	TEMPERATURE SEA	TEMPERATURE AIR	SPECIFIC HUMIDITY (G/KG)	RADIATION WATTS/M2	PRESSURE MB	WIND SPEED M/S	WIND DIRECTION DEG	SHIP SPEED KNOTS	SHIP DIRECTION DEG	CONVECTIVE CODE	CLOUD COVER
262	0	9 25.0	21 20.6	26.1	26.1	17	0	1013.9	2.4	166	12.0	90		
262	1	9 25.0	21 20.6	26.4	26.4	1A	0	1013.0	4.5	202	12.0	90		
262	2	9 26.0	20 56.8	26.0	26.0	1A	0	1012.2	4.9	205	12.0	85		
262	3	9 27.0	20 45.0	25.1	25.1	1A	0	1012.4	4.2	228	12.0	90		
262	4	9 27.0	20 33.0	25.0	25.0	1A	0	1012.1	5.5	193	12.0	90		
262	5	9 28.0	20 21.2	25.0	25.0	1A	0	1013.3	1.4	190	0	90		
262	6	9 28.0	20 0.3	24.5	24.5		0	1013.6	3.0	245	0	125		
262	7	9 30.1	20 0.6	24.2	24.2		0	1014.0	0*	0*			2	9
262	8	9 30.0	20 0.0	26.7	26.7	17	34	1014.3	0*	0*				
262	9	9 30.0	20 0.0	26.9	26.9	17	202	1014.7	1.0	169	0	94		
262	10	9 30.0	20 0.0	26.8	26.8	17	348	1015.0	1.0	195	4.0	15	2	9
262	11	9 30.0	20 0.0	26.5	26.5	17	360	1014.6	1.5	247	4.0	160	1	9
262	12	9 34.5	19 50.0	26.0	26.0	17	360	1013.6	0*	0*				
262	13	9 36.0	19 57.7	26.0	26.0	17	353	1013.1	3.4	260	4.0	50	1	9
262	14	9 38.0	19 54.2	26.0	26.0	17	390	1013.0	2.0	267	0	87	2	10
262	15	9 41.0	19 50.4	26.0	26.0	17	188	1012.8	3.4	293	0	143	3	9
262	16	9 41.0	19 50.9	26.0	26.0	14	160	1012.5	3.0	265	0	130	3	9
262	17	9 42.0	19 51.8	27.1	25.3	1A	76	1012.8	2.0	230	0	150		
262	18	9 42.0	19 51.3	27.1	25.3	1A	13	1012.8	5.9	215	0	105		
262	19	9 43.0	19 50.8	27.0	24.7		0	1014.0	3.0	215	0	105		
262	20	9 43.0	19 51.9	27.0	24.7		0	1014.4	2.5	265	0	115		
262	21	9 44.0	19 51.1	27.0	25.2	1A	0	1014.6	3.4	220	0	105		
262	22	9 44.0	19 50.6	27.1	25.1	1A	0							
262	23	9 44.0	19 50.6	27.1	25.1	1A	0							

\* INDICATES VALUES FROM SHIP LOG  
 † UNCALIBRATED SEA TEMPERATURE - DIFFERENCE WITHIN 0.3 DEG.C

Table 1. (continued).



ATLANTIC OCEANOGRAPHIC & METEOROLOGICAL LABORATORIES  
SEA AIR INTERACTION LABORATORY

COLUMBUS ISLAND (GATE) HOURLY METEOROLOGICAL OBSERVATIONS  
SEPTEMBER 20, 1974

JULIAN DAY	GMT HOUR	LATITUDE DEG MIN SEC	LONGITUDE DEG MIN SEC	TEMPERATURE DEG C	SPECIFIC HUMIDITY (G"/KGW)	RADIATION WATTS/M2 HOURLY 1/2-HR	PRESSURE MB	WIND SPEED M/S	WIND DIREC DEG	SHIP SPEED KNOTS	SHIP DIREC DEG	SHIP CONVECTIVE CODE	CLOUD COVER
263	0	9 44.5	19 50.6	27.1	17	0	1014.0	3.9*	218*	.0	95		
263	1	9 55.0	19 44.5	25.1	17	0		3.9*	218*				
263	2	10 4.0	19 40.0	25.1	17	0		3.9*	207*				
263	3	10 13.0	19 35.0	25.2	17	0		3.9*	218*				
263	4	10 23.0	19 29.5	25.6	19	0		3.9*	218*				
263	5	10 34.5	19 24.0	25.4	18	0	1011.1	.0*	0*	12.0	25		
263	6	10 45.0	19 18.0	25.6	18	0	1012.1	.0*	0*	12.0	25		
263	7	10 56.5	19 13.0	25.7	17	69	1012.4	.0*	0*	12.0	25		
263	8	11 7.0	19 7.5	26.3	19	132		.0*	0*	12.0	25		
263	9	11 18.0	19 2.5	26.2	18	376		.0*	0*	12.0	25		
263	10	11 29.0	18 57.0	26.6	18	593		.0*	0*	12.0	25		
263	11	11 30.0	18 50.0	26.8	18	774		.0*	0*	12.0	25		
263	12	11 40.0	18 47.0	27.0	18	844		2.0*	5*	12.0	25		
263	13	12 2.5	18 41.0	26.2	18	821		3.0*	15*	12.0	25		
263	14	12 15.0	18 35.5	26.3	18	551		3.9*	25*	12.0	25		
263	15	12 27.0	18 29.0	26.4	17	411		1.4*	50*	12.0	25		
263	16	12 39.5	18 23.5	26.7	16	383		1.0*	20*	12.0	25		
263	17	12 52.0	18 18.0	27.2	16	300		.0*	0*	12.0	25		
263	18	13 4.0	18 12.0	26.0	17	125		.0*	0*	12.0	25		
263	19	13 16.0	18 6.5	27.1	17	27		.0*	0*	12.0	25		
263	20	13 30.0	18 .0	27.2	17			.0*	0*	12.0	25		
263	21	13 42.0	17 54.0	27.0	18	0		.0*	0*	12.0	25		

\* INDICATES VALUES FROM SHIP LOG  
% UNCALIBRATED SEA TEMPERATURE - RELIEVED TO BE WITHIN 0.3 DEG.C

Table 1. (continued).

at 7.3 m height, the surface pressure given in Table 1 is the measured value plus a correction factor of 0.82 mb.

The hourly wind speed and direction values from the ship's log are absolute values. They are indicated in Table 1 with an asterisk. When ship's log values are used, ship speed and direction were not tabulated because they were unnecessary. Wind speed and direction relative to the ship were sampled and recorded every minute on the data acquisition system when it was operational. To obtain hourly values, ten-minute averages during a stable period around the indicated hour were made for both wind speed and direction relative to the ship. Then, the wind speed and direction were reduced to absolute values using the ship speed and direction. In Table 1, the wind speed values have been reduced to 10 m using (5.2.13). The convective code and cloud cover values in Table 1 were estimated from the cloud photographs.

The radiation, air temperature, and wind speed are displayed graphically in Figure 17. These data appear consistent in that low radiation values generally correspond to low air temperatures for moderate winds. Also, high air temperature generally corresponds to low winds for typical undisturbed radiation conditions.

# COLUMBUS ISELIN (GATE) METEOROLOGICAL OBSERVATIONS

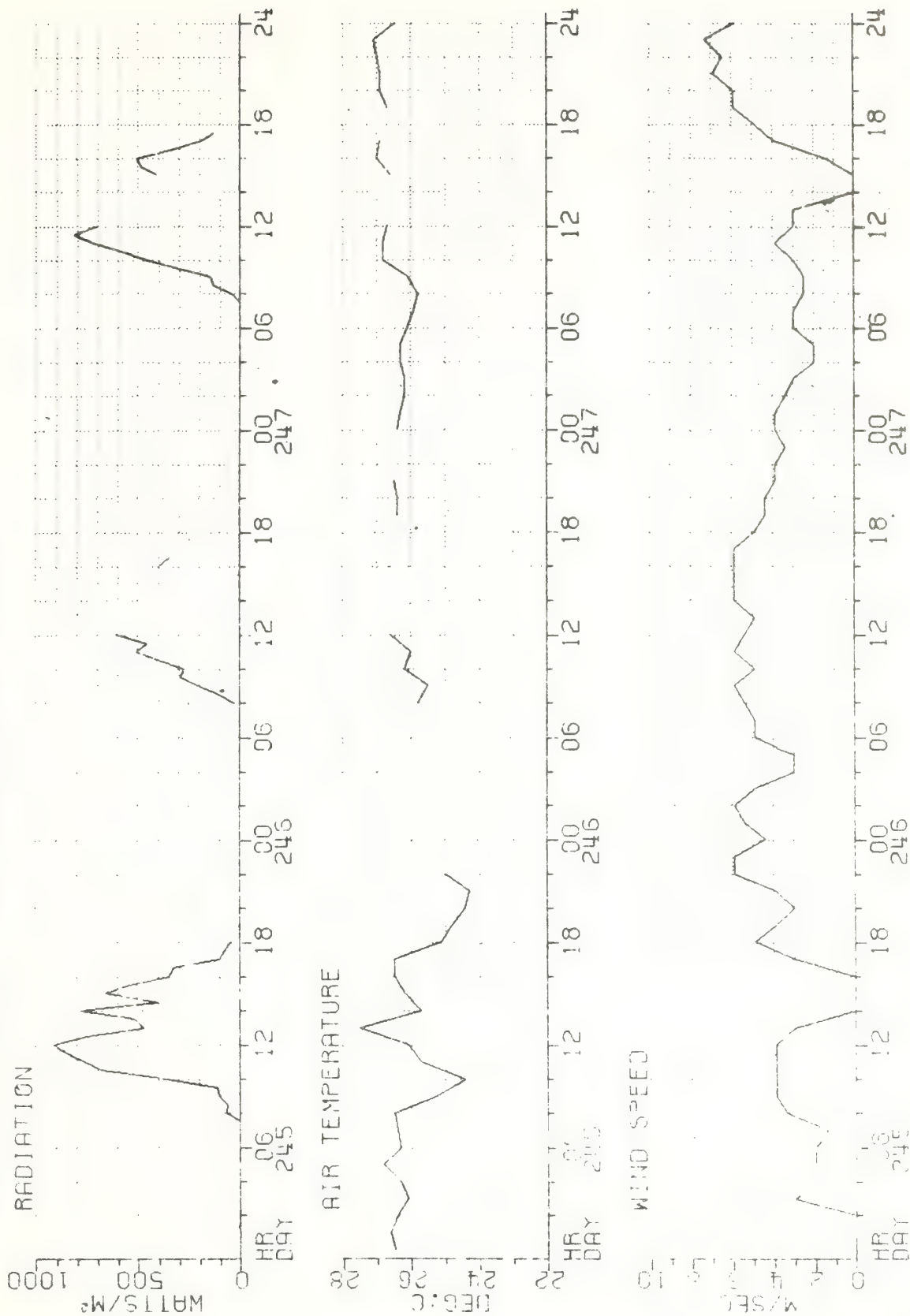


Figure 17. Radiation, air temperature, and wind speed.



[illegible]

1096

# COJUMBIA IN (GATE) METEOROLOGICAL OBSERVATIONS

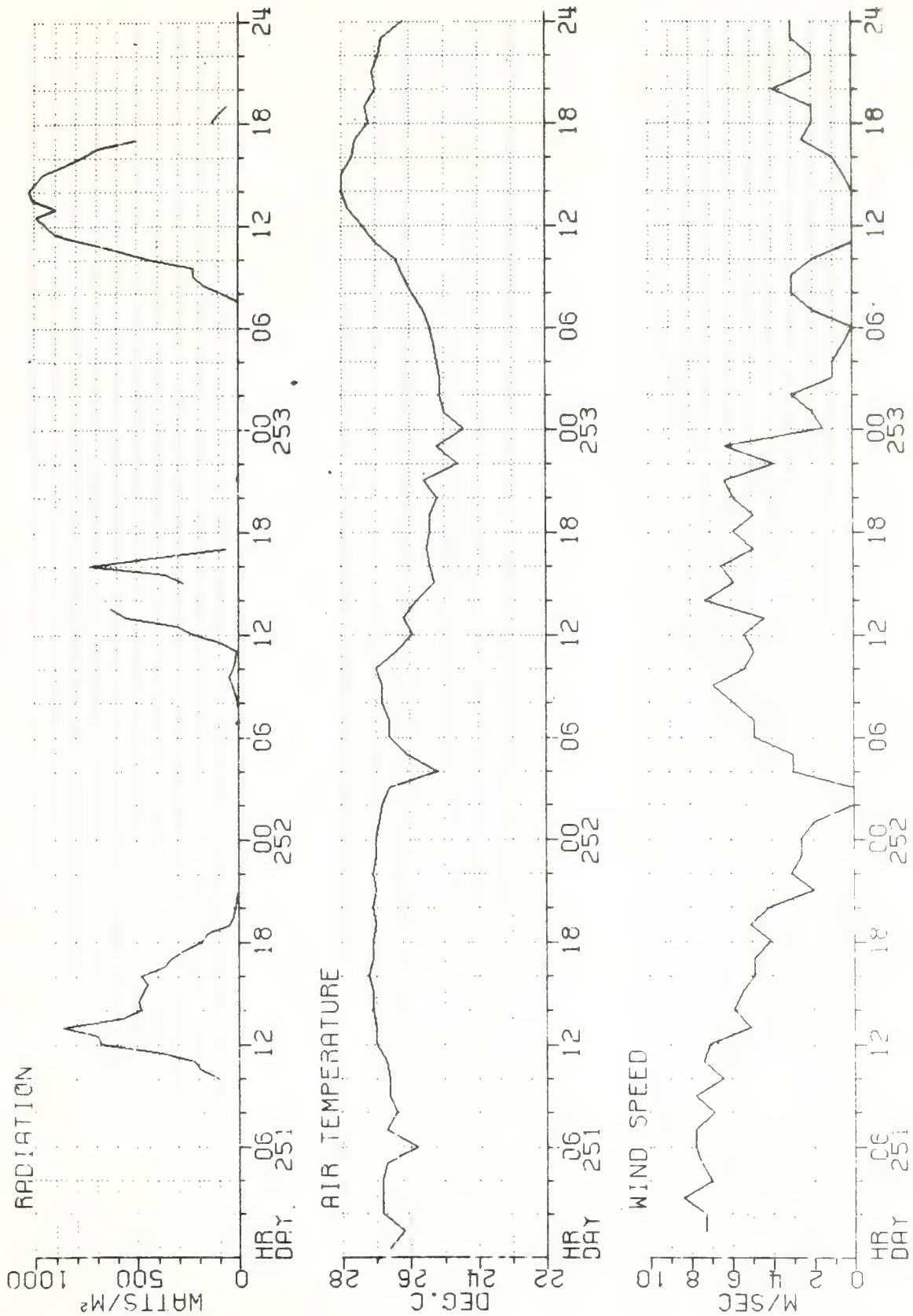


Figure 17. (continued).

# COLUMBUS ISLEIN (GATE) METEOROLOGICAL OBSERVATIONS

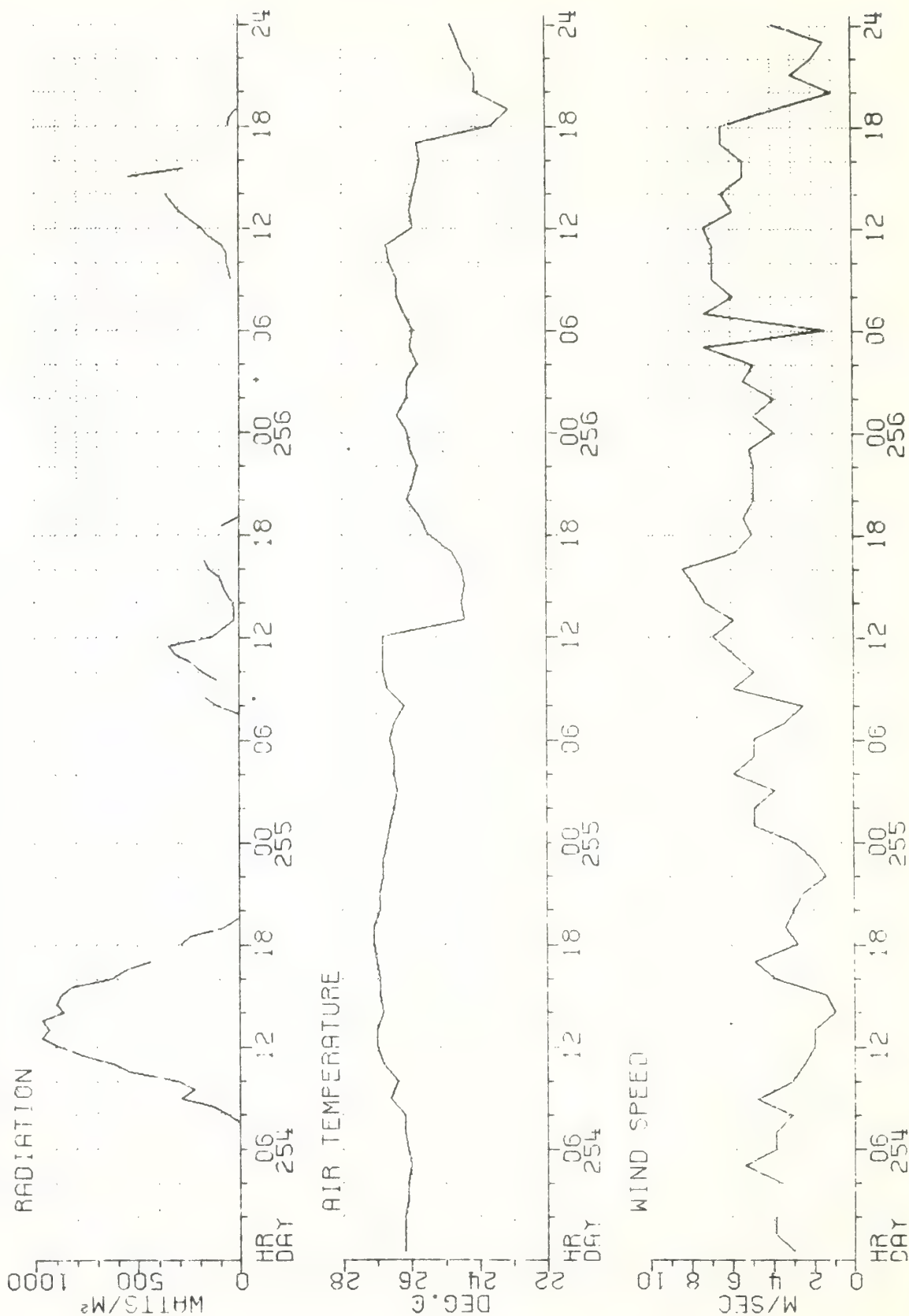


Figure 17. (continued).



[illegible]

1099

# COMPARISON OF ISFLIN (GATE) METEOROLOGICAL OBSERVATIONS

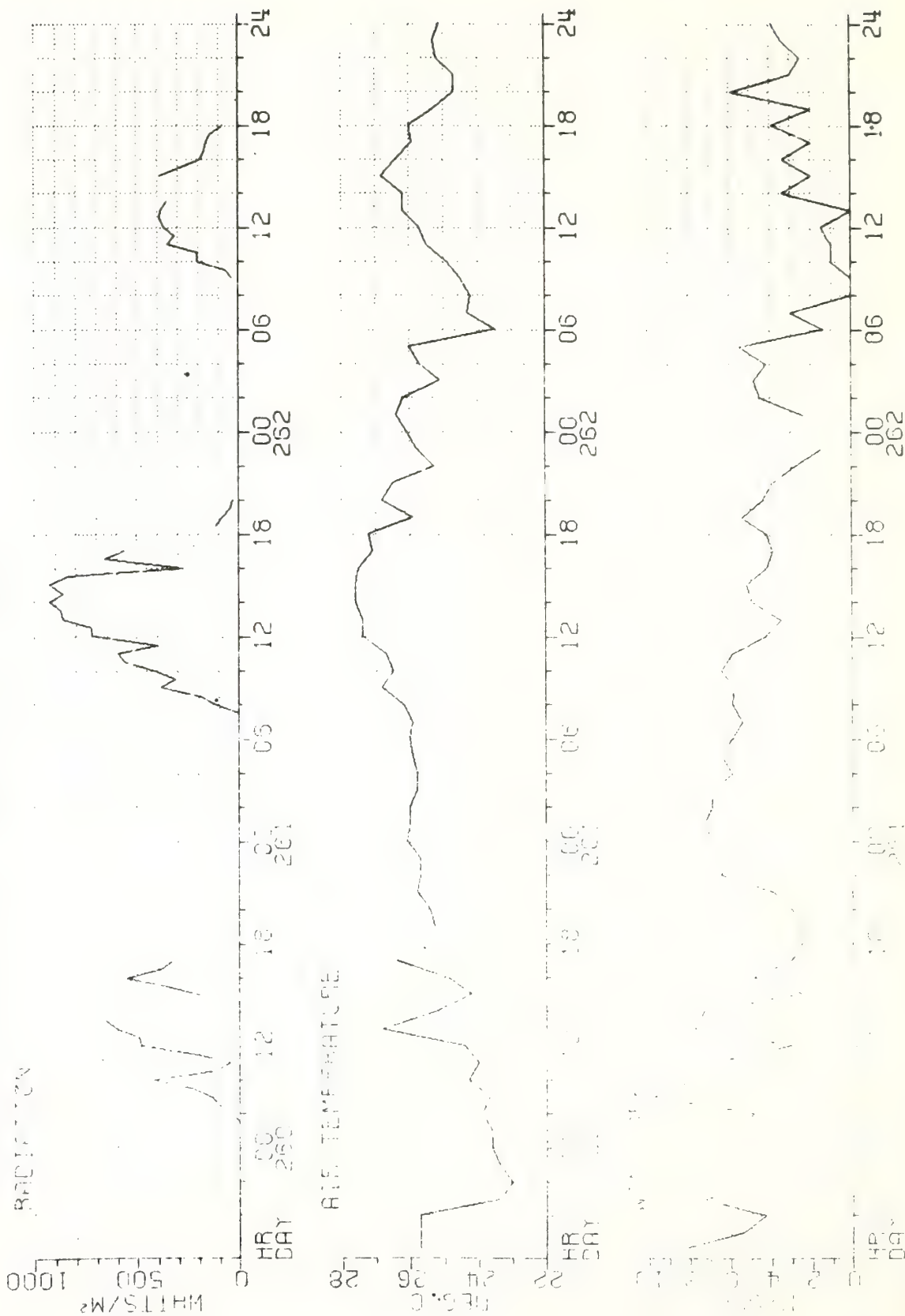


Figure 17. (continued).

COLUMBUS ISELIN (GATE)

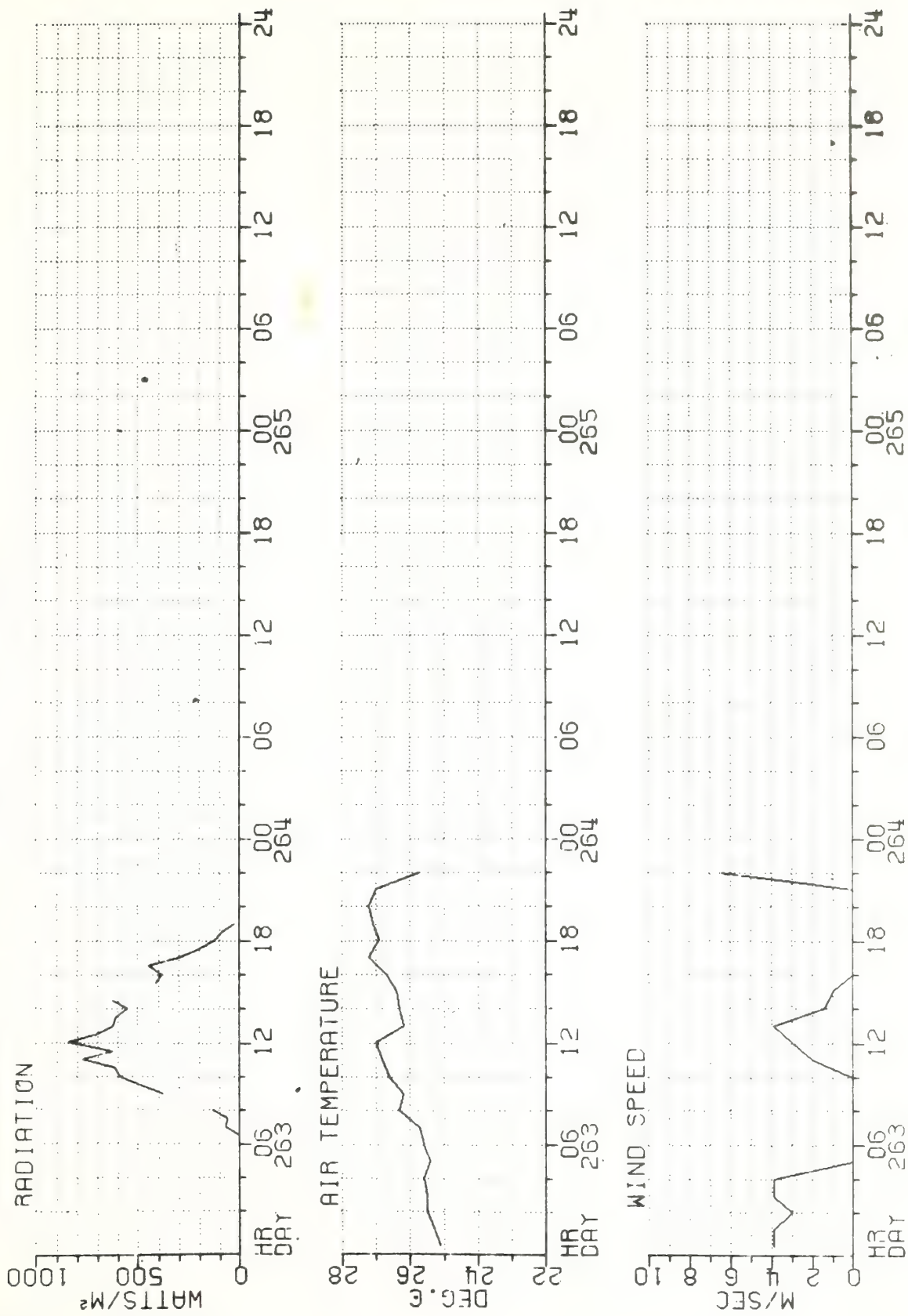


Figure 17. (continued).



## 5. CALCULATION OF MOMENTUM AND HEAT FLUXES

The bulk aerodynamic parameterization equations which include the effects of atmospheric stability have been used to calculate the latent and sensible heat fluxes and the momentum flux. The data used for the calculations are described and presented in Section 4. Since the data were collected at heights different from the standard ten-meter level, they were all reduced to that level except for the atmospheric pressure. The three basic steps in the calculation procedure for determining the heat and momentum fluxes were (1) to calculate a virtual gradient Richardson number,  $Ri_v$ , (2) to calculate the ten-meter values of wind, air temperature, and mixing ratio, and (3) to calculate the fluxes using the ten-meter values.

In Section 5.1, the bulk aerodynamic calculation procedure for the case of near-neutral stability is described. The effects of stability are included in Section 5.2. The calculation of longwave back radiation from the sea surface is given in Section 5.3.

### 5.1 Near-Neutral Stratification

For the case of near-neutral stratification, i.e., for virtual Richardson number  $<|0.01|$ , the bulk aerodynamic

parameterization equations are given by:

$$\tau = c_1 \rho_a C_0^D U^2 \quad (5.1.1)$$

$$Q_S = c_2 \rho_a C_0^S U (T_S - T) \quad (5.1.2)$$

$$Q_L = c_2 \rho_a C_0^L U (q_s - q) \quad (5.1.3)$$

where  $c_1$  and  $c_2$  are constants which adjust the units of  $\tau$ ,  $Q_S$ , and  $Q_L$ . The air density is  $\rho_a$ , and  $C_0^{D,S,L}$  are the transfer coefficients for momentum flux ( $\tau$ ), sensible heat flux ( $Q_S$ ), and latent heat flux ( $Q_L$ ), respectively. The quantities without subscript refer to ten-meter values, where  $U$  is the wind speed,  $T$  is the air temperature,  $q$  is the mixing ratio, and  $T_S$  and  $q_s$  are sea surface temperature and saturation mixing ratio. The sensible and latent heat fluxes are positive for transfer from the ocean to the atmosphere.

The mixing ratio  $q$  in units of g/g is calculated using the relation

$$q = \epsilon \frac{e}{p} \quad (5.1.4)$$

where  $\epsilon=0.622$ ,  $p$  is the observed atmospheric pressure at the sea surface, and  $e$  is the water vapor pressure. The water vapor pressure is the product of the observed relative humidity,  $r$ , and the saturation vapor pressure,  $e_s$ , i.e.,

$$e=re_s. \quad (5.1.5)$$

In the present calculations for the saturation water vapor pressure,  $e_s$ , the Goff-Gratch formula (List, 1958) was used:

$$\begin{aligned} \log e_s = & -7.90298 \left( \frac{T_{sa}}{T} - 1 \right) + 5.02808 \log \left( \frac{T_{sa}}{T} \right) \\ & - 1.3816 \cdot 10^{-7} \left[ 10^{11.344 \left( 1 - \frac{T}{T_{sa}} \right) - 1} \right] \\ & - 8.1328 \cdot 10^{-3} \left[ 10^{-3.49149 \left( \frac{T_{sa}}{T} - 1 \right) - 1} \right] + \log e_{ws} \end{aligned} \quad (5.1.6)$$

where  $T_{sa}=373.16^0\text{K}$ ,  $e_{ws}=1013.246$  mb, and  $T$  is given in degrees Kelvin.

It is assumed that the temperature and the potential temperature of the air are identical because the depth range involved in the calculations is only 10 meters. The virtual temperature,  $T_v$ , is calculated using the expression (Brocks and



Krugermeyer, 1972):

$$T_v = (1 + 0.604q)T \quad . \quad (5.1.7)$$

If  $T_v$  is in the range of  $29^{\circ}\text{C}$ , the air density,  $\rho_a$ , can be taken to be  $1.15 \times 10^{-3} \text{ g/cm}^3$ . The values of the transfer coefficients were determined by Hoeber (1969) and have the following values:

$$C_0^D = 1.25 \cdot 10^{-3} \quad (5.1.8)$$

$$C_0^S = 27.12 \text{ cal sec g}^{-1} \text{ K}^{-1} \text{ day}^{-1} \quad (5.1.9)$$

$$C_0^L = 7.94 \cdot 10^4 \text{ cal sec g}^{-1} \text{ day}^{-1} \quad (5.1.10)$$

Using a value of specific heat at constant pressure of  $0.24 \text{ cal g}^{-1} \text{ K}^{-1}$ ,  $C_0^S$  in (5.1.9) corresponds to a nondimensional sensible heat transfer coefficient of  $1.31 \times 10^{-3}$ . Using a value of latent heat of evaporation of  $580 \text{ cal g}^{-1}$ ,  $C_0^L$  in (5.1.10) corresponds to a nondimensional latent heat transfer coefficient of  $1.58 \times 10^{-3}$ .

With

$$c_1 = 0.10 \text{ nt m}^{-2} / \text{dyne cm}^{-2} \quad (5.1.11)$$

$$c_2 = 0.4843 \text{ watt m}^{-2} / \text{cal cm}^{-2} \text{day}^{-1} , \quad (5.1.12)$$

the values of the transfer coefficients given by (5.1.8) to (5.1.10) and the remaining parameters in (5.1.1) to (5.1.3) given in cgs units, the wind stress is given in units of  $\text{nt m}^{-2}$  and the heat fluxes in units of  $\text{watt m}^{-2}$ .

Although the numerical values for the transfer coefficients for neutrally stable conditions vary somewhat in the literature, the above values are considered to be most applicable to the present study. The measurements by Høefer (1969) were made on the equator at  $30^{\circ}\text{W}$  longitude from a semi-stable meteorological buoy carrying a mast of 10-meters height.

## 5.2 Non-Neutral Stability Conditions

The virtual gradient Richardson number ( $Ri_v$ ) is a measure of stability and defined by

$$Ri_v = \frac{g \frac{\partial T_v}{\partial z}}{T_v \left( \frac{\partial U}{\partial z} \right)^2} . \quad (5.2.1)$$

The following finite difference form was used to calculate  $Ri_v$ , taking into account the different heights at which the sensors were located:

$$Ri_v = g \frac{(T_v - T_{0v})}{T_v U^2} \frac{z_w^2}{z_T} , \quad (5.2.2)$$

where  $g$  is the gravitational acceleration,  $T_{0v}$  is the virtual sea surface temperature,  $T_v$  is the virtual air temperature,  $z_w$  is the height at which the wind was observed, and  $z_T$  the height at which the air temperature was measured. In this form of the equation, the wind speed at the sea surface is assumed to be zero, the air temperature at the sea surface is assumed to be the sea surface temperature, and the sea surface is at  $z=0$ . The virtual temperatures are computed from the observations using (5.1.7). The vapor pressure at the sea surface is assumed to be the saturation vapor pressure.



In order to derive corrections for the wind stress,  $\tau$ , in non-neutral cases, similarity considerations are invoked which suggest that

$$\frac{kz}{u_*} \frac{\partial U}{\partial z} = \phi_M \left( \frac{z}{L} \right) , \quad (5.2.3)$$

where  $k$  is von Karman's constant ( $\sim 0.38$ ) and  $L$  is the Monin-Obukhov length. For the case of neutral stratification,  $\phi_M(z/L)=1$ , and integration reduces (5.2.3) to the familiar logarithmic law. Following Monin and Obukhov,  $\phi_M(z/L)$  can be expanded in a power series as follows,

$$\phi_M \left( \frac{z}{L} \right) = 1 + \alpha_1 \frac{z}{L} + \dots . \quad (5.2.4)$$

Substitution of (5.2.4) into (5.2.3) yields, upon integration over a constant shear layer,

$$\frac{U}{u_*} = \frac{1}{k} \left( \ln \frac{z}{z_0} + \alpha_1 \frac{z - z_0}{L} + \dots \right) , \quad (5.2.5)$$

where  $z_0$  represents the roughness length. In the following,  $z_0$  will be neglected compared to  $z$  wherever it appears as an additive parameter. Assuming  $z/L \ll 1$ , then the drag coefficient  $C^D$ , is

$$C^D = \left( \frac{u_*}{U} \right)^2 = \frac{k^2}{\left( \ln \frac{z}{z_0} + \alpha_1 \frac{z}{L} \right)^2} .$$

Since  $C_0^D$ , the drag coefficient for the neutral case at a height of 10 m, is equal to

$$C_0^D \equiv \left( \frac{k}{\ln \frac{z}{z_0}} \right)^2 , \quad (5.2.7)$$

$C^D$  can be approximated by the relation

$$C^D \approx C_0^D \left[ 1 - 2\alpha_1 \frac{z}{L \cdot \ln \left( \frac{z}{z_0} \right)} \right] . \quad (5.2.8)$$

In order to evaluate  $z/L$ , it is assumed that

$$\frac{z}{L} \sim Ri_v .$$

Defining

$$\psi_M = 1 - \phi_M \left( \frac{z}{L} \right) \quad (5.2.9)$$

and substituting this relation into (5.2.4) obtains

$$\psi_M\left(\frac{z}{L}\right) = \alpha_1 \frac{z}{L} \quad . \quad (5.2.10)$$

From (5.2.8), the drag coefficient,  $C^D$ , for non-neutral stability is

$$C^D = C_0^D \left( 1 + \frac{2\psi_M}{\ln\left(\frac{z}{z_0}\right)} \right) \quad , \quad (5.2.11)$$

where  $z_0$  can be determined from (5.2.7). For  $z=10\text{m}$  and  $C_0^D = 1.25 \cdot 10^{-3}$ , the roughness length assumes the value of

$$z_0 = 0.0215 \text{ cm}.$$

In order to calculate the wind speed at a standard height of 10 meters from an observation at the height  $z_w$  (near the ten-meter level), it is assumed that  $\psi_M(z_w) = \psi_M(z=10\text{m}) = \psi_M$ . Combining (5.2.5) and (5.2.10) yields



$$U = \frac{u_*}{k} \ln \left( \frac{z}{z_0} - \psi_M \right) \quad . \quad (5.2.12)$$

Substituting the wind speed at 10 m and at the measured level into the above equation separately and dividing one resulting equation by the other yields a relation for reducing the measured wind speed to the 10-m wind. Thus, the 10-m wind speed can be calculated using the relation

$$U(10m) = U(z_w) \left( \frac{\ln 10^3 - \ln z_0 - \psi_M}{\ln z_w - \ln z_0 - \psi_M} \right) \quad . \quad (5.2.13)$$

The formula for the wind stress becomes

$$\tau = (0.1)(1.15 \cdot 10^{-3})(1.25 \cdot 10^{-3}) \left( 1 + \frac{2\psi_M}{\ln 10^3 - \ln z_0} \right) U^2(10m) \quad . \quad (5.2.14)$$

The correction factor,  $\psi_M$ , is evaluated by means of (5.2.9) and the following empirical relations for  $\phi_M$ :

$$\phi_M\left(\frac{z}{L}\right) = \begin{cases} (1-18 Ri_V)^{-1/4} & \text{for } Ri_V < 0 \\ 1 & \text{for } Ri_V = 0 \\ (1-4.5 Ri_V)^{-1} & \text{for } Ri_V > 0 \end{cases} \quad (5.2.15)$$

(see Brocks and Krugermeyer, 1972).

The sensible and latent heat flux corrections for non-neutral stratification are analogous to the momentum flux corrections. The analogue to (5.2.3) is

$$\frac{k}{F_\star^i} \frac{\partial F^i}{\partial z} = \phi^i\left(\frac{z}{L}\right), \quad (5.2.16)$$

where  $F_\star^i$  is defined as

$$F_\star^i = \begin{cases} -\frac{Q_s}{\rho_a c_p u_\star} & \text{for } i=s \\ -\frac{Q_L}{\rho_a u_\star} & \text{for } i=L \end{cases},$$

with  $Q_s$  the sensible heat flux,  $Q_L$  the latent heat flux, and  $F_\star^i = (T_\star, q_\star)$ . The parameter  $T_\star$  is the temperature analog of

the friction velocity, and  $q_*$  is the specific humidity analog. Expanding  $\phi^i\left(\frac{z}{L}\right)$  in a power series yields

$$\phi^i\left(\frac{z}{L}\right) = 1 + \beta_1^i\left(\frac{z}{L}\right) + \dots$$

which is analogous to (5.2.4). Integration over a constant flux ( $F^i$ ) layer gives

$$\frac{F^i - F_0^i}{F_*^i} = \frac{1}{k} \left( \ln \frac{z}{z_0^i} + \beta_1^i \frac{z}{L} \right), \quad i=S, L, \quad (5.2.17)$$

where the  $z_0^i$  are roughness lengths for sensible ( $i=s$ ) and latent ( $i=L$ ) heat flux, respectively. Then

$$C_1^i = \left( \frac{u_*}{U} \right) \frac{F_*^i}{F^i - F_0^i} = \frac{k^2}{\left( \ln \frac{z}{z_0^i} + \beta_1^i \frac{z}{L} \right) \left( \ln \frac{z}{z_0^i} + \alpha_1^i \frac{z}{L} \right)}. \quad (5.2.18)$$

To the first order in  $z/L$ , this becomes



$$C_1^i = \frac{k^2}{\ln \frac{z}{z_0} \ln \frac{z}{z_0} \left[ 1 + \left( \frac{\beta_1^i \frac{z}{L}}{\ln \frac{z}{z_0}} \right) + \left( \frac{\alpha_1 \frac{z}{L}}{\ln \frac{z}{z_0}} \right) \right]} \quad (5.2.19)$$

Defining

$$C_0^i \equiv \frac{k^2}{\ln \frac{z}{z_0} \ln \frac{z}{z_0}} \quad (5.2.20)$$

and

$$\psi^i \left( \frac{z}{L} \right) = 1 - \phi^i \left( \frac{z}{L} \right)$$

then, to the first order

$$\psi^i \left( \frac{z}{L} \right) = -\beta_1^i \frac{z}{L} \quad (5.2.21)$$

Substituting (5.2.10), (5.2.20), and (5.2.21) into (5.2.19) yields the transfer coefficient for non-neutral stratification,

$$C_1^i = C_0^i \left( 1 + \frac{\psi^i}{\ln \frac{z}{z_0^i}} + \frac{\psi_M}{\ln \frac{z}{z_0}} \right) \quad \text{for } i=S, L. \quad (5.2.22)$$

For consistency of units,

$$C_1^i = \begin{cases} 8.64 \cdot 10^4 c_p C_1^i & \text{for } i=S \\ 8.64 \cdot 10^4 L_h C_1^i & \text{for } i=L \end{cases} \quad (5.2.23)$$

where  $c_p$  is the specific heat at constant pressure, and  $L_h$  is the latent heat of evaporation. For the values of  $C_0^i$  given in (5.1.9) and (5.1.10), the corresponding roughness lengths are

$$z_0^i = \begin{cases} 0.0351 \text{ cm.} & \text{for } i=S \\ 0.203 \text{ cm.} & \text{for } i=L \end{cases} \quad (5.2.24)$$

For reducing  $T$  and  $q$  to 10 m values, the relation

$$F^i - F_0^i = \frac{F_\star^i}{k} \left( \ln \frac{z_i}{z_0} - \psi^i \right) \quad \text{for } i=S, L$$

is used. Assuming  $\psi^i(z_i) = \psi^i(z=10\text{m}) = \psi^i$ ,

$$F^i(z=10\text{m}) - F_0^i = (F^i(z_i) - F_0^i) \left( \frac{\ln 10^3 - \ln z_0^i - \psi^i}{\ln z_i - \ln z_0^i - \psi^i} \right) \quad \text{for } i=S, L. \quad (5.2.25)$$

Then, the sensible and latent heat fluxes can be calculated using the relation

$$Q_i = (0.4843)(1.15 \cdot 10^{-3}) \left[ 1 + \frac{\psi^i}{\ln\left(\frac{10^3}{z_0^i}\right)} + \frac{\psi_M}{\ln\left(\frac{10^3}{z_0}\right)} \right] U(10\text{m})$$

$$\cdot \begin{cases} 27.12 (T_S - T(10\text{m})) & \text{for } i=S \\ 7.94 \cdot 10^4 (q_S - q(10\text{m})) & \text{for } i=L. \end{cases} \quad (5.2.26)$$

For the limiting case of zero wind speed, the bulk aerodynamic equations yield zero fluxes. For wind speeds of approximately  $50 \text{ cm sec}^{-1}$  and less, turbulent convection becomes significant. For such wind speeds, the following



correction equations were used:

$$Q_S = c_3 \rho_a c_p M (T_S - T) \quad (5.2.27)$$

$$Q_L = c_3 \rho_a L_h M (q_S - q) \quad . \quad (5.2.28)$$

The parameter  $M$  is a function of the virtual sea-air temperature difference. Values used for  $M$  were taken from a graph by Webb (1975). The values of  $M$  used range from  $0.110 \text{ cm sec}^{-1}$  for a  $1^\circ\text{C}$  virtual sea-air temperature difference to  $0.260 \text{ cm sec}^{-1}$  for an  $8^\circ\text{C}$  virtual sea-air temperature difference. The parameter  $M$  has an approximately logarithmic dependence on the virtual sea-air temperature difference in this range. For virtual temperature differences less than  $1^\circ\text{C}$ ,  $Q_S$  and  $Q_L$  are set equal to zero. With the parameters on the right hand side of (5.2.27) and (5.2.28) in cgs units,  $c_3 = 4.184 \times 10^4 \text{ watts m}^{-2} / \text{cal cm}^{-2} \text{ sec}$ . Then,  $Q_S$  and  $Q_L$  are in units of  $\text{watt m}^{-2}$ .

### 5.3 Longwave Back Radiation from the Sea Surface

The effective back radiation is calculated from the formula

$$Q_B = c_2 s \sigma T_S^3 \left[ T_S (0.39 - 0.05 \sqrt{e}) (1 - KC^2) + 4(T_S - T) \right] \quad (5.3.1)$$

where  $s=0.97$ ,  $\sigma=1.189 \times 10^{-7} \text{ cal cm}^{-2} \text{ day}^{-1} \text{ K}^{-4}$ , and  $C$  is the cloudiness in tenths. The parameter  $K$  increases linearly with latitude from 0.5 at the equator to 0.8 at  $70^\circ \text{N}$ . The value  $K=0.55$  was used for the back radiation fluxes given in this report (Wyrтки, 1966).

6. MOMENTUM, HEAT AND RADIATIVE FLUXES  
IN THE VICINITY OF THE R/V C. ISELIN  
IN THE C-SCALE AREA

In order to calculate hourly fluxes from the meteorological data in Table 1, linear interpolation was used for missing temperature, humidity, and wind speed data. The sea surface temperature was assumed to have a value of  $27.5^{\circ}\text{C}$  at 0000 on September 2, 1974, and  $27.1^{\circ}\text{C}$  at 2100 on September 20, 1974. When the surface pressure was missing, it was assumed to have a value of 1013 mb. Missing cloud cover data were set equal to 3. The half-hourly radiation data were linearly interpolated where data were missing. The radiation was assumed to be zero from 2030 through 0730 if data were missing during those periods.

In Table 2, where the fluxes are given, hourly radiation data were computed using the relation

$$Q_{Ri} = 0.25(R_{i-1} + R_{i+1}) + 0.50 R_i, \quad (6.1)$$

where  $R_i$  is the measured interpolated hourly radiation value, and  $R_{i\pm 1}$  are the adjacent half-hourly values. For a wind speed greater than  $0.4 \text{ m sec}^{-1}$ , the sensible and latent heat fluxes were calculated using (5.2.26); otherwise, (5.2.27)



TABLE 2

MOMENTUM AND HEAT FLUXES

NATIONAL OCEANIC & ATMOSPHERIC ADMINISTRATION  
ATLANTIC OCEANOGRAPHIC METEOROLOGICAL LABORATORIES  
SEA AIR INTERACTION LABORATORY

FLUXES CALCULATED FROM COLOURS ISFLN (GATE) HOURLY METEOROLOGICAL OBSERVATIONS USING LINEAR INTERPOLATION FOR MISSING DATA  
SEPTEMBER 02, 1974

JULIAN DAY	GMT HOUR	SENSIBLE HEAT FLUX (WATTS/M2)	LATENT HEAT FLUX (WATTS/M2)	RADIATION (WATTS/M2)	BACK RADIATION (WATTS/M2)	LONG WAVE RADIATION (WATTS/M2)	NET RADIATION (10**4 JOULES/M2)	DAILY NET HEAT FLUX (10**4 JOULES/M2)	WIND STRESS (NT/M2)	RICHARDSON NUMBER	POWER RATIO
245	00	2.	17.	0.	0.	60.	0.	0.	.000		
245	01	2.	18.	0.	0.	60.	-21.	-28.	.000		
245	02	2.	17.	0.	0.	61.	-43.	-57.	.000		
245	03	7.	22.	0.	0.	63.	-60.	-112.	.014		.091
245	04	4.	20.	0.	0.	63.	-89.	-158.	.007		.073
245	05	3.	25.	0.	0.	59.	-110.	-200.	.007		.040
245	06	5.	22.	0.	0.	61.	-132.	-243.	.007		.087
245	07	3.	38.	0.	0.	61.	-154.	-279.	.003		.070
245	08	7.	33.	0.	51.	61.	-158.	-319.	.019		.072
245	09	16.	111.	96.	77.	69.	-148.	-355.	.025		.144
245	10	22.	126.	375.	77.	66.	-40.	-301.	.025		.176
245	11	13.	111.	760.	66.	63.	209.	-96.	.025		.120
245	12	11.	103.	854.	63.	55.	404.	148.	.025		.104
245	13	1.	83.	553.	55.	64.	673.	297.	.014		.013
245	14	4.	12.	621.	64.	66.	874.	492.	.000		
245	15	3.	26.	565.	66.	66.	1052.	660.	.000		
245	16	7.	25.	392.	66.	66.	1170.	767.	.000		
245	17	7.	100.	153.	65.	65.	1202.	761.	.014		.065
245	18	23.	137.	53.	70.	70.	1196.	697.	.030		.165
245	19	20.	133.	29.	76.	76.	1179.	625.	.025		.153
245	20	18.	96.	10.	77.	77.	1155.	560.	.014		.184
245	21	24.	120.	0.	78.	78.	1126.	477.	.025		.187
245	22	29.	124.	0.	73.	73.	1100.	374.	.057		.158
245	23	28.	185.	0.	73.	73.	1074.	271.	.057		.153
245	24	21.	139.	0.	72.	72.	1048.	188.	.032		.140

# ATLANTIC OCEANOGRAPHIC & ATMOSPHERIC A WINDS T R A T I O N SEA AREA INTERPRECTION L A N O R A T O R Y

FLUXES CALCULATED FROM COLUMNAR ISFLN (GATE) HOURLY METEOROLOGICAL OBSERVATIONS USING LINEAR INTERPOLATION FOR MISSING DATA  
SEPTEMBER 02, 1974

JULIAN DAY	GWT HOUR	SENSIRFL HEAT FLUX (WATTS/M2)	LATE-IT HEAT FLUX (WATTS/M2)	RADIATION (WATTS/M2)	BACK RADIATION (WATTS/M2)	LONG WAVE RADIATION (WATTS/M2)	NET RADIATION (10**4 JOULES/M2)	DAILY NET RADIATION (10**4 JOULES/M2)	NET HEAT FLUX (10**4 JOULES/M2)	DAILY STRESS (NT/M2)	RICHMONSON NUMBER	REF. DATA
245	00	2.	17.	0.	0.	60.	0.	0.	0.	.000		
245	01	2.	14.	0.	0.	60.	-21.	-28.	-28.	.000		
245	02	2.	17.	0.	0.	61.	-43.	-57.	-57.	.000		
245	03	7.	22.	0.	0.	61.	-60.	-112.	-112.	.014		.091
245	04	4.	40.	0.	0.	61.	-89.	-158.	-158.	.007		.071
245	05	3.	55.	0.	0.	59.	-110.	-200.	-200.	.007		.040
245	06	5.	52.	0.	0.	61.	-132.	-243.	-243.	.007		.047
245	07	3.	38.	0.	0.	61.	-154.	-274.	-274.	.003		.070
245	08	7.	03.	51.	0.	61.	-156.	-319.	-319.	.019		.072
245	09	16.	111.	96.	0.	60.	-148.	-355.	-355.	.025		.144
245	10	22.	126.	375.	760.	77.	-40.	-301.	-301.	.025		.176
245	11	13.	111.	760.	66.	66.	209.	-96.	-96.	.025		.120
245	12	11.	103.	854.	67.	67.	404.	148.	148.	.025		.104
245	13	1.	93.	553.	55.	55.	673.	297.	297.	.014		.011
245	14	4.	12.	621.	64.	64.	874.	492.	492.	.000		
245	15	3.	26.	565.	68.	68.	1052.	660.	660.	.000		
245	16	3.	25.	392.	66.	66.	1170.	761.	761.	.000		.065
245	17	7.	100.	153.	65.	65.	1202.	761.	761.	.014		.165
245	18	23.	137.	53.	70.	70.	1190.	697.	697.	.030		.151
245	19	20.	133.	29.	76.	76.	1179.	625.	625.	.025		.184
245	20	14.	26.	10.	77.	77.	1155.	560.	560.	.014		.187
245	21	24.	120.	0.	78.	78.	1120.	477.	477.	.025		.158
245	22	29.	184.	0.	73.	73.	1100.	374.	374.	.057		.151
245	23	28.	185.	0.	71.	71.	1074.	271.	271.	.057		.140
245	24	21.	139.	0.	72.	72.	1048.	188.	188.	.032		



NATIONAL OCEANOGRAPHIC ATMOSPHERIC ADMINISTRATION  
ATLANTIC OCEANOGRAPHIC & METEOROLOGICAL LABORATORIES  
SEA AIR INTERACTION LABORATORY

FLUXES CALCULATED FROM COLUMBUS ISFLTN (KATE) HOURLY METEOROLOGICAL OBSERVATIONS USING LINEAR INTERPOLATION FOR MISSING DATA  
SEPTEMBER 04, 1974

JULIAN DAY	GMT HOUR	SENSIBLE HEAT FLUX (WATTS/M2)	LATENT HEAT FLUX (WATTS/M2)	RADIATION (WATTS/M2)	RAYC (WATTS/M2)	LONG WAVE RADIATION (WATTS/M2)	NET RADIATION (10**4 JOULES/M2)	DAILY NET HEAT FLUX (10**4 JOULES/M2)	WIND STRESS (NT/M2)	RICHARDSON NUMBER	POWER RATIO
247	00	13.	125.	0.	66.	0.	0.	0.	.025	-13.8	.100
247	01	13.	119.	0.	66.	-24.	-71.	-71.	.025	-14.1	.112
247	02	12.	122.	0.	60.	-49.	-145.	-145.	.010	-20.0	.102
247	03	11.	106.	0.	70.	-74.	-212.	-212.	.014	-27.1	.102
247	04	7.	71.	0.	69.	-98.	-264.	-264.	.007	-57.3	.090
247	05	7.	73.	0.	69.	-123.	-318.	-318.	.007	-58.3	.097
247	06	12.	102.	0.	60.	-148.	-384.	-384.	.014	-27.9	.114
247	07	13.	102.	0.	71.	-174.	-451.	-451.	.014	-29.7	.124
247	08	11.	85.	54.	71.	-180.	-491.	-491.	.010	-43.4	.132
247	09	10.	81.	183.	68.	-139.	-483.	-483.	.010	-39.5	.123
247	10	3.	95.	453.	64.	2.	-380.	-380.	.014	-22.1	.087
247	11	11.	121.	713.	63.	236.	-194.	-194.	.025	-12.5	.091
247	12	9.	97.	715.	65.	470.	156.	156.	.014	-23.4	.092
247	13	9.	98.	602.	66.	821.	306.	306.	.000	-23.0	.094
247	14	4.	22.	507.	66.	957.	432.	432.	.000	-110.1	.105
247	15	4.	22.	443.	67.	1098.	554.	554.	.003	-15.0	.103
247	16	5.	48.	458.	68.	1150.	553.	553.	.025	-9.0	.098
247	17	14.	134.	213.	67.	1161.	501.	501.	.039	-5.6	.092
247	18	16.	159.	99.	66.	1150.	417.	417.	.057	-4.6	.078
247	19	17.	184.	34.	64.	1130.	333.	333.	.057	-3.9	.094
247	20	13.	167.	9.	65.	1107.	231.	231.	.076	-5.6	.099
247	21	19.	199.	0.	71.	1081.	118.	118.	.066	-4.8	.109
247	22	22.	223.	0.	73.	1055.	-16.	-16.	.087	-6.0	.132
247	23	20.	270.	0.	69.	1030.	-115.	-115.	.057		
247	24	24.	141.	0.							

Table 2. (continued).

# FLUXES CALCULATED FROM OBSERVED DATA USING LINEAR INTERPOLATION FOR MISSING DATA

SEPTEMBER 05, 1964

JULIAN DAY	GMT HOUR	TIME (H:M:S)	NET RADIATION (WATTS/M <sup>2</sup> )	LONG WAVE RADIATION (WATTS/M <sup>2</sup> )	DAILY NET RADIATION (10**4 JOULES/M <sup>2</sup> )	DAILY HEAT FLUX (JOULES/M <sup>2</sup> )	WIND STRESS (N/M <sup>2</sup> )	RICHARDSON NUMBER	BOWEN RATIO
248	00	21	181	7	0	0	.057	-6.0	.132
248	01	20	140	0	-25	-86	.030	-10.1	.131
248	02	41	262	0	-49	-216	.155	-2.5	.164
248	03	40	242	0	-74	-342	.155	-2.5	.172
248	04	31	202	0	-69	-452	.076	-5.5	.152
248	05	31	168	0	-124	-555	.076	-5.4	.161
248	06	30	217	0	-150	-672	.080	-4.1	.165
248	07	30	210	0	-175	-790	.090	-4.5	.177
248	08	30	177	6	-100	-888	.076	-5.4	.178
248	09	5	108	17	-213	-992	.057	-12.4	.250
248	10	40	108	30	-211	-1078	.057	-11.5	.231
248	11	20	111	306	-80	-1001	.010	-29.0	.197
248	12	15	172	307	11	-930	.010	-22.1	.136
248	13	20	170	211	02	-940	.057	-7.2	.150
248	14	30	170	135	119	-967	.010	-17.5	.230
248	15	25	105	207	175	-950	.010	-30.4	.215
248	16	15	134	272	240	-943	.025	-18.2	.138
248	17	13	136	207	294	-950	.025	-17.0	.131
248	18	13	137	124	312	-988	.025	-17.0	.170
248	19	13	70	26	297	-1033	.014	-26.6	.164
248	20	13	77	0	270	-1086	.014	-27.4	.164
248	21	14	00	0	252	-1149	.010	-19.4	.145
248	22	11	00	0	227	-1208	.014	-25.0	.127
248	23	7	60	0	203	-1256	.007	-52.0	.111
248	24	15	101	0	177	-1353	.030	-9.6	.080

NATIONAL OCEANOGRAPHIC ATMOSPHERIC ADMINISTRATION  
ATLANTIC OCEANOGRAPHIC METEOROLOGICAL LABORATORY  
SEA AIR INTERACTION LABORATORY

FLUXES CALCULATED FROM COLIMBUS ISELIN (GATE) HOURLY METEOROLOGICAL OBSERVATIONS USING LINEAR INTERPOLATION FOR MISSING DATA  
SEPTEMBER 06, 1974

JULIAN DAY	GMT HOUR	SENSIBLE HEAT FLUX (WATTS/M2)	LATENT HEAT FLUX (WATTS/M2)	RADIATION <sup>1</sup> (WATTS/M2)	LONG WAVE RADIATION (WATTS/M2)	NET RADIATION <sup>2</sup> (10**4 JOULES/M2)	DAILY NET RADIATION <sup>3</sup> (10**4 JOULES/M2)	NET HEAT FLUX (10**4 JOULES/M2)	DAILY STRESS (NT/M2)	RICHARDSON NUMBER	POWER RATIO
249	00	15.	101.	0.	73.	0.	0.	0.	.039	-0.6	.090
249	01	4.	22.	0.	70.	-25.	-34.	-34.	.000		
249	02	4.	25.	0.	71.	-51.	-70.	-70.	.000		
249	03	10.	110.	0.	69.	-76.	-142.	-142.	.010	-17.8	.089
249	04	10.	118.	0.	69.	-100.	-213.	-213.	.010	-17.2	.085
249	05	3.	85.	0.	64.	-123.	-269.	-269.	.014	-20.2	.080
249	06	9.	80.	0.	63.	-146.	-324.	-324.	.014	-10.8	.097
249	07	5.	87.	0.	64.	-169.	-381.	-381.	.014	-20.6	.090
249	08	7.	82.	02.	41.	-151.	-398.	-398.	.014	-20.4	.080
249	09	3.	22.	336.	65.	-53.	-309.	-309.	.000		
249	10	5.	64.	574.	56.	133.	-148.	-148.	.007	-43.6	.074
249	11	5.	82.	765.	64.	380.	73.	73.	.010	-26.7	.062
249	12	3.	113.	825.	64.	659.	303.	303.	.010	-14.6	.068
249	13	7.	124.	950.	47.	944.	581.	581.	.010	-14.3	.053
249	14	7.	116.	807.	46.	1256.	811.	811.	.010	-13.0	.057
249	15	5.	114.	623.	34.	1470.	980.	980.	.010	-13.2	.054
249	16	23.	114.	251.	57.	1540.	1000.	1000.	.010	-30.3	.202
249	17	30.	153.	240.	55.	1610.	1004.	1004.	.039	-14.0	.197
249	18	14.	67.	250.	49.	1682.	1048.	1048.	.010	-44.5	.187
249	19	15.	107.	150.	46.	1720.	1042.	1042.	.025	-14.6	.143
249	20	15.	150.	50.	65.	1714.	977.	977.	.048	-6.2	.090
249	21	14.	138.	0.	62.	1692.	900.	900.	.057	-4.5	.103
249	22	10.	104.	0.	60.	1670.	805.	805.	.086	-2.3	.052
249	23	26.	149.	0.	70.	1645.	717.	717.	.057	-6.0	.171
249	24	33.	321.	0.	75.	1615.	562.	562.	.127	-3.2	.104

Table 2. (continued).



NATIONAL OCEANOGRAPHIC & ATMOSPHERIC ADMINISTRATION  
ATLANTIC OCEANOGRAPHIC & METEOROLOGICAL LABORATORIES  
SEA AIR INTERACTION LABORATORY

FLUXES CALCULATED FROM COLUMNAR ISFLIN (SAFE) HOURLY METEOROLOGICAL OBSERVATIONS USING LINEAR INTERPOLATION FOR MISSING DATA  
SEPTEMBER 07, 1974

JULIAN DAY	GMT HOUR	SENSIBLE HEAT FLUX (WATTS/M2)	LATENT HEAT FLUX (WATTS/M2)	RADIATION (WATTS/M2)	LONG WAVE RADIATION (WATTS/M2)	NET RADIATION (10**4 JOULES/M2)	DAILY HEAT FLUX (10**4 JOULES/M2)	WIND STRESS (NT/M2)	RICHARDSON NUMBER	POWER RATIO
250	00	31.	321.	0.	75.	0.	0.	.127	-3.2	.104
250	01	12.	151.	0.	62.	-22.	-81.	.057	-4.3	.081
250	02	13.	206.	0.	61.	-44.	-182.	.098	-2.2	.065
250	03	23.	104.	0.	71.	-70.	-288.	.074	-5.3	.144
250	04	11.	221.	0.	61.	-92.	-393.	.096	-2.2	.048
250	05	13.	200.	0.	61.	-114.	-492.	.100	-2.2	.067
250	06	7.	201.	0.	60.	-135.	-588.	.086	-2.1	.037
250	07	2.	246.	5.	60.	-155.	-700.	.117	-1.6	.035
250	08	3.	150.	58.	42.	-150.	-751.	.051	-3.0	.052
250	09	5.	109.	218.	42.	-96.	-761.	.071	-2.3	.023
250	10	3.	230.	340.	43.	21.	-743.	.103	-1.9	.034
250	11	3.	184.	458.	40.	172.	-660.	.067	-2.2	.018
250	12	2.	180.	692.	57.	400.	-497.	.067	-2.0	.012
250	13	-2.	150.	866.	53.	693.	-260.	.067	-1.1	-.014
250	14	6.	161.	904.	57.	998.	-15.	.067	-2.3	.034
250	15	3.	166.	857.	48.	1249.	215.	.071	-1.0	.020
250	16	-7.	114.	905.	48.	1562.	449.	.030	-1.2	-.057
250	17	3.	166.	400.	30.	1724.	550.	.071	-1.0	.020
250	18	2.	173.	188.	47.	1775.	538.	.073	-1.7	.013
250	19	1.	135.	92.	55.	1785.	498.	.046	-2.5	.007
250	20	5.	101.	14.	57.	1769.	412.	.091	-1.6	.027
250	21	4.	169.	0.	59.	1748.	329.	.060	-2.6	.025
250	22	13.	178.	0.	61.	1726.	238.	.076	-3.0	.073
250	23	7.	151.	0.	58.	1705.	160.	.058	-3.1	.048
250	24	11.	153.	0.	57.	1685.	81.	.071	-2.8	.066

Table 2. (continued).

NATIONAL OCEANOGRAPHIC & ATMOSPHERIC ADMINISTRATION  
ATLANTIC OCEANOGRAPHIC & METEOROLOGICAL LABORATORIES  
SEA AIR INTERACTION LABORATORY

FLUXES CALCULATED FROM COLIMBUS ISFLIN (DATE) HOURLY METEOROLOGICAL OBSERVATIONS USING LINEAR INTERPOLATION; FOR MISSING DATA  
SEPTEMBER 01, 1974

JULIAN DAY	GMT HOUR	SENSIBLE HEAT FLUX (WATTS/M <sup>2</sup> )	LATENT HEAT FLUX (WATTS/M <sup>2</sup> )	RADIATION <sup>1</sup> (WATTS/M <sup>2</sup> )	LONG WAVE RADIATION (WATTS/M <sup>2</sup> )	NET RADIATION <sup>2</sup> (10**4 JOULES/M <sup>2</sup> )	DAILY NET HEAT FLUX (10**4 JOULES/M <sup>2</sup> )	WIND STRESS (NT/M <sup>2</sup> )	RICHARDSON NUMBER	BOWEN RATIO
251	00	17.	153.	0.	57.	0.	0.	.071	-2.8	.066
251	01	15.	104.	0.	62.	-22.	-97.	.085	-2.0	.077
251	02	9.	175.	0.	57.	-43.	-184.	.080	-2.1	.040
251	03	5.	203.	0.	56.	-63.	-279.	.112	-1.3	.028
251	04	4.	157.	0.	55.	-83.	-357.	.077	-1.6	.023
251	05	5.	152.	0.	57.	-103.	-444.	.090	-1.6	.028
251	06	10.	174.	0.	61.	-125.	-536.	.098	-2.5	.107
251	07	7.	177.	0.	56.	-145.	-622.	.097	-1.5	.037
251	08	0.	140.	21.	34.	-150.	-680.	.076	-2.1	.058
251	09	7.	154.	63.	34.	-140.	-738.	.097	-1.5	.036
251	10	5.	153.	120.	35.	-109.	-765.	.065	-2.4	.038
251	11	6.	151.	253.	34.	-30.	-753.	.086	-1.9	.032
251	12	2.	172.	605.	33.	170.	-610.	.070	-1.5	.014
251	13	2.	130.	748.	33.	433.	-400.	.041	-3.1	.013
251	14	1.	146.	507.	55.	596.	-290.	.056	-1.0	.004
251	15	1.	129.	472.	54.	747.	-186.	.040	-2.0	.001
251	16	-1.	121.	445.	54.	888.	-88.	.038	-2.3	-.008
251	17	-4.	117.	320.	54.	980.	-32.	.038	-2.4	-.004
251	18	-1.	103.	197.	31.	1046.	-49.	.027	-3.3	-.007
251	19	1.	116.	70.	55.	1051.	-9.	.041	-2.7	.007
251	20	1.	52.	21.	56.	1038.	-104.	.028	-4.3	.006
251	21	1.	82.	3.	56.	1019.	-142.	.007	-19.5	.013
251	22	0.	71.	0.	56.	909.	-191.	.015	-7.2	.000
251	23	4.	71.	0.	57.	979.	-238.	.011	-11.4	.006
251	24	0.	71.	0.	57.	959.	-284.	.011	-11.4	.006

Table 2. (continued).

NATIONAL OCEANIC & ATMOSPHERIC ADMINISTRATION  
ATLANTIC OCEANOGRAPHIC & METEOROLOGICAL LABORATORIES  
SEA AIR INTERACTION LABORATORY

FLUXES CALCULATED FROM COLUMBUS ISFLUX (RATE) HOURLY METEOROLOGICAL OBSERVATIONS USING LINEAR INTERPOLATION FOR MISSING DATA  
SEPTEMBER 09, 1974

JULIAN DAY	GMT HOUR	SENSEFLX HEAT FLUX (WATTS/M <sup>2</sup> )	LATENT HEAT FLUX (WATTS/M <sup>2</sup> )	RADIATION (WATTS/M <sup>2</sup> )	BACK RADIATION (WATTS/M <sup>2</sup> )	LONG WAVE RADIATION (WATTS/M <sup>2</sup> )	NET RADIATION (10**4 JOULES/M <sup>2</sup> )	DAILY NET HEAT FLUX (10**4 JOULES/M <sup>2</sup> )	WIND STRESS (NT/M <sup>2</sup> )	RICHARDSON NUMBER	POWER RATIO
252	00	4.	71.	0.	57.	0.	0.	0.	.011	-11.4	.004
252	01	1.	54.	0.	57.	-20.	-40.	-40.	.007	-20.1	.013
252	02	4.	17.	0.	57.	-41.	-67.	-67.	.000		
252	03	1.	16.	0.	57.	-62.	-94.	-94.	.000		
252	04	10.	81.	0.	67.	-86.	-150.	-150.	.014	-23.2	.121
252	05	5.	71.	0.	50.	-107.	-199.	-199.	.014	-14.1	.064
252	06	2.	109.	0.	55.	-127.	-259.	-259.	.038	-3.3	.023
252	07	3.	102.	0.	55.	-147.	-317.	-317.	.038	-3.4	.033
252	08	2.	143.	0.	33.	-156.	-378.	-378.	.056	-2.1	.014
252	09	1.	168.	35.	33.	-155.	-438.	-438.	.075	-1.5	.007
252	10	1.	136.	33.	32.	-155.	-487.	-487.	.047	-2.4	.007
252	11	4.	120.	33.	20.	-154.	-531.	-531.	.038	-4.1	.035
252	12	11.	132.	200.	30.	-92.	-521.	-521.	.048	-4.9	.095
252	13	7.	110.	500.	31.	80.	-391.	-391.	.031	-6.5	.062
252	14	16.	220.	500.	66.	239.	-316.	-316.	.087	-3.1	.074
252	15	13.	175.	324.	38.	342.	-283.	-283.	.057	-5.8	.105
252	16	12.	175.	554.	66.	518.	-177.	-177.	.068	-4.5	.109
252	17	13.	124.	105.	42.	554.	-190.	-190.	.030	-7.5	.108
252	18	13.	182.	45.	60.	546.	-270.	-270.	.057	-5.9	.101
252	19	14.	142.	27.	67.	531.	-341.	-341.	.030	-8.2	.101
252	20	20.	154.	0.	67.	511.	-424.	-424.	.057	-5.8	.127
252	21	17.	158.	3.	64.	489.	-509.	-509.	.064	-4.3	.105
252	22	17.	116.	0.	73.	463.	-583.	-583.	.025	-16.7	.150
252	23	21.	166.	0.	67.	439.	-674.	-674.	.064	-5.2	.128
252	24	7.	51.	0.	76.	411.	-723.	-723.	.004	-120.2	.147



NATIONAL OCEANOGRAPHIC & ATMOSPHERIC ADMINISTRATION  
ATLANTIC OCEANOGRAPHIC METEOROLOGICAL LABORATORY  
SEA AIR INTERACTION LABORATORY

FLUXES CALCULATED FROM COLLINS ISFLIN (RATE) HOURLY METEOROLOGICAL OBSERVATIONS USING LINEAR INTERPOLATION FOR MISSING DATA  
SEPTEMBER 10, 1974

JULIAN DAY	GMT HOUR	SENSITIVE HEAT FLUX (WATTS/M <sup>2</sup> )	HEAT FLUX (WATTS/M <sup>2</sup> )	RADIATION (WATTS/M <sup>2</sup> )	RAC <sup>2</sup> RADIATION (WATTS/M <sup>2</sup> )	LONG WAVE RADIATION (WATTS/M <sup>2</sup> )	NET RADIATION (10**4 JOULES/M <sup>2</sup> )	DAILY NET RADIATION (10**4 JOULES/M <sup>2</sup> )	NET HEAT FLUX (10**4 JOULES/M <sup>2</sup> )	DAILY HEAT FLUX (NT/M <sup>2</sup> )	RICHARDSON NUMBER	BOWMEN RATIO
253	00	7.	51.	0.	0.	76.	0.	0.	0.	.004	-120.2	.147
253	01	6.	40.	0.	0.	70.	-25.	-50.	-50.	.007	-57.5	.128
253	02	11.	24.	0.	0.	60.	-50.	-109.	-109.	.014	-25.2	.128
253	03	3.	28.	0.	0.	69.	-75.	-145.	-145.	.002	-234.7	.121
253	04	3.	25.	0.	0.	67.	-89.	-179.	-179.	.002	-210.0	.126
253	05	2.	14.	0.	0.	69.	-123.	-209.	-209.	.000	-275.9	.109
253	06	4.	16.	0.	0.	66.	-147.	-240.	-240.	.000		
253	07	5.	55.	0.	0.	65.	-170.	-285.	-285.	.007	-43.3	.096
253	08	6.	85.	82.	82.	62.	-163.	-310.	-310.	.014	-17.0	.072
253	09	5.	84.	211.	211.	62.	-109.	-289.	-289.	.014	-15.3	.055
253	10	3.	54.	420.	420.	60.	20.	-140.	-140.	.007	-30.7	.051
253	11	3.	23.	746.	746.	60.	267.	59.	59.	.000		
253	12	0.	0.	947.	947.	49.	590.	382.	382.	.000		
253	13	0.	0.	950.	950.	51.	914.	706.	706.	.000		
253	14	0.	0.	1015.	1015.	53.	1260.	1052.	1052.	.000	-62.4	-.049
253	15	-1.	14.	943.	943.	51.	1581.	1368.	1368.	.000	-46.5	-.027
253	16	-1.	30.	776.	776.	52.	1841.	1618.	1618.	.002	-8.3	-.020
253	17	-2.	77.	507.	507.	53.	2005.	1754.	1754.	.010	-20.3	.002
253	18	1.	65.	173.	173.	59.	2046.	1772.	1772.	.007	-19.1	-.003
253	19	-2.	66.	68.	68.	59.	2049.	1752.	1752.	.007	-6.5	.013
253	20	2.	129.	21.	21.	58.	2036.	1691.	1691.	.025	-24.8	.007
253	21	1.	73.	0.	0.	62.	2013.	1643.	1643.	.007	-27.6	.018
253	22	1.	70.	0.	0.	62.	1991.	1595.	1595.	.007	-13.0	.024
253	23	2.	98.	0.	0.	62.	1969.	1536.	1536.	.014	-15.1	.080
253	24	5.	68.	0.	0.	59.	1948.	1489.	1489.	.014		

Table 2. (continued).

NATIONAL OCEANIC & ATMOSPHERIC ADMINISTRATION  
ATLANTIC OCEANOGRAPHIC & METEOROLOGICAL LABORATORIES  
SEA AIR INTERACTION LABORATORY

FLUXES CALCULATED FROM COLUMBUS ISELIN (-ATE) HOURLY METEOROLOGICAL OBSERVATIONS USING LINEAR INTERPOLATION FOR MISSING DATA  
SEPTEMBER 11, 1974

JULIAN DAY	GMT HOUR	SENSIBLE HEAT FLUX (WATTS/M2)	LATENT HEAT FLUX (WATTS/M2)	RADIATION (WATTS/M2)	LONG WAVE RADIATION (WATTS/M2)	NET RADIATION (10**4 JOULES/M2)	DAILY NET HEAT FLUX (10**4 JOULES/M2)	WIND STRESS (NT/M2)	RYCHARDSON NUMBER	POWER RATIO
254	00	5.	68.	0.	59.	0.	0.	.014	-15.1	.080
254	01	7.	107.	0.	62.	-22.	-63.	.025	-9.4	.068
254	02	7.	111.	0.	62.	-45.	-128.	.025	-9.4	.065
254	03	4.	101.	0.	62.	-67.	-190.	.021	-10.5	.076
254	04	7.	89.	0.	61.	-89.	-246.	.021	-11.0	.083
254	05	12.	148.	0.	63.	-111.	-326.	.048	-5.4	.081
254	06	8.	105.	0.	62.	-134.	-389.	.025	-9.9	.077
254	07	7.	120.	0.	64.	-157.	-458.	.025	-10.0	.062
254	08	6.	104.	65.	54.	-153.	-491.	.016	-15.2	.064
254	09	6.	141.	232.	52.	-88.	-479.	.037	-5.4	.041
254	10	5.	89.	343.	55.	16.	-413.	.016	-15.0	.055
254	11	3.	72.	638.	51.	227.	-228.	.010	-19.7	.042
254	12	2.	62.	870.	55.	523.	45.	.007	-31.2	.040
254	13	3.	64.	952.	61.	944.	342.	.007	-37.0	.055
254	14	2.	30.	900.	62.	1146.	632.	.002	-169.1	.062
254	15	3.	48.	866.	64.	1435.	902.	.003	-85.4	.067
254	16	7.	125.	659.	62.	1649.	1069.	.025	-10.3	.060
254	17	9.	134.	450.	50.	1790.	1158.	.038	-6.2	.060
254	18	4.	89.	205.	61.	1874.	1209.	.013	-18.7	.040
254	19	5.	105.	106.	58.	1992.	1187.	.019	-11.5	.048
254	20	5.	86.	7.	62.	1872.	1130.	.014	-17.2	.053
254	21	4.	77.	0.	61.	1950.	1079.	.010	-23.2	.053
254	22	2.	42.	0.	60.	1828.	1042.	.003	-68.7	.050
254	23	3.	57.	0.	60.	1807.	998.	.007	-33.9	.057
254	24	5.	78.	0.	59.	1785.	947.	.014	-15.3	.064

NATIONAL OCEANIC & ATMOSPHERIC ADMINISTRATION  
ATLANTIC OCEANOGRAPHIC & METEOROLOGICAL LABORATORIES  
SEA AIR INTERACTION LABORATORY

FLUXES CALCULATED FROM COLLINS ISFLIN (GATE) HOURLY METEOROLOGICAL OBSERVATIONS USING LINEAR INTERPOLATION FOR MISSING DATA  
SEPTEMBER 12, 1974

JULIAN DAY	GMT HOUR	SENSIBLE HEAT FLUX (WATTS/M2)	LATENT HEAT FLUX (WATTS/M2)	RADIATION (WATTS/M2)	LONG WAVE RADIATION (WATTS/M2)	NET RADIATION (10**4 JOULES/M2)	DAILY NET HEAT FLUX (10**4 JOULES/M2)	WIND STRESS (N/M2)	RICHARDSON NUMBER	POWER RATIO
255	00	5.	78.	0.	59.	0.	0.	.014	-15.3	.064
255	01	3.	123.	0.	59.	-21.	-68.	.038	-5.7	.060
255	02	9.	129.	0.	60.	-43.	-140.	.038	-6.0	.060
255	03	9.	105.	0.	61.	-63.	-202.	.025	-9.5	.072
255	04	10.	152.	0.	59.	-86.	-281.	.056	-3.8	.064
255	05	0.	123.	0.	59.	-107.	-350.	.038	-5.4	.061
255	06	7.	126.	0.	59.	-129.	-419.	.038	-5.1	.053
255	07	5.	05.	0.	60.	-150.	-477.	.019	-11.2	.056
255	08	5.	61.	08.	43.	-131.	-481.	.010	-22.5	.078
255	09	7.	140.	139.	45.	-97.	-503.	.056	-3.2	.047
255	10	5.	115.	178.	44.	-49.	-498.	.038	-4.3	.043
255	11	6.	133.	303.	43.	45.	-455.	.056	-2.9	.046
255	12	7.	154.	174.	28.	06.	-460.	.075	-2.1	.046
255	13	31.	161.	42.	50.	05.	-532.	.057	-8.1	.190
255	14	35.	212.	40.	73.	83.	-633.	.087	-5.1	.167
255	15	39.	230.	82.	74.	85.	-727.	.090	-4.6	.170
255	16	42.	255.	141.	75.	109.	-810.	.114	-4.0	.164
255	17	26.	175.	153.	72.	139.	-854.	.055	-7.7	.140
255	18	16.	167.	112.	71.	153.	-905.	.040	-8.0	.097
255	19	16.	189.	32.	70.	140.	-992.	.048	-7.0	.084
255	20	11.	181.	5.	69.	116.	-1085.	.030	-7.8	.060
255	21	13.	149.	0.	66.	93.	-1167.	.030	-7.7	.084
255	22	13.	121.	0.	63.	70.	-1238.	.039	-7.4	.111
255	23	11.	138.	0.	63.	47.	-1314.	.042	-6.3	.082
255	24	3.	114.	0.	64.	24.	-1381.	.025	-10.3	.071

Table 2. (continued).



FLUXES CALCULATED FROM COLUMBUS ISLAND METEOROLOGICAL OBSERVATIONS USING LINEAR INTERPOLATION FOR MISSING DATA  
SEPTEMBER 13, 1974

ATMOSPHERIC PHYSICS AND METEOROLOGICAL LABORATORIES  
SPACIAL INTERPRETATION LABORATORY

JULIAN DAY	GMT HOUR	SENSIBLE HEAT FLUX (WATTS/M2)	LATENT HEAT FLUX (WATTS/M2)	RADIATION (WATTS/M2)	BACK RADIATION (WATTS/M2)	LONG WAVE RADIATION (WATTS/M2)	NET RADIATION (10**4 JOULES/M2)	DAILY NET RADIATION (10**4 JOULES/M2)	1/2 FT HEAT FLUX (10**4 JOULES/M2)	DAILY HEAT FLUX (M2)	WIND STRESS (NT/M2)	RICHARDSON NUMBER	POWER RATIO
256	00	9.	114.	0.	0.	64.	0.	0.	0.	-75.	.025	-10.3	.071
256	01	8.	130.	0.	0.	61.	-22.	-22.	-75.	-146.	.038	-5.7	.054
256	02	7.	125.	0.	0.	66.	-46.	-46.	-146.	-227.	.025	-11.2	.071
256	03	12.	140.	0.	0.	63.	-60.	-60.	-227.	-300.	.048	-5.4	.082
256	04	13.	126.	0.	0.	64.	-81.	-81.	-300.	-397.	.039	-7.5	.107
256	05	18.	169.	0.	0.	62.	-114.	-114.	-397.	-434.	.087	-3.0	.093
256	06	4.	17.	0.	0.	63.	-176.	-176.	-434.	-524.	.003	-12.0	.102
256	07	14.	176.	0.	0.	60.	-158.	-158.	-524.	-589.	.087	-2.6	.079
256	08	7.	140.	14.	14.	37.	-166.	-166.	-589.	-661.	.056	-3.6	.061
256	09	11.	104.	42.	42.	38.	-165.	-165.	-661.	-720.	.076	-2.0	.054
256	10	8.	170.	61.	61.	36.	-156.	-156.	-720.	-772.	.076	-2.4	.046
256	11	6.	178.	98.	98.	58.	-141.	-141.	-772.	-784.	.076	-2.1	.033
256	12	16.	175.	102.	102.	33.	-84.	-84.	-784.	-743.	.087	-2.9	.093
256	13	11.	134.	291.	291.	32.	9.	9.	-743.	-694.	.056	-3.0	.083
256	14	14.	166.	378.	378.	63.	123.	123.	-694.	-598.	.066	-3.8	.086
256	15	13.	130.	453.	453.	34.	274.	274.	-598.	-606.	.048	-5.5	.094
256	16	13.	130.	228.	228.	34.	343.	343.	-606.	-694.	.048	-5.6	.107
256	17	15.	162.	140.	140.	34.	381.	381.	-694.	-769.	.066	-4.0	.093
256	18	33.	101.	65.	65.	79.	370.	370.	-769.	-807.	.067	-8.1	.206
256	19	28.	120.	22.	22.	82.	354.	354.	-807.	-869.	.025	-24.0	.230
256	20	5.	29.	5.	5.	76.	329.	329.	-869.	-925.	.002	-32.1	.175
256	21	15.	84.	0.	0.	75.	302.	302.	-925.	-969.	.014	-60.6	.138
256	22	10.	69.	0.	0.	77.	274.	274.	-969.	-1042.	.007	-124.0	.144
256	23	5.	44.	0.	0.	73.	246.	246.	-1042.		.003	-15.4	.136
256	24	16.	114.	0.	0.	71.	222.	222.			.025		

ATLANTIC OCEAN SURFACE AIR TEMPERATURES  
SEA AIR INTERACTION LABORATORY

FLUXES CALCULATED FROM COLUMBUS ISFLUX (DATE) AIR SURFACE METEOROLOGICAL OBSERVATIONS USING LINEAR INTERPOLATION FOR MISSING DATA  
SEPTEMBER 14, 1974

JULIAN DAY	GMT HOUR	SENSIBLE HEAT FLUX (WATTS/M <sup>2</sup> )	LATENT HEAT FLUX (WATTS/M <sup>2</sup> )	RADIATION (WATTS/M <sup>2</sup> )	LONG WAVE RADIATION (WATTS/M <sup>2</sup> )	NET RADIATION (10**4 JOULES/M <sup>2</sup> )	DAILY NET HEAT FLUX (10**4 JOULES/M <sup>2</sup> )	WIND STRESS (NT/M <sup>2</sup> )	WIND-DRIVEN NUMBER	BOURN RATIO
257	00	17.	114.	0.	71.	0.	0.	.025	-15.4	.136
257	01	15.	139.	0.	67.	-24.	-80.	.039	-8.4	.108
257	02	10.	70.	0.	70.	-50.	-134.	.010	-17.6	.140
257	03	43.	221.	0.	72.	-75.	-255.	.127	-1.4	.197
257	04	35.	104.	0.	72.	-101.	-362.	.087	-4.0	.180
257	05	50.	263.	0.	75.	-128.	-502.	.146	-3.2	.188
257	06	35.	108.	0.	73.	-155.	-612.	.083	-5.3	.176
257	07	27.	161.	0.	76.	-182.	-707.	.047	-9.9	.167
257	08	24.	151.	66.	47.	-175.	-763.	.057	-6.7	.162
257	09	21.	104.	221.	50.	-113.	-779.	.076	-4.0	.100
257	10	13.	158.	439.	46.	29.	-690.	.057	-4.6	.083
257	11	12.	98.	744.	42.	291.	-485.	.025	-12.0	.117
257	12	4.	189.	851.	28.	578.	-259.	.086	-1.6	.020
257	13	29.	175.	310.	39.	679.	-231.	.099	-3.5	.168
257	14	24.	174.	408.	40.	811.	-171.	.076	-4.9	.161
257	15	37.	173.	253.	55.	882.	-176.	.057	-9.6	.216
257	16	24.	119.	153.	57.	917.	-193.	.025	-22.0	.220
257	17	16.	107.	246.	64.	982.	-172.	.039	-8.1	.150
257	18	11.	188.	244.	38.	1056.	-170.	.086	-2.4	.060
257	19	12.	103.	77.	61.	1062.	-205.	.038	-6.4	.114
257	20	5.	93.	10.	58.	1045.	-258.	.025	-7.1	.051
257	21	21.	170.	0.	65.	1022.	-350.	.085	-3.4	.124
257	22	34.	204.	0.	60.	997.	-461.	.114	-3.3	.160
257	23	22.	114.	0.	78.	969.	-538.	.025	-20.2	.197
257	24	5.	49.	0.	68.	944.	-582.	.005	-67.2	.111

Table 2. (continued).

ATLANTIC OCEAN SURFACE FLUXES AT METEOROLOGICAL STATION A1001 FOR  
SEA AIR INTERACTION LABORATORY

FLUXES CALCULATED FROM COLUMBUS JF 74 (DATE) HOURLY METEOROLOGICAL OBSERVATIONS OF THE LINEAR INTERPOLATION FOR MISSING DATA  
SEPTEMBER 15, 1974

JULIAN DAY	GMT HOUR	SENSIBLE HEAT FLUX (WATTS/M <sup>2</sup> )	LATENT HEAT FLUX (WATTS/M <sup>2</sup> )	RADIATION <sup>1</sup> (WATTS/M <sup>2</sup> )	LONG WAVE RADIATION <sup>1</sup> (WATTS/M <sup>2</sup> )	DAILY NET RADIATION <sup>1</sup> (10**4 JOULES/M <sup>2</sup> )	DAILY NET HEAT FLUX <sup>2</sup> (10**4 JOULES/M <sup>2</sup> )	DAILY STRESS <sup>3</sup> (N/T/M <sup>2</sup> )	RICHARDSON NUMBER	BOWEN RATIO
258	00		40.	0.	68.	0.	0.	.005	-17.2	.111
258	01	-2.	22.	0.	43.	-10.	-23.	.009	0.	-.070
258	02	3.	41.	0.	58.	-36.	-60.	.007	-28.5	.072
258	03	4.	64.	0.	58.	-57.	-105.	.015	-11.7	.064
258	04	2.	127.	0.	60.	-79.	-173.	.031	-4.8	.019
258	05	2.	122.	0.	50.	-100.	-240.	.031	-4.7	.018
258	06	2.	115.	0.	59.	-121.	-303.	.027	-5.4	.018
258	07	2.	107.	0.	50.	-143.	-364.	.024	-6.1	.019
258	08	2.	103.	42.	40.	-142.	-401.	.024	-6.1	.019
258	09	1.	105.	214.	40.	-90.	-377.	.024	-5.7	.013
258	10	-1.	68.	440.	56.	59.	-263.	.010	-9.0	-.002
258	11	-1.	77.	609.	46.	294.	-55.	.013	-6.4	-.013
258	12	3.	60.	744.	41.	547.	175.	.010	-17.8	.050
258	13	5.	83.	753.	41.	803.	397.	.020	-9.8	.053
258	14	7.	109.	868.	61.	1094.	645.	.025	-9.4	.068
258	15	1.	20.	893.	63.	1392.	936.	.001	-136.4	.065
258	16	1.	91.	686.	61.	1617.	1130.	.010	-22.2	.043
258	17	2.	52.	460.	55.	1763.	1257.	.004	-48.6	.038
258	18	1.	34.	263.	58.	1837.	1318.	.002	-116.9	.038
258	19	3.	63.	248.	62.	1903.	1361.	.007	-16.7	.054
258	20	2.	42.	3.	37.	1801.	1333.	.003	-50.3	.042
258	21	1.	32.	0.	60.	1870.	1299.	.002	-118.3	.047
258	22	2.	41.	0.	61.	1845.	1262.	.003	-77.7	.051
258	23	2.	42.	0.	60.	1826.	1224.	.003	-56.2	.035
258	24	2.	46.	0.	62.	1804.	1185.	.004	-59.0	.052



ANALYTICAL CALCULATIONS AT ATMOSPHERIC ADMINISTRATION  
 A T M O S P H E R I C A D M I N I S T R A T I O N  
 S E A A I R I N T E R A C T I O N L A B O R A T O R Y

FLUXES CALCULATED FROM COLIMONTS RESULTS (WATTS/M2) DAILY METEOROLOGICAL OBSERVATIONS USING LINEAR INTERPOLATION FOR MISSING DATA  
 SEPTEMBER 16, 1974

JULIAN DAY	GAT HOUR	SENSING HEAT FLUX (WATTS/M2)	LATENT HEAT FLUX (WATTS/M2)	RADIATION (WATTS/M2)	LONG WAVE RADIATION (WATTS/M2)	NET RADIATION (10**4 JOULES/M2)	DAILY NET HEAT FLUX (10**4 JOULES/M2)	WIND STRESS (N/MT/M2)	RICHARDSON NUMBER	POWER RATIO
259	00	2.	46.	7.	62.	0.	0.	.004	-50.0	.052
259	01	0.	45.	0.	62.	-25.	-56.	.010	-13.6	.098
259	02	11.	107.	0.	63.	-45.	-122.	.030	-9.2	.104
259	03	14.	106.	0.	65.	-69.	-186.	.028	-11.4	.121
259	04	15.	108.	0.	64.	-92.	-255.	.030	-7.7	.140
259	05	0.	100.	0.	62.	-114.	-319.	.025	-8.7	.056
259	06	4.	41.	0.	62.	-137.	-358.	.005	-51.3	.095
259	07	6.	57.	0.	64.	-160.	-403.	.000	-29.1	.110
259	08	2.	12.	49.	41.	-157.	-406.	.000	-1055.3	.175
259	09	5.	14.	131.	39.	-124.	-380.	.000		
259	10	0.	50.	105.	42.	-69.	-345.	.007	-40.9	.124
259	11	0.	00.	424.	39.	70.	-238.	.020	-11.9	.100
259	12	0.	68.	514.	27.	245.	-88.	.014	-8.9	.023
259	13	17.	172.	446.	35.	393.	-8.	.087	-3.1	.100
259	14	35.	155.	239.	78.	451.	-19.	.053	-9.7	.224
259	15	31.	148.	262.	77.	525.	-9.	.047	-11.0	.212
259	16	13.	138.	364.	73.	630.	38.	.030	-11.1	.166
259	17	13.	232.	282.	47.	715.	27.	.114	-3.3	.142
259	18	14.	166.	167.	65.	751.	-2.	.062	-4.5	.096
259	19	12.	223.	110.	34.	779.	-61.	.113	-2.3	.083
259	20	13.	163.	37.	63.	769.	-135.	.068	-3.9	.095
259	21	32.	155.	0.	74.	742.	-229.	.057	-8.2	.204
259	22	28.	142.	0.	72.	716.	-324.	.050	-7.2	.172
259	23	22.	161.	0.	67.	692.	-414.	.066	-5.0	.135
259	24	18.	213.	0.	63.	669.	-520.	.113	-2.2	.086

Table 2. (continued).

# MONTHLY SUMMARY OF CLIMATIC DATA FOR SEPTEMBER, 1974 STATION: 060000, CAPRICORN METEOROLOGICAL LABORATORY SEA LEVEL, ILLUMINATED LAMINAR RADIATION

FLUXES CALCULATED FROM RECORDS (1974, 1975) USING LIPMAN INTERPOLATION FOR MISSING DATA  
 SEPTEMBER 17, 1974

JULIAN DAY	GMT HOUR	SURFACE HEAT FLUX (WATTS/M <sup>2</sup> )	LATENT HEAT FLUX (WATTS/M <sup>2</sup> )	LONG WAVE RADIATION (WATTS/M <sup>2</sup> )	NET RADIATION (10**4 JOULES/M <sup>2</sup> )	DAILY NET HEAT FLUX (10**4 JOULES/M <sup>2</sup> )	WIND STRESS (NT/M <sup>2</sup> )	RICHTERSON NUMBER	BOWEN RATIO
260	00	11.	213.	61.	0.	0.	.113	-2.2	.086
260	01	11.	139.	63.	-23.	-77.	.044	-5.2	.044
260	02	11.	97.	61.	-45.	-137.	.030	-7.2	.097
260	03	40.	120.	77.	-72.	-250.	.088	-5.0	.238
260	04	33.	141.	81.	-102.	-342.	.039	-15.1	.238
260	05	40.	120.	78.	-130.	-453.	.077	-6.2	.222
260	06	20.	143.	79.	-156.	-543.	.030	-13.2	.197
260	07	30.	148.	77.	-186.	-644.	.057	-8.0	.204
260	08	20.	136.	45.	-185.	-701.	.030	-12.1	.189
260	09	50.	280.	77.	-157.	-793.	.155	-3.1	.195
260	10	30.	102.	71.	-74.	-792.	.090	-4.1	.184
260	11	30.	212.	77.	-64.	-870.	.077	-6.1	.164
260	12	10.	101.	72.	60.	-781.	.014	-28.3	.161
260	13	00.	157.	53.	253.	-645.	.097	-1.0	.010
260	14	20.	162.	53.	411.	-552.	.087	-3.2	.125
260	15	10.	45.	72.	480.	-505.	.010	-42.0	.180
260	16	10.	152.	71.	620.	-426.	.030	-9.3	.111
260	17	00.	57.	54.	725.	-348.	.014	-9.5	.044
260	18	00.	54.	42.	794.	-301.	.010	-20.8	.083
260	19	00.	60.	64.	921.	-297.	.010	-28.1	.114
260	20	00.	70.	63.	816.	-331.	.014	-18.8	.100
260	21	00.	100.	62.	793.	-392.	.025	-8.2	.073
260	22	10.	152.	62.	771.	-474.	.066	-3.5	.084
260	23	10.	132.	60.	750.	-548.	.006	-3.3	.097
260	24	00.	148.	59.	729.	-625.	.076	-2.3	.060

# ATLANTIC OCEAN SURFACE FLUXES AT WASHINGTON FIELD STATION, WASHINGTON

FLUXES CALCULATED FROM COLOURIMETRIC OBSERVATIONS USING LINEAR INTERPOLATION FOR MISSING DATA  
SEPTEMBER 18, 1974

JULIAN DAY	GMT HOUR	SENSIBLE HEAT FLUX (WATTS/M <sup>2</sup> )	LATENT HEAT FLUX (WATTS/M <sup>2</sup> )	RADIATION (WATTS/M <sup>2</sup> )	LONG WAVE RADIATION (WATTS/M <sup>2</sup> )	NET RADIATION (10 <sup>3</sup> JOULES/M <sup>2</sup> )	DAILY NET HEAT FLUX (10 <sup>3</sup> JOULES/M <sup>2</sup> )	WIND STRESS (N/M <sup>2</sup> )	RICHARDSON NUMBER	ROWLEY RATIO
261	00	0	148.	0	59.	0.	0.	.076	-2.3	.060
261	01	11.	149.	0	59.	-21.	-86.	.046	-2.2	.063
261	02	10.	158.	0	59.	-43.	-168.	.076	-2.5	.063
261	03	10.	158.	0	60.	-65.	-251.	.076	-2.9	.078
261	04	11.	171.	0	60.	-80.	-324.	.056	-3.7	.081
261	05	10.	137.	0	59.	-107.	-306.	.066	-3.0	.075
261	06	0	142.	0	60.	-109.	-474.	.056	-3.4	.059
261	07	0	117.	0	59.	-150.	-540.	.048	-4.0	.074
261	08	0	100.	106.	57.	-132.	-571.	.056	-2.9	.040
261	09	1.	127.	317.	45.	-34.	-519.	.054	-1.7	.001
261	10	3.	135.	425.	47.	102.	-433.	.065	-1.0	.025
261	11	1.	112.	537.	52.	276.	-299.	.056	-1.6	.010
261	12	-4.	82.	643.	37.	495.	-109.	.020	-4	-.051
261	13	-3.	63.	832.	48.	777.	152.	.019	-3	-.055
261	14	-10.	144.	809.	47.	1093.	410.	.055	3	-.068
261	15	-11.	163.	889.	47.	1386.	658.	.065	3	-.068
261	16	-5.	85.	509.	40.	1552.	795.	.027	-2	-.057
261	17	-2.	78.	550.	51.	1731.	947.	.024	-1.8	-.027
261	18	-3.	81.	263.	33.	1814.	1002.	.028	-1.1	-.037
261	19	8.	120.	90.	50.	1922.	963.	.048	-4.0	.067
261	20	-2.	80.	29.	30.	1821.	933.	.031	-2.2	-.003
261	21	2.	87.	0	55.	1801.	882.	.025	-4.9	.020
261	22	7.	62.	0	63.	1779.	834.	.013	-20.7	.113
261	23	3.	30.	0	59.	1756.	802.	.004	-49.9	.084
261	24	2.	48.	0	59.	1737.	762.	.006	-27.7	.046

Table 2. (continued).



FLUXES CALCULATED FROM COLUMN 5, 15, 17, 18, 19, 20, 21, 22, 23, 24, 25, 26, 27, 28, 29, 30, 31, 32, 33, 34, 35, 36, 37, 38, 39, 40, 41, 42, 43, 44, 45, 46, 47, 48, 49, 50, 51, 52, 53, 54, 55, 56, 57, 58, 59, 60, 61, 62, 63, 64, 65, 66, 67, 68, 69, 70, 71, 72, 73, 74, 75, 76, 77, 78, 79, 80, 81, 82, 83, 84, 85, 86, 87, 88, 89, 90, 91, 92, 93, 94, 95, 96, 97, 98, 99, 100, 101, 102, 103, 104, 105, 106, 107, 108, 109, 110, 111, 112, 113, 114, 115, 116, 117, 118, 119, 120, 121, 122, 123, 124, 125, 126, 127, 128, 129, 130, 131, 132, 133, 134, 135, 136, 137, 138, 139, 140, 141, 142, 143, 144, 145, 146, 147, 148, 149, 150, 151, 152, 153, 154, 155, 156, 157, 158, 159, 160, 161, 162, 163, 164, 165, 166, 167, 168, 169, 170, 171, 172, 173, 174, 175, 176, 177, 178, 179, 180, 181, 182, 183, 184, 185, 186, 187, 188, 189, 190, 191, 192, 193, 194, 195, 196, 197, 198, 199, 200, 201, 202, 203, 204, 205, 206, 207, 208, 209, 210, 211, 212, 213, 214, 215, 216, 217, 218, 219, 220, 221, 222, 223, 224, 225, 226, 227, 228, 229, 230, 231, 232, 233, 234, 235, 236, 237, 238, 239, 240, 241, 242, 243, 244, 245, 246, 247, 248, 249, 250, 251, 252, 253, 254, 255, 256, 257, 258, 259, 260, 261, 262, 263, 264, 265, 266, 267, 268, 269, 270, 271, 272, 273, 274, 275, 276, 277, 278, 279, 280, 281, 282, 283, 284, 285, 286, 287, 288, 289, 290, 291, 292, 293, 294, 295, 296, 297, 298, 299, 300, 301, 302, 303, 304, 305, 306, 307, 308, 309, 310, 311, 312, 313, 314, 315, 316, 317, 318, 319, 320, 321, 322, 323, 324, 325, 326, 327, 328, 329, 330, 331, 332, 333, 334, 335, 336, 337, 338, 339, 340, 341, 342, 343, 344, 345, 346, 347, 348, 349, 350, 351, 352, 353, 354, 355, 356, 357, 358, 359, 360, 361, 362, 363, 364, 365, 366, 367, 368, 369, 370, 371, 372, 373, 374, 375, 376, 377, 378, 379, 380, 381, 382, 383, 384, 385, 386, 387, 388, 389, 390, 391, 392, 393, 394, 395, 396, 397, 398, 399, 400, 401, 402, 403, 404, 405, 406, 407, 408, 409, 410, 411, 412, 413, 414, 415, 416, 417, 418, 419, 420, 421, 422, 423, 424, 425, 426, 427, 428, 429, 430, 431, 432, 433, 434, 435, 436, 437, 438, 439, 440, 441, 442, 443, 444, 445, 446, 447, 448, 449, 450, 451, 452, 453, 454, 455, 456, 457, 458, 459, 460, 461, 462, 463, 464, 465, 466, 467, 468, 469, 470, 471, 472, 473, 474, 475, 476, 477, 478, 479, 480, 481, 482, 483, 484, 485, 486, 487, 488, 489, 490, 491, 492, 493, 494, 495, 496, 497, 498, 499, 500, 501, 502, 503, 504, 505, 506, 507, 508, 509, 510, 511, 512, 513, 514, 515, 516, 517, 518, 519, 520, 521, 522, 523, 524, 525, 526, 527, 528, 529, 530, 531, 532, 533, 534, 535, 536, 537, 538, 539, 540, 541, 542, 543, 544, 545, 546, 547, 548, 549, 550, 551, 552, 553, 554, 555, 556, 557, 558, 559, 560, 561, 562, 563, 564, 565, 566, 567, 568, 569, 570, 571, 572, 573, 574, 575, 576, 577, 578, 579, 580, 581, 582, 583, 584, 585, 586, 587, 588, 589, 590, 591, 592, 593, 594, 595, 596, 597, 598, 599, 600, 601, 602, 603, 604, 605, 606, 607, 608, 609, 610, 611, 612, 613, 614, 615, 616, 617, 618, 619, 620, 621, 622, 623, 624, 625, 626, 627, 628, 629, 630, 631, 632, 633, 634, 635, 636, 637, 638, 639, 640, 641, 642, 643, 644, 645, 646, 647, 648, 649, 650, 651, 652, 653, 654, 655, 656, 657, 658, 659, 660, 661, 662, 663, 664, 665, 666, 667, 668, 669, 670, 671, 672, 673, 674, 675, 676, 677, 678, 679, 680, 681, 682, 683, 684, 685, 686, 687, 688, 689, 690, 691, 692, 693, 694, 695, 696, 697, 698, 699, 700, 701, 702, 703, 704, 705, 706, 707, 708, 709, 710, 711, 712, 713, 714, 715, 716, 717, 718, 719, 720, 721, 722, 723, 724, 725, 726, 727, 728, 729, 730, 731, 732, 733, 734, 735, 736, 737, 738, 739, 740, 741, 742, 743, 744, 745, 746, 747, 748, 749, 750, 751, 752, 753, 754, 755, 756, 757, 758, 759, 760, 761, 762, 763, 764, 765, 766, 767, 768, 769, 770, 771, 772, 773, 774, 775, 776, 777, 778, 779, 780, 781, 782, 783, 784, 785, 786, 787, 788, 789, 790, 791, 792, 793, 794, 795, 796, 797, 798, 799, 800, 801, 802, 803, 804, 805, 806, 807, 808, 809, 810, 811, 812, 813, 814, 815, 816, 817, 818, 819, 820, 821, 822, 823, 824, 825, 826, 827, 828, 829, 830, 831, 832, 833, 834, 835, 836, 837, 838, 839, 840, 841, 842, 843, 844, 845, 846, 847, 848, 849, 850, 851, 852, 853, 854, 855, 856, 857, 858, 859, 860, 861, 862, 863, 864, 865, 866, 867, 868, 869, 870, 871, 872, 873, 874, 875, 876, 877, 878, 879, 880, 881, 882, 883, 884, 885, 886, 887, 888, 889, 890, 891, 892, 893, 894, 895, 896, 897, 898, 899, 900, 901, 902, 903, 904, 905, 906, 907, 908, 909, 910, 911, 912, 913, 914, 915, 916, 917, 918, 919, 920, 921, 922, 923, 924, 925, 926, 927, 928, 929, 930, 931, 932, 933, 934, 935, 936, 937, 938, 939, 940, 941, 942, 943, 944, 945, 946, 947, 948, 949, 950, 951, 952, 953, 954, 955, 956, 957, 958, 959, 960, 961, 962, 963, 964, 965, 966, 967, 968, 969, 970, 971, 972, 973, 974, 975, 976, 977, 978, 979, 980, 981, 982, 983, 984, 985, 986, 987, 988, 989, 990, 991, 992, 993, 994, 995, 996, 997, 998, 999, 1000

FLUXES CALCULATED FROM COLUMN 5, 15, 17, 18, 19, 20, 21, 22, 23, 24, 25, 26, 27, 28, 29, 30, 31, 32, 33, 34, 35, 36, 37, 38, 39, 40, 41, 42, 43, 44, 45, 46, 47, 48, 49, 50, 51, 52, 53, 54, 55, 56, 57, 58, 59, 60, 61, 62, 63, 64, 65, 66, 67, 68, 69, 70, 71, 72, 73, 74, 75, 76, 77, 78, 79, 80, 81, 82, 83, 84, 85, 86, 87, 88, 89, 90, 91, 92, 93, 94, 95, 96, 97, 98, 99, 100, 101, 102, 103, 104, 105, 106, 107, 108, 109, 110, 111, 112, 113, 114, 115, 116, 117, 118, 119, 120, 121, 122, 123, 124, 125, 126, 127, 128, 129, 130, 131, 132, 133, 134, 135, 136, 137, 138, 139, 140, 141, 142, 143, 144, 145, 146, 147, 148, 149, 150, 151, 152, 153, 154, 155, 156, 157, 158, 159, 160, 161, 162, 163, 164, 165, 166, 167, 168, 169, 170, 171, 172, 173, 174, 175, 176, 177, 178, 179, 180, 181, 182, 183, 184, 185, 186, 187, 188, 189, 190, 191, 192, 193, 194, 195, 196, 197, 198, 199, 200, 201, 202, 203, 204, 205, 206, 207, 208, 209, 210, 211, 212, 213, 214, 215, 216, 217, 218, 219, 220, 221, 222, 223, 224, 225, 226, 227, 228, 229, 230, 231, 232, 233, 234, 235, 236, 237, 238, 239, 240, 241, 242, 243, 244, 245, 246, 247, 248, 249, 250, 251, 252, 253, 254, 255, 256, 257, 258, 259, 260, 261, 262, 263, 264, 265, 266, 267, 268, 269, 270, 271, 272, 273, 274, 275, 276, 277, 278, 279, 280, 281, 282, 283, 284, 285, 286, 287, 288, 289, 290, 291, 292, 293, 294, 295, 296, 297, 298, 299, 300, 301, 302, 303, 304, 305, 306, 307, 308, 309, 310, 311, 312, 313, 314, 315, 316, 317, 318, 319, 320, 321, 322, 323, 324, 325, 326, 327, 328, 329, 330, 331, 332, 333, 334, 335, 336, 337, 338, 339, 340, 341, 342, 343, 344, 345, 346, 347, 348, 349, 350, 351, 352, 353, 354, 355, 356, 357, 358, 359, 360, 361, 362, 363, 364, 365, 366, 367, 368, 369, 370, 371, 372, 373, 374, 375, 376, 377, 378, 379, 380, 381, 382, 383, 384, 385, 386, 387, 388, 389, 390, 391, 392, 393, 394, 395, 396, 397, 398, 399, 400, 401, 402, 403, 404, 405, 406, 407, 408, 409, 410, 411, 412, 413, 414, 415, 416, 417, 418, 419, 420, 421, 422, 423, 424, 425, 426, 427, 428, 429, 430, 431, 432, 433, 434, 435, 436, 437, 438, 439, 440, 441, 442, 443, 444, 445, 446, 447, 448, 449, 450, 451, 452, 453, 454, 455, 456, 457, 458, 459, 460, 461, 462, 463, 464, 465, 466, 467, 468, 469, 470, 471, 472, 473, 474, 475, 476, 477, 478, 479, 480, 481, 482, 483, 484, 485, 486, 487, 488, 489, 490, 491, 492, 493, 494, 495, 496, 497, 498, 499, 500, 501, 502, 503, 504, 505, 506, 507, 508, 509, 510, 511, 512, 513, 514, 515, 516, 517, 518, 519, 520, 521, 522, 523, 524, 525, 526, 527, 528, 529, 530, 531, 532, 533, 534, 535, 536, 537, 538, 539, 540, 541, 542, 543, 544, 545, 546, 547, 548, 549, 550, 551, 552, 553, 554, 555, 556, 557, 558, 559, 560, 561, 562, 563, 564, 565, 566, 567, 568, 569, 570, 571, 572, 573, 574, 575, 576, 577, 578, 579, 580, 581, 582, 583, 584, 585, 586, 587, 588, 589, 590, 591, 592, 593, 594, 595, 596, 597, 598, 599, 600, 601, 602, 603, 604, 605, 606, 607, 608, 609, 610, 611, 612, 613, 614, 615, 616, 617, 618, 619, 620, 621, 622, 623, 624, 625, 626, 627, 628, 629, 630, 631, 632, 633, 634, 635, 636, 637, 638, 639, 640, 641, 642, 643, 644, 645, 646, 647, 648, 649, 650, 651, 652, 653, 654, 655, 656, 657, 658, 659, 660, 661, 662, 663, 664, 665, 666, 667, 668, 669, 670, 671, 672, 673, 674, 675, 676, 677, 678, 679, 680, 681, 682, 683, 684, 685, 686, 687, 688, 689, 690, 691, 692, 693, 694, 695, 696, 697, 698, 699, 700, 701, 702, 703, 704, 705, 706, 707, 708, 709, 710, 711, 712, 713, 714, 715, 716, 717, 718, 719, 720, 721, 722, 723, 724, 725, 726, 727, 728, 729, 730, 731, 732, 733, 734, 735, 736, 737, 738, 739, 740, 741, 742, 743, 744, 745, 746, 747, 748, 749, 750, 751, 752, 753, 754, 755, 756, 757, 758, 759, 760, 761, 762, 763, 764, 765, 766, 767, 768, 769, 770, 771, 772, 773, 774, 775, 776, 777, 778, 779, 780, 781, 782, 783, 784, 785, 786, 787, 788, 789, 790, 791, 792, 793, 794, 795, 796, 797, 798, 799, 800, 801, 802, 803, 804, 805, 806, 807, 808, 809, 810, 811, 812, 813, 814, 815, 816, 817, 818, 819, 820, 821, 822, 823, 824, 825, 826, 827, 828, 829, 830, 831, 832, 833, 834, 835, 836, 837, 838, 839, 840, 841, 842, 843, 844, 845, 846, 847, 848, 849, 850, 851, 852, 853, 854, 855, 856, 857, 858, 859, 860, 861, 862, 863, 864, 865, 866, 867, 868, 869, 870, 871, 872, 873, 874, 875, 876, 877, 878, 879, 880, 881, 882, 883, 884, 885, 886, 887, 888, 889, 890, 891, 892, 893, 894, 895, 896, 897, 898, 899, 900, 901, 902, 903, 904, 905, 906, 907, 908, 909, 910, 911, 912, 913, 914, 915, 916, 917, 918, 919, 920, 921, 922, 923, 924, 925, 926, 927, 928, 929, 930, 931, 932, 933, 934, 935, 936, 937, 938, 939, 940, 941, 942, 943, 944, 945, 946, 947, 948, 949, 950, 951, 952, 953, 954, 955, 956, 957, 958, 959, 960, 961, 962, 963, 964, 965, 966, 967, 968, 969, 970, 971, 972, 973, 974, 975, 976, 977, 978, 979, 980, 981, 982, 983, 984, 985, 986, 987, 988, 989, 990, 991, 992, 993, 994, 995, 996, 997, 998, 999, 1000

JULIAN DAY	GMT HOUR	SENSIBLE HEAT FLUX (WATTS/M <sup>2</sup> )	LATENT HEAT FLUX (WATTS/M <sup>2</sup> )	RADIATION (WATTS/M <sup>2</sup> )	LONG WAVE RADIATION (WATTS/M <sup>2</sup> )	NET RADIATION (10 <sup>10</sup> 4 JOULES/M <sup>2</sup> )	DAILY NET HEAT FLUX (10 <sup>10</sup> 4 JOULES/M <sup>2</sup> )	WIND STRESS (N/MT)	DIFFUSION STRESS (N/MT)	POWER DATA
262	00	1.	65.	0.	50.	0.	0.	.006	-27.7	.046
262	01	1.	67.	0.	54.	-19.	-37.	.009	-12.7	.030
262	02	1.	67.	0.	55.	-39.	-40.	.032	-4.3	.046
262	03	1.	146.	0.	70.	-64.	-173.	.037	-9.5	.090
262	04	7.	80.	0.	50.	-80.	-228.	.029	-7.1	.084
262	05	7.	112.	0.	57.	-105.	-202.	.040	-3.3	.061
262	06	0.	36.	0.	75.	-133.	-334.	.003	-142.5	.225
262	07	12.	60.	0.	60.	-158.	-380.	.014	-26.3	.170
262	08	5.	10.	12.	53.	-173.	-400.	.000		
262	09	5.	10.	41.	69.	-183.	-424.	.000		
262	10	3.	72.	160.	65.	-145.	-396.	.002	-210.7	.145
262	11	2.	21.	303.	44.	-52.	-211.	.002	-160.3	.104
262	12	3.	36.	351.	44.	62.	-211.	.004	-61.3	.080
262	13	1.	15.	378.	50.	177.	-102.	.000		
262	14	4.	70.	367.	56.	289.	-17.	.010	-8.5	.050
262	15	2.	40.	351.	32.	408.	84.	.007	-15.0	.000
262	16	2.	76.	207.	28.	472.	120.	.010	-7.8	.030
262	17	4.	15.	157.	37.	515.	145.	.007	-31.4	.070
262	18	7.	85.	187.	37.	533.	130.	.025	-8.6	.087
262	19	0.	46.	35.	64.	523.	101.	.007	-45.0	.130
262	20	25.	138.	7.	69.	501.	20.	.057	-6.8	.195
262	21	1.	70.	0.	68.	470.	-34.	.014	-27.0	.195
262	22	0.	50.	0.	65.	453.	-82.	.010	-32.7	.146
262	23	11.	74.	0.	63.	430.	-136.	.010	-15.4	.145
262	24	10.	03.	0.	66.	406.	-197.	.025	-13.1	.147

Table 2. (continued).

NATIONAL OCEANOGRAPHIC ADMINISTRATION  
ATLANTIC OCEANOGRAPHIC METEOROLOGICAL LABORATORIES  
SPACE AIR INTERACTION LABORATORY

FLUXES CALCULATED FROM COLUMBUS ISFLIN (-14°F) HOURLY METEOROLOGICAL OBSERVATIONS USING LINEAR INTERPOLATION; FOR MISSING DATA  
SEPTEMBER 20, 1974

JULIAN DAY	GMT HOUR	SENSIBLE HEAT FLUX (WATTS/M <sup>2</sup> )	LATENT HEAT FLUX (WATTS/M <sup>2</sup> )	RADIATION (WATTS/M <sup>2</sup> )	LONG WAVE RADIATION (WATTS/M <sup>2</sup> )	NET RADIATION (10**4 JOULES/M <sup>2</sup> )	DAILY NET HEAT FLUX (10**4 JOULES/M <sup>2</sup> )	WIND STRESS (NT/M <sup>2</sup> )	RYCHARDSON NUMBER	POWER RATIO
263	00	14.	93.	0.	66.	0.	0.	.025	-13.1	.147
263	01	12.	56.	0.	50.	-21.	-46.	.025	-10.7	.217
263	02	9.	73.	0.	64.	-44.	-98.	.014	-20.0	.113
263	03	11.	96.	0.	64.	-67.	-159.	.025	-11.4	.113
263	04	10.	86.	0.	61.	-89.	-216.	.025	-10.5	.118
263	05	7.	11.	0.	63.	-112.	-244.	.000		
263	06	3.	11.	0.	61.	-134.	-271.	.000		
263	07	3.	14.	51.	62.	-138.	-281.	.000		
263	08	1.	10.	146.	55.	-105.	-253.	.000		
263	09	2.	13.	376.	58.	9.	-143.	.000		
263	10	1.	12.	574.	55.	196.	39.	.000		
263	11	1.	40.	607.	53.	428.	256.	.007	-17.4	.026
263	12	1.	61.	753.	52.	640.	486.	.014	-6.7	.008
263	13	6.	81.	636.	57.	899.	663.	.025	-7.5	.075
263	14	2.	32.	582.	57.	1076.	840.	.003	-54.8	.062
263	15	1.	24.	516.	50.	1242.	995.	.002	-122.0	.048
263	16	1.	20.	406.	50.	1367.	1113.	.000		
263	17	0.	0.	312.	57.	1459.	1205.	.000		
263	18	2.	17.	136.	57.	1488.	1227.	.000		
263	19	0.	0.	41.	55.	1483.	1222.	.000		
263	20	0.	0.	9.	55.	1466.	1206.	.000		
263	21	0.	0.	0.	54.	1447.	1186.	.000		

Table 2. (continued).

and (5.2.28) were used. The longwave back radiation was calculated using (5.3.1); the wind stress was calculated using (5.2.14). The Bowen ratio is the ratio of sensible to latent heat flux. The daily net radiation,  $R_{net}$ , is the daily total incoming less back radiation, i.e.,

$$R_{net \ ij} = \begin{cases} 0 & \text{for } i=0 \\ \sum_{k=1}^i (Q_{Rk} - Q_{Bk}) \cdot 3600 & \text{for } i=1,2,\dots,24, \end{cases} \quad (6.2)$$

where  $i$  is the hour of the day and  $j$  is the day. The daily net heat flux is the sum of the daily total incoming radiation and the sensible and latent heat transport, i.e.,

$$H_{net \ ij} = \begin{cases} 0 \\ \sum_{k=1}^i (Q_{Rk} - Q_{sk} - Q_{Lk} - Q_{Bk}) \cdot 3600 & \text{for } i=1,2,\dots,24. \end{cases} \quad (6.3)$$

The Richardson number was calculated using (5.2.2).

The values in Table 2 of sensible and latent heat fluxes and long-wave back radiation are graphically displayed in



Figure 18. The values of wind stress, daily net radiation, and daily net heat flux are graphed in Figure 19.

The net heat loss during the 18-day period of September 2 through September 19, 1974, amounts to  $2.225 \times 10^7$  joule  $\text{m}^{-2}$ . If this loss were distributed uniformly over a depth of 25 m, a net cooling of approximately  $0.2^\circ\text{C}$  would have occurred over the layer.

# COLUMBUS ISELIN (GATE) CALCULATED FLUXES

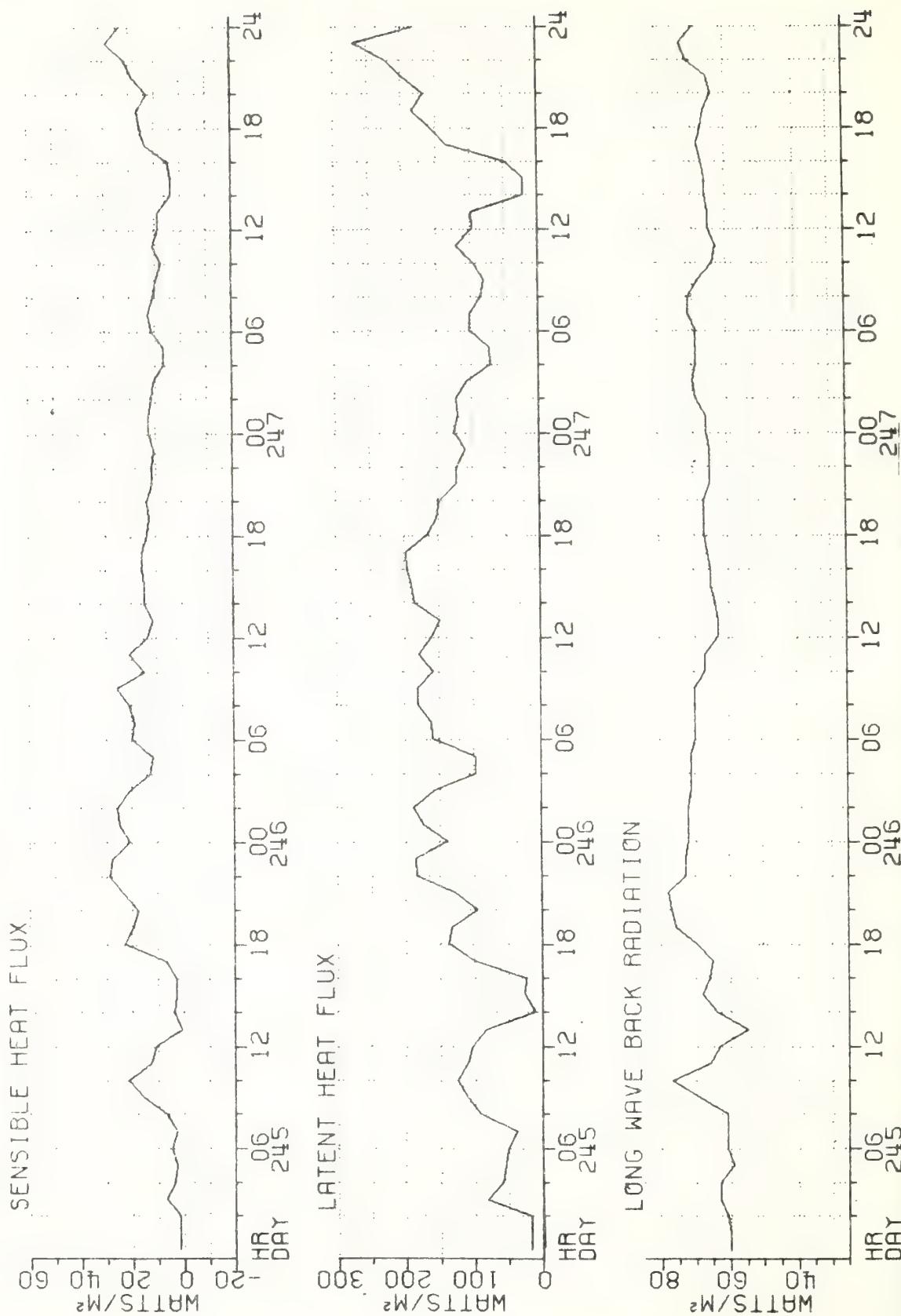
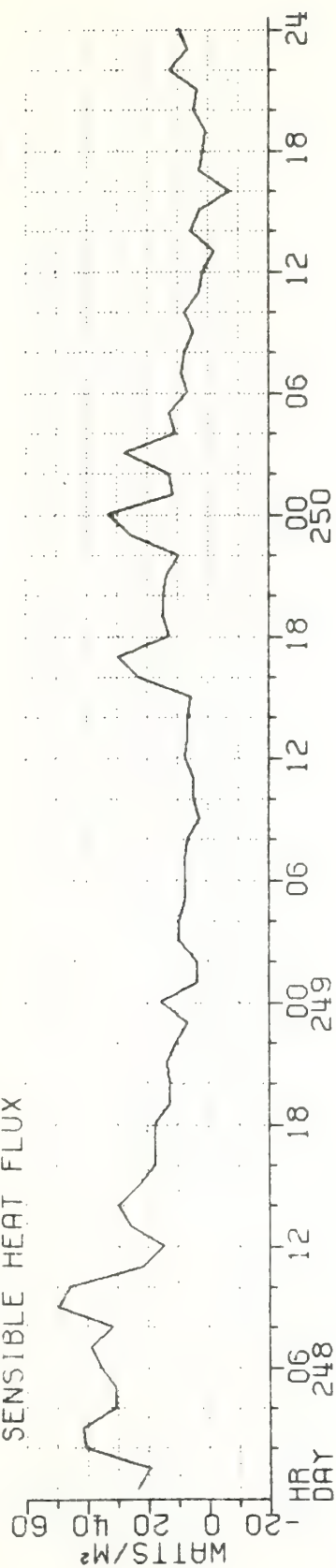
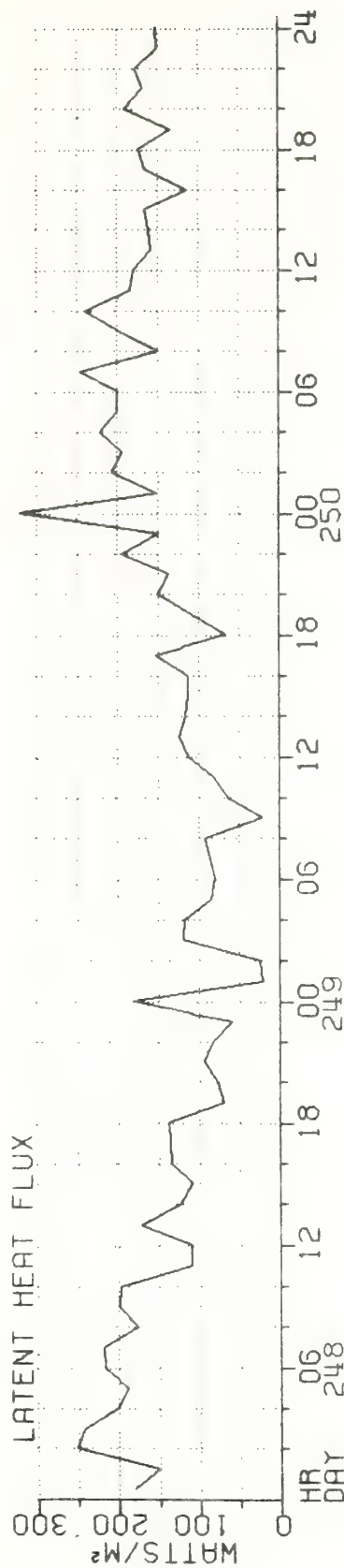


Figure 18. Sensible and latent heat fluxes and longwave back radiation

## SENSIBLE HEAT FLUX



## LATENT HEAT FLUX



## LONG WAVE BACK RADIATION

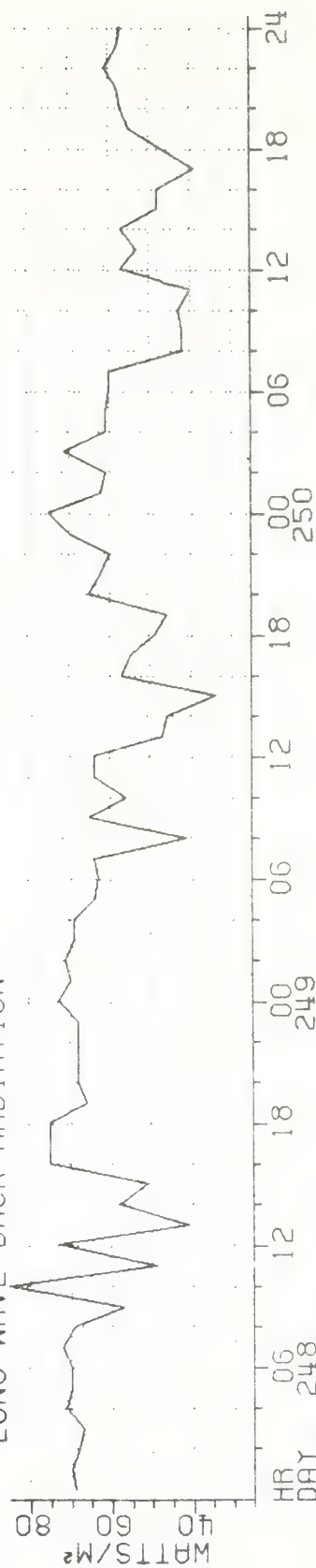


Figure 18. (continued).



# COLUMBUS ISELIN (GATE) CALCULATED FLUXES

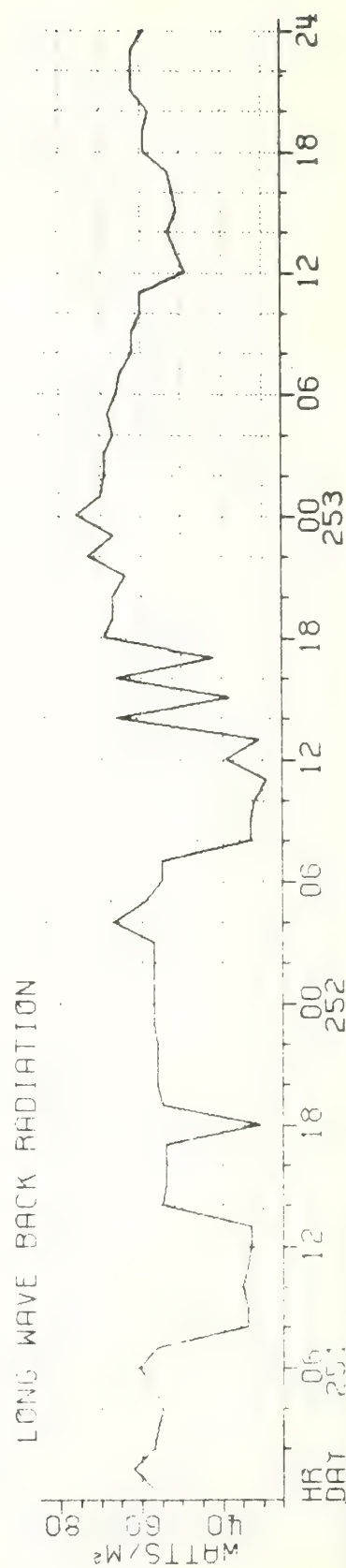
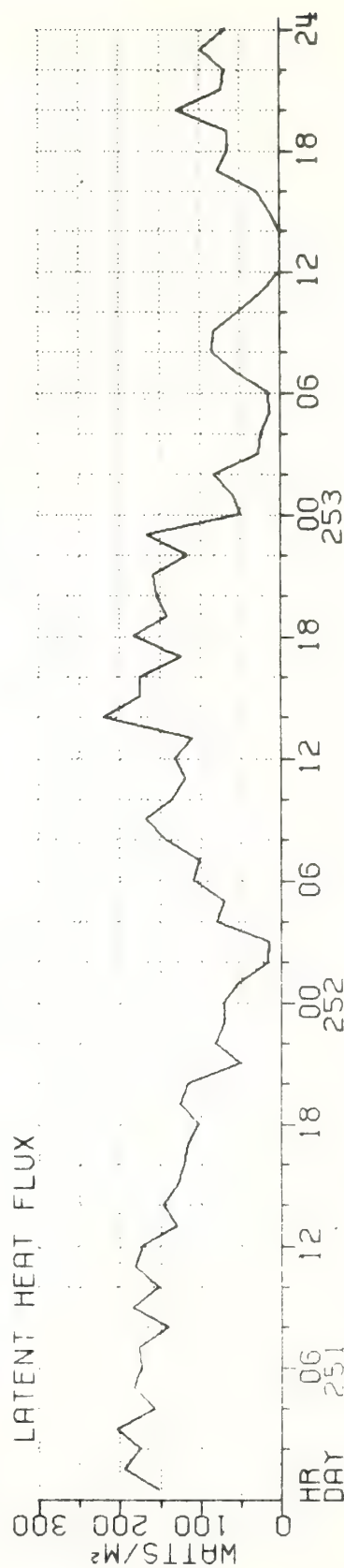
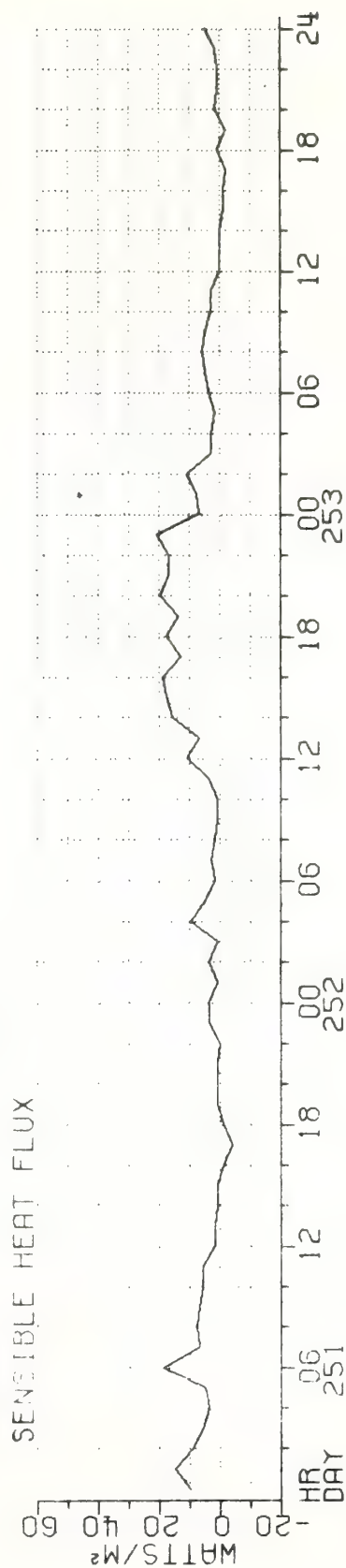


Figure 18. (continued).

# COLUMBUS ISELIN (GATE) CALCULATED FLUXES

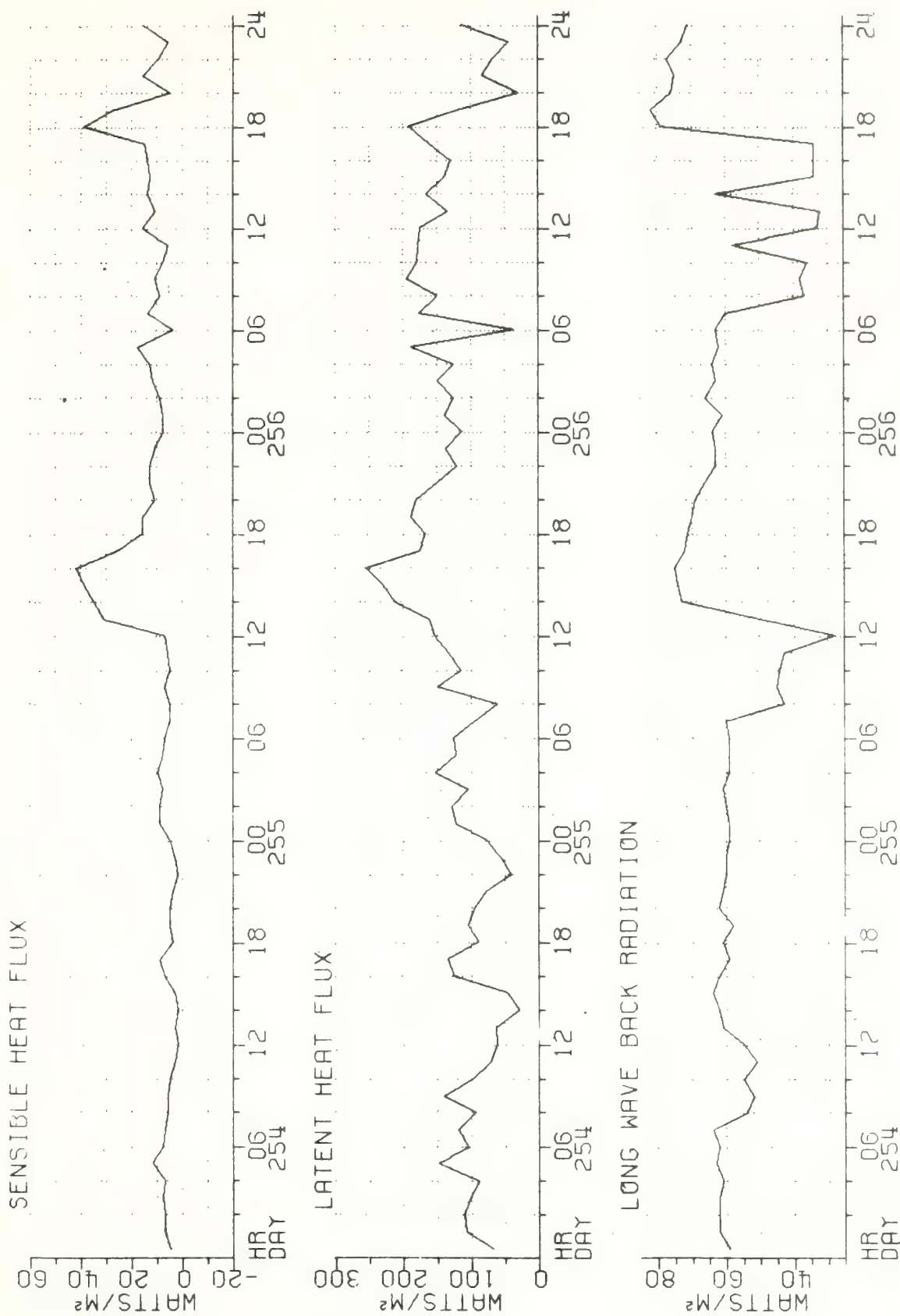


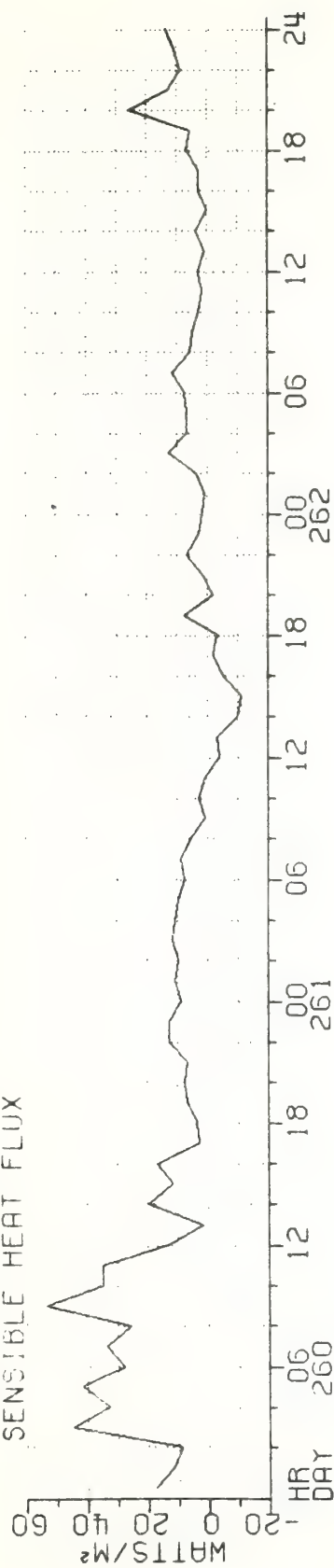
Figure 18. (continued)

[illegible]

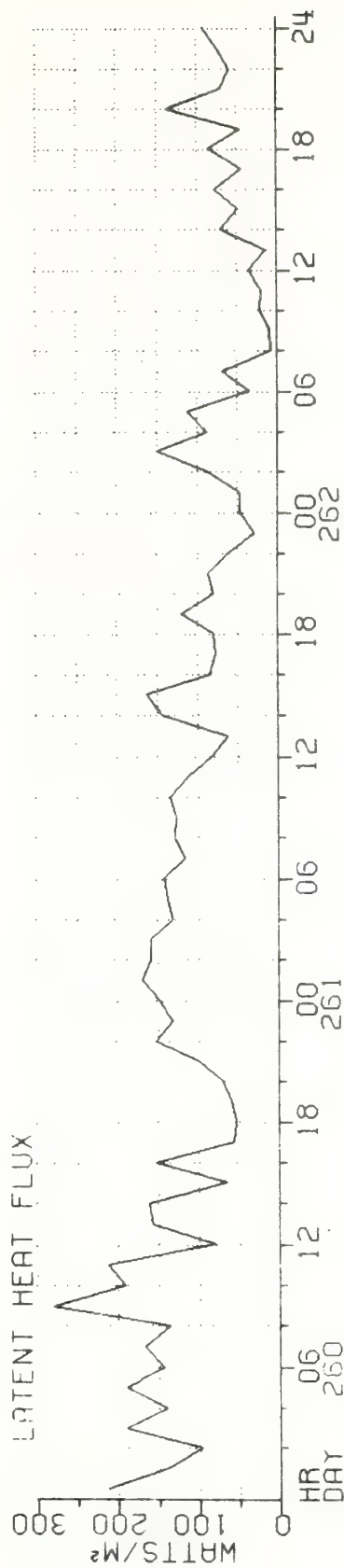
Figure 18. (continued).



# SENSIBLE HEAT FLUX



## LATENT HEAT FLUX



# LONG WAVE BACK RADIATION

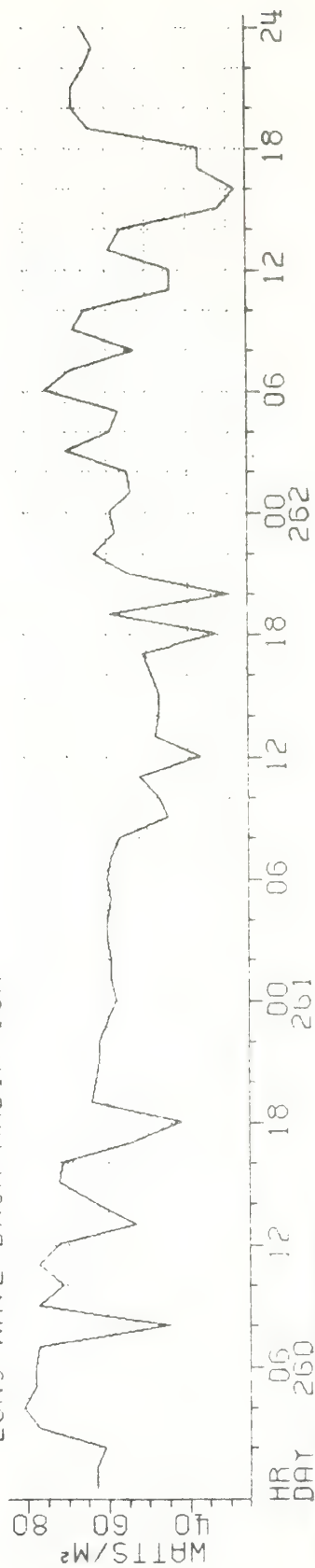
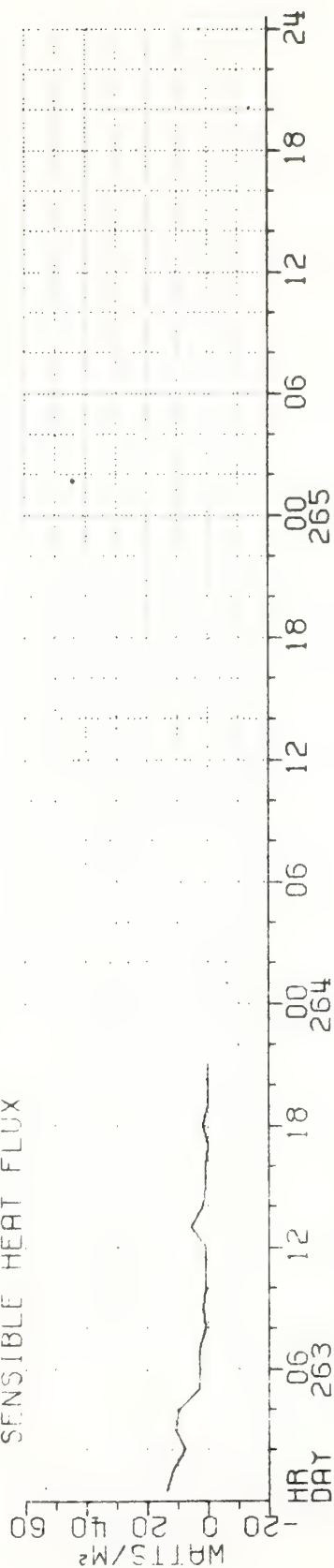


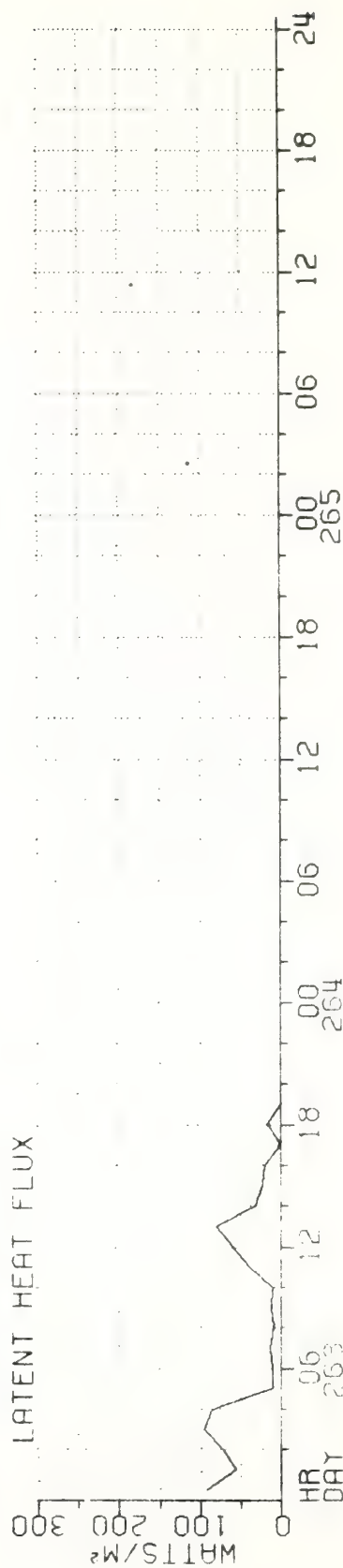
Figure 18. (continued).

# COLUMBUS ISLIN (GATE) CALCULATED FLUXES

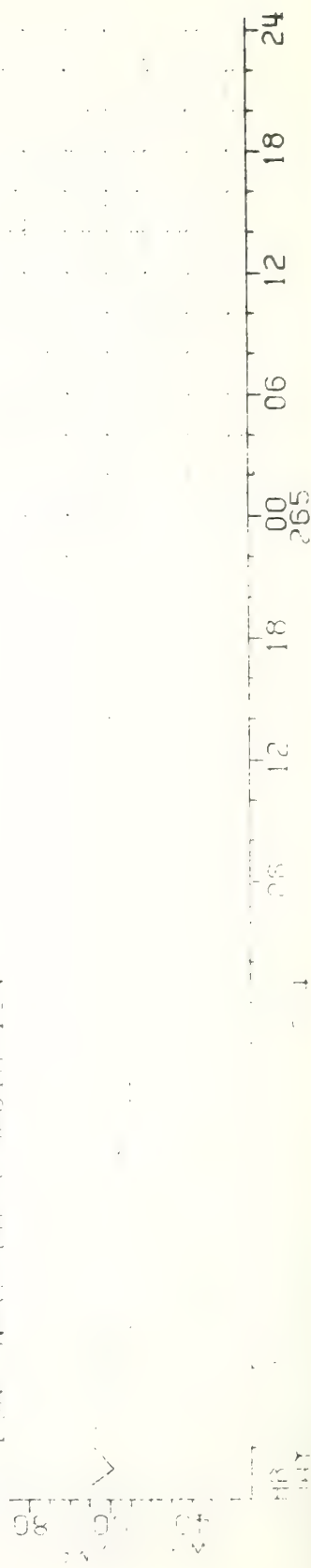
SENSIBLE HEAT FLUX



LATENT HEAT FLUX

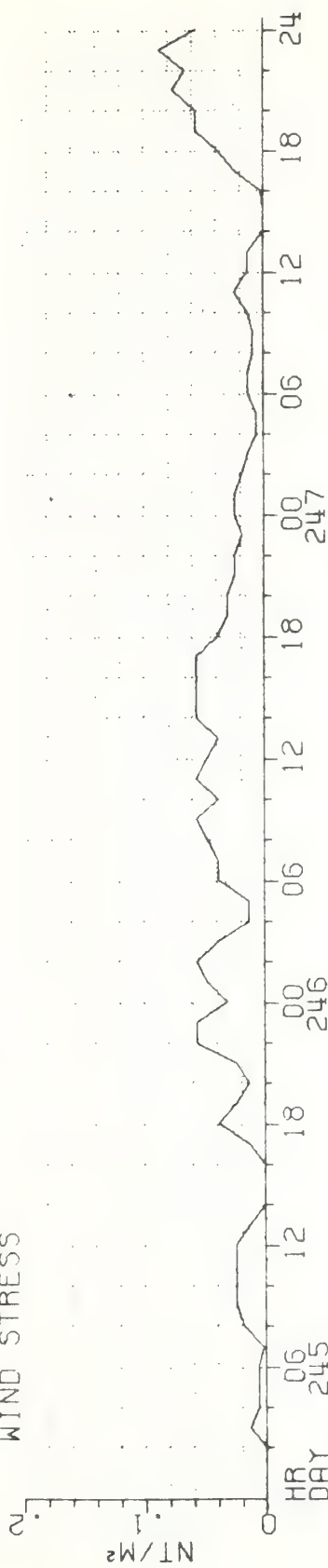


LONG WAVE RADIATION

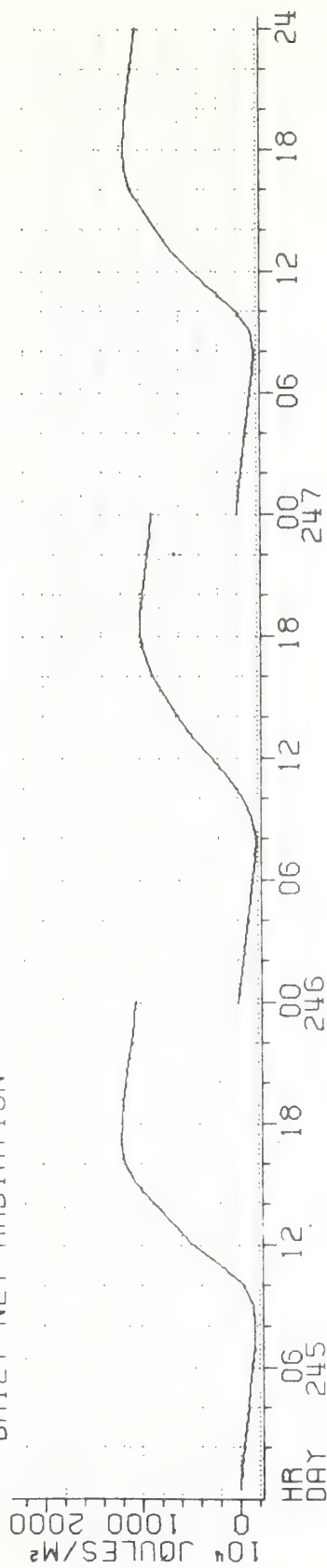


# COLUMBUS ISELIN (GATE) CALCULATED FLUXES

WIND STRESS



DAILY NET RADIATION



DAILY NET HEAT FLUX

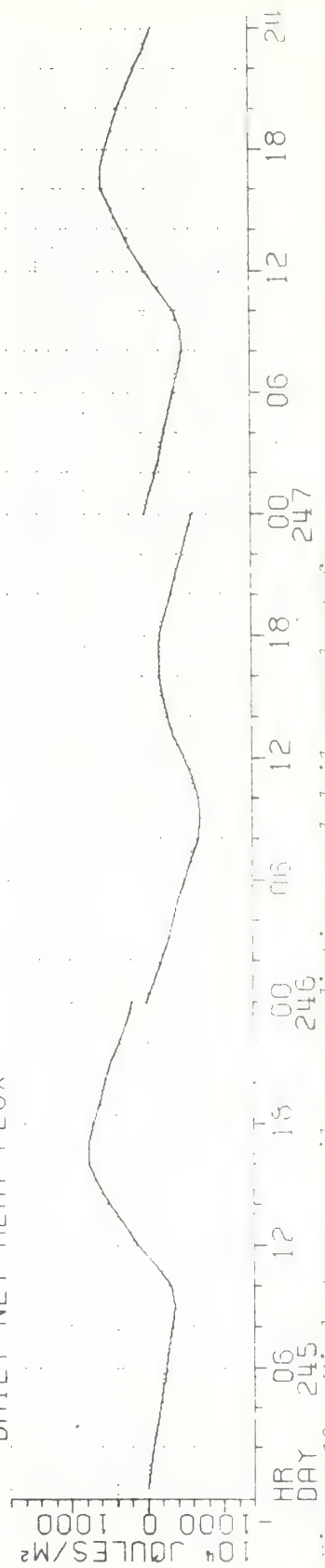


Figure 12. Wind stress, radiation, and daily net heat flux.



# COLUMBUS ISELIN (GATE) CALCULATED FLUXES

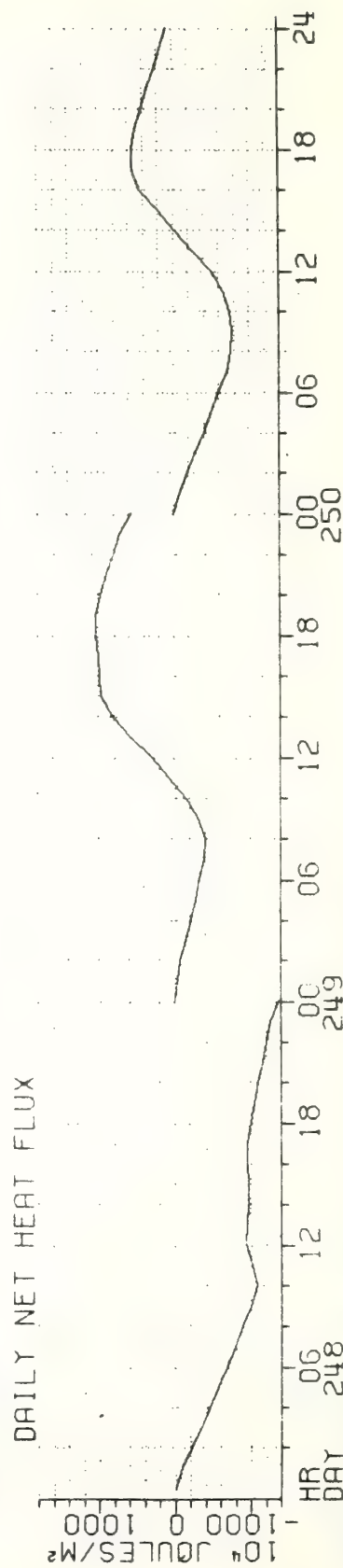
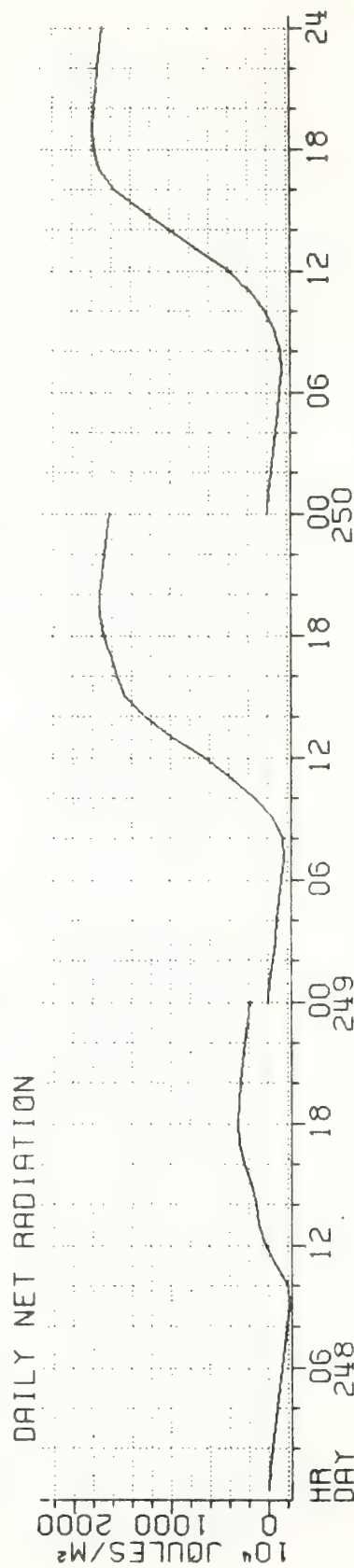
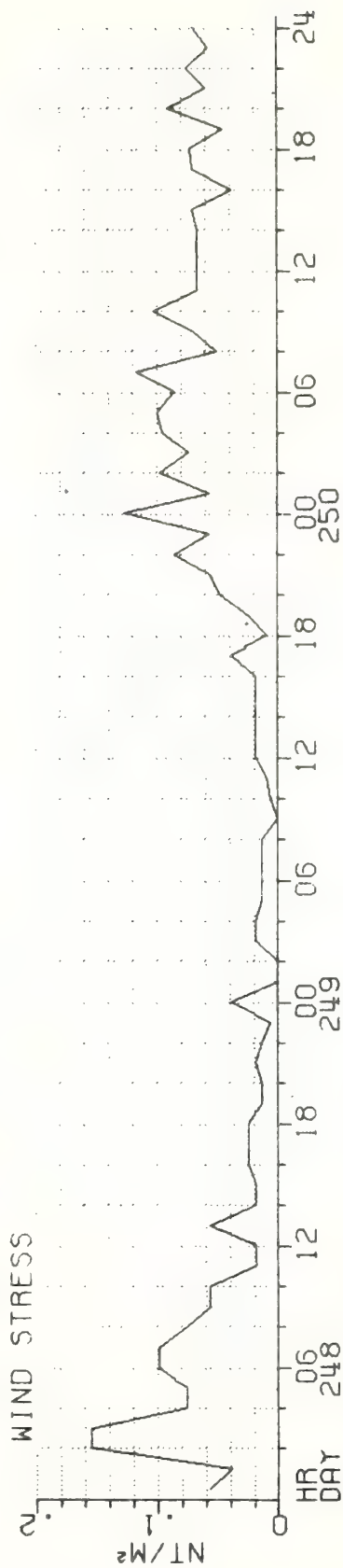


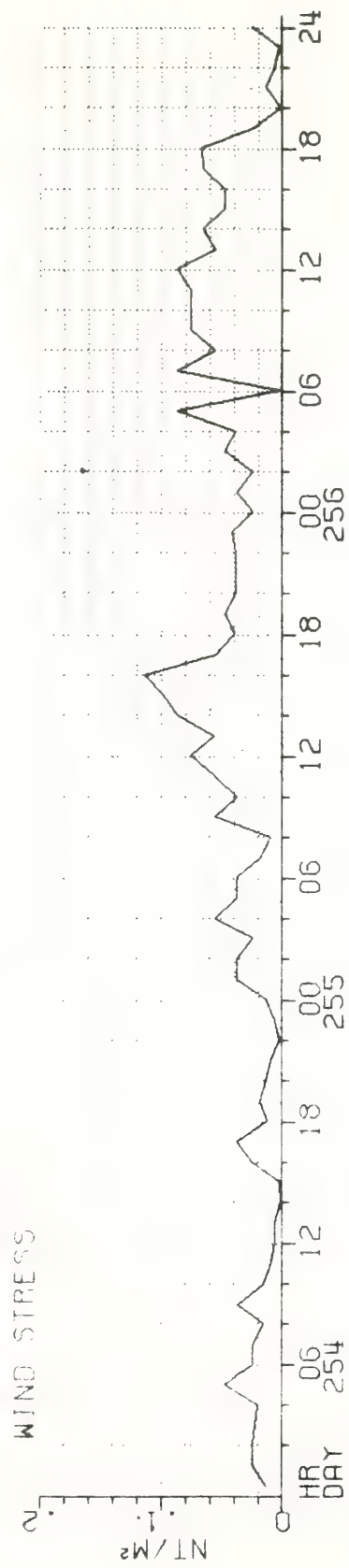
Figure 19. (continued).

The figure consists of three vertically stacked line graphs sharing a common x-axis representing time from Day 251 to Day 253. The x-axis is labeled with 'DAY' and 'HR' (Hour) and has major ticks at 00, 06, 12, 18, and 24 for each day.

- Top Graph: WIND STRESS**
  - Y-axis: NT/M<sup>2</sup>, ranging from 0 to 0.2.
  - Line: Shows highly variable wind stress throughout the period, with peaks reaching approximately 0.15 NT/M<sup>2</sup> and troughs near 0.
- Middle Graph: DAILY NET RADIATION**
  - Y-axis: 10<sup>4</sup> JOULES/M<sup>2</sup>, ranging from 0 to 2000.
  - Line: Shows a clear diurnal cycle. Radiation is near zero during the night (approx. 00-06 hours) and peaks at approximately 1800 10<sup>4</sup> JOULES/M<sup>2</sup> during the day (approx. 12-18 hours).
- Bottom Graph: DAILY NET HEAT FLUX**
  - Y-axis: 10<sup>4</sup> JOULES/M<sup>2</sup>, ranging from -1000 to 1000.
  - Line: Shows a diurnal cycle similar to radiation but with lower magnitude. It is negative (cooling) during the night, reaching about -500 10<sup>4</sup> JOULES/M<sup>2</sup>, and positive (warming) during the day, peaking at about 500 10<sup>4</sup> JOULES/M<sup>2</sup>.

Il termine *illegittimo*.

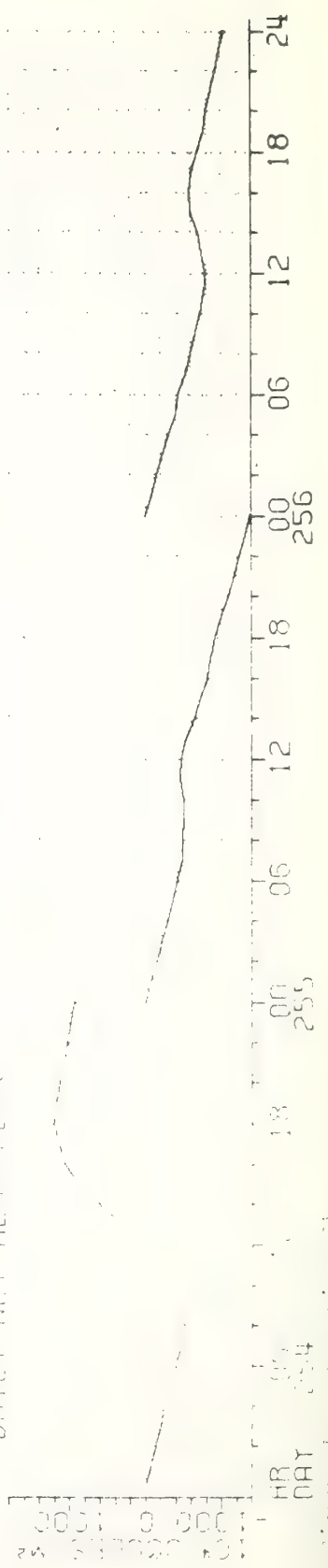
# COLUMBIA ISLE (IN IGATE) CALCULATED FLUXES



## DAILY NET RADIATION



## DAILY NET HEAT FLUX





# COLUMBUS ISELIN (GATE) CALCULATED FLUXES

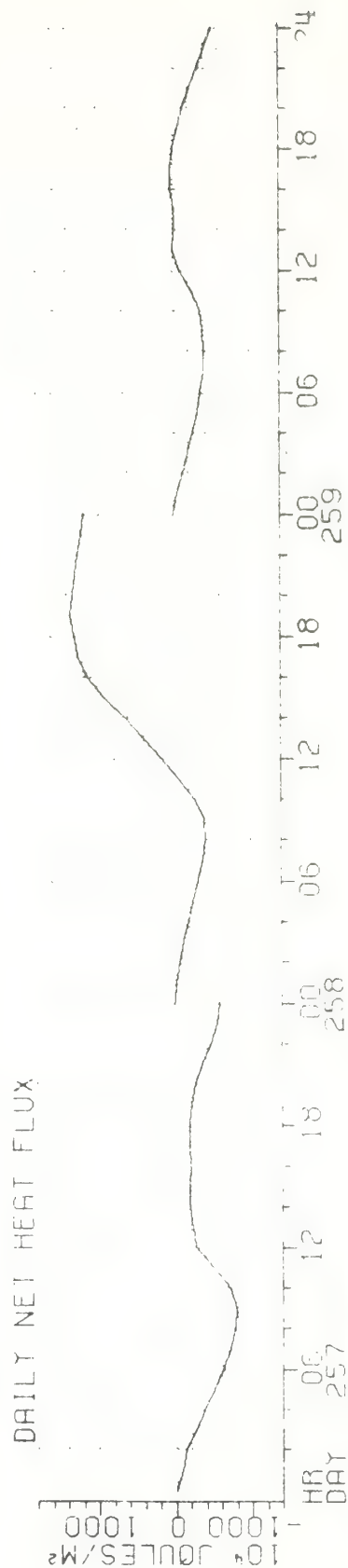
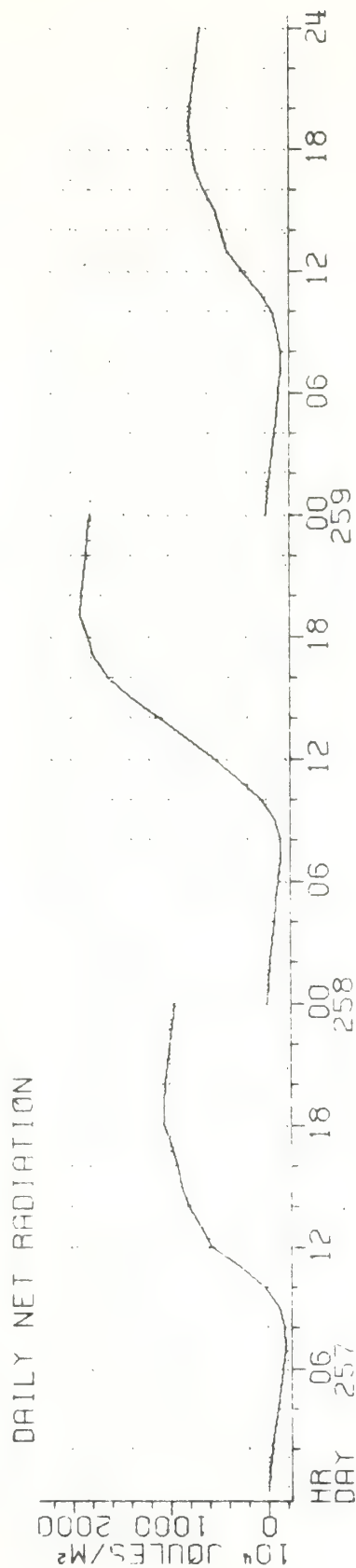
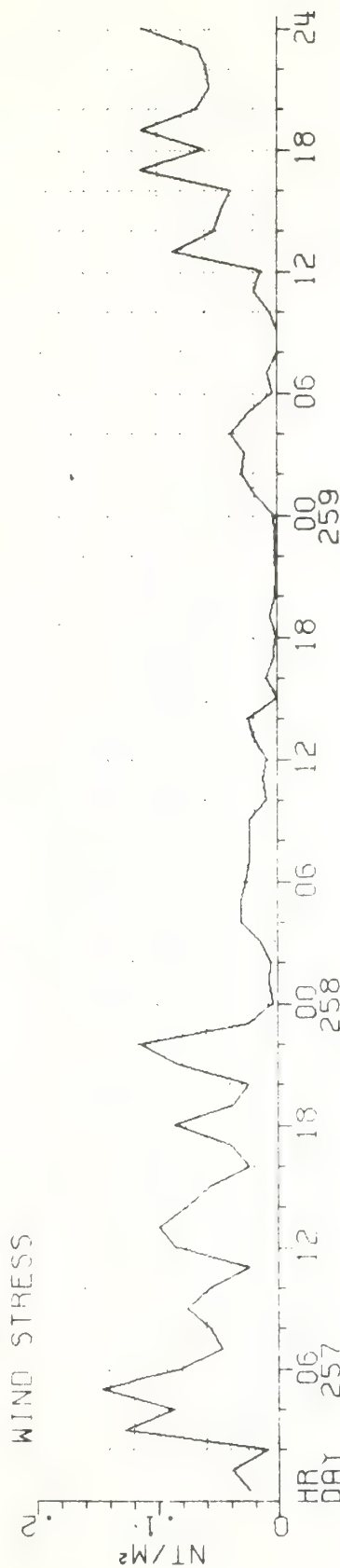
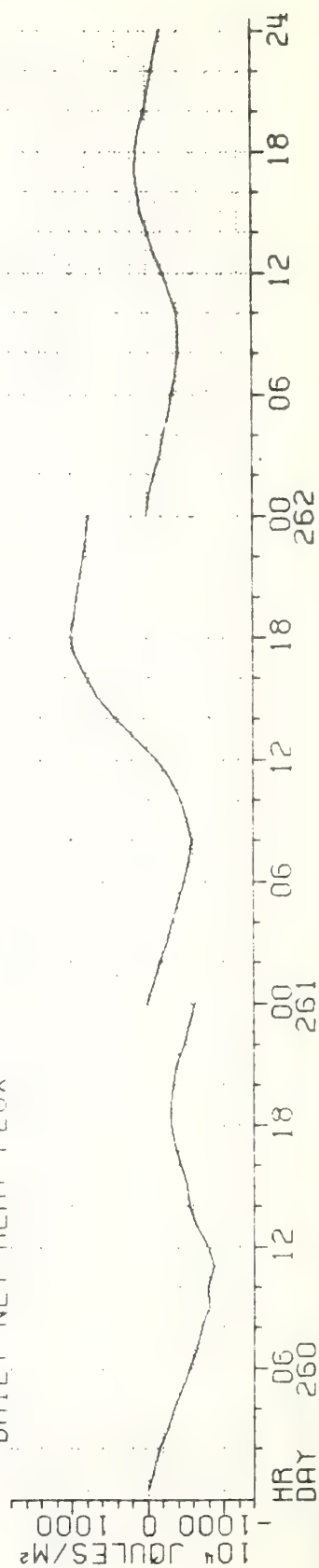
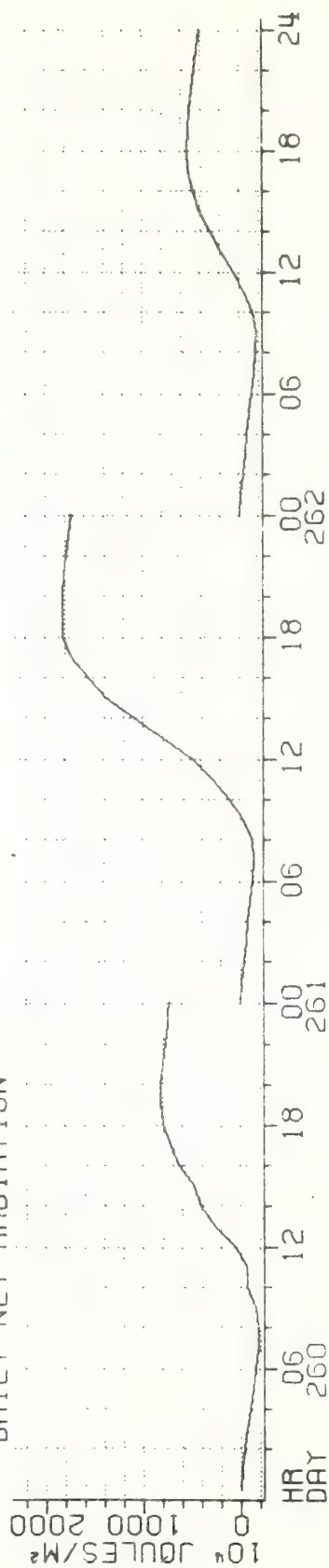


Figure 18. (contin.)

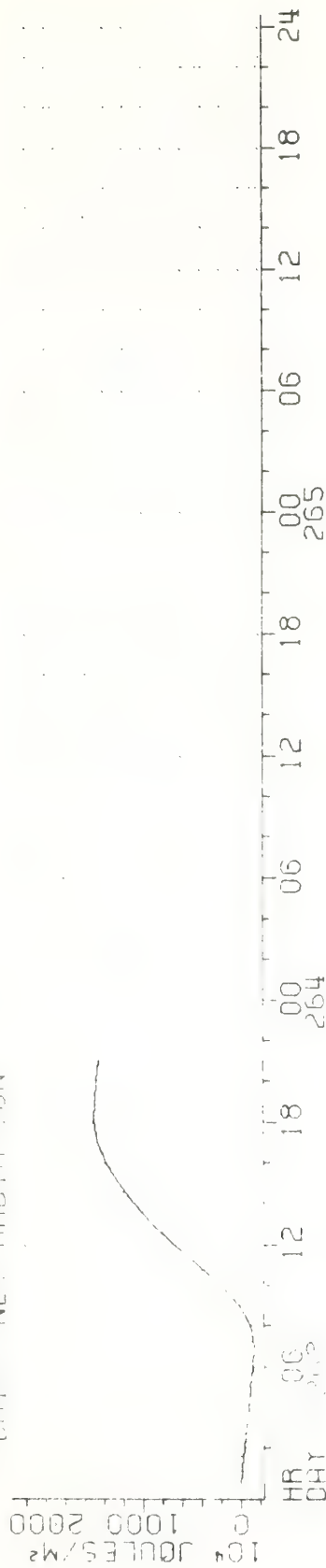


1154

COMPARISON OF PLIN (CHIEF)  
 CUMULATIVE FLUXES  
 WIND SPEEDS



DATA NET RADIATION



DATA NET HEAT FLUX





## 7. REFERENCES

- Brocks, K., and L. Krugermeyer (1972), The Hydrodynamic Roughness of the Sea Surface. Studies in Physical Oceanography, Vol. 1, Ed. A. L. Gordon, Gordon and Breach Science Publ., New York, pp. 75-92.
- Hoeber, H., (1969), Wind, Temperatur-und Feuchteprofile in der wassernahen Luftschicht über dem aquatorialen Atlantik. Meteor Forschungsergeb. Reihe B, 3, 1-26.
- List, R., (1958), Smithsonian Meteorological Tables, Sixth Revised Edition. Smithsonian Institution, 527 pp.
- Webb, E. K., (1975), Personal communication.
- Wyrtki, K., (1966), Seasonal Variation of Heat Exchange and Surface Temperature in the North Pacific Ocean, Hawaii Inst. of Geophysics, U. of Hawaii. HIG-66-3.

APPENDIX

LIST OF CLOUD PHOTOGRAPHS AVAILABLE AT SAIL

## GATE - R/V ISELIN 1974

MONTH/DAY	PICTURE NO.	TIME-GMT	DIRECTION	SIGNIFICANT WEATHER
9/1	1	1115		Squall
	2	1115		
	3	1115		
	4	1115		
9/1	1	1210		Squall
	2	1210		
	3	1210		
	4	1210		
	5	1210		
	6	1210		
	7	1210		
	8	1210		
9/2	1	0815		
	2	0815		
	3	0815		
	4	0815		
	5	0815		
	6	0815		
	7	0815		
	8	0815		
	9	0815		
	10	0815		
	11	0815		
	12	0815		
	1	0940		
	2	0940		
	1	0800		
	2	0800		
	3	0800		
	4	0800		
	5	0800		
	6	0800		
	7	0800		
	8	0800		
	9	0800		
	10	0800		
	11	0800		
	12	0800		
	13	0800		
	14	0800		
	15	0800		



MONTH/DAY	PICTURE NO.	TIME-GMT	DIRECTION	SIGNIFICANT WEATHER
9/3	16	0800		
	17	0800		
	18	0800		
	19	0800		
	20	0800		
	21	0800		
	22	0800		
	23	0800		
	24	0800		
	25	0800		
9/5	1	1010	S	
	2	1010	E	
	3	1010	N	
	4	1010	W	
	5	1010		
	6	1010		
	1	1200	N	
	2	1200	E	
	1	1400	N	
	2	1400	E	
	3	1400	S	
	4	1400	W	
	1	1500	E	
	2	1500	S	
	3	1500	W	
	4	1500	N	
	1	1600	S	
	2	1600	W	
	3	1600	N	
	4	1600	E	
	1	1730	W	
	2	1730	N	
	3	1730	E	
	4	1730	S	

## GATE - R/V ISELIN

1974

MONTH/DAY	PICTURE NO.	TIME-GMT	DIRECTION	SIGNIFICANT WEATH
9/5	1	1815	NE	Squa11
	2	1815	NE	
	3	1815	S	
	4		W	
	5	1815	N	
9/6	1	0730		
	2	0730		
	3	0730		
	4	0730		
	5			
	6			
	7			
9/6	1	1000	N	
	2	1000	S	
	3	1000	W	
9/6	1	1349	W	Squa11
	2	1349	S	
	3	1349	SE	
	4	1349	E	
	5	1349	N	
9/6	1	1525	E	Squa11
	2		S	
	3		W	
	4		N	
9/6	1	1550	E	
	2	1550	S	
	3	1550	W	
	4	1550	N	
9/6	1	1705	NW	
	2	1705	N	
	3	1705	E	
9/6	1	1810	W	
	2	1810	N	
9/6	1	1814	W	
	2	1814	N	
	3	1814	E	
	4	1814	S	

## GATE - R/V ISELIN 1974

MONTH/DAY	PICTURE NO.	TIME-GMT	DIRECTION	SIGNIFICANT WEATHER
9/6	1	1915	W	
	2	1915	NW	
	3	1915	N	
	4	1915	NE	
	5	1915	SE	
	6	1915	SE	
	7	1915	S	
	8	1915	SW	
9/7	1	0805	E	
	2	0805	S	
	3	0805	W	
	4	0805	N	
9/7	1	0910		
	2	0910		
	3	0910		
9/7	1	1000	W	
	2	1000	N	
	3	1000	E	
	4	1000	S	
9/7	1	1104	N	
	2	1104	E	
	3	1104	S	
	4	1104	W	
9/7	1	1440		
	2	1440		
	3	1440		
	4	1440		
9/7	1	1601	N	
	2	1601	E	
	3	1601	S	
	4	1601	W	
9/7	1	1745	N	
	2	1745	E	
	3	1745	S	
	4	1745	W	



## GATE - R/V ISELIN 1974

MONTH/DAY	PICTURE NO.	TIME-GMT	DIRECTION	SIGNIFICANT WEATHER
9/7	1	1810		Squall
	2	1810		
	3	1810		
9/8	1	0743	N	
	2	0743	E	
	3	0743	S	
	4	0743	W	
9/8	1	0800	S	
	2	0800	W	
	3	0800	N	
	4	0800	E	
9/8	1	0900	W	
	2	0900	N	
	3	0900	E	
	4	0900	S	
9/8	1	1000	W	
	2	1000	N	
	3	1000	E	
	4	1000	S	
9/8	1	1057	W	
	2	1057	N	
	3	1057	E	
	4	1057	S	
9/8	1	1205	W	
	2	1205	N	
	3	1205	E	
	4	1205	S	
9/8	1	1315		
	2	1315		
	3	1315		
	4	1315		
	5	1315		
	6	1315		
	7	1315		
	8	1315		

## GATE - R/V ISELIN 1974

MONTH/DAY	PICTURE NO.	TIME-GMT	DIRECTION	SIGNIFICANT WEATHER
9/8	1	1500		
	2	1500		
	3	1500		
	4	1500		
9/8	1	1800	W	
	2	1800	N	
	3	1800	E	
	4	1800	S	
9/9	1	0745	S	
	2	0745	W	
	3	0745	N	
	4	0745	E	
9/9	1	0856		
	2	0856		
	3	0856		
	4	0856		
9/9	1	0956	S	
	2	0956	W	
	3	0956	N	
	4	0956	E	
	5	0956	SE	
9/9	1	1100	E	
	2	1100	S	
	3	1100	W	
	4	1100	N	
9/9	1	1200	E	
	2	1200	S	
	3	1200	W	
	4	1200	N	
9/9	1	1300	E	
	2	1300	S	
	3	1300	W	
	4	1300	N	

## GATE - R/V ISELIN 1974

MONTH/DAY	PICTURE NO.	TIME-GMT	DIRECTION	SIGNIFICANT WEATHER
9/9	1	1430	W	
	2	1430	N	
	3	1430	E	
	4	1430	S	
9/9	1	1630	W	Squall
	2	1630	N	
	3	1630	E	
	4	1630	S	
9/10	1	0725	W	
	2	0725	N	
	3	0725	E	
	4	0725	E	
	5		S	
9/10	1	0800	W	
	2	0800	N	
	3	0800	E	
	4	0800	S	
9/10	1	0900	W	
	2	0900	N	
	3	0900	E	
	4	0900	S	
9/10	1	1000	W	
	2	1000	E	
	3	1000	S	
9/10	1	1200		
	2	1200		
	3	1200		
	4	1200		
	5	1200		
9/10	1	1600	W	
	2	1600	N	
	3	1600	E	
	4	1600	S	



## GATE - R/V ISELIN 1974

MONTH/DAY	PICTURE NO.	TIME-GMT	DIRECTION	SIGNIFICANT WEATHER
9/10	1	1728	W	
	2	1728	N	
	3	1728	E	
	4	1728	S	
9/10	1	1905	W	
	2	1905	N	
	3	1905	E	
	4	1905	S	
9/10	1	1947	W	
	2	1947	N	
	3	1947	E	
	4	1947	S	
	5	1947	SW	
9/11	1	0751	E	
	2	0751	S	
	3	0751	W	
	4	0751	N	
9/11	1	0900	E	
	2	0900	S	
	3	0900	W	
	4	0900	N	
9/11	1	1000	E	
	2		S	
	3		W	
	4		N	
9/11	1	1100	W	
	2	1100	N	
	3	1100	E	
	4	1100	S	
9/11	1	1200	W	
	2	1200	N	
	3	1200	E	
	4	1200	S	

## GATE - R/V ISELIN 1974

MONTH/DAY	PICTURE NO.	TIME-GMT	DIRECTION	SIGNIFICANT WEATHER
9/11	1	1855	W	
	2	1855	N	
	3	1855	E	
	4	1855	S	
9/12	1	0808	N	
	2	0808	E	
	3	0808	SE	
	4	0808	S	
	5	0808	W	
9/12	1	0855	W	
	2	0855	N	
	3	0855	E	
9/12	1	0859	E	
	2	0859	SE	
	3	0859	S	
	4	0859	W	
9/12	1	1004	W	
	2	1004	N	
	3	1004	E	
	4	1004	S	
9/12	1	1100	N	
	2	1100	E	
	3	1100	S	
	4	1100	W	
9/12	1	1210	N	Squall
	2	1210	E	
	3	1210	S	
	4	1210	SW	
	5	1210	W	
9/12	1	1212		Rain Shower
9/12	1	1235		Rain Shower

## GATE - R/V ISELIN 1974

MONTH/DAY	PICTURE NO.	TIME-GMT	DIRECTION	SIGNIFICANT WEATHER
9/12	1	1250	NE	Squall
	2	1250	N	
	3	1250	NW	
	4	1250	W	
	5	1250	SW	
	6	1250	S	
	7	1250	SE	
	8	1250	N	
9/12	1	1815	W	
9/13	1	0742	S	Squall
	2	0742	W	
	3	0742	NW	
	4	0742	NE	
	5	0742	E	
9/13	1	0807	W	
	2	0807	N	
	3	0807	E	
	4	0807	S	
9/13	1	0857	W	Squall
	2	0857	N	
	3	0857	NE	
	4	0857	S	
	5	0857	E	
9/13	1	1003	W	Squall
	2	1003	E	
	3	1003	S	
	4	1003	SW	
9/13	1	1153		
	2	1153		
	3	1153		
	4	1153		
	5	1153		
9/13	1	1300	N	
	2	1300	E	
	3	1300	S	
	4	1300	W	



## GATE - R/V ISELIN 1974

MONTH/DAY	PICTURE NO.	TIME-GMT	DIRECTION	SIGNIFICANT WEATHER
9/13	1	1502	W	Squa11
	2	1502	N	
	3	1502	E	
	4	1502	S	
9/13	1	1608	W	Squa11
	2	1608	N	
	3	1608	E	
	4	1608	S	
9/13	1	1701	W	Squa11
	2	1701	N	
	3	1701	E	
	4	1701	S	
9/14	1	0728	W	
	2	0728	N	
	3	0728	E	
	4	0728	S	
9/14	1	0804	S	Squa11
	2	0804	W	
	3	0804	N	
	4	0804	E	
9/14	1	0818	E	
	2	0818		
	3	0818		
	4	0818		
9/14	1	0927	W	
	2	0927	N	
	3	0927	E	
	4	0927	S	
9/14	1	1024	W	Squa11
	2	1024	N	
	3	1024	E	
	4	1024	S	
9/14	1	1114	W	
	2	1114	E	
	3	1114	S	
	4	1114	N	

## GATE - R/V ISELIN 1974

MONTH/DAY	PICTURE NO.	TIME-GMT	DIRECTION	SIGNIFICANT WEATHER
9/14	1	1220	N	Squall
	2	1220	E	
	3	1220	S	
9/14	1	1400	W	
	2	1400	N	
	3	1400	E	
	4	1400	S	
9/14	1	1520	W	
	2	1520	N	
	3	1520	E	
	4	1520	S	
9/14	1	1618	W	
	2	1618	N	
	3	1618	E	
	4	1618	S	
9/14	1	1700	W	
	2	1700	N	
	3	1700	E	
	4	1700	S	
9/14	1	1800	W	
	2	1800	N	
	3	1800	E	
	4	1800	S	
9/15	1	0753	E	
	2	0753	S	
	3	0753	W	
	4	0753	N	
9/15	1	0858	E	
	2	0858	S	
	3	0858	W	
	4	0858	N	
9/15	1	1102	W	
	2	1102	N	
	3	1102	S	

## GATE - R/V ISELIN 1974

MONTH/DAY	PICTURE NO.	TIME-GMT	DIRECTION	SIGNIFICANT WEATHER
9/15	1	1222	E	
	2	1222	S	
	3	1222	W	
	4	1222	N	
9/15	1	1301		
	2	1301		
	3	1301		
	4	1301		
	5	1301		
9/15	1	1506		
	2	1506		
	3	1506		
	4	1506		
9/15	1	1600		
	2	1600		
	3	1600		
	4	1600		
9/15	1	1656		
	2	1656		
	3	1656		
	4	1656		
9/15	1	1818		
	2	1818		
	3	1818		
	4	1818		
9/15	1	1938		
	2	1938		
	3	1938		
	4	1938		
9/16	1	0750	E	
	2	0750	S	
	3	0750	W	
	4	0750	N	
9/16	1	0900	S	
	2	0900	W	
	3	0900	N	
	4	0900	E	



MONTH/DAY	PICTURE NO.	TIME-GMT	DIRECTION	SIGNIFICANT WEATHER
9/16	1	1104	E	
	2	1104	S	
	3	1104	W	
	4	1104	N	
9/16	1	1213	S	
	2	1213	W	
	3	1213	N	
	4	1213	E	
9/16	1	1257	W	Squall
	2	1257	N	
	3	1257	E	
	4	1257	S	
9/16	1	1700	W	
	2	1700	N	
	3	1700	S	
	4	1700	E	
9/16	1	1900	S	
	2	1900	W	
	3	1900	N	
	4	1900	E	
9/17	1	0725	W	
	2	0725	N	
	3	0725	E	
	4	0725	E	
	5	0725	S	
9/17	1	0745	W	
	2	0745	N	
	3	0745	E	
	4	0745	S	
9/18	1	0733	W	
	2	0733	N	
	3	0733	E	
	4	0733		
	5	0733		

## GATE - R/V ISELIN 1974

MONTH/DAY	PICTURE NO.	TIME-GMT	DIRECTION	SIGNIFICANT WEATHER
9/18	1	1000	E	
	2	1000	S	
	3	1000	W	
	4	1000	N	
9/18	1	1206	N	
	2	1206	E	
	3	1206	S	
	4	1206	W	
9/18	1	1545		
	2	1545		
	3	1545		
	4	1545		
9/18	1	1800	E	
	2	1800	S	
	3	1800	W	
	4	1800	N	
9/19	1	1810	E	
	2	1810	S	
	3	1810	W	
	4	1810	N	
9/19	1	1100	N	Squalls
	2	1100	E	
	3	1100	S	
	4	1100	S	
	5	1100	W	
9/19	1	1200	N	Squalls
	2	1200	E	
9/19	1	1511	E	Squalls
	2	1511	S	
	3	1511	W	
	4	1511	N	

MONTH/DAY	PICTURE NO.	TIME-GMT	DIRECTION	SIGNIFICANT WEATHER
9/19	1	1610	S	Squalls
	2	1610	S	
	3	1610	W	
	4	1610	N	
	5	1610	E	
	6	1610	SE	
9/19	1	1734	S	Squalls
	2	1734	W	
	3	1734	N	
	4	1734	E	
	5	1734	SE	
9/19	1	1804	S	Squalls
	2	1804	W	
	3	1804	N	
	4	1804	E	
	5	1804	SE	



NOAA Technical Memorandum ERL AOML-26, 22 pages.

NOAA Technical Memorandum ERL AOML-26

A SPLICED NUMERICAL GRID HAVING APPLICATIONS  
TO STORM SURGE

W. C. Thacker  
Sea-Air Interaction Laboratory

Atlantic Oceanographic and Meteorological Laboratories  
Miami, Florida  
December 1976

UNITED STATES  
DEPARTMENT OF COMMERCE  
Juanita M. Krebs, Secretary

NATIONAL OCEANIC AND  
ATMOSPHERIC ADMINISTRATION  
Robert M. White, Administrator

Environmental Research  
Laboratories  
Wilmot N. Hess, Director



## DISCLAIMER

The Environmental Research Laboratories do not approve, recommend, or endorse any proprietary product or proprietary material mentioned in this publication. No reference shall be made to the Environmental Research Laboratories, or to this publication furnished by the Environmental Research Laboratories, in any advertising or sales promotion which would indicate or imply that the Environmental Research Laboratories approve, recommend, or endorse any proprietary product or proprietary material mentioned herein, or which has as its purpose an intent to cause directly or indirectly the advertised product to be used or purchased because of this Environmental Research Laboratories publication.

## CONTENTS

	Page
ABSTRACT	1
1. INTRODUCTION	1
2. ANALYTIC SOLUTION FOR A TWO-DEPTH BASIN	2
3. NUMERICAL SOLUTIONS USING A SPLICED GRID	11
4. DISCUSSION	17
5. REFERENCES	19



# A Spliced Numerical Grid Having Applications to Storm Surge

W. C. Thacker

## ABSTRACT

A spliced numerical grid, such as might be used to calculate storm surges simultaneously within bays and along the open coast, is used to obtain solutions to the shallow water wave equations. Spurious, numerically induced flow is generated at the splice, but the amplitude of this noise is small so long as there are no variations of the solution on the scale of the grid spacings. Analytical solutions are obtained for a two-depth basin, and the agreement with numerical solutions is excellent for both trapped waves and seiche waves. Such a spliced grid with the finer portion in shallow water has advantages over a uniform grid in that it resolves the waves better over the entire basin and in that the time step can be larger for the same resolution in shallow water.

## 1. INTRODUCTION

Work on a spliced grid has been motivated by the need for mathematical models capable of predicting hurricane storm surges in bays and estuaries. The National Weather Service is using the SPLASH models of Jelesnianski (1970) to predict surges along the open coast. These models have a grid spacing of 4 nmi, which is sufficient to resolve the hurricane and the flow on the continental shelf but is too large to resolve the flow within bays and estuaries. Other models (Overland, 1975; Reid and Bodine, 1968) with smaller grid spacing have been used to calculate the surge within bays. They require the results of a model such as SPLASH to provide seaward boundary conditions for bay calculations. Since there is strong

coupling between the bay and the shelf regions, it is necessary to use a model that is appropriate to both regions.

One possibility is to use a fine grid, appropriate for the bay, throughout the extended region consisting of both the bay and the shelf. However, this is undesirable for two reasons. First, more computations than necessary must be made in the shelf region in each time step because of the excess number of grid points there. More importantly, because the maximum size of the time step is inversely proportional to the square root of the greatest depth, an undesirably large number of time steps is needed.

Another possibility is to use a fine computational grid for the bay spliced to a coarse grid for the shelf. This avoids an excess of computations in the shelf region and allows for a larger time step.

As a test of such a spliced grid, normal modes of a square basin were computed and compared with analytic solutions. In particular, the important case corresponding to shallow water with a fine grid and deep water with a coarse grid was considered. Agreement between numerical and analytic solutions for both the trapped waves (edge waves) and the seiche waves was excellent.

## 2. ANALYTIC SOLUTION FOR A TWO-DEPTH BASIN

Storm surge calculations are based on the shallow water wave equations,

$$\left. \begin{aligned} \frac{\partial U}{\partial t} + gD \frac{\partial H}{\partial x} &= 0 \\ \frac{\partial V}{\partial t} + gD \frac{\partial H}{\partial y} &= 0 \\ \frac{\partial H}{\partial t} + \frac{\partial U}{\partial x} + \frac{\partial V}{\partial y} &= 0 \end{aligned} \right\} , \quad (1)$$

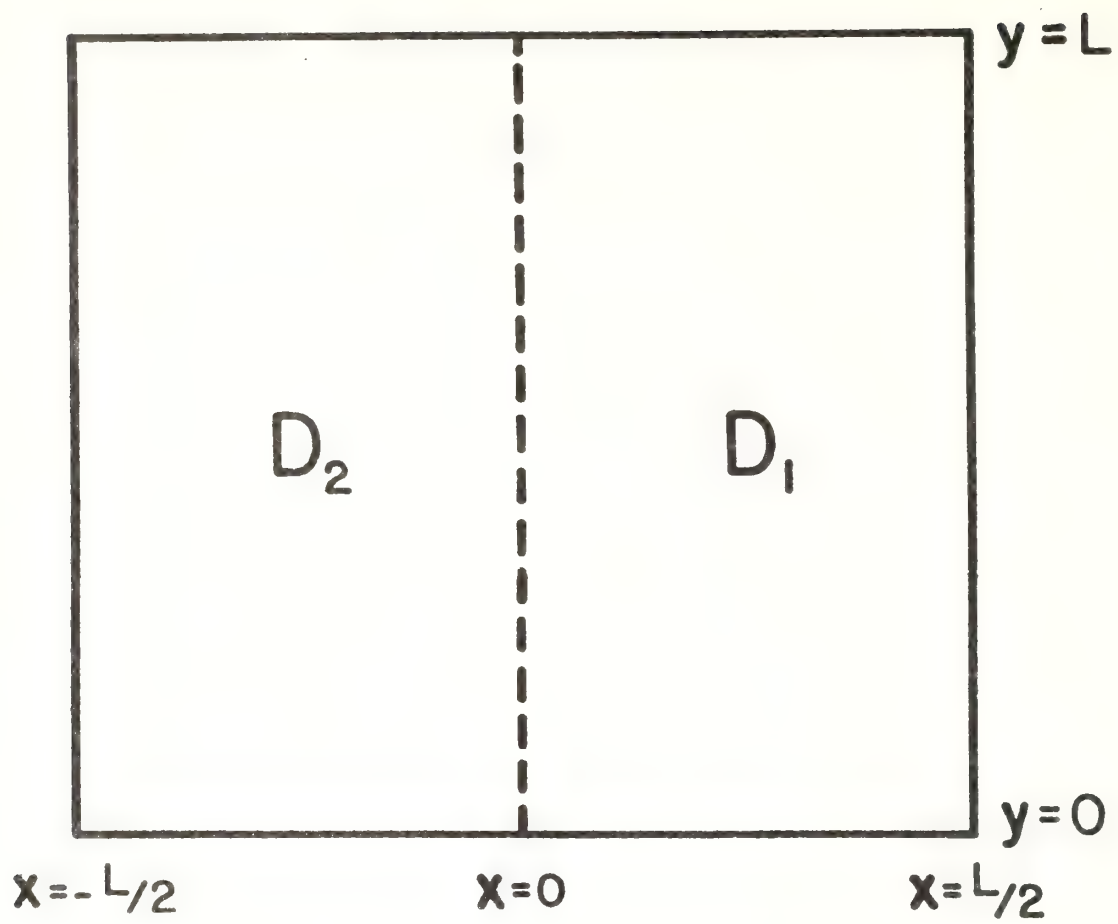
where  $U$  and  $V$  are the  $x$ - and  $y$ -components of transport,  $H$  is the elevation of water above mean sea level,  $D$  is the depth of the basin, and  $g$  is the acceleration of gravity. These equations are solved for the variable depth basin, illustrated in

Figure 1, having depths  $D_1$  for  $0 < x < L/2$  and  $D_2$  for  $-L/2 < x < 0$ . The boundary conditions are  $U=0$  for  $x=\pm L/2$ , and  $V=0$  for  $y=0$  and  $y=L$ . At  $x=0$ ,  $U$  and  $H$  must be continuous; the  $y$ -component of the velocity  $V/D$ , not the transport, must also be continuous.

In solving for the normal mode solutions,  $U_1$ ,  $V_1$ , and  $H_1$ , which are solutions for the region with depth  $D_1$  are matched to corresponding solutions  $U_2$ ,  $V_2$ , and  $H_2$ , for the region with depth  $D_2$ . These solutions are given by

$$\left. \begin{aligned}
 U_1 &= \eta_1 \left( \frac{g D_1 k_1^2}{k_1^2 + k_y^2} \right)^{\frac{1}{2}} \sin k_1 (x - L/2) \cos k_y y \sin \omega t \\
 V_1 &= \eta_1 \left( \frac{g D_1 k_y^2}{k_1^2 + k_y^2} \right)^{\frac{1}{2}} \cos k_1 (x - L/2) \sin k_y y \sin \omega t \\
 H_1 &= \eta_1 \cos k_1 (x - L/2) \cos k_y y \cos \omega t \\
 \\ 
 U_2 &= \eta_2 \left( \frac{g D_2 k_2^2}{k_2^2 + k_y^2} \right)^{\frac{1}{2}} \sin k_2 (x + L/2) \cos k_y y \sin \omega t \\
 V_2 &= \eta_2 \left( \frac{g D_2 k_y^2}{k_2^2 + k_y^2} \right)^{\frac{1}{2}} \cos k_2 (x + L/2) \sin k_y y \sin \omega t \\
 H_2 &= \eta_2 \cos k_2 (x + L/2) \cos k_y y \cos \omega t
 \end{aligned} \right\} \cdot (2)$$





To maintain continuity at  $x=0$ ,  $\omega$  and  $k_y$  must be the same for the two regions. The boundary conditions,  $V_1=V_2=0$  at  $y=0,L$ , require that  $k_y = \frac{n\pi}{L}$ , where  $n$  is an integer. The wave numbers  $k_1$  and  $k_2$  must be determined by the continuity conditions at  $x=0$ ,

$$\left. \begin{aligned} \eta_1 \cos \frac{k_1 L}{2} &= \eta_2 \cos \frac{k_2 L}{2} \\ -\eta_1 g D_1 k_1 \sin \frac{k_1 L}{2} &= \eta_2 g D_2 k_2 \sin \frac{k_2 L}{2} \end{aligned} \right\} \quad (3)$$

and by the dispersion equations,

$$\omega^2 = g D_1 (k_1^2 + k_y^2) = g D_2 (k_2^2 + k_y^2). \quad (4)$$

The solutions for  $k_2$  can be displayed graphically as the intersections of the curves  $f=f_1(\theta)$  and  $f=f_2(\theta)$ , where

$$\left. \begin{aligned} f_1 &= -D_1 \sqrt{\frac{D_2}{D_1} \theta^2 - \left(\frac{D_1 - D_2}{D_1}\right) \left(\frac{n\pi}{2}\right)^2} \tan \sqrt{\frac{D_2}{D_1} \theta^2 - \left(\frac{D_1 - D_2}{D_1}\right) \left(\frac{n\pi}{2}\right)^2} \\ f_2 &= D_2 \theta \tan \theta \\ \theta &= \frac{k_2 L}{2} \end{aligned} \right\} \quad (5)$$

A negative argument of the square root in the expression for  $f_1$ , corresponding to  $k_1^2 < 0$ , corresponds to waves trapped in the shallow regions of the basin. For those modes, the factors  $\cos k_1(x - \frac{L}{2})$  and  $\sin k_1(x - L/2)$  in (2) should be replaced

with  $\cosh \ell_1(x - \frac{L}{2})$  and  $\sinh \ell_1(x - L/2)$ , where  $\ell_1^2 = -k_1^2 < 0$ . Likewise in (3),  $\cos \frac{k_1 L}{2}$  and  $\sin \frac{k_1 L}{2}$  become  $\cosh \frac{\ell_1 L}{2}$  and  $-\sinh \frac{\ell_1 L}{2}$ , and in (4),  $k_1^2$  becomes  $-\ell_1^2$ . Then

$$f_1 = D_1 \sqrt{\left(\frac{D_1 - D_2}{D_1}\right) \left(\frac{n\pi}{2}\right)^2 - \frac{D_2}{D_1} \theta^2} \tanh \sqrt{\left(\frac{D_2 - D_1}{D_1}\right) \left(\frac{n\pi}{2}\right)^2 - \frac{D_2}{D_1} \theta^2} . \quad (6)$$

Note that this is never the case for  $n=0$ , i.e., for motion that is uniform in the direction parallel to the interface; and further note that the modes with most variation in the direction parallel to the interface are most likely to be trapped in shallow water; the greater the difference in depth, the larger the number of trapped modes. Meyer (1971) has recently reviewed waves trapped by depth variations.

The graphical solutions for  $k_2$  for a constant depth basin,  $D_1 = D_2$ , are shown in Figure 2. These solutions are the same for all values of  $n$  since, for a constant depth basin,  $k_2$  and  $k_1$  are independent of  $k_y$ . The solutions are  $k_2 = k_1 = \frac{m\pi}{L}$ . Thus the normal modes can be identified by the two integers,  $m$  and  $n$ , corresponding to the  $x$ - and  $y$ -variations.

The corresponding solutions for the case  $D_1 = 4D_2$  are shown in Figure 3. For unequal depths,  $k_2$  and  $k_1$  are no longer independent of  $k_y$ . The solutions of Figure 3 correspond to

$k_y = \frac{\pi}{L}$  ( $n=1$ ). Again, the  $x$ -variation can be identified by a non-negative integer,  $m$ , which can be chosen to be the same as that used in the limit  $D_1 \rightarrow D_2$ . The lowest mode,  $m=0$ , which corresponded to no  $x$ -variation when  $D_1 = D_2$ , now has  $x$ -variation for  $D_1 = 4D_2$  and is a trapped wave.

The solutions for the same case,  $D_1 = 4D_2$ , but for the next higher  $y$ -variations ( $n=2$ ), are shown in Figure 4. Now the two modes,  $m=0$  and  $m=1$ , are trapped waves.

Table 1 contains the values of  $k_2$  and  $k_1$  or  $\ell_1$  for modes with  $n \leq 4$  and  $m \leq 4$ . For this case  $D_1 = 4D_2$ . These values were obtained by numerical solution of (5) and (6).



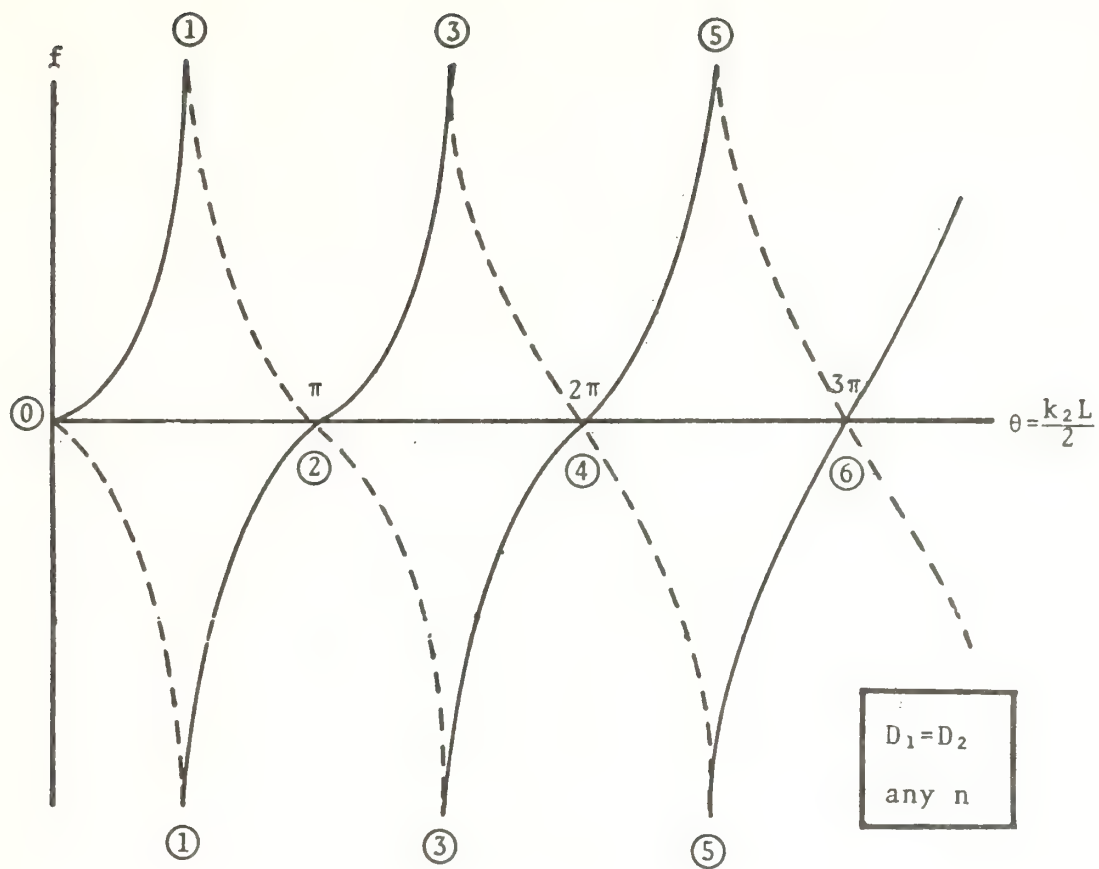


Figure 2. Solid curves represent  $f_2$ ; dashed curves,  $f_1$ . Solutions for  $k_2 = \frac{m\pi}{L}$  are represented by  $(m)$ . For odd  $(m)$ , the curves intersect at infinity.

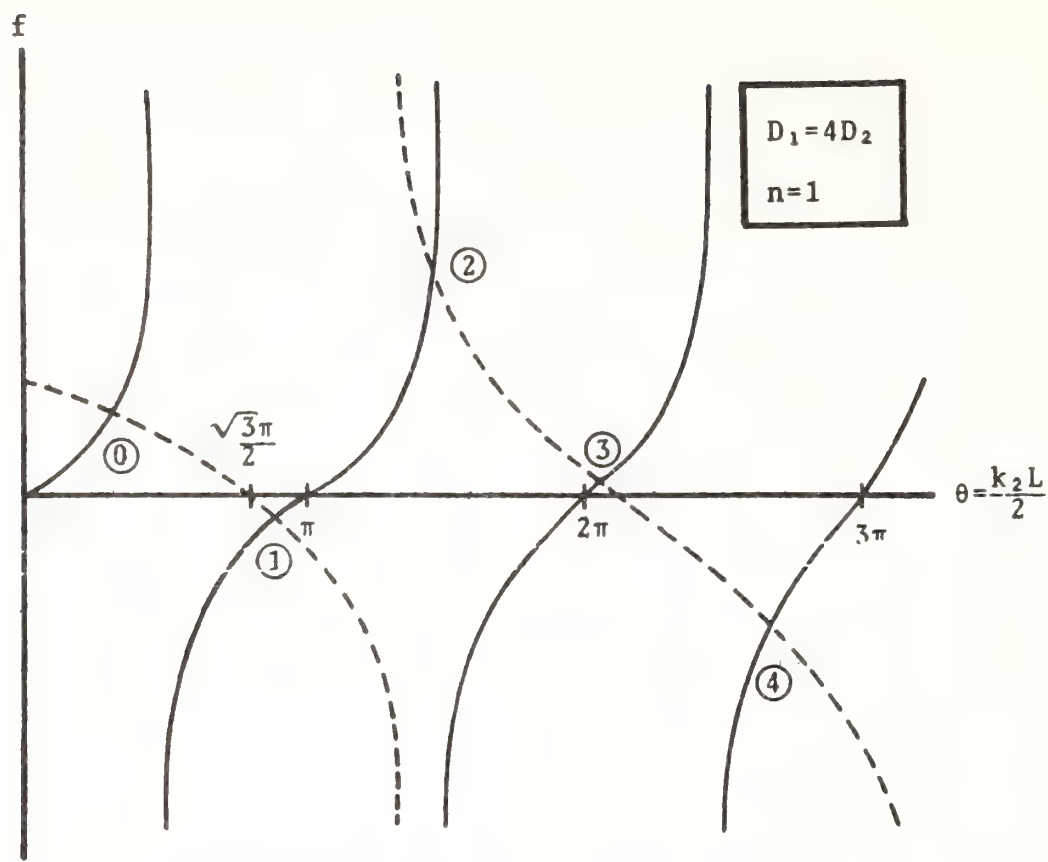


Figure 3. Solid curves represent  $f_2$ ; dashed curves,  $f_1$ . The modes are labeled  $(m)$  to correspond to Figure 2. The zeroth mode is a trapped wave.

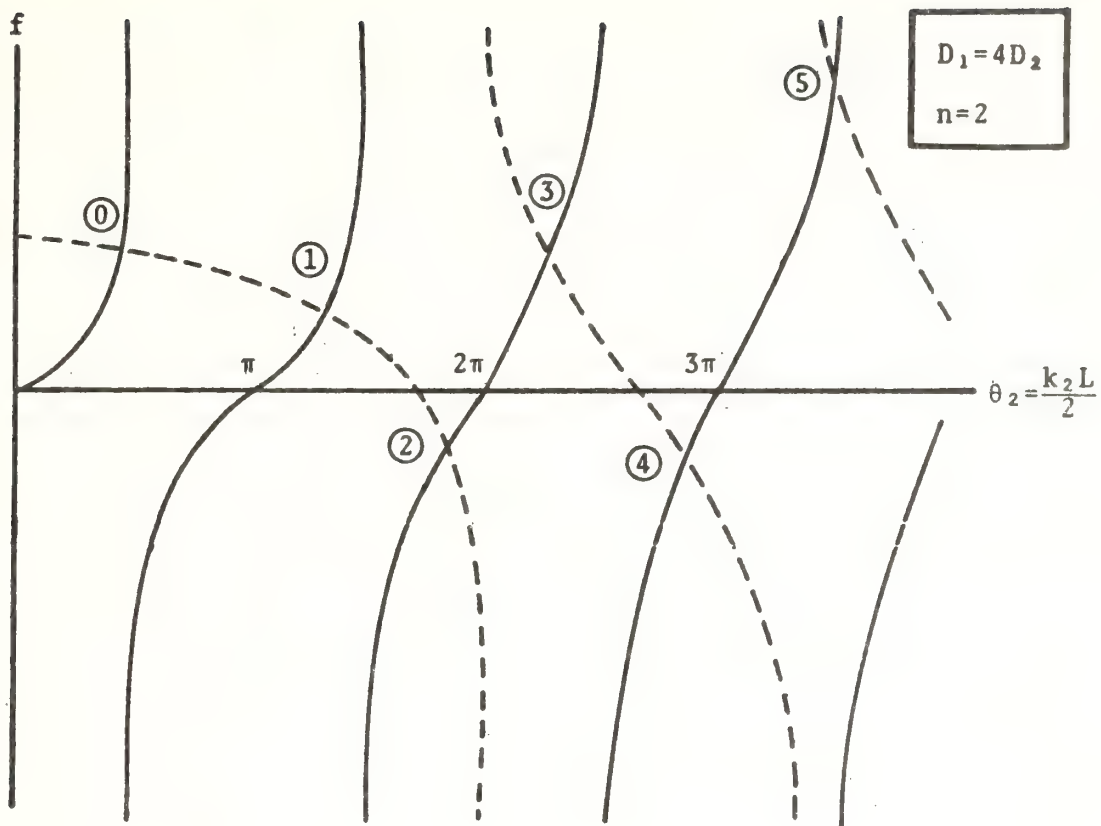


Figure 4. Intersection of solid curve ( $f_2$ ) with the dashed curves ( $f_1$ ) give the solutions for shallow-water wavenumber,  $k_2$ . Again, the modes are labeled  $(m)$  to correspond to Figure 2. Modes  $m=0$  and  $m=1$  are trapped waves.



Table 1. Values of wavenumbers and frequencies for normal modes of basin with  $D_1=4D_2$ . The integer,  $m$ , which indexes the  $x$ -variation corresponds to

$$k_1=k_2=\frac{m\pi}{L} \text{ if } D_1 \rightarrow D_2.$$

$m$	$n$	$\frac{k_2 L}{2}$	$\frac{k_1 L}{2}$	$\frac{\ell_1 L}{2}$	$\frac{k_y L}{2}$	$\frac{\omega L}{2 g D_2}$
0	0	0	0	—	0	0
1	0	1.910633	0.955317	—	0	1.910633
2	0	4.372552	2.186276	—	0	4.372552
3	0	8.193819	4.096909	—	0	8.193819
4	0	10.655737	5.327869	—	0	10.655737
0	1	1.265841	—	1.204144	1.570796	2.017363
1	1	2.859502	0.440041	—	1.570796	3.262537
2	1	4.551944	1.824691	—	1.570796	4.815350
3	1	6.561891	2.985641	—	1.570796	6.747282
4	1	8.331865	3.937568	—	1.570796	8.478642
0	2	1.433659	—	2.624568	3.141593	3.453257
1	2	4.152616	—	1.758166	3.141593	5.207094
2	2	5.696660	0.843077	—	3.141593	6.505500
3	2	7.200379	2.357787	—	3.141593	7.855893
4	2	8.879242	3.508280	—	3.141593	9.418627
0	3	1.478877	—	4.013503	4.712389	4.938997
1	3	4.401891	—	3.436684	4.712389	6.448508
2	3	7.110300	—	2.003962	4.712389	8.530122
3	3	8.495382	1.178101	—	4.712389	9.714841
4	3	9.850168	2.757081	—	4.712389	10.919360
0	4	1.501266	—	5.389375	6.283185	6.460048
1	4	4.489681	—	4.956764	6.283185	7.722412
2	4	7.417831	—	3.981553	6.283185	9.721246
3	4	10.088569	—	2.040590	6.283185	11.885186
4	4	11.2	1.435974	—	6.283185	12.890374

### 3. NUMERICAL SOLUTIONS USING A SPLICED GRID

The spliced grid used to calculate the normal modes of the two-depth basin is illustrated in Figure 5 for a simple case with very few grid points. Calculations were made with the grid spacing of  $\Delta x_1 = \Delta y_1 = L/30$  in the deep region, and  $\Delta x_2 = \Delta y_2 = L/60$  in the shallow region. The spliced grid is staggered, with U, V, and H calculated at different points. The coordinates of the variables are given in Table 2.

The finite difference equations that approximate (1) follow.

$$\left. \begin{aligned} U1_{I,J}^{T+\frac{1}{2}} &= U1_{I,J}^{T-\frac{1}{2}} - gD_1 \frac{\Delta t}{\Delta x_1} (H1_{I+1,J}^T - H1_{I,J}^T); I=1, \dots, 29; J=1, \dots, 60 \\ V1_{I,J}^{T+\frac{1}{2}} &= V1_{I,J}^{T-\frac{1}{2}} - gD_1 \frac{\Delta t}{\Delta y_1} (H1_{I,J+1}^T - H1_{I,J}^T); I=1, \dots, 30; J=1, \dots, 59 \\ H1_{I,J}^{T+1} &= H1_{I,J}^T - \frac{\Delta t}{\Delta x_1} (U1_{I,J}^{T+\frac{1}{2}} - U1_{I-1,J}^{T+\frac{1}{2}}) - \frac{\Delta t}{\Delta y_1} (V1_{I,J}^{T+\frac{1}{2}} - V1_{I,J-1}^{T+\frac{1}{2}}); \\ &I=1, \dots, 30; J=1, \dots, 60 \end{aligned} \right\}, (7a)$$

$$\left. \begin{aligned} U2_{I,J}^{T+\frac{1}{2}} &= U2_{I,J}^{T-\frac{1}{2}} + gD_2 \frac{\Delta t}{\Delta x_1} (H2_{I+1,J}^T - H2_{I,J}^T); I=1, \dots, 59; J=1, \dots, 120 \\ V2_{I,J}^{T+\frac{1}{2}} &= V2_{I,J}^{T-\frac{1}{2}} - gD_2 \frac{\Delta t}{\Delta y_1} (H2_{I,J+1}^T - H2_{I,J}^T); I=1, \dots, 60; J=1, \dots, 119 \\ H2_{I,J}^{T+\frac{1}{2}} &= H2_{I,J}^T + \frac{\Delta t}{\Delta x_1} (U2_{I,J}^{T+\frac{1}{2}} - U2_{I-1,J}^{T+\frac{1}{2}}) - \frac{\Delta t}{\Delta y_1} (V2_{I,J}^{T+\frac{1}{2}} - V2_{I,J-1}^{T+\frac{1}{2}}); \\ &I=1, \dots, 60; J=1, \dots, 120 \end{aligned} \right\}, (7b)$$

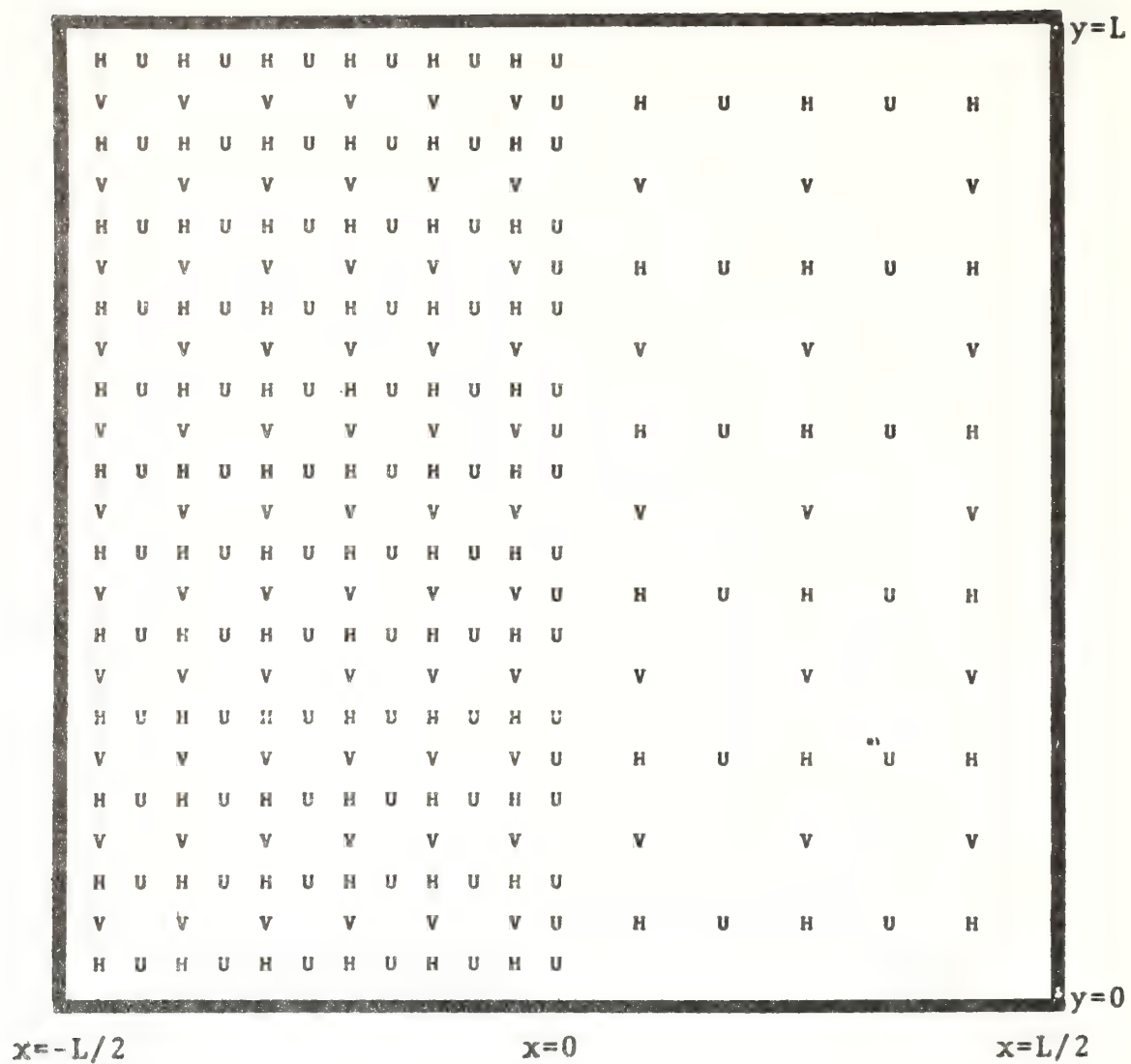


Figure 5. Numerical grid. The  $H$ ,  $U$ , and  $V$  fields are staggered. The  $U$  field is evaluated along the splice.



Table 2. Coordinates of variables on spliced grid. Note that the variables  $U1(0,J)$  and  $U2(0,J)$  are situated on the splice. Further note that the  $x$ -coordinates for  $H1$ ,  $U2$ , and  $V2$  are negative for positive values of  $I$ .

Variable	$x$ -coordinate	$y$ -coordinate	Index Ranges
$H1(I,J)$	$\left(\frac{I-1/2}{60}\right)_L$	$\left(\frac{J-1/2}{60}\right)_L$	$I=1,\dots,30; J=1,\dots,60$
$U1(I,J)$	$\left(\frac{I}{60}\right)_L$	$\left(\frac{J-1/2}{60}\right)_L$	$I=0,\dots,29; J=1,\dots,60$
$V1(I,J)$	$\left(\frac{I-1/2}{60}\right)_L$	$\left(\frac{J}{60}\right)_L$	$I=1,\dots,30; J=1,\dots,59$
$H2(I,J)$	$-\left(\frac{I-1/2}{120}\right)_L$	$\left(\frac{J-1/2}{120}\right)_L$	$I=1,\dots,60; J=1,\dots,120$
$U2(I,J)$	$-\left(\frac{I}{120}\right)_L$	$\left(\frac{J-1/2}{120}\right)_L$	$I=0,\dots,59; J=1,\dots,120$
$V2(I,J)$	$\left(\frac{I-1/2}{120}\right)_L$	$\left(\frac{J}{120}\right)_L$	$I=1,\dots,60; J=1,\dots,119$

$$\left.
\begin{aligned}
U1_{0,J}^{T+\frac{1}{2}} &= U1_{0,J}^{T-\frac{1}{2}} - g(D_1 + D_2) \frac{\Delta t}{\Delta x_1 + \Delta x_2} (H1_{1,J}^T - \frac{1}{2}(H2_{1,2J}^T + H2_{1,2J-1}^T)); \\
&J=1, \dots, 60 \\
U2_{0,2J}^{T+\frac{1}{2}} &= \frac{3}{4}U1_{0,J}^{T+\frac{1}{2}} + \frac{1}{4}U1_{0,J+1}^{T+\frac{1}{2}}; J=1, \dots, 59 \\
U2_{0,2J-1}^{T+\frac{1}{2}} &= \frac{3}{4}U1_{0,J}^{T+\frac{1}{2}} + \frac{1}{4}U1_{0,J-1}^{T+\frac{1}{2}}; J=2, \dots, 60 \\
U2_{0,120}^{T+\frac{1}{2}} &= \frac{5}{4}U1_{0,60}^{T+\frac{1}{2}} - \frac{1}{4}U1_{0,59}^{T+\frac{1}{2}} \\
U2_{0,1}^{T+\frac{1}{2}} &= \frac{5}{4}U1_{0,1}^{T+\frac{1}{2}} - \frac{1}{4}U1_{0,2}^{T+\frac{1}{2}}
\end{aligned}
\right\} , (7c)$$

and

$$\left.
\begin{aligned}
U1_{M1,J}^{T+\frac{1}{2}} &= 0; J=1, \dots, 60; T=0, 1, \dots \\
U2_{M2,J}^{T+\frac{1}{2}} &= 0; J=1, \dots, 120; T=0, 1, \dots \\
V1_{I,0}^{T+\frac{1}{2}} &= V1_{I,N1}^{T+\frac{1}{2}} = 0; I=1, \dots, 30; T=0, 1, \dots \\
V2_{I,0}^{T+\frac{1}{2}} &= V2_{I,N2}^{T+\frac{1}{2}} = 0; I=1, \dots, 60; T=0, 1, \dots
\end{aligned}
\right\} . (7d)$$

The superscripts refer to the time step, and the subscripts refer to the grid points. Equations (7a) and (7b) are very much alike. The notable difference is the sign of terms in (7b) involving  $\Delta x_2$  differ from those in (7a) involving  $\Delta x_1$ . This is because the origin of the x-axis is taken at the splice, so I increases in the positive x-direction in (7a) and in the negative x-direction in (7b). Equations (7c) govern the perpendicu-

lar transports at the splice. Only the values appropriate to the coarse grid are evaluated from values at previous time steps. Values at points on the fine grid are obtained by interpolation and extrapolation. This is done in the spirit of the approximation involved in replacing derivatives with finite differences, i.e., a linear variation between grid points must be a good approximation. For completeness, the boundary conditions are given in equations (7d).

Numerical solutions for normal modes were obtained first for a basin of uniform depth, where  $D_1=D_2$ . The numerical solutions are good if the sinusoidal functions are well resolved on the coarse grid. Two cases are notable. The first corresponds to no variations in the solutions in the direction parallel to the splice, corresponding to  $k_y=0$  in equations (3). For this case,  $V=0$  both in the analytical solution and the numerical solution. The second case corresponds to no variations in the solutions in the direction perpendicular to the splice, corresponding to  $k_x=0$  in (3). For this case,  $U=0$  for all time in the analytical solution, but  $U \neq 0$  in the numerical solution. This is due to the interpolation in (7c) necessary to join the two grids. The source of this noise in the  $U$  field is illustrated in Figure 6. The level of the noise can be controlled by controlling the number of grid points per wavelength, since linear interpolation involves the same approximation as replacing derivatives by finite differences. Although the noise is most apparent in the  $U$  field, there is also noise in the  $H$  and  $V$  fields that is less noticeable since it may be only one percent of the calculated value, rather than the entire value, which must be the case when comparing to  $U=0$ . Even the noise in the  $U$  field would not be apparent if only the first two digits of the numerical solutions were displayed. This noise due to interpolation might appear in any attempt to use a non-uniform grid. So long as there is little energy in the shortest wavelengths, this noise is not expected to be a problem.

The spliced grid shown in Figure 5 is ideally suited for the case  $D_1=4D_2$  because it resolves the normal modes equally in the two regions. This can be seen from equation (4). The wavelengths in the two regions are given by  $\lambda_1=2\pi/(k_y^2+k_1^2)^{1/2}$  or  $\lambda_1=2\pi/(k_y^2-k_1^2)^{1/2}$  and  $\lambda_2=2\pi/(k_y^2+k_2^2)^{1/2}$ , so from (4),  $\lambda_1=2\lambda_2$ . Because the grid spacing is twice as large in region 1 as in region 2, the number of grid points per wavelength is given by



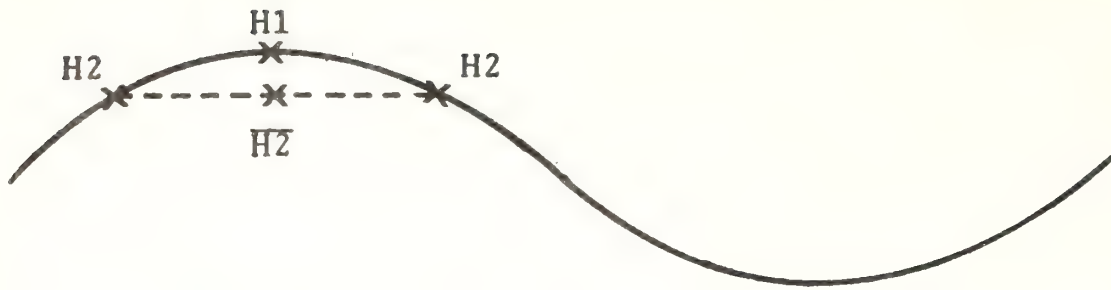


Figure 6. The sinusoid curve represents an  $H$  field along the splice. The value  $\overline{H2}$  represents an interpolated value of the  $H2$  field that should compare with the value  $H1$  directly across the splice. Although there is no change in the elevation of the  $H$  field in the analytical solutions, there is an induced slope across the splice due to the interpolation. It is this slope which leads to non-zero values of the  $U$  field in the numerical solution. When the finite difference approximation is good, linear interpolation is a good approximation, and the level of the noise in the  $U$  field is low.

$60\pi/(\omega L/2\sqrt{gD})$ , which is greater than 10 for all of the modes listed in Table 1. Thus, all of these modes are fairly well resolved on the grid, and numerical results should be good to a few percent. The maximum time step determined by the stability conditions,  $\Delta t = \Delta x_1/(2gD_1)^{1/2}$  and  $t = \Delta x_2/(2gD_2)^{1/2}$ , is the same for both regions of the grid. For a uniform grid, the time step would be determined by the deep region.

Table 3 compares the dimensionless frequencies,  $\omega L/2\sqrt{gD}$  obtained by counting the number of sign changes of the height field at each computational point in one thousand time steps with the analytical results listed in Table 1. The frequencies were found to be the same at all grid points in both regions, except for modes with  $n=4$ . For those cases, the number of sign changes was not accurately counted in regions where the height field was essentially zero at all times. For most of the points, however, the frequency was found to be constant, even for  $n=4$ . The agreement shown in Table 2 is quite good, with differences between computed and analytical results of less than a few percent as expected from the resolution of the grid.

#### 4. DISCUSSION

The excellent results of this test suggest that a similar spliced grid can be used in numerical models of storm surges for bays and estuaries. The principal restriction is that there be no wave components of the solutions that can be represented on the fine grid but not on the coarse grid. Since wave lengths increase from shallow to deep water, this restriction is not severe. Another way of stating this restriction is that the solutions must be sufficiently smooth that the interpolations necessary at the grid splice be a good approximation. But that is exactly the usual requirement that a finite difference must be a good approximation of a derivative for the numerical solution to be valid.

Table 3. A Comparison of values for  $\omega L/2\sqrt{gD}$  obtained numerically and analytically for normal modes (m,n)

Mode		Dimensionless Frequency	
m	n	Computed	Analytical
1	0	1.87	1.91
2	0	4.40	4.37
3	0	8.13	8.19
4	0	10.66	10.66
0	1	2.00	2.02
1	1	3.20	3.26
2	1	4.80	4.82
3	1	6.80	6.75
4	1	8.53	8.48
0	2	3.47	3.45
1	2	5.27	5.21
2	2	6.63	6.51
3	2	7.97	7.86
4	2	9.60	9.42
0	3	5.00	4.94
1	3	6.49	6.45
2	3	8.55	8.53
3	3	9.86	9.71
4	3	11.11	10.92
0	4	6.42	6.46
1	4	7.73	7.72
2	4	9.73	9.72
3	4	11.90	11.89
4	4	12.83	12.89



## 5. REFERENCES

- Jelesnianski, Chester P. (1970): "Bottom stress time-history" in linearized equations of motion for storm surges. Mon. Weather Rev., 98:462.
- Meyer, R. E. (1971): Resonances of unbounded water bodies. Mathematical Problems in the Geophysical Sciences, 1. Geophysical Fluid Dynamics, pp. 181-227. William H. Reid, Editor, American Mathematical Society.
- Overland, James E. (1975): Estimation of hurricane storm surge in Apalachicola Bay, Florida. NOAA Tech. Rept. NWS 17.
- Reid, Robert O., and Bernie R. Bodine (1968): Numerical model for storm surges in Galveston Bay. J. Waterways and Harbors Div., Proc. American Society of Civil Engineers, 94:33.



## **A Transformation Relating Temporal and Spatial Spectra Of Turbulent Kinetic Energy**

W. C. Thacker

Atlantic Oceanographic and Meteorological Laboratories  
Miami, Florida

February 1977

### **U. S. DEPARTMENT OF COMMERCE**

Juanita M. Kreps, Secretary

National Oceanic and Atmospheric Administration

Richard A. Frank, Administrator

Environmental Research Laboratories

Wilmot Hess, Director

Boulder, Colorado

## CONTENTS

	Page
Abstract .....	1
1. INTRODUCTION .....	1
2. THE FROST-FREE TURBULENCE TRANSFORMATION .....	2
3. A COMPARISON WITH DATA .....	4
4. A COMPARISON WITH A DIMENSIONAL ARGUMENT .....	5
5. SHEAR DISPERSION .....	6
6. SUMMARY .....	8
7. REFERENCES .....	8



# A TRANSFORMATION RELATING TEMPORAL AND SPATIAL SPECTRA OF TURBULENT KINETIC ENERGY

W. C. Thacker

**ABSTRACT.** A transformation is developed, based upon the scale dependence of turbulent diffusion, that relates temporal and spatial spectra of turbulent kinetic energy. The basic idea is that an eddy diffusivity is appropriate when scales of the flow smaller than a length  $\ell$  and a time  $t$  are unresolved. An expression similar to Heisenberg's for eddy diffusivity is used to obtain the connection between  $\ell$  and  $t$  necessary to transform temporal spectra into spatial spectra. This transformation reveals a close connection between Webster's Site D spectrum of turbulent kinetic energy in the ocean and Okubo's diagrams of oceanic mixing. Furthermore, all spectra obtained from dimensional arguments satisfy this transformation.

## 1. Introduction

An important quantity in the theory of turbulence is  $E(k)$ , the spatial spectrum of kinetic energy. To measure  $E(k)$  is difficult since it requires sampling the velocity field at many spatial points simultaneously. It is much easier to record a time series of the velocity at one point, from which  $\Phi(\omega)$ , the temporal spectrum of kinetic energy, can be obtained. Therefore a transformation is needed that will allow  $E(k)$  to be calculated if  $\Phi(\omega)$  is known. The usual transformation is based upon Taylor's (1938) hypothesis of frozen turbulence, which is valid only if there is a strong mean flow. The purpose of this paper is to present a new transformation that should be valid in the absence of a mean flow. To stress the contrast with the idea of frozen turbulence the term "frost-free turbulence" is used.

The frost-free turbulence transformation is motivated by the results of dye-diffusion experiments in the ocean as summarized by Okubo's (1971) diagrams. His first diagram, reproduced here as Figure 1, illustrates that the spatial and temporal scales of turbulence can be related. This is certainly necessary if there is to be a transformation that can relate  $\Phi(\omega)$  and  $E(k)$ . His second diagram, Figure 2, shows the scale dependence of the eddy diffusivity. An expression for scale dependent diffusivity, such as Heisenberg's (1948) expression for eddy viscosity, is central to this transformation. The transformation

is insensitive to the exact form of this expression because  $\Phi(\omega)$  and  $E(k)$  fall off rapidly with increasing  $\omega$  and  $k$ .

This transformation is obtained in two ways. First  $\Phi(\omega)$  and  $E(k)$  are related through the more general spectral density,  $S(k, \omega)$ , which expresses both spatial and temporal variations. A comparison is made with the frozen turbulence case, and a more general transformation is suggested that has the limits of frozen turbulence and frost-free turbulence, depending upon whether advection or diffusion dominates. Then a heuristic derivation is given, based upon a mechanism for turbulent mixing. The idea here is that the mixing is due to shear dispersion on all scales. The results of a two-layer model for the shear effect are iterated over all scales to obtain expressions for the scale dependence of turbulent diffusivity from which the frost-free turbulence transformation follows.

Because it is difficult to measure  $E(k)$ , it is difficult to test the validity of this transformation directly. Two indirect tests are discussed here. The first is a comparison of a temporal spectrum of kinetic energy of turbulence in the ocean obtained by Webster (1969) with the diffusion data displayed by Okubo (1971). It should be emphasized that no theory is presented for the observed shape of this spectrum. That is a dynamical problem, and the transformation discussed here should be regarded as kinematical. The

comparison shows that the two types of data are in excellent agreement. The second test is provided by a dimensional argument. If it is assumed that only one dimensional constant is important, then consistent forms for  $E(k)$  and  $\Phi(\omega)$  can be obtained. Again, it should be emphasized that it is unimportant whether such a dimensional argument can be applied to real data. What is important is that the forms for  $E(k)$  and  $\Phi(\omega)$  obtained from the dimensional argument are indeed related through the frost-free turbulence transformation.

## 2. The Frost-Free Turbulence Transformation

A turbulent velocity field can be considered to be a random function of space and time. If the turbulence is statistically homogeneous, isotropic, and stationary, then the variance in the velocity field  $\langle u^2(x, t) \rangle$  can be represented in terms of spectral density,  $S(k, \omega)$ . The temporal and spatial spectra are obtained from  $S(k, \omega)$  by integrating over wavenumbers and frequencies, respectively:

$$\left. \begin{aligned} \Phi(\omega) &= \int_0^\infty dk S(k, \omega) \\ E(k) &= \int_0^\infty d\omega S(k, \omega) \end{aligned} \right\} \quad (1)$$

Thus,  $\Phi$  is related to  $E$  through  $S(k, \omega)$ .

In general, a single frequency does not correspond to a single wavenumber. Nevertheless, it is clear that high frequencies correspond to high wavenumbers and low frequencies to low wavenumbers. For example, oceanic motion with a scale of hundreds of kilometers is expected to correspond to time variations on the scale of months, not seconds. Therefore, it should be reasonable to assume that, for any wavenumber,  $S(k, \omega)$  is sharply peaked at a single frequency and, for any frequency,  $S(k, \omega)$  is peaked at a single wavenumber. This can be expressed in two ways,

$$\left. \begin{aligned} S(k, \omega) &= E(k) \delta(\omega - f(k)) \\ S(k, \omega) &= \Phi(\omega) \delta(k - g(\omega)) \end{aligned} \right\} \quad (2)$$

which are equivalent if the functions  $f$  and  $g$  are the inverses of each other. The Dirac delta functions can be considered as approximating more general distributions with finite widths.

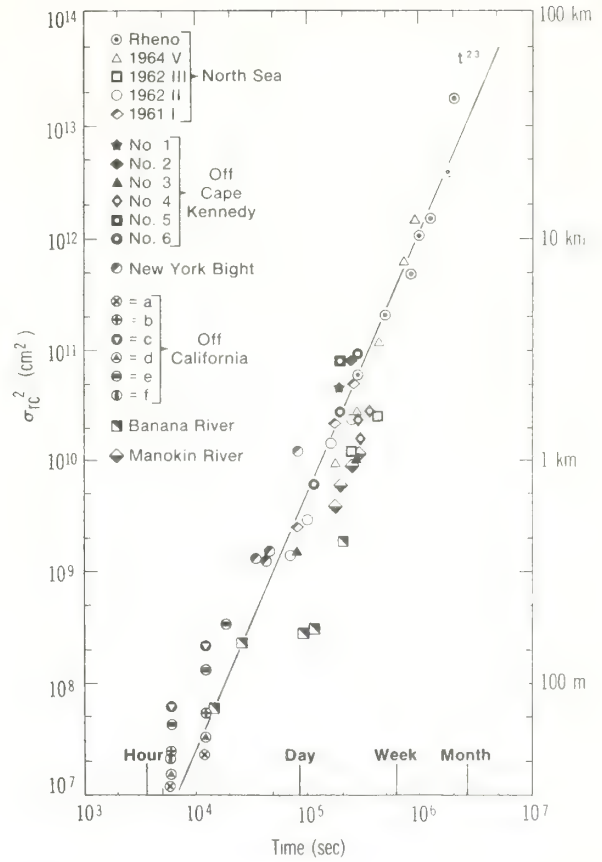


Figure 1. Variance of dye concentration (size of dye patch) versus diffusion time (time elapsed since the dye was introduced as a point source). (After Okubo, 1971.)

Using (1) with (2), transformations connecting  $E$  and  $\Phi$  can be obtained:

$$\left. \begin{aligned} \Phi(\omega) &= \frac{E(g(\omega))}{f'(g(\omega))} \\ E(k) &= \frac{\Phi(f(k))}{g'(f(k))} \end{aligned} \right\} \quad (3)$$

Thus, the frost-free turbulence transformation will depend upon the form of the function  $f$ , its inverse  $g$ , and their derivatives  $f'$  and  $g'$ .

Clues for the form of  $f$  can be found in Okubo's (1971) dye diffusion diagrams. Figure 1 shows the relationship between the width of a dye patch and the duration of the dye diffusion experiment. This is the connection between space and time scales that is to be expressed by  $f$ . The fact that the slope of the line drawn through the data is greater than one indicates that turbulent diffusion

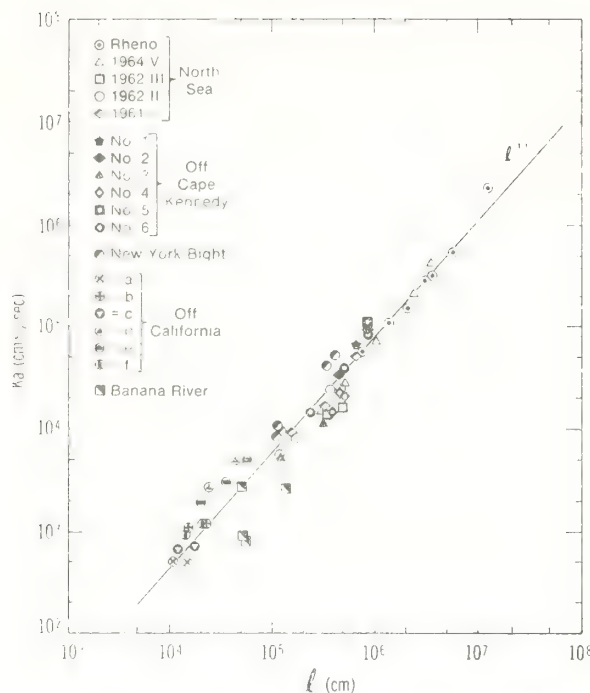


Figure 2. A diffusion diagram for apparent diffusivity versus scale of diffusion. (After Okubo, 1971.)

is scale dependent. Okubo obtains a scale dependent diffusivity  $K$  from these data using the expression

$$\ell^2 = 2Kt \quad (4)$$

to relate the width of the dye patch  $\ell$  to the duration of the experiment  $t$ . Figure 2 shows  $K$  plotted against  $\ell$ . Equation (4), plus an expression for the scale dependence of  $K$ , gives the relation between spatial and temporal scales necessary to define the functions  $f$  and  $g$ .

It is easy to understand why turbulent diffusion should be scale dependent. The spreading of the dye patch can be due only to those eddies that are smaller than the dye patch. Larger eddies serve only to advect and to distort the dye patch. At a later time when the dye patch is larger, larger eddies are available to contribute their energy to the mixing. Thus, the mixing proceeds faster as the dye patch gets larger.

Those eddies smaller than the dye patch, having wavenumbers greater than  $\frac{2\pi}{\ell}$ , are parameterized by the diffusivity  $K$ . As  $\ell$  gets larger, so does  $K$ . Thus,  $K$  is a function of  $k = \frac{2\pi}{\ell}$ . The

expression for the scale dependence used here is

$$K = \left[ C \int_k^\infty \frac{E(k') dk'}{k'^2} \right]^{1/2}, \quad (5)$$

where  $C$  is a dimensionless constant of proportionality of order one. This is an expression quite similar to that used by Heisenberg (1948) for eddy viscosity, and is exactly that found by Tchen (1973, 1975) and Nakano (1972) from their dynamic theories of turbulence. A heuristic derivation of this expression, based upon the idea that the mechanism of turbulent mixing is shear dispersion on all scales, is given below.

The parameter  $K$ , evaluated according to (5), accounts for the effects of eddies with wavenumbers larger than  $k = \frac{2\pi}{\ell}$  where  $\ell$  is the width of the dye patch. The basic assumption made here is that these eddies correspond to frequencies greater than  $\omega = \frac{2\pi}{t}$ , where  $t$  is the duration of the dye experiment corresponding to the width  $\ell$ . Thus,  $\omega$  is related to  $k$  and  $K$  by equation (4),

$$\omega = \pi^{-1} K k^2. \quad (6)$$

Equation (6) expresses the relationship between  $\omega$  and  $k$  that is necessary to transform  $\Phi(\omega)$  into  $E(k)$ . This should be thought of as a statistical assumption for several reasons. First, since, in general, there is no one-to-one relationship between frequencies and wavenumbers, the relationship expressed by (6) must be statistical in the sense that it is a "most likely" relationship. Second, it is statistical since the parameter  $K$  is assumed to represent the average effect of the small scales. It is clear that (6) should be valid only when the small scales can be described by an eddy diffusivity. Finally, implicit in (6) is the idea of ergodicity: a spatial average, a temporal average, and an ensemble average should all be equivalent. A time series of length  $t$  determines  $\Phi(\omega)$  for  $\omega > \frac{2\pi}{t}$ . Likewise, a spatial profile of length  $\ell$  determines  $E(k)$  for  $k > \frac{2\pi}{\ell}$ . If the time series is measured simultaneously with the dye experiment, it seems most reasonable to relate  $\omega$  and  $k$  according to (6). Clearly, the results for each experiment should vary somewhat, but it is reasonable to think of a most likely result that represents the average of an ensemble of experiments. It is in this way that (6) should be interpreted.



By substituting (5) into (6), the expression for  $f$  is determined;

$$f(k) = \pi^{-1} k^2 \left[ C \int_k^\infty \frac{E(k')}{k'^2} dk' \right]^{1/2}. \quad (7)$$

The corresponding expression for  $g$  is found by inverting  $f$ . The simplest way to do this is to take advantage of the fact that  $E(k)$  is simply a transformation of  $\Phi(\omega)$ . This implies that  $K$  can also be expressed as an integral of  $\Phi(\omega)$  over frequencies greater than  $\omega$ , and that expression can be used in (6) to obtain  $g$ . To obtain that expression, first write (5) in differential form as  $dK = -C \frac{E(k)dk}{2Kk^2}$ , and then use (6) and the identity  $E(k)dk = \Phi(\omega)d\omega$  to obtain  $dK = -\frac{C}{2\pi} \frac{\Phi(\omega)d\omega}{\omega}$ . This can be integrated to give

$$K = -\frac{C}{2\pi} \int_\omega^\infty \frac{\Phi(\omega')d\omega'}{\omega'}. \quad (8)$$

Now, (8) and (6) yield

$$g(\omega) = \left[ \frac{C}{2\pi^2\omega} \int_\omega^\infty \frac{\Phi(\omega')d\omega'}{\omega'} \right]^{1/2}. \quad (9)$$

Equations (7) and (9), together with (3), determine the frost-free turbulence transformation. It is simplest to write this in terms of  $K$ ,

$$\left. \begin{aligned} \Phi(\omega) &= \frac{2\pi K E\left(\sqrt{\frac{\pi\omega'}{K}}\right)}{4kK^2 - C E\left(\sqrt{\frac{\pi\omega'}{K}}\right)} \\ E(k) &= \frac{4kK^2 \Phi(\pi^{-1}Kk^2)}{2\pi K + C \Phi(\pi^{-1}Kk^2)} \end{aligned} \right\}, \quad (10)$$

where  $K$  is given by (5) and (8), respectively. Equations (5) and (8) will be discussed further in section 5. Equations (10) will be compared with results of experiments in section 3 and with results of dimensional arguments in section 4.

Equations (2) can be used to obtain the frozen turbulence transformation also. For that case,  $f(k) = Uk$  and  $g(\omega) = \omega/U$ , where  $U$  is the mean velocity that advects the frozen turbulence. Using (3), the frozen turbulence transformation is given by

$$\left. \begin{aligned} \Phi(\omega) &= \frac{1}{U} E\left(\frac{\omega}{U}\right) \\ E(k) &= U \Phi(Uk) \end{aligned} \right\}.$$

It is possible to construct a more general transformation that reduces to frozen turbulence

when advection dominates diffusion and to frost-free turbulence when diffusion dominates advection. One possibility is through the use of the function

$$f(k) = Uk + \pi^{-1} Kk^2$$

and its inverse, where  $K$  is given by (5) and (8), as before. This leads to the transformation

$$E(k) = \frac{(2\pi UK + 4kK^2)\Phi(Uk + \pi^{-1}Kk^2)}{2\pi K + C\Phi(Uk + \pi^{-1}Kk^2)}.$$

If the trend is removed from the time series from which  $\Phi$  is to be obtained, then the information concerning the mean velocity  $U$  is lost so the transformation given in (9) should be used.

### 3. A Comparison With Data

A direct test of the frost-free turbulence transformation given by equations (10) is impossible since the data necessary to evaluate  $E(k)$  are unavailable. Nevertheless, long time series of the velocity at one point in the ocean have been obtained, so  $\Phi(\omega)$  is available. Such a spectrum from Site D (Webster, 1969) is shown in Figure 3. This can be compared with Okubo's (1971) dye diffusion diagrams to check whether the transformation is reasonable.

It is possible to evaluate the diffusivity from (8) numerically using the data in Figure 3. However, for simplicity, these data are approximated by the formula

$$\Phi(\omega) \sim \omega^{-4/3}. \quad (11)$$

This does not imply that there is any dynamic significance to the exponent  $-4/3$ . This exponent was chosen simply to represent the gross behavior of the spectrum over the entire range of frequencies. The details of the tidal and inertial peaks in the spectrum should contribute, at most, shoulders to the curve of diffusivity versus frequency scale. Substituting (11) into equation (8) yields

$$K \sim \omega^{4/3}.$$

Using this in (6), with  $\ell = \frac{2\pi}{k}$  and  $t = \frac{2\pi}{\omega}$ , gives a relation between spatial and temporal scales,

$$\ell^2 \sim t^{7/3}. \quad (12)$$

This is exactly the behavior shown in Figure 1. Of course, the data in Figure 2 are well described by

$$D \sim \ell^{8/7}, \quad (13)$$

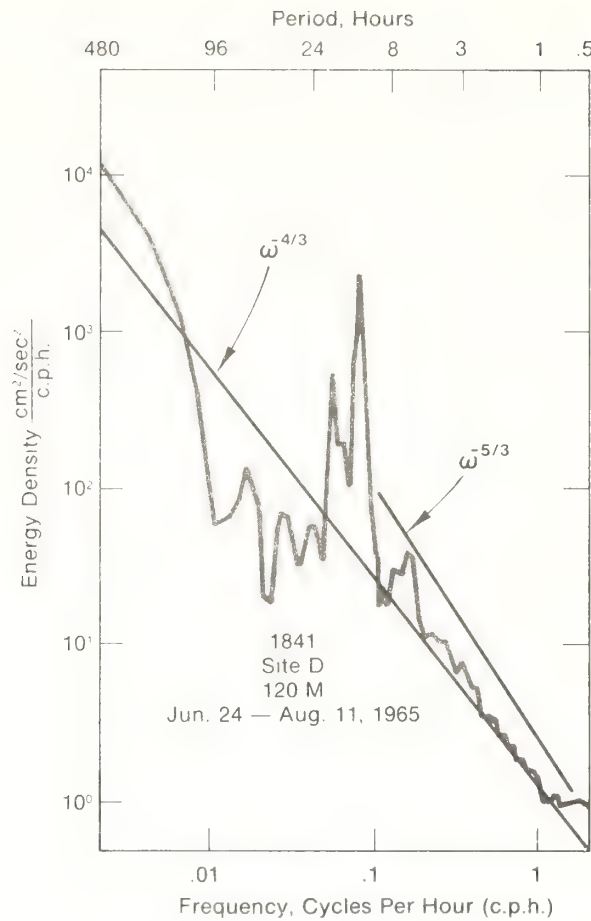


Figure 3. Kinetic energy density spectrum on a log-log plot for a set of current measurements collected at 120-m depth. Minus-four-thirds and minus-five-thirds slopes are indicated. (After Webster, 1969.)

obtained using equations (4) and (12), since Okubo uses (4) to transform the data from Figure 1 to Figure 2.

In making this comparison, two equations were used, (6) and (8). These are the two equations that define frost-free turbulence transformation. Equation (6) relates frequencies to wavenumbers through the eddy diffusivity, and equation (8) expresses the scale dependence of the eddy diffusivity. The agreement found when these two sets of data are compared in this way is evidence that this transformation is indeed valid.

#### 4. A Comparison With A Dimensional Argument

A dimensional argument also provides a transformation connecting  $\Phi(\omega)$  and  $E(k)$ . This argument is based upon the assumption that the spectra depend upon only one dimensional

constant. For example, if this constant is  $\epsilon$ , the rate of energy dissipation, then the dimensional argument gives the familiar results for the inertial subrange:  $E(k) \sim k^{-5/3}$  and  $\Phi(\omega) \sim \omega^{-2}$ . No attempt is made here to argue that a single dimensional constant is appropriate for the entire spectrum shown in Figure 3. Perhaps it is possible to divide the spectrum into subranges in which a single constant is important, but that is not assumed. The point is that if such a subrange does exist, then the dimensional argument for the subrange is in agreement with the frost-free turbulence transformation.

Suppose that the one important dimensional constant  $Q$  has dimensions  $X^a T^b$ . Then  $E$  and  $\Phi$  must have the following forms in order to be dimensionally correct:

$$\left. \begin{aligned} E(k) &\sim Q^{-\frac{2}{b}} k^{\left(\frac{2a}{b}+3\right)} \\ \Phi(\omega) &\sim Q^{\frac{2}{a}} \omega^{\frac{2b}{a}+1} \end{aligned} \right\} \quad (14)$$

For the case where  $Q$  is taken to be  $\epsilon$ , the exponents  $a$  and  $b$  are 2 and -3, respectively.

These forms can be seen to be consistent with frost-free turbulence. Suppose that  $\Phi(\omega) \sim \omega^{-p}$ , where  $p = -\left(\frac{2b}{a}+1\right)$ , and calculate  $E(k)$  using the frost-free transformation (10). The result is

$$E(k) \sim k^{\left(\frac{3p-1}{p+1}\right)}, \quad (15)$$

which is exactly what is given in (14) when

$$p = -\left(\frac{2b}{a}+1\right).$$

Dimensional arguments can also be made for the diffusivity and for the width of the dye patch:

$$\left. \begin{aligned} K &\sim Q^{-\frac{a}{b}} \ell^{2+\frac{a}{b}} \sim \ell^{\frac{2p}{p+1}} \\ \ell^2 &\sim Q^{\frac{2}{a}} \ell^{-\frac{2b}{a}} \sim \ell^{p+1} \end{aligned} \right\} \quad (16)$$

These results are also in agreement with frost-free turbulence, as can be seen from equations (5) and (6) with  $E(k)$  given by (15).

## 5. Shear Dispersion

It is possible to derive the frost-free turbulence transformation using the idea that the mechanism for turbulent mixing is shear dispersion on all scales. Such a derivation should clarify the idea of scale dependent diffusion that is intrinsic to the transformation described here. It should also clarify the manner in which the advection of small eddies by large eddies is incorporated into the transformation.

Shear dispersion was discussed by Taylor (1953, 1954) in the context of longitudinal dispersion in pipes. He found that an enhanced diffusivity was needed to account for the dispersion of contaminant introduced into the flow. This enhanced diffusivity is appropriate in conjunction with the cross-sectional average of the contaminant concentration. The enhancement is due to the combined action of shear and cross-shear mixing, features that are unresolved when we are dealing with cross-sectional averages, and whose effects are accounted for by the enhanced diffusivity.

This shear dispersion relates to turbulent diffusion in two ways. First, the eddy diffusivity can likewise be considered as parameterizing the details of the flow that are averaged out. The value of the diffusivity appropriate to a given scale is determined by those details of the flow that are smaller than this scale. Second, the mechanism of turbulent mixing is shear dispersion on all scales. At any scale there are eddies that provide shear, and there are smaller eddies that provide mixing across this shear. As the scale is increased, the eddy diffusivity must be enhanced to account for the additional shear and cross-shear mixing that is averaged out.

From the point of view of someone numerically modeling the flow, this is clear. Eddy diffusivity is used to parameterize mixing due to sub-grid scale motion. For a coarser numerical grid, a larger value of diffusivity is needed to account for the mixing that would be explicitly resolved on a finer grid.

A simple two-layer model of shear dispersion can show how the diffusivity is enhanced as the details of the shear are averaged over. This model is given by the equations,

$$\left. \begin{aligned} \frac{\partial C_1}{\partial t} + u_1 \frac{\partial C_1}{\partial x} &= -\frac{1}{T} (C_1 - C_2) + K \frac{\partial^2 C_1}{\partial x^2} \\ \frac{\partial C_2}{\partial t} + u_2 \frac{\partial C_2}{\partial x} &= -\frac{1}{T} (C_2 - C_1) + K \frac{\partial^2 C_2}{\partial x^2} \end{aligned} \right\} \quad (17)$$

governing the contaminant concentrations  $C_1$  and  $C_2$  in the layers of fluid with velocities  $u_1$  and  $u_2$ . The contaminant mixes from the more concentrated to the less concentrated layer with a mixing time  $T$ . Longitudinal diffusion within each layer is described by a diffusivity  $K$ . If both  $T$  and  $K$  are due to eddies that are unresolved in this two-layer description, then they should be related by

$$\ell^2 = 2KT, \quad (18)$$

where  $\ell$  is the thickness of the layers.

The reason for considering this model is to illustrate the relationship of the mean concentration,  $\bar{C} = \frac{1}{2} (C_1 + C_2)$ , as determined by (17), and the solution of the advection-diffusion equation,

$$\frac{\partial \bar{C}}{\partial t} + \bar{u} \frac{\partial \bar{C}}{\partial x} = K^* \frac{\partial^2 \bar{C}}{\partial x^2}, \quad (19)$$

which should be appropriate when the details of the two layers are averaged out. Here  $\bar{u} = \frac{1}{2} (u_1 + u_2)$  is the average velocity and  $K^*$  is the enhanced diffusivity.

Equations (17) can be combined to show that  $\bar{C}$  must satisfy

$$\left[ \left( \frac{\partial}{\partial t} + \bar{u} \frac{\partial}{\partial x} - K \frac{\partial^2}{\partial x^2} \right)^2 + \frac{2}{T} \left( \frac{\partial}{\partial t} + \bar{u} \frac{\partial}{\partial x} - K \frac{\partial^2}{\partial x^2} \right) - (\Delta u)^2 \frac{\partial^2}{\partial x^2} \right] \bar{C} = 0, \quad (20)$$



where  $\Delta u = \frac{1}{2}(u_1 - u_2)$ . This is not exactly equation (19); however, if the first term were negligible, then it would be the same as (19) with

$$K^* = K + \frac{1}{2}(\Delta u)^2 T. \quad (21)$$

Careful analysis (Thacker, 1975) can show that ignoring this first term is equivalent to resolving only those changes in  $C$  that are slower than the mixing time  $T$  and those spatial details that are larger than a mixing length  $x = (2K^*T)^{1/2}$ . Note that  $T$  and  $x$  are related according to equation (4), the equation that relates length and time scales for the frost-free turbulence transformation.

On the other hand, for small changes in time, the first term in equation (19) is important and the second term is negligible. The reason for this is that in a short enough time, a negligible amount of mixing between the layers occurs. In this limit, advection within each layer is important and an enhanced diffusivity parameter does not apply. However, each time a bit of contaminant crosses to the other layer, its direction reverses. This gives a long-term net effect of a random walk and diffusion-like behavior. Thus, shear dispersion is like either advection or diffusion, depending upon the scale of the observation. If all of the details of the flow are resolved, shear dispersion is differential advection. But if these details are ignored, which corresponds to filtering out high frequencies and high wavenumbers, then shear dispersion can be represented by an enhanced diffusivity.

Equation (21) can be generalized to the case of turbulent mixing. The shear of the two-layer flow can be thought of as representing an eddy of arbitrary scale in a turbulent flow and the mixing as due to smaller eddies. If the resolution is decreased, then the eddy that represented the shear contributes to the mixing across the shear of a still larger eddy. Thus, the difference  $dK \equiv K^* - K$  can be thought of as the increase in eddy diffusivity associated with a decrease in resolution. The factor  $(\Delta u)^2$  represents the energy in the scale of the shear, so it should be proportional to  $E(k)dk$  or  $\Phi(\omega)d\omega$ . The mixing time  $T = \frac{2\pi}{\omega}$  is related to the diffusivity through equation (4),  $\ell^2 = 2KT$ , if  $\ell = \frac{2\pi}{k}$  is the scale of the shear. Thus, (21) can be generalized to the differential equations

$$dK = -C \frac{E(k)dk}{2Kk^2} = \frac{C}{2\pi} \frac{\Phi(\omega)d\omega}{\omega}. \quad (22)$$

These equations can be integrated to give equations (5) and (8).

Equations (22) together with (6) are sufficient to determine the frost-free turbulence transformation. To see this, differentiate equation (6) and substitute from (21) to get an equation relating  $d\omega$  and  $dk$ ,

$$d\omega = \pi^{-1} \left[ 2Kk - C \frac{E(k)}{2K} \right]. \quad (23)$$

Now use (23) to eliminate  $d\omega$  and  $dk$  from (22). The result is exactly the transformation given by equations (21).

The principal point to be seen from this heuristic derivation is that the eddy diffusivity parameterization should only be valid for an appropriately averaged description of the flow. Such an average should filter out high frequencies and high wavenumbers, where the cut-off values are related by equation (6). The result of this averaging should be expressions like equations (5) and (8) for the diffusivity. It is the extent of the averaging that determines what should be resolved as advection and what should be parameterized as diffusion.

It is interesting to note the similarity of the ideas behind this heuristic derivation of equation (5) and those of Tchen and of Nakano who obtain the same expression for eddy viscosity. Tchen (1973, 1975) uses a hierarchy of ensembles to allow for a varying degree of resolution, which is expressed here as a differential equation. His memory chain corresponds to a hierarchy of time scales that are associated with the hierarchy of length scales. Nakano (1972) bases his theory upon the idea that smaller eddies serve to damp the larger eddies while larger eddies serve to distort and advect smaller eddies. The damping

is simply mixing of momentum, so his ideas are the same as those used here.

Recently, McComb (1974) obtained a similar expression for eddy viscosity by modifying Edwards' (1964) theory of turbulence. Their idea is that small scale advection is like random stirring, which is basically the same as the idea presented here. In the two-layer model, the random forces are provided by the shear and the cross-shear mixing. This can be seen clearly from Monin and Yaglom's (1971) derivation of equation (20) as a Fokker-Planck equation for a Markov process.

None of these dynamic theories has yet produced an equation, similar to (8), expressing the eddy viscosity as an integral over the time spectrum. For both (5) and (8) to hold, there must be a correspondence between frequencies and wavenumbers, at least in the statistical sense that an ensemble average should filter out high frequencies and high wavenumbers. Tchen's theory seems to be the closest to this. It would be interesting to see if such an expression can be obtained from these theories. If so, then a more rigorous derivation of the frost-free turbulence transformation should be possible.

## 6. Summary

The frost-free turbulence transformation presented here in equations (10) is based upon two assumptions. The first is that there is a correspondence between spatial and temporal scales of the turbulence. This is justified by the results of the dye diffusion experiments as summarized by Okubo's (1971) diagrams and by the argument that a mixing length and a relaxation time can be assigned to the averaging process that results in the eddy diffusivity. The second is that an expression such as (5) can be used to describe the

scale dependence of the eddy diffusivity. This is justified by the generalization of the results from shear dispersion and by the dynamical theories of Tchen, Nakano, Edwards, and McComb. This transformation successfully relates current records with dye diffusion data and agrees with the results of dimensional arguments. Therefore, this transformation appears to be valid and should be useful as a working hypothesis for further studies of turbulence.

## 7. References

- Edwards, S. F. (1964): The statistical dynamics of homogeneous turbulence. *J. Fluid Mech.*, 18:239-273.
- Heisenberg, W. (1948): Zur statistischen Theorie der Turbulenz. *Z. Physik.*, 124:628-657.
- Monin, A. S., and A. M. Yaglom (1971): *Statistical Fluid Mechanics*, Vol. 1. MIT Press, Cambridge, Mass., 676-693.
- McComb, W. D. (1974): A local energy-transfer theory of isotropic turbulence. *J. Phys. A*, 7:632-649.
- Nakano, T. (1972): A theory of homogeneous, isotropic turbulence of incompressible fluids. *Ann. Phys.*, 73:326-371.
- Okubo, A. (1971): Oceanic diffusion diagrams. *Deep-Sea Res.*, 18:789-802.
- Taylor, G. I. (1938): The spectrum of turbulence. *Proc. Roy. Soc. A*, 164:476.
- Taylor, G. I. (1953): Dispersion of soluble matter in solvent flowing slowly through a tube. *Proc. Roy. Soc. A*, 219:446-468.
- Taylor, G. I. (1954): The dispersion of matter in turbulent flow through a pipe. *Proc. Roy. Soc. A*, 223:466-488.
- Tchen, C. M. (1973): Repeated cascade theory of homogeneous turbulence. *Phys. Fluids*, 16:13-30.
- Tchen, C. M. (1975): Cascade theory of turbulence in a stratified medium. *Tellus*, 27:1-14.
- Thacker, W. C. (1976): A solvable model of shear dispersion. *J. Phys. Oceanogr.*, 6:66-75.
- Webster, F. (1969): Turbulence spectra in the ocean. *Deep-Sea Res.*, 16 (Suppl.):357-368.

## Irregular Grid Finite-Difference Techniques: Simulations of Oscillations in Shallow Circular Basins

W. C. THACKER

*Atlantic Oceanographic and Meteorological Laboratories, NOAA, Sea-Air Interaction Laboratory, Miami, Fla. 33149*

(Manuscript received 13 February 1976, in revised form 23 September 1976)

### ABSTRACT

Finite-difference techniques for irregular computational grids are presented. Successful simulations of transient normal mode oscillations in shallow circular basins, where analytic solutions are known, demonstrate that these techniques can yield accurate results, even in situations involving a curved boundary. These techniques should prove to be quite useful for numerically forecasting storm surges in bays and estuaries where calculations are complicated by the curving coastline.

### 1. Introduction

Numerical forecasts of storm surges in bays, estuaries or lakes are complicated by the curvature of the coastline. Straightforward finite-difference calculations (Reid and Bodine, 1968; Overland, 1975) on uniform, rectangular computational grids, which represent the coastline as a stair-step boundary, may yield well-behaved solutions away from the boundary but generate numerical noise at the coastline where the forecast is to be made. Coordinate transformation techniques (Reid and Vastano, 1966; Birchfield and Murty 1974; Jelesnianski, 1974) provided a better representation of the boundary. However, the effort involved in defining the transformation makes it difficult to implement. Finite-element methods (Wang and Conner, 1975; Norton, King, and Orlob, 1973) with irregular, triangular computational grids also provide a better representation of the boundary. However, they are time-implicit and require lengthy matrix inversion at each time step which is undesirable for forecast models. This suggests that time-explicit, finite-difference calculations on irregular, triangular grids might be a way to handle the problem of boundary curvature.

To date, little has been done to implement finite-difference techniques on irregular triangular grids. Kivisild (1954) used a grid of equilateral triangles to calculate storm surges on Lake Okeechobee. Crowley (1971), Boris *et al.* (1975) and Fritts (1976) have made finite-difference calculations using irregular grids. They were concerned with problems other than storm surge forecasting where there is an advantage that the grid points be free to move during the calculation. There seems to be no discussion in the literature of these techniques per se. For this reason, emphasis here is placed on the techniques rather than on storm surges.

However, the discussion will be restricted to two-dimensional grids and to the shallow water wave equations so that the applicability to storm surge forecasting can be seen.

The approximation of partial derivatives on irregular grids is discussed in Section 2. The basic idea is that the partial derivatives can be approximated by the slopes of a planar surface. This idea can be generalized so that an average of slopes of several planar surfaces can be used to approximate derivatives. Such approximations are first order in the grid spacings. Although higher order schemes are possible based upon the slopes of parabolic or other surfaces, they are not discussed in detail. The formulas for approximating partial derivatives have the desirable feature of satisfying a Green's theorem. For shallow water waves this guarantees that mass is conserved.

Two different schemes for approximating solutions to the shallow water wave equations are discussed. The first scheme involves two spatially staggered grids, one for the water surface elevation and the other for the momentum. This scheme yields good results when the earth's rotation is neglected, but it cannot be used when these terms must be included. The second scheme has only one grid for all variables and allows rotation to be included.

Numerical solutions to the shallow water wave equations for a circular basin calculated with these schemes are compared to corresponding exact solutions obtained analytically in closed form. Computations are initialized to normal modes of the basin and carried forward for a time approximately equal to 50 cycles of the normal mode. After 50 cycles, both the amplitudes and the frequencies of the computations are in good agreement with the exact values for the normal modes. This demonstrates that these irregular grid finite-difference



techniques do indeed provide a means for incorporating curved boundaries into numerical calculations and suggests that these techniques might be useful for forecasting storm surges.

## 2. Formulas for approximating partial derivatives

An irregular two-dimensional grid can be thought of as being a patchwork of triangular elements whose vertices are the grid points. In the vicinity of each triangle, the partial derivatives of a function can be approximated by the slopes of a plane determined by the values of the function at the vertices. This leads to the following three-point formulas for approximating partial derivatives:

$$\left. \begin{aligned} \overline{\frac{\partial f}{\partial x}} &= [f_1(y_2 - y_3) + f_2(y_3 - y_1) + f_3(y_1 - y_2)] / \Delta \\ \overline{\frac{\partial f}{\partial y}} &= -[f_1(x_2 - x_3) + f_2(x_3 - x_1) + f_3(x_1 - x_2)] / \Delta \end{aligned} \right\}, \quad (1)$$

$$\Delta = x_1(y_2 - y_3) + x_2(y_3 - y_1) + x_3(y_1 - y_2)$$

where  $f_1$ ,  $f_2$  and  $f_3$  are the values of the function at the three vertex points,  $(x_1, y_1)$ ,  $(x_2, y_2)$  and  $(x_3, y_3)$ , respectively. The overbars indicate that these are approximations. The quantity  $\Delta$  is twice the area of the triangle.

The accuracy of these formulas depends upon the point  $(x, y)$  at which the derivatives are approximated, even though the formulas do not explicitly depend upon that point. Clearly the approximation is better in the vicinity of the triangle than at some distance point. The dependence of the accuracy upon the point  $(x, y)$  can be seen by considering power series expansions of the function about that point, i.e.,

$$\left. \begin{aligned} f_1 &= f + \frac{\partial f}{\partial x}(x_1 - x) + \frac{\partial f}{\partial y}(y_1 - y) + \epsilon_1 \\ f_2 &= f + \frac{\partial f}{\partial x}(x_2 - x) + \frac{\partial f}{\partial y}(y_2 - y) + \epsilon_2 \\ f_3 &= f + \frac{\partial f}{\partial x}(x_3 - x) + \frac{\partial f}{\partial y}(y_3 - y) + \epsilon_3 \end{aligned} \right\}, \quad (2)$$

where  $\epsilon_1$ ,  $\epsilon_2$ , and  $\epsilon_3$  are higher order terms of the expansions. Solving for  $\partial f / \partial x$  and  $\partial f / \partial y$  yields corrections to (1),

$$\left. \begin{aligned} \frac{\partial f}{\partial x} \overline{\frac{\partial f}{\partial x}} &= \frac{\partial f}{\partial x} - [\epsilon_1(y_2 - y_3) + \epsilon_2(y_3 - y_1) + \epsilon_3(y_1 - y_2)] / \Delta \\ \frac{\partial f}{\partial y} \overline{\frac{\partial f}{\partial y}} &= \frac{\partial f}{\partial y} + [\epsilon_1(x_2 - x_3) + \epsilon_2(x_3 - x_1) + \epsilon_3(x_1 - x_2)] / \Delta \end{aligned} \right\}. \quad (3)$$

The terms  $\epsilon_i$  are of second order in the grid spacing and the correction terms in (3) are therefore of first order. Even if the point  $(x, y)$  is at the center of an equilateral triangle, the correction terms are first order in the grid spacing, in contrast to the case of centered differences on uniform rectangular grids in which the correction terms are second order. However, the approximation is best at the centers of the triangles,  $x = (x_1 + x_2 + x_3) / 3$  and  $y = (y_1 + y_2 + y_3) / 3$ .

The approximation to the derivatives expressed by (1) is equivalent to the approximations involved in using linear interpolating functions for finite element calculations. Higher order polynomial interpolating functions have a counterpart of higher order finite-difference approximations. The partial derivatives can be approximated by the slopes of polynomial surfaces determined by some greater number of grid points. For example, if the midpoint of each side of the triangles is also a grid point, the values of the function at each vertex and each side point of a triangle determine a parabolic surface. In this case the slope approximation does depend explicitly upon the point  $(x, y)$  where the approximation is made. In this case, the same procedure of power series expansions will yield six-point functions and their corrections, as in (3). However, no effort has been made to proceed along these lines.

These three-point formulas are best suited for approximating derivatives at the centers of the triangular elements comprising the grid. When staggered grids can be used, as in Section 3, where the centers of the triangles of one grid are the vertices of the other, then there is no difficulty other than an ambiguity due to the fact that, generally, there are more centers than vertices. It is desirable in this case to approximate the derivatives at the vertices rather than at the centers.

Each grid point is simultaneously the vertex of several triangles. The derivatives at that grid point might be approximated by the three-point formulas for any of these triangles. This suggests that an average of these formulas should be used. Because the triangles are not all the same size, the average should be weighted by the areas of the triangles. If these are  $N$  triangles with a vertex at  $(x, y)$  and their remaining vertices at  $(x_1, y_1)$ , ...,  $(x_N, y_N)$  are indexed counterclockwise about  $(x, y)$ , then this averaging procedure yields the  $N$  point formulas

$$\left. \begin{aligned} \overline{\frac{\partial f}{\partial x}} &= \sum_{i=1}^N f_i(y_{i+1} - y_{i-1}) / \Delta \\ \overline{\frac{\partial f}{\partial y}} &= - \sum_{i=1}^N f_i(x_{i+1} - x_{i-1}) / \Delta \\ \Delta &= \sum_{i=1}^N x_i(y_{i+1} - y_{i-1}) \end{aligned} \right\}, \quad (4)$$

where the summation is cyclic, modulo  $N$ , and  $\Delta$  is twice the area of the polygon formed by the  $N$  triangles.

For the case  $N=3$ , the  $N$  point formulas reduce to the three-point formulas of Eqs. (1). For the case in which the polygon  $N=4$ , is a rectangle, Eqs. (4) reduce to the usual centered-difference formulas. These formulas do not depend explicitly upon the point  $(x,y)$  where the derivatives are approximated; again, the accuracy does depend upon that point. The accuracy, still first order, is best at the centroid of the polygon formed by the  $N$  triangles.

Formulas (4) can be rewritten

$$\left. \begin{aligned} \frac{\partial f}{\partial x} &= \sum_{i=1}^N \frac{1}{2} (f_i + f_{i+1}) (y_{i+1} - y_i) / \frac{1}{2} \Delta \\ \frac{\partial f}{\partial y} &= - \sum_{i=1}^N \frac{1}{2} (f_i + f_{i+1}) (x_{i+1} - x_i) / \frac{1}{2} \Delta \end{aligned} \right\}, \quad (5)$$

so that each term can be associated with a triangle side connecting points  $i$  and  $i+1$ . The first factor,  $\frac{1}{2}(f_i + f_{i+1})$ , is the average value of the function for the side. Note that this side is shared by two triangles, unless it lies on a boundary. Therefore, because the points are taken counter-clockwise in the formulas, the terms associated with this line are equal in magnitude but opposite in sign at the two triangles where these terms contribute. This fact guarantees that a Green's theorem is satisfied.

Green's theorem (see, e.g., Taylor, 1955) states that, for two functions  $f$  and  $g$  with continuous first partial derivatives in a region  $R$  bounded by a sectionally smooth curve  $c$ ,

$$\iint \left( \frac{\partial f}{\partial x} - \frac{\partial g}{\partial y} \right) dx dy = \int_c (f dy - g dx). \quad (6)$$

On an irregular triangular grid, the corresponding theorem is

$$\frac{1}{3} \sum_{i=1}^M \left( \frac{\partial f}{\partial x} + \frac{\partial g}{\partial y} \right)_i \frac{1}{2} \Delta_i = \sum_{i=1}^B \left[ \frac{1}{2} (f_i + f_{i+1}) (y_{i+1} - y_i) - \frac{1}{2} (g_i + g_{i+1}) (x_{i+1} - x_i) \right]. \quad (7)$$

Here it is assumed that there are  $M$  grid points and that the first  $B$  points are on the boundary and indexed counterclockwise. The factor  $\frac{1}{2}\Delta_i$  is the area of the polygon formed by the triangles with a vertex at the point  $i$ . Because each triangle has three vertices, only one-third of this area can be associated with each vertex; thus the factor  $\frac{1}{3}$ . Using the fact from the preceding paragraph, it is easy to see that when evaluating the left-hand side of (7) using (5), the contributions of the internal lines cancel, leaving only the contribution of the boundary on the right-hand side of (7).

A similar Green's theorem holds for the three-point formulas of (1) on staggered grids. When applied to shallow water waves, these theorems guarantee that

the total volume of water is constant so long as no water flows in at the boundary.

So far, only approximations for first partial derivatives have been discussed. One possibility for approximating higher derivatives is by iterating the formulas for the first derivatives. However, this approximation might depend upon the order of the differentiation, in which case  $\partial^2 f / \partial x \partial y \neq \partial^2 f / \partial y \partial x$ . This is the case for the three-point formulas on staggered grids, even if the grids are composed of identical triangular elements. On regular grids, four- and six-point formulas can be iterated to form second derivatives, but for irregular grids  $\partial^2 f / \partial x \partial y \neq \partial^2 f / \partial y \partial x$ . Therefore, iterating the formulas for first derivatives does not seem attractive.

If the first derivatives had been approximated by the slopes of higher order polynomials, then the curvature of these polynomials would provide an approximation to the second derivatives. This corresponds to the fact that higher order interpolating functions must be used with the finite-element method to approximate solutions to partial differential equations involving higher derivatives.

These results for two-dimensional irregular grids can be generalized to higher dimensions. For  $k$  dimensions, the basic approximation yields  $(k+1)$  point formulas. Again, averaging should provide approximations for derivatives at the grid points. Higher order approximations to first derivatives might also be constructed, as well as higher partial derivatives.

### 3. Two irregular grid schemes for shallow water waves

The linearized shallow water wave equations in the absence of frictional stresses are

$$\left. \begin{aligned} \frac{\partial U}{\partial t} &= -gD \frac{\partial H}{\partial x} + fV \\ \frac{\partial V}{\partial t} &= -gD \frac{\partial H}{\partial y} - fU \\ \frac{\partial H}{\partial t} &= - \left( \frac{\partial U}{\partial x} + \frac{\partial V}{\partial y} \right) \end{aligned} \right\}, \quad (8)$$

where  $U$  and  $V$  are the  $x$  and  $y$  components of volume transport per unit width,  $H$  is the surface elevation,  $D$  the stillwater depth,  $g$  the gravitational acceleration and  $f$  the Coriolis parameter accounting for the earth's rotation. Two irregular grid, finite-difference schemes were used to calculate approximate solutions to these equations for the case of a closed circular basin. The first involved the use of staggered grids, one for  $U$  and  $V$  and the other for  $H$ . In the second scheme all three variables were calculated at the same grid points.

Samples of grids used for these calculations are shown in Figs. 1, 2 and 3. For scheme one, the vertices of the



triangles were taken as grid points for  $U$  and  $V$ , and the crosses at the centers of alternate triangles as those for  $H$ . (The crosses have been omitted from Fig. 3 because of the small scale of the elements.) For scheme two,  $U$ ,  $V$  and  $H$  are all calculated at the vertex points. For both schemes, there are  $U$ ,  $V$  points situated on the boundary so that the zero normal flow condition is easy to implement.

It is interesting to note that these grids are topologically equivalent to hexagonal arrays of equilateral triangles. An interior hexagonal pattern is quite evident in the interior of grid 1, but the outer triangles have been distorted to approximate the circular basin. The hexagonal pattern which can easily be recognized near the center of grids 2 and 3 is gradually distorted to the circular shape at the boundary. Because of this topological equivalence, these calculations are equivalent to coordinate transformation calculations on a hexagonal shaped grid of equilateral triangles.

The manner in which the grid points are indexed is unimportant. The convention followed was to index the  $U$ ,  $V$  points with a single integer,  $i=1, \dots, I$ , with the boundary points first,  $i=1, \dots, B$ , and the  $H$  points with the integer,  $j=1, \dots, J$ . What is important is to know which points are neighbors so that the finite-difference formulas can be evaluated. For scheme one, arrays were used to store the indices of the three  $H$  points closest to each  $U$ ,  $V$  point and the indices of the three  $U$ ,  $V$  points closest to each  $H$  point. For scheme two, six neighbor indices were stored for interior points

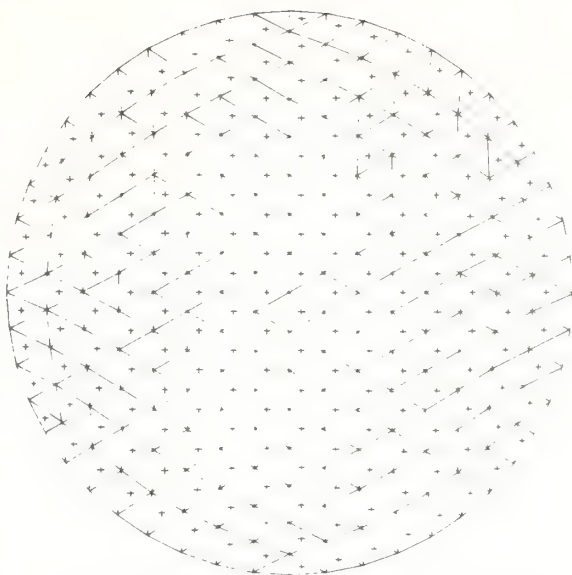


FIG. 2. Grid two.  $U$ ,  $V$  and  $H$  are calculated as for grid one. Instabilities associated with nonuniformity of the triangles were insignificant.

and four or five for boundary points, depending upon the number of triangles which meet at that point.

The finite-difference formulas depend upon the coordinates of the grid points. For numerical stability (see Section 4) it is important that the grid points be smoothly distributed. The smooth distributions for

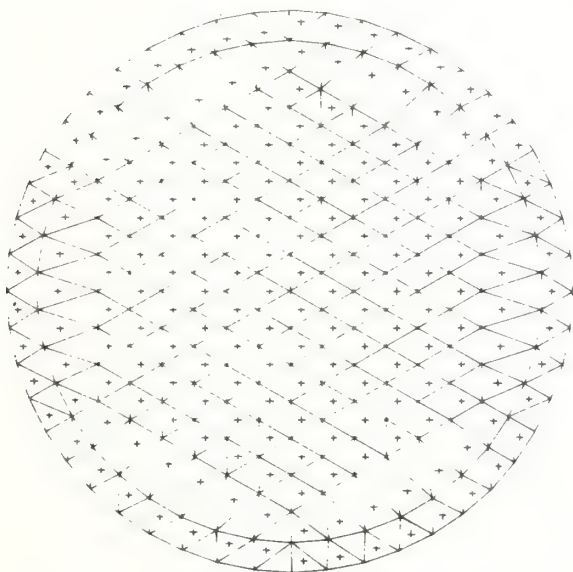


FIG. 1. Grid one. The transports  $U$  and  $V$  are calculated at the vertices of the triangles. For scheme one, the surface elevation  $H$  is calculated at the centers of the triangles marked by crosses; for scheme two, at the vertices the same as  $U$  and  $V$ . The contrast in triangle sizes is greater for this grid than for grid two, resulting in a larger growth rate for the associated instability.

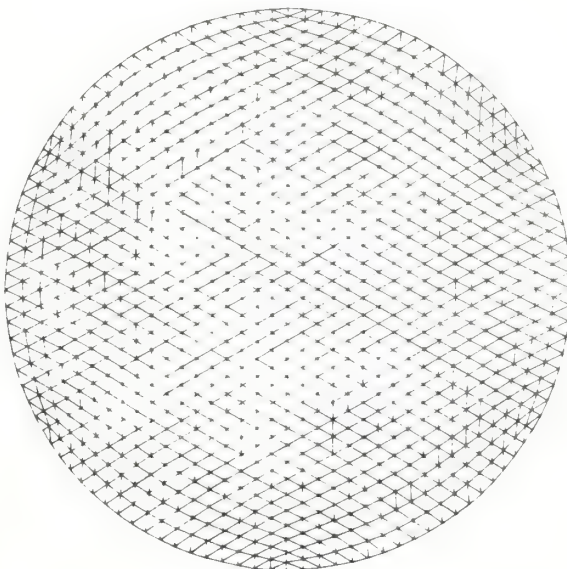


FIG. 3. Grid three.  $U$ ,  $V$  and  $H$  are calculated as for grid one, the crosses marking scheme one  $H$  points being omitted because of scale. This grid provided quite good resolution of the normal modes which were simulated.



grids 2 and 3 were obtained by solving the equations

$$\left. \begin{aligned} x_i &= \frac{1}{6} \sum_{n=1}^6 x_{i_n(i)} \\ y_i &= \frac{1}{6} \sum_{n=1}^6 y_{i_n(i)} \end{aligned} \right\}, \quad i = B+1, \dots, I, \quad (9)$$

where  $i_n(i)$ ,  $n = 1, \dots, 6$ , are the six neighboring points to the  $i$ th point on the  $U, V$  grid. Some of the neighboring points can be boundary points with coordinates,  $x_i = R \cos(2\pi i/B)$  and  $y_i = R \sin(2\pi i/B)$ ,  $i = 1, \dots, B$ . Eqs. (9) can be thought of as determining the equilibrium position of a system of springs under tension,

fixed at the boundary points. These equations were solved using an over-relaxed Jacobi technique. The staggered  $H$ -grid coordinates were then given by

$$\left. \begin{aligned} x_j &= \frac{1}{3} \sum_{n=1}^3 x_{i_n(j)} \\ y_j &= \frac{1}{3} \sum_{n=1}^3 y_{i_n(j)} \end{aligned} \right\}, \quad j = 1, \dots, J, \quad (10)$$

where  $i_n(j)$ ,  $n = 1, \dots, 3$ , are the three points on the  $U, V$ -grid closest to the  $j$ th point on the staggered  $H$ -grid.

For both schemes, the discrete analogues of (8) take the form

$$\left. \begin{aligned} U_i^{n+1} &= U_i^{n-1} - gD_i \tau \left( \frac{\partial \bar{H}}{\partial x} \right)_i^n + f\tau V_i^{n+1} \\ V_i^{n+1} &= V_i^{n-1} - gD_i \tau \left( \frac{\partial \bar{H}}{\partial y} \right)_i^n - f\tau U_i^{n+1} \\ U_i^{n+1} &= U_i^{n-1} - gD_i \tau \left[ \sin^2 \theta_i \left( \frac{\partial \bar{H}}{\partial x} \right)_i^n - \cos \theta_i \sin \theta_i \left( \frac{\partial \bar{H}}{\partial y} \right)_i^n \right] \\ V_i^{n+1} &= V_i^{n-1} - gD_i \tau \left[ \cos^2 \theta_i \left( \frac{\partial \bar{H}}{\partial y} \right)_i^n - \cos \theta_i \sin \theta_i \left( \frac{\partial \bar{H}}{\partial x} \right)_i^n \right] \\ H_j^{n+1} &= H_j^n - \tau \left[ \left( \frac{\partial U}{\partial x} \right)_j^{n+1} + \left( \frac{\partial V}{\partial g} \right)_j^{n+1} \right] \end{aligned} \right\}, \quad \begin{aligned} &i = B+1, \dots, I \\ &i = 1, \dots, B \\ &j = 1, \dots, J \end{aligned} \quad (11)$$

In scheme one, the three-point formulas were used to approximate the partial derivatives;  $(\partial \bar{H}/\partial x)_i^n$  and  $(\partial \bar{H}/\partial y)_i^n$  were calculated using the three  $H$  points nearest to the  $U$  point,  $i$ , and  $(\partial U/\partial x)_j^{n+1}$  and  $(\partial V/\partial y)_j^{n+1}$  were calculated using the three  $U, V$ -points nearest to the  $H$  point,  $j$ . For the boundary points,  $i = 1, \dots, B$ , the three closest  $H$  points form triangles which do not intersect the boundary; the slopes of these triangles were extrapolated to the boundary. In scheme two, with  $i \equiv j$  and  $I \equiv J$ , six-point formulas were used to approximate the partial derivatives except for points on the boundary,  $i = j = 1, \dots, B$ . Five-point formulas were used for all boundary points except for six corresponding to the corners of distorted hexagons for which four-point formulas were used.

The trigonometric factors  $\cos \theta_i$  and  $\sin \theta_i$  guarantee that there is no normal flow at the boundary. A leap-frog scheme was used for the time derivatives, with surface elevations calculated at times  $t = n\tau$  and momentum components calculated at times  $t = (n + \frac{1}{2})\tau$ , where  $\tau$  is the length of the time step and  $n = 0, 1, 2, \dots$ . The time differences are implicit since the Coriolis terms are evaluated at the new time levels,  $n + \frac{1}{2}$ , in

order to guarantee stability in the limit,  $g=0$ . No time-consuming matrix inversion is necessary, though, since the equations are only coupled by pairs; it is a simple matter to rewrite the equations expressing  $U_i^{n+1}$  and  $V_i^{n+1}$  in terms of  $H_i^n$ , and  $U_i^{n-1}$  and  $V_i^{n-1}$ .

#### 4. Numerical stability

By assuming the grids to be uniform and without boundaries, it is possible to analyze these two computational schemes for stability. For equilateral triangular grids, the solutions can be assumed to vary as  $\exp\{i[(2M+N)k\Delta + \sqrt{3}Nl\Delta]\}$ , where  $2\Delta$  is the distance between grid points,  $k$  and  $l$  are wave vector components, and the integers  $M$  and  $N$  index the grid points. For both schemes the eigenvalues  $\lambda$  of the amplification matrices must satisfy equations of the form

$$\left. \begin{aligned} (1-\lambda)[(1+f^2)\lambda^2 - (2-p)\lambda + 1] - iq\lambda^2 &= 0 \\ p &= 4gD(\tau^2/\Delta^2)(|z_1|^2 + |z_2|^2) \\ q &= (8/\sqrt{3})fgD(\tau^2/\Delta^2) \operatorname{Im} z_1^* z_2 \end{aligned} \right\}, \quad (12)$$

where  $i = \sqrt{-1}$  and the complex numbers  $z_1$  and  $z_2$  account for the geometry of the grid,

$$\left. \begin{aligned} z_1 &= 1 - \exp(-2ik\Delta) \\ z_2 &= \frac{1}{2}[1 + \exp(-2ik\Delta)] - \exp[i(k + \sqrt{3}l)\Delta] \end{aligned} \right\}, \text{ Scheme one}$$

$$\left. \begin{aligned} z_1 &= (1/2\sqrt{3}) \cos(k\Delta) \sin(l\Delta) \\ z_2 &= \frac{1}{6} \sin(k\Delta)[2 \cos(k\Delta) + \cos(\sqrt{3}l\Delta)] \end{aligned} \right\}, \text{ Scheme two}$$
(13)

For scheme one, if  $f=0$ , then  $|\lambda| \leq 1$  for  $\tau \leq (\Delta/3)(gD)^{1/2}$ . Thus, when the earth's rotation is neglected, scheme one is stable so long as the time step is small enough. This corresponds to the usual Courant condition for rectangular grids. For  $f \neq 0$ , because  $q \neq 0$ , scheme one is unstable. To see this, note that for small  $f$ , the eigenvalue corresponding to  $\lambda=1$  when  $f=0$  becomes  $\lambda = 1 - iq/p$ , so  $|\lambda|^2 = 1 + q^2/p^2 > 1$ . Thus, scheme one is unstable when the earth's rotation is included. The fact that  $q \neq 0$  seems to be related to the fact that  $\partial^2 H / \partial x \partial y \neq \partial^2 H / \partial y \partial x$ , even on a uniform grid, where these second derivatives are approximated by iterating the approximations for first derivatives. As the solutions step forward in time, these terms do not cancel, so they provide a numerical source of vorticity and energy. For the case  $f=0$  these terms never appear.

For scheme two,  $q=0$ . The Courant condition follows from the inequality  $2[1 - (1 + f^2)^{1/2}] \leq p \leq 2[1 + (1 + f^2)^{1/2}]$ . Thus, the Coriolis force increases the upper bound on the time step but it imposes a lower bound. So long as this Courant condition is satisfied, scheme two is stable—even when the earth's rotation is included.

The fact that these schemes are stable for uniform grids does not guarantee their stability for variable grids with boundaries. In fact, when calculations were first made on the grid shown in Fig. 1 using scheme one, instability was observed. When these calculations were repeated on the grid shown in Fig. 2, the instability was considerably suppressed.

Instabilities associated with variable grid spacing are quite like those associated with variable coefficients on uniform grids. In fact, because the grids used here can be deformed into hexagonal arrays of equilateral triangles, the calculations could be made using a coordinate transformation technique on these uniform triangular grids. In that case, the variability of the original grid would be replaced by the variability of the map factors of the transformation to the uniform grid. The instability could be attributed to the variability of the map factor coefficients.

Instabilities associated with grid irregularities should not be identified with the fact that these are finite-difference techniques. Similar effects have been reported for finite-element calculations by Wang and Conner (1975) and by Pagenkopf and Pearce (1975). In fact, the grid smoothing technique given by Eqs. (9) which were used to position the points on grids 2 and 3 might be equally as useful for smoothing grids for finite element calculations.

Calculations with scheme two exhibited instabilities with growth rates depending upon the magnitude of  $f$ . This can be attributed to the variability of the grid spacing. For irregular grids, terms proportional to  $f[(\partial^2 H / \partial x \partial y) - (\partial^2 H / \partial y \partial x)]$  provide a numerical source of energy. Thus, increasing  $f$  should increase the growth rate. For most practical problems, the growth rate is quite small. In high latitudes where  $f$  is largest, this scheme might not be feasible for highly irregular grids. Perhaps higher order schemes suitable for approximating higher partial derivatives would be more suitable in these situations.

For practical problems such as storm surge forecasting, instability should not be a problem. So long as the size of the triangles on the grid vary smoothly enough, the  $e$ -folding time due to instabilities should be on the order of a week while the duration of the surge is usually less than 24 h. The same relaxation procedure used to position the grid points in Figs. 2 and 3 can also be used to obtain smoothly varying grids for practical problems. Furthermore, when bottom friction is included in the calculations, the instability can be expected to be damped.

## 5. Normal mode simulations

The irregular grid finite-difference schemes described in Section 3 were used to simulate the normal mode oscillations of a closed circular basin of uniform depth  $D = D_0$ . These oscillations are solutions to the shallow water equations of the form (Lamb, 1945)

$$\left. \begin{aligned} H &= \eta J_n(kr) \cos(n\theta + \omega t) \\ U' &= \eta \left( \frac{\omega}{k} \right) \left\{ \left[ \frac{n}{kr} J_n(kr) + \frac{f}{\omega} J_n'(kr) \right] \sin \theta \cos(n\theta + \omega t) - \left[ \frac{n}{kr} J_n(kr) + J_n'(kr) \right] \cos \theta \sin(n\theta + \omega t) \right\} \\ V' &= -\eta \left( \frac{\omega}{k} \right) \left\{ \left[ \frac{n}{kr} J_n(kr) + \frac{f}{\omega} J_n'(kr) \right] \cos \theta \cos(n\theta + \omega t) + \left[ \frac{n}{kr} J_n(kr) + J_n'(kr) \right] \sin \theta \sin(n\theta + \omega t) \right\} \end{aligned} \right\}, \quad (14)$$

TABLE 1. Scheme one simulations,  $f=0$ , uniform depth circular basin.

Normal mode $n$ $m$		Nondimensional frequency $= \omega R (gD_0)^{-1/2}$		
		Exact	Grid 2	Grid 3
0	1	3.8317	3.8	3.83
0	2	7.0156	6.9	7.02
0	3	10.1735	$\sim 10$	10.1
0	4	13.3237	$\sim 13$	13.2
1	0	1.8412	1.8	1.84
1	1	5.3314	5.3	5.33
1	2	8.5363	$\sim 8.3$	8.54
1	3	11.7060	$\sim 12$	11.6
2	0	3.0542	3.0	3.06
2	1	6.7061	$\sim 6.7$	6.71
2	2	9.9695	$\sim 10$	9.9
2	3	13.1703	$\sim 13$	13.0

where  $\eta$  is the amplitude of the oscillation,  $J_n$  and  $J'_n$  are the Bessel function of order  $n$  and its derivative, and  $x = r \cos \theta$ ,  $y = r \sin \theta$ . The values of the eigenfrequency  $\omega$  and corresponding wavenumber  $k$  are determined by the dispersion equation and the boundary condition

$$\left. \begin{aligned} \omega^2 &= gD_0 k^2 + f^2 \\ kR J'_n(kR) + \frac{n f}{\omega} J_n(kR) &= 0 \end{aligned} \right\} \quad (55)$$

The lowest frequency normal modes are fairly well resolved by the grids shown in Figs. 1 and 2, and therefore might be expected to be fairly well approximated for several periods of oscillation by these finite-difference schemes.

For each normal mode, the calculations were initialized according to (14) with  $\eta=1$  and  $t=0$  and then stepped forward in time according to (11) for 50 cycles of the normal mode oscillation. The time steps for the simulations were  $\tau = 0.65l(gD_0)^{-1/2}$ , where  $l$  is the distance between adjacent points on the boundary.

During the 50 cycles of each normal mode simulation, tallies were kept of the number of times each  $H_j$  changed sign in order to judge how well the eigenfunctions were approximated. Because of discretization error, the estimates of frequency were expected to vary from grid point to grid point with the variation especially noticeable near the nodes of the eigenfunctions.

TABLE 2. Scheme two simulations,  $f=0$ , uniform depth circular basin.

Normal mode $n$ $m$		Nondimensional frequency $= \omega R (gD_0)^{-1/2}$	
		Exact	Grid 3
0	1	3.8317	3.79
0	2	7.0156	6.88
0	3	10.1735	9.77
0	4	13.3237	12.3

TABLE 3. Scheme two simulations,  $f=0.3(gD_0)^{1/2}/R$ , uniform depth circular basin.

Normal mode $n$ $m$		Nondimensional frequency $= \omega R (gD_0)^{-1/2}$	
		Exact	Grid 3
0	1	3.8434	3.81
0	2	7.0220	6.89
0	3	10.1779	9.78
0	4	13.3271	12.4
1	0	1.9748	1.94
1	1	5.3507	5.30
1	2	8.5458	8.30
1	3	11.7121	11.1

This was indeed the case, and the frequency estimate variation was considerably less for calculations on the finer grid which has less discretization error.

Results of simulations with scheme one are summarized in Table 1. Because scheme one is unstable when  $f \neq 0$ , only the case of  $f=0$  is considered. The integers  $n$  and  $m$  identify the normal modes which were simulated;  $n$  refers to the order of the Bessel function for that mode, corresponding to the number of radial nodes, and  $m$  indicates the number of concentric circular nodes. The exact nondimensional frequencies were taken from tabulated values of zeros of derivatives of Bessel functions given by Abramowitz and Segun (1970). The tilde is used to indicate qualitatively good results having quite a bit of scatter in values of frequency estimates over the grid points. The additional resolution of grid 3 over grid 2 reduces the scatter in frequency estimates and confines it to nodal areas of higher frequency modes.

Results of simulations with scheme two are shown in Tables 2, 3 and 4 for  $f=0$ ,  $f=0.3(gD_0)^{1/2}/R$  and  $f=1.0(gD_0)^{1/2}/R$ , respectively. The frequency estimates are systematically low. This should be expected since the averages over neighboring triangles involved in the definition of the  $N$  point formulas (4) behave numerically like viscosity. The magnitude of the computational viscosity was estimated to be  $\nu \approx 0.3(4R^2 gD)^{1/2}$ . The exact frequencies in Table 2 are the same as those in Table 1; those in Tables 3 and 4 were obtained by numerically solving (15).

During these simulations, the normal modes were approximated in amplitude and shape as well as in

TABLE 4. Scheme two simulations,  $f=1.0(gD_0)^{1/2}/R$ , uniform depth circular basin.

Normal mode $n$ $m$		Nondimensional frequency $= \omega R (gD_0)^{-1/2}$	
		Exact	Grid 3
0	1	3.9600	3.83
0	2	7.0865	6.88
0	3	10.2225	9.78
0	4	13.3612	12.30



frequency. During the phase of the oscillation when the surface should be flat, variation in the surface due to discretization error was apparent, but this variation was small compared to the maximum amplitude of the surface elevation. As expected, these schemes conserve the quantity of water in the basin. However, because of the weak instabilities associated with irregularities

of the grids, after more than 50 cycles the amplitudes and shapes, like the frequencies, are poorly simulated.

In order to test the behavior of these irregular grid finite-difference schemes for situations when the depth of the basin is not uniform, normal modes of a circular basin with a parabolic depth profile  $D = D_0[1 - (r^2/R^2)]$  were also simulated. These oscillations are of the form (see Lamb, 1945),

$$\begin{aligned} H &= \eta \left( \frac{r}{R} \right)^n \Psi_{m,n} \left( \frac{r}{R} \right) \cos(n\theta + \omega t) \\ U &= -\eta \frac{gD}{(\omega - f)R} \left( \frac{r}{R} \right)^{n-1} \left\{ n \Psi_{m,n} \left( \frac{r}{R} \right) \sin[(n-1)\theta + \omega t] + \frac{r}{R} \Psi'_{m,n} \left( \frac{r}{R} \right) \left[ \left( \frac{\omega}{\omega + f} \right) \cos\theta \sin(n\theta + \omega t) \right. \right. \\ &\quad \left. \left. - \left( \frac{f}{\omega + f} \right) \sin\theta \cos(n\theta + \omega t) \right] \right\} \quad (16) \\ V &= -\eta \frac{gD}{(\omega - f)R} \left( \frac{r}{R} \right)^{n-1} \left\{ n \Psi_{m,n} \left( \frac{r}{R} \right) \cos[(n-1)\theta + \omega t] + \frac{r}{R} \Psi'_{m,n} \left( \frac{r}{R} \right) \left[ \left( \frac{\omega}{\omega + f} \right) \sin\theta \sin(n\theta + \omega t) \right. \right. \\ &\quad \left. \left. + \left( \frac{f}{\omega + f} \right) \cos\theta \cos(n\theta + \omega t) \right] \right\} \end{aligned}$$

where  $\Psi_{m,n}(r/R) = F(-m, m+n+1; n+1; r^2/R^2)$  is a hypergeometric polynomial and  $\Psi'_{m,n}(r/R)$  is its derivative with respect to  $r/R$ . The integers  $m$  and  $n$  indicate the number of concentric circular nodes and the number of diametrical nodes, respectively, of the  $H$  field. The frequencies of these oscillations are given by solutions of the dispersion equation

$$(\omega^2 - f^2) \frac{R}{gD_0} + 2n \left( \frac{\omega - f}{\omega} \right) = 4(m+1)(m+n). \quad (17)$$

Four oscillations were simulated using both schemes with grid three. The initial conditions were determined by Eqs. (16) and (17) with  $\eta=1$  and  $t=0$ . For the modes with  $m=0$ ,  $\Psi_{0,n}=1$  and  $\Psi'_{0,n}=0$  for all values of  $r/R$ . For the modes with  $n=0$ ,

$$\Psi_{m,0}(r/R) = P_m(1 - 2r^2/R^2)$$

is a Legendre polynomial; in particular

$$\Psi_{1,0}(r/R) = 1 - 2r^2/R^2$$

(see Lamb, 1945, or Abramowitz and Stegun, 1970). As before, the time step was taken to be  $\tau = 0.65(gD_0)^{-1/2}$ .

The results of simulations using scheme one [ $f=0$ ] are given in Table 5. Those for scheme two [ $f=0$  and  $f=0.3(gD_0)^{1/2}/R$ ] are given in Tables 6 and 7, respectively. These results are as good as those for the uniform depth basin. Neither scheme has difficulty with depth variations.

## 6. Discussion

The simulations of normal mode oscillations provide particularly appropriate tests of the irregular grid finite-difference techniques since these techniques are intended for future use in modeling storm surges. The shallow water wave equations which govern these oscillations are the basis of storm surge calculations. There are other terms which must be added to these equations to account for atmospheric forcing of the water motion, dissipation due to bottom stress, and perhaps nonlinearities if the amplitude of the motion is sufficiently

TABLE 5. Scheme one simulations,  $f=0$ , parabolic depth circular basin.

Normal mode		Nondimensional frequency $= \omega R (gD_0)^{-1/2}$	
$n$	$m$	Exact	Grid 3
1	0	1.4142	1.41
2	0	2.0000	2.00
3	0	2.4495	2.43
0	1	2.8284	2.83

TABLE 6. Scheme two simulations,  $f=0$ , parabolic depth circular basin.

Normal mode		Nondimensional frequency $= \omega R (gD_0)^{-1/2}$	
$n$	$m$	Exact	Grid 3
1	0	1.4142	1.41
2	0	2.0000	1.99
3	0	2.4495	2.43
0	1	2.8284	2.80

TABLE 7. Scheme two simulations,  $f = 0.3(gD_0)^{1/2}/R$ , parabolic depth circular basin.

Normal mode		Nondimensional frequency $= \omega R(gD_0)^{-1/2}$	
$n$	$m$	Exact	Grid 3
1	0	1.5721	1.57
2	0	2.1556	2.14
3	0	2.6041	2.58
0	1	2.8443	2.83

great, but since the exact solutions to the equations with these terms added are not available for comparison, discussion of simulations of these effects will be postponed until further calculations are made which are appropriate to a particular bay. The success of the normal mode simulations indicates that these irregular grid techniques do provide a means for calculating when there are curved boundaries such as the curving coastlines of bays and estuaries and that there are no difficulties associated with variations of the depth of the basin or with rotation of the earth. Furthermore, these simulations show that the transient response to initial conditions can be accurately represented, which is important for storm surge simulation.

Although the primary motivation for these irregular grid techniques has been the problem of curved boundaries, another advantage of these techniques is that they allow for a variation in the density of grid points over the domain of the calculation. This is desirable for storm surge models for two reasons. Because the explicit time step is bounded by the smallest ratio of grid spacing to square root of depth, on a uniform grid it is controlled by the greatest depths situated farthest from the coastline where the forecast is to be made. Variable grid spacing should allow for a larger time step to be used that is equally appropriate for shallow as for deep regions of the basin. Second, because wavelengths contract as waves propagate into shallower water, the variable grid spacing would also allow for the same number of grid points per wavelength in all parts of the basin. Plans exist for investigating the use of such a grid in conjunction with calculations for a particular bay.

Finally, it should be emphasized that these irregular grid finite-difference techniques are quite general and

should be useful for a wide variety of calculations. They offer the same flexibility as do the irregular grid finite-element techniques, and they have the advantage of an explicit time step which is useful for computations of transient phenomena.

## REFERENCES

- Abramowitz, Milton, and Irene A. Stegun, Eds., 1970: *Handbook of Mathematical Functions*. Nat. Bur. Stnds., 411 pp.
- Birchfield, G. E., and T. S. Murty, 1974: A numerical model for wind-driven circulation in Lakes Michigan and Huron. *Mon. Wea. Rev.*, **102**, 157-165.
- Boris, J. P., K. L. Hain and M. J. Fritts, 1975: Free surface hydrodynamics using a Lagrangian triangular mesh. *Proc. First Intern. Conf. Numerical Ship Hydrodynamics*, 20-23 October, David W. Taylor Naval Ship Research and Development Center.
- Crowley, W. P., 1971: FLAG: A free-Lagrange method for numerically simulating hydrodynamic flows in two dimensions. *Proc. Second Intern. Conf. Numerical Methods in Fluid Dynamics*. Springer-Verlag.
- Fritts, Martin, (1976). A numerical study of free surface waves. Rep. SAI-76-528-WA, Science Applications, Inc. (To be submitted to *Phys. Fluids*.)
- Jelesnianski, Chester P., (1974). SPLASH (Special program to list amplitudes of surges from hurricanes) Part two. General track and variant storm conditions. NOAA Tech. Memo. NWS TDL-52.
- Kivisild, Hans R., 1954: Wind effect on shallow bodies of water with special reference to Lake Okeechobee. *Trans. Roy. Inst. Tech. Sweden*, **83**.
- Lamb, Horace, 1945: *Hydrodynamics*. Dover Publ., Sections 191, 193, 210, 212.
- Norton, William R., Ian P. King and Gerald T. Orlob, 1973. A finite element model for lower granite reservoir. Final report prepared for Walla Walla District, U. S. Army Corps of Engineers, Walla Walla, Wash.
- Overland, James E., 1975: Estimation of hurricane storm surge in Apalachicola Bay, Florida. NOAA Tech. Rep. NWS 17.
- Pagenkopf, James R., and Bryan P. Pearce, 1975: Evaluation of techniques for numerical calculation of storm surges. Tech. Rep. No. 199, Ralph M. Parsons Laboratory for Water Resources and Hydrodynamics, MIT.
- Reid, Robert O., and Bernie R. Bodine, 1968: Numerical model for storm surges in Galveston Bay. *J. Waterways Harbors Div. Proc. ASCE*, **94**, 33-57.
- Reid, R. O., and A. C. Vastano, 1966: Orthogonal coordinates for the analysis of long gravity waves near islands. *Coastal engineering, Proc. Santa Barbara Specialty Conf.*, Amer. Soc. Civil Eng., 1-20.
- Taylor, Angus E., (1955). *Advanced Calculus*. Ginn and Company, Chap. 13.
- Wang, John D., and Jerome J. Conner, 1975: Mathematical modeling of near coastal circulation. MIT Sea Grant Program Rep. No. MITSG 75-13.

## CORRIGENDUM

Author W. C. Thacker has found errors in the article, "Irregular Grid Finite-Difference Techniques: Simulations of Oscillations in Shallow Circular Basins" (*J. Phys. Oceanogr.*, 7, 284-292).

Eq. (12) should read

$$\left. \begin{aligned} (1-\lambda)[(1+f^2\tau^2)\lambda^2 - (2-\rho)\lambda + 1] - iq\lambda^2 &= 0 \\ \rho &= gD(\tau^2/\Delta^2)(|z_1|^2 + |z_2|^2) \\ q &= 2f\tau gD(\tau^2/\Delta^2) \operatorname{Im} z_1^* z_2 \end{aligned} \right\}. \quad (12)$$

Eq. (13) should read

$$\left. \begin{aligned} z_1 &= \frac{1}{2}[1 - \exp(-2ik\Delta)] \\ z_2 &= (1/\sqrt{3})\left\{ \frac{1}{2}[1 + \exp(-2ik\Delta)] - \exp[i(k + \sqrt{3}l)\Delta] \right\} \quad \left. \begin{array}{l} \text{Scheme one} \\ \text{Scheme two} \end{array} \right\} \\ z_1 &= \frac{1}{2} \sin(k\Delta)[2 \cos(k\Delta) + \cos(\sqrt{3}l\Delta)] \\ z_2 &= (1/\sqrt{3}) \cos(k\Delta) \sin(\sqrt{3}l\Delta) \end{aligned} \right\}. \quad (13)$$

The sentence following Eq. (13) should read:

For scheme one, if  $f = 0$ , then  $|\lambda| \leq 1$  for  $\tau \leq \Delta(3/gD)^{1/2}$ . A consequence of these changes is that  $C = (2gD)^{1/2}\tau/2\Delta$  can be as great as  $6^{1/2}/2 \approx 1.22$  for scheme one. Thus Wang's criticism (*J. Phys. Oceanogr.*, 7, 932) that  $C$  can be no greater than  $2^{1/6} \approx 0.24$  is invalid.



## Reply

W. C. THACKER

*Sea-Air Interaction Laboratory, Atlantic Oceanographic and Meteorological Laboratories, NOAA, Miami, Fla.*

1 August 1977

Instability resulting from grid irregularity can be a problem for both finite-element and finite-difference techniques. In order to demonstrate this, the simulations of normal mode oscillations for circular basins (Thacker, 1977) have been repeated using finite-element techniques similar to those described by Wang and Connor (1975). The results were the same as those obtained using irregular grid finite-difference techniques; i.e., instability was highly evident when grid one was used, but computations using grid two, which is much smoother, showed no evidence of instability for the duration of the simulation unless the Coriolis parameter was sufficiently large. This indicates that the nonlinear instability to which Wang refers is not essentially different from that which occurs in irregular grid finite-difference computations. This also indicates that the instability has nothing to do with lumped matrices.

The important point concerning instability is that, so long as the computations terminate in a time which is short in comparison with the growth time of the instability, the results can be excellent. Simulations of normal mode oscillations for circular basins (Thacker, 1977) indicate that the growth time of the instability for smoothly varying grids is greater than 50 cycles of the slowest oscillation. For natural basins,

the corresponding growth time would be a few weeks. Since the passage of a hurricane generally takes less than a day, the instability should not interfere with the predictive modeling of storm surges.

Finite-element computations are quite expensive. They require an order of magnitude more computer time than corresponding irregular grid finite-difference computations. This is due to the fact that the piecewise polynomial interpolating functions, which are intrinsic to finite-element methods, necessarily result in time-implicit discrete equations requiring matrix inversions at each time step.

It is possible to deviate from the finite-element equations by using "lumped matrices" to obtain a time-explicit system. This type of modification has led to inaccuracies in eigenvalue problems, but (see Strang and Fix, 1973) it does not have to lead to a loss of accuracy in hyperbolic problems. Shen (1977) also recommends something like the lumped matrix approach when he suggests that finite-element techniques can be useful for determining finite-difference formulas for spatial derivatives. These formulas should be similar to those used in irregular grid finite-difference calculations. In this sense the lumped matrix approach is essentially an irregular grid finite-difference method.

## REFERENCES

- Shen, Shan-fu, 1977: Finite-element methods in fluid mechanics. *Annual Reviews of Fluid Mechanics*, Vol. 9, Annual Reviews, Inc., 421-445.
- Strang, G., and G. J. Fix, 1973: *An Analysis of the Finite Element Method*. Prentice-Hall (see p. 253).
- Thacker, W. C., 1977: Irregular grid finite-difference techniques: Simulations of oscillations in shallow circular basins. *J. Phys. Oceanogr.*, **7**, 284-292.
- Wang, J. D., and J. J. Connor, 1975: Mathematical modeling of near coastal circulation. Rep. MITSG 75-13, MIT Sea Grant Program, 272 pp.



# "Shear Dispersion" in Time-Varying Flows

W. C. Thacker

Atlantic Oceanographic and Meteorological Laboratories  
Miami, Florida

May 1977

**U. S. DEPARTMENT OF COMMERCE**

Juanita M. Kreps, Secretary

National Oceanic and Atmospheric Administration

Richard A. Frank, Administrator

Environmental Research Laboratories

Wilmot Hess, Director

Boulder, Colorado



# CONTENTS

	Page
Abstract .....	1
1. Introduction .....	1
2. Closed Form Expressions .....	1
3. Parameterization as Time-Dependent Diffusion .....	5
4. Discussion .....	7
5. References .....	7

# "Shear Dispersion" in Time-Varying Flows

W.C. Thacker

**Abstract.** Shear dispersion in time-varying flows is shown to be parameterizable as effective diffusion with a time-varying diffusivity. This parameterization is appropriate only for times long in comparison with the cross-shear mixing time. High frequency variations of the flow do not contribute substantially to the mixing. Low frequency variations of the flow can be accounted for by simply allowing the parameters in the expression for the effective diffusivity to take on a time dependence.

## 1. Introduction

Previous discussions (Bowden, 1965; Schönfeld, 1961; Okubo, 1967) of harmonically varying shear have concluded that high frequency time variations do not contribute substantially to the mixing. Here it is shown that, furthermore, a time-dependent diffusivity can be introduced to parameterize time-dependent shear dispersion. A simple solvable model (Thacker, 1976) is used to obtain closed form expressions for shear dispersion with arbitrary time dependence.

## 2. Closed Form Expressions

Shear dispersion is mixing due to the combined effects of velocity shear and cross-shear mixing. A simple model, which views the shear as a flow consisting of two layers of fluid moving in opposite directions with velocities  $\pm u$  and with mixing of contaminant between the layers at a rate  $\alpha$ , can be expressed by the equations

$$\left. \begin{aligned} \frac{\partial C_1}{\partial t} + u \frac{\partial C_1}{\partial x} &= -\alpha(C_1 - C_2) + S_1 \\ \text{and} \quad \frac{\partial C_2}{\partial t} - u \frac{\partial C_2}{\partial x} &= -\alpha(C_2 - C_1) + S_2 \end{aligned} \right\} \quad (1)$$

where  $C_1(x, t)$  and  $C_2(x, t)$  are distributions of contaminant in the two layers, and  $S_1(x, t)$  and  $S_2(x, t)$  are sources of contaminant. If  $u$  and  $\alpha$  do not vary in time, then  $\bar{C} = \frac{1}{2}(C_1 + C_2)$  is well approximated by the solution of a diffusion equation with effective diffusivity given by  $K^* = u^2/2\alpha$  (Thacker, 1976). It will be shown that the same is true even if  $u$  and  $\alpha$  depend upon time.

For the case of time-independent flow, where  $u$  and  $\alpha$  are not functions of time, closed form solutions for  $\bar{C} = \frac{1}{2}(C_1 + C_2)$  and  $\Delta C = \frac{1}{2}(C_1 - C_2)$  can be obtained in terms of a Green's function,

$$G_{u,\alpha}(x, t) = \begin{cases} \frac{1}{2u} e^{-\alpha t} I_0 \left( \left[ (\alpha t)^2 - \left( \frac{\alpha x}{u} \right)^2 \right]^{\frac{1}{2}} \right); & |x| \leq ut \text{ and } t > 0 \\ 0; & \text{otherwise.} \end{cases} \quad (2)$$

The matrix notation,

$$C = \begin{pmatrix} \bar{C} \\ \Delta C \end{pmatrix}, \quad S = \begin{pmatrix} \bar{S} \\ \Delta S \end{pmatrix}, \quad \mathcal{G}_{u,\alpha} = \begin{pmatrix} \frac{\partial}{\partial t} + 2\alpha & -u \frac{\partial}{\partial x} \\ -u \frac{\partial}{\partial x} & \frac{\partial}{\partial t} \end{pmatrix} G_{u,\alpha}, \quad (3)$$

allows the solution to (1) for arbitrary initial conditions  $C(x, t=0)$  and sources of contaminant  $S(x, t)$  to be expressed compactly as

$$C(x, t) = \int_{-\infty}^{+\infty} dx' \int_0^t dt' \mathcal{G}_{u,\alpha}(x-x', t-t') S(x', t') + \int_{-\infty}^{+\infty} dx' \mathcal{G}_{u,\alpha}(x-x', t) C(x', t=0). \quad (4)$$

Equation (4) can be shown to be valid even when  $u$  and  $\alpha$  are functions of time. In this case, the matrix Green's function is given by

$$\mathcal{G}_{u(t), \alpha(t)}(x, t) = \lim_{N \rightarrow \infty} \int_{-\infty}^{+\infty} \prod_{i=1}^N dx_i \mathcal{G}_{u_i, \alpha_i}(x_i, \frac{t}{N}) \delta(x - \sum_{i=1}^N x_i) \quad (5)$$

The matrices  $\mathcal{G}_{u_i, \alpha_i}$  are the matrix Green's functions that govern the solution in  $i^{\text{th}}$  time interval, from  $(i-1)t/N$  to  $it/N$  in which the parameters have the approximately constant values  $\alpha_i$  and  $u_i$ . It is important that the matrix Green's



functions  $\mathcal{G}_{u_i, \alpha_i}$  are arranged for multiplication with the index  $i$  decreasing to the right because they do not commute. Thus,  $\mathcal{G}_{u(t), \alpha(t)}$  is the  $N$ -fold convolution of the Green's function for each of  $N$  time intervals composing the total interval from 0 to  $t$ . In the limit,  $N$  goes to infinity, so that this is an infinite convolution.

This infinite convolution is difficult to evaluate. However, it is possible to obtain closed form expressions for the moments  $\langle X^n \rangle$  of the mean contaminant distribution  $\bar{C}(x, t)$  for arbitrary functions  $\alpha(t)$  and  $u(t)$ . The Fourier transform of  $\bar{C}(x, t)$  is the generating function for these moments. Equation (4) expresses  $\bar{C}(x, t)$  in terms of convolution of initial conditions and sources with  $\mathcal{G}_{u(t), \alpha(t)}$ , which in turn is an infinite convolution. Since the Fourier transform of a convolution is a product, the problem is reduced to an easier one of evaluating an infinite product.

The Fourier transform of  $\mathcal{G}_{u(t), \alpha(t)}$  is given by

$$\Gamma_{u(t), \alpha(t)}(k, t) = \lim_{N \rightarrow \infty} \prod_{i=1}^N e^{-\frac{\alpha_i t}{N}} \begin{bmatrix} \cos \frac{\Omega_i t}{N} + \frac{\alpha_i}{\Omega_i} \sin \frac{\Omega_i t}{N} & -ik \frac{u_i}{\Omega_i} \sin \frac{\Omega_i t}{N} \\ -ik \frac{u_i}{\Omega_i} \sin \frac{\Omega_i t}{N} & \cos \frac{\Omega_i t}{N} - \frac{\alpha_i}{\Omega_i} \sin \frac{\Omega_i t}{N} \end{bmatrix}, \quad (6)$$

where  $\Omega_i = (u_i^2 k^2 - \alpha_i^2)^{1/2}$ . The moments of the distribution can be obtained by multiplying moment matrices, which are generated according to

$$\langle X^n \rangle = \left( \frac{1}{-i} \right)^n \frac{\partial^n}{\partial k^n} \Gamma_{u(t), \alpha(t)}(k, t) \Big|_{k=0}, \quad (7)$$

with the Fourier transform of the initial distribution, if there are no sources. The first few moment matrices are found to be

$$\left. \begin{aligned}
\langle X^0 \rangle &= \begin{bmatrix} 1 & 0 \\ 0 & \exp \left[ -2 \int_0^t dt' \alpha(t') \right] \end{bmatrix} \\
\langle X^1 \rangle &= \begin{bmatrix} 0 & \int_0^t dt' u(t') \exp \left[ -2 \int_0^{t'} dt'' \alpha(t'') \right] \\ \int_0^t dt' u(t') \exp \left[ -2 \int_{t'}^t dt'' \alpha(t'') \right] & 0 \end{bmatrix} \\
\langle X^2 \rangle &= \begin{bmatrix} 2 \int_0^t dt' \int_0^{t'} dt'' u(t') u(t'') \exp \left[ -2 \int_{t''}^{t'} dt''' \alpha(t''') \right] & 0 \\ 0 & 2 \int_0^t dt' \int_0^{t'} dt'' u(t') u(t'') \exp \left[ -2 \int_0^{t''} dt''' \alpha(t''') - \int_{t'}^t dt''' \alpha(t''') \right] \end{bmatrix}
\end{aligned} \right\} \quad (8)$$

Consider the case of initially localized distributions,  $\bar{C}(x, t=0) = \delta(x)$  and  $\Delta C(x, t=0) = \beta \delta(x)$ ,  $|\beta| \leq 1$ . If  $\beta = 0$ , the contaminant is initially distributed equally between the two layers; if  $\beta = \pm 1$ , it lies entirely within one of the two layers. Also, suppose that there are no continuous sources of contaminant  $\bar{S}(x, t) = \Delta S(x, t) = 0$ . Then the first few moments of  $\bar{C}(x, t)$ ,

$$\langle x^n \rangle = \int_{-\infty}^{+\infty} dx x^n \bar{C}(x, t), \quad (9)$$

are given by

$$\left. \begin{aligned}
\langle x^0 \rangle &= 1 \\
\langle x^1 \rangle &= \beta \int_0^t dt' u(t') \exp \left[ -2 \int_0^{t'} dt'' \alpha(t'') \right] \\
\langle x^2 \rangle &= 2 \int_0^t dt' \int_0^{t'} dt'' u(t') u(t'') \exp \left[ -2 \int_{t''}^{t'} dt''' \alpha(t''') \right]
\end{aligned} \right\} \quad (10)$$

These moments can be evaluated for arbitrary time dependence of the shear and mixing. The zeroth moment indicates that the total amount of contaminant is constant in time, regardless of variations of the flow. The first moment indicates that there is a horizontal asymmetry only if initially there is a vertical asymmetry. However, the magnitude of the horizontal asymmetry depends upon the time dependence of the flow parameters,  $u$  and  $\alpha$ . The second moment measures the square of the width of the distribution.

### 3. Parameterization as Time-Dependent Diffusion

A diffusion process with time-dependent diffusivity  $K^*(t)$  would yield the moments

$$\left. \begin{aligned} \langle x^0 \rangle &= 1 \\ \langle x^1 \rangle &= 0 \\ \langle x^2 \rangle &= 2 \int_0^t dt' K^*(t') \end{aligned} \right\} . \quad (11)$$

Comparison of the second moment in (10) with that in (11), shows that in some sense the expression

$$f(t) = u(t) \int_0^t dt' u(t') \exp \left[ -2 \int_{t'}^t dt'' \alpha(t'') \right] \quad (12)$$

must approach  $K^*(t)$  if the time-dependent shear effect is to behave like time-dependent diffusion. This becomes more clear after consideration of the following cases for different time dependencies of  $u$  and  $\alpha$ .

**Case One.** In the case of no time dependence, where  $u$  and  $\alpha$  are constant,

$$\left. \begin{aligned} \langle x \rangle &= \beta \frac{u}{2\alpha} (1 - e^{-2\alpha t}) \\ \langle x^2 \rangle &= \frac{u^2}{\alpha} t \left[ 1 - \frac{1}{2\alpha t} (1 - e^{-2\alpha t}) \right] \\ f(t) &= \frac{u^2}{2\alpha} (1 - e^{-2\alpha t}) \end{aligned} \right\} . \quad (13)$$

The time dependence of  $f$  should not be interpreted as time-dependent diffusion. Shear dispersion, for this case, can be parameterized as diffusion only for times long in comparison with the cross-shear mixing time; i.e.,  $\alpha t \gg 1$ . In this limit  $K^* = f = \frac{u^2}{2\alpha}$ ,  $\langle x^2 \rangle = 2(u^2/2\alpha)t$ , and  $\langle x^2 \rangle \gg \langle x \rangle^2$  (Thacker, 1976).



**Case Two.** In the case of harmonically varying shear, with  $u(t) = u_h \cos(2\pi t/T)$ , and constant  $\alpha$ ,

$$\left. \begin{aligned} \langle x \rangle &= \beta \frac{u_h}{2\alpha} \left[ 1 - e^{-2\alpha t} \left( \cos \frac{2\pi t}{T} - \frac{\pi}{\alpha T} \sin \frac{2\pi t}{T} \right) \right] R \\ \langle x^2 \rangle &= \frac{u_h^2}{4\alpha} t \left\{ 1 + \frac{T}{4\pi t} \sin \frac{4\pi t}{T} + \frac{1}{4\alpha t} \left( -\cos \frac{4\pi t}{T} \right) \right. \\ &\quad \left. - \frac{1}{\alpha t} \left[ 1 - e^{-2\alpha t} \left( \cos \frac{2\pi t}{T} - \frac{\pi}{\alpha T} \sin \frac{2\pi t}{T} \right) \right] R \right\} R \\ f(t) &= \frac{u_h^2}{2\alpha} \cos^2 \frac{2\pi t}{T} \left\{ 1 + \frac{\pi}{\alpha T} \tan \frac{2\pi t}{T} - \sec \frac{2\pi t}{T} e^{-2\alpha t} \right\} R \\ R &= \frac{(\alpha T)}{(\alpha T) + \pi^2} \end{aligned} \right\} \quad (14)$$

Each expression contains a factor  $R$ , which indicates that high frequency shear does not contribute to the dispersion, since  $R \rightarrow 0$  as  $\alpha T \rightarrow 0$ . This result was also found by Schönfeld (1961) for this model and by Okubo (1967) for another harmonic shear flow. The expressions that should be compared with time-dependent diffusion are those valid in the long time limit  $\alpha t \gg 1$ . With  $R = 1$ , these expressions are

$$\left. \begin{aligned} \langle x \rangle &= \beta \frac{u_h}{2\alpha} \\ \langle x^2 \rangle &= \frac{u_h^2}{4\alpha} t \\ f(t) &= \frac{u_h^2 \cos^2 \frac{2\pi t}{T}}{2\alpha} = \frac{[u(t)]^2}{2\alpha} \end{aligned} \right\} \quad (15)$$

Thus, low frequency harmonic shear can be parameterized as time-dependent diffusion with  $K^* = [u(t)]^2 / 2\alpha$ .

Schönfeld (1961), Bowden (1965), and Okubo (1967) have attempted to describe harmonic shear as time-independent diffusion. They obtained a diffusion coefficient given by  $(1/T) \int_0^T K^*(t) dt$ , the time average of  $K^*(t)$  over one cycle of the shear. This yields the same result for  $\langle x^2 \rangle$  in the diffusion limit, but does not allow for generalization from harmonic shear to arbitrary shear.

**Case Three.** The question remains of how the diffusivity should be parameterized for the general case in which the shear and mixing vary arbitrarily in time. The answer should be obtainable by analyzing equation (12). This

analysis is difficult because at any point in time there are three time scales that must be considered: the inverse of the mixing rate,  $t_1 = \alpha^{-1}$ ; the time over which the mixing varies,  $t_2 = \alpha / (d\alpha/dt)$ ; and the time over which the shear varies,  $t_3 = u / (du/dt)$ . On the basis of the results for cases one and two and the discussion of Thacker (1976), it seems reasonable that the result of the analysis for the general case should be

$$K^* = \frac{[u(t)]^2}{2\alpha(t)} \quad (16)$$

for  $t_2 \gg t_1$  and  $t_3 \gg t_1$ .

#### 4. Discussion

The result presented here is that shear dispersion can be parameterized as enhanced diffusion along the shear even for time-dependent flows, so long as sufficient time has elapsed for the cross-shear mixing to take place. This is an extension of a previous time-independent analysis (Thacker, 1976). All of the conclusions from that analysis should also apply for the time-dependent case. First, the diffusion parameterization of the mixing should be used when the details of the shear are not resolved. This is equivalent to ignoring variations in times shorter than the time required to mix contaminant across the shear and to ignoring variations along the shear in distances shorter than the distance over which the shear stretches the contaminant in the cross-shear mixing time. Second, the effect of turbulent mixing can be accounted for simply by adding the turbulent eddy diffusivity to the diffusivity that parameterizes the shear dispersion. Finally, a more sophisticated description of the shear flow, such as that discussed by Bowden (1965), would lead to a more complicated, and perhaps more accurate, prescription for relating the effective diffusivity parameter to the shear flow. However, the result found here should also hold for more sophisticated descriptions of the shear flow. The time-dependent diffusivity can be obtained from the expression for the time-independent diffusivity simply by allowing the flow parameters in that expression to vary in time.

#### 5. References

- Bowden, K. F., 1965. Horizontal mixing in the sea due to a shearing current. *J. Fluid Mech.*, **21**:83-95.
- Okubo, A., 1967. The effect of shear in an oscillatory current on horizontal diffusion from an instantaneous source. *Int. J. Oceanol. Limnol.*, **1**: 194-204.
- Schönfeld, J. C., 1961. The mechanism of longitudinal diffusion in a tidal river. *Bull. Int. Assoc. Sci. Hydrol.* (Louvain, Belgium), **6**(1).
- Thacker, W. C., 1976. A solvable model of "shear dispersion." *J. Phys. Oceanogr.*, **6**:66-75.

## Two-phase flow analysis of hindered settling

W. C. Thacker and J. W. Lavelle

*Atlantic Oceanographic and Meteorological Laboratories, National Oceanic and Atmospheric Administration, Miami, Florida 33149*

(Received 14 February 1977; final manuscript received 2 May 1977)

Kinematical effects which hinder settling are due to the upward return flow of the fluid and to the influence of the sediment on the hydrostatic pressure. Dynamical effects of increased drag must be accounted for with a nonlinear drag force law.

Hindered settling is a term used to designate the decrease in the fall velocity of sediment in suspension resulting from an increase in sediment concentration. This effect can be attributed to the counterflow of the suspending fluid upward through the falling sediment. There are three distinct contributions to the hindering. The first is simply the retardation that a single particle of sediment would experience in a similar upward flow. The second is due to the partitioning of the gravitational, drag, and pressure forces between the sediment and the suspending fluid. These two contributions are kinematical in nature. The third, which is dynamical, is due to the modification of the flow field in the vicinity of the sediment particles when other particles are nearby.

Maude and Whitmore<sup>1</sup> argue that the fall velocity should be diminished from that of a single particle by a factor  $(1 - C)^\alpha$ , where  $C$  is the volume fraction of sediment in suspension. The value of the exponent,  $\alpha$ , was determined to be in the range 4-9 by comparison with data. More recently, Batchelor<sup>2</sup> calculated for small  $C$  a hindering factor,  $1 - 6.55C$ , starting with the results of Goldman *et al.*,<sup>3</sup> and Stimson and Jeffery<sup>4</sup> for the motion of two falling spheres and averaging over the distribution of sediment particles. However, little has been done treating hindered settling as an aspect of two-phase flow. Soo<sup>5</sup> does discuss batch settling from this point of view, but he does not discuss hindered settling *per se*.

The purpose of this note is to point out that the two-phase flow equations, which involve the average volume

fractions and average velocities of the sediment and of the suspending fluid, are ideally suited for dealing with hindered settling. They yield results which reduce to Stokes' law in the limit of low concentration. They also allow kinematical hindering effects to be separated from dynamical effects. The dynamical hindering is attributed to increased drag due to turbulence which might develop in the counterflow and to fluctuating forces on the particles due to the necessarily asymmetric and varying flow around the particles.

If  $C$  is the volume fraction of sediment in suspension, then  $1 - C$  is the volume fraction of the suspending fluid. Each must obey its own continuity equation,

$$\partial C / \partial t + \nabla \cdot (\mathbf{v}_1 C) = 0 \quad (1)$$

and

$$\frac{\partial(1 - C)}{\partial t} + \nabla \cdot [\mathbf{v}_2(1 - C)] = 0, \quad (2)$$

where  $\mathbf{v}_1$  and  $\mathbf{v}_2$  are the velocities of the sediment and the suspending fluid, respectively. These two equations can be added to obtain the incompressibility condition for two-phase flow,

$$\nabla \cdot [\mathbf{v}_1 C + \mathbf{v}_2(1 - C)] = 0. \quad (3)$$

Momentum equations for each phase must also be satisfied,

$$\rho_1 \left[ \frac{\partial}{\partial t} (\mathbf{v}_1 C) + \nabla \cdot (\mathbf{v}_1 \mathbf{v}_1 C) \right] - \rho_1 C g \hat{k} - C \nabla p - D \quad (4)$$



and

$$\rho_2 \left\{ \frac{\partial}{\partial t} [\mathbf{v}_2(1-C)] + \nabla \cdot [\mathbf{v}_2 \mathbf{v}_2(1-C)] \right\} - \rho_2(1-C)g\hat{k} - (1-C)\nabla p + \mathbf{D}. \quad (5)$$

The density of the mixture is  $\rho_1 C + \rho_2(1-C)$ , where  $\rho_1$  and  $\rho_2$  are the densities of the sediment and fluid phases, respectively, so the gravitational force on the mixture is  $-\rho_1 C + \rho_2(1-C)g\hat{k}$ , where  $g$  is the acceleration of gravity and  $\hat{k}$  is a unit vector in the direction of the vertical. In Eqs. (4) and (5), the gravitational force is partitioned according to the mass fraction of the phases. The pressure force,  $\nabla p$ , is partitioned according to the volume fractions. The drag force,  $\mathbf{D}$ , of the suspending fluid on the sediment is equal and opposite to that of the sediment on the suspending fluid.

The drag force should depend on the relative velocity,  $\mathbf{v}_1 - \mathbf{v}_2$ , on the sediment concentration,  $C$ , and on the size and shape of the sediment particles. The usual assumption is that

$$\mathbf{D} = D_0(\mathbf{v}_1 - \mathbf{v}_2) C, \quad (6)$$

where  $D_0$  is a constant. The factor,  $C$ , is kinematical, expressing the fact that the number of particles experiencing the drag increases with increasing concentration, not that the force per particle increases. The linear dependence on the relative velocity is equivalent to Stokes' law and should be expected to be valid for small particle Reynolds numbers. For  $D_0 = 9\mu/2r^2$ , where  $\mu$  is the viscosity and  $r$  is the radius of the particles, it will be shown that (6) does yield Stokes' law in the limit of low concentration. Even in this low concentration limit, (6) should be modified if the particle Reynolds number is large enough so that turbulence develops. Furthermore, this force law will likely need to be modified with increasing concentration to account for turbulence which might develop in high shear regions of the counterflow around the particles or to account for increased drag due to fluctuating hydrodynamic forces acting on the particles as they fall.

The situation considered here is that of a horizontally homogeneous distribution of sediment particles falling through a suspending fluid. If the distribution were not homogeneous, there would likely be a return flow in regions of low sediment concentration, not the counterflow through the sediment leading to hindered settling. Processes such as settling convection<sup>6</sup> are not considered here.

This homogeneity assumption simplifies the governing equations. The horizontal components of the velocities can be neglected, and only the vertical components,  $w_1$  and  $w_2$ , need to be considered. The incompressibility condition (3) gives a relationship between them,<sup>5</sup>

$$w_2 = -[C/(1-C)]w_1. \quad (7)$$

When the sediment is falling at terminal velocity, the acceleration terms in the momentum equations (4) and (5) can be neglected, giving

$$0 = -\rho_1 C g - C(\partial p / \partial z) - D \quad (8)$$

and

$$0 = -\rho_2(1-C)g - (1-C)(\partial p / \partial z) + D. \quad (9)$$

Equations (8) and (9) express the balance of forces on the sediment and on the suspending fluid, respectively. Adding these equations results in the force balance for the mixture,

$$0 = -[\rho_1 C + \rho_2(1-C)]g - \partial p / \partial z, \quad (10)$$

which is hydrostatic. Equation (10) can be used to eliminate the pressure gradient in (8) or (9),

$$0 = -(\rho_1 - \rho_2)gC(1-C) - D. \quad (11)$$

The resultant of the gravitational and pressure forces depends upon the buoyancy factor,  $(\rho_1 - \rho_2)g$ , as expected. The factors depending on the concentration are due to the effect of the sediment on the pressure field.

If the drag force in (11) is given by  $D = D_0(w_1 - w_2)C$ , as in Eq. (6), and the relative velocity by  $w_1 - w_2 = w_1/(1-C)$  from (7), then Eq. (11) yields an expression for the fall velocity,

$$w_1 = -[(\rho_1 - \rho_2)g/D_0](1-C)^2. \quad (12)$$

In the limit,  $C=0$ , (12) should give the fall velocity of a single particle. Indeed, with  $D_0 = 9\mu/2r^2$ , (12) reduces to Stokes' law.

For  $C \neq 0$ , the factor  $(1-C)^2$  accounts for kinematical hindering of the fall velocity. This factor is due to the dependence of the counter flow on the concentration and to the effect of the concentration on the pressure field.

Because the kinematical hindering is not sufficient to account for the hindering factor  $(1-C)^\alpha$ , with  $\alpha$  in the range 4-9, found in the data study by Maude and Whitmore,<sup>1</sup> the force law given in Eq. (6) needs to be modified for the conditions considered here. A new force law is not suggested because there are two effects which cannot be separated. One is the simple effect of decreasing the distance between particles with increasing concentration. This should be incorporated in  $D$  as a dependence on  $C$  in addition to the kinematical factor already given in Eq. (6). For example, the Ergun and Orning relation<sup>5</sup> for large  $C$ ,  $D_0 = 75\mu C/2(1-C)^2 r^2$  might be used. The other is the effect of increasing the counterflow velocity with increasing  $C$ , which is particular to this case of hindered settling. This should be incorporated in  $D$  as some dependence on  $\mathbf{v}_1 - \mathbf{v}_2$  other than linear.

The dynamical hindering depends upon the nature of the counterflow. For increasing concentration, it becomes increasingly convoluted as it flows through the ensemble of falling particles. The turbulence that is likely to develop and random forces felt by the particles due to the asymmetries in the flow field can serve to increase the drag force per particle, giving dynamical hindering.

This separation of kinematical and dynamical effects clarifies the question of whether hindered settling effects should be accounted for explicitly in other flow situations. Because the kinematical effects arise naturally

from the two-phase flow equations, they are automatically included when there is counterflow, but they do not hinder the flow if there is no counterflow. The dynamical effects have to do with the dependence of the drag force on the relative velocity and the sediment concentration. This dependence is still an open question. In the limit of low concentrations of small particles, the linear drag law is appropriate, but for higher concentrations, it is likely to need modification.

<sup>1</sup>A. D. Maude and R. L. Whitmore, *Brit. J. Appl. Phys.* **9**, 477 (1958).

<sup>2</sup>G. K. Batchelor, *J. Fluid Mech.* **52**, 245 (1972).

<sup>3</sup>A. J. Goldman, R. G. Cox, and H. Brenner, *Chem. Eng. Sci.* **21**, 1951 (1966).

<sup>4</sup>M. Stimson and C. B. Jeffery, *Proc. R. Soc. London Ser. A* **111**, 110 (1926).

<sup>5</sup>S. L. Soo, *Fluid Dynamics of Multiphase Systems* (Blaisdell, Waltham, Mass., 1967), Chap. 9.

<sup>6</sup>Ph. H. Kuenen, *J. Sediment Petrol.* **38**, 817 (1968).







PENN STATE UNIVERSITY LIBRARIES



A000072832752